398

Frontiers in Artificial Intelligence and Applications

FUZZY SYSTEMS AND DATA MINING X

Proceedings of FSDM 2024, Matsue, Japan, 5-8 November 2024

Edited by
Antonio J. Tallón-Ballesteros

IOS Press

FUZZY SYSTEMS AND DATA MINING X

Frontiers in Artificial Intelligence and Applications

The book series Frontiers in Artificial Intelligence and Applications (FAIA) covers all aspects of theoretical and applied Artificial Intelligence research in the form of monographs, selected doctoral dissertations, handbooks and proceedings volumes. The FAIA series contains several sub-series, including 'Information Modelling and Knowledge Bases' and 'Knowledge-Based Intelligent Engineering Systems'. It also includes the biennial European Conference on Artificial Intelligence (ECAI) proceedings volumes, and other EurAI (European Association for Artificial Intelligence, formerly ECCAI) sponsored publications. The series has become a highly visible platform for the publication and dissemination of original research in this field. Volumes are selected for inclusion by an international editorial board of well-known scholars in the field of AI. All contributions to the volumes in the series have been peer reviewed.
The FAIA series is indexed in ACM Digital Library; DBLP; EI Compendex; Google Scholar; Scopus; Web of Science: Conference Proceedings Citation Index – Science (CPCI-S) and Book Citation Index – Science (BKCI-S); Zentralblatt MATH.

Volume 398

Recently published in this series

ISSN 0922-6389 (print)
ISSN 1879-8314 (online)

Fuzzy Systems and Data Mining X

Proceedings of FSDM 2024, Matsue, Japan, 5-8 November 2024

Edited by

Antonio J. Tallón-Ballesteros

Department of Electronic, Computer Systems and Automation Engineering, University of Huelva, Huelva city, Spain

IOS Press

Amsterdam • Washington, DC

ISBN 978-1-64368-569-4 (online)
doi: 10.3233/FAIA398

Publisher
IOS Press BV
Nieuwe Hemweg 6B
1013 BG Amsterdam
Netherlands
e-mail: order@iospress.nl

For book sales in the USA and Canada:
IOS Press, Inc.
6751 Tepper Drive
Clifton, VA 20124
USA
Tel.: +1 703 830 6300
Fax: +1 703 830 2300
sales@iospress.com

Preface

The 10th edition of FSDM, FSDM2024, attracted many professors and post-graduate students – particularly Ph.D. scholars from numerous universities worldwide – as well as technicians, policymakers and top managers of organizations and businesses from various industries. This year, as the conference celebrates its first decade, the theme is fuzzy systems and data mining. The book is divided into three parts: Part I, Fuzzy Set Theory, Algorithm and System; Part II, Data Mining; and Part III, Interdisciplinary Field of Fuzzy Logic and Data Mining. The most popular topics are feature selection, instance selection, outlier detection and missing values imputation; nonetheless in the last couple of years data normalisation has also become a trend. Fuzzy systems are present in almost every item of news containing any qualitative part, and numbers have been replaced by the word in most daily activities such as the weather forecast, the rhythm of development, or many topics such as the economy, industry and so on.

All the submitted papers were thoroughly reviewed by dedicated international Technical Programme Committee (TPC) members and anonymous reviewers and, who took into account the breadth and depth of the research topics falling within the scope of FSDM. The 71 most promising and FAIA mainstream-relevant contributions from about 237 submissions have been included in this book, resulting in an acceptance rate of 30%.

I would like to take this opportunity to thank all keynote and invited speakers, authors, programme committee members and anonymous reviewers whose work made this conference possible. Thanks are also due to the members of TPC and local committees for their efforts in fostering a successful FSDM conference. Last but not least, I would like to thank the editors and other colleagues from IOS Press for their joint efforts in publishing this volume in the book series Frontiers in Artificial Intelligence and Applications (FAIA) as the tenth edition of the FSDM conference series.

November 2024

Antonio J. Tallón-Ballesteros
https://orcid.org/0000-0002-9699-1894
Department of Electronic, Computer Systems and Automation Engineering
University of Huelva (Spain), Huelva city, Spain

About the Conference

The 10th International Conference on Fuzzy Systems and Data Mining (FSDM 2024) was held in Matsue, Japan from 5 to 8 November 2024. FSDM 2024 consisted of keynote speeches, invited speeches, oral presentations and poster presentations. FSDM 2024 attracted participants from over 20 countries and regions, including three keynote speakers: Prof. Gautam Srivastava from Canada, Prof. Alfredo Cuzzocrea from Italy, and Prof. Sheng-Lung Peng from Taiwan; four invited speakers: Prof. Dimiter Velev from Bulgaria, Prof. T.M.G. Ahsanullah from Saudi Arabia, Assoc. Prof. Sayan Kaennakham from Thailand, and Mr. Rainer Faller from the USA. With an emphasis on fuzzy theory, algorithm and system, fuzzy application, data mining and the interdisciplinary field of fuzzy logic and data mining, FSDM 2024 also included special sessions on hot topics in related research fields, including a special session on applied mathematics and intelligent algorithms for modern industry (AMIAMI), and special sessions on the application of generative AI and safeguarding AI-based automotive and automation products.

Organizing Committee

FSDM 2024 Conference Co-Chairs
Dr. Hamido Fujita, Distinguished Professor, Iwate Prefectural University, Japan
Dr. Sheng-Lung Peng, Professor, National Taipei University of Business
Dr. Guoyin Wang, Professor, Chongqing Normal University, China

FSDM 2024 Technical Programme Committee (TPC) Chairs
Dr. Mohammed Chadli, Professor, University of Paris-Saclay, IBISC Lab., France
Dr. Qixin Guo, Professor, Saga University, Japan
Dr. Shin-ichi Nishida, Professor Emeritus, Saga University, Japan

FSDM 2024 Publication Chairs
Dr. Mohammed Chadli, Professor, University of Paris-Saclay, IBISC Lab., France
Dr. Dragan Pamucar, Professor, University of Belgrade, Serbia
Dr. Yabin Shao, Professor, Chongqing University of Posts and Telecommunications, China

Contents

Part I

Fuzzy Set Theory, Algorithm and System

Fuzzy Systems and Data Mining X
A.J. Tallón-Ballesteros (Ed.)

doi:10.3233/FAIA241396

A Multi-Period Interval-Valued Fuzzy Portfolio Decision Model with Realistic Constraints

Qiansheng Zhang[a,1], Yuanjun Ou[a], Zhiyun Yin[a]
[a]*School of Mathematics and Statistics, Guangdong University of Foreign Studies, Guangzhou 510006, China*
ORCiD ID: Qiansheng Zhang https://orcid.org/0000-0001-5545-3726

Abstract. Considering the uncertainty of stock data, this paper studies interval-valued fuzzy portfolio decision model with ESG and some realistic constraints. First, a screening process is employed to identify investable stocks based on their ESG ratings. Then, a multi-period portfolio decision model with short-selling constraint is established by maximizing terminal wealth and minimizing terminal risk. By using the weighted programming method the proposed portfolio model is transformed into a single-objective model to solve the optimal decision strategy. Finally, a numerical example of stock data from the Shenzhen Stock Exchange is given to illustrate the efficiency of the presented portfolio decision model.

Keywords. Interval-valued fuzzy decision, multi-period portfolio, ESG constraint

1. Introduction

The concept of low-carbon economic development has garnered increasing attentions recently. ESG rating serves as a guide for investor to assess company's ability for sustainable development [1]. Many researchers are currently concentrated on modeling ESG investment from the perspectives of objectives [2], and screening criteria [3]. This paper will select assets based on ESG scores in the multi-period portfolio decision environment. Traditional single-period portfolio strategy postulates that the investor does not make any adjustments during the whole investment period. However, investors need to modify their investment strategies for achieving higher returns according to the change of market condition. Numerous multi-period portfolio decision models [4-6] have been presented. Most of the existing multi-period portfolio models prohibit short selling. Nonetheless, short selling plays a crucial role in the stock market, which can facilitate investors to achieve greater profits and diversify their investment strategies. Consequently, many researchers have explored portfolio selection models involving short selling constraints [7-9].

Recently, interval-valued fuzzy number (IvFN), as a useful generalization of interval and fuzzy number [10-13], has exhibited a lot of flexibilities for dealing with multicriteria risk analysis [14] and portfolio decision. Therefore, this study employs

[1] Corresponding Author, Qiansheng Zhang, Guangdong University of Foreign Studies, Guangzhou 510006, China; Email: zhqiansh01@126.com

IvFN to assess the expected return of risky asset for multi-period portfolio decision. In the multi-period portfolio process, it is vital for investor to maximize the terminal wealth and minimize the terminal risk. Due to some realistic constraints such as the short selling mechanism and transaction costs will affect portfolio decision, we establish a new IvF multi-period portfolio model with short selling proportion constraint, budget constraint, and Yager entropy. By using the weighted fuzzy programming method, the proposed multi-objective multi-period portfolio model is transformed into single-objective model for obtaining the optimal strategy.

The rest of this paper is organized as follows. Section 2 of the paper elaborates on the construction process of multi-period portfolio decision model. Section 3 of the paper empirically analyzes the impacts of ESG and other realistic constraints on the optimal portfolio strategies through a stock investment example. Section 4 summarizes the advantages and disadvantages of the model as well as the future work.

2. Construction of multi-period interval fuzzy portfolio model

Suppose an investor possesses initial wealth W_0, and plans to make multi-period portfolio including one risk-free asset and n risky assets $S = \{S_1, S_2, \cdots, S_n\}$. If the investor wants to invest in stocks with high ESG scores, he/she can set the minimum desired ESG level esg_t at the beginning of period t. Once a stock's ESG score is greater than esg_t in period t the stock will be included in the portfolio pool. Assume the investment cycle is separated into T periods, and the fund adjustment is set at the beginning of each period $t\left(t = 1, 2, ..., T\right)$. Throughout the entire investment cycle, the investor can trade short. Below we display some notations to be used in interval-valued fuzzy portfolio decision model.

$x_{t,0}$, $x_{t,i}$ are the ratios of risk-free asset and risky asset i in period t, respectively.

$r_{t,0}$, $r_{t,i}$ are the return rates of risk-free asset and risky asset i in period t, respectively.

$x_{t,i}^{+}, x_{t,i}^{-}$ are the ratios of risky asset i bought and sold in period t, respectively.

c_i^{+}, c_i^{-} are the unit transaction cost rates for buying and selling risky asset i in period t, respectively.

Considering that investor need to pay transaction costs for asset adjustments, the total transaction cost of risky asset i in period t can be calculated by

$$C_{t,i} = c_i^{+}\Delta x_{t,i}^{+} + c_i^{-}\Delta x_{t,i}^{-} \quad , \tag{1}$$

where $\Delta x_{t,i}^{+} = \max\{x_{t,i} - x_{t-1,i}, 0\}, \Delta x_{t,i}^{-} = \max\{x_{t-1,i} - x_{t,i}, 0\},$

$$x_{t,i} = (x_{t,i}^{+} - x_{t,i}^{-}), t = 1,2,\cdots,T, i = 1,2,\cdots,n.$$

So, we can compute the net return of portfolio at period t as

$$R_t = x_{t,0}r_{t,0} + \sum_{i=1}^{n}(x_{t,i}^{+} - x_{t,i}^{-})r_{t,i} - \sum_{i=1}^{n} C_{t,i} \, . \tag{2}$$

Due to the uncertain data and incomplete information, the expected return of risky asset

i in period t is expressed by IvFN $r_{t,i} = (a_{t,i}, b_{t,i}; \alpha_{t,i}, \alpha'_{t,i}, \beta_{t,i}, \beta'_{t,i})$. Then we can get the net return of portfolio in period t as IvFN $R_t = (a_t, b_t; \alpha_t, \alpha'_t, \beta_t, \beta'_t)$, where

$$a_t = x_{t,0} r_{t,0} + \sum_{i=1}^{n} (x_{t,i}^{+} a_{t,i} - x_{t,i}^{-} b_{t,i}) - \sum_{i=1}^{n} C_{t,i}, \qquad \alpha_t = \sum_{i=1}^{n} (x_{t,i}^{+} \alpha_{t,i} + x_{t,i}^{-} \beta_{t,i})$$

$$b_t = x_{t,0} r_{t,0} + \sum_{i=1}^{n} (x_{t,i}^{+} b_{t,i} - x_{t,i}^{-} a_{t,i}) - \sum_{i=1}^{n} C_{t,i}, \qquad \beta_t = \sum_{i=1}^{n} (x_{t,i}^{+} \beta_{t,i} + x_{t,i}^{-} \alpha_{t,i})$$

$$\alpha'_t = \sum_{i=1}^{n} (x_{t,i}^{+} \alpha'_{t,i} + x_{t,i}^{-} \beta'_{t,i}), \qquad \beta'_t = \sum_{i=1}^{n} (x_{t,i}^{+} \beta'_{t,i} + x_{t,i}^{-} \alpha'_{t,i}).$$

According to Zhang [15], the net return and risk of portfolio in period t are respectively calculated as

$$M(R_t) = \tfrac{1}{2}(a_t + b_t) + \tfrac{1}{12}[\beta_t + \beta'_t - (\alpha_t + \alpha'_t)] \tag{3}$$

$$V(R_t) = \tfrac{1}{4}(b_t - a_t)^2 + \tfrac{1}{12}(b_t - a_t)(\alpha_t + \alpha'_t + \beta_t + \beta'_t) + \tfrac{1}{48}((\alpha_t + \beta_t)^2 + (\alpha'_t + \beta'_t)^2), \tag{4}$$

The terminal wealth of portfolio is computed by

$$W_T = \sum_{t=1}^{T} W_0 [1 + M(R_t)]. \tag{5}$$

The terminal risk of portfolio is computed by

$$V_T = \sum_{t=1}^{T} V(R_t), \tag{6}$$

Due to that the risk of short selling is greater than the risk of buying it, we need to set the short selling proportion of all the risky assets as

$$\sum_{i=1}^{n} x_{t,i}^{-} \le \bar{s}. \tag{7}$$

Also, we set the lower and upper limits of fund ratio for each asset as follows.

$$L_i \le x_{t,i} \le U_i, t = 1,2,\cdots,T; i = 0,1,\cdots,n. \tag{8}$$

Moreover, we set the following budget constraint to ensure that the fund is fully invested at each period of investment.

$$x_{t,0} + \sum_{i=1}^{n} x_{t,i}^{+} + \sum_{i=1}^{n} m_i x_{t,i}^{-} = 1. \tag{9}$$

where m_i is the margin ratio of short selling risky asset i.

Also, investors are guaranteed a desired return for each investment period.

$$M(R_t) \ge \overline{R}_t. \tag{10}$$

Moreover, the Yager entropy constraint is employed to make portfolio $X = \{x_{t0}, x_{t1}, \cdots, x_{ti}, \cdots x_{tm}\}$ diversified.

$$H_Y(X) = \tfrac{2n}{n+1} - \sum_{i=0}^{n} \left| |x_{ti}| - \tfrac{1}{n+1} \right| = \tfrac{2n}{n+1} - \sum_{i=0}^{n} \left| x_{ti}^{+} + x_{ti}^{-} - \tfrac{1}{n+1} \right| \ge H. \tag{11}$$

So, we construct the following multi-period interval-valued fuzzy portfolio model (P1).

$$
(P1)\quad
\begin{aligned}
&\max W(x) = W_0 \prod_{t-1}^{T}\left[1+\frac{a_t+b_t}{2}+\frac{\beta_t+\beta_t'-(\alpha_t+\alpha_t')}{12}\right]\\
&\min V(x) = \sum_{t=1}^{T}\left[\frac{(b_t-a_t)^2}{4}+\frac{(b_t-a_t)(\alpha_t+\alpha_t'+\beta_t+\beta_t')}{12}+\frac{(\alpha_t+\beta_t)^2+(\alpha_t'+\beta_t')^2}{48}\right]\\
&s.t.\ \begin{cases}
M(R_t)\ge \bar{R}_t\\
\sum_{i=1}^{n} x_{t,i}^{-}\le \bar{s}\\
\frac{2n}{n+1}-\sum_{i=0}^{n}\left|x_{t,i}-\frac{1}{n+1}\right|\ge H\\
x_{t,0}+\sum_{i=1}^{n}x_{t,i}^{+}+\sum_{i=1}^{n}m_i x_{t,i}^{-}=1\\
x_{t,i}^{+}x_{t,i}^{-}=0\\
0\le x_{t,0}\le U_i, L_i\le x_{t,i}\le U_i, t=1,...,T, i=1,...,n
\end{cases}
\end{aligned}
$$

Utilizing the weighted fuzzy planning method [16], (P1) is converted to model (P2).

$$
(P2)\quad \max \lambda
$$

$$
s.t.\ \begin{cases}
\theta\lambda\le W'=\dfrac{W(x)-W^{-}}{W^{+}-W^{-}}\\
(1-\theta)\lambda\le V'=\dfrac{V^{-}-V(x)}{V^{-}-V^{+}}\\
W(x)=W_0\prod_{t-1}^{T}\left[1+\dfrac{a_t+b_t}{2}+\dfrac{\beta_t+\beta_t'-(\alpha_t+\alpha_t')}{12}\right]\\
V(x)=\sum_{t=1}^{T}\left[\dfrac{(b_t-a_t)^2}{4}+\dfrac{(b_t-a_t)(\alpha_t+\alpha_t'+\beta_t+\beta_t')}{12}+\dfrac{(\alpha_t+\beta_t)^2+(\alpha_t'+\beta_t')^2}{48}\right]\\
M(R_t)\ge \bar{R}_t\\
\sum_{i=1}^{n} x_{t,i}^{-}\le \bar{s}\\
\dfrac{2n}{n+1}-\sum_{i=0}^{n}\left|x_{t,i}-\dfrac{1}{n+1}\right|\ge H\\
x_{t,0}+\sum_{i=1}^{n}x_{t,i}^{+}+\sum_{i=1}^{n}m_i x_{t,i}^{-}=1\\
x_{t,i}^{+}x_{t,i}^{-}=0\\
0\le x_{t,0}\le U_i, L_i\le x_{t,i}\le U_i, t=1,...,T, i=1,...,n
\end{cases}
$$

where θ is the objective weight of terminal wealth, W^{+} and V^{+} denote ideal solutions for terminal wealth and risk, W^{-} and V^{-} denote non-ideal solutions for terminal wealth

and terminal risk. The parameter $\theta > 0.5$ means that the investor is risk-lover, while $\theta < 0.5$ means that the investor is risk-averse.

3. Numerical example

Assume an investor selects 29 stocks from Shenzhen Stock Exchange for multi-period portfolio plan, whose codes are 000002, 000006, 000009, 000012, 000027, 000028, 000030, 000031, 000036, 000039, 000049, 000050, 000059, 000060, 000061, 000062, 000063, 000069, 000078, 000088, 000089, 000090, 000099, 000100, 000151, 000156, 000157, 000333, 000338. When buying stocks, investor need to pay transaction cost or commission which is 0.3% of the transaction fund, i.e., $c_i^+ = 0.003$; When selling stocks, investor need to pay transaction costs that include 0.1% stamp duty in addition to commission and a margin ratio of 50%, i.e., $c_i^- = 0.004$, $m_i = 0.5$. Due to the existence of transaction costs, investment transactions should not be too frequent. Therefore, in this paper we consider three investment periods, and collect the monthly returns of the above-mentioned stocks from January 2018 to December 2023 in RESSET database. By Vercher's statistical estimation method [17], we assess the interval fuzzy return $r_{t,i} = (a_{t,i}, b_{t,i}; \alpha_{t,i}, \alpha'_{t,i}, \beta_{t,i}, \beta'_{t,i})$ of each stock at each period, where $a_{t,i} = P_{40}, b_{t,i} = P_{60}, \alpha_{t,i} = P_{40} - P_5, \alpha'_{t,i,} = P_{40} - P_3, \beta_{t,i} = P_{95} - P_{60}, \beta'_{t,i} = P_{97} - P_{60}$.

In addition, the 2018-2023 ESG rating data of the alternative stocks are selected from CSI Ratings in Wind and normalized to nine ratings from AAA to C, that take value from 1 to 0.

If we set $\overline{R}_t = 0, \bar{s} = 0.4, L_i = -0.2, U_i = 0.2, m_i = 0.5, esg = 0.4, H = 0.7$, by portfolio model (P1) we get ideal solutions $W^+ = 1.0835, V^+ = 0.0049,$ and non-ideal solutions $W^- = 1.0224, V^- = 0.0161.$

Then by utilizing portfolio decision model (P2) the return and risk of optimal portfolio under different risk preference θ can be obtained as shown in Figure 1. The fund proportion of portfolio under different risk preference parameter θ at each period are shown in Figure 2. Risk-averse investor prefers to invest in risky assets and obtain higher returns by selling assets short, while risk-averse investor prefers to invest in risk-free asset and sell a small amount of risky assets short.

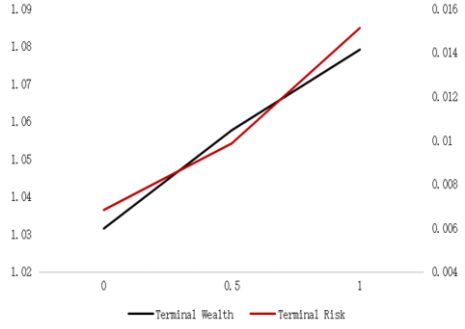

Figure 1.The terminal wealth and risk of portfolio with different risk parameter θ

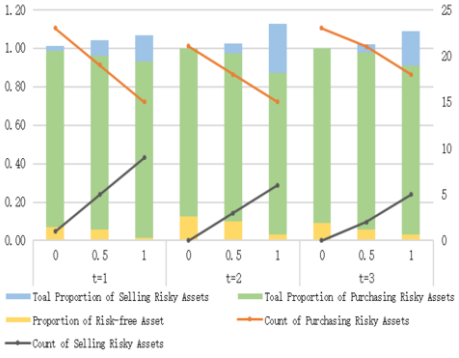

Figure 2.The investment proportion under different risk parameter θ at each period

Next, we alter the short selling proportion and make a sensitive analysis for total short selling proportion constraint.

If we keep $\overline{R}_t = 0, L_i = -0.2, U_i = 0.2, m_i = 0.5, esg = 0.4, H = 0.7$ and take $\overline{s}$ at different values 0, 0.2, 0.4 and 0.6, by using portfolio model (P2) we also get the terminal cumulative wealth and risk as shown in Figure 3. It can be observed that the terminal cumulative wealth and risk rise with the total short selling threshold $\overline{s}$ of risky assets increasing.

Further, when $\overline{s}$ varies from 0 to 0.6, the optimal portfolios at three periods are shown in Figure 4. In each period, when the value of $\overline{s}$ gradually increases, the short selling of assets increases and leads to a gradual increase in the actual investment proportion. When $\overline{s} = 0$, it means that short selling is prohibited , so the proportion of short selling assets at each period is 0, and the actual investment proportion is 1. When $\overline{s} > 0$, the fund ratios of short-selling assets at each period is greater than 0, and the actual investment proportion also exceeds 1 due to the margin ratio 0.5 of short selling. When the investors' short selling assets gradually increase, the proportions of investment in the risk-free assets decrease. From Figure 4, one can also see that the total short selling assets do not exceed 0.2, which means that investor does not sell too many assets short in pursuit of high returns.

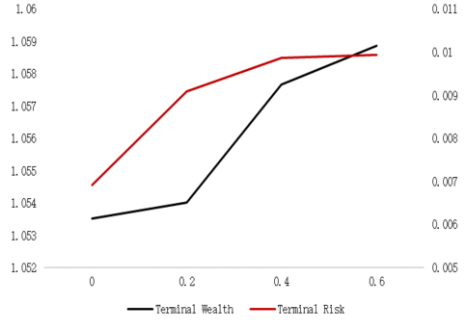

Figure 3.The optimal terminal wealth and risk for different short selling proportion threshold $\overline{s}$

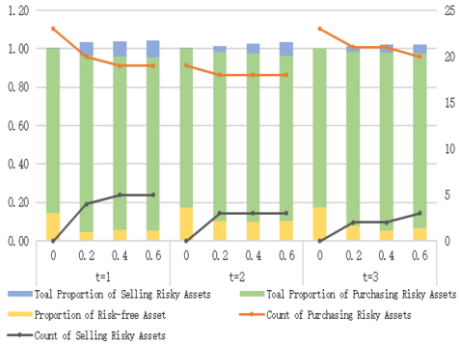

Figure 4.The investment proportion with different short selling proportion threshold $\overline{s}$ at each period

4. Conclusion

For interval fuzzy portfolio problem involving short-selling constraints, this paper examines the two perspectives for controlling asset short-selling ratio and the fund ratio constraint. Empirical analysis reveals that short-selling condition may enlarge the portfolio return and risk. The advantages of IvF portfolio model are as follows. First, IvFN is more flexible to express the uncertain return of risky asset than ordinary fuzzy number. Second, the IvF portfolio model considers multi-objective and multi-period optimization decision problem with ESG and realistic constraints. The disadvantage is that the computation of interval fuzzy possibilistic mean and risk of portfolio are complex. In the future work, we shall consider the skewness objective of portfolio and discuss the impact of liquidity of asset on the optimal strategy.

References

[1] Kanno M. Does ESG performance improve firm creditworthiness? Finance Research Letters. 2023 July; 55, 103894, doi: 10.1016/j.frl.2023.103894

[2] Xu F, Liu W, Li X, Jing K. Research on green bilevel portfolio under carbon peaking and carbon neutrality goals. Journal of Statistics and Information. 2023; 38(01): 55-70, doi: 10.3969/j.issn.1007-3116.2023.01.005

[3] Liagkouras K, Metaxiotis K, Tsihrintzis G. Incorporating environmental and social considerations into the portfolio optimization process. Annals of Operations Research. 2022; 316: 1493-1518, doi: 10.1007/s10479-020-03554-3

[4] Yang X, Chen J, Liu W, Zhao X. A multi-period fuzzy portfolio optimization model with investors' loss aversion. Soft Computing. 2023; 27: 18829-18842, doi: 10.1007/s00500-023-09030-x

[5] Li B, Zhang R, Sun Y. Multi-period portfolio selection based on uncertainty theory with bankruptcy control and liquidity. Automatica. 2023 Jan; 47: 110751, doi: 10.1016/j.automatica.2022.110751

[6] Zhang P. Multi-period possibilistic mean semivariance portfolio selection with cardinality constraints and its algorithm. Journal of Mathematical Modelling and Algorithms in Operations Research. 2015; 14: 239-253, doi: 10.1007/s10852-014-9268-6

[7] Zhang P, Zeng Y. Multiperiod mean semi-absolute deviation portfolio selection with total short selling constraints. Chinese Journal of Management Science. 2021; 29(6):60-69, doi: 10.16381/j.cnki.issn1003-207x.2017.1605

[8] Yang X, Chen S, Liu W, Zhang Y. A Multi-period Fuzzy Portfolio Optimization Model with Short Selling Constraints. International Journal of Fuzzy Systems. 2022; 24(6): 2798-2812, doi: 10.1007/s40815-022-01294-z

[9] Liu Y, Li Y, Zhang W. Background risk portfolio selection model with conservative short-selling and financial distress. Operations Research and Management Science. 2022; 32(12):128-135, doi: 10.12005/orms.2022.0397

[10] Petrović DV, Tanasijević M, Stojadinović S, Ivaz J, Stojković P. Fuzzy model for risk assessment of machinery failures. Symmetry. 2020; 12(4):525, doi: 10.3390/sym12040525

[11] Irvanizam I, Nazaruddin N, Syahrini I. Solving decent home distribution problem using ELECTRE method with triangular fuzzy number. IEEE 2018 International Conference on Applied Information Technology and Innovation; 2018 September 03-05; Padang, Indonesia: IEEE; c2018, p.139-144, doi: 10.1109/ICAITI.2018.8686768

[12] Mousavi SA, Seiti H, Hafezalkotob A, Asian S, Mobarra R. Application of risk-based fuzzy decision support systems in new product development: An R-VIKOR approach. Applied Soft Computing. 2021; 109(2): 107456, doi: 10.1016/j.asoc.2021.107456

[13] Irvanizam I, Zahara N. An extended EDAS based on multi-attribute group decision making to evaluate mathematics teachers with single-valued trapezoidal neutrosophic numbers. Handbook of Research on the Applications of Neutrosophic Sets Theory and Their Extensions in Education. IGI Global, 2023: 40-67, doi: 10.4018/978-1-6684-7836-3.ch003

[14] Chen S, Chen S. Fuzzy risk analysis based on measures of similarity between interval-valued fuzzy numbers. Computers & Mathematics with Applications. 2008; 55(8): 1670-1685, doi: 10.1016/j.camwa.2007.06.022

[15] Zhang Q, Ou Y. An interval-valued fuzzy portfolio decision model with entropy and VaR constraints. American Journal of Modeling and Optimization. 2024; 11(1): 1-6, doi: 10.12691/ajmo-11-1-1

[16] Lin C. A weighted max–min model for fuzzy goal programming. Fuzzy Sets and Systems. 2004; 142(3): 407-420, doi: 10.1016/S0165-0114(03)00092-7

[17] Vercher E, Bermúdez JD, Segura JV. Fuzzy portfolio optimization under downside risk measures. Fuzzy Sets and Systems. 2007; 158(7), 769-782, doi:10.1016/j.fss.2006.10.026

Fuzzy Systems and Data Mining X
A.J. Tallón-Ballesteros (Ed.)

doi:10.3233/FAIA241397

Sentiment and Emotion-Aware Multi-Criteria Fuzzy Group Decision Making System

Adilet YERKIN [a], Pakizar SHAMOI [a,1], Elnara KADYRGALI [a]
[a] *School of Information Technology and Engineering, Kazakh-British Technical University, Almaty, Kazakhstan*
ORCiD ID: Adilet Yerkin https://orcid.org/0009-0007-6228-7296, Pakizar Shamoi https://orcid.org/0000-0001-9682-0203, Elnara Kadyrgali https://orcid.org/0009-0000-4732-2806

Abstract. In today's world, making decisions as a group is common, whether choosing a restaurant or deciding on a holiday destination. Group decision-making (GDM) systems play a crucial role by facilitating consensus among participants with diverse preferences. Discussions are one of the main tools people use to make decisions. When people discuss alternatives, they use natural language to express their opinions. Traditional GDM systems generally require participants to provide explicit opinion values to the system. However, in real-life scenarios, participants often express their opinions through some text (e.g., in comments, social media, messengers, etc.). This paper introduces a sentiment and emotion-aware multi-criteria fuzzy GDM system designed to enhance consensus-reaching effectiveness in group settings. This system incorporates natural language processing to analyze sentiments and emotions expressed in textual data, enabling an understanding of participant opinions besides the explicit numerical preference inputs. Once all the experts have provided their preferences for the alternatives, the individual preferences are aggregated into a single collective preference matrix. This matrix represents the collective expert opinion regarding the other options. Then, sentiments, emotions, and preference scores are inputted into a fuzzy inference system to get the overall score. The proposed system was used for a small decision-making process - choosing the hotel for a vacation by a group of friends. Our findings demonstrate that integrating sentiment and emotion analysis into GDM systems allows everyone's feelings and opinions to be considered during discussions and significantly improves consensus among participants.

Keywords. group decision making, sentiment analysis, fuzzy systems, consensus

1. Introduction

Nowadays, group decision-making (GDM) is a part of many people's everyday lives. When people discuss making decisions, they use natural language to express their opinions. Traditional GDM systems generally require participants to provide explicit opi-

[1]Corresponding Author: Pakizar Shamoi; E-mail: p.shamoi@kbtu.kz

nion values to the system [1]. However, in real-life scenarios, participants often express their opinions through some text (for example, in comments, social media, messengers, etc.), which will be a challenge to computer systems. Approaches to addressing this challenge include sentiment analysis techniques, fuzzy logic, and fuzzy sets. Using sentiment analysis, we can measure the user's sentiment and subsequently determine the preference value assigned to a particular alternative by the user. This allows the computer system to incorporate the expressed opinions effectively into the decision-making process. Using fuzzy logic and fuzzy sets, groups can make decisions when there is uncertainty or ambiguity.

Discussions are one of the main tools people use to make decisions. When a decision process involves a group of people and requires multiple points of view to consider, it is commonly conducted in groups of people. GDM [2] systems are tools and processes that allow a group of people to work together to reach a consensus acceptable to all group members. GDM systems can be useful where multiple perspectives need to be considered to arrive at a decision acceptable to all group members [3], [4].

The current study presents a decision-making framework that integrates a voting system, sentiment analysis from debates, fuzzy inference systems (FIS), and consensus evaluation to perform small decision-making — determining the most suitable hotel from a set of alternatives. In our approach, experts have the flexibility to engage in GDM processes using natural language. Using sentiment analysis methods, we determine the degree to which an expert accepts a particular alternative and obtains a preference value. The methodology aims to balance quantitative evaluations with qualitative insights to enhance decision accuracy and participant satisfaction. We use FIS because of its ability to handle uncertainty and vagueness in human opinions effectively, which makes it particularly suitable because it does not rely heavily on large datasets.

The primary contribution of this paper is introducing a novel decision-making framework that integrates sentiment and emotion analysis into a fuzzy logic-based system, enhancing the effectiveness of group decision-making processes in contexts where emotional factors play a critical role.

The remainder of this paper is organized as follows: Section II reviews the relevant literature, focusing on the fuzzy approach in decision-making and sentiment and emotion analysis. Section III describes the methodology, including the preferences and voting system, sentiment analysis, and the fuzzy inference system. Section IV presents the experiment and results. Finally, Section V concludes the paper and discusses potential future research directions.

2. Related Work

Integrating sentiment and emotion awareness into multi-criteria fuzzy group decision-making systems is an emerging area of research. Recent papers include the SAR-MCMD method, combining multi-criteria decision-making, deep learning, and sentiment analysis [5], sentiment-driven fuzzy cloud multicriteria model for online product ranking [6], dual fine-tuning-based LSGDM using online reviews [7], an intuitionistic fuzzy model for consensus reaching based on public opinions and expert evaluation [8].

2.1. Fuzzy Approach in Decision Making

Group decision-making (GDM) systems use fuzzy logic [9] and fuzzy sets [10] to help groups make decisions [11] when there is uncertainty or ambiguity since its first appearance in the 1970 [12]. These systems allow group members to express their opinions [13] in a way that considers the decision-making process's fuzziness and imprecision. Fuzzy sets and logic enable the representation of imprecise or ambiguous data, which can help capture people's complex preferences and opinions in a group context. A number of works focus on applying the fuzzy approach to DM.

Kahraman et al. [14] compared four fuzzy GDM methods for selecting a facility location: Yager's weighted goals method, Blin's fuzzy model of group decision, fuzzy analytic hierarchy process, and fuzzy synthetic evaluation. All methods aimed to choose the best facility location alternative using a multi-attribute GDM system.

GDM using incomplete fuzzy preference relations is considered in [15]. This approach automates the consensus-reaching process without a moderator, using consensus and consistency criteria. Additionally, a feedback system provides recommendations to experts on adjusting their preferences to achieve a high degree of consensus.

2.2. Sentiment and Emotion Analysis for Decision Making

People usually use natural language to express their opinions during discussions [3]. Natural Language Processing (NLP) allows experts to use everyday language rather than specific formats or numbers. By extracting valuable information from large text data, NLP supports decision-making processes.

Sentiment analysis [16], [17], [18] captures the collective sentiment and emotions of group members towards a decision or option. Sentiment analysis techniques are widely used to understand the overall sentiment in chat conversations or social media discussions, guiding decision-making by considering the group's collective sentiment.

A study [17] proposed a large-scale GDM method to manage information from numerous experts using sentiment analysis. This approach extracts valuable insights from experts' comments, focusing on emotions related to positivity and aggressiveness. In another study [18], a model for GDM among experts was proposed, combining free text inputs with pairwise comparisons of alternatives.

In dynamic contexts with numerous decision alternatives, a GDM method was introduced using a perceptual computing scheme to gather expert information [16]. Sentiment analysis of debate texts provides valuable insights for selecting the best alternatives in each DM round. Further advancing this field, researchers developed a consensus model for dynamic social network GDM scenarios [19]. Additionally, a dynamic expert weight determination approach for large-scale GDM was proposed based on social media data and sentiment analysis [20]. This method dynamically identifies expert weights using sentiment analysis of social media data.

Several methods were proposed to detect and analyze emotions expressed in chat conversations. This enables a deeper understanding of participants' emotional states during decision-making processes [21], [22], [23], [24].

3. Methodology

3.1. Preferences, voting system

Figure 1 illustrates the proposed Sentiment and Emotion-aware Multi-criteria Fuzzy GDM System system.

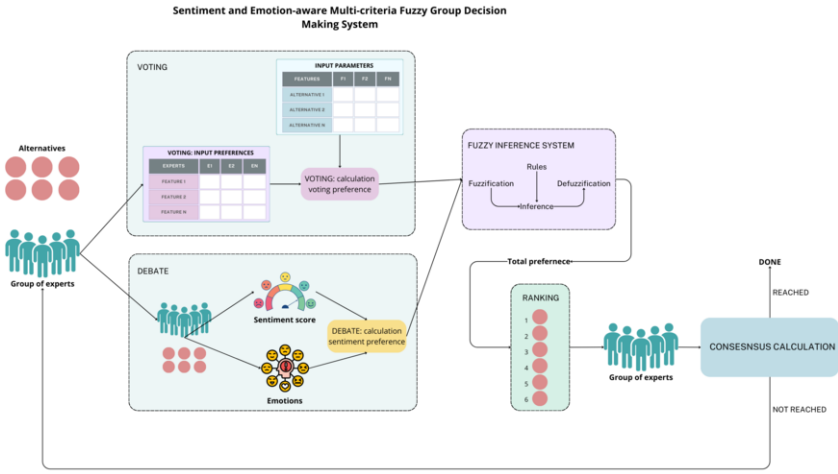

Figure 1. Sentiment and Emotion-aware Multi-criteria Fuzzy Group Decision Making System

Let a finite set of alternatives be $X = x_1, x_2, \ldots, x_n$. From the most preferred to the least preferred, these alternatives have to be ranked based on the information provided by a finite set of experts, denoted as $E = e_1, e_2, ..., e_m$. In addition, we have $F = f_1, f_2, ..., f_p$, and $Z = z_1, z_2, ..., z_{m*p}$, which are the features and the weights of the corresponding features, chosen by each of the experts $E = e_1, e_2, ..., e_m$. Because the situation in our particular setting comprises a group of friends working together to choose a hotel, the experts are considered equal. As a result of the peer-based decision-making process, every participant's opinion is given equal weight. In a GDM system, the goal is to rank the alternatives in X by considering the preference values P_k provided by each expert e_j, where j ranges from 1 to m. In addition, we have $W = w_1, w_2, ..., w_{n*p}$, which are the weights of the corresponding features for each of the alternatives $X = x_1, x_2, \ldots, x_n$. Preference assessments: "-1" - against, "0" - does not matter, and "1" – agreement. $Pref^{E_j}(X_i)$ – preference value of E_j (expert) about X_i (alternative) found using Eq. 1.

$$Pref^{E_j}(X_i) = \sum_{i,j,k=1}^{i=n,j=m,k=p} W_k(X_i) * Z_k(E_j) \tag{1}$$

3.2. Sentiment analysis

Using VADER [25] from the NLTK library, Sentiment analysis provides quantitative insights from participant discussions, enhancing our understanding of their emotional

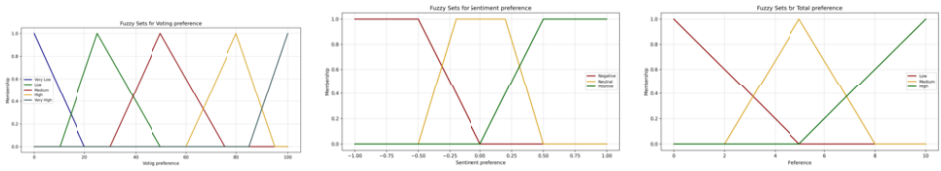

(a) Voting preferences (b) Sentiment preferences (c) Total preferences

Figure 2. Input and Output Fuzzy Sets of preference scores

responses and preferences alongside quantitative scores. We integrate emotion scores into the sentiment analysis to get the final preference score.

$$\text{Preference Score} = \alpha \cdot \text{Joint Sentiment Score} + \beta \cdot \text{Emotion Score} \tag{2}$$

Where α and β are weights that balance the influence of sentiment and emotion.

3.3. Fuzzy Inference System

The Fuzzy Inference System (FIS) integrates the quantitative results from the voting system with the qualitative results from sentiment analysis to compute a comprehensive total preference score for each option.

1. **Fuzzy Input Variables**
   - **Voting Preference.** This input variable represents the participants' aggregated voting scores for each alternative, scaled from 0 to 100. The membership function is shown in Figure 2a.
   - **Sentiment Preference.** This input variable represents the average sentiment score derived from the participants' qualitative discussions about each alternative, scaled from -1 to 1. The membership function is shown in Figure 2b.
2. **Fuzzy Output Variable. Total preference** represents the final preference score for each option, scaled from 0 to 10. The fuzzy sets are shown in Figure 2c.

Fuzzy rules define the relationship between input and output variables using IF-THEN statements. These rules combine input levels to produce an output level, forming the fuzzy control system shown in Table 1.

Table 1. Fuzzy rules. VL - Very Low, L - Low, M - Medium, H - High, VH - Very High.

Rule	1	2	3	4	5	6	7	8	9	10	11	12	13	14	15
Voting Preferences	VL	L	M	H	VH	VL	L	M	H	VH	VL	L	M	H	VH
Sentiment Preferences	L	L	L	L	L	M	M	M	M	M	H	H	H	H	H
Total Preferences	L	L	M	M	M	L	L	M	H	H	L	M	H	H	H

Table 2. Input table: Information about hotels. 0 and 1 denote the availability, e.g., whether a hotel has a pool.

id	Price, $ (per week)	Rating	Meal type	Room area, sq. m.	Star	Beach access	City closeness, minute drive	Pool
1	1165	7.7	Breakfast	42	5	1	30	1
2	133	9.6	Breakfast	32	3	0	45	0
3	783	8.1	Breakfast	50	4	1	10	1
4	525	9.2	Breakfast	35	2	0	5	1
5	4039	9	All inclusive	130	5	1	5	1
6	186	6.2	All inclusive	42	3	0	3	0
7	319	8	All inclusive	5	0	1	131	0

Table 3. Input table: Preference values of participants regarding the hotel features

id of partic.	price affordability	high rating	avail-ty of food	big room area	high star	beach access	closenes to city	avail-ty of a pool
1	0	1	-1	1	1	0	-1	0
2	1	1	0	0	1	1	1	0
3	1	1	-1	1	1	0	0	-1
4	1	1	0	0	0	1	1	0

4. Experiment and Results

We set up an experiment in which four participants make a decision about a hotel travel destination. The goal is to assess how preference analysis influences the decision-making process and outcomes, such as overall satisfaction and agreement among the participants. Experts will decide which alternatives are the most appropriate. Therefore, they should provide their preferences and opinions for a particular set of alternatives shown in Table 2. Four participants provided their preferences for each attribute using a scale from -1 to 1, where -1 indicates a negative preference, 0 indicates indifference, and 1 indicates a positive preference (see Table 3). These preferences were used to establish the initial voting system, as shown in Table 4.

The data comprises two primary components: participant preferences and hotel characteristics. We considered seven hotels, each with the following eight attributes:

- **Price per week ($):** The cost for a week's stay.
- **Rating:** The average user rating on a scale of 1 to 10.
- **Meal Type:** Whether the hotel offers breakfast only or all-inclusive meal plans.
- **Room Area (square meters):** The size of the hotel room.
- **Star Rating:** The hotel's star classification.
- **Beach Access:** Binary indicator of whether the hotel has direct access to a beach.
- **Closeness to City (minutes):** The duration of the car ride to the city center.
- **Availability of a Swimming Pool:** The hotel's swimming pool's binary indicator.

The preference score for each participant regarding each hotel is calculated by comparing the hotel's features to the group's average preferences. The steps are as follows. Continuous features such as price, rating, room area, and closeness to the city are normalized by comparing them to their respective mean values across all hotels by using the Formula Mean $= \frac{\sum_{i=1}^{n} x_i}{n}$, where n is the total number of objects, i - from 1 to n. To

Table 4. Preference matrix of experts from voting

	set 1							set 2						
hotel ID	**1**	**2**	**3**	**4**	**5**	**6**	**7**	**1**	**2**	**3**	**4**	**5**	**6**	**7**
parp1	0	1	1	0	1	-2	-1	50	56,25	56,25	50	56,25	37,5	43,75
parp2	3	2	4	4	4	2	2	68,75	62,5	75	75	75	62,5	62,5
parp3	0	2	2	1	1	0	0	50	62,5	62,5	56,25	56,25	50	50
parp4	2	2	3	4	3	2	2	62,5	62,5	68,75	75	68,75	62,5	62,5

Table 5. Collective preference matrix from voting

Hotel	hotel 1	hotel 2	hotel 3	hotel 4	hotel 5	hotel 6	hotel 7
Average Preference Score	57,81	60,94	65,62	64,06	64,06	53,12	54,69

Table 6. Sentiment preference matrix

	parp1	**parp2**	**parp3**	**parp4**	**avg. sentiment score**
hotel1	-0,5615	0,9301	-0,3561	0,2574	0,067475
hotel2	-0,5267	-0,1027	0,3612	-0,0644	-0,08315
hotel3	0	0,6597	0,8658	0,8765	0,6005
hotel4	0	0,2144	0,5478	0,7579	0,380025
hotel5	0	0,685	0,4404	0,2144	0,33495
hotel6	-0,5267	-0,831	-0,3919	-0,4497	-0,54983
hotel7	-0,296	0	0	0	-0,074

standardize the comparison of hotel attributes, we mapped the meal type attribute to numerical coefficients (0.33 for Breakfast and 1.0 for All Inclusive). For features already in binary form, values are taken without normalization.

Next, using Eq. 1 we calculated the preference value for each expert to each alternative, shown in Table 4. The preference scores, initially ranging from -8 to 8, are scaled to a more interpretable range of 0 to 100. Once all experts provide their preferences, these are aggregated into a collective preference matrix, representing the group's opinion. The group preference value is calculated by averaging the experts' preference values, as shown in Table 5.

Participants engaged in a debate about the pros and cons of each hotel through a chat messenger. This informal yet rich discussion provided valuable qualitative data. We utilized text analysis tools to extract sentiment and emotional scores from the chat. The sentiment score for each statement was calculated using the VADER sentiment analysis tool, which provides a compound score ranging from -1 (negative) to 1 (positive), as shown in Table 6. After calculating the sentiment scores for each comment, the next step is to aggregate these scores into an average sentiment score for each hotel (see Table 6).

Emotional tones (*happy, angry, surprise, sad, and fear*) were detected using the Text2Emotion library [26], which assigns scores to different emotions, as shown in Table 7. For each hotel, we calculated the average combined sentiment score. The emotion score was derived by considering the positive and negative emotions separately. It was calculated by taking the maximum of the following feelings: negative emotions included "angry," "sad," and "fear," while positive emotions included "happy" and "surprise." The difference between the positive and negative emotion scores was used to create the composite emotion score. This approach ensures that the most intense positive and negative

Table 7. Emotion preference scores

Part.	Hotel	Happy	Angry	Surprise	Sad	Fear	Positive Emotion	Negative Emotion	Emotion score
parp1	hotel1	0	0,17	0	0	0,83	0	0,83	-0,83
parp2	hotel1	0,43	0,14	0,14	0,14	0,14	0,43	0,14	0,29
parp3	hotel1	0	0	0	0	1	0	1	-1
parp4	hotel1	0,4	0	0,2	0,2	0,2	0,4	0,2	0,2
...	...	...	...	...	...	...	...	...	...
parp4	hotel7	0	0	0	0	1	0	1	-1

Table 8. Combine Sentiment and Emotion Scores into a final preference score and Total preference score after calculation by Fuzzy Inference System

Hotel	Average Combined Emotion Score	Average Combined Sentiment Score	Total Sentiment Score	Average Preference Score from Voting	Fuzzy score
hotel1	-0,34	0,07	-0,09	57,81	5,00
hotel2	0,13	-0,08	0,00	60,94	5,17
hotel3	0,31	0,60	0,49	65,62	7,52
hotel4	-0,40	0,38	0,07	64,06	5,74
hotel5	-0,19	0,33	0,13	64,06	5,88
hotel6	-0,38	-0,55	-0,48	53,12	5,00
hotel7	-0,63	-0,07	-0,29	54,69	5,00

emotions are considered, reflecting the overall emotional tone of the discussion. These Emotion and Sentiment scores were weighted and combined to form the total sentiment score: $TotalsentimentScore = EmotionScore * 0.4 + SentimentScore * 0.6$. This weighting scheme gives more importance to sentiment analysis while still considering emotional intensity.

These weights were chosen to give slightly more emphasis to sentiment analysis due to its broader contextual relevance. This weighting scheme ensures that while sentiment analysis plays a dominant role, the emotional intensity is still substantially incorporated. In general, they can be adjusted based on the context or derived from user preferences.

Next, we used the Fuzzy inference system to simulate and compute the total preference score (see Fig. 3a) based on given input values for voting preference and sentiment preference (see Fig. 4), total preference values shown in Table 8. The alternatives are ranked based on the preference levels provided by the experts.

After selecting a hotel, participants provided feedback on their agreement and confidence levels regarding the decision (see Fig. 3b). These values were computed using another fuzzy inference system to compute a feedback score (see Fig. 5). The feedback system evaluated the consistency and confidence of the participants' opinions, as shown in Table 9. Our feedback system is non-monotonic, but this behavior is justified and appropriate given the interpretation of "confidence" as the confidence level in the agreement. Our rules capture the nuanced relationship between agreement, confidence in that agreement, and feedback, leading to outputs that make sense given the inputs. Consensus metrics, including the interquartile range (IQR) and mean consensus level, were used to evaluate the overall agreement among participants, as shown in Table 10. The consensus level was classified as *high, medium*, or *low* based on the mean consensus score.

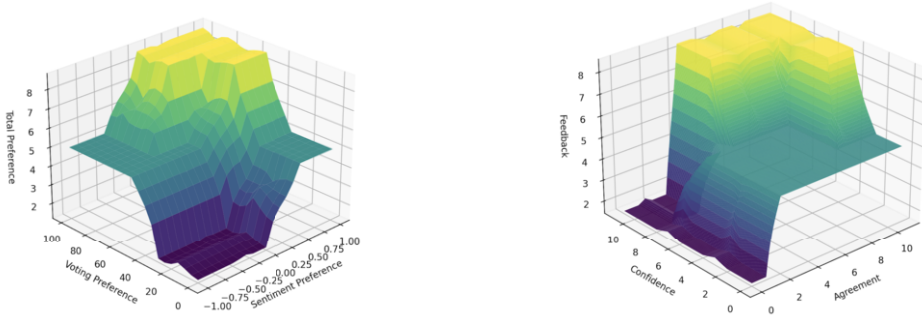

(a) Preference score (b) Feedback score

Figure 3. 3D graphic representations of a set of possible fuzzy system solutions

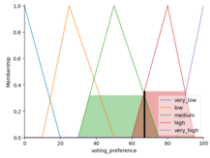

(a) Voting pref-ces

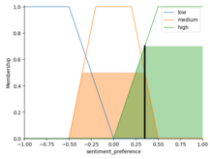

(b) Sent. pref-ces

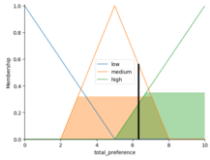

(c) Total pref-ces

Figure 4. Fuzzy Inference system preferences

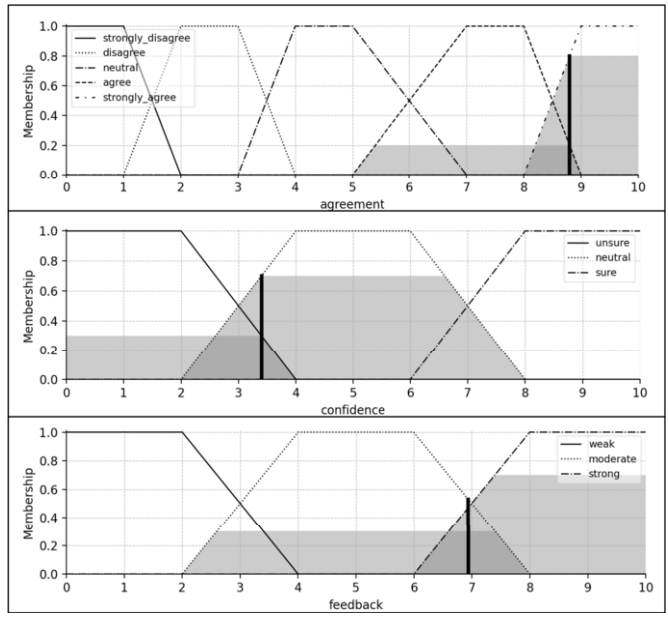

Figure 5. Visual representation of the inference process. For example, the *Agreement* value is 8.8, and the *Confidence* value is 3.4. As a result, we get a *Feedback value* ≈ 6.94.

This classification helped understand the group's satisfaction with the decision-making process.

5. Conclusion

We presented a novel decision-making framework integrating voting preferences, debate analysis, and fuzzy inference systems. The main contribution of this paper is integrating sentiment and emotion analysis into a fuzzy logic-based system, thereby making traditional group decision-making processes emotion-aware, particularly in situations

Table 9. Participants Feedback on Hotel Recommendation

id of participant	Agreement level (0-10)	Confidence level (0-10)	Feedback value
1	5	7	6.24
2	9	8	8.44
3	8	7	6.24
4	10	10	8.44

Table 10. Consensus score

IQR	Mean	Consensus level
2.19	7.34	high

where emotional factors are crucial. An example of the application of our framework is selecting a hotel. The high consensus level among participants further validates the proposed methodology. This approach can be applied to various GDM scenarios, providing a reliable method for achieving consensus. As for future works, we aim to explore the system's applicability in more complex contexts and further refine its components to increase its generalizability. While our current work shows that integrating sentiment and emotion analysis into a multi-criteria fuzzy GDM system is feasible, as demonstrated with the hotel selection example, we plan to explore its effectiveness in more varied and complex decision-making scenarios in future research. We also plan to conduct a comprehensive sensitivity analysis and compare our approach with other decision-making frameworks to evaluate its effectiveness and reliability more rigorously.

The proposed system integrates sentiment and emotion analysis, balancing both quantitative and qualitative inputs, making it well-suited for real-world scenarios like the hotel selection case study. However, its complexity due to multiple components can make implementation challenging. The system's effectiveness may also vary in different decision-making contexts, especially given the simplicity of the current case study. Additionally, the approach depends heavily on the quality of textual data, which could affect outcomes if the data is incomplete or biased.

In the future, we will explore integrating our framework with conventional multi-criteria decision support techniques like TOPSIS, ELECTRE, and PROMETHEE to enable a thorough comparison and assessment of its efficacy in various decision-making scenarios.

Acknowledgment

This research has been funded by the Science Committee of the Ministry of Science and Higher Education of the Republic of Kazakhstan (Grant No. AP22786412)

References

[1] Juan Antonio Morente-Molinera, Gang Kou, Yi Peng, Cristóbal Torres-Albero, and Enrique Herrera-Viedma. Analysing discussions in social networks using group decision making methods and sentiment analysis. *Information Sciences*, 447:157–168, 2018.

[2] Jean-Marie Blin and Mark A Satterthwaite. Individual decisions and group decisions: The fundamental differences. *Journal of Public Economics*, 10(2):247–267, 1978.

[3] F Herrera, E Herrera-Viedma, and J L Verdegay. A model of consensus in group decision making under linguistic assessments. *Fuzzy Sets and Systems*, 78:87, 1996.

[4] Enrique Herrera-Viedma, Francisco Herrera, and Francisco Chiclana. A consensus model for multiperson decision making with different preference structures. *IEEE Trans. on SMC*, 32:394–402, 5 2002.

[5] Swathi Angamuthu and P. Trojovský. Integrating multi-criteria decision-making with hybrid deep learning for sentiment analysis in recommender systems. *PeerJ Computer Science*, 9, 2023.

[6] Zaoli Yang, Qingyuan Li, Vincent Charles, Bing Xu, and Shivam Gupta. Online product decision support using sentiment analysis and fuzzy cloud-based multicriteria model through multiple e-commerce platforms. *IEEE Transactions on Fuzzy Systems*, 31:3838–3852, 2023.

[7] Xuechan Yuan, Tingyu Xu, Shiqi He, and Chao Zhang. An online review data-driven fuzzy large-scale group decision-making method based on dual fine-tuning. *Electronics*, 13(14):2702, 2024.

[8] Wei Yang and Luxiang Zhang. A multi-period intuitionistic fuzzy consensus reaching model for group decision making problem in social network. *Complex & Intelligent Systems*, pages 1–22, 2024.

[9] L.A. Zadeh. Fuzzy logic. *Computer*, 21(4):83–93, 1988.

[10] L. A. Zadeh. Fuzzy sets. *Information and Control*, 8(3):338–353, 1965.

[11] J. A. Morente-Molinera, F. J. Cabrerizo, J. R. Trillo, I. J. Pérez, and E. Herrera-Viedma. Managing group decision making criteria values using fuzzy ontologies. volume 199, pages 166–173, 2021.

[12] R. E. Bellman and L. A. Zadeh. Decision-making in a fuzzy environment. *Management Science*, 17:B–141–B–164, 12 1970.

[13] L A Zadeh. From computing with numbers to computing with words-from manipulation of measurements to manipulation of perceptions *. *Int. J. Appl. Math. Comput. Sci*, 12:546–548, 2002.

[14] Cengiz Kahraman, Da Ruan, and Ibrahim Doğan. Fuzzy group decision-making for facility location selection. *Information Sciences*, 157:135–153, 2003.

[15] Enrique Herrera-Viedma, Sergio Alonso, Francisco Chiclana, and Francisco Herrera. A consensus model for group decision making with incomplete fuzzy preference relations. *IEEE Transactions on Fuzzy Systems*, 15:863–877, 10 2007.

[16] J. A. Morente-Molinera, F. J. Cabrerizo, J. Mezei, C. Carlsson, and E. Herrera-Viedma. A dynamic group decision making process for high number of alternatives using hesitant fuzzy ontologies and sentiment analysis. *Knowledge-Based Systems*, 195, 5 2020.

[17] José Ramón Trillo, Enrique Herrera-Viedma, Juan Antonio Morente-Molinera, and Francisco Javier Cabrerizo. A large scale group decision making system based on sentiment analysis cluster. *Information Fusion*, 3 2022.

[18] J. A. Morente-Molinera, G. Kou, K. Samuylov, R. Ureña, and E. Herrera-Viedma. Carrying out consensual group decision making processes under social networks using sentiment analysis over comparative expressions. *Knowledge-Based Systems*, 165:335–345, 2 2019.

[19] Xia Liu, Yunyue Zhang, Yejun Xu, Mengqi Li, and Enrique Herrera-Viedma. A consensus model for group decision-making with personalized individual self-confidence and trust semantics: A perspective on dynamic social network interactions. *Information Sciences*, 627:147–168, 5 2023.

[20] Qifeng Wan, Xuanhua Xu, Jun Zhuang, and Bin Pan. A sentiment analysis-based expert weight determination method for large-scale group decision-making driven by social media data. *Expert Systems with Applications*, 185:115629, 2021.

[21] Neghina Mihai, Matei Alexandru, and Zamfirescu Bala-Constantin. Multimodal emotion detection from multiple data streams for improved decision making. *Procedia Comp. Science*, 214:1082–1089, 2022.

[22] Jennifer M. George and Erik Dane. Affect, emotion, and decision making. *Organizational Behavior and Human Decision Processes*, 136:47–55, 2016.

[23] David Nicoladie Tam. Variables governing emotion and decision-making: human objectivity underlying its subjective perception. *BMC Neuroscience*, 11:P96 – P96, 2010.

[24] Ricardo Santos, Goreti Marreiros, Carlos Ramos, Jose Neves, and Jose Bulas-Cruz. Personality, emotion, and mood in agent-based group decision making. *IEEE Intelligent Systems*, 26(6):58–66, 2011.

[25] C. J. Hutto and Eric Gilbert. Vader: A parsimonious rule-based model for sentiment analysis of social media text. In *Proceedings of the International AAAI Conference on Web and Social Media*, 2014.

[26] MultiMedia LLC. text2emotion 0.0.5 package, 2020.

Fuzzy Systems and Data Mining X
A.J. Tallón-Ballesteros (Ed.)

doi:10.3233/FAIA241398

Experimental Study on Appropriate Sample Size of Lagged Fibonacci Pseudorandom Number Generators for Stochastic Simulations

Hiroshi HARAMOTO [a,1], Makoto MATSUMOTO [b] and Takuji NISHIMURA [c]
[a] *Center for Data Science, Ehime University, Matsuyama 790-8577, Japan*
[b] *Freelancer, Japan*
[c] *Faculty of Science, Yamagata University, Yamagata 990-8560, Japan*
ORCiD ID: Hiroshi HARAMOTO https://orcid.org/0000-0003-4833-0108, Makoto MATSUMOTO https://orcid.org/0000-0003-1914-7208

Abstract. Pseudorandom number generators are essential for various stochastic simulations in physics, economics, engineering, etc. In this study, we propose a practical method for estimating appropriate sample sizes for lagged Fibonacci generators, one of the most traditional and widely used pseudorandom number generators. This estimation is based on an analogy with the theoretical one-dimensional random walk. The proposed method is formulated using a weight enumeration polynomial and the MacWilliams identity in coding theory. Generally, a weight enumeration polynomial requires an intractable exhaustive check of the seeds. However, under certain conditions, the MacWilliams identity allows for the direct derivation of the weight enumeration polynomial. To improve efficiency, we employ a heuristic technique to approximate the weight enumeration polynomial by truncating "non-essential" terms motivated by Fourier analysis in signal processing.

Keywords. Pseudorandom Number Generation, Lagged Fibonacci Generator, MacWilliams Identity, Binomial Distribution
2020 Mathematics Subject Classification. 11K45, 11B37, 11T71, 68Q87

1. Introduction

We consider the following simulation using a pseudorandom number generator (PRNG): this simulation corresponds to a one-dimensional random walk [1]. Let $x_0, x_1, \ldots$ denote an (unsigned) w-bit integer sequence generated by the PRNG and let m be a positive integer. We enumerate the number of 1's in the n-th least significant bit (LSB) of the subsequence $x_0, \ldots, x_{m-1}$, and denote it by R_1. Next, we enumerate the number of 1's in the n-th LSB of $x_m, \ldots, x_{2m-1}$, and denote it by R_2. By repeating this procedure N times, we obtain $R_1, R_2, \ldots, R_N$. Under the assumption that initial values of the PRNG are

[1] Corresponding Author: Hiroshi HARAMOTO, e-mail: haramoto@ehime-u.ac.jp

chosen randomly, these R_i's are random variables conforming to some distributions. If the PRNG were an ideal RNG, 0 and 1 would occur independently and equally likely, then these variables should conform to the binomial distribution with m trials and probability $1/2$. This binomial distribution is denoted by $B(m, 1/2)$.

If the PRNG has a deviation, the actual probability $\Pr(R_i = j)$, $j = 0, 1, \ldots, m$, differs from the expected probability $\binom{m}{j}/2^m$. This discrepancy becomes more apparent as N increases, which potentially undermines the reliability of the simulation. Thus, it is useful to predict an upper limit of N that does not exhibit such a discrepancy. Poorer PRNGs tend to exhibit lower upper limits than better ones. This indicates that the upper limit can serve as a figure of merit for PRNGs.

In this study, we examine the distribution of the n-th LSB of the output of lagged Fibonacci generators [2], defined by the recurrence

$$x_{k+i} = x_{l+i} + x_i \pmod{M}, \quad i = 0, 1, 2, \ldots, \tag{1}$$

where k and l are positive integers and M is 2^w with a positive integer w. Note that the n-th LSBs ($n \leq w$) of the generated sequence is the same as the most significant bit of the sequence generated by

$$x_{k+i} = x_{l+i} + x_i \pmod{2^n}, \tag{2}$$

and thus we may consider only the latter sequence from now on. These PRNGs have been implemented in various software packages as standard PRNGs. For example, a lagged Fibonacci generator based on the recursion

$$x_{31+i} = x_{28+i} + x_i \pmod{2^{32}} \quad i = 0, 1, 2, \ldots \tag{3}$$

is used as a standard random-number generator in the BSD-C library. Further, the well-known molecular dynamics program, Large-scale Atomic/Molecular Massively Parallel Simulator, uses a 97th-order lagged Fibonacci generator [3,4].

It is experimentally known that the least significant bits of lagged Fibonacci generators have significant deviations from the expected binomial distribution. To mitigate the effects of these deviations, some applications discard the LSB by right-shifting. Although this approach appears to be intuitive, we must ensure that the distribution of the second (or higher) bit in lagged Fibonacci generators is indeed better than that of the first bit.

Usually, statistical tests are performed on PRNGs to evaluate the deviation of their empirical distribution from the theoretical distribution [5,6]. However, such tests suffer from instability as different experiments yield different results. To address this issue, Matsumoto and Nishimura introduced a theoretical test called the *weight discrepancy test*, which provides upper limits for N for $\mathbb{F}_2$-linear PRNGs [7]. Subsequently, Haramoto et al. extend this test to some PRNGs based on $\mathbb{Z}/2^n\mathbb{Z}$ [8,9], where $\mathbb{Z}/2^n\mathbb{Z}$ is the residue ring modulo 2^n. The weight discrepancy test is stable, indicating that its results are independent of the initial values. On the other hand, its computational cost increases exponentially with respect to n. In fact, in a previous study [9], only the cases $n \leq 6$ were considered.

The aim of this study is to investigate an approximation of the weight discrepancy test. Although the approximation still requires exponential computation time, upper lim-

its of N for several lagged Fibonacci generators are estimated up to the 24-th LSBs with sufficient accuracy. We also present experimental results that support the practical adequacy of the approximation.

2. Chi-squared discrepancy and weight enumerator polynomial

By the reversibility of the reccurence (1), when the initial value $(x_0, ..., x_{k-1})$ is uniformly and randomly chosen, then for any positive integer t, $(x_t, ..., x_{t+k-1})$ is uniformly random. Therefore, for any i, R_i conforms to one same distribution, i.e., $\Pr(R_i = j)$ is independent of i. Thus, we may denote $\Pr(R_i = j)$ by $\Pr(R = j)$.

We recall a standard chi-squared test examining a null hypothesis:

$$\mathscr{H}_0 : R_1, R_2, \ldots, R_N \sim_{i.i.d.} B(m, 1/2) \tag{4}$$

using a goodness-of-fit (GOF) test.

Under $\mathscr{H}_0$, the probability $\Pr(R_i = j)$ is expected to be $\binom{m}{j}/2^m$, where $j = 0, 1, \ldots, m$. We categorize the R_i's into suitable classes, C_0, C_1, ..., C_ν. In this study, we focus on the categorization

$$\begin{aligned} &C_0 := \{0, 1, \ldots, s_0\}, \qquad C_j := \{s_0 + j\} \quad (1 \le j \le m - 2s_0 - 1), \\ &C_\nu := \{m - s_0, m - s_0 + 1, \ldots, m\} \end{aligned} \tag{5}$$

for suitably chosen s_0 and $\nu := m - 2s_0$. Based on the classes, we define

$$q_j := \Pr(R \in C_j) \ \text{ and } \ p_j := \sum_{i \in C_j} \frac{1}{2^m} \binom{m}{i}, \tag{6}$$

for $j = 0, 1, \ldots, \nu$. The test statistic of the GOF test called the chi-squared statistic

$$\chi^2 := \sum_{i=0}^{\nu} \frac{(\#\{j \mid 1 \le j \le N, R_j \in C_i\} - Np_i)^2}{Np_i}, \tag{7}$$

where the symbol $\#S$ means the number of elements in the finite set S. The chi-squared statistic χ^2 is known to approximately conform to the chi-squared distribution with ν degrees of freedom for large N [10].

Let χ^2_{obs} be a realization of χ^2. If the *p-value* $\Pr(\chi^2_{obs} \le X)$, where X is a random variable conforming to the chi-squared distribution with ν degrees of freedom, is less than a significance level (e.g., 0.01), we reject the null hypothesis $\mathscr{H}_0$ and conclude that the n-th LSB of the tested PRNG is far from random. When the tested sequence is ideal, the distribution $(q_j)_{j=0}^{\nu}$ coincides with the distribution $(p_j)_{j=0}^{\nu}$ arising from the binomial distribution. However, for the tested sequence generated using a PRNG, the distribution $(q_j)_{j=0}^{\nu}$ differs from $(p_j)_{j=0}^{\nu}$ in general. In particular, Matsumoto and Nishimura proved the inequality

$$\left|\mathrm{E}(\chi^2) - (\nu + N\delta)\right| \le \nu \max_{j=0,\ldots,\nu} \left|1 - \frac{q_j}{p_j}\right|, \tag{8}$$

where the distance-like function

$$\delta := \sum_{i=0}^{v} \frac{(q_j - p_i)^2}{p_i} \tag{9}$$

is called the *chi-squared discrepancy* of $(q_j)_{j=0}^{v}$ from $(p_j)_{j=0}^{v}$ [7].

Here we assume that the PRNG is rather good, and q_j is very close to p_i for each i, so that the right hand side of the above inequality is negligible compared to $E(\chi^2)$. Then

$$E(\chi^2) \approx v + N\delta. \tag{10}$$

Putting

$$N_r := \frac{\chi_v^2(0.01) - v}{\delta}, \tag{11}$$

where $\chi_v^2(0.01)$ denotes the first upper percentile of the chi-squared distribution with v degrees of freedom, we have $E(\chi^2) \approx \chi_v^2(0.01)$, and hence

$$\Pr(\mathrm{E}(\chi^2) \le X) \approx 0.01. \tag{12}$$

Thus, the chi-squared GOF test with sample size N_r often reveals the discrepancy between $(q_j)_{j=0}^{v}$ and $(p_j)_{j=0}^{v}$. Consequently, the deviation of the n-th LSB of PRNGs may ruin the reliability of simulations.

On the other hand, when considering the sample size

$$N_s := \frac{\chi_v^2(0.25) - v}{\delta}, \tag{13}$$

the chi-squared GOF test yields $\Pr(\mathrm{E}(\chi^2) \le X) \approx 0.25$. This implies that the distribution of the n-th LSB of the outputs of the PRNG can hardly be distinguished from the binomial distribution, hence expected to do no harm to the simulation.

For these reasons, N_r and N_s are termed the *risky sample size* and *safe sample size* for the chi-squared GOF test, respectively [7].

The weight discrepancy test requires the computation of q_j's, and hence, the probability $\Pr(R_i = j)$. Lagged Fibonacci generators allow us to compute these probabilities efficiently, as described below. By definition, the sequence $x_0, x_1, \ldots$ of the lagged Fibonacci generator is determined by the initial value $(x_0, x_1, \ldots, x_{k-1}) \in (\mathbb{Z}/2^n\mathbb{Z})^k$. To compute the probability $\Pr(R = j)$, we consider the function

$$O_G : (\mathbb{Z}/2^n\mathbb{Z})^k \to (\mathbb{Z}/2^n\mathbb{Z})^m; \quad (x_0, x_1, \ldots, x_{k-1}) \mapsto (x_0, x_1, \ldots, x_{m-1}). \tag{14}$$

For $(x_0, x_1, \ldots, x_{m-1}) \in (\mathbb{Z}/2^n\mathbb{Z})^m$, and for $i = 0, 1, \ldots, 2^n - 1$, we denote the number of i's among $x_0, x_1, \ldots, x_{m-1}$ by $\mathrm{wt}_i(x_0, x_1, \ldots, x_{m-1})$. Let

$$V_j := \left\{ (x_0, x_1, \ldots, x_{k-1}) \in (\mathbb{Z}/2^n\mathbb{Z})^k \;\middle|\; \sum_{i=2^{n-1}}^{2^n-1} \mathrm{wt}_i(O_G(x_0, x_1, \ldots, x_{k-1})) = j \right\} \tag{15}$$

for $j = 0, 1, \ldots, v$. According to this notation, we have

$$\Pr(R = j) = \frac{\#V_j}{\#(\mathbb{Z}/2^n\mathbb{Z})^k} = \frac{\#V_j}{2^{kn}}. \tag{16}$$

Let $C := \mathrm{Im}(O_G)$. Since $(\mathbb{Z}/2^n\mathbb{Z})^k$ is a group, and O_G is a group homomorphism, O_G is a $(\#\ker(O_G) : 1)$-mapping. Therefore, we have

$$\Pr(R = j) = \frac{1}{\#C} \# \left\{ (x_0, x_1, \ldots, x_{m-1}) \in C \;\middle|\; \sum_{i=2^{n-1}}^{2^n-1} \mathrm{wt}_i(x_0, x_1, \ldots, x_{m-1}) = j \right\}. \tag{17}$$

We also define the *weight enumeration of C* for nonnegative integers $j_0, j_1, \ldots, j_{2^n-1}$ as follows:

$$\begin{aligned} &A(j_0, j_1, \ldots, j_{2^n-1}) \\ &\quad := \#\{(x_0, x_1, \ldots, x_{m-1}) \in C \mid \mathrm{wt}_i(x_0, x_1, \ldots, x_{m-1}) = j_i \;\; (i = 0, 1, \ldots, 2^n - 1)\}. \end{aligned} \tag{18}$$

Using this, $\Pr(R = j)$ can be expressed as follows:

$$\Pr(R = j) = \frac{1}{\#C} \sum_{j_{2^{n-1}+1} + \cdots + j_{2^n-1} = j} A(j_0, j_1, \ldots, j_{2^n-1}). \tag{19}$$

Unfortunately, the computation of $A(j_0, j_1, \ldots, j_{2^n-1})$ is known to be an NP-complete problem [11]. However, the *weight enumerator polynomial of C*

$$W_C(X_0, \ldots, X_{2^n-1}) := \sum_{(j_0, j_1, \ldots, j_{2^n-1}) \in \mathbb{Z}_{\geq 0}^{2^n}} A(j_0, j_1, \ldots, j_{2^n-1}) X_0^{j_0} X_1^{j_1} \cdots X_{2^n-1}^{j_{2^n-1}}, \tag{20}$$

enables the computation of the weight enumeration of C under certain conditions.

Theorem 2.1 (MacWilliams Identity over $\mathbb{Z}/2^n\mathbb{Z}$ [12,13]) *Let $C^\perp$ be the orthogonal space of C with respect to a standard inner product*

$$\langle (x_0, \ldots, x_{2^n-1}), (y_0, \ldots, y_{2^n-1}) \rangle := \sum_{i=0}^{2^n-1} x_i y_i \in \mathbb{Z}/2^n\mathbb{Z} \tag{21}$$

and let $X'_i := \sum_{p=0}^{2^n-1} \omega^{ip} X_p$ for $i = 0, 1, \ldots 2^n - 1$, where $\omega := \exp\left(\frac{2\pi\sqrt{-1}}{2^n}\right)$. Then, we have

$$W_C(X_0, X_1, \ldots, X_{2^n-1}) = \frac{1}{\#C} W_{C^\perp}(X'_0, X'_1, \ldots, X'_{2^n-1}). \tag{22}$$

If the number of elements of $C^\perp$ is not too large, then we can compute the weight enumeration of $C^\perp$ via an exhaustive check. Using the weight enumerator polynomial $W_{C^\perp}$ and the MacWilliams identity, we obtain W_C.

When computing $\Pr(R = j)$, we require only the sum

$$\sum_{j_{2^{n-1}+1}+\cdots+j_{2^n-1}=j} A(j_0, j_1, \ldots, j_{2^n-1}), \tag{23}$$

instead of the value of each $A(j_0, j_1, \ldots, j_{2^n-1})$. Substituting indeterminates X for $X_0, \ldots, X_{2^{n-1}-1}$ and Y for $X_{2^{n-1}}, \ldots, X_{2^n-1}$ in X_i' yields

$$W_C(X, \ldots, X, Y, \ldots, Y) = \sum_{j=0}^{m} \sum_{j_{2^{n-1}+1}+\cdots+j_{2^n-1}=j} A(j_0, j_1, \ldots, j_{2^n-1}) X^j Y^{m-j}. \tag{24}$$

This substitution reduces the number of variables from 2^n to two, and thus, the right-hand side of the MacWilliams identity can be expanded efficiently using Mathematica.

3. Approximation of weight enumerator polynomial

The technique described in the previous section for computing $A(j_0, j_1, \ldots, j_{2^n-1})$ reduces the computational cost. However, the computational difficulty of $W_{C^\perp}$ increases exponentially with increasing n. Therefore, we investigate a heuristic method to approximate $W_{C^\perp}$ for the computation of W_C and δ.

Let $\mathscr{W}_{C^\perp}$ be the polynomial consisting of the monomials of the highest and second-highest degrees with respect to X_0 in $W_{C^\perp}$. Using $\mathscr{W}_{C^\perp}$, we define a weight enumerator-like polynomial $\mathscr{W}_C$ as follows:

$$\mathscr{W}_C(X_0, \ldots, X_{2^n-1}) := \frac{1}{\#C} \mathscr{W}_{C^\perp}(X_0', \ldots, X_{2^n-1}'). \tag{25}$$

Let $A_{ap}(j_0, \ldots, j_{2^n-1})$ be the coefficient of $X_0^{j_0} \cdots X_{2^n-1}^{j_{2^n-1}}$ in $\mathscr{W}_C$. If $\mathscr{W}_C$ approximates W_C in some sense, then the probability $\Pr(R = j)$ would be approximated by

$$\Pr(R = j) \approx \sum_{j_{2^{n-1}+1}+\cdots+j_{2^n-1}=j} A_{ap}(j_0, j_1, \ldots, j_{2^n-1}). \tag{26}$$

One of the reasons for considering the polynomial $\mathscr{W}_{C^\perp}$ is that low Hamming-weight elements in $C^\perp$ are known to have a detrimental effect on randomness. Several studies have been conducted on smaller weights, e.g., three and five [14,15].

Another reason is that the MacWilliams identity is a discrete Fourier transform over $\mathbb{Z}/2^n\mathbb{Z}$. The highest-degree term with respect to X_0 in $W_{C^\perp}$ corresponds to $(0, 0, \ldots, 0) \in C^\perp$, and the second-highest degree terms with respect to X_0 in $W_{C^\perp}$ correspond to the nonzero elements in $C^\perp$ with the minimum Hamming weight. Here, formally mimicking the concept of Fourier analysis in signal processing [16], we regard the highest term as an analogue of the DC component, and the second-highest terms as the low-frequency component. In Fourier analysis, the DC and low-frequency components often represent the fundamental characteristics of a signal, while the high-frequency components are often considered to be less important. Thus, we expect that $\mathscr{W}_{C^\perp}$ provides a practically adequate approximation of $W_{C^\perp}$. Figure 1 summarizes the above considerations in the

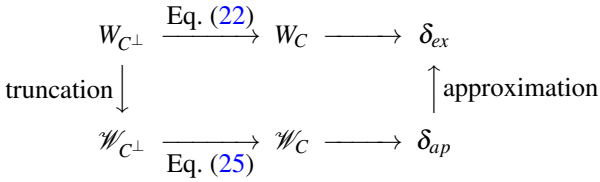

Figure 1. The relationship of W_C, $W_{C^\perp}$, δ_{ex}, $\mathscr{W}_C$, $\mathscr{W}_{C^\perp}$, and δ_{ap}.

form of a diagram: we denote by δ_{ex} the exact value of the chi-squared discrepancy derived using $W_{C^\perp}$ and by δ_{ap} the approximate value of the chi-squared discrepancy derived using $\mathscr{W}_{C^\perp}$.

Although we lack a mathematical justification for the approximation by $\mathscr{W}_C$, the observations presented below suggest that the polynomials $\mathscr{W}_{C^\perp}$ and $\mathscr{W}_C$ provide an approximation to compute δ with sufficient accuracy.

Now, we consider the aforementioned approximation of the chi-squared discrepancy for the lagged Fibonacci generator based on recurrence (3). Let $m = 34$. For $n = 1$, we have

$$W_{C^\perp}(X_0, X_1) = X_0^{34} + 3X_0^{31}X_1^3 + 3X_0^{28}X_1^6 + X_0^{25}X_1^9 \tag{27}$$

and a 2-term polynomial

$$\mathscr{W}_{C^\perp}(X_0, X_1) = X_0^{34} + 3X_0^{31}X_1^3. \tag{28}$$

For $n = 2$, we obtain a 20-term polynomial

$$W_{C^\perp}(X_0, X_1, X_2, X_3) = X_0^{34} + 3X_0^{31}X_1^2X_3 + 3X_0^{31}X_2^3 + 3X_0^{31}X_1X_3^2 + (\text{lower terms}) \tag{29}$$

and a 4-term polynomial

$$\mathscr{W}_{C^\perp}(X_0, X_1, X_2, X_3) = X_0^{34} + 3X_0^{31}X_1^2X_3 + 3X_0^{31}X_2^3 + 3X_0^{31}X_1X_3^2. \tag{30}$$

Table 1 summarizes the numbers of terms of $W_{C^\perp}$ and $\mathscr{W}_{C^\perp}$, the exact value of the chi-squared discrepancy δ_{ex}, the approximate value of the chi-squared discrepancy δ_{ap}, and the relative error $(\delta_{ap} - \delta_{ex})/\delta_{ex}$.

We can also consider another example involving a variant of a lagged Fibonacci generator, described by Knuth [17] based on a three-term recurrence:

$$x_{100+i} := -x_{63+i} + x_i \pmod{2^{30}}. \tag{31}$$

Let $m = 103$. The results are summarized in Table 2. Note that, for $n = 6$, the computation time for δ_{ex} using Mathematica 11 on an Intel Core i7 at 4.0 GHz with 16 GB of memory was 5843 seconds for the 31st lagged Fibonacci generator, and 21806 seconds for the 100th lagged Fibonacci generator, respectively. On the other hand, the corresponding computation times for δ_{ap} were only 1.2 seconds and 2.4 seconds, respectively.

Table 1. Results of the weight discrepancy test on the lagged-Fibonacci generator $x_{31+i} = x_{28+i} + x_i$ ($s_0 = 10$)

n (bit)	1	2	3
# of terms of $W_{C^\perp}$	4	20	120
# of terms of $\mathscr{W}_{C^\perp}$	2	4	8
δ_{ex}	1.24767×10^{-3}	3.11161×10^{-4}	7.77432×10^{-5}
δ_{ap}	1.24364×10^{-3}	3.10910×10^{-4}	7.77275×10^{-5}
$(\delta_{ap} - \delta_{ex})/\delta_{ex}$	-3.2289×10^{-3}	-8.0827×10^{-4}	-2.0213×10^{-4}
n (bit)	4	5	6
# of terms of $W_{C^\perp}$	816	5984	45760
# of terms of $\mathscr{W}_{C^\perp}$	16	32	64
δ_{ex}	1.94328×10^{-5}	4.84803×10^{-6}	1.21450×10^{-6}
δ_{ap}	1.94319×10^{-5}	4.85797×10^{-6}	1.21449×10^{-6}
$(\delta_{ap} - \delta_{ex})/\delta_{ex}$	-5.0538×10^{-5}	-1.2635×10^{-5}	-3.1587×10^{-6}

Table 2. Results of the weight discrepancy test on the lagged Fibonacci generator $x_{100+i} = -x_{63+i} + x_i$ ($s_0 = 30$)

n (bit)	1	2	3
# of terms of $W_{C^\perp}$	4	20	120
# of terms of $\mathscr{W}_{C^\perp}$	2	4	8
δ_{ex}	5.08657×10^{-5}	1.27154×10^{-5}	3.17878×10^{-6}
δ_{ap}	5.08601×10^{-5}	1.27150×10^{-5}	3.17875×10^{-6}
$(\delta_{ap} - \delta_{ex})/\delta_{ex}$	-1.1139×10^{-4}	-2.7849×10^{-5}	-6.9623×10^{-6}
n (bit)	4	5	6
# of terms of $W_{C^\perp}$	816	5984	45760
# of terms of $\mathscr{W}_{C^\perp}$	16	32	64
δ_{ex}	7.94690×10^{-7}	1.98672×10^{-7}	4.96680×10^{-8}
δ_{ap}	7.94688×10^{-7}	1.98672×10^{-7}	4.96680×10^{-8}
$(\delta_{ap} - \delta_{ex})/\delta_{ex}$	-1.7406×10^{-6}	-4.3515×10^{-7}	-1.0879×10^{-7}

In both cases, $\mathscr{W}_{C^\perp}$ approximates the chi-squared discrepancy with sufficient accuracy despite involving fewer terms.

We also compute δ_{ap}'s corresponding to the ninth to 24-th LSBs of the lagged Fibonacci generator based on (3) and (31). Results of all cases are listed in Table 3. Based on these results, we infer that the chi-squared discrepancy is multiplied by a factor of $1/4$ when the examined bit is shifted to the left.

In order to confirm the accuracy of δ_{ap}, we apply the chi-squared GOF test to the tenth and 15-th LSBs of the generators. Tables 4–7 present the p-values corresponding to ten random initial values for each experiment. As expected, the GOF test with the safe sample size does not detect the deviation. On the other hand, the test with the risky sample size often rejects the sequence with the significance level of 0.01.

4. Concluding Remarks

In the previous section, we observed that discarding the lower bits can reduce the discrepancy between the empirical distribution and the expected binomial distribution. While this is a natural phenomenon, it does not always hold true.

Table 3. Values of δ_{ap} for the lagged Fibonacci generators of $x_{31+i} = x_{28+i} + x_i$ and $x_{100+i} = -x_{63+i} + x_i$

bit	9	10	11	12
31st	1.89764×10^{-8}	4.74411×10^{-9}	1.18603×10^{-9}	2.96507×10^{-10}
100th	7.76063×10^{-10}	1.94016×10^{-10}	4.85039×10^{-11}	1.21260×10^{-11}
bit	13	14	15	16
31st	7.41267×10^{-11}	1.85317×10^{-11}	4.63292×10^{-12}	1.15823×10^{-12}
100th	3.03150×10^{-12}	7.57874×10^{-13}	1.89468×10^{-13}	4.73671×10^{-14}
bit	17	18	19	20
31st	2.89557×10^{-13}	7.23893×10^{-14}	1.80973×10^{-14}	4.52435×10^{-15}
100th	1.18418×10^{-14}	2.96045×10^{-15}	7.40110×10^{-16}	1.85029×10^{-16}
bit	21	22	23	24
31st	1.13109×10^{-15}	2.82749×10^{-16}	7.07102×10^{-17}	1.76889×10^{-17}
100th	4.62571×10^{-17}	1.15633×10^{-17}	2.89177×10^{-18}	7.23407×10^{-19}

Table 4. p-values of the GOF test on the tenth LSB of $x_{31+i} = x_{28+i} + x_i$ ($*$: less than 0.01)

$N_r = 3.3 \times 10^9$	2.7E-02	*5.4E-06	3.2E-01	*6.2E-06	*9.3E-05
(risky)	1.2E-02	*5.2E-05	*1.6E-04	3.6E-02	*6.1E-03
$N_s = 6.8 \times 10^8$	1.1E-01	1.9E-01	7.8E-02	*7.4E-04	5.8E-01
(safe)	*5.9E-03	2.2E-01	4.4E-01	8.9E-02	9.8E-01

Table 5. p-values of the GOF test on the 15-th LSB of $x_{31+i} = x_{28+i} + x_i$ ($*$: less than 0.01)

$N_r = 3.310^{12}$	*8.7E-05	*1.6E-04	2.5E-02	*3.8E-05	3.6E-06
(risky)	2.9E-02	*2.7E-03	2.9E-01	*1.3E-03	*4.5E-03
$N_s = 6.9 \times 10^{11}$	1.7E-01	4.4E-01	1.2E-01	5.4E-01	3.1E-02
(safe)	8.7E-01	1.5E-01	1.1E-01	6.1E-01	1.2E-01

Table 6. p-values of the GOF test on the tenth LSB of $x_{100+i} = -x_{63+i} + x_i$ ($*$: less than 0.01)

$N_r = 1.3 \times 10^{11}$	*4.1E-04	*3.7E-04	*2.1E-03	*3.1E-03	8.9E-02
(risky)	*3.6E-05	*8.6E-04	1.8E-02	2.5E-02	*4.0E-03
$N_s = 3.0 \times 10^{10}$	7.2E-01	1.7E-01	1.7E-01	*6.9E-03	9.4E-02
(safe)	5.8E-01	3.8E-01	1.9-01	2.5E-02	1.2E-01

Table 7. p-values of the GOF test on the 15-th LSB of $x_{100+i} = -x_{63+i} + x_i$ ($*$: less than 0.01)

$N_r = 1.3 \times 10^{14}$	*8.2E-06	2.2E-01	1.6E-01	1.8E-01	7.5E-02
(risky)	9.3E-02	2.2E-02	*1.9E-03	1.9E-01	*7.1E-03
$N_s = 3.1 \times 10^{13}$	9.1E-01	7.3E-01	7.8E-02	8.0E-01	1.5E-02
(safe)	6.0E-01	4.4E-01	3.0E-02	3.9E-01	4.3E-02

In the rest of this section, we consider a nine-term Multiple Recursive Generator (MRG) of order 40, defined by the recursion

$$x_{40+i} := x_{38+i} + x_{22+i} + x_{21+i} + x_{18+i} + x_{10+i} + x_{4+i} + x_{2+i} + x_i \pmod{2^n}. \quad (32)$$

The characteristic polynomial of this recurrence is primitive over $\mathbb{F}_2$ [18].

For $m = 45$ and $s_0 = 12$, the (exact) chi-squared discrepancies of the MRG are 3.36294×10^{-12} for $n = 3$ and 1.55491×10^{-11} for $n = 4$. Thus, the chi-squared dis-

crepancy of the fourth LSB is approximately 4.6 times larger than that of the third. This implies that discarding the lower bits worsens the bit distribution.

Table 8 presents the chi-squared GOF test results for the third and fourth LSBs of the nine-term MRG. The sample size of the GOF test is 1.2×10^{12}, which is roughly equal to the risky sample size for the fourth LSB. The safe sample size for the third LSB is approximately 1.7×10^{12}. The GOF test does not detect any deviations for the sequences generated by the third bit. In contrast, sequences of the fourth LSB are often rejected with the significance level of 0.01.

Table 8. p-values of the GOF test on the 9-term MRG

3rd LSB	3.0E-01	7.5E-02	4.9-01	3.1E-01	7.7E-01
	6.4E-01	1.9E-02	4.1E-01	4.6E-02	2.4E-01
4th LSB	1.2E-02	1.3E-01	*1.9E-03	*4.0E-03	*8.1E-03
	3.2E-02	*5.6E-03	2.7E-01	*3.8E-05	8.4E-02

In this paper, we investigated chi-squared discrepancies solely through empirical analysis. In future works, we aim to provide a theoretical examination of the truncated polynomial $\mathscr{W}_{C^\perp}$. Lagged Fibonacci generators can be viewed as three-term MRGs. A straightforward method to enhance the randomness of MRGs is by increasing the number of terms, which raises the minimum Hamming weight of $C^\perp$. Consequently, another objective for future research is to explore the relationship between χ^2-discrepancies and the number of terms in MRGs.

Acknowledgements

The authors would like to thank the referees for many helpful comments. This work was supported by JSPS KAKENHI Grant Numbers 17K14234, 19K03450, 22K03415, and 23K03033.

References

[1] Kneusel RT. Random Numbers and Computers. Switzerland :: Springer,; ©2018. Include index. doi:10.1007/978-3-319-77697-2.

[2] Kroese DP, Taimre T, Botev ZI. Handbook of Monte Carlo Methods. Wiley; 2011. doi:10.1002/9781118014967.

[3] Plimpton S. Fast Parallel Algorithms for Short-Range Molecular Dynamics. Journal of Computational Physics. 1995;117(1):1 19. Available from: http://lammps.sandia.gov. doi:10.1006/jcph.1995.1039.

[4] Thompson AP, Aktulga HM, Berger R, Bolintineanu DS, Brown WM, Crozier PS, et al. LAMMPS - a flexible simulation tool for particle-based materials modeling at the atomic, meso, and continuum scales. Comp Phys Comm. 2022;271:108171. doi:10.1016/j.cpc.2021.108171.

[5] L'Ecuyer P, Simard R. TestU01: a C library for empirical testing of random number generators. ACM Trans Math Software. 2007;33(4):Art. 22, 40. doi:10.1145/1268776.1268777.

[6] Bassham LE, Rukhin AL, Soto J, Nechvatal JR, Smid ME, Barker EB, et al. SP 800-22 Rev. 1a. A Statistical Test Suite for Random and Pseudorandom Number Generators for Cryptographic Applications. Gaithersburg, MD, USA; 2010.

[7] Matsumoto M, Nishimura T. A Nonempirical Test on the Weight of Pseudorandom Number Generators. In: Monte Carlo and quasi-Monte Carlo methods, 2000 (Hong Kong). Berlin: Springer; 2002. p. 381-95. doi:10.1007/978-3-642-56046-0_26.

[8] Haramoto H, Matsumoto M, Nishimura T. Computing conditional probabilities for $\mathbb{F}_2$-linear pseudorandom bit generators by splitting MacWilliams identity. Int J Pure Appl Math. 2007;38(1):29-42.

[9] Haramoto H, Matsumoto M, Nishimura T, Otsuka Y. A Non-empirical Test on the Second to the Sixth Least Significant Bits of Pseudorandom Number Generators. In: Dick J, Kuo FY, Peters GW, Sloan IH, editors. Monte Carlo and Quasi-Monte Carlo Methods 2012. Berlin, Heidelberg: Springer Berlin Heidelberg; 2013. p. 417-26. doi:10.1007/978-3-642-41095-6_19.

[10] Wasserman L. All of Statistics: A Concise Course in Statistical Inference. Springer Texts in Statistics. Springer; 2004. doi:10.1007/978-0-387-21736-9.

[11] Vardy A. The intractability of computing the minimum distance of a code. IEEE Transactions on Information Theory. 1997;43(6):1757-66. doi:10.1109/18.641542.

[12] MacWilliams FJ, Sloane NJA. The theory of error-correcting codes. I. North-Holland Publishing Co.; 1977.

[13] Klemm M. Selbstduale Codes über dem Ring der ganzen Zahlen modulo 4. Archiv der Mathematik. 1989 Aug;53:201-7. doi:10.1007/BF01198572.

[14] Vattulainen I, Ala-Nissila T, Kankaala K. Physical Tests for Random Numbers in Simulations. Phys Rev Lett. 1994 Nov;73:2513-6. doi:10.1103/PhysRevLett.73.2513.

[15] Matsumoto M, Kurita Y. Strong deviations from randomness in m-sequences based on trinomials. ACM Trans Model Comput Simul. 1996 apr;6(2):99–106. doi:10.1145/232807.232815.

[16] Bremaud P. Mathematical Principles of Signal Processing: Fourier and Wavelet Analysis. Springer New York; 2002. doi:10.1007/978-1-4757-3669-4.

[17] Knuth DE. The Art of Computer Programming, Volume 2 (3rd ed.): Seminumerical Algorithms. Addison-Wesley; 1997.

[18] Lidl R, Niederreiter H. Finite Fields. 2nd ed. Encyclopedia of Mathematics and its Applications. Cambridge University Press; 1996.

Fuzzy Systems and Data Mining X
A.J. Tallón-Ballesteros (Ed.)

doi:10.3233/FAIA241399

A Fuzzy Measurement-Based Algorithm for Spoken English Evaluation

Jinwei Dong[1], Ziting He , Hao Chen, Jinchun Zhang and Limin Zhi
Guangdong University of Foreign Studies, Guangzhou, China
ORCiD ID: Ziting He https://orcid.org/0009-0009-3795-4741,
Hao Chen https://orcid.org/0009-0004-2883-4178

Abstract. This study explored an improved English language evaluation algorithm for virtual learning environments, particularly in metaverse educational settings. By integrating big data analysis with fuzzy measure theory, the model extracted learners' language usage habits, progress, and difficulties from large datasets, overcoming the limitations of traditional subjective evaluation methods. Fuzzy measures quantified subjective factors such as clarity, fluency and intonation, while a Sugeno integral approach combined these measures into an overall score. Comparisons with traditional methods have shown significant improvements in the assessment of speaking skills across a range of proficiency levels.

Keywords. English Speaking Evaluation, Metaverse Learning, Fuzzy Measure

1. Background Information

The digital transformation of education has given rise to the Metaverse, an emerging virtual reality space that has the potential to revolutionise the field of education, particularly in the context of English language learning. Among the various forms of English learning available in the Metaverse, oral English learning is particularly prominent. The evaluation of spoken English based on a big data analysis differs from the traditional evaluation of spoken English. In the process of determining the weights of the indicators, the machine learning algorithm can employ a purely mathematical approach to calculate the degree of importance of the indicators that are susceptible to human experience. Consequently, the impact of subjective factors on the evaluation results is minimal, thereby effectively addressing the problem of evaluation accuracy.

2. Current Research at Home and Abroad

In recent years, scholars at home and abroad have explored the potential applications of meta-universe in language learning. This has included the proposal of a meta-universe learning system [1], the creation of experiential learning in meta-universe environments [2], and the establishment of campus meta-universe models. These models emphasise

[1] Corresponding Author: Jinwei Dong, School of English Education, Guangdong University of Foreign Studies, China; Email: 200110581@oamail.gdufs.edu.cn.
This study is financially supported by the Undergraduate Innovation Training Project of Guangdong University of Foreign Studies in 2024.

the potential benefits of meta-universe applications in enhancing teaching effectiveness and promoting pedagogical reform. In terms of spoken English evaluation, research has concentrated on utilising intelligent speech recognition technology, natural language processing and machine learning algorithms to automatically assess pronunciation accuracy, fluency, vocabulary utilisation and grammatical structure. For instance, studies have been conducted on intelligent assessment algorithms for spoken English pronunciation quality [3], a spoken language assessment system capable of providing real-time feedback [4] and a system for correcting and improving spoken pronunciation [5]. The implementation of these studies on English-speaking learning platforms has shown preliminary outcomes. However, more precise and individualized speaking assessment models can be developed through the integration of big data analysis with learners' linguistic habits and learning requirements.

3. English Speaking Evaluation Algorithm

Despite the automation and intelligence that have been incorporated into the existing spoken English evaluation system, it still needs improvement in terms of accuracy and personalisation. In order to further align with learners' language preferences and learning objectives, it is necessary to integrate big data analysis technology to enhance and refine the spoken English evaluation algorithm.

3.1. Features of Spoken English and Speech Recognition Technology

Some features of spoken English include liaison and pronunciation confusion. As a phonological phenomenon, Liaison occurs when, according to specific phonological rules, the final sound of a word blends seamlessly with the beginning sound of the word immediately following it. This smooth transition in pronunciation gives the listener the impression that the two words share a syllabic boundary. Pronunciation confusion, on the other hand, arises when the pronunciations of specific words become so similar as to be indistinguishable. The evaluation of speech typically relies on continuous speech recognition technology, which is scored by evaluating criteria such as pronunciation accuracy, speech similarity, speech rate and duration. Moreover, a posteriori probabilities are employed to evaluate mathematical models to ensure the accuracy of the assessment results. The process of automatic speech recognition typically comprises three principal stages, as illustrated in Figure 1.

The initial stage is the construction of the model library [6], which establishes sound databases in accordance with the pronunciation characteristics of natural language. This enables the system to utilise these pronunciation models to perform matching searches. The second stage is feature extraction, which encompasses the collection of acoustic signals, the conversion of human pronunciation into a format that can be understood by the machine, and the elimination of background noise. The final stage is information matching, whereby the extracted speech features are fed into a decoder. The computer will then search for the most appropriate matches in the sound database based on the decoding results. The most similar matches are the result of computer recognition. The assessment of spoken English pronunciation represents a fundamental prerequisite for the successful implementation of automatic speech recognition technology.

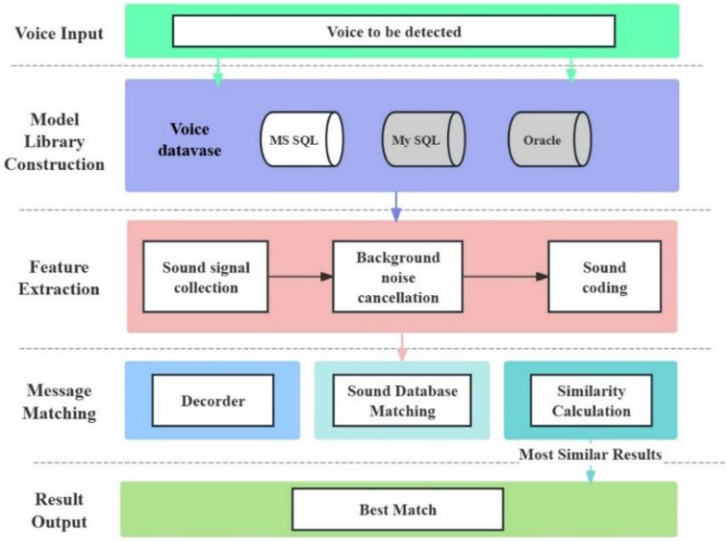

Figure 1. The process of automatic speech recognition

3.2. A Fuzzy Measurement-Based Algorithm for Spoken English Evaluation

In order to accurately quantify and address the problems of subjectivity, fuzziness and uncertainty in the field of language assessment, this paper proposed a flexible and refined evaluation framework that not only integrated multiple evaluation indicators, but also adapted to the specific needs of various types of learners. The objective of this framework is to develop a more precise, individualised and efficient system for evaluating oral English proficiency. In this paper, the features of spoken pronunciation were extracted using the deep learning technique Convolutional Neural Network (CNN). Subsequently, these features were applied to a fuzzy measure-based English-speaking evaluation algorithm to ensure comprehensive and in-depth evaluation results, thereby providing learners with more instructive advice.

3.2.1. Definition of Fuzzy Measures

The definition of fuzzy measure [7], as defined in spoken English evaluation algorithms, is based on fuzzy set theory and serves as a means of quantifying and addressing uncertainty and ambiguity in evaluation. A fuzzy measure μ is a mathematical function that maps a *set A* to a value between 0 and 1, indicating the degree of affiliation or importance of *set A* to an attribute. The closer this value is to 1, the higher the degree of membership of *set A* on that attribute, i.e., the better it represents or satisfies that attribute.

Formally, a fuzzy measure can be defined as follows:

$$\mu: 2^X \rightarrow [0,1] \tag{1}$$

Here, X represents a non-empty finite set that encompasses all potential evaluation features. 2^X denotes the power set of X, which is defined as the set of all subsets of X. The term (A) is used to denote the value of *set A* under the concept of fuzzy measure, reflecting the degree to which A fulfils the evaluation criteria.

In spoken language evaluation, the fuzzy measure can be employed to quantify features such as accuracy and fluency of pronunciation. This enables the transformation of qualitative evaluations of these features into quantitative analysis, thereby establishing a consistent and objective foundation for the evaluation of the algorithm. The membership function enables the fuzzy measure to represent the degree of affiliation of pronunciation features on different evaluation levels such as “excellent”, “good”, and so on, thereby providing a foundational framework for comprehensive evaluation.

3.2.2. Data Collection and CNN-Based Feature Extraction

In the meta-universe learning environment described in the previous section, a substantial corpus of spoken data from learners is available, including audio and video recordings. It should be noted that the data may contain background noise, unclear pronunciation and non-verbal sounds. The objective of data cleaning is to eliminate these distractions and guarantee that only unambiguous samples of spoken language are employed for analysis.

Subsequently, it is necessary to extract key linguistic features from the cleaned data. Convolutional neural networks (CNN) have demonstrated the potent capability for feature extraction in audio data. By inputting the preprocessed time-frequency representations into CNN, critical linguistic features can be effectively extracted from audio signals. In this paper, the CNN model was designated as the primary algorithmic model for audio feature extraction.

The pre-processed audio representations from the preceding stage were employed as the input to CNN. The convolutional layer of the CNN would learn to extract useful local features from the input data. In the convolutional layer, a convolutional kernel (also referred to as a filter) performs a convolution operation with local regions of the input data, thereby generating a feature map. The specific convolution operation can be expressed as follows: Here, x represents the time-frequency representation of the input, w denotes the weight of the convolution kernel, b signifies the bias term, f is the activation function, and y stands for the output of the convolutional layer. Following a series of trials, five 3X3 convolution kernels were ultimately identified, with a step size of 1 and the activation function set to ReLU.

$$y_{ll} = f\left(\sum_{m=0}^{M-1}\sum_{n=0}^{N-1} w_{mn}\, x_{(l+m)(j+n)} + b\right) \tag{2}$$

Here, x represents the time-frequency representation of the input, w denotes the weight of the convolution kernel, b signifies the bias term, f is the activation function, and y stands for the output of the convolutional layer. Following a series of trials, five 3X3 convolution kernels were ultimately identified, with a step size of 1 and the activation function set to ReLU.

After the convolutional layer, the pooling layer operation is introduced. The pooling layer aims to reduce the spatial size of the feature map, thereby increasing the sensory field of the network and reducing the amount of computation. The most common operations of pooling are maximum and average pooling. In this paper, the average pooling operation was selected, with a pooling kernel size of 2X2 and a step size of 2. This configuration enables the calculation of the average value within a local region in the audio as the output, which in turn reduces the dimensionality of the features while retaining the most important information.

After processing through multiple convolutional and pooling layers, the network generates several feature maps. These feature maps contain a set of hierarchical features extracted from the raw audio data. They can be regarded as abstract representations of

the audio signal, capturing key information and being used for subsequent speech evaluation tasks.

3.2.3. Construction of Fuzzy Comprehensive Evaluation Algorithm

The construction of the fuzzy comprehensive evaluation algorithm is a staged process, commencing with the selection of key evaluation indicator factors and the construction of a fuzzy judgement matrix. The algorithm employed the principle of fuzzy change to calculate the judgement matrix of the evaluation indicators, which typically comprises three principal stages: the construction of the fuzzy matrix, the selection of the fuzzy operator and the synthesis of the result vector. In the evaluation process, weights are assigned in accordance with the degree of influence exerted by different factors on the evaluation object. These weights are subsequently synthesised by means of fuzzy operators in order to obtain comprehensive evaluation results. In this paper, the accuracy, fluency, rhythm and intonation of pronunciation were selected as the evaluation indicators.

In constructing the fuzzy matrix, it is necessary to quantify each influencing factor. The degree of membership of each factor in the factor set is determined by defining the membership function. Commonly used membership functions include trigonometric, Gaussian and trapezoidal functions. In this paper, the trigonometric function was selected for calculation. It is defined mathematically as follows.

$$\mu(A) = \begin{cases} 0 & \text{if } |A| = 0 \\ \frac{1+\frac{|A|-\alpha}{\beta}}{2} & \text{if } 1 \le |A| \le L \\ 1 & \text{if } |A| > L \end{cases} \tag{3}$$

Here $|A|$ represents that the basis α and β of the feature *set A* are parameters that adjust the shape of the function and L is a preset threshold.

Furthermore, the Sugeno integral [8] was adopted to address the problem of fusion of different fuzzy measurements in developing the oral continuous reading evaluation model. The application of the Sugeno integral enables the algorithm to effectively assess the continuous reading group in accordance with the specific continuous reading context. To illustrate, if the continuous reading period exceeds two hours, the system will primarily assess the actual number of consecutive readings completed by the learner in order to ascertain the score for connected reading. This approach offers a more precise representation of the learner's performance in oral continuous reading.

3.2.4. Fuzzy Comprehensive Evaluation and Evaluation Result Outputs

For each evaluation indicator μ_i, the composite degree of membership (A) is calculated based on its membership function (A) and weight w_i:

$$\mu(A) = \sum_{i=1}^{n} w_i \cdot \mu_i(A) \tag{4}$$

This formula weights and sums the degree of membership of all indicators to obtain the composite membership degree. For the determination of the weights w_i associated with each evaluation indicator, here employed a machine learning approach using the Random Forest (RF) algorithm. This method leverages the ensemble learning technique

of multiple decision trees to estimate the importance of each feature, which in context corresponds to the evaluation indicators. The detailed information of the weights w_i is crucial for understanding the influence of each evaluation indicator on the overall assessment. For instance, consider a model for evaluating English oral proficiency with three assessment indicators, which is an important degree score that comes from the training of a Random Forest model: Pronunciation Clarity (u_1), Fluency (u_2), and Intonation (u_3). Employ the Random Forest (RF) algorithm to ascertain the weights for these indicators.

Dataset: A dataset of 1000 samples, each annotated with scores for the three assessment indicators and an overall evaluation grade.

Features and Target Variable: The features are Pronunciation Clarity (u_1), Fluency (u_2), and Intonation (u_3), with the target variable being the overall evaluation grade.

Training the Random Forest Model: A random forest model is trained on this dataset, which automatically computes the importance of each feature.

Feature Importance: Post training, the RF model provides importance scores for each feature. For instance:

- Pronunciation Clarity (u_1): 0.45
- Fluency (u_2): 0.30
- Intonation (u_3): 0.25

Normalization of Weights: These importance scores are normalized to ensure they sum up to one, maintaining the proportional influence of each indicator on the composite membership degree. The normalized weights w_i are:

$$\begin{aligned} w_1 &= \frac{0.45}{0.45+0.30+0.25} \approx 0.47 \\ w_2 &= \frac{0.30}{0.45+0.30+0.25} \approx 0.31 \\ w_3 &= \frac{0.25}{0.45+0.30+0.25} \approx 0.22 \end{aligned} \tag{5-7}$$

Application of Weights: These weights are applied to calculate the composite membership degree $\mu(A)$ for each sample.

Based on the calculated composite membership degree (A), the evaluation object is classified into the corresponding evaluation level. For example, the evaluation levels can be defined as “excellent”, “good”, “fair” and “poor”, with a threshold range of membership degree set for each level.

Finally, the results of the comprehensive evaluation are conveyed in a transparent and intelligible way to provide suitable feedback to the learners.

3.3. Algorithm Optimisation Strategy

In order to integrate fuzzy measures and provide different levels of assessment results, the algorithm employed the Sugeno integral [8], which is a special kind of fuzzy integral that is able to integrate multiple fuzzy measures to give an overall assessment. This method is capable of not only assessing individual articulations, but also continuous articulations, thereby providing more comprehensive and accurate results.

For each evaluation dimension, the degree of membership is calculated based on its fuzzy measure function, and then these degrees of membership are synthesised into a single value by using the Sugeno integral formula. The Sugeno integral is typically defined as the supremum of the minimum value or product of all membership degrees.

The processing of the difficult pronunciation set (HDP) refers to a specialised technique for the assessment of spoken English, specifically for the identification of confusable phonemes. Firstly, by analysing all possible pronunciations within English sentences, a database encompassing these pronunciations is constructed. Subsequently, when a learner pronounces a word, the system captures the pronunciation features and searches for the most matching pronunciation path in the database. This is then used as a basis for assessing the accuracy of the pronunciation and providing targeted feedback and suggestions for improvement.

The fundamental principle underlying the construction and utilisation of HDP sets is that it facilitates an in-depth analysis of learners' pronunciation patterns, particularly those error-prone phonemes. This approach not only assists learners in identifying and enhancing their challenging pronunciation but also enables a more sophisticated and tailored assessment of their performance, which can effectively enhance their speaking abilities and comprehension.

4. Experimental Results

4.1. Experiment Overview

In order to verify the validity of the English proficiency assessment model combining big data analysis with fuzzy measurement, a series of experiments were conducted with a total sample size of 100, ensuring a diverse representation of different proficiency levels, age groups, and language backgrounds. The aim is to test the ability of the model to accurately extract key information from learner data and effectively quantify the fuzzy factor of English ability through fuzzy measurement. After the experiment, we selected 5 samples from different populations through stratified sampling to compare the results. The study used data from learners of different levels, including individuals of different levels, ages, and backgrounds. In order to ensure the accuracy and reliability of the data, the data were cleaned and preprocessed, and about 5% of the outliers and noise data were eliminated. In addition, the assessment process is carefully reviewed by professional English teachers to ensure the accuracy and credibility of the results.

4.2. Analysis of Discrepancies

After comparison experiments we analyzed the differences between model and evaluator scores to identify potential areas for model improvement or to understand the variability of human assessments.Our enhanced fuzzy comprehensive evaluation model has been fortified with an expanded and diverse dataset. This enlargement has bolstered the model's robustness and its ability to provide nuanced assessments of learners' spoken English skills.

The membership degree remains a pivotal metric, reflecting the proficiency level of each learner across key dimensions: pronunciation clarity, fluency, and intonation. With these degrees, we can discern the proximity of a learner's performance to the ideal benchmarks, where values nearing 1.0 indicate exceptional proficiency. The incorporation of human evaluator scores has introduced a critical validation step, ensuring that our model's assessments are not only data-driven but also aligned with human judgment. The calculated average accuracies, ranging from 95.23% to 98.70%, reveal a remarkably high degree of congruence between the model's evaluations and

those of human evaluators. This affirms the reliability and trustworthiness of our model's outputs.The results highlight the model's efficacy in evaluating a wide array of learners, offering a nuanced understanding of their spoken English skills. The high average accuracy not only validates the model's dependability but also underscores its capacity to provide constructive feedback aimed at enhancing oral communication skills.

In summation, the fusion of big data analytics with fuzzy measurement theory has marked a significant leap forward in the domain of educational technology. Our model's improved accuracy and its capacity to deliver tailored feedback are instrumental in enriching the learning experience. This advancement lays a solid groundwork for the evolution of groundwork for the evolution of intelligent educational systems.

5. Conclusion

The implementation of English-speaking evaluation algorithms within the context of big data analysis on the Metaverse English learning platform presents a promising opportunity for enhancing the efficacy of English learning and the precision of English teaching. As a consequence of the ongoing advancement of information technology and the enhancement of algorithms through the analysis of big data, metaverse English learning will become increasingly intelligent and individualised. This will provide global English learners with an interactive, expansive and immersive English learning platform, thereby establishing a robust foundation for the development of a more intelligent, efficient and individualised metaverse English learning ecosystem.

References

[1] Suzuki SN, Kanematsu H, Barry DM, Ogawa N, Yajima K, Nakahira KT, Shirai T, Kawaguchi M, Kobayashi T, Yoshitake M. Virtual Experiments in Metaverse and their Applications to Collaborative Projects: The framework and its significance. Procedia Computer Science. 2020 Sep;176:2125-2132, doi: 10.1016/j.procs.2020.09.249.

[2] Sinha E. 'Co-creating' experiential learning in the metaverse- extending the Kolb's learning cycle and identifying potential challenges. The International Journal of Management Education. 2023;21(3):100875, doi: 10.1016/j.ijme.2023.100875.

[3] Xue, N. Analysis Model of Spoken English Evaluation Algorithm Based on Intelligent Algorithm of Internet of Things. Computational Intelligence and Neuroscience. 2022;2022(1):8469945, doi: 10.1155/2022/8469945.

[4] Wang J. Speech recognition sensors and artificial intelligence automatic evaluation application in English oral correction system. Measurement: Sensors. 2024;32:101070. doi:10.1016/j.measen.2024.101070.

[5] Sheng Y, Yang, K. Automatic Correction System Design for English Pronunciation Errors Assisted by High-Sensitivity Acoustic Wave Sensors. Journal of Sensors. 2021;2021(1):2853056, doi: 10.1155/2021/2853056.

[6] Lampert TA, Stumpf A, Gançarski P. An Empirical Study Into Annotator Agreement, Ground Truth Estimation, and Algorithm Evaluation. IEEE Transactions on Image Processing. 2016 Jun;25(6):2557-2572. doi:10.1109/TIP.2016.2544703.

[7] Zhao L, Liu Y, Chen L, Zhang J, Koomey JG. English oral evaluation algorithm based on fuzzy measure and speech recognition. Journal of Intelligent and Fuzzy Systems. 2019 Jul;37(1):241-248. doi: 10.3233/JIFS-179081.

[8] Enemegio R, Jurado F, Villanueva-Tavira J. Experimental evaluation of a Takagi-Sugeno fuzzy controller for an EV3 ballbot system. Applied Science. 2024;14(10):4103. doi:10.3390/app14104103

Fuzzy Systems and Data Mining X
A.J. Tallón-Ballesteros (Ed.)

doi:10.3233/FAIA241400

Overview of Interpolation Finite Difference Methods Enabling Unlimited High-Accuracy Numerical Calculations

Tsugio Fukuchi[1]
Tsubokura Ground-Survey and Design Ltd., Fukushima, Japan
ORCiD ID: Author Name https://orcid.org/0000-0002-5646-8361

Abstract. There are many different types of numerical analysis for partial differential equations. Numerical methods that have been studied over a long period of time and have been used in engineering practice include the finite difference method (FDM), finite element method (FEM), and boundary element method (BEM). This paper focuses on the FDM. Conventionally, numerical calculations using the FDM have mostly been performed with second-order accuracy. It usually guarantees a calculation accuracy of 3 to 4 significant figures, which is considered to be sufficient accuracy from an engineering perspective. We generally recognize that numerical calculations are approximate calculations. However, when the FDM is generalized in a way that incorporates the conventional theory, it becomes possible to perform unlimitedly high-accuracy numerical calculations, and it becomes possible to easily perform calculations that converge to a theoretical numerical solution with a certain number of significant figures. This type of numerical calculation system is defined as the interpolation FDM (IFDM). The essential requirement for the establishment of IFDM is the algebraic polynomial approximation of the (real number) analytic function. This paper describes this concept and outlines the theoretical features and computational examples of IFDM, which has three characteristics: (i) the ability to handle arbitrary domains and arbitrary boundary conditions, (ii) unlimited high-accuracy calculations, and (iii) high-speed calculations.

Keywords. Finite Difference Method, algebraic polynomial approximation, Unlimited High-Accuracy Calculation, High-Speed Calculation

1. Introduction

In numerical calculations using the FDM, the author makes a generalization that includes the conventional theory, finally, we expanded the concept of the FDM, which allows unlimited high-accuracy numerical calculations [1]. This new finite difference method was defined as the interpolation finite difference method (IFDM). In this paper, we outline the basic concepts of IFDM and calculation examples. “It is a phenomenological fact that most of the fundamental equations that arise in physics are second-order derivatives [2].” Physical phenomena in the continuum are expressed by second-order

[1] Corresponding Author, Tsugio Fukuchi, Tsubokura Ground-Survey and Design Ltd., Fukushima, Japan; Email: fkbandou@sunny.ocn.ne.jp

partial differential equations (PDEs), which are classified into three types: (i) parabolic PDE, (ii) elliptic PDE, and (iii) hyperbolic PDE [3]. It is a special case that a PDE has an analytical solution, and some numerical calculation methods are used to find the numerical solution. Numerical calculation methods that have been studied for a long time and used in engineering practice include the FDM, the finite element method (FEM), and the boundary element method (BEM). Each has its own unique characteristics and is an essential component of the overall picture of numerical computation of (partial) differential equations.

Regarding FDM, and FEM, which specify calculation points within a domain, the following evaluations are available [2]. FDM is the oldest method for numerical solutions of PDEs. On structured grids, the FDM is very simple and effective. It is especially easy to obtain higher-order schemes on regular grids. The disadvantage of the FDM is that certain conservation laws are not enforced unless special care is taken. Furthermore, the restriction to simple geometries is a significant disadvantage if complex flows are specified. FEM has an important advantage in being able to deal with arbitrary geometries. The principal drawback, shared by any method that uses unstructured grids, is that the matrices of the linearized equation are not as well structured as those for regular grids making it more difficult to find efficient solution methods.

The above evaluation regarding FDM and FEM is understood to be a common understanding up to now. However, neither of them can be established as a fixed doctrine, and there are many studies that utilize the strengths of each to overcome the difficulties. In that sense, there is diversity in research trends. FEM was originally developed for structural analysis, but is now being applied to the analysis of time-dependent phenomena such as heat diffusion and initial value problem [4,5,6]. To solve the grid generation problem, a meshless finite element method has been proposed [7]. For FDM, the idea of a generalized finite difference method has been introduced to freely handle irregular cross sections, and the concept of a meshless finite difference method has also been proposed [8]. There have also been some attempts to improve the accuracy of numerical calculations, and currently numerical calculations up to sixth-order accuracy have been published for the numerical analysis of the Poisson equation [9]. In principle, it would be important to perform numerical analysis of the same object using FDM and FEM and compare the characteristics of both, but this is beyond the scope of this paper. The author has also studied FDM from his own perspective, considered its ideal numerical calculation system, and published the results of his study one by one [10-25]. The author's research may also be one example of the diversity of research trends.

The (traditional) FDM is very simple and effective. If FDM could be applied to any domain and any boundary condition, enable highly accurate calculations, and be developed into a fast calculation method while maintaining its characteristics of simplicity, then such a numerical calculation method would be an ideal numerical calculation method. To achieve this, it is necessary to make some slight but essential conceptual changes to the conventional FD scheme. A characteristic of FDM is that the development of theory from 1D to 2D, and even from 2D to 3D, is often seen as a simple expansion of dimensions. (This may be a characteristic that FEM and BEM do not have.) Therefore, we will limit our explanation to 1D problems here. In the following, Section 2, we will reaffirm the meaning of solving finite difference equation (FDE) based on a numerical example of the 1D Poisson equation. Next, the algebraic polynomial approximation of the (real number) analytic function and the high-order FD scheme, which are essential requirements for the establishment of IFDM, will be explained. Section 3 describes the Runge function. It is confirmed that IFDM calculations using

overlap polynomials are independent of the Runge phenomenon. Section 4 summarizes the characteristics of IFDM and confirms its effectiveness.

2. Essential Requirements for the Establishment of IFDM

Continuum physical phenomena occur in three-dimensional space, and in this paper the 3D Poisson equation is expressed as follows:

$$\nabla^2_{(3)}u \equiv \frac{\partial^2 u}{\partial x^2} + \frac{\partial^2 u}{\partial y^2} + \frac{\partial^2 u}{\partial z^2} = f(x,y,z) \tag{1}$$

The ultimate goal is to perform a highly accurate numerical analysis of this equation in any domain and under any boundary conditions. The 1D Poisson equation is described as follows.

$$\nabla^2_{(1)}u \equiv \frac{\partial^2 u}{\partial x^2} \equiv u_{xx} \equiv u_{2x} = f(x) \tag{2}$$

The forcing term $f(x)$ is an analytic function that has no singular points on the domain including the endpoints. It is conventionally abbreviated as $\partial^2 u/\partial x^2 \equiv u_{xx}$, but since many higher-order derivative notations are required in the IFDM, it is expressed as $\partial^2 u/\partial x^2 \equiv u_{2x}$. In the IFDM calculation, the elliptic PDE is calculated using the pseudoacceleration method, where a pseudoacceleration term is added to the elliptic PDE and numerically analyzed as the parabolic PDE [13]. Therefore, the basic equation for the numerical calculation of the 1D Poisson equation, $\nabla^2_{(1)}u = f(x)$, is expressed as follows:

$$\partial u/\partial t \equiv u_t = u_{2x} - f(x) \tag{3}$$

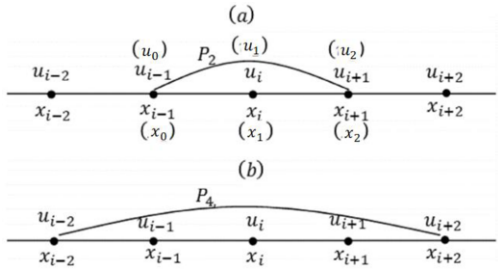

Fig. 1. Notations for second-order FD scheme and fourth-order scheme

As $t \to \infty$, $\partial u/\partial t \to 0$, and the convergent solution to Eq. (3) is the solution to $\nabla^2_{(1)}u = f(x)$. The FDE using the forward time-centered space (FTCS) scheme in Eq. (3) is expressed as follows:

$$u_i^{n+1} = u_i^n + \Delta t\left(P''_{2,x}(u_i^n) - f_i\right) \tag{4}$$

where, the second order accuracy FD scheme (FDS(2)) is defined as

$$P''_{2,x}(u_i^n) \equiv \frac{u_{i-1}^n - 2u_i^n + u_{i+1}^n}{h^2} \tag{5}$$

In Eq. (5), the FD scheme is used as a formula, but an equivalent result can be obtained as follows.

Referring to Fig.1, the three points $p_{i-1}^n(x_{i-1},u_{i-1}^n), p_i^n(x_i,u_i^n), p_{i+1}^n(x_{i+1},u_{i+1}^n)$ are written as $p_0(x_0,u_0), p_1(x_1,u_1), p_2(x_2,u_2)$. (It is common to define $(x_0=-h, x_1=0, x_2=h$.) The quadratic polynomial that passes through these three points is expressed as follows:

$$P_2(x) \equiv a_0 + a_1 x + a_2 x^2 \tag{6}$$

The following equation holds:

$$\begin{matrix} & \mathbf{X} & & \boldsymbol{a} & \boldsymbol{u} \\ \begin{bmatrix} 1 & x_0 & x_0^2 \\ 1 & x_1 & x_1^2 \\ 1 & x_2 & x_2^2 \end{bmatrix} & & \begin{bmatrix} a_0 \\ a_1 \\ a_2 \end{bmatrix} & = & \begin{bmatrix} u_0 \\ u_1 \\ u_2 \end{bmatrix} \end{matrix} \tag{7}$$

X is the Vandermonde matrix (VM), and we have the following representation:

$$\begin{matrix} \boldsymbol{a} & & \mathbf{C} \equiv \mathbf{X^{-1}} & & \boldsymbol{u} \\ \begin{bmatrix} a_0 \\ a_1 \\ a_2 \end{bmatrix} & = & \begin{bmatrix} c_{00} & c_{01} & c_{02} \\ c_{10} & c_{11} & c_{12} \\ c_{20} & c_{21} & c_{22} \end{bmatrix} & & \begin{bmatrix} u_0 \\ u_1 \\ u_2 \end{bmatrix} \end{matrix} \tag{8}$$

When it is necessary to specify the degree of the polynomial in the above expression, they will be written as $\mathbf{X}_m, \boldsymbol{a}_m, \boldsymbol{u}_m$, etc. respectively. The second derivative of Eq. (6) at x_1 is $P_2''(x_1) \equiv 2a_2$. (Due to the nature of quadratic expressions, $P_2''(x_i) \equiv 2a_2, i = 0,1,2$.) This can also be expressed from Eq. (8) as follows:

$$P_2''(x_1) = 2c_{20}u_0 + 2c_{21}u_1 + 2c_{22}u_2 \tag{9}$$

Actual numerical calculations show that whether we use Eq. (5) or $P_2''(x_1) \equiv 2a_2$ we get exactly the same results, including the convergence process. Furthermore, Eqs. (5) and (9) are also exactly equivalent. However, the method of utilizing $P_2''(x_1) \equiv 2a_2$ can only be applied to explicit methods such as the FTCS scheme, and in other high-speed calculations (fully implicit methods [16]), the expression of Eq. (9) is unavoidable.

The above method is the simplest way to derive an FD scheme for second-order derivatives through numerical calculations. There are many other discussions on deriving FD schemes [12,19,20], but for the purposes of this paper, this method is sufficient. It goes without saying that an FD scheme for first-order derivatives can also be derived instantly using a similar method. Already at this stage important generalizations have been made. In the definitions of $x_0=-h, x_1=0, x_2=h$, the calculation points are spaced equally apart, but the above discussion is also valid for $x_0=-h, x_1=0, x_2=\varphi h, ex.\ \varphi=0.5$. If necessary, $1<\varphi<2$ may be set.

In Fig. 2, there are two ways to define the FD scheme corresponding to the irregular distribution of calculation points that occurs at the right end (x_2). The first method is the SW scheme [26] published in 1938, which formalizes the FD scheme with irregular placement of calculation points, and is equivalent to the author's method [12]. The second method is the one adopted in the Ghost fluid method [27] published in 2002, which converts the irregular placement of computation points into a regular placement of

computation points by extrapolation and applies the formula, Eq. (5). Since the same quadratic formula is used, it is natural that the two values match numerically. Although it is usually not necessary to use $\varphi = 0.5$, etc., It may be $1 < \varphi < 2$, in the 1D Poisson equation, when this concept is extended to 2D and 3D domains it becomes a powerful tool for dealing with irregular domains. It can be further developed to set unstructured calculation points within the domain, if it is needed.

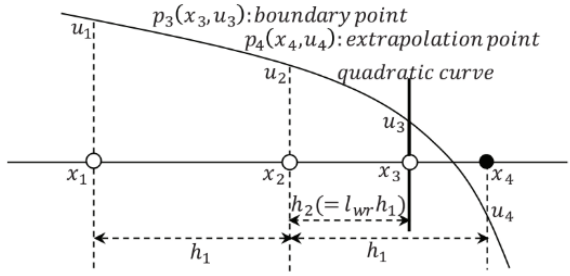

Fig. 2. Setting for the right boundary condition over irregular domain

The above discussion can be extended to the concept of high-order accuracy FD schemes. Figure 1(a) shows the second-order accuracy case, which in theory requires only central differences and is denoted as FDS(2,1). Figure 1(b) shows the case of fourth-order accuracy, which requires the definition of an FD scheme with three points, i.e., FDS(4,1), FDS(4,2) and FDS(4,3). If the number of divisions is $N_x = 10$, let us approximate this by $P_{10}(x)$. In this case, we need to define FDS$(10,k), k = 1,2,\cdots,9$. In the case of a fourth-order polynomial, it is expressed as follows:

$$P_4(x) \equiv a_0 + a_1 x + a_2 x^2 + a_3 x^3 + a_4 x^4 \tag{10}$$

$$P_4''(x) \equiv 2a_2 + 6a_3 x + 12a_4 x^2 \tag{11}$$

Then, Eq. (8) is expressed as follows:

$$\underset{\boldsymbol{a}_4}{\begin{bmatrix} a_0 \\ a_1 \\ a_2 \\ a_3 \\ a_4 \end{bmatrix}} = \underset{\mathbf{C}_4 = \mathbf{X}_4^{-1}}{\begin{bmatrix} c_{00} & c_{01} & c_{02} & c_{03} & c_{04} \\ c_{10} & c_{11} & c_{12} & c_{13} & c_{14} \\ c_{20} & c_{21} & c_{22} & c_{23} & c_{24} \\ c_{30} & c_{31} & c_{32} & c_{33} & c_{34} \\ c_{40} & c_{41} & c_{42} & c_{43} & c_{44} \end{bmatrix}} \underset{\boldsymbol{u}_4}{\begin{bmatrix} u_0 \\ u_1 \\ u_2 \\ u_3 \\ u_4 \end{bmatrix}} \tag{12}$$

Therefore, when $x = 0$, Eq. (11) can be expressed as follows:

$$P_4''(x_2) = 2c_{20}u_0 + 2c_{21}u_1 + 2c_{22}u_2 + 2c_{23}u_3 + 2c_{24}u_4 \tag{13}$$

In this case, it is necessary to define FDS(4,1), FDS(4,2) and FDS(4,3). This can be done by changing the zero point and calculating $\mathbf{X}_4^{-1}$ three times. However, if possible, it would be better to calculate the inverse matrix only once. Although we will not go into detail here, this is possible in principle by using Eqs. (11) and (12).

In placement of FD schemes, the computability is determined by whether all FD schemes overlap. There are countless possibilities for arranging overlapping polynomials. Polynomial placement of different orders may also be possible. However, to manage the calculation accuracy in IFDM, the order is always fixed. Figure 3 shows an example

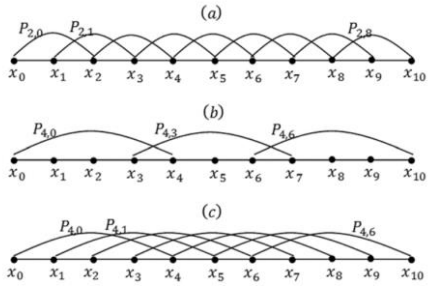

Fig. 3. Polynomial interpolation setting method (a) setting of second-order,

where the domain is divided into 10 equal parts ($N_x = 10$), and in FDS(2), the placement is unique. However, in FDS(4), many placements are possible, and when left-right symmetry is taken into account, two kinds of overlapping polynomials, (b) and (c), are possible. In the IFDM, only pattern (c) is adopted. This is called the standard fourth-order algebraic polynomial interpolation scheme and defined as SAPI(4). Other high-order accuracy numerical calculation methods include SOBI(m) and CIFD(m), which are described in the reference [25]. SOBI scheme: second-order based interpolation scheme, CIFD scheme: compact interpolation finite difference scheme

The above concepts can be easily extended to the general case. Suppose an analytic function $u(x)$ is approximated by the following algebraic polynomial:

$$u(x) \cong P_m(x) \equiv \sum_{i=0}^{m} a_i x^i \equiv a_0 + a_1 x + \cdots + a_m x^m, m = 2,4, \cdots, m_{max} \quad (14)$$

This polynomial approximation is important in all IFDM calculation methods. m can be either even or odd, but in IFDM, even numbers are used except in special cases [17]. m_{max} is the value of m at which the error is assumed to be minimal, and varies depending on several factors. However, it is clear that as the calculation precision increases, m_{max} also increases without limit. (In this paper, we distinguish between calculation accuracy and calculation precision. When we talk about double precision calculation, quadruple precision calculation, etc., we use the term “calculation precision.”)

Here, we will discuss the results of numerical calculations for a very simple function. In Fig. 4(a) the result of numerical calculations for $f(x) = 2$ is shown. Calculations are performed in double precision. Dirichlet boundary condition value is essentially arbitrary, but for the sake of simplicity, it is set as shown in the figure. A notable fact is that when calculations are performed using FDS(2), the numerical calculation error is zero. This type of calculation is defined as an intrinsic error zero (IE0) calculation. In theory, calculations using FDS(m), m = 4, 6, ... are of course IE0 calculations, but when m exceeds a certain value, the error becomes significant. This is thought to occur as a synergistic effect of roundoff error and truncation error [18].

Figure 4(a) also shows the numerical calculation results for the case $f(x) = \exp(x)$. The calculation error (average of absolute error) of FDS(2) is Er=1.3E-04. FDS(2) guarantees about four significant digits and has a wide range of application, and in such a graph of the calculation results, the results are indistinguishable from more accurate calculations. FDS(2) may be sufficient for most calculations in engineering problems. However, our realm of perception is constantly expanding. The author has dared to take on the problem of computational accuracy. Figure 4(b) is a log-log error diagram [1] of

the calculation error of $\nabla^2_{(1)}u = e^x$, calculated using SAPI(m). SAPI(2) is equivalent to the conventional second-order accuracy FD scheme. In the figure, AP-line(2) is shown as follows.

$$y = ax + b \rightarrow y = 2.0505x - 1.8404 \rightarrow log|Er| = 2.0505 \log h - 1.8404$$

AP-line means accuracy power line [1]. Under the condition of N_x =10,20,40, in SAPI(m) and double precision calculations, the AP-line can be clearly defined when m=2, 4, but is not defined when $m \geq 6$. The log-log error diagram is determined by the synergistic effect of the calculation precision, range of N_x, roundoff error, and truncation error. Actual accuracy power, $(a = 2.0505)$ is generally $a = m + \epsilon, 0 < \epsilon < 1$. The AP-line changes slightly depending on which part of the error is output, so "the correlation coefficient" is not 1.

High precision calculations are now generally possible [28]. The numerical calculations in this paper were performed using Microsoft Excel VBA. This is double precision calculation, but by introducing Microsoft Excel's Add-in, Xnumbers [29], developed by Professor Robert de Levie, calculations with arbitrary precision are

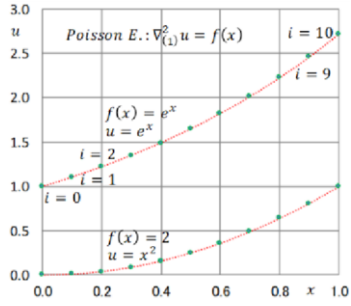

Fig. 4(a) Poisson equation calculation results

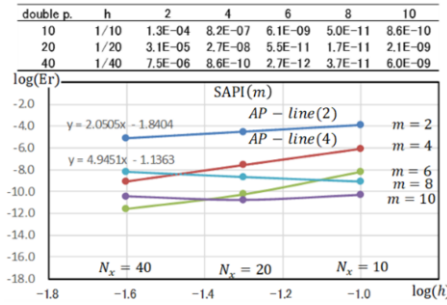

Fig. 4(b) log-log error diagram, double precision

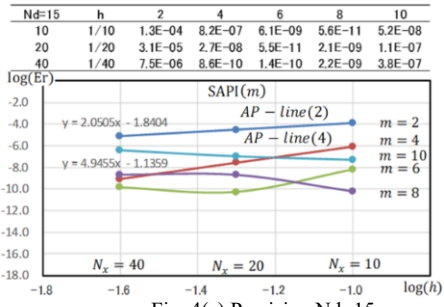

Fig. 4(c) Precision Nd=15

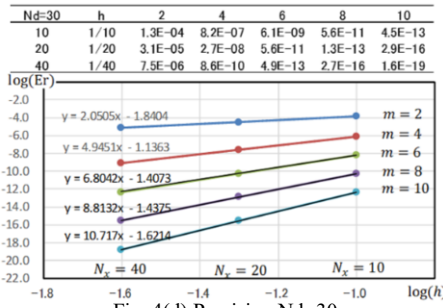

Fig. 4(d) Precision Nd=30

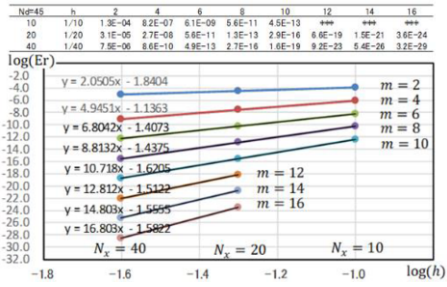

Fig. 4(e) Precision Nd=45

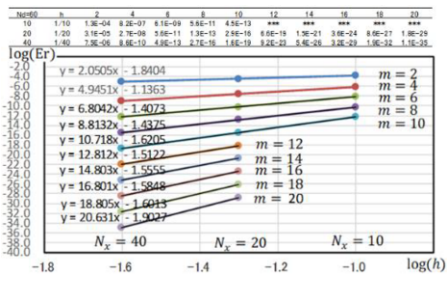

Fig. 4(f) Precision Nd=60

Double p.	h	2	4	6	8	10
10	1/10	1.3E−04	4.3E−08	7.7E−12	7.4E−16	1.3E−15
20	1/20	3.1E−05	2.6E−09	1.1E−13	2.7E−15	4.4E−15
40	1/40	7.5E−06	1.6E−10	4.6E−15	1.0E−14	6.4E−15

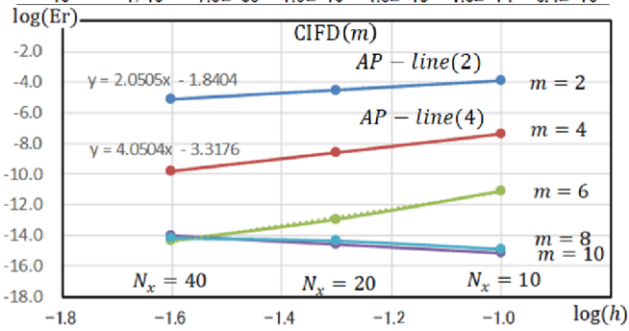

Fig. 4(g) Poisson equation calculation results, CIFD(m) log-log error diagram

possible. To perform calculations with 15 significant digits, specify digit number, Nd=15. This roughly corresponds to double precision calculation. The log-log error diagrams calculated for Nd=15, 30, 45, 60 are shown in Fig. 4(c),(d),(e),(f). The double precision calculation (Fig. 4(b) and the calculation for Nd=15 (Fig. 4(c) do not exactly match, but show a similar tendency. Fig. 4(d) For Nd=30, AP-lines are defined in all calculations for SAPI(m), $m = 2,4,\cdots,10$. Fig. 4(e) For Nd=45, AP-lines are defined up to m=16, and Fig. 4(f) for Nd=60, AP-lines are defined up to m=20. Generalizing the above tendency, it can be assumed that m_{max} in equation (14) can increase indefinitely as calculation precision increases. Abstractly, as Nd → ∞, there is a theoretical possibility that m → ∞. In this case, the AP-line will be uniquely defined in any range specified in the log-log error diagram display.

Figure 4(g) shows the result of CIFD(m), which is the most accurate calculation the author achieved in the 1D Poisson equation using double precision calculation. In this series of calculations, the maximum significant digits are about 15. (The Compact FD scheme has been defined up to sixth order accuracy [30], but in the CIFD scheme it was generalized in the 1D Poisson equation. The concept of the CIFD is also based on Eq. (14).) In this case, it is considered that there is almost no calculation error.

The following provisions exist regarding the convergence of FDM numerical calculations [3]. Convergence: A finite difference scheme is convergent if the solution of the finite difference equation approaches that of the PDE as the grid size approaches zero. In this sense, it may be possible to claim that the numerical calculation using FDS(2) can reduce the numerical calculation error without limit. According to the CIFD(m) scheme, which has the most effective convergence in the 1D Poisson equation, calculations with 15 significant figures are possible with about 5 calculation points at CIFD(14) [18] . Namely it is a VE0 calculation. On the other hand, in FSD(2), using $log|Er| = 2.0505\, log\, h - 1.8404$, the number of divisions when the significant number is 15 digits is approximately calculated as N_x=1.4×10^{13}. The crucial difference between the two is clear.

Finally, we revisit the numerical calculation of the Poisson equation. In IFDM, the pseudoacceleration method is basically used for the calculation of elliptic PDE. However, for the calculation of 1D Poisson equation, in FDS(m), the direct method using the TDMA (m=2) and BDMA (m≥4) algorithms is the fastest.[16] (TDMA: tridiagonal-matrix algorithm, BDMA: band diagonal matrix algorithm) This is because it does not

require repeated calculations. Because of the large amount of calculation, most of the calculations here are done using direct methods. The same results can be obtained using fully implicit methods. The convergence time is much shorter than that of explicit methods. However, it is generally difficult to use direct methods for the 2D Poisson equation, and a fully implicit method based on the alternating direction implicit (ADI) method is the fastest calculation method [17].

3. Runge phenomenon

There are cases where the expression in Eq. (14) is invalid. It is a well-known fact that the Runge phenomenon occurs when a function is approximated by an algebraic polynomial [24]. Figure 5 shows an example of approximating the Runge function with m =10 and m =12, and it can be seen that this function cannot be approximated by an algebraic polynomial in the range of [-1,1]. However, this is unrelated to the use of algebraic polynomials to improve the accuracy of the FD scheme. The Runge function is expressed as follows:

$$u = \frac{1}{1 + 25x^2} \tag{15}$$

The Runge phenomenon in Fig. 5 occurs when the entire domain is considered as one interval. However, the polynomial used in IFDM is a kind of piecewise polynomial, so the span of FDS(m) can be made as small as possible. Figure (6) shows the error evaluation when the Rung function is evaluated as a piecewise polynomial. The error is small at both ends and large in the center.

If this is the solution of the Poisson equation, $f(x)$ is defined as:

$$f(x) = \frac{50(-1 + 75x^2)}{(1 + 25x^2)^3} \tag{16}$$

The results of calculating this using double-precision calculation, CIFD(10) (CIFD: Compact interpolation finite difference) [18], are shown in Fig. 7. When $N_x = 100, m = 10$, the error is Er=3.1E-15. Namely, this is a VE0 calculation.

Now, let the range of the piecewise polynomial be D_k, and assume the following equation.

$$\sum_{k=1}^{K} D_k = D \tag{17}$$

D is the entire range, and in the above example, $D \rightarrow -1 \leq x \leq 1$. Each D_k is usually constant. If we think about it this way, even a "poor quality" function can be made into a "good quality" function by approximating it with a polynomial in each interval. The fact that double precision CIFD calculations become VE0 calculations is closely related to the above concept.

As the final discussion in Sections 2 and 3, we will confirm the meaning of Eq. (14) again. Many elementary functions have Taylor expansions. The following Maclaurin expansion is its special pattern.

$$g(x) = g(0) + g'(0)x + \frac{g''(0)}{2!}x^2 + \cdots + \frac{g^{(m)}(0)}{m!}x^m + R_{m+1} \tag{18}$$

Except for the Lagrange remainder term R_{m+1}, this is formally identical to the algebraic polynomial defined in Eq. (14). This statement also holds for the Taylor expansions. Approximation of a function using an algebraic polynomial is considered to have the same generality as the Taylor expansion of the function. Equation (18) is a power series expansion of the function, and it would be possible to define the convergence radius corresponding to each function. In general, the radius of convergence of the exponential function e^x is $r = \infty$. In other words, it is a function with good properties. The radius of convergence of Eq. (15) is unknown, but is likely to be quite small. In other words, it is a function with poor properties. However, even for functions with poor properties, if the interval width is set within the expected convergence radius, high-order polynomial approximation will be possible. This is the conclusion of Sections 2 and 3.

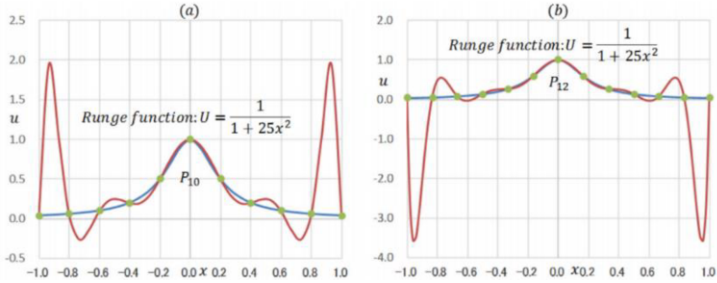

Fig. 5. Runge phenomena, (a) Runge function with 10th-order polynomial interpolation, (b) Runge function with 12th-order polynomial interpolation

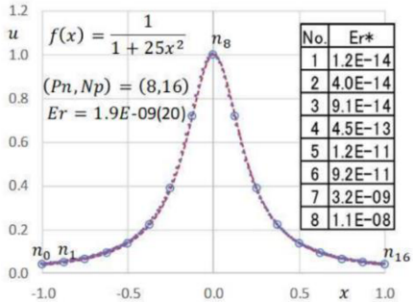

No.	Er*
1	1.2E-14
2	4.0E-14
3	9.1E-14
4	4.5E-13
5	1.2E-11
6	9.2E-11
7	3.2E-09
8	1.1E-08

Fig. 6 Runge function, approximate accuracy

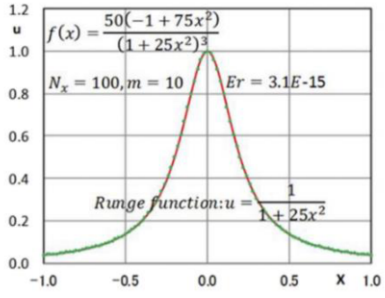

Fig. 7. Runge function, Poisson equation calculation accuracy

4. Conclusion

Conventionally, numerical calculations have been recognized as approximate calculations. However, the calculation method regarding IFDM becomes a numerical calculation system that allows unlimited high accurate calculations in an environment where any high precision calculations are possible. The essential requirement for the establishment of the IFDM numerical calculation system is the algebraic polynomial approximation of the function expressed by Eq. (14). If any single function or composite function can be reduced to an algebraic polynomial, then all calculus can be done by formal operations.

We have explained the case where the domain is one-dimensional, but this can naturally be expanded to two- and three-dimensional cases. Traditionally, the analysis of

equilibrium states has focused on how to generate the linear simultaneous equation, $\mathbf{Mu} = \mathbf{F}$. However, in IFDM numerical calculations, even in an elliptic PDE, numerical analysis is performed by starting from initial values and finding the converged value as a result of time marching. This method was defined as the pseudoacceleration method. It has the advantage of making it easier to handle non-Dirichlet boundary conditions [13,14,15]. In the FTCS scheme, which is a time-marching method, the calculation variables are replaced simultaneously. However, by adopting successive replacement, the number of steps required to converge is drastically reduced. This is defined as the time-marching successive-displacement (TMSD) method or scheme [11]. In FDS(2), this TMSD is a calculation equivalent to the successive over relaxation (SOR) method [2,11]. Furthermore, by adopting the time marching method, it becomes possible to employ a fully implicit method. In an explicit method, the time width Δt is limited, but in a fully implicit method, calculations are unconditionally stable and convergence is incomparably faster than with explicit methods.

Traditionally, FD schemes have been given as formulas. However, when dealing with several types of high-order accuracy calculations or irregular domains, "formalism" does not make sense. The FD scheme should be defined through numerical calculations before the numerical calculation routines. The same applies to 2D and 3D calculations.

We have described the limited case of the numerical analysis of the Poisson equation. However, all quadrature rules, starting with Simpson's rules, can be instantly defined by simply specifying m in a single system based on Eq. (14) [24]. It is also worth noting that while high accurate calculations of initial value problems have traditionally been performed using the fourth-order Runge-Kutter (RK4) method, the method based on polynomial approximation allows for VE0 calculations in most cases, and the calculations are completed instantly [22]. The algebraic polynomial approximation method (APAM) is a general term for the set of numerical methods (numerical differentiation, numerical integration, and numerical analysis of integral etc.) based on the concept of Eq. (14) that approximates an analytic function with an algebraic polynomial [24], and IFDM is part of that theory.

Although the numerical calculations of IFDM and APAM are considered to be new numerical calculation methods as a whole, they may not be sufficient from the perspective of mathematics and numerical calculation experts. I would appreciate the generous criticism of many scholars.

Finally, I would like to thank Shinji Tsubokura, President of Tsubokura Ground-Survey and Design Ltd., for his special consideration during the research process.

References

[1] T. Fukuchi, “Characteristic features of error in high-order difference calculation of 1D Poisson equation and unlimited high-accurate calculation under multi-precision calculation,” Mathematics and Computers in Simulation, 190(2021), 303-328. doi: 10.1016/j.matcom.2021.05.011

[2] J. H. Ferziger and M. Peric,´ Computational Methods for fluid Dynamics,” 3rd ed. (Springer, 2002), pp. 35–37.

[3] K. A. Hoffmann and S. T. Chiang, Computational Fluid Dynamics for Engineer-Volume I, Engineering Education System (Wichita, Kansas, 1993).

[4] P. Papadopoulos, “Introduction to the Finite Element Method”, Department of Mechanical Engineering, University of California, Berkeley, 2015

[5] Ireneusz Winnicki, Janusz M. Jasinski, “Finite Element Method in Hermitian Spaces in the Analysis of Irregular Atmospheric Processes, Conference Paper, 2018

[6] Md. Shafiqul Islam etc., “Numerical Solutions of IVP using Finite Element Metod with Taylor Series”,

[7] Jurica Sorić etc., "Meshless Approach as an Alternative to Finite, Element Method in Solid Mechanics Numerical Modeling", Izvorni znanstveni članak / Original scientific paper, 2019
[8] X. W. Huang1 · C. S. Wu1, A Meshless Finite Difference Method Based on Polynomial Interpolation, Journal of Scientific Computing (2019). doi: 10.1007/s10915-019-00952-z
[9] M. VAN DAELE etc., "Five-Diagonal Finite Difference Methods Based on Mixed-Type Interpolation for a Certain Fourth-Order Two-Point Boundary-Value Problem", Compstera Matin. Applić. Vol. 24, No. 10, pp. 55-76, 1992
[10] T. Fukuchi, "Numerical calculation of fully-developed laminar flows in arbitrary cross-sections using finite-difference method," AIP Advances 1(4), 042109 (2011). doi: 10.1063/1.3652881
[11] T. Fukuchi, "Numerical stability analysis and rapid algorithm for calculations of fully developed laminar flow through ducts using time-marching method," AIP Advances 3, 032101 (2013). http://dx.doi.org/10.1063/1.4794500
[12] T. Fukuchi, "Finite difference method and algebraic polynomial interpolation for numerically solving Poisson's equation over arbitrary domains," AIP Advances 4, 060701 (2014). http://dx.doi.org/10.1063/1.4885555
[13] T. Fukuchi, Numerical analyses of steady-state seepage problems using the interpolation finite difference method, Soils and Foundations, Jpn. Geotech. Soc. 54 (6) (2016) 608–626. doi: 10.1016/j.sandf.2016.07.003
[14] T. Fukuchi, New high-precision empirical methods for predicting the seepage discharges and free surface locations of earth dams validated by numerical analyses using the IFDM, Soils and Foundations, Jpn. Geotech. Soc. 58 (2018) 427–445. doi: 10.1016/j.sandf.2018.02.011
[15] T. Fukuchi, Accurate Empirical Calculation System for Predicting the Seepage Discharge and Free Surface Location of Earth Dam over Horizontal Impervious Foundation, MDPI, Eng 2020, 1, 60–95, http://dx.doi: 10.3390/eng1020005
[16] T. Fukuchi, High-order accurate and high-speed calculation system of 1D Laplace and Poisson equations using the interpolation finite difference method, AIP Adv. 9 (2019) 055312.. doi: 10.1063/1.5096395
[17] T. Fukuchi, "Higher order difference numerical analyses of a 2D Poisson equation by the interpolation finite difference method and calculation error evaluation," AIP Advances 10, 125009, (2020). doi: 10.1063/5.0018915
[18] T. Fukuchi, "A whole high-accuracy numerical calculation system for the 1D Poisson equation by the interpolation finite difference method", AIP Advances 12, 105315 (2022). doi: 10.1063/5.0093636
[19] T. Fukuchi, "Algorithm for deriving multidimensional space finite difference schemes using interpolation polynomials", ResearchGate preprint, 2022. doi: 10.13140/RG.2.2.17376.00002
[20] T. Fukuchi, "Exact calculation of multivariate finite difference schemes using multivariate Lagrange interpolation polynomial", ResearchGate preprint, 2022. doi: 10.13140/RG.2.2.35319.75689
[21] T. Fukuchi, "Calculation error estimation without assuming a theoretical solution in the numerical calculation of the 1D Poisson equation by IFDM", Research square preprint, 2022. doi: 10.21203/rs.3.rs-1748619/v2
[22] T. Fukuchi, "High-accuracy and high-speed calculation of second-order ODE by the interpolation finite difference method", Research square preprint, 2022. doi: 10.21203/rs.3.rs-1922411/v1
[23] T. Fukuchi, "Interpolation numerical integration method for extremely high-accuracy calculation of ordinary differential equations", Research square preprint, 2022. doi: 10.21203/rs.3.rs-2261296/v1
[24] T. Fukuchi, Interpolation numerical calculus for analytic functions by using algebraic polynomials", Research square preprint, 2023. doi: 10.21203/rs.3.rs-2742831/v1
[25] T. Fukuchi," A comprehensive high-accuracy numerical calculation system for the 2D Poisson equation by the interpolation finite difference method", Research square preprint, 2023. doi: 10.21203/rs.3.rs-3622031/v1
[26] G. H. Shortley and R. Weller, "The numerical solution of Laplace's equation," J. Appl. Phys. 24, 334–348 (1938).
[27] F. Gibou, R. P. Fedkiw, L. T. Cheng, and M. Kang, "A second-order-accurate symmetric discretization of the Poisson equation on irregular domains," Journal of Computational Physics, 176(1), 205–227 (2002).
[28] Web-List of arbitrary-precision arithmetic software, 2024. https://en.wikipedia.org/wiki/List_of_arbitrary-precision_arithmetic_software
[29] Web-Xnumbers, 2019, https://ipfs.io/ipfs/QmXoypizjW3WknFiJnKLwHCnL72vedxjQkDDP1mXWo6uco/wiki/XNUMBERS.html
[30] R. S. Hirsh, "Higher order accurate difference solutions of fluid mechanics problems by a compact differencing technique," J. Comput. Phys. 19, 90–109

Fuzzy Systems and Data Mining X
A.J. Tallón-Ballesteros (Ed.)

doi:10.3233/FAIA241401

A Novel Three-Way MAGDM Model Under Q-Rung Orthopair Hesitant Fuzzy Environment

Yuanyuan Chen[a], Xiuqin Ma[a,1], Hongwu Qin[a] and Yibo Wang[a]
[a] *College of Computer Science and Engineering, Northwest Normal University, China*
ORCiD ID: Xiuqin Ma: https://orcid.org/0000-0003-1569-460X

Abstract. Q-rung orthopair hesitant fuzzy set (q-ROHFS) is a powerful instrument for addressing uncertainty problems. Nevertheless, the classification methods of three-way multi-attribute group decision-making (TWD-MAGDM) under this new model have been seldom researched, and the current TWD-MAGDM method in a hesitant fuzzy environment fails to consider the psychological behavior and fuzzy correlation of decision-maker, resulting in not enough distinction among classified objects. To resolve this issue, we present a novel TWD-MAGDM classification model for a q-rung orthopair hesitant fuzzy (q-ROHF) environment. Firstly, this paper considers the fuzzy correlation by allocating weight through Shapely and combines the prospect theory and Gaussian function to develop a preference function that can accurately describe the loss and gain. Based on this function, it presents a relative utility function that can more accurately measure the utility. Secondly, we provide a conditional probability that considers psychological factors and has enhanced recognition capabilities. Finally, a novel TWD-MAGDM classification model for q-ROHF is provided based on the new relative utility function and conditional probabilities. We subsequently verify the efficacy of the proposed approach.

Keywords. Q-Rung orthopair hesitant fuzzy sets; Multi-attribute group decision-making; Three-way decision.

1. Introduction

Multi-attribute Group Decision Making (MAGDM) is a significant area of research in contemporary decision science. In the actual decision-making (DM) process, the decision-maker often conveys opinions with uncertainty due to the complexity of the problem and the environment. Thus, the DM problem in the interview background can be considered as a q-rung orthopair hesitant fuzzy[1] MAGDM (q-ROHF-MAGDM) problem. The ranking of objects is feasible with certain extant q-ROHF-MAGDM methods[2, 3]. However, the decision results of other objects are not identifiable. In response to the issues above, Yao[4] introduced the three-way decision-making (TWD) model. This model has enjoyed widespread application across various domains as an efficient approach to handling uncertainty based on human cognitive processes. Consequently, TWD-MAGDM (combining TWD and MAGDM) was proposed[5-7].

[1] Corresponding Author: Xiuqin Ma, College of Computer Science and Engineering, Northwest Normal University, Lanzhou, China; Email: maxiuqin@nwnu.edu.cn

For instance, Jiang et al.[5] developed a TWD-MAGDM categorical decision model to address the investment problem. Lei et al.[7] developed a TWD-MAGDM categorical decision model using Regret Theory (RT) to select water supply options.

However, the TWD-MAGDM approaches have different advantages and characteristics. They are insufficient in yielding reasonable results and suffer from numerous deficiencies when confronted with the complexity of real DM. The discriminability of current TWD-MAGDM classification methods is influenced by many factors, such as the inability to accurately evaluate loss (utility), identifying conditional probabilities using equivalence classes being limited in its capacity, and other factors. Furthermore, the MAGDM problem must consider a crucial factor, namely the impact of psychological behavior on decision results. However, the majority of the current MAGDM methods[2, 5, 6] fail to consider the impact of psychological behavior on accuracy. Finally, although the current MAGDM methods operate under the assumption that attributes are uncorrelated, there is a potential correlation between attributes during the actual DM process. To enhance the accuracy and differentiation of the classification model, the primary contributions of this paper are as follows. 1) The model considers the fuzzy correlation by allocating weight through Shapely and combines the prospect theory (PT)[8] and Gaussian function to develop a priority function that can accurately describe the loss and gain. Based on this function, it presents a relative utility function that can more accurately measure the utility. 2) The comparison objects derived from the priority function provide an objective conditional probability that considers psychological factors and has enhanced recognition capabilities. 3) A novel TWD-MAGDM classification model under a q-ROHF environment was given based on the novel relative utility function and conditional probabilities. The model enhances the distinctiveness of classification methods.

The subsequent portion of this investigation is presented below. Section 2 provides an overview of the q-ROHFS and its associated ideas. In Section 3, we introduce a novel relative utility function and a conditional probability, which serve as the foundation for proposing a new TWD model. In Section 4, we introduce a TWD-MAGDM approach and demonstrate its validity. Lastly, concluded in Section 5.

2. Preliminaires

Before introducing a novel model, we provide the definition and fundamental operations of q-ROHFS. Then, we review the fundamentals of regret theory, the λ-fuzzy Measure, and the Shapley index.

2.1. q-ROHFS

Definition 1[1]**.** Let $X = \{x_1, x_2, \dots, x_n\}$ be a fixed set. Then a q-ROHFS F on X is

$$F = \left\{ \langle x_i, \mu(x_i), v(x_i) \rangle_q \middle| x_i \in X \right\} \tag{1}$$

where $\mu(x_i)\ and\ v(x_i)$ are two sets of values in [0,1], which indicate qth rung possible membership degrees (MDs) and non-membership degrees (NMDs) of the element $x_i \in X$ to the set F, respectively. For a q-ROHFS, the conditions $0 \le \alpha, \beta \le 1, 0 \le (\alpha^+)^q + (\beta^+)^q \le 1$ must be met, where $\alpha \in \mu(x_i), \beta \in v(x_i)$ and $\alpha^+ = max_{\alpha \in \mu(x_i)}\{\alpha\}, \beta^+ =$

$max_{\beta \in v(x_i)}\{\beta\}$, for all $x_i \in X$. The pair $h_F = \left(\mu_F(u), v_F(u)\right)_q$ is represented as a q-rung orthopair hesitant fuzzy number (q-ROHFN). For convenience, a q-ROHFN is simplified to $h = (\mu, v)_q$. In addition, one important property of the q-ROHF hesitant degree π can be defined as $\pi = \left(1 - \frac{1}{l(\mu)}\sum_{\alpha\in\mu}\alpha^q - \frac{1}{l(v)}\sum_{\beta\in v}\beta^q\right)^{\frac{1}{q}}$, where $l(\mu)$ and $l(v)$ indicate the number of elements in μ and v, respectively.

2.2. Shapley index

In 1953, Shapley introduced the Shapley index[9]. The Shapley index assigns importance to each object based on its contribution to the combined information. Specifically, the Shapley index, derived from non-additivity measurements, incorporates the interrelationship of attributes.

Definition 6[10]. Suppose μ be a fuzzy measure on a finite set N. For any x ∈ N, the Shapley index is defined as follows:

$$S(\mu, N) = \sum_{S\subseteq N\setminus x} \frac{(N - |S| - 1)!\,|S|!}{N!}[\mu(S \cup x) - \mu(S)]. \tag{2}$$

2.3. RT

Loomes et al.[11] introduced a definition of RT that examines how the emotions developed when individuals compare their current circumstances with the past can affect choice outcomes. When decision-makers make a choice, they experience regret if they later understand that the alternative rejected was superior to the one selected. On the contrary, they have a sense of great joy.

The regret-joy function is a key component of RT. The object U_i is one of the members of a finite set. Let $\Delta U_1 = U_i - \max(U)$ and $\Delta U_2 = U_i - \min(U)$, respectively. The regret function $R(U_i)$ and the joy function $J(U_i)$ to measure the object difference are described as

$$R(U_i) = 1 - e^{-\sigma\Delta U_1}, \tag{3}$$

$$J(U_i) = 1 - e^{-\sigma\Delta U_2}, \tag{4}$$

where σ ∈ $[0, +\infty)$ is the regret aversion parameter, and greater values correspond to a higher level of regret avoidance.

3. Novel three-way decision model of q-ROHFS

3.1. The relative loss function of q-ROHFS

Liu et al.[12] introduced the relative loss function. This approach not only solves the problem but also reduces the computation of thresholds. Building upon this, Lei et al.[7] further extended the relative loss function to dual hesitant fuzzy environments. Subsequently, Zhan et al.[13] introduced the notion of a relative utility function.

Nevertheless, the approach above fails to consider the psychological behavior of the object itself when computing the relative utility function and relative loss function, which is inconsistent with reality. In previous MCGDM investigations[7], the comparison object is frequently selected based on its relation to the maximum or minimum of the dual hesitant fuzzy numbers. The optimal scheme is determined by assigning MDs a value of 1 and NMDs a value of 0, resulting in the full disregard of NMDs. Similarly, the selection for the most unfavorable scheme is when all MDs are set to 0, and all NMDs are set to 1, resulting in the complete disregard of the MDs. Thus, we construct a novel relative utility function to address these issues. The method steps are as follows.

For a q-ROHFN decision matrix $H = \left[h_{ij}\right]_{m\times n}$ with an object set $O = \{o_1, o_2, \dots, o_m\}$ and an attribute set $A = \{a_1, a_2, \dots, a_n\}$. $h_{ij} = \left(\mu_{ij}, v_{ij}\right)_q$ represents the evaluation value of the object o_i under the attribute a_j.

We utilize the standard PROMETHEE II[14] method to calculate the deviation $\mathrm{D}(\mathrm{h_{ik}}, \mathrm{h_{jk}})$ between objects o_i and o_j for the attribute a_k. We have selected the "smooth" Gaussian function from reference[15] as the preference function. We evaluate the value of gain and loss for different objects based on PT. Then, we determine the preference function $P(h_{ik}, h_{jk})$ for objects o_i and o_j under the attribute a_k, the preference function $\mathrm{P}(h_{ik}, h_{jk})$ can be considered a gain or a loss.

The Shapely index approach, introduced by Shapley et al. in 1953, allows us to determine the Shapely index of an attribute using the λ-fuzzy measure. Consider a set of attributes $A = \{a_1, a_2, \dots, a_n\}$. Let μ represent the fuzzy measure of this set of attributes. According to Equation (2), the Shapely index of the attribute a_k can be obtained

Let the weight of the attribute a_k is denoted as w_k equal to $w_k = S_k(\mu, A)$. We have the preference function and attribute weights $\mathrm{W} = \{w_1, w_2, \dots, w_n\}$. Then, the multi-attribute preference index for each pair of objects

$$\psi(o_i, o_j) = \sum_{k=1}^{n} w_k \, P(h_{ik}, h_{jk}), \tag{5}$$

where $\psi(o_i, o_j)$ represents the extent to which the alternative o_i is superior to o_j.

Ultimately, the entering flow $\phi^+(o_i) = \frac{1}{m}\sum_{j=1}^{m} \psi(o_i, o_j)$ and the leaving flow $\phi^-(o_i) = \frac{1}{m}\sum_{j=1}^{m} \psi(o_j, o_i)$ for each object are determined by the preference index and the thought that the object is better when it has a bigger leaving flow, and the bigger entering flow, the worse the object is. We get the best object $o^+ = \max\{\phi^-(o_i)\}$ and the worst object $o^- = \max\{\phi^+(o_i)\}$ by comparing objects with relative utility functions. Subsequently, the preference index $\psi(o_i, o_j)$ is used as the utility value to calculate the relative utility function based on Zhan et al.[13]. Finally, we have a state set $\Omega = \{\mathrm{C}, \mathrm{C}^\tau\}$ and an action set $\mathbb{A} = \{\mathrm{a_P}, \mathrm{a_B}, \mathrm{a_N}\}$, the relative utility functions provided in Table 1.

Table 1 The relative utility function.

o_i	C	C^τ
a_P	$O^{\mathrm{i}}_{\mathrm{PP}}$=ψ($o_i$, o^-)	O^{i}_{PN}=0
a_B	$O^{\mathrm{i}}_{\mathrm{BP}}$= ζ · ψ($o_i$, o^-)	$O^{\mathrm{i}}_{\mathrm{BN}}$=ζ · ψ($o^+$, o_i)
a_N	O^{i}_{NP}=0	$O^{\mathrm{i}}_{\mathrm{NN}}$=ψ($o^+$, o_i)

3.2. The conditional probability of q-ROHFS

Subsequently, we will construct the fundamental method for the conditional probability. Lei et al.[7] obtained conditional probability using a score function in the same environment. However, to calculate the conditional probability of the q-ROHFS environment, the following issues need to be addressed: 1) how to calculate the conditional probability using the dominance relationship under the q-ROHFS environment; 2) how to incorporate the decision-maker's psychological behavior into the calculation of the conditional probability to ensure a more realistic result; 3) the selection of the object of comparison is a critical factor, and the selection of the object of comparison tends to be at the two extremes when calculating the regret function. Thus, we construct a novel conditional probability to address these issues.

To begin with, for a q-ROHFN decision matrix $H = \left[h_{ij}\right]_{m\times n}$ with an object set $O = \{o_1, o_2, \dots, o_m\}$ and an attribute set $A = \{a_1, a_2, \dots, a_n\}$. $h_{ij} = \left(\mu_{ij}, v_{ij}\right)_q$ represents the evaluation value of the object o_i under the attribute a_j. In accordance with the concept of PROMETHEE II, the comparison object is obtained to determine the best object $o^+ = \max\{\phi^-(o_i)\}$ and the worst object $o^- = \max\{\phi^+(o_i)\}$.

Secondly, based on equations (3) and (4), we initially establish the regret function $R(o_s)$and the joy function $J(o_s)$ for the object o_s.

Definition 7. Suppose a q-ROHFN decision matrix with m objects $O = \{o_1, o_2, \dots, o_m\}$. Then, $o^+ = \max\{\phi^-(o_i)\}$ and $o^- = \max\{\phi^+(o_i)\}$ are the best object and the worst object obtained by PROMETHEE Ⅱ method, respectively. The regret function $R(o_s)$ and the joy function $J(o_s)$ of the object o_s are described as follows

$$R(o_s) = 1 - e^{-\delta\times\psi(o_s,o^+)}, \tag{6}$$

$$J(o_s) = 1 - e^{-\delta\times\psi(o_s,o^-)}, \tag{7}$$

where ψ is indicated the multi-attribute preference index by (5), $\sigma \in [0, +\infty)$ is the regret aversion parameter.

Subsequently, the regret dominance relation R^+ and the joy dominance relation J^- of the object o_s are described as follows

$$R^+ = \left\{\left((o_s, o_t) \in O \times O \middle| R(o_s) \geq R(o_t)\right)\right\}, \tag{8}$$

$$J^- = \left\{\left((o_s, o_t) \in O \times O \middle| J(o_s) \geq J(o_t)\right)\right\}, \tag{9}$$

Following that, we will construct the regret advantage class $[o_s]_{R^+}$ and the joy advantage class $[o_s]_{J^-}$for the object o_s. These classes are based on the regret advantage relation R^+ and the joy advantage relation J^- that has been previously defined. Suppose that $o_t \in [o_s]_{R^+}$,we have the object o_t is superior to o_s. Suppose that $o_t \in [o_s]_{J^-}$, we have the alternative o_t is inferior to o_s.

Finally, the RT-based conditional probabilities are determined by the RT-based regret dominance class $[o_s]_{R^+}$ and the joy dominance class $[o_s]_{J^-}$.

Definition 9. Let $[o_s]_{R^+}$ and $[o_s]_{J^-}$ are the regret advantage class and the joy advantage class, respectively, of the object o_s, based on the defined advantage class, the conditional probability calculation for each object o_s pertains to the state C is described as follows

$$P(C|o_s) = \frac{[o_s]_{J^-}}{[o_s]_{J^-} + [o_s]_{R^+}}. \tag{10}$$

The conditional probability of the object o_s with respect to $\neq \mathcal{X}$ is described as

$$P(\neq C|o_s) = \frac{[o_s]_{R^+}}{[o_s]_{J^-} + [o_s]_{R^+}}. \tag{11}$$

Proposition 1.$\mathcal{P}\left(\mathcal{X}\middle|[Q_j]_{\aleph}\right)$ and $\mathcal{P}\left(\neq \mathcal{X}\middle|[Q_j]_{\aleph}\right)$ satisfy the following property

$$P(C|o_s) + P(\neq C|o_s) = 1. \tag{12}$$

3.3. Novel three-way group decision model process of q-rung orthopair hesitant fuzzy set

The objective of this section is to create a TWD-MAGDM model. This model will be built on the relative utility function and the conditional probability that were developed in Sections 3.1 and 3.2. This model is to classify objects in the following manner.

Let $O = \{o_1, o_2, \ldots, o_m\}$ be an object set and $A = \{a_1, a_2, \ldots, a_n\}$ be an attribute set by a group of decision-makers, $\mathrm{E} = \{e_1, e_2, \ldots, e_k\}$. We have $\mathrm{W} = \{w_1, w_2, \ldots, w_k\}(w_j > 0, \sum_{j=1}^{k} w_j = 1)$ be the weight vector of the decision-makers. The evaluation value of the object o_i on an attribute a_j by the decision maker e_l is represented as a q-ROHFN $h_{ij}^{(l)} = \left(\mu_{ij}^{(l)}, v_{ij}^{(l)}\right)_q$. Then, the q-ROHFN decision matrix $H^{(l)} = \left[h_{ij}\right]_{m\times n}(l = 1, \ldots, k; i = 1, \ldots m; j = 1, \ldots, n)$ is given. Then the minimum q value that satisfies the condition is given.

[Step 1] The utility function $O_{\Delta\blacksquare}^{i(l)}$ $(l = 1, \ldots, \mathrm{k}; \Delta \in \{P, B, N\}; \blacksquare \in \{P, B, N\})$ for the object o_i, as given in **Table 1**

[Step 2] Subsequently, the conditional probability $\mathrm{P}(\mathrm{C}|o_i)$ and $\mathrm{P}(\neq \mathrm{C}|o_i)$, $(\mathrm{i} = 1,2, \ldots, \mathrm{m})$ of each object is determined for various sets of states using Eqs. (10) and (11).

[Step 3] Then, the expected utility $\mathrm{E}^{(l)}(a_\Delta|[o_i])$ $(l = 1, \ldots, \mathrm{k}; \Delta \in \{P, B, N\})$ of the object o_i is calculated using (P1) - (N1):

(P1) $\mathrm{E}^{(l)}(a_P|[o_i]) = O_{PP}^{i(l)}\mathrm{P}^{(l)}(C|o_i) + O_{PN}^{i(l)}\mathrm{P}^{(l)}(\neq C|o_i)$,

(B1) $\mathrm{E}^{(l)}(a_B|[o_i]) = O_{BP}^{i(l)}\mathrm{P}^{(l)}(C|o_i) + O_{BN}^{i(l)}\mathrm{P}^{(l)}(\neq C|o_i)$,

(N1) $\mathrm{E}^{(l)}(a_N|[o_i]) = O_{NP}^{i(l)}\mathrm{P}^{(l)}(C|o_i) + O_{NN}^{i(l)}\mathrm{P}^{(l)}(\neq C|o_i)$.

[Step 4] Based on step 3 and the expert weight vector $\mathrm{W} = \{w_1, w_2, \ldots, w_k\}$, the process of combining the values of $\mathrm{E}^{(l)}(a_\Delta|[o_i])(l = 1, \ldots, \mathrm{k}; \Delta \in \{P, B, N\})$ with their respective weights results in the composite expected utility $\widetilde{\mathrm{E}}(a_\Delta|[o_i])(\Delta \in \{P, B, N\})$. This composite expected utility is described as: $\widetilde{\mathrm{E}}(\mathrm{a_P}|[\mathrm{o_i}]) = \sum_{\mathrm{l}=1}^{\mathrm{k}} \mathrm{w_l}\,\mathrm{E}^{(\mathrm{l})}(\mathrm{a_P}|[\mathrm{o_i}])$, $\widetilde{\mathrm{E}}(\mathrm{a_B}|[\mathrm{o_i}]) = \sum_{\mathrm{l}=1}^{\mathrm{k}} \mathrm{w_l}\,\mathrm{E}^{(\mathrm{l})}(\mathrm{a_B}|[\mathrm{o_i}])$, $\widetilde{\mathrm{E}}(\mathrm{a_N}|[\mathrm{o_i}]) = \sum_{\mathrm{l}=1}^{\mathrm{k}} \mathrm{w_l}\,\mathrm{E}^{(\mathrm{l})}(\mathrm{a_N}|[\mathrm{o_i}])$.

[Step 5] Finally, we can build a TWD-MAGDM rule for each object o_i.

$(P2)$ If $\widetilde{\mathrm{E}}(\mathrm{a_P}|[\mathrm{o_i}]) \geq \widetilde{\mathrm{E}}(\mathrm{a_B}|[\mathrm{o_i}])$ and $\widetilde{\mathrm{E}}(\mathrm{a_P}|[\mathrm{o_i}]) \geq \widetilde{\mathrm{E}}(\mathrm{a_N}|[\mathrm{o_i}])$, then we have $\mathrm{o_i} \in \mathrm{POS(O)}$,

$(B2)$If $\widetilde{\mathrm{E}}(\mathrm{a_B}|[\mathrm{o_i}]) \geq \widetilde{\mathrm{E}}(\mathrm{a_P}|[\mathrm{o_i}])$ and $\widetilde{\mathrm{E}}(\mathrm{a_B}|[\mathrm{o_i}]) \geq \widetilde{\mathrm{E}}(\mathrm{a_N}|[\mathrm{o_i}])$, then we have $\mathrm{o_i} \in \mathrm{BND(O)}$,

$(N2)$If $\widetilde{\mathrm{E}}(\mathrm{a_N}|[\mathrm{o_i}]) \geq \widetilde{\mathrm{E}}(\mathrm{a_P}|[\mathrm{o_i}])$ and $\widetilde{\mathrm{E}}(\mathrm{a_N}|[\mathrm{o_i}]) \geq \widetilde{\mathrm{E}}(\mathrm{a_B}|[\mathrm{o_i}])$, then we have $\mathrm{o_i} \in \mathrm{NEG(O)}$.

4. Comparing existing method

In this section, we conduct a comparative analysis between the proposed model and existing approaches, considering three different perspectives. The results of this comparison are presented in Tables 2 and 3. The data used in these tables are sourced from literature references[7] and [2].

Table 2 Comparison with existing TWD-MAGDM method.

Method	Decision results	Optimal project
Lei et al. method[7]	$\mathrm{POS}(O) = \{o_2\}, \mathrm{Bnd(O)} = \{o_1, o_3, o_4\}$	o_2
Our proposed method	$\mathrm{POS}(O) = \{o_2\}, \mathrm{Bnd}(O) = \{o_3, o_4\}, \mathrm{NEG} = \{o_1\}$	o_2

Table 3 Comparison with existing MADM methods.

Method	Decision results	Optimal
Lai et al. CoCoSo method[2]	$o_4 \succ o_3 \succ o_5 \succ o_1 \succ o_2$	o_4
Liu et al. TOPSIS method[1]	$o_4 \succ o_3 \succ o_5 \succ o_1 \succ o_2$	o_4
Our proposed method	$o_4 \succ o_5 \succ o_3 \succ o_1 \succ o_2$ $\mathrm{POS}(O) = \{o_4\}, \mathrm{Bnd}(O) = \{o_1, o_3, o_5\}, \mathrm{NEG} = \{o_2\}$	o_4

5. Conclusion

The TWD-MAGDM classification model, introduced in this research, enhances the distinction and simplifies the group TWD problem. Future research can provide treatment plans for mental diseases.

References

[1] D. Liu, D. Peng, and Z. Liu, "The distance measures between q‐rung orthopair hesitant fuzzy sets and their application in multiple criteria decision making," *International Journal of Intelligent Systems,* vol. 34, no. 9, pp. 2104-2121, 2019.

[2] H. Lai, H. Liao, Y. Long, and E. K. Zavadskas, "A hesitant Fermatean fuzzy CoCoSo method for group decision-making and an application to blockchain platform evaluation," *International Journal of Fuzzy Systems,* vol. 24, no. 6, pp. 2643-2661, 2022.

[3] [B. Wan and J. Zhang, "Group decision making with q-rung orthopair hesitant fuzzy preference relations," *arXiv preprint arXiv:2203.17229,* 2022.

[4] Y. Yao, "Three-way decisions with probabilistic rough sets," *Information sciences,* vol. 180, no. 3, pp. 341-353, 2010.

[5] H. Jiang and B. Q. Hu, "A novel three-way group investment decision model under intuitionistic fuzzy multi-attribute group decision-making environment," *Information Sciences,* vol. 569, pp. 557-581, 2021.
[6] D. Liang and W. Cao, "q‐Rung orthopair fuzzy sets‐based decision‐theoretic rough sets for three‐way decisions under group decision making," *International Journal of Intelligent Systems,* vol. 34, no. 12, pp. 3139-3167, 2019.
[7] W. Lei, W. Ma, X. Li, and B. Sun, "Three-way group decision based on regret theory under dual hesitant fuzzy environment: An application in water supply alternatives selection," *Expert Systems with Applications,* vol. 237, p. 121249, 2024.
[8] A. Tversky and D. Kahneman, "Advances in prospect theory: Cumulative representation of Uncertainty," *Journal of Risk and uncertainty,* vol. 5, pp. 297-323, 1992.
[9] S. Ferey and P. Dehez, "Overdetermined Causation Cases, Contribution and the Shapely Value," *Chi.-Kent L. Rev.,* vol. 91, p. 637, 2016.
[10] G. Beliakov, S. James, and J. Wu, *Discrete fuzzy measures*. Springer, 2020.
[11] G. Loomes and R. Sugden, "Regret theory and measurable utility," *Economics Letters,* vol. 12, no. 1, pp. 19-21, 1983.
[12] F. Jia and P. Liu, "A novel three-way decision model under multiple-criteria environment," *Information Sciences,* vol. 471, pp. 29-51, 2019.
[13] J. Zhan, J. Ye, W. Ding, and P. Liu, "A novel three-way decision model based on utility theory in incomplete fuzzy decision systems," *IEEE Transactions on Fuzzy Systems,* vol. 30, no. 7, pp. 2210-2226, 2021.
[14] M. R. Seikh and U. Mandal, "Interval-valued Fermatean fuzzy Dombi aggregation operators and SWARA based PROMETHEE II method to bio-medical waste management," *Expert Systems with Applications,* vol. 226, p. 120082, 2023.
[15] J.-P. Brans, P. Vincke, and B. Mareschal, "How to select and how to rank projects: The PROMETHEE method," *European Journal of Operational Research,* vol. 24, no. 2, pp. 228-238, 1986.

Fuzzy Systems and Data Mining X
A.J. Tallón-Ballesteros (Ed.)

doi:10.3233/FAIA241402

A Novel Interval-Valued Hesitant Fermatean Fuzzy Multi-Attribute Group Decision-Making Method Based on Consensus

Xuli Niu[a], Xiuqin Ma [a,1], Hongwu Qin[a], Dong Ren[a] and Siyue Lei[a]
[a] *College of Computer Science and Engineering, Northwest Normal University, Lanzhou, 730020, Gansu, China*

Abstract. Interval-valued hesitant Fermatean fuzzy sets (IVHFFSs) offer a powerful mathematical tool for addressing decision-making problems full of uncertainty and ambiguity. Despite their potential, multi-attribute group decision-making (MAGDM) methods within this context have not been extensively explored. This paper addresses this gap by introducing a consensus-based MAGDM approach for IVHFFSs. First, we propose an interval-valued hesitant Fermatean fuzzy (IVHFF) distance measure without normalization, which does not generate data redundancy. Next, we propose an objective expert weighting method based on hesitancy and consensus level. Furthermore, combined with the proposed distance measure and expert weighting method, we propose an IVHFF consensus model. Since the consensus model directly adjusts the expert evaluation value through the distance matrix, it effectively improves the efficiency of consensus reaching. Finally, based on the proposed consensus model, we propose a novel MAGDM method under IVHFF environment.

Keywords. Interval-valued hesitant Fermatean fuzzy sets, Consensus, Distance measure, Multi-attribute group decision-making.

1. Introduction

Decision-making frequently involves ambiguous and uncertain data. The fuzzy sets proposed by Zadeh[1] provide significant theoretical support for such uncertainty. In recent decades, researchers have proposed a number of extensions of fuzzy sets[2-5] due to the growing complexity of fuzzy decision-making environments. Fuzzy sets incorporating the concept of hesitation have been successively offered as a way to address the possibility that decision makers will pause in specific situations while evaluating in complicated and uncertain situations[6-9]. Furthermore, it might be challenging to pinpoint the precise membership and non-membership functions due to the high degree of individualization in these roles. Using interval values to express the degree of membership (MD) and non-membership (NMD) is a more sensible method. In order to solve these problems, Mishra et al. proposed the concept of interval-valued hesitant Fermatean (IVHFF) fuzzy sets (IVHFFSs)[10], a new fuzzy set for dealing with uncertainty.

[1] Corresponding Author: Xiuqin Ma, Northwest Normal University, China. Email: maxiuqin@nwnu.edu.cn.
Funding was provided by the National Natural Science Foundation of China(62162055),the National Natural Science Foundation of China(12461094),the Gansu Provincial University Teacher Innovation Foundation (2024A-006) and the Key Research and Development Program Project of Gansu Province(24YFFA025).

It is getting harder for a single expert to weigh all the pertinent factors in a situation and make decisions as the socioeconomic environment gets more complex. Because of this, most real-world decision-making procedures involve groups of people. Multi-attribute group decision making (MAGDM) is a decision-making method where a team of specialists assesses several aspects of a problem and attempts to come up with a shared solution. Various group decision-making methods in fuzzy environments have been widely studied. Lai et al.[11] proposed a hesitant Fermatean Fuzzy CoCoSo method, and applied it to solve blockchain platform evaluation problems. Under single-valued trapezoidal neutrosophic environment, Irvanizam and Novi proposed an extended EDAS[12] and an improved RAFSI method[13] and applied them to the MAGDM problem. However, MAGDM methods in the IVHFF setting have not been studied, so it is of great interest to propose methods for MAGDM in this setting.

Consensus, a key step in the MAGDM problem, is a dynamic and iterative decision-making process that can help decision makers to bring their opinions closer. Consensus models in group decision making are generally classified into two categories: (1) Consensus models based on identification and directional rules[14, 15]; (2) Consensus models based on optimization rules[16, 17]. Li et al.[18] proposed a consensus reaching process in large-scale group decision making based on opinion leaders. However, in the feedback adjustment phase of consensus model, the weights of the decision-making experts are rarely taken into account, which to some extent ignores the importance of the experts. Therefore, it is a very meaningful thing to consider the weight of experts in the consensus process. More importantly, consensus models in the IVHFF environment have not yet been studied.

Based on the aforementioned discussion, we summarized some research motivations: (1) Existing distance measures in the IVHFF environment necessitate data normalization, which can result in redundant data. (2) Consensus plays a very crucial role in group decision making. However, there is currently no established consensus model tailored for the IVHFF context. (3) Consensus-based MAGDM methods in IVHFF environments remain underexplored and are in an emergent stage.

This paper introduces a novel consensus-based MAGDM methodology for IVHFF environment, with the following key contributions and advantages.

(1) We present a non-normalized IVHFF distance measure that avoids data redundancy in the calculation of IVHFFNs.

(2) We propose a method for determining expert weights that considers hesitancy and consensus levels, providing a more objective assessment of expert importance.

(3) We propose a consensus-based MAGDM approach in the IVHFF environment, addressing existing gaps in the literature.

The remainder of this paper consists of the following: Section 2 introduces some basic concepts. In Section 3, an IVHFF distance measure and an expert weight determination method are presented. Section 4 details the main steps of the proposed consensus-based MAGDM method for IVHFF. Finally, the conclusions are presented in Section 5.

2. Preliminaries

Some basic concepts of IVHFFSs are reviewed in this section.

Definition 2.1[10]**.** The IVHFFS H on a universe X is defined by

$$H = \{x_i, (\alpha_H(x_i), \beta_H(x_i)) | x_i \in X\} \quad (1)$$

where two sets of interval values in [0,1] $\alpha_H(x_i) = \bigcup_{[\gamma_H^l(x_i),\gamma_H^u(x_i)]\in\alpha_H(x_i)}[\gamma_H^l(x_i), \gamma_H^u(x_i)]$ and $\beta_H(x_i) = \bigcup_{[\eta_H^l(x_i),\eta_H^u(x_i)]\in\beta_H(x_i)}[\eta_H^l(x_i), \eta_H^u(x_i)]$, representing the possible MD intervals and NMD intervals, respectively, of the element $x_i \in X$ to H, with the constraints

$$0 \le \gamma_H^l(x_i) \le \gamma_H^u(x_i) \le 1, 0 \le \eta_H^l(x_i) \le \eta_H^u(x_i) \le 1,$$
$$0 \le \left(\left(\gamma_H^u(x_i)\right)^+\right)^3 + \left(\left(\eta_H^u(x_i)\right)^+\right)^3 \le 1.$$

For convenience, the pair $(\alpha_H(x_i), \beta_H(x_i))$ is called an interval-valued hesitant Fermatean fuzzy number (IVHFFN) denoted by $\zeta = (\alpha, \beta)$.

Definition 2.2[10]**.** Suppose that $\zeta = (\alpha, \beta)$ is an IVHFFN, then the score function for ζ can be defined as

$$S(\zeta) = \frac{1}{2}\left(\begin{array}{l}\left(\frac{1}{\#a}\sum_{[\gamma_H^l(x_i),\gamma_H^u(x_i)]\in\alpha_H(x_i)}\left(\gamma_H^l(x_i)\right)^3 - \frac{1}{\#b}\sum_{[\eta_H^l(x_i),\eta_H^u(x_i)]\in\beta_H(x_i)}\left(\eta_H^l(x_i)\right)^3\right) \\ +\left(\frac{1}{\#a}\sum_{[\gamma_H^l(x_i),\gamma_H^u(x_i)]\in\alpha_H(x_i)}\left(\gamma_H^u(x_i)\right)^3 - \frac{1}{\#b}\sum_{[\eta_H^l(x_i),\eta_H^u(x_i)]\in\beta_H(x_i)}\left(\eta_H^u(x_i)\right)^3\right)\end{array}\right) \quad (2)$$

where $\#a$ and $\#b$ represent the number of interval values in α and β, respectively.

3. A novel IVHFF distance measure and expert weighting method

In this section, we focus on proposing distance measure in the IVHFF setting without normalization, and expert weight computation method.

3.1. A novel distance measure under IVHFF context

Currently, the distance measures that exist in the IVHFF environment require normalization of IVHFFNs, which will produce redundant data. To address these issues, this paper first proposes a novel IVHFF distance measure that eliminates the need for normalization.

Definition 3.1. Let $\zeta_1 = (\alpha_1, \beta_1)$ and $\zeta_2 = (\alpha_2, \beta_2)$ be two IVHFFNs, then the distance between ζ_1 and ζ_2 is defined as follows:

$$d(\zeta_1, \zeta_2) = \left(\frac{1}{5}\left(\begin{array}{c}\left|\left(\varphi_{1\gamma}^l\right)^3 - \left(\varphi_{2\gamma}^l\right)^3\right|^\lambda + \left|\left(\varphi_{1\gamma}^u\right)^3 - \left(\varphi_{2\gamma}^u\right)^3\right|^\lambda + \\ \left|\left(\varphi_{1\eta}^l\right)^3 - \left(\varphi_{2\eta}^l\right)^3\right|^\lambda + \left|\left(\varphi_{1\eta}^u\right)^3 - \left(\varphi_{2\eta}^u\right)^3\right|^\lambda + \\ |(\pi_1)^3 - (\pi_2)^3|^\lambda\end{array}\right)\right)^{\frac{1}{\lambda}} \quad (3)$$

where $\varphi_{s\gamma}^l = \frac{1}{\#a_s}\sum_{i=1}^{\#a_s}\left(\gamma_i^l\right)^3$, $\varphi_{s\gamma}^u = \frac{1}{\#a_s}\sum_{i=1}^{\#a_s}(\gamma_i^u)^3$, $\varphi_{s\eta}^l = \frac{1}{\#b_s}\sum_{i=1}^{\#b_s}\left(\eta_i^l\right)^3$, $\varphi_{s\eta}^u = \frac{1}{\#b_s}\sum_{i=1}^{\#b_s}(\eta_i^u)^3$, $\#a_s$ and $\#b_s$ denote the number of MD intervals and NMD intervals in ζ_1 and ζ_2 respectively, $s = 1,2$, $\lambda > 0$, and

$$\pi_1 = \sqrt[3]{1 - \left(\frac{1}{\#a_1}\sum_{[\gamma_1^l,\gamma_1^u]\in\alpha_1}((\gamma_1^l)^3 + (\gamma_1^u)^3) + \frac{1}{\#b_1}\sum_{[\eta_1^l,\eta_1^u]\in\beta_1}((\eta_1^l)^3 + (\eta_1^u)^3)\right)},$$

$$\pi_2 = \sqrt[3]{1 - \left(\frac{1}{\#a_2}\sum_{[\gamma_2^l,\gamma_2^u]\in\alpha_2}((\gamma_2^l)^3 + (\gamma_2^u)^3) + \frac{1}{\#b_2}\sum_{[\eta_2^l,\eta_2^u]\in\beta_2}((\eta_2^l)^3 + (\eta_2^u)^3)\right)}.$$

Especially, when $\lambda = 1$, we can call Eq. (3) as IVHFF Hamming distance; when $\lambda = 2$, we can call Eq. (3) as IVHFF Euclidean distance.

3.2. A newly method for expert weighting method

Drawing inspiration from Liu et al.[15], in this paper, we propose a method for calculating expert weights based on hesitancy and consensus level.

Definition 3.3. The consensus level $CL^t(t = 1,2,\dots,k)$ between expert e^t and collective matrix $\widetilde{\mathcal{M}} = \left(\widetilde{x_{ij}}\right)_{m\times n}(i = 1,2,\dots,m, j = 1,2,\dots,n)$ is defined as follows

$$CL^t = \frac{1}{mn}\sum_{i=1}^{m}\sum_{j=1}^{n} 1 - d\left(x_{ij}^t, \widetilde{x_{ij}}\right) \tag{4}$$

where $d\left(x_{ij}^t, \widetilde{x_{ij}}\right)$ denotes distance measures between expert e^t and collective matrix.

The following are the precise stages for calculating expert weights.

Step1: Let $\mathcal{M}^t = \left(x_{ij}^t\right)_{m\times n}(i = 1,2,\dots,m, j = 1,2,\dots,n, t = 1,2,\dots,k)$ represents an IVHFF decision matrix.

Step2: Based on the uncertainty of the IVHFFNs[10], we can calculate the hesitancy of expert e^t by using Eq. (5).

$$HS^t = \frac{1}{2mn}\sum_{i=1}^{m}\sum_{j=1}^{n}\left(\pi_H^l\left(x_{ij}^t\right) + \pi_H^u\left(x_{ij}^t\right)\right) \tag{5}$$

Step3: According to Eq. (4) in Definition 3.3, we can calculate the consensus level CL^t of expert e^t.

Step4: Calculate the weight of expert e^t by using Eq. (6).

$$w_e^t = \frac{CL^t \times \sqrt{1 - HS^t}}{\sum_{t=1}^{k} CL^t \times \sqrt{1 - HS^t}} \tag{6}$$

From Eq. (6) we can derive that when the hesitancy of the expert is lower and the consensus level to the collective is higher, the expert weight will be higher. And vice versa.

4. Consensus-Based MAGDM method for IVHFFSs

Solving group decision problems generally requires a consensus reaching process and a selection process. Here, we first propose a consensus model in the IVHFF environment, followed by a selection process to accomplish the final decision.

4.1. Proposed consensus model under IVHFF setting

The specific steps of the consensus model are as follows.

Step 1: Let $\mathcal{M}^{t(r)} = \left(x_{ij}^{t(r)}\right)_{m\times n}(i = 1,2,\dots,m, j = 1,2,\dots,n, t = 1,2,\dots,k)$ represents an IVHFF decision matrix, where $x_{ij}^{t(r)} = \left(\alpha_{ij}^{t(r)}, \beta_{ij}^{t(r)}\right)$ is an IVHFFN, representing the value of the expert e^t assessment of alternative A_i under attribute C_j.

Here r denotes the number of consensus rounds, and its value should be less than the maximum number of consensus rounds r_{max}.

Step 2: Calculate the weights of the experts $w_e^{t(r)}(t = 1,2, \dots, k)$ according to the expert weighting method proposed in section 3.2.

Step 3: Apply IVHFF weighted averaging aggregation operator[10] to aggregate the k expert assessment matrices, finally generating the collective matrix $\widetilde{\mathcal{M}^{(r)}} = \left(\widetilde{x_{ij}^{(r)}}\right)_{m\times n}$.

Step 4: Consensus measure.

Consensus measure is to calculate the degree of consensus among a group of experts based on the consensus level of each expert, i.e., the group consensus level (GCL).

Step 4.1: Based on the proposed IVHFF distance measure, we can obtain the distance matrix $D\mathcal{M}^{t(r)} = \left(d_{ij}^{t(r)}\right)_{m\times n}$ between expert e^t and the collective $\widetilde{\mathcal{M}^{(r)}}$.

Step 4.2: Calculate the consensus level $CL^{t(r)}$ of expert e^t by using (4).

Step 4.3: Calculate the $GCL^{t(r)}$ by Eq. (7).

$$GCL^{t(r)} = \frac{1}{k}\sum_{t=1}^{k} CL^{t(r)} \tag{7}$$

Step 5: If the $GCL^{t(r)}$ is greater than or equal to the consensus threshold Θ, the consensus ends. Otherwise, the consensus moves to the feedback adjustment phase.

Step 6: Feedback mechanism.

The feedback mechanism facilitates consensus reaching by identifying the experts who need to modify the original assessment opinion, followed by the set direction rules to modify the assessment values of the experts, which ultimately leads to consensus reaching.

(I) Identify rules

Step 6.1: Identify experts whose consensus level $CL^{t(r)}$ does not reach consensus threshold Θ.

$$\overline{e^{(r)}} = \left\{e^t | CL^{t(r)} \le \Theta, \mathrm{t} = 1,2, \dots, \mathrm{k}\right\} \tag{8}$$

Step 6.2: Iterate through the distance matrix corresponding to the experts identified in Step 6.1, identifying the values in the distance matrix that are not reach the consensus threshold Θ.

$$\overline{d_{ij}^{t(r)}} = \left\{ d_{ij}^{t(r)} \middle| \begin{matrix} d_{ij}^{t(r)} \le \Theta \wedge e^t \in \overline{e^{(r)}} \wedge d_{ij}^{t(r)} \in D\mathcal{M}^{t(r)}, \\ i = 1,2, \dots, m, j = 1,2, \dots, n, t = 1,2, \dots, k \end{matrix} \right\} \tag{9}$$

(II) Modification rules

To better reflect the significance of experts and produce more logical and objective final decision-making outcomes, we take the experts' weight into consideration during the modification procedure. Here, we map the expert weights via the Sigmoid function to obtain the modification coefficients of experts, making use of the great property of the Sigmoid function.

Step 6.3: The expert weights $w_e^{t(r)}$ are mapped through Sigmoid function $f(x) = \frac{1}{1+e^{-k(x-x_0)}}$ to obtain the adjustment coefficient $\theta^{t(r)}$.

$$\theta^{t(r)} = \frac{1}{1 + e^{-10\left(w_e^{t(r)} - 0.5\right)}} \tag{10}$$

From Eq. (10), we can obtain that when the weight of the expert $w_e^{t(r)}$ is larger, the modification coefficient $\theta^{t(r)}$ obtained will be smaller, which suggests that for the

experts with larger weights, we can better retain their original assessment opinions. And vice versa.

Step 6.4: The corresponding value $x_{ij}^{t(r)}$ in the original evaluation matrix of expert e^t is obtained according to $\overline{d_{ij}^{t(r)}}$, then $x_{ij}^{t(r)}$ is modified by using Eq. (11).

$$\overline{x_{ij}^{t(r+1)}} = \left(\alpha_{ij}^{t(r+1)}, \beta_{ij}^{t(r+1)}\right) = \bigcup_{\substack{\left[\gamma_{ij}^{t(r)l}, \gamma_{ij}^{t(r)u}\right] \in \alpha_{ij}^{t(r)}, \\ \left[\eta_{ij}^{t(r)l}, \eta_{ij}^{t(r)u}\right] \in \beta_{ij}^{t(r)}}} \left(\begin{Bmatrix} \left[\theta^{t(r)} \times C_{\gamma}^{(r)l} + \left(1-\theta^{t(r)}\right) \times \gamma_{ij}^{t(r)l}, \right. \\ \left. \theta^{t(r)} \times C_{\gamma}^{(r)u} + \left(1-\theta^{t(r)}\right) \times \gamma_{ij}^{t(r)u} \right] \end{Bmatrix}, \begin{Bmatrix} \left[\theta^{t(r)} \times C_{\eta}^{(r)l} + \left(1-\theta^{t(r)}\right) \times \eta_{ij}^{t(r)l}, \right. \\ \left. \theta^{t(r)} \times C_{\eta}^{(r)u} + \left(1-\theta^{t(r)}\right) \times \eta_{ij}^{t(r)u} \right] \end{Bmatrix} \right) \tag{11}$$

where $C_{\gamma}^{(r)l} = \frac{1}{\#\bar{\alpha}} \sum \widetilde{\gamma_{ij}^{(r)l}}$, $C_{\gamma}^{(r)u} = \frac{1}{\#\bar{\alpha}} \sum \widetilde{\gamma_{ij}^{(r)u}}$, $C_{\eta}^{(r)l} = \frac{1}{\#\bar{\beta}} \sum \widetilde{\eta_{ij}^{(r)l}}$, $C_{\eta}^{(r)l} = \frac{1}{\#\bar{\beta}} \sum \widetilde{\eta_{ij}^{(r)l}}$.

In order to ensure that the modified values are still IVHFFNs, we set the corresponding constraints, i.e., $S\left(x_{ij}^{t(r)}\right) \leq S\left(\overline{x_{ij}^{t(r+1)}}\right) \leq S\left(\widetilde{x_{ij}^{(r)}}\right)$. In addition, for the proposed consensus model, we set a parameter of the maximum number of adjustments $\mathcal{N}$ in advance, which serves to limit the number of expert evaluation values that can be modified in each round of the consensus process. The ultimate goal is to maximize the retention of experts' original opinions and improve the efficiency of the consensus model.

Step 6: Compute the modified GCL; upon reaching the consensus threshold Θ, the consensus is considered accomplished. In the event that the GCL fails to reach the consensus threshold Θ, we need to go back to Step 2. If the consensus is reached in fewer rounds than the maximum number of rounds r_{max}, the consensus is successful; if not, it fails.

4.2. Selection process

The specific steps of the selection process are as follows.

Step 1: The IVHFF weighted averaging aggregation operator[10] is used to aggregate the collective matrix $\widetilde{\mathcal{M}^{(r)}} = \left(\widetilde{x_{ij}^{(r)}}\right)_{m \times n}$ corresponding to the expert groups that have reached consensus, obtaining the aggregated value of alternative A_i.

Step 2: Eq. (2) in Definition 2.2 is used to calculate the score of alternative A_i. The alternatives are then ranked based on the score values to determine which is the best option.

So far, we have proposed a MAGDM method based on consensus model. In order to show our proposed decision model more clearly, the framework diagram of the whole method is shown in Figure 1.

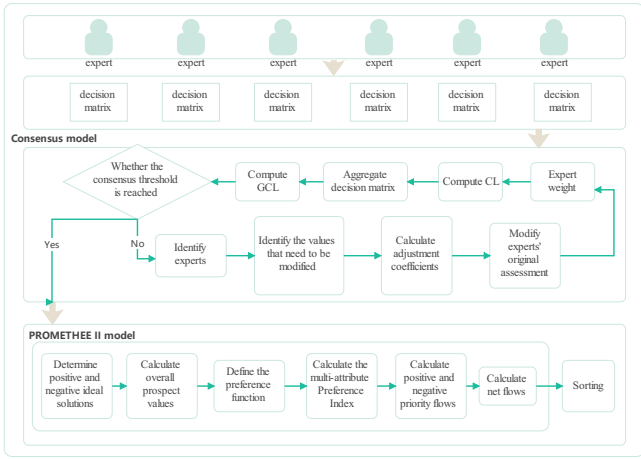

Figure 1. Diagram of the MAGDM framework based on consensus model.

5. Numerical example

An electronics company is developing a new smart home device and needs to choose the right supplier for key components. To ensure that the decision is comprehensive, the company invites three experts, e_1, e_2 and e_3, to participate in the evaluation. There are four alternatives A_1, A_2, A_3 and A_4 and the expert needs to evaluate the alternatives based on three attributes C_1, C_2 and C_3. Therefore, the experts evaluated the alternatives based on the available empirical knowledge and obtained the corresponding IVHFF decision matrix Tables 1.

Table 1. The IVHFF decision matrix M_1, M_2 and M_3 given by three experts.

	e_1			e_2			e_3		
	C_1	C_2	C_3	C_1	C_2	C_3	C_1	C_2	C_3
A_1	{[0.21,0.7]}, {[0.38,0.38]}	{[0.41,0.52]}, {[0.06,0.7],} {[0.15,0.3]}	{[0.24,0.8]}, {[0.73,0.78]}	{[0.8,0.83],} {[0.11,0.16]} {[0.52,0.64]}	{[0.52,0.61]}, {[0.25,0.33],} {[0.35,0.81]}	{[0.47,0.5],} {[0.23,0.34]} {[0.48,0.93]}	{[0.14,0.96]}, {[0.15,0.37]}	{[0.32,0.76]}, {[0.28,0.77]}	{[0.42,0.57]}, {[0.39,0.66],} {[0.14,0.28]}
A_2	{[0.37,0.8]}, {[0.12,0.35]}	{[0.65,0.67],} {[0.11,0.11]} {[0.09,0.48]}	{[0.04,0.75],} {[0.25,0.68]} {[0.29,0.43]}	{[0.43,0.53]}, {[0.01,0.3]}	{[0.74,0.85]}, {[0.17,0.53]}	{[0.34,0.47]}, {[0.39,0.92]}	{[0.83,0.92],} {[0.14,0.72]} {[0.37,0.6],} {[0.28,0.28]}	{[0.03,0.15],} {[0.21,0.44]} {[0.25,0.47]}	{[0.4,0.76]}, {[0.12,0.45],} {[0.21,0.26]}
A_3	{[0.31,0.92],} {[0.53,0.76]} {[0.12,0.41]}	{[0.07,0.54]}, {[0.03,0.76],} {[0.03,0.54]}	{[0.56,0.61],} {[0.36,0.45]} {[0.61,0.86]}	{[0.51,0.62]}, {[0.63,0.72]}	{[0.68,0.83]}, {[0.05,0.51]}	{[0.21,0.32],} {[0.65,0.78]} {[0.06,0.75],} {[0.07,0.2]}	{[0.02,0.17],} {[0.32,0.35]} {[0.15,0.78]}	{[0.54,0.92],} {[0.34,0.55]} {[0.06,0.44],} {[0.01,0.51]}	{[0.01,0.55],} {[0.09,0.44]} {[0.2,0.54]}
A_4	{[0.19,0.47]}, {[0.55,0.77],} {[0.33,0.34]}	{[0.48,0.58],} {[0.16,0.67]} {[0.41,0.54]}	{[0.63,0.88]}, {[0.12,0.44]}	{[0.15,0.3]}, {[0.76,0.84],} {[0.23,0.75]}	{[0.29,0.37]}, {[0.42,0.85],} {[0.5,0.84]}	{[0.29,0.42]}, {[0,0.15]}	{[0.11,0.33]}, {[0.08,0.2]}	{[0.03,0.74]}, {[0.14,0.63]}	{[0.55,0.66]}, {[0.14,0.25],} {[0.42,0.53]}

We then use the methodology proposed in Section 4 to solve this decision problem.

5.1. Consensus process

We specify the consensus threshold $\Theta = 0.94$, the maximum number of consensus rounds $r_{max} = 10$, and the maximum number of adjustments $\mathcal{N} = 10$.According to the proposed consensus model in Section 4.1, we obtain the following results.

Initial round ($r = 0$):

(1) The weight $w_e^{(r)}$ of each expert is obtained as follows:

$$w_e^{(0)} = \{0.33, 0.35, 0.32\}$$

(2) Aggregating multiple expert decision matrices to obtain $\widetilde{\mathcal{M}^{(0)}} = \left(\widetilde{x_{ij}^{(0)}}\right)_{4\times3}$.

(3) Consensus measure.

(i) Based on the proposed IVHFF distance measure, we can obtain the distance matrix of the experts as shown below.

$$D\mathcal{M}^{1(0)} = \begin{bmatrix} 0.9604 & 0.958 & 0.8972 \\ 0.9429 & 0.9876 & 0.9941 \\ 0.8795 & 0.9266 & 0.8718 \\ 0.9776 & 0.9856 & 0.8865 \end{bmatrix} D\mathcal{M}^{2(0)} = \begin{bmatrix} 0.8759 & 0.9767 & 0.7423 \\ 0.9661 & 0.7785 & 0.7429 \\ 0.9581 & 0.8768 & 0.9637 \\ 0.8982 & 0.9075 & 0.8971 \end{bmatrix}$$

$$D\mathcal{M}^{3(0)} = \begin{bmatrix} 0.7901 & 0.9082 & 0.9439 \\ 0.9608 & 0.9693 & 0.9123 \\ 0.9067 & 0.99 & 0.9927 \\ 0.9992 & 0.9524 & 0.9618 \end{bmatrix}$$

(ii) Use Eq. (4) to obtain expert CL.

$$CL^{t(0)} = \{0.9345, 0.8819, 0.9406\}$$

(iii) Calculate the current GCL according to Eq. (7).

$$GCL^{(0)} = 0.9190$$

(4) Because the current group consensus level $GCL^{(0)} < \Theta$, i.e., there is no consensus among experts in the Initial round ($r = 0$) of the consensus process. Therefore, we need to facilitate the GCL of experts to reach the specified consensus threshold through the feedback mechanism.

First round ($r = 1$):

(5) Feedback mechanism.

(i) Recognition rule: Identify experts whose consensus level does not reach the consensus threshold Θ.

$$\overline{e^{(0)}} = \{e_1, e_2\}$$

(ii) Find the values in the distance matrix that do not reach the consensus threshold Θ.

(iii) Modification rule: Objective mapping of expert weights $w_e^{(0)}$ through Eq.(10) yields adjustment coefficient $\theta^{t(0)}$.

$$\theta^{t(0)} = \{0.84, 0.82, 0.86\}$$

(iv) We can modify the values obtained from (ii) according to Eq. (11). For reasons of space, we omit the specific details of the modifications here.

(6) Calculate the group consensus level $GCL^{(1)}$ of the experts after the first round ($r = 1$) of adjustment.

$$GCL^{(1)} = 0.9577$$

Because $GCL^{(1)} > \Theta$, i.e., through one round of consensus, the experts have reached an acceptable level of consensus, and the consensus is over.

5.2. Selection process

Through the consensus process, a consensus has been reached among the experts. In order to further select the optimal alternatives and get the final decision result, we need to enter the selection process.

According to the specific steps of the selection process in section 4.2, we can get the scores of the alternatives as $A_1: 0.5815$, $A_2: 0.5969$, $A_3: 0.5547$ and $A_4: 0.5542$. Then we obtain the final sorting result as $A_2 > A_1 > A_3 > A_4$.

5.3. Comparative analysis

In order to demonstrate the advantages and correctness of the method proposed in this paper, we have conducted a comparative analysis. Here, we have chosen to compare with the COPRAS method proposed by Mishra et al. [10] and the TOPSIS method proposed by Wang et al[19]. The comparison results are shown in Table 2.

Table 2. Comparative results of decision-making methods.

Method	*Resulting value*				*Results*
	A_1	A_2	A_3	A_4	
Proposed method	0.5815	0.5969	0.5547	0.5542	$A_2 > A_1 > A_3 > A_4$
Mishra et al.'s method[10]	0.9806	1.0	0.9329	0.931	$A_2 > A_1 > A_3 > A_4$
Wang et al.'s method[19]	0.5385	0.5597	0.5352	0.524	$A_2 > A_1 > A_3 > A_4$

From Table 2, we can see that the ranking results obtained by our proposed method are basically the same as those obtained by the other methods, which verifies the correctness and rationality of our proposed method.

5.4. Advantage analysis

We propose a consensus-based MAGDM method that calculates expert weights objectively and does not need to normalize the raw data in the whole process of the method system, which improves the efficiency of the whole entire method. However, the methods of Mishra et al. [10] and Wang et al[19] not only do not consider the degree of consensus of the experts, but also need to normalize the data, which affects the efficiency of the operation of the whole method. To demonstrate the advantages of our proposed method, we utilize Table 3 to show the specific advantages.

Table 3. Comparison of the advantages of the proposed method.

Method	***GDM***	***Considering consensus***	***Objectivity of expert weights***	***normalization***
Proposed method	√	√	√	×
Mishra et al.' s method[10]	×	×	×	√
Wang et al.' s method[19]	×	×	×	√

6. Conclusion

In this paper, we mainly propose a consensus-based MAGDM method for IVHFF environment. Firstly, we propose a new IVHFF distance measure without normalization. Secondly, we propose an expert weighting method based on hesitancy and consensus level, which is able to calculate expert weights objectively. Then, we propose a consensus model in the IVHFF environment. In the feedback adjustment process of the consensus model, we consider the expert weights and objectively map them to obtain the adjustment coefficients, thus not only better reflecting the importance of the experts and maximizing the fit to the original opinions of the experts, but also improving the efficiency of the consensus algorithm. Further, we propose the IVHFF MAGDM method based on the proposed consensus model. Finally, we demonstrate the practicality of the proposed method through a real numerical example. The correctness and advantages of our proposed method are also further verified through comparative analysis. In order to

improve the consensus efficiency faster, the consensus feedback mechanism of the proposed method has some optimization space. In future research, we can apply the proposed decision-making method to large-scale group decision-making and three-way multi-attribute group decision-making, and also extend it to novel fuzzy environments such as Z-number.

References

[1] Zadeh LA. Fuzzy sets. Information and control. 1965;8(3):338-53.
[2] Ren D, Ma X, Qin H, Lei S, Niu X. A multi-criteria decision-making method based on discrete Z-numbers and Aczel-Alsina aggregation operators and its application on early diagnosis of depression. Engineering Applications of Artificial Intelligence. 2025;139. doi: 10.1016/j.engappai.2024.109484.
[3] Qin H, Peng Q, Ma X, Zhan J. A new multi-attribute decision making approach based on new score function and hybrid weighted score measure in interval-valued Fermatean fuzzy environment. Complex & Intelligent Systems. 2023;9(5):5359-76.
[4] Ma X, Qin H, Abawajy JH. Interval-valued intuitionistic fuzzy soft sets based decision-making and parameter reduction. IEEE Transactions on Fuzzy Systems. 2020;30(2):357-69.
[5] Ma X, Fei Q, Qin H, Li H, Chen W. A new efficient decision making algorithm based on interval-valued fuzzy soft set. Applied Intelligence. 2021;51(6):3226-40.
[6] Wang Y, Ma X, Qin H, Sun H, Wei W. Hesitant Fermatean fuzzy Bonferroni mean operators for multi-attribute decision-making. Complex & Intelligent Systems. 2024;10(1):1425-57.
[7] Qin H, Wang Y, Ma X, Abawajy JH. A Novel Choquet Integral-based VIKOR Approach under Q-rung Orthopair Hesitant Fuzzy Environment. IEEE Transactions on Fuzzy Systems. 2024.
[8] Lei S, Ma X, Qin H, Wang Y, Zain JM. A new multi-attribute group decision-making method based on Einstein Bonferroni operators under interval-valued Fermatean hesitant fuzzy environment. Scientific Reports. 2024;14(1):12370.
[9] Guo L, Zhan J, Kou G. Consensus reaching process using personalized modification rules in large-scale group decision-making. Information Fusion. 2024;103:102138.
[10] Mishra AR, Liu P, Rani P. COPRAS method based on interval-valued hesitant Fermatean fuzzy sets and its application in selecting desalination technology. Applied Soft Computing. 2022;119:108570.
[11] Lai H, Liao H, Long Y, Zavadskas EK. A hesitant Fermatean fuzzy CoCoSo method for group decision-making and an application to blockchain platform evaluation. International Journal of Fuzzy Systems. 2022;24(6):2643-61.
[12] Irvanizam I, Zahara N. An extended EDAS based on multi-attribute group decision making to evaluate mathematics teachers with single-valued trapezoidal neutrosophic numbers. Handbook of Research on the Applications of Neutrosophic Sets Theory and Their Extensions in Education: IGI Global; 2023. p. 40-67.
[13] Irvanizam I, Zahara N. An improved RAFSI method based on single-valued trapezoidal neutrosophic number and its Harmonic and Arithmetic mean operators for healthcare service quality evaluation. Expert Systems with Applications. 2024;248:123343.
[14] Xu Y, Cabrerizo FJ, Herrera-Viedma E. A consensus model for hesitant fuzzy preference relations and its application in water allocation management. Applied Soft Computing. 2017;58:265-84.
[15] Liu P, Zhang X, Pedrycz W. A consensus model for hesitant fuzzy linguistic group decision-making in the framework of Dempster–Shafer evidence theory. Knowledge-Based Systems. 2021;212:106559.
[16] Yu S-M, Zhang X-T, Du Z-j. Enhanced minimum-cost consensus: Focusing on overadjustment and flexible consensus cost. Information Fusion. 2023;89:336-54.
[17] Li J, Niu L-l, Chen Q, Li F, Wei L, Wang Z-x. A consensus reaching process with hesitant fuzzy elements considers the individuals best and worst consensus levels. Knowledge and Information Systems. 2023;65(9):3665-93.
[18] Li Y, Li G, Kou G. Consensus reaching process in large-scale group decision making based on opinion leaders. Procedia Computer Science. 2022;199:509-16.
[19] Wang L, Wang H, Xu Z, Ren Z. The interval‐valued hesitant Pythagorean fuzzy set and its applications with extended TOPSIS and Choquet integral‐based method. International Journal of Intelligent Systems. 2019;34(6):1063-85.

Fuzzy Systems and Data Mining X
A.J. Tallón-Ballesteros (Ed.)

doi:10.3233/FAIA241403

The Impact of Firefly Algorithm (FA) Optimization on Gaussian Kernel-Based Fuzzy C-Means Clustering (GKFCM) Efficiency

Narongdech DUNGKRATOKE [a], Chantana SIMTRAKANKUL [a], Janejira LAOMALA [a] and Sayan KAENNAKHAM [b,1]
[a] *Department of Interdisciplinary Science and Internationalization, Institute of Science, Suranaree University of Technology, Nakhon Ratchasima, 30000, Thailand;*
[b] *School of Mathematics and Geoinformatics, Institute of Science, Suranaree University of Technology, Nakhon Ratchasima, 30000, Thailand;*
ORCiD ID: Narongdech Dungkratoke https://orcid.org/0009-0006-7097-9666, Chantana Simtrakankul https://orcid.org/0009-0002-0873-7384, Janejira Laomala https://orcid.org/0009-0000-9350-2541, Sayan Kaennakham https://orcid.org/0000-0001-9682-559X

Abstract. This study explores the effectiveness of the traditional Firefly algorithm (FA) in optimizing the Gaussian Kernel-based Fuzzy C-means clustering (GKFCM) algorithm by adjusting 'sigma' and 'm'. We compare GKFCM with FA optimization (With FA) to without it (Without FA) using the Calinski Harabasz (CH) index and the number of iterations. For all four datasets analyzed in this study, the findings consistently indicate that the GKFCM algorithm optimized with the Firefly algorithm (FA) performs substantially better than its non-optimized counterpart, achieving higher Calinski Harabasz (CH) scores and requiring fewer iterations across various data types. Results from two initial particle distribution styles confirm FA's robustness in refining clustering outcomes and emphasize its role in enhancing clustering quality and efficiency.

Keywords. Clustering Optimization, Firefly Algorithm, Gaussian Kernel, Calinski Harabasz Index

1. Introduction

Clustering is a fundamental technique in machine learning that organizes datasets into subsets or clusters based on shared characteristics. Among the prominent methods, the Fuzzy C-Means (FCM) Algorithm enhances traditional k-means clustering by incorporating fuzziness, allowing each data point to belong to multiple clusters with varying degrees of membership [1]. A sophisticated variant, the Kernel-based FCM, excels in managing noisy datasets, data with overlapping clusters, and non-linear, complex data distributions. Notably, the Gaussian kernel function is the most popular

[1] Corresponding Author: Sayan Kaennakham, sayan_kk@g.sut.ac.th.

choice for Kernel-based FCM, as it significantly improves clustering by mapping data into a higher-dimensional space [2,3].

Despite its advancements, the Gaussian Kernel-based FCM (Gaussian K-FCM) requires careful tuning of two critical parameters: the Gaussian shape and the fuzziness level. These parameters are highly sensitive to the specific problem, necessitating skilled and experienced users for their optimal determination [4]. This challenge has spurred researchers over the past decade to develop strategies for automatic parameter adjustment. One promising approach that has emerged is the Firefly optimization algorithm (FA) [5], which aims to autonomously optimize these parameters, enhancing the practical deployment of Gaussian K-FCM.

The Firefly Algorithm (FA) is an optimization technique inspired by the bioluminescent communication behavior of fireflies. FA utilizes the principles of attraction based on brightness, where each firefly moves towards brighter ones within the search space, thereby simulating a form of natural swarm intelligence [6]. The brightness of each firefly is determined by the value of the objective function at their location, guiding their movements towards optimal solutions. This algorithm is particularly effective for solving complex optimization problems across various domains due to its simplicity, efficiency, and the ability to escape local optima [7]. While FA has previously been applied to optimize Gaussian Kernel-based FCM [8], our study builds upon this foundation by systematically evaluating its effectiveness across multiple datasets, assessing improvements in clustering quality and efficiency.

Our work will explore the application of the Firefly Algorithm for fine-tuning the parameters of the Kernel FCM, aiming to enhance its performance and applicability in various data-driven domains.

2. Methodology

2.1. The Gaussian Kernel Fuzzy C-means (GKFCM)

The objective of GKFCM is to minimize the following function

$$J_m(U,V) = \sum_{i=1}^{N}\sum_{j=1}^{C} u_{ij}^{m} \times \exp\left(-\left\|\mathbf{x}_i - \mathbf{v}_j\right\|^2 \Big/ \sigma^2\right) \tag{1}$$

where $U = \left[u_{ij}\right]$ represents the fuzzy membership matrix with u_{ij} denoting the degree of membership of the i-th data point $\mathbf{x}_i$ in the j-th cluster, $V = \left[\mathbf{v}_j\right]$ is the matrix of cluster centers in the transformed feature space, m is the fuzzification parameter ($m > 1$), controlling the level of cluster fuzziness. The Gaussian kernel function, with σ as the kernel width parameter, with the Euclidean distance, is used here.

To solve for U and V, the algorithm iteratively updates the membership u_{ij} and the cluster centers v_j using the following rules

$$u_{ij} = \left[\sum_{k=1}^{C} \left(\frac{K(\mathbf{x}_i, \mathbf{v}_j)}{K(\mathbf{x}_i, \mathbf{v}_k)} \right)^{\frac{1}{m-1}} \right]^{-1} \tag{2}$$

The cluster centers in GKFCM are typically not explicitly updated in the original feature space. Instead, they are indirectly influenced by the kernel distances in the calculation of memberships and by applying kernel methods.

2.2. The Firefly Algorithm (FA)

In FA, the brightness I_i of firefly i at a particular location $\mathbf{x}_i$ is determined by the value of the objective function $f(\mathbf{x}_i)$, i.e., $I_i \propto f(\mathbf{x}_i)$. For maximization problems, brightness is directly proportional to $f(\mathbf{x}_i)$. The attractiveness β of a firefly is a function of the distance r_{ij} between two fireflies i and j, given by

$$\beta(r_{ij}) = \beta_0 e^{-\gamma r_{ij}^2} \tag{3}$$

where β_0 is the attractiveness at $r = 0$ and γ is the light absorption coefficient, which controls how the attractiveness decreases with distance. The distance r_{ij} between two fireflies i and j located at $\mathbf{x}_i$ and $\mathbf{x}_j$, respectively, is typically calculated using the Euclidean distance, simply defined as $r_{ij} = \left\| \mathbf{x}_i - \mathbf{x}_j \right\|$. A firefly i will move towards another more attractive (brighter) firefly j according to the following equation

$$\mathbf{x}_i^{t+1} = \mathbf{x}_i^t + \beta(r_{ij})(\mathbf{x}_j^t - \mathbf{x}_i^t) + \alpha(\mathbf{rand} - 0.5) \tag{4}$$

where α is a randomization parameter, and **rand** is a random number generated uniformly from $[0,1]$.

3. The Proposed Algorithm

Step 1: Define an objective function $J(m, \sigma)$ based on Calinski Harabasz score.
Step 2: Initialize a population of fireflies, (m, σ), within their feasible ranges ($m \in (1,3), \sigma \in [0.01,5]$).
Step 3: For each firefly, update positions by moving towards brighter fireflies (i.e., better parameter sets), adjusting m and σ using

$$m_i^{t+1} = m_i^t + \beta(r_{ij})(m_j^t - m_i^t) + \alpha(rand - 0.5) \tag{5}$$

$$\sigma_i^{t+1} = \sigma_i^t + \beta(r_{ij})(\sigma_j^t - \sigma_i^t) + \alpha(rand - 0.5) \tag{6}$$

Step 4: Iterate until reaching 100 iterations or $\max_{All\_i} \left| r_i^{t+1} - r_i^t \right| \le 10^{-4}$.

Step 5: Choose the parameters from the position of the brightest firefly at the end of the iterations.

4. Experimental Setup

4.1. The datasets

Figure 1 illustrates four types of datasets under investigation. Types 1 and 2 exhibit nonlinear, spiral-like patterns; Type-1 has a tightly adherent distribution indicating low noisiness and high precision, while Type-2 shows similar patterns but with increased spread and noisiness, adding complexity to its modeling. Type-3 and Type-4 both feature two distinct clusters; Type-3 has compact clusters with low noisiness and minimal complexity, whereas Type-4's clusters are more dispersed, increasing the complexity and variability in data.

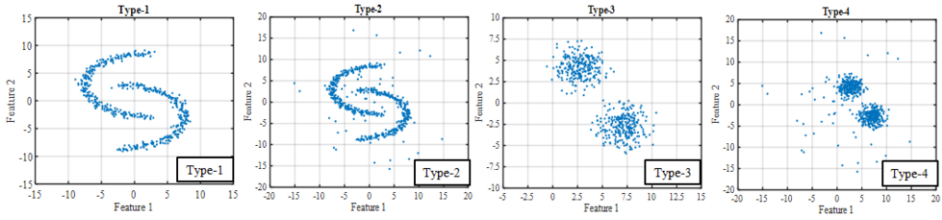

Figure 1. The four datasets: Type-1 and Type-3 each contain 500 points, while the other two contain 550 points each.

4.2. The initial FA node distribution styles

The initial node distribution in the Firefly Algorithm critically affects its performance by determining the balance between exploring the solution space and exploiting known good areas. This choice is strategic, influencing both the efficiency and effectiveness of the algorithm in response to the specific characteristics of the optimization problem. To further assess this impact, our work tested the algorithms using two styles of initial node distribution as shown in Figure 2.

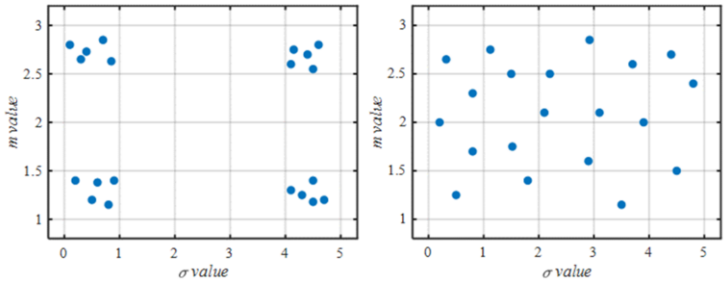

Figure 2. The initial FA node distribution styles; Left) Style-1, and Right) Style-2, containing 20 points each.

By comparing these two configurations, we aimed to understand how different initial node placements affect the algorithm's balance between exploring broadly across the solution space and concentrating on refining solutions in promising areas. Limiting the analysis to these two distinct styles also prevents excessive complexity, ensuring clear insights into the role of initial distribution without complicating the assessment with multiple configurations.

5. Main Results and General Discussions

The investigation used two numbers of fireflies; 10 and 20, each tested with two initial node distribution styles as previously shown. All simulations were performed on the same computational configuration to ensure fairness.

Table 1. Comparison of performance with and without FA, using 10 fireflies (initial distribution Style-1).

Data Type	Calinski Harabasz		No. of Iterations		(sigma, m)	
	Without FA	With FA	Without FA	With FA	Without FA	With FA
Type-1	141.1030	677.1037	42	6	(1, 2)	(5.0,2.9)
Type-2	182.1749	605.4243	102	38	(1, 2)	(5.0,1.1)
Type-3	375.3746	2751.874	57	16	(1, 2)	(4.1,2.6)
Type-4	43.6024	962.3828	97	68	(1, 2)	(4.1,2.6)

As can be seen in Table 1, the implementation of the Firefly algorithm (FA) for optimizing the Gaussian Kernel-based Fuzzy C-means clustering (GKFCM) algorithm demonstrates significant enhancements in clustering performance across various data types. The Calinski Harabasz (CH) scores, a metric assessing the ratio of between-cluster to within-cluster sums of squares, show marked improvements when optimized with FA. For example, Type-1 data sees an increase in CH score from 141.103 to 677.1037, and even more dramatically, Type-4 data's CH score escalates from 43.6024 to 962.3828. This increase signifies a more effective clustering with better defined separations between clusters when parameters are optimized by FA.

Additionally, the optimization through FA considerably reduces the number of iterations required for the GKFCM algorithm to converge, enhancing computational efficiency. Without FA, the iterations needed range from 42 to 102 across different data types, while with FA, these are reduced significantly—for instance, from 97 to 68 in Type-4 data and from 42 to 6 in Type-1 data. The optimization also influences the algorithm's parameters (σ , m), which vary with FA and are constant without it (e.g., Type-1 data with parameters changing from (1, 2) to (5, 2.9)). This tailored approach in adjusting parameters per data type contributes both to the quality of clustering and the efficiency of the algorithm, demonstrating the substantial benefits of incorporating an optimization algorithm like FA in clustering methodologies.

Table 2. Comparison of performance with and without FA, using 10 fireflies (initial distribution Style-2).

Data Type	Calinski Harabasz		No. of Iterations		(sigma, m)	
	Without FA	With FA	Without FA	With FA	Without FA	With FA
Type-1	141.1030	407.7983	42	99	(1, 2)	(3.96,2.19)
Type-2	182.1749	594.8594	102	99	(1, 2)	(4.43,2.45)
Type-3	375.3746	2751.874	57	24	(1, 2)	(4.24,2.76)
Type-4	43.6024	962.3828	97	20	(1, 2)	(4.11,2.15)

The experimental results comparing the performance of the Gaussian Kernel-based Fuzzy C-means clustering (GKFCM) algorithm with and without the optimization by the Firefly algorithm (FA) initial particle distribution style 2, as shown in Table 2, illustrate significant improvements in clustering quality and efficiency when parameters are optimized. The Calinski Harabasz (CH) index, which evaluates clustering effectiveness by measuring the ratio of between-cluster to within-cluster variance, shows substantial increases across all data types when FA is utilized. Specifically, for Type-1 data, the CH value rises from 141.103 to 407.7983, and for Type-4, it increases from 43.6024 to 962.3828. These improvements indicate that the optimized GKFCM algorithm, with tailored parameters of sigma and m, produces more distinct and well-separated clusters.

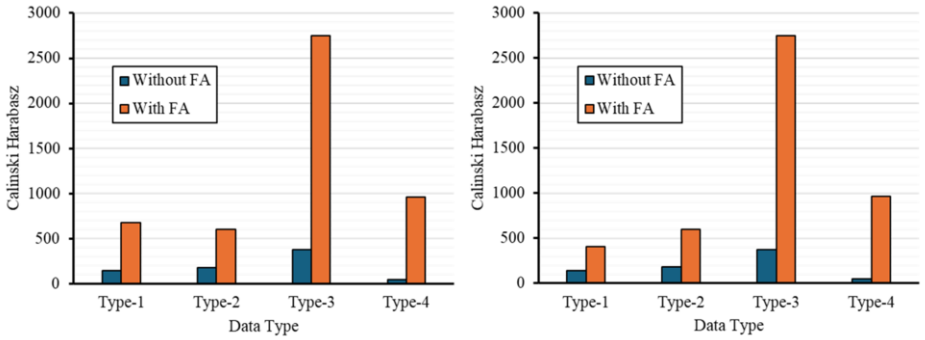

Figure 3. Calinski Harabasz values produced by both cases, using 20 fireflies, with; (left) Initial particle distribution style 1 and (right) Initial particle distribution style 2.

Contrary to the expected trend, the number of iterations needed for the algorithm to converge increased in some cases when optimized by FA. For example, Type-1 data required an increase from 42 to 99 iterations, and similar trends are observed in Type-2 and Type-3 data. This suggests that while FA enhances the clustering quality significantly, it may require more iterations to fine-tune the parameters to achieve the optimal clustering solution. The optimized parameters (sigma, m) show considerable variation across data types, demonstrating the adaptive capability of FA to tailor these parameters to specific dataset characteristics, further contributing to the enhanced performance of the GKFCM algorithm. For the case of using 20 fireflies, it was found that the overall results were similar to those discussed so far; therefore, they are not detailed here due to space limitations. Nevertheless, some results are illustrated in Figure 3.

6. Conclusion

The experiment comparing two initial particle distribution styles of the Firefly algorithm (FA) for optimizing the Gaussian Kernel-based Fuzzy C-means clustering (GKFCM) algorithm demonstrates significant benefits. FA optimization markedly improves Calinski Harabasz (CH) values, indicating better cluster separations. For instance, Type-4 data saw a CH increase from 43.6024 to 962.3828 with FA. This improvement is coupled with a reduction in iterations required for convergence, showcasing FA's computational efficiency. For Type-1 data, iterations dropped from 42 to 6. These results confirm that optimizing 'sigma' and '*m*' via FA enhances clustering quality and

accelerates convergence. Future work will extend FA-optimized GKFCM across diverse datasets and explore other optimizers, such as PSO, for optimal parameter tuning across varied applications.

Acknowledgments

This work was supported by (i) Suranaree University of Technology (SUT, http://www.sut.ac.th), (ii) Thailand Science Research Innovation (TSRI, https://www.tsri.or.th), and (iii) National Science, Research and Innovation Fund (NSRF) (NRIIS number 195619). The grant recipient is S. Kaennakham who would like to express his sincere gratitude for their support.

References

[1] Suganya R, Shanthi R. Fuzzy c-means algorithm-a review. International Journal of Scientific and Research Publications. 2012 Nov;2(11):1.

[2] Simões EC, de Carvalho FD. Gaussian kernel fuzzy c-means with width parameter computation and regularization. Pattern Recognition. 2023 Nov 1;143:109749.

[3] Chinta S, Tripathy BK, Rajulu KG. Kernelized intuitionistic fuzzy C-means algorithms fused with firefly algorithm for image segmentation. In2017 international conference on microelectronic devices, circuits and systems. 2017 Aug 10 (pp. 1-6). IEEE.

[4] Ding Y, Fu X. Kernel-based fuzzy c-means clustering algorithm based on genetic algorithm. Neurocomputing. 2016 May 5;188:233-8.

[5] Yang XS, He X. Firefly algorithm: recent advances and applications. International journal of swarm intelligence. 2013 Jan 1;1(1):36-50.

[6] Yang XS. Firefly algorithms for multimodal optimization. International symposium on stochastic algorithms 2009 Oct 26 (pp. 169-178). Berlin, Heidelberg: Springer Berlin Heidelberg.

[7] Zare M, Ghasemi M, Zahedi A, Golalipour K, Mohammadi SK, Mirjalili S, Abualigah L. A global best-guided firefly algorithm for engineering problems. Journal of Bionic Engineering. 2023 Sep;20(5):2359-88.

[8] Thomas E, Kumar SN. Fuzzy C Means Clustering Coupled with Firefly Optimization Algorithm for the Segmentation of Neurodisorder Magnetic Resonance Images. Procedia Computer Science. 2024 Jan 1;235:1577-89.

Fuzzy Systems and Data Mining X
A.J. Tallón-Ballesteros (Ed.)

doi:10.3233/FAIA241404

A Comparative Study of Distance Functions in Enhancing Cluster Quality Through Gaussian Kernel-Based Fuzzy C-Means

Chantana SIMTRAKANKUL [a], Narongdech DUNGKRATOKE [a], Janejira LAOMALA [a] and Sayan KAENNAKHAM [b,1]
[a] *Department of Interdisciplinary Science and Internationalization, Institute of Science, Suranaree University of Technology, Nakhon Ratchasima, 30000, Thailand;*
[b] *School of Mathematics and Geoinformatics, Institute of Science, Suranaree University of Technology, Nakhon Ratchasima, 30000, Thailand;*
ORCiD ID: Chantana Simtrakankul https://orcid.org/0009-0002-0873-7384
Narongdech Dungkratoke https://orcid.org/0009-0006-7097-9666
Janejira Laomala https://orcid.org/0009-0000-9350-2541
Sayan Kaennakham https://orcid.org/0000-0001-9682-559X

Abstract. This study evaluates various distance functions in Gaussian Kernel-based fuzzy C-means clustering across six datasets. Key findings include the superior performance of the Cosine distance, which consistently yielded the lowest Davies-Bouldin scores, notably 0.3823 and 0.5226 for Datasets 5 and 6, and required fewer iterations to converge, with figures as low as 7 and 8. Squared Euclidean distance also showed effectiveness, particularly with fewer iterations needed for convergence, such as 22 and 41 for Datasets 1 and 3. In contrast, Chebyshev and Minkowski distances, requiring up to 119 iterations for Dataset 2, demonstrated lower efficiency. The evaluation process also involved additional clustering quality metrics, including the Silhouette and Calinski-Harabasz indices, though only the Davies-Bouldin results are detailed in this paper. This analysis highlights the importance of choosing appropriate distance metrics to optimize clustering quality and computational efficiency.

Keywords. Fuzzy C-Means Clustering, Distance Metrics, Kernel Methods

1. Introduction

Fuzzy C-means clustering is a powerful data analysis technique that extends the traditional k-means algorithm by allowing each data point to belong to multiple clusters with varying degrees of membership [1]. This flexibility is especially valuable in fields where data elements can inherently possess ambiguous characteristics or belong to overlapping categories, such as image processing for edge detection and segmentation [2], bioinformatics for gene expression data analysis [3], and customer behavior studies

[1] Corresponding Author: Sayan Kaennakham, sayan_kk@g.sut.ac.th.

[4] where purchasing preferences may not be strictly defined. Enhancing this method, the kernel-based version of Fuzzy C-means introduces a kernel function to map the original data into a higher-dimensional feature space, effectively handling non-linearly separable data [5, 6]. Among the various kernels available, the Gaussian kernel is the most famous and widely used due to its ability to handle complex, multidimensional datasets by weighting the influence of distant points, thus smoothing the boundaries between clusters for more natural groupings.

When it comes to the Gaussian kernel [7], it is widely used in machine learning, pattern recognition, and signal processing, it is instrumental in kernel-based algorithms like support vector machines and Fuzzy C-means clustering, allowing them to capture non-linear relationships and reveal intricate patterns. Crucially, the effectiveness of the Gaussian kernel hinges on the choice of distance function used to calculate the similarity between data points. Different distance measures can dramatically influence the kernel's behavior, affecting everything from the smoothness of the data transformation to the sensitivity to outliers. Mathematical distance metrics are vital in data science for measuring object similarity or dissimilarity. Metrics like Euclidean distance, Manhattan distance, and Cosine similarity each suit different analytical needs and data types, including Minkowski distance which generalizes others. Selecting the appropriate distance metric is critical, impacting algorithm performance significantly [8].

Overall, this research focuses on examining how different distance functions affect the Gaussian Kernel-based Fuzzy C-means algorithm, highlighting the importance of metric choice in achieving optimal clustering results.

The subsequent sections of the paper are structured as follows: Section 2, Methodology, outlines the Gaussian Kernel Fuzzy C-means (GKFCM) approach and the calculations employed for data clustering. It includes the process for updating cluster centers and presents the distance functions utilized in this study, specifically Euclidean, Manhattan, and Cosine. Additionally, it discusses the appropriateness of each metric for various applications. Section 3, Datasets, details the datasets employed in the experiments, emphasizing their distinctive features that are essential for assessing the efficacy of the distance metrics. Section 4 presents the experimental findings and analysis, employing quality indicators such as the Davies-Bouldin index, Silhouette, and Calinski-Harabasz indices to evaluate clustering quality and the effectiveness of each distance metric. Section 5, Conclusion, provides a summary of the research findings and presents recommendations for future studies.

2. Methodology

2.1. The Gaussian Kernel Fuzzy C-means (GKFCM)

This method enhances the clustering performance by exploiting the Gaussian kernel's capability to capture the complex structures in data. The objective of GKFCM is to minimize the following function.

$$J_m(U,V) = \sum_{i=1}^{N}\sum_{j=1}^{C} u_{ij}^{m} \times K(\mathbf{x}_i, \mathbf{v}_j) \tag{1}$$

where $U = \left[u_{ij} \right]$ represents the fuzzy membership matrix with u_{ij} denoting the degree of membership of the i-th data point $\mathbf{x}_i$ in the j-th cluster, $V = \left[\mathbf{v}_j \right]$ is the matrix of cluster centers in the transformed feature space, m is the fuzzification parameter ($m > 1$), controlling the level of cluster fuzziness.

This work, the famous Gaussian kernel function is used and is expressed as follows

$$K(\mathbf{x}, \mathbf{v}) = \exp\left(-\frac{(d(\mathbf{x}, \mathbf{v}))^2}{2\sigma^2} \right) \tag{2}$$

with σ as the kernel width parameter, and $d(\mathbf{x}, \mathbf{v})$ represents the distance function linking between the data point $\mathbf{x}$ and cluster center $\mathbf{v}$.

To solve for U and V, the algorithm iteratively updates the membership u_{ij} and the cluster centers $\mathbf{v}_j$ using the following rules.

$$u_{ij} = \left[\sum_{k=1}^{C} \left(\frac{K(\mathbf{x}_i, \mathbf{v}_j)}{K(\mathbf{x}_i, \mathbf{v}_k)} \right)^{\frac{1}{m-1}} \right]^{-1} \tag{3}$$

Since $\mathbf{v}_j$ cannot be directly computed in the transformed feature space, the update is implicitly handled through the kernel function. The explicit update of $\mathbf{v}_j$ typically does not occur in kernelized methods; instead, $\mathbf{v}_j$ is represented as a linear combination of all data points, weighted by their memberships.

2.2. The Distance Metrics

Distance metrics (appearing as one main component of the Gaussian kernel) quantify the similarity or dissimilarity between elements in a space. They vary based on data types and applications, as outlined in Table 1.

Table 1. Mathematical formulas for various distance metrics used in clustering algorithms

Distance matric type	Mathematical Formula
Euclidean distance	$d(x,y) = \sqrt{\sum_{k=1}^{n} (x_k - y_k)^2}$
Squared Euclidean distance	$d(x,y) = \sum_{k=1}^{n} (x_k - y_k)^2$
Manhattan distance	$d(x,y) = \sum_{k=1}^{n} \lvert x_k - y_k \rvert$
Chebyshev distance	$d(x,y) = \max_{k=1}^{n} \lvert x_k - y_k \rvert$
Minkowski distance	$d(x,y) = \sqrt[p]{\sum_{k=1}^{n} \lvert x_k - y_k \rvert^p}$

Mahalanobis distance	$d(x,y)=\sqrt{(x-y)S^{-1}(x-y)^T}$
Cosine distance	$d(x,y)=\frac{\arccos(x\cdot y)}{\|x\|\|y\|}$

Choosing the right distance metric is crucial as it can significantly affect the performance and outcomes of machine learning algorithms, especially in clustering and classification tasks.

3. The Datasets

The datasets display varying characteristics, see Figure 1: Dataset-1 and Dataset-2 are nonlinear, with Dataset-2 being more complex. Dataset-3 and Dataset-6 feature distinct clusters indicating categorical data, with Dataset-6 being more complex due to multiple clusters. Dataset-4 has a noisy distribution with a slight linear trend, whereas Dataset-5 is densely clustered and shows minimal feature correlation. Each presents unique analytical challenges, from linear to complex nonlinear interactions. Dataset-1,3, and 5 contain 500 points each, and the others contain 550 points.

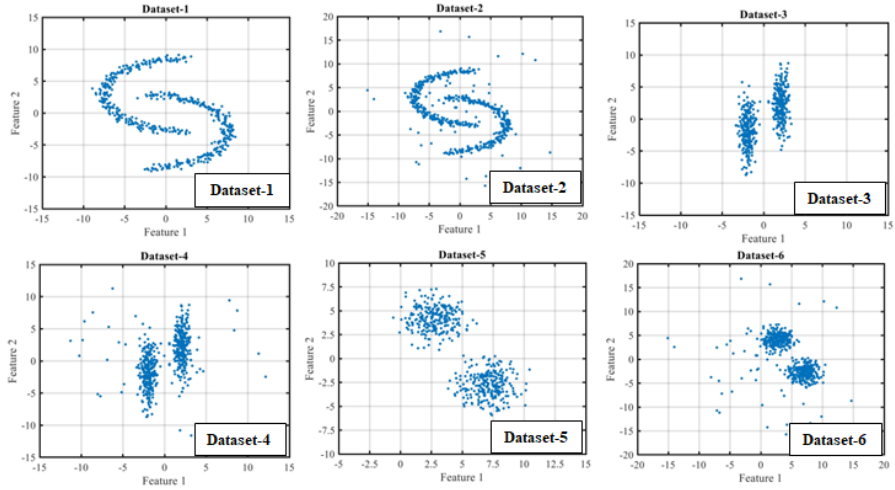

Figure 1. Manners of data point distribution.

4. Main Results and General Discussions

In this study, we utilized several well-known metrics for fuzzy clustering, including the Davies Bouldin index, Silhouette Coefficient, and Calinski Harabasz index. However, due to space constraints, only the Davies Bouldin index is presented in this document, although the other two metrics showed similar trends in the results.

Table 2. Davies-Bouldin index scores across six datasets using different distance functions.

Distance Function	Dataset-1	Dataset-2	Dataset-3	Dataset-4	Dataset-5	Dataset-6
Euclidean	0.9941826	0.8687367	2.7487063	3.2892803	0.6942038	2.3421074
Squared Euclidean	0.8357737	1.2601941	1.9501100	2.0662090	0.7159571	0.8226534
Manhattan	0.9286649	1.4894199	10.7170352	7.8536745	0.6971984	1.4666148
Chebyshev	1.1025969	0.8845497	1.4648841	1.9491796	0.6922886	14.9667797
Minkowski	1.0284561	0.8768132	1.8616782	2.3971707	0.6868385	4.1486235
Mahalanobis	1.2306699	1.1923929	1.6219738	1.0287556	4.0889937	0.5151039
Cosine	0.8127797	0.8653911	0.6880843	0.7669210	0.3823327	0.5225996

As can be seen in Table 2, the Davies-Bouldin index results for clustering using various distance functions reveal insights into cluster quality across six datasets. Cosine distance consistently demonstrates superior clustering quality with the lowest Davies-Bouldin scores, indicating tighter and more distinct clusters, with notable scores like 0.5226 and 0.3823 for Datasets 6 and 5 respectively. Squared Euclidean also shows promise, particularly in Datasets 1 and 6 with scores of 0.8358 and 0.8226, suggesting effective clustering but slightly less optimal than Cosine. On the other end, Chebyshev distance exhibits highly variable performance, with a particularly poor score of 14.9668 in Dataset 6, indicating less distinct clusters. Mahalanobis and Euclidean distances generally present moderate clustering quality, with Mahalanobis excelling in Dataset 6 with a score of 0.5151. Overall, Cosine and Squared Euclidean distances tend to provide the most effective clustering in terms of cluster compactness and separation across most datasets.

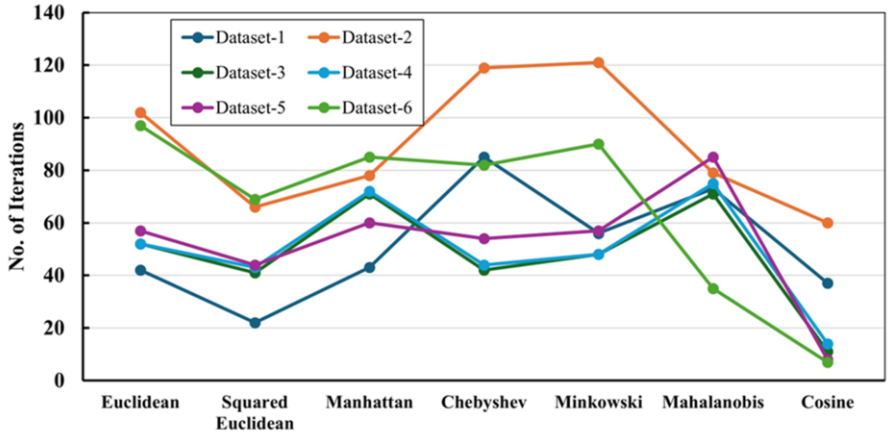

Figure 2. The number of iterations required by each distance function for each dataset.

In terms of the number of iterations each one took, Figure 2 shows that the Cosine distance function demonstrated the highest efficiency, requiring the fewest iterations to converge—7, 8, and 11 for Datasets 6, 5, and 3, respectively. Similarly, the Squared Euclidean distance consistently showed lower iteration counts, such as 22, 66, and 41 for Datasets 1, 2, and 3, suggesting its computational simplicity aids rapid convergence. In contrast, the well-known Euclidean distance required more iterations, such as 102 for Dataset 2, indicating a moderate convergence speed. Chebyshev and Minkowski

distances often required more iterations, particularly Chebyshev with 119 for Dataset 2, indicating sensitivity to dataset specifics. Mahalanobis distance excelled in Dataset 6 with only 35 iterations, underscoring its effectiveness in feature-correlated datasets. This analysis emphasizes the importance of choosing suitable distance metrics based on dataset traits to optimize clustering efficiency.

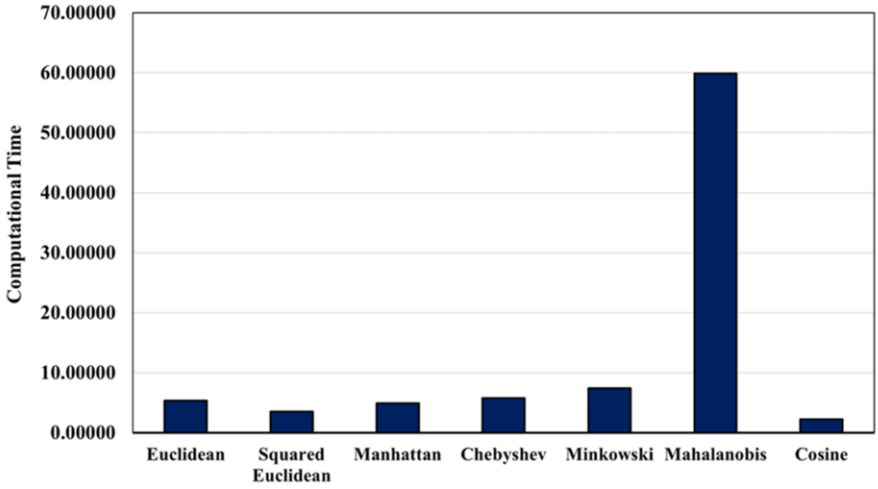

Figure 3. Computational time involved in each case.

In evaluating the computational times of various distance functions used in clustering, we see significant differences in Figure 3. The Mahalanobis distance is the most time-intensive at approximately 59.92 seconds, reflecting its complexity. At the other end, Cosine similarity is the quickest, needing only 2.24 seconds, ideal for high-dimensional data. Minkowski and Euclidean distances also require substantial time, 7.44 and 5.37 seconds respectively, due to their detailed computations. Meanwhile, simpler metrics like Manhattan and Squared Euclidean offer more efficiency at 4.92 and 3.51 seconds. This range illustrates key trade-offs between computational efficiency and the complexity of data relationships handled by each metric.

The superior performance of the Cosine and Squared Euclidean distances suggests their potential to optimize clustering in real-world applications, such as precise image segmentation for medical imaging or bioinformatics clustering for gene expression data analysis. These use cases, which often require high accuracy and distinct group separations, stand to benefit from the enhanced feature separation and computational efficiency observed with these metrics. Future work could explore integrating this approach with other optimization methods, further broadening its practical utility in dynamic, complex datasets often found in healthcare and data science domains.

5. Conclusion

Our extensive study employing Gaussian Kernel-based fuzzy C-means clustering across six datasets demonstrates that the choice of distance function significantly impacts the quality of clustering. The Cosine distance metric exhibited outstanding performance,

consistently achieving the lowest Davies-Bouldin scores, such as 0.3823 and 0.5226 for Datasets 5 and 6, respectively. This metric efficiently forms compact and distinct clusters, especially beneficial in high-dimensional data contexts. Similarly, the Squared Euclidean distance showcased robust clustering capabilities with scores like 0.8358 and 0.8226 for Datasets 1 and 6, combining effectiveness with computational efficiency. In contrast, the Chebyshev distance varied greatly in performance, with a poor score of 14.9668 in Dataset 6, highlighting its limitations in certain conditions. These findings emphasize the critical role of selecting an appropriate distance metric to optimize both the quality of clustering and the computational resources.

Acknowledgments

This work was supported by (i) Suranaree University of Technology (SUT, http://www.sut.ac.th), (ii) Thailand Science Research Innovation (TSRI, https://www.tsri.or.th), and (iii) National Science, Research and Innovation Fund (NSRF) (NRIIS number 195613). The grant recipient is S. Kaennakham who would like to express his sincere gratitude for their support.

References

[1] Suganya R, Shanthi R. Fuzzy c-means algorithm-a review. International Journal of Scientific and Research Publications. 2012 Nov;2(11):1.
[2] Hien NM, Binh NT, Viet NQ. Edge detection based on Fuzzy C Means in medical image processing system. In2017 international conference on system science and engineering (ICSSE) 2017 Jul 21 (pp. 12-15). IEEE.
[3] Gasparovica M, Aleksejeva L, Nazaruks V. Using fuzzy clustering with bioinformatics data. InProc. Int. Conf. Appl. Inf. Commun. Technologies 2013 Apr 25 (pp. 62-70).
[4] Ansari A, Riasi A. Customer clustering using a combination of fuzzy c-means and genetic algorithms. International Journal of Business and Management. 2016 Jun 21;11(7):59-66.
[5] Ding Y, Fu X. Kernel-based fuzzy c-means clustering algorithm based on genetic algorithm. Neurocomputing. 2016 May 5;188:233-8.
[6] Zhang DQ, Chen SC. Clustering incomplete data using kernel-based fuzzy c-means algorithm. Neural processing letters. 2003 Dec;18:155-62.
[7] Chung MK. Gaussian kernel smoothing. arXiv preprint arXiv:2007.09539. 2020 Jul 19.
[8] Singh A, Yadav A, Rana A. K-means with Three different Distance Metrics. International Journal of Computer Applications. 2013 Jan 1;67(10).

Fuzzy Systems and Data Mining X
A.J. Tallón-Ballesteros (Ed.)

doi:10.3233/FAIA241405

A New Three Way Multi-Attribute Group Decision-Making Method with Probabilistic Dominance Relation Based on Interval-Valued Fermatean Hesitant Fuzzy Sets

Siyue Lei[a], Xiuqin Ma[a,1], Hongwu Qin[a], Xuli Niu[a] and Dong Ren[a]
[a]*College of Computer Science and Engineering, Northwest Normal University, Lanzhou, 730020, Gansu, China*

Abstract. Interval-value Fermatean hesitant fuzzy sets (IVFHFSs) are new data model for dealing with complex, uncertain information. However, the researches on IVFHFSs score functions (SFs) have low discrimination rate and existing multi-attribute group decision-making under IVFHFSs are scarce and have no ability to classify. Therefore, this paper establishes a new three-way multi-attribute group decision-making (3W-MAGDM) based on IVFHFSs. First, novel IVFHFSs SFs are proposed. Next, the objective conditional probabilities calculation method is derived by using the probabilistic dominance relation and the relative loss functions calculation method in three-way decision is developed. The subjectivity of 3W-MAGDM under IVFHFSs is greatly reduced. Finally, a new 3W-MAGDM framework based on IVFHFSs is constructed. The new approach has a high discrimination rate in SFs and it not only has a ranking function but also has a categorization function.

Keywords. Interval-value Fermatean hesitant fuzzy sets, Three-way multi-attribute group decision-making, Score functions, Probabilistic dominance relation.

1. Introduction

With the continuous development of the information age, the expression of information is characterized by more and more complexity and uncertainty. Nowadays, complex, uncertain information often appears in various important fields, such as finance, artificial intelligence, medical care, and so on. Linking uncertain information with decision theory is a key research area for addressing real-world problems and enhancing decision-making (DM) efficiency and science.

The fuzzy sets (FSs) theory proposed by Zadeh[1] is a crucial instrument for handling complicated, ambiguous data and has drawn a lot of interest from academics. In recent years, experts have developed various optimized fuzzy models[2, 3] to enable them to describe the increasingly complex, uncertain information in reality. Then, interval-valued Fermatean hesitant fuzzy sets (IVFHFSs) were proposed by Kirişci and Şimşek[4]. IVFHFSs have greater flexibility and intelligence compared with IVFFSs by varying the number of hesitations and the range of interval values.

[1] Corresponding Author: Xiuqin Ma, Northwest Normal University, China. Email: maxiuqin@nwnu.edu.cn.
Funding was provided by the National Natural Science Foundation of China, grant number 62162055.

In order to increase the risk tolerance of DM, Yao[5] proposed the concept of 3WD on the basis of two-way decision. Some scholars have extended 3WD to multi-attribute group decision-making (MAGDM)[6] called three-way multi-attribute group decision-making (3W-MAGDM). MAGDM is able to consider multiple evaluation criteria at the same time with group intelligence idea, helping decision makers to comprehensively assess the strengths and weaknesses of each option. Then, 3W-MAGDM is based on MAGDM to further reduces DM risk. Based on degree-based linguistic term sets, Wang et al.[7] proposed the 3W-MAGDM approach by utilizing TOPSIS method. And Song et al.[8] improved VIKOR method by grey correlation analysis and constructed hybrid 3W-MAGDM model based on interval-valued intuitionistic fuzzy numbers.

However, these approaches clearly still have certain limitations: (1) As a new fuzzy model, IVFHFSs score functions (SFs) in [4] suffer from the defect of not being able to distinguish partially fuzzy data. Furthermore, the existing approaches[4, 9, 10] based on the IVFHFSs only have a sorting function and do not categorize the alternatives. (2) Critical roles are played by conditional probabilities (CPs) and loss functions during 3WD. However, the CPs of 3WD reduce the risk of DM by dominance relation[11, 12]. Furthermore, the CPs in [13] are subjective, and the loss functions in [14, 15] are subjectively awarded. (3) The current data models used in 3W-MAGDM are inflexible and have a small range of representation, which are not enough to handle the increasingly complex information changes.

Based on the above motivations, the 3W-MAGDM methodology under IVFHFSs introduces innovations in the following three ways: (1) New SFs for IVFHFSs are proposed, which can handle deficiency in existing SFs to improve the information processing capacity. (2) Introduce the probabilistic dominance class[16] which is not strict equivalence classes to 3W-MAGDM under IVFHFSs. It not only increases tolerance for risk in the DM process but also objectively calculates CPs. A novel 3WD method for objectively calculating the relative loss functions[13] (RLFs) is proposed based on the aggregation operators and the new SFs. (3) Compared with classical MAGDM in IVFHFSs, this paper combines IVFHFSs with 3W-MAGDM and establishes a 3W-MAGDM method, which not only ranks but also categorizes alternatives.

The entire paper is organized in the following manner: In Section 2, the basic concepts about IVFHFSs, probabilistic dominance relation, and 3WD are briefly described; Section 3 proposes new SFs and comparison; Section 4 presents the calculation of objective CPs and investigate a new 3WD approach based on the objective calculation of the RLFs; A novel 3W-MAGDM with probabilistic dominance relation under IVFHFSs is illustrated in Section 5; In Section 6, a conclusion is presented.

2. Preliminaries

Some basic concepts about IVFHFSs, probabilistic dominance relation, and 3WD based on decision-theoretic rough sets with RLFs are briefly reviewed in this part.

2.1. Some definitions of IVFHFSs

Definition 2.1.[4] Given a nonempty finite domain S, an IVFHFS $\mathcal{G}$ on S is performed as follows:

$$\mathcal{G} = \left\{ < s, \left(\mathcal{F}_{\mathcal{G}}(s) \right) \middle| s \in S > \right\}$$

where $\mathcal{F}_{\mathcal{G}}(s) : S \to [0,1]$ denotes the multiple possible IVFFNs. As a rule, we call $\mathcal{g}_k = [\varsigma_{kl}^-, \varsigma_{kl}^+], [\tau_{kl}^-, \tau_{kl}^+] = \mathcal{F}_{\mathcal{G}}(s)$ as an interval-valued Fermatean hesitant fuzzy number (IVFHFN), where k implies the serial number of IVFHFN and l indicates the hesitance number in IVFHFN.

Definition 2.2.[4] Let $\mathcal{g}$, $\mathcal{g}_1$, $\mathcal{g}_2$ be three IVFHFNs and λ is a constant. Then some operations are defined below:

(1) $\mathcal{g}^c = \bigcup_{([\varsigma_l^-, \varsigma_l^+], [\tau_l^-, \tau_l^+]) \in \mathcal{g}} ([\tau_l^-, \tau_l^+], [\varsigma_l^-, \varsigma_l^+])$

(2) $\lambda \mathcal{g} = \bigcup_{([\varsigma_l^-, \varsigma_l^+], [\tau_l^-, \tau_l^+]) \in \mathcal{g}} \left(\left[\sqrt[3]{1 - (1 - (\varsigma_l^-)^3)^\lambda}, \sqrt[3]{1 - (1 - (\varsigma_l^+)^3)^\lambda} \right], \left[(\tau_l^-)^\lambda, (\tau_l^+)^\lambda \right] \right)$, $(\lambda > 0)$

(3) $\mathcal{g}_1 \oplus \mathcal{g}_2 = \bigcup_{\substack{([\varsigma_{1l}^-, \varsigma_{1l}^+], [\tau_{1l}^-, \tau_{1l}^+]) \in \mathcal{g}_1, \\ ([\varsigma_{2l}^-, \varsigma_{2l}^+], [\tau_{2l}^-, \tau_{2l}^+]) \in \mathcal{g}_2}} \left(\begin{bmatrix} \sqrt[3]{(\varsigma_{1l}^-)^3 + (\varsigma_{2l}^-)^3 - (\varsigma_{1l}^-)^3 (\varsigma_{2l}^-)^3}, \\ \sqrt[3]{(\varsigma_{1l}^+)^3 + (\varsigma_{2l}^+)^3 - (\varsigma_{1l}^+)^3 (\varsigma_{2l}^+)^3} \end{bmatrix}, \begin{bmatrix} \tau_{1l}^- \tau_{2l}^-, \\ \tau_{1l}^+ \tau_{2l}^+ \end{bmatrix} \right)$

2.2. Probabilistic dominance relation

The idea of binary judgment in an order information system was presented Weng and Lv[16]. Here, we now generalize the idea to IVFHFNs by Definition 2.3.

Definition 2.3.[16] Let $\mathcal{g}_1$, $\mathcal{g}_2$ be two IVFHFNs. For $\forall \mathcal{g}_1, \mathcal{g}_2 \in S$, we obtain:

$$\mathcal{E}_q(\mathcal{g}_1, \mathcal{g}_2) = \begin{cases} 1 & (\mathcal{g}_1 | q) \geq (\mathcal{g}_2 | q) \\ 0 & \text{other} \end{cases} \quad (2-1)$$

where $\mathcal{E}_q(\mathcal{g}_1, \mathcal{g}_2)$ represents a binary judgment of $\mathcal{g}_1$ and $\mathcal{g}_2$ under attribute q. If $\mathcal{E}_q(\mathcal{g}_1, \mathcal{g}_2) = 1$, it means that $\mathcal{g}_1$ does not perform worse than $\mathcal{g}_2$ under attribute q. In contrast, if $\mathcal{E}_q(\mathcal{g}_1, \mathcal{g}_2) = 0$, it denotes that $\mathcal{g}_1$ must perform inferior to $\mathcal{g}_2$ under attribute q.

Definition 2.4.[16] Given $P = \{p_1, p_2, \dots, p_n\}$ is an object set, and $Q = \{q_1, q_2, \dots, q_m\}$ is an attribute set. For $\forall q \in Q$, $E_Q(\mathcal{g}_1, \mathcal{g}_2) = \sum_{q \in Q} \mathcal{E}_q(\mathcal{g}_1, \mathcal{g}_2) / |Q|$, where $|Q|$ indicates the cardinality of attribute set Q. Let $\boldsymbol{E}_Q = \left[E_q(\mathcal{g}_1, \mathcal{g}_2) \right]_{n \times n}$ and we call $\boldsymbol{E}_Q$ is a judgment matrix under attribute set Q.

Definition 2.5.[16] The probabilistic dominance relation under Q in the IVFHFSs can be defined as:

$$T_Q^{\geq \eta} = \left\{ (\mathcal{g}_1, \mathcal{g}_2) \in S \times S | E_q(\mathcal{g}_1, \mathcal{g}_2) \geq \eta, 0.5 \leq \eta \leq 1 \right\}$$

where η denotes confidence level, and $T_Q^{\geq \eta}$ is titled the η-probabilistic dominance relation.

Definition 2.6.[16] Given $P = \{p_1, p_2, \dots, p_n\}$ is an object set, and $Q = \{q_1, q_2, \dots, q_m\}$ is an attribute set. Let $[p_i]_Q^{\geq \eta} = \left\{ p_i \in P | \left(p_j, p_i \right) \in T_Q^{\geq \eta} \right\}$, where $i, j \in n$, then $[p_i]_Q^{\geq \eta}$ implies the η-probabilistic dominance class of p_i under Q.

2.3. The 3WD based on decision-theoretic rough sets with RLFs

For a decision-theoretic rough set, there are two states and three actions. $\Upsilon = \{Z, \neg Z\}$ denotes the set of states, where Z and $\neg Z$ indicate two reversed positions. $\psi = \{\psi_P, \psi_B, \psi_N\}$ implies the set of actions. ψ_P represents if p is accepted; ψ_B represents if p is non-committed; ψ_N represents if p is rejected, respectively. A 3 × 2 matrix provides the loss functions related to the risk of various actions. To further simplify the expression

of the loss functions, Jia and Liu[13] proposed the concept of RLFs, as shown in Table 1. In the matrix, δ_{PP}, δ_{BP}, and δ_{NP} represent the relative losses of taking acceptance, non-commitment, and rejection for the objects in state Z, respectively. Similarly, δ_{PN}, δ_{BN}, and δ_{NN} indicate the relative losses of taking acceptance, non-commitment, and rejection for the objects in state $\neg Z$, respectively.

Table 1. The RLFs

	Z	$\neg Z$
ψ_P	δ_{PP}	δ_{PN}
ψ_B	δ_{BP}	δ_{BN}
ψ_N	δ_{NP}	δ_{NN}

where the RLFs specify that $\delta_{PP} = 0$, $\delta_{NN} = 0$.

Based on the RLFs and CPs, the expression for the expected loss functions can be derived as follows:

$$\mathcal{L}(\psi_P|[p]) = \delta_{PN}\,\Omega(\neg Z|[p]) \quad (2-2)$$

$$\mathcal{L}(\psi_B|[p]) = \delta_{BP}\,\Omega(Z|[p]) + \delta_{BN}\,\Omega(\neg Z|[p]) \quad (2-3)$$

$$\mathcal{L}(\psi_N|[p]) = \delta_{NP}\,\Omega(Z|[p]) \quad (2-4)$$

where $\mathcal{L}(a_P|[p])$, $\mathcal{L}(a_B|[p])$, and $\mathcal{L}(a_N|[p])$ indicate the expected losses of making an acceptance behavior, a non-commitment behavior, and a rejection behavior, respectively. $\Omega(Z|[p])$ or $\Omega(\neg Z|[p])$ denotes the CP of Z or $\neg Z$, respectively.

By $\Omega(Z|[p]) + \Omega(\neg Z|[p]) = 1$ and Bayesian theory, we can reduce the decision rules for $(R1)$, $(R2)$, and $(R3)$ as follows:

$(R1)$ If $\Omega(Z|[p]) \geq \alpha$ and $\Omega(Z|[p]) \geq \gamma$, decide $p \in POS(Z)$;

$(R2)$ If $\Omega(Z|[p]) < \alpha$ and $\Omega(Z|[p]) > \beta$, decide $p \in BND(Z)$;

$(R3)$ If $\Omega(Z|[p]) \leq \beta$ and $\Omega(Z|[p]) \leq \gamma$, decide $p \in NEG(Z)$;

where the thresholds α, β, γ are given:

$$\alpha = \frac{\delta_{PN} - \delta_{BN}}{\delta_{PN} - \delta_{BN} + \delta_{BP}} \quad (2-5)$$

$$\beta = \frac{\delta_{BN}}{\delta_{BN} + \delta_{NP} - \delta_{BP}} \quad (2-6)$$

$$\gamma = \frac{\delta_{PN}}{\delta_{PN} + \delta_{NP}} \quad (2-7)$$

3. The new SFs under IVFHFSs

In this part, the new SFs and advantages by comparing different methods are given.

Definition 3.1. Take an IVFHFN $\mathcal{g} = ([\varsigma_l^-, \varsigma_l^+], [\tau_l^-, \tau_l^+])(l = 1,2,\ldots,x)$.

$$SF^*(\mathcal{g}) = \frac{1}{x}\sum_{l=1}^{x} \frac{2 + (\varsigma_l^-)^3 + (\varsigma_l^+)^3 - (\tau_l^-)^3 - (\tau_l^+)^3}{4} \quad (3-1)$$

is called the SF $SF^*(\mathcal{g})$ where $0 \leq SF^*(\mathcal{g}) \leq 1$. And the other SF called accuracy function $AF^*(\mathcal{g})$ is calculated as follows:

$$AF^*(\mathcal{g}) = \frac{1}{x}\sum_{l=1}^{x} \frac{(\varsigma_l^-)^3 + (\varsigma_l^+)^3 + (\tau_l^-)^3 + (\tau_l^+)^3}{2} \quad (3-2)$$

is called the where $0 \leq AF^*(\mathcal{g}) \leq 1$, where x denotes the maximum value of l.

Definition 3.2. Let $\mathcal{g}_a = ([\varsigma_{al}^-, \varsigma_{al}^+], [\tau_{al}^-, \tau_{al}^+])$ and $\mathcal{g}_b = ([\varsigma_{bl}^-, \varsigma_{bl}^+], [\tau_{bl}^-, \tau_{bl}^+])(a = 1,2,..,n, b = 1,2,\dots,n, l = 1,2,\dots,x)$ be two IVFHFNs. The ranking principle between $\mathcal{g}_a$ and $\mathcal{g}_b$ by utilizing the SF and accuracy function is defined as follows:

i. If $SF^*(\mathcal{g}_a) > SF^*(\mathcal{g}_b)$, we stipulate $\mathcal{g}_a > \mathcal{g}_b$
ii. If $SF^*(\mathcal{g}_a) < SF^*(\mathcal{g}_b)$, we stipulate $\mathcal{g}_a < \mathcal{g}_b$
iii. If $SF^*(\mathcal{g}_a) = SF^*(\mathcal{g}_b)$, then
   a) If $AF^*(\mathcal{g}_a) > AF^*(\mathcal{g}_b)$, we get $\mathcal{g}_a > \mathcal{g}_b$
   b) If $AF^*(\mathcal{g}_a) < AF^*(\mathcal{g}_b)$, we get $\mathcal{g}_a < \mathcal{g}_b$
   c) If $AF^*(\mathcal{g}_a) = AF^*(\mathcal{g}_b)$, we get $\mathcal{g}_a = \mathcal{g}_b$

From Table 2, we listed three groups of data and obtained the results of distinguishing new SFs from the existing SFs. Compared to other methods[4, 17], the proposed method is able to distinguish all groups of data in the table effectively.

Table 2**.** The comparative results of distinguishing different IVFHFNs between different SFs

	The data to be compared		The different SFs		
Group	$\mathcal{g}_1$	$\mathcal{g}_2$	SFs in [17]	SFs in [4]	Our SFs
Group 1	$\{([\sqrt[3]{0.22}, \sqrt[3]{0.32}], [\sqrt[3]{0.22}, \sqrt[3]{0.42}]), ([\sqrt[3]{0.12}, \sqrt[3]{0.22}], [\sqrt[3]{0.32}, \sqrt[3]{0.52}])\}$	$\{([\sqrt[3]{0.17}, \sqrt[3]{0.27}], [\sqrt[3]{0.17}, \sqrt[3]{0.37}]), ([\sqrt[3]{0.07}, \sqrt[3]{0.17}], [\sqrt[3]{0.27}, \sqrt[3]{0.47}])\}$	×	×	$\mathcal{g}_1 > \mathcal{g}_2$
Group 2	$\{([\sqrt[3]{0.1}, \sqrt[3]{0.2}], [\sqrt[3]{0.6}, \sqrt[3]{0.7}]), ([\sqrt[3]{0.15}, \sqrt[3]{0.35}], [\sqrt[3]{0.45}, \sqrt[3]{0.55}])\}$	$\{([\sqrt[3]{0.05}, \sqrt[3]{0.2}], [\sqrt[3]{0.6}, \sqrt[3]{0.75}]), ([\sqrt[3]{0.08}, \sqrt[3]{0.19}], [\sqrt[3]{0.65}, \sqrt[3]{0.71}])\}$	×	$\mathcal{g}_1 > \mathcal{g}_2$	$\mathcal{g}_1 > \mathcal{g}_2$
Group 3	$\{([\sqrt[3]{0.5}, \sqrt[3]{0.55}], [0,0]), ([\sqrt[3]{0.7}, \sqrt[3]{0.75}], [0,0])\}$	$\{([\sqrt[3]{0.45}, \sqrt[3]{0.6}], [0,0]), ([\sqrt[3]{0.8}, \sqrt[3]{0.9}], [0,0])\}$	$\mathcal{g}_1 < \mathcal{g}_2$	$\mathcal{g}_1 < \mathcal{g}_2$	$\mathcal{g}_1 < \mathcal{g}_2$

4. A novel 3WD model with probabilistic dominance relation under IVFHFSs

In this part, we explore the calculation of objective CPs and investigate a new 3WD approach based on the objective calculation of the RLFs.

4.1. The calculation of CPs with probabilistic dominance relation

Definition 4.1. Let $P = \{p_1, p_2, \dots, p_n\}$ be an object set and $Q = \{q_1, q_2, \dots, q_m\}$ be an attribute set. And $W = \{w_1, w_2, \dots, w_n\}$ is the weight vector for attributes. The CP of each alternative $p_i \in P$ based on the probabilistic dominance relation under the IVFHFSs is defined as follows:

$$\Omega\left(Z|[p_i]_Q^{\geq\eta}\right) = \frac{\sum_{p_i\in[p_i]_Q^{\geq\eta}} Z(p_i)}{\left|[p_i]_Q^{\geq\eta}\right|} \quad (4-1)$$

where $\left|[p_i]_Q^{\geq\eta}\right|$ implies the cardinality if the set $[p_i]_Q^{\geq\eta}$ and the good state set Z is depicted as:

$$Z(p_i) = \frac{o_1^*}{p_1} + \frac{o_2^*}{p_2} + \cdots + \frac{o_i^*}{p_i} + \cdots + \frac{o_n^*}{p_n} \quad (4-2)$$

where $o_i^* = \sum_{j=1}^m w_j SF^*\left(\mathcal{g}_{ij}\right)$ and $SF^*\left(\mathcal{g}_{ij}\right)$ is the score value of the IVFHFN $\mathcal{g}_{ij}$.

4.2. A new 3WD method based on objective calculation of the RLFs

In this section, we investigate the expression of RLFs based on IVFHFSs and establish

a new 3WD method with probabilistic dominance relation under IVFHFSs.

The set $P = \{p_1, p_2, \dots, p_n\}$ denotes the n alternatives and $Q = \{q_1, q_2, \dots, q_m\}$ implies the m attributes, which are all described by IVFHFNs $\mathcal{g}_{ij}$, where $i = 1,2, \dots, n$ and $j = 1,2, \dots, m$. In [18], the losses of taking non-commitment behavior are controlled by giving a vector of risk aversion coefficients $\theta = \{\theta_1, \theta_2, \dots, \theta_m\}(\theta \in [0,1])$. Then, by combining Table 1 and the operations of IVFHFSs in Definition 2.2, we can obtain the RLFs matrix. And based on rules $(R1)$, $(R2)$, and $(R3)$, the new classification rules are listed below:

$(R1^*)$ If $\Omega\left(Z|[p_i]_Q^{\geq\eta}\right) \geq \alpha^*$ and $\Omega\left(Z|[p_i]_Q^{\geq\eta}\right) \geq \gamma^*$, decide $p \in POS(Z)$;

$(R2^*)$ If $\Omega\left(Z|[p_i]_Q^{\geq\eta}\right) < \alpha^*$ and $\Omega\left(Z|[p_i]_Q^{\geq\eta}\right) > \beta^*$, decide $p \in BND(Z)$;

$(R3^*)$ If $\Omega\left(Z|[p_i]_Q^{\geq\eta}\right) \leq \beta^*$ and $\Omega\left(Z|[p_i]_Q^{\geq\eta}\right) \leq \gamma^*$, decide $p \in NEG(Z)$;

where the thresholds α^*, β^* and γ^* can be expressed as below:

$$\alpha^* = \frac{\delta'_{PN} - \delta'_{BN}}{\delta'_{PN} - \delta'_{BN} + \delta'_{BP}} \quad (4-3)$$

$$\beta^* = \frac{\delta'_{BN}}{\delta'_{BN} + \delta'_{NP} - \delta'_{BP}} \quad (4-4)$$

$$\gamma^* = \frac{\delta'_{PN}}{\delta'_{PN} + \delta'_{NP}} \quad (4-5).$$

5. A new 3W-MAGDM with probabilistic dominance relation under IVFHFSs

A new 3W-MAGDM based on the innovations in parts 3 and 4 is presented in this section.

The description of the MAGDM problem: Assuming that there are e experts $Y = \{y_1, y_2, \dots, y_e\}$ who need to evaluate m attributes $Q = \{q_1, q_2, \dots, q_m\}$ for n alternatives $P = \{p_1, p_2, \dots, p_n\}$. The assessed values of the experts are all described by IVFHFNs $\mathcal{g}_{ij}$, where $i = 1,2, \dots, n$ and $j = 1,2, \dots, m$. $W = \{w_1, w_2, \dots, w_m\}$ is the weight vector for attributes. $\theta = \{\theta_1, \theta_2, \dots, \theta_m\}$ is the risk aversion coefficient vector, and η implies the parameter of the probabilistic dominance class.

Step 1: Construct the assessment matrix of each expert. The expression for assessment matrix $\mathcal{K}_{n\times m}^{\varrho}(\varrho = 1,2, \dots, e)$ of each expert is obtained.

Step 2: Integrate all assessment matrixes $\mathcal{K}'_{n\times m} = (\mathcal{g}'_{ij})_{n\times m}$ by method in [10].

Step 3: Normalize the integrated assessment matrix $\mathcal{K}''_{n\times m} = (\mathcal{g}''_{ij})_{n\times m}$ by ${\mathcal{g}'_{ij}}^{c}$.

Step 4: Obtain the probabilistic dominance class for each alternative by Definition 2.3. Then, the probabilistic dominance class $[p_i]_Q^{\geq\eta}$ for each object is acquired according to Definition 2.4 ~ Definition 2.6.

Step 5: Calculate the CPs of all alternatives by Eq.(4-1).

Step 6: Compute RLFs for each alternative.

Step 7: Calculate thresholds α^*, β^* and γ^* through Eq.(4-3) ~ Eq.(4-5) and classify.

Step 8: Compute the expected losses of all alternatives and sort.

6. Conclusion

The contributions of the methodology proposed in this paper are mainly the following:

(1) The novel SFs are proposed to address the shortcoming of the existing SFs and enhance the identifying ability. (2) The probabilistic dominance class is extended to IVFHFSs, and the CPs and RLFs are objectively calculated, which improves the objectivity of the proposed method. (3) Compared with the existing MAGDM[4, 9, 10, 17], the method is more flexible in the representation of fuzzy information and complements the ability of triple categorization with the sorting function. Therefore, it incorporates group cognition while reducing DM risk, and is a scientific and effective DM method. However, current research is limited to static DM and simulation data. The introduction of dynamic DM and the conversion of real datasets into IVFHFSs are considered in future work.

References

[1] Zadeh L. Fuzzy sets. Inform Control. 1965;8:338-53.

[2] Hussain A, Ullah K. An intelligent decision support system for spherical fuzzy sugeno-weber aggregation operators and real-life applications. Spectrum of Mechanical Engineering and Operational Research. 2024;1(1):177-88.

[3] Ren D, Ma X, Qin H, Lei S, Niu X. A multi-criteria decision-making method based on discrete Z-numbers and Aczel-Alsina aggregation operators and its application on early diagnosis of depression. Engineering Applications of Artificial Intelligence. 2025;139:109484.

[4] Kirişci M, Şimşek N. Interval-Valued Fermatean Hesitant Fuzzy Sets and Infectious Diseases Application. 2022. doi: 10.21203/rs.3.rs-1273874/v1.

[5] Yao Y. Three-way decisions with probabilistic rough sets. Information sciences. 2010;180(3):341-53.

[6] Imran R, Ullah K, Ali Z, Akram M. A multi-criteria group decision-making approach for robot selection using interval-valued intuitionistic fuzzy information and aczel-alsina bonferroni means. Spectrum of Decision Making and Applications. 2024;1(1):1-32.

[7] Wang Z, Zhu P. Multi-attribute group three-way decision making with degree-based linguistic term sets. International Journal of Approximate Reasoning. 2021;137:69-93.

[8] Song J, He Z, Jiang L, Liu Z, Leng X. Research on hybrid multi-attribute three-way group decision making based on improved VIKOR model. Mathematics. 2022;10(15):2783.

[9] DemİR İ. Novel correlation coefficients for interval-valued Fermatean hesitant fuzzy sets with pattern recognition application. Turkish Journal of Mathematics. 2023;47(1):213-33. doi: 10.55730/1300-0098.3355.

[10] Lei S, Ma X, Qin H, Wang Y, Zain JM. A new multi-attribute group decision-making method based on Einstein Bonferroni operators under interval-valued Fermatean hesitant fuzzy environment. Scientific Reports. 2024;14(1). doi: 10.1038/s41598-024-62762-0.

[11] Li W, Zhou H, Xu W, Wang X-Z, Pedrycz W. Interval dominance-based feature selection for interval-valued ordered data. IEEE Transactions on Neural Networks and Learning Systems. 2022;34(10):6898-912.

[12] Li W, Xue X, Xu W, Zhan T, Fan B. Double-quantitative variable consistency dominance-based rough set approach. International Journal of Approximate Reasoning. 2020;124:1-26.

[13] Jia F, Liu P. A novel three-way decision model under multiple-criteria environment. Information Sciences. 2019;471:29-51.

[14] Liu F, Liu Y, Abdullah S. Three-way decisions with decision-theoretic rough sets based on covering-based q-rung orthopair fuzzy rough set model. Journal of Intelligent & Fuzzy Systems. 2021;40(5):9765-85. doi: 10.3233/jifs-202291.

[15] Liang D, Xu Z, Liu D, Wu Y. Method for three-way decisions using ideal TOPSIS solutions at Pythagorean fuzzy information. Information Sciences. 2018;435:282-95. doi: 10.1016/j.ins.2018.01.015.

[16] Weng Sz, Lv Yj. The sorting method and its application based on the probabilistic dominance relation. Journal of Shanxi University(Natural Science Edition). 2015;38(03):439-46. doi: 10.13451/j.cnki.shanxi.univ(nat.sci.).2015.03.009.

[17] Zeng W, Li D, Yin Q. Weighted Interval-Valued Hesitant Fuzzy Sets and Its Application in Group Decision Making. International Journal of Fuzzy Systems. 2019;21(2):421-32. doi: 10.1007/s40815-018-00599-2.

[18] Li H, Zhou X. Risk decision making based on decision-theoretic rough set: a three-way view decision model. International Journal of Computational Intelligence Systems. 2011;4(1):1-11.

Fuzzy Systems and Data Mining X
A.J. Tallón-Ballesteros (Ed.)

doi:10.3233/FAIA241406

Conformal Circular Mapping for Unbounded Multiple Connected Regions

Dan Luo and Yibin Lu[1]
Kunming University of Science and Technology, China
ORCiD ID: Dan Luo https://orcid.org/0009-0008-4371-1685

Abstract. Multiple connected regions bounded by circles are crucial from the point of view of analyzing physical problems and reducing the amount of computation. However, finding a conformal mapping function that maps a multiple connected region to circular domain is challenging. Koebe's iterative method provides a theoretically feasible path for the conformal mapping of a multiple connected region to a circular region. In this study, a numerical implementation of Koebe's iterative method is accomplished using the charge simulation method, and an algorithm for conformal circular mapping of unbounded multiple connected regions is proposed. Through numerical experiments, this paper successfully verifies the effectiveness of the proposed algorithm.

Keywords. Circular mapping, Numerical conformal mapping, Koebe's iterative method, Charge simulation method

1. Introduction

The circular mapping allows the original problem to be solved in a simpler geometrical environment by transforming the original region into a circular domain using conformal mapping [1-4]. For example, the Kirchhoff-Routh path function [1] can be solved using circular mapping to make the original flow problem easier to solve. The Kirchhoff-Routh path function is an important concept in fluid dynamics, which provides a method for analyzing the fluid flow characteristics in a flow field containing multiple obstacles. Therefore, implementing an algorithm for mapping the conformal mapping of a multi-connected region into a circular domain is crucial.

The theory of numerical methods for computing mapping functions has been continuously improved [5-7]. Among them is the numerical conformal mapping computational method based on the charge simulation method proposed by Amano [7]. The method does not require numerical integration in the solution process and uses the principle of maximum mode to evaluate the error. It is fast and easy to evaluate the computational accuracy and has become a mainstream method for solving conformal mapping functions.

However, conformal mapping is a strong constraint requiring the mapping function to satisfy local and global conformal conditions throughout the domain, but in the case of multiple connected regions, each boundary carries its boundary conditions ,which must be satisfied during the mapping process. Therefore, we consider introducing

[1] Corresponding Author: Yibin Lu, Kunming University of Science and Technology, Kunming, China. Email: lybwyz@126.com

iterative methods in the conformal mapping process. Koebe's iterative method [8,9] is used in Complex Analysis and Geometric Function Theory to find the optimal solution through a stepwise approximation, which allows each step to be adjusted according to the previous step's results. It is favorable to improve the mapping function step by step to achieve higher accuracy, and the method shows good stability, which means that the iterative process can converge to the correct solution, which is essential to ensure the reliability of the algorithm [10].

Therefore, in this study, Koebe's iterative method based on the charge simulation method for the computation of conformal mapping is introduced to provide an efficient solution for the conformal mapping from an unbounded multiple connected region to a circular domain, and a theoretical refinement of the numerical conformal mapping algorithm based on the charge simulation method is carried out. The effectiveness of the method is finally demonstrated by numerical experiments.

2. Conformal Mapping Based on the Charge Simulation Method

2.1. The Circular Mapping Function

Theorem 1. Let D be a region of connectivity $n>1$ in the extended complex plane such that $\infty \in D$. Then there exist a unique circular domain Ω of connectivity n and a unique one-to-one analytic function $f(z)$ such that $f(D)=\Omega$,see Figure 1, and f in D satisfying

$$f(z)=z+O(\frac{1}{z}) \tag{1}$$

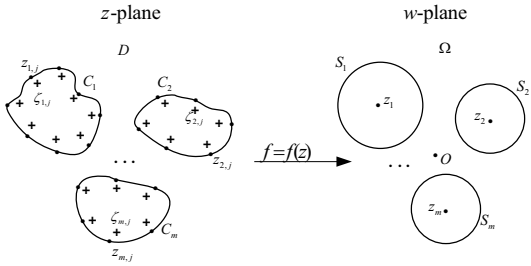

Figure 1. Conformal mapping of unbounded multiple connected region to circular domain

For unbounded D, each iteration of Koebe's method requires computing the conformal mapping from an unbounded simply connected region onto the exterior unit disk n times.

Consider a conformal mapping $f=f(z)$ from the exterior of region D consisting of a closed smooth Jordan curve C in the plane to the exterior of the unit circle S, where z is a point on region D and its boundary C. Then, one can uniquely determine the function of such a mapping by a normalization condition

$$f(\infty)=\infty, f'(\infty)>0 \tag{2}$$

which expands the function Loran at infinity as

$$f(z)=\gamma^{-1}z+a_0+a_1z^{-1}+a_2z^{-2}+\cdots \tag{3}$$

taking any point z_0 in the region enclosed by C, then at $z \to \infty$ there is

$$\log \frac{f(z)}{z - z_0} = -\log \gamma + g(z) + \mathrm{i}h(z) \tag{4}$$

where $g(z)$ and $h(z)$ are a pair of conjugate harmonic functions within the region D and $g(\infty) = 0, h(\infty) = 0$, hence the conformal mapping function can be expressed as

$$f(z) = (z - z_0)e^{-\log\gamma + g(z) + \mathrm{i}h(z)} \tag{5}$$

the $g(z)$ satisfying the Laplace equation. Therefore, under normalization conditions, $g(z)$ is a solution to the Dirichlet potential field problem that satisfies

$$\begin{cases} \nabla^2 g(z) = 0, z \in D \\ g(z) = \log \gamma - \log | z - z_0 |, z \in C \\ g(\infty) = 0 \end{cases} \tag{6}$$

reduced to the problem of finding the solution of the Dirichlet potential field problem, $g(z)$ and the conjugate summation function $h(z)$ and the radius γ.

2.2. Charge Simulation Method

With z_0 taken as the origin, approximate f, g, h, γ by F, G, H, Γ, respectively, while approximating the function $g(z) + \mathrm{i}h(z)$ by a linear combination of the complex logarithmic functions, expressed as follows

$$G(z) + \mathrm{i}H(z) = -\sum_{j=1}^{n} Q_j \left(\log | z - \zeta_j | + \mathrm{i} \arg(z - \zeta_j) \right), z \in \bar{D} \tag{7}$$

$G(z)$ and $H(z)$ are the primary combination of the real and imaginary parts of the complex logarithmic potential $\log(z - \zeta_j)$, respectively, with the charge Q_j as a coefficient to be determined, discretizing the boundary into n constraints, $z_i, i = 1, ..., n$, $\zeta_j, j = 1, ..., n$ which are simulation charge points configured inside the curve C. From Eq.(6), the approximation function $G(z)$ should satisfy the boundary conditions

$$\sum_{j=1}^{n} Q_j \log | z - \zeta_j | = \log | z - z_0 | - \log \Gamma \tag{8}$$

Secondly, according to the infinity point, it satisfies condition $g(\infty) = 0, h(\infty) = 0$, when $z \to \infty$, there is

$$\lim_{z \to \infty} \sum_{j=1}^{n} Q_j \log(z - \zeta_j) = 0 \tag{9}$$

Moreover, since the imaginary part of Eq.(7) is single-valued in the region $\bar{D}$, equivalently

$$\int_c \mathrm{d}H(z) = \int_c \mathrm{d}\sum_{j=1}^{n} Q_j \arg(z-\zeta_j) = 2\pi\sum_{j=1}^{n} Q_j = 0 \tag{10}$$

Associate the Eq.(9) and Eq.(10) to get the constraint equation

$$\sum_{j=1}^{n} Q_j \log|z_i-\zeta_j| + \log\Gamma = \log|z_i - z_0|, i = 1,...,n \tag{11}$$

Solve to obtain the values of the charge $Q_j, j = 1,...,n$ and the approximate mapping radius Γ and finally construct the approximate mapping function

$$F(z) = (z-z_0)e^{-\log\Gamma + G(z) + iH(z)} \tag{12}$$

$H(z)$ is not only single-valued on $\bar{D}$ but also required to be continuous. Since the principal values of the logarithmic function $\log(z-\zeta_j)$ are used in the calculations, and $\operatorname{Arg} z$ has a 2π discontinuity on the negative semiaxis, a simple substitution of $\arg$ for Arg would cause a discontinuity, so a point ζ_0 inside the boundary C is taken, and Eq.(10) is united to convert Eq.(7) into the mathematically equivalent continuous form

$$G(z) + iH(z) = \sum_{j=1}^{n} Q_j \log(z-\zeta_j) - \sum_{j=1}^{n} Q_j \log(z-\zeta_0) = \sum_{j=1}^{n} Q_j \log\frac{(z-\zeta_j)}{(z-\zeta_0)} \tag{13}$$

3. Koebe's Iterative Method Based on the Charge Simulation Method

This paper presents an efficient method for constructing a circular domain Ω, define the initial region $D^{0,0} = D$, the initial boundary $C_i^{0,0}, i = 1,2,...,m$, and $k = 0,1,2,...$ as the number of external iterations. The conformal mapping function $\omega: D^{0,0} \to D^{m,k}$ maps the multi-connected region $D^{0,0}$ to the circular domain $D^{m,k} = \Omega$, whose complement in the circular domain $D^{m,k}$ is the circle $\{D_1^{m,k}, D_2^{m,k}, ..., D_3^{m,k}\}$.

Region $D_i^{i-1,k}$, enclosed by curve $C_i^{i-1,k}$, is mapped to the unit circle $D_i^{i,k}$, and $C_i^{i-1,k}$ denotes the i boundary curve after the $i-1$ loop in the k iteration. The region $D_j^{i-1,k}$ enclosed by the remaining $m-1$ curves $C_j^{i-1,k}$ is mapped accordingly to $D_j^{i,k}, j \neq i$, i.e., $D_j^{i,k} = \omega^{i,k}(D_j^{i-1,k}), j = 1,..,i,..,m, i = 1,....,m$, and the number of iterations k is increased when $i = m$.

Loop each boundary in turn, and all boundaries looped once are called an external iteration. When one external iteration k is finished, the mapping function is written as

$$\hat{\omega}^k = \omega^{1,k} \circ \omega^{2,k} \circ \cdots \circ \omega^{m,k} \tag{14}$$

at this point, function $\hat{\omega}^k$ does not satisfy the normalisation condition, so function $\hat{\omega}^k$ is expanded by Laurent at ∞

$$\hat{\omega}^k(z) = bz + c_0 + c_1 z^{-1} + \cdots \tag{15}$$

the constants b and c_0 can be computed using the following equations

$$b=-\frac{1}{2\pi i}\int_C \frac{\hat{\omega}^k(z)}{z-\alpha}\frac{dz}{z-\alpha}, c_0=-\frac{1}{2\pi i}\int_C [\hat{\omega}^k(z)-bz]\frac{dz}{z-\alpha} \tag{16}$$

α is any point outside the region D. Define the correction function

$$f_k=\frac{z-c_0}{b} \tag{17}$$

the conformal mapping function after one external iteration k is obtained

$$\omega^k=\omega^k(z)=f_k\circ\hat{\omega}^k(z) \tag{18}$$

The convergence of Koebe's iterative method is proved in the [10].

Theorem 2. For unbounded region D, there exists a constant $c>0$ such that for $i=1,2,3,...$ and for all $z\in C$

$$\left\|\omega^k(z)-\omega^{k-1}(z)\right\|_\infty \le cp^k \tag{19}$$

$p=p^{'4}, p^{'4}=\max\limits_{1\le i,j\le m, i\ne j}\left|r_i+r_j/z_{0i}+z_{0j}\right|, z_{0i}=z_{0i}^{m,k-1}, r_i=\sum_{j=1}^{n}\left|z_i^{m,k-1}(j)-z_{0i}^{m,k-1}\right|/n$. It is clear that Koebe's method always converges since $0<p<1$.

The above steps are repeated, and when the convergence condition for mapping function ω^k is reached, the conformal mapping function $\omega=\omega^1\circ\omega^2\circ\cdots\circ\omega^k$ is obtained. The iterative procedure is shown in Figure 2.

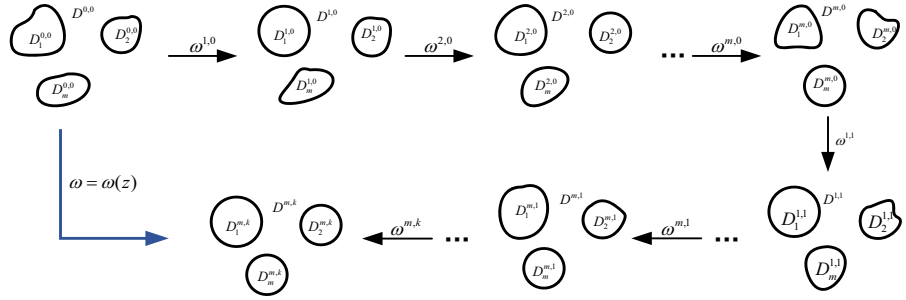

Figure 2. Illustration of Koebe's iterative method

The steps of the algorithm are as follows.

Algorithm. Koebe's iterative method based on the charge simulation method

Input: $n,\varepsilon,Max,z_{ij},\zeta_{i0},\zeta_{ij}(i=1,...,m;j=1,...,n),k=0$

Computing: $q_i=A_i/B_i,\left\|\omega^k-\omega^{k-1}\right\|_\infty, r_i=\sum_{j=1}^{n}\left|z_i^{m,k-1}(j)-z_{0i}^{m,k-1}\right|/n$

step1 while $\left\|\omega^i-\omega^{i-1}\right\|_\infty \ge p^k$ do

step2 for $i=1:m$

step3 $q_i=A_i/B_i$

step4 if $i=m$; return $\hat{\omega}^i=\hat{\omega}^k, k+1$; end if

step5 end for

step6 $b_k=\frac{1}{2\pi i}\int\hat{\omega}^k(z)/(z-z_{k0})^2\mathrm{d}z;\quad c_k=\frac{1}{2\pi i}\int(\hat{\omega}^k(z)-bz)/(z-z_{k0})\mathrm{d}z;$

step7 $\omega^k = \hat{\omega}^k((z-c_k)/b_k)$

step8 end while

Output: ω^k, ε

4. Numerical Example

A numerical example is carried out in the environment of MATLAB 2018b to consider an unbounded multiple connected region consisting of closed smooth Jordan curves. The experiment is also carried out for orange-shaped boundary curves.

For the elliptic boundary, the bound points $z_j, j=1,...,n$ of the boundary and charge points $\zeta_j, j=1,...,n$ are configured using the Joukowski transform in [11].

$$\zeta_j = J\left(\frac{\rho_2}{q}\mathrm{e}^{\mathrm{i}\theta_j}\right), z_j = J\left(\rho_2\mathrm{e}^{\mathrm{i}\theta_j}\right), J(z) = \rho_1\left(z+\frac{1}{z}\right) \tag{20}$$

where $\rho_1 = \sqrt{(a^2-1)}/2, \rho_2 = (a+1)/(a-1)$, the constraint points and charge points are uniformly distributed on the boundary and outside the problem domain.

Example. Introduces an orange-shaped boundary with equation

$C_6 : z = z_{06} + 2r(\theta)\mathrm{e}^{\mathrm{i}\theta}$, $r(\theta) = \sqrt{\cos 2\theta + \sqrt{\cos^2 2\theta + 1.1^4 - 1}}$.

the remaining elliptical boundary with equation

$Cm : (x - \mathrm{Re}\, z_{0m})^2 / a_m^2 + (y - \mathrm{Im}\, z_{0m})^2 / b_m^2 = 1,\ m = 1,2,...,5$

where $z_{01} = 3\text{-i}, z_{02} = 0.5\text{-}0.5\text{i}, z_{03} = 3\text{+}2\text{i}, z_{04} = 0.5\text{+}2\text{i}, z_{05} = \text{-}0.5\text{+i}, z_{06} = 5\text{+i}$, $a_2 = 1.7$, $a_3 = 1.5, a_4 = 0.8, a_1 = a_5 = 1, b_1 = b_3 = 0.2, b_2 = b_5 = 0.3, b_4 = 0.1$.

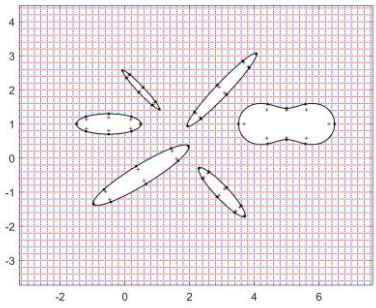

Figure 3. Original domain D

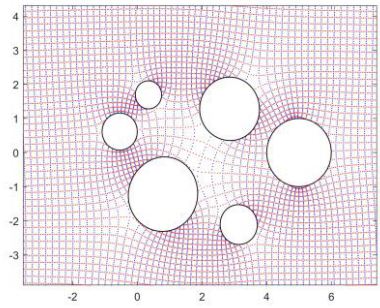

Figure 4. Circular mapping results

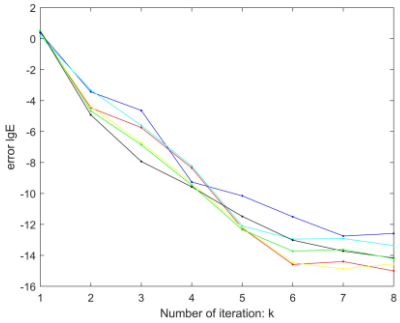

Figure 5. Numerical conformal mapping errors

Figure 3 shows the boundary of the problem domain, part of the grid, and the distribution of constraints and charge points, '·' represents the constraints, '+' represents the charge points. Figure 4 shows the image of the problem domain after the conformal mapping. Figure 5 shows the error for each boundary, the logarithm of the base of 10 is taken as the vertical coordinate and the number of iterations is taken as the horizontal coordinate. From the error plot, the method in this paper successfully realizes the circular mapping of unbounded multiple connected regions and achieves good mapping results within a small number of iterations.

5. Conclusion

This paper presents a high-precision numerical implementation of Koebe's iterative method based on the charge simulation method for computing the conformal mapping from unbounded multiple connected regions to circular domains. As verified by numerical example, it can be seen that the method of this thesis is universally feasible both in boundary shape and connectivity dimension, and a small number of iterations can obtain high accuracy mapping results. In the future, we can consider the study of bounded multiple connected region circle mapping and other forms of region conformal mapping and apply our numerical method to the computation of problems in hydrodynamics and electromagnetism.

References

[1] Crowdy DG, Marshall J. Computing the Schottky-Klein prime function on the Schottky double of planar domains[J], Computational Methods and Function Theory, 2007, 7: 293-308. doi:10.1007/BF03321646.

[2] Nasser M. Fast computation of the circular map[J]. Computational Methods & Function Theory, 2015, 15(2):1-37. doi:10.1007/s40315-014-0098-3.

[3] Chandran V, Janardhanan S, Sekar M. Numerical Study on Domain Independency for Prediction of Vortex Shedding Parameters of a Circular Cylinder[J]. 2022. doi:10.1007/978-981-16-4083-4_28.

[4] Nasser M, Rainio O, Rasila A, et al. Polycircular domains, numerical conformal mappings, and moduli of quadrilaterals[J]. Advances in Computational Mathematics, 2022, 48(5):1-34. doi:10.1007/s10444-022-09975-x.

[5] Symm GT. An integral equation method in conformal mapping[J]. Numerische Mathematik, 1966, 9(3):250-258. doi:10.1007/BF02162088.

[6] Fornberg, Bengt. A numerical method for conformal mapping of doubly connected regions[J]. Siam Journal on Scientific & Statistical Computing, 1984, 5(4):771-783. doi:10.1137/0905055.

[7] Amano K. A charge simulation method for the numerical conformal mapping of interior, exterior and doubly-connected domains[J]. Journal of Computational and Applied Mathematics, 1994, 53(3):353-370. doi:10.1016/0377-0427(94)90063-9.

[8] Koebe P. Abhandlungen zur theorie der konformen abbildung[J]. Acta math, 1916, 41: 305-344. https://doi.org/10.1515/crll.1915.145.177

[9] Zeng W, Yin X, Zhang M, et al. Generalized Koebe's method for conformal mapping multiply connected domains[C], Siam/acm Joint Conference on Geometric & Physical Modeling. ACM, 2009. doi:10.1145/1629255.1629267.

[10] Henrici P. Applied and computational complex analysis[M]. Wiley, 1974,507-526. doi:10.2307/2005805.

[11] Wu K, Lu Y. Numerical computation of preimage domains for spiral slit regions and simulation of flow around bodies[J]. Mathematical biosciences and engineering:MBE, 2023,20(1): 720-736.doi: 10.3934/mbe.2023033.

Fuzzy Systems and Data Mining X
A.J. Tallón-Ballesteros (Ed.)

doi:10.3233/FAIA241407

An Efficient Approach for Mining Temporal Fuzzy High-Utility Itemsets

Sadnan Kibria KAWSHIK [a], Zulker NAYEEN [a], Chowdhury Farhan AHMED [a,1], and Md. Tanvir ALAM [a], Carson K. LEUNG [b], Connor C.J. CONNOR [b]

[a] *University of Dhaka,Bangladesh*
[b] *University of Manitoba,Canada*

Abstract. The motivation behind fuzzy logic in data mining is to address the inherent uncertainty and imprecision in real-world data and make the mined results more interpretable for humans. Temporal Fuzzy High Utility Itemset Mining, which incorporates transaction time, is an emerging field with significant potential for analyzing time-sensitive data. Although several studies in this area have been conducted, for instance, recently fuzzy list-based approaches, a significant challenge remains in joining operations of conditional fuzzy lists when generating candidate itemsets. To solve this, we have proposed a pruning strategy based on item co-occurrences to reduce the number of join operations using anti-monotonic property. Experiments on real datasets show our approach outperforms traditional algorithms in terms of runtime and candidate generations with little memory overhead, up to 95% of non-promising candidates are pruned.

Keywords. Fuzzy utility mining, Membership function, Co-occurrence Pruning, Temporal mining, Fuzzy Set

1. Introduction

Frequent pattern mining has been one of the fundamental research issues in the field of pattern mining. However, traditional FIM algorithms overlook factors like profit and utility; thus high utility itemset mining(HUIM) was proposed. Many approaches[1] have been suggested in this field, for example, a single-phase algorithm HUI-Miner[2] proved to be much more efficient in mining. Further, FHM[3] used a triangular matrix-based data structure to store information about item co-occurrence to reduce the join operation in the pattern growth approach, paving the way for pruning efficiently.

Combining with Fuzzy set theory[4], a new framework of fuzzy high utility itemset mining(FUIM) was introduced to emulate human reasoning by mapping items' quantitative information into human linguistic terms, providing additional qualitative information (low, middle, high) of an itemset. The introduction of fuzzy utility upper bound (fuub)[5] significantly reduced the search space of candidate generation.

Transaction time plays a crucial role in different fields such as health care, insurance systems, business, weblog, etc. where time-dependent insights are necessary and thus temporal fuzzy high utility itemset mining (TFHUIM) was introduced. Mining TFHUIs

[1]Corresponding Author: Chowdhury Farhan Ahmed, farhan@du.ac.bd

initially involved a two-phase approach[6] based on the apriori algorithm. Further tree-based[7] and recently fuzzy list-based[8][9] approaches were derived considering runtime, memory, and scalability in consideration. Recently, Taewoong et al[9] proposed a scalable fuzzy list-based solution that uses global temporal fuzzy lists and considers a much faster upper bound formed with the combination of fuzzy utility and remaining utility. However, in the pattern growth approach, the join operation while creating conditional fuzzy lists is very costly. In this paper, we propose an effective pruning strategy named the *Estimated Temporal Fuzzy Utility Co-occurrence Pruning(ETFUCP)* to reduce the number of joins using the item's co-occurrence-based information.

2. Problem Definition And Related Works

To maintain the *downward closure property*, Ying Liu et al. [1] proposed a two-phase algorithm incorporating *TWU* upper bound in HUIM. FUIM is an extension of HUIM that incorporates fuzzy logic to make the output more interpretable. To address the challenge of maintaining the downward closure property, Lan et al. introduced TPFU[5] proposing the *Fuzzy Utility Upper Bound (fuub)*. The fuub of an itemset is calculated by aggregating the maximal transactional fuzzy utility(mtfu) values from transactions where the pattern appears. Here, the maximum fuzzy utility(mfu) of an item is determined by multiplying its maximum fuzzy value with its external and internal utility. The mtfu represents the total mfu of all items in a transaction, while the total transactional fuzzy utility (tfu) is the sum of fuzzy utilities for all items in that transaction. Early approaches as [5] were apriori-based generate and test algorithms, furthermore improved approaches such as FUIM[10], EA-HUFIM[11], and recently fuzzy list buffer-based algorithm, FS-IUM[12] have been introduced which performs better than its predecessors.

Temporal Fuzzy High Utility Itemset Mining (TFUIM) extends FUIM by incorporating transaction time as a temporal factor. The **temporal fuzzy utility upper bound ratio (tfuubr)** was introduced[6] to maintain downward closure property. Here, tfuubr involves the start transaction period (STP) and period set. The STP of an item is the first transaction where it appears, while the latest STP of a database,$STP(I)$,[7] is the latest STP of all items. For a pattern X, $STP(X)$, is the latest STP of all the items present in that pattern, and its period set,$PSI(X)$, spans from $STP(X)$ to the last time period of the database. The period set of a database *PS(I)*, is a set of periods from $STP(I)$ to the last period of the database. The temporal fuzzy utility upper bound ratio of an itemset, $(tfubbr(X))$ is the ratio of the fuub value of pattern to the total transactional fuzzy utility(tfu) in the $PSI(I)$, while the temporal fuzzy utility ratio $(tfur(X))$ compares the actual fuzzy utility of the itemset with the total utility in $PSI(X)$. We can use the product of minUtil and the sum of tfu in $PSI(I)$,$sumTFU(I)$ to compare with fuub[9] to prune candidates and it is also used in the algorithm.

Early methods such as TP-TFU [6] and TPM [13] were based on two-phase apriori-like algorithms, involving preprocessing and upper-bound itemset generation to identify temporal fuzzy high-utility itemsets, but these approaches were inefficient in terms of runtime and memory. Later, Tzung-Pei Hong et al. introduced two tree-based methods FHTFUP [14] and ATTFUM [7], the latter being a one-phase algorithm with an array-embedded tree structure, improved efficiency with only two database scans. Subsequent list-based techniques like FUMT [15] utilized TF-lists to compress the temporal

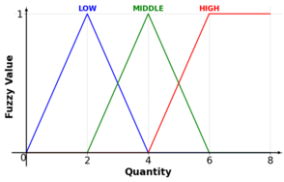

Figure 1. Fuzzy Membership Function

Period	TID	Items
P1	T0	a:4,c:1
	T1	a:3,b:3
P2	T2	a:1,c:1
	T3	a:2,b:2,c:3, d:3,e:1
P3	T4	a:2,b:4,e:1
	T5	a:2,d:3,e:1

Item	External Utility
a	2
b	6
c	4
d	2
e	4

Table 1. Transactional Database and external utility

database, enhancing speed as it was a one-phase method without candidate generation. TFUM [8] further improved performance by introducing a tighter upper bound through the remaining maximal fuzzy transactional utility.

More recently, the TFU-Miner method [9] combined fuzzy utility with remaining fuzzy utility(RFU) for a scalable solution. In transaction T, *RFU(X, T)*, is the product of the minimal fuzzy value and remaining utility(RU) of pattern X in T. The remaining utility is the total utility of items after the pattern X in transactions where it appears, excluding items derived from the same item. This method also defines an attribute called Upper Bound (UB), which is similar to the previously defined fuub. We will use it in the next sections. The TFU-Miner begins scanning the database and then calculates the upper bounds, tfu, and mtfu of all the transactions. Only items with an upper bound exceeding the minimum utility threshold are retained. In 2nd database scan, the process creates temporal fuzzy lists(TFU lists) of each item. During the mining process, a pattern growth approach is followed. From length-1 items, recursively length-2 to n-length patterns are created by joining and creating conditional lists. These join operations to create conditional lists can be time-consuming. Thus we have proposed a pruning strategy named Estimated Temporal Fuzzy Utility Co-occurrence Pruning(ETFUCP) that uses the item's co-occurrence information to prune the candidate space of high utility upper bound itemsets and recursively reduces the join operations. A hashmap-based structure (ETFUCPS) is employed to store this co-occurrence data. Further details are described in the following sections. An example transactional database (Table1) with 5 items and 5 transactions, with 3 phases, including external utility values and a fuzzy membership function (Figure 1) with three linguistic regions (Low, Middle, High), is provided.

3. Proposed Method

This section introduces our algorithm, FTFUM(Fast Temporal Fuzzy Utility Miner), an extended version of TFU-Miner that incorporates a pruning strategy called Estimated Temporal Fuzzy Utility Co-occurrence Pruning(ETFUCP).

In the first database scan, each item's utilities are fuzzified and the fuzzy utility (fu) and maximal fuzzy utility (mfu) are calculated. From this, the transactional fuzzy utility (tfu) and maximal transactional fuzzy utility (mtfu) for each transaction, along with each item's upper bounds are calculated, while identifying a set of items, *I**, with upper bounds above a minimum utility threshold.

In the second DB scan, the algorithm constructs global temporal fuzzy utility lists *(TFU-lists)* for each item. The TFU-lists contain occurrence data, utilities, and upper bounds for item-linguistic term pairs. Each occurrence list entry contains transactionID

(TID), fuzzy value (FV), the utility of item(U), and remaining utility (RU) which represents each transaction thus encapsulating the whole database.Each transaction is fuzzified and sorted based on the upper bound ascending order,$(a.M < c.M < d.L < d.M < b.L < c.L < b.M < e.L < a.L)$. For transaction $T_0 = \{a.M, c.L\}$, already sorted, so in reverse order c.L's fuzzy list was created with entry$\langle T_0, 0.5, 4, 0\rangle$ inserted in its occurrence list. Then, a.M's list is created with entry $\langle T_0, 1, 8, 4\rangle$ where 4 is the remaining utility of a.M which is the utility of c.L.The process is followed, and other fuzzy lists are formed. For two items a.M and c.L, fuzzy lists are shown in table2 (right). The three columns represent the upper bound(UB), fuzzy utility(FU), and remaining fuzzy utility(RFU) of that particular item in the whole database. For a.M, UB(a.M) = mtfu(T_0)+mtfu(T_1) = 10+12=22, FU(a.M) =$1 \times 8 + 0.5 \times 6 = 11, RFU(a.M) = 1 \times 4 + 0.5 \times 18 = 13$. Here our ETFUCPS (Estimated Temporal Fuzzy Utility Co-occurrence Pruning Structure) structure is also built. It consists of a set of triples,(a,b,c) where $a, b \in I^*$, a and b are derived from different items for example (a.L, a.M not allowed here) and UB(a,b) = c where UB is the upper bound value. ETFUCPS structure can be created as a triangular matrix as Table2 (left) or with hashmap, where the key is (a,b) and value is c$\neq$0 for fuzzy item's derived from different items. As very few items co-occur with each other, the size of the hashmap is smaller, which is very memory efficient than maintaining a matrix. Building the ETFUCPS is very fast, as it is done within a single database scan. For example, consider a.M and c.L which co-occur with each other at the transaction,T_0 only.Here the mtfu value of T_0 is = mfu(a,T_0)+mfu(c,T_0) = max(1,0,0)*4*2+max(0.5,0,0)*1*4 = 10. Thus the upper bound of pair (c.L, a.M) is 10 which we can see in the triangular matrix in Table2(right) 's row c.L and column a.M.

a.M	**22**	**11**	**13**
TID	**FV**	**U**	**RU**
0	1	8	4
1	0.5	6	18

c.L	**40**	**10**	**5**
TID	**FV**	**U**	**RU**
0	0.5	4	0
2	0.5	4	2
3	0.5	12	8

item	**a.M**	**a.L**	**b.L**	**b.M**	...
a.L	0				
b.L	12	39			
b.M	12	42	0		
c.L	10	30	27	0	
c.M	0	27	27	0	
...	...	...	...	...	...

Table 2. Fuzzy list for items a.M and c.L(left) and ETFUCPS triangular matrix

Then mining is done based on the pattern growth approach of TFU-Miner. The fuzzy lists are processed one by one and recursively the high utility upper bound itemsets and high utility itemsets are discovered using conditional TFU lists. These lists are built by combining the current TFU lists through the join operation, in this process, the unpromising itemsets having upper bound values less than minUtils are removed. Thus patterns of length (1,2,3....n) are mined and returned as results. The mining procedure is stated in pseudocode 1.

The main novelty in our algorithm is the pruning mechanism named ETFUCP (Estimated Temporal Fuzzy Utility Co-occurrence Pruning) based on the ETFUCPS structure. ETFUCP is a pruning strategy that eliminates the low utility extension of itemsets and all their transitive extensions without constructing their utility lists. This is done on line 18 on the *miner* procedure in the pseudocode 1. The pruning condition is that if there is no tuple (k, l, c) in ETFUCPS such that $c \geq \text{minUtil} \times sumTFU(I)$, then P_{kl} represents a pattern formed combining k and l, and all its supersets are low-utility itemsets and do

not need to be explored. This is based on the downward closure property which states if an itemset Y is a subset of X and $tfuubr(X) < minUtil$ then, X and all its supersets are low-utility itemset. Again, we don't need to check the condition for all distinct pairs $a,b \in P_{kl}$ subset pairs of a superset when generating conditional lists, as the check is done recursively for all subset pairs. For example, the itemset Z = $\{a.L, b.M, c.L, d.M\}$ is formed by combining subsets $\{a.L, b.M, c.L\}$ and $\{a.L, b.M, d.M\}$, which are further formed by combining $\{a.L, b.M\}$,$\{a.L, c.L\}$ and $\{a.L, d.M\}$ in a recursive procedure. So the ETFUCPS condition check had already occurred for all the subsets of Z mentioned and we only need to check $\{c.L, d.M\}$ only.

Algorithm 1 Mining Algorithm for FTFUM

Require: A set of TFU-lists, UL, The prefix pattern, $pref$, The prefix OI-list, P, The Estimated Temporal Fuzzy Utility Co-occurrence Pruning Structure, $ETFUCPS$
Ensure: A set of high temporal fuzzy utility patterns, $HTFUP_r$

```
1: function MINER(UL, pref, P, ETFUCPS)
2:     PUs ← ∅ , HTFUP_r ← ∅
3:     if P ≠ ∅ then
4:         PUs ← a transaction-id to utility map for pref
5:         for s in P do
6:             PUs.insert(⟨s.TID, s.U⟩)
7:     for U_k in UL do
8:         if U_k.UB ≥ δ · sumTFU(I) then
9:             if (U_k.UB + U_k.RFU) ≥ δ · sumTFU(I) then
10:                X ← pref ∪ U_k.item
11:                Calculate sumTFU(X) using STP(X) and TFU-table
12:                if U_k.FU ≥ δ · sumTFU(X) then
13:                    HTFUP_r.insert(X)
14:                CL ← ∅
15:                for U_l in UL.after(U_k) do
16:                    if k.i = l.i then
17:                        continue
18:                    if ∃(k,l,c) ∈ ETFUCPS such that c ≥ δ · sumTFU(I) then
19:                        C ← Combine(U_k, U_i, PUs)
20:                        if C ≠ ∅ then
21:                            CL.insert(C)
22:                if |CL| ≥ 1 then
23:                    HTFUP_r ← HTFUP_r ∪ MINER(CL, X, UL.OI_list, ETFUCPS)
24:    return HTFUP_r
```

4. Performance evaluation

We performed experiments on various datasets to evaluate our algorithm. For experimentation, a computer with an Intel 12th generation core i7 processor with 16 GB RAM was used. All the algorithms were implemented using Python programming language. For comparison, we used TFU-Miner (which used TF lists)[9]. We used 3 datasets. Mushroom is a dense dataset with 8,124 transactions and 120 items. Retail and Kosarak are sparse, containing 88,162 transactions with 16,470 items and 990,002 transactions with 41,270 items, respectively.

Two phases were considered and quantities were considered from 1 to 6. In dense datasets like Mushroom, we can see runtime and memory usage are almost similar as

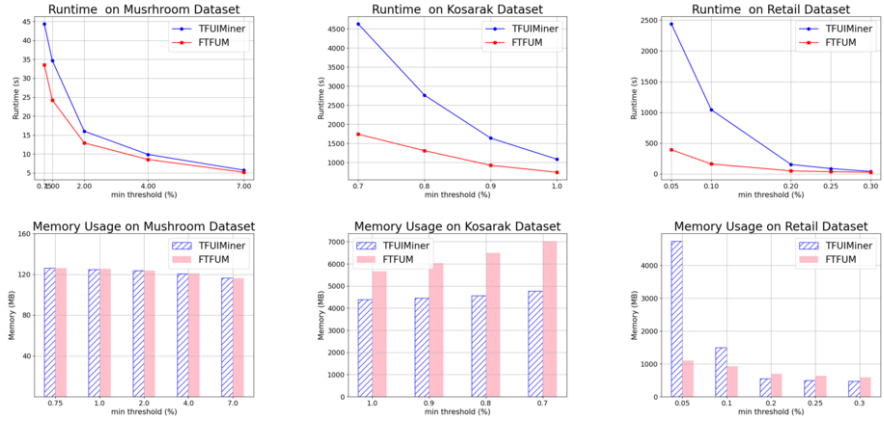

Figure 2. Runtime and memory usage for Mushroom, Retail, and Kosarak datasets.

items frequently co-occur, although our proposed FTFUM is faster. However, the performance difference is noticeable in sparse datasets such as Retail and Kosarak. For the 0.05% threshold, FTFUM(392sec) performs almost 5 times faster than TFU-Miner (2102sec). As the threshold is increased, pattern count decreases and runtime decreases too. But the FTFUM algorithm still works 3 to 4 times faster. In Kosarak, for the 0.8% threshold, FTFUM (1310s) works almost double faster than TFU-Miner (2764). As for memory usage, FTFUM requires more memory to store the hashmap of the itemset pairs' upper bound, so memory usage should have been higher. But by using the ETFUCP pruning strategy, reducing numerous unnecessary fuzzy lists, we can see memory usage is also lower. In Retail, for 0.05% threshold, FTFUM requires approximately **80% less** RAM than TFU-Miner. But in Kosarak, the memory usage of FTFUM is much higher, because this dataset contains 41270 items, hashmap of this size incurs significant overhead. For 0.7%, FTFUM (7GB) requires almost 1.5 times more memory than TFU-Miner (4.7GB). To prove the efficiency of our ETFUCP pruning strategy, we have listed the number of generated candidates in table 3.

Mushroom		
Threshold	TFU	FTFUM
0.75	813	772
1	417	370
2	39	38

Retail		
Thres	TFU	FTFUM
0.05	61075398	48577
0.1	14160175	15514
0.3	71392	1601

Kosarak		
Thres	TFU	FTFUM
1	372832	12611
0.9	79588	20496
0.8	1821446	40009

Table 3. Candidate generation Comparison

As we can see, except for the mushroom dataset, candidate generation through joining is up to 95% lower in our FTFUM algorithm. In sparse datasets, item co-occurrence within each transaction is less frequent, resulting in lower upper bounds for pairs, which enables more efficient pruning of unpromising candidates. So we can conclude that our provided hashmap-based algorithm works faster and efficiently for mining temporal fuzzy high utility itemsets.

5. Conclusion

Fuzzy high-utility itemset mining adds a new layer to discovering real-world patterns by converting item utility into human-understandable fuzzy forms (e.g., low, mid, high). In this paper, we have provided an algorithm named FTFU-Miner(FTFUM), incorporating an ETFUCPS structure to reduce joining operation on fuzzy lists, enabling faster and more efficient pruning and less candidate generation. We performed experimentation on real-life databases and found that our algorithm works faster than the current state-of-the-art TFU-miner algorithm. In the future, we have intentions to further our research on providing a more efficient approach for mining temporal fuzzy itemsets. Also, we are willing to provide faster algorithms to work on data streams.

Acknowledgement

This work is partially supported by (a) University of Dhaka, (b) Natural Sciences and Engineering Research Council of Canada (NSERC), and (c) University of Manitoba.

References

[1] Y. Liu, W.-k. Liao, and A. Choudhary, "A fast high utility itemsets mining algorithm," in *Proceedings of the 1st international workshop on Utility-based data mining*, 2005, pp. 90–99.

[2] M. Liu and J. Qu, "Mining high utility itemsets without candidate generation," in *Proceedings of the 21st ACM international conference on Information and knowledge management*, 2012, pp. 55–64.

[3] P. Fournier-Viger, C.-W. Wu, S. Zida, and V. S. Tseng, "Fhm: Faster high-utility itemset mining using estimated utility co-occurrence pruning," in *Foundations of Intelligent Systems*, T. Andreasen, H. Christiansen, J.-C. Cubero, and Z. W. Raś, Eds. Cham: Springer International Publishing, 2014, pp. 83–92.

[4] L. A. Zadeh, *Fuzzy Sets, Fuzzy Logic, and Fuzzy Systems*. World Scientific Publishing Company, 1996.

[5] G.-C. Lan, T.-P. Hong, Y.-H. Lin, and S.-L. Wang, "Fuzzy utility mining with upper-bound measure," *Applied Soft Computing*, vol. 30, pp. 767–777, 2015.

[6] W.-M. Huang, T.-P. Hong, G.-C. Lan, M.-C. Chiang, and J. C.-W. Lin, "Temporal-based fuzzy utility mining," *IEEE Access*, vol. 5, pp. 26 639–26 652, 2017.

[7] T.-P. Hong, C.-Y. Lin, W.-M. Huang, S.-M. Li, S.-L. Wang, and J. C.-W. Lin, "A one-phase tree-structure method to mine high temporal fuzzy utility itemsets," *Applied Sciences*, vol. 12, no. 6, p. 2821, 2022.

[8] S. Wan, Z. Ye, W. Gan, and J. Chen, "Temporal fuzzy utility maximization with remaining measure," *arXiv preprint arXiv:2208.12439*, 2022.

[9] T. Ryu, H. Kim, C. Lee, H. Kim, B. Vo, J. C.-W. Lin, W. Pedrycz, and U. Yun, "Scalable and efficient approach for high temporal fuzzy utility pattern mining," *IEEE Transactions on Cybernetics*, vol. 53, no. 12, pp. 7672–7685, 2023.

[10] S. Wan, W. Gan, X. Guo, J. Chen, and U. Yun, "Fuim: Fuzzy utility itemset mining," *arXiv preprint arXiv:2111.00307*, 2021.

[11] F. Yang, N. Mu, X. Liao, and X. Lei, "Ea-hufim: Optimization for fuzzy-based high-utility itemsets mining," *International Journal of Fuzzy Systems*, pp. 1–17, 2021.

[12] G. Xu, J. Chen, S. Wan, C. Peng, and Y. Liu, "Explainable itemset utility maximization with fuzzy set," *Journal of Internet Technology*, vol. 24, no. 2, pp. 257–266, 2023.

[13] W.-M. Huang, T.-P. Hong, M.-C. Chiang, and J. C.-W. Lin, "Using multi-conditional minimum thresholds in temporal fuzzy utility mining," *International Journal of Computational Intelligence Systems*, vol. 12, no. 2, pp. 613–626, 2019.

[14] T.-P. Hong, C.-Y. Lin, W.-M. Huang, K. S.-M. Li, L. S.-L. Wang, and J. C.-W. Lin, "Using tree structure to mine high temporal fuzzy utility itemsets," *IEEE Access*, vol. 8, pp. 153 692–153 706, 2020.

[15] Z. Ye, S. Wan, W. Gan, J. Chen, and L. Tang, "Fuzzy utility mining on temporal data," in *2022 4th International Conference on Data Intelligence and Security (ICDIS)*. IEEE, 2022, pp. 366–373.

Fuzzy Systems and Data Mining X
A.J. Tallón-Ballesteros (Ed.)

doi:10.3233/FAIA241408

Adaptive Density Peak Clustering Based on Fuzzy Neighborhood

Meijiao WANG, Libo HE, Yunyun WU[1], Haoshun CAO, Ling LIU
Yunnan Police College, Kunming, China
Key Laboratory of Smart Drugs Control(Yunnan Police College), Ministry of Education Key, Kunming, China
Yunnan Key Laboratory of Smart Drugs Control, Kunming, China

Abstract. Density peak clustering is a clustering strategy that groups data points based on their density in the datasets, which determines cluster centers by finding density peak points and clustering around these centers. It does not require iterative process, nor does it require the user to input too many parameters, which makes it more efficient and easy to use. However, selecting cluster centers manually by decision graph is a major limitation of the algorithm. In the existing research, automatically generate cluster centers methods were proposed, but it didn't take the contribution of different distances when calculating the local density. In this paper, fuzzy neighborhood was employed to measure the proximity between data points to automatically identify the cluster centers. We redefine the fuzzy local density and the fuzzy relative distance in density peak clustering based on fuzzy neighborhood, and automatically generate cluster center based on their statistics. Compared to traditional algorithms, this method has not added any additional parameters. To verify the effectiveness of the proposed algorithm, we conducted comparative experiments with existing algorithms.

Keywords. Data Mining, Density peak clustering, fuzzy neighborhood, fuzzy local density

1. Introduction

In unsupervised learning, clustering analysis[1] is an efficient data mining technique, which can effectively classify complex information. This technology has been widely used across various domains, including image processing[2,3], pattern recognition[4], text data mining[5], social network analysis[6], etc. Through cluster analysis, valuable information can be extracted from the data set. In today's era of rapid development of information technology, a large number of newly emerged data are raw data without processing and lack of reliable basis. Therefore, cluster analysis has shown great potential and is expected to be more widely used in practice.

The conventional clustering method can be categorized into several categories: partition clustering[7], hierarchical clustering[8], grid clustering method[9], density

[1] Corresponding Author: Yunyun WU, Yunnan Police College, China; E-mail: 156799251@qq.com

clustering[10]. However, these methods have their own shortcomings, and it poses a challenge to fully meet the high requirements of modern society for clustering effect.

In 2014, the algorithm of Density Peak Clustering (DPC algorithm) is proposed in Science[11]. The core idea of the DPC algorithm is to identify those data points with higher local density and greater relative distance as cluster centers, then assigns data points from non-clustering centers to these centers.

The DPC algorithm is straightforward, no iteration and convenient to implement, and it can recognize arbitrary shape cluster structures. Since its proposal, it has garnered widespread attention. However, its disadvantages are equally obvious. Firstly, DPC utilize decision graph to select cluster center manually. For complex data sets, the decision graph will become very complex, which makes it very difficult to correctly select cluster center points, and it is common to miss out some potential cluster center points or mistakenly select pseudo-cluster center points. To overcome the aforementioned limitation, adaptive density peak clustering algorithms with automatically generating cluster centers are proposed[12-15]. Secondly, DPC makes a binary judgment on the neighborhood relationship between sample points, which does not differentiate the proximity of neighboring points within a sample's cutoff distance neighborhood (d_c-neighborhood), resulting in an inaccurate calculation of the sample's local density. Fuzzy set theory is an effective strategy to tackle the lack of precision in binary neighborhood relationship judgments, and it is applied to fuzzy c-means (FCM) [16] analysis for the first time.

To address both of the above two issues, we introduce an adaptive density peak clustering algorithm based on fuzzy neighborhood, which generates cluster centers automatically. We first define the membership function of fuzzy neighborhood. The algorithm calculates the local density and relative distance for every sample points based on this membership function, then finds all the density peaks according to the statistical properties of the fuzzy local density and the fuzzy relative distance. Each peak is regarded as a local cluster. The remaining data points are sorted by density and are classified into the group of the nearest data point with high density.

Section 2 describes the classic density peak clustering. Section 3 presents the fuzzy density peak clustering. In Section 4, experiments are conducted to evaluate the proposed algorithm. Finally, the paper concludes with a summary provided in Section 5.

2. Related Work

The Density Peak Clustering (DPC) algorithm operates on the principle of density-based clustering. Its core idea is to identify high density regions segmented by low density regions. This method hinges on two essential assumptions:

(1) The cluster center point possesses a sufficiently high density, being encircled by data points that do not exceed its density.

(2) The center point of one cluster is significantly farther from the center point of other clusters with higher density.

The DPC algorithm introduces two key parameters: local density and distance relativity. It identify the cluster centers according to these two metrics and assign other instances to the clusters in one step without iteration. The definitions of these two parameters are described below.

Definition 1 (Local density). Let ρ_i be the local density of a data point s_i . ρ_i is defined as the number of data points in S whose distance from s_i is no greater than the radius of d_c-neighborhood . Thus , ρ_i can be expressed as follows:

$$\rho_i = \sum_j \chi(d_{ij} - d_c) \tag{1}$$

where, d_c is called the cutoff distance, i.e., the radius of neighborhood. $\chi(x)$ is a 0-1 function, the function value is 0 when x is greater than d_c, is 1 when x is less or equal than d_c. d_{ij} is the Euclidean distance between any two data points s_i and s_j.

Determining a suitable value is not an easy task. Experiments have shown that the choice of d_c has a minimal impact on the final clustering results in large datasets. Users determine the value of d_c by a given percentage. For selecting the cutoff distance, all pairwise distances between data points is sorted from lowest to highest. The value corresponding to a percentage(recommended range of 0.5% to 5%) given by user is selected as the radius of d_c-neighborhood .

Definition 2(relative distance). The relative distance δ_i of a data point s_i is determined by measuring the shortest distance between s_i and any other point in the set S that has a higher local density. In the special case where s_i possesses the highest local density among all points in S, its relative distance is defined as the greatest distance between s_i and any other point in S. This can be formulated as follows:

$$\delta_i = \begin{cases} \min_{j:\rho_j > \rho_i} (d_{ij}) & if\ \exists j\ \ s.t.\ \ \rho_j > \rho_i \\ \max_{j:j:\rho_j < \rho_i} (d_{ij}) & otherwise \end{cases} \tag{2}$$

The DPC algorithm are outlined below:

Algorithm 1. the DPC algorithm

Input: $S = \{ s_1, s_2, \ldots, s_n \}$: the datasets p: percent of the cutoff distance d_c **Output:** The cluster center of each cluster and the data points it contains.	**Steps:** (1) calculate ρ_i from Eq. 1 (2) calculate δ_i from Eq. 2 (3) determine the cluster centers by decision graph (4) allocate non-centers points to cluster centers

The main steps of the DPC algorithm are elaborated in the following:

First, the algorithm calculates for each data point a combination of two elements (ρ_i,δ_i) from Eq.1 and Eq.2.

Then, the algorithm draws a decision graph using these two elements as axes. In this diagram, ρ_i is the horizontal axis and δ_i is the vertical axis.

On the decision graph, the user needs to manually pick out the points with high ρ_i and δ_i values. These points are usually located in the upper right corner of the graph and are clearly distinguished from other data points, and they are selected as the cluster centers.

Once the cluster centers are determined, the algorithm begins to assign the remaining data points to the individual clusters. This process follows the principle of one-step allocation, which assigns data points in order of local density from largest to smallest. Each remaining data point is assigned to the cluster to the nearest cluster center with higher local density.

3. Fuzzy Density peak clustering

We introduce fuzzy set theory to define a membership function based on Euclidean distance, which can be smoothly reduced as the distance increases. This approach describes the degree to which a data point is associated with a particular cluster. The fuzzy neighbors of the data set are defined according to this function. Two crucial parameters, fuzzy local density and fuzzy relative distance, are defined based on fuzzy neighborhood. Then, a statistical strategy is given to automatically select the cluster center according to the mean value of fuzzy local density and the standard deviation of fuzzy relative distance.

3.1 Relative Definition

Definition 3(fuzzy neighborhood(FN)) . Let D be the Euclidean distance set between data points in datasets S. The fuzzy neighborhood (FN) of S is defined as a fuzzy subset on D. Let $\mu(\bullet)$ be the membership function of FN. The Euclidean distance between any two data points in S is denoted as $d(d \in D)$. Then FN is described as follows:

$$\begin{aligned} &\mathrm{FN}: \ D \to [0,1], d \to \mu(d) \\ &\mu(d_{ij}) = \begin{cases} 1 - \dfrac{d_{ij}}{d_c} & if \ d_{ij} < d_c \\ 0 & otherwise \end{cases} \end{aligned} \tag{3}$$

where, $\mu(d_{ij})$ is the membership value of d_{ij} to FN, and it is also called the proximity index between data points.

Let s_i and s_j are any two data points in S. Then FN can be expressed as following:

$$\mathrm{FN} = \{ < (s_i, s_j,), \mu(d_{ij}) > | \, s_i, s_j \in S \} \tag{4}$$

Definition 4(fuzzy local density). Fuzzy local density ρ_i^f of is the sum of the proximity index of between s_i and data points in S whose distance from s_i is no greater than d_c .

$$\rho_i^f = \sum_j \mu(d_{ij}) \tag{5}$$

In the classic DPC algorithm, local density is the most important parameters for the clustering results. However, when determining the density of a data point within its local neighborhood, the differences in proximity between this point and other data points within its neighborhood are not taken into account. As shown in Figure 1, assume there are two data points s_1 and s_2 with the same number of data points within d_c-neighborhood. When employing Eq.1 to calculate the local density, the local densities of point s_1 and s_2 are the same; however, when employing Eq.5 to compute the local density of a data point, the local density of point s_2 is significantly greater than that of s_1. Therefore, the accuracy of local density can be improved by calculating local density through Eq.5.

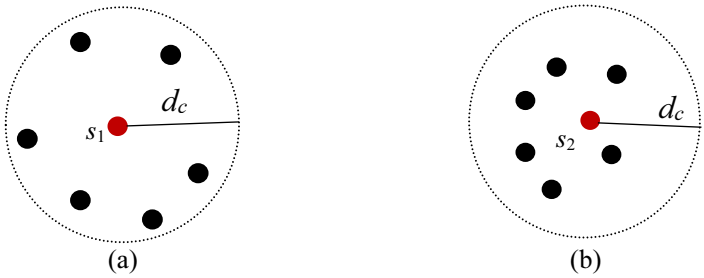

Figure 1. Local density

Although membership functions may have other definitions, an outstanding advantage of the given membership function is that it does not add any new parameters, the only parameter is the radius of d_c-neighborhood in the classic DPC algorithm.

As can be seen in Figure 2, the binary neighborhood in DPC maps the distance map distance to 0 or 1, but the fuzzy neighborhood transforms the distance into an interval value of [0,1]. An membership value $\mu(d_{ij})$ close to 1 indicates high proximity between instances, while $\mu(d_{ij})$ close to 0 indicates that two instances are far apart. This method describes the degree of proximity between spatial instances in detail, and provides a finer measurement tool for spatial data analysis.

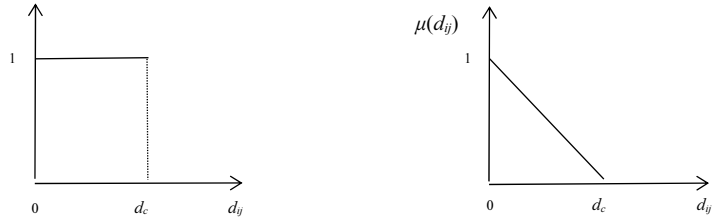

(a) the binary neighborhood (b) the fuzzy neighborhood

Figure 2. membership function of the binary neighborhood and fuzzy neighborhood

Definition 5(fuzzy relative distance). The fuzzy relative distance δ_i^f can be defined from Ep.5 as follows:

$$\delta_i^f = \begin{cases} \min_{j:\rho_j > \rho_i} (d_{ij}) & if \ \exists j \ \ s.t. \ \ \rho_j^f > \rho_i^f \\ \max_{j:j:\rho_j^f < \rho_i^f} (d_{ij}) & otherwise \end{cases} \tag{6}$$

Let $E(\rho_i^f)$ be the mean of fuzzy local density of all data points. Let $\sigma(\delta_i^f)$ be the standard deviation of the relative distance of all data points. A data point is **the cluster center** if it satisfy:

$$\begin{cases} \rho_i^f > E(\rho_i^f) \\ \delta_i^f > 2\sigma(\delta_i^f) \end{cases} \tag{7}$$

Different from the manual selection of cluster centers in the classical algorithm, the cluster centers can be automatically generated by computing the statistics of fuzzy local density and fuzzy relative distance through the above set of inequalities.

3.2 Algorithm description

Based on the above definitions, as an improvement to Algorithm 1, we propose the Adaptive density peak clustering based on fuzzy neighborhood (ADPC_FN), which is outlined as below:

Algorithm 2. the ADPC_FN algorithm

Input:

$S = \{ s_1, s_2, \ldots, s_n \}$: the dataset

p: percent of the cutoff distance d_c

Output:

The label vector of cluster index

Steps:

(1) calculate FN from Eq. 3

(2) calculate ρ_i^f from Eq. 5

(3) calculate δ_i^f from Eq. 6

(4) automatically identify the cluster centers from Eq. 7

(5) allocate non-centers points to cluster centers

Table 1. The description of experimental dataset

Datasets	Objects	Dimentions	Classes
D31	3100	2	31
Sprial	312	2	3
S2	5000	2	15
Aggregation	788	2	7
R15	600	2	15
Compound	399	2	4
Iris	150	4	3
seeds	210	7	3

4. Experiments

In this section, experiments are conducted on both synthetic and actual data sets to evaluate the performance of ADPC_FN algorithm. We selected six synthetic datasets and two real data sets with different shape and density characteristics as test objects, and compared ADPC_FN with the conventional density peak clustering algorithm (DPC) and the DBSCAN algorithm. The data set used in the experiment is shown in the Table 1. The experiments focuses on three clustering performance evaluation indexes, including accuracy, rand index and normalized mutual information (NMI) to comprehensively evaluate the effectiveness of ADPC_FN algorithm and its performance advantages on complex data sets.

In the experiment, python was used to write and compile the algorithm. The algorithm was run on a computer equipped with the Windows 10 operating system, 32GB of RAM, a 3.8GHz frequency, and an AMD Ryzen 7 7840HS processor with Radeon 780M graphics.

As observed in Figure 3 and Table 2. The ADPC_FN algorithm has shown excellent performance in processing spherical, ellipsoidal and curved data clustering tasks. In the experimental data set R15 and S2, as large data sets with different cluster numbers, verify the high robustness of ADPC_FN in the number of clusters. Even in the face of significant changes in data set size and cluster number, the algorithm can still find the cluster structure in the data stably and accurately. The ADPC_FN algorithm performs well on three data sets with different sizes and shapes. These experiments not only confirm the algorithm's adaptability to shape and size changes, but also highlight its ability to handle complex data set structures. According to three clustering evaluation metrics, ADPC_FN outperforms both DPC and DBSCAN, with only a slight disadvantage on the Sprial and the Compound datasets.

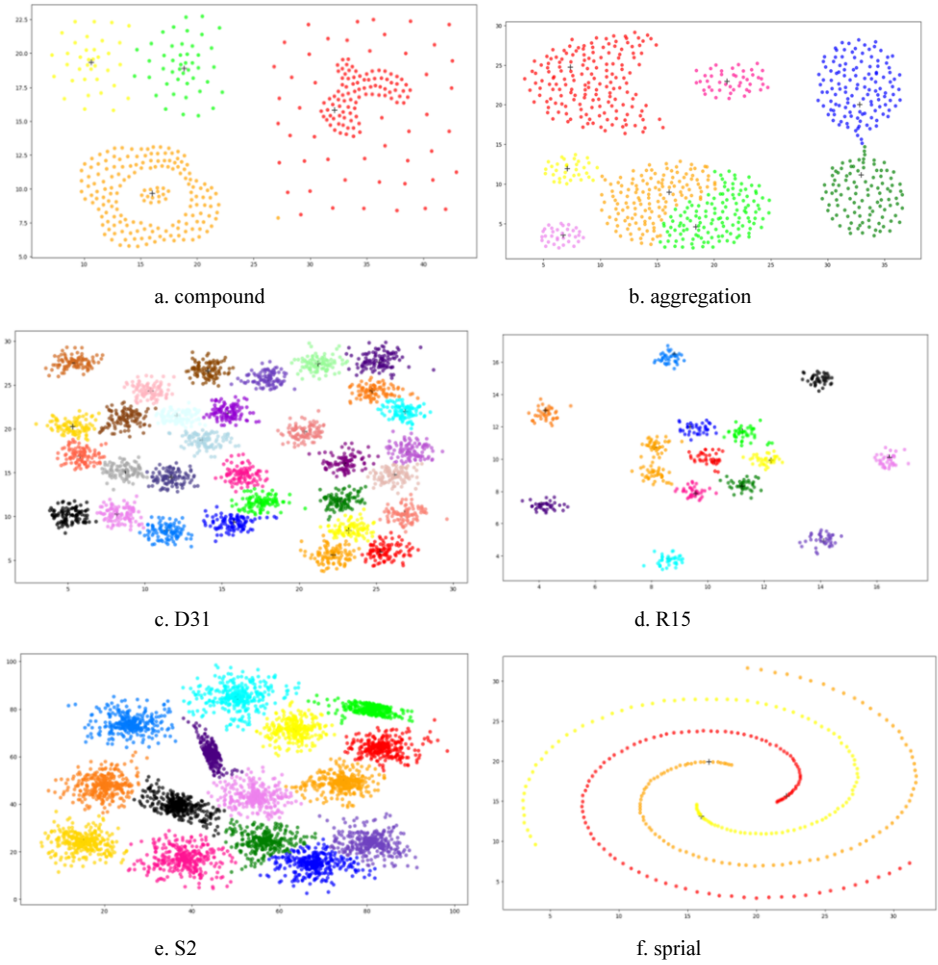

a. compound b. aggregation

c. D31 d. R15

e. S2 f. sprial

Figure 3. Effects on different data sets

Table 2. Performance Evaluation

Data sets	ADPC_FN				DPC				DBSCAN				
	ACC	ARI	NMI	*p*	ACC	ARI	NMI	*p*	ACC	ARI	NMI	eps	min_samples
D31	0.958	0.916	0.944	2.5	0.777	0.737	0.893	0.5	0.653	0.634	0.873	1	28
Sprial	0.994	0.981	0.967	2.5	0.966	0.952	0.934	2	1	1	1	2	2
S2	0.965	0.928	0.938	2	0.734	0.660	0.846	1	0.864	0.594	0.740	1	2
Aggregation	0.991	0.552	0.800	2	0.909	0.681	0.828	5	0.996	0.971	0.971	2	18
R15	0.902	0.858	0.928	1	0.865	0.821	0.913	1	0.534	0.264	0.743	1	2
Compound	0.829	0.772	0.828	2.5	0.716	0.476	0.667	1.5	0.927	0.869	0.885	2	8
Iris	0.940	0.765	0.744	0.5	0.913	0.765	0.748	2.5	0.685	0.557	0.710	1	16
seeds	0.885	0.694	0.686	2.5	0.880	0.677	0.652	5	0.794	0.442	0.535	1	16

5. Conclusions

In order to solve the limitation of manual selection of cluster centers by density peak clustering algorithm (DPC), a method based on fuzzy neighborhood method is introduced to automatically generate cluster centers. We construct a new statistical index based on fuzzy neighborhood to automatically identify cluster centers, thus avoiding the tedious and subjectivity of manual selection. The experimental results demonstrate that our proposed method can effectively generate cluster centers automatically, and shows better performance than the traditional DPC algorithm and the classical DBSCAN algorithm in clustering evaluation indexes. This improvement enhances its applicability and accuracy in practical applications.

Acknowledgments

This work is supported by the project of Science and Technology Department of Yunnan Province(No.202401AT070151), the projects of Yunnan Education Department (No.2023J0788) and the projects of Yunnan Police College (No.23A001,No.21A026), by the Sub-topic of the National Key Research and Development Program Project (No.2022YFC3320801, No.2022YFC3320802).

References

[1] Jain A. Data clustering: 50 Years beyond K-means[J]. Pattern Recognition Letters, 2010, 31(8):651-666.
[2] Hou Jian, Liu Weixue, et al. Towards Parameter-Independent Data Clustering and Image Segmentation[J]. Pattern Recognition, 2016, 60(C): 25-36, DOI:10.1016/j.patrec.2009.09.011.
[3] Sulaiman S N, Isa N A M. Adaptive Fuzzy-K-means Clustering Algorithm for Image Segmentation[J]. IEEE Transactions on Consumer Electronics, 2010, 56(4): 2661-2668, DOI:10.1109/tce.2010.5681154 .
[4] Cherikbayeva L, Yerimbetova A, Daiyrbayeva E .Research of Cluster Analysis Methods for Group Solutions of the Pattern Recognition Problem[C].2021 6th International Conference on Computer Science and Engineering (UBMK), 2021:1-4.DOI:10.1109/UBMK52708.2021.9558884.
[5] Qian S Y, Liu H H, Dai-Yi LI. Research and Application of Improved K-means Algorithm in Text Clustering[J]. DEStech Publications, 2018. DOI:10.12783/dtcse/pcmm2018/23653.
[6] Saha S K, Gosswami T. A Study of Triangle Inequality Violations in Social Network Clustering[J]. Journal of Computer and Communications, 2024, 12(1): 67-76.DOI: 10.4236/jcc.2024.121005.
[7] Lahari K, Murty M R, Satapathy S C. Partition based clustering using genetic algorithm and teaching learning based optimization: performance analysis[C]//Emerging ICT for Bridging the Future-Proceedings of the 49th Annual Convention of the Computer Society of India CSI Volume 2. Springer International Publishing, 2015: 191-200.
[8] Laksitowening K A, Prasetya M D, Suwawi, D D J, Herdiani, A. Capturing Students' Dynamic Learning Pattern Based on Activity Logs Using Hierarchical Clustering[J]. Jurnal RESTI (Rekayasa Sistem dan Teknologi Informasi), 2023, 7(1): 34-40. DOI:10.29207/resti.v7i1.4655.
[9] Wang W, Yang J, Muntz RR. STING: a statistical information grid approach to spatial data mining [C]. Proc. International Conference on Very Large Data Bases, 1997: 186-195.
[10] Ester M, Kriegel H P, Xu X. A density-based algorithm for discovering clusters a density-based algorithm for discovering clusters in large spatial databases with noise[C]. Proc. International Conference on Knowledge Discovery and Data Mining. AAAI Press, 1996:226-231.
[11] Rodriguez A, Laio A. Clustering by fast search and find of density peaks[J]. Science, 2014, 344(6191):1492. DOI:10.1126/science.1242072.
[12] Bie R, Mehmood R, Ruan S, Sun Y, Dawood H. Adaptive fuzzy clustering by fast search and find of density peaks[J]. Personal and Ubiquitous Computing, 2016. DOI:10.1007/s00779-016-0954-4.
[13] Mehmood R, Bie R, Jiao L, Dawood H, Sun Y. Adaptive cutoff distance: Clustering by fast search and find of density peaks[J]. Journal of Intelligent & Fuzzy Systems, 2016. DOI:10.3233/jifs-169102.

[14] Yaohui L, Zhengming M, Fang Y. Adaptive density peak clustering based on K-nearest neighbors with aggregating strategy[J]. Knowledge-Based Systems, 2017, 133(oct.1):208-220. DOI:10.1016 / j.knosys. 2017. 07.010.

[15] Ding S, Du W, Xu X, Shi, T, Wang Y, Li C. An improved density peaks clustering algorithm based on natural neighbor with a merging strategy[J]. Information Sciences, 2023, 624:252-276. DOI:10.1016/ j.ins.2022.12.078.

[16] Bezdek J C, Ehrlich R, Full W. FCM: The fuzzy c-means clustering algorithm[J]. Computers & Geosciences, 1973, 10(2) : 191-203. DOI:10.1016/0098-3004(84)90020-7.

Fuzzy Systems and Data Mining X
A.J. Tallón-Ballesteros (Ed.)

doi:10.3233/FAIA241409

Pruning Fuzzy Neural Network Using Group Sparsity Regularization

Xin Yuan[a,b], Jun Yang[b], Fuxi Wang[b], Yongyong Xu[b] and Tao Gao[b,1]

[a] *Tsinghua University, Beijing, China*
[b] *The 15th Research Institute of China Electronics Technology Group Corporation, Beijing, China*

Abstract. As one interpretable technique, fuzzy neural network (FNN) can be equipped into any deep models, but it faces the problem of high dimension when FNN is used for designing deep networks. To break the curse of dimensionality, in this paper, we use regularization method to reduce the influence of dimensionality on FNN, and based on $L_{2,1}$ norm (Group Lasso) two different regularizer terms are designed. Using the gradient method, FNN can learn to evaluate the importance of features and rules, respectively, and then realizes feature selection (FS) and rule generation (RG). By dint of the simulation results on the benchmark classification problems Iris and Sonar, the validity of our proposed fuzzy classifier is verified, i.e., without decreasing the classification performance, the structure of the fuzzy model can be simplified. The regularized FNN can be easily used for interpretable deep model design.

Keywords: Regularization, fuzzy model, feature selection, rule generation

1. Introduction

Regularization is regarded as an effective strategy to improve generation ability and solve overfitting problem, and it refers to the modifications for one known learning algorithm, which can improve the generalization capability of the corresponding learning technique [1]. A survey of regularization in traditional machine learning and deep learning is summarized in details [2].

For fuzzy models [3-5], the appliance of regularization is not extensively studied. Using Tikhonov regularization, the robustness of identified Takagi-Sugeno (TS) fuzzy systems is improved [6]. To improve the explanation of fuzzy rule based models, one regularization term focusing on deleting the redundant fuzzy membership is integrated into the traditional loss function during training [7]. To prune the unnecessary rules, the L_1 norm based regularizer is designed for first order fuzzy model [8-9]. The difference between [8] and [9] is that Lughofer et al. use the rule weight to design the L_1 regularizer, but the L_1 regularization term is designed by the consequent part parameters [9]. In addition, the unnecessary features in the consequent parts are pruned using the consequent weights based regularizer [8], and it is a pity that the

[1] Corresponding Author, Tao Gao, The 15th Research Institute of China Electronics Technology Group Corporation, Beijing, China; Email: gaotao_1989@126.com

corresponding features in the antecedent parts is not deleted. The $L_{2,1}$ regularizer [10] is designed and it is employed to penalize the widths and consequent parts of zero [11] and first [12] order TS fuzzy model, respectively. To integrate the mini-batch gradient descent (MBGD) and regularizer for first order TS fuzzy system learning, the L_2 regularized loss function for regression problems is devised based on the consequent parameters [13]. Furthermore, combining uniform regularization (UR) and L_2 regularization term , a novel cross-entropy based loss function is presented to train the TS fuzzy classifier [14]. To realize feature selection and identify system simultaneously, a smoothing Group Lasso (GL, i.e., $L_{2,1}$ norm) based regularization term for interval type-2 fuzzy model is created [15]. To promote the robustness of fuzzy neural network, a statistical sensitivity is defined and two kind of sensitivity based regularizers are proposed to construct the error function to optimize the fuzzy model [16]. Considering feature redundancy, using feature modulator and Pearson correlation based regularizer, controlling redundancy based feature selection method is used to realize FS in a fuzzy rule based classifier [17]. A novel regularization term, which uses Group Lasso based Pearson correlation coefficient, is introduced to delete the unimportant input nodes for FNN [18]. Inspired by Group Lasso, the Group Lasso regularizer is applied for first order TS fuzzy neural network to remove oscillations [19]. We use the GL regularizer to prune the feature nodes to simplify the network structure [20]. Observing the structure of FNN in Fig. 1, it is easy to find that except for the input nodes and output nodes, the complexity is also influenced by the second and third layer, i.e., fuzzy set nodes and rule nodes, and it is obvious there may exist unnecessary rule nodes. Hence, in this paper, we furtherly extend the GL regularizer to prune the rule nodes.

The following part is organized as: section 2 introduces the regularized FNN that can realize feature selection and rule pruning simultaneously; to prove the effectiveness of our proposed structure slimming method, the simulation results are summarized in section 3; section 4 presents the conclusions and future works.

2. Regularized FNN

The structure of type-1 zero order TS FNN for multiple-input and multiple-output problems is presented in Fig. 1.

Supposing $\{\mathbf{x}_j, \mathbf{o}_j\}$ is the preprocessed sample set, where $\mathbf{x}_j = (x_{j1}, x_{j2}, \cdots, x_{jm})$ corresponds to j^{th} normalized input vector, $\mathbf{o}_j = (o_{j1}, o_{j2}, \cdots, o_{jp})$ denotes the corresponding ideal output. For one given problem, the input dimension m and output number p are fixed, so the complexity of Fig. 1 mainly depends on the second layer (feature selection layer) and third layer (rule layer). To simplify the network, we employ the group sparsity regularization to design feature selection and rule generation method.

$$\mathrm{R}_{i_\kappa}^{TS}: If\ x_1\ is\ A_{1i}\ and\ x_2\ is\ A_{2i}\ and \cdots and\ x_m\ is\ A_{mi}, then\ y_\kappa\ is\ u_{i_\kappa}^2. \quad (1)$$

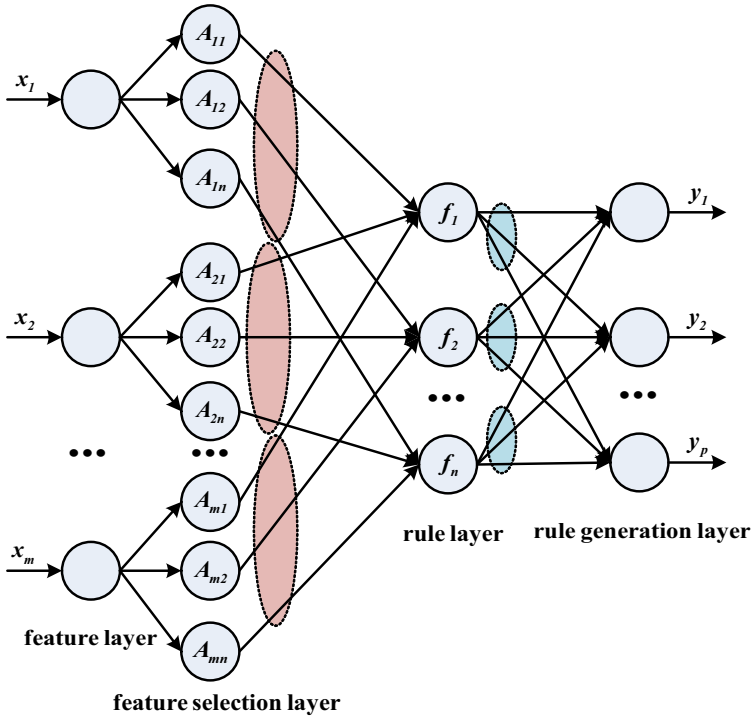

Figure 1. The type-1 zero order TS fuzzy rule based network for classification problems. For this model, the fuzzy rule base (1) is employed to design the classifier.

2.1. Feature Selection Regularizer

To realize feature selection for fuzzy models, we should change the values of membership functions for the bad feature to be 1, without considering the fuzzification method and the T-norm operation employed. Then the feature will cause no influence on the fuzzy inference outputs. The regularizer based feature selection model is designed as below:

$$E^{FS}(\mathbf{w}) = \sum_{j=1}^{J_{Tr}} E(\mathbf{f}_j \mathbf{U}) + \partial \sum_{l=1}^{m} \| \mathbf{b}_l \| = \frac{1}{2} \sum_{j=1}^{J_{Tr}} \| \mathbf{y}_j - \mathbf{o}_j \|^2 + \partial \sum_{l=1}^{m} \| \mathbf{b}_l \|. \quad (2)$$

For the l^{th} feature, $\| \mathbf{b}_l \| = \sqrt{b_{l1}^2 + b_{l2}^2 + \cdots + b_{ln}^2}$, if $\| \mathbf{b}_l \|$ is penalized to be 0 using ∂, then all the Gaussian membership values computed using $\mu_{A_{li}}(x_l) = \exp(-(x_l - a_{li})^2 b_{li}^2)$ are 1 for x_l.

In (2), where $\mathbf{w}$ is called independent variables, i.e., $\sum_{j=1}^{J_{Tr}} E(\mathbf{f}_j \mathbf{U})$ is a function of $\mathbf{w}$, and $\mathbf{w}$ is composed of a_{li}, b_{li} and the element of consequent part matrix $\mathbf{U}$.

$\mathbf{f} = (f_1, f_2, \cdots, f_n)$, $f_i = \prod_{l=1}^{m} \mu_{A_{li}}(x_l)$, $\mathbf{U} = \begin{bmatrix} \mathbf{u}_1 \\ \mathbf{u}_2 \\ \cdots \\ \mathbf{u}_n \end{bmatrix}_{n \times p}$, $\mathbf{u}_i = (u_{i1}^2, u_{i2}^2, \cdots, u_{ip}^2)$,

$\mathbf{y}_j = (y_{j1}, y_{j2}, \cdots, y_{jp}) = \mathbf{f}_j \mathbf{U}$, $y_{j\kappa} = f(\mathbf{w}) = \sum_{i=1}^{n} f_{ji} u_{i\kappa}^2$. In this paper, we directly use f_{ji} to defuzzify the fuzzy value rather than the $f_{ji} / \sum_{i=1}^{n} f_{ji}$.

$$E(\mathbf{f}_j \mathbf{U}) = E(\mathbf{y}_j) = \frac{1}{2}(y_{j1} - o_{j1})^2 + \frac{1}{2}(y_{j2} - o_{j2})^2 + \cdots + \frac{1}{2}(y_{jp} - o_{jp})^2 = \frac{1}{2} \| \mathbf{y}_j - \mathbf{o}_j \|^2$$

.

2.2. Rule Generation Regularizer

Be similar to x_l , the firing strength value f_i in Fig. 1 is also fanned out, and it is connected to p output nodes using $\mathbf{u}_i = (u_{i1}^2, u_{i2}^2, \cdots, u_{ip}^2)$. During training the Gaussian parameters, it is hard for us to guarantee the different variations of various parameters. That is to say, there may exist similar fuzzy sets and rules after tuning. Hence, during training, we should design some strategy to identify the redundant (similar but unimportant) rules and make corresponding treatments. The consequent part $u_{i\kappa}^2$ employed in this paper can evaluate the importance of f_{ji}, and if $u_{i\kappa}^2 = 0$, the firing strength f_{ji} has no effect on the output $y_{j\kappa}$, i.e., $f_{ji} u_{i\kappa}^2 = 0$, which means that the firing strength is not fired for the κ^{th} output. For f_{ji}, there are p supports $\{u_{i1}^2, u_{i2}^2, \cdots, u_{ip}^2\}$. Therefore, when all the supports tend to 0, the influence of i^{th} rule on the reasoning outputs will be eliminated, then the structure nodes in layer 2 and layer 3 can be deleted. To control the value of p supports simultaneously, the group term $\| \mathbf{u}_i \| = \| (u_{i1}^2, u_{i2}^2, \cdots, u_{ip}^2) \| = \sqrt{u_{i1}^4 + u_{i2}^4 + \cdots + u_{ip}^4}$ for f_{ji} is used as the evaluation criterion for the importance of the i^{th} rule, and if the value of $\| \mathbf{u}_i \|$ tends to zero, the firing strength f_{ji} is considered unimportant, i.e., the i^{th} rule is unimportant; otherwise, it is useful. The rule generation regularizer based fuzzy model is as below:

$$E^{RG}(\mathbf{w}) = \sum_{j=1}^{J_{Tr}} E(\mathbf{f}_j \mathbf{U}) + \beta \sum_{i=1}^{n} \| \mathbf{u}_i \| = \frac{1}{2} \sum_{j=1}^{J_{Tr}} \| \mathbf{y}_j - \mathbf{o}_j \|^2 + \beta \sum_{i=1}^{n} \| \mathbf{u}_i \|. \quad (3)$$

2.3. Training Strategy

Using any optimization method, the loss function (2) and (3) can be optimized. In this paper, we use the gradient descent method and the update rule is as below:

$$\mathbf{w}^{k+1} = \mathbf{w}^{k} + \eta(-E_{\mathbf{w}}(\mathbf{w}^{k})), k \in (1,2,\cdots), \tag{4}$$

where k is the iteration number, η is the step size (learning rate), $E_{\mathbf{w}}(\mathbf{w})$ denotes the gradient of the error function $E(\mathbf{w})$.

3. Simulation Results

In general, two methods can be used to determine the optimal number of rules. One refers to the growing method, which starts with no rule and then the rule numbers tend to a valid fixed value. The pruning method, as another strategy, initializes the rule base with a larger number and the unimportant/bad rules are pruned. In this paper, we focus on the second method. To prove the effectiveness of our method, two classification problems in Tab. 1 are used to conduct the experiments.

Table 1. Summary of the data sets used.

	Data name	No. of samples ($J_{Tr} + J_{Te}$)	No. of inputs (m)	No. of outputs (p)	Data source
Classification	Iris	150 (135+15)	4	3	[18]
	Sonar	208 (187+21)	60	2	[18]

3.1. Iris

For Iris, among all the four features, there are many researches proving that the last feature Petal Width is important. Hence, if the feature selection model works, then the last feature will be selected. After one trial, the feature selection procedure of our model is plotted in Fig. 2 (a). From it, we find that for feature 4 (F4), the optimal value of $\|\mathbf{b}_4\|$ tends to nonzero, but the norm values of remaining three features converge to zero, which means that feature 4 is important, and our model can recognize and select it.

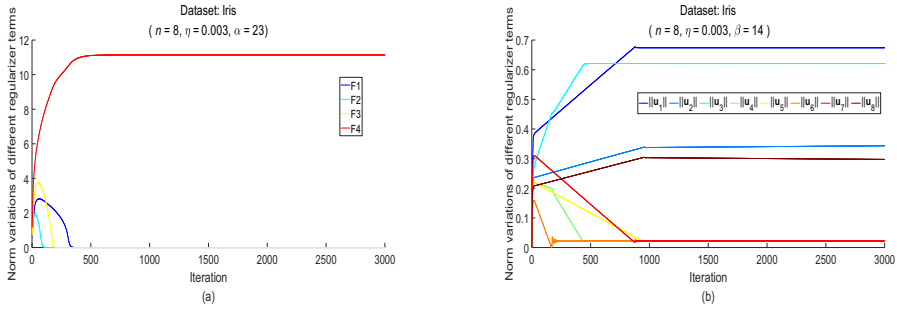

Figure 2. Feature selection process (a) and rule generation process (b) of our model for Iris.

After feature selection, the same training samples with the selected features are employed to validate the effectiveness of rule pruning strategy, and the training process is illustrated in 2 (b). At the training start, all the rules are considered unimportant by setting the value of $\| \mathbf{u}_i \|$ s to be almost 0. With the iteration increasing, our model can identify the important rules automatically. For the important rules, $\| \mathbf{u}_i \|$ s tend to nonzero values, but for the bad rules, the values of $\| \mathbf{u}_i \|$ s are penalized to be lower values by β. The fuzzy sets before and after rule pruning are plotted in Fig. 3, which proves that the redundant rules can be deleted by our rule generation strategy.

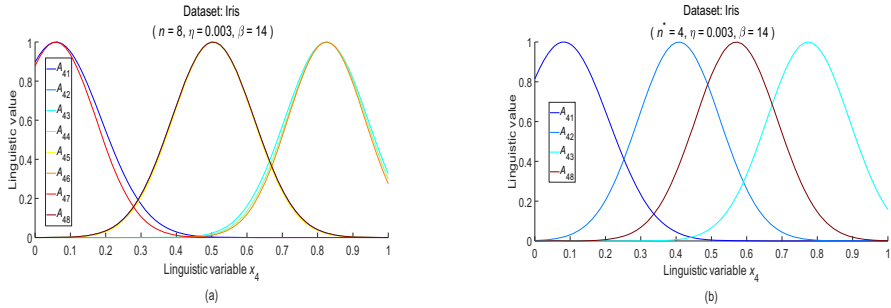

Figure 3. Fuzzy sets for Iris before pruning (a) and after pruning (b).

3.2. Sonar

Be similar to Iris, our model also works for the Sonar data on the feature selection and rule generation. For feature selection and rule generation, our model firstly judges the features and rules carefully with the very low values. Then it automatically optimizes the value of norms with the help of gradient method. Lastly, the training strategy helps our model to converge to different values. The whole feature selection and rule generation process is depicted in Fig. 4. Observing Fig. 4, seven features are selected from the sixty features and the optimal rule number n^* is 6, and the classification performance of our simplified model is illustrated quantificationally using the recorded test classification accuracy 75.4%. For the selected feature 36, we plot the linguistic value variation in Fig. 5, and this comparison figure illustrates our rule pruning method can optimize the fuzzy sets.

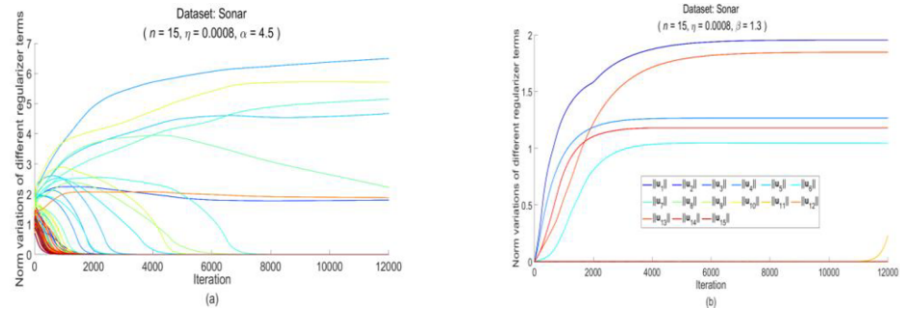

Figure 4. Feature selection process (a) and rule generation process (b) of our model for Sonar.

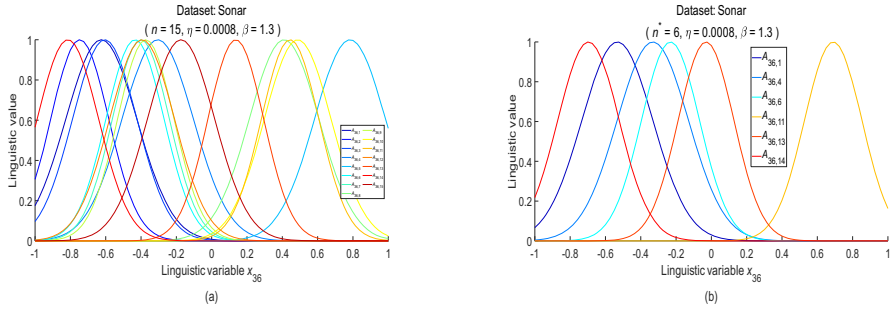

Figure 5. Fuzzy sets for Sonar before pruning (a) and after pruning (b).

4. Conclusions and Future Works

To simplify the fuzzy neural network, two different structure pruning philosophies based regularization terms are used to design the feature selection and rule generation method, respectively. One philosophy considers the value 1 has no contribution for the multiplication operation, and the other one thinks that the value 0 contributes nothing for the additive operation. Using the benchmark classification problems, the effectiveness of our structure compact method is proved.

It is a pity that our proposed method is not suitable for the real high dimensional problems (where the number of input features is higher than 1000), for we use t-norm to compute the firing strength value. In addition, the regularization term based error function is not differential in the original point ,which may be problematic when using gradient method to optimize it. Hence, in the future work, we focus on solving the existing drawbacks.

References

[1] Goodfellow I, Bengio Y, Courville A. Deep learning. Cambridge, MA, USA: MIT press, 2017
[2] Tian Y, Zhang Y. A comprehensive survey on regularization strategies in machine learning. Information Fusion. 2022 April; 80: 146-166, doi: 10.1016/j.inffus.2021.11.005
[3] Hussain A, Ullah K. An intelligent decision support system for spherical fuzzy Sugeno-Weber aggregation operators and real-life applications. Spectrum of Mechanical Engineering and Operational Research. 2024; 1(1): 177-188, doi: https://doi.org/10.31181/smeor11202415
[4] Hussain A, Ullah K, Pamucar D, Haleemzai I, Tatić D. Assessment of solar panel using multiattribute decision-making approach based on intuitionistic fuzzy aczel alsina heronian mean operator. International Journal of Intelligent Systems. 2023 May; 1: 6268613, doi: https://doi.org/10.1155/2023/6268613
[5] Wu D, Lin C T, Huang J, Zeng Z. On the functional equivalence of TSK fuzzy systems to neural networks, mixture of experts, CART, and stacking ensemble regression. IEEE Transactions on Fuzzy Systems. 2019; 28(10): 2570-2580, doi: 10.1109/TFUZZ.2019.2941697
[6] Johansen T A. Robust identification of Takagi-Sugeno-Kang fuzzy models using regularization. Proceedings of IEEE 5th International Fuzzy Systems (New Orleans: LA/USA). 1996, 1: 180-193, doi: 10.1109/FUZZY.1996.551739
[7] Jin Y. Fuzzy modelling of high-dimensional systems: Complexity reduction and interpretability improvement. IEEE Transactions on Fuzzy Systems. 2000; 8(2): 212-221, doi: 10.1109/91.842154
[8] Lughofer E, Kindermann S. SparseFIS: Data-driven learning of fuzzy systems with sparsity constraints. IEEE Transactions on Fuzzy Systems. 2010; 18(2): 396-411, doi: 10.1109/TFUZZ.2010.2042960
[9] Luo M, Sun F, Liu H. Dynamic T-S fuzzy systems identification based on sparse regularization. Asian Journal of Control. 2015; 17(1) : 274-283, doi: https://doi.org/10.1002/asjc.890

[10] Xu Z, Zhang H, Wang Y, Chang X, Liang Y. $L_{1/2}$ regularizer. Science China Information Sciences. 2010 May; 53: 1159-1169, doi: https://doi.org/10.1007/s11432-010-0090-0
[11] Liu Y, Wu W, Fan Q, Yang D, Wang J. A modified gradient learning algorithm with smoothing $L_{1/2}$ regularization for Takagi-Sugeno fuzzy models. Neurocomputing. 2014 August; 138: 229-237, doi: https://doi.org/10.1016/j.neucom.2014.01.041
[12] Liu Y, Yang D. Convergence analysis of the batch gradient-based neuro-fuzzy learning algorithm with smoothing $L_{1/2}$ regularization for the first-order TS system. Fuzzy Sets and Systems. 2017 July; 319: 28-49, doi: https://doi.org/10.1016/j.fss.2016.07.003
[13] Wu D, Yuan Y, Tan Y. Optimize TSK fuzzy systems for big data regression problems: mini-batch gradient descent with regularization, DropRule and AdaBound (MBGD-RDA). IEEE Transactions on Fuzzy Systems. 2020 May; 28(5): 1003-1015, doi: 10.1109/TFUZZ.2019.2958559
[14] Cui Y, Wu D, Huang J. Optimize TSK fuzzy systems for classification problems: mini-batch gradient descent with uniform regularization and batch normalization. IEEE Transactions on Fuzzy Systems. 2020 December; 28(12): 3065-3075, doi: 10.1109/TFUZZ.2020.2967282
[15] Gao T, Wang C, Zheng J, Wu G, Ning X, Bai X, Yang J, Wang J. A smoothing Group Lasso based interval type-2 fuzzy neural network for simultaneous feature selection and system identification. Knowledge-Based Systems. 2023; 280: 111028, doi: https://doi.org/10.1016/j.knosys.2023.111028
[16] Wang J, Chang Q, Gao T, Zhang K, Pal N R. Sensitivity analysis of Takagi-Sugeno fuzzy neural network. Information Sciences. 2022; 582: 725-749, doi: https://doi.org/10.1016/j.ins.2021.10.037
[17] Chung I F, Chen Y C, Pal N R. Feature selection with controlled redundancy in a fuzzy rule based framework. IEEE Transactions on Fuzzy Systems. 2018 April; 26(2): 734-748, doi: 10.1109/TFUZZ.2017.2688358
[18] Gao T, Bai X, Zhang L, Wang C, Wang J. Redundancy-controlled feature selection for fuzzy neural networks. 2021 International Conference on High Performance Big Data and Intelligent Systems (HPBDIS) (Macau/China). 2021: 172-176, doi: 10.1109/HPBDIS53214.2021.9658345
[19] Liu Y, Wang R, Liu Y Q, Shao Q, Lv Y, Yu Y. A novel learning approach to remove oscillations in first-order TS fuzzy system: gradient descent-based neuro-fuzzy algorithm using smoothing Group Lasso regularization. Advanced Theory and Simulations. 2024 November; 7(2): 2300545, doi: https://doi.org/10.1002/adts.202300545
[20] Gao T, Bai X, Zhang L, Wang J. Feature selection for fuzzy neural networks using group Lasso regularization. 2021 IEEE Symposium Series on Computational Intelligence (SSCI) (Orlando: FL/USA). 2021: 1-8, doi: 10.1109/SSCI50451.2021.9659548

Fuzzy Systems and Data Mining X
A.J. Tallón-Ballesteros (Ed.)

doi:10.3233/FAIA241410

The Construction of Probabilistic Boolean Networks: New Algorithms and Lower Bound

Christopher H. FOK [a,1], Wai-Ki CHING [a] and Chi-Wing WONG [a]
[a] *Department of Mathematics, The University of Hong Kong, Hong Kong, China*

Abstract. Boolean Networks (BN) and Probabilistic Boolean Networks (PBNs) are useful models for genetic regulatory networks, healthcare service systems, manufacturing systems and financial risk. This paper focuses on the construction problem of PBNs. We propose the Division Pre-processing algorithm (DPre), which breaks a non-negative integer matrix P with constant positive column sum into two non-negative integer matrices $\tilde{Q}$ and $\tilde{R}$, each with constant column sum, such that $P = d\tilde{Q} + \tilde{R}$ for some positive integer d. We combine DPre with two existing PBN construction algorithms to form a novel PBN construction algorithm called the Single Division Pre-processed SER2-GER algorithm (SDS2G). Our computational experiments reveal that SDS2G gives significantly better performance compared with other existing PBN construction algorithms, and that SDS2G is fast. Lastly, we derive a new lower bound related to PBN construction, and this new theorem generalizes a lower bound theorem in a previous paper.

Keywords. Boolean Networks, Probabilistic Boolean Networks, Sparse Representation, Pre-Processing Algorithms

1. Introduction

1.1. Background

The Boolean Network model (BN) is used for studying apoptosis, genetic regulatory networks, T cell receptor signaling and the yeast cell-cycle network ([1,2,3,4,5,6,7]). A BN consists of a set of nodes $V = \{v_1, v_2, \ldots, v_n\}$, and each node v_i is associated with a Boolean function f_i mapping from $\{0,1\}^n$ to $\{0,1\}$. To understand further the mathematical details of BNs, the interested readers can refer to [1,2,3]. The point important to us is that we can represent an n-node BN using a special $2^n \times 2^n$ matrix A (called the BN matrix of the BN). Each column of A is a standard unit vector in $\mathbb{R}^{2^n}$. We define $\tilde{B}_n$ to be the set of all $2^n \times 2^n$ matrices A' such that each column of A' is a standard unit vector in $\mathbb{R}^{2^n}$. In other words, $\tilde{B}_n$ is the set of all $2^n \times 2^n$ BN matrices.

In 2002, Shmulevich et al. proposed a probabilistic extension of the BN model—called Probabilistic Boolean Network (PBN)—for modeling genetic regulatory networks [8]. Since then, PBNs have found applications in many other areas including biomedicine

[1]Corresponding Author: Christopher H. Fok; E-mail: christopherfok2015@outlook.com

[9], the study of brain connectivity [10], credit default modeling [11] and manufacturing process modeling [12]. We will skip providing the mathematical details of PBNs and the interested readers can refer to [8,13] for such information. The key is that we can represent an n-node PBN by a $2^n \times 2^n$ transition probability matrix P (called the PBN matrix of the PBN). An $a \times a$ real-valued non-negative matrix Q is said to be an $a \times a$ transition probability matrix (TPM) if for all $j \in \{1,2,\ldots,a\}$, $\sum_{i=1}^{a} Q(i,j) = 1$.

1.2. Problem Formulation

To describe our research problem clearly, first we need to define some terminologies.

Firstly, if $P \in \mathbb{R}^{a\times a}$ is a matrix such that $P = p_0 Q$ for some real number $p_0 \geq 0$ and $a \times a$ TPM Q, then P is said to be an $a \times a$ p_0-transition probability matrix ($a \times a$ p_0-TPM). In particular, the 0-TPM is the zero matrix. If an $a \times a$ p_0-TPM P further satisfies that all entries of P are integers, then P is said to be an $a \times a$ integerized p_0-TPM. Secondly, consider any non-zero $2^n \times 2^n$ p_0-TPM P. If $x_1, x_2, \ldots, x_K \in \mathbb{R}$ are positive and $A_1, A_2, \ldots, A_K \in \tilde{B}_n$ are distinct BN matrices such that $\sum_{i=1}^{K} x_i A_i = P$, then $x_1, x_2, \ldots, x_K$ and $A_1, A_2, \ldots, A_K$ are said to define a decomposition of P with length K.

Our research problem is: given a non-zero $2^n \times 2^n$ p_0-TPM P, find a decomposition of P whose length is as small as possible. This problem is called the construction problem of PBNs. Let P be a non-zero $2^n \times 2^n$ p_0-TPM and q be any positive real number. We remark that the task of finding decompositions of P with small lengths is equivalent to the task of finding decompositions of qP with small lengths. This is because: for any decomposition $x_1, x_2, \ldots, x_K$ and $A_1, A_2, \ldots, A_K$ of P, $qx_1, qx_2, \ldots, qx_K$ and $A_1, A_2, \ldots, A_K$ define a decomposition of qP; and for any decomposition $y_1, y_2, \ldots, y_L$ and $\tilde{A}_1, \tilde{A}_2, \ldots, \tilde{A}_L$ of qP, $\frac{y_1}{q}, \frac{y_2}{q}, \ldots, \frac{y_L}{q}$ and $\tilde{A}_1, \tilde{A}_2, \ldots, \tilde{A}_L$ define a decomposition of P.

1.3. Our Contributions

Our contributions are twofold.

First, we come up with the Division Pre-processing algorithm (DPre). For any $2^n \times 2^n$ non-zero integerized p_0-TPM P and any positive integer d, DPre outputs an integerized $\tilde{q}_0$-TPM $\tilde{Q}$ and an integerized $\tilde{r}_0$-TPM $\tilde{R}$, where $\tilde{q}_0, \tilde{r}_0 \geq 0$, satisfying $P = d\tilde{Q} + \tilde{R}$. We combine DPre with two previously proposed PBN construction algorithms (called SER 2 and GER, proposed in [14] and [15] respectively) to form the Single Division Pre-processed SER2-GER algorithm (SDS2G) for tackling the construction problem of PBNs. Our computational experiments reveal that SDS2G gives significantly better performance than other existing state-of-the-art PBN construction algorithms. We also measured the execution time of SDS2G and found that SDS2G is a fast algorithm.

Second, we derive a new lower bound related to the construction problem of PBNs. Our lower bound generalizes the lower bound theorem given in [16, Theorem 4.8].

1.4. Organization of the Rest of This Paper

Section 2 describes the Division Pre-processing algorithm (DPre) and the Single Division Pre-processed SER2-GER algorithm (SDS2G). Section 3 details the numerical experiments we conducted. Section 4 explains our new lower bound related to the construction problem of PBNs. Section 5 provides the conclusion and discusses some possible extensions of this work.

1.5. Some Notations and Terminologies

Throughout this paper, MATLAB-style matrix notation will be used. For instance, $B(k,l)$ is the (k,l)-entry of a matrix B and $B(:,3)$ is the 3rd column of B. For any real-valued matrix D and any real number x, we define the column frequency of x in D to be the number of columns of D containing x as an entry, and we define $S^+(D)$ to be the set of positive entries of D. For example, if $D = \begin{pmatrix} 1 & 2 & 3 & 4 \\ 0 & 5 & 2 & 2 \\ 1 & 0 & 4 & 2 \\ 8 & 3 & 1 & 2 \end{pmatrix}$, then the column frequency of 1 in D equals 2 because 1 is an entry of $D(:,1)$ and $D(:,3)$ only. Moreover, $S^+(D) = \{1,2,3,4,5,8\}$. For any natural numbers a and b, $\mathbf{O}_{a\times b}$ refers to the $a \times b$ matrix consisting of zeros. The column vector in $\mathbb{R}^a$ consisting of ones is represented using the notation $\vec{1}_a$. For any real vector $\vec{v}$, we define $\|\vec{v}\|_0$ to be the number of non-zero entries of $\vec{v}$. For all natural number y, we define $[y]$ to be the set of integers from 1 to y.

2. The Division Pre-Processing Algorithm (DPre) and the Single Division Pre-Processed SER2-GER Algorithm (SDS2G)

The Division Pre-processing algorithm (DPre) and the Single Division Pre-processed SER2-GER algorithm (SDS2G) are designed with an aim to produce shorter-length decompositions for non-zero integerized p_0-TPM P with these two properties: $|S^+(P)|$ is large, and most of the positive values x in $S^+(P)$ have low column frequencies in P. We remark that for non-zero integerized p_0-TPMs P with these two properties, the value of p_0 is usually large. For example, consider the following two matrices of the same size:

$$R_1 = \begin{pmatrix} 1 & 2 & 3 & 4 \\ 0 & 5 & 2 & 2 \\ 1 & 0 & 4 & 2 \\ 8 & 3 & 1 & 2 \end{pmatrix}, \quad R_2 = \begin{pmatrix} 102 & 216 & 300 & 358 \\ 9 & 418 & 200 & 198 \\ 125 & 46 & 400 & 195 \\ 764 & 320 & 100 & 249 \end{pmatrix}.$$

Note that $S^+(R_1) = \{1,2,3,4,5,8\}$ and $S^+(R_2) = \{9,46,100,102,125,195,198,200,216,249,300,320,358,400,418,764\}$. Therefore, $|S^+(R_1)| = 6$ and $|S^+(R_2)| = 16$ so $|S^+(R_2)|$ is relatively large compared to $|S^+(R_1)|$. We can also see that the column frequencies of $1,2,3,4,5,8 \in S^+(R_1)$ in R_1 are 2, 3, 2, 2, 1, 1 respectively while the column frequency of every element of $S^+(R_2)$ in R_2 equals 1. Note that R_1 is an integerized 10-TPM and R_2 is an integerized 1000-TPM, and that 1000 is relatively large compared to 10.

From our empirical experience, we discover that the Greedy Entry Removal algorithm (proposed in [15] and abbreviated as GER) and the Simple Entry Removal Algorithm 2 (proposed in [14] and abbreviated as SER 2) usually outputs decompositions with large lengths when executed on integerized p_0-TPMs with the aforementioned two properties. This motivates us to come up with DPre and SDS2G for finding decompositions of such integerized p_0-TPMs with short lengths.

Before we introduce DPre and SDS2G, we need to consider the procedure of merging decompositions of p_0-TPMs. Let Q be a non-zero $2^n \times 2^n$ q-TPM and R be a non-zero $2^n \times 2^n$ r-TPM. Let $\{x_i\}_{i\in[K]}$ (positive real numbers) and $\{A_i\}_{i\in[K]}$ (distinct BN ma-

trices) define a decomposition of Q. Let $\{y_j\}_{j\in[L]}$ (positive real numbers) and $\{B_j\}_{j\in[L]}$ (distinct BN matrices) define a decomposition of R. Define $\tilde{A} := \{A_1, A_2, \ldots, A_K\}$ and $\tilde{B} := \{B_1, B_2, \ldots, B_L\}$. Define two functions $f, g : \tilde{A} \cup \tilde{B} \to \mathbb{R}_{\geq 0}$ as follows:

- For all $A \in \tilde{A} \cup \tilde{B}$, if $A = A_k$ for some A_k in $\tilde{A}$, then $f(A) = x_k$; otherwise, $f(A) = 0$.
- For all $A \in \tilde{A} \cup \tilde{B}$, if $A = B_l$ for some B_l in $\tilde{B}$, then $g(A) = y_l$; otherwise $g(A) = 0$.

Then, $\{f(A) + g(A)\}_{A\in\tilde{A}\cup\tilde{B}}$ and $\tilde{A} \cup \tilde{B}$ define a decomposition of the $(q+r)$-TPM $Q+R$, because for all $A \in \tilde{A} \cup \tilde{B}$, $f(A) + g(A) > 0$ and $\sum_{A\in\tilde{A}\cup\tilde{B}}(f(A) + g(A))A = Q + R$. $\{f(A) + g(A)\}_{A\in\tilde{A}\cup\tilde{B}}$ and $\tilde{A} \cup \tilde{B}$ is said to be the decomposition of $Q + R$ formed by merging $(\{x_i\}_{i\in[K]}, \{A_i\}_{i\in[K]})$ (a decomposition of Q) and $(\{y_j\}_{j\in[L]}, \{B_j\}_{j\in[L]})$ (a decomposition of R).

The key idea behind DPre and SDS2G is as follows. Let P be a $2^n \times 2^n$ non-zero integerized p_0-TPM such that $|S^+(P)|$ is large and most of the positive values x in $S^+(P)$ have low column frequencies in P. As remarked above, p_0 is likely to be a large positive integer. Let's assume that this is true. First, we choose a suitable positive integer d. Then, we find $\tilde{Q}$ and $\tilde{R}$ such that $\tilde{Q}$ is a $2^n \times 2^n$ non-zero integerized $\tilde{q}_0$-TPM, $\tilde{R}$ is a $2^n \times 2^n$ non-zero integerized $\tilde{r}_0$-TPM and $P = d\tilde{Q} + \tilde{R}$. Note that $\tilde{q}_0 > 0$ is the sum of entries of any column of $\tilde{Q}$ and $\tilde{r}_0 > 0$ is the sum of entries of any column of $\tilde{R}$. Clearly, $p_0 = d\tilde{q}_0 + \tilde{r}_0$. If d, $\tilde{Q}$, $\tilde{R}$ are suitably chosen, then $\tilde{q}_0$ and $\tilde{r}_0$ would be significantly smaller than p_0. Hence, certain positive entries of $\tilde{Q}$ may be associated with high column frequencies in $\tilde{Q}$, and certain positive entries of $\tilde{R}$ may be associated with high column frequencies in $\tilde{R}$. Then, GER or SER 2 is applied to $\tilde{Q}$ to obtain a decomposition $(\{x_i\}_{i\in[K]}, \{A_i\}_{i\in[K]})$ of $\tilde{Q}$ whose length K may be small as a result. GER or SER 2 is also applied to $\tilde{R}$ to obtain a decomposition $(\{y_j\}_{j\in[L]}, \{B_j\}_{j\in[L]})$ of $\tilde{R}$ whose length L may be small as well. Note that $(\{dx_i\}_{i\in[K]}, \{A_i\}_{i\in[K]})$ is a decomposition of $d\tilde{Q}$. Finally, we merge $(\{dx_i\}_{i\in[K]}, \{A_i\}_{i\in[K]})$ and $(\{y_j\}_{j\in[L]}, \{B_j\}_{j\in[L]})$ to form a decomposition of $P = d\tilde{Q} + \tilde{R}$ with length at most $K + L$. If L and K are both small, then $K + L$ will also be small, which is what we want.

Now, we present the pseudocode of the DPre algorithm.

Algorithm 1 The Division Pre-Processing Algorithm (DPre)

Require: A $2^n \times 2^n$ non-zero integerized p_0-TPM P, and a positive integer d.
Ensure: A $2^n \times 2^n$ integerized $\tilde{q}_0$-TPM $\tilde{Q}$ and a $2^n \times 2^n$ integerized $\tilde{r}_0$-TPM $\tilde{R}$ such that $\tilde{q}_0, \tilde{r}_0 \geq 0$ and $P = d\tilde{Q} + \tilde{R}$.

For all entries p_{ij} of P, find the unique non-negative integers $\tilde{q}_{ij}$ and $\tilde{r}_{ij}$ such that $0 \leq \tilde{r}_{ij} \leq d-1$ and $p_{ij} = d\tilde{q}_{ij} + \tilde{r}_{ij}$. Define the $2^n \times 2^n$ matrices $\tilde{Q} := (\tilde{q}_{ij})$ and $\tilde{R} := (\tilde{r}_{ij})$.
For all $1 \leq j \leq 2^n$, let $\vec{r}_j$ be the j-th column of $\tilde{R}$. For all $1 \leq j \leq 2^n$, set $\tilde{r}_j \leftarrow \vec{1}_{2^n}^{\top} \vec{r}_j$. Set $\tilde{r}_0 \leftarrow \max_{1 \leq j \leq 2^n} \{\tilde{r}_j\}$.
for $j = 1, 2, 3, \ldots, 2^n$ **do**
    Set $i \leftarrow 1$.
    while $\tilde{r}_j < \tilde{r}_0$ **do**
        if $d\tilde{Q}(i,j) < \tilde{r}_0 - \tilde{r}_j$ **then**
            Set $\tilde{R}(i,j) \leftarrow \tilde{R}(i,j) + d\tilde{Q}(i,j)$.
            Set $\tilde{r}_j \leftarrow \tilde{r}_j + d\tilde{Q}(i,j)$.
            Set $\tilde{Q}(i,j) \leftarrow 0$.
        else
            Set $\tilde{R}(i,j) \leftarrow \tilde{R}(i,j) + (\tilde{r}_0 - \tilde{r}_j)$.
            Set $\tilde{Q}(i,j) \leftarrow \tilde{Q}(i,j) - \left(\frac{\tilde{r}_0 - \tilde{r}_j}{d}\right)$.
            Set $\tilde{r}_j \leftarrow \tilde{r}_0$.
        Increment i by 1.
return $\tilde{Q}$, $\tilde{R}$

Remark 2.1 *It is possible that one of the outputs $\tilde{Q}$, $\tilde{R}$ of the DPre algorithm equals the zero matrix.*

Combining the DPre algorithm, SER 2 and GER, we form the Single Division Pre-processed SER2-GER algorithm (SDS2G) for tackling the construction problem of PBNs. Our numerical experiments (Section 3) demonstrate that SDS2G outperforms existing state-of-the-art PBN construction algorithms.

Algorithm 2 The Single Division Pre-Processed SER2-GER Algorithm (SDS2G)

Require: A $2^n \times 2^n$ non-zero integerized p_0-TPM P.
Two positive integers $d_{\text{low}} \leq d_{\text{high}}$.
A positive real number $z > 1$ (to be used as the score parameter of GER).
Ensure: A list of positive real numbers $\mathbf{x}$ and a list of distinct BN matrices $\mathbf{A}$ such that $(\mathbf{x}, \mathbf{A})$ defines a decomposition of P.

Set $K \leftarrow +\infty$. Initialize the variables $\mathbf{A}, \mathbf{x}$ as empty lists.
for $d = d_{\text{low}}, d_{\text{low}}+1, \ldots, d_{\text{high}}$ **do**
  Apply the DPre algortihm to P and d to obtain two matrices $\tilde{Q}$, $\tilde{R}$ such that $P = d\tilde{Q} + \tilde{R}$.
  if $\tilde{Q} \neq \mathbf{O}_{2^n \times 2^n}$ and $\tilde{R} \neq \mathbf{O}_{2^n \times 2^n}$ **then**
    Execute SER 2 on $\tilde{Q}$ to obtain a decomposition $(\{x_i^{(1)}\}_{i\in[K_1]}, \{A_i^{(1)}\}_{i\in[K_1]})$ of $\tilde{Q}$.
    Execute GER on $\tilde{Q}$ with z as the score parameter to obtain a decomposition $(\{x_i^{(2)}\}_{i\in[K_2]}, \{A_i^{(2)}\}_{i\in[K_2]})$ of $\tilde{Q}$.
    Execute SER 2 on $\tilde{R}$ to obtain a decomposition $(\{y_i^{(1)}\}_{i\in[L_1]}, \{B_i^{(1)}\}_{i\in[L_1]})$ of $\tilde{R}$.
    Execute GER on $\tilde{R}$ with z as the score parameter to obtain a decomposition $(\{y_i^{(2)}\}_{i\in[L_2]}, \{B_i^{(2)}\}_{i\in[L_2]})$ of $\tilde{R}$.
    for all $(j,k) \in [2] \times [2]$ **do**
      Merge $(\{dx_i^{(j)}\}_{i\in[K_j]}, \{A_i^{(j)}\}_{i\in[K_j]})$ and $(\{y_i^{(k)}\}_{i\in[L_k]}, \{B_i^{(k)}\}_{i\in[L_k]})$ to form a decomposition $(\mathbf{x}_{(j,k)}, \mathbf{A}_{(j,k)})$ of P, where $\mathbf{x}_{(j,k)}$ is a list of positive real numbers and $\mathbf{A}_{(j,k)}$ is a list of distinct BN matrices.
      if the length of $(\mathbf{x}_{(j,k)}, \mathbf{A}_{(j,k)})$ is smaller than K **then**
        Set K to be the length of $(\mathbf{x}_{(j,k)}, \mathbf{A}_{(j,k)})$. Set $\mathbf{x} \leftarrow \mathbf{x}_{(j,k)}$, $\mathbf{A} \leftarrow \mathbf{A}_{(j,k)}$.
return $\mathbf{x}$, $\mathbf{A}$

3. Computational Experiments

To assess the performance of SDS2G, we conducted computational experiments and compared SDS2G with three other PBN construction algorithms, namely SER 2 [14], GER [15] and SER 1 [14]. The experiments were done with JupyterLab. Our codes can be found at https://github.com/christopherfok2015/DPre-SDS2G.git

We tested the four PBN construction algorithms with four matrices: P_1 (an integerized 10000-TPM), P_2 (an integerized 23320-TPM), Q_1 (an integerized 20000-TPM), Q_2 (an integerized 86605-TPM). These matrices are defined below.

$$P_1 = \begin{pmatrix} 1599 & 2501 & 1271 & 1964 & 2501 & 0 & 0 & 242 \\ 184 & 1618 & 1906 & 0 & 0 & 1906 & 1308 & 2501 \\ 1308 & 0 & 224 & 198 & 173 & 2494 & 2469 & 1895 \\ 0 & 1308 & 0 & 1599 & 1906 & 1271 & 2494 & 2520 \\ 0 & 198 & 2494 & 2480 & 1290 & 1567 & 0 & 1578 \\ 2494 & 2480 & 0 & 0 & 1592 & 2538 & 1927 & 1264 \\ 1895 & 0 & 2538 & 2469 & 2538 & 224 & 1578 & 0 \\ 2520 & 1895 & 1567 & 1290 & 0 & 0 & 224 & 0 \end{pmatrix}, \quad P_2 = \begin{pmatrix} 2154 & 2220 & 0 & 3741 & 3214 & 4677 & 2208 & 4640 \\ 3208 & 3183 & 3209 & 3440 & 577 & 8883 & 8826 & 351 \\ 577 & 9424 & 8908 & 2222 & 8875 & 3225 & 3208 & 8833 \\ 30 & 3420 & 400 & 400 & 19 & 3402 & 3420 & 2192 \\ 8859 & 0 & 584 & 0 & 2177 & 369 & 358 & 3225 \\ 4652 & 389 & 2177 & 4684 & 3397 & 2154 & 572 & 609 \\ 3451 & 4684 & 3397 & 0 & 4678 & 610 & 4678 & 50 \\ 389 & 0 & 4645 & 8833 & 383 & 0 & 50 & 3420 \end{pmatrix}.$$

$$Q_1 = \begin{pmatrix}
2810 & 0 & 2080 & 2676 & 782 & 0 & 1840 & 1832 & 1981 & 685 & 1164 & 0 & 2806 & 1824 & 0 & 331 \\
2660 & 0 & 1172 & 2030 & 0 & 1175 & 1219 & 2886 & 2061 & 0 & 2665 & 1607 & 1255 & 452 & 999 & 0 \\
0 & 2080 & 1205 & 0 & 2825 & 1172 & 1007 & 2649 & 999 & 2597 & 1607 & 0 & 1180 & 0 & 1820 & 2000 \\
0 & 2690 & 0 & 2597 & 1156 & 1112 & 2495 & 1205 & 0 & 0 & 1236 & 661 & 2762 & 1175 & 2495 & 1989 \\
1277 & 0 & 350 & 1915 & 0 & 339 & 1521 & 0 & 0 & 1172 & 1832 & 2080 & 1989 & 0 & 2044 & 0 \\
2511 & 1879 & 0 & 0 & 1236 & 0 & 669 & 0 & 1879 & 2721 & 2841 & 355 & 0 & 1490 & 1502 & 1219 \\
1071 & 2500 & 2810 & 0 & 2030 & 724 & 0 & 452 & 685 & 2810 & 2080 & 2704 & 1505 & 710 & 0 & 1277 \\
2030 & 1175 & 2597 & 1160 & 1820 & 1521 & 1255 & 1985 & 1191 & 0 & 710 & 1832 & 0 & 0 & 331 & 0 \\
347 & 1112 & 696 & 724 & 2657 & 1915 & 2855 & 1505 & 2480 & 1521 & 1010 & 0 & 0 & 2905 & 2676 & 1071 \\
1981 & 0 & 991 & 331 & 0 & 2556 & 2645 & 2016 & 1505 & 1989 & 0 & 1175 & 2030 & 1981 & 1180 & 2676 \\
1494 & 1236 & 2044 & 2830 & 339 & 2830 & 1981 & 760 & 2657 & 1040 & 2480 & 2061 & 2539 & 2657 & 741 & 1915 \\
724 & 2822 & 2649 & 999 & 1521 & 0 & 411 & 0 & 0 & 1835 & 0 & 1040 & 0 & 2500 & 0 & 0 \\
1255 & 661 & 0 & 0 & 0 & 2641 & 0 & 1156 & 452 & 1219 & 331 & 1160 & 1026 & 1191 & 1255 & 1502 \\
0 & 1521 & 1566 & 1997 & 1015 & 1985 & 0 & 2500 & 2905 & 1981 & 2044 & 2511 & 335 & 2061 & 2927 & 685 \\
0 & 339 & 1840 & 1175 & 2539 & 2030 & 2102 & 0 & 0 & 0 & 0 & 2814 & 1832 & 0 & 2030 & 2810 \\
1840 & 1985 & 0 & 1566 & 2080 & 0 & 0 & 1054 & 1205 & 430 & 0 & 0 & 741 & 1054 & 0 & 2525
\end{pmatrix}.$$

$$Q_2 = \begin{pmatrix}
0 & 5750 & 13587 & 3407 & 13616 & 18379 & 0 & 12038 & 13574 & 13566 & 3217 & 6668 & 0 & 18387 & 13577 & 4819 \\
4813 & 9470 & 2153 & 3260 & 1660 & 13992 & 3352 & 18385 & 2137 & 829 & 3751 & 1617 & 7117 & 806 & 3325 & 143 \\
143 & 4590 & 3334 & 3769 & 9511 & 15837 & 18533 & 2269 & 2292 & 11971 & 13597 & 2003 & 0 & 3733 & 6668 & 0 \\
15173 & 4851 & 825 & 9453 & 4833 & 2311 & 4838 & 6683 & 2279 & 3734 & 3343 & 2271 & 9601 & 4789 & 2262 & 6658 \\
844 & 0 & 2279 & 14398 & 2272 & 4797 & 4555 & 2271 & 15305 & 2059 & 4788 & 2128 & 13593 & 2272 & 2004 & 2178 \\
3792 & 11989 & 11978 & 154 & 2270 & 9461 & 8877 & 158 & 4799 & 6658 & 6695 & 2325 & 2055 & 1646 & 12038 & 3788 \\
2282 & 13567 & 6695 & 0 & 816 & 0 & 3193 & 1607 & 18422 & 4856 & 18362 & 3755 & 4852 & 2149 & 3755 & 2306 \\
3334 & 197 & 1996 & 2012 & 12003 & 134 & 0 & 3213 & 3213 & 2288 & 2045 & 18387 & 3263 & 11995 & 9453 & 2028 \\
13574 & 3202 & 1664 & 14256 & 1995 & 3370 & 0 & 843 & 1673 & 158 & 1605 & 9468 & 13576 & 2288 & 4821 & 11995 \\
1627 & 20507 & 18404 & 18381 & 3326 & 1664 & 17301 & 3725 & 9476 & 1646 & 9453 & 3201 & 2139 & 3237 & 3237 & 3352 \\
6683 & 0 & 3256 & 3907 & 3213 & 3732 & 9488 & 13630 & 178 & 3203 & 11981 & 11971 & 0 & 201 & 2282 & 0 \\
11731 & 3396 & 2294 & 0 & 18381 & 862 & 816 & 2045 & 7512 & 2279 & 2294 & 3336 & 6651 & 13630 & 862 & 4017 \\
2146 & 1629 & 9474 & 0 & 6681 & 3213 & 12043 & 4815 & 2020 & 18399 & 799 & 160 & 3067 & 2005 & 1646 & 11040 \\
2045 & 7457 & 4799 & 6661 & 143 & 0 & 2005 & 9461 & 0 & 9476 & 2325 & 4856 & 0 & 3356 & 18381 & 2272 \\
18418 & 0 & 143 & 6947 & 2153 & 2192 & 0 & 2128 & 0 & 2149 & 2196 & 848 & 2306 & 9443 & 141 & 13587 \\
0 & 0 & 3724 & 0 & 3732 & 6661 & 1604 & 3334 & 3725 & 3334 & 154 & 13611 & 18385 & 6668 & 2153 & 18422
\end{pmatrix}.$$

Concerning how the parameters of SDS2G and GER were set in our numerical experiments, we set their parameters in the following way:

(SDS2G) For all four matrices, we set d_{low}, d_{high}, z to be 30, 200, 10 respectively.

(GER) For each of the four matrices, we tried executing GER with the score parameter $z = 2, 3, 4, \ldots, 20$. Then, we chose the decomposition with the shortest length out of the 19 executions.

Table 1 shows the lengths of the decompositions of P_1, P_2, Q_1, Q_2 output by SDS2G, SER 2, GER, SER 1.

Table 1. Results of executing the four PBN construction algorithms on P_1, P_2, Q_1, Q_2. The numbers in the table are the lengths of the decompositions of P_1, P_2, Q_1, Q_2 output by the four algorithms.

	P_1	P_2	Q_1	Q_2
SDS2G	12	15	24	34
GER	20	30	60	83
SER 1	41	51	119	164
SER 2	16	22	38	59

As shown in Table 1, for each of the four integerized p_0-TPMs, SDS2G outputs a decomposition with the shortest length. We conclude that among the four PBN construction algorithms, SDS2G performs the best.

Next, we measure the execution time of the four algorithms for P_1, P_2, Q_1, Q_2. This information is shown in Table 2.

Table 2. The execution time (in seconds) of SDS2G, SER 2, GER, SER 1 for P_1, P_2, Q_1, Q_2

	P_1	P_2	Q_1	Q_2
SDS2G	2.977563	4.361493	10.595228	15.332155
GER (max.)	0.051339	0.270271	0.356680	1.838730
GER (average)	0.031439	0.183380	0.242593	1.407377
GER (min.)	0.024683	0.151033	0.199324	1.178561
SER 1	0.002299	0.003136	0.018212	0.016908
SER 2	0.001001	0.002047	0.002020	0.002406

Note that for each of the four integerized p_0-TPMs, GER was executed for 19 times with $z = 2, 3, \ldots, 20$. We remark that in Table 2, for each integerized p_0-TPM, we have shown the maximum, the average and the minimum of the execution time of the corresponding 19 executions.

As shown in Table 2, SER 1 and SER 2 are the fastest PBN construction algorithms and they took milliseconds to run for P_1, P_2, Q_1, Q_2. GER is also fast and took less than 2 seconds to run for the four matrices. SDS2G took seconds to execute and is slower than GER. This can be explained by the fact that during the execution of SDS2G, SER 2 and GER are executed multiple times. Although SDS2G is the slowest among the four PBN construction algorithms, its execution durations for P_1, P_2, Q_1, Q_2 are still short. Therefore, we conclude that SDS2G is a fast algorithm and it is worth spending extra time to get a significant reduction of the length of decompositions.

4. A New Lower Bound Theorem

Let P be any $2^n \times 2^n$ non-zero p_0-TPM. Let $\{x_i\}_{i\in[K]}$ (positive real numbers) and $\{A_i\}_{i\in[K]}$ (distinct BN matrices) define an arbitrary decomposition of P. The lower bound problem related to PBN construction asks this question: can we determine some strong lower bounds for the value K from P? We have derived a new lower bound (Theorem 4.3). Before we prove this main result, we need to state and prove two lemmas.

Lemma 4.1 *Let K, d be natural numbers satisfying $K \geq d > 0$. For any partition $\{Y_1, Y_2, \ldots, Y_d\}$ of $[K]$, $|\{l \in [d] : |Y_l| = 1\}| \geq 2d - K$.*

Proof:

$$\begin{aligned} K = \sum_{l=1}^{d} |Y_l| &= \sum_{\substack{l\in[d] \text{ s.t.} \\ |Y_l|=1}} |Y_l| + \sum_{\substack{m\in[d] \text{ s.t.} \\ |Y_m|\geq 2}} |Y_m| \\ &\geq |\{l \in [d] : |Y_l| = 1\}| + 2|\{l \in [d] : |Y_l| \geq 2\}| \\ &= |\{l \in [d] : |Y_l| = 1\}| + 2(d - |\{l \in [d] : |Y_l| = 1\}|) \\ &= 2d - |\{l \in [d] : |Y_l| = 1\}|. \end{aligned}$$

Therefore, $|\{l \in [d] : |Y_l| = 1\}| \geq 2d - K$. □

Lemma 4.2 *Let P be a $2^n \times 2^n$ TPM. Let $\{x_i\}_{i\in[K]}$ (positive real numbers) and $\{A_i\}_{i\in[K]}$ (distinct BN matrices) define an arbitrary decomposition of P. For any $j \in [2^n]$, if $d(j) := \|P(:,j)\|_0$, then there exists a set $S(j) \subseteq [K]$ with cardinality $\geq \max(0, 2d(j) - K)$ such that for all $m \in S(j)$, x_m is a positive entry of $P(:,j)$.*

Proof: There are two possible cases: $d(j) \leq \frac{K}{2}$ and $d(j) > \frac{K}{2}$.

Case 1: $d(j) \leq \frac{K}{2}$. The lemma trivially holds because we can take $S(j) := \varnothing$.

Case 2: $d(j) > \frac{K}{2}$. By Proposition 4.1 of [16], $K \geq d(j)$. Let $P(i_1^j, j)$, $P(i_2^j, j)$, ..., $P(i_{d(j)}^j, j)$ be the positive entries of column j of P. By Lemma 4.3 of [16], there exists a partition $\{X_1^j, X_2^j, \ldots, X_{d(j)}^j\}$ of $[K]$ such that for all $l \in [d(j)]$, $\sum_{m\in X_l^j} x_m = P(i_l^j, j)$. By Lemma 4.1, $|\{l \in [d(j)] : |X_l^j| = 1\}| \geq 2d(j) - K > 0$. Fix arbitrary $l \in [d(j)]$ such that $|X_l^j| = 1$. Write X_l^j as $\{a(l)\}$. Then, $P(i_l^j, j) = \sum_{m\in X_l^j} x_m = x_{a(l)}$. Hence, $x_{a(l)}$ is a positive entry of $P(:,j)$. Define $S(j)$ to be the union of all X_l^j's such that $|X_l^j| = 1$. Then, $|S(j)| \geq 2d(j) - K = \max(0, 2d(j) - K)$ and for all $m \in S(j)$, x_m is a positive entry of $P(:,j)$. □

We are now ready to prove the new lower bound.

Theorem 4.3 *Let P be a $2^n \times 2^n$ TPM. For all $j \in [2^n]$, let $d(j) := \|P(:,j)\|_0$ and C_j be the set of positive entries of $P(:,j)$. Let c be a positive integer and $j_1, j_2, \ldots, j_c$ be distinct integers in $[2^n]$ such that $C_{j_1}, C_{j_2}, \ldots, C_{j_c}$ are pairwise disjoint. Then, any decomposition of P has length not less than $\left(\frac{2}{c+1}\right)\sum_{l=1}^{c} d(j_l)$.*

Proof: There are two possible cases: $c = 1$ and $c \geq 2$.

Case 1: $c = 1$. By considering Proposition 4.1 of [16], we can see that the result trivially holds.

Case 2: $c \geq 2$. Let $x_1, x_2, \ldots, x_K$ (positive real numbers) and $A_1, A_2, \ldots, A_K$ (distinct BN matrices) be an arbitrary decomposition of P. By Lemma 4.2, for each $m \in [c]$, there exists $S(j_m) \subseteq [K]$ with cardinality $\geq \max(0, 2d(j_m) - K)$ such that for all $l \in S(j_m)$, x_l is a positive entry of $P(:, j_m)$.

Note that for all $a \neq b \in [c]$, $S(j_a)$ and $S(j_b)$ are disjoint. To see this, suppose that this is not true. Then there exists $l \in [K]$, $a \neq b \in [c]$ such that $l \in S(j_a)$ and $l \in S(j_b)$. Hence, x_l is a positive entry of $P(:, j_a)$ and $P(:, j_b)$. But this contradicts with the fact that C_{j_a} and C_{j_b} are disjoint. Because $S(j_1), S(j_2), \ldots, S(j_c)$ are subsets of $[K]$, we have

$$K \geq \left|\bigcup_{m=1}^{c} S(j_m)\right| = \sum_{m=1}^{c} |S(j_m)|$$

$$\geq \sum_{m=1}^{c} \max(0, 2d(j_m) - K) \geq \sum_{m=1}^{c} (2d(j_m) - K) = \left(2\sum_{m=1}^{c} d(j_m)\right) - cK.$$

Rearranging, we get $K \geq \left(\frac{2}{c+1}\right)\sum_{m=1}^{c} d(j_m)$. □

Remark 4.4 *Let Q be any non-zero $2^n \times 2^n$ q-TPM and r be any positive real number. As explained in Section 1.2, the task of finding decompositions of Q with small lengths*

is equivalent to the task of finding decompositions of rQ with small lengths. Therefore, Theorem 4.3 is also true even when P is a non-zero $2^n \times 2^n$ p_0-TPM.

Remark 4.5 *By imposing the restriction $c = 2$ and $d(j_1) = d(j_2)$ in Theorem 4.3, we can recover Theorem 4.8 of [16]. In other words, Theorem 4.3 generalizes Theorem 4.8 of [16].*

Let's demonstrate how Theorem 4.3 can be used.

Note that any two of $P_1(:,3)$, $P_1(:,4)$, $P_1(:,8)$ have no positive entries in common and $\|P_1(:,3)\|_0 = \|P_1(:,4)\|_0 = \|P_1(:,8)\|_0 = 6$. By the theorem, the length of any decomposition of P_1 is at least $\frac{2}{3+1}(6+6+6) = 9$.

On the other hand, note that any two of $Q_2(:,2)$, $Q_2(:,6)$, $Q_2(:,7)$, $Q_2(:,10)$, $Q_2(:,11)$, $Q_2(:,13)$ have no common positive entries. Moreover, $\|Q_2(:,2)\|_0 = 12$, $\|Q_2(:,6)\|_0 = 14$, $\|Q_2(:,7)\|_0 = 12$, $\|Q_2(:,10)\|_0 = 16$, $\|Q_2(:,11)\|_0 = 16$, $\|Q_2(:,13)\|_0 = 12$. Because $\frac{2}{6+1}(12+14+12+16+16+12) = 23.42\ldots$, the length of any decomposition of Q_2 is at least 24.

Similarly, Theorem 4.3 can be applied to $P_2(:,2)$, $P_2(:,3)$, $P_2(:,6)$ to deduce that the length of any decomposition of P_2 is at least 10. Also, by applying the theorem to $Q_1(:,4)$, $Q_1(:,7)$, $Q_1(:,8)$, we can deduce that the length of any decomposition of Q_1 is at least 18.

5. Conclusion

This paper focuses on the construction problem of PBNs. We propose the Division Pre-processing algorithm (DPre), which breaks a non-negative integer matrix P with constant positive column sum into two non-negative integer matrices $\tilde{Q}$ and $\tilde{R}$ such that $P = d\tilde{Q} + \tilde{R}$ for some chosen positive integer d. Then, by combining DPre and two existing PBN construction algorithms, we form the Single Division Pre-processed SER2GER algorithm (SDS2G) for tackling the construction problem of PBNs. Our computational experiments reveal that SDS2G not only is fast but also performs significantly better than other existing PBN construction algorithms. Lastly, we derive a new lower bound related to PBN construction, and this new lower bound generalizes a previous lower bound that we derived.

There are three possible future directions of research related to this paper. First, new lower bounds related to PBN construction can be derived. Second, new algorithms for PBN construction can be formulated. Third, new pre-processing algorithms for breaking positive multiples of transition probability matrices into multiple non-negative matrices can be designed.

Acknowledgments

This work was supported by the Hong Kong Research Grants Council under Grant Numbers 17301519 and 17309522.

References

[1] Kauffman SA. Metabolic stability and epigenesis in randomly constructed genetic nets. J Theor Biol. 1969;22(3):437-67. PubMed PMID: 84204953; 5803332.

[2] Kauffman S. Homeostasis and Differentiation in Random Genetic Control Networks. Nature (London). 1969;224(5215):177-8. doi: 10.1038/224177a0.

[3] Kauffman SA. The origins of order: self organization and selection in evolution. New York: Oxford University Press; 1993.

[4] Bornholdt S. Boolean network models of cellular regulation: prospects and limitations. Journal of the Royal Society interface. 2008;5(Suppl 1):S85-S94. doi: 10.1098/rsif.2008.0132.focus.

[5] Li F, Long T, Lu Y, Ouyang Q, Tang C. yeast cell-cycle network is robustly designed. Proceedings of the National Academy of Sciences - PNAS. 2004;101(14):4781-6. doi: 10.1073/pnas.0305937101.

[6] Saez-Rodriguez J, Simeoni L, Lindquist JA, Hemenway R, Bommhardt U, Arndt B, et al. A logical model provides insights into T cell receptor signaling. PLoS Comp Biol. 2007;3(8):1580-90. doi: 10.1371/journal.pcbi.0030163.

[7] Schlatter R, Schmich K, Avalos Vizcarra I, Scheurich P, Sauter T, Borner C, et al. ON/OFF and Beyond - A Boolean Model of Apoptosis. PLoS Comp Biol. 2009;5(12). doi: 10.1371/journal.pcbi.1000595.

[8] Shmulevich I, Dougherty ER, Zhang W. From Boolean to probabilistic Boolean networks as models of genetic regulatory networks. Proceedings of the IEEE. 2002;90(11):1778-92. doi: 10.1109/JPROC.2002.804686.

[9] Trairatphisan P, Mizera A, Pang J, Tantar AA, Schneider J, Sauter T. Recent development and biomedical applications of probabilistic Boolean networks. Cell communication and signaling. 2013;11(1):46-. doi: 10.1186/1478-811X-11-46.

[10] Ma Z, Wang ZJ, McKeown MJ. Probabilistic Boolean Network Analysis of Brain Connectivity in Parkinson's Disease. IEEE journal of selected topics in signal processing. 2008;2(6):975-85. doi: 10.1109/JSTSP.2008.2007816.

[11] Gu J-W, Ching W-K, Siu T-K, Zheng H. On modeling credit defaults: A probabilistic Boolean network approach. Risk and decision analysis. 2013;4(2):119-29. doi: 10.3233/RDA-2012-0086.

[12] Rivera Torres PJ, Serrano Mercado EI, Anido Rifon L. Probabilistic Boolean network modeling and model checking as an approach for DFMEA for manufacturing systems. J Intell Manuf. 2018;29(6):1393-413. doi: 10.1007/s10845-015-1183-9.

[13] Shmulevich I, Dougherty ER, Kim S, Zhang W. Probabilistic Boolean networks: a rule-based uncertainty model for gene regulatory networks. Bioinformatics. 2002;18(2):261-74. doi: 10.1093/bioinformatics/18.2.261.

[14] Ching WK, Chen X, Tsing NK. Generating probabilistic Boolean networks from a prescribed transition probability matrix. IET systems biology. 2009;3(6):453-64. doi: 10.1049/iet-syb.2008.0173.

[15] Fok CH, Ching WK, Wong CW. The Construction of Sparse Probabilistic Boolean Networks: A Discrete Perspective. 2023 IEEE International Conference on Bioinformatics and Biomedicine (BIBM); 2023 5-8 Dec. 2023.

[16] Fok CH, Wong C-W, Ching W-K. A Discrete Perspective Towards the Construction of Sparse Probabilistic Boolean Networks. 2024. doi: 10.48550/arxiv.2407.11543.

Part II

Data Mining

Fuzzy Systems and Data Mining X
A.J. Tallón-Ballesteros (Ed.)

doi:10.3233/FAIA241412

Classification Using U-Net CN on Multi-Resolution CT Scan Image

Sugiyarto Surono [a,1], Muhammad Rivaldi [a] and Nursyiva Irsalinda[a]
[a] *Department of Mathematics, FAST UAD Yogyakarta Indonesia*
ORCiD ID: Sugiyarto Surono https://orcid.org/0000-0001-6210-7258
Nursyiva Irsalinda https://orcid.org/0000-0001-7622-5060

Abstract. Image processing has become a central topic in the era of big data, particularly within computer vision, due to the growing volume and diverse resolutions of images. Low-resolution images introduce uncertainty, underscoring the need for high-performance classification methods. Convolutional Neural Networks (CNN), especially the U-Net architecture, are widely applied for pixel-level segmentation due to their encoder-decoder structure. This study applied U-Net on a CT scan image dataset to segment lung images, followed by a CNN classifier to classify lung cancer stages (I, II, IIIa, IIIb). The U-Net model outperformed standard CNNs, achieving 99% in accuracy, precision, sensitivity, and F1 score, compared to the conventional CNN's 97%, 95%, 97%, and 96%, respectively.

Keywords. U-Net; Image Segmentation; CNN; Image Classification; Multi-resolution Image Processing

1. Introduction

Technological developments have increased the amount of data in the form of numerical data, sound data, video data and data in the form of images. The image data is generated by various tools such as cameras with different specifications. Not all image capture tools have good specifications resulting in poor-quality images [1]. These problems also tend to increase the amount of image data, which is more diverse and cause the classification method to produce low accuracy values [2]. This provides a great opportunity for researchers to explore research related to image data quality improvement techniques which implies a quality classification model that is needed to achieve high performance. As stated in [3], the multi-resolution image classification model tends to enhance the effectiveness of the image classification process when image data, obtained from various optical sensors with differing resolutions, increases [3]. This makes the model more flexible since image classification applies to images with different resolutions.

Computer Vision frequently plays a central role in image classification, with Deep Learning as a commonly utilized approach in its development [4]. According to [5], Deep Learning methods have achieved success across numerous fields. Deep Learning, or Deep Neural Networks (DNNs), refers to intricate, multi-layered Artificial Neural Networks (ANNs) and encompasses commonly used models like Convolutional Neural Networks (CNNs), which are among the most popular techniques in the field of Deep

[1] Corresponding Author, Sugiyarto Surono, FAST UAD Yogyakarta Indonesia; Email: sugiyarto@math.uad.ac.id

Neural Networks [6]. Convolutional Neural Networks (CNNs) are widely applied in image processing and computer vision tasks because they can automatically extract hierarchical features from image data, minimize computational complexity by sharing parameters, and deliver exceptional performance in tasks like image classification, object detection, and segmentation [7]. CNN has shown significant advancements, particularly in tasks related to image processing and computer vision [8], making it well-suited for the rapid developments in Artificial Intelligence technology, which has recently gained popularity, especially in image processing applications. Image processing offers numerous advantages, including its use in classification, clustering, segmentation, and other. The technique for segmenting images based on information about each image pixel used to predict the category of each predicted image pixel called Semantic segmentation.

Semantic segmentation provides pixel-level categorical information, which has proven valuable in numerous real-world applications, including self-driving cars, pedestrian detection, disability identification, therapy planning, and computer-assisted diagnosis [9]. According to [10], it assigns a label to each pixel in an image. This pixel-level semantic information data enables intelligent systems to comprehend spatial positions and make critical decisions. Deep CNNs have been extensively applied in the medical field to address challenges in biomedical segmentation [11]. Recently, CNNs, particularly in the context of segmentation models [12], have seen significant advancements, with U-Net CN being one notable architecture [13]. U-Net, introduced in 2015, utilizes an encoder-decoder architecture that employs skip connections to merge high-level semantic features from the low-level decoders in the encoder [12]

Biomedical image processing is a rapidly developing field that encompasses the acquisition of biomedical signals, the generation of images processing and display for medical diagnosis are derived from these signals. Clinical imaging systems combine hardware and software, with the growing number of medical imaging sensors attracting significant attention [14]. Notably, image classification techniques are commonly used in medical imaging to analyze and interpret medical images [15]. As highlighted in [16], lung cancer is the most lethal type of cancer, with non-small cell lung cancer (NSCLC) often diagnosed at advanced stages. In 2018, lung cancer accounted for 18.4% of all cancer-related deaths worldwide [17]. Hence, there is a critical need for methods to detect NSCLC early, enabling more effective treatment.

An essential process in training machine learning models is tunneling. This process allows the model to achieve good results through parameter selection or hyperparameters [18], [19]. In previous research, the CNN model applied ADAM optimization to training the model. The result of selecting the right hyperparameter increases the speed of training the model [20].

This study explores the use of the CN U-Net classification method for multi-resolution CT scan images of lung cancer. Building on the work in [21], which suggested using multi-resolution image data for image processing, this approach focuses on multi-resolution image classification. The first part of the study discusses lung image segmentation using the U-Net architecture. Next, the application of the CNN classification method for determining the stages of non-small cell lung cancer (NSCLC) is presented.

2. Dataset

The data is sourced from NSCLC-Radiomics, accessible at https://wiki.cancerimagingarchive.net/display/Public/NSCLC-Radiomics. The data used is licensed under CC BY 3.0 and publicly accessible. A sample image from the NSCLC-Radiomics dataset containing CT scan image data, lung mask images, and metadata from patients with Non-Small Cell Lung Cancer (NSCLC) is shown in Figure 1. Furthermore, the NSCLC-Radiomics data were obtained from 421 non-small cell lung cancer (NSCLC) patients with 4 grades of disease. The image data were of the Dicom data type, and approximately 20 lung CT scan images and 1 lung mask image were used for each patient. Next, the data were then tested using the CN U-Net classification method. The data contains 1773 images with 338 class I training data, 480 class II, 436 class IIIa, and 469 class IIIb. In comparison, the 1:9 test data has 197 images with 91 class I data, 29 class II, Class IIIa 77, and IIIb 120. The data contained low-severity Stage I Cancer, moderate-severity Stage II Cancer, medium-severity Stage IIIa Cancer, and high-severity Stage IIIb Cancer.

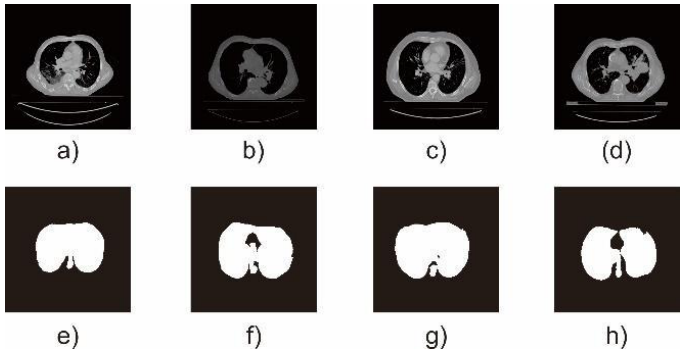

Figure 1. CT scan and mask preview. a) - d) is the CT scan images of stage I, II, IIIa, and IIIb respectively of NSCLC. e) – h) is the lung masks for image a), b), c), and d) respectively.

3. Method

This section explains how the dataset passes through the data preparation stage before being processed by the U-Net Network. The lungs in the image dataset were segmented using the U-Net network and later cropped in the lung area. The segmentation results were then classified with CNN.

3.1. Data Preparation

Define Before the segmentation stage, the data were prepared to ensure that the input could also be used in the network. The first step was to resize the resolution of the entire CT scan and mask the images to ensure they were uniform. The second step was to normalize the data using the min-max scaler.

- Resize Data

  Multi-resolution data has been resized to a uniform resolution of 256x256. This allows the data to enter the U-Net network for segmentation.

The min-max scaler is a normalization method used to transform data values into a range of probabilities, typically from 0 to 1, based on the minimum and maximum values of the data [22]. This technique is represented by Equation 1.

$$x_{scaled} = \frac{x_i - x_{min}}{x_{max} - x_{min}}, \quad (1)$$

3.2. U-Net Segmentation

As deep neural networks evolve, the semantic segmentation model's performance improves. This has led to several developments to overcome limitations in this area [23]. According to [24], U-Net is a semantic segmentation network architecture built on fully convolutional networks, consisting of two main layers: the encoder and the decoder. In this study, U-Net architecture was applied to data that underwent the preparation stage, with its structure illustrated in Figure 2 and detailed in Tables 1 and 2.

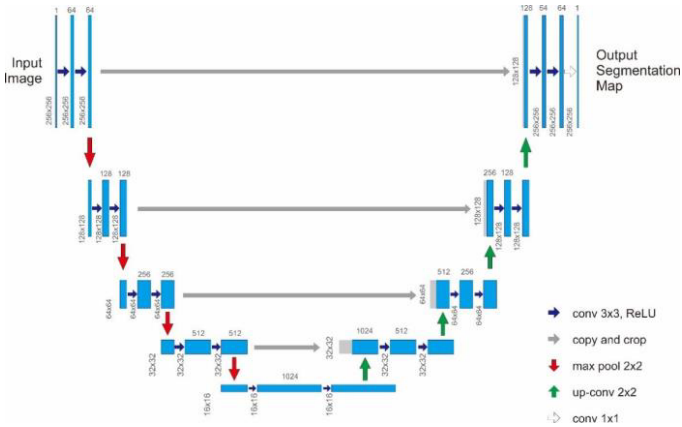

Figure 2. U-Net architecture for image segmentation..

3.3. CNN Classification

Once the image data was segmented and cropped, it was subjected to a classification process using CNN, a technique that has seen significant growth in the field of computer vision. As noted in [25], CNN consists of several layers of neural network connections that require minimal systematic processing. Due to its crucial role, CNN has been widely applied in various image processing tasks, including image recognition, segmentation, and object detection [26].

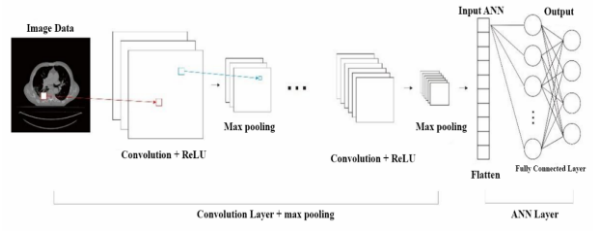

Figure 3. CNN architecture for image Classification.

4. Discussion And Experimental Result

4.1. Experimental Setup

The proposed method was implemented using Python in a Jupyter Notebook environment on a computer with a 2-core Intel(R) Xeon(R) CPU running at 2.20GHz and 32GB of RAM.

4.2. Training Process

Image segmentation and classification task, respectively. In the 20 epochs' U-Net training stage, the CT scan multi-resolution image data were used as the input data, while the mask image was utilized as the label for the prediction. Furthermore, the input image was cropped based on the appropriate area on the mask image. Meanwhile, in the CNN testing stage with 4 epochs, the image data was trimmed, and the predicted mask generated on the U-Net network was utilized as input and output in the form of 4 classes, namely stages I, II, IIIa, and IIIb. This model is trained with Adam optimization, setting hyperparameter bath size = 16 and learning rate = 0.001.

4.3. Result

The results demonstrate the performance of the U-Net CN model in classifying image data and its comparison with the CNN model used for classifying lung cancer stages. In addition to this comparison, the U-Net segmentation model was assessed by evaluating how effectively the multi-resolution data was resized to 256×256. The evaluation was based on the loss value, along with metrics such as accuracy, precision, recall, and F1 score. The computational time was also measured to assess the performance of the proposed classification model. A confusion matrix was employed to determine the accuracy, precision, recall, and F1 score values, providing insights into the model's prediction performance. Table 1 and Figure 4 illustrate the loss value changes for each epoch during the application of the segmentation model, showing both validation and training loss over 20 epochs.

TABLE 1 SEGMENTATION MODEL PERFORMANCES

Epoch	Dice Loss	Dice Coefficient	Time (seconds)
1	0.4580	0.5420	42
2	0.2764	0.7236	25
3	0.1133	0.8867	25
4	0.0862	0.9138	27
5	0.0725	0.9275	26
6	0.0583	0.9417	26
7	0.0458	0.9542	26
8	0.0376	0.9624	27
9	0.0308	0.9692	27
10	0.0231	0.9769	26
11	0.0199	0.9801	27
12	0.0179	0.9821	27
13	0.0161	0.9839	26
14	0.0149	0.9851	27
15	0.0136	0.9864	27
16	0.0126	0.9874	26
17	0.0119	0.9881	26

18	0.0113	0.9887	27
19	0.0106	0.9894	26
20	0.0101	0.9899	26
			542

The training results show slight dice loss, and the dice coefficient is close to 1.0000. This indicates that the model has a small error, and the processed pixel values have perfect consistency so that the model can distinguish the predictions of each class well.

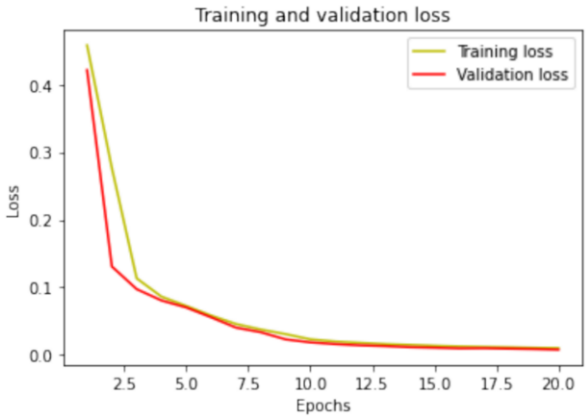

Figure 4. Training loss of the U-Net segmentation model.

Figure 4 shows the prediction results of the mask image generated by the model trained on the ratio and resolution type of the dataset. It also shows the results of cropping the CT scan image in the area corresponding to the pixels of the mask image. It was observed from the change in the loss value of each epoch in the training data that as the training ratio increased, the difference in loss from one generation to another became more stable. After obtaining the cropped image in the U-Net CN model using the predicted mask image, the CNN was used for classification. In contrast, the image data was used without performing the segmentation process. The confusion matrix of the U-Net CN and CNN models showing the numbers of correct predictions is also shown in Figure 6.

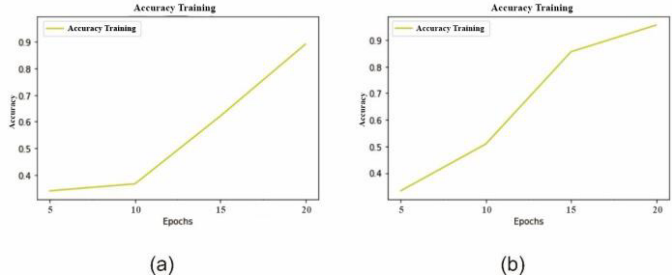

Figure 5. Accuracy for classification results using training data. a) CNN training accuracy. b) U-Net CN training accuracy.

Figure 5 (b) shows that there is an increase in the accuracy at epoch 5. Compared to the CNN model, the U-Net CN model has a significant increase in accuracy that occurs from epoch 5 until epoch 20.

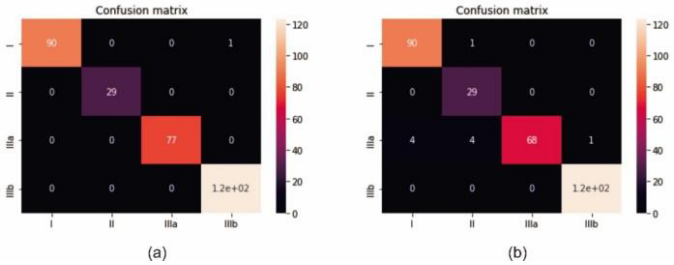

Figure 6. Confusion matrix for classification results using testing data. a) U-Net CN confusion matrix. b) CNN confusion matrix.

Figure 6 shows the confusion matrices of two CNN models and U-Net CN model. The results show that U-Net CN has better testing accuracy. This is due to the more negligible data error bias. After obtaining the value of the confusion matrix, the model will be calculated using several metrics. Based on the results of the matrix calculation, the classification can be determined. Table 2 and Table 3 show the classification results of data testing.

TBALE 2. U-NET CN PERFORMANCE USING TESTING DATA

Class	Accuracy	Precision	Recall	F1-Score
I	99%	100%	99%	100%
II	99%	100%	100%	100%
IIIa	99%	100%	100%	100%
IIIb	99%	99%	100%	99%

TBALE 3 CNN PERFORMANCE USING TESTING DATA

Class	Accuracy	Precision	Recall	F1-Score
I	97%	96%	99%	97%
II	97%	85%	100%	92%
IIIa	97%	100%	88%	94%
IIIb	97%	99%	100%	100%

Based on Tables 2 and Table 3 it can be seen that the metrics produced by the U-Net CN model are much better by producing a larger average than the CNN model. This aligns with the results from the confusion matrix of the U-Net CN model, which exhibits minimal prediction bias. The improvement in accuracy can be attributed to the use of an appropriate segmentation method. U-Net CN uses encoder-decoder based segmentation so that the image to be classified becomes clearer through this process. The pixel points will be uniformed with their respective classes through an encoder-decoder process. Due to the two stages, the encoder, the time required to train the model is somewhat time consuming. From the results of this training, the model that has been created can be made to predict future events and can reduce these cases. This aligns with the findings from research on adaptive moment estimation, which aims to minimize squared error in the backpropagation algorithm [26].

5. Conclusions

The analysis led to the following conclusions: During the data testing phase, the U-Net CN classification method demonstrated outstanding performance, achieving an average of 99% in accuracy, precision, sensitivity, and F1 scores, outperforming the CNN method, which had an average of 96.25%.Various problems, including the choice of the CNN model, the activation function, and hyperparameters in the tunneling step, influence the acquisition of model metrics. Considering the limitations of this study, we suggest that further research use segmentation methods, parameters, and activation functions that can increase accuracy and speed up training time.

Acknowledgment

The authors are grateful to the Ministry of Education and Culture for funding the PUDPT research for the fiscal year 2022 with contract number 029/PB.PDUPT/BRIn.LPPM/VI/2022.

Funding Statement

This research was funded by the Ministry of Education and Culture for the fiscal year 2022 with the contract number 157/E5/PG.02.00.PT/2022,1989.10/LL5-INT/PG.02.00/2022, 029/PB.PDUPT/BRIn.LPPM/VI/2022.

Conflicts of Interests

This research has no conflict of interest regarding the publication of this manuscript.

References

[1] Singh S, Mittal N, Singh H. Multifocus image fusion based on the multiresolution pyramid and bilateral filter. IETE Journal of Research. 2020 Jan; 68(4): 2476–2487, doi: 10.1080/03772063.2019.1711205

[2] Peryanto, A., Yudhana, A. & Umar, R. Klasifikasi Citra Menggunakan Convolutional Neural Network dan K Fold Cross Validation. J. Appl. Informatics Comput. 4, 45–51 (2020).

[3] Duarte, D., Nex, F., Kerle, N. & Vosselman, G. Multi-resolution feature fusion for image classification of building damages with convolutional neural networks. Remote Sens. 10, 10 (2018).

[4] Voulodimos, A., Doulamis, N., Doulamis, A. & Protopapadakis, E. Deep learning for computer vision: A brief review. Comput. Intell. Neurosci. (2018).

[5] Soydaner, D. A comparison of optimization algorithms for deep learning. Int. J. Pattern Recognit. Artif. Intell. 34, (2020).

[6] Albawi, S., Bayat, O., Al-Azawi, S. & Ucan, O. N. Social touch gesture recognition using convolutional neural network. Comput. Intell. Neurosci. (2018).

[7] Sharma, N., Jain, V., & Mishra, A. (2018). An Analysis of Convolutional Neural Networks for Image Classification. *Procedia Computer Science*, *132*, 377–384. https://doi.org/10.1016/j.procs.2018.05.198

[8] Khan, A., Sohail, A., Zahoora, U. & Qureshi, A. S. A survey of the recent architectures of deep convolutional neural networks. Artif. Intell. Rev. 53, (2020).

[9] Hao, S., Zhou, Y., & Guo, Y. (2020). A Brief Survey on Semantic Segmentation with Deep Learning. *Neurocomputing*, *406*, 302–321. https://doi.org/10.1016/j.neucom.2019.11.118

[10] Hao, S., Zhou, Y. & Guo, Y. A brief survey on semantic segmentation with deep learning. Neurocomputing 406, (2020).

[11] Salehi, S. S. M., Erdogmus, D. & Gholipour, A. Tversky loss function for image segmentation using 3D fully convolutional deep networks. Int. Work. Mach. Learn. Med. imaging (2017).

[12] Huang, H. et al. Unet 3+: A full-scale connected unet for medical image segmentation. ICASSP 2020-2020 IEEE Int. Conf. Acoust. Speech Signal Process. (2020).

[13] Ronneberger, O., Fischer, P. & Brox, T. U-net: Convolutional networks for biomedical image segmentation. Int. Conf. Med. image Comput. Comput. Interv. (2015).

[14] Nair, R. R. & Singh, T. Multi‐sensor medical image fusion using pyramid‐based DWT: a multi‐resolution approach. IET Image Process. (2019).

[15] Yadav, S. S. & Jadhav, S. M. Deep convolutional neural network based medical image classification for disease diagnosis. J. Big Data (2019).

[16] Berghmans, T., Durieux, V., Hendriks, L. E. & Dingemans, A. M. Immunotherapy: from advanced NSCLC to early stages, an evolving concept. Front. Med. (2020).

[17] Arbour, K. C. & Riely, G. J. Systemic therapy for locally advanced and metastatic non–small cell lung cancer. Jama (2019).

[18] Elbaz, K., Yan, T., Zhou, A. & Shen, S.-L. Deep learning analysis for energy consumption of shield tunneling machine drive system, Tunnelling and Underground Space Technology. Elsevier (2022)

[19] Shen, S., Elbaz, K. & Shaban, W. M. Real-time prediction of shield moving trajectory during tunnelling. Acta Geotech (2022) doi:https://doi.org/10.1007/s11440-022-01461-4.

[20] Yan, T., Shen, S.-L., Zhou, A. & Chen, X. Prediction of geological characteristics from shield operational parameters by integrating grid search and K-fold cross validation into stacking classification algorithm. J. Rock Mech. Geotech. Eng. (2022).

[21] Soomro, T. A. et al. Strided fully convolutional neural network for boosting the sensitivity of retinal blood vessels segmentation. Expert Syst. Appl. (2019).

[22] Phaladisailoed, T. & Numnonda, T. Machine learning models comparison for bitcoin price prediction. 2018 10th Int. Conf. Inf. Technol. Electr. Eng. (2018).

[23] Zheng, S. et al. Rethinking semantic segmentation from a sequence-to-sequence perspective with transformers. Proc. IEEE/CVF Conf. Comput. Vis. pattern Recognit. (2021).

[24] Xiao, Z., Liu, B., Geng, L., Zhang, F. & Liu, Y. Segmentation of lung nodules using improved 3D-UNet neural network. Symmetry (Basel). (2020).

[25] Ting, F. F., Tan, Y. J. & Sim, K. S. Convolutional neural network improvement for breast cancer classification. Expert Syst. Appl. (2019).

[26] Yao, P. et al. Fully hardware-implemented memristor convolutional neural network. Nature (2020).

Fuzzy Systems and Data Mining X
A.J. Tallón-Ballesteros (Ed.)

doi:10.3233/FAIA241413

A Graph Neural Network-Based Community Search System over Dynamic Graph

Yixin Song, Lihua Zhou[1]
Information Science and Engineering, Yunnan University, Kunming 650091, China

Abstract. Community search (CS), aiming to find a densely connected subgraph containing given query vertices, is an important research topic in social network analysis and is widely used in similar recommendation, team organization, friendship recommendation and other practical applications. The purpose of the CS system is to display searched community in a visual form to users. It can help users better understand and analyze networks, making better decisions. However, the exist CS systems are mostly designed for static graphs, they cannot capture the dynamic attributes and cannot intuitively display the dynamic changes of the community. In this paper, we develop a CS system over dynamic graph based on graph neural network (GNN), aiming to locate the community with cohesive attributes over dynamic graph and visualize the community to intuitively display the dynamic changes of vertices and the relationships between them. We design a GNN-based method to capture the dynamic changes of attributes and design a friendly front-end interface that visualizes the result community in the form of a timeline. It allows users to view the status of the result community at any snapshot and fine-tune the result community according to their own conditions.

Keywords. Community search system, graph neural network, dynamic graphs, attribute cohesiveness

1. Introduction

Community search (CS)[1-3] is an important research topic in graph analysis, aiming to search for a structure cohesive subgraph with query vertices that satisfies the given conditions. However, the results of CS are relatively abstract, and it's difficult to intuitively compare the advantages and disadvantages of two result communities. CS system is a system that uses visualization technology to graphically display the community. It receives the query conditions specified by users and displays the result community to users visually. Thus, CS systems can help researchers and users to explore the graph data and the result community. For this reason, Chen and Gao[4] proposed a visual interactive system (VICS-GNN) for CS with similar attributes via GNN. VICS-GNN is the first system to support interactive, flexible CS guided by user's labeling. However, VICS-GNN cannot display the dynamic changes of the communities, because it is designed for static graphs.

In this paper, we develop a CS system over dynamic graph to search for a community with similar attributes and allows users to intuitively explore the dynamic changes of

[1] Corresponding Author: Lihua Zhou, Information Science and Engineering, Yunnan University, Kunming 650091, China; E-mail: lhzhou@ynu.edu.cn.

attributes and relations between vertices. To the best of our knowledge, our proposed system is the first CS system over dynamic graphs.

Our proposed system contains a front-end and a back-end. The front-end designs a friendly visualization interface for users to explore result community easily and intuitively. Generally, a dynamic graph is a sequence of static graphs (snapshots), which represents the dynamic changes of edges, vertices and the related attributes. To visualize the dynamic changes of vertices and edges, we design a timeline to show the community at each snapshot, which allows user to explore the result in any snapshots. The back-end aims to search community with similar attributes by capturing the dynamic change of vertices' attributes. The dynamic changes of vertices' attributes reflect more comprehensive characteristics of real entities in real-world applications. For example, a user prefers action movies for a while, and then prefers science fiction movies after a while. So how to capture the dynamic changes of vertices' attributes is of great significance for CS.

Unfortunately, the most of CS methods over dynamic graphs are only consider the structure, ignoring the attributes of vertices. Although attribute community search (ACS)[5-7] can consider the attributes of vertices for CS, they cannot handle the dynamic changes of attributes. In addition, most of ACS methods are searching communities based on specified keywords, which means they cannot handle the non-linear attributes. For example, the keywords "Natural Language Processing" and "Machine Learning" are totally different, although both are closely related to the "Artificial Intelligence".

Due to the effectiveness of GNN in handling the non-linear attributes, we design a GNN based method as the default method of the back-end to capture the dynamic changes of attributes. Of course, other CS methods over dynamic graphs can also be used in the back-end.

2. System Overview

In this section, we give the framework of the CS system we proposed and introduce each module of it. The framework of the proposed CS system is shown in Figure 1, which consists of front-end and back-end. The front-end is used for a user to configure the parameters and visualize the results of CS. The parameters configured by the front-end are provided to the back-end for preprocessing and conducting subsequent community searches. The back-end is used to mine the dynamic changes of attributes, and performing the community search.

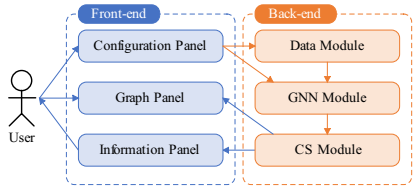

Figure 1. The framework of our CS system.

2.1. Front-end

We design a friendly visual interface for users to explore the dynamic community in a form of timeline. Figure 2(a) shows the front-end of the CS system we proposed, which includes 3 panels, namely configuration panel (box 1), graph panel (box 2) and information panel (box 3). Each panel is described as below.

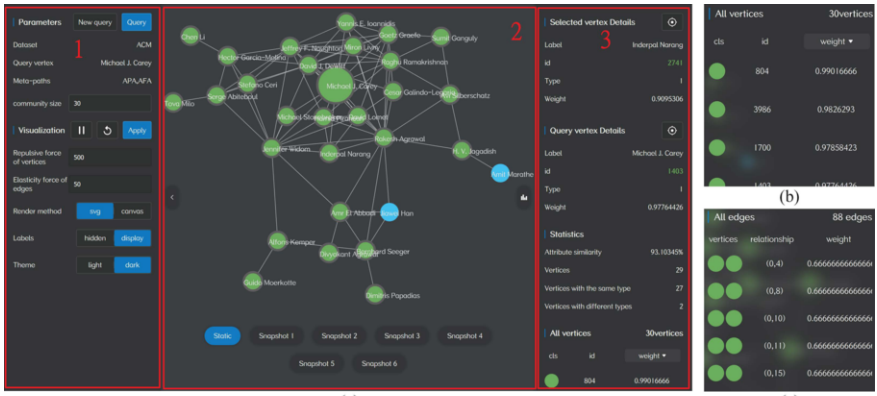

Figure 2. The front-end of our CS system (a) and the list of vertices and edges (b-c).

Configuration Panel. It allows users to set the parameters of CS and visualization. Once the user creates a new query, he/she needs to upload the dataset (a dynamic graph), set the query vertex and the meta-paths (if the uploaded dynamic graph is heterogeneous), and these three parameters will not change in this query. Then, the user sets the community size and the parameters of visualization to driving the back-end for CS. The community size constraint is commonly used in practical applications[8], such as only accepting a certain number of people to join a team due to the budget constraints.

Graph Panel. It provides users with a visual interface for exploring the result community in a form of timeline. It displays the result community in a static graph by default. The static graph contains the vertices and edges of all snapshots. Different colors in the graph represent different attribute categories of vertices. Floating below the graph panel is the timeline. It arranges all snapshots in chronological order. Users can choose to view the community status of any snapshot.

Information Panel. It shows the detail information of the vertex that the user selected in graph panel and the query vertex. It shows statistical information on the vertices and edges of the result community, which can help users judge the reliability of the results on a macroscopic level. In addition, the information of all vertices and edges in result community are also displayed to the user in the form of a list (Figure 2(b-c)).

2.2. Back-end

The back-end contains three modules and it does not involve the database, because the data is uploaded from users. Each module of the back-end is described as below.

Data Module. This module is responsible for processing the data uploaded by the user into a unified dynamic graph data structure. A dynamic graph data structure is a sequence of snapshots, and every snapshot is a static graph with vertices and edges in a specific time. If the snapshots in a dynamic graph are heterogeneous graphs, it will transform the heterogeneous graph into a homogeneous graph based on multiple symmetric meta-paths, i.e., only retain one type of vertices and edges, the edges represent the relationships between vertices with respect to multiple symmetric meta-paths.

GNN Module. This module aiming to capture the dynamic changes of attributes and calculates the attribute similarity between each vertex by GNN-based method. GNN[9] can learn high-dimensional embeddings of vertices by capturing attributes and structural information over a static graph. GNN has many variants, such as GCN[10], GAT[11] etc.

To capture the dynamic changes of attributes and structures over a dynamic graph, this module uses a two-level (spatial- and temporal-level) GAT model to fuse the embeddings of vertices from spatial and temporal perspectives respectively.

Specifically, let $\mathbf{H}^t \in \mathbb{R}^{N\times M}$ represents the initial embeddings of vertices, where N is the number of vertices and M is the dimension of the initial embedding. The spatial-level GAT is responsible for learning the embedding of vertex *u* based on the initial embedding of *u* and its neighbors *v* in the *t*-th snapshot. Firstly, the spatial-level GAT calculates the importance $\boldsymbol{\alpha}^t[u,v] \in \mathbb{R}$ of *v* to *u* by Eq. (1):

$$\boldsymbol{\alpha}^t = softmax(att_{spa}(\mathbf{A}^t, \mathbf{H}^t)), \tag{1}$$

where $\boldsymbol{\alpha}^t \in \mathbb{R}^{N\times N}$, $softmax(\bullet)$ is the normalized exponential function, $att_{spa}(\bullet)$ is the attention mechanism in spatial-level GAT, $\mathbf{A}^t \in \mathbb{R}^{N\times N}$ is the adjacency matrix of the *t*-th snapshot. Then, it fuses the embeddings of each *v* according to the importance to obtain the spatial embedding $\mathbf{Z}^t[u] \in \mathbb{R}^{1\times F}$ of vertex *u*, shown in Eq. (2).

$$\mathbf{Z}^t = \sigma(\boldsymbol{\alpha}^t \times \mathbf{H}^t), \tag{2}$$

where $\mathbf{Z}^t \in \mathbb{R}^{N\times F}$, F is the dimension of embedding, $\sigma(\bullet)$ denotes the activation function. Finally, the temporal-level GAT calculates the importance of each snapshot to vertex *u* and obtains the final embedding $\mathbf{Z}[u] \in \mathbb{R}^{1\times F}$ of vertex *u* by fusing the embeddings of each snapshot:

$$\mathbf{Z} = \sigma(softmax(att_{tem}(\mathbf{Z}^1, \mathbf{Z}^2, \cdots, \mathbf{Z}^T)) \times \mathbf{Z}^t), \tag{3}$$

where $\mathbf{Z} \in \mathbb{R}^{N\times F}$, $att_{tmp}(\bullet)$ is the attention mechanism in temporal-level GAT. To calculate the attribute similarity between each vertex, we classify all vertices into two categories (category 1 is the vertices with similar attributes to the query vertex, category 2 is the vertices with dissimilar attributes to the query vertex) based on the final embeddings $\mathbf{Z}$, and finally we will obtain the probability that each vertex belongs to category 1, e.g., the attribute similarity. To this end, we use an MLP to calculate the attribute similarity (denote as $\mathbf{AS} \in \mathbb{R}^{N\times 1}$), shown in Eq. (4). To optimize $att_{spa}(\bullet)$, $att_{tmp}(\bullet)$ and MLP, we choose cross-entropy to define the loss function, shown in Eq. (5).

$$\mathbf{AS} = \mathrm{MLP}(\mathbf{Z}), \tag{4}$$

$$loss = \sum_{u\in\mathcal{V}} \Big[-u.label \times \log(\mathbf{AS}[u]) - (1-u.label) \times \log(1-\mathbf{AS}[u]) \Big], \tag{5}$$

where $u.label$ is the label of vertex *u*, $u.label = 1$ if *u* belongs to the same category as the query vertex, otherwise $u.label = 0$. After all networks converge (the loss function is no longer decreased), the output of MLP is the desired attribute similarity. Of course, this module can also use other GNN based methods to calculate the attribute similarity, such as CS-TGN[12], DySAT[13], TGAT[14], etc.

CS Module. This module aims to complete the process of CS and return the target community C to the front-end in the form of dynamic graph data. In general, C is a

connected graph. In a dynamic graph $\mathcal{G}$, if a vertex has no edges connected to other vertices in any snapshot, then the vertex is an isolated vertex. Thus, if there are no isolated vertices in C, then C is connected. This means that verifying whether C is a connected graph requires traversing all snapshots, which is time-consuming. In order to improve the efficiency, this module will construct a union graph G based on $\mathcal{G}$. The union graph G contains all vertices and edges on all snapshots, it preserves the connectivity between vertices in $\mathcal{G}$. Formally, this module is designed to locate a target community C in a union graph G that meet the following conditions: (1) C contains q and is connected in G; (2) $|C|=s$; (3) $\sum_{q,v\in C}\alpha_{qv}$ is maximum, where q is the query vertex, s is the community size and α_{qv} is the attribute similarity between vertex q and v. To locates the target community, we can use BFS based CS algorithms such as the CS algorithms in ICS-GNN[15], CS-TGN[12] etc.

3. Effectiveness Evaluation

To verify whether our proposed system can search for a community with similar attributes over dynamic graph, we choose three representative baseline methods, including two ACS methods over static graph (BASCS[5] and Greedy-T[15]) and one CS method over dynamic graph (BU-Search[16]). We apply all methods on three real-world datasets (ACM, IMDB and DBLP)[17] and use the accuracy metric (calculated by $\left(\left|V_C \cap V_{C'}\right|\right)/\left(\left|V_C\right|\right)$, where V_C is the set of vertices in the result community, $V_{C'}$ is the set of vertices belonging to the same category as the query vertex) to evaluate the result community C searched by each method.

We implement each algorithm by using Python-3.7.15. For datasets, we divide each dataset into multiple snapshots by the timestamps in it to apply each dataset to the methods over dynamic graphs. For GNN, we set the number of iterations to 200, learning rate to 0.001, and use the Adam optimizer. To avoid the coincidence of experimental results, we randomly use 20 query vertices for experiments and calculate the average value of each metric for each algorithm. Codes of our proposed system are publicly available on GitHub (https://github.com/yixiso/CS-System). The results are shown in Table 1.

Table 1. The accuracy values for different methods

Dataset	BASCS	BU-Search	Greedy-T	Our Method
ACM	0.34674	0.42111	0.53500	**0.99667**
IMDB	0.23438	0.36082	0.51833	**0.81000**
DBLP	0.24833	0.59859	0.60667	**0.99833**

On three datasets, the accuracy values of our method are 57.56%, 64.99% and 75% higher than the best accuracy values of all the baseline methods respectively. This is because the baseline methods are not considering the dynamic changes of attributes, while our method can capture the dynamic changes of attributes, thereby improving the attribute cohesion of the resulting community.

4. Demonstration Scenario

In this section, we illustrate the CS system we proposed in a scenario of recommending similar users. For example, a user named Peter found that he/she was very interested in the research direction and articles written by “Michael J. Carey” when he/she was

reading the literature. So, he/she wanted to find more authors similar to "Michael J. Carey". To this end, the following steps maybe required.

Step 1. Configure Query Parameters. Peter click the "new query" button in the "parameter panel", and then upload the dataset (take ACM as an example), set "Michael J. Carey" as the query vertex, and set the meta-paths to initialize the query (users can leave the meta-paths out to use default parameters) in the pop-up dialog box (Figure 3(a)).

Step 2. Seach and Explore the Community. Peter inputs the community size and click "Query" button (Figure 3(b)) to execute the CS. Then, the result community will be visualized as a static graph in the "Graph Panel" in Figure 2(a) by default. There is a timeline float below the "Graph Panel", and Peter can view each snapshot individually. Each snapshot in this scenario is shown in Figure 4. It can be observed that "Michael J. Carey" has no relations with other authors in snapshot 1 and has many relations in snapshots 2-6. In addition, Peter can also observe which authors "Michael J. Carey" has relations with on each snapshot and discover which authors "Michael J. Carey" has the most frequent relations with. In addition, Peter also can check the details of all vertices and edges in the "Information Panel" as shown in Figure 2(b-c).

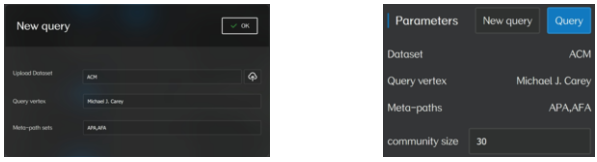

(a) The pop-up dialog box (b) The parameters of community search

Figure 3. The pop-up dialog box.

Step 3. Fine-tune the Community. Peter may not be satisfied with the current result community. For example, there are too few/many authors in the result community. Peter can increase/decrease the community size parameter appropriately and click the "Query" button again to re-search the community. The results are shown in Figure 5(a)/(b). Notice that the process of re-searching the community takes very little time. This is because the back-end only need to re-execute the CS module rather than re-execute the whole back-end. So, Peter can adjust the result community easily and quickly. However, if Peter wants to change the query vertex to search for the community, he/she needs to create a new query and re-execute the whole back-end, which means that the efficiency of the system is not ideal for changing the query vertex.

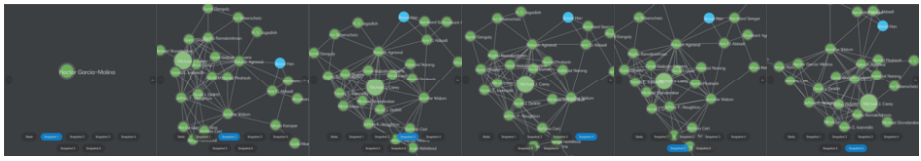

Figure 4. The status of the community at each snapshot.

(a) The community size is 60 (b) The community size is 10

Figure 5. The result community with different community size.

5. Conclusion

We design a CS system over dynamic graph based on graph neural network, making up for the limitation that existing CS systems cannot handle dynamic graphs. Our CS system uses the GNN based methods to capture the dynamic changes of attributes. In addition, it provides users with a friendly interface to conduct CS in dynamic graphs intuitively and it can quickly respond to users' fine-tuning of the results.

Acknowledgments

This research is supported by the National Natural Science Foundation of China (62062066, 62266050 and 62276227), Yunnan Fundamental Research Projects (202201AS070015); the Block-chain and Data Security Governance Engineering Research Center of Yunnan Provincial Department of Education; the Postgraduate Research and Innovation Foundation of Yunnan University (KC-22222861).

References

[1] Y. Fang, X. Huang, L. Qin, Y. Zhang, W. Zhang, R. Cheng, and X. Lin. A survey of community search over big graphs. The VLDB Journal, 2020; 29: 353-392.
[2] Y. Fang, K. Wang, X. Lin, and W. Zhang. Cohesive subgraph search over large heterogeneous information networks. Springer, 2022.
[3] Y. Fang, K. Wang, X. Lin, and W. Zhang. Cohesive subgraph search over big heterogeneous information networks: Applications, challenges, and solutions. In: 2021 International Conference on Management of Data, 2021, pp. 2829-2838.
[4] J. Chen, and J. Gao. VICS-GNN: A visual interactive system for community search via graph neural network. In: 38th International Conference on Data Engineering, 2022, pp. 3150-3153.
[5] J. Wang, L. Zhou, X. Wang, L. Wang, and S. Li. Attribute-sensitive community search over attributed heterogeneous information networks. Expert Systems with Applications, 2024; 235: 121153.
[6] Y. Fang, C. Cheng, S. Luo, and J. Hu. Effective community search for large attributed graphs. Proceedings of the VLDB Endowment, 2016.
[7] X. Huang, and L. V. Lakshmanan. Attribute-driven community search. Proceedings of the VLDB Endowment, 2017; 10(9): 949-960.
[8] B. Liu, F. Zhang, W. Zhang, X. Lin, and Y. Zhang. Efficient community search with size constraint. In: 37th International Conference on Data Engineering, 2021, pp. 97-108.
[9] F. Scarselli, M. Gori, A. C. Tsoi, M. Hagenbuchner, and G. Monfardini. The graph neural network model. IEEE Transactions on Neural Networks, 2008; 20(1): 61-80.
[10] T. N. Kipf, and M. Welling. Semi-supervised classification with graph convolutional networks. International Conference on Learning Representations, 2017.
[11] P. Veličković, G. Cucurull, A. Casanova, A. Romero, P. Lio, and Y. Bengio. Graph attention networks. International Conference on Learning Representations, 2018.
[12] F. Hashemi, A. Behrouz, and M. Rezaei Hajidehi. CS-TGN: Community search via temporal graph neural networks. In: Companion Proceedings of the ACM Web Conference, 2023, pp. 1196-1203.
[13] A. Sankar, Y. Wu, L. Gou, W. Zhang, and H. Yang. Dysat: Deep neural representation learning on dynamic graphs via self-attention networks. In: 13th International Conference on Web Search and Data Mining, 2020, pp. 519-527.
[14] D. Xu, C. Ruan, E. Korpeoglu, S. Kumar, and K. Achan. Inductive representation learning on temporal graphs. arXiv preprint arXiv:2002.07962, 2020.
[15] J. Gao, J. Chen, Z. Li, and J. Zhang. ICS-GNN: Lightweight interactive community search via graph neural network. Proceedings of the VLDB Endowment, 2021; 14(6): 1006-1018.
[16] L. Li, Y. Zhao, Y. Li, F. Wahab, and Z. Wang. The most active community search in large temporal graphs. Knowledge-Based Systems, 2022; 250: 109101.
[17] X. Wang, H. Ji, C. Shi, B. Wang, Y. Ye, P. Cui, and P. S. Yu. Heterogeneous graph attention network. In: World Wide Web, 2019, pp. 2022-2032.

Fuzzy Systems and Data Mining X
A.J. Tallón-Ballesteros (Ed.)

doi:10.3233/FAIA241414

A Meta-Path Guided Pre-Training Method for Sequential Recommendation

Wenbing Zhang, Hongmei Chen [1], Lihua Zhou, Qing Xiao
School of Information Science and Engineering,Yunnan University,Kunming,China
ORCiD ID: Wenbing Zhang https://orcid.org/https://orcid.org/0009-0000-9641-4205,
Hongmei Chen https://orcid.org/https://orcid.org/0000-0002-4054-3654

Abstract. Sequential recommendation aims to predict users' next preferred items according to their interaction sequences. Existing methods mainly utilize user-item interaction information, which may suffer from the issue of semantic information loss. In the paper, a Meta-Path guided Pre-training method for sequential Recommendation (MPPRec) is proposed to capture rich and meaningful semantic information between users and items. Specifically, MPPRec firstly learns the node embeddings guided by meta-paths in the pre-training phase. Then, the node embeddings are optimized according to task in the fine-tuning phase. Extensive experiments conducted on four real datasets demonstrate MPPRec outperforms the baseline methods.

Keywords. Pre-training, Meta-path, Node embedding, Sequential recommendation

1. Introduction

Sequential recommendation [1,2], a popular methodology of recommendation, aims to predict users' next preferred items according to their interaction sequences.

Early works use matrix factorization models [3] or Markov chains. Recently, some methods use deep learning models such as recurrent neural networks (RNNs), convolutional neural networks (CNNs) and self-attention mechanisms [4] to learn good representations of user preferences by characterizing user-item interaction sequences. However, these methods mainly utilize user-item interaction information, and don't properly consider semantic information in interaction sequences, such as the two users that purchase the same product. Besides, most methods also ignore time semantic information which is important for recommendation. To address the above issues, we propose a novel method called Meta-Path guided Pre-training method for sequential Recommendation(MPPRec). The main contributions of the paper are as follows:

- We use meta-paths to learn the embeddings of items and users in the pre-training phase, which can capture more semantic information.
- In the fine-tuning phase, we incorporate time semantic information into the embeddings of users and items to enhance the recommendation performance.
- Experiments conducted on four real datasets show MPPRec is effective.

[1]Corresponding Author: Email: hmchen@ynu.edu.cn.

2. Related Work

Sequential recommendation models can be broadly categorized into non-pretrained models and pretrained models.

Non-pretrained models estimate the transition probabilities between items and recommend the next items with high probabilities to users. Caser [2] utilizes horizontal and vertical convolutions to obtain Markov chains for recommending the next items to users. FM [3] exploits factorized model to predict the next interactions between users and items. REBUS [5] identifies the most relevant items for recommendation by finding frequent subsequences, which are embedded in a unified model based on user dynamical preferences. FMLP-Rec [6] combines the filtering mechanism with MLP and replaces the attention mechanism with filters to improve the recommendation performance. These models do not perform well when training data are sparse.

Pretrained models first capture general patterns or features from data, then the models are optimized by using task-specific data to improve the recommendation performance. S^3-Rec [1] learns the relevance between item, attribute, subsequence and sequence to enhance the embeddings for recommendation. FDSA [7] introduces feature sequences and learns feature transition patterns by exploiting the feature self-attention. TPTS-Rec [8] introduces the time embedding matrix to obtain the correlations between items and time when pre-training, and amplified sequences from the time dimension when fine-tuning. These methods have achieved better results.

Distinct from exiting pretrained models, we present a Meta-Path guided Pre-training method for sequential Recommendation (MPPRec) to capture both structural and semantic information between users and items by meta-paths when pre-training, and fuse time information when fine-tuning, leading to effective embeddings.

3. Related Definition and Problem Statement

Definition 1 (**Heterogeneous information network** [9])**.** A HIN is a graph $G = (N, E, T_N, T_E, \phi, \varphi)$, in which N and E are the sets of nodes and edges. T_N and T_E are the sets of node types and edge types, and $|T_N|+|T_E| > 2$. A HIN is associated with the function of nodes $\phi: N \rightarrow T_N$ and the function of edges $\varphi: E \rightarrow T_E$.

Definition 2 (**Meta-path** [9])**.** Given a HIN $G = (N, E, T_N, T_E, \phi, \varphi)$, a meta-path m is a sequence of node types t_{n_i} or edge types t_{e_i} , i.e. $t_{n_1} \xrightarrow{t_{e_1}} t_{n_2} \xrightarrow{t_{e_2}} \cdots \xrightarrow{t_{e_l}} t_{n_{l+1}}$ (a.k.a $t_{n_1}\ t_{n_2}\ \cdots\ t_{n_{l+1}}$), where l is the length of m, $t_{n_i} \in T_N$ and $t_{e_i} \in T_E$. A meta-path defines a semantic relationship between nodes n_1 and n_{l+1}, where $n_1, n_{l+1} \in N, \phi(n_1) = t_{n_1}, \phi(n_{l+1}) = t_{n_{l+1}}$.

Problem Statement: Given a user's interaction sequence with items: $I^u = \{i_1, \cdots, i_n\}^u$, n is the length of interaction sequence, $i_t (1 \leq t \leq n)$ is the item that the user u interacted with at the t-th step. Sequential recommendation aims to recommend the user u preferred item at the $(n + 1)$-th step.

4. The MPPRec model

In the paper, a Meta-Path guided Pre-training method for sequential Recommendation (MPPRec) is presented to properly capture rich and meaningful structural and semantic

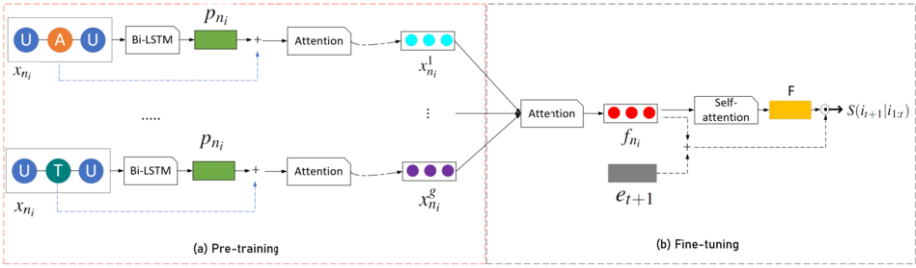

Figure 1. The MPPRec model

information between users and items based on meta-paths. Fig. 1 shows the MPPRec model, including two phase: pre-training and fine-tuning.

4.1. Pre-training

In the pre-training phase of the MPPRec model, we obtain the node embeddings by learning the embeddings of instances of meta-paths, following the approaches in [10]. Unlike the method in [11], which only consider the head and tail nodes, we consider all the nodes in an instance of the meta-path and we also incorporate the position and importance of nodes in the instance by the Bi-LSTM model and the vanilla attention [12] to enhance the node embedding. The pre-training phase is illustrated in Fig. 1(a).

Specifically, an instance of the meta-path can be seen as a sequence. Thus, we first encode the position information p_{n_i} of each node n_i in the instance by the Bi-LSTM model. Then, we compute the importance α_{n_i} of each node n_i by the vanilla attention, and sum the weighted embedding of each node n_i to obtain the instance embedding. The procedure can be described by the formula (1-4).

$$h_{x_{n_i}} = LSTM(\overrightarrow{h_{x_{n_{i-1}}}}, x_{n_i}) \oplus LSTM(\overleftarrow{h_{x_{n_{i+1}}}}, x_{n_i}) \tag{1}$$

$$p_{n_i} = Sigmoid(w^T h_{x_{n_i}} + b) \tag{2}$$

$$\alpha_{n_i} = \frac{Softmax(exp(w^T(x_{n_i} + p_{n_i}))}{\sum_{k=1}^{l+1} exp(w^T(x_{n_i} + p_{n_i}))} \tag{3}$$

$$M = \sum_{i=1}^{l+1} \alpha_{n_i}(x_{n_i} + p_{n_i}) \tag{4}$$

where M denotes the instance embedding, x_{n_i} is the embedding of node n_i in the instance.

Then, we fed the meta-path instance embedding M into a two-layers FC to generate the existing probability $\hat{p}$ of the instance by the formula (5).

$$\hat{p} = \sigma_2(w_2^T(\sigma_1(w_1^T M + b_1)) + b_2) \tag{5}$$

where σ_2 and σ_1 are sigmoid and ReLU activation function, respectively.

We train the model using both the valid instances of meta-paths and the corrupted instances in the pre-training phase. Following [10], we first obtain the valid instances of meta-paths by random walk, and obtain a corrupted instance for each valid instance by randomly replacing either the head or tail node using a node with the same type. Then, we optimize the binary cross-entropy objective function in the formula (6).

$$L_1 = -\{p\log(\hat{p}) + (1-p)\log(1-\hat{p})\} \tag{6}$$

where $p \in \{1,0\}$, p=1 denotes the valid instance and p=0 denotes the corrupted instance.

4.2. Fine-tuning and recommendation

After obtaining node embeddings under different meta-paths, we employ attention mechanism to fuse node embeddings, due to the different importances of meta-paths. Specifically, for each node n_i in meta-path instances, we learn a weight $\beta_{n_i}^j$ by the formula (7). Then, we generate the final node embedding f_{n_i} of node n_i by the formula (8).

$$\beta_{n_i}^j = Softmax(a^T x_{n_i}^j) \tag{7}$$

$$f_{n_i} = \sum_{j=1}^{g} \beta_{n_i}^j x_{n_i}^j \tag{8}$$

where a denotes the trainable attention vector, $x_{n_i}^j$ denotes the embedding of node n_i in the j-th meta-path and g denotes the number of meta-path.

Similar to [1], we fuse node embeddings by self-attention mechanism, which is described by formula (9). Further, when predicting a user's preference score for an item i at the $(t+1)$-th step, we incorporate the time embedding e_{t+1} into the node embedding f_{n_i} of the item i, and compute the score $S(i_{t+1}|i_{1:t})$ by formula (10).

$$F = Attention(f_{n_i}w_q^T, f_{n_i}w_k^T, f_{n_i}w_v^T) = Softmax(\frac{(f_{n_i}w_q^T)(f_{n_i}w_k^T)^T}{\sqrt{d}})(f_{n_i}w_v^T) \tag{9}$$

$$S(i_{t+1}|i_{1:t}) = (f_{n_i} + e_{t+1})^T \cdot F \tag{10}$$

Then, we utilize the pairwise rank loss to optimize the model, which can be calculate by formula (11).

$$L_2 = -\sum_{t=1}^{n-2} log\sigma\{S(i_{t+1}|i_{1:t}) - S(i_{t+1}^-|i_{1:t})\} \tag{11}$$

where σ is *sigmoid* activation function and i_{t+1}^- is the negative item.

5. EXPERIMENTS

5.1. Datasets

We evaluate the models on the four real datasets Beauty, Sports, Toys and LastFM [8]. Beauty, Sports and Toys are Amazon's three-category product purchase datasets, which includes User nodes (U) and Product nodes (P), the meta-path U-P-U indicates that two users purchase the same product. There are three relationships between products, also Viewed (V), also Bought (B) and bought Together (T). LastFM is a music playback and rating dataset, which includes User nodes (U), Album nodes (A) and Tag nodes (T), the meta-path A-T-A indecates that two albums have the same tag. The datasets and meta-paths used are shown in Table 1.

Table 1. The datasets and meta-paths used in experiments.

	Beauty	Sports	Toys	LastFM
# Users	22363	35598	19412	1090
# Items	12100	18357	11924	3646
# Avg. Interactions / User	8.5	8.2	8.3	45.2
# Avg. Interactions / Item	15.8	15.9	13.6	14.4
# Interactions	198502	296337	167597	52551
Meta-paths	U-P-U; $P\xrightarrow{V}P$; $P\xrightarrow{B}P$; $P\xrightarrow{T}P$			U-A-U; U-T-U; A-U-A; A-T-A

5.2. Metric and baselines

We employ the widely used Mean Reciprocal Rank (MRR), top-k Hit Ratio (i.e., HR@$\{1, 5, 10\}$) and Normalized Discounted Cumulative Gain (i.e., NDCG@$\{5, 10\}$) to evaluate the performance [13].

We compare the proposed MPPRec model with three non-pretrained models (FM [3], Caser [2] and $GRU4Rec_F$ [14]) and three pretrained models (BERT4Rec [4], FDSA [7] and S^3-Rec [1]).

5.3. Results

Table 2 shows the best results of experiments, where the best results are in bold. It can be seen that pretrained models achieve better than all non-pretrained models. MPPRec outperforms the baseline models, demonstrating that MPPRec is capable of effectively capturing more semantic information to enhance the performance of sequential recommendation.

5.4. Ablation Study

We design two variants of MPPRec, denoted by MPPRec-pre and MPPRec-time, which follow the same framework of MPPRec, but remove the pre-training and time embedding respectively. The results are given in Table 3. It can be observed that both removing pre-training and time embedding degrade the model performance, which demonstrates the effectiveness of the proposed components.

Table 2. The results of experiments.

Dataset	evaluate	FM	Caser	GRU4Rec$_F$	BERT4Rec	FDSA	S^3-Rec	MPPRec
Beauty	MRR	0.1076	0.2318	0.2751	0.2614	0.2933	0.334	**0.3967**
	HR@1	0.0405	0.1337	0.1702	0.1531	0.1841	0.2192	**0.3102**
	HR@5	0.1461	0.3125	0.3725	0.364	0.4511	0.4502	**0.4864**
	NDCG@5	0.0934	0.2268	0.2759	0.2622	0.2974	0.3407	**0.3969**
	HR@10	0.2311	0.4106	0.4753	0.4739	0.5096	0.5506	**0.5934**
	NDCG@10	0.1207	0.2484	0.309	0.2975	0.3324	0.3732	**0.3871**
Toys	MRR	0.0719	0.1973	0.2717	0.2338	0.2863	0.3202	**0.4599**
	HR@1	0.0267	0.0997	0.1671	0.1262	0.1717	0.2003	**0.3107**
	HR@5	0.0979	0.2795	0.3697	0.3344	0.3994	0.442	**0.5478**
	NDCG@5	0.0614	0.1919	0.2719	0.2327	0.2903	0.327	**0.5866**
	HR@10	0.1815	0.3896	0.4782	0.4493	0.5139	0.553	**0.6859**
	NDCG@10	0.0851	0.2274	0.307	0.2698	0.3271	0.3629	**0.4313**
Sports	MRR	0.1201	0.2191	0.2549	0.2378	0.2748	0.3071	**0.4934**
	HR@1	0.0389	0.116	0.1466	0.1255	0.1585	0.1841	**0.2212**
	HR@5	0.1503	0.3055	0.3547	0.3375	0.3994	0.4267	**0.5274**
	NDCG@5	0.1088	0.2126	0.2535	0.2341	0.2756	0.3104	**0.4363**
	HR@10	0.2481	0.4299	0.4758	0.4722	0.5136	0.5614	**0.5915**
	NDCG@10	0.1344	0.2527	0.2925	0.2775	0.3171	0.3538	**0.4768**
LastFM	MRR	0.0641	0.2033	0.2201	0.2424	0.1884	0.3072	**0.4576**
	HR@1	0.0163	0.0899	0.1147	0.1221	0.0936	0.1743	**0.2165**
	HR@5	0.0944	0.2982	0.3073	0.3569	0.2624	0.4523	**0.5743**
	NDCG@5	0.0542	0.196	0.2113	0.2409	0.1766	0.3156	**0.4088**
	HR@10	0.1577	0.4431	0.4569	0.4991	0.4055	0.5835	**0.6927**
	NDCG@10	0.0755	0.2428	0.2594	0.2871	0.2225	0.3583	**0.4469**

6. Conclusion

A Meta-Path guided Pre-training method for Sequential Recommendation (MPPRec) is presented in the paper. MPPRec learns the node embeddings guided by meta-path when pre-training, and fused time information when fine-tuning. The results of experiments show MPPRec outperforms the baseline methods.

In the future work, we will investigate auxiliary data from multi-view [15], such as reviews and locations, when learning the features of users and items.

Acknowledgments
This work is supported by the National Natural Science Foundation of China (62266050, 62276227), the Program for Young and Middle-aged Academic and Technical Reserve Leaders of Yunnan Province (202205AC160033), Yunnan Provincial Major Science and Technology Special Plan Projects (202202AD080003), Yunnan Fundamental Research Projects (202201AS070015), the Program of Yunnan Key Laboratory of Intelligent Systems and Computing (202205AG070003).

Table 3. The results of ablation study.

Datasets	Metrics	MPRec-pre	MPRec-time	MPRec	Datasets	Metrics	MPRec-pre	MPRec-time	MPRec
Beauty	MRR	0.0355	0.3807	**0.3967**	Toys	MRR	0.0555	0.4398	**0.4599**
	HR@1	0.0512	0.2902	**0.3102**		HR@1	0.0415	0.2805	**0.3107**
	HR@5	0.0956	0.4804	**0.4864**		HR@5	0.0887	0.5281	**0.5478**
	NDCG@5	0.1156	0.3719	**0.3969**		NDCG@5	0.0956	0.5676	**0.5866**
	HR@10	0.1766	0.5101	**0.5934**		HR@10	0.1458	0.6331	**0.6859**
	NDCG@10	0.1322	0.3845	**0.3871**		NDCG@10	0.1055	0.4309	**0.4313**
Sports	MRR	0.0531	0.4434	**0.4934**	LastFM	MRR	0.0623	0.4084	**0.4576**
	HR@1	0.0113	0.201	**0.2212**		HR@1	0.031	0.1966	**0.2165**
	HR@5	0.084	0.5131	**0.5274**		HR@5	0.0744	0.5444	**0.5743**
	NDCG@5	0.0982	0.4161	**0.4363**		NDCG@5	0.0881	0.3885	**0.4088**
	HR@10	0.1671	0.5765	**0.5915**		HR@10	0.132	0.599	**0.6927**
	NDCG@10	0.1154	0.4233	**0.4768**		NDCG@10	0.1077	0.4149	**0.4469**

References

[1] Zhou K, Wang H, Zhao WX, Zhu Y, et al. S^3-Rec: Self-Supervised Learning for Sequential Recommendation with Mutual Information Maximization. CIKM; 2020. p. 1893-902. doi: 10.1145/3340531.3411954.

[2] Tang J, Wang K. Personalized Top-N Sequential Recommendation via Convolutional Sequence Embedding. WSDM; 2018. p. 565-73. doi: 10.1145/3159652.3159656.

[3] Rendle S. Factorization Machines. IEEE Computer Society; 2010. p. 995-1000. doi: 10.1109/ICDM.2010.127.

[4] Sun F, Liu J, Wu J, Pei C, Lin X, Ou W, et al. BERT4Rec: Sequential Recommendation with Bidirectional Encoder Representations from Transformer. CIKM; 2019. p. 1441-50. doi: 10.1145/3357384.3357895.

[5] Lonjarret C, Auburtin R, Robardet C, Plantevit M. Sequential recommendation with metric models based on frequent sequences. Data Min Knowl Discov. 2021;35:1087-133.

[6] Zhou K, Yu H, Zhao WX, Wen JR. Filter-enhanced MLP is all you need for sequential recommendation. WWW; 2022. p. 2388-99. doi: 10.1145/3485447.3512111.

[7] Zhang T, Zhao P, et al. Feature-level Deeper Self-Attention Network for Sequential Recommendation. IJCAI; 2019. p. 4320-6. doi: 10.24963/ijcai.2019/600.

[8] Chen W, Chen H, Zhou L, Fang Y. Time-aware pre-training method for sequence recommendation. Computer Science. 2023.

[9] Yan B, Yang C, Shi C, Fang Y, Li Q, Ye Y, et al. Graph Mining for Cybersecurity: A Survey. ACM Trans Knowl Discov Data. 2024;18(2):47:1-47:52. doi: 10.1145/3610228.

[10] Huang C, Fang Y, Lin X, Cao X, Zhang W. ABLE: Meta-Path Prediction in Heterogeneous Information Networks. ACM Trans Knowl Discov Data. 2022;16(4):73:1-73:21.

[11] Fu X, Zhang J, et al. MAGNN: Metapath Aggregated Graph Neural Network for Heterogeneous Graph Embedding. WWW; 2020. p. 2331-41. doi: 10.1145/3366423.3380297.

[12] Luong T, Pham H, Manning CD. Effective Approaches to Attention-based Neural Machine Translation. The Association for Computational Linguistics; 2015. p. 1412-21. doi: 10.18653/v1/d15-1166.

[13] Du K, Zhang W, Zhou R, Wang Y, Zhao X, Jin J, et al. Learning enhanced representation for tabular data via neighborhood propagation. NeurIPS. 2022:16373-84.

[14] Hidasi B, Quadrana M, Karatzoglou A, Tikk D. Parallel Recurrent Neural Network Architectures for Feature-rich Session-based Recommendations. RecSys; 2016. p. 241-8. doi: 10.1145/2959100.2959167.

[15] Zhou L, Du G, Lü K, Wang L, Du J. A Survey and an Empirical Evaluation of Multi-view Clustering Approaches. ACM Comput Surv. 2024. doi: 10.1145/3645108.

Fuzzy Systems and Data Mining X
A.J. Tallón-Ballesteros (Ed.)

doi:10.3233/FAIA241415

Evaluation of Technical Support in Software Promotion Effectiveness Based on Causal Machine Learning

Jiayi Weng, Zihang He, Siqi Liu and Lei Zhang[1]
School of Economics and Management, Beijing Jiaotong University, Beijing, 100044, China
ORCiD ID: Jiayi Weng https://orcid.org/0009-0001-3969-9926
Zihang He https://orcid.org/0009-0005-6907-3560
Siqi Liu https://orcid.org/0009-0009-3475-7769
Lei Zhang https://orcid.org/0000-0001-7217-6919

Abstract. Precise and effective software promotion strategies are crucial for software companies. By introducing causal machine learning techniques to analyze software promotion data provided by software companies, we aim to reveal the extent to which the promotion strategy of technical support services affects sales effectiveness and explore the heterogeneity of this effectiveness across different customer groups. The results show that the introduction of technical support can generate a 60% increase in sales revenue for software companies. By comparing multiple causal machine learning models, Linear DML emerge as the optimal model, which is used to further explore customer subgroups with high causal effects and to interpret the model with SHapley Additive exPlanations (SHAP). We find that features such as larger company size, more personal computers, fewer employees, and less IT spending are customer features that are more responsive to technical support services. The findings are expected to provide software companies with a theoretical basis for developing more effective promotion strategies and identifying promotional customer groups.

Keywords. Causal Machine Learning, Precision Marketing, Software promotion, SHapley Additive exPlanations

1. Introduction

Under the digital transformation environment, outsourcing services are widely used as an effective cost-saving and resource-optimizing strategy [1]. The maturity of outsourcing has increased global competition in the software market, making effective promotional strategies critical to attracting consumers. A study by Alford and Biswas (2002) revealed the significant effect of discount promotions in increasing consumers' perceived value of a product and thereby influencing purchase decisions [2]. In terms of service provision as the main promotional strategy, the study by Nasir et al. (2021) emphasizes the central role of quality services, especially after-sales and technical support, in building consumer satisfaction and loyalty [3]. These studies suggest that

[1] Corresponding Author: Lei Zhang, School of Economics and Management, Beijing Jiaotong University, Beijing, 100044, China. Email: zhlei@bjtu.edu.cn.

high quality customer service and price promotions are both important promotional strategies that not only boost sales in the short term, but also enhance brand and market competitiveness in the long term.

With the advancement of technologies such as big data, more scholars adopted these methods for sales forecasting and evaluation of promotional methods. In the field of machine learning applications for business intelligence, Khan et al. (2020) concluded that the generalized approximation capabilities of feedforward neural networks (FNNs) make them very effective in solving complex nonlinear problems, which helps to enhance decision-making by efficiently processing high-dimensional data [4]. In applying machine learning to promotional forecasting, Almeida et al. improved the accuracy of sales forecasts by refining a tree-based model [5]. Qiu et al. generated weighted predictions through a collection of sub-model predictions under multiple model sizes to improve the accuracy of sales forecasting, and demonstrated through empirical studies that the combination of promotions has the most significant impact on improving store sales [6]. However, traditional promotion evaluation mainly employs machine learning to predict sales, ignoring confounding factors and heterogeneity, making it difficult to establish a causal relationship between promotion and sales. Due to the trend of "precision marketing" and the increasing demand for more precise analysis in the marketing industry, the significance of causal inference has become increasingly apparent and is becoming a key tool for connecting promotional behaviors with actual sales results [7].

Regarding the application of causal machine learning, Carbo-Valverde et al. (2020) employed causal machine learning models such as causal forests on the results of a consumer finance survey to explore the causal relationships that exist in the digitization process. The results suggest that segmenting customers based on preferences and providing personalized digital services are key to digitization [8]. Simonian et al. employed double machine learning in finance considering the weekly return of the S&P 500 index below a specific threshold as a treatment variable and the weekly return of a single major non-U.S. market as an outcome, examining market contagion while considering other non-U.S. markets as confounders [9]. This revealed the value of information intervention and data causal inference in optimizing consumer behavior and business decisions.

In summary, our research contributions are as follows: First, we utilize causal machine learning techniques to directly assess the impact of technical support promotions on software sales. This method allows us to clearly understand the causal relationships between promotional interventions and their outcomes, distinguishing it from traditional correlation-based market analysis. Second, we identify and analyze the heterogeneity in responses to promotional strategies among different customer groups, revealing which groups are most responsive to technical support promotions, aiding the implementation of targeted marketing strategies. Moreover, we incorporate SHAP (SHapley Additive exPlanations) values to enhance the interpretability of our causal machine learning model. This approach enables us to explain the model's predictive outcomes in a detailed and comprehensible manner, which is crucial for decision-makers to make informed decisions based on model predictions. Finally, through our analytical insights, we provide practical guidance for software companies, helping them to tailor their marketing strategies based on the causal effects and specific responses of customers, to maximize effectiveness.

2. Method

2.1. Causal machine learning

Causal machine learning is a method for estimating the causal effects of treatments on outcome variables. In contrast to traditional predictive models, causal machine learning focuses on understanding the direct effect of the treatment on the outcome, not simply the correlation between both. This distinction is critical for developing effective intervention strategies.

We first define two causal effect metrics: Average Treatment Effect (ATE) and Conditional Average Treatment Effect (CATE).

ATE is a statistical concept for measuring causal effects, defined as the average amount of change in the expected outcome for individuals in the population when they receive a particular treatment [10].

$$ATE = E[Y(1) - Y(0)] \tag{1}$$

Where, $E[\,]$ denotes expected value, $Y(1)$ denotes the software sales with technical support (with treatment), and $Y(0)$ denotes the software sales without technical support (without treatment).

ATE measures the difference in outcomes between the treatment and control groups under the assumption of random assignment, which ensures that the treatment is independent of potential confounders, both observed and unobserved, thereby isolating the treatment effect from other influences and thus effectively quantifying causal effects.

CATE further explores causal effects within specific subgroups, allowing to understand the variability of treatment effects under different conditions (e.g., different features).

$$CATE(X) = E[Y(1)\big|X] - E[Y(0)\big|X] \tag{2}$$

Where, $E[Y(1)|X]$ denotes the expected outcome of receiving the intervention given the covariate X, and $E[Y(0)|X]$ denotes the expected outcome without the intervention under the same conditions. X can be any relevant set of features, such as the size of the costumer companies.

CATE distinguishes between different groups responding to the same treatment, and this distinction helps to identify which subgroups benefit more or less from treatment, thus providing a nuanced understanding of causal effects that may be missed by ATE, especially in heterogeneous populations.

Furthermore, we use the Area Under the Uplift Curve (AUUC) to evaluate the predictive performance of the model. AUUC is a statistical metric for evaluating the performance of predictive causal machine learning models that considers the cumulative uplift in positive outcomes as the intervention is applied to individuals at different probability thresholds. This metric helps to determine whether the model can correctly distinguish those individuals who respond the best to the intervention.

2.2. Meta-Learners and Double Machine Learning

Meta-Learner estimates the potential outcomes of individuals in different treatment conditions by constructing single or multiple predictive models that include T-Learner, S-Learner, and X-Learner. T-Learner is appropriate when the treatment and control group data are similarly structured. S-Learner learns the relationship between the

treatment effect and other features by inputting the treatment condition as a feature into a single model. X-Learner is designed for situations where the treatment effect is highly heterogeneous across individuals [11]. While Double Machine Learning (DML) is a two-step approach that independently predicts the potential outcomes of treatments and outcomes before estimating the causal effects of the treatments, suitable for contexts where the treatment effects are due to individual differences [12]. We compare multiple methods to determine which is most effective in assessing the effects of software promotions.

2.3. SHAP

SHAP (Shapley Additive exPlanations) is a technique for interpreting machine learning model predictions using Shapley values from game theory. It explains model predictions by quantifying each feature's contribution. SHAP applies to any machine learning model, aiming to enhance model transparency and interpretability, enabling a deeper understanding of model decision-making processes [13]. Compared to other mainstream methods of model interpretability, SHAP (Shapley Additive exPlanations) offers distinct advantages. For instance, unlike LIME and other local interpretability models, SHAP provides a global explanation, capable of offering distinct explanations for different sub-samples. Moreover, in contrast to Partial Dependence Plots, SHAP also considers the interactions between features, thereby providing a more comprehensive depiction of the complexity of feature influences.

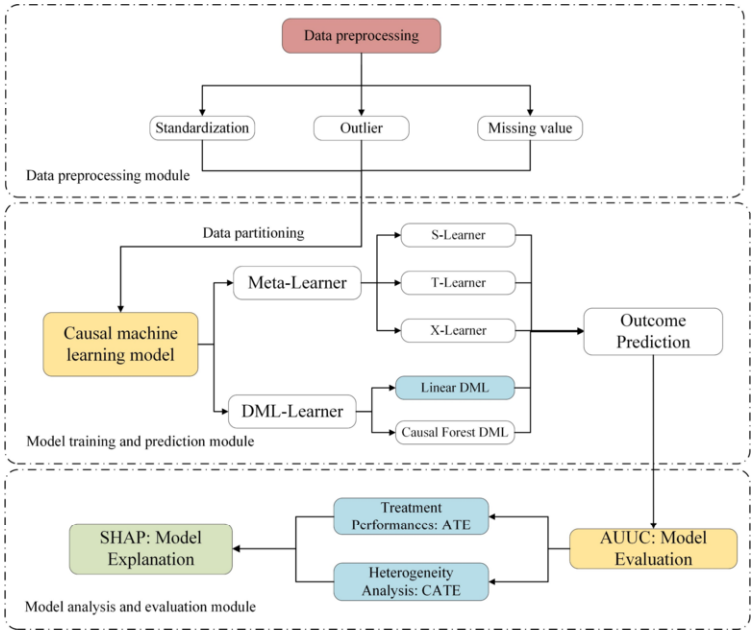

Figure. 1 Research flowchart

Our study consists of three modules:

- Data preprocessing module: Data preprocessing of the software sales dataset, including outlier processing, missing value processing and standardization.

- Model training and prediction module: Train multiple causal machine learning models using the processed data and predict the output.
- Model analysis and evaluation module: Compare the performance of different models to evaluate the effectiveness of promotions; interpret the heterogeneity of model results.

In our study, we use EconML, an open-source Python package released by Microsoft Research, to perform causal analysis [14]. Our experimental setup involved training models on a laptop with an Intel Core i7 processor and 16GB of memory. We carefully set the hyperparameters for our causal machine learning models. For the Linear DML, we used Gradient Boosting Regression Trees (GBRT) for outcome modeling and Logistic Regression with automatic cross-validation for treatment modeling, configured to handle discrete treatments without using linear models initially. The Causal Forest DML employs a Gradient Boosting Classifier for treatment and a Regressor for outcomes, with inference enabled to improve estimate reliability. The T-Learner, S-Learner, and X-Learner all use Gradient Boosting Regressors for estimating potential outcomes, with the X-Learner additionally using a Gradient Boosting Classifier for propensity modeling.

3. Data

The dataset for this research comprises 2,000 entries from a software promotions datase t provided by a software company. It includes details on promotional activities, notably technical support (Tech Support), customer attributes, and software purchase volumes. For further information: https://www.kaggle.com/datasets/hwwang98/software-usage-promotion-campaign-uplift-model. All continuous variables in the dataset were standardi zed using z-scores to minimize scale and bias effects. Then, we divided the dataset into training and testing sets, allocating 80% of the data for training and 20% for testing, in order to evaluate the effectiveness of the models.

4. Result

4.1. Treatment performance and model comparison

In this section, we use a causal machine learning model not only to estimate the overall average effect (i.e., ATE) of technical support of a software company's sales performance, but also to compare the predictive performance of different causal machine learning models.

The ATE reflects the change in sales that would be expected as a result of providing technical support (Treatment) to all customers. Higher ATE values indicate that technical support has a greater positive effect on software sales. The results show that the ATE values are mostly around 0.6 (Table 1), means that the introduction of technical support can contribute to approximately 60% of the increase in sales for software companies. T-Learner has the highest ATE of 0.607 with 95% CI = [0.594, 0.621].

Table 1. Model Performance Comparison

Model	ATE	ATE 95% CI	AUUC
Linear DML	0.605	[0.593, 0.614]	132438.324
Causal Forest DML	0.582	[0.572, 0.589]	132390.374
T-Learner	0.607	[0.594, 0.621]	131521.228
S-Learner	0.589	[0.577, 0.597]	131430.986
X-Learner	0.597	[0.566, 0.587]	132011.293

We also compared the performance of five causal machine learning models in estimating the effect of technical support on software company sales (Table 1). In our study, AUUC reflects the model's capability to identify customers' increased purchasing behaviors due to technical support under different thresholds. Higher AUUC values indicate that the model is better at identifying which customers are more likely to increase their purchases due to technical support. All models perform similarly on this metric, with Linear DML performing the best, indicating that it is more effective at predicting customer purchase behavior. Therefore, the Linear DML model is also employed in further heterogeneity analyses.

4.2. Heterogeneity Analysis

The Conditional Average Treatment Effect (CATE) provides a more detailed analytical perspective than the Average Treatment Effect (ATE). CATE reveals the heterogeneity of intervention effects, i.e., the average effect of the intervention may be different in different subgroups.

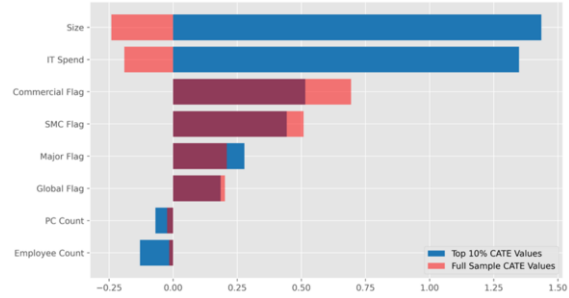

(a) Comparison of Average CATE Values

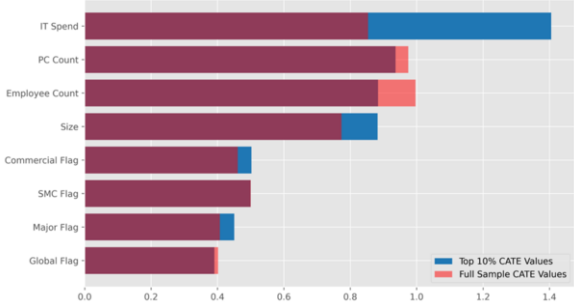

(b) Comparison of CATE Values Variability

Figure. 2 Comparing CATE: Average and Variability for Top 10% vs. Full Sample.

To explore the effect of technical support on different groups of customers, our study followed to the methodology of Wu et al. for heterogeneous groups by selecting the sample in the top 10% of the Conditional Average Treatment Effect (CATE) and analyzing this subset compared to the full sample [15]. Figure 2 illustrates the difference in CATE values between the top 10% of the effect value and the overall population of customers on the differences in CATE values on different features. The blue color represents the top 10% of customers and the orange color represents all customers.

The overlap between the two is represented by the dark red color. Taking the feature "Commercial Flag" in the figure (a) as an example, the top 10% of customers exhibit lower CATE average values relative to all customers, indicating that companies with less commercial nature exhibit higher sensitivity to technical support services. Most of the other features demonstrate significant differences in both average values and standard deviations. We note that for two features, "Size" and "IT spend", the averages for the high CATE group are significantly higher than the full sample average, as well as in distinctly different directions. This indicates that larger companies and those with higher IT spending are more responsive to technical support. Additionally, companies with operations less inclined towards commercial activities may exhibit a greater demand for third-party software.

4.3. Model Interpretability

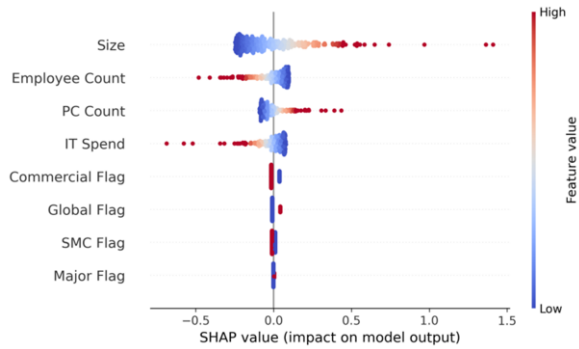

Figure 3. SHAP summary plot for software promotion.

To further investigate the features that influence the prediction results of the software promotion model, we employed the SHAP summary plot for our analysis (Figure. 3). Within this causal framework, the analysis of SHAP values focuses on assessing the impact of covariates X on the potential outcomes after a given treatment (Tech Support), rather than on the treatment variable itself. The plot visualizes the rank order of the contribution of different features to the model's prediction results, as well as the directional information (degree of positive or negative contribution) of each feature to the model's prediction. The importance of features decreases from top to bottom. Features with higher importance are "Size", "Employee Count", "PC Count" and "IT Spend", while features labeled by customers (e.g., Global Flag) exhibit lower importance.

The SHAP summary plot also provides directional information regarding how the features affected the prediction results: each dot represents an observation with the color of the dot closer to red indicating a higher value of the feature, and closer to blue indicating the opposite. Positions on the horizontal coordinate indicate the magnitude of the SHAP value for the observation, with those located to the right of the zero indicating

a positive contribution to the model's predicted results, and those to the left indicating a negative contribution. Take "Size" as an example, we see that the red dots are mostly concentrated to the right of the zero, indicating that in most cases, larger company size tends to increase the likelihood that the company will purchase third-party software. Similarly, for "Employee Count", "PC Count", "IT Spend" exhibit directionality. "PC Count" contributes positively to the likelihood of purchasing software from third-party companies, while "Employee Count" and "IT Spend" contribute negatively.

5. Conclusion

Our study employs causal machine learning methods to analyze promotional data from software companies and assess the effect of technical support on sales, revealing that technical support boosts sales by about 60%. Further analysis indicates that customers with larger company size, more number of personal computers, fewer employees, and less IT spending respond more positively to technical support. Through SHAP value analysis, we identified "Size", "Employee Count", "PC Count" and "IT Spend" as the key factors affecting model predictions. This finding provides software companies a basis for marketing strategy optimization, especially in targeting potential customers and adjusting promotional measures.

Our study innovatively applies causal machine learning techniques to analyze the effectiveness and heterogeneity of product promotions. We also utilize the SHAP method to enhance the transparency and interpretability of our findings, which is crucial for making informed decisions based on information. However, it is important to acknowledge that our study has certain areas for improvement. The dataset used in our analysis may not encompass all potential factors influencing the effectiveness of promotions, such as competitive market conditions. Additionally, while we did evaluate the effects of technical support, we did not investigate the combined effects of multiple promotional strategies.

Acknowledgement

The work was supported by the National Natural Science Foundation of China (No.72271017).

References

[1] Khan SU, Niazi M, Ahmad R. Factors influencing clients in the selection of offshore software outsourcing vendors: An exploratory study using a systematic literature review. Journal of Systems and Software. 2011;84(4):686-699. https://doi.org/10.1016/j.jss.2010.12.010

[2] Alford BL, Biswas A. The effects of discount level, price consciousness and sale proneness on consumers' price perception and behavioral intention. Journal of Business Research. 2002;55(9):775-783. https://doi.org/10.1016/S0148-2963(00)00214-9

[3] Nasir M, Adil M, Dhamija A. The synergetic effect of after sales service, customer satisfaction, loyalty and repurchase intention on word of mouth. International Journal of Quality and Service Sciences. 2021;13(3):489-505. https://www.researchgate.net/publication/373927319

[4] Khan W A, Chung S H, Awan M U, Wen X. Machine learning facilitated business intelligence (Part I): Neural networks learning algorithms and applications. Industrial Management & Data Systems. 2020;120(1):164-195. https://doi.org/10.1108/IMDS-07-2019-0361

[5] de Almeida PS, Barbosa G. A machine learning approach to promotional sales forecasting. 2018. https://repositorio-aberto.up.pt/bitstream/10216/111161/2/257774.pdf
[6] Qiu Y, Wang W, Xie T, Yu J, Zhang X. Boosting Store Sales Through Machine Learning-Informed Promotional Decisions. SSRN. 2023 Oct 18; Available from: https://ssrn.com/abstract=4605803
[7] Langen H, Huber M. How causal machine learning can leverage marketing strategies: Assessing and improving the performance of a coupon campaign. Plos one, 2023 Jan;18(1):e0278937. https://doi.org/10.1371/journal.pone.0278937
[8] Carbo-Valverde S, Cuadros-Solas P, Rodríguez-Fernández F. A machine learning approach to the digitalization of bank customers: Evidence from random and causal forests. Plos one. 2020;15(10):e0240362. https://doi.org/10.1371/journal.pone.0240362
[9] Simonian J. A causal analysis of market contagion: A double machine learning approach. Journal of Financial Data Science. 2023;5(2). https://doi.org/10.3905/jfds.2023.1.122
[10] Pearl J. Causality. In: Causality: Models, Reasoning, and Inference. Cambridge: Cambridge University Press, 2009.
[11] Künzel SR, Sekhon JS, Bickel PJ, Yu B. Meta-learners for estimating heterogeneous treatment effects using machine learning. Proceedings of the national academy of sciences. 2019;116:4156–65. https://doi.org/10.1073/pnas.1804597116
[12] Chernozhukov V, Chetverikov D, Demirer M, Duflo E, Hansen C, Newey W. Double/debiased/neyman machine learning of treatment effects. American Economic Review. 2017;107(5):261-5. https://doi.org/10.1257/aer.p20171038
[13] Lundberg S, Lee SI. A unified approach to interpreting model predictions. In: Proceedings of the 31st International Conference on Neural Information Processing Systems; 2017. p. 4768–77. https://proceedings.neurips.cc/paper_files/paper/2017/file/8a20a8621978632d76c43dfd28b67767-Paper.pdf
[14] Microsoft Research. EconML: A Python Package for ML-Based Heterogeneous Treatment Effects Estimation. Version 0.15.0. 2024. Available from: https://github.com/microsoft/EconML
[15] Wu X, Liu X, Pan F, Zhao H, Feng Y, Wang S, Ji X, Zhang Z, Wang Q, Xue F. Assessment of individualized treatment effect of antidiabetic prescriptions for type 2 diabetes based on uplift model. Chinese Journal of Disease Control & Prevention. 2021;25(6):644-649, 678. https://doi.org/10.16462/j.cnki.zhjbkz.2021.06.005

Fuzzy Systems and Data Mining X
A.J. Tallón-Ballesteros (Ed.)

doi:10.3233/FAIA241416

Product Sales Forecasting Model Driven by Multi-Source Data Integration Based on XGBoost

Xue-xia Liang [a], Bin Lu [a], Chao Deng [a,1], Yue Gu [a], Kai-di Chen [a], Yu-hua Mo [a], Liang-ben Xu [a], Pai-yu Li [a], Xi-peng Liu [a] and Meng Liu [a]
[a] *China Tobacco Guangxi Industrial Co., Ltd., Nanning Guangxi 530001, China*
ORCiD ID: Xue-xia Liang https://orcid.org/0009-0002-9184-6062
Chao Deng https://orcid.org/0000-0001-9484-8923

Abstract. In the rapidly evolving landscape of e-commerce, online shopping has gradually gained widespread acceptance. Yet, physical retail channels continue to exert a significant influence on product sales. Within this framework, sales forecasting occupies a pivotal position in traditional commerce and is indispensable for guiding corporate strategy formulation. However, most existing forecasting models fail to fully harness the potential impact of multi-source external information on consumer purchasing behavior. To address these challenges, this study proposes a novel sales forecasting model that synergizes the Extreme Gradient Boosting (XGBoost) algorithm with multi-source data integration techniques. Not only have we comprehensively collected an extensive range of external data, but we have also integrated the embedding and aggregation techniques of Point of Interest (POI) data to enrich the set of external information features available to the model. Leveraging feature engineering techniques, these heterogeneous data are transformed into formats amenable to model training. Relying on the nonlinear modeling capabilities of XGBoost and its efficacy in handling large-scale datasets, we trained and optimized the model. Empirical results indicate that our proposed method, predicated on multi-source data integration, significantly outperforms traditional models based on a single data source, thereby enhancing prediction accuracy and providing more precise inventory management strategy support for businesses.

Keywords. Multi-source data integration, POI embedding, XGBoost algorithm, Sales forecasting

1. Introduction

Despite the surge in e-commerce, physical stores maintain a vital role within the contemporary retail sector. Within conventional business paradigms, precise sales forecasting significantly influences a firm's long-term viability and short-term efficacy. This practice is instrumental for real-time decision-making, resource allocation, and is fundamental to day-to-day operations and inventory management [1]. Over time, the methodologies for product sales forecasting within the retail sector have undergone substantial transformations. Initially, traditional time series analysis techniques such as

[1] Corresponding Author: Chao Deng, China Tobacco Guangxi Industrial Co., Ltd., Nanning Guangxi 530001, China; Email: dengch021@hotmail.com

moving averages and weighted averages have progressively been supplanted by more intricate models including exponential smoothing, linear regression, evolving into advanced models like the Autoregressive Integrated Moving Average (ARIMA) and its seasonal variant SARIMA models [2], as well as Fourier analysis [3]. Furthermore, state-space models have also been incorporated into this domain [4]. These conventional methods are typically confined to the analysis of internal sales data.

Additionally, with the rapid development of big data technology, researchers in recent years have begun to leverage advanced analytical techniques driven by models, such as machine learning [5], convolutional neural networks [6], Extreme Gradient Boosting (XGBoost) models [7], and score-driven models [8], as well as integrating multi-dimensional influencing factors including calendar events, weather conditions, store locations, etc., to augment the precision and dependability of predictions [6, 9]. In comparison to conventional time series analysis, these approaches are better equipped to dissect the intricate relationships within the data, offering a more nuanced and holistic view for sales forecasting. This paradigm shift has propelled prediction models towards an elevated stage of evolution.

In the realm of sales forecasting, the significance of leveraging external data, particularly Points of Interest (POIs) data, is increasingly evident, holding substantial promise for augmenting the predictive capabilities of models. Research by Kang indicates that elements associated with the business environment, agglomeration effects, and geographic positioning—such as consumer mobility, land utilization, and demographic information—can substantially influence product sales [10]. Other studies have corroborated the intimate association between POIs data and collective behaviors, as well as urban socio-economic traits [11-13]. These findings collectively suggest that the amalgamation of conventional sales data with these dynamic external datasets could encapsulate a more exhaustive array of multidimensional factors impacting sales. Despite this, extant research, which includes graph neural network models like GraphSAGE, GAT, PinSage, and P-GNNs, endeavors to augment model efficacy via the incorporation of external feature information, yet continues to encounter impediments such as deficient data richness and challenges in managing high-dimensional features [14-17], thereby impeding the model's capacity to discern intricate spatial relationships among nodes. In our study, we aim to surmount the obstacle of limited features by adopting POI embedding and aggregation methodologies previously established [18]. The application of these methodologies enhances the richness and resilience of feature representations, thereby facilitating a more accurate comprehension and prediction of user behaviors and preferences within various regions, and consequently, bolstering the model's ability to discern and assimilate complex patterns. An elaboration on related works and the technical minutiae will follow in subsequent sections.

Therefore, this study endeavors to construct a novel commodity sales forecasting model that harnesses the potential of the XGBoost algorithm coupled with multi-source data. The research methodology encompasses four pivotal stages: (1) Acquiring an array of pertinent external data, comprising consumer demographic characteristics, retail business district features, urban economic and population metrics, as well as indicators of urban consumption levels; (2) Implementing innovative techniques for POI data embedding and aggregation, aimed at enhancing feature representation; (3) Fusing embedded features with supplementary external data to collaboratively facilitate model training; (4) Leveraging the XGBoost algorithm's efficiency to train and refine the integrated dataset. Upon empirical validation utilizing actual datasets, the forecasting approach devised in this study has demonstrated remarkable efficacy in augmenting the

precision of commodity sales predictions. This accomplishment not only actualizes the objective of establishing a highly precise and dependable commodity sales forecasting model but also infuses pioneering theoretical dynamism into the realm of sales forecasting, thereby offering tangible guidance and contributing to the progression of both scholarly research and commercial applications within this domain.

2. Related Work

2.1. Product Sales Forecasting

The interrelation between commodity demand forecasting and sales volume prediction exists an inseparable and close connection. Demand forecasting offers profound insights into market dynamics and consumer preferences, while sales volume prediction substantiates the tangible manifestation of these trends. They are mutually reinforcing, collectively informing corporate strategic decision-making. In the context of rapidly evolving modern technology, significant strides in big data, cloud computing, and sophisticated computational storage and processing technologies have considerably streamlined the process of acquiring and managing vast datasets. This technological metamorphosis has laid a robust foundation for the application of machine learning in industry demand forecasting, positioning it as an efficient and practical solution within the domain [5]. In Kim's research, a comparative analysis was executed on the performance of two cutting-edge machine learning techniques - Extreme Gradient Boosting and Neural Networks - against traditional predictive models. The findings indicated that machine learning techniques consistently demonstrated superior predictive prowess [19]. Kharfan et al. combined machine learning techniques with in-depth analysis of historical product feature, adhering to the principle of similarity, providing fashion retailers with an effective tool to enhance the precision of demand forecasting [5]. Xu et al. proposed a sports apparel sales prediction model that integrates Multilayer Perceptron (MLP) and Convolutional Neural Network (CNN) technologies. This model encompasses a myriad of retail prediction factors, including time series sales data, product attributes, distribution strategies, and store dimensions [6].

2.2. POI embedding and aggregation technology

In the current landscape where data resources are proliferating, strategies for managing data pools are frequently viewed as effective methods to augment prediction efficacy. However, their success is contingent on the prominent data features and variables that substantially influence sales volume and potential demand [20]. To harness the full potential of this data, feature engineering becomes particularly crucial. Feature engineering not only facilitates the creation of novel features, thereby augmenting the explanatory potency in demand forecasting, but also during the process of feature selection, we can acquire an in-depth understanding of each feature's significance and its substantial effect on prediction precision [5]. Amidst this context, POIs are regarded by scholars as a valuable and readily available data source for augmenting regional attributes. Nonetheless, an exclusive reliance on POI categories might disregard a plethora of significant contextual information, which is vital for establishing interconnections between diverse POIs. Techniques for POI embedding, through the processes of dimensionality reduction and feature extraction, have the capacity to

encapsulate more comprehensive spatial context information. This enhances the model's capability to discern nonlinear relationships, consequently elevating the precision of predictions [21]. Furthermore, after POIs embedding, aggregation processing is frequently necessary. Achieving effective POI embedding in an unsupervised setting becomes particularly crucial. Therefore, this study incorporates POI embedding and aggregation techniques developed in previous research. Specifically, the method trains using a combination of Delaunay Triangulation (DT), random walks, and the Skip-gram model to obtain secondary category embeddings of POIs and employs an average pooling aggregation strategy for regional embedding to acquire enhanced high-dimensional feature representations.

2.3. Advantages of XGBoost in Prediction Tasks

The XGBoost algorithm, as an efficient, flexible, and highly portable gradient boosting classification algorithm, has significantly optimized the processing of structured data, computational efficiency, and the generalization performance of models. Moreover, optimizations in memory usage and support for distributed computing have enabled it to effectively handle large-scale datasets [22]. Therefore, when confronted with complex sales data, XGBoost can quickly provide accurate and easily interpretable prediction results, meeting the needs of commercial environments for rapid iteration and deployment of predictive models. For instance, Song et al. built a consumer purchase prediction model for an e-commerce platform based on the XGBoost algorithm, highlighting its application potential in the field of sales data analysis [23]. Choi et al. found that using XGBoost combined with median imputation to handle missing data could achieve the highest accuracy when comparing various machine learning algorithms for predicting future store revenues [24]. These studies further confirm the effectiveness and applicability of XGBoost in solving practical sales forecasting problems. Given its clear advantages in data processing and analysis, this study constructs a product sales forecasting model based on the XGBoost algorithm.

3. Methodology

3.1. Regional Division and Data Processing

To forecast product sales within a specific region, segmenting the area strategically is crucial. This segmentation necessitates a thorough assessment of the similarities and disparities among different areas. Drawing from empirical evidence, this research advocates for partitioning urban spaces into unit grids of 750 × 750 meters. Given that the population within each grid fluctuates over time, reliance on the population flow at any singular point in time as an indicative index is deemed inappropriate. Consequently, our study utilizes the average population flow over an extended period as an external data metric. Regarding POI data, it primarily encompasses information about structures such as commercial zones, hospitals, and educational institutions, which exhibit relative stability in the short run and can be readily incorporated as raw feature data inputs. The representational efficacy of regional attributes is augmented through the subsequent embedding process of POIs.

3.2. POI Embedding for Enhancing Regional Feature Representation

To more comprehensively capture spatial context information and further enhance the accuracy of sales forecasts, this study adopts the POI embedding and aggregation method proposed in previous research [18]. This method first applies the Delaunay Triangulation algorithm [25] to construct a network model, treating all POIs within the urban area as nodes to form a graph structure. The Delaunay triangulation algorithm is a widely used method for constructing geometric structures. It connects a series of discrete points into a triangular network, ensuring that the circumcircle of each triangle does not contain other nodes, thereby effectively capturing the spatial proximity relationships between points [25]. Then, it utilizes a spatially explicit random walk strategy (By simulating a random walk process on the graph to reveal the relationships between nodes, considering both spatial proximity and category similarity, it can better handle complex spatial relationships in the real world) to explore and exploit the category co-occurrence patterns between POIs. In this strategy, three types of transition biases are introduced. Specifically, α_d ensures that spatially adjacent candidate nodes are preferentially selected. Here, D represents the length of the diagonal of the minimum bounding rectangle formed by all POIs in the study area, and d denotes the spatial distance between two nodes p_2 and x. Moreover, $hop_{p,x}$ signifies the minimum number of hops required from p (the previous node) to candidate node x. Let $R = \{r_1, \ldots, r_n\}$ be a collection of n spatially disjoint regions, then r_i and r_k represent two distinct, non-overlapping regions in space.

Based on the above, the unnormalized transition probability from the current node p_2 to each candidate node x is calculated. The specific formula is shown as follows:

The first is an inverse-distance transition bias α_d:

$$\alpha_d(p_2, x) = \log\left(\frac{(1+D^{1.5})}{(1+d_{p_2,x}^{1.5})}\right) \tag{1}$$

The second transition bias α_b balances the local and long distance co-occurrence bias between POIs:

$$\alpha_b(p_2, x) = \begin{cases} \alpha_b^{loc}, & \text{if } hop_{p_2,x} = 0 \\ 1, & \text{if } hop_{p_2,x} = 1 \\ \alpha_b^{glob}, & \text{if } hop_{p_2,x} = 2 \end{cases} \tag{2}$$

The third transition bias α_r is defined as:

$$\alpha_r(p_{2,x}) = \begin{cases} 1, & \text{if } \{p_{2,x}\} \subseteq P_i \\ \alpha_r^{inter-region}, & \text{if } p_2 \in P_i \text{ and } x \in P_k \text{ and } r_i \neq r_k \end{cases} \tag{3}$$

The unnormalized transition probability is:

$$tp(p_{2,x}) = \alpha_d(p_{2,x}) \times \alpha_b(p_{2,x}) \times \alpha_r(p_{2,x}) \tag{4}$$

Subsequently, the proposed sampling strategy involves initiating multiple random

walks from each node, with the objective of capturing the hierarchical classification of POIs. Throughout this process, each POI is denoted by its respective second-level class, c_i^2. For every sampled sequence, the initial POI within the sequence is designated as the target category, whereas the remaining POIs within the sequence are regarded as context categories. To enhance the quality of the second-level class embedding for each POI, an approximate form of the skip-gram neural network model, which is based on negative sampling, is deployed to minimize the subsequent objective functions:

$$\mathcal{L}_{co-occurrence} \approx \sum_{c\in C^2} \sum_{c_q \in N_{R(c)}} -\left(\log\left(\sigma\left(\boldsymbol{c}^T \boldsymbol{c}_q'\right)\right) - \sum_{i=1}^{k} \log\left(\sigma\left(\boldsymbol{c}^T \boldsymbol{c}_{n_i}'\right)\right)\right) \quad (5)$$

Where σ represents the sigmoid function, c represents target embeddings; C^2 denotes the set of vector embeddings for the second-level categories; $\boldsymbol{c}_q$ stands for a specific neighbor node directly connected to node c; $R(c)$ represents the set of all nodes directly connected to c; $N_{R(c)}$ represents the set of context categories of c captured in the random walk; $\boldsymbol{c}^T$ indicates the transpose of vector c; c' represents context embeddings and c_{n_i} represents the categories obtained through the negative sampling process, that is, those categories that do not co-occur with c in the data [26, 27].

The training of the Skip-Gram model involves maximizing the log-likelihood of the context embedding of the Points of Interest (POI). Specifically, the objective function for model training is the cross-entropy loss. The formula is as follows:

$$L(\theta) = -\sum_{(w,c)\in D} \log\, p(c|w;\theta) \quad (6)$$

The function $L(\theta)$ denotes the loss function, where D comprises the collection of all positive sample pairs (w, c). In this context, w signifies the target word, c denotes the context word, and θ represents the model parameter.

After obtained the class embeddings of the POIs, this study employed average pooling technology to effectively integrate the POI embeddings into the respective regional grids. The fundamental principle of average pooling involves calculating the mean value of all POI embeddings within each grid region, thereby deriving a comprehensive feature representation for that area. This approach recognizes that each grid region contains a diverse set of POIs, with varying categories and quantities. To execute POI embedding effectively in an unsupervised setting, we utilized the average pooling technique to determine the feature representation of each grid region. By adopting average pooling technology, this study ensures optimal performance in the absence of supervision. Through this approach, we ultimately obtain a cumulative feature that comprehensively encapsulates all POI embedded information within the grid region, thereby providing a rich feature set for the subsequent prediction model, which in turn enhances the model's capability to capture spatial context information. To elucidate the step-by-step process of our method, we have provided the flowchart depicted in Figure 1.

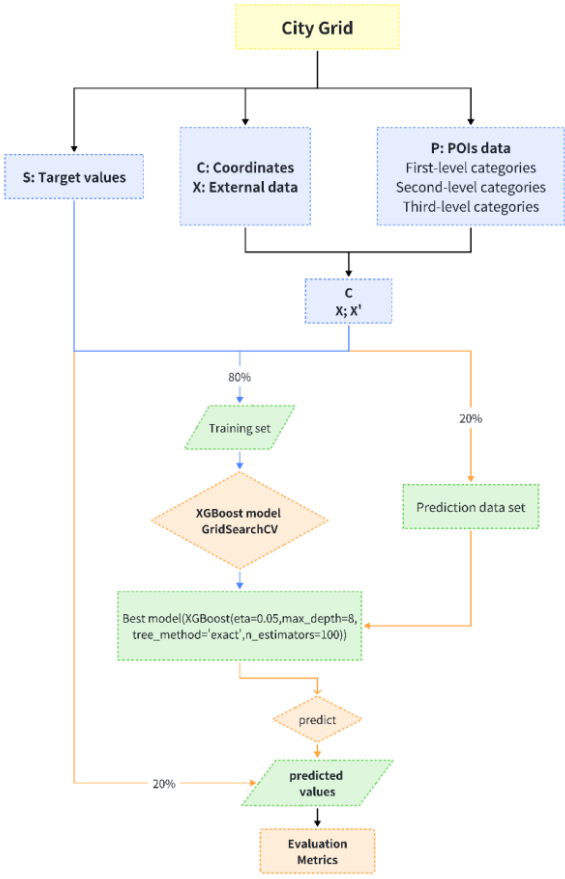

Figure 1. Flowchart of the Methodology.

4. Experiments

4.1. Experimental Setup

In the physical retail sector, cigarettes are considered a pivotal commodity due to their extensive consumer base and stable market demand. The high frequency of purchases, substantial consumer demographics, and the ongoing demand for sales data enable the effective mapping of consumer purchasing behavior patterns and market trends. These characteristics provide a reliable foundation for sales forecasting based on cigarette sales volume, which subsequently aids in enhancing the operational efficiency of retailers. Therefore, the utilization of cigarette sales data not only contributes to the improvement of physical retailers' operational efficiency but also possesses a certain representativeness, serving as a reference for the sales forecast of other commodities.

Datasets. We selected a dataset related to a specific cigarette product in Chongqing. In accordance with the grid division method previously outlined, the urban area of Chongqing was segmented into unit grids, each measuring 750m×750m, culminating in

the acquisition of 5,270 grid data points. These grid data points pre-exist in the database, and the dataset originates from an actual sales environment. The per-grid (buss-id) based dataset contains the following:

(1) C: Represents the grid coordinates selected from the center point of the grid, including longitude and latitude information. This dataset contains a total of 5270×2 data pieces of information.

(2) X: Represents external grid data, including consumer demographic attributes, retail business district attributes, urban business district economic and population attributes, as well as urban business district consumption level attributes, etc. This dataset contains a total of 5270×247 pieces of data information.

(3) S: Reflects the target predicted value of the model in the grid, reflecting the sales volume data within the grid. It contains a total of 5270 pieces of data information.

(4) P: Represents POIs data. Data is obtained through the Amap Open Platform API, and the original information is stored, resulting in categorized data. Each POI data includes the POI's longitude and latitude, as well as the POI's primary category, secondary category, and tertiary category, containing a total of 1098168 pieces of data information. Some examples are shown in Table 1.

Table 1. Amap POI Category Information Sample Table.

Number	Level 1 Category	Level 2 Category	Level 3 Category
1	Shopping Services	Specialty Store	Liquor and Tobacco Store
2	Shopping Services	Home Improvement Market	Hardware Store
3	Food and Beverage Services	Fast Food Restaurant	KFC
4	Food and Beverage Services	Chinese Restaurant	Sichuan Cuisine Restaurant
5	Accommodation Services	Hotel	Five-Star Hotel

The objective of this investigation is to confirm the efficacy of employing POI embedding features to augment the precision of sales forecasting. To attain this end, XGBoost has been chosen as the fundamental architecture for model training. By evaluating the impacts of diverse feature datasets on model training and prediction efficacy, and utilizing standardized datasets and assessment standards for control analysis, we guarantee the impartiality and trustworthiness of the experimental outcomes. In conclusion, we shall ascertain the most efficacious approach in practical application based on the experimental data, thereby offering a guideline for future research progression and model refinement.

Models. In this study, we adopted the XGBoost regression algorithm as the core method of the prediction model. The detailed process of the algorithm is described as follows:

1. Input and output.

(1) Input training sample set: $D = \{(x_1, y_1), (x_2, y_2), \dots, (x_N, y_N)\}$

(2) Output the final regression tree $f(x)$.

2. Model initialization.

Set λ, γ. Assumes that the initialization of weak learning $f_0(x_i) = c_i$, cost function $cost(c) = \sum_{i=1}^{N} L(y_i, c)$, the $c = argmin \sum_{i=1}^{N} L(y_i, c)$. When the loss function is a squared loss function, $c = \frac{1}{N} \sum_{i=1}^{N} y_i$. The initialization of the model will affect the iteration efficiency.

3. Iteration.

For $t = 1,2,\dots,T$ iteration:

(1) Calculate the negative gradient for the ith a sample, the negative gradient $r_{t,i} = -\frac{\partial L(y_i,f(x))}{\partial f(x)}|_{f(x)=f_{i-1}(x_i)}$. For regression algorithms, the commonly selected loss function is the squared loss function, that is $L\big(y,f(x)\big) = \frac{1}{2}\big(y-f(x)\big)^2$, then $r_{t,i} = y_i - f_{t-1}(x_i)$.

(2) The use of negative gradient generated regression tree: build a new data set using negative gradient $D_t = \{(x_1, r_{t,1}), (x_2, r_{t,2}), \dots, (x_N, r_{t,N})\}$. Calculate $g_{t,i}, h_{t,i}, i = 1,2,\dots,N$, compute G_j, H_j. The round decision tree $w_t(x)$ is generated according to the greedy algorithm. The region of the leaf node is $R_{t,j}, j = 1,2,\dots,J_t$, whose value $w_{t,j} = -\frac{G_j}{H_j+\lambda}$.

(3) Update the strong learner.

$$f_t(x) = f_{t-1}(x) + w_t(x) = f_{t-1}(x) + \sum_{j=1}^{J_t} w_{t,j} I\big(x \epsilon R_{t,j}\big) \tag{7}$$

If the termination condition is not satisfied, the iterative process persists. Invariably, during the execution of the model, the learning rate increments progressively.

(4) Finalization of the Learner.

In the Tth iteration, the process terminates when the value of the objective function falls below a predefined threshold or other specified termination criteria are satisfied (such as the maximum number of iterations, the performance metrics of the classifier on the training or test set, etc.).

$$f(x) = f_T(x) = f_0(x) + \sum_{t=1}^{T}\sum_{j=1}^{J_t} w_{t,j} I\big(x \epsilon R_{t,j}\big) \tag{8}$$

Test Scheme Design. In this study, we utilized three distinct external feature sets to train the model: external data only, a combination of external data and POI data, and a fusion of external data with embedded POI data. These datasets were incorporated into the XGBoost model for training, with 80% allocated for constructing the training model, while the remaining 20% was designated for validating the model's predictive accuracy. Furthermore, by employing GridSearchCV, we identified the optimal parameter configurations for the model as follows:

(1) eta=0.05: The learning rate of the model is 0.05.

(2) max_depth=8: The depth of each tree is 8.

(3) tree_method= 'exact': The decision tree is constructed with an exact method, that is, each slice of each feature is evaluated to find the best slice.

(4) n_estimators=100: There are 100 decision trees.

4.2. Evaluation Metrics

In this study, we have chosen Root Mean Square Error (RMSE), Mean Absolute Error (MAE), and the Determination Coefficient (R^2) as our primary evaluation criteria. These metrics collectively offer an in-depth and comprehensive assessment of the prediction model's performance. The RMSE and MAE provide insights into the accuracy of the predictions, while R^2 measures the model's capability to elucidate variations within the

dataset, ensuring a thorough and objective evaluation. A detailed breakdown of these indicators is as follows:

(1) RMSE: This metric is extensively employed for gauging the accuracy of continuous data predictions. It derives the square root of the mean of the squared differences between the predicted and actual observed values. A lower RMSE value indicates a reduced overall deviation between the predicted and actual values, signifying enhanced prediction accuracy within the model.

(2) MAE: This metric constitutes another prevalent evaluation measure for regression models, quantifying the average absolute discrepancy between the projected and actual values. A diminished MAE value reflects a decreased average divergence between the forecasted outcomes and the actual results, thereby corroborating a more dependable predictive performance of the model.

(3) R^2: Also recognized as the coefficient of determination, it serves as an indicator for assessing the extent to which a model elucidates the variance within the data. It is frequently utilized for appraising the model's adequacy of fit to the dataset. The R^2 value oscillates between 0 and 1, with values approaching 1 denoting an improved capacity of the model to interpret the data, consequently augmenting the confidence in the prediction results.

4.3. Prediction Results

In this research, a series of comparative experiments were designed to thoroughly assess the impact of diverse feature sets on prediction performance. We evaluated three distinct configurations of external feature sets: utilizing only external data, integrating external data with Point of Interest (POI) data, and merging external data with POI embedded data. The primary objective of these comparative analyses is to identify an optimal feature set combination strategy that will enhance the prediction model's performance in practical applications. The results of the performance evaluation indicators under each experimental configuration are presented in Table 2. The notations 'only_ext', 'with_poi', and 'with_emb' represent the use of solely external data, the combination of external data with POI data, and the integration of external data with POI embedded data, respectively. It was observed that the integration of external data with POI embedded data consistently delivered the best performance across all metrics. Specifically, this method resulted in improvements of 48.66% in RMSE, 42.24% in MAE, and 24% in R^2 compared to the use of external data alone, and 17.91% in RMSE, 16.75% in MAE, and 3.33% in R^2 compared to the combination of external data and POI data. This demonstrates that the utilization of POI embedding and aggregation technology to integrate multi-source external feature information can significantly enhance the precision of sales prediction.

Table 2. The results of evaluation metrics.

Feature Set	RMSE	MAE	R^2
only_ext	1329.69	561.67	0.75
with_poi	831.58	389.67	0.9
with_emb	**682.68**	**324.4**	**0.93**

Note: The best one is shown in bold.

To quantify the prediction accuracy of the model, this study employs a widely recognized evaluation index for data distribution concentration. The performance comparison chart indicates that a higher concentration of data points around the diagonal

correlates with increased prediction accuracy. Figure 2 vividly illustrates the model's prediction accuracy across three distinct feature set configurations. It is evident from the figure that the model, which integrates external feature data with Point of Interest (POI) embedded data (represented by green dots), significantly outperforms other configurations. This outcome not only substantiates the efficacy of the multi-source data fusion approach but also offers valuable insights for future feature engineering endeavors.

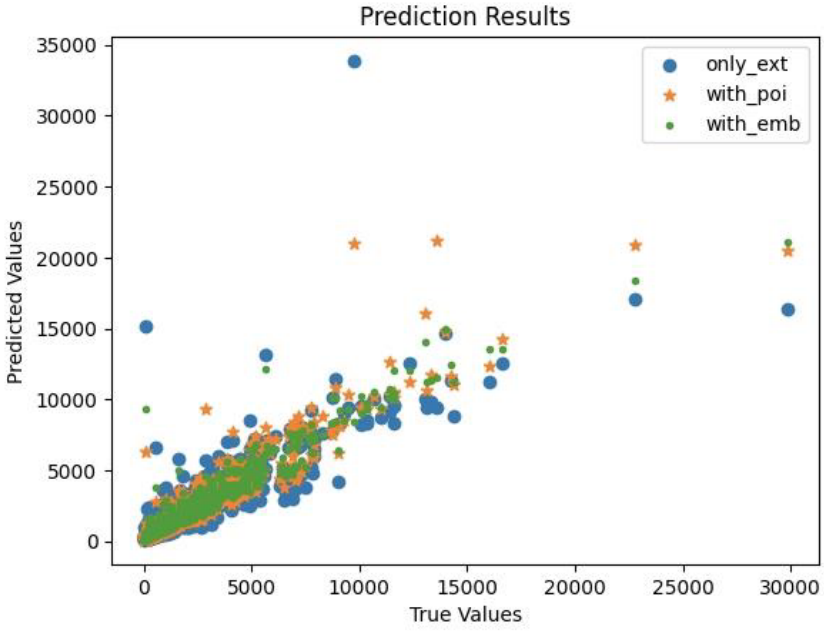

Figure 2. Comparison of Model Prediction Accuracy Under Different Feature Sets.

To further assess the predictive performance of the model, this study compares the discrepancies between predicted and actual values across various feature sets. This analysis facilitates a clear assessment of the impact of feature sets on the model's prediction accuracy. As depicted in Figure 3, the graph illustrates the disparities between the model's predicted values and the true values under different feature set configurations. In this plot, the x-axis represents the diverse data samples, while the y-axis denotes the variance - the deviation between the predicted and true values. The closer the deviation is to zero, the higher the concordance between the predicted and actual values, which directly mirrors the efficacy of the model's prediction. To more accurately illustrate the model's performance in most instances, we have included a supplementary comparison plot with extreme values excluded, as depicted in Figure 4. A comparative analysis of the various methods in both plots reveals that the accuracy of model predictions significantly improves as the feature set becomes increasingly comprehensive and refined. Notably, our method (represented by green markers) exhibits the smallest deviation, thereby demonstrating its superiority.

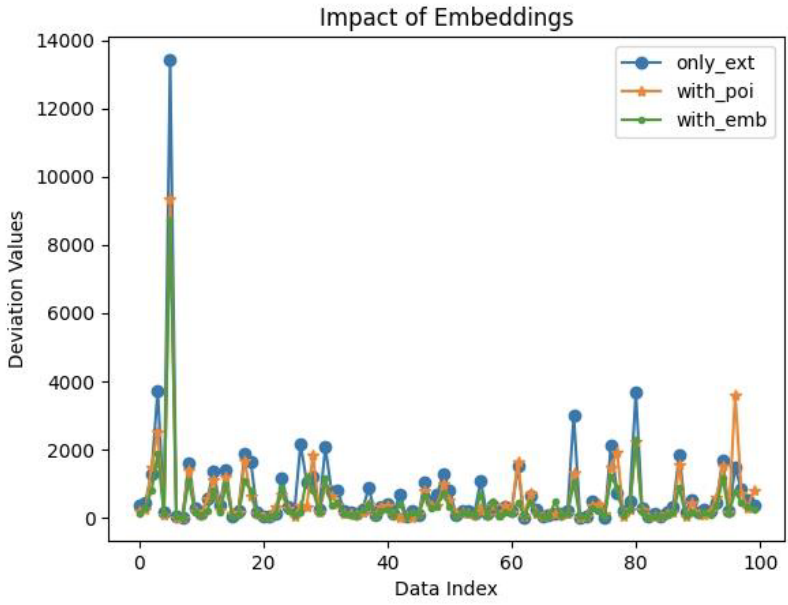

Figure 3. Comparison of Predicted and Actual Values Across Different Feature Sets.

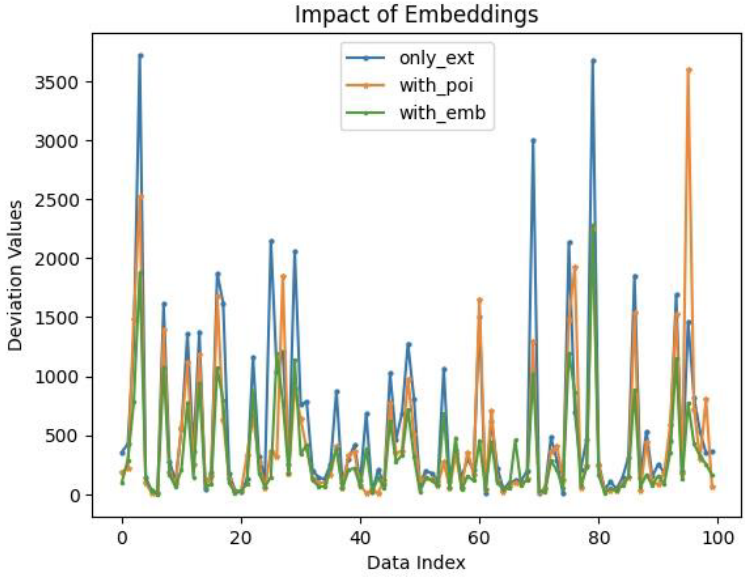

Figure 4. Comparison of Predicted and Actual Values Across Different Feature Sets after Removing Extreme Values.

5. Conclusion

Addressing the pivotal challenges in product sales forecasting within the physical retail sector, this paper proposes an innovative model that integrates multi-source data for

enhanced commodity sales prediction. Our research extends beyond internal sales data, tapping into the untapped potential of external information such as POI data. By employing embedding and aggregation techniques, we significantly augment the feature set accessible to our model. Moreover, the model is trained and refined using the XGBoost algorithm. The empirical outcomes robustly validate the efficacy of our approach, demonstrating that the amalgamation of diverse data sources coupled with embedded data fusion technology markedly enhances the predictive model's precision. In essence, the novelty of our study is anchored in the synergy between the XGBoost algorithm and the multi-source data fusion strategy, offering an innovative perspective and solution for forecasting commodity sales volumes. This research yields findings with substantial practical relevance and application potential, furnishing more precise data support for corporate strategic planning and aiding enterprises in sustaining a competitive edge in the intense market arena.

Despite the notable accomplishments of our study, certain limitations persist. Initially, although Point of Interest (POI) data has provided innovative insights for our model, potential valuable external data sources remain unexplored. Furthermore, the data fusion method utilized in this research has demonstrated commendable performance; however, it may not represent the most optimal solution. Additionally, our investigation was predominantly concentrated on specific categories of internal sales data and POI data. For diverse industries and retail establishments varying in size, the data fusion approach could necessitate meticulous adjustments and customization. Consequently, subsequent research endeavors should encompass the exploration of supplementary external data sources, such as social media tendencies and economic indicators. This exploration should go alongside the refinement of data fusion and feature engineering methodologies, as well as the use more advanced neural network models to enhance the model's precision and adaptability. Concurrently, it is imperative to consider an extensive array of datasets and industrial contexts to substantiate the model's versatility and practical application.

References

[1] Q. Q. He, C. Wu, and Y. W. Si, "LSTM with particle Swam optimization for sales forecasting," Electronic Commerce Research and Applications, vol. 51, Jan-Feb 2022, Art. no. 101118. doi: 10.1016/j.elerap.2022.101118

[2] Z. X. Guo, W. K. Wong, and M. Li, "A multivariate intelligent decision-making model for retail sales forecasting," Decision Support Systems, vol. 55, no. 1, pp. 247-255, 2013. doi: 10.1016/j.dss.2013.01.026

[3] A. Fumi, A. Pepe, L. Scarabotti, and M. M. Schiraldi, "Fourier Analysis for Demand Forecasting in a Fashion Company," International Journal of Engineering Business Management, vol. 5, 2013. doi: 10.5772/56839

[4] P. Ramos, N. Santos, and R. Rebelo, "Performance of state space and ARIMA models for consumer retail sales forecasting," Robotics and Computer-Integrated Manufacturing, vol. 34, pp. 151-163, 2015. doi: 10.1016/j.rcim.2014.12.015

[5] M. Kharfan, V. W. K. Chan, and T. F. Efendigil, "A data-driven forecasting approach for newly launched seasonal products by leveraging machine-learning approaches," Annals of Operations Research, vol. 303, no. 1-2, pp. 159-174, Aug 2021. doi: 10.1007/s10479-020-03666-w

[6] J. Xu, Y. Zhou, L. Zhang, J. M. Wang, and D. Lefloch, "Sportswear retailing forecast model based on the combination of multi-layer perceptron and convolutional neural network," Textile Research Journal, vol. 91, no. 23-24, pp. 2980-2994, Dec 2021, Art. no. 00405175211020518. doi: 10.1177/00405175211020518

[7] L. Andrade and C. B. Cunha, "Disaggregated retail forecasting: A gradient boosting approach," Applied Soft Computing, vol. 141, Jul 2023, Art. no. 110283. doi: 10.1016/j.asoc.2023.110283

[8] R. Sarlo, C. Fernandes, and D. Borenstein, "Lumpy and intermittent retail demand forecasts with score-driven models," European Journal of Operational Research, vol. 307, no. 3, pp. 1146-1160, Jun 2023. doi: 10.1016/j.ejor.2022.10.006

[9] N. Caglayan, S. I. Satoglu, and E. N. Kapukaya, "Sales forecasting by artificial neural networks for the apparel retail chain stores- An application," Journal of Intelligent & Fuzzy Systems, vol. 39, no. 5, pp. 6517-6528, 2020. doi: 10.3233/jifs-189115

[10] C. D. Kang, "Effects of Commercial Environments and Agglomeration on Retail Sales in Cluster Hierarchies: Evidence from Seoul, Republic of Korea," Journal of Urban Planning and Development, vol. 148, no. 4, Dec 2022, Art. no. 05022028. doi: 10.1061/(asce)up.1943-5444.0000866

[11] Z. B. Sojahrood and M. Taleai, "A POI group recommendation method in location-based social networks based on user influence," Expert Systems with Applications, vol. 171, Jun 2021, Art. no. 114593. doi: 10.1016/j.eswa.2021.114593

[12] J. Tang, J. Jin, Z. Miao, B. Zhang, Q. An, and J. Zhang, "Region-aware POI Recommendation with Semantic Spatial Graph," presented at the 2021 IEEE 24th International Conference on Computer Supported Cooperative Work in Design (CSCWD), 2021. doi: 10.1109/cscwd49262.2021.9437810

[13] S. G. Wang, "Point of Interest recommendation for social network using the Internet of Things and deep reinforcement learning," Mathematical Biosciences and Engineering, vol. 20, no. 9, pp. 17428-17445, 2023. doi: 10.3934/mbe.2023775

[14] W. Hamilton, Z. Ying, and J. Leskovec, "Inductive representation learning on large graphs," presented at the NeurIPS, 2017. https://dl.acm.org/doi/10.5555/3294771.3294869.

[15] P. Veličković, G. Cucurull, A. Casanova, A. Romero, P. Li`o, and Y. Bengio, "Graph Attention Networks," presented at the ICLR, Vancouver, Canada,, 2018. https://arxiv.org/abs/1710.10903.

[16] R. Ying, R. He, K. Chen, P. Eksombatchai, W. L. Hamilton, and J. Leskovec, "Graph Convolutional Neural Networks for Web-Scale Recommender Systems," presented at the KDD, London, United Kingdom, 2018. doi: 10.1145/3219819.3219890

[17] J. You, R. Ying, and J. Leskovec, "Position-aware Graph Neural Networks," presented at the ICML, 2019. https://arxiv.org/abs/1906.04817.

[18] C. Deng, X. X. Liang, X. Yan, Y. H. Mo, S. Bai, B. Lu, K. D. Chen, X. P. Liu, and Z. Chen, "Joint Urban Modeling With Graph Convolutional Networks and Crowdsourced Data: A Novel Approach," Ieee Access, vol. 12, pp. 57796-57805, 2024. doi: 10.1109/access.2024.3390156

[19] J. B. Kim, "Predicting Retail Consumers' Repeat Purchase Behaviors Using Machine Learning Methods," Korean Journal of Marketing, vol. 36, no. 3, pp. 133-147, 2021. doi: 10.15830/kjm.2021.36.3.133

[20] R. Fildes, S. Ma, and S. Kolassa, "Retail forecasting: research and practice," International journal of forecasting, 2020. doi: 10.1016/j.ijforecast.2019.06.004.

[21] L. Chen, L. Zhang, S. S. Cao, Z. Wu, and J. Cao, "Personalized itinerary recommendation: Deep and collaborative learning with textual information," Expert Systems with Applications, vol. 144, Apr 2020, Art. no. 113070. doi: 10.1016/j.eswa.2019.113070

[22] T. Chen and C. Guestrin, "XGBoost: A Scalable Tree Boosting System.," presented at the Proceedings of the 22nd ACM SIGKDD International Conference on Knowledge Discovery and Data Mining (KDD '16). New York, USA, 2016. doi: 10.1145/2939672.2939785

[23] P. Y. Song and Y. T. Liu, "An XGBoost Algorithm for Predicting Purchasing Behaviour on E-Commerce Platforms," Tehnicki Vjesnik-Technical Gazette, vol. 27, no. 5, pp. 1467-1471, Oct 2020. doi: 10.17559/tv-20200808113807

[24] J. Choi, H. Y. Yang, and O. H. A. Young, "Store Sales Prediction Using Gradient Boosting Model," Journal of the Korea Institute Of Information and Communication Engineering, vol. 25, no. 2, pp. 171-177, 2021. doi: 10.6109/jkiice.2021.25.2.171

[25] X. Yan, T. Ai, M. Yang, and H. Yin, "A graph convolutional neural network for classification of building patterns using spatial vector data," ISPRS Journal of Photogrammetry and Remote Sensing, vol. 150, pp. 259-273, 2019. doi: 10.1016/j.isprsjprs.2019.02.010

[26] T. Mikolov, I. Sutskever, K. Chen, G. Corrado, and J. Dean, "Distributed Representations of Words and Phrases and their Compositionality," Advances in Neural Information Processing Systems, vol. 2, pp. 3111-3119, 2013. https://arxiv.org/abs/1310.4546.

[27] W. Huang, L. Cui, M. Chen, D. Zhang, and Y. Yao, "Estimating urban functional distributions with semantics preserved POI embedding," International Journal of Geographical Information Science, vol. 36, no. 10, pp. 1905-1930, 2022. doi: 10.1080/13658816.2022.2040510

Fuzzy Systems and Data Mining X
A.J. Tallón-Ballesteros (Ed.)

doi:10.3233/FAIA241417

Knowledge Graph-Powered Question Answering System with Random Forest-Assisted Diagnosis for Elderly Healthcare

Yunlei Meng[a] and Rui Dai[a*]
[a] *School of Mathematics and Statistics, Beijing Technology and Business University, Beijing, China*

Abstract. As a knowledge representation tool, knowledge graph (KG) has been widely used. In this study, a question answering (Q&A) system for geriatric diseases based on knowledge graph was constructed to help the elderly obtain medical information. Initially, a total of 6,376 disease data items were collected and analyzed in order to identify the characteristics of these diseases. Then, the KG is constructed by Neo4j graph database. The establishment of Q&A system starts from semantic recognition. The Aho-Corasick (AC) automaton is utilized to filter user input questions. The Cypher language is employed for querying graph databases, and the obtained results are then imported into predefined templates for output. The accuracy of our system for different categories of questions is 87% and 94%, respectively. Finally, the random forest model is introduced to solve the problem of disease diagnosis. The feature variables were vectorized using TF-IDF model and the target variables were vectorized using one-hot model. In general, we introduce a novel Knowledge graph-driven Q&A system. Provide a new tool for health management of the elderly population. And the construction of Q&A system will promote the development of smart medicine and solves the health confusion of the elderly.

Keywords. medical knowledge graph, question answering system, random forest

1. Introduction

1.1. Background and Motivation

The Knowledge graph has received a lot of attention since it was proposed by Google in 2012. Knowledge graphs present knowledge in the form of triples that are easy to discover and reason about[1]. Knowledge graph-driven question answering systems appear in various vertical fields. For example, the knowledge map is constructed with the relationship between epidemic cases and personnel as the data source to visually and clearly present the complex information about the patients and their relationships[2]. In the field of insurance, entity extraction technology is used to build the insurance knowledge graph to realize the recommendation of life insurance knowledge and the query of life insurance product attributes[3].

* Corresponding Author: Rui Dai, Beijing Technology and Business University, Beijing, China; E-mail addresses: dr.dairui@hotmail.com

In addition, in the field of medicine, medical question answering systems utilize knowledge graph to store medical knowledge and provide accurate answers[4]. By integrating medical literature, clinical guidelines and expert knowledge, the medical knowledge graph containing various diseases, symptoms, drugs and other information is constructed. Provide basic data and knowledge support for question answering system. However, the current research mainly focuses on a certain type of diseases such as cardiovascular and cerebrovascular diseases[5]. Knowledge graph based on data from specific populations are still lacking. The elderly population has its particularity, even if some intelligent medical systems has been available, but there are still problems such as program, lack of personalization, real-time lag and so on[6][7]. Based on these problems, this study turns the face to knowledge graph-driven Q&A system to the elderly to provide them with real-time and accurate medical services.

1.2. Contributions

- Previous studies on knowledge graph were mostly based on a certain industry, but this study extends it to a certain group of people.
- This study sorted out an effective standard to classify diseases encountered by the elderly in real life.
- A large number of previous studies focused on the innovation of a certain method in the process of system construction, while this study completed the entire process from data to system construction.

1.3. Structure

Firstly, we collect data and analyze it with visual tools. Secondly, we construct the knowledge graph and build the question answering system based on it. Finally, the various parts of the system and their functions are as follows:

- Knowledge graph: Data is stored in Neo4j graph database and queried through Cypher.
- Semantic recognition module: Semantic recognition of user input questions, the specific process is AC automata word filtering[8].
- Classification model: The TF-IDF model and one-hot model were respectively used to vectorize the variables and then random forest classification model was trained.
- Answer retrieval and output module: Build Cypher statements to retrieve answers from KG and add them to the template for output.

2. Knowledge Graph

2.1. Data Acquisition and Analysis

The data comes from a project called QA Based on Medical Knowledge Graph on Github. The project data are uploaded by professional scientists and cover a wide range of disease information. The data of this project came from a disease-focused vertical medical website, which crawled data via python containing 44,000 knowledge entities and 300,000 entity relationships[9].

Data processing phase includes data cleansing, error filtering, entity identification and screening (e.g., disease, symptom, department), and attribute selection (e.g., disease description, symptom characteristics). The first step is to remove errors or missing information, such as large chunks of text or illogical text. The second step is the completion of information, complete the missing information by the Internet. The third step is the screening of the core entity that is the screening of diseases in the elderly[10]. The elderly were defined by age (≥ 65 years) and disease characteristics (e.g., cardiovascular disease, eye disease). It is classified according to its high incidence, impact on specific populations, impact on quality of life, and feasibility of prevention and treatment[11]. Through data collection, screening and classification, a total of 6,376 diseases were identified. Finally, for the screening of attribute data, the system in this study is not to provide a large number of disorganized information like a search engine, but to screen more useful information for display. Such as symptoms, appropriate food, avoid food, drugs, inspection departments and other attributes[12].

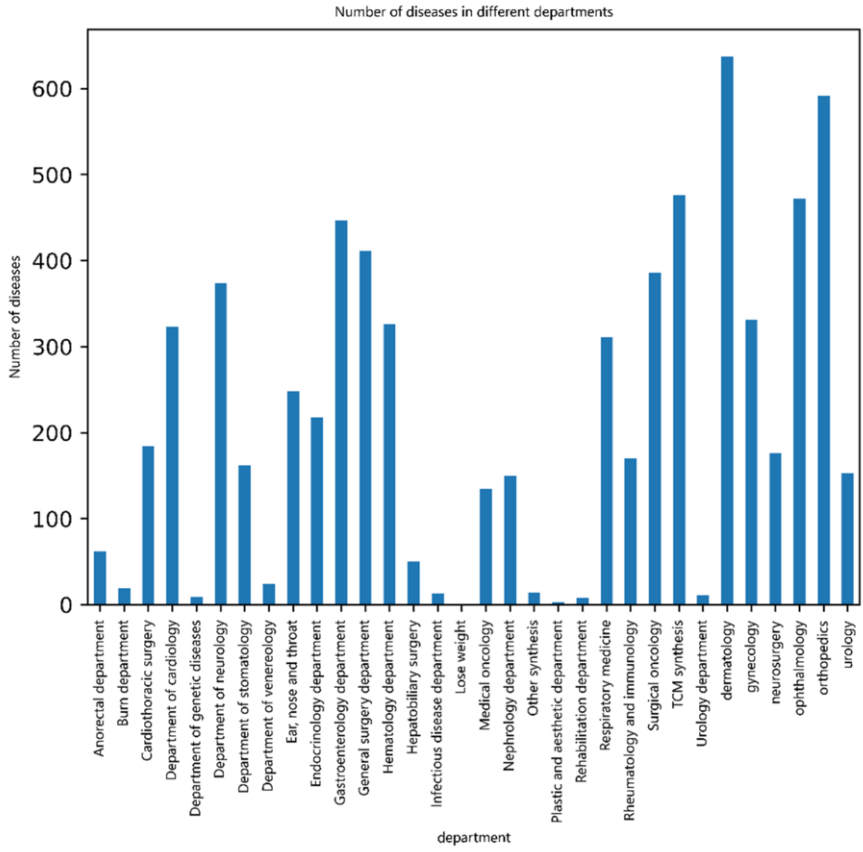

Figure 1. The figure shows the number of common diseases of the elderly in each department.

There is a lot of information in the disease data of the elderly. In order to optimize the allocation of medical resources and improve the efficiency of diagnosis and treatment, this study drew the distribution map of geriatric disease departments and analyzed their clustering in each department. Figure 1 shows the result. The diseases of the elderly are mainly concentrated in the departments of cardiology, respiratory medicine, neurology

and so on. Cluster analysis is helpful for medical institutions to optimize resource allocation, build professional medical teams, and improve the quality of diagnosis and treatment of senile diseases.

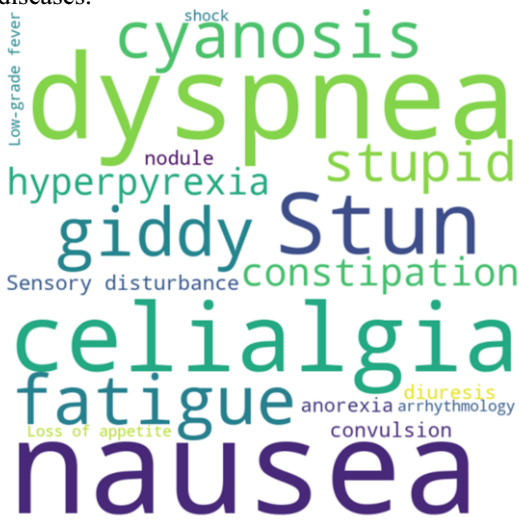

Figure 2. The figure shows the common symptoms of diseases in the elderly.

Data on disease symptoms in the elderly are also worth studying. Figure 2 shows that fatigue and difficulty breathing are common symptoms of disease in the elderly and are essential for early recognition. These symptoms are associated with multiple underlying diseases, which complicate diagnosis and treatment. It is necessary to consider a variety of factors and develop an individualized treatment plan to improve the diagnostic accuracy.

2.2. Knowledge Graph Construction

After statistical analysis of the data, it is necessary to process the triplet data suitable for constructing KG. This includes steps such as cleaning, standardization, normalization, and conversion of data. Clean data to ensure quality and accuracy, standardize uniform data formats, and transform data into triples to build knowledge graph[13]. In the E-R-E(Entity-Relation-Entity) pattern, entities represent concepts and relationships represent associations between entities. For example, in the film knowledge graph, entities are films, actors, directors, etc., and relationships are participating in and directing, etc. Complex association networks are established to explore entity relationships. In E-A-V(Entity-Attribute-Value) mode, an entity is a concrete object, attributes describe its characteristics, and attribute values represent specific values[14]. Figure 3 shows the basic units of the knowledge graph. For example, in the medical knowledge graph, the entity is disease, drug, symptom, etc., the attribute is name, dose, description, etc., and the attribute value corresponds to the specific value. By associating entities with attributes, attribute information can be stored and retrieved.

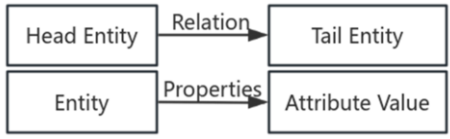

Figure 3. The figure shows the basic units of the knowledge graph.

The knowledge graph involved in the research is generally composed of interconnected entities and their properties[15]. A knowledge graph is a relational database that stores data in the form of graph. At present, most knowledge graphs involved in the research are made based on Neo4j graph database. Neo4j is a database management system based on graph database model, which stores and processes data in the form of graph and provides powerful graph database functions. Neo4j graph database is a powerful database system with many important features. First, it provides ACID (Atomicity, Consistency, Isolation, and Persistence) transaction support, ensuring data reliability and consistency. Neo4j's data model includes:

Node: indicates a node, including labels, attributes, attribute values, and ids.

Relation: Relation, including labels, attributes, attribute values, and ids.

Cypher is Neo4j's query language for graph data retrieval and manipulation, has been widely used because of its simple and intuitive syntax. This section uses Python's py2neo library and Neo4j graph database to build a medical KG.

The specific construction process is as follows: First, register the account of Neo4j graph database and connect with Python. Label the data after it is imported. Secondly, Cypher statement is used to construct the relationship between each label data. Finally, the database is retrieved, and the data are respectively popped into the knowledge graph model.

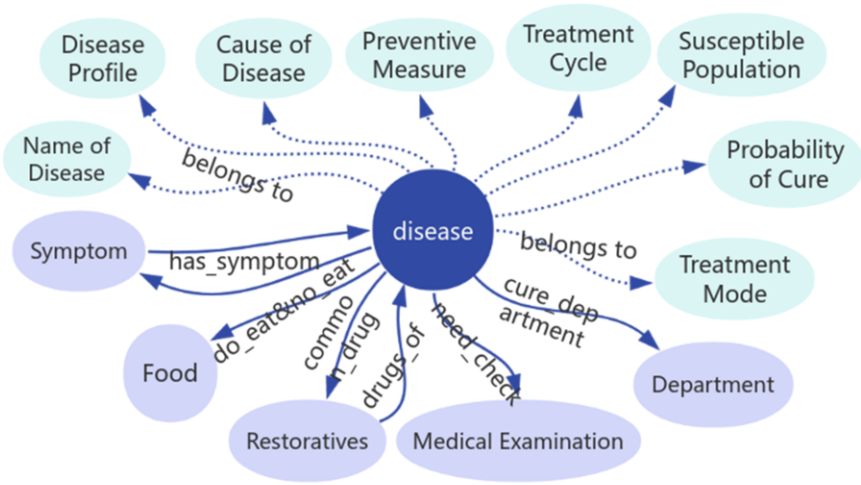

Figure 4. The figure shows all the entities, attributes, and relationships covered in this article. With the disease entity as the core, dotted arrows point to its attributes and solid arrows point to its associated entities.

Figure 4 shows the basic units of the knowledge graph in this study. Neo4j graph database supports the direct use of Cypher statements for data query and presentation. Figure 5 shows a visual example of the query results.

Figure 5. This figure shows the knowledge graph. The graph matches all nodes of the disease type named elderly diabetes and finds all nodes related to it. The right side of the database will provide the entity type, relationship type, and number of all retrieved contents. When you select an entity, the right section of the database displays the appropriate properties for that entity.

3. Q&A System

3.1. Q&A System Construction

The first step to construct a Q&A system is to judge the semantic meaning of the input[16]. In this study, the AC tree model is used to filter the problem, implemented through python's ahocorasick library, which is a string matching algorithm. The following details the specific process of building an AC automaton, there are two steps in simple terms:

1. Basic Trie structure: String all patterns together to form a Trie.
2. KMP: Construct failure Pointers for all nodes in the Trie tree. Then the AC automata can be used to implement the multi-pattern matching task. Figure 6 illustrates this process.

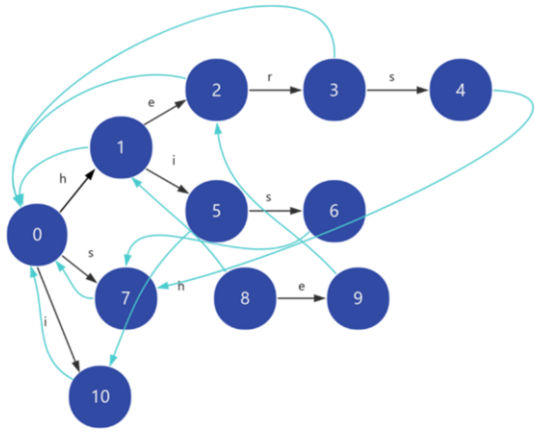

Figure 6. The figure shows how an AC automaton works. The following describes the pointing logic of failure Pointers, take node 6 as an example to illustrate the construction process of fail pointer: Find the parent node 5 of 6, fail[5]=10. But node 10 doesn't have an edge with the letter s; Continue to skip to the fail pointer of 10, where fail[10]=0. It is found that node 0 has an edge connected by the letter s, pointing to node 7; So fail[6]=7.

The filtering process is as follows: The first step is to construct a trie to filter the question word by word. The feature words required for trie are the data required for knowledge graph construction. Failure Pointers make filtering very efficient. The second step is the establishment of the question vocabulary, which requires manual input of various question words (such as what symptoms you have and what you can eat). The third step is to identify the keywords and question words in the question (some questions do not contain question words) and then pop them into the corresponding empty list. After successfully identifying the entity, intention and category in the question, type recognition is carried out[17]. For cases where the intention is not accurately identified, the disease description are returned if the entity is a disease, and the symptoms are returned if the entity is a symptom. Finally, after successfully identifying the type of the question, the corresponding Cypher statement is called and the query is executed. Table 1 shows an example of a cypher statement that performs answer retrieval after recognizing the question type.

Table 1. Example of a query statement.

Question Type	Sample Query Statement
Inquire about the cause of the illness	sql = ["MATCH (m: Disease) where m.name = '{0}' return m.name, m.cause".format(i) for i in entities]
Query the cure probability of the disease	sql = ["MATCH (m: Disease) where m.name = '{0}' return m.name, m.cured_prob".format(i) for i in entities]
Known food for disease	sql = ["MATCH (m: Disease)-[r:no_eat]->(n: Food) where n.name = '{0}' return m.name, r.name, n.name".format(i) for i in entities]

3.2. Random Forest

In the Q&A system based on KG, the random forest model is introduced to complete the classification task in order to improve the efficiency of disease diagnosis. Random forests are predicted by a combined decision tree model[18][19]. When we diagnose diseases in hospitals, in addition to using professional instruments for detection, doctors often pay attention to the patient's age, symptoms, past medical history and other factors. In this study, due to the limited data and considering the usefulness of variables, age and symptoms were selected as the characteristic variables for disease diagnosis. The age affects disease risk, and the symptoms are diagnostic clues. Because of the uniqueness of the disease data, a disease in most cases has only one professional name. Disease variables are vectorized by One-Hot Encoding, converting text data into vectors with the value of 1 for the location of the disease and 0 for the rest. The characteristic variables, age and symptoms, are disordered categorical variables (age is regarded as unordered here), so only the effective vectorization method for short text data is considered. TF-IDF model is the most widely used model to deal with this problem. The feature variables are vectorized using the TF-IDF model.

The numerical data is then trained and predicted using a random forest model, which consists of multiple decision trees that make decisions by voting or averaging the predicted results[20]. Table 2 illustrates these special visits and the target variables. Random forest is suitable for processing high-dimensional features and big data, and has good generalization ability and anti-overfitting ability, which is suitable for disease diagnosis. During the training of random forest model, the feature sparse matrix obtained

by TF-IDF model was taken as the feature variable, the disease vector was taken as the target variable, the proportion of test sets were 20% and 10% respectively, and the random number seed was 42.

Table 2. Examples of variables used by classification models.

Disease	Symptom_Features	Susceptible_Features
Chordoma	Sciatica	It occurs in the middle and old age of 50 ~ 60 years old
Squamous Cell Carcinoma	Epidermal Keratosis	It is most common in men over the age of 50

3.3. Results

In collecting real-life problems, we first categorize them. One is to diagnose the disease based on symptoms, and the other is to ask for various information about the disease[21].

Question Type 1 Example Question: What is the disease that causes sudden loss of memory and disorientation in the elderly?

Answer Sample Answer: Alzheimer's Disease

Question Type 2 Sample Question: What symptoms may indicate that you have heart disease?

Answer Sample Answer: Angina pectoris, shortness of breath, weakness, palpitations, etc

Once the question answer data is obtained, the question and answer are processed and identified through Python. When evaluating the accuracy of the question answering system, the physical match between the answer and the standard answer is taken as the criterion. Due to the text differences between the standard answer and the answer from Q&A system. The standard answer contains only the target word, while the system outputs the answer as a complete sentence. Only accuracy is selected. If the standard answer entity appears in the output answer, it is considered correct; Otherwise, it is an error. This approach is concise and intuitive, but it may overlook the nuances and grammatical correctness of the answers. Suitable for specific question answering tasks, other types of systems may require more evaluation indicators.

Table 3. Results of accuracy evaluation of question answering system.

Question Type	Total Number of Questions	Correct Answers	Accuracy Rate
Type 1	114	99	0.87
Type 2	115	108	0.94

The results of the evaluation in Table 3 show that the system responded well to 229 questions. Of the 114 questions asked about the disease, 87 percent were accurate; Of the 115 questions that asked about attributes, 94 percent were accurate. The system can provide users with accurate information, meet the query requirements of diseases and attributes, and show high reliability and usefulness. We also conducted research on incorrect questions. Research has found that a large portion of the errors from inaccuracies in the wording.

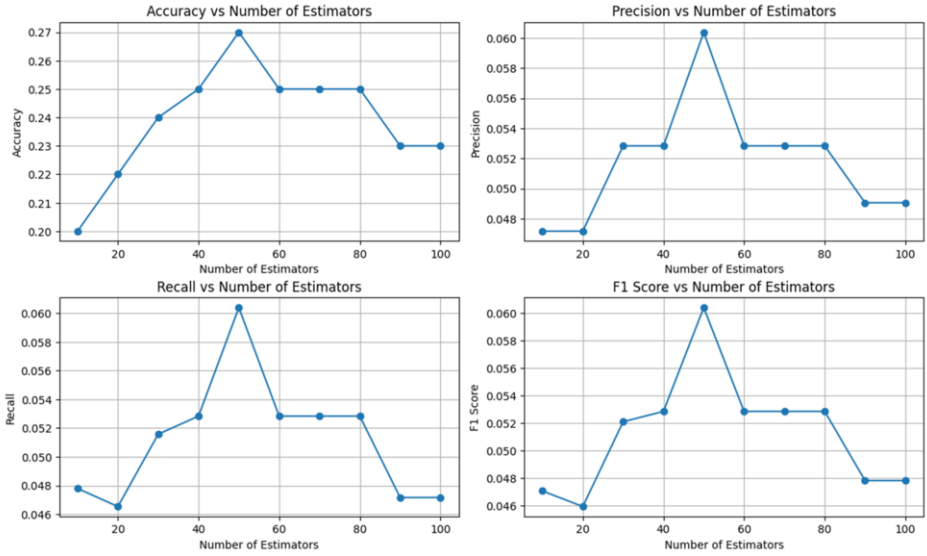

Figure 7. This figure shows the effect of the model with different number of decision trees.

The parameter setting of the random forest model has a great influence on the results. Figure 7 shows the effect of the model with different number of decision trees. We can see that when the number of decision trees is 50, the four indicators all present good results.

Table 4. Evaluation results of random forest model.

Test-Size	0.1	0.2
accuracy	0.62	0.59
precision	0.91	0.91
recall	0.62	0.59
f1	0.73	0.71

Table 4 show that the model has a low accuracy and recall in disease prediction, but a high precision. The F1 value is medium, indicating that the model has certain forecasting ability, but it still needs to be improved. We will continue to optimize the model parameters and increase the training sample size to improve the model performance. Figure 8 shows the interface of the Q&A system constructed in this study.

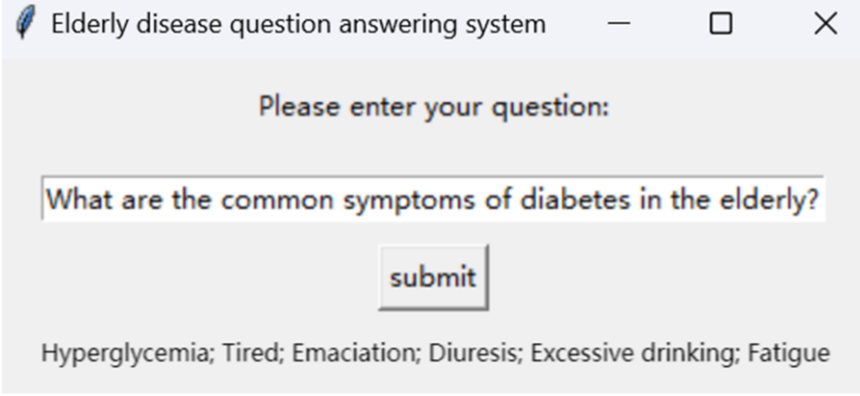

Figure 8. The figure shows the page of the question answering system. Enter the question in the input box and click Submit to get the answer.

4. Conclusion and Discussion

4.1. Summary

With the increase of the elderly population, medical resources are becoming increasingly scarce. We propose a knowledge graph-driven system to solve this problem. Based on Neo4j graph database, the Q&A system of elderly diseases is constructed. AC tree and Cypher query were used to achieve efficient question-answering, and random forest model was introduced to assist diagnosis. Finally, the results verify the good performance of the question answering system.

4.2. Limitation

Firstly, the data involved in this study is limited, and the data expansion module has not been built. Due to the limitation of equipment performance, the amount of data used in this study does not meet the standard of building a large-scale question answering system. Secondly, this study does not propose some effective algorithm improvement schemes. Finally, this study only completed a single round of questions and answers, and could not conduct multiple related questions and answers.

4.3. Future Work

In the future, we will continue to pay attention to the users in order to timely update the system. In addition, with the continuous updating of technology, we also expect to update the semantic recognition and vectorization tools used in this research to obtain higher accuracy. Finally, the issue of data privacy should also be paid attention to, and the data involved in this system should have a good protection to avoid information disclosure.

References

[1] Wu X, Duan J, Pan Y, Li M. Medical knowledge graph: Data sources, construction, reasoning, and applications. Big Data Mining and Analytics. 2023, 6(2): 201-217, doi: 10.26599/BDMA.2022. 9020021

[2] Ji S, Pan S, Cambria E, Marttinen P, Philip SY. A survey on knowledge graphs: Representation, acquisition, and applications. IEEE transactions on neural networks and learning systems; 2021 Apr 26; c2021. p. 494-514, doi: 10.1109/TNNLS.2021.3070843

[3] Zou X. A survey on application of knowledge graph. Journal of Physics: Conference Series. 2020, 1487(1): 012016, doi: 10.1088/1742-6596/1487/1/012016

[4] Ren Y, Shi Y, Zhang K, Chen Z, Yan Z. Medical treatment migration prediction based on GCN via medical insurance data. IEEE Journal of Biomedical and Health Informatics; 2020 Jul 10; c2020. p. 2516-2522, doi: 10.1109/JBHI.2020.3008493

[5] Li J, Liu J, Liu X, Yang F, Xu Y. A medical insurance fraud detection model with knowledge graph and machine learning. International Conference on Computer Application and Information Security (ICCAIS 2021); 2021; Wuhan, China: SPIE Press. c2022. p. 12260: 531-540, doi: 10.1117/12.2637418

[6] Bekoulis G, Deleu J, Demeester T, Develder C. Joint entity recognition and relation extraction as a multi-head selection problem. Expert Systems with Applications. 2018, 114: 34-45, doi: 10.1016/j.eswa.2018. 07.032

[7] Chandak P, Huang K, Zitnik M. Building a knowledge graph to enable precision medicine. Scientific Data. 2023, 10(1): 67, doi: 10.1038/s41597-023-01960-3

[8] Yang R, Ye Q, Cheng C, Zhang S, Lan Y, Zou J. Decision-making system for the diagnosis of syndrome based on traditional Chinese medicine knowledge graph. Evidence-Based Complementary and Alternative Medicine. 2022, 2022, doi: 10.1155/2022/8693937

[9] Wu X, Zhu X, Wu GQ, Ding W. Data mining with big data. IEEE transactions on knowledge and data engineering; 2013 Jun 26; c2013. p. 97-107, doi: 10.1109/TKDE.2013.109
[10] He B, Guan Y, Dai R. Classifying medical relations in clinical text via convolutional neural networks. Artificial intelligence in medicine. 2019, 93: 43-49, doi: 10.1016/j.artmed.2018.05.001
[11] Petkovic D, Altman R, Wong M, Vigil A. Improving the explainability of Random Forest classifier–user centered approach. In Pacific symposium on biocomputing 2018: proceedings of the pacific symposium. 204-215, doi: 10.1142/9789813235533-0019
[12] Guo Q, Zhuang F, Qin C, Zhu H, Xie X, Xiong H, He Q. A survey on knowledge graph-based recommender systems. IEEE Transactions on Knowledge and Data Engineering; 2020 Oct 07; c2020. p. 34(8): 3549-3568, doi: 10.1109/TKDE.2020.3028705
[13] Li L, Wang P, Yan J, Wang Y, Li S, Jiang J, Sun Z, Tang B, Chang T, Wang S, Liu Y. Real-world data medical knowledge graph: construction and applications. Artificial intelligence in medicine. 2020, 103: 101817, doi: 10.1016/j.artmed.2020.101817
[14] Gong F, Wang M, Wang H, Wang S, Liu M. SMR: medical knowledge graph embedding for safe medicine recommendation. Big Data Research. 2021, 23: 100174, doi: 10.1016/j.bdr.2020.100174
[15] Zhao C, Jiang J, Xu Z, Guan Y. A study of EMR-based medical knowledge network and its applications. Computer methods and programs in biomedicine. 2017, 143: 13-23, doi: 10.1016/j.cmpb. 2017.02.016
[16] Yin Y, Zhang L, Wang Y, Wang M, Zhang Q, Li G. Question answering system based on knowledge graph in traditional Chinese medicine diagnosis and treatment of viral hepatitis. BioMed research international. 2022, 2022, doi: 10.1155/2022/7139904
[17] Chai X. Diagnosis method of thyroid disease combining knowledge graph and deep learning. IEEE Access; 2020 Aug 14; c2020. p. 149787-149795, doi: 10.1109/ACCESS.2020.3016676
[18] Lei Z, Sun Y, Nanehkaran YA, Yang S, Islam MS, Lei H, Zhang D. A novel data-driven robust framework based on machine learning and knowledge graph for disease classification. Future Generation Computer Systems. 2020, 102: 534-548, doi: 10.1016/j.future.2019.08.030
[19] Teng F, Yang W, Chen L, Huang LF, Xu Q. Explainable prediction of medical codes with knowledge graphs. Frontiers in bioengineering and biotechnology. 2020, 8: 867, doi: 10.3389/fbioe.2020.00867
[20] Li Z, Geng P, Cao S, Hu B. Few-shot knowledge graph completion based on data enhancement. International Conference on Bioinformatics and Biomedicine (BIBM); 2022 Dec 06-08; Las Vegas, NV, USA: IEEE Press; p. 1607-1611, doi: 10.1109/BIBM55620.2022.9995024
[21] Tao X, Pham T, Zhang J, Yong J, Goh WP, Zhang W, Cai Y. Mining health knowledge graph for health risk prediction. World Wide Web. 2020, 23: 2341-2362, doi: 10.1007/s11280-020-00810-1

Fuzzy Systems and Data Mining X
A.J. Tallón-Ballesteros (Ed.)

doi:10.3233/FAIA241418

An Improved Swin Transformer with Dilated Convolution for Fault Classification of Transformer Substation

Zhiliang Lu[a], Hua Zheng[a,1] and Cheng Jiang[a]
[a] *CSG AI Technology Co., Ltd., Guangzhou, China*
ORCiD ID: Zhiliang Lu https://orcid.org/0009-0008-3105-3128
Hua Zheng https://orcid.org/0009-0006-0402-129X
Cheng Jiang https://orcid.org/0009-0002-9417-6383

Abstract. Defect detection of substation equipment components is an indispensable part of grid security situational awareness, and the regular inspection of equipment is related to the secure operation of the power system. For the current problem of low recognition accuracy of the defect classification model of substation equipment components, this paper proposes a defect classification method based on the improved Dilated Convolution Swin Transformer (DC-Swin). First, an improved Dilated Convolution Self-Attention Module is constructed for extracting the regions of equipment components that contain rich defect-specific information; Secondly, this paper constructs an image dataset using infrared imaging of defects of equipment components to pre-train the module, which enables the Self-Attention Module to learn the important regions in the image and reduces other ineffective information interfering with the model; Finally, this paper incorporates pre-trained modules, which have undergone preliminary training on flawed infrared imaging datasets, with the Swin Transformer, specifically in the channel dimension. By seamlessly integrating crucial feature regions into the original image, the network model is empowered to delve deeper into the intricate dependencies among various features, resulting in an enhanced and more discriminative feature representation capability. The proposed method improves the accuracy by 6.17% compared to the original Swin Transformer model. The results show that the method achieves the optimal utilization of the defect classification model on the acquired dataset and provides a solid foundation for substation safety situational awareness.

Keywords. Transformer substation, Fittings fault classification, Swin Transformer, Dilated convolution

1. Introduction

Transformer substations are integral components of the power system, tasked with converting and distributing electrical energy. They accomplish this by transforming high-voltage electrical energy into low-voltage electrical energy, making it suitable for use in residential and commercial settings. Ensuring the safety of transformer substations is crucial for maintaining the stability and security of the power supply [1]. Identifying and categorizing defects in transformer substation components is a highly important step.

[1] Corresponding Author, Hua Zheng, CSG AI Technology Co., Ltd., Guangzhou, China; Email: zhenghua@csg.cn

Numerous studies have been conducted on the classification of external defects in transformer substation equipment. These defects include metal corrosion, meter breakage, oil leakage from equipment, suspended objects (such as foreign objects), discoloration of breather silicone, and oil leakage from the breather. How to establish a classification system of external defects of Transformer substation equipment to timely detect and eliminate these safety hazards that affect the normal operation of Transformer substation equipment is the direction of future in-depth investigation [2].

In this paper, an image enhancement + image defect classification vision scheme based on deep learning is designed. The model is pretrained by the collected infrared images of Transformer substation fittings, which enhances the model's ability to learn the key features of the fittings and solves the problem that the model is unable to extract the key features under the complex environment; the model's ability to learn at multiple scales is enhanced by the introduction of the Dilated Convolution Self-Attention module; the model's ability to learn at multiple scales is improved by incorporating the Dilated Convolution Self-Attention module with the Swin Transformer feature channel on the splicing, to solve the Transformer substation fittings are many types, classification accuracy is difficult to meet the actual needs of the difficult problem, so that the classification model to meet the different fittings complex scenarios, for the inspection to achieve the real-time state identification of fittings defects to provide a stable Support.

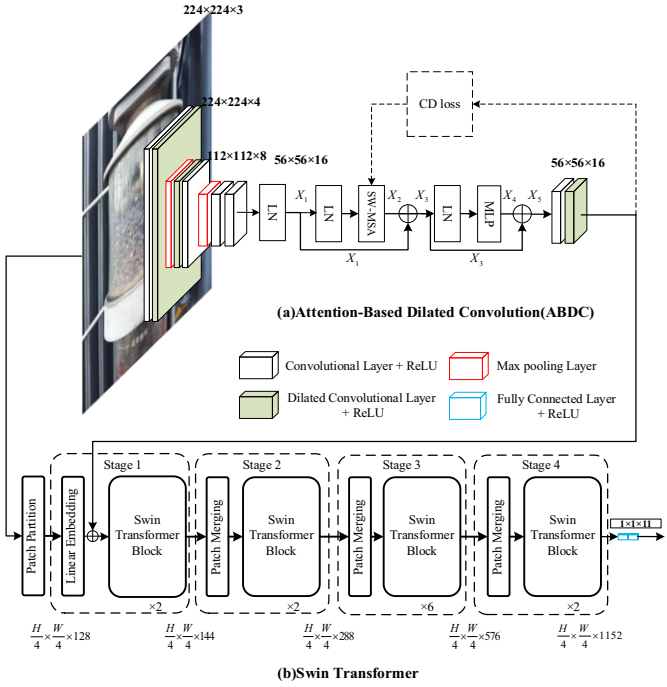

Figure 1. Dilated Convolution Swin Transformer

2. Related Work

With the increasing application of computer vision technology in the field of power detection, the application of deep learning neural network model based on self-attention mechanism for substation detection becomes more and more widespread, most of the existing research on the classification of defects in substation components focuses on defects such as substation breathers, meters, insulators, bird nests and so on [3]. The methods for classification and detection of defects are also gradually increasing, and currently there are mainly image processing methods, machine learning methods and deep learning methods[4]. In the literature [5], an R-FCN-based target detection method for fittings is improved on the basis of full convolutional network by using online difficult sample mining, soft non-maximum suppression, sample optimization, etc., which improves the detection accuracy and makes the model adaptable to the multi-type and multi-scale target detection task. However, the method has high requirements on the dataset, and the detection accuracy is not stable. Literature [6] used a deep learning target detection model SSD [7] to realize the identification and localization of transformers on the basis of extracting the deep features of substation images; furthermore. In literature [8], a deep convolutional neural network (DCNN) based on transfer learning is utilized to identify various typical incipient faults in electrical substation equipment. Initially, high-dimensional features of the electrical substation equipment images are extracted using classical pre-trained DCNN architectures through the transfer learning approach. Subsequently, the fully-connected (FC) neural network, employing the SoftMax activation function, classifies these different incipient faults. Literature [9] replaces the feature extraction network on the original Faster R-CNN model with SCNet and proposes the PinFPN network to enhance the model's ability to extract the underlying semantic and location information, but it also causes an increase in the number of references and the amount of computation, which raises the requirements for the equipment. Literature [10] proposes to use the multi-scale pre-trained YOLOv3 target detection network to frame and intercept the bird-proof spurs region in the sharpened power inspection image, and then process the intercepted bird-proof spurs region to realize the bird-proof spurs fault detection.

Although the above models have achieved more effective results in the defect classification of certain parts of the substation, they are conducted under the condition of limited dataset, which ignores the problem that the models have weaker feature learning ability under the real complex conditions. Evidently, there are two urgent difficulties to be resolved in the state recognition of substation high-voltage electrical control cabinets: firstly, the substation fittings that require recognition, including four types of breathers, meters, insulators, and bird's nests; the former two types of images are prone to color distortion in the case of strong light, and it is difficult to identify the switching state condition. The latter two types of images have the problems of weak light source, poor visibility, and high noise interference. Secondly, the meter device display screen, protective device indication area, etc. require more types of recognition, and require both real-time and accuracy.

3. DC-Swin

In order to classify substation defect images more accurately, this paper proposes an improved cavity convolution Swin Transformer based model (DC-Swin), which contains

two kinds of modules, namely, dilated convolution self-attention module and Swin Transformer module.

3.1. Dilated Convolution Self-Attention Module

Dilated Convolution Self-Attention Module starts with the part of convolution as the core of the module, first of all, the image information is input to a layer of convolution kernel size of 3×3 and a layer of Dilated Convolution, the dilated convolution was fixed to 2 dilation, and its convolution kernel step size is setting to 1 pixel, and in order to ensure that the spatial resolution remained unchanged after the convolution operation, the cavity convolution was spatially filled. The module after the two convolutional layers was the max- pooling convolution, with a step size of 2 for the max-pooling layer, which was processed through a pixel window to maximize the pooling of the convolutional layer inputs. Subsequently the image information again passes through the same configuration of convolution layer, dilated convolution layer and maximum pooling layer as above, at which point the image information undergoes preliminary processing in the convolution layer. In order to enable the image information to be integrated with the information from the Swin Transformer in the later stages, the information is fed into two convolutional layers with a convolutional kernel size of 3×3. In all the convolutional layers, the rectification nonlinearity is deployed at the later side. After completing the convolutional processing, the later module is the self-attention mechanism part. The output of a single self-attention mechanism is shown below:

$$S_{n_1} = soft\max\left(\frac{Q' \cdot K'^{T}}{\sqrt{c_K}}\right) \cdot V \tag{1}$$

Finally, the information output from the self-attention mechanism is again passed through two convolutional layers with convolutional kernel size of 3×3. At this point, the final information matrix obtained is the final output of the Dilated Convolution Self-Attention Module.

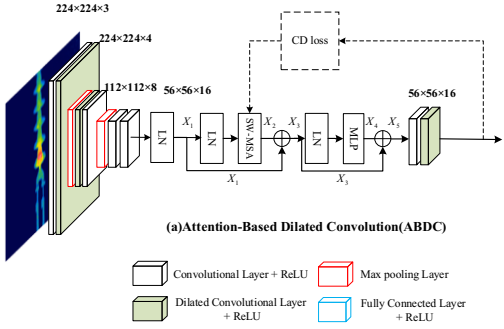

Figure 2. Dilated Convolution Self-Attention Module

3.2. Swin Transformer Module

Swin Transformer model based on the moving window multi-head self-attention mechanism is a new direction in computer vision research in recent years. Swin Transformer successfully realizes the effective capture and extraction of long-dependent features and global contextual information through its unique self-attention mechanism and hierarchical feature extraction approach. Its superior performance is not only due to its ability to capture long dependency features, but also due to its ability to deeply explore and integrate global context information through its self-concern mechanism. Swin Transformer will first process the image initially, split the image into independent patches, enter these patches into the Swin Transformer Block for information exchange between patches, and then downsample the image through the Patch Merging layer and then through the same Swin Transformer Block for information exchange between patches. After multiple downsampling and multi-head self-attention mechanism, the model realizes multi-scale self-attention computation, which enables the model to learn multi-scale information of the image, and extract more powerful information by fusing and extracting the features learned by the model and learning the relationship between different features of the image. Figure 1 shows the structure of Swin Transformer model.

In this paper, we propose a novel approach that integrates the Dilated Convolution Self-Attention Module and the Swin Transformer Module. Specifically, the size of the information matrix after processing of the original image information by the Dilated Convolution Self-Attention Module is changed to $56 \times 56 \times 16$, while the Linear Embedding layer of the Swin Transformer Module is changed to $56 \times 56 \times 128$ after processing of the original image information. By concatenating these two outputs along the channel dimension, we achieve a combined feature representation that preserves both the original input image's structure and features, while also incorporating features that have been processed by the shallow convolutional layer and the multi-head attention mechanism of the Swin Transformer. This stitching operation ensures that the fused representation contains a rich mix of local and global contextual information, which can enhance the model's ability to capture complex patterns and relationships within the data.

3.3. Loss function

During the course of the experiment, there may have been significant overlap between the self-attention probes, especially in the information-dense regions, where the self-attention probes were focused on some of the most obvious areas of the fittings features. This overlapping phenomenon between self-attention probes may lead to a waste of learning resources and can cause the model to ignore other important fittings features. To alleviate this overlap problem, this paper introduces a new overlap function, CDLoss, by using the application of this loss function to guide model training. The overlap loss function CDLoss is shown in Eqs. 2 as follows.

$$L_{CDLoss} = \sum_{\substack{n_1, n_2 \\ n_1 \neq n_2}}^{n} \sum_{h'}^{h} \sum_{w'}^{w} \frac{S_{n_1}(h', w')}{V_{n_1}} \cdot \frac{S_{n_2}(h', w')}{V_{n_2}} \tag{2}$$

In the multi-head attention mechanism, each probe functions independently, generating a unique weight matrix that signifies the focal region it attends to. This weight

matrix is a precise reflection of the region's significance, where richer fittings-specific information corresponds to a larger magnitude in the matrix. Crucially, when the overlap loss, calculated as the product of all these weight matrices, reaches zero, it signifies a distinct absence of overlap between the regions of interest captured by different probes. This absence of overlap ensures that the multiple attention probes are not redundantly focusing on the same area simultaneously, thus optimizing the model's ability to extract diverse and complementary features from the input data.

In this paper, we use the cross-entropy loss function as the loss function for single classification, and the total loss function is Eq3:

$$Loss = \sum_x s(x_i) \times \log_2 \frac{1}{s(x_i)} + \lambda * \sum_{\substack{n_1, n_2 \\ n_1 \neq n_2}}^{n} \sum_{h'}^{h} \sum_{w'}^{w} \frac{S_{n_1}(h', w')}{V_{n_1}} \cdot \frac{S_{n_2}(h', w')}{V_{n_2}} \tag{3}$$

4. Experimental Evaluation

4.1. Datasets

This paper presents a comprehensive collection and curation of aerial images captured by unmanned aerial vehicles (UAVs). Following rigorous data screening, a Transformer-based substation equipment dataset was constructed, focusing on various critical fittings within power substations. The dataset encompasses 11 distinct types of fittings, such as breathers, wattmeters, and insulators, totaling 8562 high-quality images. To facilitate experimental evaluation, the dataset was divided into a training set and a validation set, adhering to a 4:1 ratio. Figure 3 provides a visual representation of some sample images from this diverse dataset, showcasing the variability and complexity of the substation equipment. The detailed composition of the dataset, including the breakdown of images per fitting type, is outlined in Table 1, offering a comprehensive overview of the dataset's structure and content.

Table 1. Transformer substation equipment dataset

Fittings	Nums	Fittings	Nums
Breathers with iron shell (normal)	1637	Rusty Fittings	1737
Breathers with iron shell (discoloured)	1042	Normal wattmeter	531
Breathers without iron shell (normal)	160	Blur wattmeter	107
Breathers without iron shell (discoloured)	306	Broken wattmeter	125
Glass insulator without coating	334	Bird nest	1799
Insulator self-explosion	784		

Figure 3. Examples of fittings

This paper also gathers aerial infrared imaging via unmanned aerial vehicles. Following data screening, an infrared image dataset of substation equipment is assembled. Comprising 1682 images, this dataset encompasses 11 types of accessories, including transformers and insulators. Refer to Figure 4 for a few illustrative images from the dataset. In the task of infrared image recognition, since the characteristics of infrared images (e.g., gray value distribution, texture features, etc.) are different from those of visible light images, it is often difficult to achieve the desired recognition effect by applying the traditional model directly or without pre-training. Therefore, we use the infrared image dataset to pre-train the model so that the model can learn the feature representation specific to infrared images.

During the pre-training process, the model gradually learns how to extract key information from infrared images and associate this information with corresponding labels (e.g., different kinds of substation equipment accessories) through continuous iteration and optimization. This process not only enhances the model's ability to adapt to infrared image data, but also improves the model's ability to generalize to unknown data.

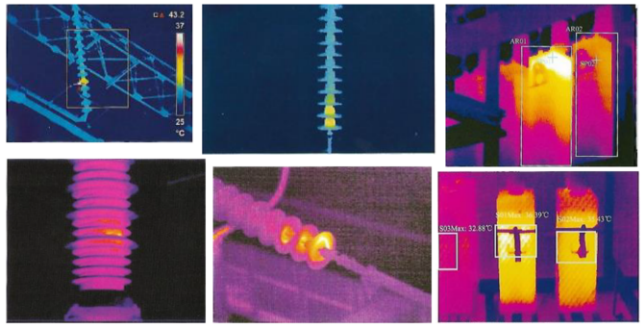

Figure 4. Examples of infrared fitting

4.2. Experimental Results and Analysis

In the experiment, we conducted a comparative analysis of our model with several other classification models, utilizing the gathered dataset. To highlight the distinct advantages

of our approach, we adopted the Single Classification Accuracy metric as a quantitative measure of model performance. The resulting qualitative experimental outcomes are presented in Table 2.

Table 2. Experimental comparison of different models

Method	Acc(%)
AlexNet	69.81
VGG16	73.48
Resnet18	76.12
Resnet34	78.66
Resnet50	79.97
Vision transformer	83.64
Swin transformer	85.42
DC-Swin(Ours)	90.69

The method was compared with classical classification models VGG, ResNet and Swin Transformer. As can be seen from the table, this paper's method has higher single classification accuracy and more accurate target recognition. It is believed that this is due to the fact that the DC-Swin's dilated convolution attention mechanism and infrared image pre-training work in the defective regions of the image fittings and different fittings, respectively, which improves the classification accuracy. Our proposed classification method, DC-Swin, achieves the best results in the evaluation metrics , which indicates that the accuracy of classified samples for substation fittings defect recognition performed by our method is higher. Compared to the base model Swin transformer, our improved DC-Swin single classification accuracy is improved. This enhancement proves that the effective combination of the ABDC module with Swin Transformer and the pre-training using infrared image dataset enables further enhancement of the network's learning capability, especially when dealing with the complex task of classifying substation fittings defects.

The results of the accuracy experiments for each fittings of accessory in the experimental dataset are shown in Table 3.

Table 3. Accuracy of various types of fittings

Fittings	Nums	Fittings	Nums
Breathers with iron shell (normal)	90.21	Rusty Fittings	98.85
Breathers with iron shell (discoloured)	74.52	Normal wattmeter	89.62
Breathers without iron shell (normal)	50.01	Blur wattmeter	66.67
Breathers without iron shell (discoloured)	78.69	Broken wattmeter	68.01
Glass insulator without coating	96.97	Bird nest	98.89
Insulator self-explosion	94.64		

The DC-Swin model seamlessly integrates crucial fitting defect feature regions identified by the ABDC module algorithm with the original input images, subsequently feeding them into the Swin Transformer Block for image classification. This approach not only maintains the inherent structure and characteristics of the original images but also incorporates features refined through shallow convolutional layers and the multi-head attention mechanism of the Swin Transformer. The DC-Swin model gains access to more significant fitting features and their intricate dependencies. The result is a fused representation that encapsulates both local and global contextual information, significantly bolstering the model's capability to decipher complex patterns and relationships within the data. The introduction of the ABDC module provides a significant complementary advantage for Swin Transformer. Although Swin Transformer has a strong remote dependency mining capability when processing images, it has a significant complementary advantage in processing fittings features. The introduction of ABDC module brings significant complementary advantages to Swin

Transformer, which has powerful remote dependency mining capability but has some limitations in dealing with local information and translation invariance of images. ABDC effectively compensates for this shortcoming by accurately extracting and splicing key defective feature regions. It enables Swin Transformer to capture and utilize these key information more comprehensively by combining the regions containing rich information about fittings features with the original image, and thus improves its ability to recognize fittings features. In addition, the addition of the ABDC further stimulates Swin Transformer's long-dependent learning capability.

The results of the ablation experiment are summarized in Table 4.Introducing the Self-Attention module sans dilated convolution in the baseline model elevated accuracy by 1.72%. Incorporating the dilated convolutional attention mechanism further boosted accuracy by 3.15%. Combining these two advancements, DC-Swin achieved the highest classification accuracy, with a single-class accuracy of 88.57%, validating our approach. Additionally, pre-training with the novel infrared fittings dataset improved the model's accuracy by 2.12%, achieving optimal results and demonstrating the effectiveness of the methods employed.

Table 4. Ablation experiment

Method			Acc(%)
Dilated convolution	**ABDC(without dilated convolution)**	**Pre-trained**	
			85.42
		√	86.92
	√		87.14
√	√		88.57
	√	√	89.31
√	√	√	90.69

5. Conclusion

In this paper, we propose a transformer substation defect classification method based on an improved Dilated Convolution Swin Transformer model. By introducing the Dilated Convolution Self-Attention module, the model is enabled to enhance the ability to recognize fittings features by more comprehensively capturing and utilizing areas of the image that contain critical feature information. In additional, the fusion of information from both modules in the channel dimension amplifies the Swin Transformer's capacity to discern feature relationships, maximizing the benefits of the Dilated Convolution Self-Attention module and the inherent strengths of the Swin Transformer. Finally, the model was pre-trained using the dataset of infrared imaging to reduce the interference of other irrelevant information in the common dataset, thus improving the key feature region extraction ability of the attention mechanism. Through experiments, it verifies the effectiveness and accuracy of the method in this paper, which provides a more accurate and efficient solution for the task of fittings classification.

References

[1] Song Z, Huang X, Ji C, Zhang Y. Deformable YOLOX: detection and rust warning method of transmission line connection fittings based on image processing technology. IEEE Transactions on Instrumentation and Measurement. 2023;72: 1-21, doi: 10.1109/TIM.2023.3238742

[2] Wang C., Fu Z., Zhang Z., Wang W., Chen H., Xu D. Fault Diagnosis of Power Transformer in One-Key Sequential Control System of Intelligent Substation Based on a Transformer Neural Network Model[J]. Processes, 2024, 12(4): 824, doi: 10.3390/pr12040824

[3] T Wen, W Liu, S Jiao, J Zhu. Quantitative evaluation method of operation reliability of substation relay protection device based on improved neural network algorithm[C]//Journal of Physics: Conference Series. IOP Publishing, 2024, 2704(1): 012002, doi: 10.1088/1742-6596/2704/1/012002

[4] W Xuan, Z Li, H Chen, H Peng, Y Guo, X Wang, L Song, H Wang. Exploration on Intelligent Detection Methods for Substation Equipment Based on Deep Learning[C]//2024 IEEE 4th International Conference on Power, Electronics and Computer Applications. IEEE, 2024: 332-335, doi: 10.1109/ICPECA60615.2024.10471052

[5] Jifeng Dai, Yi Li, Kaiming He, Jian Sun. R-fcn: Object detection via region-based fully convolutional networks[J]. Advances in neural information processing systems, 2016, 29, https://proceedings.neurips.cc/paper/2016/hash/577ef1154f3240ad5b9b413aa7346a1e-Abstract.html

[6] Wei Y, Tong L, Luo L. An exterior defects detecting method of main transformer based on convolutional neural networks[J]. Zhejiang Electric Power, 2019, 38(04): 61-68, doi: 10.19585/j.zjdl.201904011

[7] Liu W., Anguelov D., Erhan D., Szegedy C., Reed S., Fu C. Y., Berg A. C. Ssd: Single shot multibox detector[C]//Computer Vision–ECCV 2016: 14th European Conference, Amsterdam, The Netherlands, October 11–14, 2016, Proceedings, Part I 14. Springer International Publishing, 2016: 21-37, https://link.springer.com/chapter/10.1007/978-3-319-46448-0_2

[8] Guan X., Gao W., Peng H., Shu N., Gao D. W. Image-based incipient fault classification of electrical substation equipment by transfer learning of deep convolutional neural network[J]. IEEE Canadian Journal of Electrical and Computer Engineering, 2021, 45(1): 1-8, doi: 10.1109/ICJECE.2021.3109293

[9] Li X F, Liu H Y, Liu G H, Su H S. Transmission line pin defect detection based on deep learning[J]. Power System Technology, 2021, 45(8): 2988-2995, doi: 10.13335/j.1000-3673.pst.2020.1028

[10] Miao X., Lin Z. C., JIANG H., CHENG J., LIU X., ZHUANG S. Fault detection of power tower anti-bird spurs based on deep convolutional neural network[J]. Power System Technology, 2021, 45(1): 126-133, doi: 10.13335/j.1000-3673.pst.2019.1775

Fuzzy Systems and Data Mining X
A.J. Tallón-Ballesteros (Ed.)

doi:10.3233/FAIA241419

A Data Mining Approach to Modeling Annual CO2 Emission Per Capital for Asian Countries

ChienHsing WU[a, 1] and Shu-Chen KAO[b]
[a]*National University of Kaohsiung, Taiwan*
[b]*Kun Shan University, Taiwan*
ORCiD ID: ChienHsing WU https://orcid.org/0000-0003-1331-8790

Abstract. Using the classification-based data mining approach, this study aims to model annual CO2 emission (A-CO2 E) per capital for Asian countries. The dataset collected for the model contains 1287 cases from year 1985 to 2022 with 41 countries involved. The original dataset was granulated to investigate existence of noise label to ensure usefulness, followed by selecting the best one with highest classification accuracy (CA) and robustness (AUC) among five classifiers. Demographics of variables and generated decision rules are presented. Main findings are as follows. (1) Tree-based model reveals the best classifier with CA 0.9067 and AUC 0.962, (2) Country code presents the highest classification power of level of A-CO2 E, showing an individual sign leading to the level of A-CO2 E, (3) The A-CO2 E of some countries higher than that of the World oscillate as year goes, (4) Asian averages of A-CO2 E from 5.8405 (1985) to 7.2950 (2022) are higher than that of the World after year 2000, but this trend likely goes flat, signifying that Asian countries increasingly put efforts on reducing A-CO2 E while increasing GDP.

Keywords. Classification-based model, CO2 emission, granulation, noise label, decision rule

1. Background

Classification-based data mining models have been successfully used to support making decisions in various domains. While creating better living environment toward better human welfare, higher industrialization has been producing more such negative outcomes as air and water pollution and carbon (e.g., CO2) emission, resulting in severe climate changes towards deadly disasters in the past few decades [1-2]. To alleviate their impacts on human welfare, various efforts have been made from various aspects for the past years. Particularly, emphasis has been placed on the issue of carbon emission [3-6], which is regarded as one of the main sources leading to negative influences on climate changes. Consequently, modeling CO2 emission has been one of the main issues dealing with policymaking to weaken effects of the changes.

Existing literature have been constantly revealing insights to obtain relevant solutions from a wide range of aspects into promoting the quality of making strategies and policies [2]. The ultimate goal is to minimize the potential damages caused by CO2 emission by

[1] Corresponding Author: ChienHsing Wu, National University of Kaohsiung, 700, Kaohsiung University Rd., Nanzih District, Kaohsiung 811, Taiwan, E-mail: chwu@nuk.edu.tw

proposing prediction models and determinants linking to CO2 emission. Although obvious merits reported, decision support by modelling annual CO2 emission (A-CO2 E) mostly centered on dealing with quant to derive adequate insights [1-6]. Individual country, or a region, may embed with their own levels of A-CO2 E, and in consequence resulting in the needs of distinct strategies and policies [4].

To address this issue, the current research employs the classification-based data mining approach to model A-CO2 E for Asian countries. The country code along with year are particularly considered, with a combination of three quantitative features including GDP, GDP growth, and electricity production (EP) to co-classify levels of A-CO2 E. The related concepts which outline some existing studies addressing models, variables, findings, and suggestions are reviewed. The method used to develop the classification model is presented, followed by data source used and results revealed and discussed. The final section addresses the research conclusion.

2. A Review of Literature

The global warming has been demonstrating deleterious influences on human environment. One of the main issues associated with the influences is carbon emission, which generally comes along with industrialization. For the context of environment safety, previous studies have conducted extensively studies to look for solutions on how to balance the dilemma problem, as higher industrialization generally leads to more carbon emission. Open public data has been widely used to look deeply into what had happened until now and what should be doing next to support making adequate decisions. In response to this issue, prediction models embedded with creative analysis techniques have shown considerable merits modeling CO2 emission [2, 5-6].

For example, dynamic simultaneous-equations models and generalized method of moments were used to reveal the relationships among carbon dioxide (CO2) emissions, health spending and GDP growth for 51 countries [1]. Main finding is that green total factor productivity reduces CO2 emission. Particularly, a few studies examined the role that clean energy plays in alleviating effect on CO2 emission. For example, dynamic ordinary least squares method was used based on annual data from 1990 to 2020 in Vietnam [2] and revealed positive influences of GDP and energy consumption but negative effects of innovative technique, sustainable agricultural, and forest preservation on CO2 emission.

Moreover, extreme learning machine was utilized with confirmed performance better than both genetic programming and artificial neuron network to predict GDP based on CO2 emission [6], deepening the insights into how CO2 emission is generated by GDP. The causal relationships using machine learning of causal direction from dependency among solar and wind energy production, coal consumption, economic growth, and CO2 emissions were examined with data from 1971 to 2016 for China, USA, and India [5]. The study explored that renewable sources of energy used reduced overall carbon emission in China and USA, whereas India unlikely appeared the same. Approach of two-stage recurrent neural networks was used to predict per capital economic growth for 94 countries by considering energy consumption and carbon emission [4]. One of the main findings showed that mid-low and low level of income countries demonstrated a better development with less carbon emission and energy consumption because of lower level of infrastructure not conducive to higher growth. To improve prediction accuracy of CO2 emission on GDP, the intuitionistic fuzzy transfer learning model was proposed

and compared better than extreme learning machine, support vector regression, and generalized regression neural networks by training data of developed nations and testing that of developing nations [7]. This study demonstrated an alternative prediction model for CO2 emission to extend the understanding of relationship with GDP.

Obviously, these proposed models have demonstrated considerable merits prone and conducive to support making effective strategies and policies. Alternatively, knowledge discovery (KD) using classification-based learning model has shown its merits in domains. Although not a new KD mechanism, one of the advantages of classification-based model is using features (e.g., country code, GDP) to classify labels (e.g., levels of A-CO2 E) [7-8]. Different from the aforementioned models, our current research adopted supervised classification-based learning model to develop a prediction model describing levels of A-CO2 E for Asian countries. Original data was granulated for quantitative features to ensure non-noise labels used in the model and five classifiers (Tree-based, Random forest, Support vector machine, AdaBoost, and Stochastic gradient decedent) were tested and selected with highest performance. Knowledge with the form of decision rules was discovered, followed by interpretation and discussion.

3. Method

3.1 Research design

The study followed the four-phase analysis method to obtain research results, including data collection, pre-processing, classifier selection, and implementation (Table 1). The data collection deals with combinations of various data sources to form a useful dataset. The pre-processing comprehends the collected data sources such as missing data removal, data completion, data integration, and data granulation using unsupervised equal width interval approach. The classifier selection chooses the best one among five with the best classification performance (i.e., accuracy and robustness). The implementation conducts knowledge discovery in the dataset with the form of rules.

Table 1: Design characteristics

Characteristics	Description
Objective	- Modeling annual CO2 emission for Asian countries via data mining approach.
Datasets	- Collecting online data from Our World Data (https://ourworldindata.org/co2-emissions) for annual CO2 emission per capital and electricity production [9], and The World Bank (https://data.worldbank.org/) for GDP and GDP growth.
Data preprocessing	- Processing the data sources such as missing data removal, data completion, data integration, and data granulation (unsupervised equal with interval), and noise label detection.
Classification model	- Comparing classification performance among five classifiers using 70-30% testing criteria (decision tree (DT), random forest (RF), support vector machine (SVM), AdaBoost (AB), and stochastic gradient descent (SGD)) - Choosing supervised tree-based algorithm to develop decision tree
Mining outputs	Decision tree (or decision rules)

3.2 Dataset

The original data was collected from the open data websites, including Our World Data (https://ourworldindata.org/co2-emissions) for annual CO2 emission per capital and

electricity production [9], and The World Bank (https://data.worldbank.org/) for GDP and GDP growth. The data sources were combined according to year to derive two datasets, one with 1946 cases is for demographics from 1961 to 2022 for Asian countries, and another with 1287 cases is for variables relationships and data mining that requires complete data for all features and labels. There are 41 countries in total considered because data of some countries are not available. Moreover, previous studies regarded the collected data as either time series or a whole dataset mainly due to research focus and the analysis techniques used [1-2]. The current study considered the collected dataset as a whole and performed the tasks of application of classification model.

4. Findings and Discussions

4.1 Findings with demographic

There are data analysis results. First, it is found that GDP of some countries is higher than that of World. Overall, GDP of Asian countries goes higher with years. If dividing the samples into two period groups, one is before year 2000 (denoted by B-2000) and another is in and after 2000 (denoted by A-2000), it shows that the average GDP of B-2000 is almost less than USD10000 whereas A-2000 higher than 10000. GDP of some individual country in both periods are lower than that of World, but averages of both periods are higher than that of World GDP. However, the ratio (i.e., averages of Asian to World) are likely deceasing as year goes (see Figure 1).

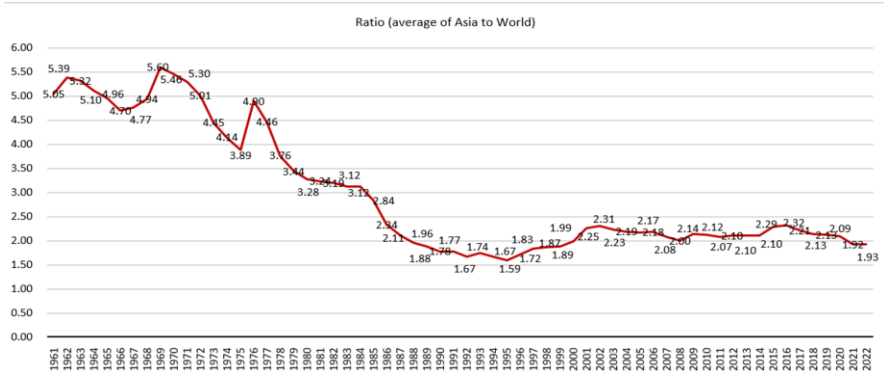

Figure 1: Ratio of GDP average of Asian countries to World

Second, regarding the GDP growth, both averages of Asian and World oscillate with years, even after the year 2000. Concerning the electricity production (kWh), both profiles of Asia and World go smoothly and little higher as year goes. Some countries likely have more efforts producing higher electricity after the year 2000 while others keep slightly increasing. Overall, the Asian average maintains higher than that of World after the year 2000, signifying that for the past two decades Asian countries likely need more energy to support more economic activities, and therefore creating higher GDP.

Third, as for the A-CO2 E, while some individual countries higher than that of the World oscillate as year goes (Figure 2), the Asian averages always keep higher than that of the World for the period of A-2000. However, trend of which likely goes flat. This implies that Asian countries put efforts on reducing A-CO2 E while increasing GDP.

However, the average values from year 1985 (5.8405 tons) to 2022 (7.2950 tons) are still far away from expected value of 2.3 tons by 2030 announced by The Institute for European Environmental Policy [10].

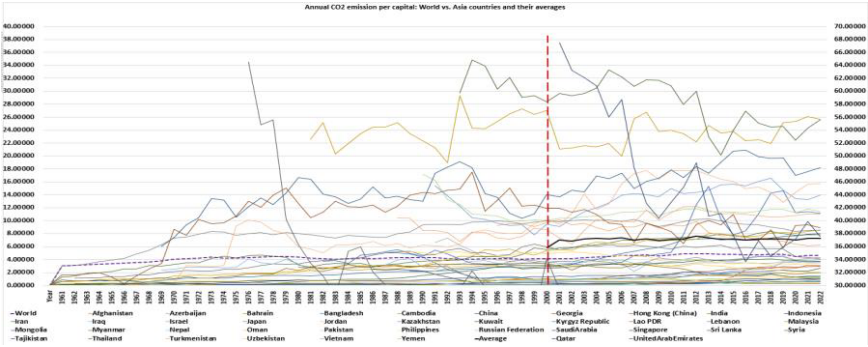

Figure 2: CO2 emission- World vs. Asian countries and their average

Finally, Table 2 summarizes the relationships among GDP, GDP growth, EP, and A-CO2 E, followed by multiple regression model development where some empty data were removed to keep consistent covering year interval from 1985 to 2022, and each year-case in every country is considered as a data point in the model. The results reveal that variables GDP, EP, and A-CO2 E have strong relationships, 0.8027, 0.7809, and 0.8720, respectively, except GDP growth. The regression model also shows that both GDP and EP are significant predicators of A-CO2 E (p-value<0.0001) with high R2 (0.779). This implies that higher A-CO2 E generally come from higher GDP and more EP in Asia, which are consistent with findings by most previous studies in other regions [2, 5-6, 8].

Table 2: Relationships and regression model for variables

Relationships among variables				
n=1287	GDP	GDP growth	EP	A-CO2 E
GDP	1			
GDP growth	-0.1171	1		
EP	0.8027	-0.1321	1	
A-CO2 E	0.7809	-0.1316	0.8720	1
Multiple regression model				
Dep. variable: A-CO2 E				
Ind. variable	Coefficient	t value	p value	
Intercept	0.2850	1.711026	0.087318	
GDP	9.181E-05	10.3253***	< 0.0001	
GDP growth	-0.0198	-1.0632	0.287892	
EP	0.00138	31.1903***	<0.0001	
R square: 0.7790, F=1507.885, p-value<0.0001				

***p<0.01, EP: electricity production per capita (Wh), A-CO2 E: Anneal CO2 emission per capital

4.2 Findings with knowledge discovery

The dataset used in data mining containing 1287 cases and five features (country name, year, GDP, GDP growth, EP) plus one label with 11 levels (A-CO2 E) was granulated to examine existence of noise label. The granulation technique used was equal with interval (EWI) which is an unsupervised technique binning feature values into k non-overlapped intervals. The k is the smallest value meeting that $2^k \geqq n$, n is 1287, the dataset size, and

was determined to be 11 by histogram development regulation. Each interval was given a linguistic term. The existence of noisy label was checked zero, implying same feature value combination leads to a unique level of label. Five classifiers were utilized to examine performance. Based on 70-30% testing criteria with setting tunings, the performance (Accuracy, AUC) of the selected five classifiers, DT, RF, SVM, AB, SGD, are (0.9145, 0.980), (0.8938, 0.989), (0.9041, 0.950), (0.8316, 0.963, (0.9067, 0.975), respectively. The tree-based classifier was therefore used to hierarchically develop decision tree for the dataset, followed by decision rules generation.

The tree-based algorithm (ID3) [11] was utilized to reveal the classification power of features to predict label covering 11 levels of A-CO2 E. It is based on the information theory, using a top-down induction approach to return the classification power that a variable (i.e., feature) can separate the other. The ranking order of classification power is County code (1.2368), EP (0.8745), GDP (0.5863), Year (0.1102), and GDP growth (0.0616). It shows that the Country code holds the highest rank to classify CO2 emission, implying that countries themselves likely lead individually to the level of annual CO2 emission. The entire decision tree was generated according to the order, followed by generated rules, as part of Table 3 where rules with one, two, and tree conditions are shown in the form of IF condition(s) THEN conclusion.

Table 3: Part of generated rules

A	B	C	D	E	F	G	H	I	J	K	L	M	N	O	P	Q	R	S	T	U
IF	Name	in	[Mongolia]	and	Year	in	[Y2022]	THEN	A-CO2E	in	["\'B2of11\'"]	with	accuracy	1	on	(0,1,0,0,0,0,0,0,0,0)	1			
IF	Name	in	[Myanmar]	THEN	A-CO2E	in	["\'B1of11\'"]	with	accuracy	1	on	(23,0,0,0,0,0,0,0,0,0)	23							
IF	Name	in	[Nepal]	THEN	A-CO2E	in	["\'B1of11\'"]	with	accuracy	1	on	(23,0,0,0,0,0,0,0,0,0)	23							
IF	Name	in	[Oman]	and	Gdp	in	["\'B1of11\'"]	and	Year	in	[Y1991]	THEN	A-CO2E	in	["\'B1of11\'"]	with	accuracy	1	on	(1,0,0,0,0,0,0,0,0,0
IF	Name	in	[Oman]	and	Gdp	in	["\'B1of11\'"]	and	Year	in	[Y1992]	THEN	A-CO2E	in	["\'B1of11\'"]	with	accuracy	1	on	(1,0,0,0,0,0,0,0,0,0
IF	Name	in	[Oman]	and	Gdp	in	["\'B1of11\'"]	and	Year	in	[Y1993]	THEN	A-CO2E	in	["\'B2of11\'"]	with	accuracy	1	on	(0,1,0,0,0,0,0,0,0,0
IF	Name	in	[Oman]	and	Gdp	in	["\'B1of11\'"]	and	Year	in	[Y1994]	THEN	A-CO2E	in	["\'B2of11\'"]	with	accuracy	1	on	(0,1,0,0,0,0,0,0,0,0
IF	Name	in	[Oman]	and	Gdp	in	["\'B1of11\'"]	and	Year	in	[Y1995]	THEN	A-CO2E	in	["\'B2of11\'"]	with	accuracy	1	on	(0,1,0,0,0,0,0,0,0,0
IF	Name	in	[Oman]	and	Gdp	in	["\'B1of11\'"]	and	Year	in	[Y1985]	THEN	A-CO2E	in	["\'B2of11\'"]	with	accuracy	1	on	(0,1,0,0,0,0,0,0,0,0
IF	Name	in	[Oman]	and	Gdp	in	["\'B1of11\'"]	and	Year	in	[Y1986]	THEN	A-CO2E	in	["\'B2of11\'"]	with	accuracy	1	on	(0,1,0,0,0,0,0,0,0,0
IF	Name	in	[Oman]	and	Gdp	in	["\'B1of11\'"]	and	Year	in	[Y1987]	THEN	A-CO2E	in	["\'B1of11\'"]	with	accuracy	1	on	(1,0,0,0,0,0,0,0,0,0
IF	Name	in	[Oman]	and	Gdp	in	["\'B1of11\'"]	and	Year	in	[Y1988]	THEN	A-CO2E	in	["\'B2of11\'"]	with	accuracy	1	on	(0,1,0,0,0,0,0,0,0,0
IF	Name	in	[Oman]	and	Gdp	in	["\'B1of11\'"]	and	Year	in	[Y1989]	THEN	A-CO2E	in	["\'B1of11\'"]	with	accuracy	1	on	(1,0,0,0,0,0,0,0,0,0
IF	Name	in	[Oman]	and	Gdp	in	["\'B1of11\'"]	and	Year	in	[Y1990]	THEN	A-CO2E	in	["\'B2of11\'"]	with	accuracy	1	on	(0,1,0,0,0,0,0,0,0,0
IF	Name	in	[Oman]	and	Gdp	in	["\'B2of11\'"]	THEN	A-CO2E	in	["\'B2of11\'"]	with	accuracy	0.8889	on	(0,8,0,0,1,0,0,0,0,0)	9			
IF	Name	in	[Oman]	and	Gdp	in	["\'B3of11\'"]	THEN	A-CO2E	in	["\'B3of11\'"]	with	accuracy	1	on	(0,0,0,0,5,0,0,0,0,0)	5			
IF	Name	in	[Oman]	and	Gdp	in	["\'B4of11\'"]	THEN	A-CO2E	in	["\'B3of11\'"]	with	accuracy	1	on	(0,0,0,0,13,0,0,0,0,0)	13			
IF	Name	in	[Pakistan]	THEN	A-CO2E	in	["\'B1of11\'"]	with	accuracy	1	on	(38,0,0,0,0,0,0,0,0,0)	38							
IF	Name	in	[Philippines]	THEN	A-CO2E	in	["\'B1of11\'"]	with	accuracy	1	on	(38,0,0,0,0,0,0,0,0,0)	38							
IF	Name	in	[Qatar]	and	Gdp	in	["\'B10of11\'"]	THEN	A-CO2E	in	["\'B7of11\'"]	with	accuracy	1	on	(0,0,0,0,0,0,0,0,0,3)	3			

For example (in Table 3), IF country code = Oman and GDP= level 1 (["\'B1of11\'"] (between USD842.805 and 15316.30) and Year = 1985~1992 THEN the level of A-CO2 E = level 1 or 2 (["\'B1of11\'"] between 0.053 and 12.305) with only one case each year, but Year = 1993 ~ 1995 appears only level 2 (["\'B2of11\'"], between 6.181 and 12.305). Moreover, as GDP goes higher (level 2 and 3, between USD15316.30 and 29789.79), level of A-CO2 E increases firmly to be level 2 or 3 with much more evidences (more than 25 cases) without Year involved. This implies that level of A-CO2 E keeps stable in level 1 between 1985 to1992, but goes to level 2 between year 1993 to 1994. Moreover, one level higher with GDP leads to one level higher with A-CO2 E.

As for the generated rules, findings are addressed from two perspectives, the number of rules generated and levels of A-CO2 E. First, there are 288 rules generated with one removed due to low accuracy (0.3333), and of which 26 with 1 condition (named R-1) containing 788 cases, 177 with 2 conditions (R-2) containing 411 cases (3 removed), and 85 with 3 conditions (R-3) containing 85 cases. These reveal that R-1 receives the highest supports and generation quality (788/26=30.31), followed by R-2 (2.32) and R-3 (1.00). Second, focusing on the levels of annual CO2 emission, in R-1 there are 23 countries grouped in level 1 (0.053 ~ 6.180) and remaining 3 in level 2 (6.181 ~ 12.307). This shows that more than half countries in Asia rank in low annual CO2 emission. In R-2, the conditions can be a combination of Country and one of EP, GDP, Year, and GDP

growth. It reveals that there are 2 cases with Country and EP ranked in level 1 whereas 66 cases with various combinations (GDP, Year, and GDP growth) ranked in level 2 and 3 (from 6.181 to 18.435). Finally, at the level 4 and above (18.436 ~), the combined conditions are Country code with mostly either high GDP or year after 2000. This signifies that high A-CO2 E comes mainly from high GDP after the year 2000.

5. Conclusion

The current research presents two purposes, one is the utilization of classification-based leaning approach (i.e., tree-based) as a prediction model to predict A-CO2 E and another is to discover knowledge in the form of decision rules revealing insights into how features leads to levels of A-CO2 E for Asian countries. The main finding reveals that country code appears the highest classification power on A-CO2 E, which existing reports has yet addressed. The next research will focus on increasing the number of relevant features for the proposed model to sufficiently describe A-CO2 E, particularly the clear energy index used as the balancing mechanism between GDP and CO2 emission. Moreover, findings may be different from the perspective of time windows (e.g., decade-by-decade) as the present study regarded the collected data as a whole. Furthermore, continuously looking for innovative prediction models with adequate variables for the A-CO2 E is also one of the next directions.

References

[1] Chaabouni S, Saidi K. The dynamic links between carbon dioxide (CO2) emissions, health spending and GDP growth: A case study for 51 countries, Environmental Research, 2017; 158, 137–144, http://doi.org/10.1016/j.envres.2017.05.041
[2] Raihan A, Hasan MA, Voumik LC, Pattak DC, Akter S, Ridwan M. Sustainability in Vietnam: Examining economic growth, energy, innovation, agriculture, and forests' impact on CO2 emissions, World Development Sustainability, 2024; 4, https://doi.org/10.1016/j.wds.2024.100164.
[3] Sadati SE, Rahbar N, Kargarsharifabad H. Energy assessment, economic analysis, and environmental study of an Iranian building: The effect of wall materials and climatic conditions, Sustainable Energy Technologies and Assessments, 2023, l(5), https://doi.org/10.1016/j.seta.2023.103093
[4] Lianos C, Kristjanpoller W. Causal treatment effects in time series: CO2 emissions and energy consumption effect on GDP, Energy, 2022; 249(36), 12–25, https://doi.org/10.1016/j.energy.2022.123625
[5] Magazzino C, Mele M, Schneider N. A machine learning approach on the relationship among solar and wind energy production, coal consumption, GDP, and CO2 emissions, Renewable Energy, 2021; 1(4), 99–115, https://doi.org/10.1016/j.renene.2020.11.050
[6] Marjanovic V, Milovancevic M, Mladenovic I. Prediction of GDP growth rate based on carbon dioxide (CO2) emissions, Journal of Co2 Utilization, 2016; 16, 212–7.
[7] Kumar S, Shukla AK, Muhuri PK, Lohani QMD. CO2 emission-based GDP prediction using intuitionistic fuzzy transfer learning, Ecological Informatics, 2023; 77, https://doi.org/10.1016/j.ecoinf.2023.102206
[8] Wu CH, Kao SC, Hong RQ, Chen LH. Profiling effects of filtering noise labels on learning performance, Knowledge-Based Systems, 2024; 294, https://doi.org/10.1016/j.knosys.2024.111667.
[9] Ember (2024). Energy Institute - Statistical Review of World Energy (2023); Population based on various sources (2023) – with major processing by Our World in Data. “Total electricity generation per person – Ember and Energy Institute” [dataset]. Ember, “Yearly Electricity Data”; Energy Institute, “Statistical Review of World Energy”; Various sources, “Population” [original data]. Retrieved June 9, 2024 from https://ourworldindata.org/grapher/per-capita-electricity-generation
[10] Gore T. Carbon inequality in 2030: Per capita consumption emissions and the 1.5C goal, The Institute for European Environmental Policy (2021), last accessed 2024/03/10, https://ieep.eu/publications/carbon-inequality-in-2030-per-capita-consumption-emissions-and-the-1-5c-goal/
[11] Quinlan JR. Induction of decision tree, Machine Learning, 1986; 1, 81-106.

Fuzzy Systems and Data Mining X
A.J. Tallón-Ballesteros (Ed.)

doi:10.3233/FAIA241420

Discovering Innovative Ideas in Social Posts for Sustainable Product Development via Data Mining Approach

Shu-Chen KAO [a,1] and Rui-Jie HUANG [b]
[a] *Kun Shan University, Taiwan*
[b] *National University of Kaohsiung, Taiwan*
ORCiD ID: Shu-Chen KAO https://orcid.org/0000-0003-4308-5457

Abstract. With the increasing awareness of environmental protection, the demand for sustainable product design has been an important issue for the past few decades. This research aims to propose an idea development model by leveraging advanced NLP, machine learning, and deep learning techniques. It collects 3,016 posts from sustainability-related social communities to compare the identification performance of seven classifiers. Through model verification using 75-25% criteria, the experimental results reveal that Word2Vec accompanied with SVM performs the best (F1=0.72, AUC=0.75). Based on 1704 creative posts, LDA is adopted to categorize four topics containing 243, 285, 412 and 764 articles, respectively. By employing Apriori and association rules, the discovered knowledge containing 30, 5110, 42 and 103 rules for each topic are extracted as a basis for idea generation conducive to sustainable products development. Discussion and implication are addressed.

Keywords. idea development, creativeness identification, semantic representation, knowledge extraction

1. Introduction

Over the past few decades, environmental protection has been attracting increasing attention to governments pursuing a sustainable living environment. By viewing various complex challenges posed by resource depletion, innovative solutions in the realm of environmental protection are proposed with diverse approaches, such as green energy creation, resources recycle, etc. to response to the high alert of sustainable requirements. Thus, the issues discussing how to cultivate the ideas of sustainable products by increasing exploitation of existing resources to adapt to dynamic market has attracted increasing attentions from those companies committing to environmental protection [1,2].

User innovation (or open innovation), proposed by von Hippel (1982) advocating the importance of user involvement in innovation outcome [3], provides companies with alternative approaches to benefit innovation [4,5]. Increasing popularity of social media provides a convenient channel to foster innovation by collecting diverse opinions or comments conducive to sustainability [6,7]. However, for those companies pursuing to

[1] Corresponding Author: Shu-Chen KAO, Department of Information Management, Kun Shan University, Tainan, R.O.C.; E-mail: kaosc@mail.ksu.edu.tw.

find innovative ideas by exploiting social media resources, the questions they are concerned with may be: (1) How to efficiently identify the creative articles from a huge number of social posts for product innovation; (2) How to well-organize and extract useful knowledge from the identified creative posts to develop idea for sustainable products.

To process huge corpus, natural language processing (NLP) is developed to represent semantic for those unstructured documents on social media platforms [1,8,9]. Bag-of-words or TF-IDF (Term Frequency-Inverse Document Frequency) primarily assessing semantic concepts according to the frequency of terms decomposed from documents, is one of the commonly used techniques for text mining. By calculating frequency of the terms in documents, TF-IDF can produce term/document matrix as the basis for purpose of new product development (NPD) [1,5,10]. The Word2Vec is a technique of word embedding by mapping word onto a value vector space. By estimating the distances between words with the vector of words and documents, it can represent suitable semantics of a word regardless document context. Owing to its remarkable performance on word embedding, Word2Vec is usually used for opinion mining to find out valuable information beneficial for product improvement or development [11,12]. BERT (Bidirectional Encoder Representations from Transformers), developed by Google in 2018, is a bidirectional transformer-based language model trained on Wikipedia and BooksCorpus. Based on transformer architecture, BERT provides a deep bidirectional and context-aware language model to has given state-of-the-art results on a wide variety of NLP tasks including new product development [1,5,13]. Despite various merits reported for these techniques, one may be better than others for a specific application context but not for all. Technique selection is a necessary step to find a suitable one for an application.

On the other hand, support vector machine (SVM), a well-known technique of machine learning algorithm, has been used for supporting the tasks of identification in many fields [14,15]. In additions, deep learning algorithms also contribute to catch classification features by extending the structure of neuro networks. Some successful applications also reveal that deep learning has made significant progress in solving various problems, including identification, prediction and recognition [14,16,17]. In deep learning algorithms, Convolutional neural networks recurrent (CNN) and long short-term memory (LSTM) are usually used for event detection or prediction, and achieved good results [5,11,14].

To achieve better identification performance, different semantic representation techniques are usually combined with SVM or LSTM to help identify creative posts [1,5]. In the research work of Kodati and Dasari, for example, deep learning algorithms such as CNN and LSTM also get remarkable performance on emotion detection [18]. However, as dataset characteristics vary, it may lead to different techniques applicable to execute the task of classification. Thus, the technical combinations suitable particularly for the task of discovering innovative ideas conducive to development of sustainable products is critical to success of model applications.

Furthermore, topic modeling, another technique of NLP, is developed to categorize a large corpus by estimating the probability distribution of topics/words. Latent Dirichlet Allocation (LDA), the most recognized technique of topic modeling, has been widely applied in topic extraction for achieving diverse practical purposes of document clustering, event detection, recommendation system, etc. [19,20,21]. However, whether LDA is applicable for sustainability innovation are still under examination. Moreover, how to reveal insights into the potential contents by extracting knowledge from a large-

scale of social posts is also a crucial issue needed to be discussed. Association rules has been effectively adopted to reveal the possible direction of conversation by examining co-occurrence of words [22,23].

To address the aforementioned issues, this paper proposes and conducts an idea development model to extract useful knowledge from online posts beneficial for innovative idea development of sustainable product design. It contains two main tasks. One is to utilize NLP and classification algorithms to explore the suitability of technical combinations for identifying the creative posts. Based on the creative posts, another employs the techniques of LDA and association rules to extract topics and obtain frequent itemset relationships for each topic as a foundation of innovative idea development for sustainable products design.

2. Research framework

To achieve research goal, the classifier is developed and selected with the best performance, followed by creative knowledge extraction using the best classifier. The research framework and their components are illustrated in Figure 1, including classifier selection and knowledge extraction, and each contains three main operations.

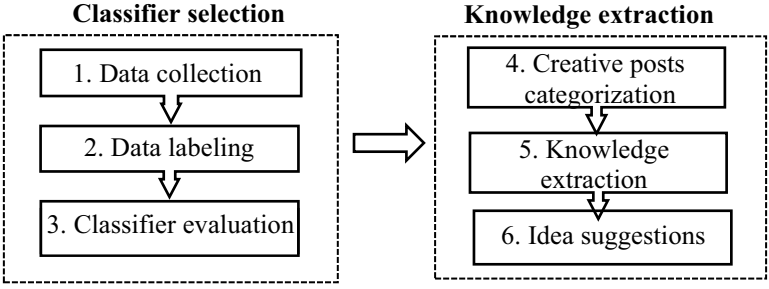

Figure 1. Research framework

2.1 Data collection

By keywords searching such as “environmental sustainability idea”, “green life idea”, “environmental protection creativeness”, “eco-friendly life idea”, etc. and web crawling, related articles were collected from Facebook, online communities, forums, and blogs. Only article contents were considered in this research for analysis use.

2.2 Data labeling

For labeling posts, three experts with domain-related expertise were invited to participate in data annotation. Basically, the article can be labeled ‘1’ to represent creative enough, otherwise it was marked ‘0’. The majority decision is adopted for inconsistent annotation results. Finally, an extra column of ‘creativeness’ was added into the dataset to identify the labeling result for each article, where value of each article was added (1 or 0) according to the decision of expert annotation.

2.3 Classifier evaluation

TF-IDF, Word2Vec and BERT, the main techniques usually used in semantic representation, are utilized to develop language model [1,5,10,11,12,13,24]. To avoid unnecessary noise, all punctuation marks and numbers are removed first, and then the words usually appeared but with no discriminative power in the documents are removed too. After eliminating sparsity words, each article was transformed into corresponding forms to represent semantics for corpus with Python packages.

Based on the outcomes of semantic modeling, classifiers were developed by paring SVM, CNN and LSTM. The BERT itself is considered to operate alone in the research. With relevant Python packages, seven classifiers were individually trained with 75% of the sample data whereas the remaining 25% be the testing dataset. The performances are compared regarding the following measure metrics: time for data training and data testing, accuracy, precision, recall, F1-score, and AUC. To better assess the model's ability to correctly classify positive instances while minimizing both false positives and false negatives, the metrics developed in the experiments also reveal AUC value (area under the ROC) and F1-score, in addition to accuracy [1,5,20].

2.4 Creative posts categorization

LDA is utilized to extract topics according to the probability distribution of terms and a specific topic. Based on the predefined number of topics, LDA can determine the appropriate topic for each post by calculating the relationships between terms and the topic distribution of each document.

2.5 Knowledge extraction

To discover the rules for the term-sets frequently appear in majority of the creative posts, Apriori algorithm and association rules are used. Upon the consideration that the diversity of the article contents may lead to distinct term-sets appearing in the analysis results, the thresholds of support and confidence are initially set to be 0.01 and adjusted depending on analysis needs.

2.6 Idea suggestions

According to the term-sets for each topic, the results can be referenced by individual company for sustainable products development. Because all the generated rules have been properly categorized by the characteristics of themes, companies can efficiently retrieve relevant knowledge. By examining the terms shown in the association rules, companies can also expand their thinking space to inspire more possible applications associated with sustainable products to meet users' requirements.

3. Research results

3.1 Classifier development and comparison

This research focused on Facebook, online communities, forums, and blogs and

collected 3,235 user posts during the period from 2023/4/1 to 2024/3/31. After removing the articles containing non or less than ten words, 3016 articles in total were used, of which 2262 articles were randomly selected for model training, whereas the remaining 754 ones were used for model testing. The manual annotation by experts produced 1704 creative articles and 1312 noncreative ones.

Seven classifiers were developed with Python packages including scikit-learn, keras, torch and tensorflow, etc. The experiment results are illustrated in Table 1 and Figure 2. They reveal that Model 4 that uses Word2Vec paired with SVM has gained the best performance (F1=0.72, AUC=0.75), which usually performs better than TF-IDF-series models. In additions, BERT also performs well (F1=0.69, AUC=0.74). Although Model 7 requires more training time, it can significantly reduce the time needed in identification, once accepted to be used. Furthermore, SVM has superior performance in approximately the same training time compared to other classification algorithms. Surprisingly, LSTM does not perform well in our experiment on the dataset used.

Table 1. Performance comparison of classifiers

	Model 1	Model 2	Model 3	Model 4	Model 5	Model 6	Model 7
Time for data training	00:50	00:50	00:57	00:51	00:51	00:54	09:54
Time for data testing	00:23	00:22	00:23	00:24	00:24	00:24	00:16
Accuracy	0.66	0.62	0.63	0.68	0.67	0.64	0.68
Precision	0.66	0.63	0.64	0.67	0.68	0.68	0.70
Recall	0.73	0.70	0.68	0.77	0.78	0.60	0.69
F1-score	0.70	0.66	0.66	0.72	0.71	0.63	0.69
AUC	0.72	0.69	0.68	0.75	0.73	0.70	0.74

Model 1: TF-IDF vs SVM, Model 2: TF-IDF vs CNN, Model 3: TF-IDF vs LSTM, Model 4: Word2Vec vs SVM, Model 5: Word2Vec vs CNN, Model 6: Word2Vec vs LSTM, Model 7: BERT

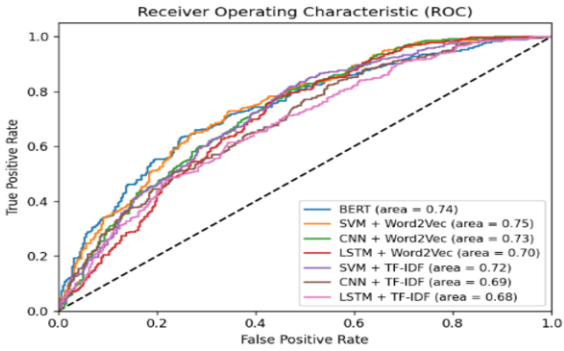

Figure 2. ROC curves and AUC values of classifiers.

3.2 Knowledge extraction

Based on the creative posts, LDA is used to extract four topics and the number of articles for each topic is 243, 285, 412 and 764 respectively. By adopting Apriori algorithm and association rules, knowledge containing frequent itemset and the relationships existing among terms are extracted. Given that support≥0.01, confidence≥0.1 and lift>1, the number of rules attained are 30, 5110, 42 and 103 respectively. Part of the rules for topic 2 is demonstrated in Figure 3. With the association rules, innovators can select topic they are interested in and further inspect the rules close to the concepts of the specific

sustainable product to assist in inspiring more ideas for eco-friendly materials or products. For example, according to the association rules and frequent itemset filtered with the keyword of "fashion" (as Figure 3 and Figure 4), important rules and various combination of terms associated with fashion can be retrieved. Particularly, rule #5108 in Figure 3 and frequent itemset #530 in Figure 4 reveal the relationship between "fashion" and "fiber, dining ware, biodegradation, organism", signifying that these terms are mostly discussed by online users. Thus, for the companies attempting to design fashionable dining ware, they should pay more attention to fiber materials used for dining ware with features of biodegradation and organism. To do so, they can focus mainly on developing creative ideas for dining ware materials that align with these features conducive to matching the users' preferences. With the similar way to extend their thinking space, companies can focus on any other rules or the term combinations they are interested in to generate possible ideas.

	antecedents	consequents	antecedent support	consequent support	support	confidence	lift
0	(regeneration)	(plastic)	0.185965	0.280702	0.077193	0.415094	1.478774
1	(plastic)	(regeneration)	0.280702	0.185965	0.077193	0.275000	1.478774
2	(plastic)	(cycle)	0.280702	0.140351	0.080702	0.287500	2.048438
3	(cycle)	(plastic)	0.140351	0.280702	0.080702	0.575000	2.048438
4	(plastic)	(materials)	0.280702	0.147368	0.066667	0.237500	1.611607
...	...	...	...	...	...	...	...
5105	(plastic, organism)	(fashion, fiber, dining ware, biodegradation, ...	0.073684	0.010526	0.010526	0.142857	13.571429
5106	(cycle, organism)	(fashion, fiber, dining ware, biodegradation, ...	0.045614	0.010526	0.010526	0.230769	21.923077
5107	(plastic, cycle)	(fashion, fiber, dining ware, biodegradation, ...	0.080702	0.010526	0.010526	0.130435	12.391304
5108	(fashion)	(fiber, dining ware, biodegradation, organism,...	0.101754	0.010526	0.010526	0.103448	9.827586
5109	(dining ware)	(fashion, fiber, biodegradation, organism, pla...	0.063158	0.010526	0.010526	0.166667	15.833333

Figure 3. Part of association rules for Topic2

	support	itemsets
34	0.035088	(fashion, plastic)
52	0.038596	(fashion, regeneration)
65	0.031579	(cycle, fashion)
77	0.024561	(fashion, materials)
89	0.028070	(fashion, biodegradation)
...	...	...
529	0.010526	(cycle, fashion, fiber, dining ware, plastic, ...
530	0.010526	(fashion, fiber, dining ware, biodegradation, ...
531	0.010526	(cycle, fashion, toy, furniture, regeneration,...
532	0.010526	(cycle, fashion, fiber, dining ware, biodegrad...
533	0.010526	(cycle, fashion, fiber, dining ware, biodegrad...

Figure 4. Frequent itemset containing "fashion"

4. Conclusion

To achieve sustainability innovation, the creativeness discovered in users' opinions on social communities are valuable to inspire ideas development for sustainable products. This research aims to proposes an idea development model by using the data mining approach with various techniques. The research contributes the insights into the model selection for companies to identify creative posts for developing sustainable products in the future. It also provides companies with an alternative user-cocreation approach conducive to product idea generation from online posts. Although revealing the ideal technical combinations for our current research, other models such as Glove may produce competitive outcomes, which will be one of our future research focuses.

References

[1] Ozcan S, Suloglu M, Sakar O, Chatufale S. Social media mining for ideation: Identification of sustainable solutions and opinions. Technovation. 2021;107, doi:10.1016/j.technovation.2021.102322.

[2] Doorn VJ, Risselada H, Verhoef PC. Does sustainability sell? The impact of sustainability claims on the success of national brands' new product introductions. Journal of Business Research. 2021;137:182-193, doi:10.1016/j.jbusres.2021.08.032

[3] von Hippel E. Lead Users: A Source of Novel Product Concepts. Management Science. 1986;32(7):791-805
[4] Choi J, Oh S, Yoon J, Lee JM, Coh BY. Identification of time-evolving product opportunities via social media mining. Technological Forecasting & Social Change. 2020;156, doi:10.1016/j.techfore.2020.120045
[5] Zhang M, Fan B, Zhang N, Wang W, Fan W. Mining product innovation ideas from online reviews. Information Processing and Management., 2021;58, doi: 10.1016/j.ipm.2020.102389
[6] Hutton S, Demir R, Eldridge S. How does open innovation contribute to the firm's dynamic capabilities?. Technovation. 2021;106, doi:10.1016/j.technovation.2021.102288
[7] Shin H, Perdue RR. Developing creative service ideas through hotel customer engagement for open innovation: Focused on empowerment and motivation processes. International Journal of Hospitality Management. 2022;100, doi:10.1016/j.ijhm.2021.103077
[8] Aman A, Reji DJ. EnvBert: An NLP model for Environmental Due Diligence data classification. Software Impacts. 2022;14, 10.1016/j.simpa.2022.100427
[9] Kaur K, Kaur P. BERT-CNN: Improving BERT for Requirements Classification using CNN. Procedia Computer Science. 2023; 218:2604-2611, doi:10.1016/j.procs.2023.01.234
[10] Sun H, Guo W, Sha H, Rong B. Dynamical mining of ever-changing user requirements: A product design and improvement perspective. Advanced Engineering Informatics, 2020;46, doi:10.1016/j.aei.2020.101174
[11] Gozuacik N, Sakar O, Ozcan S. Social media-based opinion retrieval for product analysis using multi-task deep neural networks. Expert Systems with Applications. 2021;183, doi:10.1016/j.eswa.2021.115388
[12] Lee C, Jeon D, Ahn JM, Kwon O. Navigating a product landscape for technology opportunity analysis: A word2vec approach using an integrated patent-product database. Technovation. 2020;96-97, doi:10.1016/j.technovation.2020.102140
[13] Lauriola I, Lavelli A, Aiolli F. An introduction to Deep Learning in Natural Language Processing: Models, techniques, and tools. Neurocomputing. 2022;470:443-456, doi:10.1016/j.neucom.2021.05.103
[14] Ali M, Hassan M, Kifayat K, Kim JY, Hakak S, Khan MK. Social media content classification and community detection using deep learning and graph analytics. Technological Forecasting and Social Change. 2023;188, doi: 10.1016/j.techfore.2022.122252
[15] Luo J, Luo J, Nan G, Li D. Fake review detection system for online E-commerce platforms: A supervised general mixed probability approach. Decision Support Systems. 2023;175, doi:10.1016/j.dss.2023.114045
[16] Kodati D, Dasari CM. Negative emotion detection on social media during the peak time of COVID-19 through deep learning with an auto regressive transformer. Engineering Applications of Artificial Intelligence. 2024;127, doi:10.1016/j.engappai.2023.107361107361
[17] Vishwanath T, Shirwaikar RD, Jaiswal WM, Yashaswini M. Social media data extraction for disaster management aid using deep learning techniques. Remote Sensing Applications: Society and Environment. 2023;30, doi: 10.1016/j.rsase.2023.100961
[18] Messaoudi C, Guessoum Z, ben Romdhane L. A Deep Learning Model for Opinion mining in Twitter Combining Text and Emojis. Procedia Computer Science. 2022;207:2628-2637, doi:10.1016/j.procs.2022.09.321
[19] Wang W, An A. Identification of market power abuse in Chinese electricity market based on an improved cost-sensitive support vector machine. International Journal of Electrical Power & Energy Systems. 2024;158, doi: 10.1016/j.ijepes.2024.109907
[20] Akrouchi EM, Benbrahim H, Kassou I. End-to-end LDA-based automatic weak signal detection in web news. Knowledge Based Systems. 2021;212, doi:10.1016/j.knosys.2020.106650
[21] Ma J, Wang L, Zhang YR, Yuan W, Guo W. An integrated latent Dirichlet allocation and Word2vec method for generating the topic evolution of mental models from global to local. Expert Systems with Applications. 2023;212, doi:10.1016/j.eswa.2022.118695
[22] Wang J, Liu YL. Deep learning-based social media mining for user experience analysis: A case study of smart home products. Technology in Society. 2023;73, doi:10.1016/j.techsoc.2023.102220
[23] Huang S, Zhang J, Yang C, Gu Q, Li M, Wang W. The interval grey QFD method for new product development: Integrate with LDA topic model to analyze online reviews. Engineering Applications of Artificial Intelligence. 2022;114, doi:10.1016/j.engappai.2022.105213
[24] Lee C, Jeon D, Ahn JM, Kwon O. Navigating a product landscape for technology opportunity analysis: A word2vec approach using an integrated patent product database. Technovation. 2020;96-97, doi:10.1016/j.technovation.2020.102140

Fuzzy Systems and Data Mining X
A.J. Tallón-Ballesteros (Ed.)

doi:10.3233/FAIA241421

A Study on ERP Autonomous Experiment Assisted by Digital Intelligence Fusion

Weibo Huang[1], Ziting He, Xiaopeng Xie and Haolin Chen
Guangdong University of Foreign Studies, Guangzhou, China.

Abstract. This study applied Digital Intelligence Fusion to explore an autonomous experimental model for ERP learning systems to enhance the practical experience for the undergraduates. Using AI's ability to create virtual environments, the proposed model simulated real-life scenarios to provide students with an immersive educational experience. The study employed big data analysis to build an intelligent ERP system through data warehousing and data mining techniques to improve data quality and automatically correct inaccuracies. The model performs well in capturing contextual features and generating responses that are very similar to the actual responses. This novel approach demonstrated a unique contribution to this field, enhancing ERP education through AI-driven immersive learning and big data analytics.

Keywords. ERP, AI, Digital Intelligence Fusion, Autonomous Experiment

1. Introduction

The rapid development of artificial intelligence provides new possibilities for the reform of the teaching in economics and management courses. It is necessary to address the challenges of ERP systems that are developing in sync with today's social innovation, which has led to an urgent demand for ERP educational tools [1]. The capacity of AI to construct virtual environments allows it to simulate complex scenes in the real world and provide students with an immersive learning experience that closely resembles the real situation [2]. This not only compensates for the deficiencies of traditional laboratories and AI experimental platforms in simulating the workflow and environment of enterprises and institutions, but also eliminates geographical and temporal constraints, thereby enhancing the flexibility of practical teaching [3].

In recent years, a significant number of higher education institutions, both domestic and international, have engaged in active research and development concerning the potential applications of artificial intelligence in the field of education. [4] For example, at Stanford University Business School, AI is being introduced into the fields of economics and management education with the aim of enabling students to gain a deeper understanding of complex business concepts and strategies. This is achieved by simulating business environments and decision-making scenarios. Similarly, at Wharton

[1] Corresponding Author: Weibo Huang, Center for Contemporary Education Technology, Experimental Teaching Center, Guangdong University of Foreign Studies, China; Email: 172564946@qq.com.

This study is financially supported by the Undergraduate Innovation Training Project of Guangdong University of Foreign Studies in 2024, and is also financially supported by the Experimental Teaching and Teaching Laboratory Construction Research Project of Guangdong University of Foreign Studies in 2024.

Business School, AI is being used to deliver financial and investment education, aiming to improve students' investment decision-making and risk management skills. In this context, developing an ERP autonomous experimental model can provide students with more practical learning opportunities. By combining artificial intelligence technology with the ERP autonomous experimental model, students can apply their learned knowledge in real environments, thereby strengthening their practical operation and problem-solving abilities, and helping them better adapt to the challenges and opportunities of future business environments.

2. ERP Autonomous Experiment Model Based on Big Data

The use of big data technology to construct an intelligent ERP system with a big data centre to develop an enterprise resource planning system for e-commerce companies based on data warehousing and data mining technology [5], in which the input of fundamental data is charged to the application of algorithms to quality mining and automatically rectify the data [6].

In the analysis centre, particularly in the customer management module, neural network algorithms and other such techniques will be employed to analyse the potential consumption patterns of customers, utilising the characteristics of microservice architecture. The big data centre system establishes an ERP autonomous experimentation model, as illustrated in Figure 1.

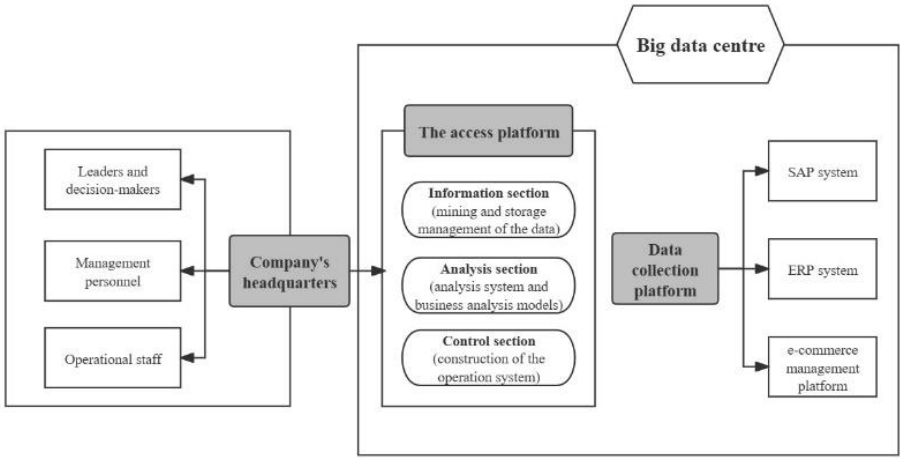

Figure 1. Autonomous ERP experiment model built through the big data centre system

The entire big data centre is managed by the company's headquarters. Leaders and decision-makers, management personnel, as well as operational staff can access the big data centre through the access platform [7]. The centre is divided into three core sections.

The information section bears responsibility for the mining and storage management of the contained data, which maintains the basic data required for the ERP system is retained [8]. Additionally, the information section will encompass a customer management module dedicated to data processing, which can be utilized by operational staff for the analysis of the data.

The role of the analysis section is to undertake analysis of the system and to process business analysis models. Operators and managers analyse the operation and processing of the basic business service modules and the modules of microservices architecture in this section, employing analytical tools to ascertain whether the business modules are fulfilling their intended function. Under the microservice architecture, ERP systems are divided into multiple independent services, each responsible for a portion of business functions, with its own database, and capable of independent deployment and expansion. Additionally, microservices may need to call each other.Furthermore, the section analyses data from the customer management module, examining the consumption requirements of each disparate computer customer, which can be represented as data within the analysis section.

The control section is responsible for the construction of the operation system of the entire big data centre. This includes eight different data categories: data security management, data quality management, data model management, master data management, data standard management, HI data management, data model management, data lifecycle management, and basic data management. Based on the data category, corresponding data processing systems are used for data control.

The data collection platform is primarily constituted by the SAP system, the ERP system, and the e-commerce management platform.

3. Artificial Intelligence Autonomous Experiment Information Push

The collaborative filtering recommender system is based on the Transformer model, which is advantageous in natural language processing and widely applied in the field of natural language processing (NLP), self-attention mechanism is its core.The input information is encoded and mathematical computations are performed to obtain the predicted values. These values are then compared with the pre-training results on the corpus to determine the final output. In this study, the GPT model (decoder structure only) in Transformer is employed. Its training process commences with unsupervised pre-training on a substantial corpus, followed by fine-tuning utilising supervised data from the current task. This step will be undertaken here with the aforementioned fine-tuned corpus. The initial stage will involve the introduction of a tokeniser, that is to say a lexical module, which will perform the automatic segmentation of the input lexicon. Subsequently, each input word is transformed into a word vector through the application of a position embedding algorithm, which typically entails a sequence of matrix and weighting operations. In order to clearly represent the question-answer position relation, a new token is added to the word list as a segmentation in this module.

For example, <CLS><sentQ>question<sentA>answer<SEP>

The token [CLS], which is similar to token [BOS] and is frequently employed in classification tasks to mark the beginning of a sequence, will be appended before each sentence in the training set. Subsequently, the token [SEP], which is analogous to the token [EOS] used to segment different sentences or sequence fragments, will be added. The position corresponding to each [CLS] is the sentence vector of each sentence.

The sentQ and sentA are labelled with the starting position of the question and answer respectively. They are placed at the beginning or end of the sentence to serve as spacers that enable the model to grasp the interval between two sentences, thereby facilitating the recognition and reinforcement of learning associated with these key markers.

In the position encoding stage, the segmentation embedding, which has been processed as described above, is summed up with the input token embedding and position embedding in Formula 1. The resultant values of the fusion calculation are then output.

$$\text{embedding} = \text{token} + \text{segment} + \text{position} \tag{1}$$

In the pre-training phase of GPT, a multilayer decoder is employed. After positional encoding of the input, the decoder performs multi-head self-attention operations on the input contextual vocabulary. This is followed by a Feed-Forward Neural (FFN) layer, which conducts linear transformations on the attention scores. Ultimately, the output of the target sentence was generated. The process of learning the text from the unsupervised labelled corpus and thus generating the predicted next sentence can be summarised in Formula 2 to Formula 5.

$$L_1(U) = \sum_i log\, P(u_i|u_{i-k}, \dots, u_{i-1}; \Theta) \tag{2}$$

$$h_0 = UW_e + W_p \tag{3}$$

$$h_l = transformer\_block(h_{l-1}) \forall i \in [1, n] \tag{4}$$

$$P(u) = softmax(h_n W_e^T) \tag{5}$$

Here, U=(u-k, …, u-1) denotes the context vector of the input participle. k is the size of the context window, n is the number of layers, P represents the conditional probability of the generated result, W_e is the participle embedding matrix, W_p is the positional embedding matrix, and the above two matrices are evolved from the basic GPT model embedding layer.

Following the completion of the aforementioned extensive corpus training, the model adjusts its parameters in accordance with the specific requirements of the prediction task. In this context, the model is designed to meet the needs of the prediction service, as outlined in this paper. The textual corpus data is drawn from the target users themselves and their surrounding users. If dataset D has been created following the application of manual labelling, each instance will comprise a sequence of input tokens $(\mathrm{x}^1, \dots, \mathrm{x}^\mathrm{m})$. These inputs are then passed through the model that has completed its initial training phase to obtain the final activation value of the Transformer module, represented by h_l^m. This activation value is subsequently fed into an additional linear output layer with parameter W_y, which allows for the continuation of the prediction process in depth, as illustrated by the following Formula 6.

$$P(y|x^1, \dots, x^m) = \text{softmax}\left(h_l^m W_y\right) \tag{6}$$

At the same time, the pre-trained model, as previously described, will undergo fine-tuning through the use of language modelling (LM). The initial phase of language modelling pre-training is primarily concerned with word and word sense level processing. This implies that the language model must also possess the capacity to comprehend sentences and the relationships between them. Consequently, this LM-based fine-tuning can accelerate the convergence of the model and simultaneously enhance the generalisation of the supervised model. In other words, the model is capable of predicting

the vocabulary with greater frequency, taking into account the contextual information of the input, and is also able to identify and rectify errors on occasion.

Its training process is to predict the next word based on the previous word sequence. For a long sequence of words S, as shown in Formula 7. where w denotes different parameters:

$$S = \{w_1, \ldots, w_{|S|}\} \tag{7}$$

After completing the above steps, the probability value of the next maximum probability word will be predicted based on the previous inputs or existing words in the process shown in Formula 8:

$$\mathcal{L}_1(S) = \sum_{i=1}^{|S|} \log P(w_i | w_0, w_1, \ldots, w_{i-1}) \tag{8}$$

For the specific LM objectives of this study, the loss function for the language modeling fine-tuning module (hereinafter referred to as Loss) is constructed by calculating the log-likelihood function using the logits derived from the normalized hidden states via the softmax function and the actual labels. The formula for log-likelihood computation is as follows:

$$\text{Loss}(\text{x}, \text{class}) = -\frac{1}{\text{n}} \sum_{\text{j}=1}^{\text{n}} \text{log}\big(\text{Pr}(\text{x[j]} | \text{x[class]})\big) \tag{9}$$

Here, x[class] denotes the normalised probability value of x under class.

In the experimental process, the modelling process of LM is optimised by weights μ, as shown in Formula 10.

$$\text{L}_3(\text{D}) = \text{L}_2(\text{D}) + \mu(\text{L}_1(\text{D})) \tag{10}$$

The only additional parameters required during the fine-tuning process are the parameter W_y derived from the preceding output layer and the recently incorporated separator tags <CLS> and <SEP> as previously outlined.

After completing the transformer model pre-training and fine-tuning, the target user's raw data is used to input into the transformer and predict the output. The model generates the results, extracts the integration information, checks the keywords, and reintroduces them into the collaborative filtering recommender system. It then calculates the similarity between the transformer prediction generation results and other users, re-generates the target user's neighbourhood matrix, and obtains a new nearest-neighbour UserNeig of the target user.

The final stage is to forecast the target user's u-rating for the target user neighbourhood, $\text{newUserNeig}(\text{u})$, generated by the aforementioned module. This is achieved through the utilisation of a weighted average method to compute the scoring method, which then allows for the generation of a list of recommendation results. The N highest-rated items are then selected for recommendation to the user for reference.

Here, $\text{P}_{\text{u,j}}$ denotes the predicted rating value of the target user u for item j, $\overline{\text{R}_\text{u}}$ denotes the average rating of the target user u for the completed rated items, $\text{R}_{\text{v,j}}$ denotes the rating of the neighbouring user v of the target user u for item j, $\overline{\text{R}_\text{v}}$ denotes the average rating of the user v for the completed rated items, n denotes the

number of the neighbours of the target user u, and $\mathrm{newSim}(v,u)$ denotes the similarity between users v and u calculated using this method, λ is the start-up coefficient $0<\lambda\leq 1$. If the target user or item is a new user or item, it will face the cold start problem. The start-up coefficient will weaken the effect of this problem and reduce the interference of the new user or item on the predicted rating value until enough interaction data is collected. θ is the personalisation coefficient ($\theta>0$), which is determined by the user's historical behaviour and preferences obtained by speculating on consumer psychology and behaviour. This coefficient increases the predicted score value more or less according to the personalisation choices of the target user.

After verifying the accuracy of the model and the practicality of the mathematical formulas, we conducted a control group experiment through model calculations to validate the model's ability to improve the effectiveness of ERP experimental teaching through digital prediction and feedback.

Step 1: Put the two types of sample datasets into the Adaboost algorithm for iterative classification of sample weights.

Step 1: Input the sample data set Z=(mi, ri), where i=1,2,... n. Execute SVM algorithm.

Step 2: Find the hyperplane that can best partition the two types of data samples, i.e., satisfy r (T'h *mi+u)1 $\geq$ 0, calculate the objective function min ?

Step 3: Determine whether the sample data can be classified well under general constraints; if not possible, add a relaxation variable T to soften the maximum interval soft margin between the maximum support vectors. This allows for a small number of classification errors to occur.

Step 4: Find the optimal parameter T best, and obtain the corresponding optimal hyperplane expression.

Step 5: Substitute into the new sample dataset Z, calculate in the solved optimal hyperplane expression, obtain the result. Does the ERP autonomous experimental model using the integration of data and intelligence have a significant effect?

The application of these mathematical principles and mechanisms of the Transformer model in the autonomous experimental mode of ERP can improve the efficiency and accuracy of data processing, especially when dealing with large amounts of business data and conducting complex business logic analysis. By using Transformer models, ERP systems can better understand and predict business processes, optimize resource allocation, and make decisions

4. Results Analysis

The ideal generative model should be able to create responses that are not only logically sound, but also exhibit rich diversity in types and scope. In other words, an efficient generative model should be able to generate both reasonable and diverse responses.

After processing the sample dataset from the second experimental teaching, we can clearly see that the model we use is more accurate, and the learning ability, practical ability, and scenario application ability of the student group using our AI autonomous experimental information push model are significantly better than those using the original ordinary teaching mode.

The improved model of this paper generated significantly more accurate responses than information retrieval-based models such as Boolean Model 25 in all three types of

datasets. In addition, on the 1st-4th indicators of the BLEU metric, the model constructed in this study has shown higher efficiency and better level of accuracy compared to the current optimal model BART in NLG under the Qingyun database test, which demonstrated that the statements generated by this model were more similar to the real replies. Therefore, the GPT model constructed in this paper achieved better results in capturing contextual features. Therefore, it provided more complete and comprehensive input information for the collaborative filtering recommender system and improved the overall recommendation accuracy.

5. Conclusions

The ERP course emphasises the interconnection and mutual reinforcement between theoretical knowledge, practical application, and artificial intelligence, particularly within the context of artificial intelligence-based pedagogical approaches. Based on our improved model, we can set up, for example, an intelligent recommendation system that recommends personalized learning resources based on students' learning preferences and behavioral data, achieving personalized teaching, or a learning situation analysis system that collects and analyzes students' learning data, uses machine learning models to evaluate students' learning progress and mastery, and helps teachers provide accurate teaching feedback. The acquisition of theoretical knowledge furnishes the requisite guidance and support for practical operation and artificial intelligence. Conversely, practical operation and artificial intelligence represent the specific application and deepening of theoretical knowledge. The three elements are mutually reinforcing, facilitating students' comprehensive engagement with the subject matter and fostering a deeper understanding of ERP courses, thereby contributing to the development of highly skilled professionals.

References

[1] Sollosy M, McInerney M. Artificial intelligence and business education: What should be taught. The International Journal of Management Education. 2022;20(3):100720, doi: 10.1016/j.ijme.2022.100720.

[2] Kumar S, Rao P, Singhania S, Verma S, Kheterpal M. Will artificial intelligence drive the advancements in higher education? A tri-phased exploration. Technological Forecasting and Social Change. 2024;201:123258, doi: 10.1016/j.techfore.2024.123258.

[3] Gangwar H, Mishra R, Kamble S. Adoption of big data analytics practices for sustainability development in the e-commerce supply chain: a mixed-method study. International Journal of Quality & Reliability Management. 2023;40(4):965-989, doi: 10.1108/IJQRM-07-2021-0224.

[4] Bandara F, Jayawickrama U, Subasinghage M, Olan F, Alamoudi H, Alharthi M. Enhancing ERP Responsiveness Through Big Data Technologies: An Empirical Investigation. Information Systems Frontiers. 2024;26:251-275, doi: 10.1007/s10796-023-10374-w.

[5] Alaskari O, Pinedo-Cuenca R, Ahmad MM. Framework for implementation of Enterprise Resource Planning (ERP) Systems in Small and Medium Enterprises (SMEs): A Case Study. Procedia Manufacturing. 2021;55:424-430, doi: 10.1016/j.promfg.2021.10.058.

[6] Chen L, Chen P, Lin Z. Artificial Intelligence in Education: A Review. IEEE Access. 2020;8:75264-75278, doi: 10.1109/ACCESS.2020.2988510.

[7] Li B. Research and development of e-commerce ERP system based on artificial intelligence technology. International Journal of Knowledge-Based Development. 2023;13(2-4):327-343, doi: 10.1504/IJKBD.2023.133333.

[8] Romero JA, Abad C. Cloud-based big data analytics integration with ERP platforms. Management Decision. 2022;60(12):3416-3437, doi: 10.1108/MD-07-2021-0872.

Fuzzy Systems and Data Mining X
A.J. Tallón-Ballesteros (Ed.)

doi:10.3233/FAIA241422

Electric Power Load Forecasting: Discovering Causal Links with Meteorological Data

Hongwei Ma[a], Huimin Peng[b,*] and Weijie Ren[a]
[a] *College of Intelligent Systems Science and Engineering, Harbin Engineering University, Harbin 150001, China*
[b] *State Key Laboratory of Technology and Equipment for Defense against Power System Operational Risks, Nari Technology Co., Ltd. , Nanjing, Jiangsu, 211106, China*

Abstract. Power system load forecasting is the foundation of power system operation and planning. Meteorological factors such as temperature, humidity, and wind speed have a significant impact on the load of the power system. In recent years, with the popularity of data-driven methods, power system load forecasting has developed. However, in existing research on power systems, the study of relationships between variables is predominantly based on correlation, with little mention of the concept of causality. In this paper, an adaptive time window strategy is proposed to identify time periods where causal relationships may change. Then, the Time Causal Discovery Framework (TCDF) was used at each time window to explore the causal relationship between electricity load and climate data. Finally, compared with the traditional correlation-based analysis method, the experiment shows that our method not only explains the causal relationship between power load and climate, but also effectively improves the prediction performance.

Keywords. Causal discovery, Power system load forecasting, Time series

1. Introduction

With the rapid development of the global economy and the continuous advancement of urbanization, the demand for electricity has shown a significant upward trend[1-4]. Electric load forecasting, as the foundation of power system planning, dispatching, and operational management, has received increasing attention. The primary task of electric load forecasting is to make accurate predictions of future electricity demand by analyzing historical load data and related influencing factors. This not only helps power dispatch centers formulate reasonable power generation plans and operational strategies to ensure the stable operation of the power system but also provides scientific decision-making bases for participants in the electricity market.

Traditional load forecasting methods establish a direct correlation between predicted values and historical values[5]. These methods can demonstrate a significant relationship between independent and dependent variables, but due to their simple structure and failure to consider various load factors, the accuracy of the calculations is low[6]. To

* Corresponding Author: Huimin Peng, penghuimin@sgepri.sgcc.com.cn.

improve the accuracy of load forecasting, data-driven model-based[7] load forecasting methods have gained increasing attention. For example, Ghore et al. [8]proposed a short-term load forecasting model for Chhattisgarh using historical weather data as input variables, based on an artificial neural network (ANN). Khwaja et al. [9]presented an ensemble ANN predictive model to enhance shortterm electricity load forecasting. Atef and Eltawil [10] proposed a deep-stacked LSTM forecasting model to forecast electricity demand. Additionally, the work of Jin et al. [11]used a GRU model to improve the prediction accuracy related to temperature, wind speed, and humidity data used in agriculture. Li et al. [12]combined LSTM with time series decomposition to provide short-term load forecasting for a city in China, and used Mean Absolute Percentage Error (MAPE), Mean Absolute Error (MAE), and Root Mean Square Error (RMSE) to compare the accuracy results. Although methods such as deep learning can effectively handle these large-scale data, the black-box nature of deep learning models results in a lack of interpretability, making it nearly impossible to determine which inputs in the original data lead to the network's outputs.

Causal discovery methods can identify the causal structure within data, which helps in understanding the underlying mechanisms of data generation. Since power system data, including power load, is influenced by seasonal cycles, the causal relationships may change over different time periods. To address the issue of time-varying causality, this paper proposes an Seasonal-Trend decomposition based on Loess (STL) [13]guided adaptive time window mechanism.

- This paper aims to explore the causal relationship between short-term power system load and climate change in a specific region, and to forecast the short-term future power demand. The contributions of this paper are as follows: Introduced the Temporal Causal Discovery Framework (TCDF) [14] to investigate the causal relationships between power load and meteorological data, enhancing the interpretability of deep learning models for power load forecasting.
- Proposed a new time window partitioning strategy to address the issue of changing causal relationships across different seasons or time periods.

2. Related work

In this subsection, the STL method is introduced first. Then, the related work on time series causal discovery is reviewed.

2.1. Seasonal-Trend Decomposition Based on Loess

The STL method is a filtering process that decomposes a time series into three additive components based on LOESS smoothing. Due to its simple design and fast computation speed, it is widely used for handling large-scale time series data. Assuming the time series is X_t, STL can decompose the global time series into three additive components as follows.

$$X_t = T_t + S_t + R_t \tag{1}$$

Where T_t is the trend component, S_t is the seasonal component, and the residual R_t is the remainder component. The trend component T_t reflects the long-term changes in the time series and can be obtained by smoothing the original time series. The seasonal component S_t represents the recurring periodic fluctuations in the time series, typically obtained by smoothing the time series within each period. The residual R_t is the part of the time series that does not belong to the trend or seasonal variations, reflecting the random fluctuations in the time series.

2.2. Time Series Causal Discovery

The earliest method for time series causal discovery is the Granger causality test [15] proposed by Granger in 1969. This method is based on predictive testing; that is, if considering the past values of sequence *Y*, the addition of past values of *X* can significantly improve the prediction of *Y*, then X is considered to be a Granger cause of *Y*.

Traditional Granger causality analysis methods typically assume linear time series dynamics and construct vector autoregressive models. However, this approach cannot handle nonlinear scenarios[16]. In recent years, many methods have introduced deep neural networks to help infer nonlinear Granger causality. Tank et al. [17] modeled each output component separately, using group sparse Lasso to penalize the weights of the first layer to infer Granger causality. Structured component-based MLP and LSTM with sparse input layers are referred to as cMLP and component cLSTM, respectively, and this approach has gained wide recognition.

Additionally, another effective method for time series causal discovery using neural networks is the Temporal Causal Discovery Framework (TCDF) proposed by Nauta et al. [14] This method utilizes Convolutional Neural Networks (CNNs) and attention mechanisms to effectively handle non-linear and complex dependencies in time series data. The attention mechanism emphasizes important time points and variables in the time series data, thereby enhancing the interpretability and accuracy of causal relationship inference.

Inspired by these studies, we introduce causal discovery into power system load forecasting. We also incorporate STL into time series causal discovery, as it can capture the seasonal and trend components of time series and guide the division of time windows. Using a causality-based forecasting method leverages the underlying causal relationships between variables for prediction, offering better interpretability and greater adaptability to changes in the data.

3. Methodology

This chapter describes the overall process of our proposed method. First, a brief review of the related TCDF is provided. Then, the STL-Guided Time Windows for TCDF is introduced. Finally, the chapter explains how to use the STL-Guided Time Windows for TCDF for power load forecasting.

3.1. Temporal Causal Discovery Framework

TCDF is composed of *N* independent depthwise separable convolutional neural networks (CNNs) with attention mechanisms, as shown in Figure 1. They have the same structure but different target sequences.

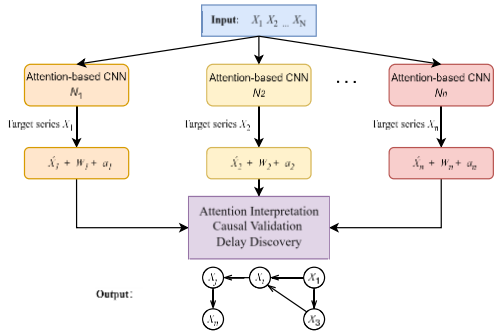

Figure 1. Diagram of the Temporal Causal Discovery Framework

The i-th neural network N_i predicts the target sequence X_i by minimizing the loss between the predicted value and the actual value. In addition to predicting the target sequence X_i, each convolutional neural network outputs its corresponding weight W_i and attention score a_i. Through attention interpretation, PIVM causal validation, and lag discovery, TCDF will output a temporal causal graph. For the task of electric load forecasting, the input time series X_1 to X_n typically include the total power demand of a specific region as well as other factors that influence power demand, such as the temperature, specific humidity, wind speed, and liquid water content in that region.

3.2. STL-Guided Time Windows for TCDF

This section introduces the process of our proposed method for prediction tasks. First, the target time series is decomposed using STL to obtain the corresponding trend, seasonal, and residual components, as shown in Figure 2.

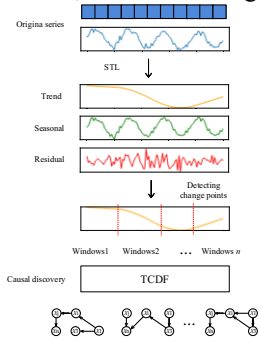

Figure 2. STL-Guided Time Windows for TCDF

Then, change point detection methods are used to detect significant changes in the trend component, assuming that periods of significant trend changes indicate shifts in causal

relationships. Based on the locations of the change points, the original series is divided into multiple time windows. Finally, TCDF is applied to each time window to obtain causal graphs for different periods. During prediction, the parent nodes (causal variables) of the target variable in each time window are selected for prediction, as these variables are involved in data generation.

4. Experiments and Results

The dataset used comes from Kaggle's Short-Term Electric Load Forecasting (Panama Case Study). The data includes the national electricity demand for the region from 2015 to June 2020, as well as meteorological data from three stations: temperature, specific humidity, total column-integrated liquid water, and wind speed. We first used the STL-Guided Time Windows for TCDF method to explore the causal relationships between electricity demand and meteorological data and to predict short-term electricity load. Then, we used some correlation methods for comparison to verify the effectiveness of our method.

4.1. Time Window and Causality Testing

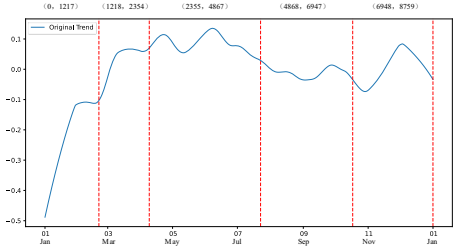

Figure 3. STL-Guided Time Windows

The data records hourly electricity demand and meteorological data, with a total of 8760 time points. We use the data from 2018-2019 as the training set, and the resulting time window segmentation is shown in Figure 3. The blue curve in the figure represents the trend component of electricity demand extracted through STL. The y-axis indicates the standardized values of the trend component, typically ranging from -1 to 1. A negative trend value usually indicates that the data is decreasing or at a lower level during that period. For electricity demand data, if the trend value is negative at a certain time, it may suggest that the electricity demand is below the long-term average at that moment. Conversely, if the trend value is positive, it may indicate that the electricity demand is above the long-term average at that time. Based on the intervals of different time points, the dataset is divided into 5 time windows. Using TCDF in each time window can reveal time-varying causal relationships. The causal graph is shown in Figure 4.

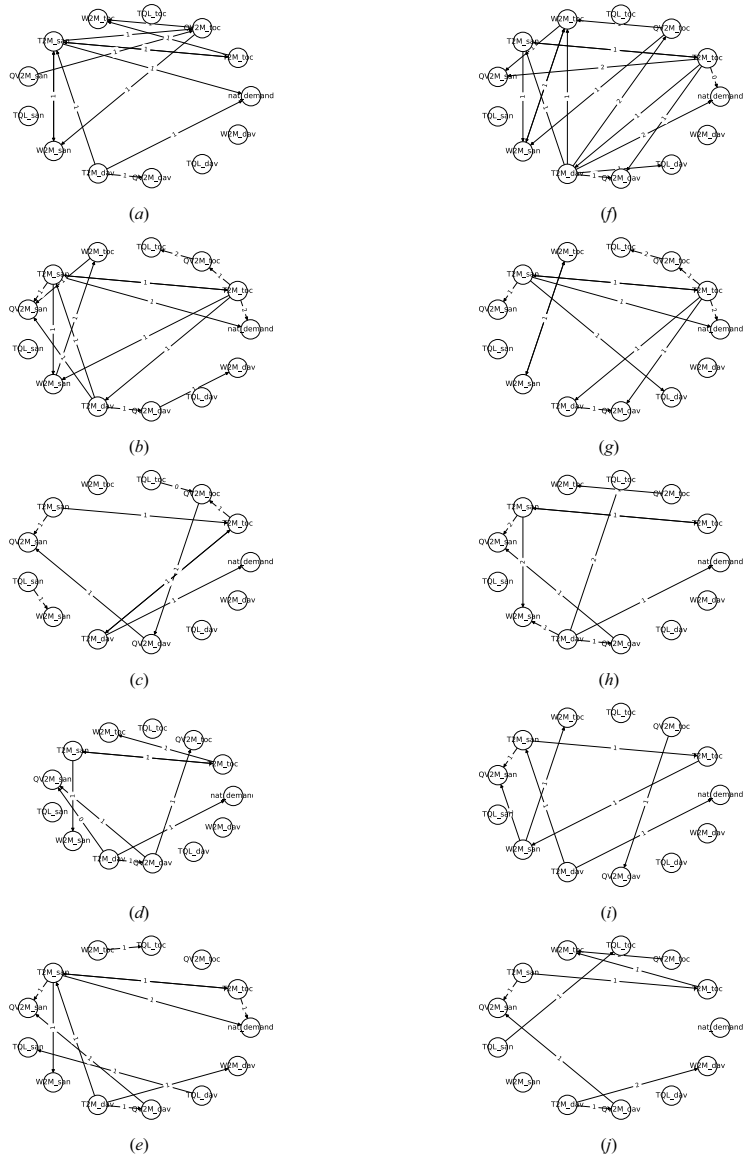

Figure4. Causal Graphs in Five Windows over Two Years (Left: 2018, Right: 2019)

In the figure, "nat_demand" represents the national electricity demand. "T2M", "QV2M", and "W2M" represent the temperature observed at 2 meters above the ground, the specific humidity, and the wind speed, respectively. "TQL" stands for total liquid water path. "toc", "san" and "dav" refer to specific weather stations at particular locations. For example, "T2M_toc" represents the temperature measured at 2 meters above the ground at the "toc" weather station. Subplots (a) to (e) represent the causal relationships within the five time windows in 2018, while (f) to (j) show the causal relationships within the five time windows in 2019. The numbers on the arrows in each causal graph indicate the time delay that causes the effect.

From the figures, it can be observed that the causal relationships between electricity demand and various meteorological factors in the same time windows of 2018 and 2019 are similar. The temperature in the observation station areas is the most direct factor influencing electricity demand. Additionally, the factors influencing electricity demand exhibit clear seasonality, changing significantly with the seasons. In 2018, subplots (*a*) and (*b*) represent the spring period, where the temperatures in the "san" and "dav" observation station areas directly affect electricity demand. Subplots (*c*) and (*d*) correspond to the summer and autumn periods, during which the temperature in the "dav" area is the direct factor influencing electricity demand. However, in winter, as shown in subplot (*e*), the temperature in the "dav" area is no longer the factor affecting electricity demand; instead, the temperature in the "san" observation area becomes the influencing factor. Similarly, in 2019, as shown in subplot (*f*) and (*g*), the factor influencing electricity demand is again the temperature observed at the "san" station, as in 2018. During the summer and autumn periods, subplots (*h*) and (*i*) show that the temperature observed in the "dav" area remains the direct factor influencing electricity demand. However, in winter, as shown in subplot (*j*), the temperature in the "dav" area is no longer the factor affecting electricity demand. The reason might be that the most influential factor affecting electricity demand in winter has shifted from T2M_dav to T2M_san. Therefore, it can be seen that the most direct factor by which climate influences electricity demand is the temperature in a specific region.

4.2. Short-Term Electric Load Forecasting under Different Algorithms

Using the first two years of data as the training set, the causal relationships between variables in the corresponding time periods are determined. Our proposed causal framework is compared with variables selected using correlation analysis in a neural network model to predict the next year's electricity demand in the corresponding time windows. To better capture complex nonlinear relationships, we employed the Mutual Information-based feature selection method, the minimal-redundancy-maximal-relevance criterion (mRMR) [18]. The top 5 features selected by mRMR, along with the load sequence itself, were used as inputs to the neural network prediction model. In contrast, our causal analysis approach used the top 5 causal variables with the shortest time delays. Using the first time window as an example, as shown in Figure 5.

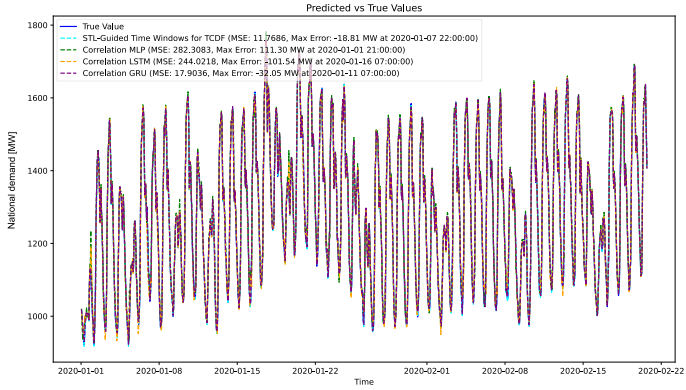

Figure5. Comparative Experiments on Electric Load Forecasting Using Different Algorithms

Mean Squared Error (MSE) is a commonly used metric to measure the difference between a model's predicted results and the actual values. MSE calculates the average of the squared differences between the predicted values and the actual values. To more clearly compare the prediction performance of the causal analysis method and the correlation-based methods, the MSE between the predicted and actual values was calculated for different algorithms. Additionally, the maximum absolute error (MAE) and the time at which it occurred were displayed in the figure. A positive error indicates that the algorithm predicted a higher load at the time of the maximum error. The formula for calculating the MSE is as follows:

$$MSE = \frac{1}{n}\sum_{i=1}^{n}\left(\hat{y}_i - y_i\right)^2 \tag{2}$$

Where n is the number of samples, $\hat{y}_i$ is the predicted value for the i-th sample, and y_i is the actual value for the i-th sample. To more clearly confirm the experimental results, Table 1 summarizes the findings.

Table 1. Comparative Experiments on Electric Load Forecasting Using Different Algorithms

Algorithm	MSE	MAE	Time of MAE Occurrence
STL-Guided Time Windows for TCDF	**11.77**	**-18.81**	2020-01-07 22:00
Correlation MLP	282.31	111.30	2020-01-01 21:00
Correlation LSTM	244.02	-101.54	2020-01-16 07:00
Correlation GRU	17.90	-32.05	2020-01-11 07:00

Based on the experimental results, the prediction error of STL-Guided Time Windows for TCDF is significantly lower than that of other correlation-based methods. This indicates that predictions based on causal relationships outperform those based on correlations. The results are more accurate because the causal framework uses variables that actually cause changes in the load, rather than merely correlated variables, to guide the prediction of electricity load changes. The lower prediction performance of correlation-based MLP and LSTM compared to GRU might be due to GRU's stronger capability in time series prediction. However, compared to the correlation GRU, STL-Guided Time Windows for TCDF achieved a 34.27% improvement. The formula for calculating the improvement rate is as follows:

$$Improvement\ rate = \frac{Correlation\ GRU's\ MSE - Causal's\ MSE}{Correlation\ GRU's\ MSE} \times 100\% \tag{3}$$

Additionally, the maximum error for each algorithm occurred during the first half of January 2020, which could be due to the neural network not having enough past time samples in the early stages, or the presence of extreme weather conditions around this period, leading to inaccurate predictions.

5. Conclusion

This paper proposes a new time window partitioning strategy based on the seasonality and trend of time series and introduces the TCDF causal discovery method for application in power system load forecasting. Experimental results show that our method not only explains the causal relationships between power load and various climatic variables but also effectively improves forecasting performance.

References

[1] Nti IK, Teimeh M, Nyarko-Boateng O, Adekoya AF. Electricity load forecasting: a systematic review. J Electr Syst Inf Technol. 2020;7:1-19. doi: 10.1186/s43067-020-00021-8.
[2] Ahmad N, Ghadi Y, Adnan M, Ali M. Load forecasting techniques for power system: research challenges and survey. IEEE Access. 2022;10:71054-71090. doi: 10.1109/ACCESS.2022.3187839.
[3] Xiao Z, Fu X, Zhang L, et al. Big data driven vessel trajectory and navigating state prediction with adaptive learning, motion modeling and particle filtering techniques. IEEE Trans Intell Transp Syst. 2020;23(4):3696-3709.
[4] Morais LBS, Aquila G, de Faria VAD, et al. Short-term load forecasting using neural networks and global climate models: An application to a large-scale electrical power system. Applied Energy. 2023;348:121439. doi: 10.1016/j.apenergy.2023.121439.
[5] Hou H, Liu C, Wang Q, et al. Review of load forecasting based on artificial intelligence methodologies, models, and challenges. Electric Power Systems Research. 2022;210:108067.
[6] Ekonomou L, Christodoulou CA, Mladenov V. A short-term load forecasting method using artificial neural networks and wavelet analysis. Int J Power Syst. 2016;1: p. 64-68.
[7] He Y, Zhu D, Chen C, Wang Y. Data-driven control of singularly perturbed hybrid systems with multi-rate sampling. ISA Trans. 2024;148:490-499. doi: 10.1016/j.isatra.2024.03.021.
[8] Ghore S, Goswami A. Short term load forecasting of Chhattisgarh grid using artificial neural network. Int J Eng Dev Res. 2015;3: p. 391-397.
[9] Khwaja AS, Anpalagan A, Naeem M, et al. Joint bagged-boosted artificial neural networks: Using ensemble machine learning to improve short-term electricity load forecasting. Electr Power Syst Res. 2020;179:106080.
[10] Atef S, Eltawil AB. Assessment of stacked unidirectional and bidirectional long short-term memory networks for electricity load forecasting. Electr Power Syst Res. 2020;187:106489.
[11] Jin XB, Yang NX, Wang XY, et al. Hybrid deep learning predictor for smart agriculture sensing based on empirical mode decomposition and gated recurrent unit group model. Sensors. 2020;20(5):1334.
[12] Li K, Huang W, Hu G, et al. Ultra-short term power load forecasting based on CEEMDAN-SE and LSTM neural network. Energy Build. 2023;279:112666.
[13] Cleveland R, Cleveland W, McRae J, Terpenning I. STL: A seasonal-trend decomposition procedure based on Loess (with discussion). J Off Stat. 1990;6(1):3.
[14] Nauta M, Bucur D, Seifert C. Causal Discovery with Attention-Based Convolutional Neural Networks. Mach Learn Knowl Extr. 2019;1:312-340. https://doi.org/10.3390/make1010019.
[15] Granger CWJ. Investigating causal relations by econometric models and cross-spectral methods. Econometrica. 1969;37(3):424-438.
[16] Assaad CK, Devijver E, Gaussier E. Survey and evaluation of causal discovery methods for time series. J Artif Intell Res. 2022;73:767-819. doi: 10.1613/jair.1.13428.
[17] Tank A, Covert I, Foti N, et al. Neural Granger causality. IEEE Trans Pattern Anal Mach Intell. 2021;44(8):4267-4279.
[18] Peng H, Long F, Ding C. Feature selection based on mutual information criteria of max-dependency, max-relevance, and min-redundancy. IEEE Trans Pattern Anal Mach Intell. 2005 Aug;27(8):1226-38. doi: 10.1109/TPAMI.2005.159.

Acknowledgements

This work was supported by the State Key Laboratory of Smart Grid Protection and Operation Control (SGNR0000KJJS2302140) and the National Natural Science Foundation of China (62206071).

Fuzzy Systems and Data Mining X
A.J. Tallón-Ballesteros (Ed.)

doi:10.3233/FAIA241423

Vision Transformers and CNN-Based Knowledge-Distillation for Histopathological Image Classification

Seddik BOUDISSA [a,1], Shyam Sundar DEBSARKAR [b] and Hiroharu KAWANAKA [a]
Bruce ARONOW [b,c,d,e] V. B. Surya PRASATH [b,c,d,e]

[a] *Graduate School of Engineering, Mie University, 1577 Kurima-machiya, Tsu, Mie 514-8507, Japan*
[b] *Department of Computer Science, University of Cincinnati, OH 45221, USA*
[c] *Division of Biomedical Informatics, Cincinnati Children's Hospital Medical Center, Cincinnati, OH 45229, USA*
[d] *Department of Pediatrics, University of Cincinnati, OH 45267, USA*
[e] *Department of Biomedical Informatics, College of Medicine, University of Cincinnati, OH 45267, USA*

ORCiD ID: Seddik Boudissa https://orcid.org/0009-0001-1824-2361, Shyam Sundar Debsarkar https://orcid.org/0009-0002-3448-0535, Hiroharu Kawanaka https://orcid.org/0009-0007-6601-9213, Bruce Aronow https://orcid.org/0000-0001-5109-6514, V. B. Surya Prasath https://orcid.org/0000-0001-7163-7453

Abstract. Histopathological image analysis remains at the forefront of computational pathology presenting numerous challenges and demanding tasks, primarily due to the complex nature of tissue structures and the extensive scale of whole slide images (WSIs). Deep learning models have been widely used in histopathology image analysis, especially convolutional neural network (CNN)-based models for classification. However, CNNs have certain limitations due to their small receptive field . Recent works employed adaptations of the classical transformer architecture to visual data [1] [2]. Models such as Vision Transformer (ViT) and Swin Transformer leverage the powerful multi-head self-attention mechanism and have demonstrated comparable or superior performance to state-of-the-art CNN-based classification models. Despite their successes, these models require huge amounts of training data to effectively learn representations as they lack the inherent inductive biases of CNNs. This work compares Vision Transformers with baseline CNN models using a breast cancer histopathological dataset. Further, we employ a novel knowledge-distillation approach to enhance the learning efficiency of vits, When trained with a limited amount of data, Unlike previous works, we aimed to minimize convolution operations when generating patch embeddings to preserve spatial information before reaching the transformer attention layers, we achieved an accuracy of 87.7% for the ViT-base trained as a student of ResNet50, which represents a 1.2% improvement in accuracy over the standalone ViT-base . [3]

[1]Corresponding Author: Seddik BOUDISSA, Graduate School of Engineering, Mie University, mrseddikboudissa@gmail.com .

Keywords. Histopathology; image classification; deep learning; convolutions; attention mechanism; vision transformers.

1. INTRODUCTION

Deep learning (DL) models in general and convolutional neural networks (CNNs) [4–6] in particular have long been dominant in medical computer vision. However, Transformers [7], originally developed for natural language processing (NLP) [8], are effective in capturing long-range dependencies between tokens (e.g., words in a paragraph) thanks to their self-attention mechanism. Recently, this architecture has been adapted to address vision tasks. Inspired by Transformers' architecture [7] success in NLP [8], [3] presented the Vision Transformer (ViT) as the first pure transformer architecture for image recognition tasks that treats images the same way the classical transformer treats a sequence of words, with each image patch acting as a word in a sentence. ViT has shown great performance when pretrained with massive amounts of data (JFT-300 M [9]), and transferred to smaller image recognition tasks (ImageNet [10], CIFAR-100 [11], etc.) However, ViT [3] encounters some limitations when pre-trained due to its quadratic complexity to the image size. ViT [3] computes attention scores between all tokens, processing such massive images becomes computationally impractical. In computational pathology domain, whole slide images (WSIs) typically can reach sizes of $35,000 \times 46,000$ pixels, highlighting the scalability challenge with respect to ViT's high complexity.

To address these limitations, Liu et al [12] introduced the Swin Transformers. This novel architecture utilizes a hierarchical structure with "shifted windows". This approach significantly improves efficiency by restricting self-attention calculations to local, non-overlapping windows while enabling connections between windows. This hierarchical design allows Swin Transformers to model information at various scales while maintaining a linear computational complexity to image size, making them ideal for handling high-resolution images. To this point, CNNs like classic ResNets [4] remain dominant in the realm of image recognition tasks owing to their robust inductive biases, particularly in scenarios where extensive datasets are not available for training transformers. The inherent strengths of CNNs lie in their ability to exploit their locality inductive bias and translation invariance nature. However, in certain tasks requiring capturing fine details and handling complex features with long-range dependencies, Vits [3] can outperform state-of-the-art CNNs due to their inherent globality, allowing them to establish connections between distant parts of the input while maintaining high-resolution feature maps, this applies when a big amount of labeled data is available.

In this work, we assess Vision Transformers against CNN base models on a breast cancer "Breakhis" dataset [13]. There have been a wealth of DL models applied to computational pathology datasets [14], and majority of the models involve CNNs and transformers [15, 16] or hybrid combinations [17]. In this study, we propose a novel knowledge distillation (KD) approach between Vits and CNN-based models, utilizing a flexible weighting between the student loss and the teacher distillation loss. This approach aims to effectively combine convolutional and self-attention mechanisms to improve the learning efficiency of Vits without imposing the inductive bias limitations of CNNs on the transformer's learning. Using Mean Attention (MA) distance plots we shed light on how encouraging a transformer to minimize CNN loss can impact its receptive field and learning behavior. The primary contributions of our work can be stated as follows:

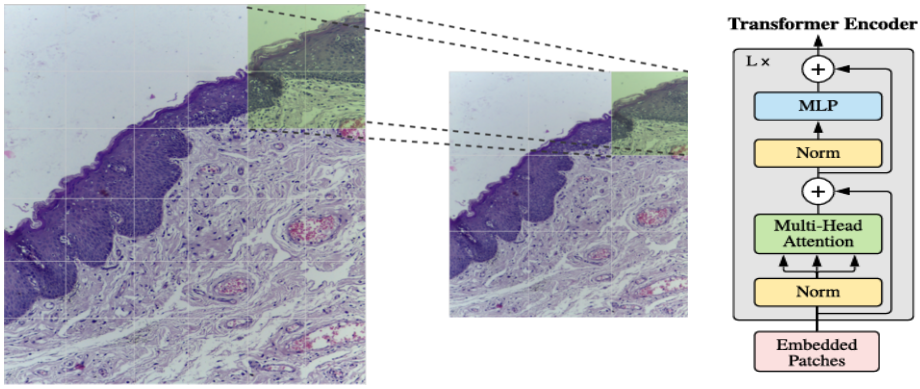

(a) (b)

Figure 1. Convolution and attention. (a) CNN's receptive field, demonstrating how the receptive field of CNNs is relatively small since In early layers, it is limited to neighboring pixels. (b) Transformer's encoder block.

- A comprehensive comparative study between the internal architectures and behaviors of CNNs (ResNet's [4], VGG's [18]) and Vision Transformers [3] [12] on a breast cancer histopathological dataset [13].
- Incorporating a novel knowledge distillation approach, we impart more locality to Vision Transformers by training on the CNN model's loss, using the mean attention distance of the early layers as a factor to adjust the weighting between the student loss and the distillation loss. This enables the models to learn effectively with less data and achieve better accuracy
- Mean Attention Distances plots to assess the Vision Transformers' receptive field.

2. BACKGROUND

2.1. Convolution and Attention

2.1.1. Convolutions

CNNs utilize sliding windows to leverage the inherent spatial relationships within the data. These relationships, such as neighboring pixels, are effectively captured thanks to the local nature of the convolutional operations. The process begins with a small receptive field that grows over layers. By incorporating such desirable inductive biases that guide the learning process, CNNs reduce computational complexity by connecting only to neighboring units, thereby optimizing spatial data processing. Receptive field of the CNN's capture the localized information images, see Figure 1(a). The number of inputs at each layer by which the output is computed is given as follows,

$$r_l = s_l . r_{l-1} + (k_l - s_l), \tag{1}$$

where r - receptive field, l - layer, s - stride, k -the kernel size.

2.1.2. *Self Attention in Transformers*

The Transformer encoder contains alternating layers of multiheaded self-attention and multi-layer perceptron (MLP) blocks. Layer normalization (LN) with residual connections is applied before each block as shown in Figure 1(b). The attention used in the transformer is a variant of the attention mechanism, that first generates for each input embedding, a query, a key, and value matrices. These matrices are obtained after multiplying the input matrix X by trainable parameters (Wq,Wk,Wv), then the attention map matrix is calculated with the following equation :

$$Attention(Q,K) = \frac{softmax(QK^t)}{\sqrt{dk}} \tag{2}$$

Q and K are the Query and Key matrices generated for each patch embedding through a linear layer.
dk is the dimension of the the key matrice

2.2. *Mean Attention Distance*

The mean attention distance is a value that indicates the importance assigned by a specific token to all other tokens, determined by the distance between them in the sequence.

Taking a look at the self-attention mechanism, we know that each token attends to all other tokens, also we have multiple layers of attention blocks, with each block containing multiple heads. To compute the mean attention distance for every head:

- A Key and Query vectors are generated for each input token.
- An attention weight is computed between every pair of tokens.
- Then a pixel distance matrix ”D” is calculated between every pair of tokens, multiplied by the correspondent weight score ”WS” and averaged over all tokens to get the attention distance ”dk”,

$$Attentiondistance = \frac{(WS * D)}{dk}. \tag{3}$$

A large attention distance means that most of the ’faraway patches’ have large attention weights. In other words, most of the attention is ’global,’ meaning that most of the features are obtained through relationships between distant parts of the image . Inversely, a small attention distance means the attention is local.

3. Method

An overview of the proposed knowledge-distillation approach is presented in Figure 2. The goal is to transfer the CNN teacher’s behavior and representation learning, including locality, to the Vision Transformer (ViT) student [3], enabling the ViT to learn accurate representations with fewer data instances. Images are fed to the ViT student as a sequence of patches, processed through layers of Multi-Headed Self-Attention [7] to capture long-range dependencies. In contrast, the CNN teacher processes images as a

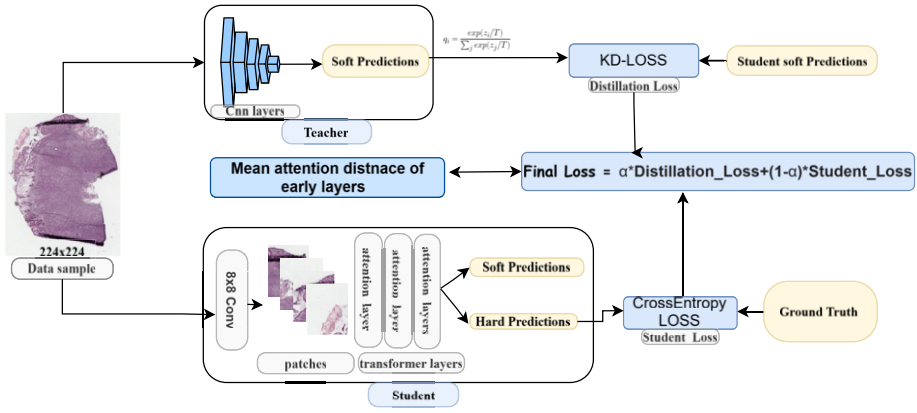

Figure 2. Our proposed approach for histopathological image classification. Distilling knowledge from a CNN-based model into a Vision Transformer (ViT) involves training the ViT by minimizing the loss between its predictions and the predictions of the CNN teacher. The input is provided as a whole to the teacher and as a sequence of patches to the student ViT. The teacher provides no intermediate layers knowledge.

whole using convolutional sliding windows to focus locally when extracting features. After obtaining soft predictions from both models using a high temperature (T $>$ 1), the student minimizes the loss [19, 20] between these predictions.

$$DestillationLoss = KLLoss(Tsoftpred, Ssoftpred) \tag{4}$$

$$StudentLoss = CELoss(Shardpred, GroundTruth). \tag{5}$$

We also push the student to learn from the ground truth by minimizing the loss between its hard predictions and the Ground truth labels, to keep the student getting knowledge from the real labels,

In previous works, patch embeddings are generated using a convolutional layer with a stride of 16 and a kernel size of 16 . This reduces the input size from 224x224x3 to an output of 14x14x768. Each patch corresponds to a pixel from each output channel, resulting in 196 patches. In our implementation, we reduce the convolutional layer's kernel size to 8 and the stride to 8. This adjustment changes the input from 224x224x3 to an output of 28x28x768. This reduction is designed to preserve more of the spatial information from the input image, which is crucial given the fine-grained and microscopic details in the tissue data we are working with . Moreover, this adjustment gives the Vision Transformer more flexibility to detect global patterns in the input feature map, rather than being constrained and limited by the inductive bias of the CNN,less limitations means more representation power. Since the complexity of the Vision Transformer is quadratic with respect to the number of patches, we maintain the same number of patches as in the previous implementation (196). However, each patch now corresponds to a 2x2 pixel area from every output feature map.

$$GlobalLoss = \alpha * DestillationLoss + (1 - \alpha)StudentLoss. \tag{6}$$

To reduce the limitations imposed by the CNN's inductive biases during learning, we introduce a new approach in the distillation process, a flexible alpha parameter. Alpha represents the weighting between the student's own loss and the distillation loss from the teacher. This parameter is dynamically adjusted based on the mean attention distance of the early layers in the Vision Transformer.

As the mean attention heads in the early layers begin to focus more on local features during training, alpha is gradually shifted more towards the student's own loss. This allows the student model to develop its own local and global understanding, while still benefiting from the teacher's guidance.

4. Experiments

We evaluate the capabilities of ResNet variants [4], VGG [18], Vision Transformer model (ViT) [3], Swin Transformer [12], and our distilled vision transformer models through multiple tests on the BreakHis dataset. Next, we analyze the effect of distillation on the receptive fields of the ViT using mean attention distance plots.

Dataset: Our models are evaluated on a breast cancer dataset, namely the BreakHis [13] which is composed of 7909 microscopic images of breast tumor tissue collected from 82 patients using different magnifying factors (40X, 100X, 200X, and 400X). It contains 2,480 benign and 5,429 malignant samples.

Metrics: To evaluate the DL models we used two evaluation metrics. Accuracy which is the correctness of the model's predictions across all classes. accuracy is calculated as the sum of all correct predictions overall predictions. In addition to accuracy, we used the F1-score which is calculated as follows,

$$F1 = 2 * \frac{Precision + Recall}{Precision * Recall}, \tag{7}$$

where,

- *Precision:* This measures the accuracy of positive predictions. It is the ratio of true positive predictions (correctly predicted positive instances) to the total predicted positive instances (both true positives and false positives). Precision focuses on minimizing false positives.
- *Recall*: This measures the ability of a model to identify positive instances correctly. It is the ratio of true positive predictions to the total actual positive instances (true positives and false negatives). Recall focuses on minimizing false negatives.

4.1. Classification Results

On the Breakhis [13] dataset, ResNet50, ResNet152 and VGG19 achieved accuracies of 84.57%, 85.12% and 83.10% respectively. In contrast, Vision Transformer (ViT)-Base obtained 86.5%, and the vit large achieved 87.3%, Although the data size isn't sufficient for ViTs, they still outperform CNN-based models. This is due to their ability to capture complex features that require a global perspective of the whole slide image, which CNNs struggle to achieve due to their inherent locality. ResNets would usually achieve much higher accuracy on simpler tasks using the same amount of data used here.

Table 1. Experiments on Breakhis dataset with various DL CNN, Transformers, and our proposed knowledge-distillation-based combinations.

Model	*Param*	*Accuracy*	*F1-score*
ViT-Base	86M	86.5%	0.8615
ViT-Large	307M	87.3 %	0.8687
Swin-S	50M	83.30	0.8317
ResNet50	25M	84.57	0.8337
ResNet152	60M	85.12	0.8426
VGG19	144M	83.10	0.8426
Ours(Swin-S+ResNet50 s)	75M	84.1%	0.8314
Ours(ViT-B+Resnet50 s)	111M	**87.7**%	**0.8756**
Ours(ViT-B+VGG19 s)	111M	**87.25**%	**0.8680**
Ours(Swin-S+ResNet50 h)	75M	84.52%	0.8380
Ours(ViT-B+Resnet50 h)	111M	**87.45**%	**0.8710**

Distilling soft knowledge from ResNet50 to Vit_Base obtained 87.7% which brings an additional 1.2% accuracy over the ViT-base and 0.4% over the ViT large with less number of parameters. Hard distillation gave better results also with 87.45% for the ViT-base. Moreover, the Swin-S [12] achieved (83.3%) distilled obtained a relative gain of 0.8%, 84.1%, and 1.2% respectively when distilled with hard predictions. These are provided in Table 1 along with the number of parameters of each of tested models and the knowledge-distillation models. As can be seen, our proposed knowledge-distillation approach that combines CNN (Teacher), and ViT (Student) models obtain the top 3 accuracies and F1-scores.

4.2. *Mean Attention Distance*

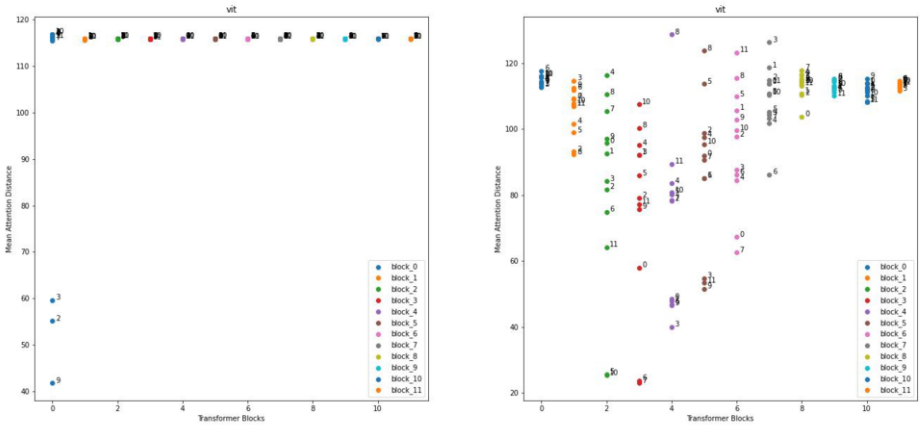

(a) ViT-base Mean Attention Distance (b) Distilled ViT-base Mean Attention Distance

Figure 3. Mean Attention Distance for (a) ViT-base and (b) distilled ViT-base models

We calculated the pixel distance attended to by each attention head, taking into account the attention weights, and then we got the average of these distances across all data points (BreakHist [13]) to obtain the *average attention head distance*.

From Figure 3a, we observe that almost all the layers of our ViT model have high mean attention head distances (Global heads), which means all layers tend to focus globally during the learning process. In other words, ViT does not infer on what to focus and lacks all sorts of guidance. The property highlights that for ViT's to learn meaningful features it requires a huge amount of data. This contrasts with CNNs, which are hardcoded to attend only locally in the lower layers. From Figure 3b we can see that when distilled, the VIT attends locally in the early layers, distillation here transfers the locality inductive bias of the ResNet to the ViT hence making it able to discern on what to focus from early layers thus, it gave better results using smaller amounts of data. Dosovitskiy [3] found similar outcomes when pretrained the vision transformer on the JFT300 [9] dataset (over 300M instances).

5. Limitations and Future Research

One of the key challenges in working with Transformers is understanding precisely what the model is learning throughout its layers. Currently, we lack clear visibility into the specific types of features that Transformers learn, and how these features compare to those learned by CNN-based models.

Gaining deeper insights into the nature of the features learned by Transformers could significantly enhance our ability to optimize their training while preserving the flexibility inherent in the attention mechanism. The primary advantage of attention is its ability to learn without being constrained by predefined biases, so maintaining this freedom is crucial.

To explore these questions further, we could leverage metrics such as Centered Kernel Alignment (CKA). This metric could help us compare the representations learned by our model with those learned by other models, providing valuable insights into their similarities and differences it can also give better insights into the roles and functions of the different attention heads within the Transformer. Understanding which heads are focusing on specific features or aspects of the input data allows us to analyze how each head contributes to the model's overall representation.,With this knowledge, we can apply targeted weighting to the attention heads, potentially enhancing their ability to capture relevant features and generate more powerful representations.

6. Conclusion

In this study, we compared the attention mechanisms of Vision Transformers with classical convolutional networks [6] on a histopathological dataset. We explored the internal mechanisms of models employing convolution and self-attention, emphasizing how data size and feature complexity affect the model performance, We also evaluated the impact of knowledge-distillation from CNN-based models (ResNet [4], VGG [18]) to self-attention-based models (ViT [3], Swin [12]) on the receptive field and learning capabilities of our models. This analysis involved plotting the mean attention distances of

each attention head to assess how the attention mechanism of Vision Transformers behaves when learning from the signal of a CNN-based model. Our experimental results indicate that our approach benefits ViTs trained on limited data as shown on a breast cancer histopathology classification task. Notably, previous works [3] demonstrated ViT and Swin achieving comparable results after pretraining on large datasets, highlighting the efficacy of extensive data in VIT's performance, which is unavailable in domains like histopathology. Our future works include the use of the proposed knowledge-distillation approach to segmentation challenges in the computational pathology domain.

References

[1] Touvron H, Cord M, Douze M, Massa F, Sablayrolles A, Jégou H. Training data-efficient image transformers & distillation through attention. In: International Conference on Machine Learning. PMLR; 2021. p. 10347-57.

[2] Zhao B, Song R, Liang J. Cumulative spatial knowledge distillation for vision transformers. In: Proceedings of the IEEE/CVF International Conference on Computer Vision; 2023. p. 6146-55.

[3] Dosovitskiy A, Beyer L, Kolesnikov A, Weissenborn D, Zhai X, Unterthiner T, et al. An image is worth 16x16 words: Transformers for image recognition at scale. arXiv preprint arXiv:201011929. 2020.

[4] He K, Zhang X, Ren S, Sun J. Deep residual learning for image recognition. In: IEEE Conference on Computer vision and Pattern Recognition; 2016. p. 770-8.

[5] Dabeer S, Khan MM, Islam S. Cancer diagnosis in histopathological image: CNN based approach. Informatics in Medicine Unlocked. 2019;16:100231.

[6] LeCun Y, Bengio Y, Hinton G. Deep learning. Nature. 2015;521(7553):436-44.

[7] Vaswani A, Shazeer N, Parmar N, Uszkoreit J, Jones L, Gomez AN, et al. Attention is all you need. Advances in Neural Information Processing Systems. 2017;30.

[8] Chowdhary K, Chowdhary K. Natural language processing. Fundamentals of Artificial Intelligence. 2020:603-49.

[9] Sun C, Shrivastava A, Singh S, Gupta A. Revisiting unreasonable effectiveness of data in deep learning era. In: IEEE International Conference on Computer Vision; 2017. p. 843-52.

[10] Deng J, Dong W, Socher R, Li LJ, Li K, Fei-Fei L. Imagenet: A large-scale hierarchical image database. In: IEEE Conference on Computer Vision and Pattern Recognition. Ieee; 2009. p. 248-55.

[11] Krizhevsky A, Hinton G, et al. Learning multiple layers of features from tiny images. University of Toronto, ON, Canada; 2009.

[12] Liu Z, Lin Y, Cao Y, Hu H, Wei Y, Zhang Z, et al. Swin transformer: Hierarchical vision transformer using shifted windows. In: IEEE/CVF International Conference on Computer Vision; 2021. p. 10012-22.

[13] Spanhol FA, Oliveira LS, Petitjean C, Heutte L. A dataset for breast cancer histopathological image classification. IEEE Transactions on Biomedical Engineering. 2015;63(7):1455-62.

[14] Hayakawa T, Prasath VBS, Kawanaka H, Arronow BJ, Tsuruoka S. Computational nuclei segmentation methods in digital pathology : A Survey. Archives of Computational Methods in Engineering. 2021;28(1):1-13.

[15] Yonekura A, Kawanaka H, Prasath VBS, Aronow BJ, Takase H. Glioblastoma Multiforme tissue histopathology images based disease stage classification with deep CNN. In: IEEE 6th International Conference on Informatics, Electronics & Vision (ICIEV). Himeji, Hyogo, Japan; 2017. .

[16] Van der Laak J, Litjens G, Ciompi F. Deep learning in histopathology: the path to the clinic. Nature Medicine. 2021;27(5):775-84.

[17] Nakagaki R, Debsarkar SS, Kawanaka H, Aronow BJ, Prasath VS. Deep learning-based IDH1 gene mutation prediction using histopathological imaging and clinical data. Computers in Biology and Medicine. 2024;179:108902.

[18] Simonyan K, Zisserman A. Very deep convolutional networks for large-scale image recognition. arXiv preprint arXiv:14091556. 2014.

[19] Günder M, Piatkowski N, Bauckhage C. Full Kullback-Leibler-Divergence Loss for Hyperparameter-free Label Distribution Learning. arXiv preprint arXiv:220902055. 2022.

[20] Mao A, Mohri M, Zhong Y. Cross-entropy loss functions: Theoretical analysis and applications. In: International Conference on Machine learning. PMLR; 2023. p. 23803-28.

Fuzzy Systems and Data Mining X
A.J. Tallón-Ballesteros (Ed.)

doi:10.3233/FAIA241424

A Feature Extraction Method for Distributed Photovoltaic Ledger Information Based on Multi-Source Heterogeneous Data Fusion

Zhihai Li [a,b,*] , Baoju Li[c], Haoyong Yi [a,b], Jiyue Fu[c], Dongjun Tang [a,b] and Guanqun Zhuang[c]
[a] *State Grid Electric Power Research Institute Co., Ltd, China*
[b] *Nanjing NARI Information & Communication Technology Co., Ltd. Nanjing, China*
[c] *State Grid Jilin Electric Power Co., Ltd, China*
ORCiD ID: Zhihai Li https://orcid.org/0009-0002-7117-393X

Abstract. Solar photovoltaic power generation has become one of the most important means of securing the world's energy supply strategy, drastically reducing emissions and ensuring sustainable development by taking advantage of the cleanliness and safety of the energy source. The development of photovoltaic (PV) power stations in pieces and the formation of PV power station clusters have become a new issue. Most traditional methods use ledger data from a single source for feature extraction, and it is difficult to achieve complete extraction of their features. In this paper, a distributed PV plant cluster ledger feature extraction method based on multi-source heterogeneous data fusion is proposed to achieve accurate prediction of PV power cluster power. Firstly, the information integration equipment is used to aggregate the power generation status information of the PV power plant cluster, including natural environment information, module parameters, battery energy storage, shadow coverage, etc. to achieve the collection of heterogeneous data from multiple sources. Secondly, the energy conversion calculation is performed based on the above information, and the unit time failure rate information is integrated to optimize the energy conversion through the failure rate calculation model. Finally, the LSTM neural network is used to process the above information, and the neural network is used to predict the PV power to optimize the operation of the PV power system. The comparison with the linear regression model proves that the model proposed in this paper has a higher prediction effect.

Keywords. multi-source heterogeneous data fusion, distributed photovoltaic power plants, Feature Extractions

1. Introduction

In recent years, countries around the world have paid more and more attention to clean energy, and clean energy has become an important trend in global energy development. New energy and grid-connected power generation has become a hot issue in the power industry [1]. At the same time, countries around the world have introduced many policies

* Corresponding Author: Zhihai Li; Email: Zhihai-Li@outlook.com

to promote the development of new energy and photovoltaic power plants. With the growth of the demand for PV power plant monitoring system, many PV monitoring system manufacturing enterprises have emerged, and the related technology is becoming more and more mature[2]. PV power plant monitoring system mainly provides necessary data and technical support for the relevant personnel in the PV industry by collecting data such as environmental information, light resources, ambient temperature, and anomaly information.

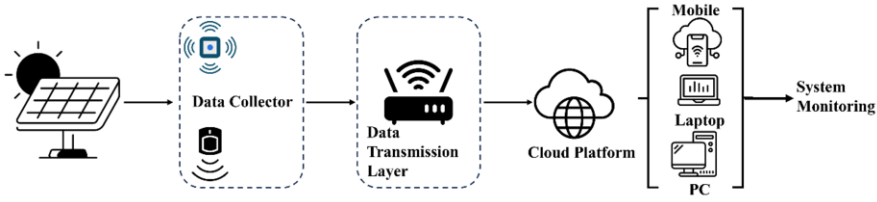

Figure 1. Architecture of common PV monitoring system

Figure 1 shows the main architecture of a common PV power generation monitoring system, which is composed of a data collection layer, a data transmission layer, a cloud platform construction layer and an application layer. The above layers enable system monitors to effectively and conveniently monitor the status of the system. The information obtained through the monitoring system is known as PV ledger information, which contains a variety of information such as environment and power generation. This information is usually heterogeneous and therefore an efficient extraction method is needed to enable feature extraction of multi-source heterogeneous ledger information from PV plants to optimize the operation of PV network systems.

The contributions of this paper are as follows: a) The use of multiple sources of heterogeneous PV power plant information provides multiple sources of information for monitoring and controlling the system, which can improve the efficiency and accuracy of monitoring and controlling. b) The use of multi-source information for the calculation of energy conversion of PV power generation can reduce the information blindness in the calculation and improve the adaptability of the system. c) Feature calculation using LSTM neural network for accurate prediction of PV power.

2. Related Work

Information fusion refers to the technology that integrates information collected from different sources, structures and architectures. The most common is multi-sensor information fusion, which refers to the fusion of information from multiple sensors in order to expand the information surface and ultimately improve the performance of the pattern recognition system. In terms of multi-source heterogeneous power data fusion, Yuan et al [3] proposed an edge intelligence-based multi-source data processing and fusion method for power distribution IoT. The method adopts the Z-score method based on Box-Cox transform to unify the magnitude and scale of multi-source heterogeneous data, and constructs a data fusion model through principal component analysis on this basis to solve the conflict phenomenon in the fusion of data sources and to ensure the effective fusion of power distribution data from different domains. Su et al [4] proposed a new energy power station remote monitoring and early warning system based on the fusion of multi-source information, and used the multipole learning particle swarm

optimization algorithm to predict the equipment operating parameters. The experimental results show that the method can monitor the equipment operation status in real time and judge the failure trend in advance. A distribution network fault location method based on power system state estimation using smart meter data was proposed by Dashtdar et al[5]. Kou [6] et al. proposed a fault monitoring model for distribution networks based on heterogeneous data from multiple sources, which uses transient phase currents as inputs to train deep feedforward network classifiers, reducing the dependence on mathematical models of faults. The experimental results demonstrate the use of transient synthetic features to improve the classification accuracy of the fault diagnostic classifier and enhance the reliability of the model. In the area of sensor information fusion, Zheng [7] et al. proposed a data fusion framework for fault diagnosis in mechanical transmission systems. Gou [8] et al. used a fused Kalman filter to diagnose faults in an aero-engine control system by integrating data from multiple sensors. Kuriakose et al.[9] compared the results of artificial neural network, linear regression and support vector machine in solar photovoltaic power prediction. Yang et al. [10]proposed a hybrid photovoltaic power prediction model based on multi-source data fusion and deep learning.

In summary, many systems have begun to utilize multi-source heterogeneous information for pattern recognition. However, they all ignored the temporal nature of photovoltaic ledger information during feature extraction, resulting in incomplete feature extraction. In this paper, an intelligent extraction method of distributed PV ledger information based on multi-source heterogeneous data fusion is proposed to achieve accurate extraction of PV ledger features.

3. The proposed methodology

Figure 2 illustrates the structure of the model proposed in this paper. The model proposed in this paper is roughly composed of four parts. The first is the multi-source heterogeneous information integration module, which integrates distributed PV power plant cluster power generation status information using PV power plant cluster information integration equipment; Secondly, there is a module for calculating the failure rate information per unit time of the PV plant group, through which the failure rate information is calculated to provide information support for the calculation of the energy conversion module at the later stage; Then comes the energy conversion calculation module through which the energy conversion matrix of the PV plant cluster is calculated; Finally, the LSTM neural network prediction module was used to calculate the relationship between the energy conversion matrix and power of the PV plant cluster by LSTM in order to assess the effectiveness of the feature extraction method.

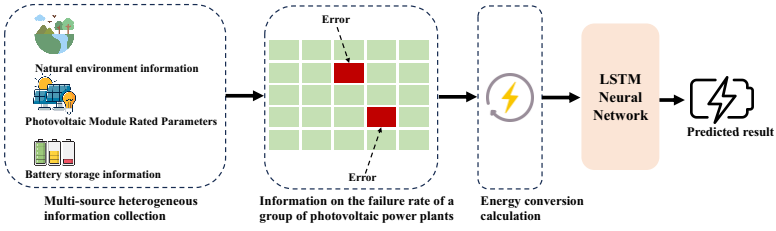

Figure 2. Model structure

3.1. Multi-source heterogeneous information collection module

In different regional environments, each photovoltaic power station is deployed with a dynamic photovoltaic power generation monitoring system with multi-source data fusion in the cloud, which utilizes the PV power station cluster information integration equipment to integrate distributed photovoltaic power station cluster power generation status information, including the natural environment information of the power generation of the photovoltaic power station cluster, photovoltaic module rating parameter, battery storage information, and shadow coverage parameter. The above multi-source heterogeneous information can provide data support for the extraction of ledger features of PV power plant clusters.

$$MData = \{H, Y, X\} \tag{1}$$

As shown in Equation 1, this paper represents the above information using a set. Where H denotes the natural environment parameters of PV power plant cluster generation, Y denotes the PV module rating parameters, and X denotes the shadow coverage parameters.

3.2. Failure Rate Calculation Module for PV Plant Groups

After obtaining the information of multi-source heterogeneous PV power plant clusters, in order to improve the performance of the model, this paper further calculates the information of PV power plant clusters' failure rate per unit time. By calculating the PV power plant cluster unit time failure rate information, the model is made to more accurately utilize the PV power plant cluster unit time failure rate information and heterogeneous information such as PV power plant cluster power generation natural environment information, PV module rating parameter, battery storage information, and shadowing coverage parameter to make efficient PV power cluster power prediction. Its calculation is shown in Equation 2.

$$Q_s = \begin{vmatrix} \mathrm{A}_{11} & \cdots & \mathrm{A}_{1\mathrm{n}} \\ \vdots & \vdots & \vdots \\ \mathrm{A}_{\mathrm{n}1} & \cdots & \mathrm{A}_{\mathrm{nn}} \end{vmatrix} \otimes \left(\mathrm{R} \frac{D^u}{F_c} \right) \tag{2}$$

In Equation 2, Q_s denotes the failure rate per unit time for different PV power plant groups, $\mathrm{A}_{11} \ldots \mathrm{A}_{1\mathrm{n}} \ldots \mathrm{A}_{\mathrm{n}1} \ldots \mathrm{A}_{\mathrm{nn}}$ denotes the matrix of failure factors per unit time for different PV power plant groups, $\otimes$ denotes the convolution calculation, R denotes the error coefficient of fault detection, which is a constant and takes a value in the range of 0-1, and D^u denotes the number of PV power plant groups in normal operation, F_c denotes the total number of PV power plant groups.

3.3. Energy conversion calculation

After calculating the unit time failure rate of different PV power plant groups, this paper will use the information of the unit time failure rate of PV power plant groups and the information of the natural environment of the power generation of PV power plant groups, the PV module rating parameter, the battery energy storage information, and the shadow coverage parameter to carry out the energy conversion calculations by using the calculation model of the unit time failure rate of different PV power plant groups. It is calculated as shown in Equation 3.

$$E_v^j = \begin{vmatrix} H & Y \\ X & B \end{vmatrix} (\xi \mathrm{G_i} + \omega \mathrm{K_i}) \otimes Q_s \tag{3}$$

In Equation 3, E_v^j denotes the energy conversion function, H denotes the natural environmental parameters of the PV power plant cluster generation, Y denotes the PV module rating parameter, X denotes the shadow coverage parameter, B denotes the shadow coverage parameter, ξ denotes the energy conversion efficiency of the controllable solar panels, G_i denotes the total amount of solar energy per unit time, ω denotes the energy conversion error compensation coefficient, and K_i denotes the energy conversion error compensation .

3.4. Results Output Module

Since the failure rate per unit time of different PV plant clusters as well as their sensor information is recorded by means of time series, the energy conversion matrix is processed in this paper using LSTM neural network. LSTM (Long Short-Term Memory Network) is a deep learning model commonly used to process sequence data. Compared with the traditional RNN (Recurrent Neural Network), LSTM introduces three gates (Input Gate, Forget Gate, Output Gate, as shown in the figure below) and a cell state, which are mechanisms that allow LSTM to better deal with long term dependencies in sequences. Its model structure is shown in Fig. 3.

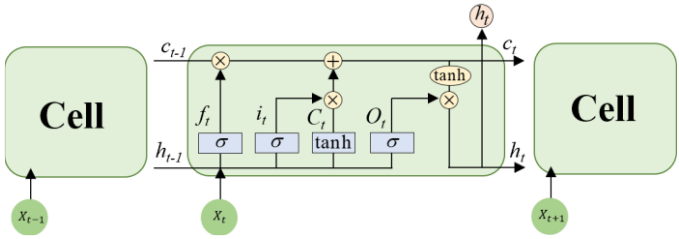

Figure 3. LSTM model structure

As shown in Figure 3, there are three main gates in the LSTM neural network: the first sigmoid function is called the forgetting gate, which determines the unimportant information to be forgotten. The second gate consists of the sigmoid function and the tanh function, called the input gate, which determines the new information to be updated and saved. The third sigmoid function, called the output gate, determines the information to be output from the memory cell. The update equation is shown in Equation 4.

$$\begin{cases} f_t = \sigma(\widetilde{f_t}) = \sigma(W_{xf}x_t + W_{hf}h_{t-1} + b_f) \\ i_t = \sigma(\widetilde{i_t}) = \sigma(W_{xi}x_t + W_{hi}h_{t-1} + b_i) \\ \widetilde{c_t} = tanh(c_t) = \tanh'(W_{xc}x_t + W_{hc}h_{t-1} + b_c) \\ c_t = c_{t-1} \odot f_t + \widetilde{c_t} \odot i_t \\ o_t = \sigma(\widetilde{o_t}) = \sigma(W_{xo}x_t + W_{ho}h_{t-1} + b_o) \end{cases} \tag{4}$$

In Equation 4, f_t,i_t and o_t refer to the forgetting gate, input gate, and output gate, respectively. x_t refers to the current input vector, W refers to the parameter matrix of each gate, and b refers to the bias. The above three gating units allows the LSTM to choose to forget the redundant information, store the useful information, and output the important information through the gate-passing unit according to the loss function.

By calculating the information of multi-source heterogeneous PV power plants through the above several threshold units, the LSTM model can store the important energy conversion information and forget the unimportant ones. In this way, the model improves the accuracy of power prediction and ultimately optimizes the operation of the power station.

4. Experimentation

To test the validity of the proposed model, this paper uses a dataset on the relationship between weather and PV system production provided by a PV plant in the United States to test the evaluation of our model. The platform for the experiment was a computer with 16GB of RAM, an i7-11800H, and an NVIDIA GeForce RTX 3050Ti GPU. The experimental environment was Python 3.9 and TensorFlow 2.0, and the model was trained using the loss function provided in Equation 5. The test results are the MSE and RMSE of the model on the test set, which is calculated as shown in Equations 5 and 6 below. Where y_i refers to the actual value, $\hat{y}_i$ refers to the predicted value and n is the number of samples. Table 1 shows the settings of the LSTM model. The data is normalized using the normalization method of Equation 8 to perform feature scaling.

Table 1. Model Setting

Number of Layers	Activation Function	Number of neurons
2	ReLU	50

$$MSE = \frac{1}{n}\sum_{i=1}^{n}(y_i - \hat{y}_i)^2 \tag{5}$$

$$RMSE = \sqrt{\frac{1}{n}\sum_{i=1}^{n}(y_i - \hat{y}_i)^2} \tag{6}$$

$$MAE = \frac{1}{n}\sum_{i=1}^{n}|y_i - \hat{y}_i| \tag{7}$$

$$X_{max-min} = \frac{X - X_{min}}{X_{max} - X_{min}} \tag{8}$$

Table 2. Experimental results

Model	Evaluation metrics	Result
Ours	MSE	0.01
	RMSE	0.06
	MAE	0.02
Kuriakose[9] et al.	MSE	0.10
	RMSE	0.19
	MAE	0.12

Its experimental results are shown in Table 2. From Table 2, the MSE and NMSE of the model on the test dataset are under 0.1, which means that the error between the predicted and actual values of the model is small. This indicates that the model fits the data well. At the same time, the MSE, RMSE and MAE values of the model proposed in this paper are lower than those of the compared models. This is because the model proposed in this paper has a strong ability to extract time series features while combining multi-source heterogeneous data.

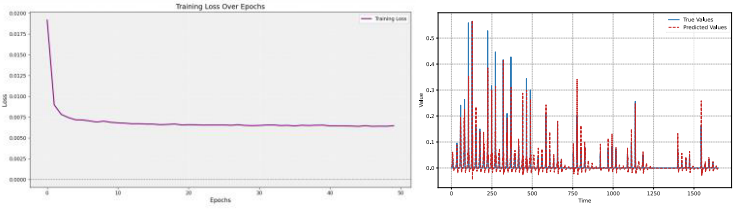

(a) Training Loss (b) Test Result

Figure 4. Training Loss and test result

Fig. 4(a) shows how the model's loss changes during the training process. From Fig. 4, the model proposed in this paper converges faster, and the model has converged under a desirable loss value after about 10 Epochs of training. This indicates that the model possesses efficient convergence, which helps to improve the efficiency of model development and resource utilization. The poor computational resources of a PV power plant often make it incapable of deploying models with excessive training time or high training complexity, which further demonstrates the high applicability of the model.

Figure 4(b) shows the prediction performance of the model on the test set, from which the model proposed in this paper can fit the true values well. The figure further demonstrates that the model can fit most of the real data, but is slightly less predictive in the early part of the test cycle.

5. Conclusions

Traditional feature methods are difficult to achieve effective extraction of multi-source heterogeneous PV ledger features, further limiting the optimization of PV power plant clusters. This paper proposes a feature extraction method for distributed photovoltaic ledger information based on multi-source heterogeneous data fusion. Firstly, the collection of heterogeneous data from multiple sources is realized by aggregating the power generation state information of a cluster of PV power plants, including natural environment information, module parameters, battery energy storage, shadow coverage, and so on. Secondly, energy conversion calculations are performed based on this information and the energy conversion calculation process is optimized by a failure rate calculation model. Finally, an LSTM neural network is used to process this information and predict the PV power to validate the effectiveness of the proposed feature extraction method. The experiment proves that the model proposed in this paper has a strong performance along with fast convergence and has good engineering applicability. However, the model’s spatial feature extraction capability is insufficient. In the future, we will further enhance the model’s spatial feature extraction capability.

Acknowledgements

This paper is supported by the State Grid Corporation of China Headquarters Management Technology Project "Research on Large scale Distributed Photovoltaic Multi level Information Fusion and Collaborative Control Technology" (Project Code: 4000-202329100A-1-1-ZN).

References

[1] Schmietendorf K, Peinke J & Kamps O. The impact of turbulent renewable energy production on power grid stability and quality. The European Physical Journal B, 2017, 90: 1-6. doi: https://doi.org/10.1140/epjb/e2017-80352-8

[2] Liu, Ximei, & Junjie Ma. "Application of the ubiquitous power internet of things in state monitoring of power equipment." Power system protection and control 48.14 (2020): 69-75. https://link.cnki.net/doi/10.19783/j.cnki.pspc.201980

[3] Yuan, Q., Pi, Y., Kou, L., Zhang, F., Li, Y., & Zhang, Z. Multi-source data processing and fusion method for power distribution internet of things based on edge intelligence. Frontiers in Energy Research, 2022, 10: 891867. doi: https://doi.org/10.3389/fenrg.2022.891867

[4] Su, D., Qiu, T., Yin, Q., & Li, G. Research on Remote Monitoring and Early Warning System of New Energy Station Based on Multi-source Information Fusion. 2021 6th Asia Conference on Power and Electrical Engineering (ACPEE). IEEE, 2021: 1168-1173. doi: https://doi.org/10.1109/ACPEE51499.2021.9436923

[5] Dashtdar M, Sadegh Hosseinimoghadam S M & Dashtdar M. Fault location in the distribution network based on power system status estimation with smart meters data. International Journal of Emerging Electric Power Systems, 2021, 22(2): 129-147. doi: https://doi.org/10.1515/ijeeps-2020-0126

[6] Kou, L., Liu, C., Cai, G. W., Zhang, Z., Zhou, J. N., & Wang, X. M. Fault diagnosis for three-phase PWM rectifier based on deep feedforward network with transient synthetic features. ISA transactions, 2020, 101: 399-407. Doi: https://doi.org/10.1016/j.isatra.2020.01.023

[7] Yan, S. F., Ma, B., Zheng, C. S., & Chen, M. Weighted evidential fusion method for fault diagnosis of mechanical transmission based on oil analysis data. International Journal of Automotive Technology, 2019, 20: 989-996. doi: https://doi.org/10.1007/s12239-019-0093-9

[8] Gou L, Sun R & Han X. FDIA System for Sensors of the Aero-Engine Control System Based on the Immune Fusion Kalman Filter. Mathematical Problems in Engineering, 2021, 2021(1): 6662425. doi: https://doi.org/10.1155/2021/6662425

[9] Kuriakose, A. M., Kariyalil, D. P., Augusthy, M., Sarath, S., Jacob, J., & Antony, N. R. Comparison of artificial neural network, linear regression and support vector machine for prediction of solar PV power .In 2020 IEEE Pune section international conference (PuneCon). IEEE, 2020: 1-6. doi: https://doi.org/10.1109/PuneCon50868.2020.9362442

[10] Si, Z., Yang, M., Yu, Y., Ding, T., & Li, M. A hybrid photovoltaic power prediction model based on multi-source data fusion and deep learning. In 2020 IEEE 3rd Student Conference on Electrical Machines and Systems (SCEMS). IEEE, 2020: 608-613. doi: https://doi.org/10.1109/SCEMS48876.2020.9352398

Fuzzy Systems and Data Mining X
A.J. Tallón-Ballesteros (Ed.)

doi:10.3233/FAIA241425

Satellite Telescope Self-Calibration Through Precise Stellar Data Mining

Konstantin RYABININ [a,1], Gerasimos SARRAS [a], Wolfgang LÖFFLER [a], Olga EROKHINA [a], and Michael BIERMANN [a]

[a] *Astronomisches Rechen-Institut, Center for Astronomy of Heidelberg University*

ORCiD ID: Konstantin Ryabinin https://orcid.org/0000-0002-8353-7641, Gerasimos Sarras https://orcid.org/0009-0005-5316-4062, Wolfgang Löffler https://orcid.org/0009-0003-1319-5601, Olga Erokhina https://orcid.org/0000-0002-2207-7979, Michael Biermann https://orcid.org/0000-0002-5791-9056

Abstract. This paper is devoted to the development of an astrometric solver aiming to reveal precise stellar parameters by mining the data provided by a satellite telescope. First, we focus on the self-calibration model of the satellite telescope intended to absorb the telescope's optical and mechanical distortions and the satellite's imprecise attitude. Our experiments reveal that the calibration model based on the Legendre polynomials can cope with different types of input data distortions. Second, we demonstrate the performance of the solver for different test cases on the CPU cluster. So far we showed that 275 millions of stellar observations can be processed on 64 cluster nodes within 2.5 hours. The viability of this approach is proven along with the indication of bottlenecks and challenges for future work.

Keywords. Astrometry, High-Performance Computing, Calibration Model, Legendre Polynomials, Data Mining

1. Introduction

Modern astronomy is tightly connected with data mining, which allows for the extraction of knowledge about celestial objects from the vast number of observations made by different types of telescopes. Astrometric star catalogues as created by dedicated space missions are among the most fundamental astronomic data, upon which astronomic science is based. These catalogues contain information about the positions and motions of stars (either in true 3d space or as projected onto the celestial sphere) as well as other stellar parameters like brightness, colour and so on.

Space-based telescopes have the great advantage over earth-bound telescopes that they are not affected by atmospheric absorption, refraction and turbulence. This results in a much higher light sensitivity and angular resolution. The price to pay is a requirement of a much more accurate instrument calibration. This is due to dramatical change of instrument properties during and after launch by outgassing, solar radiation and geomagnetic effects. This means that the electronics, optics and spatial orientation (atti-

[1] Corresponding Author: Konstantin Ryabinin, konstantin.riabinin@uni-heidelberg.de

tude) of the instrument need to be constantly recalibrated in space using either additional on-board instruments dedicated to calibration or, as in the case of self-calibrating space astrometry, the much more accurate observations of the science instrument itself.

This study is carried out in the Institute for Computational Astronomy (Astronomisches Rechen-Institut, ARI) of Heidelberg University, Germany, in preparation for the Japanese Astrometric Satellite Mission for INfrared Exploration (JASMINE) [1] the scientific goal of which is to produce a catalogue of stars in the neighbourhood of the Galactic Centre. Here we discuss the software pipeline ARI JASMINE Astrometric Solver (AJAS) [2] for solving the JASMINE astrometric problem, examine the distortion effects AJAS can calibrate out from the input data and the AJAS performance on small CPU clusters.

2. Astrometric Problem

Each observation made by the telescope can be expressed as an equation $o_{\ell,\lambda} = f(\vec{p}_\lambda) + g(\vec{c}_\ell)$, where o is a point in the image captured by the telescope, $\ell \in [1..L]$ is the number of observation, $\lambda \in [1..\Lambda]$ is a star observed, f is a function of stellar parameters, $\vec{p}$ is a vector of stellar parameters (position, proper motion, parallax, etc.), g is the calibration model, and $\vec{c}$ is a set of calibration parameters. To reveal the parameters, the system of these equations should be solved. Generally, the function f is not known, but its Taylor expansion can be represented as follows:

$$o_{\ell,\lambda} = f(\hat{\vec{p}}_\lambda) + g(\hat{\vec{c}}_\ell) + \frac{\mathrm{d}}{\mathrm{d}\vec{p}} f(\vec{p})\bigg|_{\hat{\vec{p}}_\lambda} \Delta\hat{\vec{p}}_\lambda + \frac{\mathrm{d}}{\mathrm{d}\vec{c}} g(\vec{c})\bigg|_{\hat{\vec{c}}_\ell} \Delta\hat{\vec{c}}_\ell + O\left(\Delta\hat{\vec{p}}_\lambda{}^2\right) + O\left(\Delta\hat{\vec{c}}_\ell{}^2\right), \quad (1)$$

where $\hat{\vec{p}}_\lambda$ is the initial guess of the stellar parameters for the star λ (data from the existing star catalogue) and $\Delta\hat{\vec{p}}_\lambda$ is the update of the stellar parameters (refinement of the existing star catalogue), $\hat{\vec{c}}$ is initial calibration parameters (may be zero at the beginning of data mining procedure), and $\Delta\hat{\vec{c}}_\ell$ is the update of the calibration parameters (actually representing the distortions being calibrated out).

Eq. (1) can be linearized and then for all L available observations, it results in the system of linear equations $\mathscr{D}\vec{x} = \vec{l}$, where $\mathscr{D}$ is a design matrix that is a Jacobian of the calibrated observation function, $\vec{x}$ contains both stellar parameters $\vec{p}$ and calibration parameters $\vec{c}$, and $\vec{l}$ is the vector of differences between observed and predicted stellar coordinates. Here we use Field-of-View Reference System (FoVRS), the reference system fixed to the telescope and co-rotating with the satellite.

Typically, the number of equations in this system is much larger than the number of unknowns. Due to the inevitable noise of measurements, the additional equations are mostly linearly independent, so this overdetermined system has no exact solution. Therefore, the astrometric solution is then defined as the best possible fit that can be derived by the least squares adjustment by solving the equation system:

$$\mathscr{N}\vec{x} = \vec{b}, \quad (2)$$

where $\mathscr{N} = \mathscr{D}^{\mathsf{T}}\mathscr{D}$ is normal matrix and $\vec{b} = \mathscr{D}^{\mathsf{T}}\vec{l}$.

Generally, there are two fundamental challenges in solving the astrometric problem. The first one is the formulation of a proper calibration model that allows for the de-

sired accuracy of the final solution by removing the unwanted distortions of observations while keeping the important information intact. The second challenge is the computational complexity of solving the system due to the large input data. For the 3-year-long JASMINE mission, the design matrix $\mathscr{D}$ is expected to be on the size of $10^{10} \times 10^{7}$.

AJAS software aims to benefit from modern high-performance computing ensuring the direct solution of the JASMINE astrometric problem within a reasonable time and prescribed accuracy. We take the best practices of the ESA Hipparcos [3] and the ESA Gaia [4] space astrometry missions for the AJAS JASMINE direct solver problem formulation. For the solver architecture, we adapt Astrometric Global Iterative Solution (AGIS) [5] and Gaia One Day Astrometric Solution (ODAS) [6].

3. AJAS Pipline

AJAS implements a direct (non-iterative) solution of the JASMINE astrometric problem. For this, a reduced normal matrix $\mathscr{M}$ is calculated from the normal matrix $\mathscr{N}$ (see Eq. 2) by forward-eliminating the part of $\mathscr{N}$ that corresponds to the fast-changing calibration parameters. Then, a pseudo-inverse $\mathscr{M}^{+}$ is calculated using singular value decomposition. Based on $\mathscr{M}^{+}$, the partial solution for source parameters and slow-changing calibration parameters is derived. Finally, the rest of the solution for the fast-changing parameters is revealed via the backsubstitution. The further details can be found in [2]. Fig. 1 shows the main blocks of the AJAS pipeline.

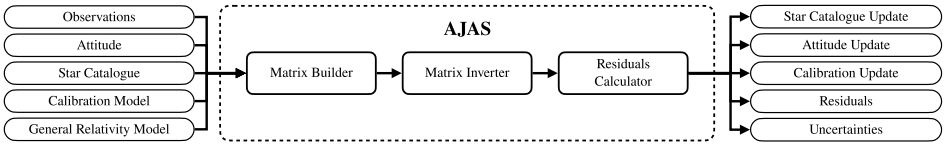

Figure 1. AJAS pipeline (blocks are input/output data and computational modules; arrows indicate data flow).

The AJAS input data include *Observations* and *Attitude*, which are the data obtained from the satellite telescope. *Star Catalogue* is the initial knowledge about the observed stars where the scientific goal of JASMINE is to improve this knowledge. *Calibration Model* and *General Relativity Model* are the assumptions of physical effects to be accounted for the improvement of the solution accuracy. The detailed technical description of the 3 main AJAS modules (*Matrix Builder*, *Matrix Inverter*, and *Residuals Calculator*), as well as the mathematics behind them, are provided in [2].

The output data of AJAS include the updates for the star catalogue, calibration, and attitude. The quality of the solution can be estimated by analyzing the distribution of post-adjustment residuals and uncertainties of individual elements of the solution.

AJAS is written in C++ utilizing the hybrid parallelism model leveraged by MPI, OpenMP, and POSIX-based threads. The computational core is based on EigenExa [7] and ScaLAPACK [8] libraries, which are state-of-the-art tools for inverting huge dense matrices on the CPU clusters. To inspect the solution, a set of tools is designed including the plotting and statistical analysis scripts. Currently, these scripts are written in Python and JavaScript to allow for preliminary validation of the solver's viability. For the real mission, they should be replaced by more mature data mining and visual analytics tools capable of handling the full size of JASMINE data. Creating full-fledged software for

the inspection of astrometric solutions is a complex research task that is mainly a part of future work.

4. Calibration Model

The goal of the calibration model is to absorb the distortions of observations caused by imperfections of the telescope optics, detector, and measurement errors of the satellite attitude. Here we use shifted Legendre polynomials up to 5^{th} order to describe distortions. These polynomials are flexible enough to represent shift, scaling, tilt, rotation, and different wavy patterns. In the angular space of FoVRS, the distortion pattern is modeled as:

$$\begin{cases} \eta = \eta^{(0)} + \eta^{(1)}(\kappa,\mu) + \sum\limits_{r=0}^{5}\sum\limits_{s=0}^{5-r} \eta_{rs} L_r(\tilde{\kappa}) L_s(\tilde{\mu}) \\ \zeta = \zeta^{(0)} + \zeta^{(1)}(\kappa,\mu) + \sum\limits_{r=0}^{5}\sum\limits_{s=0}^{5-r} \zeta_{rs} L_r(\tilde{\kappa}) L_s(\tilde{\mu}) \end{cases}, \tag{3}$$

where κ, μ – pixel-space coordinates of the observation, $\tilde{\kappa}, \tilde{\mu} \in [0;1]$ – normalized pixel-space coordinates of the observation relative to the detector center, $\eta^{(0)}, \zeta^{(0)}$ – FoVRS coordinates of the detector center, $\eta^{(1)}, \zeta^{(1)}$ – FoVRS coordinates of the observation, η_{rs}, ζ_{rs} – calibration parameters, $L_n(x)$ – shifted Legendre polynomial of order n defined as follows:

$$L_n(x) = (-1)^n \sum_{k=0}^{n} \binom{n}{k} \binom{n+k}{k} (-x)^k. \tag{4}$$

The initial guess for the calibration is $\eta_{rs} = \zeta_{rs} = 0$ for each $r,s \in [0..5]$. The calibration updates $\Delta\eta_{rs}, \Delta\zeta_{rs}$, are then a part of the solution calculated by AJAS. Therefore, the new calibration parameters $\eta'_{rs} = \eta_{rs} + \Delta\eta_{rs}$, $\zeta'_{rs} = \zeta_{rs} + \Delta\zeta_{rs}$ are substituted in Eq. 3 instead of η_{rs} and ζ_{rs}.

Calibration order 0 (where order $a = r + s$) represents a shift that can be introduced either by the imprecise position of the detector on the telescope's focal plane or an imprecisely measured attitude. Order 1 represents scale and tilt, which combination can also express rotation. The cause of these effects can be improper attitude, accidental rotation of the detector, floating of the focal length, tilt of the focal plane, or their combination. Effects modeled by higher orders (2–5) are expected to be very subtle and correspond to different types of bending as a result of the thermal expansion of the focal plane and telescope's mirror.

For testing the calibration model, we develop a tool called DJ Legendre. It allows for generating a synthetic observation catalogue of an artificial grid-shaped constellation with tunable distortions. On the next step, the observation catalogue is loaded to the solver which in turn calibrates out the distortions and calculates star catalogue updates. DJ Legendre is written in JavaScript and available online a as web application: https://scivi.tools/djlegendre. Fig. 2 demonstrates two test cases, for which the observational data were generated by DJ Legendre and the solution was calculated by AJAS.

As mentioned above, AJAS uses the singular value decomposition to find the pseudo-inverse of the reduced normal matrix of the observation equation system. This

involves solving the eigenproblem and then zeroing out the eigenvalues, which carry no meaningful information about the solution. These values are the smallest in the spectrum and their number can be derived from the nature of the astrometric problem. Here, careful analysis of the problem is required because zeroing out too few values will cause the mathematically perfect but unphysical solution as shown in Fig. 2b and 2e. While the residuals of these solutions are perfectly fitted by a Gaussian of the correct width (which is a condition of a mathematically perfect solution), the grid pattern is not restored. Cutting too many eigenvalues will in turn reduce the accuracy of the solution. Fig. 2c and 2f demonstrate the solution where the correct number of eigenvalues is cut, whereby the grid pattern is successfully recovered. In Fig. 2f, the square grid is cut on the borders because some stars appear outside of the detector and were not observed due to initial distortion. In both cases, the residuals are again perfectly fitted by a Gaussian of the correct width, which indicates that the mathematical quality is achieved as well.

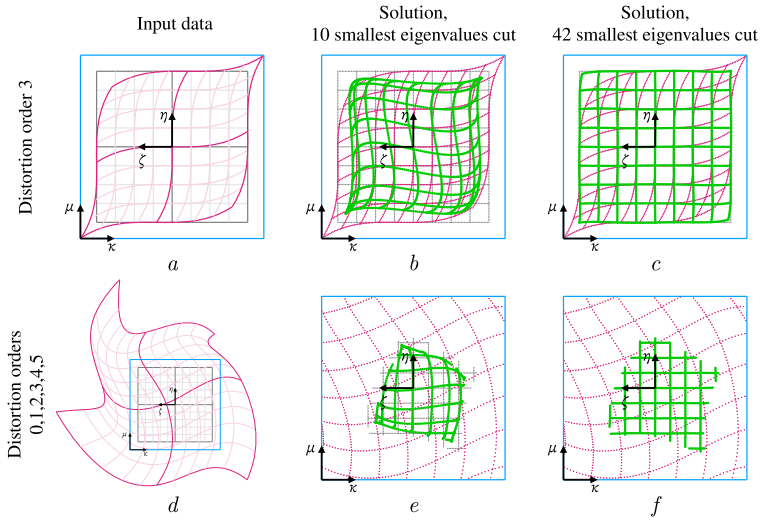

Figure 2. Test cases demonstrating the capabilities of the calibration model based on Legendre polynomials. $(\kappa;\mu)$ denote a pixel space of the telescope's detector; $(\eta;\zeta)$ denote FoVRS; blue line indicates the detector; grey indicates the star catalogue; pink indicates the observations; green indicates the updated star catalogue.

In the case of JASMINE, the number of eigenvalues to be cut must correspond to the number of calibration model parameters multiplied by the number of telescope detectors (here this number is 42, i.e. 2 directions (η and ζ) multiplied by 21 calibration parameters and one detector). The reason is the degeneracy between the calibration model and stellar positions. The solution has the freedom to incorporate the update either into the calibration parameters or into the stellar positions to minimize the residuals. We discovered this non-obvious fact using our preliminary data mining tools analyzing both mathematical and physical properties of the solution.

The physical correctness of the solutions of test cases in Fig. 2c and 2f is obvious from the visual inspection. However, in the real mission, advanced data mining tools should be included in the solution quality assessment. As a first step, we develop a tool that generates HTML-based interactive reports for every AJAS run. Reports contain information for the basic data mining of the solution, e.g. interactive histograms of residu-

als. Histograms allow visual estimating, whether residuals have systematics or just random noise. If there are still systematics after the solution, this indicates that the calibration model do not pick up all the regular effects of the input data and thereby should be improved. For our simple test cases, Legendre polynomials are capable of removing all the systematics. To assess more complicated tests, more sophisticated data mining tools are needed, which will require a full-fledged client-server architecture of a visual analytics pipeline.

5. AJAS Performance Testing

We use a JASMINE test data generator written in Java to create the input observation catalogue for the performance testing of AJAS. The data generator consists of three principal parts, namely, the input star catalogue, the mission formulation, and the observation catalogue. The input star catalogue can be read from the file or generated within a given target region. The independent next step is the mission formulation which includes defining physical parameters and implementing a pointing strategy that, in turn, defines the exact time and coordinates of the captured part of the sky. And the last part is the creation of an observation catalogue by projecting stars to every detector focal plane and defining which stars are captured by detectors during every exposure. The example of the JASMINE-like mission is shown in Fig. 3 using the reduced mock data star catalogue [9].

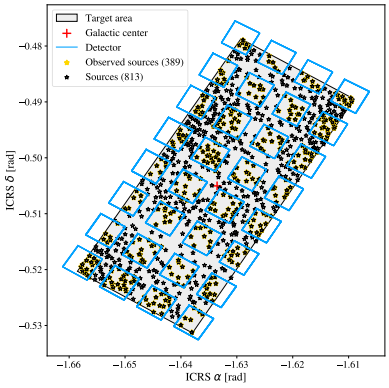

Figure 3. A small example of a JASMINE-like mission created by a test data generator using a reduced mock catalogue shown as a combination of different time snapshots with moving detector.

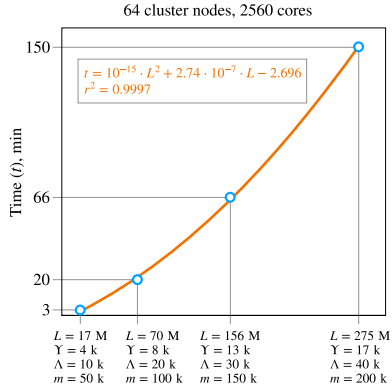

Figure 4. Performance of AJAS. L is number of observations, Υ is number of exposures, Λ is number of stars, $m \times m$ is size of $\mathscr{M}$, r^2 is goodness of the trend curve fit.

AJAS performance is tested on the 16×16 process grid using 64 nodes of the academic Baden-Württemberg (Germany) cluster bwUniCluster 2.0. Each node has 40 Intel®Xeon Gold 6230 2.1 GHz CPU cores, 96 Gb RAM, and 4 NUMA nodes. The latter is the reason of running 4 processes per node, each one is tied to an individual NUMA node. The performance and scaling of AJAS are shown in Fig. 4. As seen, the time scaling with the number of observations is close to linear. The main bottleneck is disk and RAM data access. The JASMINE astrometric problem lacks the locality of data access, which makes calculations cache-unfriendly and therefore limits CPU performance dramatically.

6. Conclusion

In this work, we demonstrate that AJAS can cope with linear and non-linear distortions of the input data and performs well enough to solve the astrometric problem with up to 275 million observations of 40 thousand stars within 2.5 hours. Weak scaling test (increase of the problem size with constant number of CPU cores) shows nearly linear dependency of the calculation time on the number of observations. This is still only the first step towards the solution of the full JASMINE astrometric problem as the real mission is estimated to have 3 times more stars and 100 times more observations than the largest case we have tested so far. The objectives of future work include testing of strong scaling (constant problem size with increasing number of CPU cores), assessing more complex test cases, e.g. setup with a multi-detector telescope and distortion formulation adhering to different functions like Zernike polynomials, as well as dedicated optimizations to alleviate the data access bottleneck.

Acknowledgments This work was financially supported by the German Aerospace Agency (Deutsches Zentrum für Luft- und Raumfahrt e.V., DLR) through grant 50OD2201. The authors acknowledge support by the state of Baden-Württemberg through bwHPC. The authors also thank the National Astronomical Observatory of Japan (NAOJ) fruitful discussions for the JASMINE specifics.

References

[1] Kawata D, Kawahara H, Gouda N, Secrest NJ, Kano R, Kataza H, et al. JASMINE: Near-infrared astrometry and time-series photometry science. Publications of the Astronomical Society of Japan. 2024;76(3):386-425. Available from: https://doi.org/10.1093/pasj/psae020.

[2] Ryabinin K, Sarras G, Löffler W, Biermann M. Direct Solver Aiming at Elimination of Systematic Errors in 3D Stellar Positions. Lecture Notes in Computer Science. 2024;14838:309-23. Available from: https://doi.org/10.1007/978-3-031-63783-4_23.

[3] ESA. The Hipparcos and Tycho Catalogues. ESA SP-1200. 1997. Available from: https://www.cosmos.esa.int/web/hipparcos/catalogues.

[4] Gaia Collaboration, Prusti T, de Bruijne JHJ, Brown AGA, Vallenari A, Babusiaux C, et al. The Gaia mission. Astronomy & Astrophysics. 2016 Nov;595:A1. Available from: https://ui.adsabs.harvard.edu/abs/2016A&A...595A...1G.

[5] Lindegren L, Lammers U, Hobbs D, O'Mullane W, Bastian U, Hernàndez J. The astrometric core solution for the Gaia mission. Overview of models, algorithms, and software implementation. Astronomy & Astrophysics. 2012 Feb;538:A78. Available from: http://cdsads.u-strasbg.fr/abs/2012A%26A...538A..78L.

[6] Löffler W, Bastian U, Biermann M, Jordan S, Brüsemeister T, Stampa U, et al. The One-Day Astrometric Solution for the Gaia Mission. Astronomy & Astrophysics. in preparation.

[7] Sakurai T, Futamura Y, Imakura A, Imamura T. In: Sato M, editor. Scalable Eigen-Analysis Engine for Large-Scale Eigenvalue Problems. Singapore: Springer Singapore; 2019. p. 37-57. Available from: https://doi.org/10.1007/978-981-13-1924-2_3.

[8] Blackford LS, Choi J, Cleary A, D'Azevedo E, Demmel J, Dhillon I, et al. ScaLAPACK Users' Guide. Philadelphia, PA: Society for Industrial and Applied Mathematics; 1997.

[9] Ramos P, Ohsawa R. Input catalogue of JASMINE (GCS window). Zenodo; 2024. Available from: https://doi.org/10.5281/zenodo.13119966.

Fuzzy Systems and Data Mining X
A.J. Tallón-Ballesteros (Ed.)

doi:10.3233/FAIA241426

Efficient Early Sparsification for Accelerating Solutions to the Traveling Salesman Problem

Yonglu JIANG [a], Hongyu XING [b,c] Hanchen SHI [b,c] Zijing WEI [b,c] and Zhongguo YANG [a,d,1]

[a] *School of Information Science and Technology, North China University of Technology, Beijing, China*
[b] *School of London Brunel, North China University of Technology, Beijing, China*
[c] *Department of Mathematics, Brunel University London, London, UK*
[d] *Beijing Key Laboratory on Integration and Analysis of Large-Scale Stream Data, North China University of Technology, Beijing, China*

Abstract. The Travelling Salesman Problem (TSP) is a well-established NP-hard problem, often tackled using heuristic algorithms. While state-of-the-art learning-driven approaches for TSP perform comparably to classical solvers when trained on trivially small instances, they struggle to generalize the learned policy to larger, practical-scale instances. Consequently, as the number of cities increases, the efficiency of these algorithms diminishes significantly. This paper focuses on the early elimination of non-advantageous edges while retaining advantageous ones, thereby accelerating the TSP solution. Our approach involves capturing the differential frequencies of various edges during the early stages of an intelligent evolutionary algorithm, which we term as "knowledge" derived from the evolutionary process. We then design effective features to characterize the similarities and differences between edges. Leveraging this "knowledge", we label edges as either advantageous or non-advantageous. By integrating the guidance of a predictor, we intervene in the intelligent evolutionary algorithm to sparsify the TSP graph, ultimately enhancing the TSP solution. Our method effectively prunes edges in TSP instances, preserving the optimal path while minimizing redundant edges. Experimental results demonstrate that our approach significantly improves both computational efficiency and solution quality on the TSP50 and TSP100 test sets compared to other models. This methodology offers a novel perspective by extracting and utilizing latent knowledge among edges, thereby enhancing the performance of intelligent evolutionary algorithms in solving the TSP. Our findings not only improve current methodologies but also encourage further exploration and development in related fields and practical applications.

Keywords. Traveling Salesman Problem, Intelligent Evolutionary Algorithm, Machine Learning, Knowledge, Speed up

[1]Corresponding Author: Dr.Zhongguo Yang, E-mail: yangzhongguo@ncut.edu.cn

1. Introduction

The Traveling Salesman Problem (TSP) is a classic example of a combinatorial optimization problem with significant real-world implications. Originating in the fields of logistics and routing, it involves finding the shortest route that visits each city exactly once before returning to the starting point. Despite its apparent simplicity, the TSP is classified as an NP-hard problem, making the determination of an exact optimal solution computationally intractable as the number of cities increases, due to the problem's exponential time complexity. This challenge has driven the exploration of alternative approaches to efficiently tackle large-scale instances of the TSP.

While state-of-the-art learning-driven TSP approaches perform comparably to classical solvers when trained on trivially small instances, they struggle to generalize the learned policy to larger, practical-scale instances. As the number of cities grows, the efficiency of these algorithms significantly diminishes. Traditional exact algorithms are also constrained by their exponential time complexity, rendering them impractical for real-world scenarios with numerous locations. To alleviate this computational burden, heuristic and approximation methods have been developed, though their limitations become apparent as the problem size increases [1]. Graph sparsification has emerged as a critical technique for addressing the TSP by reducing the solution search space. Researchers, including James Fitzpatrick, have investigated TSP instance sparsification using supervised learning models on the MATILDA dataset's CLKhard and LKCChard categories [2]. Their approach seeks to eliminate edges unlikely to be part of the optimal path. However, the effectiveness of this method is limited when faced with constrained data or the need for rapid processing, underscoring the necessity for enhanced generalization capabilities.

Fitzpatrick's work offered valuable insight into the unlikelihood of certain edges appearing in the optimal solution, which inspired our approach. By tracking the behavior of different edges within a TSP instance, we observed that the selection dynamics of edges within the population undergo significant changes as the algorithm iterates. Some edges gradually withdraw from selection, while others are consistently chosen, indicating early patterns. As depicted in Figure 1 (a) and (b), advantageous edges are swiftly identified and continually selected, reducing the number of iterations required for convergence. Conversely, Figure 1 (c) and (d) illustrates the rapid decline of non-advantageous edges, facilitating their early elimination and leading to effective graph sparsification. This method leverages empirical knowledge from the intelligent evolutionary algorithm, obviating the need for a pre-training dataset, to accelerate the sparsification of TSP problems and significantly enhance generalization ability. Our approach enhances the efficiency and effectiveness of TSP solutions by concentrating on promising edges and discarding less relevant ones. In the work of Liu, Bokai and Lu, Weizhuo[3], machine learning methods were employed to enhance computational efficiency, utilizing particle swarm optimization (PSO), which inspired our approach to combinatorial optimization.

To operationalize this approach, we designed a set of features based on edge fitness and adjacency, extracting a feature set for each edge at the start of the iteration. As the algorithm progresses, we collect historical data on edge appearances and the optimal routes at various stages, using this information to create dynamic labels. Through this iterative

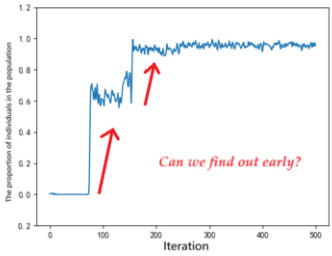

(a) Early recognition of advantageous

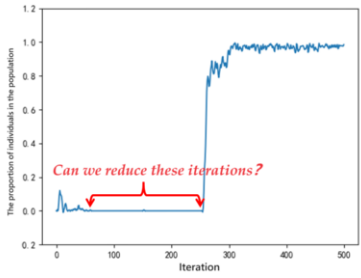

(b) Iteration reduction of advantageous

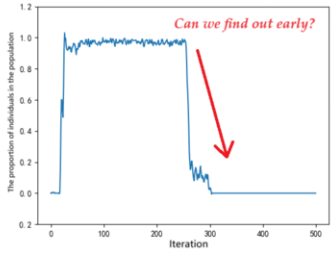

(c) Early detection of non-advantageous

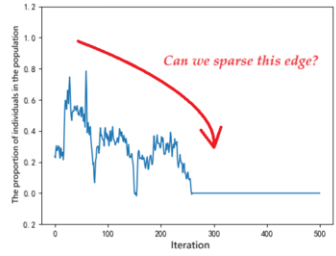

(d) Sparsification potential

Figure 1. Introducing edge frequency-based sparsification

process, we identify dominant edges likely to appear in the optimal solution and non-dominant edges that are less likely to do so.

In subsequent iterations, we apply this knowledge to prune TSP instances. Non-dominant edges are deliberately removed from the population, while edges likely to appear in the optimal solution are retained. This strategy ensures the quality of the population, fosters its evolution, and further accelerates the sparsification of the TSP problem.

Our original contributions in this paper can be summarized as follows:

- **Knowledge-driven Feature Engineering:** We apply principles from intelligent evolutionary algorithms, integrating knowledge from iterative processes with carefully designed features to dynamically improve algorithm performance.
- **Graph Sparsification Enhancement through Intelligent Edge Analysis:** By dynamically identifying and prioritizing edges based on their likelihood of being part of the optimal solution, we achieve more effective graph sparsification. This reduces the search space and accelerates convergence.
- **Improved Generalization Capability of Swarm Evolution Algorithms:** Our algorithm does not rely on pre-existing datasets. Instead, it extracts knowledge directly from the input TSP instance, reducing dependency on external data and enhancing generalization capability.

Through comprehensive exploration and empirical evaluation, we aim to validate the effectiveness of our proposed methodology relative to existing approaches. These contri-

butions collectively highlight the novelty and potential impact of our methodology in solving large-scale TSP instances.

2. Related Work

In our research, we built upon the optimization algorithms and methodologies developed by previous scholars. By integrating their innovative approaches and collective expertise, we aimed to advance existing algorithms and contribute meaningfully to the discourse on TSP. This collaborative foundation enabled us to enhance the performance and effectiveness of TSP solutions, driving forward the field with improved methodologies.

2.1. Exact, Heuristic, Hybrid Solvers

The Concorde TSP solver is a leading tool for solving TSP instances [4]. It employs a range of efficient algorithms, including branch and bound, cutting planes, linear relaxation, and dynamic programming, to achieve high accuracy. The Lin-Kernighan-Helsgaun (LKH) TSP solver, an extension of the classic Lin-Kernighan algorithm improved by Keld Helsgaun, is a highly effective heuristic for large-scale TSP problems, demonstrating exceptional performance with thousands to millions of cities [5]. Google's OR-Tools provides a comprehensive suite of open-source libraries for solving complex optimization problems, including various algorithms for TSP, such as heuristic, exact, and hybrid methods [6]. Additionally, heuristic methods like nearest insertion and farthest insertion offer simplicity and effectiveness for small-scale problems. Despite the strengths of these tools, opportunities for improvement exist in computational resource utilization and the generalization of algorithms for very large-scale TSP instances.

2.2. Graph Neural Network Solution

Deep learning has shown promise in solving the TSP. Oriol Vinyals introduced the pointer network, a neural architecture designed to handle output sizes that vary with input sequence length [7]. By generating one million training samples, Ptr-Net can produce paths close to the optimal solution for small-scale problems, paving the way for deep learning applications in TSP. Similarly, Chaitanya K. Joshi developed a method using a graph convolutional neural network to solve the TSP, employing a highly parallelized beam search to generate non-autoregressive travel routes [8]. Although these methods excel in solution quality, reasoning speed, and sample efficiency, they face challenges when scaled to larger TSP instances. Issues include substantial training data requirements, limited solution accuracy, and restricted generalization. Additionally, as black box models, neural networks often present challenges in interpretability and verification, complicating their use in critical applications.

2.3. Graph Sparsification

The goal of graph sparsity is to reduce the number of edges, enhancing efficiency and simplifying computational tasks. For the TSP, this means removing edges unlikely to be part of the optimal solution. Yuan Sun's work involves extracting various features from

TSP instances, including topological and path features, and using an SVM model to predict and eliminate these less likely edges [9]. Similarly, James Fitzpatrick's approach utilizes a supervised model to achieve graph sparsity in the TSP [2], while Yong Wang generates sparse maps by analyzing frequency plots and applying frequency thresholds, which helps reduce the search space and complexity [10].

Our method builds on these approaches but differs by avoiding pre-trained models. Instead, we collect frequency information during the optimization process of an intelligent evolutionary algorithm to achieve graph sparsity.

3. Methodology

In this section, we outline the theoretical framework that supports our research and provide a detailed explanation of our methodology and its specific components. Our approach begins with an extensive feature extraction process that evaluates all edges within the problem domain. We then track the evolution of these edges throughout the iterations of the intelligent evolutionary algorithm. By examining changes in edge selection patterns, we classify edges as either advantageous or non-advantageous. Furthermore, we integrate a predictive model to estimate the potential advantages or disadvantages of other edges. The entire process is depicted in Figure 2.

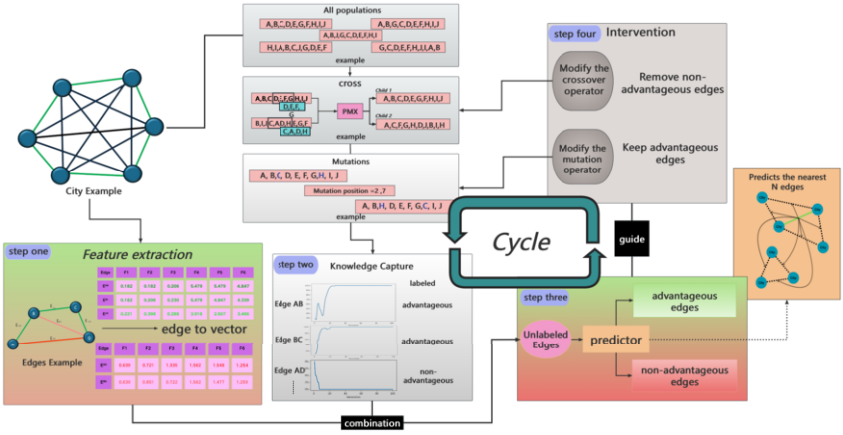

Figure 2. Knowledge-driven sparse graph optimization for TSP

3.1. Features Extraction

The work by Fitzpatrick et al. constructs six local features [2], which play a key role in guiding the decision-making process of classifiers. These features are grounded in the Euclidean distance between cities (i.e., $dist_{ij}$). Specifically, six features, denoted as F1 through F6, were designed to represent different proportional relationships, capturing normalized distance metrics. F1 quantifies the distance between two cities relative to the longest edge in the network, while F2 and F3 measure the distance between each city

and its farthest neighbor. To account for the inverse strength of these relationships, the reciprocals of these distances were also computed, corresponding to F4, F5, and F6.

$$dist_{ij} = \sqrt{(x_i - x_j)^2 + (y_i - y_j)^2},$$

$$F1 = \frac{dist_{ij} + 1}{\text{max\_edge} + 1}, \quad F2 = \frac{dist_{ij} + 1}{\text{max\_dist\_from\_i} + 1}, \quad F3 = \frac{dist_{ij} + 1}{\text{max\_dist\_from\_j} + 1},$$

$$F4 = \frac{\text{max\_edge} + 1}{dist_{ij} + 1}, \quad F5 = \frac{\text{max\_dist\_from\_i} + 1}{dist_{ij} + 1}, \quad F6 = \frac{\text{max\_dist\_from\_j} + 1}{dist_{ij} + 1}.$$

These ratio-based features, incorporating both absolute distances and their relative relationships, form a comprehensive feature set that encapsulates the spatial interrelationships between cities within the TSP network. By considering both the magnitude of distances and the relative positions of cities, the model gains a deeper understanding of the spatial dynamics in play. This dual consideration of absolute and relative metrics enriches the model's capacity to detect patterns and dependencies within the TSP structure.

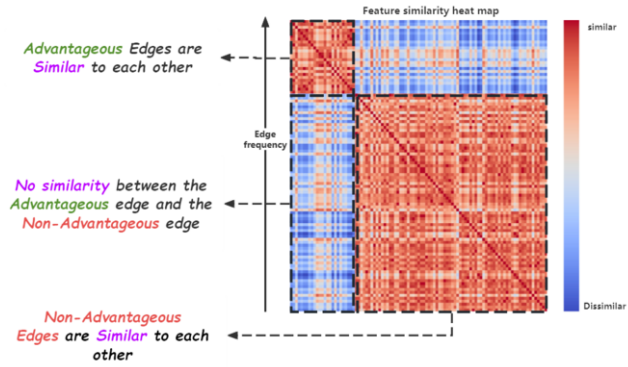

Figure 3. Heatmap of edge differences in feature space

Figure 3 presents a heatmap illustrating the feature differences across various edges. It is evident that significant distinctions exist between edges with high frequency (advantageous edges) and those with low frequency (non-advantageous edges). The similarity among advantageous edges is high, as is the similarity among non-advantageous edges, while the similarity between these two groups remains low.

By learning these features and incorporating edge frequency data, the predictive model can be effectively trained. This approach allows the model to grasp the complex spatial interrelationships within the TSP network, providing a robust framework for predicting the behavior of coordinate networks.

3.2. Knowledge Capture

By analyzing the structure of the optimal solution for the TSP, we observe that a significant portion of the edge set does not appear in the optimal solution. Inspired by previous research [7] [8], such edges can be identified in advance. During the initial phase of the intelligent evolutionary algorithm, we monitor each edge in the population, recording the frequency of their appearance across iterations. As illustrated in Figure 4, the frequency of certain edges varies as the algorithm progresses. For example, Edge 3 and Edge 4 display distinct behaviors: Edge 3 is identified as non-advantageous, while Edge 4 is classified as advantageous—representing what we term "accurate knowledge". Conversely, Edges 1 and 2 initially exhibit advantageous or non-advantageous traits, but these characteristics diminish in later iterations, signifying "incorrect knowledge".

To reduce the impact of such incorrect knowledge, we introduce a sampling and labeling strategy, which helps to mitigate its influence. Based on this process, we categorize the edges we track into two distinct groups:

- **Advantageous Edges** Edges that appear with high frequency in high-quality solutions (i.e., those with shorter tour lengths) are classified as advantageous.
- **Non-Advantageous Edges** Edges that appear infrequently or predominantly in lower-quality solutions are classified as non-advantageous.

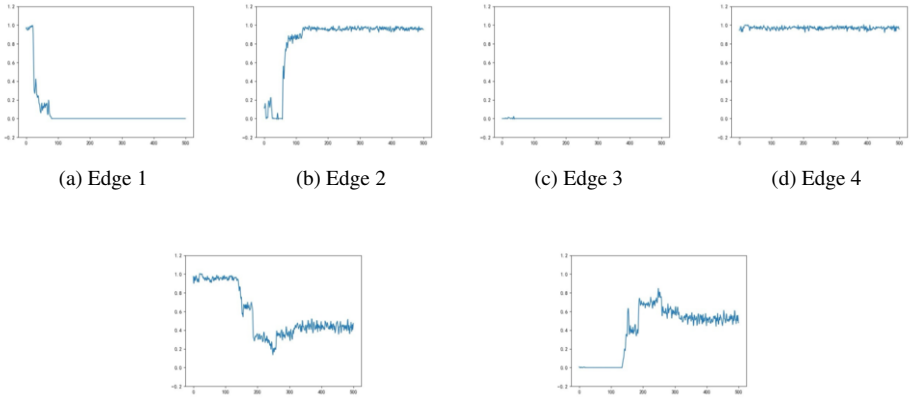

(a) Edge 1 (b) Edge 2 (c) Edge 3 (d) Edge 4

(e) Edge 5 (f) Edge 6

Figure 4. Trace the typical edges of the evolutionary process

Regarding Edge 5 and Edge 6 in Figure 4, their frequency change graphs exhibit complementary patterns, indicating a competitive relationship. Therefore, we handled these edges separately and included them in the search space. As described in Section 3.4, we subsequently selected the optimal edge from this competitive set.

3.3. Knowledge-driven predictor

Building on insights from Section 3.2, we predict unmarked edges in the search space to identify both promising and non-promising edges, with Edge 1 and Edge 2 in Figure 4

serving as key examples.

We begin by using features from Section 3.1 and the knowledge from Section 3.2 to label a subset of the population. This labeled subset is then used to evaluate the entire population, identifying N edges that are most and least advantageous in the feature space.

Frequency data is gathered every 10 iterations, with high-frequency edges labeled as 1 and low-frequency edges labeled as 0. Significant frequency changes, like those seen with Edge 1 and Edge 2, result in inverse labeling. For edges labeled 1 but similar in features to those labeled 0, their inclusion in the marked set is determined by an internal voting mechanism. Finally, marked edges are flagged as 1, and the K-nearest neighbors algorithm is applied to find the N nearest neighbors, helping to identify dominant and non-dominant edges, thereby enhancing the search process through intelligent evolution.

3.4. Intervention algorithm for sparse

We utilize the insights from Section 3.3 to identify both advantageous and non-advantageous edges within the population. This information is then used to guide and adjust the genetic algorithm operators, effectively reducing the search space and enabling edge pruning. To select the next generation of parent solutions, we apply a tournament selection mechanism. In this approach, a random subset of solutions is selected from the population, and the best-performing solution within this subset is chosen as the parent. This process is repeated to select additional parents, incorporating predicted dominant edges to increase the likelihood of selecting superior solutions.

The selected parent solutions undergo crossover operations to generate offspring, introducing variability and promoting exploration of the solution space. We utilize partial mapping crossover (PMX) and order crossover (OX) [11]. To maintain population diversity and prevent premature convergence, mutation operations are applied to the offspring, including exchange and inversion mutations [12]. During mutations, dominant edges are avoided, focusing on non-dominant edges to encourage high-quality mutations.

Additionally, we introduce a repair operator designed to correct edges unlikely to appear in the optimal solution. This involves checking new individuals in each generation and replacing suboptimal edges through local optimization or replacement operations. The fitness function is adjusted to reward individuals containing high-quality edges by incorporating an edge reward term: the more high-quality edges an individual contains, the higher the reward. This helps retain superior edges for the next iteration.

These four operations collectively eliminate non-advantageous edges and retain advantageous ones, effectively reducing the search space and sparsifying the graph. This iterative approach accelerates the TSP solution process. As depicted in the flowchart in Figure 2, these steps form a continuous loop. Given that incorrect information may arise during execution, it is crucial to continuously update and integrate the latest knowledge to maintain the robustness and efficiency of the graph sparsification process.

For more information we refer the reader to the following surveys [13][14].

4. Experiments and Results

In this section, we discuss benchmark problem instances, outline the procedures for conducting training and experiments, and evaluate the effectiveness of our method on instances from Ruprecht-Karls-Universität Heidelberg and other notable cases with distinct characteristics [15][16]. Specifically, our approach was implemented using Python (3.8), SciPy (1.7.3), NumPy (1.21.5), and Pandas (1.4.2) libraries for numerical operations, the Scikit-learn (1.0.2) library for machine learning tasks, and the Matplotlib (3.5.1) library for visualizing experimental results. The experiments were conducted on a Windows 11 system equipped with an Intel i9 processor, 16GB of RAM, and an Nvidia 4060 GPU. These details provide a comprehensive overview of the software and hardware environment utilized in our experiments.

4.1. Learn Features and Predict Advantageous Edges

Features The experimental results identified six key features (F1-F6), represented as ratios. These features capture the relative significance of edges, city distances, and overall network properties. By combining these features with edge frequency data from the Traveling Salesman Problem (TSP), we utilize a frequency-based ranking system to better understand edge importance. This approach highlights the role of feature extraction and frequency ranking in improving optimization accuracy and emphasizes the importance of understanding the interaction between various features in predicting optimal routes.

Predict of Edge Frequencies The experimental process begins with loading a sorted and merged dataset containing both TSP features and actual edge frequencies. The data is split into features and labels, with the first 'n' entries used as the training set. A K-Nearest Neighbors Regression model predicts edge frequencies, while a Nearest Neighbors model identifies the closest unlabeled neighbors for each sample. The results, including the predicted labels and corresponding edges, are stored in a DataFrame.

To improve accuracy, duplicate entries are filtered, keeping only edges with the highest predicted values. The refined results are saved to a new CSV file. This method demonstrates the potential of machine learning models in route prediction and emphasizes the importance of data preprocessing in optimizing the accuracy of practical solutions.

4.2. Analysis of Frequency Dynamics of Advantageous and Non-Advantageous Edges

Figure 5 illustrates the evolutionary dynamics of edge selection frequencies during TSP optimization using a learning-based algorithm. The central network graph represents a TSP instance, with nodes as cities and edges as potential paths. Edges are classified based on their contribution to optimal or near-optimal solutions.

The left panel displays the frequency dynamics of advantageous edges, while the right panel focuses on non-advantageous edges across successive generations of the genetic algorithm.

- **Advantageous Edges (Left Panel)** The three plots show the proportion of advantageous edges increasing rapidly, stabilizing near 100% by the 30th generation. This indicates the algorithm effectively identifies and reinforces useful edges.

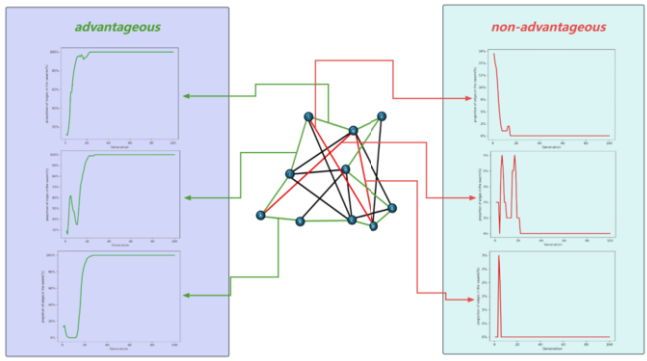

Figure 5. Frequency dynamics of advantageous and non-advantageous edges

- **Non-Advantageous Edges (Right Panel)** The plots illustrate a rapid decline in the frequency of non-advantageous edges, approaching 0% within the first 30 generations, highlighting the algorithm's ability to eliminate less optimal edges.

Overall, Figure 5 demonstrates how edge frequencies evolve during optimization. By tracking these changes, edges can be categorized into advantageous and non-advantageous groups, reducing the search space and sparsifying the TSP graph. Focusing on advantageous edges enhances both the efficiency and generalization of the optimization process, with the frequency dynamics validating the algorithm's effectiveness.

4.3. Sparsification of Complete Graphs based on Prediction Results

To assess the sparsification performance of our feature-based prediction model, we tested three TSPLIB instances: wi29, dj38, and st70 [15]. We first solved these instances using a traditional genetic algorithm and then applied our prediction model. The number of iterations required for each algorithm to converge was compared. Figure 6 shows the results for the predictive model.

Instance 1 The prediction model converged to the optimal solution at the 44th iteration, and the sparse result contained 100% of the optimal solution at the 30th iteration.

Instance 2 The prediction model converged to the optimal solution at the 49th iteration, and the sparse result contained 100% of the optimal solution at the 30th iteration.

Instance 3 The prediction model converged to the optimal solution at the 63th iteration, and the sparse result contained 100% of the optimal solution at the 40th iteration.

The model demonstrated rapid convergence across all test cases, highlighting its efficiency in feature extraction and knowledge utilization, which resulted in faster convergence to optimal solutions.

Specific Analysis Instance 3 Using Instance 3 (st70.TSP) as an example, we explored the sparsification process (Figure 7). After 200 iterations, the graph's initial 4556 edges were reduced to 441 edges. Notably, these sparsified edges contained all the optimal so-

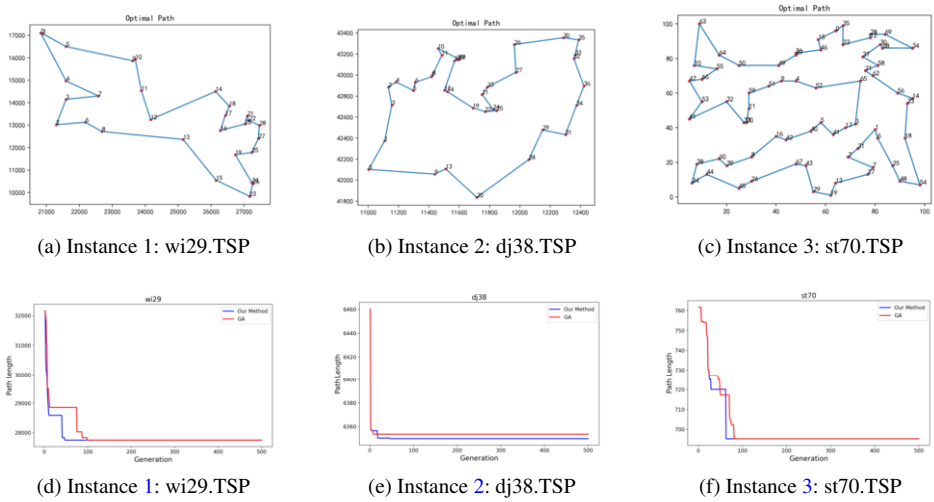

(a) Instance 1: wi29.TSP (b) Instance 2: dj38.TSP (c) Instance 3: st70.TSP

(d) Instance 1: wi29.TSP (e) Instance 2: dj38.TSP (f) Instance 3: st70.TSP

Figure 6. Optimal solution obtained by prediction model

lutions identified by the genetic algorithm at the 985th iteration. This result underscores the effectiveness of the prediction model in identifying and predicting optimal edge selections, significantly reducing problem complexity.

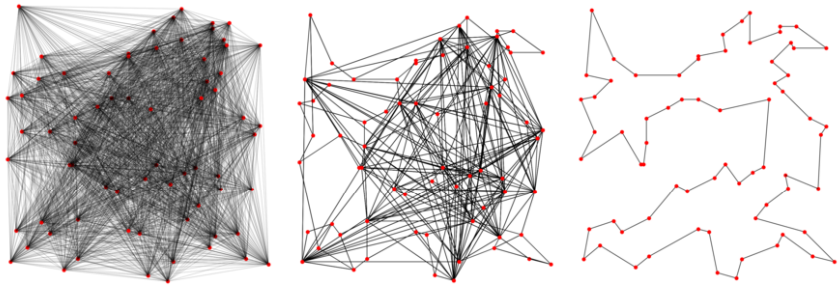

(a) Complete Graph (b) Sparse of the 200th (c) Optimum of 985th

Figure 7. Instance 3: st70.TSP sparsification process

4.4. Comparative Analysis of Algorithm Performance

Instances Experiments To assess the performance of our method, we tested it against established optimization algorithms on 16 TSPLIB benchmark instances [15]. The algorithms compared include Ant Colony Optimization (ANT), Genetic Algorithm (GA), Particle Swarm Optimization (PSO), Simulated Annealing (SA), and Tabu Search (TS). We evaluated the optimum solution and the number of iterations required to achieve this optimum. Figure 8 presents a scatter plot of these results, with the horizontal axis showing the optimum found and the vertical axis representing the iteration at which the last change occurred. The TSP instances are indicated as numbers within circles.

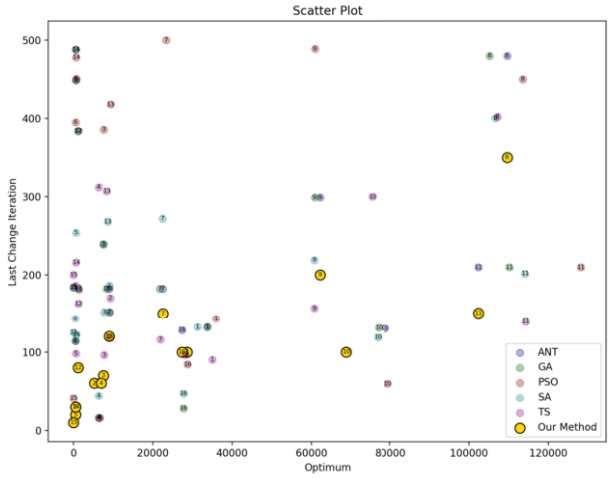

Figure 8. Scatter plot of optimum and iteration counts for TSPLIB instances across various algorithms

Our method exhibits competitive efficiency, achieving optimal solutions in fewer iterations compared to most other algorithms. For instance, our method reached the optimum within the first 100 iterations for several instances (e.g., instances 1, 2, and 3), outperforming others in convergence speed.

While many algorithms achieve similar optimum values, our method consistently delivers near-optimal or optimal solutions. The clustering of brown markers at lower optimum values indicates robust performance. Although algorithms like GA and SA also show clusters of low optimum values, their higher iteration counts suggest a trade-off between solution quality and computational effort.

Certain outliers in the scatter plot reveal instances where some algorithms either significantly underperform or require more iterations to reach the optimum. For example, instance 8 shows higher optimum values with ANT and PSO, indicating challenges in those cases. Our method avoids such extreme outliers, demonstrating greater reliability and consistency across diverse problem instances.

Numerical Experiments During testing, our model was evaluated using beam search and demonstrated superior performance with the smallest error. Table 1 compares our model against methods from existing literature, including GA, PSO, and SAA, as well as heuristic methods like Nearest Insertion and Farthest Insertion for TSP50 problems [16].

The results reveal that while GA, PSO, and SAA provide competitive objective values with minimal optimality gaps (ranging from 0.40% to 0.42%), they require slightly more computational time compared to our model, which achieves the best balance between solution quality and efficiency. Heuristic methods such as Nearest Insertion and Farthest Insertion, though fast, exhibit much higher optimality gaps (22.94% and 5.53%). Our model excels by providing high-quality solutions with reduced computational time, making it ideal for scenarios where both speed and accuracy are critical.

Table 1. Comparison of results for 10,000 instances of TSP50 instances

Method	Objective	Optimality Gap	Total Time	Inference Time
Our Model	5.707	0.31%	13.7s	0.07s
GA [17]	5.3	0.40%	14.5s*	0.09s
PSO [18]	5.1	0.42%*	14.8s*	0.08s
SAA [19]	5.2	0.41%*	14.2s*	0.085s
Nearest Insertion	7.00*	22.94%*	0s*	-
Farthest Insertion	6.01*	5.53%*	2s*	-

* Approximate values.

5. Discussion and Conclusions

The proposed knowledge-driven hybrid method for predicting and sparsifying paths in the TSP represents a notable advancement in optimizing algorithm efficiency. By leveraging insights from an intelligent evolutionary algorithm, the method effectively prunes non-advantageous edges while retaining beneficial ones, leading to a more streamlined solution space. This approach accelerates the TSP solution process and enhances solution quality.

A key strength of this method is its dynamic adaptation and learning from the evolutionary process, which reduces reliance on extensive pre-training datasets and improves generalization. However, challenges remain with high-dimensional and complex data structures, and future research should consider integrating advanced techniques such as graph neural networks (GNNs) and topological structure analysis. In the work of Liu Bokai et al. [20], a hybrid machine learning method was used to predict the thermal conductivity of PNC. They combined ANN with PSO, which provides valuable insights and potential directions for future research. Additionally, while efforts are made to avoid local optima, the risk of knowledge solidification persists. Adaptive parameter adjustments and search strategies could help maintain diversity and prevent premature convergence.

Overall, this study introduces a novel approach by combining knowledge-driven prediction with intelligent evolutionary methods, demonstrating significant improvements in efficiency and accuracy, particularly for TSP50 and TSP100 with Euclidean distances. Future work should focus on refining feature extraction techniques and exploring adaptive strategies to enhance robustness and effectiveness. The promising results underscore the potential of knowledge-driven approaches in solving complex combinatorial optimization problems and suggest avenues for further advancement in this field.

References

[1] CK Joshi, Q Cappart, LM Rousseau, T Laurent, and X Bresson. Learning tsp requires rethinking generalization. arxiv 2020. *arXiv preprint arXiv:2006.07054*.

[2] James Fitzpatrick, Deepak Ajwani, and Paula Carroll. Learning to sparsify travelling salesman problem instances. In *International Conference on Integration of Constraint Programming, Artificial Intelligence, and Operations Research*, pages 410–426. Springer, 2021.

[3] Bokai Liu and Weizhuo Lu. Surrogate models in machine learning for computational stochastic multi-scale modelling in composite materials design. *International Journal of Hydromechatronics*, 5(4):336–365, 2022.

[4] David L Applegate, Robert E Bixby, Vasek Chvatal, and William J Cook. *The traveling salesman problem: a computational study*. Princeton University Press, 2006.

[5] Keld Helsgaun. *An extension of the Lin-Kernighan-Helsgaun TSP solver for constrained traveling salesman and vehicle routing problems*. Roskilde University, Roskilde, 2017.

[6] Google. Or-tools: Google's operations research tools, 2015.

[7] Oriol Vinyals, Meire Fortunato, and Navdeep Jaitly. Pointer networks, 2017.

[8] Chaitanya K Joshi, Thomas Laurent, and Xavier Bresson. An efficient graph convolutional network technique for the travelling salesman problem. *arXiv preprint arXiv:1906.01227*, 2019.

[9] Yuan Sun, Andreas Ernst, Xiaodong Li, and Jake Weiner. Generalization of machine learning for problem reduction: a case study on travelling salesman problems. *Or Spectrum*, 43(3):607–633, 2021.

[10] Yong Wang. An approximate method to compute a sparse graph for traveling salesman problem. *Expert Systems with Applications*, 42(12):5150–5162, 2015.

[11] Colin R Reeves. Genetic algorithms. *Handbook of metaheuristics*, pages 109–139, 2010.

[12] Noraini Mohd Razali, John Geraghty, et al. Genetic algorithm performance with different selection strategies in solving tsp. In *Proceedings of the world congress on engineering*, volume 2, pages 1–6. International Association of Engineers Hong Kong, China, 2011.

[13] Samuel A Oluwadare, Bosede A Ogunsanmi, and John C Nwaiwu. Towards solving travelling salesperson problem using hybrid of genetic algorithm and lin-kernighan algorithm: A comparative evaluation with neural network model. *International Journal of Computer Applications*, 975:8887.

[14] Bladimir Toaza and Domokos Esztergár-Kiss. A review of metaheuristic algorithms for solving tsp-based scheduling optimization problems. *Applied Soft Computing*, page 110908, 2023.

[15] G. Reinelt. Tsplib - a traveling salesman problem library, 1991.

[16] Xavier Bresson and Thomas Laurent. The transformer network for the traveling salesman problem. *arXiv preprint arXiv:2103.03012*, 2021.

[17] Fei Liu and Guangzhou Zeng. Study of genetic algorithm with reinforcement learning to solve the tsp. *Expert Systems with Applications*, 36(3):6995–7001, 2009.

[18] Kang-Ping Wang, Lan Huang, Chun-Guang Zhou, and Wei Pang. Particle swarm optimization for traveling salesman problem. In *Proceedings of the 2003 international conference on machine learning and cybernetics (IEEE cat. no. 03ex693)*, volume 3, pages 1583–1585. IEEE, 2003.

[19] Xiutang Geng, Zhihua Chen, Wei Yang, Deqian Shi, and Kai Zhao. Solving the traveling salesman problem based on an adaptive simulated annealing algorithm with greedy search. *Applied Soft Computing*, 11(4):3680–3689, 2011.

[20] Bokai Liu, Nam Vu-Bac, and Timon Rabczuk. A stochastic multiscale method for the prediction of the thermal conductivity of polymer nanocomposites through hybrid machine learning algorithms. *Composite Structures*, 273:114269, 2021.

Fuzzy Systems and Data Mining X
A.J. Tallón-Ballesteros (Ed.)

doi:10.3233/FAIA241427

Research on Crane Scene Recognition Technology Combining Digital Twins with Neural Networks

Wensheng SU[a] , Jia XU [a1] and Xinren WANG[a]
[a] *Special Equipment Safety Supervision Inspection Institute of Jiangsu Province, Nanjing, 210036, China*

Abstract. In the fields of computer vision and intelligent recognition, with the increasing complexity and dynamism of crane scenes, how to use digital twins technology and artificial intelligence technology to improve the accuracy and efficiency of crane image recognition has become a research hotspot. Based on the combination of digital twin technology, convolutional neural networks, and long short-term memory networks (DTE-CNN-LSTM), an algorithm has been developed to achieve intelligent recognition and semantic understanding of complex crane operation scenes by introducing a virtual simulation environment for image feature optimization and processing. The research results indicate that the DTE-CNN-LSTM algorithm performs well in multiple crane scenarios. After optimization, the recognition accuracy of night cranes reached 100%, the recognition accuracy of rainy scenes increased to 95%, and the misclassification rate decreased to 5%. The recognition accuracy of obstacle has reached 98%, and the recognition accuracy of crane operation area has reached 90%, significantly reducing the misclassification rate. Overall, the DTE-CNN-LSTM algorithm achieved an accuracy rate of 96.70% and an F1 value of 96.64% in classification tasks for different crane scenarios. Its robustness and generalization ability in complex crane working environments have been verified, demonstrating high potential for application.

Keywords. Artificial intelligence; computer vision; digital twins; image recognition; convolutional neural network; crane operation scenario

1. Introduction

With the rapid development of digital twins technology, the application of computer vision in crane scene recognition has gradually become a research focus. As an important branch of computer vision, image recognition is particularly widely used in identifying crane scenes. However, due to the differences in working environments and job contents of different cranes, traditional image recognition technology is inadequate in dealing with complex and ever-changing crane work scenarios [1-3]. The operation scenario of a crane not only includes various static and dynamic elements such as on-site command and signal lights, but is also affected by various environmental factors such as lighting, weather, and perspective, which poses great challenges to the recognition of related scenarios [4-5]. In recent years, deep learning, especially Convolutional Neural

[1] Corresponding Author: Jia Xu, Special Equipment Safety Supervision Inspection Institute of Jiangsu Province, Nanjing, 210036, China; Email: xj13914451158@outlook.com.

Networks (CNN), has achieved significant results in the field of image recognition. It can extract high-level feature information from massive data and demonstrate extremely high accuracy in classification tasks. Although CNN performs well in static image classification tasks, its ability to handle dynamic crane operation scenes involving time series information is limited [6-7], and there is an urgent need to develop a suitable recognition system based on the working environment of the crane.

Long Short Term Memory (LSTM) networks, as an effective tool for processing time series data, can capture temporal dependencies in the data, thus showing great potential in semantic understanding of crane images. However, despite significant advances in digital twin technology and deep learning algorithms in their respective fields, there are still many challenges in combining the two for recognition in different crane operation scenarios [8-9]. In existing research, it is often overlooked how to effectively integrate spatiotemporal information in complex crane operation scenarios, resulting in the need to improve the generalization ability and practical application effectiveness of the model.

Furthermore, Physics-Informed Neural Networks (PINNs) not only learn from data but also enhance their generalization ability through physical constraints [10-11]. This approach is particularly suitable for dealing with complex physical environments such as crane dynamics and air resistance, providing stronger interpretability and stability for crane scene recognition [12-13]. Sensitivity analysis allows for a quantitative assessment of the impact of different input variables (e.g., weather, lighting, crane speed) on the model's output results. It not only aids in identifying which factors play a decisive role in crane scene recognition but also provides directions for further optimization of the model. Based on this, the research will integrate Convolutional Neural Networks (CNNs) and Long Short-Term Memory (LSTM) networks with Digital Twin technology, while also incorporating PINNs, to explore intelligent recognition and semantic understanding algorithms suitable for crane scenes[14-16]. The aim is to overcome the shortcomings of current technologies and promote the further development of Intelligent Transportation Systems (ITS).

2. Construction of Graphical Image Intelligent Recognition and Crane Operation Scene Semantic Understanding Algorithm Based on Digital Twin

2.1. Design of Graphical Image Intelligent Recognition Algorithm

Driven by digital twin technology, the graphical image intelligent recognition algorithm aims to achieve efficient processing and accurate recognition of complex image data. The algorithm design integrates Convolutional Neural Networks (CNNs) with digital twin technology to comprehensively optimize the performance of image feature extraction and processing. The design of the graphical image intelligent recognition algorithm is primarily based on the feature extraction capabilities of CNNs, combined with the virtual simulation environment provided by digital twin technology, to achieve efficient image data processing and analysis. The design approach encompasses three main steps: image data preprocessing, feature extraction, and algorithm optimization based on the digital twin environment. Among these, image preprocessing is a crucial step in the intelligent recognition algorithm as it directly affects the effectiveness of feature extraction. In this step, image data first undergoes normalization to reduce the

influence of environmental factors such as lighting and noise. Assuming the input image is denoted as X, its normalization process can be represented by Equation (1).

$$X` = \frac{X - \mu}{\sigma} \tag{1}$$

In Equation (1), μ represents the mean value of the image, and σ denotes the standard deviation. After normalization, the image data enters the Convolutional Neural Network (CNN) for feature extraction. The core of CNN in image feature extraction lies in extracting local features through convolutional layers, reducing computational complexity through pooling layers, and completing feature mapping through fully connected layers. Assuming the convolutional kernel is W and the input image is X, the convolutional operation can be represented by Equation (2).

$$Y_{i,j} = \sum_{m=1}^{M} \sum_{n=1}^{N} W_{m,n} \cdot X_{i+m-1, j+n-1} \tag{2}$$

In Equation (2), $Y_{i,j}$ represents the convolution result, while M and N denote the dimensions of the convolutional kernel. By stacking multiple convolutional layers, the network gradually extracts higher-level features. Following the convolutional layers, a max pooling operation is applied to reduce the dimensions of the feature maps, thereby decreasing the computational complexity. The max pooling operation can be represented by Equation (3).

$$Z_{i,j} = \max\left\{Y_{2i-1,2j-1}, Y_{2i-1,2j}, Y_{2i,2j-1}, Y_{2i,2j}\right\} \tag{3}$$

In Equation (3), $Z_{i,j}$ represents the result after pooling. This process not only compresses the size of the feature maps but also retains important feature information. In digital twin-driven image processing optimization, digital twin technology provides a virtual simulation environment that enables further processing and optimization of image data within the virtual setting. The digital twin environment can simulate real-world scenarios, offering abundant contextual information to enhance the effectiveness of feature extraction. Assuming that within the digital twin environment, the features of the input image are represented as $F(X)$, higher-quality feature representations $F`(X)$ can be obtained through correlation with the virtual environment, as expressed in Equation (4).

$$F`(X) = \alpha \cdot F(X) + \beta \cdot E(V(X)) \tag{4}$$

In Equation (4), α and β represent weight parameters, while $E(V(X))$ denotes the additional features extracted from the virtual environment. This optimization process can effectively improve the accuracy of image recognition. After feature extraction, a fully connected layer is used to map the extracted features and generate classification results. Assuming the input features are H and the weights of the fully connected layer are W_f, the output can be expressed as Equation (5).

$$O = W_f \cdot H \tag{5}$$

The weight parameters are continuously optimized through the Backpropagation algorithm to improve the classification accuracy of the network. In summary, the design of the graphical image intelligent recognition algorithm encompasses the entire process from image preprocessing, feature extraction, to digital twin optimization. Multi-level feature extraction is performed using Convolutional Neural Networks (CNNs), and the features are further optimized through digital twin technology to achieve efficient and accurate image recognition.

In the implementation process, the input image is first normalized to reduce the impact of noise and environmental factors. Subsequently, image features are extracted

through a multi-layer Convolutional Neural Network (CNN), and the pooling layer is applied to reduce the dimensions of the feature maps. Finally, the extracted features are optimized using digital twin technology, and the classification results are output through the fully connected layer. The specific implementation flowchart of the algorithm is shown in Figure 1.

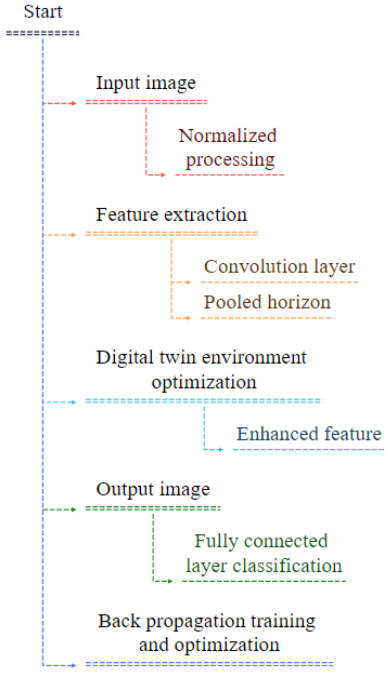

Figure 1. Specific implementation flow of the algorithm.

As shown in Figure 1, specifically, the input image X undergoes normalization to obtain $X`$. The convolutional and pooling layers are then applied to $X`$ for feature extraction, resulting in the feature map Y. The feature map Y is input into the digital twin environment for optimization, yielding enhanced features $F`(X)$. The fully connected layer is used to classify $F`(X)$, resulting in the output O. The network is trained and optimized using the backpropagation algorithm until convergence is achieved.

The time complexity of the algorithm is primarily determined by the operations in the convolutional layers. Assuming the size of the convolutional kernel is $k \times k$ and the size of the input image is $n \times n$, the time complexity of a single convolution operation is $O(k^2 \cdot n^2)$. The operation complexity of the pooling layer is relatively low, typically $O(n^2)$. By incorporating digital twin technology into the optimization process, the algorithm enhances feature extraction and classification accuracy.

2.2. Semantic Understanding Algorithm for Crane Operation Scenes Based on LSTM

In the semantic understanding of complex scenes, capturing the correlation between dynamic information and sequential data is crucial. Long Short-Term Memory (LSTM) networks, with their superior capability in processing time series data, have emerged as a key tool for handling various complex semantic understanding tasks. The LSTM-based

semantic understanding algorithm for complex scenes can effectively extract information from temporal image data, enabling accurate analysis and comprehension of complex scenarios. In the operation and maintenance scenario of cranes, real-time detection and analysis of dynamic objects such as temperature, crane working signs, and machine signal lights are required. Due to the strong temporal correlation and complex scene transition characteristics of the above scenarios, relying solely on static image processing techniques is difficult to meet practical needs. Therefore, it is necessary to harness the memory capability of LSTM networks to process continuous temporal image sequences, capturing the hidden dynamic relationships within the scene and subsequently enhancing the precision of semantic understanding. By incorporating forget gates, input gates, and output gates, LSTM networks overcome the gradient vanishing issue encountered by traditional Recurrent Neural Networks (RNNs) when processing long sequences, enabling them to effectively capture long-term dependencies [10-11]. The core structure of an LSTM unit is detailed as follows: Forget Gate: Determines the extent to which the state information from the previous moment is retained at the current moment. The forget gate's calculation formula is presented as Equation (6).

$$f_t = \sigma(W_f \cdot [h_{t-1}, x_t] + b_f) \tag{6}$$

In Equation (6), f_t represents the output of the forget gate, W_f is the weight matrix for the forget gate, h_{t-1} is the hidden state from the previous moment, x_t is the current input, b_f is the bias term, and σ is the sigmoid activation function. The Input Gate: It is used to update the memory cell state at the current moment. The computation of the input gate consists of two parts, with the update formula for the input gate presented in Equation (7).

$$i_t = \sigma(W_i \cdot [h_{t-1}, x_t] + b_i) \tag{7}$$

In Equation (7), i_t represents the output of the input gate, W_i is the weight matrix for the input gate, and b_i is the bias term. Subsequently, the update formula for the candidate memory cell state is presented in Equation (8).

$$\widetilde{C}_t = \tanh(W_C \cdot [h_{t-1}, x_t] + b_C) \tag{8}$$

In Equation (8), $\widetilde{C}_t$ denotes the candidate memory cell state, W_C is the weight matrix, b_C is the bias term, and $\tanh$ is the hyperbolic tangent function. Memory Cell Update: The memory cell state C_t at the current moment is updated according to Equation (9).

$$C_t = f_t \cdot C_{t-1} + i_t \cdot \widetilde{C}_t \tag{9}$$

In Equation (9), C_{t-1} represents the memory cell state at the previous time step. Based on the aforementioned LSTM architecture, in the context of semantic understanding of crane operation scenes, the LSTM network is utilized to process consecutive sequences of crane operation scene images. The specific implementation steps encompass data preprocessing, training, and optimization of the LSTM model. Crane operation scene data typically consists of continuous image frame sequences, and in order to effectively leverage the LSTM network, these data require preprocessing. Assuming the input image sequence is denoted as $\{X_1, X_2, X_3, \Lambda, X_T\}$, where T signifies the total number of image frames. Initially, feature extraction is performed on each frame to obtain the corresponding feature vectors $\{F_1, F_2, F_3, \Lambda, F_T\}$. The feature extraction method can be chosen as one based on Convolutional Neural Networks (CNNs), as described in Equation (10).

$$F_t = CNN(X_t) \tag{10}$$

The preprocessed feature vector sequence $\{F_1, F_2, F_3, \Lambda\ , F_T\}$ serves as the input to the LSTM network. Following data preprocessing, the LSTM model is utilized to train the crane operation scene sequence data. Assuming the training dataset is denoted as $\{(X^1, y^1), (X^2, y^2), (X^3, y^3), \Lambda\ , (X^N, y^N)\}$, where X^i represents the i-th sequence and y^i the corresponding label. The objective of the LSTM is to optimize the model parameters by minimizing the following loss function *L*, as stated in Equation (11).

$$L(\theta) = -\frac{1}{N}\sum_{i=1}^{N} y^i \log(h_T^i) + (1 - y^i)\log(t - h_T^i) \tag{11}$$

In Equation (11), h_T^i represents the output of the i-th sequence at time step T, and θ denotes the set of model parameters. Through the iterative updating of model parameters θ using the backpropagation algorithm and stochastic gradient descent, the value of the loss function L is continuously minimized. Ultimately, the trained LSTM model can be employed for semantic understanding of actual crane operation scenes.

In digital twin systems, LSTM models can not only handle real-life crane operation and maintenance scenarios, but also collaborate with virtual simulation environments. Leveraging digital twin technology, the simulation environment can provide additional virtual data, enriching the training samples for LSTM, and consequently enhancing the model's generalization capability. Assuming the virtual data is denoted as X^v, the loss function for training incorporating virtual data can be expressed as Equation (12).

$$L`(\theta) = \alpha L(\theta) + \beta L_v(\theta) \tag{12}$$

In Equation (12), $L_v(\theta)$ represents the loss function for the virtual data, while α and β are weight coefficients. By adopting this approach, the LSTM model is not only capable of comprehending the semantics within real-world scenarios but also able to acquire additional information from the virtual environment, further enhancing its understanding of complex crane operation scenes.

1.3 Optimization of Crane Scene Recognition Algorithms Based on Physics-Informed Neural Networks and Sensitivity Analysis

In the process of intelligent recognition of crane scenes, while relying solely on deep neural networks to process image data can achieve high accuracy, the model lacks understanding of the physical laws in actual scenes, which may lead to insufficient generalization ability in certain extreme cases. Therefore, physical constitutive equations are introduced and combined with artificial neural networks to form Physics-Informed Neural Networks (PINNs), thereby enhancing the recognition capability for complex crane scenes.

Assuming that the crane scenes being processed involve crane movement and air resistance, these can be modeled through physical constitutive equations.

$$\frac{\partial u}{\partial t} + u\frac{\partial u}{\partial x} = -\frac{1}{\rho}\frac{\partial p}{\partial x} + v\frac{\partial^2 u}{\partial x^2} \tag{13}$$

In this context, u represents the velocity field, p denotes the pressure field, ρ stands for density, and v is the viscosity coefficient. In the neural network, the predicted output of the neural network is constrained with the physical constitutive equations to form the loss function of the Physics-Informed Neural Network (PINN). The loss function is composed of both data-driven errors and errors constrained by physical equations. Furthermore, to evaluate the impact of different input parameters on model performance, Sensitivity Analysis is introduced. Sensitivity Analysis is capable of

quantifying the influence of input parameters on model outputs, aiding in identifying which input parameters are crucial to model performance. In crane scene recognition, factors such as ambient lighting, weather conditions, and crane flow can all affect recognition effectiveness. Assuming the input parameters of the model are $x=[x_1, x_2, x_3, \Lambda\ , x_n]$, the objective of Sensitivity Analysis is to calculate the partial derivative of each input parameter with respect to the model output, as shown in Equation (14).

$$S_i = \frac{\partial y}{\partial x_i} \tag{14}$$

Where y represents the output result of the model, and x_i denotes the i-th input parameter. Therefore, by introducing Physics-Informed Neural Networks (PINNs) and Sensitivity Analysis, the model's predictive capability for complex scenarios is enhanced, its interpretability of different input variables is improved, and the robustness and generalization of the model are further advanced.

3. Experiments and Results Analysis

3.1. Experimental Environment and Dataset Selection

In the experimental process of semantic understanding of crane operation and maintenance scenarios, the hardware and software environment of the experiment is as follows: the experimental hardware configuration uses the Intel Core i9-9900K processor released in 2019, which has 8 cores, 16 threads, and a frequency of 3.6 GHz to ensure multitasking capability. 64 GB DDR4 memory and 2 TB NVMe SSD provide efficient data storage and fast access capabilities. The NVIDIA RTX 2080 Ti graphics card supports parallel computing of large-scale deep learning models, combined with TensorFlow 2.0 and PyTorch 1.4 frameworks, running on Ubuntu 18.04 LTS system to ensure the efficiency and reliability of experiments.

In terms of dataset, this article obtained multiple crane scene images and crane system operation and maintenance data, as shown in Figure 2.

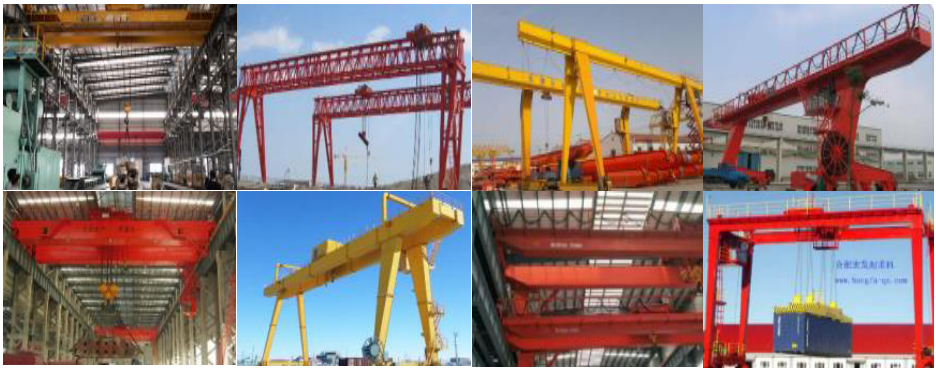

Figure 2. Crane System Dataset.

The dataset we collected contains 3000 finely annotated images of crane operation scenes, covering various scene elements such as static, dynamic, and operation signs, as well as a variety of changing conditions such as extreme weather, different types of cranes, and geographical locations. The image resolution of this dataset is 2048x1024, and it is divided into 2100 training sets, 300 validation sets, and 600 test sets.

3.2. Algorithm Experimental Analysis

In the algorithm experimental analysis, experimental methods were employed to validate and evaluate the performance of the proposed intelligent recognition algorithm in practical applications. Key indicators such as recognition effect evaluation, comparison of precision and accuracy, and algorithm performance under different scenarios were analyzed. The robustness and generalization ability of the algorithm in processing complex crane operation environments were also investigated. Among these, the evaluation results of image recognition effects are presented in Figure 3.

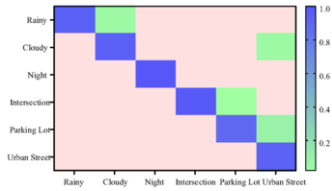

Figure 3. Image recognition effect evaluation results.

As shown in Figure 3, the image recognition effect evaluation results of the proposed Digital Twin Enhanced Convolutional Neural Network and Long Short-Term Memory (DTE-CNN-LSTM) optimization algorithm are presented. The performance of the optimized model has significantly improved in various scenarios. The recognition accuracy of the night crane operation scene remains at 100%, reflecting the stability of the model under low light conditions. The recognition accuracy of outdoor crane scenes on rainy days has reached 95%, with a misclassification rate reduced to 5%, significantly reducing the situation of misidentifying rainy days as cloudy. For the recognition of crane operation markers, the accuracy rate reaches 98%, with only a misclassification rate of 2%. The recognition accuracy of work signal lights reaches 90%, with a misclassification rate of only 10%. The recognition accuracy of command and dispatch has reached 93%, and the overall performance of the model has been significantly enhanced in complex crane operating environments.

The recognition results of different algorithm models for crane operation scenarios are shown in Table 1. It can be seen that the DTE-CNN-LSTM model performs the best, with an accuracy of 96.70% and an F1 value of 96.64%. It has excellent recognition ability in complex crane operation scenarios. In contrast, the Inception-ResNet-V2 model achieves an accuracy of 90.50% and an F1 score of 90.59%, which, while high, falls slightly behind the DTE-CNN-LSTM. ResNet101 achieves an accuracy of 87.80% and an F1 score of 87.65%. DenseNet121 performs robustly with an accuracy of 84.20% and an F1 score of 84.12%. EfficientNet-B0 and VGG16 exhibit accuracies of 72.30% and 79.45%, respectively, showing a decline in precision and recall when dealing with more complex crane operation scenes. Overall, DTE-CNN-LSTM leads in all indicators, demonstrating great potential in efficient and accurate crane scene recognition tasks.

Table 1. Crane operation scene classification and comparison results

Model	Accuracy	Precision	Recall	F1-score
VGG16	0,7945	0,8012	0,789	0,795
EfficientNet-B0	0,723	0,7385	0,741	0,7397
DenseNet121	0,842	0,8475	0,835	0,8412
ResNet101	0,878	0,889	0,8645	0,8765
Inception-ResNet-V2	0,905	0,913	0,899	0,9059
DTE-CNN-LSTM	0,967	0,97	0,963	0,9664

4. Conclusion

With the rapid development of intelligent operation of cranes, intelligent recognition of crane operation scenarios plays a crucial role in safety management. Based on this, we study a theoretical algorithm for intelligent recognition of graphic images and semantic understanding of crane scenes that combines digital twin technology, convolutional neural networks, and long short-term memory networks. By constructing a digital twin environment and using virtual simulation technology to enhance the accuracy of feature extraction and processing, combined with LSTM network to effectively capture dynamic information in complex crane operation scenes, the recognition ability of the model in practical scenarios has been improved. The experimental results show that the DTE-CNN-LSTM model performs well in various complex scenarios, with a recognition accuracy of 96.70% and an F1 value of 96.64%. Especially in poor lighting or weather conditions such as nighttime and rainy days, the performance of the model remains stable, with a recognition accuracy of 100% for nighttime scenes and 95% for rainy scenes. In addition, for different working scenarios of cranes in different states, the recognition accuracy of the model reached 98% and 90% respectively, demonstrating strong robustness and adaptability. Compared to other models such as Inception ResNet-V2 and ResNet101, DTE-CNN-LSTM has significant advantages in various indicators. However, despite achieving high accuracy in multiple tests, the DTE-CNN-LSTM model still has certain limitations. The accuracy of the model still needs to be further improved in terms of data processing efficiency and real-time performance; Therefore, future research will focus on optimizing the computational efficiency of the model and further improving its adaptability in diverse scenarios.

Acknowledgments

This work was supported partly by Science and Technology Plan Project of Special Equipment Safety Supervision Inspection Institute of Jiangsu Province (KJ(Y)2023035).

References

[1] D Dai, Y Li, Y Wang, H Bao, G Wang. Rethinking the image feature biases exhibited by deep convolutional neural network models in image recognition[J].CAAI Transactions on Intelligence Technology, 2022, 7(4):721-731.
[2] Zhang Z , Wang Y , Luo Z ,et al.Automatic detection of hazardous scenarios during spatial interaction between tower cranes and workers[J].Journal of Tsinghua University (Science and Technology), 2024, 64(2):198-204.DOI:10.16511/j.cnki.qhdxxb.2023.22.047.
[3] Gheisari M E B .Applications and requirements of unmanned aerial systems (UASs) for construction safety[J].Safety science, 2019, 118.
[4] Zhong D , Lv H , Han J ,et al.A Practical Application Combining Wireless Sensor Networks and Internet of Things: Safety Management System for Tower Crane Groups[J].Sensors (Basel, Switzerland), 2014, 14(8).DOI:10.3390/s140813794.
[5] Wu H , Zhong B , Li H ,et al.On-site safety inspection of tower cranes: A blockchain-enabled conceptual framework[J].Safety Science, 2022.DOI:10.1016/j.ssci.2022.105815.
[6] Teizer,Jochen,Venugopal,et al.Ultrawideband for Automated Real-Time Three-Dimensional Location Sensing for Workforce, Equipment, and Material Positioning and Tracking[J].Transportation Research Record: Journal of the Transportation Research Board, 2008, 2081:56-64.DOI:10.3141/2081-06.
[7] GUO H L, ZHANGZT, YU R, et al. Action recognition based on 3D Skeleton and LSTM for the monitoring of construction workers' safety harness usage[J]. Journal of Construction Engineering and Management, 2023, 149(4):04023015.
[8] Yang Z , Yuan Y , Zhang M, et al. Safety Distance Identification for Crane Drivers Based on Mask R-CNN[J].Sensors, 2019, 19(12):2789.DOI:10.3390/s19122789.
[9] Huang Y , Fan J Y , Hu J Z Y .TBi-YOLOv5: A surface defect detection model for crane wire with Bottleneck Transformer and small target detection layer[J].Proceedings of the Institution of Mechanical Engineers, Part C. Journal of mechanical engineering science, 2024, 238(6):2425-2438.
[10] Q Jiang, C Shu, L Zhu, L Yang, Y Liu, Z Zhangl.Applications of finite difference-based physics-informed neural networks to steady incompressible isothermal and thermal flows[J].International Journal for Numerical Methods in Fluids, 2023,10(95):1565-1597.
[11] Junchao S , Yong C , Xiaoyan T .Physics-Informed Neural Networks with Two Weighted Loss Function Methods for Interactions of Two-Dimensional Oceanic Internal Solitary Waves[J].Journal of Systems Science & Complexity, 2024, 37(2):545-566.
[12] Lorenzen F , Zargaran A , Janoske U .Potential of physics-informed neural networks for solving fluid flow problems with parametric boundary conditions[J].Physics of fluids, 2024,1(36):1-12.
[13] Junchao S , Yong C , Xiaoyan T .Physics-Informed Neural Networks with Two Weighted Loss Function Methods for Interactions of Two-Dimensional Oceanic Internal Solitary Waves[J].Journal of Systems Science & Complexity, 2024, 37(2):545-566.
[14] Jiang Wang, Yi Yang, Junhua Mao, Zhiheng Huang, Chang Huang, and Wei Xu. Cnn-rnn: A unified framework for multi-label image classification[C]. In CVPR, 2016.
[15] Yangtao Wang, Yanzhao Xie, Yu Liu, Ke Zhou, and Xiaocui Li. Fast graph convolution network based multi-label image recognition via cross-modal fusion[C]. In Proceedings of the 29th ACM International Conference on Information & Knowledge Management, pages 1575–1584, 2020
[16] Jin Ye, Junjun He, Xiaojiang Peng, Wenhao Wu, and Yu Qiao. Attention-driven dynamic graph convolutional network for multi-label image recognition[C]. In ECCV, 2020

Fuzzy Systems and Data Mining X
A.J. Tallón-Ballesteros (Ed.)

doi:10.3233/FAIA241428

Investigating XGBoost Efficiency on Diverse Time-Series Data Through PSO Parameter Tuning

Khwanchai HUAILUK [a], Natthapon KHETKRATHOK [a], Pirapong INTHAPONG [a], Sayan KAENNAKHAM [b], and Nara SAMATTAPAPONG [c,1]
[a] *Department of Interdisciplinary Science and Internationalization, Institute of Science, Suranaree University of Technology, Nakhon Ratchasima, 30000, Thailand;*
[b] *School of Mathematics and Geoinformatics, Institute of Science, Suranaree University of Technology, Nakhon Ratchasima, 30000, Thailand;*
[c] *School of Industrial Engineering, Institute of Engineering, Suranaree University of Technology, Nakhon Ratchasima, 30000, Thailand;*
ORCiD ID: Khwanchai Huailuk https://orcid.org/0009-0008-9502-334X, Natthapon Khetkrathok https://orcid.org/0009-0003-9810-1626, Pirapong Inthapong https://orcid.org/0009-0006-1618-4619, Sayan Kaennakham https://orcid.org/0000-0001-9682-559X, Nara Samattapapong https://orcid.org/0000-0002-2230-6591

Abstract. This study investigates the effectiveness of Particle Swarm Optimization (PSO) in enhancing the performance of the XGBoost algorithm on three distinct types of time-series datasets: intermittent (Dataset-1), multi-seasonal (Dataset-2), and non-stationary (Dataset-3). Time-series data often exhibit complex patterns, making hyperparameter tuning crucial for improving model accuracy. In this research, two PSO variants, PSOv1 and PSOv2, were applied to optimize key hyperparameters, specifically the learning rate (LR) and Max Depth (MxD), in order to minimize the Root Mean Square Error (RMSE). Both PSOv1 and PSOv2 demonstrated significant improvements over the baseline XGBoost model, with PSOv2 showing faster and more stable convergence across all datasets. Notably, the PSO algorithms were particularly effective for multi-seasonal and non-stationary time-series, where the convergence rate was faster compared to intermittent data. These results highlight PSO's ability to fine-tune hyperparameters for better generalization, reducing overfitting and improving performance on unseen data. This work underscores the importance of swarm intelligence algorithms in optimizing machine learning models for complex time-series forecasting tasks, paving the way for future research in hybrid optimization techniques and the exploration of additional hyperparameters.

Keywords. XGBoost, Time-Series Prediction, Particle Swarm Optimization (PSO), Hyperparameter Tuning, Forecasting Applications

1. Introduction

Time-series data plays a pivotal role in a wide range of industries [1], from finance [2] and healthcare [3] to energy management [4], supply chains [5], and climate forecasting [6]. Accurate modeling and prediction of time-series patterns are essential for informed decision-making, optimizing resource allocation, and enhancing operational efficiency.

[1] Corresponding Author: Nara Samattapapong, nara@g.sut.ac.th.

The inherent complexity of time-series data, which often exhibits varied patterns such as seasonal trends, cyclical behaviors, or irregular fluctuations, adds a layer of difficulty when selecting the most effective predictive model[7]. In recent years, XGBoost has emerged as one of the most robust machine learning algorithms for time-series forecasting, known for its scalability, efficiency, and ability to handle missing data while reducing overfitting through regularization [8]. However, its full potential can only be realized through careful tuning of its hyperparameters, which are key to maximizing predictive accuracy. Given the time-consuming and challenging nature of manual parameter tuning, there is a growing interest in automated approaches to optimize models like XGBoost.

One promising approach to optimizing XGBoost's hyperparameters lies in swarm intelligence algorithms [9] three, particularly Particle Swarm Optimization (PSO). PSO mimics the social behavior of organisms such as birds or fish to navigate and search the hyperparameter space effectively, making it a highly efficient method for automatic tuning [10]. Unlike traditional optimization techniques, PSO does not require gradient information, making it especially well-suited for optimizing non-differentiable, multidimensional problems such as hyperparameter tuning in machine learning models. Moreover, recent developments have introduced Adaptive PSO, an advanced variant that dynamically adjusts its parameters throughout the optimization process, allowing for greater flexibility and potentially yielding better results than the standard PSO approach [11]. This research focuses on investigating the effectiveness of both Standard PSO and Adaptive PSO in fine-tuning XGBoost for time-series prediction across a variety of datasets, each with distinct characteristics.

This study evaluates the performance of XGBoost on three diverse time-series datasets, representing different types of patterns, by comparing the impact of two PSO variants on its hyperparameter optimization [10]. By automating the tuning process, we aim to alleviate the burden on data analysts and engineers, allowing XGBoost to perform at its best without the need for exhaustive manual interventions. The findings from this comparative analysis will shed light on the suitability of XGBoost for different time-series structures and the effectiveness of the PSO variants in improving forecasting accuracy. Additionally, this research will provide valuable insights for practical applications in industries that rely heavily on time-series data, offering a framework for improving decision-making processes and optimizing operational outcomes using advanced machine learning techniques. In doing so, we aim to contribute to the growing body of knowledge in both time-series forecasting and the use of optimization algorithms in machine learning.

2. Methodology

2.1. Extreme Gradient Boosting

XGBoost [12] is a powerful ensemble learning algorithm that builds decision trees sequentially, optimizing a regularized loss function to enhance predictive accuracy. At each iteration t, the objective function is expressed as follows

$$L^{(t)} = \sum_{i=1}^{n} l\left(y_{i,} \hat{y}_i^{(t)}\right) + \sum_{k=1}^{t} \Omega\left(f_k\right). \tag{1}$$

Here, $l\left(y_i \hat{y}_i^{(t)}\right)$ represents the loss between the true label y_i and the predicted value $\hat{y}_i^{(t)}$. Common loss functions include squared error for regression and logistic loss for classification. The regularization term $\Omega\left(f_k\right)$ helps prevent overfitting. The second term, regularizes the model to avoid overfitting and is defined as

$$\Omega\left(f_k\right) = \gamma T_k + \frac{1}{2}\lambda \sum_{j=1}^{T_k} \omega_j^2 \tag{2}$$

where T_k is the number of leaves in the *k*-th tree, γ controls model complexity, and ω_j are the leaf weights, with λ serving as a regularization parameter. The prediction at iteration *t* is updated as follows

$$\hat{y}_i^{(t)} = \hat{y}_i^{(t-1)} + \eta f_t\left(x_i\right), \tag{3}$$

where η is the learning rate, and $f_t\left(x_i\right)$ is the prediction from the *t*-th tree. The tree f_t is constructed to minimize the first and second-order Taylor expansion of the loss function with respect to the model output expressed as

$$L^{(t)} \approx \sum_{i=1}^{n}\left[q_i f_t\left(x_i\right) + \frac{1}{2} h_i f_t^2\left(x_i\right)\right] + \Omega\left(f_t\right), \tag{4}$$

where $q_i = \dfrac{\partial l\left(y_i, \hat{y}_i^{(t-1)}\right)}{\partial \hat{y}_i^{(t-1)}}$ and $h_i = \dfrac{\partial l\left(y_i, \hat{y}_i^{(t-1)}\right)}{\partial \hat{y}_i^{(t-1)2}}$ are the first and second-order gradients, respectively. The final model is the sum of all tree predictions, producing the optimized output as shown in the following equation.

$$\hat{y}_i = \sum_{t=1}^{T} \eta f_t\left(x_i\right). \tag{5}$$

Thus, XGBoost balances predictive power and complexity through gradient boosting and regularization, [13].

2.2. Particle Swarm Optimization (PSO)

2.2.1 Classical Particle Swarm Optimization (CPSO)

The classical Particle Swarm Optimization (CPSO) algorithm involves a set of particles (solutions) moving in the search space to find the optimal solution. Each particle's position is updated based on its velocity, which is influenced by the particle's personal best position ($P_i(t)$) and the global best position ($G(t)$) among all particles. The velocity and position update equations are given, respectively, as

$$v_i(t+1) = w v_i(t) + c_1 r_1\left[P_i(t) - x_i(t)\right] + c_2 r_2\left[G(t) - x_i(t)\right], \tag{6}$$

$$x_i(t+1) = x_i(t) + v_i(t+1), \tag{7}$$

where $v_i(t)$ and $x_i(t)$ represent the velocity and position of particle i at iteration t, respectively. $P_i(t)$ is the personal best position of particle i, and $G(t)$ is the global best position. The constants c_1 and c_2 are the cognitive and social learning coefficients, and

r_1 and r_2 are random numbers uniformly distributed between 0 and 1. The inertia weight ω controls the trade-off between exploration and exploitation in the search space.

2.2.2 Inertia Weight Adaptation Strategies (APSO)

Several strategies have been proposed to adapt the inertia weight ω to improve convergence. One common approach is to set a fixed inertia weight, with ω=0.7298 being widely adopted in many PSO variants. a chaotic map can be employed to adjust the inertia weight. The inertia weight is dynamically updated using the following expression

$$w(t) = \left(w_{\max} - w_{\min}\right)\frac{T-t}{T} + w_{\min} \cdot p(t) \tag{8}$$

where $\rho(t)$ is a chaotic term defined as:

$$\rho(t) = 4 \cdot \rho(t-1) \cdot (1-\rho(t-1)) \in (0,1), \tag{9}$$

$\rho(0)$ is a random number. This chaotic adaptation allows the inertia weight to follow a non-linear behavior, which may enhance the algorithm's exploration capability by preventing early convergence to local optima.

The acceleration coefficients c_1 and c_2 determine the relative importance of the cognitive component (p-best) and the social component (g-best) in the velocity update. In some PSO variants, these coefficients are set to fixed values, typically $c_1 = c_2 = 2.0$. However, to improve the balance between exploration and exploitation over time, time-varying acceleration coefficients have been proposed.

A time-varying acceleration strategy reduces the cognitive component while increasing the social component over the course of the iterations. The equations for the time-varying acceleration coefficients are as follows

$$c_1(t) = c_1^{\max} - \left(c_1^{\max} - c_1^{\min}\right)\frac{t}{T}, \tag{10}$$

$$c_2(t) = c_2^{\max} - \left(c_2^{\max} - c_2^{\min}\right)\frac{t}{T}, \tag{11}$$

where $c_1^{\max} = c_2^{\max} = 2.5$ and $c_1^{\min} = c_2^{\min} = 0.5$. This strategy encourages early exploration of the search space by initially prioritizing the cognitive component, but gradually shifts toward exploiting the global best solution as the number of iterations increases.

3. Experimental Setup

3.1 Dataset Description and Preprocessing

The study uses three types of time-series datasets. The first, intermittent data with many zeros or missing values, is typical in sporadic demand and requires specialized handling. The second exhibits multi-seasonal patterns, common in energy consumption, requiring analysis of different cycles. The third, non-stationary data, like in financial markets, needs stabilization before modeling. For XGBoost, the "Date" column is converted to datetime, and time-based features (Hour, Day, Month, Year) are added. The dataset is split into training (80%, 70%) and testing sets (20%, 30%).

3.2 XGBoost Configuration and PSO Optimization

The In this study, XGBoost optimizes two key hyperparameters: learning rate and max depth. The learning rate controls model adjustments, while max depth determines tree complexity. Using 100 estimators, the model minimizes RMSE, with time-based features (Hour, Day, Month, Year) added to the dataset. The data is split 80% for training and 20% for testing, ensuring effective handling of diverse time-series patterns. Two PSO variants—Classical and Adaptive—are employed to tune these hyperparameters. Classical PSO uses a fixed inertia weight (0.5), while Adaptive PSO adjusts inertia dynamically from 0.9 to 0.4 over 30 iterations. With 10 particles, both PSOs automatically minimize RMSE, improving model performance without manual tuning. The objective function for executing the PSOs is defined to consider both the effect of accuracy recorded on the training and that of the test set, as defined in the following

$$PSO - Objective\_Function = \beta \cdot RMSE_{Train} + (1-\beta) \cdot RMSE_{Test}, \tag{12}$$

where β is the weight.

4. Main Results and General Discussions

The performance of the XGBoost algorithm, along with two versions of Particle Swarm Optimization (PSO), was evaluated across three distinct time-series datasets by optimizing two hyperparameters: the learning rate (LR) and Max Depth (MxD). For Dataset-1, the baseline XGBoost model with an LR of 0.01 and an MxD of 3 resulted in RMSE values of 14.1009 on the training set and 12.1001 on the testing set. Optimizing with PSOv1 (LR: 0.3564, MxD: 10) significantly improved the performance, reducing the RMSE to 0.1145 on the training set and 3.9612 on the testing set. PSOv2 (LR: 0.5573, MxD: 10) yielded similar results, with RMSE values of 0.0049 for training and 4.0023 for testing. For Dataset-2, the baseline XGBoost model (LR: 0.01, MxD: 3) recorded RMSEs of 9.6056 and 13.3153 for training and testing, respectively. PSOv1 optimization (LR: 0.0490, MxD: 10) further improved these values, with an RMSE of 0.0071 on the training set and 1.0439 on the testing set. PSOv2 (LR: 0.4001, MxD: 10) achieved comparable performance, with RMSEs of 0.0088 for training and 1.0437 for testing.

In the case of Dataset-3, the baseline XGBoost model with the same hyperparameters (LR: 0.01, MxD: 3) produced RMSEs of 9.6697 for training and 12.8992 for testing. After applying PSOv1 optimization (LR: 0.6899, MxD: 10), the RMSE was reduced to 0.0025 for training and 4.9810 for testing. PSOv2 (LR: 0.8568, MxD: 10) slightly outperformed PSOv1, with RMSE values of 0.0018 for training and 4.9782 for testing. Overall, both PSO versions demonstrated significant improvements over the baseline XGBoost model, with PSOv2 providing marginally better results in most cases.

PSO algorithms significantly improved XGBoost by fine-tuning the learning rate and Max Depth, reducing RMSE across all datasets and enhancing model robustness. Future work could explore hybrid PSOs, optimize additional hyperparameters like subsample and gamma, or integrate PSO with advanced techniques like neural networks for further performance gains.

Table 1. RMSE comparison of XGBoost and PSO-optimized XGBoost models across three time-series datasets.

Model	Dataset-1			Dataset-2			Dataset-3		
	LR, MxD	RMSE Training	RMSE Testing	LR, MxD	RMSE Training	RMSE Testing	LR, MxD	RMSE Training	RMSE Testing
XGBoost	0.01, 3.0	14.1009	12.1001	0.01, 3.0	9.6056	13.3153	0.01, 3.0	9.6697	12.8992
XGBoost with PSOv1	0.3564, 10	0.1145	3.9612	0.4490, 10	0.0071	1.0439	0.6899, 10	0.0025	4.9810
XGBoost with PSOv2	0.5573, 10	0.0049	4.0023	0.4001, 10	0.0088	1.0437	0.8568, 10	0.0018	4.9782

The convergence plots for PSOv1 and PSOv2 across the three datasets reveal distinct differences in the speed and stability of convergence. In all datasets, both PSO versions show rapid convergence within the first few iterations, followed by a stable plateau, indicating minimal RMSE fluctuations. For Dataset-1, PSOv1 converged to a stable RMSE around the 5th iteration, while PSOv2 demonstrated a slightly faster and more stable convergence, reaching a similar RMSE earlier. In Dataset-2, both PSOv1 and PSOv2 achieved rapid convergence within 3 iterations, but PSOv2 maintained a more consistent and lower RMSE throughout the subsequent iterations. Similarly, in Dataset-3, both PSO versions converged quickly by the 5th iteration, but PSOv2 again displayed a smoother and slightly lower RMSE compared to PSOv1. Overall, PSOv2 exhibits more consistent and efficient convergence across all three datasets, outperforming PSOv1 in terms of both speed and stability.

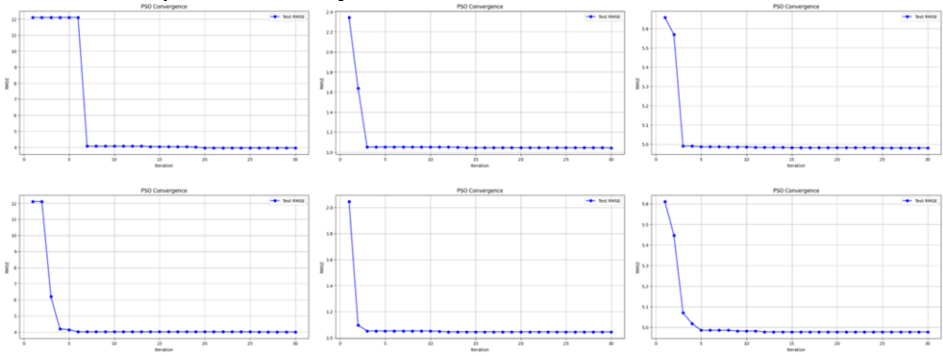

Figure 1. PSOv1 vs. PSOv2 convergence for RMSE minimization on three time-series datasets.

5. Conclusion

The application of PSO to optimize the learning rate and Max Depth in XGBoost significantly improved forecasting accuracy across intermittent, multi-seasonal, and non-stationary time-series datasets. Both PSOv1 and PSOv2 successfully reduced RMSE, with PSOv2 demonstrating faster convergence rates and more stable performance. The convergence behavior varied slightly depending on the dataset type, with faster convergence observed in the multi-seasonal and non-stationary datasets compared to the intermittent dataset. This suggests that the nature of the data impacts the optimization process, as more structured datasets like multi-seasonal time-series benefit more from

the PSO fine-tuning. These findings underline the effectiveness of PSO for time-series forecasting, encouraging future work to explore additional hyperparameter optimization and integration with other machine learning techniques to enhance performance across diverse data types.

References

[1] N. Kashpruk, C. Piskor-Ignatowicz, and J. Baranowski, "Time Series Prediction in Industry 4.0: A Comprehensive Review and Prospects for Future Advancements," *Applied Sciences,* vol. 13, no. 22, p. 12374, 2023.

[2] D. Cheng, F. Yang, S. Xiang, and J. Liu, "Financial time series forecasting with multi-modality graph neural network," Pattern Recognition, vol. 121, p. 108218, 2022.

[3] M. A. Morid, O. R. L. Sheng, and J. Dunbar, "Time series prediction using deep learning methods in healthcare," ACM Transactions on Management Information Systems, vol. 14, no. 1, pp. 1-29, 2023.

[4] N. Mounir, H. Ouadi, and I. Jrhilifa, "Short-term electric load forecasting using an EMD-BI-LSTM approach for smart grid energy management system," Energy and Buildings, vol. 288, p. 113022, 2023.

[5] J. Feizabadi, "Machine learning demand forecasting and supply chain performance," International Journal of Logistics Research and Applications, vol. 25, no. 2, pp. 119-142, 2022.

[6] H. Acaroğlu and M. Güllü, "Climate change caused by renewable and non-renewable energy consumption and economic growth: A time series ARDL analysis for Turkey," Renewable Energy, vol. 193, pp. 434-447, 2022.

[7] S. Li, W. Xu, and Z. Li, "Review of the SBAS InSAR Time-series algorithms, applications, and challenges," Geodesy and Geodynamics, vol. 13, no. 2, pp. 114-126, 2022.

[8] M. Niazkar et al., "Applications of XGBoost in water resources engineering: A systematic literature review (Dec 2018–May 2023)," Environmental Modelling & Software, p. 105971, 2024.

[9] X. Xiong, X. Guo, P. Zeng, R. Zou, and X. Wang, "A short-term wind power forecast method via xgboost hyper-parameters optimization," Frontiers in energy research, vol. 10, p. 905155, 2022.

[10] M. Jain, V. Saihjpal, N. Singh, and S. B. Singh, "An overview of variants and advancements of PSO algorithm," Applied Sciences, vol. 12, no. 17, p. 8392, 2022.

[11] D. Wang, D. Tan, and L. Liu, "Particle swarm optimization algorithm: an overview," Soft computing, vol. 22, no. 2, pp. 387-408, 2018.

[12] T. Chen and C. Guestrin, "Xgboost: A scalable tree boosting system," in Proceedings of the 22nd acm sigkdd international conference on knowledge discovery and data mining, 2016, pp. 785-794.

[13] W. Li, Y. Yin, X. Quan, and H. Zhang, "Gene expression value prediction based on XGBoost algorithm," Frontiers in genetics, vol. 10, p. 1077, 2019.

Fuzzy Systems and Data Mining X
A.J. Tallón-Ballesteros (Ed.)

doi:10.3233/FAIA241429

Evaluating the Effectiveness of the Generalized Sigmoid in YOLOv8 for Drug Detection and Classification

Anan PANPHUECH [a] ,Songkiat LOWMUNKHONG [a], Ratapong ONJUN [a], Patthra JANTHAWANNO [a] and Sayan KAENNAKHAM [b,1]
[a] *Department of Interdisciplinary Science and Internationalization, Institute of Science, Suranaree University of Technology, Nakhon Ratchasima, 30000, Thailand*
[b] *School of Mathematics and Geoinformatics, Institute of Science, Suranaree University of Technology, Nakhon Ratchasima, 30000, Thailand*
ORCiD ID: Anan Panphuech https://orcid.org/0009-0001-3296-1434, Songkiat Lowmunkhong https://orcid.org/0009-0001-0280-3072, Ratapong Onjun https://orcid.org/0009-0001-9724-5762, Patthra Janthawanno https://orcid.org/0009-0009-3289-0232, Sayan Kaennakham https://orcid.org/0000-0001-9682-559X

Abstract. In this study, we investigate the potential of the Generalized Sigmoid (GS), $\sigma(x;a,b)=\left(1+e^{-a(x-b)}\right)^{-1}$ as an adaptive activation function within the YOLOv8 framework for drug detection and classification tasks. Medication errors, particularly in identifying pills and tablets, present serious challenges in healthcare due to visual similarities and environmental factors. We propose the use of the GS, which allows flexible parameter tuning, to enhance detection accuracy. Various configurations of the GS are evaluated against the widely-used SiLU and standard sigmoid functions. Our experiments reveal that optimal tuning of GS parameters, specifically with a=1.50 and b=1.50, improves model performance in terms of mean Average Precision (mAP) and overall classification accuracy. These findings suggest that the GS can surpass standard activation functions, offering a promising advancement in deep learning applications for healthcare.

Keywords. YOLOv8, Generalized Sigmoid (GS), Drug Detection, Deep Learning in Healthcare

1. Introduction

Medication errors, particularly in drug dispensing and classification, remain a serious challenge in the healthcare and pharmaceutical sectors [1]. Ensuring the accurate detection and classification of different drug forms, such as capsules and tablets, is crucial to maintaining patient safety. Misclassifications can result in incorrect dosing, improper administration, and adverse health outcomes. With hospitals and pharmacies handling thousands of medications daily, the complexity of managing such processes

[1] Corresponding Author: Sayan KAENNAKHAM, School of Mathematics and Geoinformatics, Institute of Science, Suranaree University of Technology, Nakhon Ratchasima, 30000, Thailand; Email: sayan_kk@g.sut.ac.th

necessitates more reliable and advanced automated solutions. As such, improving the accuracy of drug detection and classification systems can substantially reduce medication-related risks and improve patient care [2].

YOLOv8, a state-of-the-art object detection model, has demonstrated substantial success across various domains due to its speed and precision [3]. However, the detection and classification of medications present unique challenges that demand further refinement. Capsules and tablets, though medically distinct, often appear visually similar, complicating their classification. Environmental factors such as lighting variability, overlapping objects, and subtle size differences further intensify the complexity of this task. This makes it essential to explore innovative strategies for enhancing YOLOv8's ability to handle such nuanced scenarios.

In this study, we introduce the Generalized Sigmoid [4] as an adaptive activation strategy within YOLOv8, aiming to explore its potential in improving drug detection and classification performance. While the GS function [5] is known for its flexibility, this research delves deeper into understanding how different components of the function influence the detection and classification process in this specific context. By analyzing the impacts of its parameters, such as slope and inflection points, we hope to shed light on their behavior and uncover insights into how they can be fine-tuned to optimize performance. The modified YOLOv8 framework is evaluated using key metrics, including mean Average Precision (mAP), and classification accuracy, to demonstrate its effectiveness [6]. Through this study, we aim to contribute both to safer drug dispensing practices and to advancing the field of object detection by refining activation function strategies in specific but challenging use cases.

2. Mathematical Background

2.1. YOLOv8

YOLO (You Only Look Once) [7] is an advanced object detection algorithm specifically designed for real-time detection, localization, and classification of objects within images. A typical architecture of YOLOv8 is illustrated in Figure 1 and is structured into three primary components: the Backbone, Neck, and Head, with a brief introduction as follows.

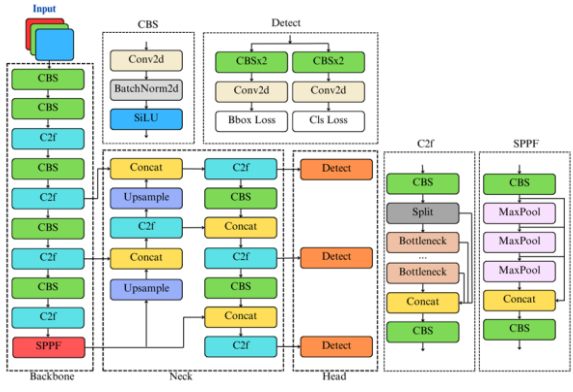

Figure 1. Typical architecture of YOLOv8.

Given an input image I of size $W \times H \times C$ (Width, Height, Channels), the backbone of YOLOv8 extracts features by applying a series of convolutional layers. The convolutional layers apply filters, represented as:

$$F_k = \sigma(W_k \cdot I + b_k). \tag{1}$$

Where F_k is the feature map from the *k*-th convolutional layer, W_k are the weights of the convolutional filters, bk is the bias term, and $\sigma(\cdot)$ is an activation function, on which this work focuses. The Neck of YOLOv8 implements a Feature Pyramid Network (FPN) to create multi-scale feature maps, allowing detection of objects at different sizes. Suppose the feature maps at different levels of the FPN are P_1, P_2, P_3, etc. These are used to detect objects at varying scales.

The multi-scale feature representation is computed as

$$P_i = f(F_{\text{out}}, i). \tag{2}$$

Where P_i is the feature map at the i-th scale, and $f(\cdot)$ is a function that aggregates feature maps through upsampling and merging operations. The Head of YOLOv8 predicts bounding boxes, objectness scores, and class probabilities. For each bounding box, four parameters are predicted: (*x*,*y*,*w*,*h*), where: (*x*,*y*) are the center coordinates of the bounding box, *w* and *h* are the width and height of the bounding box. The objectness score *o* indicates the likelihood of an object being present in the box, and the class probabilities c_i (for each class *i*) determine what the object is.

The output for each anchor box can be expressed as follows

$$\text{Box}(i) = \left(\sigma(t_x) + x_a, \sigma(t_y) + y_a, e^{t_w} \cdot w_a, e^{t_h} \cdot h_a\right). \tag{3}$$

The final class probability for class *i* and the objectness score are calculated as $P_{\text{class}_i} = \sigma(c_i) \cdot o$, where c_i is the class score for class *i*, and *o* is the objectness score.

The loss function in YOLOv8 is a combination of three losses

1. Classification Loss (cls_loss): This loss measures the error in predicting object classes. YOLOv8 utilizes the Binary Cross-Entropy (BCE) loss for this purpose:

$$L_{cls\_loss} = -\frac{1}{N}\sum_{i=1}^{N}\left[y_i \log(p_i) + (1 - y_i)\log(1 - p_i)\right] \tag{4}$$

   where N is the number of objects, y_i denotes the ground truth class label, and p_i is the predicted probability for class *i*.

2. Bounding Box Loss (box_loss): YOLOv8 employs Complete Intersection over Union (CIoU) loss for bounding box regression. CIoU incorporates factors such as IoU, distance between predicted and ground truth box centers, and aspect ratio consistency into its formulation:

$$L_{box\_loss} = 1 - IoU + \frac{\rho^2(b, b_{gt})}{c^2} + \alpha v \tag{5}$$

Where IoU is the Intersection over Union of the predicted and ground truth boxes, $\rho^2(b, b_{gt})$ denotes the Euclidean distance between the centers of the two boxes, c is the diagonal length of the smallest enclosing box covering both boxes, v measures the consistency of aspect ratios, and α is a positive trade-off parameter.

3. Distribution Focal Loss (dfl_loss): This loss enhances the precision of bounding box predictions by focusing on the distribution of predicted box coordinates. It is formulated as:

$$L_{\text{dfl\_loss}} = -\frac{1}{N}\sum_{i=1}^{N}\sum_{c=1}^{C}\left[q_{i,c}\log(p_{i,c})\right] \tag{6}$$

Where N is the total number of objects, C is total number of possible classes, $q_{i,c}$ is ground truth class label for the $i-th$ object and class c, and $p_{i,c}$ is predicted probability that the $i-th$ object belongs to class c

The total loss is the sum of these three components:

$$L_{\text{total}} = L_{\text{cls\_loss}} + L_{\text{box\_loss}} + L_{\text{dfl\_loss}} \tag{7}$$

2.2. The Sigmoid Function and Its Generalized Form

The sigmoid function is a mathematical function with an "S" shape, commonly used in machine learning, especially for logistic regression and neural networks. It is defined as expressed as

$$\sigma(x) = \frac{1}{1+e^{-x}} = \left(1+e^{-x}\right)^{-1} \tag{8}$$

In YOLOv8, studying the GS function is crucial because it introduces parameters that allow control over the curve's shape, enhancing model flexibility. The generalized form is as follows

$$\sigma(x;a,b) = \frac{1}{\left(1+e^{-a(x-b)}\right)} = \left(1+e^{-a(x-b)}\right)^{-1} \tag{9}$$

This form enables fine-tuning the steepness, midpoint, and vertical shift, improving predictions by adjusting the output behavior based on the specific task at hand, such as object detection in YOLOv8.

3. Experimental Setups

3.1. Dataset and Model Configuration

The dataset, sourced from Roboflow [8], contains 1,659 images of capsules and tablets. It was split into 1,446 training images, 135 validation images, and 78 test images, with each image resized to 640×640 pixels. Data augmentation techniques, including flips, zooms, rotations, and brightness adjustments, were applied to enhance model robustness. For each parameter setting of the GS (with a ranging from 0.25 to 1.75 and b from 0.00 to 1.75), as well as for the baseline YOLOv8 with the SiLU [9], we trained the model on the training set. The validation set was used during training for hyperparameter tuning and early stopping to select the best-performing model for each configuration. Finally, the test set was used to evaluate the generalization performance of each model.

3.2. Training and Evaluation

The model was trained for 150 epochs using a batch size of 32 and a learning rate of 0.001, with the AdamW optimizer for adaptive learning. Validation was conducted after each epoch using the validation set. Performance was evaluated using Precision, Recall, F1-Score, mean Average Precision (mAP) at thresholds of 0.50 (mAP50) and 0.50 to 0.95 (mAP50-95), for bounding box accuracy, as shown below,

$$Pn = \frac{TP}{TP + FP},\ Rl = \frac{TP}{TP + FN},\ Fe = 2 \times \frac{Pn \times Rl}{Pn + Rl},\ \text{and}\ mAP = \frac{1}{N}\sum_{i=1}^{N} AP_i, \tag{10}$$

where Pn is Precision, Rl is Recall, Fe is F1-Score, TP is True Positives, FP is False Positives, and FN is False Negatives. The mean Average Precision (mAP) was calculated as the mean of the Average Precision (AP) over different IoU thresholds. Where N is the number of IoU thresholds, and AP_i is the Average Precision at the i -th threshold.

4. Main Results and Discussion

Table 1 compares the performance of the SiLU activation function, the baseline in the YOLOv8, with various configurations of the GS function in terms of Precision (Pn), Recall (Rl), and F1-Score (Fe) across the Train, Validation, and Test datasets. While GS with a=1.00, b=1.00 represents the standard Sigmoid function. The SiLU is defined as $f(x) = x \cdot \sigma(x)$. The SiLU achieves a strong overall performance, with an F1-Score of 0.716, Precision of 0.775, and Recall of 0.665 on the Test set, providing a reliable baseline. In comparison, the GS function, when tuned with different parameters, yields varying results. Lower values, such as a=0.25, b=0.00, underperform with an F1-Score of 0.566. As aaa increases, performance improves, with a=1.50, b=0.00 achieving an F1-Score of 0.702. Further tuning to a=1.50, b=1.50 produces an F1-Score of 0.711, Precision of 0.773, and Recall of 0.658, while a=1.75, b=1.75 yields one of the highest F1-Scores at 0.707. These results indicate that with optimal tuning, GS can match or exceed SiLU's performance, though it is sensitive to parameter selection in drug detection and classification tasks.

Table 1. Comparison of SiLU and GS in YOLOv8 across Precision (Pn), Recall (Rl), and F1-Score (Fe) on Train, Validation, and Test datasets.

Activation Function	Train			Val			Test		
	Pn	Rl	Fe	Pn	Rl	Fe	Pn	Rl	Fe
SiLU	0.828	0.780	0.803	0.828	0.780	0.803	0.775	0.665	0.716
a=1.00,b=0.00	0.790	0.721	0.754	0.792	0.720	0.754	0.771	0.623	0.689
a=0.25,b=0.00	0.647	0.567	0.604	0.638	0.569	0.602	0.588	0.546	0.566
a=0.50,b=0.00	0.754	0.718	0.736	0.753	0.720	0.736	0.703	0.629	0.664
a=0.75,b=0.00	0.769	0.741	0.755	0.768	0.743	0.755	0.720	0.667	0.693
a=1.25,b=0.00	0.814	0.762	0.787	0.815	0.762	0.788	0.761	0.647	0.700
a=1.50,b=0.00	0.859	0.748	0.800	0.859	0.748	0.800	0.742	0.666	0.702
a=1.75,b=0.00	0.807	0.743	0.774	0.807	0.743	0.774	0.794	0.648	0.714
a=1.00,b=0.25	0.795	0.747	0.770	0.795	0.749	0.771	0.657	0.693	0.675
a=1.00,b=0.50	0.839	0.716	0.772	0.840	0.716	0.773	0.773	0.650	0.706
a=1.00,b=0.75	0.803	0.772	0.787	0.802	0.772	0.787	0.741	0.653	0.694
a=1.00,b=1.00	0.836	0.772	0.803	0.836	0.773	0.803	0.749	0.667	0.706
a=1.00,b=1.25	0.811	0.770	0.790	0.817	0.763	0.789	0.729	0.659	0.692
a=1.00,b=1.50	0.817	0.783	0.800	0.817	0.783	0.799	0.786	0.648	0.710
a=1.00,b=1.75	0.831	0.774	0.801	0.830	0.774	0.801	0.746	0.672	0.707
a=0.25,b=0.25	0.633	0.566	0.598	0.634	0.567	0.599	0.597	0.531	0.562
a=0.50,b=0.50	0.769	0.696	0.731	0.771	0.696	0.732	0.691	0.623	0.655
a=0.75,b=0.75	0.807	0.725	0.764	0.811	0.725	0.765	0.771	0.640	0.700
a=1.25,b=1.25	0.833	0.756	0.793	0.832	0.756	0.792	0.745	0.685	0.714
a=1.50,b=1.50	**0.848**	**0.776**	**0.810**	**0.847**	**0.774**	**0.809**	**0.773**	**0.658**	**0.711**
a=1.75,b=1.75	0.833	0.747	0.788	0.834	0.747	0.788	0.780	0.647	0.707

Figure 2 illustrates that GS with a=1.50 and b=1.50 shows notable performance compared to the standard sigmoid function (a=1.00 and b=0.00). While both activation functions converge in mean average precision (mAP) as the number of epochs increases, the GS with a=1.50 and b=1.50 exhibits a higher initial mAP and improved stability beyond 50 epochs. This highlights the influence of tuning parameters a and b on achieving better performance. Additionally, GS with a=0.25 and b=0.00 performs poorly, emphasizing the importance of parameter tuning. Although SiLU also performs well, the optimized GS surpasses it in stability and mAP, underscoring its potential for this application.

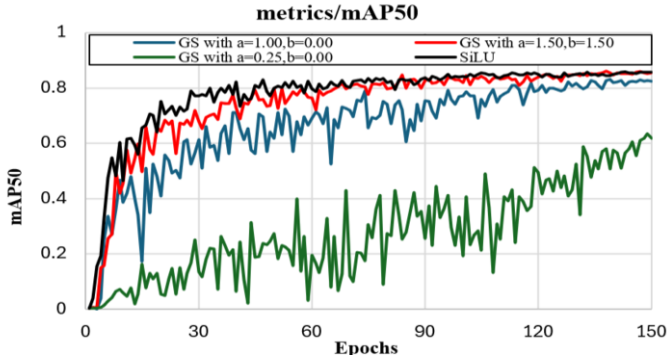

Figure 2. Performance of GS vs. SiLU: Optimized GS Outperforms Standard Sigmoid and SiLU in mAP50.

5. Conclusions

This study demonstrates the potential of the GS function as an adaptive activation strategy for drug detection and classification using YOLOv8. By carefully tuning the parameters a and *b*, we observed notable performance improvements over both the standard sigmoid and SiLU functions. The results suggest that GS, with optimized parameters such as a=1.50 and b=1.50, provides enhanced stability, higher mAP, and improved classification accuracy, particularly after 50 epochs. These findings underscore the value of exploring and fine-tuning activation functions in deep learning models to achieve better results in complex tasks like drug classification, ultimately contributing to safer healthcare practices. Future research could explore applying GS to other medical image detection tasks, testing it on larger datasets, or combining it with optimization techniques like swarm intelligence to enhance model performance further.

Acknowledgements

This work was supported by (i) Suranaree University of Technology (SUT, http://www.sut.ac.th), (ii) Thailand Science Research Innovation (TSRI, https://www.tsri.or.th), and (iii) National Science, Research and Innovation Fund (NSRF) (NRIIS number 195619). The grant recipient is S. Kaennakham who would like to express his sincere gratitude for their support.

References

[1] Morimoto T, Gandhi TK, Seger AC, Hsieh TC, Bates DW. Adverse drug events and medication errors: detection and classification methods. Quality and Safety in Health Care. 2004 May;13(4):306-14, doi: 10.1136/qshc.2004.010611

[2] Goedecke T, Ord K, Newbould V, Brosch S, Arlett P. Medication Errors: New EU Good Practice Guide on Risk Minimisation and Error Prevention. Drug Safety. 2016 Mar;39(6):491-500, doi: 10.1007/s40264-016-0410-4

[3] Li Y, Fan Q, Huang H, Han Z, Gu Q. A modified YOLOv8 detection network for UAV aerial image recognition. Drones. 2023 May;7(5):304, doi: 10.3390/drones7050304

[4] Kyurkchiev N, Markov S. Sigmoid functions: some approximation and modelling aspects. Saarbrucken: LAP LAMBERT Academic Publishing; 2015. 110 p.

[5] Narayan S. The generalized sigmoid activation function: Competitive supervised learning. Information sciences. 1997 Jun;99(1-2):69-82, doi: 10.1016/S0020-0255(96)00200-9

[6] Sohan M, SaiRam T, RamiReddy CV. A review on yolov8 and its advancements. International Conference on Data Intelligence and Cognitive Informatics; 2024 Jan. Singapore, Springer. p. 529-45, doi: 10.1007/978-981-99-7962-2_39

[7] Redmon J. You only look once: Unified, real-time object detection. Proceedings of the IEEE conference on computer vision and pattern recognition; 2016.

[8] Pills Detection Dataset. 2023. Available at:https://universe.roboflow.com/seblful/pills-detection-s9ywn/dataset/19. Accessed on September 28, 2024.

[9] Nwankpa C, Ijomah W, Gachagan A, Marshall S. Activation functions: Comparison of trends in practice and research for deep learning. arXiv preprint arXiv:1811.03378, 2018 Nov. doi: 10.48550/arXiv.1811.03378

Fuzzy Systems and Data Mining X
A.J. Tallón-Ballesteros (Ed.)

doi:10.3233/FAIA241430

Performance Assessment of Fourier Convolutional Neural Networks in Medical Image Analysis for Breast Cancer Diagnosis

Songkiat LOWMUNKHONG [a], Anan PANPHUECH [a], Patthra JANTHAWANNO [a], Ratapong ONJUN [a] and Sayan KAENNAKHAM [b,1]
[a] *Department of Interdisciplinary Science and Internationalization, Institute of Science, Suranaree University of Technology, Nakhon Ratchasima, 30000, Thailand*
[b] *School of Mathematics and Geoinformatics, Institute of Science, Suranaree University of Technology, Nakhon Ratchasima, 30000, Thailand*
ORCiD ID: Songkiat Lowmunkhong https://orcid.org/0009-0001-0280-3072
Anan Panphuech https://orcid.org/0009-0001-3296-1434
Patthra Janthawanno https://orcid.org/0009-0009-3289-0232
Ratapong Onjun https://orcid.org/0009-0001-9724-5762
Sayan Kaennakham https://orcid.org/0000-0001-9682-559X

Abstract. Breast cancer remains a major global health concern, and early diagnosis is crucial for improving patient outcomes. This study explores the performance of Fourier Convolutional Neural Networks (FCNNs) in comparison to traditional Convolutional Neural Networks (CNNs) like VGG16 for classifying breast cancer using ultrasound images. We evaluated the models on key performance metrics, including accuracy, precision, recall, and AUC-ROC, while also considering computational factors such as training time and memory consumption. Results show that VGG16 consistently delivers stable performance across different learning rates, while FCNN16 significantly outperforms VGG16 at a lower learning rate of 0.0001, achieving near-perfect classification metrics. These findings highlight the potential of FCNNs for breast cancer diagnosis, though further research is necessary to fully optimize this approach.

Keywords. Convolutional Neural Networks, Fourier Convolutional Neural Networks, Breast Cancer Diagnosis, Ultrasound Medical Image, Ultrasound Breast Images for Breast Cancer Datasets

1. Introduction

Breast cancer remains one of the most prevalent cancers worldwide, with early detection playing a critical role in improving survival rates and optimizing treatment outcomes [1]. Ultrasound imaging has emerged as a pivotal tool in breast cancer diagnosis, providing a non-invasive, accessible, and cost-effective method for detecting abnormal tissue

[1] Corresponding Author: Sayan Kaennakham, School of Mathematics and Geoinformatics, Institute of Science, Suranaree University of Technology, Nakhon Ratchasima, 30000, Thailand; Email: sayan_kk@g.sut.ac.th

structures [2]. In recent years, the use of machine learning techniques, particularly Convolutional Neural Networks (CNNs) [3], has revolutionized medical image analysis by automating feature extraction and enhancing diagnostic accuracy. However, while CNNs have shown substantial success in this domain [4, 5], there is growing interest in exploring more efficient and powerful network architectures that can further improve both the accuracy and computational efficiency of image-based diagnosis.

Fourier Convolutional Neural Networks (Fourier CNNs) offer an advancement over traditional CNNs by utilizing the Fourier Transform [6] to capture more complex patterns and structures in medical images, enhancing feature extraction. This approach addresses limitations of conventional convolutional operations and provides computational advantages by reducing model training and inference time and optimizing memory usage. As real-time diagnostic tools become increasingly critical in clinical settings, these improvements position Fourier CNNs as a strong alternative for large-scale medical image analysis tasks.

This study compares the performance of Fourier CNNs and traditional CNNs for classifying breast cancer as benign or malignant using ultrasound images from a Kaggle dataset. We evaluate key metrics, including accuracy, precision, recall, and AUC-ROC, while also analyzing training time and memory use. Statistical analysis via SPSS highlights the practical advantages of Fourier CNNs for potential clinical integration in breast cancer diagnosis.

2. Mathematical Background

2.1. Convolutional Neural Networks

Convolutional Neural Networks (CNNs) are specialized neural networks for analyzing image data, using convolutional layers to apply filters and extract features. This allows CNNs to capture patterns effectively for tasks like image classification and object detection. The filters slide across input data, creating feature maps, with weights learned during training to automatically identify relevant features.

Mathematically, the convolution operation can be expressed as Eq. (1)

$$Z_{k_1,k_2} = \sum_{l_1=-m_x/2}^{m_x/2} \sum_{l_2=-n_x/2}^{n_x/2} K_{l_1,l_2} \odot u_{k_1-l_1,k_2-l_2}, \tag{1}$$

where Z_{k_1,k_2} represents the output feature map, K_{l_1,l_2} is the convolutional filter, and u_{k_1,k_2} is the input matrix. The symbol $\odot$ denotes element-wise multiplication. The summation across indices l_1 and l_2 accounts for the size of the filter as it moves across the input. Through this process, the network learns to detect important features, leading to effective feature extraction.

2.2. The VGG16

VGG16 (Very Deep Convolutional Networks for Large-Scale Image Recognition, [7]) is a convolutional neural network with 16 layers that have weights. It comprises 13 convolutional layers, 5 max pooling layers, and 3 dense layers. VGG16 processes input images of size 224x224 with 3 color channels (RGB). The first convolutional layer

(conv-1) has 64 filters, followed by 128 in conv-2, 256 in conv-3, and 512 in conv-4 and conv-5. After the convolutional layers, there are three fully connected layers, followed by a final classification layer. A classification layer then processes the output to determine the final class probabilities.

2.3. The Fourier Transformation

Fourier analysis is a mathematical technique used to decompose signals into simpler components known as sinusoids. The Discrete Fourier Transform (DFT) is specifically designed for processing digital signals, utilizing real numbers for both the input and output. The DFT is central to Fourier decomposition, which transforms a signal from the time (or spatial) domain into the frequency domain, providing a frequency representation of the original signal. The DFT is mathematically represented as Eq. (2)

$$X[k] = \sum_{n=0}^{N-1} x[n] e^{-j2\pi nk/N} \tag{2}$$

where $x[n]$ is the input signal, $X[k]$ is the transformed signal in the frequency domain, and N is the total number of points in the signal. The inverse Discrete Fourier Transform (IDFT) allows for the reconstruction of the original signal from its frequency components. The formula for the inverse DFT is given by Eq. (3)

$$x[n] = \frac{1}{N} \sum_{k=0}^{N-1} X[k] e^{j2\pi nk/N} \tag{3}$$

where $X[k]$ represents the frequency domain signal, and $x[n]$ is the recovered signal in the time domain.

2.4. The Fourier Convolutional Neural Networks (FCNN)

This project aims to enhance convolution efficiency using Fourier convolution, which leverages the Fast Fourier Transform (FFT) based on the Discrete Fourier Transform (DFT). By applying FFT to sequences, multiplying elements, and using the inverse FFT, this method achieves results similar to traditional convolution, as shown in Figure 1. Additionally, frequency domain manipulations improve feature extraction in ultrasound images by capturing distinct frequency characteristics and reducing noise, unlike spatial domain methods [8].

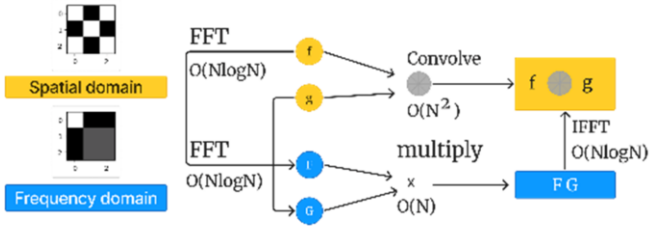

Figure 1. The process of Fourier Convolution using the Fast Fourier Transform (FFT).

3. Experimental Setups

3.1. Dataset Description

This study utilized an ultrasound breast cancer dataset from Kaggle, created by Vuppala Adithya Sairam of Rajalakshmi Engineering College, Chennai, India. The dataset contains both benign and malignant images, depicted as Figure 2, with a resolution of 224 x 224 pixels in RGB format. Only one channel was used for analysis as all channels contained identical values. Data augmentation, including rotation and sharpening, was applied to increase sample size.

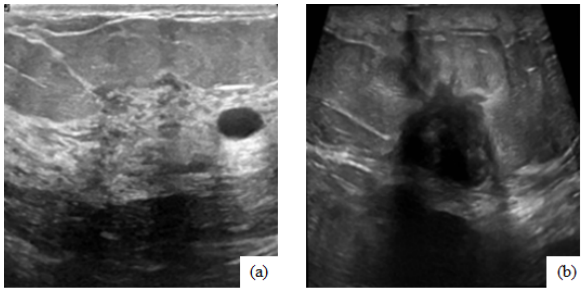

Figure 2. Samples of ultrasound breast cancer images (a) Benign. (b) Malignant.

The dataset was divided into three parts: 80% for training (7,305 images), 10% for validation (811 images), and 10% for testing (900 images). 5-fold cross-validation was used to ensure robust training and validation.

3.2. Model Architectures

The proposed system utilizes a Fourier Convolutional Neural Network (FCNN) to classify breast cancer ultrasound images. We modified the Conv1-1 layer of the VGG16 architecture. To perform FCNN, the input images are pre-processed to 1 channel, and a random kernel $F(k) \in \mathbb{C}^{\mathrm{M}\times\mathrm{N}}$ of the same size is prepared for the Fourier Transform. The input image $x \in \mathbb{C}^{height\times width}$ and kernel $k \in \Re^{k\times l}$ are zero-padded at the right and bottom and then transformed using FFT. After applying the Fourier Transform to both $F(x)$ and the random kernel K, both must be complex-valued. For a random kernel, real and imaginary components are initialized from a Gaussian distribution. The pointwise multiplication of complex numbers follows the rectangular form. If $\mathcal{F}(x) = A + Bi$ and $K = C + Di$, their product is defined as Eq. (4)

$$\mathcal{F}(x) \times K = (AC - BD) + (AD + BC)i\,, \tag{4}$$

where the corresponding diagram is illustrated as Figure 3.

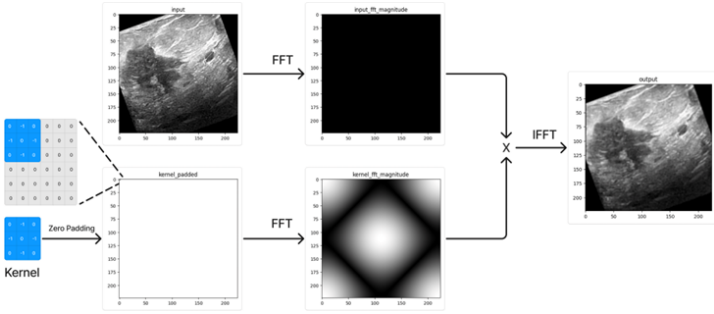

Figure 3. The FCNN Flow Diagram

3.3. Model Training and Evaluation

To evaluate the performance of VGG16 and FCNN models, a hyperparameter search was conducted, testing various learning rates (0.001, 0.0001), batch sizes (16, 32), and 10 epochs using 5-fold cross-validation. Both models were optimized with AdamW and assessed using accuracy, precision, recall, and F1-score to address class imbalances. The confusion matrix, ROC curve, AUC, and precision-recall curve further evaluated model discrimination, especially in imbalanced datasets. Python and Google Colab with A100 GPUs were utilized to streamline the workflow and enhance processing efficiency.

4. Main Results and Discussion

As shown in Table 1, VGG16 performs consistently across learning rates and classes, with AUC values of 0.94-0.95 and F1-scores of 0.84-0.88, indicating reliable classification. In contrast, FCNN16 struggles at a 0.001 learning rate, particularly for malignant cases, with a F1-score of 0. However, at a 0.0001 learning rate, FCNN16 improves significantly, achieving near-perfect AUC and F1-scores close to 1.0, showing greater sensitivity to learning rate adjustments than VGG16.

Table 1. Comparison of Performance Metrics for VGG16 and FCNN16 Models at Different Learning Rates with 10 epochs and a Batch Size of 16

Model	Learning Rate	AUC	Precision-Recall	Accuracy	Precision	Recall	F1-score	Class
VGG16	0.001	0.95	0.96	0.87	0.87	0.89	0.88	benign
VGG16	0.001	0.95	0.93	0.87	0.86	0.84	0.85	malignant
VGG16	0.0001	0.94	0.96	0.86	0.87	0.88	0.88	benign
VGG16	0.0001	0.94	0.91	0.86	0.85	0.84	0.84	malignant
FCNN16	0.001	0.5	0.56	0.56	0.56	1	0.71	benign
FCNN16	0.001	0.5	0.44	0.56	0	0	0	malignant
FCNN16	0.0001	0.99	0.99	0.95	0.96	0.95	0.95	benign
FCNN16	0.0001	0.99	0.98	0.95	0.93	0.95	0.94	malignant

In Table 2, VGG16 maintains consistent performance with a batch size increase, achieving stable AUC values of 0.95 and F1-scores between 0.86 and 0.89 across benign and malignant classifications, regardless of the learning rate. In contrast, FCNN16 shows

poor results at a 0.001 learning rate, particularly for malignant cases with an F1-score of 0. However, reducing the learning rate to 0.0001 allows FCNN16 to achieve perfect scores (AUC, precision, recall, and F1-score of 1.0), outperforming VGG16. This highlights FCNN16's sensitivity to learning rate adjustments and demonstrates that a lower rate can mitigate noise and avoid local minima during frequency domain transformations of ultrasound images.

Table 2. Comparison of Performance Metrics for VGG16 and FCNN16 Models at Different Learning Rates with 10 epochs and a Batch Size of 32

Model	Learning Rate	AUC	Precision-Recall	Accuracy	Precision	Recall	F1-score	Class
VGG16	0.001	0.95	0.96	0.88	0.88	0.9	0.89	benign
VGG16	0.0001	0.95	0.92	0.88	0.86	0.87	0.86	malignant
FCNN16	0.001	0.5	0.56	0.56	0.56	1	0.71	benign
FCNN16	0.0001	1	1	0.99	0.99	1	0.99	malignant

Figure 4 shows that both VGG16 and FCNN16 models demonstrate strong performance, with minimal signs of overfitting and close alignment between training and validation losses. VGG16 steadily improves, achieving 98-99% training accuracy and 97% validation accuracy, indicating robust generalization. FCNN16, on the other hand, converges rapidly within the first 20 epochs, reaching near-perfect accuracy (99-100%) for both training and validation. Overall, both models exhibit efficient learning, with FCNN16 showing slightly faster convergence and higher accuracy.

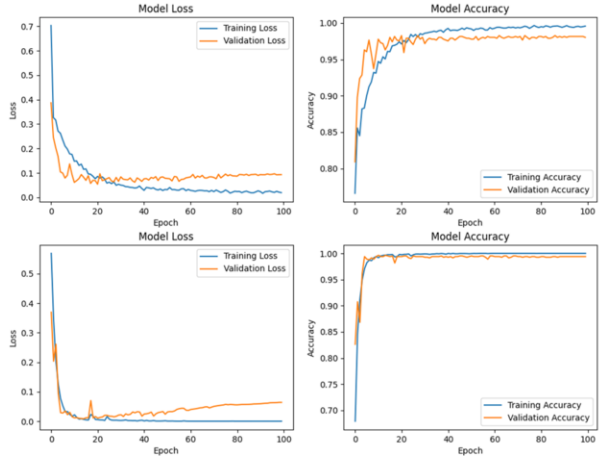

Figure 4. Training and validation curves for VGG16 (top) and FCNN16 (bottom).

5. Conclusions

The results of this study highlight the potential of Fourier Convolutional Neural Networks (FCNNs) for breast cancer diagnosis using ultrasound images. While VGG16 consistently provided stable performance across different learning rates, FCNN16 demonstrated superior capabilities when optimized with a lower learning rate of 0.0001, achieving near-perfect classification metrics. This study suggests that, with proper

hyperparameter tuning, FCNNs can outperform traditional CNNs, such as VGG16, in terms of accuracy and computational efficiency. Future research should focus on further refining FCNNs to fully realize their potential in medical image analysis.

Acknowledgements

This work was supported by (i) Suranaree University of Technology (SUT, http://www.sut.ac.th), (ii) Thailand Science Research Innovation (TSRI, https://www.tsri.or.th), and (iii) National Science, Research and Innovation Fund (NSRF) (NRIIS number 195613). The grant recipient is S. Kaennakham who would like to express his sincere gratitude for their support.

References

[1] Sohan M, SaiRam T, RamiReddy CV. A review on yolov8 and its advancements. International Conference on Data Intelligence and Cognitive Informatics; 2024 Jan 7; Springer, Singapore. p. 529-45, doi: 10.1007/978-981-99-7962-2_39

[2] Sushanki S, Bhandari AK, Singh A. A review on computational methods for breast cancer detection in ultrasound images using multi-image modalities. Archives of Computational Methods in Engineering. 2024 Nov;31(8):1277-96, doi: 10.1007/s11831-023-10015-0

[3] Krichen M. Convolutional neural networks: A survey. Computers. 2023 Jul;12(8):151, doi: 10.3390/computers12080151

[4] Khan MH, Jahangeer NB, Dullull W, Nathire S, Gao X, Sinha GR, Nagwanshi KK. Multi-class classification of breast cancer abnormalities using Deep Convolutional Neural Network (CNN). Plos one. 2021 Aug;16(8):e0256500, doi: 10.1371/journal.pone.0256500

[5] Onjun R, Dungkratoke N, Sriwichai K, Kaennakham S. Wavelet Pooling in Convolutional Neural Networks for Breast Cancer Detection with Ultrasound Images. International Conference on Computational & Experimental Engineering and Sciences; 2023 May 5; Springer International Publishing; p. 709-19, doi: 10.1007/978-3-031-42515-8_49

[6] Duoandikoetxea J. Fourier analysis. Bilbao: American Mathematical Society; 2024. 222 p.

[7] Albashish D, Al-Sayyed R, Abdullah A, Ryalat MH, Almansour NA. Deep CNN model based on VGG16 for breast cancer classification. 2021 International conference on information technology (ICIT); 2021 Jul 14-15; Amman, Jordan. IEEE. p. 805-10, doi: 10.1109/ICIT52682.2021.9491631

[8] Ritesh M, Ambica P, Gopalakrishnan T, Priya S, Geet S, Mohan K. FourierCNN: Skin cancer Classification using Convolution Neural Network Fortified with Fast Fourier Transform. 2024 IEEE International Conference on Interdisciplinary Approaches in Technology and Management for Social Innovation (IATMSI); Gwalior, India, 2024, pp. 1-4, doi: 10.1109/IATMSI60426.2024.10502458

Fuzzy Systems and Data Mining X
A.J. Tallón-Ballesteros (Ed.)

doi:10.3233/FAIA241431

Investigating the Performance of LSTM Models Optimized by Firefly Algorithms on Diverse Time-Series Data

Krankamon PHUKHRONGHIN [a], Narongdech DUNGKRATOKE [b], Papon TANTIWANICHANON [b], and Sayan KAENNAKHAM [c,1]

[a] *Faculty of Engineering and Technology, Rajamangala University of Technology Isan, 744 Suranarai Road, Muang Disrtict, Nakhon Ratchasima, 30000, Thailand;*
[b] *Department of Interdisciplinary Science and Internationalization, Institute of Science, Suranaree University of Technology, Nakhon Ratchasima, 30000, Thailand;*
[c] *School of Mathematics and Geoinformatics, Institute of Science, Suranaree University of Technology, Nakhon Ratchasima, 30000, Thailand;*
ORCiD ID: Krankamon Phukhronghin https://orcid.org/0009-0005-5526-8439, Narongdech Dungkratoke https://orcid.org/0009-0006-7097-9666, Papon Tantiwanichanon https://orcid.org/0009-0008-4336-8901, Sayan Kaennakham https://orcid.org/0000-0001-9682-559X

Abstract. This study investigates the performance of Long Short-Term Memory (LSTM) models optimized by three variants of the Firefly Algorithm (FA) for time-series forecasting across diverse datasets. The datasets include a multi-seasonal series, a non-stationary series, and a series with spikes and drops, each posing unique challenges for prediction. The optimization was conducted using the Traditional Firefly Algorithm (FA), Distance-Based Firefly Algorithm (DFA), and Logarithmic Weighted Firefly Algorithm (LWFA). Results show that DFA achieved the highest Nash-Sutcliffe Efficiency (NSE), reaching 0.9917 for non-stationary data and 0.9865 for data with spikes and drops, outperforming FA and LWFA. These findings highlight the effectiveness of swarm-based optimization in improving the accuracy of LSTM models, especially in handling complex time-series patterns.

Keywords. Time-series forecasting, LSTM Parameter Optimization, Firefly Optimization Algorithm (FA), Optimization for Variable Time-Series Data

1. Introduction

Time-series forecasting plays a crucial role across a wide array of industries, from finance and energy to healthcare and supply chain management, where accurate predictions can significantly influence decision-making processes [1]. Recurrent Neural Networks (RNNs), particularly Long Short-Term Memory (LSTM) models, have emerged as a powerful tool for tackling sequential data challenges [2]. LSTMs are designed to handle the complexities of time-dependent data, such as long-term dependencies and nonlinearities, by effectively controlling the flow of information

[1] Corresponding Author: Sayan Kaennakham, sayan_kk@g.sut.ac.th.

through their gates. However, despite their advantages, tuning the parameters of LSTM models, such as time steps, batch size, and the number of hidden units, remains a challenge, as it can significantly impact the model's predictive performance [3, 4].

Recent advancements in swarm intelligence-based optimization algorithms, such as the Firefly Algorithm (FA) and its variants [5], have shown promise in optimizing the hyperparameters of LSTM models to improve forecasting accuracy. Traditional Firefly Algorithm (FA), Distance-Based Firefly Algorithm (DFA), and Logarithmic Weighted Firefly Algorithm (LWFA) offer different strategies to enhance the exploration and exploitation of parameter spaces [6]. These methods adapt to the challenges of different types of time-series data, including multi-seasonal patterns, non-stationary sequences, and time series with abrupt spikes and drops [7]. This study aims to investigate the effectiveness of these FA variants in optimizing LSTM models for three distinct types of time-series data, each posing unique forecasting challenges [8].

The datasets used in this study reflect common complexities in real-world time-series data: Dataset-1 is a multi-seasonal series with recurring patterns, Dataset-2 is a non-stationary series with changing statistical properties, and Dataset-3 is characterized by sudden spikes and drops. By applying FA variants to LSTM models across these datasets, this research seeks to highlight the advantages and limitations of each optimization algorithm, providing insights into how swarm-based optimization can improve time-series forecasting performance in diverse scenarios.

2. Methodology

2.1. Long-Short-Term Memory Neural Network

Long Short-Term Memory (LSTM) [9] is a recurrent neural network (RNN) designed to model sequential data while avoiding the vanishing gradient problem. Each LSTM unit has a cell state C_t and uses three gates: f_t, input gate i_t, and output gate o_t, to control information flow. The forget gate determines how much of the previous cell state C_{t-1} to keep, defined as follows

$$f_t = \sigma\left(W_f \cdot \left[h_{t-1}, x_t\right] + b_f\right), \tag{1}$$

The input gate determines what new information to store in the cell state, defined as follows

$$i_t = \sigma\left(W_i \cdot \left[h_{t-1}, x_t\right] + b_i\right). \tag{2}$$

The new candidate values $\tilde{C}_t$ for the cell state are computed using the hyperbolic tangent function

$$\tilde{C}_t = \tanh\left(W_C \cdot \left[h_{t-1}, x_t\right] + b_C\right) \tag{3}$$

Finally, the cell state is updated

$$C_t = f_t * C_{t-1} + i_t * \tilde{C}_t \tag{4}$$

The output gate o_t determines the next hidden state h_t, which influences the output

$$h_t = o_t * \tanh\left(C_t\right) \tag{5}$$

These mechanisms allow LSTM to control the flow of information effectively over long time periods, making it suitable for time-series tasks.

2.2. The Firefly Algorithm (FA)

2.2.1 Traditional Firefly Algorithm (FA)

In FA, [10], the brightness I_i of firefly i at a particular location $\mathbf{x}_i$ is determined by the value of the objective function $f\left(\mathbf{x}_i\right)$, i.e., $I_i \propto f\left(\mathbf{x}_i\right)$. For maximization problems, brightness is directly proportional to $f\left(\mathbf{x}_i\right)$. The attractiveness β of a firefly is a function of the distance r_{ij} between two fireflies i and j, given by

$$\beta(r_{ij}) = \beta_0 e^{-\gamma r_{ij}^2} \tag{6}$$

where β_0 is the attractiveness at $r = 0$ and γ is the light absorption coefficient, which controls how the attractiveness decreases with distance. The distance r_{ij} between two fireflies i and j located at $\mathbf{x}_i$ and $\mathbf{x}_j$, respectively, is typically calculated using the Euclidean distance. A firefly i will move towards another more attractive (brighter) firefly j according to the following equation

$$\mathbf{x}_i^{t+1} = \mathbf{x}_i^t + \beta(r_{ij})(\mathbf{x}_j^t - \mathbf{x}_i^t) + \alpha(\mathbf{rand} - 0.5) \tag{7}$$

where α is a randomization parameter, and **rand** is a random number generated uniformly from $\left[0,1\right]$.

2.2.2 Distance-Base Firefly Algorithm (DFA)

The distance-based adaptive strategy aims to improve the Firefly Algorithm (FA) by dynamically adjusting the light absorption coefficient based on distances between fireflies. A static coefficient can cause issues: either fireflies become too visible to each other (when γ approaches 0), or they move randomly without direction (when γ is too high). To overcome this, the following mean distance calculation is introduced for each firefly

$$dis_i = \frac{1}{N-1} \sum_{j=1, j\neq i}^{N} \sqrt{\sum_{k=1}^{D} \left(x_{i,k} - x_{j,k}\right)^2} \tag{8}$$

where N is the total number of fireflies, and D is the problem's dimensionality. Using this, the distance ratio (Dr) is defined as $Dr = \left(dis_{opt} - dis_{\min}\right) \Big/ \left(dis_{\max} - dis_{\min}\right)$. Here, dis_{opt} is the distance to the global best firefly, while $dis_{\max}$ and $dis_{\min}$ represent the maximum and minimum distances among fireflies. The adaptive absorption coefficient (A_c) is then formulated as $A_c = \frac{1}{1+\sigma e^{-\rho \cdot Dr}}$, where σ controls the scale of A_c and ρ determines its sensitivity to changes in Dr. This adaptive coefficient allows the fireflies to balance exploration and exploitation during the search. By replacing the constant absorption coefficient with A_c, the new attractiveness is defined as $\tau = Dr \cdot e^{-A_c r^2}$. This adaptive strategy enables the fireflies to adjust their trajectories based on distance information, improving the search efficiency across diverse problem landscapes.

2.2.3 Logarithmic Weighted Firefly Algorithm (LWFA)

The Logarithmic Weighted Firefly Algorithm (*LWFA*) enhances the standard *FA* by introducing a minimum attraction (β_{ij}) to avoid near-zero attraction between distant fireflies. The adjusted attraction formula is expressed as follows

$$. \beta_{ij}\left(r_{ij}\right) = \beta_{\min} + \left(\beta_0 - \beta_{\min}\right) e^{-\gamma r_{ij}^2} . \tag{9}$$

LWFA also incorporates a self-adaptive inertia weight $w(t)$ for balancing exploration and exploitation, defined $w(t) = w_1 - \beta\left(w_1 - w_2\right)\log\left(T/t\right)$, where w_1 and w_2 are the initial and final weights, and T is the maximum number of iterations. Additionally, the dynamic step size c is given by $c = \theta^D \times T \times e^{-\frac{t}{T}}$. These updates ensure better exploration early on and more precise adjustments later in the search, making *LWFA* more effective for high-dimensional optimization.

3. Experimental Setup

3.1. The Datasets

The datasets include three distinct time series, each posing unique challenges for LSTM models. Dataset-1 is a multi-seasonal time series with repeating patterns, requiring the model to capture long-term dependencies. Dataset-2 is non-stationary, with changing statistical properties, making consistent predictions difficult. Dataset-3 features spikes and drops, with sudden fluctuations that are hard to predict. These characteristics make the datasets ideal for testing LSTM optimization algorithms' robustness.

3.2. LSTM Configuration and Firefly Algorithm Settings

The LSTM models in this study were optimized using a population of 10 fireflies over 20 generations, with key parameters such as time steps, batch size, and the number of LSTM cells being adjusted. The attractiveness coefficient β_0 was set to 1, and the light absorption coefficient γ was fixed at 1. The randomization factor α, initialized at 0.5,

decreased over generations to allow more precise search refinement. The Logarithmic Weighted Firefly Algorithm (LWFA) introduced a Levy flight parameter λ=1.5, enabling enhanced exploration by allowing random steps based on the Levy distribution. The models' performance was evaluated using the Nash-Sutcliffe Efficiency (NSE), a measure of prediction accuracy where values close to 1 indicate strong performance. The FA variants, including Traditional FA, Distance-Based FA, and LWFA, were used to optimize the LSTM hyperparameters, with the goal of maximizing NSE and improving model performance across three distinct time-series datasets.

4. Main Results and General Discussions

Table 1 compares the performance of LSTM models optimized by the Traditional Firefly Algorithm (FA), Distance-Based Firefly Algorithm (DFA), and Logarithmic Weighted Firefly Algorithm (LWFA) across three distinct datasets: a multi-seasonal time series with a single feature (Dataset 1), a non-stationary time series (Dataset 2), and a time series with spikes and drops (Dataset 3). The baseline LSTM model, using fixed parameters (24 time steps, 32 batch size, and 50 cells), performs modestly across these datasets, achieving NSE scores of 0.5696, 0.9713, and 0.9180 for Datasets 1, 2, and 3, respectively. When optimized using the FA, the performance improves, with NSE scores rising to 0.7980 for Dataset 1, 0.9865 for Dataset 2, and 0.9845 for Dataset 3, indicating that the FA adjusts parameters effectively for different time series characteristics.

The DFA, however, shows the best performance overall, particularly for the complex datasets. It achieves NSE scores of 0.8497 for Dataset 1, 0.9917 for Dataset 2, and 0.9865 for Dataset 3, indicating its superior ability to handle both non-stationary data and time series with spikes and drops. By optimizing time steps, batch size, and cell count, DFA consistently outperforms both FA and LWFA, especially in Dataset 1, where it selects 4 time steps and 256 cells to handle the multi-seasonal nature. While LWFA also improves over the baseline, with NSE scores of 0.7826 for Dataset 1 and 0.9864 for Dataset 2, it tends to perform slightly below DFA, particularly in datasets with abrupt changes like Dataset 3, where it scores 0.9822. Thus, DFA proves to be the most versatile and robust algorithm across the varying characteristics of the three datasets.

Table 1. Comparison of LSTM Models Optimized by FA, DFA, and LWFA with NSE Scores Across Three Datasets (Time Steps define the past data used, Batch Size is the number of sequences processed at once, and Num Cells are the LSTM units that determine learning capacity).

Dataset	Prediction Model	Parameters			NSE
		Time Steps	Batch Size	Num Cells	
1	*LSTM*	24.0000	32.0000	50.0000	0.5696
	LSTM with *FA*	4.1012	52.7725	138.3546	0.7980
	LSTM with *DFA*	4.0000	25.6677	256.0000	0.8497
	LSTM with *LWFA*	6.1123	59.7953	190.3343	0.7826
2	*LSTM*	24.0000	32.0000	50.0000	0.9713
	LSTM with *FA*	28.6919	46.3929	112.7169	0.9865
	LSTM with *DFA*	4.1904	60.4139	187.7732	0.9917
	LSTM with *LWFA*	18.0415	29.7117	41.1821	0.9864
3	*LSTM*	24.0000	32.0000	50.0000	0.9180
	LSTM with *FA*	20.2256	27.7986	52.8772	0.9845
	LSTM with *DFA*	4.5301	24.4437	223.6061	0.9865
	LSTM with *LWFA*	14.2770	43.3155	133.9430	0.9822

The convergence behavior across the three datasets, as depicted in Figure 1, shows that while the Traditional Firefly Algorithm (FA) and Logarithmic Weighted Firefly Algorithm (LWFA) tend to converge faster, the Distance-Based Firefly Algorithm (DFA) consistently provides more gradual and stable improvements in performance. In Dataset-1 (multi-seasonal time series), DFA steadily optimizes the LSTM model, whereas FA and LWFA converge quickly but plateau early. A similar pattern is observed in Dataset-2 (non-stationary time series), where DFA's gradual increase leads to slightly higher final NSE values compared to FA and LWFA, which reach near-optimal solutions faster. In Dataset-3 (spikes and drops time series), DFA once again shows more consistent improvement, outperforming FA and LWFA in final performance. Overall, DFA proves more effective in handling complex datasets, while FA and LWFA offer faster but less fine-tuned convergence.

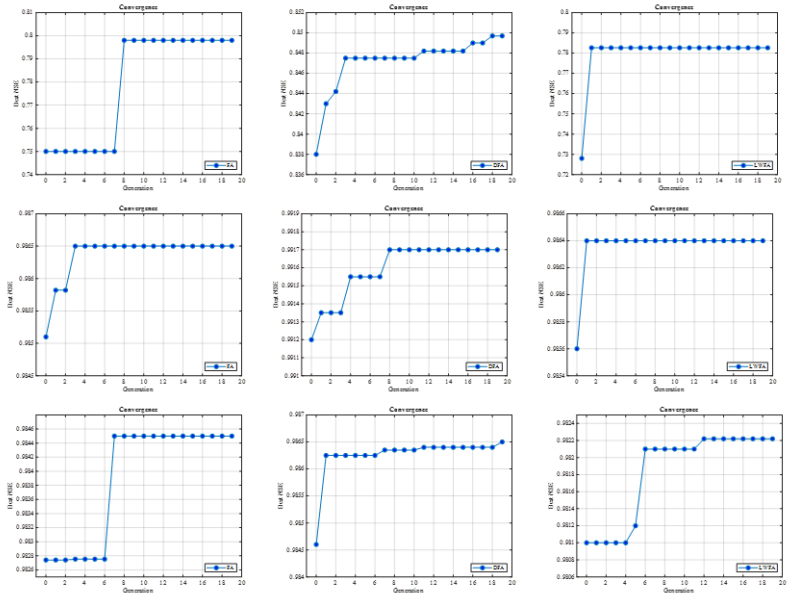

Figure 1. Convergence Behavior of LSTM Models Optimized by FA, DFA, and LWFA: Top Row (Dataset-1), Middle Row (Dataset-2), Bottom Row (Dataset-3).

5. Conclusion

This study demonstrates the effectiveness of Firefly Algorithm variants in optimizing LSTM models for time-series forecasting across diverse datasets. The Distance-Based Firefly Algorithm (DFA) consistently outperformed the Traditional Firefly Algorithm (FA) and Logarithmic Weighted Firefly Algorithm (LWFA), achieving the highest Nash-Sutcliffe Efficiency (NSE) scores, particularly on Dataset-2 (non-stationary time series) with an NSE of 0.9917 and Dataset-3 (spikes and drops time series) with 0.9865. The baseline LSTM model, without optimization, showed moderate performance, with NSE values of 0.5696 for Dataset-1, 0.9713 for Dataset-2, and 0.9180 for Dataset-3. Optimizing the LSTM models using FA variants significantly improved performance across all datasets, with DFA providing the most consistent and stable improvements.

These findings underscore the value of using swarm-based optimization for fine-tuning LSTM parameters, particularly for complex, dynamic time-series data.

Optimized LSTM models using FA variants hold great potential for breast cancer detection and monitoring by analyzing non-stationary patient data patterns, predicting disease progression, and tracking treatment responses. This approach can lead to earlier detection and more timely interventions. The models' effectiveness extends to other areas such as financial market predictions, energy consumption, and industrial anomaly detection [11]. Future research could combine FA with other optimization methods to further enhance LSTM performance across diverse time-series datasets [12]. Applying this technique to real-time patient data could foster adaptive models, improving responsiveness and predictive accuracy in breast cancer care.

Acknowledgments

This work was supported by (i) Suranaree University of Technology (SUT, http://www.sut.ac.th), (ii) Thailand Science Research Innovation (TSRI, https://www.tsri.or.th), and (iii) National Science, Research and Innovation Fund (NSRF) (NRIIS number 195613). The grant recipient is S. Kaennakham who would like to express his sincere gratitude for their support.

References

[1] Torres JF, Hadjout D, Sebaa A, Martínez-Álvarez F, Troncoso A. Deep learning for time series forecasting: a survey. Big Data. 2021 Feb 1;9(1):3-21.
[2] Van Houdt G, Mosquera C, Nápoles G. A review on the long short-term memory model. Artificial Intelligence Review. 2020 Dec;53(8):5929-55.
[3] Zhang N, Shen SL, Zhou A, Jin YF. Application of LSTM approach for modelling stress–strain behaviour of soil. Applied Soft Computing. 2021 Mar 1;100:106959.
[4] Xu Y, Hu C, Wu Q, Jian S, Li Z, Chen Y, Zhang G, Zhang Z, Wang S. Research on particle swarm optimization in LSTM neural networks for rainfall-runoff simulation. Journal of hydrology. 2022 May 1;608:127553.
[5] Kumar V, Kumar D. A systematic review on firefly algorithm: past, present, and future. Archives of Computational Methods in Engineering. 2021 Jun;28:3269-91.
[6] Ariyaratne MK, Fernando TG. A comprehensive review of the firefly algorithms for data clustering. Advances in Swarm Intelligence: Variations and Adaptations for Optimization Problems. 2022 Oct 2:217-39.
[7] Williams AT, Sperl RE, Chung SM. Anomaly Detection in Multi-Seasonal Time Series Data. IEEE Access. 2023 Sep 20.
[8] Abbasimehr H, Shabani M, Yousefi M. An optimized model using LSTM network for demand forecasting. Computers & industrial engineering. 2020 May 1;143:106435.
[9] Sundermeyer M, Schlüter R, Ney H. Lstm neural networks for language modeling. InInterspeech 2012 Sep 9 (Vol. 2012, pp. 194-197).
[10] Fister I, Fister Jr I, Yang XS, Brest J. A comprehensive review of firefly algorithms. Swarm and evolutionary computation. 2013 Dec 1;13:34-46.
[11] Okwu MO, Tartibu LK. Firefly Algorithm. In: Metaheuristic Optimization: Nature-Inspired Algorithms Swarm and Computational Intelligence, Theory and Applications. Springer; 2020. p. 61-69.
[12] Gangula R, Vutukuru MM, Kumar MR. Intrusion Attack Detection Using Firefly Optimization Algorithm and Ensemble Classification Model. Wireless Personal Communications. 2023;132:1899-916.

Fuzzy Systems and Data Mining X
A.J. Tallón-Ballesteros (Ed.)

doi:10.3233/FAIA241432

Comparative Analysis of Radial Basis Functions and Cubic Splines for Data Imputation

Wisut KITCHAINUKOON [a], Amornrat SANGSUWAN[b], Pornthip PONGCHALEE [c], and Krittidej CHANTHAWARA [d,1]

[a] *Department of Mathematics, Faculty of Science and Technology, Loei Rajabhat University, Loei, 42000, Thailand*

[b] *Department of Mathematics, Faculty of Education, Loei Rajabhat University, Loei, 42000, Thailand;*

[c] *Department of Applied Mathematics and Statistics, Faculty of Science and Liberal Arts, Rajamangala University of Technology Isan, Nakhon Ratchasima, 30000, Thailand;*

[d] *Program of Mathematics, Faculty of Science, Ubon Ratchathani Rajabhat University, Ubon Ratchathani, 34000, Thailand*

Abstract. This study evaluates the effectiveness of Radial Basis Function (RBF) approaches, specifically Gaussian and Multiquadric RBFs, compared to Cubic and Adaptive Splines for data imputation in time-series datasets. Three datasets—multi-seasonal, non-stationary, and spikes and drops—were used, with varying data corruption levels to simulate real-world scenarios. Imputation performance was assessed using Root Mean Square Error (RMSE). The results indicate that spline-based methods, particularly Cubic and Adaptive Splines, consistently deliver lower RMSE values, showcasing superior robustness to data variability and high corruption levels compared to RBF methods. This comparative analysis offers insights into selecting appropriate techniques for effective data imputation in time-series analysis.

Keywords. Data Imputation, Radial Basis Function, Cubic Splines, Interpolation Techniques, Imputation Accuracy, Missing Values

1. Introduction

Data imputation has become a vital component in data preprocessing, especially in fields where missing values can severely impact the integrity of analytical results. In areas like time-series analysis, healthcare [1], finance [2], and scientific research, incomplete datasets are common, and if left untreated, can skew conclusions or even render the analysis meaningless [3]. The imputation of missing data is not merely about filling in gaps but ensuring that the imputed values reflect the underlying patterns and trends in the data as accurately as possible. This requires advanced techniques that can offer both

[1] Corresponding Author: Krittidej CHANTHAWARA, Program of Mathematics, Faculty of Science, Ubon Ratchathani Rajabhat University, Ubon Ratchathani, 34000, Thailand; Email: krittidej.c@ubru.ac.th

precision and adaptability to various data types and structures. Interpolation is suitable for imputation in time series data as it leverages the continuity and sequential patterns, providing accurate estimates for missing values in short gaps. Two prominent interpolation techniques, Radial Basis Functions (RBFs) [4] and cubic splines [5], are widely recognized for their ability to handle missing data by generating smooth, continuous approximations. Each method is rooted in distinct mathematical principles, making it essential to examine their respective advantages and limitations in different imputation contexts[6, 7].

Radial Basis Functions, particularly in their multiquadric form, offer a flexible global interpolation approach that is highly effective in handling high-dimensional, scattered data. The multiquadric RBF generates smooth approximants by calculating distances between data points, allowing for the capture of complex, nonlinear relationships that may exist in the data [8]. This characteristic makes RBFs particularly valuable in applications where the data points are irregularly spaced or come from multidimensional sources [9]. Conversely, cubic splines operate on a different premise, relying on piecewise cubic polynomials to interpolate between points. These splines ensure smooth transitions between intervals with continuous first and second derivatives, making them highly suitable for structured, lower-dimensional datasets where a more localized approach to imputation is beneficial. By focusing on these distinct approaches, this study seeks to offer a nuanced understanding of how RBFs and cubic splines perform in different data environments, particularly when applied to time-series datasets with various characteristics [10].

In this research, we investigate six imputation strategies, including Gaussian RBFs (with two values of sigma), two forms of multiquadric RBF, and two variations of cubic splines, to assess their performance across diverse time-series datasets. These strategies are evaluated based on several key metrics, such as imputation accuracy, computational efficiency, and robustness, particularly under different missing data scenarios. The role of hyperparameters, such as the shape parameter in RBFs and the placement of knots in cubic splines, is also explored to understand their influence on imputation outcomes. By conducting a detailed comparative analysis of these methods, this study aims to provide practical guidance for selecting the most suitable technique for data imputation, depending on the specific requirements of the dataset. The results will offer valuable insights for researchers and practitioners seeking to maintain data integrity and improve the reliability of analytical results, contributing to the broader field of data science and interpolation methods. In sections 2, we present the mathematical background of interpolation and approximation techniques. In sections 3 and 4, we prepare datasets for testing interpolation methods and performing data imputation. The imputation phase involves filling in missing values, during which we assess the performance of different methods in terms of accuracy and reliability using root mean square error and comparative analysis.

2. Mathematical Background

2.1. Radial Basis Functions (RBFs)

Radial Basis Functions are widely used for interpolation and approximation, particularly in scattered data scenarios. The approximation function $f(x)$ is expressed as a linear

combination of radially symmetric functions centered at data points $\{x_i, y_i\}$, where $x_i \in \mathbb{R}^d$ and $y_i \in \mathbb{R}$. The general RBF approximation is given by

$$f(x) = \sum_{i=1}^{N} \lambda_i \phi\left(\|x - x_i\|\right), \tag{1}$$

where λ_i are coefficients, $\phi\left(\|x - x_i\|\right)$ is the RBF, depending on the Euclidean distance $\|x - x_i\|$. This distance serves as the input to the radial basis function, making RBF interpolation a function of the relative distance between points, which allows for flexibility and smoothness in the resulting approximation. In this work, two popular choices of RBF are paid attention to, they are defined as follows

$$\phi\left(\|\mathbf{x} - \mathbf{x}_i\|\right) = \begin{cases} \left(\|\mathbf{x} - \mathbf{x}_i\|^2 + \sigma^2\right)^{\beta} & ; \quad \textit{Generalized MQ} \\ \exp\left(-\|\mathbf{x} - \mathbf{x}_i\|^2 / 2\sigma^2\right) & ; \quad \textit{Gaussian RBF} \end{cases}, \tag{2}$$

where $\sigma > 0$ is the shape parameter controlling the function's flatness. A smaller σ results in a more peaked RBF, while a larger σ produces a flatter response. In the case of the generalized MQ function, the additional parameter β controls the degree of flatness and is generally set to values between β=0.5 and β=1.5 [11], depending on the smoothness of the data. The Gaussian RBF, in contrast, provides a smooth, bell-shaped function that decays exponentially as the distance increases, controlled solely by the σ parameter. These RBF formulations are highly flexible and can be adapted for various types of interpolation and approximation problems, making them particularly well-suited for time-series data imputation in this study. By adjusting the parameters σ and β, the RBF can be fine-tuned to achieve the desired smoothness and accuracy in the interpolated results.

2.2. Cubic Schemes

The adaptation of cubic spline interpolation is a method for generating data using third-order polynomials. This method uses the initial data $x_{i-2}, x_{i-1}, x_i, x_{i+1}, x_{i+2}$ to create the polynomial by cubic spline. The cubic spline is defined as follows

$$P_3(x) = \sum_{i=-2}^{2} B_i(x) y_i \tag{3}$$

when

$$B_i(x)=\begin{cases}\dfrac{(x-x_{i-2})^3}{(x_{i+1}-x_{i-2})(x_i-x_{i-2})(x_{i-1}-x_{i-2})} & for \quad x_{i-2}\le x<x_{i-1}\\ \dfrac{(x-x_{i-2})^2(x_i-x)}{(x_{i+1}-x_{i-2})(x_i-x_{i-2})(x_i-x_{i-1})}+\dfrac{(x-x_{i-2})(x_{i+1}-x)(x-x_{i-1})}{(x_{i+1}-x_{i-2})(x_{i+1}-x_{i-1})(x_i-x_{i-1})} & for \quad x_{i-1}\le x<x_i\\ +\dfrac{(x_{i+2}-x)(x-x_{i-1})^2}{(x_{i+2}-x_{i-1})(x_{i+1}-x_{i-1})(x_i-x_{i-1})}\\ \dfrac{(x-x_{i-2})(x_{i+1}-x)^2}{(x_{i+1}-x_{i-2})(x_{i+1}-x_{i-1})(x_{i+1}-x_i)}+\dfrac{(x_{i+2}-x)(x-x_{i-1})(x_{i+1}-x)}{(x_{i+2}-x_{i-1})(x_{i+1}-x_{i-1})(x_{i+1}-x_i)} & for \quad x_i\le x<x_{i+1}\\ +\dfrac{(x_{i+2}-x)^2(x-x_{i+2})}{(x_{i+2}-x_{i-1})(x_{i+2}-x_i)(x_{i+1}-x_i)}\\ \dfrac{(x_{i+2}-x)^3}{(x_{i+2}-x_{i-1})(x_{i+2}-x_i)(x_{i+2}-x_{i+1})} & for \quad x_{i+1}\le x<x_{i+2}\\ 0 & for \quad otherwise\end{cases} \tag{4}$$

The polynomial is then used to evaluate the value at x_i and to calculate the error. If the error is greater than 5%, a midpoint knot x_i^* is added between x_i and x_{i+1}, and the cubic spline is recomputed by using data $x_{i-2}, x_{i-1}, x_i, x_i^*, x_{i+1}$. In step of recovering missing values at $\hat{x}_i$: choose polynomial for $x_i \le \hat{x}_i < x_{i+1}$ to calculate missing values by $P_3(\hat{x}_i)$.

3.Experimental Setups

The study uses three time-series datasets: a multi-seasonal time series with regular periodic patterns (Dataset-1), a non-stationary time series with trends and abrupt shifts (Dataset-2), and a spikes and drops time series with irregular, sudden changes (Dataset-3). These datasets were selected to evaluate the performance of interpolation methods under diverse and challenging conditions.

To simulate real-world missing data scenarios, three levels of data corruption—10%, 25%, and 50%—were introduced by randomly removing data points from each time-series dataset. These corruption levels represent varying degrees of data loss, allowing us to assess the performance and robustness of each interpolation method in recovering missing values across different levels of data degradation.

The performance of each interpolation method was evaluated using the Root Mean Square Error (RMSE), which measures the difference between the imputed and actual values. RMSE was chosen as it effectively captures both the magnitude and consistency of errors, making it a reliable metric for comparing the accuracy of different techniques across varying levels of data corruption. Lower RMSE values indicate better imputation performance.

4.Main Results and Discussion

The results presented in Table 1 reveal notable differences in the performance of various interpolation techniques for data imputation across different corruption levels of a multi-seasonal time series dataset. Gaussian RBF with a standard deviation of 0.1 exhibits higher RMSE values compared to the other methods, with errors progressively increasing

as the corruption level rises, reaching 61.63 for 50% corruption. The Multiquadric RBF method, particularly with β=3/2, offers a comparatively lower RMSE, achieving 4.60, 5.14, and 5.69 across 10%, 25%, and 50% corruption levels, respectively. The spline-based methods, Cubic and Adaptive, generally outperform the RBF methods, with the Cubic Spline consistently demonstrating the lowest RMSE at each corruption level (e.g., 3.88 for 10% corruption and 4.04 for 25% corruption). The Adaptive Spline exhibits slightly higher RMSE values compared to its cubic counterpart, though the difference remains marginal, especially at higher corruption levels where the RMSE increases to 4.62. Overall, the spline-based methods demonstrate superior robustness to data corruption when compared to the RBF approaches, particularly in cases of lower corruption levels.

Table 1 Root Mean Square Error (RMSE) comparison of various interpolation methods at different data corruption levels (10%, 25%, and 50%) for Dataset-1: a multi-seasonal time series dataset.

Data Corruption Level	Gaussian RBF		Multiquadric RBF		Spline	
	$\sigma = 0.5$	$\sigma = 0.1$	$\beta = 1/2$	$\beta = 3/2$	Cubic	Adaptive
10%	54.787810	72.393950	4.203230	4.604818	3.880803	3.914182
25%	58.355514	72.095816	4.407891	5.145134	4.043455	4.263847
50%	61.634992	72.140857	4.709776	5.691994	4.469533	4.624455

Table 2 illustrates the RMSE performance of different interpolation methods applied to the non-stationary time series dataset under varying levels of data corruption. The Multiquadric RBF with β=1/2 demonstrates remarkable accuracy, achieving minimal RMSE values close to zero for all corruption levels, notably 0.000028 for 10% corruption and 7.04 for 50% corruption, significantly outperforming all other methods. The Gaussian RBF (σ=0.5) shows inconsistent results, with RMSEs ranging from 2.08 at 50% corruption to over 10.47 at 10% corruption. The performance of the Spline methods remains relatively stable across corruption levels, with RMSE values hovering around 0.72–0.80, indicating robustness in dealing with non-stationary data. While the Adaptive Spline slightly outperforms the Cubic Spline in some cases, the difference is marginal. Overall, the Multiquadric RBF method is most effective for this dataset, particularly at lower corruption levels.

Table 2 Root Mean Square Error (RMSE) comparison of various interpolation methods at different data corruption levels (10%, 25%, and 50%) for Dataset-2 : a non-stationary time series dataset.

Data Corruption Level	Gaussian RBF		Multiquadric RBF		Spline	
	$\sigma = 0.5$	$\sigma = 0.1$	$\beta = 1/2$	$\beta = 3/2$	Cubic	Adaptive
10%	10.472248	10.775935	0.000028	0.379259	0.728446	0.731239
25%	11.111204	14.873718	0.707081	0.772658	0.710826	0.717327
50%	2.081957	14.884052	7.043845	0.913856	0.803558	0.807143

Table 3 summarizes the RMSE performance of different interpolation methods on the spikes and drops time series dataset at varying corruption levels. The Gaussian RBF method (σ=0.1) shows significantly higher RMSE values compared to other methods, ranging from 19.31 to 25.97 as the corruption level increases. In contrast, the Multiquadric RBF, particularly with β=1/2, delivers much lower RMSEs, with the values

consistently around 3.44 to 2.82 across all corruption levels. Both Cubic and Adaptive Splines exhibit superior performance, with RMSE values in the range of 3.10 to 2.65 for Cubic Spline and 3.10 to 2.70 for Adaptive Spline, demonstrating their robustness in handling this challenging dataset. Notably, the spline methods outperform the Multiquadric RBF as the corruption level increases, highlighting their efficiency in handling time series with sudden spikes and drops. Overall, the spline-based methods, particularly the Adaptive Spline, show the most stable and lowest RMSE performance, especially at higher corruption levels.

Table 3 Root Mean Square Error (RMSE) comparison of various interpolation methods at different data corruption levels (10%, 25%, and 50%) for Dataset-3 : a spikes and drops time series dataset

Data Corruption Level	Gaussian RBF		Multiquadric RBF		Spline	
	$\sigma = 0.5$	$\sigma = 0.1$	$\beta = 1/2$	$\beta = 3/2$	**Cubic**	**Adaptive**
10%	19.693816	25.967805	3.441154	3.539726	3.106099	3.107410
25%	19.310685	25.796492	3.019679	3.154228	2.857276	2.858678
50%	21.335702	25.870687	2.820384	3.190294	2.657555	2.703954

The results across the three datasets and corresponding interpolation methods reveal distinct patterns in performance, highlighting the strengths and limitations of each technique under varying data corruption levels. Gaussian RBF consistently exhibits the highest RMSE values across all datasets, with particularly poor performance on the spikes and drops dataset (e.g., RMSE of 19.69 for 10% corruption) and non-stationary dataset (RMSE of 14.88 for 50% corruption). In contrast, the Multiquadric RBF demonstrates superior accuracy, particularly with β=1/2, where it achieves the lowest RMSE of 0.000028 for the non-stationary dataset at 10% corruption. However, its performance is less stable on the spikes and drops dataset, with RMSE values decreasing from 3.44 to 2.82 as corruption levels rise. The spline-based methods (Cubic and its adaptive version) consistently outperform the RBF methods, particularly in handling challenging datasets with higher corruption levels, such as in the spikes and drops dataset, where the Cubic Spline achieves an RMSE of 2.65 at 50% corruption. Overall, the spline methods exhibit robustness across all datasets, maintaining low RMSEs even at higher corruption levels, making them the most reliable for data imputation, especially when dealing with erratic patterns or high corruption rates.

5.Conclusions

This study provides a detailed comparison of interpolation techniques—Gaussian RBF, Multiquadric RBF, Cubic Spline, and Adaptive Spline—applied to various time-series datasets with differing corruption levels. The results demonstrate that spline-based methods consistently outperform RBF approaches, particularly in datasets with high levels of corruption and irregular patterns. The Cubic and Adaptive Splines exhibited robust performance across all datasets, showing stable RMSE values even in more challenging scenarios, such as the spikes-and-drops dataset. The Multiquadric RBF (β=1/2) showed excellent accuracy in the non-stationary dataset, achieving an RMSE as low as 0.000028, but its effectiveness declined in more complex datasets with sudden fluctuations. In contrast, the Gaussian RBF consistently produced higher RMSE values

across all datasets, indicating its limitations in handling irregularities and higher corruption rates. These findings highlight the superiority of spline-based methods for practical time-series data imputation, especially in complex real-world scenarios. Future research could explore hybrid techniques that combine the strengths of different interpolation methods, with a focus on further improving performance in highly corrupted datasets or those with erratic behaviors.

Acknowledgment

We would like to express our sincere gratitude to *Loei Rajabhat University*, Rajamangala University of Technology Isan, Ubon Ratchathani Rajabhat University for their invaluable support throughout this research project. The resources, guidance, and encouragement provided by the faculty and staff have been instrumental in the successful completion of this work.

References

[1] Z. Zhang, "Missing data imputation: focusing on single imputation," *Annals of translational medicine,* vol. 4, no. 1, 2016.

[2] S. Mehtab and J. Sen, "Analysis and forecasting of financial time series using CNN and LSTM-based deep learning models," in *Advances in Distributed Computing and Machine Learning: Proceedings of ICADCML 2021*, 2022: Springer, pp. 405-423.

[3] L. Libkin, "Incomplete data: what went wrong, and how to fix it," in *Proceedings of the 33rd ACM SIGMOD-SIGACT-SIGART symposium on Principles of database systems*, 2014, pp. 1-13.

[4] J. Luengo, S. García, and F. Herrera, "A study on the use of imputation methods for experimentation with radial basis function network classifiers handling missing attribute values: The good synergy between rbfns and eventcovering method," *Neural Networks,* vol. 23, no. 3, pp. 406-418, 2010.

[5] S. McKinley and M. Levine, "Cubic spline interpolation," *College of the Redwoods,* vol. 45, no. 1, pp. 1049-1060, 1998.

[6] G. Wolberg, "Cubic spline interpolation: A review," 1988.

[7] V. Skala, "RBF interpolation with CSRBF of large data sets," *Procedia Computer Science,* vol. 108, pp. 2433-2437, 2017.

[8] Y.-L. Zou, F.-L. Hu, C.-C. Zhou, C.-L. Li, and K.-J. Dunn, "Analysis of radial basis function interpolation approach," *Applied geophysics,* vol. 10, no. 4, pp. 397-410, 2013.

[9] P. G. Papaioannou, R. Talmon, I. G. Kevrekidis, and C. Siettos, "Time-series forecasting using manifold learning, radial basis function interpolation, and geometric harmonics," *Chaos: An Interdisciplinary Journal of Nonlinear Science,* vol. 32, no. 8, 2022.

[10] D. Pollock, "Smoothing with cubic splines," ed: Queen Mary and Westfield College, Department of Economics, 1993.

[11] P. Pongchalee, P. Paewpolsong, P. Inthapong, T. Singin, and S. Kaennakham, "Numerical Investigation on β= 3/2 in the Generalized Multiquadric Neural Networks for Classification Challenge," in *International Conference on Computational & Experimental Engineering and Sciences*, 2023: Springer, pp. 735-747.

Fuzzy Systems and Data Mining X
A.J. Tallón-Ballesteros (Ed.)

doi:10.3233/FAIA241433

Linguistic Text Mining

Alberto POSTIGLIONE [a,1]
[a] *Department of Business Sciences - Management & Innovation Systems (DISA-MIS), University of Salerno, ITALY*
ORCiD ID: Alberto Postiglione https://orcid.org/0000-0001-6411-6529

Abstract. This paper explores the challenges of processing the increasing volume of natural language text, which often surpasses traditional methods' real-time processing abilities. These texts are typically authored by individuals from diverse educational, cultural, and experiential backgrounds. The paper highlights the main linguistic and semantic issues that arise in the analysis of natural language text.

Linguistic Text Mining is a computational approach that combines linguistic principles with computational techniques to extract high-quality information from natural language texts. Despite the frequent mentions of "Linguistic" and "Text-Mining" in scientific literature, no formal definition exists; this paper proposes one. It further explores LTMs potential in enhancing knowledge extraction by emphasizing linguistic features, such as multi-word units (MWUs).

Traditional text analysis relies heavily on statistical methods, focusing on simple words, which are often polysemous, or on aggregating words without semantic context and this limits systems' ability to interpret domain-specific semantics. By contrast, MWUs, like "credit card", convey specific, unambiguous meanings, critical for identifying specialized domains. MWUs are typically organized within ontologies that represent distinct knowledge domains.

Building on previous work, the study compares AUTOMETA, an ontology-based approach using finite automata for MWU identification, with large language model (LLM)-based and other ontology-driven Linguistic Text Mining methods. Findings suggest that integrating linguistic frameworks significantly improves information extraction, offering a deeper understanding of complex language structures.

Keywords. Linguistic, Text Mining, Linguistic Text Mining, Natural Language Processing, Multi-Word Unit, Finite Automata

1. Introduction

1.1. The Volume of Natural Language Documents

This paper examines natural language (NL) texts, which are commonly either unstructured, such as free-text content like emails and social media posts, or semi-structured, such as XML, JSON, or HTML files, which exhibit some degree of organization but do not have the structure required for database storage.

In recent years, the volume of this data has increased significantly, sourced from books, scientific publications, news articles, emails, and web pages. The growing presence of social media in everyday life (including forums, chats, and blogs), and the rise

[1]Corresponding Author: Alberto Postiglione, DISA-MIS, University of Salerno, ITALY, ap@unisa.it

of interactive tools like chatbots [1,2,3,4] has further amplified this surge. This increase is also driven by several converging trends: the expansion of corporate data systems, the rapid development of Big Data [5,6,7,8,9,10,11], and the widespread adoption of the Internet of Things (IoT) [12,13,14,15,16,17,18] and the Industrial Internet of Things (IIoT) [19,20,21,22,23]. In addition, government worldwide policies, aimed at reducing paper-based documentation, further contribute to this expansion.

Some estimates suggest that over 80% of all global data is semi-structured or unstructured [24], with some analyses indicating that this figure could be as high as 85% [25], in contrast to structured data, which is typically organized in relational databases or spreadsheets. Currently, around 25-30% of documents on the indexed web are text-based (such as HTML[2], Word documents, PDFs, blog posts[3], etc.), while the remainder consists of images, videos, databases, and multimedia content.

In addition to visible web content, a significant portion of documents on the Deep Web is also text-based. Research suggests that the Deep Web holds trillions of unindexed documents, including numerous public records and academic papers.

Regardless of the precise percentage, the current scale of unstructured and semi-structured textual data aligns with the characteristics of Big Data: vast volume, diverse formats, lack of standardization, and continuous generation. Its enormous volume now exceeds the capacity of traditional databases and algorithmic approaches, which often struggle to manage and process this data efficiently, especially in real-time scenarios. This underscores the need for advanced data management and analysis techniques, as these data types require specialized methods, such as NLP, machine learning, and data lakes, for effective storage and processing.

1.2. Main Issues in Natural Language Textual Documents

When search engines retrieve partially incorrect or loosely related results, it is often a consequence of limitations in linguistic analysis during computational processing and indexing. While humans can effortlessly understand unstructured text, computers face significant challenges due to their inability to fully comprehend semantics and context. Some of the key issues include:

1.2.1. Standardization and Formatting Issues

Natural language texts come from a wide variety of different sources, and are produced by authors from diverse educational, cultural, and experiential backgrounds, which gives rise to heterogeneous writing styles and inconsistencies.

Differences may arise in the use of *punctuation*, *capitalization*, and *accented* characters[4]. There are also variations in the use or choice of *apostrophes*, in lexical differences between *American English and British English* (e.g., center (American) vs. centre (British)), and in the use of *Abbreviations and Contractions* (e.g., "Dr." for "Doctor" or "didnt" for "did not"). In addition, differences in *sentence structure* are common.

[2] At this moment, there are over 2 billions of websites worldwide - see https://techjury.net/blog/internet-statistics/.

[3] An estimate of over 2.7 trillion blog posts were written in 2022 - see above url.

[4] For instance, the vowel 'a' can appear in various forms, such as $\acute{a}, \grave{a}, \hat{a}, \check{a}, \breve{a}, \tilde{a}, \bar{a}, \vec{a}, \dot{a}, \ddot{a}$

Furthermore, *colloquial expressions* appear in many contexts, such as literature, politics, and journalism, further complicating computational processing. The lack of standardized writing conventions adds to the complexity for computational systems.

1.2.2. Ill-formed expressions

Texts often contain errors, non-existent words, or expressions used incorrectly due to human oversight. Examples include spelling mistakes (e.g., "banc", a non-existent word, or "band" instead of "bank") or incorrect usage influenced by dialect or lack of knowledge.

1.2.3. Lexical and Semantic Ambiguity

A common phenomenon in natural language is *polysemy*, where words have multiple meanings that often require contextual information to disambiguate (e.g., "park" can refer to both a public space and the act of parking). The frequent emergence of *neologisms*, often borrowed from online discourse (e.g., "B2C" for "business-to-consumer"), presents additional challenges.

Semantic ambiguity can also arise at the sentence level, where multiple interpretations may arise. For example, the sentence "Alice saw Bob at the stadium with binoculars" could imply different scenarios:

1. Alice is at the stadium and saw Bob, who may be in an unknown location and has binoculars.
2. Alice is at the stadium and, using her binoculars, saw Bob, who may be in an unknown location.
3. Alice saw Bob, who is at the stadium and has binoculars.
4. Alice, using her binoculars, saw Bob, who is at the stadium.

1.2.4. Significant deep layers

One of the most significant challenges of NLP is to decipher how individuals use language to convey *feelings, emotions and thoughts*. This encompasses rhetorical devices such as metaphors, allusions, irony, euphemisms, aphorisms, and other implicit ideas, all of which obscure meaning beneath the surface of the text.

Grasping these deeper layers poses a considerable challenge for technology, as it necessitates advanced reasoning and understanding that remain largely unattainable with current systems. For instance, the phrase "Bob left us yesterday" can suggest various interpretations (e.g., relocating, changing employment, or passing away), while "You are the apple of my eye" serves as a metaphorical expression.

1.2.5. In conclusion

The challenges outlined are inherent to natural language texts and must be addressed in any form of linguistic analysis. While meticulous and effective pre-processing can mitigate some of these issues, many remain unresolved by current algorithms. Some challenges are particularly intricate, making it difficult even for humans to address them without supplementary information from other senses (such as sight) or external knowledge.

1.3. Semantic-Based Methods for Processing Natural Language Texts

This section outlines fundamental methods rooted in semantics for processing natural language, which focus on understanding the contextual meanings of words, phrases, and sentences. Key semantic-based approaches include:

1. *Word Sense Disambiguation (WSD)* [26,27,28]. WSD determines the correct meaning of polysemous words based on context, such as distinguishing between "bank" (financial institution) and "bank" (riverbank).
2. *Named Entity Recognition (NER)* [29,30,31]. NER identifies and categorizes proper nouns, such as people, organizations, locations, and dates, which are crucial for extracting meaningful information from text.
3. *Semantic Role Labeling (SRL)* [32,33,34]. SRL labels the roles words play in sentences, such as identifying in "Alice gave Bob a book" the giver ("Alice"), recipient ("Bob"), and object ("book").
4. *Distributional Semantics* [35,36,37]. This approach suggests that words sharing similar contexts tend to have related meanings. Techniques such as Word2Vec [35] and GloVe [36] leverage extensive corpora to generate word embeddings, effectively capturing semantic relations among words.
5. *Ontology-Based Analysis* [38,39,40]. Ontologies represent knowledge domains, capturing concepts and their relationships to infer meaning from text.
6. *Latent Semantic Analysis (LSA)* [41,42,43]. LSA utilizes singular value decomposition (SVD) to reveal underlying semantic structures by examining word co-occurrence patterns within reduced-dimensional spaces.
7. *Semantic Parsing* [44,45]. This method converts natural language into formal representations like logic or knowledge graphs, enabling better machine understanding of meaning.
8. *Frame Semantics* [46]. Based on Fillmore's frame theory, this approach explores how words evoke certain scenarios, helping in the comprehension of relationships within these scenarios.

1.4. Multi-Word Units (MWUs)

In a text, words are usually divided into two categories: *single words*, which are cohesive and meaningful sequences of letters, separate from each other, and *multi-word units (MWUs)* [47,48], which are combinations of two or more single words that, together, convey a unitary meaning.

Simple words, such as *credit* or *card*, are often *polysemous*, meaning they have multiple interpretations depending on the context. For example, "credit" may refer to concepts in banking, psychology, mathematics, industry, or economics, while "card" could relate to commerce, materials, medicine, literature, or computer science. Most text processing techniques focus on analyzing simple words, but their polysemy poses challenges in determining their precise meanings.

MWUs, such as *"credit card"*, are typically *monosemous*; they are not arbitrary combinations of simple words but rather fixed expressions that form a single semantic unit, conveying a specific meaning independent of their individual components. An MWU identifies a distinct semantic area or object. Examples of MWUs include:

- Idiomatic Expressions: e.g., *Spill the beans* (to reveal a secret).
- Collocations: e.g., *Catch a glimpse*, *Run a business*, *Heavy traffic*.
- Phrasal Verbs: e.g., *Give up* (surrender), *Hold on* (wait).
- Proverbs: e.g., *A stitch in time saves nine* (dealing with a problem early prevents more work later).
- Technical Terms: e.g., *Machine learning*, *Renewable energy*.
- Compound Words: e.g., *Notebook* (note + book), *Toothbrush* (tooth + brush).
- Fixed Expressions: e.g., *For the time being* (temporarily), *In a nutshell* (briefly).
- Named Entities: e.g., *Mona Lisa* (picture's name), *Eiffel Tower*.
- Acronyms and Initialisms: e.g., *NASA*, *UNESCO*, *FBI*.
- Technical or Scientific Terminology: e.g., *Quantum mechanics*, *Nuclear fusion*.

There is a strong relationship between specialized terminology and MWUs, to the extent that field-specific vocabularies are predominantly composed of MWUs. However, this relationship is not limited to specialized fields; it also spans a broad spectrum of semantic areas. Linguistic studies have shown that a significant portion of cognitive information in natural language is conveyed through MWUs. While single words often require context for disambiguation, MWUs tend to retain their meaning consistently across contexts.

Although some methods analyze aggregates of simple words, they often rely on statistical criteria and are generally inefficient. Transitioning from simple word-based analysis to MWU-based investigation offers deeper semantic insights but introduces computational challenges. Unlike simple words, which are easily identified by spaces or punctuation, MWUs lack explicit markers to indicate their boundaries. This makes automatic detection difficult, as MWUs can vary in length and involve unpredictable word combinations. Consequently, identifying MWUs in text requires more sophisticated and computationally intensive analysis techniques.

2. Text Mining

Text mining [49,50,25,24,51] is an interdisciplinary field that integrates Natural Language Processing (NLP), statistical techniques, and computer science. Its main goal is to automatically uncover patterns, extract insights, and generate knowledge from semi-structured or unstructured text data. As a specialized branch of data mining [52,25], text mining focuses specifically on unstructured and semi-structured data, in contrast to traditional data mining, which primarily addresses structured datasets.

Text mining is applied across numerous areas, including feature extraction, summarization, document classification, trend analysis, sentiment analysis, topic modeling, opinion mining, and named entity recognition, making it a highly adaptable tool in sectors such as industry, academia, web applications, and beyond.

A key aspect of NLP is text annotation, which involves adding labels to enhance the structure, context, or meaning of texts. This annotation can be performed manually or through automated methods and frequently necessitates domain expertise, especially for tasks like classifying brief scientific texts, which typically include only a title, abstract, and keywords, or processing medical documentation [53,54,55].

Text mining has extensive applications across numerous sectors, including finance [56,57], risk management [58], predictive maintenance [59], policy-making [60], educa-

tion [61], agriculture [62], psychiatry [63], biomedicine [64], healthcare [65,66,67], and social media analysis [68,69,70].

In [24], a text mining system is divided into pre-processing, text representation, and four operational phases: Dimensionality Reduction, Feature Extraction, Document Classification, and Evaluation. The primary objective of the pre-processing and text representation phases is to convert unstructured and semi-structired text into structured features, ensuring that the input text is standardized into a uniform format. This process includes preparing and cleansing the raw text data for analysis.

3. Linguistic vs. Non-Linguistic Text Mining

Search engines often retrieve unstructured documents that only partially match user queries due to limitations in linguistic analysis during computational processing and indexing. Non-linguistic text analysis systems primarily rely on statistical and mathematical methods, focusing on identifying patterns without considering linguistic features. These systems analyze quantitative aspects of the text, such as word frequency and co-occurrence. Common tasks include document categorization, keyword extraction, and similarity analysis, with the main objective of identifying patterns and trends while overlooking the nuances of language.

Nevertheless, this statistical approach has inherent limitations. It typically necessitates large datasets and frequently produces irrelevant results (noise) or overlooks significant information (silence) because of its lack of semantic focus. As a result, the analysis may misinterpret the true meaning of the text, necessitating complex rules to enhance accuracy. This has given rise to the development of *rule-based text mining*, which improves precision by more effectively differentiating relevant information from noise.

3.1. Linguistic-Based Text Mining

Although there is no universally accepted formal definition for "Linguistic Text Mining", the terms "Linguistic" and "Text-Mining" appear in the title, abstract, or keywords of about a thousand scientific articles currently indexed in SCOPUS (see, for example, [71, 72,73,74,75,76]). In this paper, we propose a working definition for this concept.

Linguistic-based text mining focuses on identifying semantically meaningful information from text and involves the extraction, transformation, and analysis of text to identify patterns, entities, relationships, and insights, converting raw text into structured data for further analysis and decision-making. This approach uses NLP techniques grounded in linguistic principles, including linguistic rules, text annotation, and semantic analysis. Key techniques encompass discourse analysis, syntactic parsing, part-of-speech tagging, sentiment analysis, named entity recognition, knowledge discovery, and more.

Definition *Linguistic(-based) Text Mining (LTM) is a computational process that extracts meaningful, high-quality information and knowledge from unstructured or semi-structured natural language text by combining linguistic principles with computational techniques.*

4. A Finite-Automaton and Linguistic-Based Text-Mining System for MWUs

In [77], we presented an innovative text mining system called AUTOMETA. This system employs a finite automaton and a formalized representation of natural language, focusing particularly on the concept of *unit of meaning*. The scientific foundation of AUTOMETA builds upon research in Lexicon-Grammar (LG) [78,79,80] and string matching using finite automata [81,82,83,84].

AUTOMETA is a product of interdisciplinary research in computational linguistics and computer science, and represents a major step forward compared to its predecessor, CATALOGA [85,86]. In 2021, we undertook a thorough redefinition, redesign, and rewriting of CATALOGA, resulting in the birth of AUTOMETA, in 2024. While maintaining the approach of its predecessor and reusing certain ontologies (currently under review), every other component underwent extensive redesign. This includes improving algorithms, optimizing data structures, introducing new technology updates, refining source code, and tweaking the user interface, to improve performance.

4.1. AUTOMETA Overview

AUTOMETA is designed for efficient Multiword Unit (MWU) identification and semantic domain assignment within natural language texts, leveraging predefined ontologies. These ontologies contain MWUs associated with unique identifiers linked to specific knowledge domains. When a relevant ontology isnt available, it must be created with input from subject matter experts. AUTOMETA supports integration across multiple domain-specific ontologies, enabling seamless mapping and facilitating broader applications.

Each MWU within these lexical ontologies is tagged with identifiers that serve as metadata, aligning terms with distinct semantic contexts. This system, termed a “lexical ontology”, bridges MWUs in specific terminologies with corresponding knowledge domains, providing clarity for domain-specific interpretation. For example, the MWU *diatonic chords* is tagged with ”MUSIC” for the music domain, while *Mathematical Analysis* is tagged with ”MATHE” for mathematics. Unlike encyclopedic databases, these ontologies are streamlined for precise and standardized terminology, enhancing AUTOMETA’s focus on capturing essential domain knowledge efficiently.

4.2. A case study

In a case study from [77], AUTOMETA was tested on 100 texts from various media sources, ranging in length from 103 (644 characters) to 8,800 words (56,715 characters), with an average length of 766 words and 5,436 characters per text. The system utilized a broad ontology of 21,396 Multi-Word Units (MWUs) across 21 domains to assess its categorization accuracy compared to human expert classifications. The evaluation followed a three-step methodology:

1. Manual Review: Domain experts manually categorized each text, assigning up to three primary domains.
2. AUTOMETA Processing: The same texts were processed by AUTOMETA.

Table 1. Accuracy Categories

85% or higher:	Objective fully achieved
70% to 84%:	Objective well achieved
50% to 69%:	Objective achieved
30% to 49%:	Objective poorly achieved
Below 30%:	Objective not reached

3. Accuracy Comparison: The system's categorization was matched to human classifications and scored according to a defined accuracy scale (Table 1), ranging from "fully achieved" (85%+ match) to "not reached" (below 30

AUTOMETA demonstrated both efficiency and accuracy. Ontology-based finite automata were built within 12 seconds, while, for the input texts, preprocessing and processing times averaging under 2.9 and 1.3 seconds, respectively, and peak memory usage of 709 MB. AUTOMETAs performance on standard hardware was robust, with no need for specialized equipment.

The results showed high reliability: 91% of the texts achieved the desired classification accuracy, with 83% in close agreement with human classifications, particularly effective for very short texts, even a few hundred words (see table 2).

Table 2. Test summary

Goal	# Documents	# Words (Avg)	# Characters (Avg)	Average percentage
Fully Achieved	52	721.50	5,279.87	93.56%
Well Achieved	31	956.93	6,731.37	75.97%
Achieved	8	698.25	4,598.13	52.50%
Poorly Achieved	2	581.50	3,687.50	37.50%
Not Achieved	7	440.71	2,716.14	2.86%

Thus, AUTOMETA proved capable of rapid, accurate, scalable tool for domain-specific semantic analysis across varied text lengths, without pre-training, requiring minimal system resources and delivering rapid processing times, marking it as a practical tool for large-scale linguistic text mining applications.

4.3. Ethical Considerations

AUTOMETAs focus on MWUs minimizes ambiguity, promoting precise domain categorization. MWUs have limited synonymy and strong specificity, making them less susceptible to misinterpretation than simple words. However, the models neutrality necessitates human oversight for handling ethically sensitive or harmful content. For instance, in cases of input text containing incitements to violence, encouragements of suicide, or promotion of unethical ideologies (e.g., Nazism), the model objectively identifies the associated semantic domains without moral or ethical judgment: it does not inherently assess the quality, truthfulness, or societal impact of that content. This neutrality can be advantageous for identifying and categorizing harmful content, supporting applications in content moderation. AUTOMETA could be a valuable tool help to ensure that such data is excluded from pre-training datasets of other models, such as Large Language Models (LLMs), reducing the risk of perpetuating biases or misinformation. This limitation calls

for human oversight to avoid risks such as censorship, over-filtering, or unintentional bias in content selection, where some material may be unfairly excluded or included.

In summary, while AUTOMETA categorizes content based on semantics, it does not assess factual accuracy or societal implications, emphasizing the need for human intervention in complex ethical evaluations.

5. Comparisons

5.1. PLM Family Systems: Main Issues

LLMs [87,88], especially Large Pre-Trained Language Models (PLMs), have transformed NLP in recent years, enabling more accurate and relevant text interpretation and generation. This section addresses critical issues in PLMs, as outlined by Zhang et al. [89] and supported by sources like MIT Technology Review[5] and OpenAI[6]:

Pre-training issues:

PLMs require extensive, diverse datasets, raising several concerns:

- **Data size:** PLMs require enormous datasets; for instance, GPT-3 was trained on 570 GB of text , equivalent to about 300 billion words[90].
- **Ethical and Moral Concerns and Data Quality:** Schramowski et al. [91] argue that the huge amount of unfiltered pre-training data inevitably affects model reliability, as it causes PLMs to absorb factual inaccuracies, biases, social stereotypes and misinformation or retain sensitive or inappropriate content, resulting in biased or ethically questionable results and potential legal and privacy risks [92].

AUTOMETA does not require pre-training, and therefore focuses only on the document to be analyzed, without other documents influencing its analysis.

Tokenization:

Tokenization, based on statistical models, breaks text into discrete units, or tokens, that are numerically encoded for processing. The tokenization process breaks the natural cohesion of complex expressions, treating sentences such as “natural language processing” as independent tokens (“natural”, “language”, “processing”), rather than recognizing them as a cohesive unit, thus missing the deep semantic understanding of each “semantic unit”.

AUTOMETA bypasses traditional tokenization, preserving MWUs as cohesive units for clearer semantic understanding.

Semantics and MWUs:

Tokenization also hinders the accurate interpretation of MWUs and creates challenges in handling polysemy (words with multiple meanings), leading to interpretative ambiguities. This inherent ambiguity complicates precise understanding and interpretation.

[5] https://www.technologyreview.com/2021/02/24/1014369/10-breakthrough-technologies-2021
[6] https://openai.com/blog/chatgpt

By recognizing MWUs as cohesive entities, AUTOMETA reduces synonymy issues and provides a clearer understanding of the texts semantic structure.

Text Flaws and Pre-processing:

Datasets for PLMs pre-training often contain typos, misspellings, or inconsistent formatting, making pre-processing complex and costly, with common errors such as homophones easily missed. Furthermore, focusing mainly on simple words can lead to frequent misinterpretations, since they are numerous and often not clearly distinguished from each other, which makes them easily confused. For example, a lexical error such as "my band is far away" (instead of "my bank") may not be detected during training or text mining.

AUTOMETA minimizes pre-processing by focusing on spelling normalization for MWUs, reducing data dimensionality without extensive pre-processing efforts.

Rare or Unknown Topics:

PLMs struggle with rare topics or concepts not commonly seen in training data, often producing inaccurate results.

AUTOMETA focuses on identifying highly informative MWUs, thus it performs effectively with texts containing only a few key multi-word expressions, enabling it to perform reliably on specialized or unfamiliar content across domains. AUTOMETA excels in processing texts on rare or unfamiliar topics, even with brief documents.

Resource Requirements and Management:

PLMs demand substantial computational resources, energy consumption, and financial investment, restricting access to institutions with high-end infrastructure, which limits accessibility and raises transparency issues.

AUTOMETA operates with minimal computational power. Building an ontology is a one-time and relatively inexpensive operation; there are also many open access ontologies (e.g. OBO Foundry[7], SUMO[8]) that can be used immediately. This allows AUTOMETA to maintain low operating costs, while providing high-value domain knowledge for effective text processing.

Overall, AUTOMETA offers a lightweight, accessible alternative to PLMs, addressing many limitations by avoiding pre-training, reducing dependency on extensive resources, and enhancing semantic precision through MWU recognition.

5.2. Traditional Ontological-Based Strategies: Main Issues

MWU identification in the input text

For a document consisting of n words, the process of identifying MWUs from an ontology of size m necessitates $O(\log m)$ accesses to a sorted data structure for each search. In total, this results in $O(n)$ accesses to the structure for each word, as the method needs to evaluate subsequent words in a sequence to identify potential MWUs. Consequently, a comprehensive analysis of the text entails a minimum of $O(n \log m)$ accesses per word, culminating in an overall time complexity of $O(n^2 \log m)$ for the entire document.

[7] https://cacm.acm.org/research/ontologies-and-the-semantic-web/
[8] https://www.ontologyportal.org/

AUTOMETAs approach leverages a finite automaton as an online data structure that encapsulates the entire ontology, diverging from conventional methods. The finite automaton reads the text sequentially, identifying MWUs without requiring feedback loops, thus achieving linear time complexity: it processes an input text of k characters in $O(k)$ elementary steps. AUTOMETA overcomes the limitations of traditional systems when dealing with MWUs: it allows seamless handling of MWUs, regardless of their length or the number of simple words they comprise, and recognizes both partially and fully overlapping MWUs without incurring additional computational costs.

Ontology size

In conventional ontological-based text-mining approaches, matching individual words or MWUs against an ontology can be computationally costly, with processing times that scale with the ontology's size. Since the complexity performance depends from the size of the ontology, more the ontology is big, more time is necessary for each search operation.

AUTOMETA works efficiently, regardless of the size of the ontology.

Ontology management

Ontology management tasks, such as deleting, inserting, or modifying entries while preserving structure, can further increase processing time. Maintaining an ordered structure for rapid retrieval can require at least $O(\log m)$ accesses for each operation, often necessitating costly memory rearrangements.

AUTOMETA's design does not require a sorted ontology structure, allowing for cost-free operations, such as additions, modifications, or deletions. This flexibility means words can be added, modified, or removed without affecting the ontologys integrity or triggering resource-intensive reordering. AUTOMETA stores ontologies in central memory, significantly reducing access times compared to traditional systems that rely on slower, secondary memory.

Input text dimension

traditional systems that rely on simple words tend to perform better on longer texts, where statistical patterns emerge, but struggle with shorter documents that lack sufficient word counts to reveal these patterns.

AUTOMETAs efficiency in processing both short and long documents makes it a versatile and robust solution for text-mining applications.

AUTOMETAs computational approach advantages over traditional ontology-based text-mining systems. Key benefits include its linear processing time, simplicity and flexibility in handling multi-word units (MWUs), and efficient ontology management.

6. Conclusions, Future Directions and Research Limits

6.1. Conclusions

This paper addresses the complexities of analyzing natural language text, often unstructured or semi-structured, and highlights the limitations of traditional databases and algorithms in managing such data, especially where real-time processing is crucial. The di-

versity of authorship, cultural backgrounds, and stylistic conventions in natural language adds to the variability and ambiguity, with lexical and semantic inconsistencies posing significant challenges for computational systems. While human readers navigate these nuances with ease, machines struggle to interpret semantics and context, particularly in the absence of sensory or external information.

Traditional text analysis methods primarily rely on statistical and mathematical techniques, relying on quantitative features like word frequency and co-occurrence. These techniques, however, require large datasets and often yield results that include irrelevant information (noise) or omit essential elements (silence), leading to a lack of semantic depth. To address these issues, linguistic text mining incorporates semantic and contextual layers, leveraging resources like lexicons, grammars, and ontologies. The identification of multi-word units plays a key role, as they represent much of the cognitive content in texts, allowing for clearer representation of specific knowledge domains.

Although the terms "Linguistic" and "Text Mining" are frequently cited together in titles, abstracts, or keywords in scientific literature, with about a thousand papers indexed in SCOPUS, a formal definition for "Linguistic Text Mining" has not been established. This paper aims to establish a working definition for this term.

In a previous paper ([77]), we introduced AUTOMETA, an ontology-based approach that utilizes finite automata for efficient MWU identification. In Section 4.2, we summarize a test conducted on AUTOMETA as reported in [77]. AUTOMETA demonstrated excellent computational performance and high linguistic accuracy in recognizing knowledge within texts.

In this paper, we further compare AUTOMETA with LLM-based methods and other ontology-driven language technology management approaches.

Thus, AUTOMETA emerges as a scalable, domain-specific, and efficient tool for semantic analysis, requiring no pre-training and minimal system resources. These capabilities establish it as a valuable asset for large-scale linguistic text mining applications, adaptable across constantly evolving languages and fields.

6.2. Future Directions

Future development of AUTOMETA could focus on several key areas to enhance its functionality and adaptability:

- Ontology Updates and Expansion: Continuous updating of existing ontologies and developing new ones for emerging fields like e-Government, biomedicine, and sustainability would enhance AUTOMETAs applicability across diverse domains.
- Comprehensive Validation: Expanding validation and testing on larger and more varied corpora will help refine AUTOMETAs performance and reliability across different text types and domains.
- Web Integration: Embedding AUTOMETA within websites and online platforms could enable collection of usability feedback and improve user experience through real-world applications.

To keep pace with evolving linguistic needs, it is essential to examine how language shifts in response to new communicative demands. Several promising directions for future research include:

- Adaptive Ontology Systems: Developing ontology-based systems capable of dynamically incorporating new terms and concepts would improve responsiveness to fast-changing fields like technology and healthcare.
- Multilingual Capabilities: Expanding AUTOMETAs multilingual functionality to include widely spoken languages, such as Spanish, Chinese, and Japanese, would increase its global applicability.
- Multi-Modal and Knowledge Integration: Incorporating external knowledge sources or multi-modal data (e.g., visual or audio information) could help resolve contextual ambiguities that text-based processing alone may struggle with.
- Translation Feature for MWUs: Adding an accurate translation feature for MWUs could address common errors in technical and scientific translation. Given that MWUs typically convey meaning as a unified whole, translating them requires more than the translation of individual terms.

6.3. Research Limits

Despite the encouraging outcomes of this study, certain limitations in the linguistic text mining approach highlight areas for further research. A primary constraint lies in its reliance on predefined ontologies to accurately recognize and categorize MWUs within specific domains. Since these ontologies require regular updates to capture new language developments and terminology, this reliance can limit the systems adaptability to emerging or previously unrepresented domains. It's real that there are also many open access ontologies (e.g. OBO Foundry, SUMO) that can be used immediately.

Another challenge is processing idiomatic and highly ambiguous text. The system effectively identifies MWUs and domain-specific terms but encounters difficulties with expressions where meaning depends on subtle context or metaphor. This challenge reflects a broader limitation in natural language processing, as current technologies struggle to interpret the subtleties that human readers grasp intuitively. Expanding the systems ability to manage contextual and figurative language will be essential for handling more sophisticated text forms.

Furthermore, the current approach is predominantly rule-based for MWU recognition, which could be enhanced by incorporating machine learning techniques. While rule-based models deliver high accuracy within established domains, they lack the flexibility and adaptability that data-driven approaches offer. Future research could explore hybrid models that combine rule-based techniques with machine learning, potentially leveraging deep learning models for improved contextual interpretation, to increase the system's robustness and versatility.

References

[1] Ana Paula Chaves and Marco Aurelio Gerosa. How should my chatbot interact? A survey on social characteristics in Human–Chatbot interaction design. *International Journal of Human-Computer Interaction*, 37(8):729–758, 2021. Cited by: 156.

[2] Amon Rapp, Lorenzo Curti, and Arianna Boldi. The human side of human-chatbot interaction: A systematic literature review of ten years of research on text-based chatbots. *International Journal of Human Computer Studies*, 151, 2021. Cited by: 152.

[3] Bei Luo, Raymond Y. K. Lau, Chunping Li, and Yain-Whar Si. A critical review of state-of-the-art chatbot designs and applications. *Wiley Interdisciplinary Reviews: Data Mining and Knowledge Discovery*, 12(1), 2022. Cited by: 61.

[4] Giuseppe Fenza, Francesco Orciuoli, Angela Peduto, and Alberto Postiglione. Healthcare conversational agents: Chatbot for improving patient-reported outcomes. *Lecture Notes in Networks and Systems*, 661 LNNS:137–148, 2023.

[5] Min Chen, Shiwen Mao, and Yunhao Liu. Big data: A survey. *Mobile Networks and Applications*, 19(2):171–209, 2014. Cited by: 2252.

[6] C.L. Philip Chen and Chun-Yang Zhang. Data-intensive applications, challenges, techniques and technologies: A survey on Big Data. *Information Sciences*, 275:314–347, 2014. Cited by: 2208.

[7] Chun-Wei Tsai, Chin-Feng Lai, Han-Chieh Chao, and Athanasios V. Vasilakos. Big data analytics: A survey. *Journal of Big Data*, 2(1), 2015. Cited by: 546; All Open Access, Gold Open Access.

[8] Ahmed Oussous, Fatima-Zahra Benjelloun, Ayoub Ait Lahcen, and Samir Belfkih. Big data technologies: A survey. *Journal of King Saud University - Computer and Information Sciences*, 30(4):431–448, 2018. Cited by: 581.

[9] Amina Adadi. A survey on data-efficient algorithms in big data era. *Journal of Big Data*, 8(1), 2021. Cited by: 80.

[10] Liang Zhao. Event prediction in the big data era: A systematic survey. *ACM Computing Surveys*, 54(5), 2022. Cited by: 63.

[11] Haolan Zhang, Sanghyuk Lee, Yifan Lu, Xin Yu, and Huanda Lu. A survey on big data technologies and their applications to the metaverse: Past, current and future. *Mathematics*, 11(1), 2023.

[12] Luigi Atzori, Antonio Iera, and Giacomo Morabito. The internet of things: A survey. *Computer Networks*, 54(15):2787–2805, 2010. Cited by: 10936.

[13] Chun-Wei Tsai, Chin-Feng Lai, Ming-Chao Chiang, and Laurence T. Yang. Data mining for internet of things: A survey. *IEEE Communications Surveys and Tutorials*, 16(1):77–97, 2014. Cited by: 496.

[14] Ala Al-Fuqaha, Mohsen Guizani, Mehdi Mohammadi, Mohammed Aledhari, and Moussa Ayyash. Internet of things: A survey on enabling technologies, protocols, and applications. *IEEE Communications Surveys and Tutorials*, 17(4):2347–2376, 2015. Cited by: 5626.

[15] Li Da Xu, Wu He, and Shancang Li. Internet of things in industries: A survey. *IEEE Transactions on Industrial Informatics*, 10(4):2233–2243, 2014. Cited by: 3715.

[16] Lalit Chettri and Rabindranath Bera. A comprehensive survey on internet of things (IoT) toward 5G wireless systems. *IEEE Internet of Things Journal*, 7(1):16–32, 2020. Cited by: 1174.

[17] Dinh C. Nguyen, Ming Ding, Pubudu N. Pathirana, Aruna Seneviratne, Jun Li, Dusit Niyato, Octavia Dobre, and H. Vincent Poor. 6G internet of things: A comprehensive survey. *IEEE Internet of Things Journal*, 9(1):359–383, 2022. Cited by: 587.

[18] Ibrahim Kahraman, Alper Kose, Mutlu Koca, and Emin Anarim. Age of information in internet of things: A survey. *IEEE Internet of Things Journal*, 11(6):9896–9914, 2024.

[19] Emiliano Sisinni, Abusayeed Saifullah, Song Han, Ulf Jennehag, and Mikael Gidlund. Industrial internet of things: Challenges, opportunities, and directions. *IEEE Transactions on Industrial Informatics*, 14(11):4724–4734, 2018. Cited by: 1317.

[20] Hugh Boyes, Bil Hallaq, Joe Cunningham, and Tim Watson. The industrial internet of things (IIoT): An analysis framework. *Computers in Industry*, 101:1–12, 2018. Cited by: 824.

[21] Diego G.S. Pivoto, Luiz F.F. de Almeida, Rodrigo da Rosa Righi, Joel J.P.C. Rodrigues, Alexandre Baratella Lugli, and Antonio M. Alberti. Cyber-physical systems architectures for industrial internet of things applications in Industry 4.0: A literature review. *Journal of Manufacturing Systems*, 58:176–192, 2021. Cited by: 285.

[22] Yujiao Hu, Qingmin Jia, Yuan Yao, Yong Lee, Mengjie Lee, Chenyi Wang, Xiaomao Zhou, Renchao Xie, and F. Richard Yu. Industrial internet of things intelligence empowering smart manufacturing: A literature review. *IEEE Internet of Things Journal*, 11(11):19143–19167, 2024.

[23] Xiaoshao Mu and Maxwell Fordjour Antwi-Afari. The applications of Internet of Things (IoT) in industrial management: A science mapping review. *International Journal of Production Research*, 62(5):1928–1952, 2024. Cited by: 20.

[24] Chengqing Zong, Rui Xia, and Jiajun Zhang. *Text Data Mining*. Springer Singapore, 2021. Cited by: 23.

[25] Sayali Sunil Tandel, Abhishek Jamadar, and Siddharth Dudugu. A survey on text mining techniques. In *2019 5th International Conference on Advanced Computing and Communication Systems, ICACCS*

2019, pages 1022–1026. Institute of Electrical and Electronics Engineers Inc., 2019. Cited by: 31.

[26] Roberto Navigli. Word sense disambiguation: A survey. *ACM Computing Surveys*, 41(2), 2009. Cited by: 1431.

[27] Yinglin Wang, Ming Wang, and Hamido Fujita. Word Sense Disambiguation: A comprehensive knowledge exploitation framework. *Knowledge-Based Systems*, 190, 2020. Cited by: 100; All Open Access, Hybrid Gold Open Access.

[28] Michele Bevilacqua, Tommaso Pasini, Alessandro Raganato, and Roberto Navigli. Recent trends in word sense disambiguation: A survey. In Zhou Z.-H., editor, *IJCAI International Joint Conference on Artificial Intelligence*, pages 4330–4338. International Joint Conferences on Artificial Intelligence, 2021. Cited by: 97.

[29] Erik F. Tjong Kim Sang and Fien de Meulder. Introduction to the CoNLL-2003 shared task: Language-independent named entity recognition. In *Proceedings of the 7th Conference on Natural Language Learning, CoNLL 2003 at HLT-NAACL 2003*, pages 142–147. Association for Computational Linguistics (ACL), 2003. Cited by: 2489.

[30] Zara Nasar, Syed Waqar Jaffry, and Muhammad Kamran Malik. Named entity recognition and relation extraction: State-of-the-art. *ACM Computing Surveys*, 54(1), 2021. Cited by: 125.

[31] Jing Li, Aixin Sun, Jianglei Han, and Chenliang Li. A survey on deep learning for named entity recognition. *IEEE Transactions on Knowledge and Data Engineering*, 34(1):50–70, 2022. Cited by: 747.

[32] Xavier Carreras and Lluís Márquez. Introduction to the CoNLL-2005 shared task: Semantic role labeling. In *CoNLL 2005 - Proceedings of the Ninth Conference on Computational Natural Language Learning*, pages 152–164, 2005. Cited by: 495.

[33] Luheng He, Kenton Lee, Mike Lewis, and Luke Zettlemoyer. Deep semantic role labeling: What works and what's next. In *ACL 2017 - 55th Annual Meeting of the Association for Computational Linguistics, Proceedings of the Conference (Long Papers)*, volume 1, pages 473–483. Association for Computational Linguistics (ACL), 2017. Cited by: 339.

[34] Amelia Devi Putri Ariyanto, Diana Purwitasari, and Chastine Fatichah. A systematic review on semantic role labeling for information extraction in low-resource data. *IEEE access : practical innovations, open solutions*, 12:57917–57946, 2024.

[35] Tomas Mikolov, Kai Chen, Greg Corrado, and Jeffrey Dean. Efficient estimation of word representations in vector space. In *1st International Conference on Learning Representations, ICLR 2013 - Workshop Track Proceedings*. ICLR, 2013. Cited by: 21489.

[36] Jeffrey Pennington, Richard Socher, and Christopher D. Manning. GloVe: Global vectors for word representation. In *EMNLP 2014 - 2014 Conference on Empirical Methods in Natural Language Processing, Proceedings of the Conference*, pages 1532–1543. Association for Computational Linguistics (ACL), 2014. Cited by: 25461.

[37] Gemma Boleda. Distributional semantics and linguistic theory. *Annual Review of Linguistics*, 6:213–234, 2020. Cited by: 125.

[38] Sébastien Harispe, Sylvie Ranwez, Stefan Janaqi, and Jacky Montmain. Semantic similarity from natural language and ontology analysis. *Synthesis Lectures on Human Language Technologies*, 8(1):1–256, 2015. Cited by: 142.

[39] Melinda McDaniel and Veda C. Storey. Evaluating domain ontologies: Clarification, classification, and challenges. *ACM Computing Surveys*, 52(4), 2019. Cited by: 76.

[40] Alberto Postiglione. Text mining with finite state automata via compound words ontologies. *Lecture Notes on Data Engineering and Communications Technologies*, 193:194–205, 2024.

[41] Ali Hassani, Amir Iranmanesh, and Najme Mansouri. Text mining using nonnegative matrix factorization and latent semantic analysis. *Neural Computing and Applications*, 33(20):13745–13766, 2021. Cited by: 25.

[42] Raja Muhammad Suleman and Ioannis Korkontzelos. Extending latent semantic analysis to manage its syntactic blindness. *Expert Systems with Applications*, 165, 2021. Cited by: 21.

[43] G. Deena and K. Raja. Keyword extraction using latent semantic analysis for question generation. *Journal of Applied Science and Engineering*, 26(4):501–510, 2023.

[44] Luke S. Zettlemoyer and Collins Michael. Learning to map sentences to logical form: Structured classification with probabilistic categorial grammars. In *Proceedings of the 21st Conference on Uncertainty in Artificial Intelligence, UAI 2005*, pages 658–666. AUAI Press, 2005. Cited by: 449.

[45] Jonathan Berant, Andrew Chou, Roy Frostig, and Percy Liang. Semantic parsing on freebase from question-answer pairs. In *EMNLP 2013 - 2013 Conference on Empirical Methods in Natural Language*

Processing, Proceedings of the Conference, pages 1533–1544. Association for Computational Linguistics (ACL), 2013. Cited by: 1401.

[46] C.J. Fillmore and C.F. Baker. Frame semantics for text understanding. *Proceedings of WordNet and Other Lexical Resources Workshop*, 2001. Cited by: 138.

[47] Ivan A. Sag, Timothy Baldwin, Francis Bond, Ann Copestake, and Dan Flickinger. Multiword expressions: A pain in the neck for NLP. *Lecture Notes in Computer Science (including subseries Lecture Notes in Artificial Intelligence and Lecture Notes in Bioinformatics)*, 2276:1–15, 2002. Cited by: 593.

[48] Mathieu Constant, Gülşen Eryiğit, Johanna Monti, Lonneke Van Der Plas, Carlos Ramisch, Michael Rosner, and Amalia Todirascu. Multiword expression processing: A survey. *Computational Linguistics*, 43(4):837–892, 2017. Cited by: 129.

[49] Charu C. Aggarwal and ChengXiang Zhai. A survey of text classification algorithms. In Charu C. Aggarwal and ChengXiang Zhai, editors, *Mining Text Data*, pages 163–222. Springer US, Boston, MA, 2012. Cited by: 1243.

[50] Kamran Kowsari, Kiana Jafari Meimandi, Mojtaba Heidarysafa, Sanjana Mendu, Laura Barnes, and Donald Brown. Text classification algorithms: A survey. *Information (Switzerland)*, 10(4):article no. 150, 2019. Cited by: 587.

[51] Mukesh Kumar, Sushil Kumar, and Saneh Lata Yadav. *Data Mining for the Internet of Things: A Survey*. Apple Academic Press, 2023.

[52] Vishal Gupta and Gurpreet S. Lehal. A survey of text mining techniques and applications. *Journal of Emerging Technologies in Web Intelligence*, 1(1):60–76, 2009. Cited by: 476.

[53] Juan Miguel Cejuela, Peter McQuilton, Laura Ponting, S.J. Marygold, Raymund Stefancsik, Gillian H. Millburn, and Burkhard Rost. Tagtog: Interactive and text-mining-assisted annotation of gene mentions in PLOS full-text articles. *Database-the Magazine of Electronic Database Reviews*, 2014:article no. bau033, 2014. Cited by: 49.

[54] Gleb Danilov, Timur Ishankulov, Konstantin Kotik, Yuriy Orlov, Mikhail Shifrin, and Alexander Potapov. *The Classification of Short Scientific Texts Using Pretrained BERT Model*. IOS Press, 2021.

[55] I.K. Kusakin, O.V. Fedorets, and A.Y. Romanov. Classification of short scientific texts. *Scientific and Technical Information Processing*, 50(3):176–183, 2023.

[56] B. Shravan Kumar and Vadlamani Ravi. A survey of the applications of text mining in financial domain. *Knowledge-Based Systems*, 114:128–147, 2016. Cited by: 161.

[57] Aaryan Gupta, Vinya Dengre, Hamza Abubakar Kheruwala, and Manan Shah. Comprehensive review of text-mining applications in finance. *Financial Innovation*, 6(1):1–25, article no. 39, 2020. Cited by: 58.

[58] Chih-Yuan Chu, Kijung Park, and Gül E. Kremer. A global supply chain risk management framework: An application of text-mining to identify region-specific supply chain risks. *Advanced Engineering Informatics*, 45:1–17, article no. 101053, 2020. Cited by: 69.

[59] Alberto Postiglione and Mario Monteleone. Predictive maintenance with linguistic text mining. *Mathematics*, 12(7):1–18, paper no. 1089, 2024.

[60] E.W.T. Ngai and P.T.Y. Lee. A review of the literature on applications of text mining in policy making. In PACIS, editor, *Pacific Asia Conference on Information Systems, PACIS 2016 - Proceedings*, page article no. 125137. Pacific Asia Conference on Information Systems, 2016. Cited by: 19.

[61] Rafael Ferreira-Mello, Máverick André, Anderson Pinheiro, Evandro Costa, and Cristobal Romero. Text mining in education. *Wiley Interdisciplinary Reviews: Data Mining and Knowledge Discovery*, 9(6):1–49, article no. e1332, 2019. Cited by: 102.

[62] B. Drury and Mathieu Roche. A survey of the applications of text mining for agriculture. *Computers and Electronics in Agriculture*, 163:1–13, article no. 104864, 2019. Cited by: 29.

[63] Adeline Abbe, Cyril Grouin, Pierre Zweigenbaum, and Bruno Falissard. Text mining applications in psychiatry: A systematic literature review. *International Journal of Methods in Psychiatric Research*, 25(2):86–100, 2016. Cited by: 75.

[64] Sudha Cheerkoot-Jalim and Kavi Kumar Khedo. A systematic review of text mining approaches applied to various application areas in the biomedical domain. *Journal of Knowledge Management*, 25(3):642–668, 2020. Cited by: 15.

[65] Ignacio Rodríguez-Rodríguez, José-Víctor Rodríguez, Niloofar Shirvanizadeh, Andrés Ortiz, and Domingo-Javier Pardo-Quiles. Applications of artificial intelligence, machine learning, big data and the internet of things to the COVID-19 pandemic: A scientometric review using text mining. *International Journal of Environmental Research and Public Health*, 18(16):article no. 8578, 2021. Cited by: 26.

[66] Fotis A Baltoumas and al. OnTheFly2.0: A text-mining web application for automated biomedical entity recognition, document annotation, network and functional enrichment analysis. *NAR Genomics and Bioinformatics*, 3(4):article no. lqab090, 2021. Cited by: 11.

[67] V. Giannella, F. Bardozzo, A. Postiglione, R. Tagliaferri, R. Sepe, and E. Armentani. Neural networks for fatigue crack propagation predictions in real-time under uncertainty. *Computers and Structures*, 288, 2023.

[68] Rizwana Irfan, Christine K. King, Daniel Grages, Sam Ewen, Samee U. Khan, Sajjad A. Madani, Joanna Kolodziej, Lizhe Wang, Dan Chen, Ammar Rayes, Nikolaos Tziritas, Cheng-Zhong Xu, Albert Y. Zomaya, Ahmed Saeed Alzahrani, and Hongxiang Li. A survey on text mining in social networks. *Knowledge Engineering Review*, 30(2):157–170, 2015. Cited by: 87.

[69] Said A. Salloum, Mostafa Al-Emran, Azza Abdel Monem, and Khaled Shaalan. A survey of text mining in social media: Facebook and Twitter perspectives. *Advances in Science, Technology and Engineering Systems*, 2(1):127–133, 2017. Cited by: 151.

[70] Alberto Postiglione and Giustino De Bueriis. On Web's contact structure. *Journal of Ambient Intelligence and Humanized Computing*, 10(7):2829–2841, 2019.

[71] Jan Dědek, Peter Vojtáš, and Marta Vomlelová. Fuzzy ILP Classification of web reports after linguistic text mining. *Information Processing and Management*, 48(3):438–450, 2012.

[72] Yang-Cheng Lu, Chung-Hua Shen, and Yu-Chen Wei. Revisiting early warning signals of corporate credit default using linguistic analysis. *Pacific Basin Finance Journal*, 24:1–21, 2013. Cited by: 28.

[73] Frederik Cailliau and Ariane Cavet. Mining automatic speech transcripts for the retrieval of problematic calls. *Lecture Notes in Computer Science (including subseries Lecture Notes in Artificial Intelligence and Lecture Notes in Bioinformatics)*, 7817 LNCS(PART 2):83–95, 2013. Cited by: 9.

[74] Francisco Villarroel Ordenes, Babis Theodoulidis, Jamie Burton, Thorsten Gruber, and Mohamed Zaki. Analyzing customer experience feedback using text mining: A linguistics-based approach. *Journal of Service Research*, 17(3):278–295, 2014. Cited by: 139.

[75] R. Jindal and S. Taneja. A novel weighted classification approach using linguistic text mining. *International journal of computer applications*, 180(2):9–15, 2017.

[76] Tobias Nießner, Daniel H. Gross, and Matthias Schumann. Evidential strategies in financial statement analysis: A corpus linguistic text mining approach to bankruptcy prediction. *Journal of Risk and Financial Management*, 15(10), 2022.

[77] Alberto Postiglione. Finite state automata on multi-word units for efficient text-mining. *Mathematics*, 12(4):1–20, paper no. 506, 2024.

[78] Maurice Gross. Lexicon-grammar and the syntactic analysis of French. In *10th International Conference on Computational Linguistics, COLING 1984 and 22nd Annual Meeting of the Association for Computational Linguistics, ACL 1984*, pages 275–282. Association for Computational Linguistics (ACL), 1984. Cited by: 26.

[79] Maurice Gross. The construction of electronic dictionaries; [La construction de dictionnaires électroniques]. *Annales Des Télécommunications*, 44(1-2):4–19, 1989. Cited by: 21.

[80] Maurice Gross. The use of finite automata in the lexical representation of natural language. *Lecture Notes in Computer Science (including subseries Lecture Notes in Artificial Intelligence and Lecture Notes in Bioinformatics)*, 377 LNCS:34–50, 1989. Cited by: 25.

[81] Alfred V. Aho and Margaret J. Corasick. Efficient string matching: An aid to bibliographic search. *Communications of the ACM*, 18(6):333–340, 1975. Cited by: 2250.

[82] Maxime Crochemore, Christophe Hancart, and Thierry Lecroq. *Algorithms on Strings*, volume 9780521848992. Cambridge University Press, 2007. Cited by: 391.

[83] Ramanpreet Singh and Ali A. Ghorbani. EfficientPMM: Finite automata based efficient pattern matching machine. In Lees M., Sloot P., Krzhizhanovskaya V., Dongarra J., and Koumoutsakos P., editors, *Procedia Computer Science*, volume 108, pages 1060–1070. Elsevier B.V., 2017.

[84] Saqib Iqbal Hakak, Amirrudin Kamsin, Palaiahnakote Shivakumara, Gulshan Amin Gilkar, Wazir Zada Khan, and Muhammad Imran. Exact string matching algorithms: Survey, issues, and future research directions. *IEEE access : practical innovations, open solutions*, 7:69614–69637, 2019. Cited by: 61.

[85] Annibale Elia, Mario Monteleone, and Alberto Postiglione. Cataloga: A software for semantic-based terminological data mining. In *1st International Conference on Data Compression, Communication and Processing,IEEE,Palinuro(SA),June 21-24*, pages 153–156. IEEE Computer Society, 2011.

[86] Annibale Elia, Alberto Postiglione, Mario Monteleone, Johanna Monti, and Daniela Guglielmo. CATALOGA©: A software for semantic and terminological information retrieval. In *ACM International*

Conference Proceeding Series, pages 1–9, 2011.

[87] Muhammad Usman Hadi, qasem al tashi, Rizwan Qureshi, Abbas Shah, amgad muneer, Muhammad Irfan, Anas Zafar, Muhammad Bilal Shaikh, Naveed Akhtar, Jia Wu, and Seyedali Mirjalili. Large language models: A comprehensive survey of its applications, challenges, limitations, and future prospects. *Authorea Preprints*, 2023.

[88] Bonan Min, Hayley Ross, Elior Sulem, Amir Pouran Ben Veyseh, Thien Huu Nguyen, Oscar Sainz, Eneko Agirre, Ilana Heintz, and Dan Roth. Recent advances in natural language processing via large pre-trained language models: A survey. *ACM Computing Surveys*, 56(2), 2023. Cited by: 12.

[89] Min Zhang and Juntao Li. A commentary of GPT-3 in MIT technology review 2021. *Fundamental Research*, 1(6):831–833, 2021. Cited by: 32.

[90] Tom B. Brown and et al. Language models are few-shot learners. In *Advances in Neural Information Processing Systems*, volume 2020-December. Neural information processing systems foundation, 2020. Cited by: 6032.

[91] Patrick Schramowski, Cigdem Turan, Nico Andersen, Constantin A. Rothkopf, and Kristian Kersting. Large pre-trained language models contain human-like biases of what is right and wrong to do. *Nature Machine Intelligence*, 4(3):258–268, 2022. Cited by: 51.

[92] Jie Huang, Hanyin Shao, and Kevin Chen-Chuan Chang. Are large pre-trained language models leaking your personal information? In Goldberg Y., Kozareva Z., and Zhang Y., editors, *Findings of the Association for Computational Linguistics: EMNLP 2022*, pages 2038–2047. Association for Computational Linguistics (ACL), 2022.

Fuzzy Systems and Data Mining X
A.J. Tallón-Ballesteros (Ed.)

doi:10.3233/FAIA241434

Early Drought Prediction Using MODIS Time Series with LSTM: A Study of the Western United States

Somsak Limchupanpanich[a], Tanakorn Sritarapipat[b,1], Sayan Kaennakham[b] and Suwit Ongsomwang[b]
[a] *Department of Interdisciplinary Science and Internationalization, Institute of Science, Suranaree University of Technology, Nakhon Ratchasima, 30000, Thailand*
[b] *School of Mathematics and Geoinformatics, Institute of Science, Suranaree University of Technology, Nakhon Ratchasima, 30000, Thailand*
ORCiD ID: Somsak Limchupanpanich https://orcid.org/0009-0002-4740-8903
Tanakorn Sritarapipat https://orcid.org/0009-0009-0557-527X
Sayan Kaennakhamhttps://orcid.org/0000-0001-9682-559X
Suwit Ongsomwang https://orcid.org/0000-0002-2296-0374

Abstract. Droughts impose severe global challenges by affecting water resources, agricultural productivity, and ecosystems, and presenting considerable socioeconomic risks. In the Western United States, increasing aridity and reliance on limited water sources aggravate these issues. Accurate and timely drought forecasting is essential for effective water management, mitigating agricultural impacts, and addressing broader economic and environmental concerns. This research introduces a novel approach for early drought prediction by using remotely sensed data, with a specific focus on the drought-prone states of California and Nevada. We analyse MODIS (Moderate Resolution Imaging Spectroradiometer) time series data from 2001 to 2015 to derive indices such as the Vegetation Condition Index (VCI) and Temperature Condition Index (TCI), These indices serve as monthly indicators of drought severe. We utilize the Long Short-Term Memory (LSTM) model to predict the Vegetation Condition Index (VCI), Temperature Condition Index (TCI). Subsequently, the annual average values of these indices are employed with linear regression to estimate drought severity levels. The results indicate that this hybrid approach enhances predictive accuracy by effectively integrating temporal dynamics with vegetation indices, providing actionable drought forecasts.

Keywords. Vegetation Condition Index (VCI), Temperature Condition Index (TCI), LSTM model

1. Introduction

Droughts are a major global challenge, posing significant threats to agriculture, ecosystems, and human well-being [1, 2]. These natural events are complex, driven by intricate factors like precipitation and soil moisture, and characterized by diverse features ranging from intensity to spatial extent [1, 2]. Drought forecasting with long lead times

[1]Corresponding Author, Tanakorn Sritarapipat; Email: tanakorn.s@sut.ac.th

is crucial for developing early warning systems and effective risk management strategies, especially in the Western US, which is highly susceptible to drought [1, 2, 3]. The problem of accurate long-term drought forecasting, up to a year in advance, is critical for agriculture planning and insurance [4]. However, this remains an unsolved problem due to data complexity and the stochastic nature of aridity [4].

Traditional methods relied on historical data, limiting their ability to capture complex drought patterns. Recent studies emphasize integrating remote sensing data with machine learning, as demonstrated by Gyaneshwar et al. (2023) and Nandgude et al. (2023), which highlight deep learning models' capacity to capture non-linear relationships and spatiotemporal dependencies [5,6]. Nay et al. (2018) further illustrate the improvement in forecasting accuracy through machine learning frameworks utilizing remotely sensed vegetation health data [7]. Advances in remote sensing technologies, such as MODIS Leaf Area Index (LAI) products, have bolstered drought early warning systems, as shown by Barrett et al. (2020) and Wang et al. (2022) [8,9]. Additionally, Zhong et al. (2019) and Kratzert et al. (2019) emphasize the effectiveness of long short-term memory (LSTM) networks in modeling long-term drought characteristics and addressing climate change impacts [10,11]. Overall, combining remote sensing with machine learning is transforming drought prediction methodologies and improving management strategies in vulnerable regions.

This research explores the potential of deep learning, specifically Long Short-Term Memory (LSTM) networks, to improve drought prediction in the Western United States, a region particularly vulnerable to drought due to rising aridity and limited water resources [1, 2, 3]. Our findings demonstrate that LSTMs can effectively model the complex spatiotemporal patterns of drought, leading to significantly improved prediction accuracy, particularly for longer-term forecasting horizons. Our model shows promising results for shorter-term forecasting.

2. Methodology

2.1 Dataset and Study Area

In this study, we utilize the Moderate Resolution Imaging Spectroradiometer (MODIS) to monitor drought conditions by analyzing vegetation and temperature indices. The dataset includes the Normalized Difference Vegetation Index (NDVI), derived from the MOD13A2 product, which indicates vegetation health, and Land Surface Temperature (LST), extracted from the MOD11A2 product.

To understand the specific severity of a drought, it's essential to refer to the classifications used by the particular drought monitoring organization or research project. Drought Severe Level is a general term that can refer to various levels of drought severity. One widely recognized system is the U.S. Drought Monitor, which classifies droughts into five levels: N(Normal): Normal situation, D0 (Abnormally Dry): Below-normal topsoil moisture, minimal impacts on crops. D1 (Moderate Drought): Significant moisture deficits affecting crops and water supplies. D2 (Severe Drought): Widespread crop losses and increasing water shortages. D3 (Extreme Drought): Severe crop losses, major water shortages, risk of wildfires. D4 (Exceptional Drought): Widespread crop failures and extreme water shortages with major economic impacts [12].

We chose to focus on the Western US, particularly California and Nevada, due to its unique drought challenges and heavy reliance on irrigation in agriculture [6]. The

region's semi-arid climate, compounded by climate change and population growth, significantly impacts crop yields and livestock [13]. Additionally, complex water rights and over-reliance on groundwater lead to aquifer depletion. Understanding these issues is crucial for developing effective strategies for sustainable agricultural practices in this vital area.

2.2 Method

2.2.1 MODIS Time Series Data

The MOD13A2 product provides the Normalized Difference Vegetation Index (NDVI) data every 16 days, while the MOD11A2 product offers Land Surface Temperature (LST) data every 8 days, both at a spatial resolution of 1 km. To facilitate a comprehensive analysis of long-term drought trends, the data from these products were aggregated into monthly intervals.

2.2.2 Calculation of VCI and TCI

The Vegetation Condition Index (VCI) [14] and Temperature Condition Index (TCI) [15] are calculated to assess drought stress on vegetation at a county level and monthly.

$$VCI = \frac{(NDVI - NDVI_{min})}{(NDVI_{max} - NDVI_{min})} * 100 \quad (1)$$

Where NDVImin and NDVImax represent the minimum and maximum NDVI values over the historical period.

High VCI values indicate healthy vegetation, while lower values suggest drought stress.

$$TCI = \frac{(LST_{max} - LST)}{(LST_{max} - LST_{min})} * 100 \quad (2)$$

where LSTmax and LSTmin represent the maximum and minimum historical LST values.

High TCI values indicate low thermal stress, while lower values suggest significant thermal stress, often associated with drought.

2.2.3 Forecasting VCI and TCI Using LSTM

To leverage the temporal relationships inherent in weather and drought patterns, we use Long Short Term Memory (LSTM) networks [16], specifically incorporating the Vegetation Condition Index (VCI) and Temperature Condition Index (TCI) derived from MODIS data along with the US Drought Monitor datasets. This approach emphasizes forecasting the Vegetation Condition Index (VCI) and Temperature Condition Index (TCI). Initially, the data is scaled to normalize the values within a range of 0 to 1. The Long Short-Term Memory (LSTM) model is structured with a single hidden layer containing 100 units, followed by one output unit that predicts continuous values for both VCI and TCI. In this study, we varied the input lengths to 3 months, 6 months, and 9 months to assess the model's predictive performance over extended observation periods. The formulas for LSTM for each layer and each element in the input sequence are shown in (Eqn. 3):

Input Gate: $i_t = \sigma(\omega_i[h_{t-1}, x_t] + b_i)$ (3)

Forget Gate: $f_t = \sigma(\omega_f[h_{t-1}, x_t] + b_f)$

Cell Input: $g_t = tanh(\omega_c[h_{t-1}, x_t] + b_c)$

Output Gate: $o_t = \sigma(\omega_o[h_{t-1}, x_t] + b_o)$

Cell State Update: $c_t = f_t * c_{t-1} + i_t * g_t$

Hidden State Update: $h_t = o_t * tahn(c^t)$

where:
σ represent sigmoid function
ω_x is weight for the respective gate(x) neuron
h_{t-1} is output of the previous LSTM block (at time stamp t-1)
x_t is input at current timestamp
b_x is biases for the respective gates(x)

For tuning the LSTM model, we used the Adam optimizer with a learning rate of 0.001 to minimize mean square error (MSE), a batch size of 1, and trained the model for 20 epochs. Early stopping was applied if the validation error increased twice consecutively.

2.2.4 Prediction of Drought Severity Levels

Agricultural drought occurs when prolonged dry conditions affect crops and soil moisture. Predicting drought severity requires understanding long-term conditions, as short-term weather fluctuations may not provide sufficient insight into the broader trends affecting agriculture. In this research, we developed a model to predict yearly drought severity levels by leveraging the average annual TCI and VCI.. A linear regression model is well-suited for this task, particularly when the relationship between these indices and drought severity is approximately linear. The dataset is divided into training (70%) and testing (30%) subsets, allowing the model to learn the correlation between TCI, VCI, and drought severity during training, while the testing phase evaluates its predictive accuracy. We examined the model's performance under three conditions: 1) using VCI, 2) using TCI, and 3) using both VCI and TCI. The linear regression equation is: (Eqn. 4).

$$y = b_0 + b_1 * x_1 + b_2 * x_2 \quad (4)$$

where:
y is the predicted annual drought severity level ([0-5])
(N=0, D0=1, D1 =2 D2 =3, D3=4, D4=5)
b_0 is the intercept.
b_1, b_2 are the regression coefficients.
x_1, x_2 are the annual average annual VCI and TCI, respectively.

For early predictions of drought severity, we utilized linear regression with actual and forecasted annual average VCI and TCI. The prediction horizons were varied as

follows: 3 months (using actual indexes from January to March and forecasted indexes from April to December), 6 months (using actual indexes from January to June and forecasted indexes from July to December), and 9 months (using actual indexes from January to September and forecasted indexes from October to December)

3. Experimental Results

In this section, we present the results of the experiments conducted to evaluate the performance of the LSTM model in forecasting VCI and TCI (3.1). Then, the evaluation of predicting yearly drought severity is given (3.2). Finally, we evaluated the early prediction of yearly drought severity (3.3).

3.1 Evaluation of Forecasting VCI and TCI

We applied the LSTM model to forecast the VCI and TCI over varying lengths of 3, 6, and 9 months, utilizing data from 2001 to 2010 for training. The model's performance was evaluated using data from 2011 to 2015 (Table 1).

Table 1. RMSE of forecasted TCI and VCI over varying period months in California and Nevada

	California		**Nevada**	
	RMSE of forecasted VCI	RMSE of forecasted TCI	RMSE of forecasted VCI	RMSE of forecasted TCI
3 months	0.224	0.315	0.164	0.154
6 months	0.225	0.329	0.378	0.184
9 months	0.309	0.341	0.363	0.198

3.2 Evaluation of Predicting Drought Severity Levels

We applied a linear regression model in predicting drought severity levels with the actual average VCI and TCI over the period from 2001 to 2015, with 70% of the data for training and 30% for testing. The R-Square is given in table 2.

Table 2. R-square of predicting drought severity varying variables in California and Nevada

	California	Nevada
	R-Square	R-Square
Annual average VCI	0.06	0.03
Annual average TCI	0.48	0.29
Annual average VCI and TCI	0.52	0.32

3.3 Evaluation of Early Predicting Drought Severity Levels

Then, we employed the linear regression model using the actual and forecasted annual average VCI and TCI, focusing on a 3-month forecast length over the period from 2011 to 2015, and the performance of the models across varying actual and forecasted indexes with 3, 6, and 9 months is given in Table 3.

Table 3. RMSE of early predicting drought severity varying actual and forecast months using annual average VCI and TCI in California and Nevada

	California	Nevada
	RMSE of early predicting drought varying	RMSE of early predicting drought varying
3 months (Jan-Mar)	1.70	1.06
6 months (Jan-Jun)	1.09	0.80
9 months (Jan-Sep)	1.07	0.99

4. Discussion

Based on the results in section 3.1, the average RMSE across both states is 0.277 for the VCI and 0.254 for the TCI, indicating the LSTM model's effectiveness in forecasting these indices. In California, the average RMSE is 0.253 for VCI and 0.328 for TCI, whereas Nevada shows a lower average RMSE of 0.302 for VCI and 0.179 for TCI. The results indicate similar performance across California and Nevada, implying consistent model accuracy in both states. For varying forecast lengths, the model demonstrated high accuracy across 3, 6, and 9 months in predicting VCI and TCI, with the 3-month forecast consistently providing nearly the highest accuracy for both indices in California and Nevada. Therefore, a 3-month forecast period is suggested for optimal accuracy in predicting TCI and VCI in this study.

In section 3.2, the experimental results demonstrate that using the combined annual average VCI and TCI yields the highest accuracy for predicting drought severity, particularly in California, with an R-Square of approximately 0.52. In Nevada, the combined model shows a lower R-Square of 0.32. The performance of models using annual average VCI and TCI together (California: R-Square 0.52, Nevada: R-Square 0.32) and TCI alone (California: R-Square 0.48, Nevada: R-Square 0.29) is quite similar, while using only VCI results in significantly lower accuracy (California: R-Square 0.06, Nevada: R-Square 0.03). Consequently, this research adopts a linear regression approach with the combined annual average VCI and TCI to achieve more reliable drought severity predictions.

Based on section 3.3, the experimental results indicate that RMSE values are low, demonstrating a general trend of decreasing RMSE as the number of actual value months increases. Specifically, the 9-month forecast shows RMSE values of 1.07 for California and 0.99 for Nevada, and the 6-month forecast yields RMSE values of 1.09 for California and 0.80 for Nevada, both reflecting high accuracy. In contrast, the 3-month forecast exhibits lower accuracy, with RMSE values of 1.70 for California and 1.06 for Nevada. This research underscores the effectiveness of early prediction, particularly with the 6-month forecast, suggesting that the proposed model for predicting drought severity operates efficiently. This implies that by utilizing actual data from January to June, the model can predict drought severity with RMSE values around 1 (on drought severity levels of 0 to 5). Consequently, this model can be employed for timely drought planning and mitigation strategies.

5. Conclusions

This research proposed a combined approach utilizing the Vegetation Condition Index (VCI) and Temperature Condition Index (TCI) to predict yearly drought severity levels in California and Nevada. The experimental results demonstrated that the Long Short-

Term Memory (LSTM) model achieved progressively lower RMSE values over longer forecast periods, with average RMSE values of 0.252 for VCI and 0.328 for TCI in California, and 0.302 for VCI and 0.179 for TCI in Nevada, indicating superior predictive accuracy, particularly in Nevada. In California, while the model showed a consistent decrease in RMSE for VCI, the performance for TCI exhibited slight variability. Additionally, linear regression analysis highlighted that using both VCI and TCI enhanced prediction accuracy across varying forecast horizons, with average RMSE values of 1.09 for the combined indices at the 6-month forecast in California and 0.80 for Nevada. These findings underscore the significance of employing advanced modeling techniques and appropriate indices in drought forecasting, which can provide critical insights for agricultural and resource management strategies in drought-prone regions.

References

[1] Bolen, Bennett, et al. "Drought Prediction in the Western U.S. Using a Long Short-Term Memory (LSTM) Model." CS230: Deep Learning, Winter 2021, Stanford University, CA. (LateX template borrowed from NIPS 2017.)

[2] Mohammed, S., Elbeltagi, A., Bashir, B., Alsafadi, K., Alsilibe, F., Alsalman, A., Harsányi, E., 2022. A comparative analysis of data mining techniques for agricultural and hydrological drought prediction in the eastern mediterranean. Computers and Electronics in Agriculture 197, 1–19.

[3] Ghozat, A., Sharafati, A., Asadollah, S.B.H.S., Motta, D., 2023. A novel intelligent approach for predicting meteorological drought based on satellite based precipitation product: Application of an emd-dfa-dbn hybrid model. Computers and Electronics in Agriculture 211.

[4] Alexander Marusov, Vsevolod Grabar, Yury Maximov, Nazar Sotiriadi, Alexander Bulkin, Alexey Zaytsev, 2024. Long-term drought prediction using deep neural networks based on geospatial weather data. arXiv:2309.06212v6 [cs.LG]. https://doi.org/10.1016/j.envsoft.2024.106127.

[5] Gyaneshwar A, Mishra A, Chadha U, Raj Vincent PMD, Rajinikanth V, Pattukandan Ganapathy G, Srinivasan K., 2023. A Contemporary Review on Deep Learning Models for Drought Prediction. Sustainability 15, 6160. https://doi.org/10.3390/su15076160

[6] Nandgude N, Singh TP, Nandgude S, Tiwari M., 2023. Drought Prediction: A Comprehensive Review of Different Drought Prediction Models and Adopted Technologies. Sustainability 15, 11684. https://doi.org/10.3390/su151511684

[7] Nay, John & Burchfield, Emily & Gilligan, Jonathan, 2018. A Machine Learning Approach to Forecasting Remotely Sensed Vegetation Health. International Journal of Remote Sensing. 39. 1800-1816. 10.1080/01431161.2017.1410296.

[8] Adam B. Barrett, Steven Duivenvoorden, Edward E. Salakpi, James M. Muthoka, John Mwangi, Seb Oliver, Pedram Rowhani, 2020. Forecasting vegetation condition for drought early warning systems in pastoral communities in Kenya. Remote Sensing of Environment, Volume 248, 2020, 111886, ISSN 0034-4257, https://doi.org/10.1016/j.rse.2020.111886.

[9] Wang J, Si H, Gao Z, Shi L, 2022. Winter Wheat Yield Prediction Using an LSTM Model from MODIS LAI Products. Agriculture 12, 1707. https://doi.org/10.3390/agriculture12101707

[10] S. Zhong, L. Di, Z. Sun, Z. Xu and L. Guo, 2019. Investigating the Long-Term Spatial and Temporal Characteristics of Vegetative Drought in the Contiguous United States. IEEE Journal of Selected Topics in Applied Earth Observations and Remote Sensing, VOL. 12, NO. 3, MARCH 2019, 836-848. doi: 10.1109/JSTARS.2019.2896159.

[11] Kratzert, Frederik & Klotz, Daniel & Brandstetter, Johannes & Hoedt, Pieter-Jan & Nearing, Grey & Hochreiter, Sepp. (2019). Using LSTMs for climate change assessment studies on droughts and floods. 10.48550/arXiv.1911.03941.

[12] U.S. Drought Monitor. Drought Classification. Available at: U.S. Drought Monitor.

[13] Barrett, A. B., et al. (2020). Forecasting vegetation condition for drought early warning systems in pastoral communities in Kenya. Remote Sensing of Environment, 248, 111886. DOI: 10.1016/j.rse.2020.111886.

[14] Zhou, L., & H. E. M. R. (2008). "MODIS Vegetation Condition Index and Drought Monitoring." International Journal of Remote Sensing, 29(3), 675-695.

[15] Zhou, L., & G. M. (2010). "MODIS Temperature Condition Index (TCI) for Monitoring Drought: An Example for the Central United States." Remote Sensing of Environment, 114(1), 112-123.

[16] Zhang, Y., Liu, Y., & Chen, T. (2020). Long short-term memory networks for machine learning: A survey. Expert Systems with Applications, 102, 109–117.

Fuzzy Systems and Data Mining X
A.J. Tallón-Ballesteros (Ed.)

doi:10.3233/FAIA241435

Correlation Analysis over Big Multidimensional Datasets: A Powerful Paradigm for Next-Generation Big Data Analytics Research−Definitions, Models, Implementations

Alfredo CUZZOCREA[a,b, 1]
[a] *iDEA Lab, University of Calabria, Rende, Italy*
[b] *Department of Computer Science, University of Paris City, Paris, France*
ORCiD ID: Alfredo Cuzzocrea https://orcid.org/0000-0002-7104-6415

Abstract. *Correlation analysis* has been a powerful paradigm to discover and analyze *hidden properties* and *patterns* of large-scale datasets for decades. At now, correlation analysis turns to be a perfect tool for supporting *big multidimensional data* analysis and mining, with a wide range of relevant properties, including the amenity of supporting meaningfully exploration and discovery of multidimensional ranges kept in such kind of datasets. These operators are thus the basis for several *multidimensional big data analytical tools* that can be designed and implemented on top of the foundations defined by correlation functions. In line this this scientific area, the talk will provide introduction and motivations, models and algorithms, and, finally, best-practices guidelines for effective and efficient implementations of correlation-analysis-based tools over big multidimensional datasets.

Keywords. Big data, Big data analytics, Correlation analysis, Advanced big data analytics

1. Introduction

Nowadays, the emergence of *big data* has revolutionized various sectors, ranging from scientific research to *Business Intelligence* (BI), by offering unprecedented opportunities for discovering hidden insights from vast and complex datasets. In particular, the ability to find meaningful patterns between variables has become a critical driver of progress in fields such as *healthcare*, *finance*, *environmental science*, and so forth (e.g., [1,2]). One of the most prominent analytical tools to achieve this is *correlation analysis*. Historically, correlation analysis has served as an essential method for understanding relationships between variables by quantifying the degree to which they move together or apart. Over time this has been found to be effective when it comes to various data-oriented issues, right from simple bilinear relationships to several variable complications. In this context,

[1] Corresponding Author. E-mail: alfredo.cuzzocrea@unical.it – This research has been made in the context of the Excellence Chair in Big Data Management and Analytics at University of Paris City, Paris, France

as data volume, variety and velocity grow exponentially, the importance of correlation analysis amplifies, particularly when applied to *large-scale multidimensional datasets* (e.g., [3,4]).

The shift from traditional data analysis to big data analytics has increased the scope and volume of datasets while simultaneously posing fresh challenges in terms of complexity, dimensionality, and computing capability. Multidimensional data is common in a variety of disciplines, including sensor networks (e.g., [5]), geographical information systems (e.g., [6]), genomics (e.g., [7]), and financial markets (e.g., [8]), where datasets contain a large number of related variables that must be examined concurrently. While correlation analysis has long been used to uncover linear correlations between variables (e.g., [9]), applying it to multidimensional datasets necessitates dealing with a very complex data field in which patterns are difficult to detect. Despite its complexities, correlation analysis is particularly well-suited to big data analytics because it may be used as a strong exploratory technique to uncover previously unknown important patterns, anomalies, and connections (e.g., [10]).

Indeed, correlation analysis enables analysts to examine not just pairwise correlations but higher-order relationships that span multiple dimensions (e.g., [11]). These multidimensional correlations reveal intricate dependencies among variables, which are critical for applications like recommendation systems (e.g., [12,13]), risk management (e.g., [14]), and anomaly detection (e.g., [15,16]). Despite its advantages, the application of correlation analysis to big multidimensional datasets presents several challenges. One of the most prominent difficulties lies in managing the computational complexity inherent in analyzing large datasets with many dimensions. As the number of dimensions increases, so too does the complexity of the correlation functions required to analyze the data. This phenomenon, often referred to as the *curse of dimensionality* (e.g., [17,18]) results in computational bottlenecks, where the resources needed for analysis become prohibitively high. Thus, advanced techniques are required to filter out irrelevant data, mitigate the effects of noise, and ensure that correlation results are both accurate and reliable.

In light of these drawbacks, current research has centered on creating new models, algorithms, and tools for doing efficient and effective correlation analysis on large multidimensional data sets. Several computational methodologies, including dimensionality reduction techniques, parallel processing, and distributed computing, have been developed to overcome the scalability challenge. For instance, techniques like as *Principal Component Analysis* (PCA) (e.g., [19]) and *Single Value Decomposition* (SVD) (e.g., [20]) can minimize the number of dimensions in a dataset while maintaining the most essential variables, simplifying the study without sacrificing vital information. These developments, together with the development of powerful algorithms capable of handling high-dimensional spaces, have prepared the way for next-generation big data analytics that fully use correlation analysis.

Following these considerations, this paper aims to advance the current state of research in this domain by providing a comprehensive examination of correlation analysis applied to big multidimensional datasets. In doing so, it aims to contribute to both the theoretical and practical dimensions of big data analytics. Specifically, this paper will explore the fundamental definitions and models that reinforce correlation analysis in a multidimensional context, by offering insights into the mathematical and statistical foundations of the technique.

2. Related Work

In this Section, we provide a comprehensive overview of key research proposals that are closely aligned with our work on correlation analysis over big multidimensional datasets. We examine a range of studies that have addressed similar challenges in managing and analyzing high-dimensional data, with a particular focus on methods developed to uncover complex correlations across multiple variables.

[21] proposes eBoF, a novel visualization approach based on the *Bag-of-Features* (BoF) model, aimed at analyzing time-varying ensemble data. The eBoF method extracts simple, monotonic intervals from target variables in ensemble scalar data, which serve as local feature patches. Previous works in *ensemble data visualization* have mainly focused on static models or traditional clustering techniques, which often lose *geo-spatial information* and provide less detailed insights into temporal dynamics. Existing methods like topic modeling or clustering algorithms tend to overlook the temporal correlations and geographic features critical for comprehensive data analysis. eBoF addresses these limitations by incorporating *temporal correlation* into *feature clustering*, preserving spatial information that is often lost in conventional methods. The authors build on these limitations by introducing an approach that clusters *feature patches-based* on their temporal similarity, which offers a probability distribution across different clusters. This enables more insightful clustering results, which are validated using domain knowledge. Through case studies and performance evaluations, the authors demonstrate the effectiveness of eBoF in *ensemble simulation data analysis*, by comparing it against traditional methods in order to show its superior ability to retain *spatial-temporal insights*.

In [22], the authors introduce a novel approach leveraging *Canonical Correlation Analysis* (CCA) to explore the intricate relationships between electricity consumption, gas consumption, and climate factors within a *smart grid environment*. Unlike traditional approaches, which predominantly focused on *coarse-grained time* series analyses, which often rely on methods like *Autoregressive Distributed Lag* (ARDL) models to investigate long-term relationships over monthly or yearly intervals, this research addresses the emerging need for *fine-grained*, *high-resolution* data analysis. The increasing deployment of smart grids and *Internet of Things* (IoT) devices has enabled the collection of multidimensional, hourly consumption data, capturing complex interactions between internal factors, such as consumer behavior, and external variables, including climate, location, and building types. Traditional CCA methods, while effective for small-scale datasets, struggle with the computational demands and complexity introduced by these large, dynamic, and multidimensional datasets. This paper significantly extends the application of CCA by proposing an optimized model, called *Canonical Correlation Analysis with an Optimal Result Selection Mechanism* (CCASM), which is specifically designed to handle the volume and granularity of big data. CCASM improves upon classical CCA by offering enhanced computational efficiency and the ability to manage large-scale multivariable datasets, providing a more scalable and accurate means of analyzing fine-grained relationships in energy consumption patterns. By segmenting consumers based on geographic and climatic factors, this model not only allows for a more detailed understanding of consumption behaviors but also enables cross-sectional analysis across various demographic and environmental conditions.

[23] addresses the computational challenges of *Generalized Canonical Correlation Analysis* (GCCA) in handling *large-scale multi-view* data. While classical GCCA has been extensively studied for integrating information across multiple feature spaces, many

existing algorithms face significant memory and computational demands, limiting their scalability. To overcome these issues, the authors propose *scalable* and *distributed* GCCA algorithms that reduce complexity by scaling linearly with the number of data points, while also efficiently handling sparse data. Previous works have introduced formulations like *sum-of-correlations* (SUMCOR) and *maximal variation* (MAX-VAR) for GCCA, but these often relied on *deflation-based methods*, which can lead to error propagation and computational inefficiencies. This paper improves upon those approaches by avoiding bottlenecks such as whitening processes, which traditionally increase computational load. By leveraging distributed computing, the proposed method enables more efficient analysis of large-scale datasets, which significantly enhances the scalability of GCCA for big data applications.

In [24], they delve into the application of correlation analysis within medical science, addressing the critical challenge of managing imprecise or uncertain data. It introduces an *improved Z-test* for correlation, explicitly designed to account for the inherent uncertainty often present in real-life datasets. While previous studies have predominantly relied on classical Z-tests, which assume precise and well-defined data, practical applications in fields like medicine frequently involve data with indeterminate values or interval-based measurements due to factors such as measurement error or variability in biological processes. To overcome these limitations, this paper extends conventional statistical approaches by incorporating *neutrosophic statistics*, a framework developed to handle *uncertainty*, *imprecision*, and *indeterminacy* in data. The improved Z-test is applied to assess the correlation between medical variables, such as *heartbeat* and *temperature*, where uncertainty in measurements is common. By comparing the performance of the proposed method against traditional statistical tests, the authors demonstrate its superiority in scenarios where data precision is uncertain, which highlights its practical significance in medical decision-making and diagnostics. This work not only improves the robustness of correlation analysis in medical contexts but also extends the applicability of statistical methods in fields where data reliability is a challenge.

When working with big, complicated datasets, correlation analysis is a frequently utilized method for exploratory data analysis. Three popular correlation techniques are compared with *Kendall's Rank Correlation, Spearman's Rank Correlation, and Pearson's Product-Moment Correlation*. In [25], they examine the association between the operational condition of industrial pumps and more than 207,000 variables in a *high-dimensional vibration dataset* using Spearman's rank correlation coefficient, a non-parametric measure. Because Spearman's correlation can capture monotonic correlations between variables and is resilient when dealing with *non-normally* distributed data, it was selected as the preferred method. Because of this, it works especially well in situations involving *non-linear* or *distribution-free* data. They employ Spearman's method to pinpoint important factors that have a strong correlation with the states of the pump. This allows for a more focused approach to further analysis, particularly in the development of unsupervised machine learning models. [25] makes a further contribution by using the *R Programming Language* and effective computational techniques to manage the enormous dataset and calculate correlation values. Their findings are important for machine diagnostics and predictive maintenance since the vibration analysis they conducted identifies mechanical problems early on, which may assist avoid expensive machine failures.

In [26], the authors investigate how China's targeted poverty alleviation through education may be addressed through the use of machine learning models and

spatiotemporal correlation analysis. The *Average Education Years* (AEY) and *Gross Domestic Product per Capital* (GDP/C) are the main subjects of their research, which finds a strong positive association between the two. The authors using a combination of remote sensing data and geospatial analysis, offering insights into how enhancing education may fight poverty, examine the distribution of poverty among provinces. In order to identify important factors impacting education levels, such as population distribution and economic development, the study uses *Principal Component Analysis* (PCA). A *Linear and Residual Integration Model* (LRIM) is then constructed. This model uses a *Back Propagation* (BP) neural network to handle nonlinear residuals and linear time series models (ARIMA) to forecast trends in educational progress. Furthermore, using nighttime light data, they categorize impoverished counties using *Random Forest* algorithms, attaining great accuracy in the spatiotemporal analysis of poverty distribution from 1995 to 2010. Their method combines *cutting-edge* big data processing and machine learning techniques to deliver practical insights for educational policy meant to combat poverty. By fusing classical statistical models with spatial analysis, this work advances the discipline and provides a fresh viewpoint on focused education-based initiatives to reduce poverty.

Using data mining techniques and clustering algorithms, the authors investigate the association between middle school student subjective well-being and physical activity in this paper. In order to gauge the amount of physical activity and subjective well-being of 1,848 students from five cities in Sichuan Province, China, the authors performed a study and gathered information via questionnaires. They discovered that student overall levels of physical activity were inadequate, with girls exhibiting noticeably lower levels of exercise. A strong relationship between life happiness, emotional balance, and exercise frequency was found by the data analysis. Pupils who exercised on a regular basis reported feeling better about themselves subjectively than those who did not. The scientists optimized data processing and increased accuracy in assessing the correlations between variables by using a clustering technique based on swarm intelligence, which is comparable to ant colony models. Overall, [27] highlights the value of physical education in enhancing overall well-being and offers insightful recommendations for enhancing middle school kids physical and mental health. The authors come to the conclusion that encouraging young people to participate in sports, especially girls, is crucial to advancing their mental and physical development.

Authors of [28] use the *Hilbert-Huang Transform* (HHT) to analyze spatial spatiotemporal large data, addressing the difficulties in doing so. They understand that *non-stationary* signals, which are a feature of geographic data, cannot be processed by conventional techniques like *Fourier* or *wavelet* transformations. Authors suggest utilizing the HHT to calculate the instantaneous frequency of geographic data in order to get around these restrictions. This method offers a more precise and flexible representation of non-stationary and non-linear signals. They supplement this by assessing correlations between non-stationary variables across several scales using an absolute *entropy-based* correlation technique that is based on *Kullback-Leibler* (KL) divergence. This method captures both local and global correlations in the data, which enables a more thorough understanding of the connections between geographic elements. The authors used five geographic elements from Beijing and Tianjin across several decade population, civil vehicles, business volume of post and telecommunications, local phone users, and undergraduate students to validate their strategy. They show that, especially when dealing with *non-stationary* data, their method outperforms better-established correlation techniques like *spectral angle mapping* and *Pearson correlation*.

In summary, this research clearly demonstrates that by utilizing these enhanced correlation insights, the suggested method not only provides more precise correlation analysis for spatial spatiotemporal large data but also paves the way for future research, including predictive modeling.

3. Correlation Analysis over Big Multidimensional Datasets

In this Section, we introduce the main approach of this paper, which consists of presenting a comprehensive framework designed to facilitate efficient correlation analysis over big multidimensional datasets.

In the context of the rapidly evolving landscape of big data analytics, the need for frameworks that can handle complex, hierarchical data structures while preserving privacy is paramount. This is where the Drill-CODA framework [29] brings significant advancements to the field of multidimensional big data analytics.

Drill-CODA is a composite framework designed to support drill-across multidimensional big data analytics over big co-occurrence aggregate hierarchical data, while simultaneously preserving privacy. The framework addresses critical challenges faced by big data analytics, including the complexity and scale of real-life hierarchical datasets. By combining data processing metaphors and multidimensional analysis principles, Drill-CODA enhances the expressive power and accuracy of decision-making processes. In [29], Drill-CODA is presented as a framework that allows for the execution of drill-across queries in a way that both respects the hierarchical structure of the data and ensures privacy through aggregation and co-occurrence analysis. This innovative approach allows the extraction of valuable insights from big hierarchical data while maintaining privacy constraints through anonymization and multidimensional aggregation.

Figure 1 shows our proposed reference architecture for supporting efficient and effective correlation analysis over big multidimensional datasets.

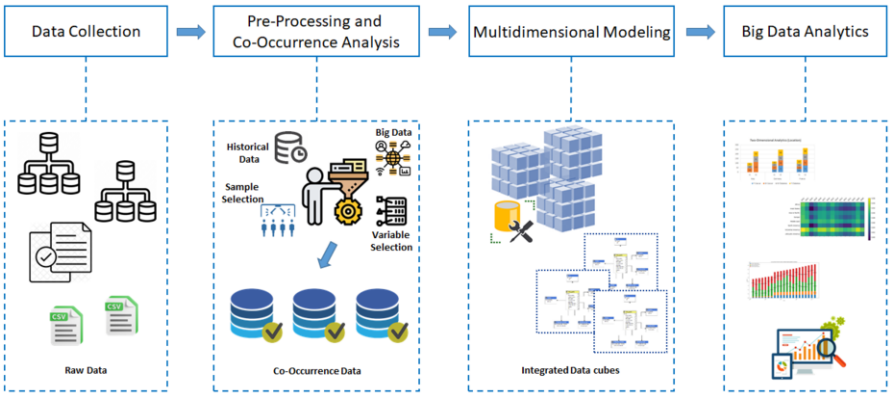

Figure 1. Reference Architecture for Supporting Correlation Analysis over Big Multidimensional Datasets.

As shown in Figure 1, our architecture encompasses several functional components that work collaboratively to enable correlation analysis over big multidimensional datasets, which we describe as follows:

- *Raw Data Collection Layer*: it is the foundation of the architecture, responsible for gathering all relevant data from various sources. These data come from multiple types of sources, including transactional databases, IoT sensors, social media platforms, and so forth.
- *Pre-Processing and Co-Occurrence Analysis Layer*: Once the raw data is collected, the next phase consists of a two-stage process. The first one is *data pre-processing*, which consists of cleaning data by removing duplicates, handling missing values, correcting data inconsistencies, as well as converting the data into a uniform format. The next phase is to apply *co-occurrence analysis* over the pre-processed datasets, which aims to identify patterns and correlations between different variables (e.g., how frequently two or more attributes occur together). Moreover, co-occurrence analysis can be used for *privacy-preserving aggregation*, as *sensitive* data can be anonymized during this stage.
- *Multidimensional Modeling Layer*: in this step, the co-occurrence data are organized into a *multidimensional data model*. This involves structuring data into OLAP data cubes, where dimensions such as *time* and *location* can be analyzed. This multidimensional modeling enables complex analyses like slicing, dicing, and pivoting of data.
- *Big Data Analytics and Visualization Layer*: this is the final layer of the architecture, where large-scale correlation analyses are performed over pre-processed and multidimensional data. This layer is designed to exploit the full potential of big data, by enabling highly efficient computation of complex queries and delivering valuable insights from vast and high-dimensional data collections. It supports a variety of analytical methods, including correlation analysis, trend discovery, and pattern recognition, through seamless integration with OLAP cubes.

However, it should be noted that in addition to the architecture implementation, [29] provides an extensive experimental assessment and evaluation of the Drill-CODA framework. The results demonstrated the framework's effectiveness in handling large-scale data processing while preserving privacy. The experimental setup involved real-life datasets, where Drill-CODA's performance in terms of processing time, scalability, and privacy preservation was rigorously tested. This further validates the practical application of the architecture described.

4. Conclusions and Future Work

Starting from the foundations of big data analytics, and the extended multidimensional big data analytics paradigm, this paper has presented models, issues and algorithms of correlation analysis tools for supporting big data analytics, along with the overview of a state-of-the-art proposal.

Future work is mainly oriented to *performance aspects* (e.g., [30-35]), which play a leading role when big multidimensional datasets must be accessed and processed.

Acknowledgments

This research is supported by the ICSC National Research Centre for High Performance Computing, Big Data and Quantum Computing within the NextGenerationEU program (Project Code: PNRR CN00000013).

References

[1] Jones DE, Ghandehari H, Facelli JC. A Review of the Applications of Data Mining and Machine Learning for the Prediction of Biomedical Properties of Nanoparticles. *Computer Methods and Programs in Biomedicine* 2016; 132: 93–103, doi: https://doi.org/10.1016/j.cmpb.2016.04.025

[2] Focardi SM, Fabozzi FJ. *The Mathematics of Financial Modeling and Investment Management*, John Wiley & Sons, 2004.

[3] Russom P. Big Data Analytics. *TDWI Best Practices Report, Fourth Quarter* 2011; 19(4): 1–34.

[4] Tsai C, Lai C, Chao H, Vasilakos AV. Big Data Analytics: A Survey. *Journal of Big Data* 2015; 2: 21, doi: https://doi.org/10.1186/s40537-015-0030-3

[5] Rao P, Kwon J, Lee S, Subramaniam LV. Advanced Big Data Management and Analytics for Ubiquitous Sensors. *International Journal of Distributed Sensor Networks* 2015; 11: 174894, doi: https://doi.org/10.1155/2015/174894

[6] Stefanidis A, Crooks A, Radzikowski J. Harvesting Ambient Geospatial Information from Social Media Feeds. *GeoJournal* 2013; 78: 319–338, doi: https://doi.org/10.1007/s10708-011-9438-2

[7] O'Driscoll A, Daugelaite J, Sleator RD. 'Big Data', Hadoop and Cloud Computing in Genomics. *Journal of Biomedical Informatics* 2013; 46(5): 774–781, doi: https://doi.org/10.1016/j.jbi.2013.07.001

[8] Ahmed M, Choudhury N, Uddin S. Anomaly Detection on Big Data in Financial Markets. In: *9th IEEE/ACM International Conference on Advances in Social Networks Analysis and Mining*. 2017 July 31 - August 03; Sydney, Australia. pp. 998–1001, doi: https://doi.org/10.1145/3110025.3119402

[9] Spearman C. The Proof and Measurement of Association between Two Things. *International Journal of Epidemiology* 2010; 39(5): 1137–1150, doi: https://doi.org/10.1093/ije/dyq191

[10] Tran H, Hu J. Privacy-Preserving Big Data Analytics: A Comprehensive Survey. *Journal of Parallel and Distributed Computing* 2019; 134: 207–218, doi: https://doi.org/10.1016/j.jpdc.2019.08.007

[11] Zhou X, Liang W, Wang KI, Yang LT. Deep Correlation Mining Based on Hierarchical Hybrid Networks for Heterogeneous Big Data Recommendations. *IEEE Transactions on Computational Social Systems* 2021; 8(1): 171–178, doi: https://doi.org/10.1109/TCSS.2020.2987846

[12] Wu Z, Yin W, Cao J, Xu J, Cuzzocrea A. Community Detection in Multi-Relational Social Networks. In: *14th International Conference on Web Information Systems Engineering*; 2013 October 13-15; Nanjing, China. pp. 43–56, doi: https://doi.org/10.1007/978-3-642-41154-0_4

[13] Leung CK, Kajal A, Won Y, Choi JMC. Big Data Analytics for Personalized Recommendation Systems. In: *IEEE DASC/PiCom/DataCom/CyberSciTech*. 2019 August 5-8; Fukuoka, Japan; pp. 1060–1065, doi: https://doi.org/10.1109/DASC/PiCom/CBDCom/CyberSciTech.2019.00190

[14] Yang R, Yu L, Zhao Y, Yu H, Xu G, Wu Y, Liu Z. Big Data Analytics for Financial Market Volatility Forecast based on Support Vector Machine. *International Journal of Information Management* 2020; 50: 452–462, doi: https://doi.org/10.1016/j.ijinfomgt.2019.05.027

[15] Chandola V, Banerjee A, Kumar V. Anomaly Detection: A Survey. *ACM Computing Surveys* 2009; 41(3): 1–58, doi: https://doi.org/10.1145/1541880.1541882

[16] Cuzzocrea A. CAMS: OLAPing Multidimensional Data Streams Efficiently. In: *11th International Conference on Data Warehousing and Knowledge Discovery*; 2009 August 31 - September 2; Linz, Austria. pp. 48–62, doi: https://doi.org/10.1007/978-3-642-03730-6_5

[17] Cuzzocrea A, Darmont J, Mahboubi H. Fragmenting Very Large XML Data Warehouses via K-Means Clustering Algorithm. *International Journal of Business Intelligence and Data Mining* 2009; 4(3/4): 301–328, doi: https://doi.org/10.1504/IJBIDM.2009.029076

[18] Vervliet N, Debals O, Sorber L, De Lathauwer L. Breaking the Curse of Dimensionality Using Decompositions of Incomplete Tensors: Tensor-Based Scientific Computing in Big Data Analysis. *IEEE Signal Processing Magazine* 2014; 31(5): 71–79, doi: https://doi.org/10.1109/MSP.2014.2329429

[19] Wold S, Esbensen K, Geladi P. Principal Component Analysis. *Chemometrics and Intelligent Laboratory Systems* 1987, 2(1-3): 37–52.

[20] Golub GH, Reinsch C. Singular Value Decomposition and Least Squares Solutions. In: *Handbook for Automatic Computation: Volume II: Linear Algebra*, Springer, pp. 134–151, 1971.

[21] Ding Z, Han J, Qian R, Shen L, Chen S, Yu L, Zhu Y, Liu R. eBoF: Interactive Temporal Correlation Analysis for Ensemble Data Based on Bag-of-Features. *IEEE Transactions on Big Data* 2023; 9(6): 1726–1737, doi: https://doi.org/10.1109/TBDATA.2023.3324482

[22] Jiang Z, Yuan Q, Lin R, Yang F. Canonical Correlation Analysis and Visualization for Big Data in Smart Grid. *IEEE Journal of Emerging and Selected Topics in Circuits and Systems* 2023; 13(3): 702–711, doi: https://doi.org/10.1109/JETCAS.2023.3290418

[23] Fu X, Huang K, Papalexakis EE, Song HA, Talukdar PP, Sidiropoulos ND, Faloutsos C, Mitchell TM. Efficient and Distributed Generalized Canonical Correlation Analysis for Big Multiview Data. *IEEE Transactions on Knowledge and Data Engineering* 2019; 31(12): 2304–2318, doi: https://doi.org/10.1109/TKDE.2018.2875908

[24] Aslam M. Analysis of Imprecise Measurement Data Utilizing Z-Test for Correlation. *Journal of Big Data* 2024; 11(1): 4, doi: https://doi.org/10.1186/s40537-023-00873-7

[25] Xiao C, Ye J, Esteves RM, Rong C. Using Spearman's Correlation Coefficients for Exploratory Data Analysis on Big Dataset. *Concurrency and Computation: Practice and Experience* 2016; 28(14): 3866–3878, doi: https://doi.org/10.1002/cpe.3745

[26] Han Y, Liu L, Sui Q, Zhou J. Big Data Spatio-Temporal Correlation Analysis and LRIM Model Based Targeted Poverty Alleviation through Education. *ISPRS International Journal of Geo-Information* 2021; 10(12): 837, doi: https://doi.org/10.3390/ijgi10120837

[27] Song Q, Rong B. Correlation Analysis of Middle School Students' Happiness and Sports in the Context of Big Data. *International Journal of Web-Based Learning and Teaching Technologies* 2024; 19(1): 1–14, doi: https://doi.org/10.4018/ijwltt.337605

[28] Song W, Wang L, Xiang Y, Zomaya AY. Geographic Spatiotemporal Big Data Correlation Analysis via the Hilbert-Huang Transformation. *Journal of Computer and System Sciences* 2017; 89: 130–141, doi: https://doi.org/10.1016/j.jcss.2017.05.010

[29] Cuzzocrea A, Soufargi S. Privacy-Preserving Big Hierarchical Data Analytics via Co-Occurrence Analysis. In: *13th International Conference on Data Science, Technology and Applications*; 2024 July 9-11; Dijon, France. pp. 93–103, doi: https://doi.org/10.5220/0012767800003756

[30] Cuzzocrea A, Saccà D, Serafino P. Semantics-Aware Advanced OLAP Visualization of Multidimensional Data Cubes. *International Journal of Data Warehousing and Mining* 2007; 3(4): 1–30, doi: https://doi.org/10.4018/jdwm.2007100101

[31] Cuzzocrea A, Moussa R, Xu G. OLAP*: Effectively and Efficiently Supporting Parallel OLAP over Big Data. In: *3rd International Conference on Model and Data Engineering*; 2013 September 25-27; Amantea, Italy. pp. 38–49, doi: https://doi.org/10.1007/978-3-642-41366-7_4

[32] Cuzzocrea A. Improving Range-SUM Query Evaluation on Data Cubes via Polynomial Approximation. *Data & Knowledge Engineering* 2006; 56(2): 85–121, doi: https://doi.org/10.1016/j.datak.2005.03.011

[33] Yu B, Cuzzocrea A, Jeong DH, Maydebura S. On Managing Very Large Sensor-Network Data Using Bigtable. In: *12th IEEE/ACM International Symposium on Cluster, Cloud and Grid Computing*; 2012 May 13-16; Ottawa, Canada. pp. 918–922, doi: https://doi.org/10.1109/CCGrid.2012.150

[34] Jiang R, Lu R, Choo KR. Achieving High Performance and Privacy-Preserving Query over Encrypted Multidimensional Big Metering Data. *Future Generation Computer Systems* 2018; 78: 392–401, doi: https://doi.org/10.1016/j.future.2016.05.005

[35] Ramdane Y, Boussaid O, Boukraâ D, Kabachi N, Bentayeb F. Building a Novel Physical Design of a Distributed Big Data Warehouse over a Hadoop Cluster to Enhance OLAP Cube Query Performance. *Parallel Computing* 2022; 111: 102918, doi: https://doi.org/10.1016/j.parco.2022.102918

Fuzzy Systems and Data Mining X
A.J. Tallón-Ballesteros (Ed.)

doi:10.3233/FAIA241436

Top-k Local Co-Location Pattern Mining Based on Weighted Voronoi Diagram

Can Jin[a], Lizhen Wang[b,1] Peizhong Yang[a], and Xiaoxu Wang[b]
[a] *School of Information Science and Engineering,Yunnan University, Kunming, China*
[b] *School of Science and Technology, Dianchi College, Kunming, China*

Abstract. Local co-location pattern (LCP) mining is an important branch of spatial co-location pattern mining, which aims to discover co-location patterns that prevalently co-occur in local regions. The LCPs can reveal the implicit association relationships among spatial features in local regions but not on a global scale. Existing LCP mining algorithms cannot effectively identify artificially divided local regions, and it is difficult to set an appropriate prevalence threshold for selecting prevalent LCPs. To address these problems, we propose a novel top-*k* LCPs mining algorithm based on weighted Voronoi diagram (called Top-*k* LCPM-WVD). This algorithm effectively identifies LCP distribution regions formed by human factors using the weighted Voronoi diagram, and proposes a top-*k* mining framework to efficiently mine the *k* most prevalent LCPs within regions. Extensive experimental evaluations are conducted on both real-world and synthetic datasets. Compared to the existing state-of-the-art algorithms, our proposed Top-*k* LCPM-WVD algorithm yields more interpretable LCPs with good efficiency.

Keywords. pattern mining, local co-location pattern, weighted Voronoi diagram, top-*k* mining framework

1. Introduction

With the rapid development of Global Positioning System and remote sensing technologies, a large amount of spatial data has been generated. Against this background, spatial data mining techniques have emerged, aiming to extract potential and valuable knowledge from massive spatial data [1]. As an important task of spatial data mining, spatial co-location pattern (co-location) mining is proposed to discover subsets of spatial features whose instances are prevalently located in adjacent locations.

Due to the heterogeneity of spatial data distribution, some co-locations may only be distributed in certain local regions. Consequently, local co-location pattern (LCP) mining has emerged, which aims to discover co-locations that are not prevalent in the global scope but prevalent in local regions. LCP mining can not only discover local co-location relationships among spatial features, but also identify the specific regions where these relationships occur, which can provide important insights for urban planning and construction [2], public health [3], and other fields [4].

[1] Corresponding Author: Lizhen Wang; E-mail: lzhwang@ynu.edu.cn.
This work is supported by the National Natural Science Foundation of China (62276227, 62306266), the Yunnan Fundamental Research Projects (202201AS070015, 202401AT070450), and the Postgraduate Research and Innovation Foundation of Yunnan University (KC-23235527, TM-23236919).

Traditional LCP mining methods usually involve two main stages: (1) dividing the global study area into several local regions using specified regional partitioning method; and (2) mining LCPs within each region.

In the regional partitioning stage, existing methods often use partitioning rules [5, 6] or clustering algorithms [7, 8] based on the geographical proximity between instances, which can effectively identify local regions naturally formed by geographical factors. However, since these methods do not consider non-geographic factors such as economics, they perform poorly in identifying local regions formed by human factors, making it difficult to explain the mined LCPs and their prevalent regions. To address this problem, Ghosh et al. [3] proposed that artificially divided administrative districts be directly used as local regions for LCP mining. Under the ideal situation of ignoring the flow of population across administrative districts, administrative districts, as the fundamental spatial units for people to carry out social production and life for a long time, can be regarded as the distribution regions of LCPs related to human activities, i.e., formed by human factors. However, spatial behavior criteria of human activities are usually based on the principle of the closest distance [9]. In view of this, the Voronoi diagram, as an efficient spatial division method based on the nearest neighbor principle, can be used to redefine the human activity space according to the spatial location of administrative districts, yielding results superior to traditional administrative divisions. However, due to the large differences in economic and other strengths of different administrative districts, the human activity spaces often do not strictly follow the regular Voronoi diagram under the competition among administrative districts. To address this, we further consider the comprehensive strengths of administrative districts, converting them into weights and incorporating them into the Voronoi diagram to construct a weighted Voronoi diagram. This approach more accurately depicts the spatial distribution of human activities, thereby effectively obtaining the distribution region of LCP formed by human factors, and ultimately optimizing the interpretation and application value of LCP mining results.

In the pattern mining stage, traditional LCP mining methods apply a uniform prevalence threshold to filter prevalent LCPs. However, users are typically more interested in the most prevalent patterns among the mining results. Specifying a desired number of patterns is also more intuitive than setting a prevalence threshold. Moreover, the introduction of local regions significantly increases the computational complexity of LCP mining. To address these issues, we propose a top-k LCP mining framework to more efficiently mine the k most prevalent LCPs within regions.

2. Concepts and Methods

2.1. Spatial Colocation Pattern

In space, different types of entities are abstracted as **spatial features**. All features in space constitute the spatial feature set, denoted as $F = \{f_1, f_2, ..., f_n\}$. The occurrences of spatial features at specific geographical locations are considered as **spatial instances**, denoted as $S = \{S_1, S_2, ..., S_n\}$, where S_i $(1 \le i \le n)$ is the instance set of feature f_i. Two instances are said to satisfy the spatial neighbor relationship NR if their Euclidean distance is not greater than a given neighbor distance threshold d, expressed as $NR(o, o') \Leftrightarrow (\text{distance}(o, o') \le d)$, where $\text{distance}(o, o')$ represents the Euclidean distance between instance o and o'. For an instance o, the set of all instances that satisfy the

neighbor relationship with o and have different feature types from o is called the **neighbor set** of o, expressed as $Neigh(o) = \{o' \mid NR(o, o') = true \wedge o'.t \neq o.t\}$, with $o.t$ representing the feature type of instance o. A **spatial co-location pattern** $c = \{f_1, f_2, ..., f_l\} (l \leq n)$ is a non-empty subset of the spatial feature set F, whose instances of different features prevalently appear in close proximity in space.

2.2. Regional Partitioning Method

Definition 1. Weighted distance: Given an instance o and its weight w, for an instance o', the weighted distance between o' and o is defined as the ratio of the Euclidean distance between o' and o to w, expressed as:

$$d_w(o', o) = \frac{\text{distance}(o', o)}{w}, w > 0 \quad (1)$$

Definition 2. Weighted Voronoi region: Given a set of spatial instances $G = \{o_1, o_2, ..., o_m\}$, where $G \subseteq S$, the instances in G are called **generators**, also given a set of weight $W = \{w_1, w_2, ..., w_m\}$, where w_i is the weight of generator o_i. For $o_i \in G$, its corresponding weighted Voronoi region $V(o_i, w_i)$ is the set of all spatial instances whose weighted distance to o_i is less than that to any other generator $o_j \in G$ $(j \neq i)$, expressed as:

$$V(o_i, w_i) = \left\{ o_x \mid o_x \in S \wedge d_w(o_x, o_i) < d_w\left(o_x, o_j\right), \forall j \neq i \right\} \quad (2)$$

The set of weighted Voronoi regions of all generators in G is called the **weighted Voronoi diagram** of G, denoted as $V(G, W) = \{V(o_1, w_1), V(o_2, w_2), \ldots, V(o_m, w_m)\}$.

When using the weighted Voronoi diagram to divide regions, administrative centers (represented by the government locations) serve as generators, and the comprehensive strengths of their corresponding administrative districts are quantified as weights using the weight determination method in literature [9]. Each weighted Voronoi region, reflecting the attraction range of an administrative district concerning human and economic resources, is shaped by the administrative district's geographical location and comprehensive strength.

Taking Yunnan Province as an example, Figure 1(a) illustrates the prefecture-level administrative divisions. Figure 1(b) presents the regular Voronoi diagram created using the government locations of these districts as generators (red five-pointed stars), while Fig. 1(c) displays the weighted Voronoi diagram incorporating the comprehensive strength weights (red numbers) of the districts. The geographical boundaries of the administrative districts and the Voronoi regions are depicted by black lines, with colored dots representing POI instances of various feature types.

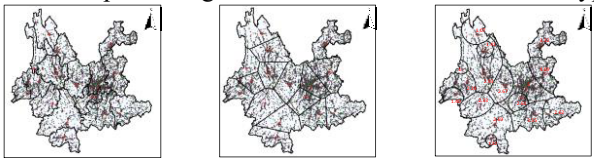

(a) **(b)** **(c)**

Figure 1. Comparison of regional partition results for Yunnan Province. **(a)** Administrative division. **(b)** Regular Voronoi diagram. **(c)** Weighted Voronoi diagram.

2.3. Top-k LCP Mining

2.3.1. Basic Concepts and Prevalence Measures of LCPs

Given a local region R, LCP $c = \{f_1, f_2, ..., f_l\} (l \geq 2)$ is a non-empty subset of the spatial feature set F_R in R ($c \subseteq F_R$), where the number of features contained in c is called the order of the pattern, denoted by $|c|$. Given a set of instances $RI = \{o_1, o_2, ..., o_l\}$, if (1) the number of instances contained in RI is equal to the order of c, and the instances in RI cover all feature types of c, (2) any two instances in RI have a neighbor relationship NR, then the instance set RI is called a **row instance** of c. If an instance o_j of f_i ($o_j.t = f_i$) is included in any row instance of c, then o_j is a **local participating instance** of f_i in c. The set of all local participating instances of f_i in c is called the **local participating instance set** of f_i, denoted as $LPIns(c, f_i, R)$. The **local participation ratio** (LPR) of feature f_i in pattern c is the ratio of the number of local participating instances of feature f_i in c to the total number of instances of feature f_i in region R. The **local participation index** (LPI) of LCP c is the minimum value of the local participation ratio of all features in c, which is widely used to measure the prevalence of LCP.

2.3.2. Concept of top-k prevalent LCP mining

Definition 3. Top-*k* LCPs: Let $L = \{c_i \mid c_i \text{ is an LCP in } R\}$ be the set of all LCPs in the local region R. After sorting the LCPs in L by descending LPI, the set of the first k LCPs, $L_k = \{c_j \mid c_j \in L, j \leq k\}$, is the top-$k$ LCPs in R.

LCP $c \in L_k$ is called the **top-*k* prevalent LCP**, represented as a tuple $<c, R>$.

2.3.3. Pruning strategy based on local star participation index

Since no prevalence threshold is set, mining top-k prevalent LCPs needs to generate all LCPs and sort them by LPI to obtain top-k LCPs, which is time-consuming. To optimize this, we first generate local star patterns and calculate their local star participation ratios. Only qualifying local star patterns can form local co-location patterns.

For an instance $o \in S(f_i, R)$, its **local feature neighbor transaction** is denoted as $LFNT(o) = \{f_i \mid f_i = o.t \vee f_i \in E\}$ where $o.t$ is the **reference feature** and E is the set of different features of neighbor set $Neigh(o, R)$ of o in R. The **local feature neighbor transaction set** of f_i, denoted as $LFT(f_i)$, is composed of the feature neighbor transactions of all instances in $S(f_i, R)$. A **local star pattern** $starC_{fi} = \{f_i, f_1, ..., f_{i-1}, f_l\} (l \geq 2)$ is a non-empty subset of $LFNT(o)$, where f_i is reference feature of $LFNT(o)$. The **local star participation ratio** (LSPR) of $starC_{fi}$ is the proportion of feature neighbor transactions containing $starC_{fi}$ to the number of feature neighbor transactions with f_i as the reference feature. LCP $c = \{f_1, f_2, ..., f_l\} (l \geq 2)$ is formed by combining all local star patterns that cover all features in c. The minimum LSPR of all contributed local star patterns of c is called the **local star participation index** (LSPI) of c. According to the literature [10], it is not difficult to prove that the LPI of LCP c is not greater than its LSPI. Therefore, when the LSPI of pattern c is less than the minimum LPI in the current L_k, there is no need to generate c or its supersets.

To generate LCPs step by step and quickly calculate their LSPIs through bit operations, we convert the local feature neighbor transaction set into a vertical structure and instance number sets into bit strings.

Definition 4. Local vertical feature neighbor transaction set and bit string-based local vertical feature neighbor transaction set: Given the local feature neighbor transaction set $LFT(f_i)$ of feature f_i, the local vertical feature neighbor transaction set $LVFT(f_i)$ of f_i consists of all non-repeating features in $LFT(f_i)$ and all instance numbers where the features appear in $LFT(f_i)$, denoted as:

$$LVFT(f_i) = \{f_j, \{o.id \mid f_j \in LFNT(o) \wedge LFNT(o) \in LFT(f_i)\}\} \quad (3)$$

The instance number set in $LVFT(f_i)$ is converted into a bit string, where each bit represents whether a feature appears in a specific transaction, to obtain the bit string-based local vertical feature neighbor transaction set $bLVFT(f_i)$.

3. Algorithm and Analysis

After partitioning the region based on weighted Voronoi diagram (Section 2.2), we proposed an efficient algorithm (Algorithm 1) for mining top-k LCPs in regions.

Algorithm 1 Top-k LCPM

Input: spatial feature set F_R and spatial instance set S_R in region R, distance threshold d, desired number of LCP k.

Output: L_k within the region R

1. Calculate neighbor relationships between instances, and materialize as neighborhood sets (NSs);
2. bLVFNTs = genVerticalFeatureNeighborTransactions(NSs);
3. initialize $L_k = \emptyset$, $C_1 = F_R$, $S_1 = b$LVFNTs, $\theta = 0$, l=2;
4. **While** $C_{l\text{-}1} \neq \emptyset$ **do**
5. (C_l, S_l)= genLCPsWithLocalStarPatterns (L_k, $S_{l\text{-}1}$, l);
6. C_l_sorted = calculateLocalStarPIAndSort(C_l, S_l);
7. **For each** $c \in C_l\_sorted$ **do**
8. **If** $|L_k| == k$ and c.LSPI < θ **then**
9. break;
10. LPIns = searchLocalParticipatingInstances(c, NSs);
11. LPI = calculateTrueLPI(c, LPIns);
12. If $|L_k| < k$ or $|L_k| == k$ and LPI $\geq \theta$ **then**
13. insert (c, LPI, L_k, θ);
14. l++;
15. **Return** L_k.

Algorithm 1 describes the process of mining top-k LCPs within a local region R. Firstly, the neighbor relationships between instances are materialized into the neighbor sets of each instance, and the bit string-based local vertical feature neighbor transaction sets are constructed from them (lines 1-2). An ordered list L_k with capacity k is initialized to dynamically store the current k largest LPIs and their corresponding LCPs, where the variable θ represents the smallest LPI value in L_k (line 3). Starting from order 2, when the l-1 order LCP set $C_{l\text{-}1}$ is not empty, the l-order LCP set C_l is generated by combining the local star patterns in the l-order local star pattern set S_l. Calculate the LSPI of each LCP in C_l and sort these LCPs in descending order by LSPI. (lines 5-6). Next, the sorted l order LCP set C_l_sorted is traversed. If L_k is full and the LSPI of the current LCP c is lower than θ, the current iteration is terminated and moves to the next stage (lines 8-9). Otherwise, the column-based calculation method [11], which can significantly reduce the search space, is used to search for the local

participating instance set of the current pattern c to calculate its LPI (lines 10-11). When L_k is not full, c and its LPI are directly inserted into L_k in order; when L_k is full, it needs to be compared with θ, and if c's LPI is not less than θ, it is inserted into the corresponding position of L_k and the minimum LPI and its LCPs are removed from L_k (lines 12-13). Finally, the order l is incremented, and proceed to the next stage (line 14).

Finally, since each region is independent, we can use the parallel technique proposed in literature [7] to simultaneously mine top-k LCPs within multiple regions, maximizing the overall efficiency of LCP mining.

4. Experiments and Analysis

In this section, we conduct extensive experiments on both real-world and synthetic datasets to evaluate the effectiveness and performance of the proposed Top-k LCPM-WVD algorithm.

4.1. Experiment Setup

The real dataset. The POI dataset of Yunnan Province crawled from Google Maps, which contains 208,257 instances with 51 features.
The synthetic datasets: The synthetic datasets are generated following the method in reference [11].
Experimental environment. All algorithms are implemented in C++ and executed on a computer equipped with an Intel(R) Core(TM) i7-7820X CPU and 64 GB memory.

4.2. Analysis of effectiveness

In this section, we evaluate the effectiveness of the Top-k LCPM-WVD algorithm's regional partitioning method and LCP mining results using the real-world dataset. The POI dataset mainly contains urban facilities related to people's production and life. Consequently, we only compare our approach with the method proposed in the literature [3], which uses administrative districts as local regions for LCP mining.

4.2.1. Effectiveness of the regional partitioning method

An effective regional division is essential for subsequent LCP mining. In Figure 1, taking Kunming as an example, as a city with the highest comprehensive strength weight, Kunming has a strong attraction to POI instances, prompting these instances to form a dense and large cluster around its administrative center. However, as can be seen from the figure, the geographical boundary of Kunming city incorrectly divides this POI cluster, and the regular Voronoi region also fails to fully contain this cluster. In contrast, the weighted Voronoi region, by considering the city's geographical location and comprehensive strength, is able to contain the POI cluster more completely.

4.2.2. Effectiveness of the LCP mining results

After regional partition, we set the distance threshold to 100 meters and mine the top-10 LCPs. The LCP {Chinese restaurant, company} is prevalent in both the regular

Voronoi region (green line) and weighted Voronoi region (red line) of Qujing City but not within its geographic boundary (black line). As shown in Figure 2(a), instances of this co-location appear outside Qujing's geographic boundary due to the city's attraction. These instances are mostly covered by the two Voronoi regions, resulting in the prevalent LCP {Chinese restaurant, company}. Figure 2(b) shows the distribution of company and furniture market instances within Kunming City's weighted Voronoi region. These two features prevalently co-locate in this region, forming the prevalent LCP {Chinese restaurant, furniture market}. However, neither the geographical boundaries of Kunming City nor the regular Voronoi region can identify this prevalent pattern whose many instances are located outside the boundaries of both.

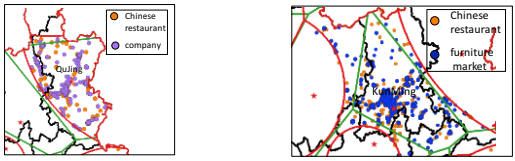

(a) (b)

Figure 2 LCP instance distribution across different regions. **(a)** {Chinese restaurant, company} in Qujing City. **(b)** {Chinese restaurant, furniture market} in Kunming City.

4.3. Performance Evaluation

This section evaluates the Top-*k* LCPM-WVD algorithm's performance using synthetic datasets, examining the effects of the number of instances $|I|$, the number of features $|F|$, distance threshold d and the number of most prevalent LCPs to be mined k on the algorithm's running time. As this is the first top-*k* LCPs mining method, we compared our algorithm with TopKColoc-WVD, an adapted version of Yoo et al.'s [10] top-*k* co-location mining algorithm (which is more efficient than traditional co-location mining algorithms) incorporating our partitioning method.

Figure 3(a) illustrates the effect of the number of input instances on the algorithm's running time. Set parameters $|F| = 25$, $d = 40$, $k = 20$. As $|I|$ increases, instance density of each region rises, leading to increased running times for both algorithms. However, Top-k LCPM-WVD consistently outperforms TopKColoc-WVD, especially with larger datasets, maintaining stable performance.

Figure 3(b) illustrates the effect of the number of features on the algorithm's running time. Set parameters $|I| = 400000$, $d = 40$, $k = 20$. More features result in exponential growth in LCPs and neighboring relationships, increasing running times. The performance gap between the algorithms widens with more features, with Top-*k* LCPM-WVD running significantly faster.

Figure 3(c) illustrates the effect of distance threshold d on the algorithm's running time. Set parameters $|I| = 400000$, $|F| = 25$, $k = 20$. As d increases, more spatial neighbor relationships form, creating more row instances. Although the running time of both algorithms increases with d, the Top-*k* LCPM-WVD algorithm consistently exhibits a lower running time. This is because Top-*k* LCPM-WVD searches fewer instances of the LCP for the calculation of LPI compared to TopKColoc-WVD.

Figure 3(d) illustrates the effect of the number of most prevalent LCPs to be mined k on the algorithm's running time. Set parameters $|I| = 400000$, $|F| = 25$, $d = 40$. Increasing k raises the number of LCPs to be processed, and the algorithm running time increases accordingly. As can be seen that the running time of the Top-*k* LCPM-WVD algorithm is always significantly lower than that of the TopKColoc-WVD algorithm.

This is because the improved FP-tree structure employed by TopKColoc-WVD needs to generate all LCPs and calculate their LSPIs at once.

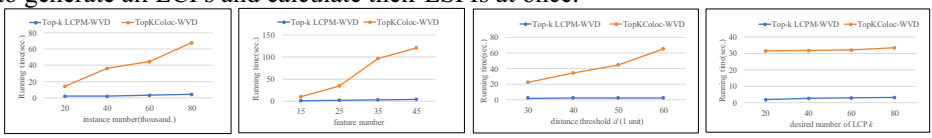

(a) **(b)** **(c)** **(d)**

Figure 3. Effect of parameters on execution time. **(a)** Running time vs. instance number. **(b)** Running time vs. feature number. **(c)** Running time vs. *d*. **(d)** Running time vs. *k*.

5. Conclusion

In this paper, we first propose a novel region partitioning method based on weighted Voronoi diagram to obtain local regions formed by human factors. Subsequently, we introduce the top-*k* concept to mine the *k* most prevalent LCPs within each region. Finally, we verify the effectiveness of the proposed partitioning method and LCP mining results through a real-world dataset, and conduct extensive experiments on synthetic datasets to further demonstrate the efficiency and scalability of the algorithm.

References

[1] Wang L, Fang Y, Zhou L. Preference-based spatial co-location pattern mining. Singapore: Springer, 2022, doi: 10.1007/978-981-16-7566-9.

[2] Wang S, Huang Y, Wang XS. Regional Co-locations of Arbitrary Shapes. In Proceedings of the13th International Symposium, 2013, pp. 19-37. doi: 10.1007/978-3-642-40235-7_2.

[3] Ghosh S, Gupta J, Sharma A, et al. Towards geographically robust statistically significant regional colocation pattern detection. In Proceedings of the 5th ACM SIGSPATIAL International Workshop on GeoSpatial Simulation, 2022, pp. 11-20. doi: 10.1145/3557989.3566158.

[4] Deng M, Cai J, Liu Q, et al. Multi-level method for discovery of regional co-location patterns. Int. J. Geogr. Inf. Sci., 2017, 31(9): 1846-1870, doi: 10.1080/13658816.2017.1334890.

[5] Li Y, Shekhar S. Local Co-location Pattern Detection: A Summary of Results. In Proceedings of the 10th International Conference on Geographic Information Science, 2018, pp. 1-10. doi: 10.4230/LIPIcs.GISCIENCE.2018.10.

[6] Wang D, Wang L, J X, et al. RCPM_CFI: A regional core pattern mining method based on core feature influence. Inf. Sci., 658 (2024) 119895, doi: 10.1016/j.ins.2023.119895.

[7] Jiang X, Wang L, Vanha T. A parallel algorithm for regional co-location mining based on fuzzy density peak clustering. Sci Sin Inform, 2023(53): 1281–1298, doi: 10.1360/SSI-2022-0004.

[8] Wang D, Wang L, Wang X, et al. An approach based on maximal cliques and multi-density clustering for regional co-location pattern mining. Expert Systems with Applications, 248(2024):123414, doi: 10.1016/j.eswa.2024.123414.

[9] Wang X, Liu J, Zhuang D, et al. Application of Voronoi Diagram in Determining the Spatial Organization of Urban Economic Influence Areas. Journal of Central China Normal University (Natural Sciences), 2003(02): 256-260, doi: 10.19603/j.cnki.1000-1190.2003.02.032.

[10] Yoo JS, Bow M. Mining top-k closed co-location patterns. In Proceedings 2011 IEEE International Conference on Spatial Data Mining and Geographical Knowledge Services, 2011, pp. 100-105. doi: 10.1109/ICSDM.2011.5969013.

[11] Yang P, Wang L, Wang X, et al. Parallel co-location pattern mining based on neighbor-dependency partition and column calculation. In Proceedings of the 29th International Conference on Advances in Geographic Information Systems, 2021, pp. 365-374. doi: 10.1145/3474717.

Part III

Interdisciplinary Field of Fuzzy Logic and Data Mining

Fuzzy Systems and Data Mining X
A.J. Tallón-Ballesteros (Ed.)

doi:10.3233/FAIA241438

Application of Hybrid Model Based on NeuralProphet Model and Error Correction in Wind Power Prediction

Zai-hong HOU [a,1], and Yu-long BAI [a]
[a] *College of Physics and Electrical Engineering, Northwest Normal University, Lanzhou, Gansu, 730070, China.*
ORCiD ID: Yu-long Bai https://orcid.org/0000-0002-3323-0211

Abstract. Wind power prediction is essential for the optimal operation of wind farms. Therefore, a novel combined model is proposed to improve the prediction performance for the short-term wind power forecasting. First, the wavelet threshold denoising (WTD) technique is used to preprocess the original wind power data. Second, the NeuralProphet (NP) model is used to predict the preprocessed wind power data. Then, the error sequence predicted by the NP model is subjected to ICEEMDAN-VMD quadratic decomposition to reduce its complexity. The sparrow search algorithm (SSA) optimization algorithm is used to optimize the library for support vector machines (LIBSVM) hyperparameters to predict the decomposed error subsequences. Finally, the predicted error sequence results and the NP prediction results are combined to obtain the final prediction results. A hybrid WTD-NP-ICEEMDAN-VMD-SSA-LIBSVM model is proposed for wind power prediction. To evaluate the model's performance and reliability, we compared the prediction effects of 6 single models and 6 hybrid models through two sets of experiments. Four evaluation indices were used to assess the model. It is evident that the model demonstrates high accuracy and efficiency in wind power prediction.

Keywords. NeuralProphet, wavelet threshold denoising, sparrow search algorithm, quadratic decomposition.

1. Introduction

As an important renewable energy source in China, wind power has developed rapidly in recent years, but its intermittence and regional differences bring power supply stability and management challenges[1]. Therefore, the economic dispatch based on wind power prediction is very important for the coordinated development and safe operation of power system.

Related research primarily comprises two approaches: single models and hybrid models for wind power estimation.The primary tools for single-model prediction are

[1]Corresponding Author: Yu-long Bai, College of Physics and Electrical Engineering, Northwest Normal University, Lanzhou, Gansu, 730070, China, E-mai: baiyulong@nwnu.edu.cn

physical models, statistical models, and intelligent models[2]. The physical model uses the laws and principles of physics to describe and predict time series data. Statistical models overcome the shortcomings of traditional physical methods by avoiding the need to consider the geographical conditions of wind farms. The intelligent model uses machine learning technology and a large amount of data for training, and has strong nonlinear processing, self-learning and fault-tolerant capabilities. It is widely used in the field of dynamic wind power forecasting[3].

Due to the time-dependent and complex nature of wind power fluctuations, it is challenging to capture the hidden characteristics of an irregular wind power sequence through a single forecasting model, and it is impossible to obtain satisfactory prediction results in this way[4]. Therefore, hybrid prediction methods have become the mainstream trend because of their excellent nonlinear processing ability and good forecasting accuracy.

The main contributions and innovations of this paper lie in the use of a more advanced prediction model for wind power forecasting. A new quadratic decomposition method is proposed to process the error sequence, and an intelligent optimization algorithm is used to optimize the hyperparameters of the error sequence prediction model. The rationality and superiority of the proposed model are confirmed through the analysis of wind power data.

2. Related work

2.1. Data Analysis and Processing

Wavelet threshold denoising is a technique used to improve the quality and readability of the signal. The noise in the signal is removed by wavelet transform of the signal and using the minimaxi criterion and hard threshold processing and symlet wavelet basis.[5].

The ICEEMDAN-VMD secondary decomposition method further reduces the complexity of the error sequence, thereby improving the accuracy of the overall prediction.

The ICEEMDAN algorithm is described as follows[6]:

Step 1: White noise is added to the actual signal $E_i\left[w^{(i)}\right]$ to obtain Eq. (1):

$$x^{(i)} = x + \beta_0 E_i\left[w^{(i)}\right] \tag{1}$$

where $[w^{(i)}]$ represents theth added noise component and x is the signal to be decomposed. β_0 is to adjust the intensity of the noise added to the signal.

Step 2: The value of modal component IMF_1 is calculated from Eq. (2):

$$\widetilde{d_1} = x - r_1 = x - \frac{1}{I}\sum_{i=1}^{I} M\left[X^i\right] \tag{2}$$

where $M(.)$ is the local mean function and r_1 represents the residual of the first group.

Step 3: The value of IMF_2 is calculated from Eq. (3):

$$\widetilde{d_2} = r_1 - r_2 = r_1 - \frac{1}{I}\sum_{i=1}^{I} M\left\{r_1 + \beta_1 E_2\left[w^i\right]\right\} \tag{3}$$

Step 4: The value of the kth modal component IMF_k is calculated from Eq. (4):

$$\widetilde{d}_k = r_{k-1} - r_k = r_{k-1} - \frac{1}{I}\sum_{i=1}^{I} M\left\{r_{k-1} + \beta_{k-1} E_k\left[w^i\right]\right\} \tag{4}$$

where $k = 3,4...n$[6].

The process of the VMD algorithm is as follows[7]:

Step 1. Initialize u_k^1, ω_k^1, $\hat{\lambda}^1$.

Step 2. The values of u_k, ω_k, and λ are updated according to Eqs. (5–7):

$$\hat{u}_k^{n+1}(\omega) = \frac{\hat{f}(\omega) - \sum_{i\neq k}\hat{u}_i^n(\omega) - \frac{\hat{\lambda}(\omega)}{2}}{1 + 2\alpha(\omega - \omega_k)^2} \tag{5}$$

$$\omega_k^{n+1} = \frac{\int_0^\infty \omega\left|\hat{u}_k^{n+1}(\omega)\right|^2 d\omega}{\int_0^\infty \left|\hat{u}_k^{n+1}(\omega)\right|^2 d\omega} \tag{6}$$

$$\hat{\lambda}^{n+1}(\omega) = \hat{\lambda}^n(\omega) + \tau\left[\hat{f}(\omega) - \sum_k \hat{u}_k^{n+1}(\omega)\right] \tag{7}$$

Step 3. Step 2 is repeated until the iteration termination condition is satisfied:

$$\sum_k \frac{\left\|\hat{u}_k^{n+1} - \hat{u}_k^n\right\|_2^2}{\left\|\hat{u}_{k^n}\right\|_2^2} < \varepsilon \tag{8}$$

where ε is a given accuracy requirement.

2.2. NeuralProphet

NeuralProphet is a time series prediction library based on PyTorch.Inspired by the PROPHET model, it combines time series analysis and deep learning. It consists of multiple modules, such as trend and seasonality, which interact in the internal neural network layer to improve the accuracy of prediction[8].

$$\hat{y}_t = T(t) + S(t) + E(t) + F(t) + A(t) + L(t) \tag{9}$$

where, $T(t)$ represents the trend at time t, which can be modeled either as a linear trend or as a piecewise linear trend by specifying change points[9].

$S(t)$represents the seasonal effect at time t. Seasonality is modeled using Fourier terms, so the model can deal with multiple seasonality characteristics in high-frequency data.

$E(t)$represents special events, representing outliers in time series data.

$F(t)$represents the regression effect of future known exogenous variables at time t.

$A(t)$represents the autoregressive effect at time t based on past observations.

$L(t)$represents the regression effect of lagging observations of external variables at time t.

2.3. Proposed hybrid model framework

This section describes the architecture of the proposed hybrid model and the related submodels.

(a) Wavelet threshold denoising : wavelet threshold denoising is used to effectively denoise wind power data and improve data smoothness.

(b) Multi-model selection : After considering the six single models of ELM, LSTM, CNN, Prophet, LIBSVM and NP, the NP model is selected, which has the most accurate prediction performance.

(c) NP model : a prediction model combining time series analysis and neural network technology.

(d) NP prediction : The data is divided into training set and test set, and the NP model is used to train and predict the error sequence.

(e) Error sequence processing : ICEEMDAN-VMD secondary decomposition is used to decompose the complex error sequence into multiple subsequences, which are input into the SSA-LIBSVM model to obtain the prediction results.

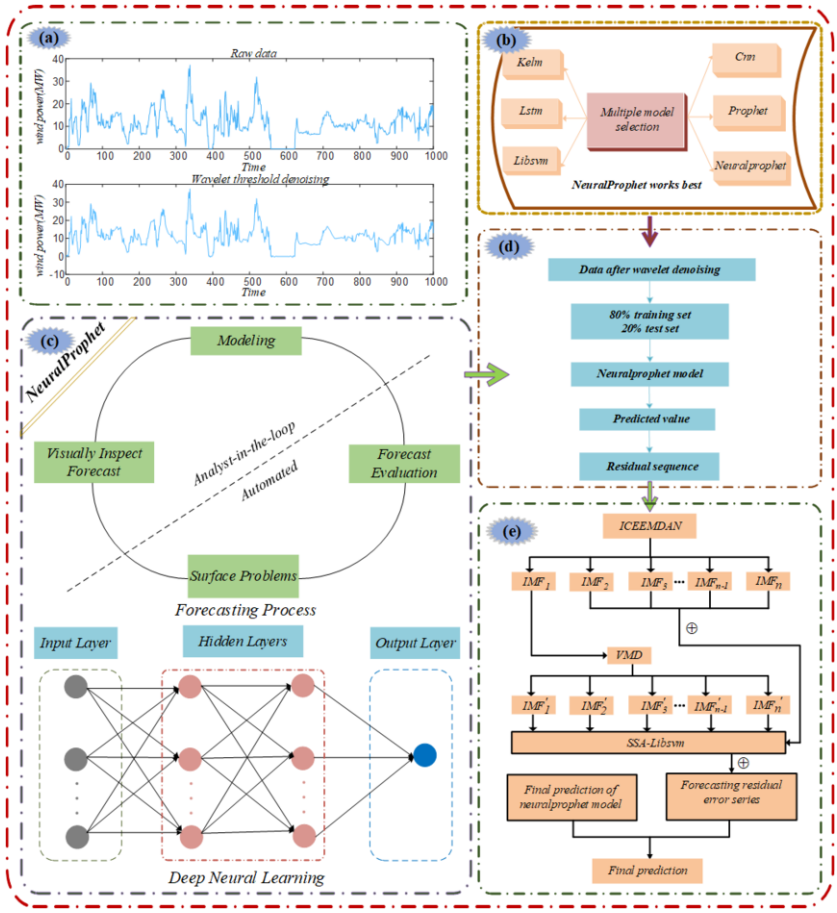

Figure 1. Proposed hybrid model framework

3. Data description and experimental analysis

This paper uses historical wind power data for future predictions and evaluates the proposed model by comparing it to six single models and six other hybrid models through two experiments, thus confirming its superiority and reliability.

3.1. Data description

The experimental data set is the wind power data of Bestielike Township in Xinjiang in 2017. The GW77 wind turbine is used with a single unit capacity of 1 500 kW and a total capacity of 49.5 MW. As shown in Figure 2, the data is collected every 15 minutes[10].

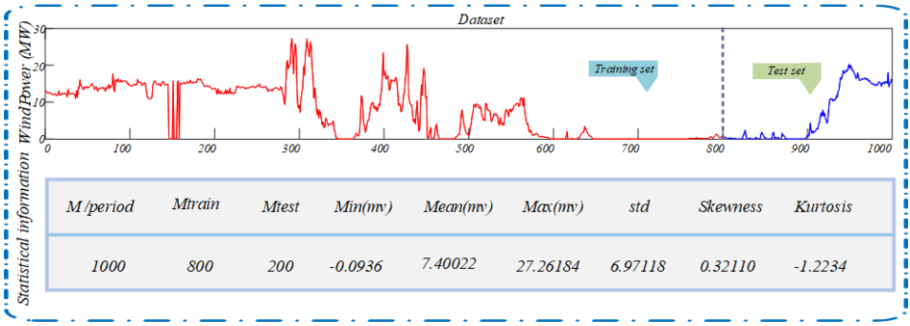

Statistical information

M /period	Mtrain	Mtest	Min(mv)	Mean(mv)	Max(mv)	std	Skewness	Kurtosis
1000	800	200	-0.0936	7.40022	27.26184	6.97118	0.32110	-1.2234

Figure 2. Original wind power data

In order to evaluate the impact of different data segmentation ratios on model performance, we compared the wind power prediction capabilities of LSTM and CNN models at 8 : 2,9 : 1 and 7 : 3 ratios in Table 1. Considering the instability of the single prediction results, we conducted 10 experiments and used the average of these experiments as the final prediction results. The results show that the segmentation ratio of 8 : 2 training set and test set provides the best prediction effect for these models.

Table 1. Set different segmentation ratios

Model	Ration	MSE	MAE	MAPE	RMSE	R^2
	7:3	1.254	0.955	0.467	1.120	0.9878
LSTM	9:1	1.187	0.895	0.474	0.474	0.9882
	8:2	**1.153**	**0.889**	**0.470**	**1.074**	**0.9880**
	7:3	0.794	0.674	0.513	0.891	0.9892
CNN	9:1	1.310	0.857	0.521	1.145	0.9910
	8:2	**0.683**	**0.678**	**0.501**	**0.826**	**0.9908**

3.2. Evaluation indicators

To evaluate the predictive capability of the hybrid model proposed in this paper, we adopted the following four accuracy evaluation metrics: Mean Absolute Percentage Error (MAPE), Root Mean Squared Error (RMSE), Theil's Inequality Coefficient (TIC), and Theil's U statistic.

Table 2. Error evaluation indicators

Metric	Definition	Equation
RMSE	The square root of the mean of the square of the prediction error	$RMSE = \sqrt{\frac{1}{N}\sum_{i=1}^{N}(\hat{x}_i - x_i)^2}$
MAPE	Average of N absolute percentage errors	$MAPE = \frac{1}{N}\sum_{i=1}^{N}\left\lvert\frac{x_i-\hat{x}_i}{x_i}\right\rvert$
Theil's U	Evaluate the accuracy of the prediction model	$Theil'sU = \frac{\sqrt{\sum_{i=1}^{N}(\hat{x}_i - x_i)^2}}{\sqrt{\sum_{i=1}^{N}\hat{x}_i^2}+\sqrt{\sum_{i=1}^{N}x_i^2}}$
TIC	Measure the inequality of a distribution	$TIC = \sqrt{\frac{\sum_{i=1}^{n}(x_i-\hat{x}_i)^2}{\sum_{i=1}^{n}\hat{x}_i^2}}$

As shown in Table 2,where $\hat{x}_i$ and x_i denote the true value and the predicted value of the ith sample respectively, $\bar{x}$ is the mean of the true value, and N is the number of samples.

3.3. Single model comparative experiment

Six single models were employed to analyze and compare the prediction results in Table 3. The data after wavelet threshold denoising were directly predicted by the ELM, LSTM, CNN, PROPHET, LIBSVM and NP models. Due to the instability of the wind power prediction results from a single model, the final result for each model was obtained as the average value after 10 tests, and the value predicted by the best single model is marked.

Table 3. Comparison of single model test results

Model	MAPE	RMSE	Theil's U	TIC
ELM	5.1031	1.1904	0.06310	0.08510
LSTM	7.8355	0.8824	0.04602	0.06220
CNN	7.8623	0.8875	0.04630	0.06258
PROPHET	2.4256	0.8183	0.04184	0.05587
LIBSVM	3.6516	0.7742	0.04008	0.05366
NeuralProphet	**0.0320**	**0.1298**	**0.00674**	**0.00900**

(1)Among ELM, LSTM, CNN, PROPHET, LIBSVM and NP models, the prediction effect of NP model is the best, followed by LIBSVM. As shown in Figure. 3, the prediction curve of the NP model almost coincides with the original curve. Therefore, NP is selected as the main model and LIBSVM is the error correction model.

(2) The data predicted by the NP model are more closely correlated with the original data. The scatter plot in Figure. 3 shows that the correlation between the wind power data predicted by the NP model and the original data is close to 1.

(3) The NP model can more accurately fit the data points at inflection points in the wind power. NP provides a novel growth mode to allow trend interruptions and jumps. From the line chart in Figure. 3, it can be seen that the fitting effect of NP prediction is the best, while the fitting effect of PROPHET is the worst.

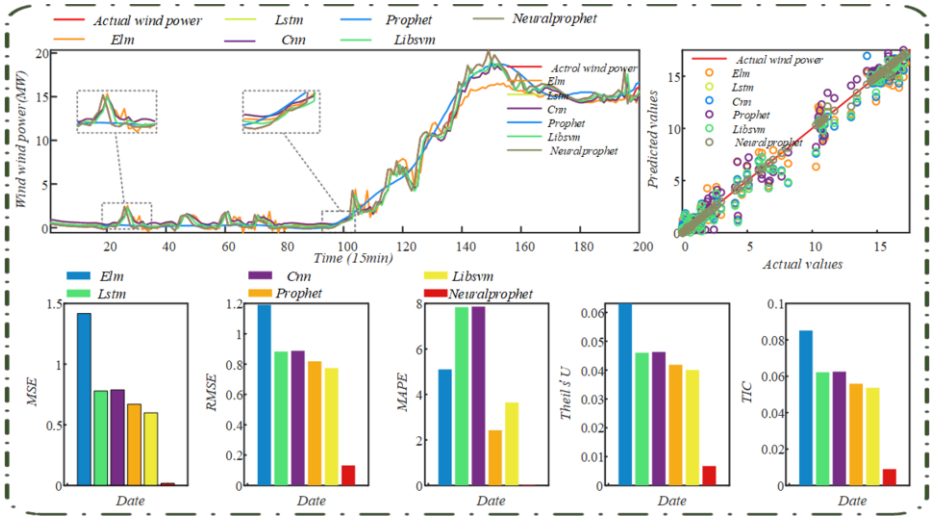

Figure 3. Comparison diagram of the single-model experiment

3.4. Hybrid model comparative experiment

The experimental results are shown in Table 4, where the value predicted by the best hybrid model is shown in bold. Figure. 4 shows Theil's U radar chart and bar chart of the four performance indices in the six hybrid model experiments as well as line charts and scatter diagrams of the prediction results of each hybrid model.

Table 4. Comparison of hybrid-model test results

Model	MAPE	RMSE	Theil's U	TIC
WTD-NP-LIBSVM	0.0392	0.1299	0.00664	0.00886
WTD-NP-VMD-SSA-LIBSVM	0.1458	0.0801	0.00409	0.00547
WTD-NP-VMD-ICEEMDAN-SSA-LIBSVM	0.2268	0.0996	0.00509	0.00679
WTD-NP-ICEEMDAN-SSA-LIBSVM	0.5724	0.0978	0.00500	0.00667
WTD-NP-ICEEMDAN-ICEEMDAN-SSA-LIBSVM	0.5154	0.1042	0.00532	0.00710
WTD-NP-ICEEMDAN-VMD-SSA-LIBSVM	**0.5168**	**0.0600**	**0.00307**	**0.00409**

(1) In time series prediction, different models exhibit varying predictive power for different time series. Therefore, this paper aims to compare the prediction performance of six commonly used time series models. The order of prediction accuracy from low to high is ELM, LSTM, CNN, PROPHET, LIBSVM, and NeuealProphet.Therefore, NeuealProphet is selected as the main model and LIBSVM is used as the error correction model.

(2) In the process of error sequence correction, ICEEMDAN-VMD quadratic decomposition can improve the prediction accuracy more than other decomposition methods. In Figure. 4, the evaluation index bar chart of data are compared. In addition to the MAPE, the other indicators show that the best correction effect of a combined model is obtained by means of the ICEEMDAN-VMD quadratic decomposition method. The scatter plots for this combined model are close to the regression line, which proves that the model is reasonable and effective.

(3) When the SSA is used as an intelligent optimization algorithm to optimize the hyperparameters of the LIBSVM model, the error is reduced relative to that obtained in the case of manual parameter adjustment, thus significantly improving the prediction accuracy.

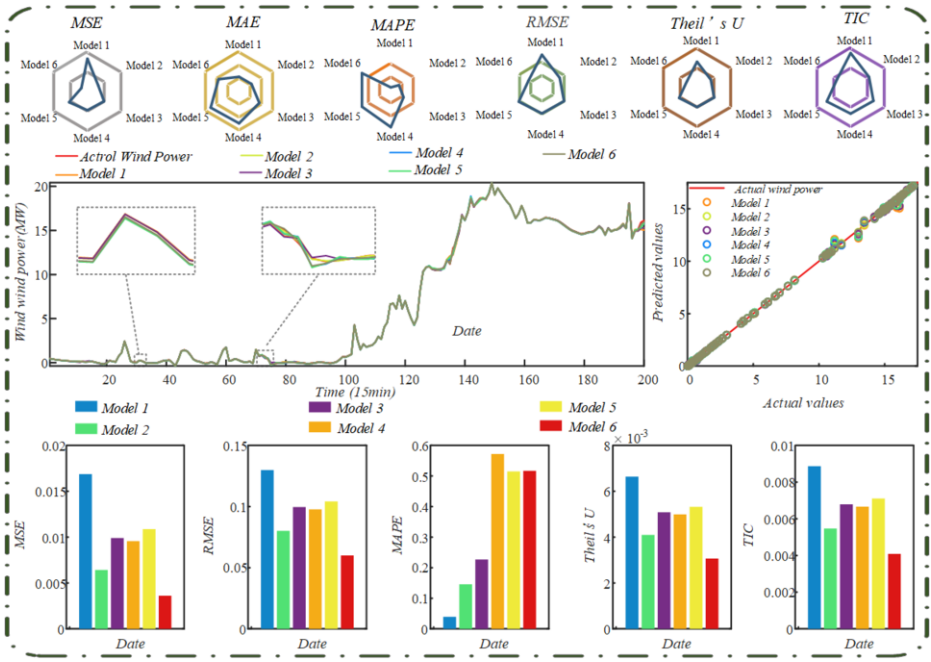

Figure 4. Comparison diagram of the hybrid-model experiment

4. Conclusion And Future Works

4.1. Conclusion

To accurately and effectively predict changes in the wind power trend, a hybrid framework that combines the wavelet threshold denoising method, the NP model, ICEEMDAN-VMD quadratic decomposition and an SSA-LIBSVM model is established. Based on two sets of experiments, four evaluation indices, the following conclusions can be drawn:

(1)The NP model achieves the best effect in wind power prediction among the six compared single models.

(2)The ICEEMDAN-VMD quadratic decomposition method proposed in this paper has the best effect in data decomposition. This method decomposes the highly complex error sequence into multiple error subsequences, which improves the prediction accuracy of the overall model.

(3)When the SSA is used as an intelligent optimization algorithm to optimize the hyperparameters of the LIBSVM model, this reduces the error obtained in the case of manual parameter adjustment and greatly improves the prediction accuracy.

4.2. Future Works

The wind power prediction model uses historical and meteorological data to predict the capacity of wind farms in advance, so it is very important to provide real-time high-precision wind field information. With the advantages of high precision, high spatial resolution and wide measurement range, wind lidar is regarded as the most suitable measurement technology to provide detailed information of wind field.

By measuring wind speed and wind direction remotely, wind lidar helps to optimize the operation of wind turbines, improve energy efficiency and achieve effective wind farm management. The next step is to improve the temporal resolution of wind field measurement by wind lidar technology, explore the application in wind turbine wake analysis, develop high spatial and temporal resolution data processing algorithms, verify the effectiveness, and provide high-precision wind speed monitoring and wake analysis to optimize wind farm operations.

5. Acknowledgments

This research was funded by the NSFC (National Natural Science Foundation of China) project (grant number: 42371377,41861047)

References

[1] J.M. González-Sopea, Pakrashi V , Ghosh B .An overview of performance evaluation metrics for short-term statistical wind power forecasting[J].Renewable and Sustainable Energy Reviews, 2021, 138:110515-.DOI:10.1016/j.rser.2020.110515.

[2] Li M , Li Y , Choi S S .Dispatch Planning of a Wide-Area Wind Power-Energy Storage Scheme Based on Ensemble Empirical Mode Decomposition Technique[J].IEEE Transactions on Sustainable Energy, 2021, 12(2):1275-1288.DOI:10.1109/TSTE.2020.3042385.

[3] Triebe O , Hewamalage H , Pilyugina P ,et al.NeuralProphet: Explainable Forecasting at Scale[J].arXiv e-prints, 2021.DOI:10.48550/arXiv.2111.15397.

[4] Han Y , Tong X .Multi-Step Short-Term Wind Power Prediction Based on Three-level Decomposition and Im-proved Grey Wolf Optimization[J].IEEE Access, 2020, PP(99):1-1.DOI:10.1109/ACCESS.2020.2984851.

[5] Bokde N ,Feijóo, Andrés, Villanueva D ,et al.A Review on Hybrid Empirical Mode Decomposition Models for Wind Speed and Wind Power Prediction[J].Energies, 2019, 12(2).DOI:10.3390/en12020254.

[6] Han Y , Tong X .Multi-Step Short-Term Wind Power Prediction Based on Three-level Decomposition and Im-proved Grey Wolf Optimization[J].IEEE Access, 2020, PP(99):1-1.DOI:10.1109/ACCESS.2020.2984851.

[7] Zhao Z , Nan H , Liu Z ,et al.Multi-step interval prediction of ultra-short-term wind power based on CEEMDAN-FIG and CNN-BiLSTM[J].Environmental science and pollution research international, 2022, 29(38):58097-58109.DOI:10.1007/s11356-022-19885-6.

[8] Wong J , Wang R , Bu S .Comparison analysis of deep learning forecasting models with hybrid structure for short-term wind power prediction[J].12th IET International Conference on Advances in Power System Control, Operation and Management (APSCOM 2022), 2022.DOI:10.1049/icp.2023.0076.

[9] Bao, Y.; Tan, C.; Jia, J. Fast Dual-LiDAR Reconstruction for Dynamic Wind Field Retrieval. Atmosphere 2022, 13, 905. https://doi.org/10.3390/atmos13060905

[10] Liu, Z.; Barlow, J.F.; Chan, P.-W.; Fung, J.C.H.; Li, Y.; Ren, C.; Mak, H.W.L.; Ng, E. A Review of Progress and Applications of Pulsed Doppler Wind LiDARs. Remote Sens. 2019, 11, 2522. https://doi.org/10.3390/rs11212522

Fuzzy Systems and Data Mining X
A.J. Tallón-Ballesteros (Ed.)

doi:10.3233/FAIA241439

Analysis of Turn to Turn Short Circuit Fault of Marine Propulsion Motor

Rui Chen, Kefeng Zhu and Kaiqi Zhao[1]
Harbin Engineering University, Harbin, 150001, China

Abstract. With the long development of the Marine industry, the diversity of the Marine power system is getting higher and higher, but at the same time, there are more and more types of faults, such as transformer faults and Marine propulsion motor faults, etc. This paper takes the relevant data of a 146-meter-long ship as an example to analyze the turn to turn short circuit fault of the propulsion motor by simulation. The simulation and analysis of ship integrated electric propulsion system by computer can comprehensively test the target system, provide data support for system design and modification, and ensure the stable and reliable operation of the system in harsh conditions. The use of pre-simulation has attracted attention in the international field of ship electric power system design.

Keywords. Ship power system; modeling; fault simulation; turn to turn short circuit fault

1. Introduction

The main function of the ship's power system is to provide electrical energy for various mechanical equipment on the ship, and to distribute electrical energy to each electrical equipment through transmission lines. In recent years, electric propulsion has been well promoted by virtue of its good maneuverability and flexible operation[1]. At the same time, the ship has many operating conditions, so the fault analysis of the ship's power system is more critical. The common fault types of Marine power system include large load disturbance, short circuit, relay fault and so on[2]. When a fault occurs in a certain part of the ship's power system, it is likely to affect other electrical equipment and even spread to the whole power system, resulting in serious consequences. If a fault occurs somewhere, the system can immediately identify the fault and eliminate the fault, which can ensure the normal operation of the ship[3]. For example, the relay in the opening and closing process will produce arc due to a variety of reasons, resulting in ablation, electromagnetic interference, increased loss and many other hazards. Therefore, in order to protect the relay contacts and extend the service life, there are a variety of arc extinguishing methods, such as Capacitance, RC (resistance-capacitance circuit) circuit, and blowing arc extinguishing chamber and other circuits and physical methods to reduce the possibility of arc generation; RC circuit is mainly used in this paper[4].

[1] Corresponding Author, Kaiqi Zhao, Harbin Engineering University, Harbin, 150001, China Email: zhaokaiqi@hrbeu.edu.cn

Using computer digital simulation technology, the variation of various parameters in the power system can be obtained by modeling and simulation without actual fault, which provides effective data support for the study of fault mechanism[5].

In the shipbuilding industry, ships using electric propulsion system are obviously superior to traditional mechanical propulsion ships in many aspects, including economy, environmental protection, safety and stability:

(1) good economy, low maintenance cost of integrated power system, and small fuel consumption;

(2) Low noise, constant speed operation of the prime mover, small structural noise, especially the cancellation of the gear box, reducing the vibration noise;

(3) Good safety and reliability.

In the research and design stage of Marine integrated power system, in order to meet the requirements of power system index, it is necessary to carry out equipment matching and internal fault research of electric propulsion system. In order to find the appropriate parameters and energy conversion mode, and obtain the best design scheme, it is necessary to analyze the operation mode of ship, engine and paddle energy conversion under different sea conditions and various working conditions, and the change law obtained during the voyage[6]. In this case, the parts of the scheme are designed to be suitable for any navigational conditions, and under this scheme, the energy consumption of the ship can be minimized in the completion of the established navigation tasks. Therefore, in the form of energy shortage, it is very urgent to study the best energy conversion of electric propulsion equipment for the purpose of saving energy, which is also one of the important directions for the development of shipbuilding industry.

2. Marine propulsion motor model

2.1 Motor modeling

The propulsion motor in the integrated electric propulsion system is a high-order, nonlinear, and strongly coupled multivariable complex system. It is difficult to establish a complete dynamic mathematical model of asynchronous motors through mechanism analysis modeling. In order to facilitate the analysis and simplification of the internal physical relationships of asynchronous motors, an equivalent circuit analysis method similar to the transformer modeling method can be used to convert the rotor winding of asynchronous motors into an equivalent rotor with the same phase number, winding turns, and winding coefficient as the stator side, Transform the complex original motor dynamic model into an equivalent asynchronous motor model with a relatively stationary coordinate system. Therefore, when establishing the mathematical model of an asynchronous motor, the main physical characteristics of the motor are considered, and a simplified assumption is made for the asynchronous motor: when ignoring the core loss, magnetic circuit saturation phenomenon, and the variation of winding resistance with temperature, and assuming a symmetrical distribution of three-phase windings, the original asynchronous[7]. Original motor model shown in the figure 1 can be obtained.

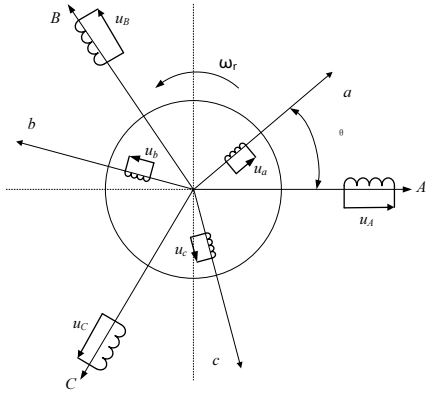

Figure 1. Original motor model of asynchronous motor

2.2 Propulsion motor hardware system

The propulsion motor mentioned in this paper is mainly a squirrel-cage three-phase asynchronous motor, the hardware part of which mainly includes power circuit and control circuit.

2.2.1Power circuit

This design uses AC-DC-AC voltage inverter, the power circuit is mainly divided into two parts: rectification part, AC-DC; Inverter part, DC-AC (DC-AC).

2.2.2Control circuit

The control circuit mainly includes DSP minimum system, optocoupler isolation circuit, current detection circuit, speed detection circuit, bus voltage detection circuit, overvoltage detection circuit, undervoltage protection circuit, IPM fault output isolation circuit, fault protection circuit, serial communication circuit.

3. Three-phase motor control strategy

In the 1980s, German Professor Dipenbrok and Japanese scholar Takahashi proposed the Direct Torque Control (DTC) model. This mode abandonds the decoupling method in traditional vector control and adopts the idea of stator flux orientation and instantaneous space vector, which has good dynamic and static performance[8].

In this system, the electromagnetic torque of the motor can be directly controlled, so that the AC motor can obtain excellent dynamic and static performance, and it has gradually become a hot spot in AC speed regulation.

In direct torque control system, the mathematical model of asynchronous motor is changed to a two-phase static coordinate system.

In the previous section, the mathematical model of induction motor based on rotating coordinate system is introduced. The mathematical model of asynchronous motor under static coordinates is obtained by coordinate transformation[9]. The coordinate transformation relationship is shown in Figure 2.

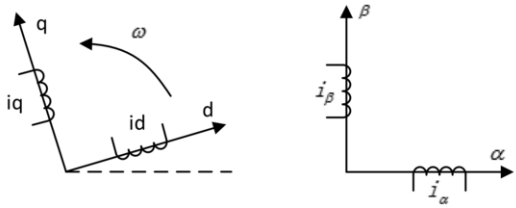

Figure 2. Coordinate transformation diagram

The voltage equation after transformation is expressed as:

$$\begin{bmatrix} u_{s\alpha} \\ u_{s\beta} \\ u_{r\alpha} \\ u_{r\beta} \end{bmatrix} = \begin{bmatrix} R_s & 0 & 0 & 0 \\ 0 & R_s & 0 & 0 \\ 0 & 0 & R_r & 0 \\ 0 & 0 & 0 & R_r \end{bmatrix} \begin{bmatrix} i_{s\alpha} \\ i_{s\beta} \\ i_{r\alpha} \\ i_{r\beta} \end{bmatrix} + \frac{d}{dt} \begin{bmatrix} \Psi_{s\alpha} \\ \Psi_{s\beta} \\ \Psi_{r\alpha} \\ \Psi_{r\beta} \end{bmatrix} + \begin{bmatrix} 0 \\ 0 \\ \omega\Psi_{r\beta} \\ -\omega\Psi_{r\alpha} \end{bmatrix}$$

The flux linkage equation is expressed as:

$$\begin{bmatrix} \Psi_{s\alpha} \\ \Psi_{s\beta} \\ \Psi_{r\alpha} \\ \Psi_{r\beta} \end{bmatrix} = \begin{bmatrix} L_s & 0 & L_m & 0 \\ 0 & L_s & 0 & L_m \\ L_m & 0 & L_r & 0 \\ 0 & L_m & 0 & L_r \end{bmatrix} \begin{bmatrix} i_{s\alpha} \\ i_{s\beta} \\ i_{r\alpha} \\ i_{r\beta} \end{bmatrix}$$

The torque equation is expressed as:

$$T_e = n_p L_m \left(i_{s\beta} i_{r\alpha} - i_{s\alpha} i_{r\beta} \right)$$

The equation of motion is expressed as:

$$\frac{d\omega}{dt} = \frac{n_p}{J} (T_e - T_L - B\omega)$$

Because the squirrel cage induction motor is used, the rotor side is always in a short circuit state, and $u_{r\alpha}, u_{r\beta}$ is directly assigned to zero in the calculation[10].

In direct torque control system, the stator parameters are directly used for calculation, and the change of rotor side parameters has no effect on the system. Through the analysis and combination of the above voltage equation, flux equation and torque equation, the state equation of the asynchronous motor with $\omega - i_s - \Psi_s$ as the state variable under αβ static coordinates is as follows:

$$\begin{cases} \dfrac{d\omega}{dt} = \dfrac{n_p^2}{J} \left(i_{s\beta} \Psi_{s\alpha} - i_{s\alpha} \Psi_{s\beta} \right) - \dfrac{n_p}{J} T_L \\ \dfrac{d\Psi_{s\alpha}}{dt} = -R_s i_{s\alpha} + u_{s\alpha} \\ \dfrac{d\Psi_{s\beta}}{dt} = -R_s i_{s\beta} + u_{s\beta} \\ \dfrac{di_{s\alpha}}{dt} = \dfrac{1}{\sigma L_s T_r} \Psi_{s\alpha} + \dfrac{1}{\sigma L_s} \omega \Psi_{s\beta} - \dfrac{R_s L_r + R_r L_s}{\sigma L_s L_r} i_{s\alpha} - \omega i_{s\beta} + \dfrac{u_{s\alpha}}{\sigma L_s} \\ \dfrac{di_{s\beta}}{dt} = \dfrac{1}{\sigma L_s T_r} \Psi_{s\beta} + \dfrac{1}{\sigma L_s} \omega \Psi_{s\alpha} - \dfrac{R_s L_r + R_r L_s}{\sigma L_s L_r} i_{s\beta} - \omega i_{s\alpha} + \dfrac{u_{s\beta}}{\sigma L_s} \end{cases}$$

The principle structure of the direct-torque control system controlled by stator flux is shown in Figure 3. In the figure, both ATR and AΨR adopt a two-point control with hysteresis loop, and their structures are respectively output according to the electromagnetic torque deviation ΔT_e and flux amplitude deviation $\Delta\Psi_s$, as shown in Figure 4. The reference value Ψ_s^* of the stator flux in the figure is related to the actual motor speed ω: if the speed is lower than the rated speed, Ψ_s^* remains unchanged; When the speed exceeds the rated speed, the flux reference value Ψ_s^* is inversely

proportional to the speed ω. P/N is a polarity discriminator for a given torque[11]. If the target torque is positive, the P/N adjustment output is 1; If the target torque is negative, the P/N adjustment output is 0. For different P/N regulation outputs, even if the same electromagnetic torque controller output, the control effect will be different.

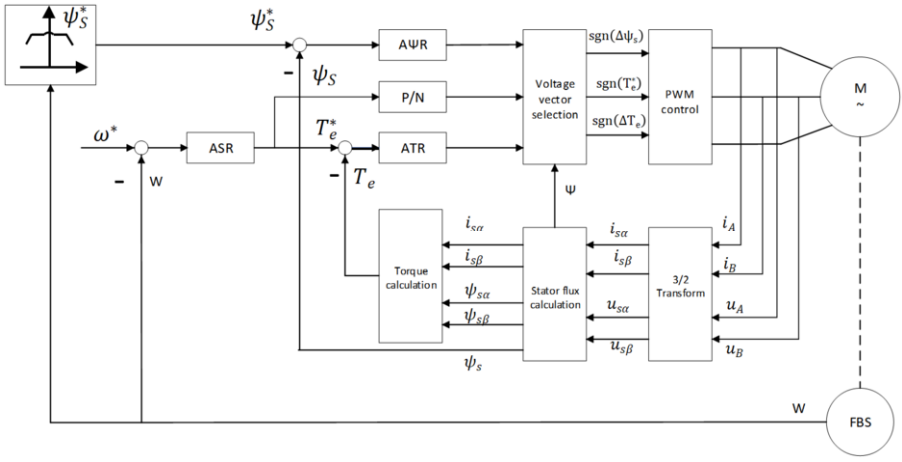

Figure3. Direct torque control system schematic structure

When the forward electromagnetic torque is expected to be obtained, when the output value of P/N regulation is "1", if the deviation of electromagnetic torque $(\Delta T_e = T_e^* - T_e)$ is greater than 0, the symbol function sgn(ΔT_e) output is "1", then the stator flux should rotate forward, so that the electromagnetic torque T_e becomes larger. If the electromagnetic torque deviation $(\Delta T_e = T_e^* - T_e)$ is less than 0, its sign function sgn(ΔT_e) output is "0", the stator flux should stop rotating, making the electromagnetic torque smaller. When the reverse electromagnetic torque is expected, the output of P/N regulation is "0". If the deviation $(\Delta T_e = T_e^* - T_e)$ of the electromagnetic torque is less than 0, the output of the symbol sgn(ΔT_e) function is "0", and the stator flux should rotate in the reverse direction, so that the electromagnetic torque T_e increases in the reverse direction. If the deviation $(\Delta T_e = T_e^* - T_e)$ of the electromagnetic torque is greater than 0, the output of the symbol function sgn(ΔT_e) is "1", which controls the stator flux vector of the motor to stop rotating, so that the electromagnetic torque decreases in the reverse direction.

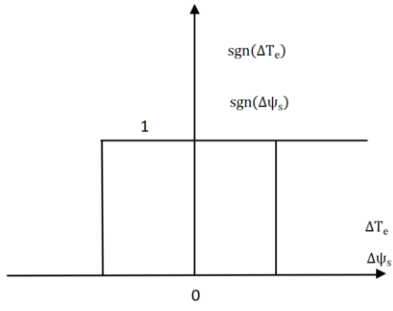

Figure 4. Two-position controller with hysteresis

4. Modeling of interturn short circuit fault of propulsion motor

Squirrel-cage induction motor is the most widely used propulsion motor in Marine integrated power system operating in a wet environment, the electrical fault of the motor cannot be ignored, especially the inter-turn short circuit fault and the single-phase open circuit fault, which make the longest fault in the three-phase asynchronous motor. Failure of asynchronous motor may cause a series of adverse reactions in Marine integrated electric propulsion system. Depending on the severity of the situation, it will affect the normal operation of the system, cause shutdown, and even endanger the stability of the whole system. It can be seen that the safe and stable operation of the power system is closely related to the running state of the motor, and the motor failure will threaten people's lives in serious cases[12]. Therefore, the operating state of the motor should be continuously monitored, so as to diagnose the fault in time, maintain the equipment, and minimize the time and scope of the fault. For three-phase asynchronous motors, winding faults are mostly stator inter-turn short circuit faults. If the faults are not diagnosed and discharged in time, the faults may develop into serious faults such as interphase short circuit and ground short circuit , and eventually lead to the system being forced to stop. This typical motor failure poses a great threat to the stability of the ship's electric propulsion system.

The stator current of the motor is three-phase symmetric given the three-phase symmetric voltage, and the angles between them are different 120 degrees with equal amplitudes. However, when the motor turns short circuit, the three-phase current symmetry is affected. The inter-turn short-circuit fault will produce a huge loop current in the short-circuit circuit. When the number of open turns is small, the motor can continue to run. When the number of short circuit turns is relatively large, it is easy to cause single-phase grounding, inter-phase short-circuit and other faults, affecting the operation of the system. Therefore, it is only necessary to detect the change of the current value of the motor stator to know whether there is an inter-turn short circuit fault.

Assuming that the stator winding of the induction motor adopts the star connection method, the structure of the induction motor with inter-turn short circuit fault in the A-phase winding is shown in Figure 5. Where $s\alpha_2$ indicates the number of short circuit turns.μ indicates the percentage of short circuit turns. And assume that the impedance is resistance R_f.

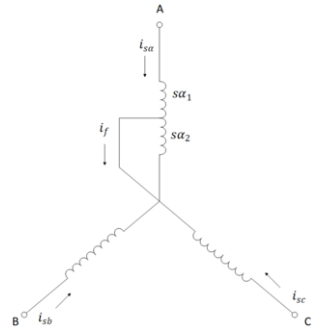

Figure 5. Induction motor stator A phase winding between turns short circuit fault

Figure 6 shows the equivalent circuit diagram of single-phase stator winding of asynchronous motor. Figure f_1 is the frequency at which the motor drive circuit is supplied with power. $\dot{U}_1$ is the phase voltage of the single-phase stator winding. $\dot{I}_1$ is the phase current of the corresponding single-phase stator winding. r_1 and x_1 are the

resistance and leakage reactance of each phase stator winding, respectively. $\dot{E}_1$ is the induced electromotive force of the stator winding in the rotating magnetic field.

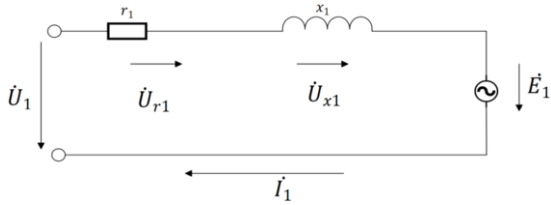

Figure 6. Stator winding equivalent circuit diagram of asynchronous motor

Induction electromotive force of rotating magnetic field of induction motor:

$$E_1 = 4.44 f_1 w_1 k_{w1} N \phi_M$$

By analyzing the equivalent circuit diagram of the stator winding of the motor, the expression of the stator current $\dot{I}_1$ can be obtained as follows:

$$\dot{I}_1 = \frac{\dot{U}_1 - \dot{E}_1}{r_1 + jx_1} = \frac{U_M \angle \phi_U}{Z_M \angle \phi_Z} = I_M \angle \phi_M$$

The stator winding of the asynchronous motor is three-phase symmetrical during normal operation. The parameters of the resistance and inductance of the single-phase stator winding of the motor are basically equal, and the electromotive force of the stator winding of each phase is also equal, and the phase difference of the three-phase current is equal. When the stator winding has an inter-turn short circuit, the resistance and inductance of the phase will decrease. It can be seen from the above equation that although the induced electromotive force changes little at this moment, the amplitude of the phase current $\dot{I}_1$ of the phase will increase, so that the phase angle of the three-phase phase current of the stator of the asynchronous motor is no longer 120 degrees different from each other[13].

In the simulation platform of Marine integrated electric propulsion system, the mathematical modeling of the asynchronous motor with inter-turn short circuit fault is carried out. The voltage equations of stator and rotor of induction motor after inter-turn failure are as follows:

$$\begin{cases} d\dfrac{\Psi_{s\alpha}}{dt} = -R_s i_{s\alpha} + u_{s\alpha} - \dfrac{2}{3}\mu R_s i_f \\ d\dfrac{\Psi_{s\beta}}{dt} = -R_s i_{s\beta} + u_{s\beta} \\ d\dfrac{\Psi_{s\alpha}}{dt} = -R_r i_{r\alpha} - \omega_r \Psi_{r\beta} \\ d\dfrac{\Psi_{r\beta}}{dt} = -R_r i_{r\beta} + \omega_r \Psi_{r\alpha} \end{cases}$$

The flux linkage equation is expressed as:

$$\begin{bmatrix} \Psi_{s\alpha} \\ \Psi_{s\beta} \\ \Psi_{r\alpha} \\ \Psi_{r\beta} \end{bmatrix} = \begin{bmatrix} L_s & 0 & L_m & 0 \\ 0 & L_s & 0 & L_m \\ L_m & 0 & L_r & 0 \\ 0 & L_m & 0 & L_r \end{bmatrix} \begin{bmatrix} i_{s\alpha} \\ i_{s\beta} \\ i_{r\alpha} \\ i_{r\beta} \end{bmatrix} - \frac{2}{3}\mu \begin{bmatrix} L_s \\ 0 \\ L_m \\ 0 \end{bmatrix} i_f$$

Short-circuit winding voltage and flux linkage equation are expressed as:

$$u_{\alpha s2} = R_f i_f = \mu Rs\left(i_{s\alpha} - i_f\right) + \frac{d\Psi_f}{dt}$$

The torque equation is expressed as:

$$T_e = \frac{3}{2} n_p L_m \left(i_{s\beta} i_{r\alpha} - i_{s\alpha} i_{r\beta} \right) - n_p \mu L_m i_f i_{r\beta}$$

$u_{r\alpha}, u_{r\beta}$ are directly assigned to zero value during calculation, and the equation of motion is unchanged, the reason for this is that the squirrel cage induction motor is equivalent to a short circuit on the rotor side[14].

Through the analysis and combination of the above voltage equation, flux equation and torque equation, the state equation of asynchronous motor with $\omega - i_s - \Psi_s$ as the state variable under $\alpha\beta$ static coordinate is as follows:

$$\begin{cases} \dfrac{d\omega}{dt} = \dfrac{n_p^2}{J} \left(i_{s\beta} \Psi_{s\alpha} - i_{s\alpha} \Psi_{s\beta} \right) - \dfrac{n_p}{J} T_L \\ d\dfrac{\Psi_{s\alpha}}{dt} = -R_s i_{s\alpha} + u_{s\alpha} - \dfrac{2}{3} \mu R_s i_f \\ d\dfrac{\Psi_{s\beta}}{dt} = -R_s i_{s\beta} + u_{s\beta} \\ d\dfrac{\Psi_{r\alpha}}{dt} = -R_r i_{r\alpha} - \omega_r \Psi_{r\beta} \end{cases}$$

5. Simulation analysis of interturn short circuit fault of propulsion motor

The Marine electric propulsion system is in a relatively humid environment, and the windings of the propulsion motor are affected by moisture and insulation aging. In order to analyze the characteristics of the Marine electric propulsion system under the inter-turn short-circuit fault, the inter-turn short-circuit fault is simulated and analyzed. The simulation time is t=6s. When the generator set is started without load, the system reaches stability when t=1.5s, the propulsion system is put into operation when t=1.5s, and the fault is simulated when t=4s. The simulation results are shown in Figure 7:

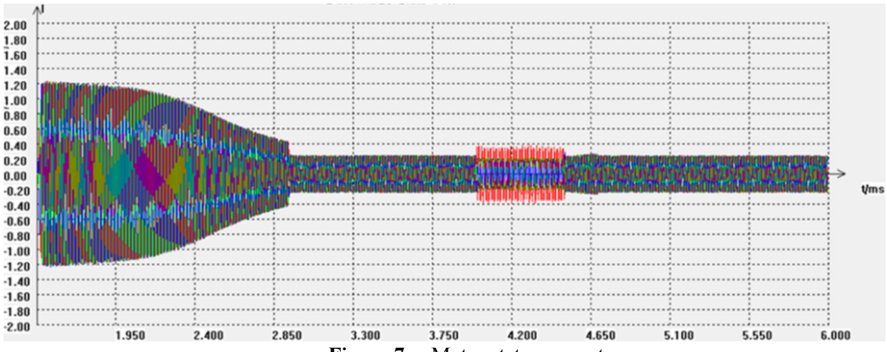

Figure 7. Motor stator current

It can be seen that the current fluctuation of the propulsion motor occurs when t = 4s, which is mainly manifested as the rapid increase of the A-phase stator current, the corresponding decrease of the other two-phase current, and the asymmetry of the three-phase stator current. It can be seen that the inter-turn short circuit fault occurred in the propulsion motor when t = 4s.

6. Conclusion

The turn to turn short-circuit fault occurs in the propulsion motor at t=4s, and the motor speed fluctuates slightly, but the A-phase stator current increases rapidly, the other two-phase current decreases correspondingly, and the three-phase stator current is asymmetrical. The control mode of the propulsion motor is direct torque control, but due to the turn to turn short-circuit fault, the electromagnetic torque still severely oscillates. After t=4.5s, the system detects the inter-turn short-circuit fault of the propulsion motor, and applies the stator current directional control mode. The stator current directional control plays a regulating role within 0.3s after the system detects the fault, reducing the fault current amplitude and restoring the motor speed.

References

[1] Guohua Y ,Yihuai H ,Qingguo S .A Convolutional Neural Network-Based Method of Inverter Fault Diagnosis in a Ship's DC Electrical System[J].Polish Maritime Research,2022,29(4):105-114.
[2] John P .Analysis of unbalanced fault operating conditions of ship electric networks via Millman's theorem[J].Journal of Marine Engineering Technology,2022,21(6):324-333.
[3] Daniele B ,Giovanni G ,Stefano P , et al. Weighted Bandwidth Method for Stability Assessment of Complex DC Power Systems on Ships[J].Energies,2021,15(1):258-258.
[4] Shuangqi Y .Research on Design, Detection and Realization of Monitoring System Based on Ship Power Grid Parameter[J].Journal of Physics: Conference Series,2021,2023(1):
[5] German-Galkin S ,Tarnapowicz D ,Matuszak Z , et al. Optimization to Limit the Effects of Underloaded Generator Sets in Stand-Alone Hybrid Ship Grids[J].Energies,2020,13(3):
[6] Haring M ,Skjong E ,Johansen A T , et al. Extremum-Seeking Control for Harmonic Mitigation in Electrical Grids of Marine Vessels.[J].IEEE Trans. Industrial Electronics,2019,66(1):500-508.
[7] Tixador P P ,A. B ,G. A , et al. Superconducting Fault Current Limiter for Ship Grid Simulation and Demonstration[J].IEEE Transactions on Applied Superconductivity,2017,27(4):1-5.
[8] Li W ,Bai M ,Lu R , et al. The Design of Portable Ship Power Grid Harmonic Analysis System based on USB[C]//IEEE Beijing Section, Global Union Academy of Science and Technology, Chongqing Global Union Academy of Science and Technology. Proceedings of 2016 IEEE Advanced Information Management, Communicates, Electronic and Automation Control Conference(IMCEC 2016).Institute of Electrical and Electronics Engineers,2016:5.
[9] Staudt V ,Bartelt R ,Heising C .Fault Scenarios in DC Ship Grids[J].IEEE Electrification Magazine,2015,3(2):40-48.
[10] Staudt ,Volker, Bartelt , et al. Fault Scenarios in DC Ship Grids: The advantages and disadvantages of modular multilevel converters.[J].IEEE electrification magazine,2015,3(2):40-48.
[11] V. M ,V. Z ,G. V , et al. Identification of the Parameters of a Three-Phase Asynchronous Motor for Intelligent Monitoring Systems[J].Latvian Journal of Physics and Technical Sciences,2022,59(2):23-36.
[12] K ,V. K,I. V.Frequency-current method of controlling an asynchronous three-phase motor[J].Transactions of the Krylov State Research Centre,2020,4(394):
[13] Malyar S V ,Malyar V V .ESTABLISHED MODES AND STATIC CHARACTERISTICS OF THREE-PHASE ASYNCHRONOUS MOTOR POWERED WITH SINGLE PHASE NETWORK[J].Izvestiâ Vyssih Učebnyh Zavedenij i Ènergetičeskih ob Edinennij SNG. Ènergetika,2016,59(6):536-548.
[14] Liu J H ,Wang L J ,Bao D F .Modeling of the Three-Phase Asynchronous Motor Based on MATLAB/Simulink[J]. Applied Mechanics and Materials,2013,2370(313-314):1042-1045.

Fuzzy Systems and Data Mining X
A.J. Tallón-Ballesteros (Ed.)

doi:10.3233/FAIA241440

ZJ19 Cigarette Crimper Joint Detector and Exclusion Device and Applications

Tongshan LIU, Yuanyuan CHEN, Yali ZHANG, Andong Bi, Fang XU, You LIU[1]
Baoding Cigarette Factory, Hebei Baisha Tobacco Co., Ltd, 999 Hehua Road, Baoding 071000, China
ORCiD ID: Tongshan LIU https://orcid.org/0009-0002-6218-1639

Abstract. This study aimed to comprehensively analyze the types of joint cigarettes and the structure and working principle of the joint detector and exclusion device of the original equipment to identify specific reasons for the inability of the ZJ19 cigarette crimper [1] to effectively detect and exclude joint cigarettes. An implementation plan was determined through repeated experiments and numerous discussions. A built-in joint detector was designed and installed to address the inability of the original equipment to detect built-in joints [2], keeping the original joint detector unchanged [3], thus ensuring the detection of all joints. A filter was installed in the exclusion air path to address the issue of missing exclusion of splicing joint cigarettes during the production process, and improvements were made to the material of the removal block, reducing the failure rate of the excluded part. The addition of a secondary exclusion function further ensured the exclusion of all joint cigarettes, thereby improving product quality

Keywords. Detector; filter; joint cigarette; removal block; secondary exclusion; ZJ19 cigarette crimper

1. Introduction

The quality of cigarette products is fundamental to the survival and development of cigarette companies [4] and is an increasing concern for consumers. When using the ZJ19 cigarette crimper during production, joint cigarettes often flow into the next processes, thereby affecting product quality. If they are not detected promptly, they can enter the market, posing a risk to consumer interests and tarnishing the corporate image. Generally, joint cigarettes are considered defective and fall under category A defects. Therefore, the urgent priority is ensuring the complete exclusion of all joint cigarettes during the production process.

[1] Corresponding author, You Liu, Hebei Baisha Tobacco Co., Ltd., Baoding Cigarette Factory, Baoding, Hebei, 071000; E-mail: 156026590@qq.com

2. Cause Analysis

2.1 Types and Frequency Statistics of Unexcluded Joint Cigarettes

The types of joint cigarettes that appear during the production process include the following: rolling paper built-in joints, rolling paper joints, tipping paper built-in joints, and tipping paper joints (Fig. 1) [5]

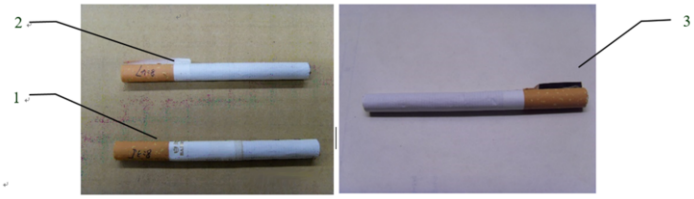

Figure 1. Images of real joint cigarettes: 1.rolling paper built-in joint or rolling paper joint; 2. tipping paper built-in joint; 3.tipping paper joint.

A statistical table was generated based on the quality process control data statistics from March to May 2010, (Table 1).

Table 1. Statistics of types and number of joint cigarettes unexcluded by the ZJ19 Cigarette Crimper from March to May 2010

No.	Quality defect item		Number of unexcluded joint cigarettes (joint cigarettes)		% of the total unexcluded joint cigarettes
1	Built-in joint	Rolling paper built-in joint	28		
		Tipping paper built-in joint	16	44	77.2
2	Splicing joint	Rolling paper joint	8		
		Tipping paper joint	5	13	22.8

As shown in Table 1, 57 unexcluded joint cigarettes appeared in 3 months, with a frequency of 19 joint cigarettes per month. The number of unexcluded cigarettes with built-in joints accounted for 77.2% of the total unexcluded joint cigarettes, highlighting it as the key issue to be addressed. Although the number of joint cigarettes that failed to be excluded during production was relatively small, it could not be overlooked, as joint cigarettes are considered defective cigarettes and fall under category A defects. Therefore, cause analysis was required.

2.2 Analysis of the Joint Detection and Exclusion Process of Original Equipment

2.2.1 Analysis of Tipping Paper Joint Detection and Exclusion Process of Original Equipment

When the roll of the tipping paper reached the set diameter , the paper feed roller accelerated by 12.5% and the paper storage began. When the paper storage reached 8 m in length, the splicing device was activated. It cut off the head of the tipping paper in use and the tail of the spare tipping paper, and spliced the tipping paper with black tape on the surface of the joint. As the spliced tipping paper joint passed through the joint detector

[6], the joint detector emitted a pulse signal to the exclusion controller board due to the weak reflection of light from the black tape [7]. The signal was then shifted and amplified, leading to the electrification of the double-length exclusion solenoid valve within the elimination drum wheel [8]. Then, compressed air was passed, and the double-length joint cigarettes were blown off through the exclusion hole on the removal block (Fig. 2).

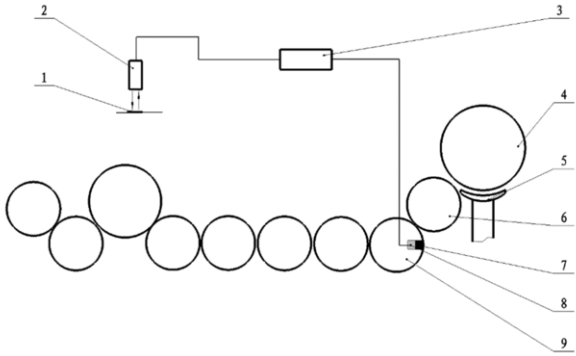

Figure 2. Schematic diagram of joint detection and exclusion process: 1.Black tape joint; 2. joint detector; 3.exclusion signal processing controller; 4. tipping paper drum wheel; 5. washboard; 6. removal drum wheel; 7. removal block; 8.double-length exclusion valve; 9. elimination drum wheel.

2.2.2 Analysis of Rolling Paper Joint Detection and Exclusion Process of Original Equipment

The rolling paper joints of the original equipment do not have a dedicated detector. The exclusion process of the joints was as follows: detecting the splicing signal, shifting and amplifying the signal, and finally outputting the signal to the double-length exclusion solenoid valve of the elimination drum wheel to eliminate the joint cigarettes.

2.3 Cause Analysis of Unexcluded Built-in Joints

The tipping paper and the rolling paper of supplied materials often contain joints. The tipping paper detector of the original equipment is a reflective photoelectric switch, which can detect only darker black tape joints (with reduced intensity of reflected light). In contrast, the double-sided tape of the tipping paper built-in joint is inside the joint. This means that when the joint passes through the detector, the detector can detect only the tipping paper but not the built-in joint (as the intensity of the reflected light remains largely unchanged). Hence, all tipping paper built-in joint cigarettes are not excluded, allowing joint cigarettes to flow into the next process (Fig. 3).

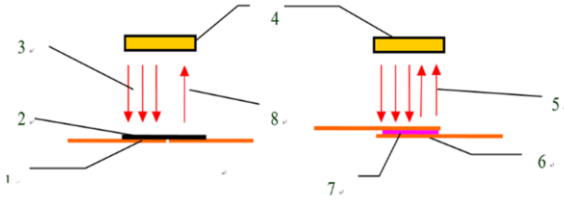

Figure 3. Joint detector: 1. Black tape joint; 2. black tape; 3.emitted light by the detector; 4. reflective joint detector; 5. reflected light from the built-in joint (strong); 6. built-in joint; 7. double-sided tape; 8. reflected light from black tape (weak).

Both rolling paper built-in joints and joints produced during production are joined with double-sided tape, and the rolling paper joints lack a detector. Hence, the inability to detect built-in joints is the fundamental reason why cigarettes with built-in joints cannot be excluded.

2.4 Cause Analysis of Unexcluded Joints

Besides the missing exclusion of built-in joints, the joints produced during production are also frequently not excluded [9], which is mainly due to the exclusion device failure. The causes and frequency of the exclusion device failures were statistically analyzed (Table 2).

Table 2. Some of the exclusion device failures from February to August 2010

Month	Causes of exclusion failures				
	Faults of solenoid valve (*n*)	Wear of removal block (*n*)	Wear of elimination drum wheel (*n*)	Cracking of compressed air pipe due to aging (*n*)	Others (*n*)
February	2	2	1	0	0
March	4	1	0	0	1
April	3	2	1	0	0
May	1	1	0	0	0
June	2	3	0	1	1
July	6	2	0	0	0
August	3	2	1	1	0
Total	21	13	3	2	2
Ratio	51.2%	31.7%	7.3%	4.9%	4.9%

As indicated, the solenoid valve failures occurred 21 times, accounting for 51.2% of the exclusion device failures. By inspecting the compressed air pipeline, we found that the compressed air indeed contained particulate impurities, condensation water, and oil. Consequently, the solenoid valve was blocked or operating inflexibly, thus causing poor exclusion of joint cigarettes. Therefore, the presence of impurities in the compressed air was the direct cause of solenoid valve failures, leading to the ineffective exclusion of joint cigarettes. The failures due to the wear of the removal block occurred 13 times in 7 months, from February to August 2010, accounting for 31.7% of the exclusion device failures. An investigation into the actual wear of the removal block after 1 month of use was conducted, and a statistical table was created (Table 3).

Table 3. Statistics of the wear amount of the removal block

Machine No.	*1*	*2*	*3*	*4*	*5*	*6*	**Average**
Thickness before installation (mm)	22.45	22.46	22.45	22.50	22.39	22.52	22.46
Thickness after 1 month of use (mm)	22.03	22.08	22.09	22.11	22.00	22.19	22.08
Wear amount (mm)	0.42	0.38	0.36	0.39	0.39	0.33	0.38

As indicated, the average wear amount of the removal block after 1 month of use was 0.38 mm. Only when the removal block in the elimination drum wheel was tightly fitted to the drum wheel could joint cigarettes be effectively excluded. The removal block was made of bakelite, which has low toughness and is easily worn. If not promptly expelled, tobacco residue and particles produced by wear can cause accelerated wear of the removal block. The worn removal block cannot fit tightly to the drum wheel, causing leaks in the negative pressure suction in the drum wheel and dispersion of the exclusion compressed air. This makes it impossible for the exclusion device to completely exclude defective cigarettes. The diagram of the elimination drum wheel exclusion structure is shown in Figure 4.

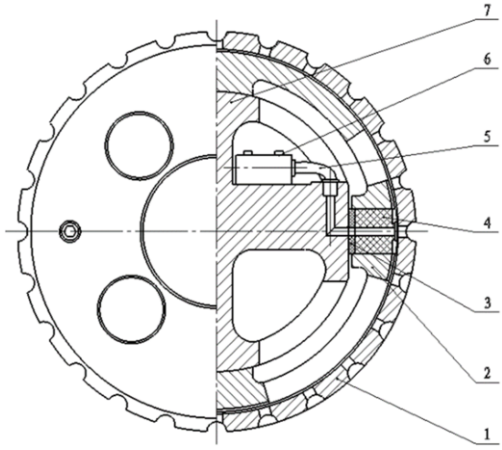

Figure 4. Diagram of the elimination drum wheel exclusion structure: 1. Elimination drum wheel; 2. negative pressure distribution valve; 3. adjustment spacer; 4. removal block; 5.compressed air pipe; 6.double-length exclusion solenoid valve; 7. drum wheelbase.

In summary, the main causes of failures to exclude joint cigarettes in cigarette crimpers are as follows:

1) Lack of a built-in joint detector in raw materials
2) Impurities in compressed air
3) Lack of wear resistance of the removal block.

3. Solution

Given multiple reasons for the failure to exclude joint cigarettes, comprehensive consideration is necessary:

The issue of tipping paper built-in joints not being detected can be addressed by requiring manufacturers to modify their production methods to accommodate the joint detector. However, as multiple suppliers of raw materials exist in the market, achieving this change in the short term may be difficult. Moreover, as rolling paper lacks joint detectors, installing an additional tipping paper joint detector and a rolling paper joint detector without altering the existing detection setup is a feasible solution.

The problem of impurities in the compressed air can be easily resolved by choosing an appropriate filter.

The performance of various materials should be compared to address the issue of the nonwearable removal block. Then, a material that is both performance-efficient and complies with food safety conditions should be selected to replace the bakelite material.

3.1 Solution 1: Detection of Built-In Joints in Raw Materials

3.1.1 Detector Selection

The tapes of both rolling paper and tipping paper built-in joints were located inside the joints. As a result, detecting the joints from the perspectives of color difference and reflection intensity was difficult. Given that the built-in joints were made of two layers of rolling paper or tipping paper bonded with a double-sided tape and their thickness was about three times the thickness of a single layer of tipping paper or rolling paper, joint thickness detection was a feasible method for detecting joints. As the thickness difference between a joint and a single layer of paper was extremely small, directly detecting the thickness of rolling paper or tipping paper joints was challenging. However, experiments have revealed a significant difference in light transmittance between the single-layer paper and the joint. Therefore, reflective photoelectric sensors were chosen after comparing the functions of various photoelectric detectors. Furthermore, considering the flexible and convenient installation of reflective fiber optic sensors, reflective fiber optic sensors were specifically chosen to detect tipping paper or rolling paper joints.

The selected fiber optic sensor model was KEYENCE FS-V21R, which consisted of a transmitter, a receiver, fiber optics, and a fiber optic amplifier. This sensor had high sensitivity, could recognize objects as narrow as 3 mm, and had an operating frequency response of ≤0.1 ms. Thus, it could detect the normal splicing of rolling paper/tipping paper and built-in joints of about 8 mm within the entire rolling paper, resulting in economical, practical, and reliable performance.

3.1.2 Determination of Detector Position

The criteria for determining the detector position were as follows: (1) The running state of the rolling paper and tipping paper must be stable. Only with stable operation can the detector reliably work without causing false detections. (2) The paper travel distance from the detector to the exclusion device must be constant to ensure the accuracy of signal shifting and precise exclusion of joint cigarettes. (3) The detector should be installed after the splicing device of the original equipment. This detected not only built-in joints but also joints produced during production, allowing for the detection of joints even if the original detector fails.

The position of the tipping paper joint detector that met the aforementioned three criteria was after the original joint detector and before the first paper-guide roller after the tipping paper base, as shown in Figure 5.

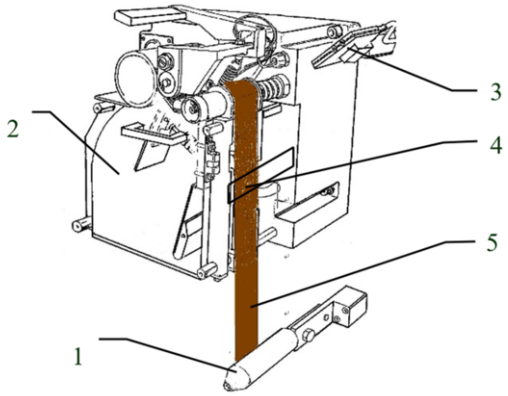

Figure 5. Arrangement of detectors for built-in joints in the tipping paper: 1. Paper-guide roller; 2. tipping paper base; 3. original tipping paper joint detector; 4. arrangement of built-in joint detectors; 5.tipping paper.

The detectors for rolling paper joints were arranged after the rolling paper guide track and before the cigarette pipe paper-guide roller, as shown in Figure 6.

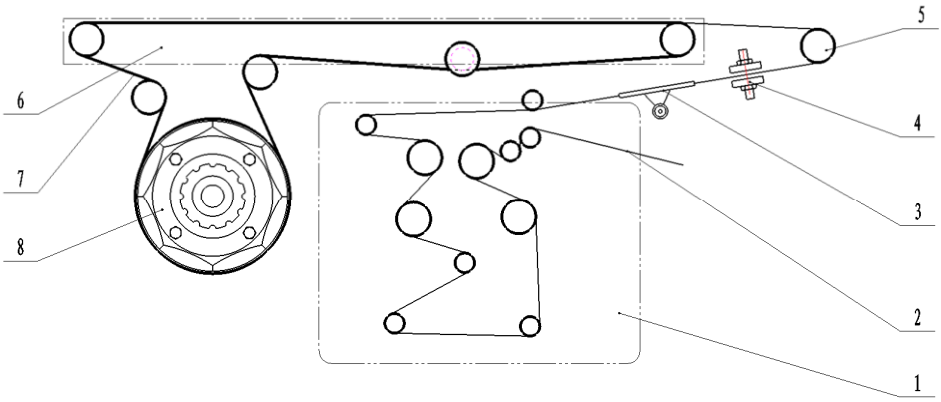

Figure 6. Arrangement of detectors for built-in joints in the rolling paper: 1. Brand case; 2. rolling paper; 3. rolling paper guide track; 4. joint detector; 5. cigarette pipe rolling paper guide track; 6. cigarette pipe; 7. cotton tape; 8. tape drum.

3.1.3 Detection Principle

The reflective fiber optic sensor detects the intensity of light. When a joint reaches the detection position, the joint blocks most of the light. Consequently, the intensity of the received light is below a set value. The sensor then recognizes the existence of a joint and sends a signal to the exclusion controller. After signal shifting and amplification by the exclusion controller, the signal is outputted to the elimination drum wheel, which energizes the exclusion solenoid valve to exclude the joint cigarettes, as shown in Figure 7.

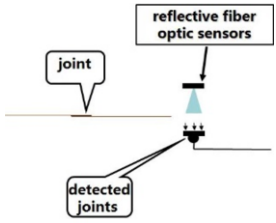

Figure 7. Schematic of built-in joint detection.

3.1.4 Determination of Detection Range

The faces of the two fiber optic connectors were positioned facing each other on opposite sides of the paper [10]. If the distance between them was too great, the emitted light diverged, reducing the intensity of the received light and making it susceptible to interference from other light sources. Conversely, if the distance was too close, it affected the paper perforation work of operators, caused wear on the fiber optic connectors, and resulted in paper dust sticking to them, negatively impacting detector performance. Through testing, a distance of 6 mm between the two fiber optic connectors was determined, to ensure stable detector operation without affecting the paper perforation work of operators (Fig. 8).

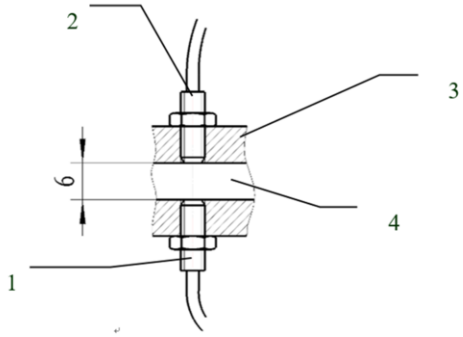

Figure 8. Diagram of the distance between fiber optic connectors: 1. Emitting fiber optic connector; 2. receiving fiber optic connector; 3. fiber optic connector fixing support; 4. detection channel.

3.1.5 Design of Processing Drawings

After the detector model and the installation position were determined, the production required design drawings for the fiber optic connector support, fiber optic amplifier base, and support base. Figure 9 shows the three-view drawing of the fiber optic connector support.

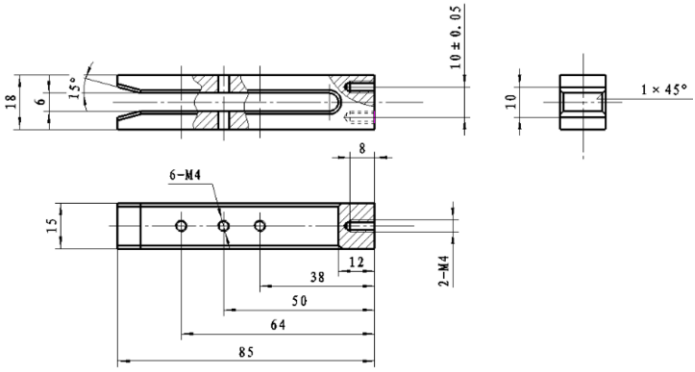

Figure 9. Three-view drawing of the detector support.

3.1.6 Circuit Design

The upgraded circuit on the original equipment used two Omron counters (H7CX-AWD1) and four optocouplers to initially process the joint signal. Then, the signal passed through the detector interface board and the high-flow exclusion board before being outputted to the exclusion solenoid valve of the elimination drum wheel to exclude the joint cigarettes. Figure 10 illustrates the working principle.

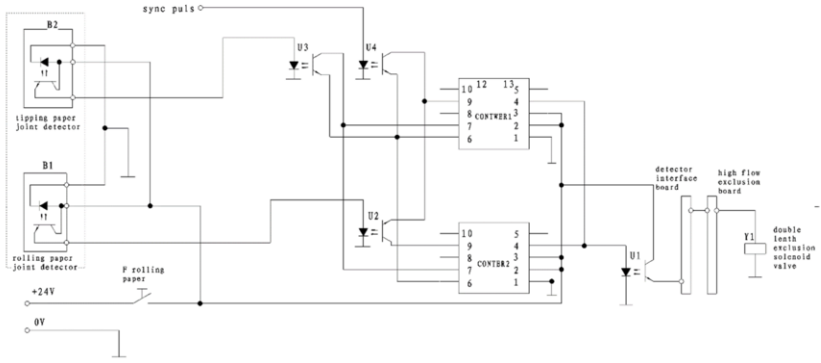

Figure 10. Schematic of the joint detector.

3.1.7 Installation and Debugging

The system was first tested and debugged on Machine No. 3, as shown in Figure 11.

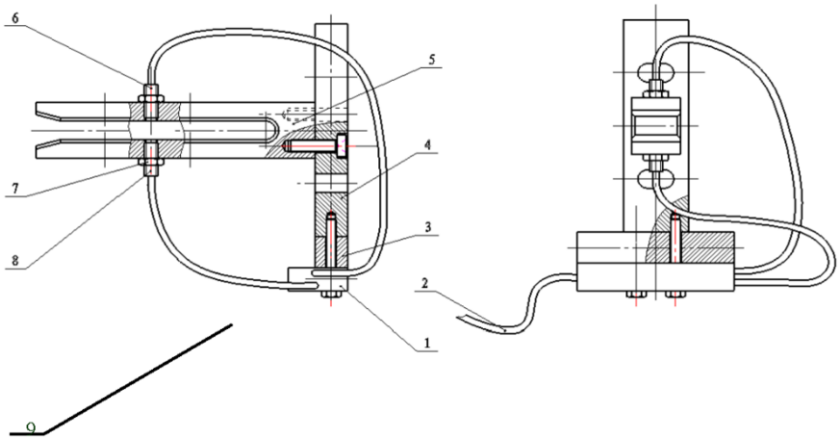

Figure 11. Diagram depicting detector installation: 1. Fiber optic amplifier; 2. power supply and signal line; 3. fiber optic amplifier support; 4. fiber optic connector support base; 5. fiber optic connector support; 6. transmitter; 7. locknut; 8.receiver; 9. fiber optic.

The debugging process and key points were as follows: (1) The FS-V21R fiber optic sensor digitally presented the intensity of received light. The higher light transmittance in the paper resulted in increased light intensity detected by the sensor, leading to a higher displayed value. After testing, the set value was determined to be half the displayed value for a single layer of paper. (2) In accordance with process requirements, the number of cigarettes excluded upon joint detection was set to 6–10 double-length cigarettes. (3) The initial number of shift steps from detection to exclusion position was preliminarily set based on calculations and then accurately tuned through testing to ensure precise exclusion of joint cigarettes.

After joint detection and exclusion testing, all joints in the rolling paper and the tipping paper were detected, and all joint cigarettes were successfully excluded.

3.1.8 Promotion

After successful testing on Machine No. 3, this improvement was extended to the other ZJ19 cigarette crimpers. Joint detection and exclusion tests were conducted on all six ZJ19 cigarette crimpers, and all built-in joints were successfully excluded under the premise that the exclusion device functioned correctly.

3.2 Solution 2: Arrangement of a Filter for the Exclusion Device

In this study, a filter with a powder metallurgy porous filter element was selected. Powder metallurgy porous materials possess excellent permeability, making them suitable for uniformly filtering distributed fluids and for use in permeation devices. When used as filters, they offer a high filtration rate. For example, filters made of sintered titanium sponge powder demonstrate a filtration rate six times higher than ceramic filters when used for filtering electrolytic zinc sulfate solution. Similarly, filters made of sintered green steel powder boast a flow rate four times greater than that of pleated paper filters and six times that of cotton yarn filters. Additionally, the pore size and porosity can be controlled, ensuring high filtration accuracy. The materials also exhibit good gas separation performance while retaining certain metallic and alloy characteristics such as

thermal conductivity, electrical conductivity, and weldability. Also, they possess sufficient strength and toughness to operate under high-pressure conditions. The failure rate of the solenoid valve was significantly reduced after separately installing a filter with 0.5-μm powder metallurgy porous filter element for the exclusion device. From October to November 2010, the number of failures of the solenoid valve was zero.

3.3 Solution 3: Optimization of the Removal Block Material

The original material used for the removal block was bakelite. It is known in the plastics industry as phenol formaldehyde plastic, primarily using wood powder as filler. Plastic products made from bakelite powder through pressing are called bakelite products. The removal block in the elimination drum wheel is made of bakelite, exhibiting high rigidity, high brittleness, and average wear resistance. Further, the particles generated from wear accelerate the deterioration of both the removal block and the drum wheel.

After extensive comparisons, ultra-high-molecular-weight polyethylene (UHMWPE), an engineering plastic, was selected as the material for the removal block due to its exceptional wear resistance, impact resistance, excellent compressive strength, crack resistance, good self-lubrication, anti-adhesiveness, unique low-temperature resistance, and excellent chemical stability. The dimensions of the original removal block were measured for processing (Fig. 12).

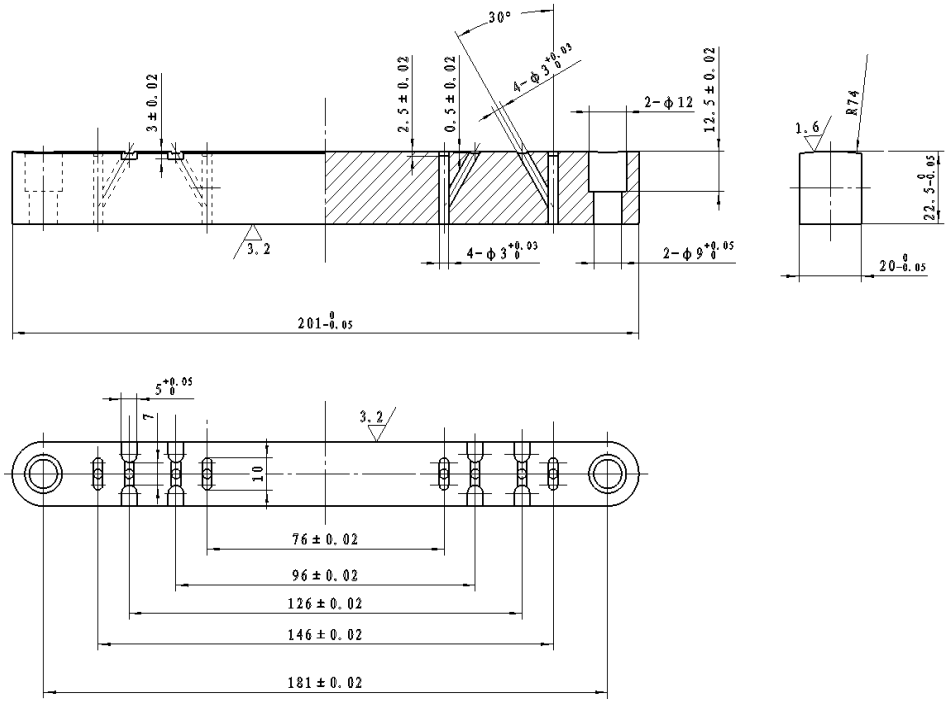

Figure 12. Three-view drawing of the removal block.

Testing on Machine No. 1 revealed that the wear amount of the UHMWPE removal block after 1 month of use was only 0.12 mm. The statistics of the wear amount of the UHMWPE removal block after 1 month of use are presented in Table 4.

Table 4. Statistics of wear amount

Machine No.	1	2	3	4	5	6	Average
Thickness before installation (mm)	22.45.	22.49	22.46	22.45	22.48	22.43	22.46
Thickness after 1 month of use (mm)	22.33	22.38	22.33	22.32	22.36	22.28	22.33
Wear amount (mm)	0.12	0.11	0.13	0.13	0.13	0.15	0.13

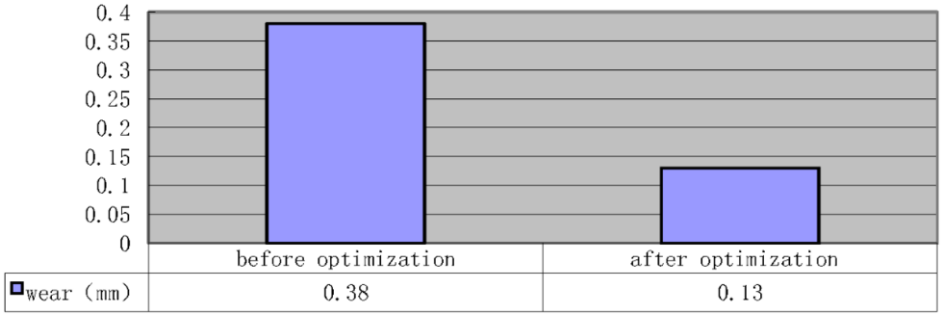

Figure 13. Wear amount of the UHMWPE removal block after 1 month of use before and after improvement.

As shown in Table 4 and Figure 13, the average wear amount of the UHMWPE removal block after 1 month of use was 0.13 mm, showing a significant reduction in wear compared with that before the improvement.

3.4 Further Enhancement of Joint Cigarette Exclusion Function: Improving Secondary Exclusion Capability

After the improvements, a 1-month follow-up investigation on six cigarette crimpers revealed a joint cigarette exclusion failure in Machine No. 2 due to the malfunction of the exclusion device. Thus, despite detecting all joints, instances of joint cigarette exclusion failure might still occur if the exclusion device malfunctioned. From December 2010 to February 2011, the number of exclusion device failures was statistically analyzed and compared with the data from June to August 2010, as depicted in Table 5.

Table 5. Causes and number of exclusion failures

Month		Causes of exclusion failures					
		Faults of solenoid valve	Wear of removal block	Wear of elimination drum wheel	Cracking of compressed air pipe due to aging	Others	Total
June to August 2010 (before the improvement)	Number of failures	11	7	1	2	2	23
December 2010 to February 2011 (after the improvement)	Number of failures	0	1	0	1	2	4

The number of exclusion device failures significantly reduced after the improvement compared with before the improvement, but occasional failures still occurred (Table 5). Further reducing the number of exclusion device failures was challenging, and hence an alternative solution to address the issue of missing exclusion of joint cigarettes was required. After extensive research and experiments, a solution was devised to ensure the complete exclusion of joint cigarettes in the final exclusion drum wheel in the event of a malfunction of the exclusion device in the elimination drum wheel.

The working principle of secondary exclusion is as follows: Normally, when a joint is detected, the signal reaches the primary exclusion controller and the output signal of the controller is split into two signals. One signal targets the elimination drum wheel to exclude the joint cigarettes, whereas the other, after being processed by the secondary exclusion controller, targets the final exclusion drum wheel to clear the exclusion hole. If the primary exclusion fails, the joint cigarettes cannot be excluded at the elimination drum wheel position but can be excluded at the secondary exclusion position, that is, the final exclusion drum wheel (Fig. 14).

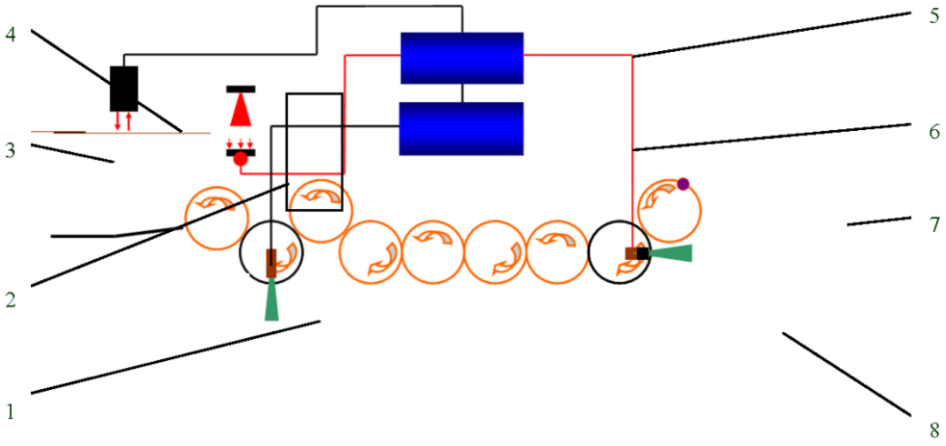

Figure 14. Schematic of secondary exclusion: 1. Exclusion drum wheel; 2. fiber optic detector; 3. joint; 4. black tape joint detector; 5.primary exclusion signal processing controller; 6. secondary exclusion signal processing controller; 7. joint cigarette; 8. elimination drum wheel.

The exclusion testing was conducted on each YJ19 cigarette crimper. After setting the elimination drum wheel exclusion device to a failed state, the joint cigarettes could not be excluded at the primary exclusion position but instead were all excluded at the secondary exclusion position. Therefore, after the addition of a secondary exclusion function for joint cigarettes, joint cigarettes could still be excluded even if the exclusion device of the elimination drum wheel failed, providing a double assurance for the exclusion of joint cigarettes.

4. Improvements

After the improvements, the statistics of defective cigarettes in the six ZJ19 cigarette crimpers in the packaging workshop showed zero joint cigarettes from March 10, 2011, to June 30, 2011, indicating ideal performance of the improvements (Fig. 15).

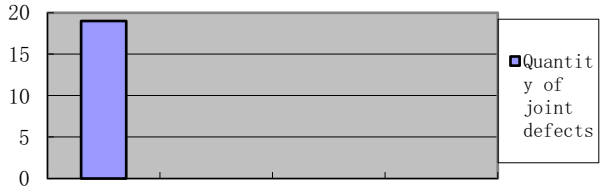

Figure 15. Quantity of joint defects before and after improvement.

After the improvement, the failure rates of the exclusion devices reduced. In virtue of the presence of the secondary exclusion device, the unqualified cigarettes could be eliminated by the last elimination drum even if the exclusion device at the elimination drum failed. Hence, maintenance could be completed in off-operation slots instead of operation slots, thereby improving the effective operation rate. Table 6 and Figure 16 illustrate the failure frequency and maintenance time of exclusion devices before and after improvement.

Table 6. Failure frequency and maintenance time of exclusion devices before and after improvement

		Causes of exclusion failure					
Period	Item	Blockage of solenoid valve	Wear of elimination block	Wear of elimination drum	Aging and cracking of compressed air pipe	Others	Total
June to August 2010 (before improvement)	Failure frequency	11	7	1	2	2	23
	Maintenance time (h)	7.3	3.5	0.5	3	1	15.3
March to May 2011 (after improvement)	Failure frequency	1	1	0	1	2	5
	Maintenance time (h)	0	0	0	0	0.5	0.5

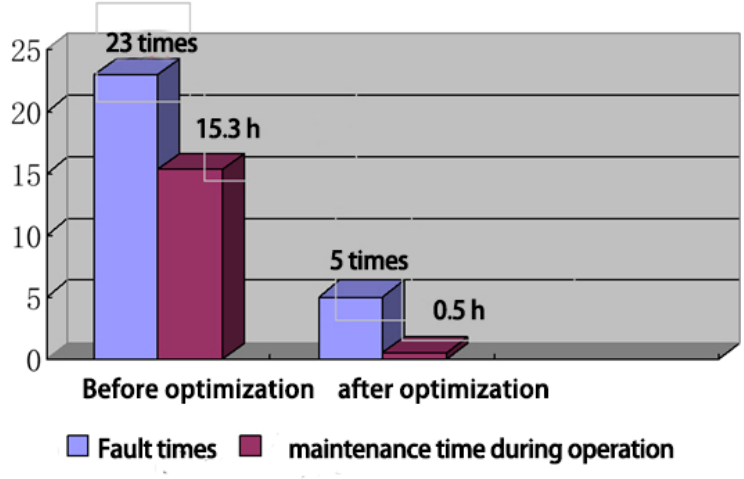

Figure 16. Failure frequency and maintenance time of exclusion devices before and after improvement.

5. Conclusions

The improvements proposed in this study addressed the issues of undetectable cigarettes with built-in joints and missing exclusion of joint cigarettes, thereby enhancing product quality, protecting consumer interests, and upholding corporate reputation. Additionally, they resulted in a reduction in the number of the exclusion device failures, saved maintenance time, and improved the effective operation rate of the equipment. This improvement process introduced new ideas for problem identification, analysis, and resolution, enhanced coordination and teamwork skills, and provided valuable references for future maintenance and improvements.

References

[1] Huang C, Xu Z, The design and implementation of cigarette culling device in Protos 70 cigarette maker. Study of Science and Engineering at RTVU. 2021;(02):9-12. DOI:10.19469/j.cnki.1003-3297.2021.02.0009

[2] Li G. Application of Static Lapping in KDF2 Paper Lapping System. Science and Technology Innovation Herald. 2013; (05): 71. DOI: 10.16660/j.cnki.1674-098x.2013.05.169

[3] Wang G, Zhou Y, Ren H. The application of ultrasonic technology in the detection of paper tray joints. Plant Maintenance Engineering. 2021; (20): 97-98. DOI: 10.16621/j.cnki.issn1001-0599.2021.10D.54

[4] Bian Y. Training materials for tobacco machinery repair technicians, Vocational Skills Appraisal and Guidance Center of the National Tobacco Monopoly Administration, 2002 (12): 18-29. https://www.docin.com/p-616304710.html

[5] Zhang D, Chu L, Ma Y. Application of AC servo control system in ZJ17 cigarette maker for non-adhesive tape splicing. Journal of Shandong Industrial Technology. 2018; (18):36. DOI: 10.16640/j.cnki.37-1222/t.2018.18.031

[6] Li P. Improvement of the detection technology for the tipping paper joint of ZJ17 cigarette unit. Scientific and Technological Innovation. Scientific and Technological Innovation. 2021; (34): 170-172. https://kns.cnki.net/kcms2/article/abstract?v=vAdbs87d_CmJsMf-MdU3A5LsHxIdKofy_0fR3daNUyM9KDHRPRKc-FNGK1KEF9RrABOSbplzvQ9bDy9U7VvRxYh92JbhT3EqbVQko4Absn4Llfw3Dc2wSCuNcf3jouYxDo_DI6jqYa4Gylm1x4upIg==&uniplatform=NZKPT&language=CHS

[7] Yu T, Li C, He C, An J, Du W. Design of Formed Paper Joint Tracking and Rejection System Based on PLC. Mechanical Engineering & Automation. 2023; (04): 153-155. https://kns.cnki.net/kcms2/article/abstract?v=vAdbs87d_ClKoRM0ELBAehXczTbzO34wPOpCoDAeNZJ6FfsCaBQoHT0VMKRgQ72fgFcR0vGSWg9IGp3WuEb9WpnMGnieLGDbxWikkOTax5fDHxlCu41GmCKgCmDE0VucIzvHg7r-SuqaV7VkiiZsxQ==&uniplatform=NZKPT&language=CHS

[8] Zhang B. Improvement of ZJ19 Cigarette Machine Eliminating Drum Double Length Cigarette Removal Device. China Science and Technology Information. 2021; (13): 42-43. https://kns.cnki.net/kcms2/article/abstract?v=vAdbs87d_CkFmzfK1k-D06VLCWPRAteZtoLsbCv-pc316zoqPI03Qyk8D9HJcsZAlkru7Sc0aswvyVKKgNNKke7hhz2YrFTs0z5kWNY6vnp7jHsKB7V-3rbnzZMGy9uEKDCCCk9c_mN9Qo67-oLXyg==&uniplatform=NZKPT&language=CHS

[9] Wei X, Guo W, Zhao Y. Development of a detection and removal system for tipping paper joints in cigarette machines. China Plant Engineering. 2006 (08): 49-50. https://kns.cnki.net/kcms2/article/abstract?v=vAdbs87d_CmXkpgROSvJvT6yp2ZjuiBkKsQ-UfkeZYiUmciUYLamnQw2TzQU1rwVOtlMPW1tBnedSjzZDY-1s45O7US34Wcau0PhABCu3CUk5uTZ2_Sfkv0rMrKmh8wCT7GOY2hOGyw=&uniplatform=NZKPT&language=CHS

[10] Qian J, Shi J, Shen T, Wang Y, Yang S. Design of Detection for Paper Joint in Cigarette Machine Based on Digital Fiber Optic. Plant Maintenance Engineering. 2022; (23): 99-101. DOI: 10.16621/j.cnki.issn1001-0599.2022.12.41

Fuzzy Systems and Data Mining X
A.J. Tallón-Ballesteros (Ed.)

doi:10.3233/FAIA241441

An Adaptive IMM for Tracking Maneuvering Target with High Variability of Environment

Tran Thi THANH[a,1], Tran Trung KIEN[a], Nguyen Van KHUONG[a], Tran Quoc TUAN[a], Tran Vu HOP[a] and Nguyen Van LOI[a]
[a] *Radar Center, Viettel High Technology and Industries Corporation, Vietnam*
ORCiD ID: Thanh Tran https://orcid.org/0009-0000-1531-860X

Abstract. This paper introduces a novel approach for tracking maneuvering targets in highly variable environments. An adaptive interacting multiple model algorithm, which is a combination of the modified adaptive Kalman algorithm and the interacting multiple model algorithm, is proposed to enhance tracking performance. One notable aspect of this method is its ability to continuously adjust the residual values of each sub-filter in the interacting multiple model algorithm, leading to improved adaptation to the target's high mobility and increased accuracy in position estimation. In comparison to the classical interacting multiple model algorithm, the results from both simulation and real data suggest that the proposed adaptive interacting multiple model algorithm has shown a 38.3% increase in overall tracking accuracy in position and approximately 28% in velocity.

Keywords. Maneuvering target, highly variable environments, Kalman algorithm, adaptive interacting multiple model, residual adjustment

1. Introduction

In recent years, tracking and estimating the positions of moving targets has become an extremely important and increasingly necessary problem in many different fields such as military and aerospace, traffic management and many other applications [1]. However, with the increase in structural complexity and flexible movement of targets in complex terrain conditions, accurate and effective tracking of targets is posing great challenges for both technology and science worldwide.

The Kalman filter (KF) is a commonly used technique in target tracking, providing an optimal solution to linear filtering problems in state-space dynamical systems. The effectiveness of Kalman filters relies on the assumption that the linear dynamic system model is accurately known beforehand, and the process and measurement noises are zero-mean, jointly standard Gaussian with known covariance matrices. On the other hand, a conventional linear system model may fail to represent the true sensor measurements in many actual applications [2-3], such as an intermittent sensor fault. The sensor measurement may on occasion only contain noise and be unaffected by the system being observed , and the performance of the KF may degrade when this pure noise is presented in the measurement update [4]. Moreover, many studies have also shown that the

[1] Corresponding Author: Tran Thi Thanh, Radar Center, Viettel High Technology and Industries Corporation, Ha Noi, Viet Nam; E-mail: tranthithanhbg1995@gmail.com.

traditional Kalman filter and its modified versions, still face difficulties when the target is mobile and changes velocity rapidly or is nonlinear [5-7].

The interacting multiple model (IMM) algorithm is a technique that combines different state hypotheses from various filter models to improve the estimation of targets with dynamic behavior [8]. Filter models are chosen based on the target's characteristics and a Markov chain controls the switching between these models. The final output is a weighted average of tracking results from all models. The IMM Kalman filter incorporates multiple states of target movement, each with a certain weight that influences the final fusion results. Throughout the target's movement, the IMM Kalman filter is able to promptly adjust the weight for each model, particularly when the target's motion state undergoes a change. Nevertheless, the IMM Kalman filter may have limitations when not all target motion models are included, leading to weakened tracking or divergence, particularly when targets exhibit unpredictable and nonlinear maneuvers [9].

The literatures [10-11] use a neural network to correct the filter result of IMM Kalman filter, to achieve the goal of improving the performance of IMM Kalman filter in maneuvering target tracking. Compared with the traditional IMM, maneuvering target tracking using IMM Kalman filter aided by Elman neural network is more valid. Application of fuzzy interacting multiple model unscented Kalman filter (FUZZY-IMMUKF) approach to integrated navigation processing for maneuvering vehicles has been proposed in [12]. The FUZZY-IMMUKF algorithm displays notable enhancements in navigation estimation accuracy when compared to the UKF and IMMUKF approaches. A nonlinear tracking solution for maneuvering aerial targets based on an adaptive IMM framework and unscented Kalman filters (AIMM-UKF) has been studied in [13] to obtain more accurate estimates, better consistency of the tracker, and more robust prediction during sensor outages. The study demonstrated that the AIMM-UKF exhibited rapid adaptation to the maneuver, as evidenced by a decrease in velocity settling time. The AIMM-UKF produces a noise reduction factor ranging from 0.36 to 0.43. A novel adaptive Kalman filter (AKF) to estimate the unknown probability of measurement loss using the IMM filtering framework has been investigated in [14]. The state, Bernoulli random variable, and measurement loss probability are jointly inferred based on the variational Bayesian approach. Reference [15] developed a tracking method using IMM algorithm combined with Probabilistic Data Association algorithm to solve the problem of low data-rate measurement. The experimental results indicate that the algorithm is capable of significantly enhancing the accuracy of target tracking, as well as effectively addressing issues related to incorrect tracking and loss of maneuvering targets. However, the application of those methods to conditions of inaccurate measurement has not been fully mentioned.

Recently, the association of physical sensors and computational models to enhance additional information about system states, inputs, and/or parameters has been termed virtual sensing. The virtual sensing is gaining popularity in various industries, including machinery, robotics and especially in the control of unmanned devices [16]. In a recent study published in [17], researchers have proposed a new method using deterministic artificial intelligence to effectively control the movement of unmanned underwater vehicles. The approach aims to eliminate errors in tracking motion trajectories by accurately following user commands, even if they are unknown or arbitrary. This innovative approach involves learning from parameters that are traditionally assumed to be constant in classical linear, time-invariant (LTI) methods, allowing for more precise control of the vehicles. The study in literature [18] utilizes a computational model which

is formulated using Pontryagin's treatment of Hamiltonian systems to obtain optimal and near-optimal results based on the selected algorithm. The simulation results demonstrate that the method proposed leads to a 69–72% enhancement in state estimation, a 29–33% increase in rate improvement, while simultaneously achieving minimal costs in the utilization of guidance, navigation, and control decision criteria. Real-time optimal (nonlinear) state estimation using the Moore– Penrose pseudoinverse has been found to be the most recommended approach with very highly accurate estimates and mathematically optimal low utilization costs. However, the application of those methods to conditions of high variability of environment has not been fully mentioned.

In this paper, a combination of the new adaptive Kalman algorithm and IMM is presented. Firstly, the paper describes the proposed adaptive interacting multiple model algorithm, which involves continuously adjusting the residual values of sub-filters in the IMM to enhance flexibility and applicability, ultimately improving tracking performance. Secondly, simulation and real data results concerning the performance of the proposed algorithm are given. A general conclusion of the obtained results is presented in the last section.

2. Methodology

The proposed adaptive interacting multiple model (AIMM) algorithm is divided into three parts: model interaction or mixer, individual model filtering, and model combination. Two sub-filters are utilized to capture common motion models of targets. The first sub-filter is a linear Kalman filter for constant velocity segments, while the second is an augmented-state Unscented Kalman filter for horizontal turn segments. In the second part of the AIMM algorithm, an adaptive update is implemented for each sub-filter in response to anomalies in detection measurements. The diagram of the proposed method is illustrated in Figure 1.

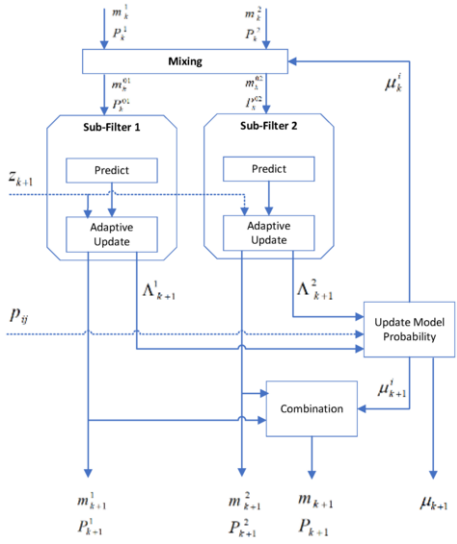

Figure 1. Algorithm of the proposed method

Part 1: Interaction

Assume the probability of each model M^j is μ_k^j at the moment k, we have:

$$\mu_k^j = P\{M_k^j\} \tag{1}$$

The normal factor is defined as:

$$\overline{c_j} = \sum_{i=1}^{N} p_{ij}\mu_k^i \tag{2}$$

where N represents the total number of the filter models in the model set; p_{ij} is the transition probability.

Then the mixture probability converting from model i to model j is written as:

$$\mu_{k+1}^{i|j} = \frac{1}{\overline{c_j}} p_{ij}\mu_k^i \tag{3}$$

Let the state estimation and the covariance matrix of each sub filter in IMM Kalman filter at the moment k be m_k^i and P_k^i respectively. Accordingly, the mixture state estimation of all filters m_k^j and the corresponding mixture covariance matrix P_k^j are shown as follows:

$$m_k^{0j} = \sum_{i=1}^{N} \mu_{k+1}^{i|j}\, m_k^i \tag{4}$$

$$P_k^{0j} = \sum_{i=1}^{N} \mu_{k+1}^{i|j} * \left\{P_k^i + \left[m_k^i - m_k^j\right]\left[m_k^i - m_k^j\right]^T\right\} \tag{5}$$

Part 2: Filter

Perform Kalman filter for each model M respectively:

$$\left[m_{k+1}^{-,i}, P_{k+1}^{-,i}\right] = Filter_{predict}\left(m_k^j, P_k^j, A_k^i, Q_k^i\right) \tag{6}$$

$$\left[m_{k+1}^i, P_{k+1}^i\right] = Filter_{update}\left(m_{k+1}^{-,i}, P_{k+1}^{-,i}, y_{k+1}, H_{k+1}^i, R_{k+1}^i\right) \tag{7}$$

The proposed adaptive interacting multiple model (AIMM) method aims to adjust parameters in each sub-filter based on input data to adapt to variability and uncertainty in the environment, optimizing estimation performance in challenging situations. However, the complexity of the problem necessitates a new solution for more effective parameter calculation to reduce errors and increase reliability. One approach in this method is fine-tuning the residual value of each sub-filter in the IMM algorithm. The residual in each sub-filter is typically the difference between the observed value and the predicted value from the system state estimate. Enhancing the residual can enhance filter performance. The ratio between the residual and the square root of the residual covariance matrix is used to create an index measuring the difference between prediction and observation in each sub-filter. The formula for this index can be written as follows:

$$\boldsymbol{adapThres(i)} = \frac{\boldsymbol{Res(i)}}{\sqrt{\boldsymbol{ResCov(i,i)}}} \tag{8}$$

The larger the *adapThres*, the larger *Res* relative to its variation, may indicate that the filter's prediction may not be reliable. On the contrary, if *adapThres* is smaller, it can indicate that the filter's prediction has a higher level of confidence. We utilize the statistical "3-sigma rule" to assess the variability and stability of a system, process, or data [19]. This principle is based on measuring the dispersion or variability of data through the standard deviation and applying a threshold based on multiple standard deviations. In particular, the 3-sigma rule shows that in a normal distribution (Gaussian distribution), about 99.7% of the observations are within ±3 standard deviations of the

mean. This means that variation usually occurs within this range and only a small fraction (about 0.3%) falls outside this range. Therefore, if the *adapThres* is greater than 3, this may suggest that the difference between prediction and measurement at time k has an uncertainty greater than the threshold of 3 standard deviations. This may indicate that there is a significant or imprecise difference occurring at this time, beyond the estimated level of uncertainty. It is an indication of abnormal or error conditions. Then we need to consider the scale ratio based on the difference between the predicted and measured parameters:

$$\boldsymbol{scale} = \frac{\left(\frac{\boldsymbol{Res(i)}}{\boldsymbol{adapThres}}\right)^{\mathbf{2}} - \boldsymbol{R(i,i)}}{\widetilde{\boldsymbol{P}}\boldsymbol{(i,i)}} \tag{9}$$

Then, we apply the data recalibration by adjusting the *Res* value. If the *scale* exceeds the *maxCovScale* threshold, we will update the *Res* value to smooth the data according to the following formula:

$$\boldsymbol{Res(i)} = \boldsymbol{adapThres}\sqrt{\boldsymbol{maxCovScale}\widetilde{\boldsymbol{P}}\boldsymbol{(i,i)} + \boldsymbol{R(i,i)}} \tag{10}$$

The *maxCovScale* value is the cut threshold which is determined based on the distribution of the scale values. Figure 2 shows the histogram with the distribution fit of scale values in the low measurement accuracy case as described in section 3.2. The *maxCovScale* value in that case is approximately equal to 2.25.

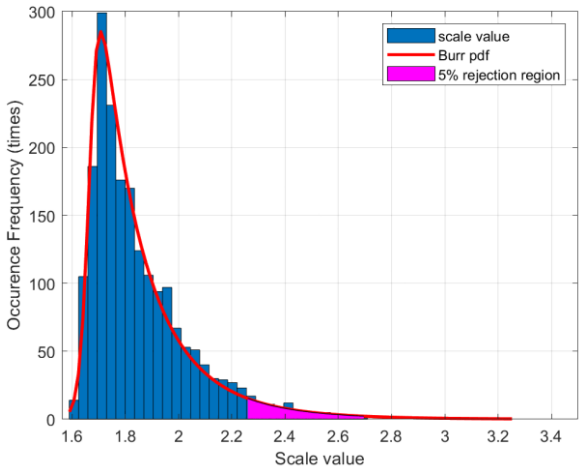

Figure 2. The histogram with the distribution fit of scale value

Calculate the likelihood value of model i:

$$\Lambda_{k+1}^{i} = \mathcal{N}\left(v_{k+1}^{i}; 0; S_{k+1}^{i}\right) \tag{11}$$

where $\mathcal{N}(\cdot)$ represents Gaussian distribution function; v_{k+1}^{i} and S_{k+1}^{i} represent the observation innovation and its covariance matrix, respectively.

The model probability at the moment $(k+1)$ is:

$$\mu_{k+1}^{i} = \frac{1}{c}\Lambda_{k+1}^{i}\overline{c_i} \tag{12}$$

where c is the normalization coefficient:

$$c = \sum_{i=1}^{n} \Lambda_{k+1}^{i} \, \overline{c_j} \tag{13}$$

Part 3: Combination

The estimated output of IMM Kalman filter is:

$$m_{k+1} = \sum_{i=1}^{N} \mu_{k+1}^{i} \, m_{k+1}^{i} \tag{14}$$

$$P_{k+1} = \sum_{i=1}^{N} \mu_{k+1}^{i} \left\{ P_{k+1}^{i} + \left[m_{k+1}^{i} - m_{k+1} \right] \left[m_{k+1}^{i} - m_{k+1} \right]^{T} \right\} \tag{15}$$

3. Result and discussion

To demonstrate the effectiveness of the proposed adaptive interacting multiple model (AIMM) method, we now consider tracking a target using the models and parameters mentioned above. Initially, the target is positioned at (x, y, z) = (7000 m, 7000 m, 800 m) with an initial velocity of 150 m/s. The tracking process unfolds as follows: For the first 100 sampling periods, the target follows the constant velocity (CV) model. From sampling period 101 to 120, the target switches to the constant acceleration (CA) model with an acceleration of 0.1 m/s². Between sampling periods 121 to 200, the target adopts the constant turn (CT) model with a rotation rate of 0.4 deg/s. In sampling periods 201 to 300, another CT model is employed, but with a rotation rate of -0.3 deg/s. Finally, from sampling periods 301 to 400, the target reverts to the CV model. The trajectory of the target is illustrated in Figure 3(a). The radar is located at Cartesian coordinates (0 m, 0 m, 0 m) with a sampling interval of T = 10s. To simulate different levels of measurement accuracy, we conducted two test cases: test case 1 with high measurement accuracy, and test case 3 with low measurement accuracy.

In these experiments, the conventional interacting multiple model (IMM) [8], IMM Aided by Elman Neural Network (IMM-ENN) [11] and our proposed adaptive IMM (AIMM) are implemented and compared. The position root-mean-square error (RMSE) is utilized to estimate the performance.

3.1. High measurement accuracy case

In the first case, the process noises are assumed to be zero-mean white Gaussian with standard deviations of range, azimuth and elevation measurements are σ_r = 50 m, σ_a = 0.2 deg and σ_e = 0.2 deg, respectively. In most cases with the high measurement accuracy, all three methods achieve the same track performance, as shown in Figure 3(b). The proposed algorithm and IMM-ENN method give results that are closer to the true path than the traditional IMM method. However, the difference is not too much.

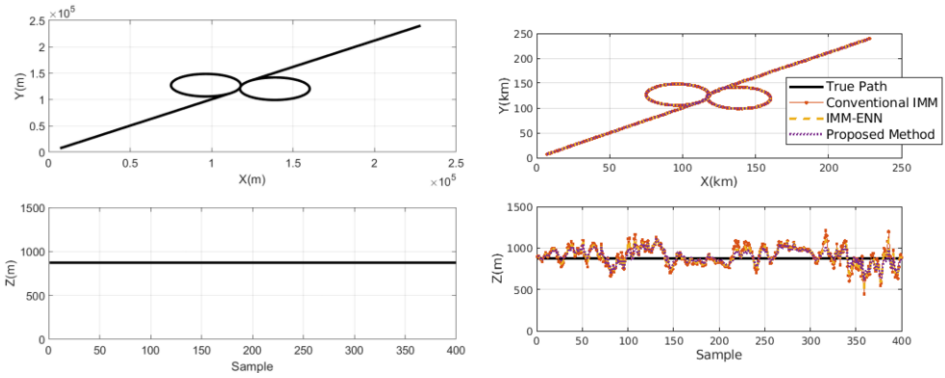

(a) (b)

Figure 3. Trajectory of simulated target (a) and Tracking result with the high measurement accuracy (b)

Figure 4(a) illustrates the position error, including range, azimuth, and elevation, when employing three different methods in comparison to the true path. The range and azimuth errors of the proposed method closely align with those of the IMM-ENN and traditional IMM methods. However, there is a noticeable reduction in the elevation error, particularly in the turning section (from sample 121 to sample 300). In Figure 4(b), the velocity RMSE resulting from the use of three different methods is compared to the true path. In terms of numerical values, as indicated in Table 1, it is evident that the range RMSE of the proposed method improves by approximately 6% compared to the IMM-ENN method and roughly 11% compared to the traditional IMM method. The azimuth RMSE of the proposed algorithm closely matches that of IMM-ENN and demonstrates an improvement of approximately 12% compared to the traditional IMM method. Furthermore, the elevation RMSE displays an improvement of approximately 17% compared to IMM-ENN and a substantial 29% improvement in comparison to the traditional IMM method. As for velocity RMSE, it shows an improvement of approximately 10% and 25% compared to IMM-ENN and the traditional IMM method, respectively.

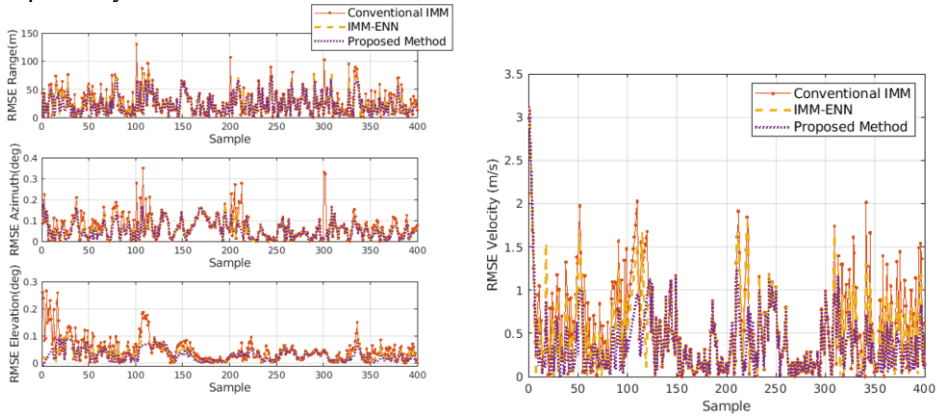

(a) (b)

Figure 4. Position RMSE (a) and Velocity RMSE (b)

Table 1. The RMSE of each method

	Conventional IMM	IMM-ENN	Proposed Method
RMSE Range (m)	38	36.3	34.1
RMSE Azimuth (deg)	0.09	0.082	0.08
RMSE Elevation (deg)	0.07	0.06	0.05
RMSE Velocity (m/s)	1.2	1.0	0.9
RMSE of CV Model Mode Probability	0.09	0.08	0.076

Figure 5 shows the mode probability of the constant turn (CV) model with three methods with respect to the true mode. As shown in the figure, the proposed method has the result of updating the CV model probability quite similar to the IMM-ENN and conventional IMM method. In particular, the CV model mode probability RMSE improved approximately 5% compared with IMM-ENN, and approximately 16% compared with the traditional IMM method.

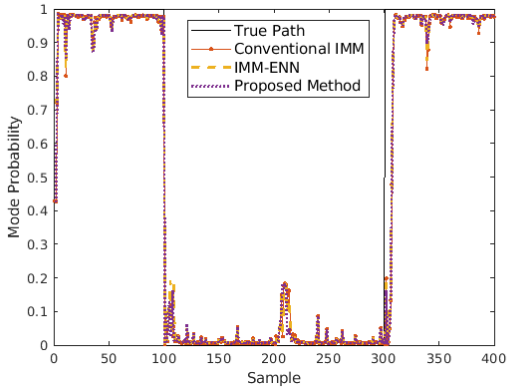

Figure 5. The mode probability of CV model

3.2. Low measurement accuracy case

In the second case, standard deviations of range, azimuth and elevation measurements are σ_r = 250 m, σ_a = 1.5 deg, and σ_e = 1.5 deg, respectively. Figure 6(a) shows the tracking result of three methods. For this case, the proposed method shows significantly better results than the two reference methods.

Figure 7(a) and Figure 7(b) show the position and velocity RMSE of three methods under the condition of high measurement error. It can be seen that the IMM Aided by Elman Neural Network (IMM-ENN) method and the proposed method have lower position error than the traditional IMM method. The proposed method has a much lower elevation RMSE than the IMM-ENN method. Numerically, as shown in Table 2, we can see that the range RMSE of the proposed method improves by approximately 15% compared to the IMM-ENN method, and approximately 25% with respect to that of the traditional IMM method. The azimuth RMSE of the proposed method also improves by approximately 12% and 30% compared with the IMM-ENN method and the traditional

IMM method, respectively. In particular, the elevation RMSE improved approximately 45% compared with IMM-ENN, and approximately 60% compared with the traditional IMM method. The velocity RMSE improved approximately 17% and 28% compared with IMM-ENN and the traditional IMM method, respectively.

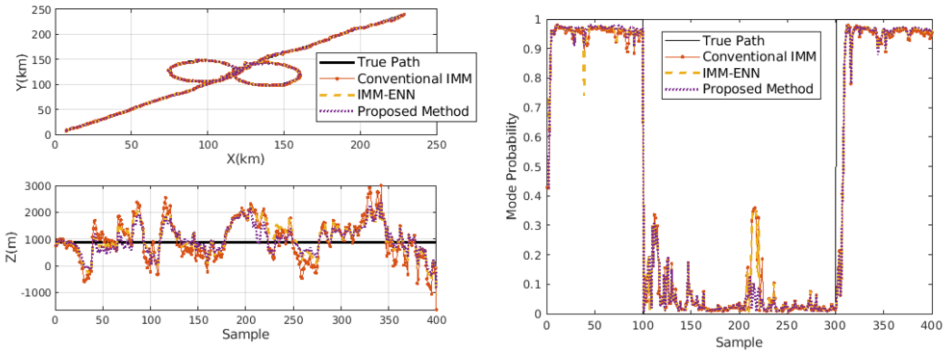

(a) (b)

Figure 6. Tracking result with the low measurement accuracy (a) and the mode probability of CV model (b)

Figure 6(b) shows the mode probability of the CV model with the IMM Aided by Elman Neural Network (IMM-ENN), the conventional IMM and proposed adaptive interacting multiple model (AIMM) with respect to the true mode. It is evident that the mode probability of the proposed algorithm closely aligns with the true mode probability in the sample ranges 1-100 and 300-400 when compared to the two reference methods. In particular, the proposed method gives much better results at the maneuvering section (in the sample ranges 200-250). Numerically, the CV model mode probability RMSE improved approximately 13% compared with IMM-ENN, and approximately 17% compared with the traditional IMM method.

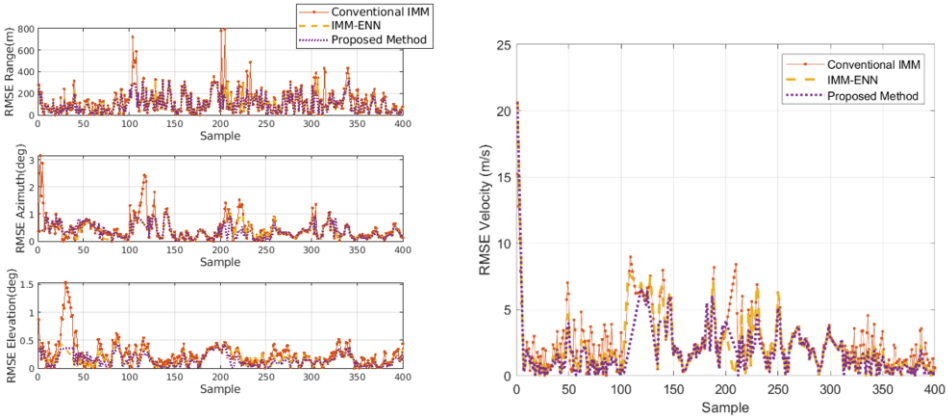

(a) (b)

Figure 7. Position RMSE (a) and Velocity RMSE (b)

Table 2. The RMSE of each method

	Conventional IMM	IMM-ENN	Proposed Method
RMSE Range (m)	172	152	129
RMSE Azimuth (deg)	0.58	0.45	0.4
RMSE Elevation (deg)	0.3	0.22	0.12
RMSE Velocity (m/s)	3.6	3.1	2.6
RMSE of CV Model Mode Probability	0.095	0.09	0.079

The proposed method was utilized in testing at an air surveillance radar station. The tracking results of an aircraft target are shown in Figure 8. At some detection points with large measurement errors, the traditional IMM method displayed non-seamless trajectory tracking (left figure), whereas the proposed method showed smooth tracking results (right figure). As a result, the position and velocity errors were reduced by approximately 15% and 18% compared to the traditional IMM method, respectively. It is important to note that both IMM methods utilized the same structure and parameters.

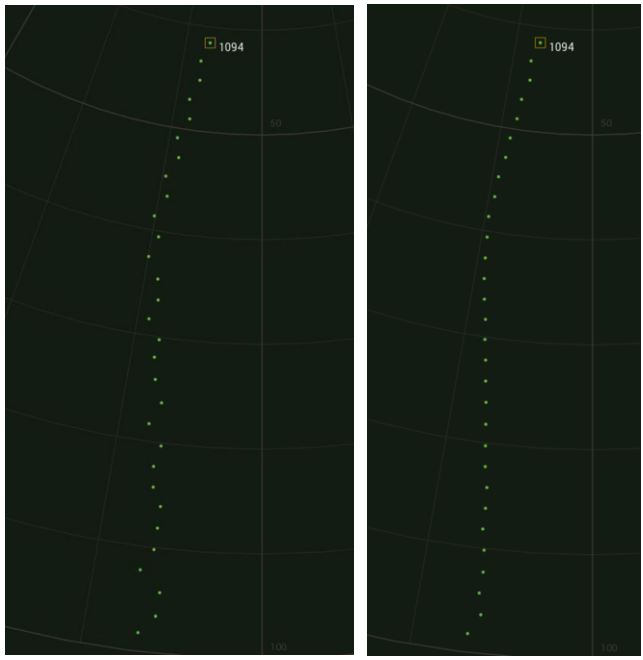

Figure 8. Target tracking result with the traditional IMM (left) and proposed method (right)

4. Conclusion

This paper provides an in-depth exploration of a novel approach for tracking maneuvering targets under conditions of low-accuracy measurement. We investigate an

Adaptive Interacting Multiple Model (AIMM) algorithm, which combines elements of the adapted Kalman algorithm with the IMM algorithm to create a more comprehensive method aimed at enhancing tracking performance. We propose a continuous adjustment of the residual values within each sub-Kalman filter of the IMM algorithm, with the goal of adapting to the high mobility of the target and improving position estimation accuracy. Based on simulated data, our study demonstrates the effectiveness of our proposed method in terms of enhancing the accuracy of target state estimation under conditions of low measurement accuracy. Notably, the proposed method achieves a notable reduction in the Root Mean Square Error (RMSE) for range, approximately 15% compared to the IMM-ENN method, and an even more significant improvement of approximately 25% compared to the traditional IMM method. Similarly, the azimuth RMSE of the proposed method experiences enhancements of approximately 12% and 30% when compared to the IMM-ENN and traditional IMM methods, respectively. Of particular significance is the elevation RMSE, which witnesses a remarkable improvement of approximately 45% compared to IMM-ENN and an impressive 60% improvement relative to the traditional IMM method. Additionally, the velocity RMSE demonstrates substantial enhancements of approximately 17% and 28% when compared to IMM-ENN and the traditional IMM method, respectively.

References

[1] M. Zhao, X. Zhang, & Q. Yang, “Modified Multi-Mode Target Tracker for High-Frequency Surface Wave Radar,” Remote Sensing, July 2018, doi:10.3390/rs10071061

[2] D. Zhang and D. Ionescu, "A New Method for Measuring Packet Loss Probability Using a Kalman Filter," *IEEE Transactions on Instrumentation and Measurement*, vol. 58, no. 2, pp. 488-499, Feb. 2009, doi: 10.1109/TIM.2008.2003324.

[3] J. Zhang and K. You, “Kalman filtering with unknown sensor measurement losses,” IFAC-Papers OnLine, vol. 49, no. 22, pp. 315–320, Sep. 2016, doi: https://doi.org/10.1016/j.ifacol.2016.10.416

[4] M. Joerger and B. Pervan, “Kalman filter-based integrity monitoring against sensor faults,” J. Guid., Control Dyn., vol. 36, no. 2, pp. 349–361, Mar. 2013, doi: 10.2514/1.59480

[5] Y. Bar-Shalom, X. Rong Li, and T. Kirubarajan, “Estimation with Applications to Tracking and Navigation,” New York: John Wiley and Sons, Inc., 2001.

[6] N. Kaempchen, K. Weiss, M. Schaefer and K. C. J. Dietmayer, "IMM object tracking for high dynamic driving maneuvers," *IEEE Intelligent Vehicles Symposium, 2004*, Parma, Italy, 2004, pp. 825-830, doi: 10.1109/IVS.2004.1336491.

[7] S. A. Gadsden, S. R. Habibi and T. Kirubarajan, "A novel interacting multiple model method for nonlinear target tracking," *2010 13th International Conference on Information Fusion*, Edinburgh, UK, 2010, pp. 1-8, doi: 10.1109/ICIF.2010.5712021.

[8] Blackman, Samuel, and Robert Popoli, "Design and analysis of modern tracking systems," Norwood, MA: Artech House, 1999.

[9] De-Ping Yuan and Juan-Yi Zheng, "Interacting multiple model target tracking algorithm based on particle filtering," *Proceedings of 2011 IEEE CIE International Conference on Radar*, Chengdu, China, 2011, pp. 1907-1910, doi: 10.1109/CIE-Radar.2011.6159947.

[10] Z. Zhu, W. Liu and X. Dai, “Maneuvering Target Tracking Method Based on RBF Neural Network and Interacting Multi Models,” Journal of Missiles and Guidance, vol.26, pp. 329-333, 2006, doi: 10.1109/IHMSC.2015.241

[11] M. Sun, Z. Ma and Y. Li, "Maneuvering Target Tracking Using IMM Kalman Filter Aided by Elman Neural Network," *2015 7th International Conference on Intelligent Human-Machine Systems and Cybernetics*, Hangzhou, China, pp. 144-148, 2015, doi: 10.1109/IHMSC.2015.241.

[12] D. -J. Jwo and C. -H. Tseng, "Fuzzy adaptive interacting multiple model unscented Kalman filter for integrated navigation," *2009 IEEE Control Applications, (CCA) & Intelligent Control, (ISIC)*, St. Petersburg, Russia, 2009, pp. 1684-1689, doi: 10.1109/CCA.2009.5281068.

[13] A. C. Alvaro and A.V. Mariano, “Adaptive IMM-UKF for Airborne Tracking”, Advances in Air Traffic and Airspace Control and Management, 2023, doi: https://doi.org/10.3390/aerospace10080698

[14] W. Youn, N. Y. Ko, S. A. Gadsden and H. Myung, "A Novel Multiple-Model Adaptive Kalman Filter for an Unknown Measurement Loss Probability," in *IEEE Transactions on Instrumentation and Measurement*, vol. 70, pp. 1-11, 2021, Art no. 8500511, doi: 10.1109/TIM.2020.3023213.
[15] D. Zhang, X. Ma, S. Quan, H. Wang and D. Xu, "Tracking of High Maneuvering Targets in Low Data Rate Measurement," *2020 IEEE MTT-S International Wireless Symposium (IWS)*, Shanghai, China, 2020, pp. 1-3, doi: 10.1109/IWS49314.2020.9360037.
[16] Cuadrado, J.; Naya, M.Á. Editorial of Special Issue "Combining Sensors and Multibody Models for Applications in Vehicles, Machines, Robots and Humans". *Sensors*. 2021; 21(19): 6345. https://doi.org/10.3390/s21196345
[17] Sands T. Development of Deterministic Artificial Intelligence for Unmanned Underwater Vehicles (UUV). Journal of Marine Science and Engineering. 2020; 8(8): 578, doi: 10.3390/jmse8080578
[18] Sands T. Virtual Sensoring of Motion Using Pontryagin's Treatment of Hamiltonian Systems. Sensors. 2021; 21(13): 4603, doi: https:// doi.org/10.3390/s21134603
[19] Pukelsheim, Friedrich, "The Three Sigma Rule," The American Statistician, vol. 48, no. 2, 1994, pp. 88–91, doi: https://doi.org/10.2307/2684253.

Fuzzy Systems and Data Mining X
A.J. Tallón-Ballesteros (Ed.)

doi:10.3233/FAIA241442

An Intelligent Service System Model for Chronic Diseases from the Perspective of DIKW

Mingliang Tan[a], Qianghua You[a], Jialu Lyu[a], Jie Li[a], Yawen Deng[a,1]
[a]*School of Management, North Sichuan Medical College, Nanchong 637100, China*
ORCiD ID: Mingliang Tan https://orcid.org/0000-0002-9832-7508
ORCiD ID: Yawen Deng https://orcid.org/0009-0004-1982-8059

Abstract. Massive data resources about chronic diseases could be analyzed and organized by new information technologies to finally converge on intelligent health knowledge services. This has very significant consequences for improving health management of chronic diseases, reducing the economic burdens of patients, alleviating serious pressure on health care, and improving the current uneven distribution of medical resources. This paper appeals to DIKW, a well-known framework in the field of information science and knowledge management, to build an intelligent service system model for chronic diseases through theories and methods related to data mining, knowledge organization, artificial intelligence, and knowledge services. This model involves 3 stages: Data Acquisition and Data Processing, Ontology Construction and Semantic Annotation, and Demand Mining and Knowledge Exploitation. These stages realize a shift and transition from data to information, from information to knowledge, and from knowledge to wisdom.

Keywords. DIKW framework, big data, knowledge organization, intelligent chronic disease service, system model construction

1. Introduction

Deaths and disease burdens in the world are mainly caused by chronic diseases such as hypertension, diabetes, stroke, coronary heart disease, chronic obstructive pulmonary disease, and cancers. Reports from the World Health Organization show that over 40 million people die from chronic diseases every year, accounting for over 70% of all deaths around the world in the same year. About 300 million Chinese people suffer from chronic diseases, and this number is roughly one-fifth of China's total population. Moreover, chronic diseases are also causally responsible for over 85% of total deaths and over 80% of total disease burdens in China. Chronic patients generally need long-term medication, regular condition monitoring, and scientific health management because chronic diseases are characterized by complex causes, insidious onset, a long duration, a high repeated visiting rate, many complications, easy recurrence, and difficult treatment. This is why chronic patients should have dynamic and continuous access to

[1] Corresponding Author: Yawen Deng, School of Management, North Sichuan Medical College, Nanchong 637100, China; Email: dengyawenscu@163.com.

health knowledge regarding their medication, disease detection, diets, treatments, follow-up checks, and health care.

Traditionally, face-to-face communication with medical specialists is a leading way for chronic patients to have access to health management knowledge relevant to chronic diseases. However, this way is seriously restricted spatially and temporally and is characterized by a propensity of rough indoctrination of knowledge, so then patients' access to health knowledge lacks enough independence and convenience and is accompanied by heavy economic burdens and high time costs.

New opportunities have come up with the rapid development and widespread application of information technologies like information communication, the Internet, database, and cloud computing. Chronic patients, whatever time and place they are at, can now seek necessary health knowledge concerning their diseases online by using terminals like smartphones and desk computers. In the context of big data, the sheer amount, heterogeneous sources, and variable quality are typical of health-related information available on the Internet. Therefore, given China's national development strategy of big data, artificial intelligence, and "Internet+" health care, it would be of huge academic value and practical significance to provide high-quality personalized intelligent health knowledge services for chronic patients, in virtue of delving deep into massive data resources and organizing them.

2. Related research

Recently, a new generation of information technologies like big data mining, deep neural networks, natural language processing, machine learning, and artificial intelligence have been used to develop the health management of chronic diseases and relevant services. In China and other countries, this has been one of the hot research topics in computer science, information management, and medical informatics..

Wang et al. appealed to natural language processing techniques and a domain knowledge base to develop a knowledge-based health recommender system, which reveals chronic patients' potential needs based on their health data and then recommends the most relevant health education materials to them [1]. Roca et al. presented chronic patients with a microservice chatbot architecture for chronic patients to satisfy requirements in patients' data storage, remote monitoring of diseases, and timely medication reminding [2]. Elhadj et al. collected data from terminals like wearable devices and then presented a healthcare monitoring system for chronic patients in terms of dynamic knowledge reasoning [3]. Omisore et al. designed and implemented a system used for diagnosis and personalized management of diabetes, including a multimodal self-adaptive neuro-fuzzy inference model and a knowledge-based diets recommender model [4]. Nenova et al. appealed to big data analysis and case-based reasoning to predict chronic disease progression based on data across multiple dimensions, for example, of patients' clinical visits, laboratory tests, vital signs, and so on [5].

Researchers actively explore different new information technologies and apply them to various cases of health care of chronic diseases and relevant services, including patients' profiles, diet monitoring and personalized recommendations, knowledge retrieval and quizzes, disease progression predictions, intelligent medication recognitions, online medical quality-of-service evaluations and so on. Their research integrates methods, technologies, and tools across multiple areas to solve practical problems, and thus achieved some good results, manifesting the huge potential of

information technologies. However, most of current researches are done from the perspective of computer science and AI technologies, focusing on the application of various intelligent tools in particular cases involving health management and service for chronic diseases. But this means from the perspective of information management and knowledge organization that a holistic scheme design of the whole intelligent chronic disease service system is still lacking. Therefore, given DIKW, a theoretical framework in the field of information science and knowledge management, this paper is aimed at integrating multidisciplinary methods to construct a DIKW-based intelligent service system model for chronic diseases and then analyzing the structural functions of this model and its technological approach in detail.

3. The DIKW Framework

The Data-Information-Knowledge-Wisdom framework (DIKW) is one of the most well-known classical theoretic models in the field of information science and knowledge management. It has been also widely used in other different fields such as the library and information science, journalism and communication, medical informatics, information systems, industrial engineering, educational digitalization, and philosophical epistemology [6]. Such a framework can be traced back to a famous poem called "The Rock" (1934) written by the winner of the Nobel Prize in Literature, T. S. Eliot. Later in a 1989 essay called "From data to wisdom," American system theorist Russell Ackoff expounded definitions of data, information, knowledge, and wisdom, their relationships, and a hierarchical structure involving them [7]. Since the 1990s, the DIKW framework has been further extended and improved by specialists, and consequently, a hierarchical pyramid system was thus generated. As depicted in Figure 1, there is a progressive relationship between data, information, knowledge, and wisdom: Wisdom stems from knowledge, which stems from information, which in turn stems from data.

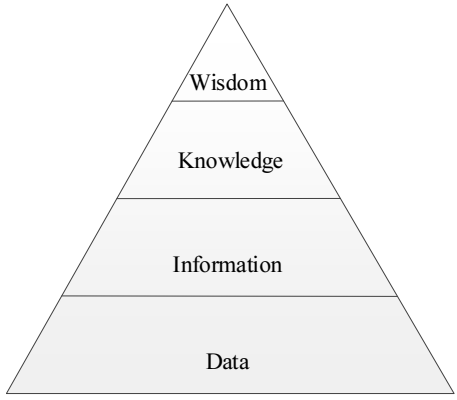

Figure 1. The DIKW Pyramid.

Data is the most fundamental kind of materials transferred, stored, and processed by computers. Specifically speaking, it is a record and description of things, observations, events, and activities [8], existing in various forms of a number, text, image, audio, and video.

Information is a particular kind of data organized and processed for some purpose [9], generated from the processing of data through selection, ordering, classification,

aggregation, computation, and statistical inference. A process of selection, processing, and explanation allows data to correlate with particular scenarios, objectives, and problems, and it also supplements data with a corresponding context. In this way, data becomes relevant, valuable, and meaningful for a receiver.

Knowledge is a kind of useful material resulting from filtering, processing, summarizing, and extracting relevant information [10]. It is acquired through a process of discovering, understanding, organizing, and refining patterns and relationships in information.

Wisdom is grounded by knowledge. It is an ability to solve practical problems by accumulating, selecting, applying, and activating relevant knowledge [11].

To sum up, the DIKW framework holistically models the whole process of machines processing data very well [12].

4. A DIKW-based Intelligent Service System Model for Chronic Diseases

Given the DIKW theoretic framework, this paper is to build a DIKW-based intelligent service system model for chronic diseases (as shown in Figure 2), through theories and methods in the fields of data mining, knowledge organization, artificial intelligence, and knowledge services. Three stages are included in this model: Data Acquisition and Data Processing, Ontology Construction and Semantic Annotation, and Demand Mining and Knowledge Exploitation. They realize a shift and transition from data to information, from information to knowledge, and from knowledge to wisdom, respectively. In such a closely connected and progressive way, accurate personalized intelligent health knowledge services for chronic diseases would be achieved through these successive stages to effectively promote the health management and disease recovery of chronic patients.

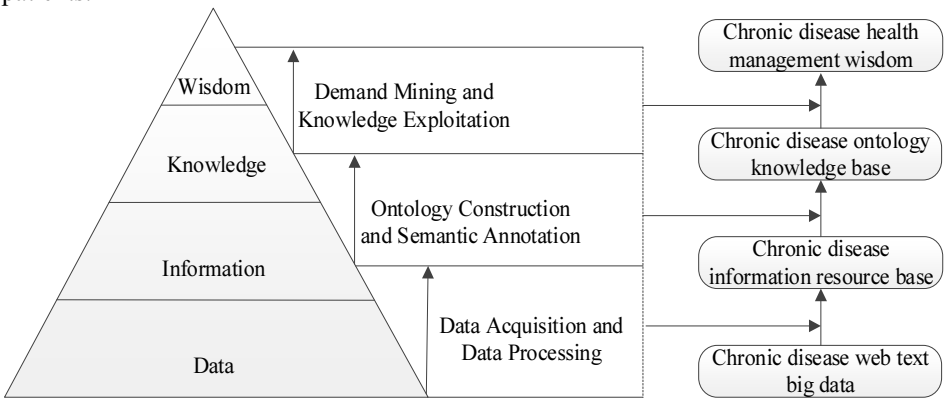

Figure 2. A DIKW-based Intelligent Service System Model for Chronic Diseases.

4.1 Data Acquisition and Data Processing

The internet is a typical big data repository, including various data resources. It carries typical features of big data: huge capacity, diverse types, fast generation speed, and a low value density. On the internet, most of the data resources relevant to health management of chronic diseases exist in unstructured textual forms of Q&A sessions on

online health communities, online encyclopedia entries of diseases, and articles posted by WeChat public accounts. In light of this, the stage of Data Acquisition and Data Processing should contain two main tasks or objectives:

- Collects and processes textual data resources necessary for intelligent chronic disease services online.
- Forms an information resources base for chronic diseases, achieving a transition from data to information.

More specifically, three particular sub-processes shall be included in this stage: data collection, data cleaning, and data selection.

4.2 Ontology Construction and Semantic Annotation

This paper organizes domain knowledge of chronic diseases using an ontology, which is an explicit formal specification of a shared conceptual model. Specifically speaking, an ontology models and formally describes domain knowledge by its basic elements: concepts, relations, and instances. The stage of Ontology Construction and Semantic Annotation involves three tasks or objectives:

- Constructs a domain ontology of chronic diseases to semantically describe a conceptual model about the corresponding domain.
- Semantically tags chronic disease information resources based on the given domain ontology, allowing machines to understand semantic contents of unstructured texts and to build semantic connections between knowledge units.
- Forms a chronic disease ontology knowledge base, achieving a transition from information to knowledge

A Semantic Annotation process results in a chronic disease ontology knowledge base when it establishes the connection and mapping between ontology knowledge elements and knowledge units of texts, appeals to concepts and relations in a domain ontology of chronic diseases to reveal and describe semantic contents of texts, and then realizes a formal expression of the meaning of texts and an ordered organization of resources. In such a process, knowledge units in textual resources about chronic diseases are linked to a globalized knowledge network, and thus machines can implement deep understanding and intelligent processing of the meaning of texts, laying a foundation for knowledge computing operations such as retrieval and reasoning in an ontology knowledge base.

4.3 Demand Mining and Knowledge Exploitation

For intelligent chronic disease services to be accurate and personalized, user profiles are required to be comprehensive and clear in order to have an appropriate understanding of health knowledge demands from chronic patients, thus establishing a precise match and dynamic mapping between users' demands and knowledge resources. The stage of Demand Mining and Knowledge Exploitation thereby involves the following tasks or objectives:

- Delves deep into chronic patients' demands.
- Implements knowledge computing operations such as accessing, matching, retrieving, and reasoning in a chronic disease ontology knowledge base, providing users with various forms of intelligent health knowledge services.

- Transform knowledge to wisdom in the sense that chronic patients' knowledge is activated as their wisdom in self-health management.

This stage consists of two sub-processes: one is demand mining, and one is knowledge exploitation. The sub-process of knowledge exploitation is an interface of chronic disease ontology knowledge base and users' demands. Health knowledge could be given to chronic patients in five main forms, including intelligent retrieval service, intelligent Q&A service, intelligent navigation service, intelligent recommendation service, intelligent reasoning service.

5. Conclusion

It is of great practical significance to improve the quality and level of health knowledge services for chronic diseases using new information technologies such as big data, cloud computing, text mining, machine learning, natural language processing, and deep neural network. In this study, a DIKW-based intelligent service system model for chronic diseases, as a holistic and systematic architectural design, is constructed as a viable approach to developing a chronic disease knowledge service system in the context of big data and artificial intelligence.

Future studies could combine rule-based methods with statistical machine-based methods to extract ontology knowledge elements from unstructured texts. Deep learning technologies will also be applied to realize the multi-granularity Semantic Annotation of textual information resources about chronic diseases. Besides, future studies can also appeal to the idea of agile development and rapid prototyping to develop an intelligent chronic disease service system, and then improve and optimize it according to actual feedback from chronic patients.

Acknowledgments

This paper was supported by the following funding projects: The Ph.D. Start-up Project of North Sichuan Medical College (Project No.: CBY21-QD37 and CBY23-QDA25); 2023 National College Student Innovation and Entrepreneurship Training Program project (Project No.: 202310634004X).

References

[1] Wang Z, Huang H, Cui L, Chen J, An J, Duan H, Ge H, Deng N. Using Natural Language Processing Techniques to Provide Personalized Educational Materials for Chronic Disease Patients in China: Development and Assessment of a Knowledge-Based Health Recommender System. JMIR Medical Informatics. 2020 April; 8(4): e17642, doi: 10.2196/17642

[2] Roca S, Sancho J, García J, Alesanco A. Microservice chatbot architecture for chronic patient support. Journal of Biomedical Informatics. 2020 February; 102: 103305, doi: 10.1016/j.jbi.2019.103305

[3] Elhadj HB, Sallabi F, Henaien A, Chaari L, Shuaib K, Thawadi MA. Do-Care: A dynamic ontology reasoning based healthcare monitoring system. Future Generation Computer Systems. 2021 May; 118: 417-431, doi: 10.1016/j.future.2021.01.001

[4] Omisore OM, Ojokoh B A, Babalola AE, Igbe T, Folajimi Y, Nie Z, Wang L. An affective learning-based system for diagnosis and personalized management of diabetes mellitus. Future Generation Computer Systems. 2021 April; 117: 273-290, doi: 10.1016/j.future.2020.10.035

[5] Nenova Z, Shang J. Chronic disease progression prediction: Leveraging case-based reasoning and big data analytics. Production and Operations Management. 2022 January; 31(1): 259-280, doi: 10.1111/poms.13532
[6] Kirsch P, Hine A, Maybury T. A model for the implementation of industry-wide knowledge sharing to improve risk management practice. Safety Science. 2015 December; 80: 66-76, doi: 10.1016/j.ssci.2015.07.009
[7] Ackoff RL. From data to wisdom. Journal of applied systems analysis. 1989 January; 16: 3-9. http://faculty.ung.edu/kmelton/Documents/DataWisdom.pdf
[8] Ardolino M, Rapaccini M, Saccani N, Gaiardelli P, Crespi G, Ruggeri C. The role of digital technologies for the service transformation of industrial companies. International Journal of Production Research. 2018; 56(6): 2116-2132, doi: 10.1080/00207543.2017.1324224
[9] Rowley J. The wisdom hierarchy: representations of the DIKW hierarchy. Journal of Information Science. 2007 April; 33(2): 163-180, doi: 10.1177/0165551506070706
[10] Yu L, Duan Y. Trusted service provider discovery based on data, information, knowledge, and wisdom. International Journal of Software Engineering and Knowledge Engineering. 2021; 31(1): 3-19, doi: 10.1142/S0218194021400015
[11] Gee PM, Greenwood DA, Kim KK, Perez SL, Staggers N, DeVon HA. Exploration of the e-patient phenomenon in nursing informatics. Nursing Outlook. 2012; 60(4): e9-e16, doi: 10.1016/j.outlook.2011.11.005
[12] Ma L. Meanings of information: The assumptions and research consequences of three foundational LIS theories. Journal of the American Society for Information Science and Technology. 2012 April; 63(4): 716-723, doi: 10.1002/asi.21711

Fuzzy Systems and Data Mining X
A.J. Tallón-Ballesteros (Ed.)

doi:10.3233/FAIA241443

Precise Services in Smart Cultural Tourism for Tourists

Xinhai Liao [1] , Jiaqi Wu, Zilin Jia and Jiaxing Xian
Guangdong University of Foreign Studies, Guangzhou, China

Abstract. In response to the specific problems encountered in addressing the needs of tourists in the cultural and tourism industry, innovations have been introduced how Big Data enhances precision services in smart tourism through a tourist-centric framework that improves personalization and accuracy using advanced algorithms. A service model centered on tourists and utilizing information technology to achieve precise smart cultural and tourism services has been proposed. Based on collaborative filtering recommendation systems, combined with the transformer model, predictions are made on tourist needs and behavior in order to provide personalized and precise service recommendations to tourists. Recommendations have also been made to promote the transformation of the cultural and tourism industry towards smart cultural and tourism based on this model.

Keywords. Precision Services, Smart Cultural Tourism, Big Data, Tourist Demands, Transformer Model

1. Introduction

In the era of Big Data, new data information is generated every moment, making it difficult for people to find what they truly need. At the same time, people's demands are becoming more diverse and personalized. In this context, meeting the needs of tourists has become a key issue facing the cultural and tourism industry [1]. By using digital technology to identify the target audience accurately and implementing smart precision marketing with the assistance of new media marketing methods, it will become a major trend for the transformation and development of the cultural and tourism industry's marketing model in the future [2].

By utilizing the functionality of collecting massive information through Big Data for intelligent analysis, a solid foundation is laid for the transformation of the traditional marketing model of the cultural and tourism industry towards smart precision marketing [3]. On the other hand, digital technology based on Big Data can also effectively promote cross-industry integration and fusion, accelerate industry convergence through digital empowerment, and further improve the travel experience for tourists [4].

[1] Corresponding Author: Xinhai Liao, Center for Contemporary Education Technology, Experimental Teaching Center, Guangdong University of Foreign Studies, China; Email: 200311155@oamail.gdufs.edu.cn.
This study is financially supported by the Undergraduate Innovation Training Project of Guangdong University of Foreign Studies in 2024.

2.Application Scenarios of Smart Precision Service in the Big Data Era of Cultural and Tourism Industry

2.1. Tourism Information Promotion Based on Tourist Profiles

In order to efficiently meet the personalized needs of users by categorizing them effectively, the concept of user profiles has been introduced. One way to understand "user profiles" is that the creation of user profiles is "data-driven" rather than "assumption-driven." Another way to understand it is that user profiles are a type of persona profile where real people are abstracted into a set of data [5]. User profiles usually also describe behavior patterns, goals, skills, and attitudes. Tourist profiles can be seen as an extension of user profiles in the realm of smart culture and tourism. It is based on massive tourist data, exploring tourist behaviors and preferences, and building tourist profile models based on their needs [6].

By following a cycle of "identifying user needs - providing personalized services - collecting user feedback - identifying user needs," the platform can enhance cultural and tourism promotional services [7]. Additionally, the smart culture and tourism platform can also track tourist activity participation, investigate the most popular activities and themes, provide feedback to the responsible personnel for cultural and tourism promotional activities, and plan and carry out activities accordingly. Through this feature, tourists can also offer suggestions for promotional content.

2.2.Resource Push Mechanism Oriented by Tourist Needs

Tourists acquire resources through two methods: actively searching for information on social platforms by entering keywords; and receiving intelligent resource recommendations based on Big Data. Initially, when a user uses the search function for the first time, the platform can provide initial recommendations based on user gender, age, major, and other personal information and keep a record of the user's resource selections and independent keyword searches. The platform collects user information and behavior traces left during information searches, mines user demand information from this data, further organizes and categorizes it, and uses algorithm tools to analyze these data. Based on the analysis results, a "one-on-one" personalized push mechanism is established. Subsequently, when users need to search again, relevant resources are prioritized for recommendation, with a user feedback function in place for users to express satisfaction or dissatisfaction, thus evaluating the accuracy of resource recommendations.

By effectively leveraging these components, organizations can create robust marketing campaigns, enhance tourist experiences, and foster positive relationships with their audience. Future research should examine how evolving digital landscapes further shape these elements and influence the decisions of cultural tourists.

3.Smart Tourism Precision Service Framework Centered on Tourists in the Big Data Era

Based on the analysis in the previous section on smart cultural and tourism precision services in the context of Big Data for users, resources, and product service providers, a

smart cultural and tourism precision service framework centered on tourists in the era of Big Data is constructed, as shown in Figure 1.

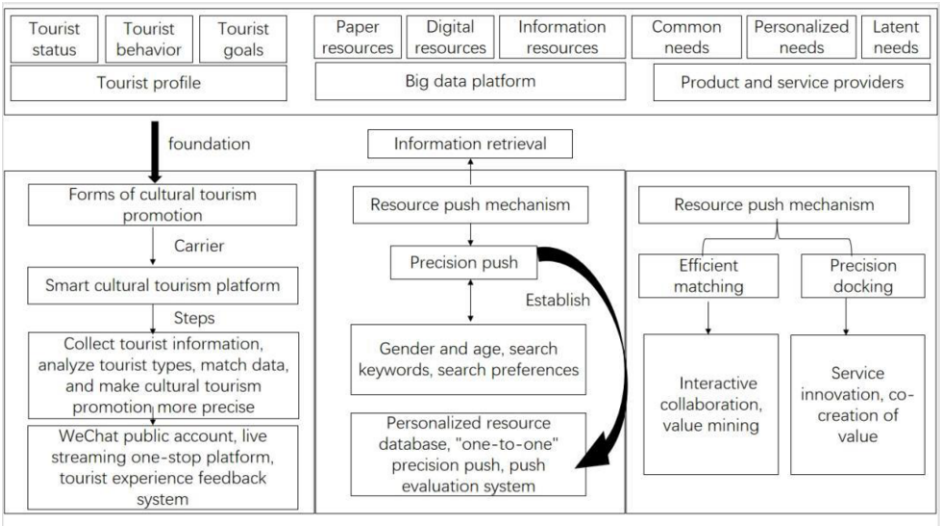

Figure 1. Summary of the literature review

In the era of Big Data, cultural and tourism enterprises primarily focus on building tourist profiles, managing Big Data platforms, and standardizing product service providers to improve cultural and tourism promotion, resource push, and product service supply. Cultural and tourism enterprises construct reader profile models by collecting and analyzing tourist status, behavior, and goals to change the form of cultural and tourism promotion. Cultural and tourism enterprises use smart cultural and tourism platforms as the carrier for cultural and tourism promotion, promoting precisely based on personal information in the backend on platforms like WeChat public accounts and live one-stop platforms, and using a tourist experience feedback system to help the platform make improvements centered around tourists. The Big Data platform categorizes massive paper resources, digital resources, network information resources, and other resource collections and constructs a new resource database, based on reader gender, age, and traces of active information retrieval, for "one-on-one" precise tourist push. Product service providers should adhere to a service concept oriented toward tourist needs, deducing common and individual needs of tourists through Big Data analysis, speculating on tourists' latent needs, and providing matching products and services for various requirements.

4.Algorithm implementation and experimental results

4.1 Algorithm Implementation

This study will be based on collaborative filtering recommender system, combined with transformer model, the tourists' demand and behavior prediction, so as to provide tourists with personalized and accurate service recommendation. The specific method is, in the target user image, features are not significant and unclear, its demand or behavior is uncertain conditions, with the help of collaborative filtering recommender system by

virtue of a small amount of existing information to find the most similar to the target user and several other users, and then the behavior of these related users and demand for new information aggregated sorted and weighted, and the target user's existing information together with the formation of the corpus dataset, which is used for the training. This dataset is used to train the transformer model and output behavior or demand predictions. After that, the predicted data is used to improve the feature set of the target user and enrich the user profile of the user. Finally, the perfected target user generated by the transformer model is imported into the collaborative filtering recommendation system to generate the target user's recommended items, realizing the precise service delivery of intelligent tourism centered on tourists' needs.

Therefore, first of all, it is to obtain other similar users in the neighborhood of the target user from the collaborative filtering recommendation algorithm. In the collaborative filtering recommendation system, the user-item scoring relationship matrix is often used, which indicates the degree of liking or disliking of a user for a certain item through the user's explicit or implicit scores, generally the higher the score, the more the user loves the item, and vice versa the more the user dislikes it, and this is used as the input data for the recommendation. This system uses an implicit rating feedback mechanism because it does not require users to provide ratings directly. Instead, the user's behavioral data, such as browsing history, click preference, dwell time, and even message comments, are analyzed to infer the user's preference for the item. Usually, the construction of the scoring matrix does not require manual calculation of scores and can be done automatically by the system. Since in reality there are multiple users and multiple projects at the same time, i.e., the two belong to a form of many-to-many.

m and n respectively denote the number of users and the number of items entered into the system. The element Rij represents the score of user i on item j, where there is a large amount of unrated information, reflecting the sparsity of the user-item score matrix. In this method, Rij takes values in the range of $\{R_{ij} \mid -100 \le R_{ij} \le 100, R_{ij} \in Z\}$and the meanings represented by the high and low scores can be referred to above. When user Ui has no rating for item Ij, the default Rij=0. It can be seen that there are more null values due to the initial input data not filled by transformer prediction.

After obtaining the user-item rating relationship matrix, the similarity between different users is calculated using an improved high-dimensional similarity measure based on a function with the following equation

$$\mathrm{Sim}(u,v) = \frac{\sum_{i \in I(u) \cap I(v)} \frac{R_i}{|R_{u,i} - R_{v,i}| + R_i}}{|I(u,v)|} \tag{1}$$

Where, u and v are two different users, $I(u,v) = I(u) \cap I(v)$ represents the common rating items of user u and user v, R_i represents the average value of the first item in the common rating items, $R_{u,i}$ is the user u's rating of the item i, $R_{v,i}$ as the same. $\mathrm{Sim}(u,v)$ represents the similarity between users.

In practice, the recommendation system has to deal with a large number of users and items, and the present improved module treats the ratings of a user for all items as a vector, which gives the vector a high-dimensional nature. Therefore, the above formula calculation process is better in terms of clarity and simplicity than the traditional similarity calculation method. The core idea of collaborative filtering recommendation algorithm is to recommend the target user based on the common rating items of two

users. Therefore, the above formula is also designed based on the common rating items of users. Meanwhile, in order to improve the accuracy of similarity, the average rating of the items is added to the above formula. When two users do not all agree on the ratings of the common items, the accuracy of similarity can be effectively increased by measuring the rating similarity between two items by utilizing the average score of the items. Completion of the above steps results in a matrix of user similarity that is used to represent the similarity between different users. [8]

$\{U_1, U_2, \ldots, U_m\}$ denotes the number of users included in the system, so after the matrix is constructed it will be a matrix of $m * m$ to represent the degree of similarity between users. The element S_{ij} represents the degree of similarity between user U_i and user U_j.

Then, it is necessary to arrange the values of each row in the user similarity matrix in descending order, and after completing the sorting, the nearest neighbor method is used to select the appropriate number of user neighbors for each user, which in turn prepares for the generation of recommendations. In order to scientifically obtain the k-value, to prevent the occurrence of too many similar users leading to the subsequent training scale up algorithm efficiency decline or overfitting, k-value will be obtained through the particle swarm optimization algorithm based on the convergence factor, the process is as follows.

In the dimensional search space, the position of the particle $i(i = 1,2, \ldots, n)$ is $X_i = (x_{i1}, x_{i2}, \ldots, x_{iD})$. The position movement distance of the particle i is $V_i = (v_{i1}, v_{i2}, \ldots, v_{iD})$. $P_i = (p_{i1}, p_{i2}, \ldots, p_{iD})$ indicates the optimal position in the movement history of the particle i and the particle's historical optimal position (value). $P_g = (p_{g1}, p_{g2}, \ldots, p_{gD})$ indicates the population's historical optimal position, i.e., the global optimal position or value, and the particle updates the velocity and position according to the following two formulas.

Velocity update formula:

$$v_{id}(t+1) = \varphi \times \left[v_{id}(t) + c_1 \times \text{rand}() \times \left(p_{id}(t) - x_{id}(t)\right) + \times \text{rand}() \times \left(p_{gd}(t) - x_{gd}(t)\right)\right] \quad (2)$$

The convergence factor φ can be defined as:

$$\varphi = \frac{2}{\left|2 - (c_1 + c_2) - \sqrt{|(c_1 + c_2)^2 - 4(c_1 + c_2)|}\right|} \quad (3)$$

Position update formula:

$$x_{id}(t+1) = x_{id}(t) + v_{id}(t+1) \quad (4)$$

The t denotes the number of iterations, c1 and c2 are the learning factor, rand( ) is the random number between 0 to 1. In order to improve the convergence performance of the algorithm, enhance the ability of local search and improve the stability of the algorithm, the convergence factor φ is newly introduced into this module instead of the inertia weights ω, because the convergence factor φ can improve the stability of the algorithm when dealing with high-dimensional optimization problems, accelerate the speed of convergence, and reduce the sensitivity to the parameter settings.

At the same time, in order to "accelerate" the particle movement in the module, so that the algorithm can complete the search in all the space, and then in the later stages of the algorithm to let the particles "decelerate" so that the search is more accurate,

therefore, the optimization module used in this study makes the following improvements to the learning factor.

Improve the learning factor formula:

$$\mathbf{c_1 = 2 - \sin\left(\frac{k\pi}{t_{max}}\right)} \quad (5)$$

$$\mathbf{c_2 = 1 + \sin\left(\frac{k\pi}{t_{max}}\right)} \quad (6)$$

k is the current number of iterations, t_{max} represents the maximum number of iterations, when the iteration conditions $t \leq t_{max}$ are met, calculate and update the speed and position of each particle, so that the learning factor c with the increase in the number of iterations k, c_1 linearly decreasing, c_2 linearly increasing. This improvement can make the reassignment of the position of a particle when it is the optimal position can prevent falling into the local optimal solution, thus largely improving the possibility of discovering the global optimal solution.

After obtaining the ideal k value the neighbor (Neig) matrix can be generated $\{U_1, U_2, \ldots, U_m\}$ denotes the number of users included in the algorithm, and the $m * k$ neighbor matrix is represented by the matrix of one, where N_{ij} denotes the neighbor j of the user i.

Up to this point, we have obtained k users similar to the original neighborhood of the target user, after which we collect the related information of these k users, such as consumption request, service evaluation, experience message and other related text information, and aggregate and combine them with the existing information of the target user to generate a fine-tuned corpus.

4.2 Experimental Results

BLEU is mainly used to measure the accuracy rate, and its similarity ranges from 0 to 1. The closer the score is to 1, the higher the prediction quality. For the perplexity level (PPL), the PPL of the model in this thesis is low, meaning that it performs well when evaluating the correlation between the system-generated answer and the user's previous utterance, thus indicating a strong connection between the two utterances. Meanwhile, in the generation class task, the model proposed in this thesis has a PPL of less than 200, which means that the generated utterances are able to achieve a level of similarity with humans to some extent and outperform the seq2seq model across the board. It shows that the results generated after the prediction of this transform module can be well fused with the neighboring user information, so that the collaborative filtering recommender system can better identify the potential needs and preferences of the target user, and then provide accurate recommended content.

Both filter recommendation systems and transformative models represent critical components in enhancing the cultural tourism experience. While filter recommendation systems offer personalized suggestions based on user data and preferences,

transformative models strive to create meaningful and impactful experiences that resonate with visitors on multiple levels. Together, they can significantly improve engagement, satisfaction, and the overall sustainability of cultural tourism practices.

The effectiveness of filter recommendation systems and transformative models relies heavily on the quality and relevance of data inputs, as well as the clarity of the outputs produced by the algorithms. By leveraging user data, item attributes, and contextual factors, these systems can deliver meaningful, personalized recommendations and transformative cultural experiences, ultimately enriching the cultural tourism landscape.

5.Conclusion

Digital technology has brought significant challenges and opportunities to the development of the cultural and tourism industry. The integrated development of digital cultural tourism itself is a complex and rich process, and applying digital technology to the marketing of cultural and tourism enterprises will further optimize market positioning accuracy, business resource consumption, tourist satisfaction, and more. The digital transformation and construction of cultural and tourism enterprises' marketing will effectively drive the development of emerging formats within the industry and innovate management methods, playing an important role in the transformation and upgrade of operations within the cultural and tourism industry, providing a scientific basis for smart tourism and precision marketing. Regardless of the era, services in the cultural and tourism industry should be efficient and precise. With the increasing emphasis on personalized services, the digital development of smart cultural and tourism is an inevitable trend. Therefore, how to improve the application of Big Data technology in the cultural and tourism industry remains a continuous subject of research.

References

[1] Marpaung B.O.Y., Tania Felicia. Visitor Satisfaction and Tourist Attraction Image. International Journal of Psychological Studies. doi:10.5539/IJPS.V13N2P33

[2] Imjai N ,Swatdikun T ,Rungruang P , et al. Empowering generation z accountants in the era of data complexity and open innovation: Nurturing Big Data analytics, diagnostic, and forensic accounting skills Journal of Open Innovation: Technology, Market, and Complexity, 2024,10. doi:100308-. doi:10.1016/J.JOITMC.2024.100308, doi: 10.3390/APP11198989

[3] Rinaldi A .A novel application based on a heuristic approach for planning itineraries of one-day tourist.Applied Sciences. 2024, 09. DOI:10.3390/app11198989.

[4] Xu M . Research on Network Information Security Control in the Big Data Era. Journal of Electronics and Information Science, 2024, 9(2), doi: 10.23977/JEIS.2024.090212

[5] Chen N . Study on the Activation Strategy of Historical and Cultural Blocks from the Perspective of Smart Cultural Tourism—A Case Study of the Three Lanes and Seven Alleys in Fuzhou City. Advances in Social Science and Culture, 2024, 6 (3), doi: 10.22158/ASSC.V6N3P40

[6] Hou W . Exploration of high-quality development path of tourism and culture industry in the context of smart tourism. Applied Mathematics and Nonlinear Sciences, 2024, 9 (1), doi:5.1.1.10.2478/AMNS-2024-0863

[7] Tobias G ,Chackartchi T ,Mann J , et al. Survival Rates of Amalgam and Composite Resin Restorations from Big Data Real-Life Databases in the Era of Restricted Dental Mercury Use. Bioengineering (Basel, Switzerland), 2024, 11(6): 579-579, doi:10.3390/BIOENGINEERING11060579

[8] Zhou Yingying. Improving collaborative filtering recommendation algorithm using outlier detection. Nanjing University of Posts and Telecommunications, July18, 2024. DOI:CNKI:CDMD:2.1015.728917.

Fuzzy Systems and Data Mining X
A.J. Tallón-Ballesteros (Ed.)

doi:10.3233/FAIA241444

Application of the YOLOv8x Model in Visual Stem Detection During Cigarette Production

Jiangtao Zhang, Baohua Li, Ying Qin, Dan Yan, Yali Zhang and You Liu[1]
Baoding Cigarette Factory, Hebei Baisha Tobacco Co., Ltd, Baoding, China
ORCiD ID: Jiangtao Zhang https://orcid.org/0009-0004-0771-3457

Abstract. The rapid separation of tobacco shreds and stems is a critical stage in the cigarette production process. Compared to traditional mechanical separation devices, machine vision technology combined with deep learning models offers advantages in accuracy, adaptability, and flexibility for automated air separation equipment. However, intelligent separation mechanisms based on machine vision also face operational challenges, including imbalanced training sample distribution, motion artifacts in targets, difficulty in sample annotation, and the small size of tobacco shreds and stems, which makes feature extraction challenging. This study first collected actual images from the outlet of the ZJ17 cigarette making machine, constructing a dataset consisting of 105 annotated static images of tobacco shreds and stems, and 50 dynamic images, divided into training and testing sets in an 8:2 ratio. Next, this study used the YOLOv8 model to train and predict the tobacco shreds and stems dataset, achieving classification and detection of tobacco shreds and stems. Finally, the model's performance was evaluated using mAP50, Precision, Recall, and Confidence metrics, achieving an overall mAP50 of 0.796, Precision of 0.81, and Recall of 0.8068. Specifically, the Precision was 0.855 for stems and 0.764 for shreds, with Recalls of 0.764 and 0.647, respectively. Visualization of the detection results showed high consistency between the model's predictions and the original annotations, demonstrating its reliability and accuracy in practical applications. This study successfully solved the challenge of accurate small target multi-scale feature extraction and demonstrated the effectiveness of the model in real-world scenarios.

Keywords. ZJ17 cigarette making machine; deep learning; YOLOv8 model; stem detection

1. Introduction

In the cigarette production process, the separation of tobacco shreds and stems is one of the critical stages. The ZJ17 cigarette making machine, as a high-speed cigarette equipment, has integrated various intelligent detection and control systems that can perform real-time quality inspection of cigarettes and accurately reject defective cigarettes [1], as shown in Figure 1(a). Figure 1(b) illustrates the secondary air separation

[1] Corresponding author, You Liu, Hebei Baisha Tobacco Co., Ltd., Baoding Cigarette Factory, Baoding, Hebei, China; E-mail: 156026590@qq.com

mechanism of the ZJ17 cigarette making machine. This separation mechanism achieves the secondary separation of tobacco stems and leaves by adjusting the air pressure of the suction head, making it one of the critical sorting structures of the ZJ17 cigarette making machine. With the increasing market demand for product quality, traditional separation techniques are unable to meet market needs. Traditional techniques for separating tobacco shreds and stems rely on mechanical separation devices, which, although capable of basic separation tasks, have certain limitations in terms of precision, adaptability, and flexibility[2]. Automated equipment in cigarette production can separate tobacco shreds and stems (Figure 2), which can enhance production efficiency, ensure product quality, reduce production costs, and optimize resource utilization, thereby improving product quality and corporate competitiveness.

Figure 1. Diagram of the ZJ17 Cigarette Making Machine

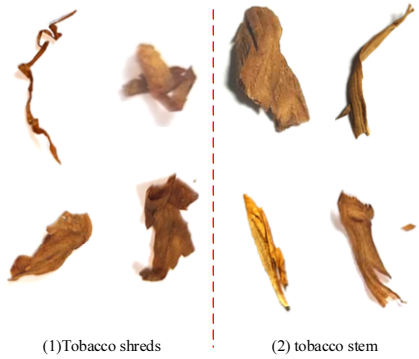

Figure 2. Tobacco shreds and stems with significant visual differences

However, the aforementioned separation and detection technologies exhibit limitations in precision and identification speed when applied to the separation assessment of tobacco shreds and stems in high-speed and scale-variable separation devices. Consequently, there is a need for a classification and detection algorithm tailored to high-speed motion and multi-scale targets of tobacco stems and shreds to meet production requirements. This study employed the YOLOv8 neural network, renowned for its exceptional multi-scale feature capture and small object detection capabilities, combined with high-speed blur denoising preprocessing methods, as an effective solution to these problems.

2. Related Works

Machine vision technology combined with deep learning models offers new solutions. Machine vision simulates the human visual system by capturing and analyzing images using image processing algorithms [3]. Deep learning learns complex features from data, achieving precise recognition and classification. By capturing images of the operating state of the tobacco shreds in Figure 1(b) using machine vision and employing deep learning technology for estimating the separation degree of tobacco shreds and stems, the level of automation in the production line can be further improved, reducing manual intervention and lowering production costs. Integrated with intelligent detection and control systems, machine vision provides detailed information for identifying tobacco shreds and stems, enhancing the intelligence of the production process.

Significant advances have been achieved in tobacco fragment and stem separation technology through machine vision and deep learning. Kang Xiaozhen et al. [4] utilized industrial cameras and image processing algorithms to perform online quantitative analysis of tobacco fragment quality characteristics, achieving precise measurements of non-overlapping tobacco fragment lengths and widths with an average accuracy error of less than 5% and width errors within 0.1 mm. Wei Jiaxin et al. [5] developed an image recognition-based method to extract the skeleton of tobacco fragments and establish a fitting model, achieving more accurate statistics on whole leaves and fragment rates with an average relative error ≤5%, demonstrating high accuracy and feasibility. Further, Xiao Leiyu et al. [6] used deep learning models to address manual sorting issues during threshing and re-drying processes, developing an online classification and recognition system for tobacco stems. The improved YOLOv3 model demonstrated outstanding performance in recognition accuracy and anti-interference capability, achieving an accuracy rate of 95.01%, surpassing the SSD (Single Shot MultiBox Detector) and Mask R-CNN (Mask Regional Convolutional Neural Network) models.

Additionally, Yang Guang et al. [7] designed a self-learning system using image recognition methods for online detection of tobacco fragment widths. Zhong Yu et al. [8] conducted research based on residual neural networks to quickly and accurately identify different types of tobacco fragments. The optimized model surpassed traditional convolutional neural networks in recognition rate and robustness, with accuracy and recall rates exceeding 96% in the test set. Hu Shilong et al.[9] proposed a method combining deep learning and precision measurement to accurately identify defective stems in tobacco fragments, improving cigarette combustion safety quality with a recognition rate exceeding 98% and width calculation error less than 0.03 mm. Gao Zhenyu et al.[10] utilized convolutional neural networks to improve the accuracy of identifying tobacco fragment compositions significantly.

Recent research from 2023 onward has focused on enhancing the precision and stability of tobacco separation and detection, especially in overcoming lighting challenges in complex industrial settings. Shen Kai et al. [11] developed a method based on image recognition to describe the granularity and shape of tobacco leaf fragments for numerical simulation modeling, achieving a deviation of less than 1.3% from experimental results. Fu Yongmin et al. [12] introduced HOG (Histogram of Oriented Gradients) and LBP (Local Binary Patterns) features and a cascaded AdaBoost classifier to achieve dynamic recognition and real-time detection of tobacco impurities, effectively responding to environmental changes. Wu Yusheng et al. [13] established an integrated online tobacco detection system combining visual inspection and deep learning, capable

of detecting foreign objects in tobacco fragments, cigarette defects, and cigarette packaging appearance.

Research on the automatic grading of flue-cured tobacco using spectral technology has shown that spectral analysis can efficiently and accurately classify tobacco fragments. Compared to traditional manual grading, it offers high speed, accuracy, and repeatability. Tao Fazhan et al. [14] developed a hyperspectral imaging system and machine learning model to precisely classify stems in tobacco fragments, maintaining high accuracy under varying lighting conditions and overcoming traditional detection limitations. Zhang Ying et al. [15] developed a rapid identification method for tobacco leaf components based on near-infrared spectroscopy, providing new insights into tobacco leaf grade evaluation. Li Shijing et al. [16] studied the application of hyperspectral information in tobacco leaf grade classification, achieving an accuracy rate of 96% using multivariate scatter correction preprocessing and support vector machine models, demonstrating the feasibility of using hyperspectral information for tobacco leaf grading.

In conclusion, machine vision, deep learning, and spectral technology have shown significant advantages and application potential in the field of tobacco separation and grading. This study introduces a significant contribution to the field by addressing the unique challenges of high-speed tobacco stem and shred detection in industrial environments. By employing the YOLOv8 model, known for its superior multi-scale feature extraction and small object detection capabilities, this research enhances the precision and efficiency of tobacco stem and shred separation. The proposed methodology not only improves detection accuracy but also reduces manual intervention, thereby optimizing the overall tobacco production process and increasing production efficiency.

3. Engineering Problem Analysis and Solutions

3.1 Problem Analysis

Despite the progress made with existing technologies and research, several shortcomings remain. The main issues are as follows:

(1)When processing large volumes of tobacco inspection data, deep learning models face sample distribution imbalances between tobacco shreds and stems, resulting in low training accuracy.

(2)In the air separation devices, tobacco shreds and stems are in a high-speed motion state, and constructing a clear dataset requires substantial human resources.

(3)During detection, the small size and scale differences of the targets, namely tobacco shreds and stems, make it challenging to capture each target's features accurately, leading to low model accuracy [17].

The YOLOv8 model's label distribution and framework characteristics in the detection of tobacco shreds and stems are shown in Figure 3.

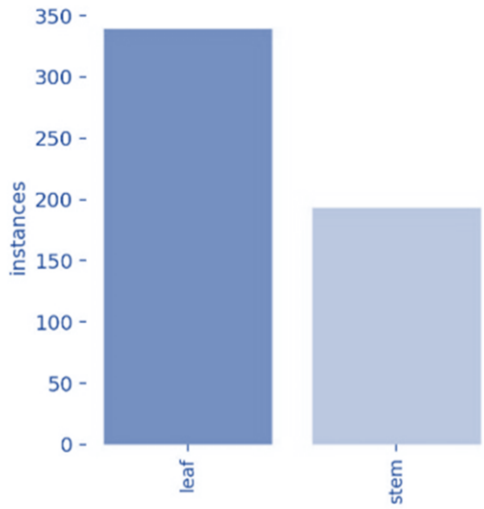

Figure 3. Framework Diagram of the YOLOv8 Tobacco Leaf Detection Model

The bar chart indicates that the number of instances labeled "leaf" significantly exceeds those labeled "stem." The box plot in the top right corner shows the concentrated distribution of detection boxes. The scatter plot in the bottom left corner displays the spatial distribution of targets (x, y coordinates) within the image, indicating a fairly even distribution across the entire image. The scatter plot in the bottom right corner shows the width and height distribution of the targets, with most targets having widths between 0.1 and 0.3 and heights between 0.05 and 0.25. Overall, the model processes targets that are uniformly distributed spatially and concentrated in size distribution.

Addressing the issue of small targets and large background proportions, Niu Qunfeng et al. [18]used the Otsu method to determine the threshold distinguishing the foreground region containing tobacco shreds from the irrelevant background. This threshold was then used to convert grayscale images into binary images. Liu Jiangpeng et al. [19]utilized K-means clustering on denoised images to separate the foreground and background, completing the segmentation process. However, these studies primarily focus on preprocessing stages for small target recognition rather than the recognition of multi-scale small targets within the model itself.

In the domain of high-speed imaging, several effective methods have been proposed to address noise and motion blur. Apart from the use of high-speed cameras to effectively mitigate noise, Daoyu Li et al.[20] introduced an efficient frame decomposition technique that decomposes a single motion-blurred image into multiple sharp video frames, thereby enhancing frame rate while maintaining high spatial resolution. Weihao Zhuang et al.[21] proposed a deep learning-based method for denoising underexposed images, addressing the trade-off between motion blur and underexposure noise in high-speed imaging. This approach significantly improves the acquisition rate of high-speed cameras while maintaining image quality. Additionally, G. Boracchi et al. [22] provided a statistical model to evaluate the performance of deblurring algorithms under arbitrary motion conditions. By employing a Monte Carlo method, this model analyzes the balance between motion blur and noise, optimizing image quality.

3.2 Solution

To address the aforementioned issues, this study first collected static and dynamic image samples of tobacco shreds and stems manually to enhance the training dataset, thereby strengthening the intrinsic features of the tobacco shreds and stems. Subsequently, the images underwent a series of preprocessing steps. As shown in Figure 4, image normalization was performed to standardize the pixel value range. This was followed by histogram equalization to improve the contrast distribution across the images. After histogram equalization, contrast adjustment was applied to enhance the visibility of features. Wiener filtering was then used to reduce motion blur and improve image clarity. These preprocessing and enhancement techniques facilitated better feature extraction from the images, laying a solid foundation for subsequent classification and detection tasks. Then, by adjusting model parameters and updating optimizers, the classification process of tobacco shreds and stems was modeled using YOLOv8. Finally, the effectiveness of the classification model was analyzed through experimental evaluation. The application of machine vision technology combined with deep learning models to the ZJ17 cigarette making machine set can significantly contribute to the technological advancement and industrial upgrading of the tobacco manufacturing industry.

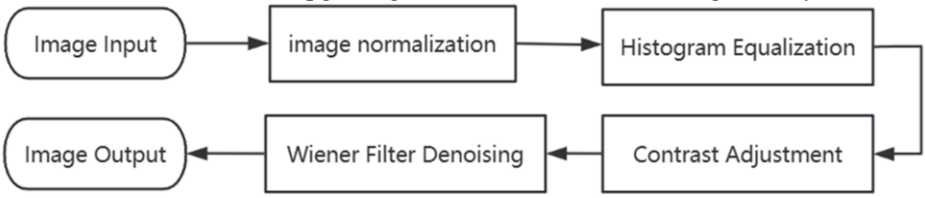

Figure 4 Data Preprocessing Workflow

The YOLOv8 (You Only Look Once version 8) neural network is renowned for its exceptional multi-scale feature capture and small target detection capabilities[23]. By integrating multi-layer feature maps, YOLOv8 extracts rich image information at different scales, effectively enhancing the detection accuracy of small targets. The improved Feature Pyramid Network (FPN) [24] and Path Aggregation Network (PANet)[25] further enhance multi-scale feature fusion, enabling accurate recognition of small targets even in complex backgrounds. YOLOv8 employs a more efficient anchor mechanism and loss function design, maintaining high-efficiency real-time processing capabilities while significantly improving detection performance [26].

As shown in Figure 5, the overall structure is divided into three main parts: Backbone, Neck, and Head. The Backbone is primarily responsible for extracting basic image features through a series of CBS (Convolution, Batch Normalization, and SiLU activation function) and C2F (Cross Stage Partial Networks) modules, gradually downsampling the image to generate feature maps of different scales. These feature maps contain information at various levels within the image, providing rich feature representations for subsequent target detection.

The Neck aims to further integrate these feature maps to enhance the semantic information of feature representations. This part adopts the concept of the Feature Pyramid Network (FPN), which, through upsampling and concatenation operations, merges feature maps of different scales. Specifically, the Neck performs two rounds of upsampling and concatenation, merging low-resolution, high-semantic feature maps with high-resolution, low-semantic feature maps, generating multi-scale, multi-level feature maps. These integrated feature maps can better capture the various scale information of targets within the image.

The Head is the critical part of the entire model, responsible for the final target detection and classification. Each Head corresponds to a specific scale of the feature map and consists of two main branches: one for boundary box (BBox) prediction and loss calculation, and the other for class (Cls) prediction and loss calculation. Specifically, the Head extracts further features through convolution layers, then separately calculates the losses for boundary box regression and class prediction. The three Heads handle feature maps of different scales, ensuring that the model can accurately detect and classify tobacco shreds targets of various sizes.

Overall, this framework, through multi-scale feature fusion and detection, effectively improves the detection accuracy and robustness of the model for targets of different sizes. Particularly in the task of tobacco shreds target detection, the model can accurately identify and classify tobacco shreds of varying sizes and shapes, making it suitable for industrial applications in complex background scenarios[27]. The multi-scale detection mechanism designed in this manner ensures the model's high flexibility and accuracy in practical applications.

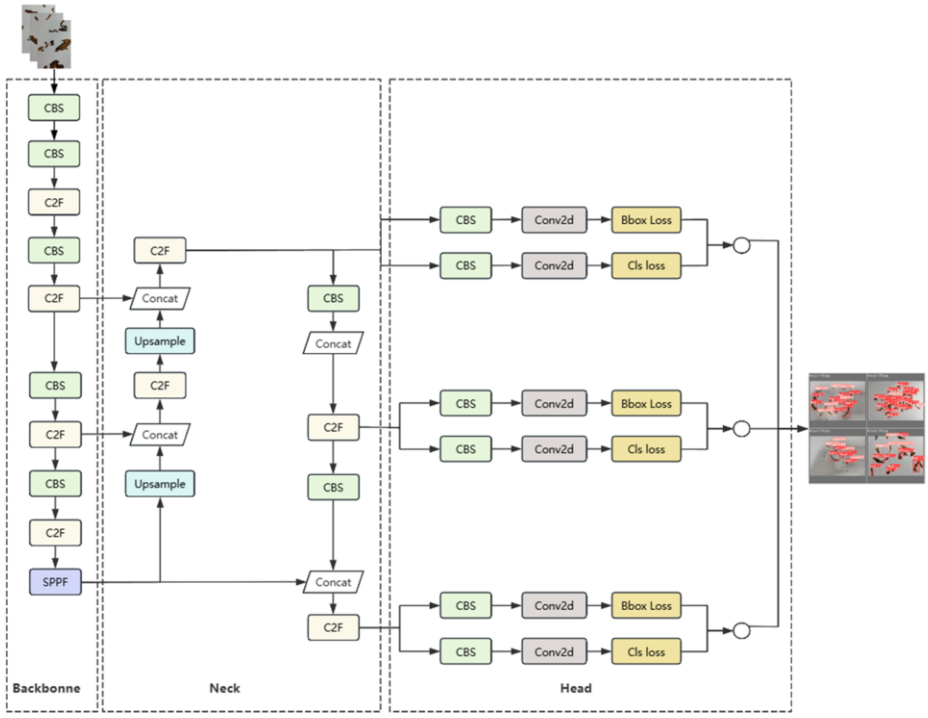

Figure 5. Framework diagram of the YOLOv8 tobacco leaf target detection model

4. Experiment and Results Analysis

4.1 Experimental Setup

The experiments in this study were conducted on a Windows 11 system. The hardware configuration included an Intel i5-12490 processor with a base frequency of 3.6 GHz, 16

GB of RAM, and an Nvidia GeForce RTX 4070 GPU with 12 GB of GPU memory. The software environment consisted of the PyCharm IDE, utilizing the PyTorch deep learning framework, with Python 3 as the programming language for network training and testing.

The camera used was a Keyence CV-200C industrial camera [28], as shown in Table 1. The camera's dimensions are 23mm x 45mm, making it suitable for deployment in the secondary air separation mechanism of the ZJ17 cigarette making machine. Its maximum resolution reaches up to 1600x1200, and at this resolution, the maximum frame rate is approximately 17 fps, which is appropriate for image acquisition of small, high-speed moving mixtures of tobacco shreds and stems.

Table 1. Specific Parameters of the CV-200C Series

Model	CV-200C
Parameters and Performance	6 Megapixel 1/1.8" CMOS USB3.0 Industrial Area Camera
Sensor Type	CCD
Sensor Component	1/1.8 inch Color CCD Image Sensor, Square Pixel/Full Pixel Readout 2.01 Megapixels, Pixel Size: 4.4x4.4 μm
Effective Pixels	1.92 Megapixels, 1600 (Horizontal) x 1200 (Vertical)
Pixel Transmission Frequency	40 MHz
Scanning System	Progressive (58.5 ms: 2 Megapixel Mode, 47.6 ms: 1 Megapixel Mode)
Transmission System	Digital Serial Transmission
Electronic Shutter	1/15--1/10000, can be set between 0.05 msec to 9000 msec
Lens Mount	C-Mount
Environmental Temperature Resistance	0 to +40°C
Relative Humidity Resistance	35 to 85 % RH (Non-condensing)
Weight	Approx. 110 g (without lens)

4.2 Model Performance Evaluation

In this study, the classification and detection results of tobacco shreds and stems based on the YOLOv8 model demonstrated high performance, as shown in Table 2 and Figure 6. Table 2 lists the model's evaluation metrics, including mAP50, Precision, and Recall. The overall mAP50 value is 0.796, indicating that the model has a good average accuracy at different confidence thresholds. Additionally, the overall Precision and Recall of the model are 0.81 and 0.8068, respectively, showing excellent performance in predicting positive samples and capturing actual positive samples.

Regarding specific category performance, the model's detection performance for tobacco stems surpasses that for tobacco shreds. The Precision for tobacco stems is 0.855, while it is 0.764 for tobacco shreds; the Recall for tobacco stems is 0.764, compared to

0.647 for tobacco shreds. This difference may be due to the more distinct morphological features of tobacco stems, making them easier for the model to recognize.

Table 2. Model Prediction Results

	R	mAP50	Precision	Recall
All	0.796	0.81	0.8068	0.77031
Leaf	0.761	0.764	0.647	
Stem	0.83	0.855	0.764	

As depicted in Figure 6, both Precision and Recall significantly increase with the number of training steps, stabilizing at approximately 0.75 and 0.80, respectively, indicating the model's effectiveness in reducing false positives and capturing positive samples. The metrics mAP50 and mAP50-95 also show a significant upward trend, stabilizing at around 0.80 and 0.40, respectively, demonstrating high detection performance across different IoU thresholds. Therefore, all the model's metrics exhibit outstanding performance, effectively distinguishing between tobacco shreds and stems, highlighting its high application value.

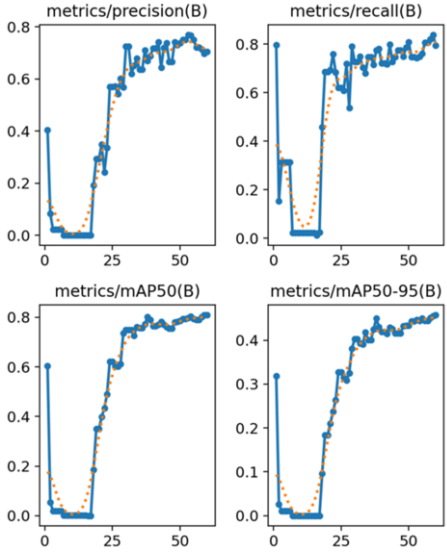

Figure 6. Model Prediction Results

4.3 Model Performance in Leaf and Stem Classification

Figure 7 and Figure 8 present the confusion matrix and the normalized confusion matrix of the YOLOv8 model, reflecting its performance in classifying tobacco shreds, stems, and background. Most data with the actual value "leaf" were correctly classified, but a small portion was misclassified as "stem" and "background." Similarly, for data with the actual value "stem," most were correctly classified, but some were misclassified as "leaf" and "background."

The classification proportions are illustrated in Figure 8: the proportion of actual "leaf" correctly classified is 0.89, with misclassification proportions as "stem" and "background" being 0.09 and 0.08, respectively. Overall, the model performs well in

classifying "leaf" and "stem," but there is still some error in distinguishing "leaf" from "background."

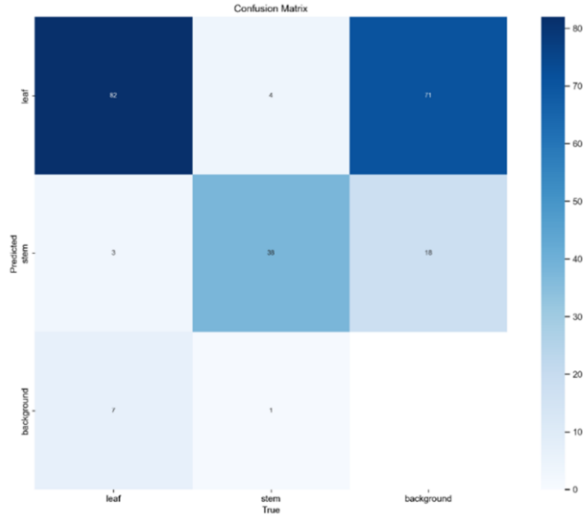

Figure 7. Confusion Matrix

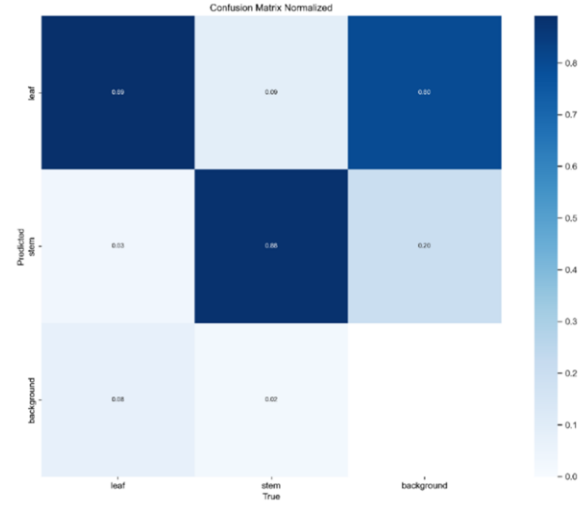

Figure 8. Normalized Confusion Matrix

4.4 Model Detection Relationship Curves

Figure 9 illustrates the F1-Score curve at different confidence thresholds. Overall, as confidence increases from 0 to 1, the F1-Score initially rises and then falls. For "leaf," the F1-Score peaks at a confidence of approximately 0.3, whereas the F1-Score for "stem" performs better at higher confidence levels. The best overall F1-Score for all categories is 0.75, corresponding to a confidence of 0.36, indicating the model's optimal comprehensive performance at this confidence level.

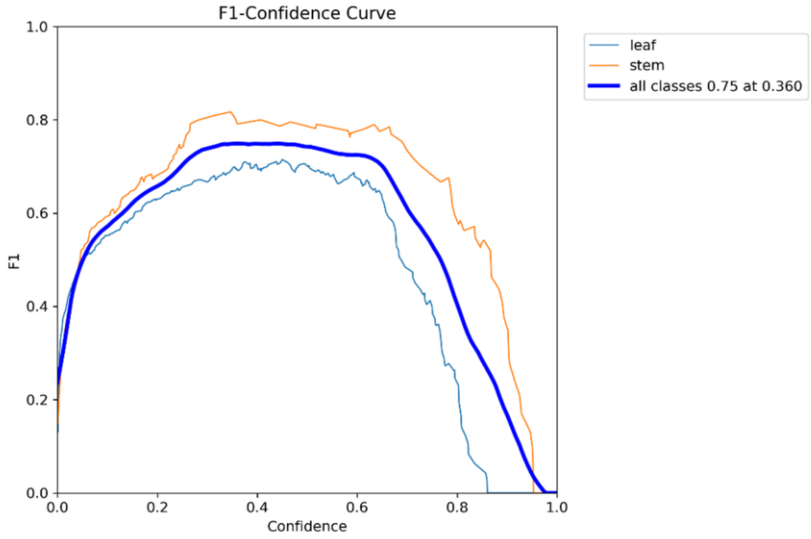

Figure 9. F1-Score Curve

Figure 10 shows the relationship curves between Precision, Recall, and Confidence for the YOLOv8 model in the classification tasks of tobacco shreds and stems. Figure 10 (a) presents the Precision-Confidence curve, indicating that precision increases with confidence and eventually stabilizes at around 0.8 at high confidence levels, demonstrating the model's high accuracy at high confidence. Figure 10 (b) displays the Precision-Recall curve, showing the model's precision performance at different recall rates, with the overall curve indicating that precision decreases at higher recall rates. Figure 10 (c) shows the Recall-Confidence curve, revealing that recall decreases with increasing confidence, stabilizing between 0.6 and 0.8 at high confidence levels. Overall, the model's performance is balanced across different confidence levels, maintaining high precision while achieving good recall, making it suitable for effective detection of tobacco shreds and stems.

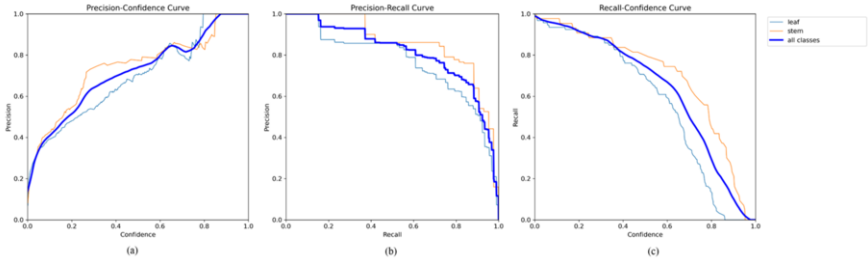

Figure 10. Precision-Recall-Confidence Curves

4.5 Loss Function Training Process

Figure 11 illustrates the trends of different loss functions during the training process of the YOLOv8 model. Figure 11 (a) shows the box regression loss[30], which gradually decreases from approximately 2.0 to around 1.4 as training iterations increase, indicating the model's progressive optimization in target boundary localization. Figure 11 (b) depicts the classification loss[29][30], which exhibits a more significant decline from

about 3.5 to around 1.0, demonstrating substantial improvements in the model's target classification capability. Figure 11 (c) represents the distribution focal loss, which also shows a downward trend, stabilizing at around 1.4, indicating enhanced performance in predicting target distributions. The concurrent decline of all three losses suggests continuous improvement in the model's overall performance, enabling more accurate target detection and classification.

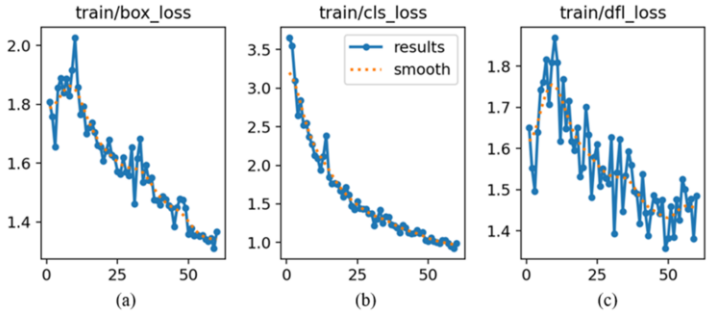

Figure 11. Changes in Loss Functions During Training

4.6 Visualization of Detection Results

The study visualizes the model's classification and detection results, as shown in Figure 12, illustrating the YOLOv8 model's actual performance in the classification and detection tasks for tobacco shreds and stems. The upper part of each image set represents the original annotations, while the lower part displays the model's predictions. The model accurately identifies and annotates tobacco shreds and stems, assigning corresponding confidence scores. Despite some errors, such as mislabeling certain shreds as stems or background, the overall recognition effect is satisfactory. Notably, the model can distinguish and accurately label each target even in densely populated scenarios. Comparing the model's predictions with the original annotations shows a high degree of consistency, demonstrating its reliability and accuracy in practical applications.

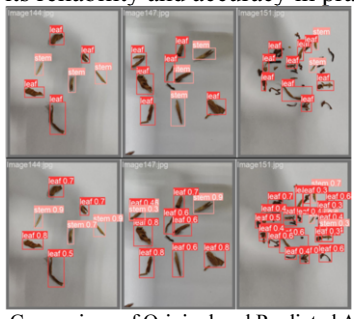

Figure 12. Comparison of Original and Predicted Annotations

5. Conclusion

In this study, the YOLOv8x model was employed for classifying and detecting tobacco shreds and stems, achieving notable results. The model's overall mean average precision at 50% intersection over union (mAP50) is 0.796, with a precision of 0.81 and a recall of 0.8068, demonstrating high detection performance. It performs better in detecting

stems, with a precision of 0.855 and a recall of 0.764, compared to shreds, which have a precision of 0.764 and a recall of 0.647. The model enhances multi-scale feature fusion through multi-layer feature maps and an improved feature pyramid network, allowing accurate identification of small targets in complex backgrounds. Additionally, the decrease in loss functions during training indicates continuous optimization in target localization, classification, and distribution prediction. Visualization of results shows high consistency between model predictions and original annotations, confirming its reliability and accuracy in practical applications.

Compared with current advanced technologies, the model in this study also highlights its advantages in complex industrial application scenarios. For example, the JIT-PLS strategy demonstrated high accuracy in predicting chemical constituents in tobacco[31], and the HPLC-HRMS method provided efficient pesticide residue analysis [32]. However, the YOLOv8x model excels in real-time detection and classification of physical characteristics, maintaining high accuracy and speed in complex environments, making it more suitable for practical industrial applications.

Overall, the YOLOv8x model's advantages in precise detection of small targets and multi-scale features have significant practical implications in the tobacco industry, contributing to the automation of tobacco shreds and stem separation, improving production efficiency and product quality. However, the adoption of this technology faces potential obstacles including imbalanced training sample distribution and difficulties in sample annotation, which can hinder its industrial implementation. Future research should focus on enhancing training data diversity, developing more robust models to handle high-speed motion and complex industrial environments, and improving automated annotation techniques to ensure accurate detection and classification.

References

[1]Wang Zhen, Zhang Jianlong, Li Duanduan, Liu Haozhe, Fu Zhiqiang, Li Guang. Mechanism of Primary Wind Distribution in ZJ17 Rolling Unit Based on Fluent. Journal of Machine Design. 2024;(03): 130-135. DOI: 10.13841/j.cnki.jxsj.2024.03.020

[2]Bai Xue, Jiang Xiaowei, Cai Peiliang, Yang Jianfeng, Zhou Meifen, Li Ming, Feng Lingfan. Design of Online Stem and Leaf Separation System in ZJ17 Cigarette Machine. Packaging Engineering. 2018; (21): 32-36, doi:10.19554/j.cnki.1001-3563.2018.21.007

[3]Shi Xu, Gao Song, Liu Shuai, Ma Shiquan, Huang Kun, Pan Yuanhong, Guo Jian, Song Wenfeng, Zhang Tiehuai, Guan Qunrong, Xiao Changdong, Wu Jinhui, Long Baoan, Pu Enping, Shi Xiaohui, and Wu Si. Exploration of Smart Tobacco Agriculture Development Based on Artificial Intelligence Technology. Zhejiang Agricultural Science. 2024; 65(04): 942-948, doi:10.16178/j.issn.0528-9017.20221226

[4]Kang Xiaozhen, Yang Yi, Xie Shangyu, Sun Zhe, Fang Shijie Online Quantitative Analysis of Tobacco Quality Characteristics Based on Machine Vision. Technological Innovation and Application. 2022; 12 (27): 56-62, doi:10.19981/j.CN23-1581/G3.2022.27.014

[5]Wei Jiaxin, Li Qi, Ma Fei, Ding Meizhou, Jin Yawei, Wang Yibin, Xu Wenwu, Wang Xiaoming. Tobacco structure detection and tobacco component analysis based on image recognition. Journal of Light Industry. 2022; 37 (3): 82-87, doi: 10.12187/2022.03.011

[6]Xiao Lei Yu, Wang Shu, Liu Yuangen, Zhang Long, Wang Ling, Du Jinsong, Xu Dayong. Classification and recognition of tobacco stem morphology based on deep learning technology. Tobacco Technology. 2021; 54 (06): 65-74, doi:10.16135/j.issn1002-0861.2020.0522

[7]Yang Guang, Huang Chuanxi, Xu Yonghu, Xing Yingjie, Yang Fanfan. Image Processing and Width Calculation of Tobacco Shreds Based on Image Recognition Method. Optical Frontier. 2023, 1(176): 87-89.

[8]Zhong Yu, Zhou Mingzhu, Xu Yan, Liu Dexiang, Wang Hongqiang, Dong Hao, Yu Jian, Li Xiaohui, Yang Jin, Xing Jun. Establishment of Tobacco Shred Type Recognition Method Based on Residual Neural

Network. Tobacco Science & Technology. 2021; 54(05): 82-89, doi:10.16135/j.issn1002-0861.2020.0602

[9]Hu Shilong, Chen Jianqiang, Lai Donghui, Zhou Lei. Detection Method of Defective Leaf Stems and Tobacco Shreds Based on Machine Vision [J]. Computer Applications, 2019, 39(S1): 215-218.

[10]Gao Zhenyu, Wang An, Dong Hao, Liu Yong, Wang Jinping, Zhou Mingzhu, Xia Yingwei, Zhang Long. Identification Method of Tobacco Shred Composition Based on Convolutional Neural Network. Tobacco Science & Technology. 2017;(07): 68-75. doi: 10.16135/j.issn1002-0861.2016.0502

[11]Shen Kai, Fan Hu, Han Leyuan, Li Xu, Wang Siyuan, Han Jiawei, Wang Peng, Guo Yu, Wang Canxing, Zhu Qiang, Lin Jianzhong, Xia Chen, Pan Fanda. Characterization and Numerical Simulation of Tobacco Leaf Shred Morphology Based on Image Recognition. China Tobacco Journal: 1-17 [2024-06-12]. http://kns.cnki.net/kcms/detail/11.2985.TS.20240205.1330.002.html.

[12]Fu Yongmin, Fan Lei, Li Changjin, Wu Qinghua. Cascade Detection Method of Tobacco Shred Impurities Based on Computer Vision and Machine Learning. Journal of Light Industry. 2023;38(04): 113-121.

[13]Wu Yusheng, Li Anhu, Wan Yaming, Meng Tian-chen. Progress in Research on Tobacco Online Inspection Technology Based on Machine Vision. Laser & Optoelectronics Progress. 2024; 61(8): 0800003, doi: 10.3788/LOP231332

[14]Tao Develop-Fa, Yang Dong, Hong Weiling, Su Ziqi, Fu Zhu-mu, Lin Zhi-ping. Study on Classification and Recognition of Stems in Tobacco Shreds Based on Hyperspectral Imaging. Journal of Henan University of Science and Technology (Natural Science Edition). 2024; 45(03): 32-42+5, doi: 10.15926/j.cnki.issn1672-6871.2024.03.005

[15]Zhang Ying, He Liyuan. Automatic Grouping Method of Flue-cured Tobacco Shreds Based on Near-infrared Spectroscopy. Transactions of the Chinese Society of Agricultural Engineering. 2011; 27(04): 350-354

[16]Li Shijing, Pan Xi, Chen Xizhuo, Zhu Junyan, Wu Bizhi, Xie Xiaofang, Wen Yongxian. Comparative Study on Grading Methods of Tobacco Shreds Based on Hyperspectral Information. Tobacco Science & Technology. 2021;54(10): 82-91, doi: 10.16135/j.issn1002-0861.2021.0213

[17]Du Youmei, Guo Jizhou, Wang Xiaoyu, Xie Wei, Huang Yanjun, Liu Ruihong, Liu Zechun, Xie Fuwei. Analysis Method of Cigarette Smoke Component Retention by Tobacco Shred Segments. Tobacco Science & Technology. 2022, 55(05): 32-40.

[18]Niu Qunfeng, Yuan Qiang, Jin Yi, Wang Li, Liu Jiangpeng. Tobacco Shred Type Recognition Based on Improved VGG16 Convolutional Neural Network. Foreign Electronic Measurement Technology. 2022; 41(09): 149-154, doi: 10.19652/j.cnki.femt.2203982.

[19]Liu Jiangpeng, Niu Qunfeng, Jin Yi, Chen Xia, Wang Li, Yuan Qiang. Research on Tobacco Shred Image Recognition Method Based on Efficient Channel Attention Mechanism and Multi-scale Feature Fusion. Henan Agricultural Sciences. 2022; 51(11): 145-154, doi: 10.15933/j.cnki.1004-3268.2022.11.017

[20]Huang Kun, Qi Zhaojian, Wang Juanmin, Hu Qian, Hu Weichao, Pi Jianyong. Dense Pedestrian Detection Model Based on Improved YOLOv8. Computer Engineering. [2024-06-12], doi: 10.19678/j.issn.1000-3428.0069026

[21]Weihao Zhuang, Tristan Hascoet, Ryoichi Takashima, Tetsuya Takiguchi. Learn to See Faster: Pushing the Limits of High-Speed Camera with Deep Underexposed Image Denoising. 2022. doi.org/10.48550/arXiv.2211.16034.

[22]Giacomo Boracchi, Alessandro Foi. (2012). Modeling the Performance of Image Restoration From Motion Blur. IEEE Transactions on Image Processing, 21, 3502-3517. https://doi.org/10.1109/TIP.2012.2192126.

[23]Xu Yanwei, Li Jun, Dong Yuanfang, Zhang Xiaoli. Review of YOLO Series Target Detection Algorithms [J/OL]. Computer Science and Exploration: 1-19 [2024-06-12]. http://kns.cnki.net/kcms/detail/11.5602.TP.20240611.1631.006.html.

[24]Jingyi Zhao, Shengnan Hao, Chenxu Dai, Haiyang Zhang, Hanlin Ji, Li Zhao, & Ivan Ganchev. (2022). Improved vision-based vehicle detection and classification by optimized YOLOv4. IEEE Access, 10, 8590-8603. https://doi.org/10.1109/access.2022.3143365

[25]Shijing Li, Yong Wang, Chunlin Feng, Dingwen Zhang, Huijun Li, Wei Huang, Liang Shi. A Thermal Imaging Flame-Detection Model for Firefighting Robot Based on YOLOv4-F Model. 2022; 5(5): 172. DOI: https://doi.org/10.3390/fire5050172

[26] Huang Kun, Qi Zhaojian, Wang Juanmin, Hu Qian, Hu Weichao, Pi Jianyong. Dense Pedestrian Detection Model Based on Improved YOLOv8 [J/OL]. Computer Engineering: 1-11 [2024-06-12]. https://doi.org/10.19678/j.issn.1000-3428.0069026.

[27]Bo Xu, Xiang Cui, Wei Ji, Hao Yuan, Juncheng Wang. Apple grading method design and implementation for automatic grader based on improved YOLOv5[J]. Agriculture, 2023, 13(1): 124. doi.org/10.3390/agriculture13010124

[28]Dashan Zhang, Jie Guo, Xiujun Lei, Changan Zhu. A High-Speed Vision-Based Sensor for Dynamic Vibration Analysis Using Fast Motion Extraction Algorithms, Sensors (Basel, Switzerland). 2016; (4): 572, doi: https://doi.org/10.3390/s16040572

[29]Hao Zhang, Shuaijie Zhang. Focaler-IoU: More Focused Intersection over Union Loss. 2024. arXiv:2401.10525v1 [cs.CV]. https://arxiv.org/abs/2401.10525v1.

[30]Yi-Fan Zhang, Weiqiang Ren, Zhang Zhang, Zhen Jia, Liang Wang, Tieniu Tan. Focal and Efficient IOU Loss for Accurate Bounding Box Regression. 2021. arXiv preprint arXiv:2101.08158.

[31]Youyan Liang, Le Zhao, Junwei Guo, Hongbo Wang, Shaofeng Liu, Luoping Wang, Li Chen, Mantang Chen, Nuohan Zhang, Huimin Liu, Cong Nie. Just-in-Time Learning-Integrated Partial Least-Squares Strategy for Accurately Predicting 71 Chemical Constituents in Chinese Tobacco by Near-Infrared Spectroscopy. ACS Omega. 2022; 7(43), 38650–38659, doi:10.1021/acsomega.2c04139.

[32]Anindita Paul, Zareen Khan, Arijita Bhattacharyya, Sujan Majumder, Kaushik Banerjee. Multiclass pesticide residue analysis in tobacco (Nicotiana tabacum) using high performance liquid chromatography-high resolution (Orbitrap) mass spectrometry: A simultaneous screening and quantitative method. Journal of Chromatography A. 2021 Jul;1648, 462208, doi:10.1016/j.chroma.2021.462208

Fuzzy Systems and Data Mining X
A.J. Tallón-Ballesteros (Ed.)

doi:10.3233/FAIA241445

Super-Resolution Reconstruction Technology of Beidou Satellite Transmission Images Based on Adaptive Mechanism

Lanyong Zhang[a,1] , Yuanlin Yao[a] and Sheng Liu[a]
[a] *College of Intelligent Systems Science and Engineering, Harbin Engineering University, Harbin 150001, China*
ORCiD ID: Lanyong Zhang https://orcid.org/ 0000-0002-2683-2732

Abstract. Satellite image transmission is crucial for distant sea monitoring and navigation safety. Beidou satellite communication has low cost, high security and confidentiality, and has broad development potential in the field of satellite image transmission. However, the communication capacity of Beidou satellites is limited. In order to increase the transmission rate of images, the images are compressed and sent. The shore end receives and decodes images with lower resolution. Therefore, the shore end designs super-resolution reconstruction technology to perform image processing on the received images. The improvement of resolution, improving the quality and texture details of images and making them clearer and more realistic are urgent problems that need to be solved. This paper proposes a generative adversarial network super-resolution reconstruction method based on an adaptive mechanism. This method uses a new perceptual loss function combination to integrate pixel loss, feature loss based on an adaptive weight mechanism, and adversarial loss to achieve a total loss function. At the same time, an adaptive weight mechanism is introduced in the feature loss, and a spatial attention mechanism is introduced in the generator and discriminator of SRGAN, thereby effectively distinguishing the salient areas and background areas of the image, and fully retaining the high-frequency details and edge features of the image. This solves the problems of low resolution, edge smoothness and detail distortion of images received at the shore end. Experimental results show that the image details of the overall area of the ship image (including the salient area and the background area) reconstructed by this method are clearer than existing super-resolution reconstruction methods such as EnhanceNet, ESPCN, and SRCNN, and the edge integrity of the salient area is better.

Keywords. Adaptive mechanism; Beidou satellite; Ship image; Super-resolution reconstruction.

1. Introduction

In the field of modern offshore monitoring and navigation safety, high-quality satellite image transmission plays a vital role. However, although the Beidou satellite communication system has obvious advantages in terms of cost and security, its communication capacity limitation has become a major problem in improving the quality

[1] Corresponding Author: Lanyong Zhang, zhanglanyong@hrbeu.edu.cn.

of remote transmission images. Especially in complex marine environments and emergency response, high-resolution images are the key to accurate monitoring and decision-making. Therefore, how to improve image resolution and detail restoration while ensuring image transmission efficiency has become an urgent scientific problem that needs to be solved.

Image super-resolution reconstruction technology aims to reconstruct high-resolution images from low-resolution images, thereby improving the visual quality, detail and clarity of the image. Harris [1] first proposed the concept of image super-resolution reconstruction, focusing on single frame images to restore lost frequency details. Based on this, Tasi [2] et al. achieved super-resolution restoration by applying Fourier transform to multiple frames of low-resolution images. Super-resolution reconstruction technology is of great significance in the field of video surveillance. The rapid development of deep learning has also indirectly promoted the improvement of super-resolution reconstruction technology. Currently, image super-resolution reconstruction technology is mainly divided into four main categories: interpolation method [3], reconstruction method [4], shallow learning method [5] and deep learning method [6]. The super-resolution reconstruction method based on interpolation expands the image pixel information through the interpolation process [7-10], but the optimization of the interpolation method still has flaws, that is, the texture details of the reconstructed image are missing. In order to solve this problem, the image texture needs to be considered. Reconstruction-based super-resolution reconstruction technology [11-13] infers the high-frequency details lost in the image by considering the degradation model, but the performance of the degradation model depends largely on the quality and diversity of the training data. The cost of data collection and preprocessing is high, so targeted methods need to be introduced to improve the performance of image super-resolution reconstruction and restoration. Aiming at the limitations of reconstruction methods in super-resolution reconstruction, shallow learning methods [14-17] retrieve high-resolution (HR) images that are most similar to low-resolution (LR) input images from a specific training set or image patches, and then splice or fuse the retrieved high-resolution image patches to form a complete high-resolution image. However, shallow learning methods are often constrained by the inherent limitations of manually crafted feature extraction in tasks such as image super-resolution, as well as their limited generalization ability. This results in suboptimal performance and outcomes when dealing with intricate image data..

Different from shallow learning, deep learning methods [18] demonstrate excellent performance and stronger generalization capabilities in complex tasks such as image super-resolution by automatically learning complex and high-level features of data. Compared with shallow learning, deep learning can process large-scale data sets more effectively and generate more detailed and realistic image reconstruction results. Due to the emergence of network models with different characteristics in deep learning, super-resolution reconstruction technology has achieved unprecedented development.

The SRCNN model [19] achieves image super-resolution reconstruction for the first time through a three-layer nonlinear transformation network. Although its network architecture is simple, the output high-resolution reconstruction effect is significantly better than traditional methods. Dong [20] et al. proposed an improved FSRCNN, using small convolution and deconvolution technology to solve the computational redundancy problem. The ESPCN method proposed by Shi [21] et al. directly learns the mapping relationship from low resolution (LR) to high resolution (HR) images through sub-pixel convolution layer, which effectively improves the speed and efficiency of super-

resolution reconstruction. Through its unique game learning mechanism, the introduction of generative adversarial networks (GANs) [22-26] in the field of super-resolution reconstruction has led to significant advancements. Compared with decades of traditional neural network research, generative adversarial networks represent a new branch of machine learning. Therefore, in terms of model development and practical applications, it is still necessary to conduct in-depth research on generative adversarial networks and apply them to the field of image reconstruction. The exploration of adversarial networks needs to continue, and many aspects require in-depth research.

Based on the communication characteristics of Beidou satellites, this study proposes a generative adversarial network super-resolution reconstruction method based on an adaptive mechanism, and designs a perceptual loss function based on adaptive weights, including pixel loss, feature loss of adaptive weights, and adversarial loss to optimize the overall loss function. At the same time, a feature loss based on an adaptive weight mechanism is proposed to effectively distinguish the salient areas and background areas of the image, fully retaining the high-frequency details and edge features of the image. Finally, by incorporating the spatial attention mechanism into the discriminator of the SRGAN (Super-Resolution Generative Adversarial Network), the model is able to more effectively focus on key areas and salient features of the image, thereby enhancing its performance.. This method can not only significantly improve the resolution and quality of images transmitted through satellites, but also provide technical support for a variety of applications such as offshore monitoring, disaster warning, navigation, etc. It has important theoretical value and broad application prospects. By improving the resolution and detail restoration of images, the Beidou satellite system can be more effectively used for real-time monitoring and management of offshore operations, further promoting the development of remote sensing technology in the fields of marine science and navigation safety.

The second part of this article introduces the model architecture of SEAP-SRGAN and elaborates on the innovation of the SeAp SRGAN model in using a combination of perceptual loss functions during its training phase. The third part provides a detailed introduction to the overall loss function of this article, covering the process of reconstructing low resolution images received from shore decoding and those reconstructed by the generative model in the shore super-resolution reconstruction module. In order to verify whether the proposed method can achieve good results in super-resolution reconstruction of ship images transmitted from Beidou satellite to shore in practical applications, experimental verification and analysis were conducted in the fourth part. Finally, a conclusion summary was made in the sixth section.

2. Model framework

This paper proposes a generative adversarial network (SeAp-SRGAN) based on an adaptive optimization mechanism, aiming to achieve super-resolution reconstruction of images. The network's core architecture is built on the Generative Adversarial Network (GAN) framework, by simultaneously training a generator and a discriminator, which compete with each other during the training process: the generator's task is to produce high-resolution images that are as close to the real world as possible. The discriminator is tasked with distinguishing whether an input image is generated by the generator or is a real sample, while the rate image (or potentially a related output, depending on context) provides information that may aid in this distinction. As the recognition ability of the

discriminator increases, the generator continuously improves the quality of the generated image through adaptive optimization of the loss function. The ultimate goal is to improve the similarity between the generated image and the real sample image, and effectively improve the resolution and vision of the image received by the shore. SeAp-SRGAN introduces a spatial attention mechanism in both its generator and discriminator and optimizes the loss function. As shown in Figure 1, the innovative points of the combination of perceptual loss functions used by the SeAp-SRGAN model in its training phase include:

(1) The designed perceptual loss function combines pixel loss, adaptive weight feature loss and adversarial loss to optimize the overall loss function.

(2) A feature loss based on an adaptive weight mechanism is proposed, and the weight is adjusted according to different local structures such as the salient area and background area of the image received at the shore. Therefore, the objective is to effectively distinguish between the salient areas and background areas of the image, while fully retaining the high-frequency details and edge features, which are crucial for preserving the image's fidelity and quality..

(3) Introduce a spatial attention mechanism into the generator and discriminator of SRGAN, and add a spatial attention module to the generator to dynamically adjust the generator's attention to different areas of the image; add a global attention module to the discriminator. The pooling layer is used to extract the global features of the image, and then weight the global features through the spatial attention mechanism to improve the discriminator's ability to perceive image details, allowing the model to pay more attention to important areas and features in the image, thereby improving generation.

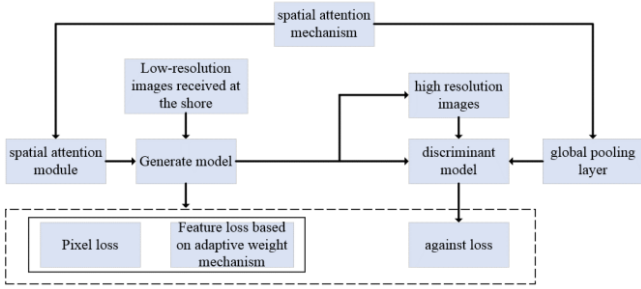

Figure 1 SeAp-SRGAN model architecture

3. Total loss function

3.1. Pixel loss

Pixel loss plays a key role in evaluating the content consistency between the reconstructed high-resolution image and the original uncompressed image, thereby optimizing the pixel space of the SeAp-SRGAN model. In order to enhance edges, contours and other high-frequency details during the image reconstruction process, this section introduces the Charbonnier loss function proposed by the LapSRN model to calculate the pixel loss L_{Pix}^{SR}, as shown in Equation (1):

$$L_{Pix}^{SR} = \frac{1}{N}\sum_{n=1}^{N}\sqrt{\left(G_{\theta_G}\left(I_n^{LR}\right) - I_n^{HR}\right)^2 + \varepsilon^2} \tag{1}$$

In the formula: $G_{\theta_G}\left(I_n^{LR}\right)$ represents the reconstructed image, I_n^{HR} represents the uncompressed original image collected by the ship, I_n^{LR} is the layered compressed image of the ship's image processing module, $n=1,...,N$ represents the network parameter set of the generator, ε is close to the Charbonnier penalty constant term of 0, according to experimental tests, has the best effect when ε is set to 0.001.

3.2. Feature loss based on adaptive weight mechanism

Feature loss is used to evaluate the semantic similarity between the high-resolution image reconstructed by the shore-end super-resolution reconstruction module and the original image collected by the ship-end before compression, so as to optimize the feature expression ability of the SeAp-SRGAN model. This paper optimizes the feature loss function into a weighted perceptual loss function, where the loss of each pixel is weighted by its adaptive weight. By applying the pre-trained VGG network as a feature extractor, the perceptual loss function can be expressed as follows:

$$\mathrm{L}_{\mathrm{adVGG}}=\sum_{i,j} w_{ij}\ \mathrm{P}\phi(G_{\theta_G}\left(I^{LR}\right))_{ij}-\phi(I^{HR})_{ij}\ \mathrm{P}_2^2 \tag{2}$$

In the formula: $\phi(G_{\theta_G}\left(I^{LR}\right))_{ij}$ and $\phi(I^{HR})_{ij}$ represent the feature representation of the generated image and the real image at the i row and j column respectively, $\mathrm{P}\cdot\mathrm{P}_2^2$ represents the Euclidean distance between features, and w_{ij} represents the adaptive weight at the i row and j column position.

This method uses the local contrast information of the image to measure the importance levels of different pixels, and uses the pixels with larger local contrast as the image information of the salient area to construct an adaptive dynamically adjusted spatial information weight $W_{i,j}$ as follows:

$$W_{i,j}=\frac{1}{1+\beta C_{i,j}} \tag{3}$$

In the formula: $C_{i,j}$ represents the local contrast of the image at the i row and j column, and β is the adjustment parameter that controls the weight range. Pixels with larger local contrast will be given smaller weights so that the loss function pays more attention to the. salient area of the image.

For different areas of the image, the local contrast $C_{i,j}$ is calculated as follows:

$$C_{i,j}=\sqrt{\frac{1}{N}\sum_{i=1,j=1}^{N}\left(I_{i,j}-\mu\right)^2} \tag{4}$$

In the formula: $I_{i,j}$ represents the gray value of the i,j pixel, $\mu=\frac{1}{N}\sum_{i=1,j=1}^{N} I_{i,j}$ is the average pixel value in the local area, and N represents the total number of pixels in the area.

3.3. Fighting losses

The adversarial loss is used to measure the similarity between the image reconstructed by the generative model and the real image. The cross-entropy of the discriminator to distinguish the generated image from the real high-resolution image is used to define the adversarial loss. The calculation formula is as follows:

$$L_{Adv}^{SR} = \sum_{n=1}^{N} -\log D_{\theta_D}\left(G_{\theta_G}\left(I^{LR}\right)\right) \tag{5}$$

In the formula: D_{θ_D} is the probability that the generated super-resolution image is true, and $G_{\theta_G}\left(I^{LR}\right)$ is the generated super-resolution image.

4. Introduce attention mechanism

By introducing the attention mechanism, the generative model pays special attention to salient areas and key features during the image reconstruction process to enhance the edge and texture details of the image, thereby significantly improving image quality and detail performance.

This paper introduces a spatial attention mechanism based on the SRGAN algorithm. The SRGAN generation model and discriminant model architecture are shown in Figure 2, including two opposing networks, the generation model G and the discriminant model D. k represents the convolution kernel size, and n represents the number of feature maps, s represents the convolution step size. The generative model G uses the residual network structure to take the hierarchically compressed low-resolution image received by the shore as input, and reconstructs the super-resolution image as the output. The discriminant model D is a depth convolution accumulation network with 8 convolutional layers..

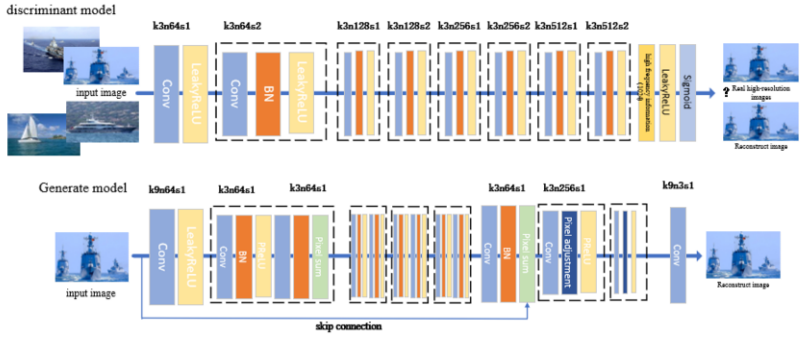

Figure 2 SRGAN generation model and discriminant model architecture diagram

"k3n64s1" represents a convolutional layer with a kernel size of 3x3, outputting 64 feature maps, and a stride of 1 for the convolution operation. This configuration is typically used to maintain the spatial dimensions (height and width) of the feature map unchanged, while increasing the depth (number of channels) of the feature map. On the contrary, "k3n64s2" represents a convolutional layer with a kernel size of 3x3, outputting

64 feature maps, but with a stride of 2 for the convolution operation. This configuration is typically used to reduce the spatial dimension of feature maps (halving the height and width), while potentially increasing or decreasing the depth of feature maps. A spatial attention mechanism is added to the generative model G and the discriminant model D to improve the texture information and details of the salient areas of the image. A spatial attention module is added to the generative model G to learn the relationship between different areas in the I^{LR} image, thereby making the generative model can dynamically adapt to adjust the degree of attention to the salient areas and background areas of the I^{LR} image. First, feature transformation is performed. The input image I^{LR} is subjected to three linear transformations to obtain three feature maps I_f^{LR}、I_g^{LR}、I_h^{LR}. Assume that the dimension of the I^{LR} image is H, the number of channels is $H \times W \times C$, and the converted dimension is $H \times W \times C_1$, where C_1 is the converted channel number.

$$I_f^{LR} = I^{LR} \cdot W_f + b_f \tag{6}$$

$$I_g^{LR} = I^{LR} \cdot W_g + b_g \tag{7}$$

$$I_h^{LR} = I^{LR} \cdot W_h + b_h \tag{8}$$

In the formula: W_f, W_g, W_h is the weight matrix used for conversion respectively, b_f, b_g, b_h is the bias term, both are parameters that need to be learned, and are implemented through convolution operations. Each operation corresponds to a convolution kernel.

Calculate the similarity matrix S between I_f^{LR} and I_g^{LR}, as shown in the following formula:

$$S_{ij} = I_f^{LR}(i,j) \cdot (I_f^{LR})^T \tag{9}$$

In the formula: S_{ij} represents the similarity between the feature at position (i, j) and the features at other positions.

After processing the similarity matrix with the softmax function, the attention weight matrix A of each position is calculated: $A_{ij} = soft\max(S_{ij})$, where A_{ij} represents the attention weight at the position, and then the weighted feature calculation is performed to obtain the weighted feature map I_Y^{LR}, $I_{Y_{ij}}^{LR} = \sum_{k=1}^{H \times W} A_{ij} \cdot I_h^{LR}(k)$, where $I_{Y_{ij}}^{LR}$ represents the weighted feature at (i, j); finally, the weighted feature map I_Y^{LR} is fused with the original feature map I^{LR} through element-level addition to generate the final output feature map I_Z^{LR}.

$$I_{Z_{ij}}^{LR} = I_{X_{ij}}^{LR} + I_{Y_{ij}}^{LR} \tag{10}$$

In the formula: $I_{Y_{ij}}^{LR}$ represents the final feature at position (i, j).

The discriminator adds a global pooling layer, which aims to extract comprehensive features of the image and use the spatial attention mechanism to weight these features to enhance the recognition of details. The global pooling layer converts the feature map into

a fixed-length vector to capture the overall information of the image. By performing global pooling on the input feature map $G(I^{LR})$, this layer generates a fixed-length vector P that represents the global features of the image. The global average pooling operation is defined as follows:

$$P = \frac{1}{H \times W} \sum_{i=1}^{H} \sum_{j=1}^{W} I_{X_{ij}}^{LR} \tag{11}$$

The spatial attention mechanism dynamically adjusts the importance of each position in the feature map by weighting the global feature P. Specifically, the spatial attention mechanism learns a weight matrix W_a and applies it to global features to generate weighted global features P_a. The calculation formula of the spatial attention mechanism is as follows:

$$P_a = P \cdot W_a \tag{12}$$

In the formula: W_a is the weight matrix obtained by learning, which is used to weight global features. The weighted global feature P_a contains important information at different locations in the image and can better reflect the details and structural features of the image.

During training, adversarial and perceptual loss functions are used for model optimization, and spatial and channel attention weights are balanced to improve the quality and details of the generated images.

5. Experimental results and analysis

5.1. Model training

In order to verify whether the proposed method can achieve good super-resolution reconstruction effects of ship images transmitted from Beidou satellites to the shore in practical applications, experimental verification was carried out. The experiment adopted the torch-GPU framework for algorithm implementation. The experimental equipment environment is indicated in Table 1.

Table 1 Experimental equipment environment and parameters

Equipment environment	**Parameter**
Operating system name	Ubuntu 20.04
processor	Intel@ Core™ i9-10900K CPU @ 3.70GHzx20
graphics card	NVIDIA GeForce RTX 3070 Ti
Memory	62.5GB
programming language	Python3.8
Training set	VOC2023

In model training, the Nadam optimization algorithm is used, which combines the characteristics of Nesterov momentum and Adam algorithm. On the basis of maintaining the advantages of the Adam algorithm, the stability and convergence efficiency of the optimization process are enhanced by introducing Nesterov momentum and correcting the learning rate deviation. The optimal parameters are adjusted through experiments:

Learning rate: $\alpha = 10^{-4}$,

Momentum parameters: $\beta_1 = 0.9$,

Gradient decay rate: $\beta_2 = 0.999$,

Number of iterations: 2×10^4 times

The experimental test set is the ship images transmitted by Beidou satellite, as shown in Figure 3.

Figure 3 Experimental part test set

The total variation model is used in the spatial loss calculation to retain the edge and texture information of the image as much as possible, thereby optimizing the image reconstruction quality. By adjusting the parameter β, the weight of the spatial information W can be controlled, and its impact on the transmitted image can be tested through different settings. The impact of super-resolution performance is to effectively use spatial information weights to retain image edges and high-frequency details. Experimental results show that when the parameter $\beta = 0.1$, the image reconstruction effect is optimal.

5.2. Comparative analysis of methods

The image super-resolution reconstruction method proposed in this article is compared with other classic super-resolution algorithms. The experiments used the open source codes of three classic methods and the same data set as the method in this article for experimental verification and analysis. The results were evaluated and compared from both subjective and objective aspects.

In the subjective evaluation, a test set of layered compression coding distortion images transmitted through Beidou satellites was used to compare the visual effects reconstructed by different methods. Comparison of results shows that because existing super-resolution reconstruction methods such as EnhanceNet, ESPCN, and SRCNN use traditional perceptual losses for full-image optimization, the reconstructed images have deficiencies in edge smoothing and detail distortion. Specifically, the image reconstruction by SRCNN has the most obvious distortion and blurred edge details; while EnhanceNet and ESPCN do not handle local edge details well. Experimental analysis shows that using the SeAp-SRGAN super-resolution reconstruction method proposed in this article can significantly improve the detail clarity of ship images (including salience and background areas) and the integrity of the edges of the salience area. The comparison of subjective visual effects of super-resolution reconstruction of test images is shown in Figure 4.

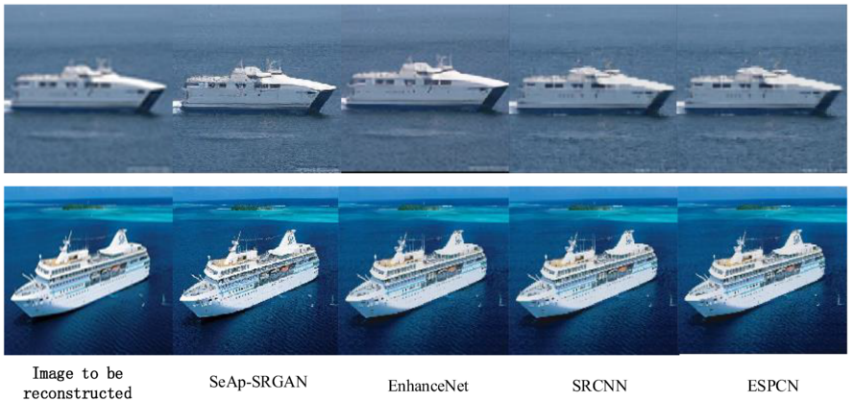

Figure 4 Comparison of subjective visual effects of test image super-resolution reconstruction

Objective evaluation uses PSNR and SSIM indicators to quantify the quality of image reconstruction. This paper comprehensively applies PSNR and SSIM indicators to evaluate the super-resolution reconstruction of transmission distortion images, taking into account numerical differences, structure and perceptual quality to comprehensively evaluate the reconstruction performance. The comparison results of PSNR and SSIM quantitative indicators of different image reconstruction methods are shown in in Tables 2 and 3. The comparison chart of PSNR and SSIM indicators using different methods is shown in Figure 5.

Table 2 Comparison of PSNR indicators of different methods

reconstruction image	SRCNN	EnhanceNet	ESPCN	SeAp -SRGAN
1	31.08	28.34	25.95	29.78
2	27.12	25.78	27.11	28.34
3	26.91	23.88	26.50	26.68
4	25.36	23.64	25.75	26.92
average value	27.62	25.41	26.33	27.93

Table 3 Comparison of SSIM indicators of different methods

reconstruction image	SRCNN	EnhanceNet	ESPCN	SeAp -SRGAN
1	0.918	0.911	0.924	0.916
2	0.915	0.916	0.919	0.916
3	0.917	0.917	0.919	0.918
4	0.917	0.920	0.912	0.920
average value	0.917	0.916	0.918	0.918

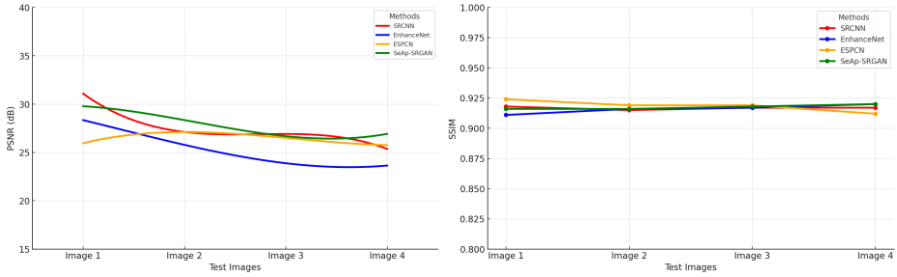

Figure 5 Comparison chart of PSNR and SSIM indicators of different methods

The comparison results show that the SeAp-SRGAN method designed in this article has better overall effect in different test images. In terms of PSNR index, the average value of SeAp-SRGAN reaches 27.93, which is 0.31, 2.52 and 1.6 higher than SRCNN, EnhanceNet and ESPCN respectively; in terms of SSIM index, the average value of SeAp-SRGAN is 0.918, exceeding SRCNN and EnhanceNet respectively 0.001 and 0.002, which are comparable to ESPNN. Experimental results show that this research method is superior to other comparison methods in image quality evaluation, and significantly improves the edge detail reconstruction effect of images.

6. Conclusion

This paper proposes a super-resolution reconstruction method based on an adaptive mechanism Generative Adversarial Network (GAN), aiming to improve the resolution and quality of images transmitted through Beidou satellites. By introducing a new combination of perceptual loss functions, including pixel loss, adaptive weight mechanism-based feature loss, and adversarial loss, we successfully optimize the total loss function and significantly improve the visual quality of the image. In addition, this method also introduces a spatial attention mechanism in the generator and discriminator, which effectively distinguishes the salient areas and background areas of the image, and fully retains the high-frequency details and edge features of the image.

Through comparative experiments with other classic super-resolution algorithms (ESPCN, EnhanceNet, SRCNN), this method shows obvious advantages in edge smoothing and detail preservation. Subjective evaluation results show that the SeAp-SRGAN method can significantly improve the detail clarity and edge integrity of the reconstructed image, especially in the salience and background areas of the ship image. The objective evaluation indicators PSNR and SSIM also prove that the SeAp-SRGAN method is superior to the contrasting super-resolution method in terms of image quality, with the average PSNR reaching 27.93 and the average SSIM being 0.918. These data show that this method maintains the image structure and improves image quality. Image quality is excellent.

The super-resolution reconstruction technology proposed in this study is not only innovative in theory, but also shows great potential in practical applications, especially in fields such as offshore monitoring and navigation safety. Future work will focus on further optimizing the operating efficiency and adaptability of the algorithm to adapt to a wider range of application scenarios and more complex image processing needs.

References

[1] Benjamin, R, Harris.Image-Inclusive Instruction[J]. College & Undergraduate Libraries. 2007, 14(2): 65-75.
[2] Burnik U, Tasi J. An Algebraic Approach to Two-Dimensional Digital Image Restoration [J]. 2002, 5(04): 182-183.
[3] Patel V, Mistree K, Gopalbhai C. A Review on Different Image Interpolation Techniques for Image Enhancement [J]. 2013, 17(20): 147-149.
[4] Hong Gongyi, Jiang Yuming, Wu Yuan. Research on super-resolution image reconstruction algorithm [J]. Microelectronics and Computers, 2004, 21(4): 4-8.
[5] Li Yinghua, Liu Yue, Liu Ying. Review and prospects of learning-based image super-resolution technology [J]. Journal of Xi'an University of Posts and Telecommunications, 2022, 27(02): 72-87.
[6] Jiang Shu, Wang Junying, Dong Dai, et al. Brief analysis of image super-resolution reconstruction method based on deep learning [J]. Yangtze River Information and Communications, 2022, 35(12): 28-34.
[7] XieQifang, YaoGuoqing, LiuPin. Super-resolution Reconstruction of Satellite Video Images Based on Interpolation Method [J]. Procedia Computer Science, 2017, 24(03): 63-65.
[8] Wang S, Li Z, Li X, et al. A new method of super-resolution reconstruction based on wavelet and subpixel interpolation[C]. 2015 International Computer Conference on Wavelet Active Media Technology & Information Processing, 2015: 398-405.
[9] Jian L. Super-resolution image reconstruction based on contourlet and fractal interpolation [J]. Electronic Measurement Technology, 2010, 20(3): 331-334.
[10] Ding N, Liu Y P, Fan L W, et al. Single Image Super-Resolution via Dynamic Lightweight Database with Local-Feature Based Interpolation [J]. Journal of Computer Science and Technology: English Edition, 2019, 34(3): 13-18.
[11] Zhou H, Gao H, Tian X. A Super-resolution Reconstruction Method of Remotely Sensed Image Based on Sparse Representation [J]. Sensors and Transducers, 2013, 160(12): 229-236.
[12] Yu C, Pei H. Super-resolution reconstruction method of face image based on attention mechanism [J]. IEEE Access, 2021, (99): 1-6.
[13] Qifang X, Guoqing Y, Pin L. Super-resolution Reconstruction of Satellite Video Images Based on Interpolation Method [J]. Procedia Computer Science, 2017, (107): 454-459.
[14] Mcdonnell M D, Vladusich T. Enhanced Image Classification With a Fast-Learning Shallow Convolutional Neural Network [J]. IEEE, 2015, 68(8): 7944-7956.
[15] Li Y, Yang M, Zhang Z. Multi-View Representation Learning: A Survey from Shallow Methods to Deep Methods [J]. 2016, 7(01): 109-117.
[16] Jaramillo-González R, Aristizábal E, García-Aristizábal E F. Rainfall Thresholds for Shallow Landslides by coupled Physically- Based Models and Machine Learning methods in Colombian Andes Basins [J]. 2021, 6(3): 1-13.
[17] Garajeh M K, Weng Q, Haghi V H, et al. Learning-Based Methods for Detection and Monitoring of Shallow Flood-Affected Areas: Impact of Shallow-Flood Spreading on Vegetation Density [J]. Canadian journal of remote sensing, 2022, (9): 503-520.
[18] Takam C A, Samba O, Kouanou A T, et al. Spark Architecture for deep learning-based dose optimization in medical imaging [J]. Informatics in Medicine Unlocked, 2020, 19(100): 335-340.
[19] Fleet D, Pajdla T, Schiele B, et al. Learning a Deep Convolutional Network for Image Super-Resolution [J]. Lecture Notes in Computer Science, 2014, 978(3):10319-10593.
[20] Dong C, Loy C C, Tang X. Accelerating the Super-Resolution Convolutional Neural Network [J]. Springer, Cham, 2016, 30(12): 28-36.
[21] Shi W, Caballero J, Huszár F, et al. Real-Time Single Image and Video Super-Resolution Using an Efficient Sub-Pixel Convolutional Neural Network [J]. arXiv e-prints, 2016,62(09): 1368-1376.
[22] Yang Yun, Yang Xinyue, Zhang Xiaoxuan. Generative adversarial network image super-resolution reconstruction based on attention mechanism [J]. Journal of Shaanxi University of Science and Technology, 2024, 42(02): 216-223.
[23] Si Yazhong, Zhang Xulong, Yang Fan, et al. Multi-feature fusion defogging technology based on generative adversarial network [J]. Big Data, 2014, 34 (01): 1-14.
[24] Li Xiaolin, Gao Yuwei, Fu Guoqing. Research on text-to-image conversion based on generative adversarial networks [J]. Computer Applications and Software, 2024, 41(03): 188-219.
[25] Gong Ying, Xu Wentao, Zhao Ce, et al. Review of the application of generative adversarial networks in image restoration [J]. Computer Science and Exploration, 2024, 18(03): 553-573.
[26] Chen Jingxia, Lin Wentao, Long Minxiang, et al. Video anomaly detection based on UNet3+ generative adversarial network [J]. Computer Engineering and Design, 2024, 45(03): 777-784.

Fuzzy Systems and Data Mining X
A.J. Tallón-Ballesteros (Ed.)

doi:10.3233/FAIA241446

A Preliminary Investigation into the Current Status and Prospects of Visual Analysis of Acoustic Properties for the Singing Voice

Jie HUA[a,1] and Wei YI[b]
[a] *Faculty of Information Engineering Shaoyang University, China*
[b] *Guangdong Song and Dance Theatre, China*
ORCiD ID: Jie Hua https://orcid.org/0000-0002-3409-2076
Wei Yi https://orcid.org/0009-0009-9030-4625

Abstract. Acoustic analysis is an objective measurement approach commonly used in the assessment of the singing voice. It involves parameters such as fundamental frequency, formant, intensity, vibrato pattern, and others, providing parameters on the internal view of the singing voice. However, presenting multi-dimensional voice data from multiple audio files simultaneously in current studies is a challenging task. This review summarises existing methodologies, highlighting their limitations and proposing future directions, particularly integrating Information and Communications Technology to enhance vocal analysis visualisation. This study also emphasises the critical role of advanced visualisation methods in enhancing the accuracy, accessibility, and impact of vocal analysis, and it aims to enhance the understanding of vocal mechanisms, support singers and students in vocal practice, and drive forward the field of vocal research through innovative, user-friendly technologies. Our future work will focus on developing interactive visualisation techniques to simplify and enrich the interpretation of vocal data, making complex acoustic properties accessible to a broader audience, including non-experts.

Keywords. Acoustic Analysis, Acoustic Property, Graph Drawing, Multi-dimensional Parameters, Singing Voice, Visual Analysis, Vocal Analysis

1. Introduction and Background

Acoustic analysis is an objective measurement in the field of singing voice research [1]. Understanding relevant properties is essential for improving vocal techniques, delivering appropriate vocal expression, and accurately conveying music styles. Despite significant progress in this field, most existing research has primarily focused on voice analysing using software such as VoceVista [2], Praat [3] and Sonic Visualiser [4]. While these tools are powerful in providing visual representations, including spectrograms, spectra, and electroglottography (EGG) of acoustic parameters, they often have limited capability when it comes to comparing the multi-dimensional structure of the singing voice across multiple audio samples. This limitation is crucial to address for a holistic understanding

[1] Corresponding Author: Jie HUA, jie.hua@alumni.uts.edu.au.

of the singing voice, especially in the analysis of vocal techniques in crossover singing [5]. Praat, an open-source tool, offers black-and-white graphical analysis and can directly extract parameters such as pitch, formant, intensity, and vibrato. Meanwhile, Sonic Visualiser and VoceVista both provide colour visualisation options, with Sonic Visualiser also offering real-time spectrogram analysis of acoustic data.

Vocal technique involves coordinating the respiratory, phonatory, and resonance systems [6-8]. Breathing patterns and vocal fold vibrations affect sound pressure level (SPL), which influences loudness and voice quality through subglottal pressure (*P*sub) [9]. Phonation controls the fundamental frequency (f_0), impacting pitch and varying with muscle dominance [7, 10-11]. The resonance system, including the larynx, tongue, jaw, lips, soft palate, and nose [10, 12-13], shapes vowels, consonants, and timbre [12, 14], which are analyzed using parameters like formant, jitter, and shimmer [7, 15]. Voice quality, influenced by anatomical and physiological factors [10], is a multi-dimensional construct [1] and key to distinguishing timbre and vocal style [16]. Acoustic analysis, often used to assess voice quality [1], primarily relies on spectrograms and spectra, but current visual tools like line [2, 17-21], bar [20, 22] charts, and scatter plots [20, 23-26] struggle to display multiple dimensions of acoustic data, such as frequency, amplitude, vibrato, and duration [27]. The lack of interactive features [6] further complicates complex analysis and comparison.

Despite advancements in vocal analysis, a major challenge remains the usability and accessibility of methods for handling complex vocal datasets. Many tools require significant technical expertise, limiting their widespread adoption. This review aims to summarise the advantages, disadvantages, and challenges of existing vocal analysis methodologies. It will also explore future directions, particularly focusing on applying Information and Communications Technology (ICT) methods to address gaps in visualisation applications for singing voice research. The review will evaluate the importance of visual graphics in analysing multiple acoustic data attributes, providing preliminary assessments and guidance for further study.

In the following parts of this paper, Section 2 provides the methodology of this work. An overview of existing works is given in Section 3. Section 4 presents the challenges of ICT adoption in the field. Future directions are discussed in Section 5. Section 6 summarises the essential findings and outlines our future research.

2. Methodology

This study is an integrative review that brings together literature from acoustic analysis in singing voice research and data visualization methods to provide an interdisciplinary perspective. The aim is to utilise visualisation technologies to address gaps in the graphical representation of acoustic research on singing voices as a preliminary step and to propose new research directions. Accordingly, this literature review integrates relevant findings from these two disciplines, identifies their key themes and theories, and proposes comprehensive conclusions.

To ensure a high-quality selection of studies for this literature review, we conducted a thorough search using the Google Scholar database, covering publications from 2000 to 2024. Keywords “acoustic analysis” and “singing voice” were employed to identify relevant literature. The selection process involved a systematic review and analysis of 22 research papers, applying strict inclusion criteria focused on the relevance of the papers, their discussion of technological advancements, practical implementations, and the

citation impact. This assessment was conducted by two experts with extensive experience in their respective fields. One expert in data analysis ensured the selected papers met high technical standards and aligned with current technological trends. The other, an experienced researcher in singing, brought deep domain knowledge to ensure novel methodologies that advanced acoustic properties in voice analysis, resulting in a well-rounded and high-quality selection.

The selected literature was categorised based on key features, advantages and disadvantages, acoustic analysis tools, visualisation tools, and statistical techniques. This approach provided an overview of existing studies, identified challenges, and pointed to future directions. Key themes, methodologies, findings, and gaps were extracted, enabling a detailed understanding of the research landscape. Each paper's quality was assessed for methodological rigour, relevance, and significance, ensuring the inclusion of high-quality studies. The synthesis involved comparing findings, identifying recurring themes, and summarising advancements and challenges in singing voice analysis. This comprehensive review offers insights into technological advancements, educational strategies, and future directions, while also identifying persistent challenges and suggesting future research to advance the field of acoustic properties analysis.

3. Overview of Existing Research

This Section provides a comprehensive overview of the existing research landscape in singing voice analysis, by synthesising these key features, advantages and disadvantages.

- Key Features in Vocal Analysis

f1: Accuracy and precision
f2: Visualisation methods
f3: Advanced analysis techniques
f4: Ease of use and accessibility
f5: Integration with other thchnologies

Publication	Reference	Publication	Reference	Publication	Reference
Paper_1	[27]	Paper_9	[10]	Paper_17	[30]
Paper_2	[1]	Paper_10	[24]	Paper_18	[19]
Paper_3	[32]	Paper_11	[17]	Paper_19	[2]
Paper_4	[23]	Paper_12	[35]	Paper_20	[20]
Paper_5	[22]	Paper_13	[33]	Paper_21	[21]
Paper_6	[34]	Paper_14	[25]	Paper_22	[31]
Paper_7	[28]	Paper_15	[26]		
Paper_8	[29]	Paper_16	[18]		

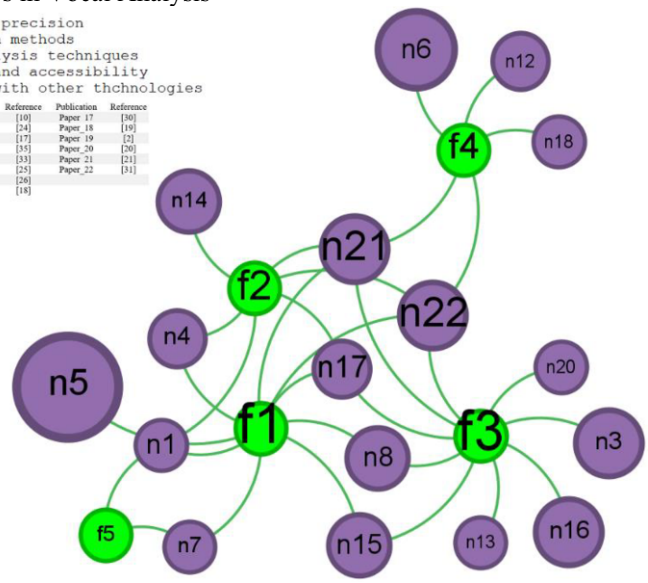

Figure 1. Key features and publications' social network.

Accuracy and precision are crucial for reliable vocal assessments, ensuring that tools and methods deliver dependable results. Studies [21-23, 26-31] emphasize the importance of these elements in creating robust vocal analysis frameworks. Visualisation methods like spectrograms are key for interpreting acoustic data, helping identify patterns, correlations,

and anomalies. However, visualisation tools often struggle with truly multi-dimensional data [21, 23, 25, 27, 30-31]. Advanced analysis techniques, including machine learning and statistical methods, are increasingly prevalent, providing deeper insights into vocal properties and enhancing assessment accuracy. Studies [18, 20-21, 26, 29, 30-33] highlight how these methods offer a more nuanced understanding of vocal phenomena.

The ease of use and accessibility of vocal analysis tools are vital for broader adoption in research and practice. Research stresses the need for user-friendly tools that can be easily integrated into various settings, making them accessible to a wider audience [19, 21, 31, 34-35]. The integration with other technological fields is a growing trend, enhancing the scope and applicability of vocal analysis. Interdisciplinary approaches, such as combining acoustics, physiology, and pedagogy [27-28], or integrating advanced digital tools [27], lead to more sophisticated methods for understanding and improving vocal performance.

Figure 1 shows connections between key features and publications in this review. Nodes without connections are removed, with node size based on citations and label font size on connection degree. It highlights a lack of focus on ease of use, accessibility, and technological integration, while visualisation tools struggle with high-dimensional datasets. Note that node size does not reflect the importance of publications and features.

- Advantages of Existing Research

Existing research on acoustic analysis for the singing voice presents several notable advantages. Many studies have highlighted acoustic analysis as an objective measurement that provides trustworthy parameters for assessing the singing voice [1-2, 21-22, 31]. Some studies have also incorporated subjective measurements of auditory perception of the singing voice, considered the influence of emotional expression and language articulation [19, 21, 26-27, 29-30, 32], as well as variation of physiology and anatomy [10, 17-18, 20-21, 26, 29-30] on the acoustic properties of the singing voice. Comprehensive methods enhance the understanding of vocal mechanisms, develop vocal pedagogy and support both vocal research and practical vocal performance applications.

Moreover, numerous studies have introduced innovative methods and tools, such as BioVoice, RespTrack System, and advanced acoustic analysis software [1, 18, 26-27]. Furthermore, a few studies have combined ICT to propose visualisation of the singing voice for more effective feedback [1, 21, 27, 35]. Other studies have delved into the linguistic properties of the singing voice under the context of musical style through acoustic analysis [16, 33]. These interdisciplinary approaches broaden the scope and impact of vocal analysis research, promoting collaborations across different fields and leading to more comprehensive and innovative solutions.

- Disadvantages of Existing Research

Current research on acoustic properties in singing voice analysis has predominantly focused on individual song segments, utilising simple data tables and basic charts. They have limited the exploration of data from multiple sources and resulted in visual analyses that are either overly simplistic or excessively complex, especially in the context of crossover singing research [5, 21, 30]. Consequently, a comprehensive view of vocal characteristics across musical styles has been constrained. Although significant advancements have been made in analysing single song segments, these methods fall short in integrating diverse musical data into a unified analysis. Additionally, many studies suffer from small sample sizes, which affects the generalisability of the findings [18, 21, 24, 26, 29-30, 32]. Increasing sample sizes in future research would enhance the robustness and applicability of the results. Notably, the complexity of the methods and the steep learning curve required for effective use hinder widespread adoption [21, 26-

27, 29-30, 34]. The dependence on sophisticated technology and software can be a barrier, particularly in less-resourced settings [21-22, 27]. Developing more accessible and affordable tools would help mitigate this issue and make vocal analysis more widely available. Furthermore, the accessibility and cost of tools and methods are significant drawbacks, limiting their use in broader educational or clinical settings [21, 27, 35].

4. Challenges of ICT Adoptions in Vocal Analysis Technologies

Challenges particularly in managing and integrating the multiple dimensions of vocal data, which can hinder their usability and accessibility. Additionally, interpreting visual and acoustic data requires specialised expertise, and existing methods often struggle to capture the full range of vocal characteristics effectively. To address these challenges, ongoing efforts are needed to refine tools and techniques, with a focus on improving their ability to handle and integrate diverse data attributes.

Acoustic Analysis Tools: Acoustic analysis software has been pivotal in vocal research, providing tools for measuring various vocal parameters such as formant, intensity, jitter, and shimmer [35], as well as spectrogram, spectrum, and EGG [23, 25, 27, 34-35], have been widely used in research. They are sophisticated tools designed for detailed acoustic analysis, providing high precision and a broad range of analytical features [23]. Spectrograms are used to visualise vocal signals over time, including the fundamental frequency and its harmonic series, as well as the intensity and vibrato parameters [21], the interface of a spectrogram is shown in Figure 2. The concentrated areas in the harmonic series are known as formants [7], labelled F_1, F_2, F_3, F_4, F_5 and so on [36]. Among them, F_1 and F_2 are associated with the vowels being sung, while F_3 to F_5 form a singer's timbre [12]. Spectra are displayed in two dimensions, showing frequency peaks and amplitude for a short time slice [21]. They all provide a detailed insider view of vocal information and its variations [23, 25, 27]. However, most existing tools are designed for analysing individual audio files. When dealing with multi-dimensional data that requires comparing multiple audio files, these tools can only provide visual comparisons or require users to click a movable cursor to read and extract parameters [21], which can then be compared in other software. This manual selection process can reduce the accuracy of the data.

Visualisation Tools: They are essential for presenting vocal data visually [25, 27], which have unique advantages but also face challenges when addressing multiple data attributes. Although effective for summarising complex data, heat maps can oversimplify information, potentially leading to subjective interpretations and missing nuanced details. Radar Charts are useful for identifying overall patterns across various dimensions but can become cluttered when too many variables are included. This clutter can limit their effectiveness for detailed analysis and may obscure specific trends within the data. Scatter Plots display relationships between two variables, helping to identify correlations and outliers [25]. While straightforward to create and interpret, scatter plots are limited to examining two variables simultaneously. This restriction can be problematic when uncovering more complex patterns or interactions among multiple vocal parameters.

Statistical and Machine Learning Techniques: Machine Learning can manage large and complex datasets, uncovering patterns that might not be apparent through traditional methods [18, 33]. However, it requires substantial data for training and is computationally intensive, and this can limit accessibility and make it challenging to apply relevant techniques to diverse or underrepresented datasets. Statistical analysis

employs various techniques to examine vocal data and derive insights [18, 20, 32]. While offering robust tools for data interpretation, statistical methods often require advanced knowledge and can be time-consuming. This complexity can be a barrier for researchers aiming to integrate and analyse multiple data attributes effectively. These techniques are crucial for analysing vocal features and classifying vocal qualities [18, 20, 33]. Despite their capabilities, adopting them also encounters challenges in handling complex datasets.

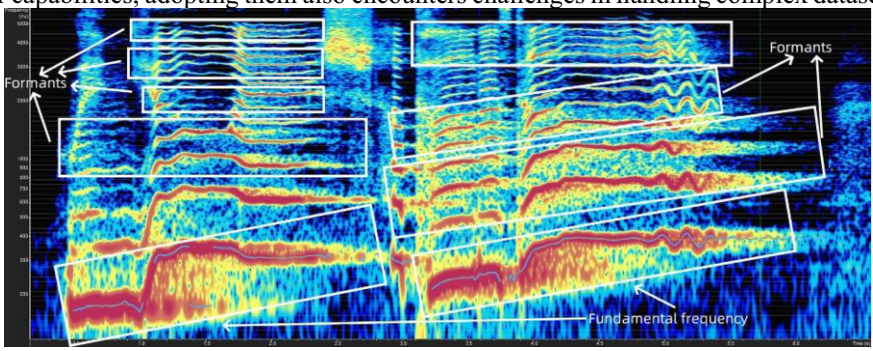

Figure 2. A spectrogram for a segment of audio in the jazz style is extracted from VoceVista. The X-axis represents time, and the Y-axis represents the frequency of the sound. The lowest line corresponds to the fundamental frequency, which is related to pitch. Above that are the harmonics that are superimposed in multiples, with concentrated areas representing formants that determine the timbre. The colour shade is related to voice intensity, and the wavering of the harmonics corresponds to vibrato, while a flat line indicates the absence of vibrato [7, 11].

5. Future Directions

This chapter explores the key future directions for singing voice analysis technologies, focusing on their adoption and impact on research and practice.

Broader Studies and Integration of Multimodal Data: Expanding studies to include larger and more diverse sample populations is crucial [18, 29, 32]. Broader participant groups help validate findings and gain a comprehensive understanding of vocal characteristics across different demographics. Integrating vocal data with other physiological and environmental data can offer a holistic view of vocal performance and its influencing factors [19, 24, 27], allowing researchers to explore complex interactions and gain deeper insights into how various variables affect vocal characteristics.

Advanced Analytical Techniques: Developing sophisticated analytical techniques is crucial in this field [18, 20, 32-33]. Emerging methods such as advanced machine learning algorithms and statistical models, promise deeper insights into vocal properties and patterns. Leveraging large datasets and refining algorithms will allow researchers to uncover previously inaccessible patterns and insights.

Integration into Educational Curricula: Incorporating new findings and technologies into vocal training curricula is essential for enhancing educational outcomes [17, 23, 27]. The integration will improve the quality of vocal training and equip the next generation of researchers and practitioners with the skills to utilise these advanced technologies.

Technological Enhancements: More accessible technologies are vital for broadening the use of vocal analysis [22, 27, 33]. Enhancements in software and hardware will make these tools more user-friendly and widely applicable, facilitating greater adoption in both research and practical settings.

Improved Usability of Tools: Making vocal analysis tools more user-friendly and accessible to non-experts is essential for broader adoption [34-35]. Simplifying interfaces, providing intuitive designs, and offering comprehensive training resources will enable users from diverse backgrounds to engage with these technologies more effectively. Enhancing usability will facilitate the integration of vocal analysis tools into various contexts, including educational and clinical settings.

Real-time Analysis Capabilities: Real-time feedback and analysis are critical for improving the immediacy and relevance of vocal assessments [17, 23]. These capabilities will facilitate dynamic and interactive research and training, allowing users to make adjustments as needed. This development will enhance the practicality and effectiveness of vocal analysis tools in both research and applied settings.

Data Visualisation Methods: Applying advanced visualisation methods to analyse multiple acoustic data attributes is an emerging area of research. Interactive visualisation techniques can offer new insights into complex vocal data by presenting it in more accessible and interpretable formats. These methods will aid in identifying patterns and correlations across diverse data attributes, enhancing the overall analysis of vocal performance. Future research should focus on developing and refining these interactive visualisation techniques along with improving the comprehensiveness and clarity of vocal data analysis. Our previous work generated a dashboard that includes a wind rose, statistical table, and parallel coordinates graph, along with interaction features. This dashboard aims to offer users an easy-to-use tool for analysing multiple attributes of singing voice data, please refer to [5].

6. Conclusions and Future Work

This study reviews existing research on vocal analysis, evaluating current methods, identifying challenges, and outlining future directions. We highlight the limitations of existing methods, which often involve complex, disparate data that are difficult to integrate and interpret. However, the literature was collected based on keywords, citations, and the researcher's experience. Consequently, the final conclusions may have subjective restrictions. To address this issue, we plan to involve more experts in the field to provide a more comprehensive and objective perspective.

Our future work will focus on the potential of advanced visualisation methods. We aim to refine and implement interactive visualisation techniques to enhance the understanding of vocal characteristics. By improving the interpretability of vocal data through these methods, we will present data in an easy-to-understand manner with interactive features. These techniques offer more precise and intuitive representations of multifaceted acoustic data, making it accessible even to those without professional expertise in the field. This approach aims to address current challenges related to data complexity and integration, promoting the broader adoption of innovative technologies in vocal research and pedagogy. Furthermore, it will provide additional support to singers and students engaged in vocal performance practice, helping them understand vocal mechanisms more effectively. Figure 3 offers a dataset sample of the recorded song "When You Wish Upon a Star" (Leigh Harline, Ned Washington) in four vocal styles. We will conduct different types of graphs, validate them with experts in the singing field, and determine suitable structures for presenting the multiple properties of the dataset.

In conclusion, this study underscores the importance of visualisation methods in advancing acoustic analysis of the singing voice. By focusing on easy-to-understand

graphs for analysing multiple data attributes, we aim to enhance the accuracy, accessibility, and impact of vocal analysis technologies. This will drive the field forward and unlock new possibilities for understanding and improving vocal performance.

Style	Parameter	Lyrics	When	you	wish	upon	a	star
Jazz	Formant	F1	218.51	378.27	618.8	662.36	432.26	722.02
		F2	1362.18	1546.33	1612.37	1421.63	1405.45	1271.37
		F3	2469.66	2470	2691.12	2619.73	2144.68	1892.51
		F4	3548.42	3718.76	3585.08	3963.17	3504.34	3563.59
	Intenity	dB	78.91	79.19	77.17	80.28	83.43	80.08
	Jitter (local)	Periodicity	0.58%	0.96%	0.88%	1.67%	0.59%	0.74%
	Shimmer (local)	Oscillation amplitude	4.52%	8.50%	5.82%	10.72%	5.27%	6.48%
Pop	Formant	F1	239.58	362.92	455.14	432.97	361.47	703.24
		F2	1612.08	1318.98	1530.2	1117.07	961.04	1254.45
		F3	2398.62	2303.96	2494.23	1846.21	1919.35	1857.68
		F4	3518.02	3447.27	3509.84	3647.9	3531.67	3679.1
	Intenity	dB	78.76	79.16	73.21	82.32	83.21	76.43
	Jitter	Periodicity	0.48%	1.68%	0.94%	1.21%	0.25%	0.60%
	Shimmer	Oscillation amplitude	3.23%	8.99%	10.31%	2.49%	6.04%	5.99%
Legit	Formant	F1	203.52	406.24	461.94	475.03	577.7	685.42
		F2	1423.31	1195.32	1440.12	1009.99	1440.14	1245.53
		F3	2408.82	1826.23	2491.26	2001.66	2707.77	2338.06
		F4	3382.57	3072.05	3480.69	3764.16	4057.95	3844.08
	Intenity	dB	78.55	80.7	75.42	81.15	80.67	79.73
	Jitter	Periodicity	0.31%	0.93%	0.86%	0.35%	0.22%	0.61%
	Shimmer	Oscillation amplitude	2.28%	6.94%	5.58%	2.66%	4.58%	5.07%

		Lyrics	无	论	你	身	在	何	处
Mandarin	Formant	F1	211.46	406.98	364.52	385.57	336.79	419.28	453.9
		F2	1127.22	1255.94	1429.07	1478	1102.66	994.13	1337.48
		F3	2270.53	2218.28	2673.54	2205.95	2229.88	1982.12	2075.86
		F4	3330.85	3528.52	3241.36	3616.63	3478.66	3495.82	3548.75
	Intenity	dB	80.49	79.56	76.02	78.32	81.04	79.9	74.75
	Jitter	Periodicity	0.44%	2.18%	0.58%	0.64%	0.90%	0.31%	0.89%
	Shimmer	Oscillation amplitude	3.05%	14.54%	5.00%	2.80%	5.42%	2.58%	5.11%

Figure 3. Sample data of acoustic properties for the singing voice.

References

[1] Barsties, B. and De Bodt, M., 2015. Assessment of voice quality: current state-of-the-art. Auris Nasus Larynx, 42(3), pp.183-188.

[2] Miller, T. E., & Shahriari, A. (2020). World music: A global journey. Routledge.

[3] Praat: Doing Phonetics by Computer. (2011). Ear and hearing, 32(2), 266-266.

[4] www.sonicvisualiser.org. Sonic Visualiser. Available at: https://www.sonicvisualiser.org/index.html.

[5] Hua, J. and Yi, W., 2023, July. Visual Analysis of Voice in Crossover Singing. In 2023 27th International Conference Information Visualisation (IV) (pp. 198-203). IEEE.

[6] Shah, P., & Freedman, E. G. (2011). Bar and Line Graph Comprehension: An Interaction of Top-Down and Bottom-Up Processes. Topics in cognitive science, 3(3), 560-578.

[7] McCoy, S. J. (2005). Your voice, an inside view: multimedia voice science and pedagogy (2nd printing, with corrections. ed.). Inside View Press.

[8] Spivey, N., Saunders-Barton, M., & Uhre, M. (2018). Cross-training in the voice studio: a balancing act. Plural Publishing, Inc.

[9] Björklund, S., & Sundberg, J. (2016). Relationship Between Subglottal Pressure and Sound Pressure Level in Untrained Voices. Journal of Voice, 30(1), 15-20.

[10] Steinhauer, K., McDonald Klimek, M., & Estill, J. (2017). The Estill voice model: theory & translation. Estill Voice International.

[11] Miller, D. G. (2008). Resonance in singing: voice building through acoustic feedback (Library version 1.0. ed.). Inside View Press.

[12] Björkner, E. (2006). Why so different?-Aspects of voice characteristics in operatic and musical theatre singing: Aspects of voice characteristics in operatic and musical theatre singing KTH.

[13] Henrich, N., Smith, J., & Wolfe, J. (2011). Vocal tract resonances in singing: Strategies used by sopranos, altos, tenors, and baritones. J Acoust Soc Am, 129(2), 1024-1035.

[14] Cho, T., & Mücke, D. (2020). Articulatory Measures of Prosody. In C. Gussenhoven & A. Chen (Eds.), The Oxford Handbook of Language Prosody (pp. 14-28).

[15] Hakanpaa, T., Waaramaa, T., & Laukkanen, A. M. (2019). Emotion Recognition from Singing Voices Using Contemporary Commercial Music and Classical Styles. J Voice, 33(4), 501-509.
[16] YI, W., 2022. Vocal resonance and musical style (Doctoral dissertation, Macquarie University).
[17] Mitchell, H.F., 2005. Defining vocal quality in female classical singers: pedagogical, acoustical and perceptual studies.
[18] Scherer, K.R., Sundberg, J., Tamarit, L. and Salomão, G.L., 2015. Comparing the acoustic expression of emotion in the speaking and the singing voice. Computer Speech & Language, 29(1), pp.218-235.
[19] Hakanpää, T., Waaramaa, T. and Laukkanen, A.-M. (2021). Comparing Contemporary Commercial and Classical Styles: Emotion Expression in Singing. Journal of Voice, 35(4), 570–580.
[20] Schellenberg, M. H. (2013). The realisation of tone in singing in Cantonese and Mandarin (T). UBC. Retrieved from https://open.library.ubc.ca/collections/ubctheses/24/items/1.0073581
[21] Miller, D. G. (2008). Resonance in singing: voice building through acoustic feedback (Library version 1.0.). Inside View Press.
[22] Degottex, G., Kane, J., Drugman, T., Raitio, T. and Scherer, S., 2014, May. COVAREP—A collaborative voice analysis repository for speech technologies. In 2014 ieee international conference on acoustics, speech and signal processing (icassp) (pp. 960-964). IEEE.
[23] Larrouy-Maestri, P., Magis, D. and Morsomme, D., 2014. Effects of melody and technique on acoustical and musical features of western operatic singing voices. Journal of Voice, 28(3), pp.332-340.
[24] Guzman, M., Lanas, A., Olavarria, C., Azocar, M.J., Muñoz, D., Madrid, S., Monsalve, S., Martinez, F., Vargas, S., Cortez, P. and Mayerhoff, R.M., 2015. Laryngoscopic and spectral analysis of laryngeal and pharyngeal configuration in non-classical singing styles. Journal of Voice, 29(1), pp.130-e21.
[25] Smith, C.G., Finnegan, E.M. and Karnell, M.P., 2005. Resonant voice: spectral and nasendoscopic analysis. Journal of Voice, 19(4), pp.607-622.
[26] Fantini, M., Succo, G., Crosetti, E., Torre, A.B., Demo, R. and Fussi, F., 2017. Voice quality after a semi-occluded vocal tract exercise with a ventilation mask in contemporary commercial singers: acoustic analysis and self-assessments. Journal of Voice, 31(3), pp.336-341.
[27] F.M. and Fiuza, M.B., 2022. Real-time visual feedback in singing pedagogy: current trends and future directions. Applied Sciences, 12(21), p.10781.
[28] Mitchell, H.F. and Kenny, D.T., 2008. Open throat: acoustic and perceptual support for pedagogic practice. Journal of Singing, 64(1), pp.429-441.
[29] LeBorgne, W.D., Lee, L., Stemple, J.C. and Bush, H., 2010. Perceptual findings on the broadway belt voice. Journal of Voice, 24(6), pp.678-689.
[30] Bourne, T. and Kenny, D., 2016. Vocal qualities in music theater voice: perceptions of expert pedagogues. Journal of voice, 30(1), pp.128-e1.
[31] Steinhauer, K., McDonald, M.M. and Estill, J., 2017. The Estill voice model: Theory & translation. Estill Voice International.
[32] Scherer, K.R., Sundberg, J., Fantini, B., Trznadel, S. and Eyben, F., 2017. The expression of emotion in the singing voice: Acoustic patterns in vocal performance. The Journal of the Acoustical Society of America, 142(4), pp.1805-1815.
[33] Sha, C.Y., Yang, Y.H., Lin, Y.C. and Chen, H.H., 2013, May. Singing voice timbre classification of Chinese popular music. In 2013 IEEE International Conference on Acoustics, Speech and Signal Processing (pp. 734-738). IEEE.
[34] Roubeau, B., Henrich, N. and Castellengo, M., 2009. Laryngeal vibratory mechanisms: the notion of vocal register revisited. Journal of voice, 23(4), pp.425-438.
[35] Manfredi, C., Barbagallo, D., Baracca, G., Orlandi, S., Bandini, A. and Dejonckere, P.H., 2015. Automatic assessment of acoustic parameters of the singing voice: application to professional western operatic and jazz singers. Journal of Voice, 29(4), pp.517-e1.
[36] Titze, I. R., Baken, R. J., Bozeman, K. W., Granqvist, S., Henrich, N., Herbst, C. T., Howard, D. M., Hunter, E. J., Kaelin, D., Kent, R. D., Kreiman, J., Kob, M., Löfqvist, A., McCoy, S., Miller, D. G., Noé, H., Scherer, R. C., Smith, J. R., Story, B. H., . . . Wolfe, J. (2015). Toward a consensus on symbolic notation of harmonics, resonances, and formants in vocalisation. The Journal of the Acoustical Society of America, 137(5), 3005-3007.

Fuzzy Systems and Data Mining X
A.J. Tallón-Ballesteros (Ed.)

doi:10.3233/FAIA241447

VReport 2.0: Report Generator to Support Independent Learning for the Visually Impaired Students in Science and Engineering

Yubin Ok[a] and Jongwoo Lee[b,1]
[a]*Dept. of IT Engineering, Sookmyung Women's University, Seoul, Republic of Korea*
[b]*Dept. of IT Engineering / Research Institute of ICT Convergence, Sookmyung Women's University, Seoul, Republic of Korea*
ORCiD ID: Yubin Ok https://orcid.org/0009-0002-1526-7034
Jongwoo Lee https://orcid.org/0000-0003-1093-7430

Abstract. In recent years, the education landscape has undergone major changes, such as the pandemic, the introduction of digitalization, and advanced technologies that facilitate the dissemination of contactless services. All of these are driving innovations in the learning experience. Furthermore, the United Nations has declared a digital bill of rights, which seeks to define digital as a fundamental human right beyond the concept of expanding digital access or bridging the gap. However, the issue of poor information accessibility for the disadvantaged remains a significant challenge, both domestically and internationally. In order to face this reality, this paper implemented a function based on LaTex that allows the visually-impaired students to enter formulas by voice in there reports. The performance and usability evaluation of this feature was analysed by T-Test, and it was discovered that the report generator has a significant effect on enabling independent learning for blind students. Therefore, this feature is expected to not only foster independence in learning for blind students in science and technology, but also to ensure general social integration and digital accessibility for blind students through the introduction of technology that is in line with the times.

Keywords. Visually impaired, Report generator, Voice-based command, Math formulas, Mobile application

1. Introduction

To be valuable, education needs to be flexible enough to evolve with the times, be equitable for all, and incorporate current technology [1]. Recently, the education environment has been undergoing a major transformation with the introduction of digitization and advanced technology [2], which is causing innovation in the learning experience. In the era of the Fourth Industrial Revolution, teaching with the right software is widely used and plays a big role in improving students' imagination and problem-solving skills [3]. In addition, as part of the 「2022 Digital Strategy of the

[1] Corresponding Author: Jongwoo Lee, bigrain@sookmyung.ac.kr.

Republic of Korea」, the government has declared a "Digital Bill of Rights" to ensure digital accessibility for people with disabilities, re-defining digital content as a universal right that everyone can access[4].

In addition, the pandemic has promoted the spread of online services in many fields, including education, which created accessibility limitations for visually-impaired people who are disadvantaged in obtaining information. To solve this problem, among various educational environments, extended reality has shown promise in terms of educational inclusion and educational opportunities for the visually-impaired [5]. In particular, in order to realize the inclusion for visually-impaired in the educational space of schools, it has been necessary to foster the independence of visually-impaired students in doing their own academic work [6].

In our current reality, this research is necessary not only to help those with disability learn, but also to ensure social inclusion and digital accessibility for them. In particular, we want to help blind students to obtain an equal learning experience as sighted students especially in online educational environments.

This paper builds on previous research [7] and aims to improve and enhance the application at hand. In particular, we focus on the math formula input and the reading-aloud functions for blind students of science and engineering. Blind people have difficulty in reading and understanding formulas because, for obvious reasons, they do not perceive formulas visually. To solve this problem, we implement a formula input based on the formula reading rules of the service provided by the National Library for the Disabled [8].

The main goals of this paper are:

1) enable blind users to insert formulas into reports with their voice and check the formulas they've inserted, eliminating such barriers for learning in the sciences
2) bridge the gap between blind and sighted users in software accessibility

2. Related Works

2.1. LaTex

LaTex is an editor for writing science and engineering documents and is often used for writing academic papers and reports. Because it is command-based, it is convenient for general people to enter formulas and diagrams and is especially popular in the sciences. However, the commands for entering formulas in LaTex are complex and require a lot of learning and practice to use. Also, LaTex does not provide a screen reader function, which makes it difficult for blind or visually-impaired users to use [9].

2.2. Screen Reader

Screen Reader is a software that utilizes TTS technology to read out text on the screen to the user. Screen readers help people who are blind or visually-impaired to understand information on the screen by speaking it aloud. They also support the ability to enter formulas, but only if the formula is entered in Braille and then converted and documented, or if the formula is entered in LaTex grammar using a specific program. Also, it can only process textual information, so information such as diagrams or images without alternative text cannot be read to a blind person [10].

2.3. National Library for the Disabled

The National Library for the Disabled in South Korea provides a "formula reading service" to help create alternative materials for the visually-impaired [8]. Many countries and their respective organizations are creating alternative materials in a variety of contents and media to support blind people in studying and working. However, there have been difficulties in replacing the formulas with speech due to the lack of standardized rules [11]. To solve this problem, the National Library for the Disabled has established rules for the voice-conversion of formulas and symbols. Based on these rules, the reading service is able to provide substantial help. However, there are still many symbols and formulas that are not supported, and the service is not developed for the visually-impaired, so it is difficult for the visually-impaired to use.

2.4. Limitations of existing services

LaTex is not a service for the visually-impaired, so it has limitations that make it difficult for the visually-impaired to use. On the other hand, the formula-reading service that the National Library for the Blind provides is somewhat helpful to the blind, but it has limitations in that it is difficult to use and does not yet support all the formulas or symbols. Finally, Screen Reader is a service for the visually-impaired, but they are not very convenient because they can only read text, and require a specific device or program to enter the formulas. Therefore, to improve the limitations of the above three services, this paper aims to help blind users in insert formulas, images, and diagrams, including text, into reports using voice.

3. Design and Implementation of VReport 2.0

In this paper, we developed a voice report generator application (VReport 2.0) for the visually-impaired in science and engineering to enable them to generate reports with similar speed as general users. Because VReport 2.0 works by clicking a button and then entering the user's voice, blind users can utilize a bluetooth remote control device, a device that helps them click the buttons. In this chapter, we will explain the process from the design to the implementation of the system based on Figure 1. In particular, it implements formula-input and reading-aloud via voice, which are the main concerns of this thesis paper. In Figure 1, the images corresponding to "Add Image" and "Add Chart" are implemented in the previous version of VReport+ [12], so we do not describe them.

3.1. Improving the Existing Formula Reading Service

In the existing formula reading service [8], formulas or symbols are often not converted properly and the level of conversion is often insufficient. Therefore, this paper aims to improve the limitations of the formula-reading service provided by the National Library for the Disabled and then provide it to relevant users.

Table 1. Differences between reading formulas in existing service vs. VReport 2.0

Formula	Existing service	VReport 2.0
$\log_a b$	Subscript a b	Log start subscript start a subscript end b log end
$(a+b)^2$	Additional case studies are required.	Open parentheses a plus b close parentheses squared
$\sum_{n=1}^{10} a_n a_{n+1}$	n opens the tens parenthesis, a subscript to a subscript to n, a subscript to start n plus a subscript to end n, and a subscript to end the parenthesis.	Sigma start n equals 1 to 10 of a subscript start n subscript end a subscript start n plus 1 subscript end sigma end
$\int_a^b x\,dx$	a b x dx	Integral start a to b of x dx integral end
x^{a*b}	Additional case studies are required.	x squared of a multiplied b

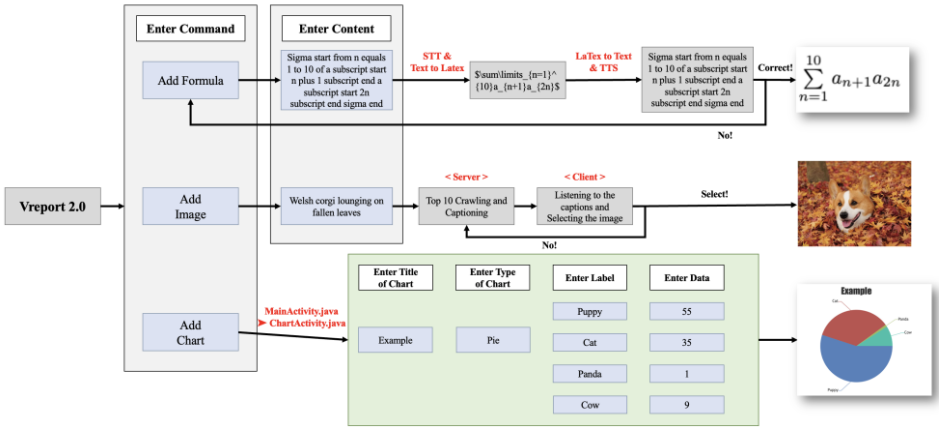

Figure 1. How VReport 2.0's main features work.

Table 1 summarizes some of the cases where operator symbols are not readable when used by themselves, and some of the ways to improve them. In the existing service, when the user enters any of those symbols, the service displays the phrase "Additional case study is required". Table 1 also summarizes cases where the level of conversion is insufficient and some of the ways to improve them. It summarizes cases where operator symbols work well when used alone but do not convert well when connected to operands when creating formulas.

In this paper, we also improve various cases where the existing service does not provide monosyllabic entities, as shown in Table 1, to allow users to enter more formulas.

3.2. Inserting a Formula Based on Voice Command

The formula input for this system is based on the formula reading service provided by the National Library for the Blind and Low-Vision, which has established rules for the speech conversion of formulas and math symbols for the blind and low vision [8]. The system also utilizes LaTex, which is commonly used by science and engineering students to write papers and reports. We utilize LaTex's formula input syntax to insert formulas into HTML reports.

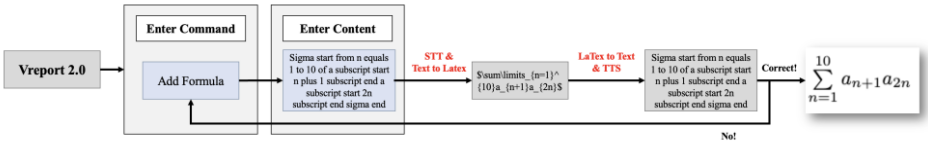

Figure 2. Formula insertion process in VReport 2.0.

The algorithm for inserting formulas is a one-to-one bidirectional mapping. Inserting a formula works based on the voice command "Add Formula" and the process of speaking the formula that the user wants to insert, as shown in Figure 2. As the user speaks the command and the formula, the system generates the formula in LaTex syntax. Then, the generated formula is read aloud to the user, and if it is deemed correct, it is inserted into the report. If the formula is deemed incorrect, the user must enter the formula again.

If the user has entered a text that does not conform to the formula-reading rules or any typos, or if the STT process has not received and translated the user's voice correctly, there is no LaTex grammar system that maps to that text. Therefore, in these cases, the system beeps out an alarm and prompts the user to re-type.

The example run shown in Figure 2 is from the formula of $\sum_{n=1}^{10} a_{n+1}a_{2n}$ and shows one of the formulas that the existing service cannot read. As a user can see in Table 1, VReport 2.0 can input, convert, and read the sigma symbol, whereas the existing service cannot. However, due to the wide range of mathematical symbols and formulas, we limit the implementation to the level of a first-year high schooler, i.e., Common Mathematics 1 and Common Mathematics 2 of the 2022 revised curriculum [13].

4. Evaluation

4.1. Setting of Evaluation

Given that the primary users of the system are visually-impaired students, the experiment aims to evaluate the impact of sight on the use of VReport 2.0. Therefore, we want to compare the performance general people to those of the visually-impaired in two cases: with and without blocked vision. The subjects are 20 people of different ages and professions, including students majoring in science and engineering.

Since the experiment aims to test the performance of VReport 2.0, we measure the report creation time and count the number of formula-entry errors to determine whether the view is blocked or not. When generating a report, subjects are tested under the criteria shown in Table 2. In particular, when entering formulas, subjects should select one of the formulas listed in Table 3 below, as the time and number of errors will vary greatly depending on the length of the formula.

Table 2. What to enter when evaluating performance

Task	Command	Criteria
Creating File	"File Name"	1 to 3 words
Inserting Formula	"Add Formula"	One of the Table 3
Creating Chart	"Add Chart"	data & label: 4 pieces
Inserting Image	"Add Image"	5 to 10 words

Table 3. Candidate formulas for entry

Formula	Text
$\int x^3 e^x \, dx$	Integral start x cubed e to the x-th power dx integral end
$\log_a x^{a+b}$	Log start subscript start a subscript end x squared of a plus b log end
$\frac{\sqrt[3]{x}}{\sqrt{y}}$	Fraction start root start y root end numerator root start 3 and x root end fraction end
$-b \pm \sqrt{b^2 - 4ac}$	Minus b plus minus root start b squared minus 4ac root end

4.2. Analyzing Evaluation Results

The criteria for analyzing the results are:

1) The first criterion is the difference in execution time with and without visual blocking, which is analyzed using a t-test to check for heterogeneity in the sample to see if the results are statistically significant [14].
2) The second criterion is the number of errors made while entering formulas.

As stated above, the results are analyzed using a t-test to check for heterogeneity in the sample to ensure that the results are statistically significant [14]. When generating a report with VReport 2.0, we want to analyze the efficiency and accuracy with t-tests. The number of errors refers to the number of times a user needs to re-enter a formula because the desired formula is not entered.

4.2.1 First criteria: Execution time.

Table 4 shows the average execution time per task. When analyzing the results for the formula entry task, it is discovered that the average time for formula entry is 33.85 seconds for the blind and 32.05 seconds for the non-blind. The t-test for both cases shows a P-value of 0.17, which exceeds the alpha value of 0.05. Therefore, the two groups are statistically similar to this aspect of the formula-entry task.

4.2.2 Second criteria: Number of formula insertion errors.

Table 5 shows the average number of formula-entry errors caused by or related to impaired vision. On average, there is 0.6 errors in formula entry for the blind and 0.5 errors for the non-blind. The t-test for both cases shows a P-value of 0.34, which exceeds the alpha value of 0.05. Therefore, the two groups are statistically similar to this aspect of the formula-entry task.

Therefore, blind or non-blind performance are not found to have a statistically significant difference in the performance of VReport 2.0, suggesting that the system is suitable for visually-impaired people to perform similarly to the people without such disability. However, there is a limitation in that we were not able to remove outliers that we did not detect during the analysis of the results and writing of the paper, which may have affected the results of the analysis in some way. This should be taken into consideration when conducting future evaluations with real visually impaired people.

Table 4. Evaluation results - average time spent per task and P-Value of T-Test results for each task

-	Add Formula (Blind)	Add Formula (Non-Blind)	Add Chart (Blind)	Add Chart (Non-Blind)	Add Image (Blind)	Add Image (Non-Blind)
Average Number	33.85 (s)	32.05 (s)	97.95 (s)	95.4 (s)	121.55 (s)	119.6 (s)
P-Value	0.34		0.09		0.11	

Table 5. Evaluation results – average number of formula insertion errors and P-Value of T-Test result

-	Blind	Non-Blind
Average Number	0.6	0.5
P-Value	0.34	

5. Conclusion

In order to ensure the social inclusion of the visually-impaired, educational provision must be flexible and respond well to rapidly changing environments. Efforts must be made to empower the visually-impaired to be independent and self-reliant. As one of the efforts to help and mitigate this issue, this paper advances the voice report generator, which in turn supports the independent learning of the visually-impaired. Such mitigation is achieved by adding to the functions of formula insertion, image insertion, and chart creation.

The performance evaluation of VReport 2.0 implemented in this paper was conducted by measuring the execution time and the number of errors. The results of the evaluation show that visual limitations do not make a significant difference in using the application, which means that blind people can perform similarly to the general people when using VReport 2.0. When visually-impaired people use VReport 2.0 to generate reports by voice, we expect them to be able to generate high quality reports that include an adequate amount of information and visuals in addition to text. We also expect them to be able to learn independently without assistance. As independence in learning is important for blind people, this paper is a step forward for the inclusion of visually-impaired people in the field of STEM education.

However, there are still limitations as the usability evaluation was not conducted with actually visually-impaired people, and the range of possible formula input was limited to the first-year high school level. Therefore, if follow-up studies are conducted to expand the scope and improve the system for the visually-impaired people, it is expected that delving into the above-mentioned issues may expand the accessibility and inclusion of visually-impaired people in education.

Acknowledgments

This work was supported by the National Research Foundation of Korea (NRF) grant funded by the Korea government (MSIT) (No.2022R1F1A1063408). This research was supported by the MSIT (Ministry of Science and ICT), Korea, under the ICAN (ICT Challenge and Advanced Network of HRD) program (IITP-2024-RS-2022-00156299) supervised by the IITP (Institute of Information & Communications Technology Planning & Evaluation).

References

[1] Sukkyung Jeon. 2023. A Study of Time and Space Changes in the Digital Age from the Perspective of Educational Philosophy. The Korean Journal of Philosophy of Education, 45(3), 29–52. https://doi.org/10.15754/jkpe.2023.45.3.002

[2] Boeun Yang, Jinkyung Jung, Sohee·Kwon, Seungmi Lee, Daeun Jung, and Hyunjin Jang. 2023. A study on the research trends in non-face-to-face culture and arts education from the perspective of the endemic COVID-19. Journal of Education & Culture, 29(5), 77-102.

[3] Voskoglou, M.G. (2024). The Role of Computers in Education in the Era of the Fourth Industrial Revolution. In: Papadakis, S. (eds) IoT, AI, and ICT for Educational Applications. EAI/Springer Innovations in Communication and Computing. Springer, Cham. https://doi.org/10.1007/978-3-031-50139-5_6

[4] Ministry of Science and ICT. 2022. Korea's National Digital Strategy. South Korea.

[5] Hamash, Mahmoud, Hanan Ghreir, and Peter Tiernan. 2024. Breaking through Barriers: A Systematic Review of Extended Reality in Education for the Visually Impaired. Education Sciences 14, 4: 365. https://doi.org/10.3390/educsci14040365

[6] Hulten, Thomas & Junger, Alex & Oliveira, Victor & Lui, Márcio De La Cruz & Fernandes, Vera & Pinto, Marcelo. 2023. Dialoguing teaching for visual impairment from the perspective of inclusive special education. Revista de Gestão e Secretariado (Management and Administrative Professional Review). 14. 12819-12836. 10.7769/gesec.v14i8.2578

[7] Jungyoon Choi, Yoojeong Song, and Jongwoo Lee. 2022. Implementation of Voice-Based Report Generator Application for Visually Impaired. Electronics 11, 12: 1847. https://doi.org/10.3390/electronics11121847

[8] Seon-Kyung Oh. 2017. A Study on the Improvement and the Production State of Alternative Materials of Special Libraries for the Visually Disabled in Korea. Journal of the Korean Society for Library and Information Science, 51(3), 215-246, http://dx.doi.org/10.4275/KSLIS.2017.51.3.215

[9] S. J. Park, S. B. Lim, and J. H. Yook. 2021. An analysis on the understanding and satisfaction of optimal math reading methods for people with visual disabilities. Journal of Rehabilitation Welfare Engineering & Assistive Technology, 15(2), 60-68, 10.21288/resko.2021.15.2.60

[10] Ather Sharif, Sanjana Shivani Chintalapati, Jacob O. Wobbrock, and Katharina Reinecke. 2021. Understanding Screen-Reader Users' Experiences with Online Data Visualizations. In Proceedings of the 23rd International ACM SIGACCESS Conference on Computers and Accessibility (ASSETS '21). Association for Computing Machinery, New York, NY, USA, Article 14, 1–16. https://doi.org/10.1145/3441852.3471202

[11] Joo Hyun Park, Hyun-Young Kim, and Yoojeong Song .2021. Mathematical sound generation and voice conversion service for the visually impaired. Korean Institute of Information Scientists and Engineers.

[12] Yubin Ok, Soon-Bum Lim, Jongwoo Lee. 2024. Implementation of Chart Creation Functionality in Voice-Based Report Generator for the Visually Impaired. Proceedings of Ninth International Congress on Information and Communication Technology, 3, 371-380, https://doi.org/10.1007/978-981-97-3559-4

[13] Ministry of Education. 2022. Ministry of Education Bulletin No. 2022-33 [Attachment 8]. South Korea.

[14] Janczyk, M., Pfister, R. 2023. Difference Hypotheses for Up to Two Means: t-Tests. In: Understanding Inferential Statistics. Springer, Berlin, Heidelberg. https://doi.org/10.1007/978-3-662-66786-6_5

Fuzzy Systems and Data Mining X
A.J. Tallón-Ballesteros (Ed.)

doi:10.3233/FAIA241448

Automated Detection of Abnormal Vibration in Connecting Rod of Vibrating Groove Based on DS Theory Integrating Image and Sound Signals

Xudong Li [a], Wu Wen [b], Fei Guo [a], Minchang Liu [b], Rongya Zhang [b,1], Xin Jin [a], Yang Liu [b], Yingjun Han [a], Hua Hu [a], Wu Hu [a], Yaping Ma [b] and Tingjie Bao [b]
[a] *Chengdu Cigarette Factory, China Tobacco Sichuan Industrial Co., Ltd., No. 56, Section 1, Chenglong Avenue, Jinjiang District, Chengdu, Sichuan 610066, China*
[b] *Technology Center, China Tobacco Sichuan Industrial Co., Ltd., Section 2, Chenglong Avenue, Longquanyi District, Chengdu, Sichuan 610100, China*
ORCiD ID: Rongya Zhang https://orcid.org/0009-0005-9486-3281

Abstract. [Objective] Because of the aging of parts and mechanical structure, the vibration of connecting rod is easy to produce abnormal state, while the abnormal vibration states are difficult to detect in a timely manner,thus resulting in shutdown and material breakage during the tobacco processing process, or uneven tobacco screening, thereby reducing the quality of tobacco products . In order to solve this problem, an automatic detection technology based on Dempster-Shafter (DS) theory is proposed in this paper, so as to deal with the abnormal vibration of connecting rod in time. [Methods]The image data inside the tobacco sieve vibrating groove were collected, and the Kanade-Lucas-Tomasi (KLT) algorithm was used to track the continuous frames of the image and extract the connecting rod feature points at adjacent moments of the tobacco sieve vibrating groove. A series of microphones are constructed to obtain the location of noise source signals, and the noise source signals are denoised using wavelet coefficients. DS theory was used to fuse the image features and sound signals, calculate the vibration state conflict factor of connecting rod, judge the vibration state of connecting rod according to the conflict factor, and complete the automatic detection of abnormal vibration of connecting rod in the vibration groove of tobacco screen. [Results] The experimental results show that the proposed method can accurately identify the fault position of the connecting rod and classify the abnormal vibration level, and the results of abnormal vibration amplitude of the connecting rod in the vibrating groove of tobacco screening are highly consistent with the actual results. [Conclusion] The vibration anomaly automated detection technology designed in this article can be used for the analysis of the state of connecting rod mechanical components in the tobacco industry and the diagnosis of faults.

Keywords. DS theory, Connecting rod vibration, KLT algorithm, Wavelet coefficient, Image and sound signals fusion, vibration state conflict factor

[1] Corresponding Author: Rongya Zhang, Technology Center, China Tobacco Sichuan Industrial Co., Ltd., Section 2, Chenglong Avenue, Longquanyi District, Chengdu, Sichuan 610100, China; Email: rongyazhang@126.com
Xudong Li and Wu Wen are Co-first authors.

1. Introduction

The tobacco industry has consistently been a significant sector in China, and its production process necessitates the use of numerous mechanical devices to execute various operations [1]. Among these, the tobacco sieve separation vibrating slot is a critical component in the processing of tobacco leaves. This device efficiently and accurately grades tobacco shreds, thereby ensuring the quality of tobacco products [2]. However, as the equipment usage time increases, the internal parts and mechanical structure of the tobacco sieve separation vibrating slot gradually age, causing the equipment to loosen and wear out [3]. This can result in abnormal vibration of the connecting rod. Unfortunately, it is difficult to detect vibration anomalies in a timely manner, which can easily cause material interruption and shutdown during the silk making process or lead to uneven screening of tobacco shreds, affecting the quality of tobacco products. Once the vibration anomaly escalates to a serious level, the incurred loss will be substantial, directly impacting the shredded tobacco production capacity and significantly affecting the production line. Therefore, early detection of low-level anomalies, as well as statistics on changes and trends in anomalies, is of great value for daily maintenance, especially for preventing major anomalies.

Current scholars have extensively researched the detection of abnormal vibrations in mechanical equipment. Li and Peng [4] proposed a method for detecting anomalies in bearing vibration based on an improved autoencoder network. They utilized Mahalanobis distance to reduce the volume of training data for the autoencoder network, thereby enhancing training efficiency and achieving low-dimensional detection of bearing vibration anomalies. Despite its efficacy, this method fails to facilitate swift online detection and classification due to the issue of protracted detection duration. Wang et al. [5] suggested a method for detecting abnormal vibrations in refrigeration compressors based on autoencoders. They constructed an autoencoder model to establish a basis for determining compressor vibration anomalies, which improved the accuracy of abnormal vibration detections. However, the computational power of this method requires further verification, and it also necessitates a substantial number of training samples to achieve satisfactory detection performance. Xue et al. [6] proposed a method for detecting mechanical abnormal sounds based on self-supervised feature extraction. They converted sound samples into spectrograms and constructed a self-supervised feature extractor to achieve unsupervised recognition of abnormal sounds in mechanical equipment. However, this method does not incorporate image processing, and there is room for improvement in detection accuracy.

Xu et al. [7] suggested using the effective value of equipment vibration signals as a monitoring indicator to detect early faults in equipment and assess the degree of fault severity. Currently, some research on anomaly detection for tobacco vibratory channels has been conducted. Tang et al. [8] combined wavelet networks to extract fault characteristics of tobacco leaf processing equipment, thereby determining the type of fault and significantly improving the maintenance level of tobacco leaf processing equipment. Fu et al. [9] used professional fault detection tools to conduct fault detection on the tobacco leaf production line. Huang et al. [10] proposed a vision-based fault detection system for tobacco vibratory channels, which processes video sequences through deep convolutional methods, reducing the cost of traditional manual inspections in cigarette factories. Wei et al. [11] collected signals from tobacco packaging machinery and performed wavelet denoising, then constructed a fault signal recognition model through neural networks, providing reliable technical conditions for the operation and

maintenance of tobacco packaging machinery. However, the detection quality of this method still needs to be further improved. Wang et al. [12] derived and constructed a theoretical model of the BP neural network in tobacco equipment, which can effectively identify faults in tobacco equipment. However, this study only tests the design results from a single dimension and fails to select multiple tobacco production units for practical application. The effectiveness of the experimental method still needs further verification. At present, research on anomaly detection for tobacco vibratory channels is mainly based on single signals, such as sound or image information. However, such research methods have problems in application, such as excessive noise in signals. At the same time, some detection methods are severely affected by external factors in practical applications, and there are many problems such as poor timeliness of detection results, the study of vibration anomalies in tobacco vibratory channels through the integration of multi-source information is still ongoing.

The Dempster-Shafter (DS) theory is a mathematical theory that utilizes uncertain reasoning [13]. It computes and consolidates the confidence levels of various hypotheses to ascertain the final conclusion's confidence level. DS theory has been extensively utilized in fields such as fault diagnosis [14], quality evaluation [15], comprehensive assessment [16], and pattern determination [17]. Consequently, this paper proposes an automatic detection technology for abnormal vibrations in the connecting rod of tobacco sieve separation vibrating channels based on DS theory. By integrating continuous frame tracking images and denoised sound signals with DS theory, it diagnoses the operational status of the screening vibrating channels, thereby achieving the detection of abnormal vibrations in the connecting rod of the tobacco sieve separation vibrating channels.

2. Materials and Methods

2.1. Image Sequence Tracking Based on KLT Algorithm

The Kanade-Lucas-Tomasi (KLT) algorithm is a prevalent feature point tracking method in computer vision. This algorithm effectively tracks a series of feature points across successive image frames, estimating their motion. Multiple sensors are affixed to the inspection robot, enabling it to gather images of the tobacco sieve separation vibrating trough connecting rod via sensing technology. The process of feature point matching and tracking for this trough connecting rod necessitates only recognizable feature points within the image, eliminating the requirement for known labels. Consequently, employing the KLT algorithm [18] can augment computational efficiency.

Assuming the floating point image frame of the tobacco sieve separation vibrating slot connecting rod at time t is $I(x, y, t)$, and the first frame floating point image is created as $I_1(x_1, y_1, t)$. Applying Gaussian blurring to $I_1(x_1, y_1, t)$ based on a two-dimensional Gaussian function:

$$I_1'(x_1, y_1, t) = \frac{1}{2\pi\sigma^2} e^{-\frac{x^2+y^2+t^2}{2\sigma^2}} \tag{1}$$

In the equation, (x, y, t) represents the pixel coordinates in the horizontal and vertical directions of the image at time t, and σ is the variance of x_1. Decompose $I_1'(x_1, y_1, t)$ into a multi-scale pyramid image sequence, and use a Gaussian kernel (5*5) to convolve it to suppress noise:

$$Q_1 = \begin{bmatrix} 1 & 4 & 6 & 4 & 1 \\ 4 & 16 & 24 & 16 & 4 \\ 6 & 24 & 36 & 24 & 6 \\ 4 & 16 & 24 & 16 & 4 \\ 1 & 4 & 6 & 4 & 1 \end{bmatrix} \tag{2}$$

Calculate the Difference of Gaussian (DOG) operator and apply non-maximum suppression to compute the feature points of the vibrating slot connecting rod:

$$\zeta = wQ_{1max}, 0 < w < 1 \tag{3}$$

In the equation, w is the image threshold; $Q_{1_{max}}$ is the maximum feature value calculated. Extract the feature points in the reference frame through gradient calculation.

Similarly, the feature points for the adjacent frame I_2 are computed using a comparable method:

$$\zeta' = wQ_{2max}, 0 < w < 1 \tag{4}$$

According to the KLT target tracking benchmark, we calculate the pixel point translation distance of $I_2(x_2, y_2, t)$:

$$I_i(x_i, y_i, t) = I_i(x_i + dx_i, y_i + dy_i, t + dt) \tag{5}$$

Taylor expansion to obtain the displacement vector:

$$I_i(x_i, y_i, t) = I_i(x_i, y_i, t) + \frac{\partial I_i}{\partial x_i}dx_i + \frac{\partial I_i}{\partial y_i}dy_i + \frac{\partial I_i}{\partial t}dt + \varepsilon \tag{6}$$

Where ε represents the minimal sum of squares of the image gray difference. By disregarding the second-order parameters, the transformation results in:

$$\frac{\partial I_i}{\partial x_i}dx_i + \frac{\partial I_i}{\partial y_i}dy_i + \frac{\partial I_i}{\partial t}dt = 0 \tag{7}$$

Assign the image feature points of the tobacco sieve separation vibrating slot connecting rod to set I to facilitate continuous tracking, thereby offering data support for subsequent image feature fusion.

In practical scenarios, discrepancies in the positioning of the vibrating slot and fluctuations in shooting angles introduce substantial challenges related to angle and lighting variations when capturing vibrating slot features in images, as illustrated in Figure 1.

Figure 1. The Problems of Angle and Illumination Changes in Continuous Tracking of Actual Images.

To address this issue, the framework employs a tracking technique based on the KLT algorithm and a feature point detection method utilizing a lightweight depth detection network. The detailed implementation is illustrated in Figure 2. For consecutive image frames at T1 and T2, Gaussian smoothing is initially applied, followed by feature point extraction. Subsequently, KLT optical flow tracking is performed on these extracted feature points, and the displacement vector of successive frames is computed using the tracking outcomes.

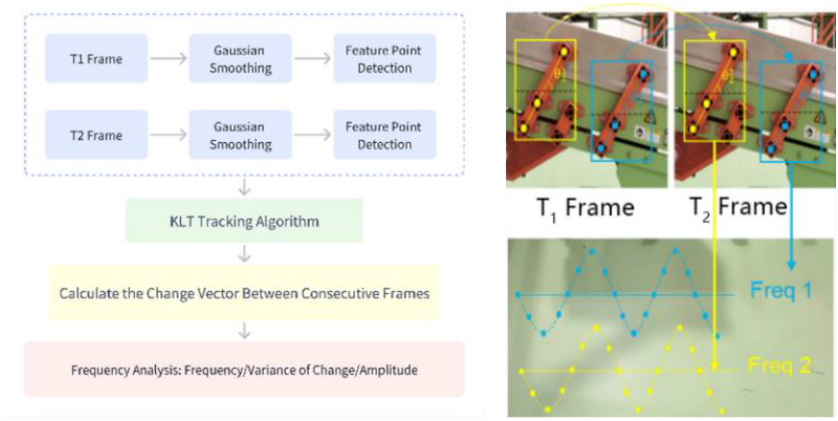

Figure 2. Visual Tracking Method for Vibration Grooves Based on KLT.

The You Only Look Once (YOLO) algorithm utilizes a single Convolutional Neural Network (CNN) model to facilitate end-to-end object detection. The core concept of YOLO is to transform object detection into a regression problem, using the entire image as input to the network and obtaining the position of the bounding box and its category through just one neural network. Therefore, the feature points chosen in this study are the central coordinates of key components on the vibrating slot. These are identified using a lightweight Yolo detection network. The detection of these feature points is carried out for each frame, and if tracking is interrupted, newly detected feature points are employed to resume tracking, thereby enhancing robust continuous tracking capabilities.

2.2. Denoising of Sound Signals Based on Wavelet Coefficients

In the context of tobacco processing, various noise sources contribute to the overall noise profile, with the slot being the predominant source. However, other personnel and equipment also contribute to the noise. This study employs a wavelet coefficient-based method for sound signal denoising, leveraging the unique distribution characteristics of these noises. To ensure high-quality sound data, an acoustic camera is utilized. The acoustic camera is a microphone array, which consists of multiple high-sensitivity microphones arranged in a specific pattern. It generates a sound pressure level distribution on a plane using array signal processing algorithms, visualizing sound with color contour maps. Multiple microphones are used to simultaneously capture the vibration sound signals of the tobacco sieve separation vibrating slot connecting rod:

$$r_k(g) = \sum_{l=1}^{M} p_k(\upsilon_l) s_l(g) e^{-j2\pi(k-1)d\,sin(\upsilon_l)/\lambda} + u_k(g) \tag{8}$$

Where M is the output of each element in the matrix, $p_k(\upsilon_l)$ is the signal sensitivity of the k-th microphone array to the υ_l direction, and $s_l(g)$ is the signal emitted by the l target source. $u_k(g)$ is the noise on the k-th array; λ is the wavelength of the sound wave.

The base bursts column output is:

$$V_k(n) = \sum_{c=1}^{M} b_k z_c(n - \tau_k) \tag{9}$$

In the equation, b_k represents the weighting coefficient for the k-th microphone array element; $z_c(n)$ is the input sound signal received by the c-th target source, and τ_k is the time delay for the sound signal to reach the k-th microphone array element.

Based on the phase difference between microphone signals, determine the location of the noise source signal emission:

$$H = \frac{f_k(n)\varphi}{1-M^2} \tag{10}$$

In the equation, φ denotes the phase of the noise source signal. To suppress the wavelet coefficients of the noise source signal, soft and hard thresholds are set. The hard threshold is defined in Equation (11), while the soft threshold is defined in Equation (12):

$$\hat{d}_{j,k} = \begin{cases} d_{j,k}, |d_{j,k}| > \lambda \\ 0, |d_{j,k}| \le \lambda \end{cases} \tag{11}$$

$$\dot{d}_{j,k} = \begin{cases} sgn(d_{j,k})\left(|d_{j,k}| - \lambda\right), |d_{j,k}| > \lambda \\ 0, |d_{j,k}| \le \lambda \end{cases} \tag{12}$$

In the equation, $d_{j,k}$ represents the vibration signal function; $sgn(d_{j,k})$ denotes the sign function. The noise-suppressed vibration signal is obtained by reconstructing the signal:

$$\iota = \sum_{l=n+1}^{M} c_l(t)\chi \tag{13}$$

In the equation, $c_l(t)$ represents the signal component after wavelet threshold denoising, and χ denotes the reconstructed signal.

Further information such as the peak, frequency, and amplitude of the vibration signal can be extracted. The processed sound information from a vibrating slot operating normally approximately follows a normal distribution, displaying relatively stable peak and trough information. However, a vibrating slot in an abnormal state may experience peak shifts.

The complete process of denoising is illustrated in Figure 3. First, the sound signal undergoes a wavelet transform for decomposition. Subsequently, soft and hard thresholds are applied to suppress the wavelet coefficients. The final step involves reconstructing the suppressed wavelet coefficients to obtain the denoised sound signal. Figure 4 provides a comparison of the time domain and frequency domain of the denoised signal before and after processing. This comparison demonstrates that sound denoising based on wavelet coefficients can effectively suppress noise.

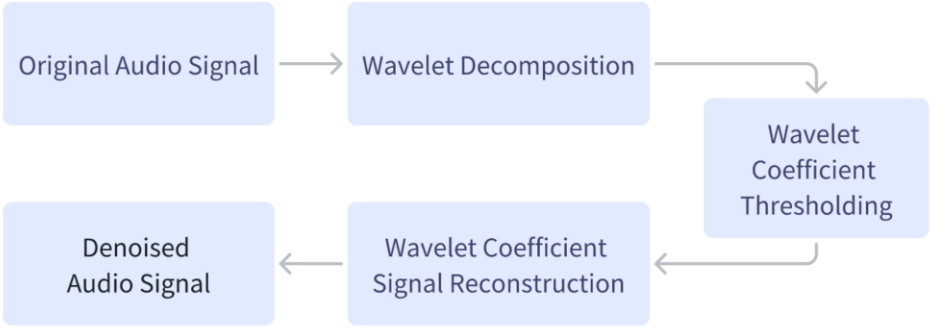

Figure 3. Process Flow of Sound Denoising Method Based on Wavelet Coefficients.

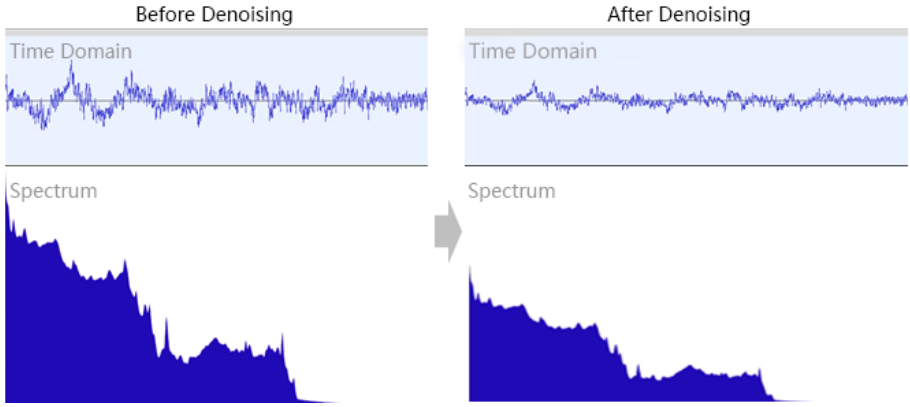

Figure 4. Sound Denoising Effect Based on Wavelet Coefficients.

2.3. Image Sequence Tracking Based on KLT Algorithm

In the pursuit of automating the detection of anomalous vibrations within the tobacco sieve separation vibrating slot's connecting rod, DS theory is primarily employed to merge image characteristics and sound signals. This integration allows for an assessment of the vibration state of the connecting rod, thereby accomplishing automated detection. The comprehensive framework is illustrated in Figure 5.

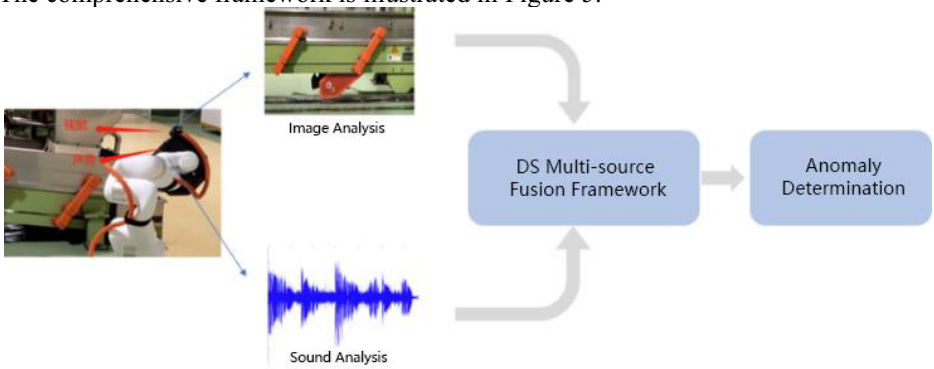

Figure 5. An Anomaly Detection Framework Based on DS Theory Fusion of Image and Sound Signals.

It is important to note that all proposition sets are represented using a discernment frame. In order to accurately differentiate the degree of belief in propositions within the discernment frame, analysis and calculation are performed using the Basic Probability Assignment (BPA) function.

In this study, we introduce interval number theory and construct an interval number model to integrate image features and sound signals. According to industrial design, the vibration frequency of a vibrating slot should be a fixed value when it is without faults. To obtain the frequency value for each vibrating slot, we extract feature points from continuous frame images and construct a feature point function. Under ideal conditions, the distribution of frequency values should follow a normal distribution with the expectation as the mean. Similarly, after processing, the vibration audio signal

approximates a normal distribution, representing the stability of the equipment. Normally, the audio signal should have stable peaks:

$$P_t^i = l^i * q_{con}^t \tag{14}$$

In the equation, l^i represents the feature point function of the i-th floating image, which indicates the probability of the vibrating slot operating normally based on the extracted image features. q_{con}^t is the characteristic function corresponding to the processed audio signal, which also represents the probability of the vibrating slot operating normally based on the extracted sound signal.

Based on the aforementioned foundation, the data structures of two signal sources are integrated to establish the identification framework:

$$m = \{m(A), m(B), m(C), m(\emptyset)\} \tag{15}$$

The equation above illustrates four distinct scenarios for a vibrating slot: faulty, non-faulty, uncertain, and an empty set. The symbol ∅ represents an empty set, which arises when the intersection of interval numbers across all categories equals zero.

Shannon entropy serves as a measure of information content; a functioning vibrating slot operates in an orderly and regular manner, thereby containing less information. Conversely, a faulty vibrating slot contains specific fault information, leading to an increased amount of information content. Shannon entropy parameters are employed to quantitatively assess the vibration of the tobacco sieve separation vibrating slot's connecting rod. The subsequent equation quantifies the information contained in the slot's movement during a single observation:

$$k = \sum_{j=1}^{M} a^j \, log \, a^j \tag{16}$$

In the equation, a^j denotes the probability associated with the movement of the tobacco sieve separation vibrating slot, while M signifies the total number of events within the discernment framework. To enhance the precision of the final judgment criteria and to refine the quantitative indicators for the normal operation of the vibrating slot, a comprehensive analysis is undertaken by comparing the discrepancies between the actual measured values and the theoretical values. At a specific moment t during an observation, its deviation is calculated:

$$\sum_{\alpha=1}^{M} f(x + x_a, y + y_a, t) - f(x, y, t) = \sum_{\alpha=1}^{M} f_x'(x, y, t) x_a - f_y'(x, y, t) y_\alpha \tag{17}$$

To concentrate on the operational state of the vibrating slot, two scenarios are taken into account: fault-free and faulty. Additionally, as per the prior analysis, the signal post-integration maintains a normal distribution; hence, the aforementioned equation can be streamlined:

$$\sum_{\alpha=1}^{M} f_x'(x, y, t) x_a - f_y'(x, y, t) y_a = \sum_{\alpha=1}^{M} f'(x, y, t) * \omega * \varphi_\alpha \tag{18}$$

Where,

$$f'(x, y, t) = \exp\left(-\frac{\sigma_x (x-\mu_x)^2 + \sigma_y (y-\mu_y)^2}{2\sigma_x \sigma_y}\right) \quad \omega = \frac{A}{2\pi^2 \sigma_x \sigma_y} \quad \varphi_\alpha = \left(\frac{x}{2\sigma_y} - \frac{y}{2\sigma_y}\right) \tag{19}$$

For the sake of simplicity, the function $f'(x, y, t)$ is denoted as $D(t)$, which represents the similarity function. The constant term ω signifies the fusion dependency between image features and sound signals. The signal fusion dimension for both is represented by φ_α. The weight factor is determined by the information amount calculated using Shannon entropy. Based on this, the conflict factor τ [19]is computed.

$$\tau = \kappa D(t) \sum_{a=1}^{M} \omega \varphi_a \tag{20}$$

The conflict factor, denoted as τ, serves as a metric to evaluate the vibrational state of the connecting rod. Typically, its absolute value is confined within the range of 0 to

1. The irregular vibrations exhibited by the tobacco sieve separation vibrating slot's connecting rod are categorized into five distinct levels, as delineated in Table 1.

Table 1. Classification of Vibration in Tobacco Sieve Slot Connecting Rod.

$\|\tau\|$	Abnormal level	Vibration description
$0<\|\tau\|\leq 0.05$	level 1	Minor vibration, does not affect screening efficiency or equipment lifespan
$0.05<\|\tau\|\leq 0.2$	level 2	Moderate vibration, still meets the requirements for screening efficiency and equipment lifespan
$0.2<\|\tau\|\leq 0.5$	level 3	Significant vibration, affecting screening efficiency, requires timely handling
$0.5<\|\tau\|\leq 0.7$	level 4	Severe vibration, has caused damage to equipment components, requires shutdown for maintenance
$0.7<\|\tau\|\leq 1.0$	level 5	Extremely severe vibration, has resulted in serious equipment failure, necessitates emergency repairs or equipment replacement

As the absolute value of $|\tau|$ increases, the vibration of the tobacco sifting vibrating slot's connecting rod becomes more anomalous. By evaluating the magnitude of $|\tau|$, one can swiftly ascertain the operational condition of the tobacco sifting vibrating slot, thereby facilitating the automated detection of vibration irregularities.

3. Results and Discussion

3.1. Experimental Environment and Calculation Process

To validate the efficacy of automated detection technology for anomalous vibrations in the tobacco sieve separation vibrating slot connecting rod, based on DS theory, comparative tests were conducted. Given that different methods exhibit certain discrepancies in quantitative indicators, to facilitate a comprehensive comparison of the results obtained from various methods, all calculation results were normalized and mapped to a range between [-1,1]. The normalized index is represented by the variable 'nor'. Similar to the conflict factor, the closer the absolute value of this index is to 0, the more optimal the working state of the vibrating slot; conversely, the closer it is to 1, the more suboptimal the working state of the vibrating slot. A ZS series linear vibrating screening equipment, produced by a specific company, was chosen as the test subject (comprising one group of equipment that had faults and was eliminated, and one group of equipment currently in use). Vibration motor excitation was employed as the vibration source to propel the tobacco onto the screen, while simultaneously advancing in a straight line. Through multiple layers of screens, several specifications of materials above and below the screen were produced and discharged from their respective discharge ports to complete the screening operation. The actual tobacco sifting equipment is depicted in Figure 6.

Figure 6. Actual Image of Tobacco Sieve Separation Equipment.

The screening vibrating slot of the tobacco sieve separation equipment is depicted in Figure 7.

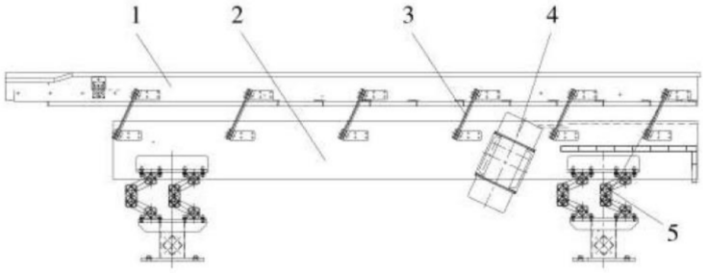

1- tank body; 2- rack; 3- pendulum rod assembly; 4- vibration exciter; 5- with elastic device

Figure 7. Structural Diagram of Tobacco Sieve Separation Equipment.

By utilizing the tobacco sieve separation equipment displayed in Figure 6, we are able to simulate the real-world operating conditions of the connecting rod within the vibration in tobacco sieve slot. In order to regulate and fine-tune the precise vibration state, a composite signal, derived from the amalgamation of image features and sound signals, is employed as the input signal. Concurrently, the corresponding conflict factor, denoted as τ, serves as the output signal. The computational procedure is delineated in Figure 8.

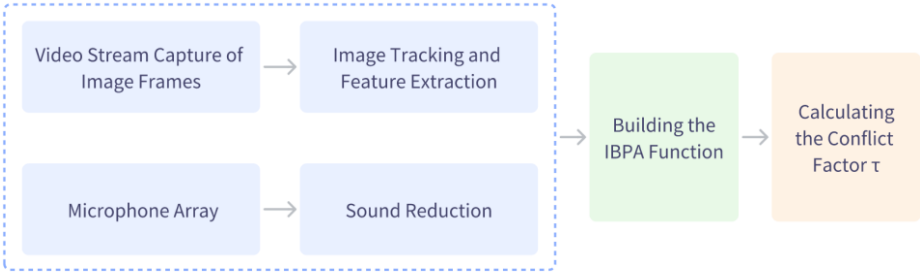

Figure 8. The Process of Experimental Calculation.

3.2. Experimental Results and Analysis

3.2.1. Connecting Rod Fault Location Identification and Grading Test

According to the structure diagram in Figure 7, the fault location of the ZS series linear vibrating screening equipment is the pendulum rod assembly. The pendulum rod assembly is a crucial component of the linear vibrating screening equipment. If the pendulum rod assembly fails, it will diminish the screening efficacy of the linear vibrating screening equipment and reduce the screening effect of the screening equipment.

The method developed in this research is employed to compute the similarity index function for components of linear vibrating screening equipment, including the tank body, frame, pendulum rod assembly, vibrator, and elastic device. It also determines the τ value and classifies the vibration anomaly level of the connecting rod. The detailed results are presented in Table 2.

Table 2. Connecting Rod Vibration Classification of the Test Tobacco Sieve Slot.

Test point	$\|\tau\|$ value	Abnormal level
1	0	level 1
2	0	level 1
3	0.9	level 5
4	0.01	level 1
5	0.02	level 1

According to the data presented in Table 2, the values of τ for test points 1, 2, 4, and 5 are all less than 0.05, indicating no fault positions that could affect the linear vibrating screening equipment. However, a τ value greater than 0.7 for test point 3 suggests a fault in the pendulum rod assembly device, with the abnormal level classified as level 5. The results obtained from the method designed in this study align with the actual fault locations in the linear vibrating screen equipment, thereby confirming the accuracy of the proposed method in identifying fault locations within the linear vibrating screen equipment.

3.2.2. Vibration Signal Detection Accuracy Test

To validate the efficacy of the proposed automatic detection system for vibration anomalies in the connecting rod of a tobacco sieve separating vibration groove, this study employs two comparative methods: the bearing vibration anomaly detection technique based on an enhanced self-coding network [4], and the refrigeration compressor abnormal vibration detection approach grounded on the autoencoder [5]. The accuracy of vibration signal detection across various test groups is analyzed to ascertain the precision of the method designed in this research. The correlation between the velocity of the oscillating motor and the standardized index of the connecting rod vibration under standard conditions is as follows:

Combined with the information shown in Figure 9, it is evident that at a motor speed of 360r/min, anomalies in vibration manifest within the connecting rod of the tobacco screen's separation groove. Concurrently, the maximum absolute value of nor is 1. Incorporating the above data, three distinct techniques were employed to ascertain the vibration state of the connecting rod at the aforementioned motor speed. The efficacy of each technique was gauged by comparing the congruity between the computed normalized mapping index and the observed vibration outcomes. A higher congruity

indicates superior methodology. The detailed experimental findings are presented in Figure 10.

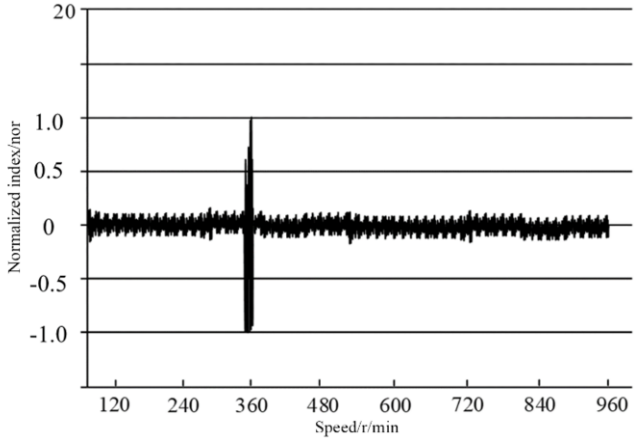

Figure 9. Relationship Between Actual Vibration Motor Speed and Normalized Index of Connecting Rod Vibration.

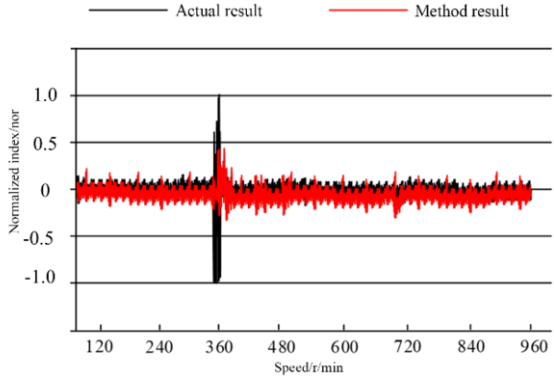

(a) Results of Bearing Vibration Anomaly Detection Method Based on Improved Autoencoding Network. [4]

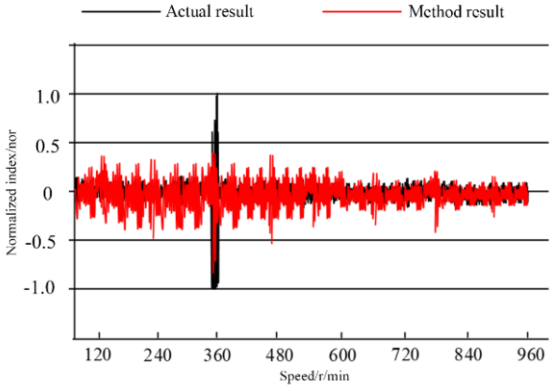

(b) Results of Abnormal Vibration Detection Method of Refrigeration Compressor Based on Autoencoder. [5]

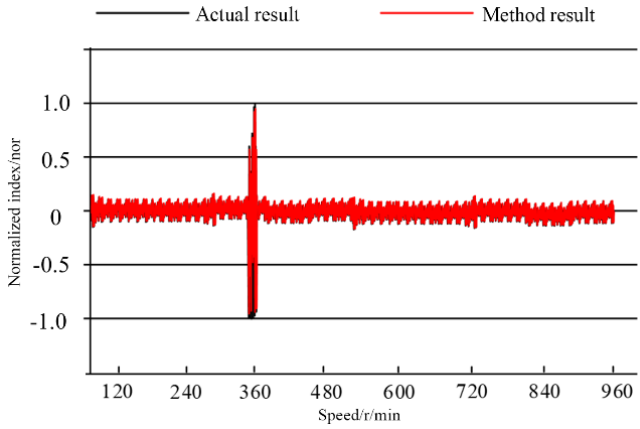

(c) Results Using the Method Proposed in This Article.

Figure 10. Comparative Diagram of Abnormal Vibration Amplitude Results Using Different Methods.

The test results depicted in Figure 10 demonstrate a discrepancy between the vibration anomaly amplitude detected by the bearing vibration anomaly detection method based on the improved autoencoder network [4] and the refrigeration compressor vibration anomaly detection method based on the autoencoder [5], when compared to the actual vibration results of the vibration motor. When the vibrating motor operates at a speed of 360 r/min, the normalized index detected by the bearing vibration anomaly detection method, which is based on the enhanced self-coding network [4], ranges from -0.4 to 0.4. In contrast, the normalized index identified by the autoencoder-based refrigeration compressor anomaly detection method [5] spans from -0.8 to 0.4. This discrepancy arises because the self-coding network [4-5] processes high-dimensional signals related to the input device by self-encoding and compressing them, followed by classification judgments for anomaly detection. Owing to the substantial dimensions of the input data and numerous network parameters, there is a propensity for the training dataset to achieve a commendable fitting effect, while the actual verification data may exhibit suboptimal outcomes and overfitting. The self-coding network approach necessitates extensive data training. However, in real-world production scenarios, the quantity of anomalous data is limited. This scarcity facilitates the training of a network capable of reconstructing the normal signal but hinders the effective training of features that distinctly highlight anomalous data. Consequently, the anomaly detection may not align with empirical results. The normalized index detected by the method proposed in this paper ranges from -0.98 to 0.95, which is in good agreement with the actual results. This is because the method designed in this study adopts DS theory to fuse the collected continuous frame feature points and the noise signal after noise reduction, and convert the visualized graphics into data, thereby improving the accuracy of automatic detection of vibration anomalies. It is proven that the method designed in this study has high precision in the automatic detection of the vibration abnormality of the connecting rod in the separating vibration groove of the tobacco screen.

4. Application Effect

To further elucidate the superiority of the proposed method, a long-term observation was

conducted in the tobacco sieve separation workshop to obtain more comprehensive and accurate actual data verification. The subsequent table presents the verification results.

Table 3. Test Result.

Time	Test point	$\|\tau\|$ value	Abnormal level
2023/03/08	1	0.03	level 1
	2	0	level 1
	3	0.85	level 5
	4	0.1	level 2
	5	0.03	level 1
2023/04/20	1	0.015	level 1
	2	0.01	level 1
	3	0.05	level 1
	4	0.1	level 1
	5	0.03	level 1
2023/06/10	1	0.02	level 1
	2	0.2	level 2
	3	0.62	level 4
	4	0.032	level 2
	5	0.012	level 1
2023/08/06	1	0.036	level 1
	2	0.04	level 1
	3	0.96	level 5
	4	0.05	level 1
	5	0.01	level 1

The table above displays four randomly selected verification results from continuous observation in 2023. The calculation results indicate that level 5 faults were detected on March 8 and August 6, while a level 4 fault was detected on June 10. These findings are consistent with work and maintenance records, demonstrating the strong applicability of this method in practical applications. It effectively monitors the working state of the tobacco vibrating tank.

5. Conclusion

This study innovatively proposes an automated detection technology for abnormal vibration of tobacco sieve screening chute connecting rods based on DS theory, addressing the limitations and shortcomings of traditional detection methods. By incorporating advanced techniques such as gradient computation, image grayscale difference matching, KLT algorithm, and wavelet coefficient denoising, it achieves effective integration and efficient processing of multi-source data, constructing a more robust and adaptable model for automated detection of vibration abnormalities. This model not only enhances detection accuracy and efficiency but also maintains stable performance under complex working conditions, providing strong technical support for the state analysis and fault judgment of mechanical components like vibratory chute connecting rods in the tobacco industry. It can well meet the daily detection needs of the production line, improve production efficiency and product quality, and has significant practical application value and research significance for the development of the tobacco industry. In subsequent research, we will attempt to combine DS theory with other advanced theories or algorithms, continuously optimize existing image processing and feature extraction algorithms, to build a more intelligent and efficient vibration

abnormality detection model, constantly improving the technology and methods for detecting vibration abnormalities.

References

[1] Zhang SW, Zhang ZY, Guo WM, Xu WT, Peng YF, Chang NJ, et al. Establishment and application of a leaf classification system for Henan "Golden Leaf" cigarettes. Tobacco Science & Technology. 2022;55(07):73-82. doi: 10.16135/j.issn1002-0861.2022.0013
[2] Xiang H, He XQ, Wang L, Zou YS, Liu GY, Yang T, et al. The optimal quantity of cut tobacco rolling back calculating model for cigarette machine based on its feature and the principle of cigarette processing. Food and Machinery. 2018;34(10):217-20. doi: 10.13652/j.issn.1003-5788.2018.10.043
[3] Zhang YH, Li S, Xu L, Liu GY. Study on the Dynamic Response and Influencing Factors of Vibration Trough in Vibration Conveyor. Hoisting and Conveying Machinery. 2013(07):61-4.
[4] Li BB, Peng L. Bearing Vibration Abnormal Detection Based on Improved Autoencoder Network. Journal of Frontiers of Computer Science and Technology. 2022;16(01):163-75.
[5] Wang YT, Feng T, Sun Q, Wang J, Wang YH. Anomaly vibration detection method of the refrigeration compressor based on autoencoder. Food and Machinery, 2021;37(04):120-3+8. doi: 10.13652/j.issn.1003-5788.2021.04.022
[6] Xue YJ, Chen X, Zhou SB, Liu YS, Han W. Mechanical Abnormal Sound Detection Based on Self-Supervised Feature Extraction. Laser & Optoelectronics Progress, 2022;59(12):361-71.
[7] Xu D. Research on analysis and prediction method of fatigue remaining life of ball bearings. National University of Defense Technology. 2011;14-28.
[8] Tang JS, Qin NB, Wei DJ, Ding L. Tobacco silk-making equipment shutdown fault detection method based on wavelet network. Equipment management and maintenance, 2022(10):32-3. doi: 10.16621/j.cnki.issn1001-0599.2022.05D.16
[9] Fu ZJ, Li YJ. Example application of professional fault detection toolbox based on Profibus in tobacco silk production line. Domestic and International Mechatronics Technology, 2010; (07):3.
[10] Huang YH, Ni Y, Chen GX. A vision-based tobacco vibration groove fault detection system: CN202210192952.2. CN115841444A. 2010.
[11] Wei DJ, Tang JS, Qin NB, Liu XS. Tobacco packaging machinery fault signal detection method based on neural network. Equipment Management and Maintenance. 2022(10):133-4. doi: 10.16621/j.cnki.issn1001-0599.2022.05D.66
[12] Wang X, Lu J, Xu Z, Zhang JH. Early fault monitoring and optimization of tobacco machinery plastic gears based on BP neural network algorithm. Plastics Technology. 2021;49(02):91-4. doi: 10.15925/j.cnki.issn1005-3360.2021.02.023
[13] Shafer G. Dempster-shafer theory. Encyclopedia of artificial intelligence. 1992;1:330-331.
[14] Gao JQ, Liu JL. Application of the Improvement of DS Evidence Theory on Fault Diagnosis of Aeronautic AC Generator. Small & Special Electrical Machines. 2016;44(06):37-40.
[15] Sun Q, Zhang T, Wang XY, Chen ZB. Air quality evaluation method based on progressive DS evidence theory. Journal of Beijing Forestry University. 2022;44(03):119-28.
[16] Li B. Synthesis assessment method based on Pignistic similarity and improved DS evidence theory. Application Research of Computers. 2018;35(12):3682-4+8.
[17] Wang YB, Cheng SY, Zhou YP, GuO PC, Zhou DQ, Luo CY. Air-to-air Operation Modes Recognition of Airborne Fire Control Radar Based on DS Evidence Theory. Modern Radar. 2017;39(05):79-84. doi: 10.16592/j.cnki.1004-7859.2017.05.017
[18] Lu JJ. Design of KLT tracking image mosaic model based on computer vision. Modern Electronics Technique. 2021;44(13):41-5. doi: 10.16652/j.issn.1004-373x.2021.13.009
[19] Li Y, Deng Y. Intuitionistic evidence sets. IEEE Access. 2019;7:106417-106426.

Fuzzy Systems and Data Mining X
A.J. Tallón-Ballesteros (Ed.)

doi:10.3233/FAIA241449

Corrugated Cardboard Defect Detection Based on Attention Mechanism and Lightweight Improvements in YOLOv8

Yali Zhang, Fang XU, You Liu[1], Guowei Zhang, Tongshan Liu and Dan Yan
Hebei Baisha Tobacco Co., Ltd., Baoding Cigarette Factory, Baoding, Hebei, 071000, China
ORCiD ID: Yali Zhang https://orcid.org/ 0009-0006-5393-4378

Abstract. Corrugated cardboard is a crucial component of packaging materials, and its surface defects directly affect the quality and aesthetics of the products. To address the challenges posed by the diverse and uneven distribution of defects on cardboard surfaces, we propose the YOLOv8-GSP, a detection algorithm based on attention mechanisms and lightweight improvements in YOLOv8 for surface defects of corrugated cardboard. Firstly, to tackle the insufficient size of the cardboard defect dataset, Projected GAN was employed to augment the dataset, thereby enhancing the training effectiveness of the detection model. Then, Ghost convolution was introduced to reduce the computational complexity and improve the operational speed. Additionally, an SE attention module was incorporated into the Neck network to emphasize the feature information of the corrugated cardboard surface, thereby enriching feature fusion. We improved YOLOv8 by incorporating Ghost convolution and attention mechanisms to enhance the efficiency and accuracy of the detection model. These improvements not only reduce the computational complexity of the model but also enhance detection performance by better focusing on target features. Our method is experimentally validated on a self-constructed dataset, providing a more efficient and accurate solution for the automatic detection of corrugated cardboard surface defects. Indeed, the proposed method's mean Average Precision (mAP) increased by 1.6% compared to the standard YOLOv8.

Keywords. YOLOv8; Corrugated cardboard defect detection; Ghost convolution; SE attention; Projected GAN

1. Introduction

As a key component of green packaging materials, corrugated cardboard plays a critical role in promoting the sustainable development of various industries in China, including the express delivery and packaging industries [1]. However, during the manufacturing process of cardboard, various defects such as damage, cracks, scratches, and stains may occur due to multiple factors. If these defects are not promptly detected and resolved, they can lead to significant economic losses and resource waste. Hence, high-precision

[1] Corresponding Author, You Liu, Hebei Baisha Tobacco Co., Ltd., Baoding Cigarette Factory, Baoding, Hebei, 071000, China; E-mail: 156026590@qq.com

automatic detection of corrugated cardboard is essential for early fault prediction, which is important for the safe operation of related industries.

Conventional manual inspection of product surfaces is time-consuming, labor-intensive, and highly subjective, leading to potential fluctuations in detection accuracy [2-5]. Given the significant growth in cardboard production, conventional detection approaches can no longer meet the existing demands. Thus, improving detection efficiency, accuracy, and real-time performance is necessary.

With the rapid development of Deep learning (DL), computer vision has achieved significant breakthroughs, and target detection is one of the key tasks in computer vision [6]. Ai et al. [7] proposed an online detection method by integrating neural network technology into cardboard surface defect detection, aiming to relieve BP neural networks' slow convergence speed and high computational amount issues. This method eliminated the effects of sample order and allowed for parameter adjustments, resulting in more accurate and reliable recognition results, with a recognition rate of 91%. Qu et al. [8] proposed a cardboard defect detection method based on the Gabor filter and Laplace algorithm, and this method can effectively extract edge images of defects. However, low efficiency and poor anti-interference capability often limit conventional detection algorithms. To resolve these limitations, Qu et al. [9] proposed a low-contrast detection algorithm based on artificial bee colony optimization. It used the dispersion matrix of the filtered defective cardboard image as the objective function for bee colony optimization to obtain the optimal segmentation threshold for detection. Jiang et al. [10] reported an improved YOLOv5 algorithm. It improved the accuracy of cardboard defect localization by optimizing the activation and loss functions and using the prediction box screening method.

Although the above methods could achieve corrugated cardboard defect detection, they still fall short of meeting the actual production requirements. To achieve faster and more accurate recognition of various cardboard defects during practical production, this study detects corrugated cardboard defects based on the YOLOv8 target detection model. It improves this model based on the characteristics of the corrugated cardboard dataset. The YOLOv8 model is the next-generation target detection network proposed in early 2023. In response to the challenges of corrugated cardboard defect detection, we propose an improved method based on YOLOv8. By adopting a more lightweight backbone network, adding attention modules, and using generative adversarial networks (GAN) to expand the dataset, the detection performance is improved, and the accuracy and reliability of corrugated cardboard defect detection are significantly enhanced. The results demonstrate that the proposed method achieves high detection accuracy on the corrugated cardboard defect detection dataset.

2. YOLOv8 target detection network

YOLOv8 is a one-stage target detection algorithm, and its structure is shown in Figure 1. It consists of three modules: Backbone, Neck, and Head. The Backbone refers to the backbone network, responsible for feature extraction; the Neck is responsible for feature fusion; and the Head is responsible for the regression calculation of target categories and positions in target detection.

The Backbone module comprises three components, including CBS, C2f, and cross-stage partial (SPPF); the CBS module consists of the convolution layer (Conv), batch normalization (BN), and sigmoid linear unit (SiLU) activation function. The C2F module

draws on the Cross Stage Partial structure [11]. The SPPF module improves spatial pyramid pooling (SPP) [12]. The Neck module retains the PANet structure from YOLOv5, and it comprises a feature pyramid network (FPN) [13] and a path aggregation network (PAN) [14]. The Head module adopts a Decoupled Head, separates localization and classification into two branches, and shifts from Anchor-Based in YOLOv5 to Anchor-Free.

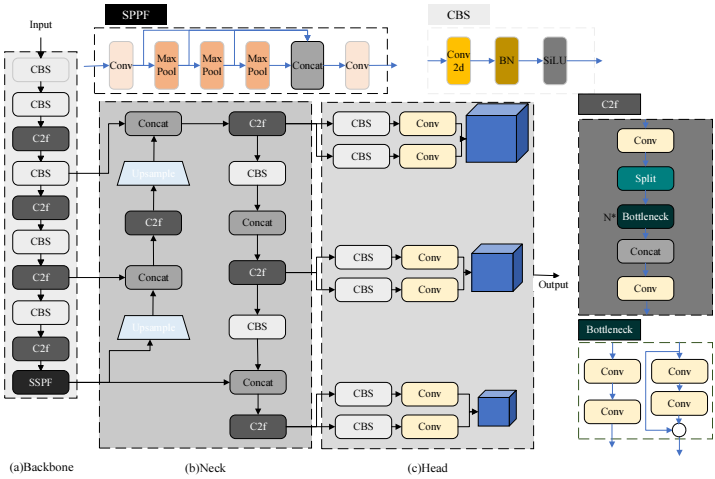

Fig. 1. Structure of YOLOv8

Detecting defects on corrugated cardboard often requires lightweight models to accommodate the large volume of corrugated cardboard being processed and the limited computational resources available in the production environment. Although YOLOv8 performs well in target detection, its model size is still relatively large, leaving room for improvement, especially for embedded devices or scenarios requiring real-time processing. Additionally, the complex texture of corrugated cardboard and the variety of defect types, such as damage, cracks, and stains, present challenges for achieving high detection accuracy with a single-stage network. In this study, we propose an improved YOLOv8 model, which enhances the accuracy and efficiency of corrugated cardboard defect detection by combining lightweight design and attention mechanisms. By adopting a lightweight backbone network and introducing attention mechanisms, this model can more effectively capture and fuse the feature information of corrugated cardboard, thereby improving detection performance and real-time processing capability while reducing computational resource demands.

3. YOLOv8-GSP improved detection network

Two improvements are made for YOLOv8-GSP: (1) the convolution module in the Backbone network is replaced with Ghost convolution to reduce its computational amount and achieve a lightweight design. (2) the attention mechanism module is added to the original YOLOv8 Neck network, which makes the detection network focus more on the target features in the feature map and thus improves detection accuracy. Figure 2 shows the structure of the improved model network.

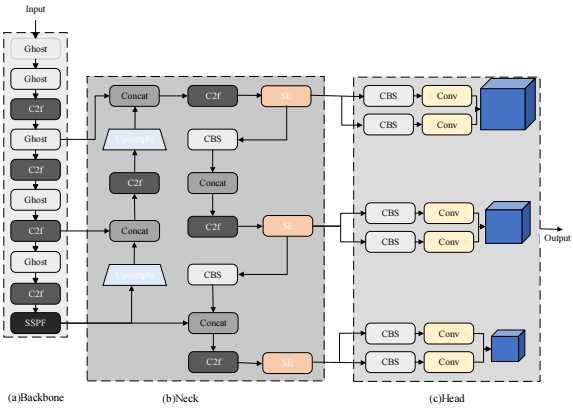

Fig. 2. Structure of YOLOv8-GSP

3.1. Ghost convolution

Ghost convolution is a common method used to reduce CNN's computational complexity and parameter count [15] while keeping the model performance barely affected. Ghost convolution is inspired by ResNet-50 [16], where many feature maps are highly similar and redundant. Instead of using expensive convolution operations to generate these feature maps, Ghost convolution efficiently creates them from the original features using linear transformation operations, which require significantly fewer computational resources. Ghost convolution mainly consists of two steps: first, a small number of convolution kernels are used to perform preliminary feature extraction on the images, and then, low-cost depthwise convolution is used to generate redundant feature maps. These feature maps are also concatenated (ConCat) to obtain the final feature map. The process is shown in Figure 3.

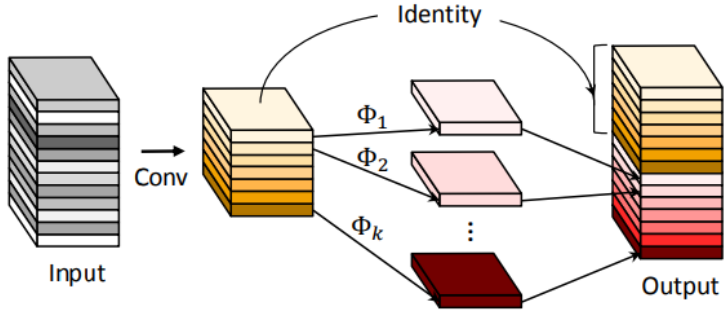

Fig. 3. Process of Ghost convolution

Ghost convolution is computationally efficient and has fewer parameters. Replacing the convolution operations in the YOLOv8 backbone network with Ghost convolution significantly reduces the model's parameter count. It minimizes performance losses, which can meet the practical factory requirements for lightweight model deployment.

3.2. SE attention mechanism

The squeeze-and-excitation (SE) attention mechanism is a common method for enhancing CNN performance [17]. As shown in Figure 4, the SE module consists of Squeeze and Excitation.

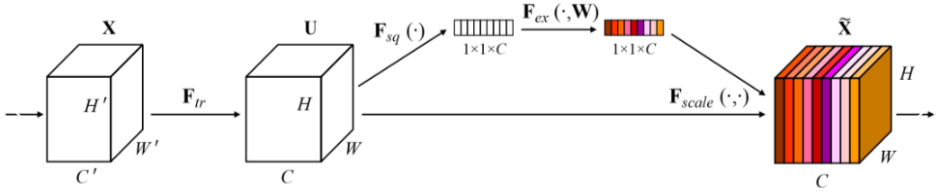

Fig. 4. Structure of SE attention mechanism

In Squeeze, the SE module compresses the spatial feature encoding of each channel through global average pooling. It converts the information into a global feature, and the output feature map has a dimension of 1×1×C. In Excitation, the SE module learns the weight of each channel through a fully connected layer, thereby characterizing the importance of each channel. Additionally, the weight values calculated by the SE module are multiplied with the corresponding 2D matrix of the original feature map for each channel to achieve feature recalibration and learning of the relationships between channels, resulting in an adjusted feature map. The SE module can strengthen important features, suppress unimportant information, reduce interference in the network, and enhance robustness. Introducing this attention mechanism into the YOLOv8 Neck network can enhance the feature response for detection tasks, improve network expressive capability, enhance detection performance, and meet the detection requirements of practical factories.

3.3. Projected GAN

Projected GAN [18] is a variate of GAN [19], and its core idea is to introduce a projection mechanism to project data into a low-dimensional space for adversarial training. Projected GAN comprises three parts: generator, discriminator, and projection module. The generator learns the data distribution from random noise vectors, generating real samples. The discriminator is used to distinguish between real samples and generated samples. Discriminator and generator exist in pairs, continuously competing to optimize the generated effects. Compared with conventional GANs, the projected GAN discriminator also makes judgments in the projected low-dimensional feature space. The projection module maps high-dimensional input data into low-dimensional feature space.

Projected GAN is highly effective and can generate high-quality image samples. Training Projected GAN to expand the dataset can enhance model performance, which is important in practical production.

4. Experimental

4.1. Dataset and experimental setup

A corrugated cardboard defect dataset was established in strict accordance with the COCO dataset standards, and LabelMe was used for detailed annotation of corrugated cardboard defects. The dataset contains 1043 images (with 813 generated images), of which 80% is classified into the training set, and 20% is classified into the validation set. The training set has 184 original and 650 generated images, while the validation set includes 46 original and 163 generated images.The details of the hardware environment and software versions are shown in Table 1. The BatchSize is set to 64 for hyper-parameter settings, the training count is 100 epochs, and the learning rate is dynamically adjusted using the cosine annealing method. The input image size for the network is set to 640×640, and other settings are kept at their default values.

Table 1. Experimental setup

Configuration Name	Version Parameters
CPU	AMD EPYC 7453
GPU	NVIDIA GeForce RTX 4090
Operating System	Ubuntu 20.04
CUDA	12.2
Programming Language	Python 3.8.19
Deep Learning Framework	Torch 1.13.0+cu117

4.2. Indicators

Trained models usually require indicators to assess their performance. In this study, multiple indicators are used, including mean Average Precision (mAP), computational complexity (GFLOPs), and inference speed (FPS) [20]. mAP is the most commonly used indicator in target detection, which measures average detection precision at different thresholds. mAP@0.5 and mAP@0.5:0.95 are used to assess detection accuracy. GFLOPs denote the number of floating-point operations required during inference, which are used here to measure the model's computational complexity. FPS denotes the number of image frames processed per second to evaluate the model's inference speed. Higher FPS values suggest better real-time performance of the model.

4.3. Results and analysis

To validate the superiority of the proposed method in detecting defects of corrugated cardboard, experiments were conducted on the current defect dataset to compare the proposed method and the most common algorithms, as shown in Table 2.

Table 2. Comparison of the proposed method and the most common algorithms

Model	mAP@0.5	mAP@0.5:0.95	GFLOPS
Faster RCNN [21]	0.948	0.642	41.1
RetinaNet [22]	0.925	0.614	36.2
SSD-300 [23]	0.841	0.537	11.5
YOLOv5s	0.954	0.648	16.3
YOLOv8n	0.943	0.636	8.2
UAV-YOLOv8[24]	0.962	0.663	10.3
Proposed method	**0.959**	**0.665**	**5.4**

The proposed method was compared with dual-stage Faster RCNN and other single-stage networks (e.g., RetinaNet, SSD, YOLOv5s, YOLOv8n). Compared with the dual-stage model Faster RCNN, the proposed single-stage model achieved higher detection accuracy and had lower computational complexity. The proposed method demonstrated certain advantages in detection accuracy and computational complexity compared with other single-stage models. Compared with YOLOv8n, the proposed model exhibited an increase of mAP by 1.6% and a decrease of FLOPS by 2.8G, resulting in improved performance. Although the difference in detection accuracy compared to UAV-YOLOv8 is minimal, our model demonstrates a significant advantage in terms of size. Overall, the proposed method achieved the best-corrugated cardboard defect detection performance.

Ablation experiments were conducted to validate each module's further contribution to performance improvement, and the results are shown in Table 3.

Table 3. Results of ablation experiments

Improvement			FPS	mAP@0.5:0.95	GFLOPs
Dataset expansion	Ghost	SE			
×	×	×	211	0.867	8.2
√	×	×	212	0.943	8.2
×	√	×	248	0.858	5.3
×	×	√	199	0.892	8.3
√	√	×	246	0.936	5.3
√	×	√	197	0.963	8.3
×	√	√	231	0.884	5.4
√	√	√	229	0.959	5.4

Through the ablation experiments, we first observed that using Projected GAN to expand the dataset could improve detection accuracy without affecting the number of parameters or inference speed. Then, replacing ordinary convolution with Ghost convolution in the backbone network reduced the number of parameters by 2.9GFLOPs and increased FPS (reflecting model inference speed) from 211 to 248, making the model more lightweight and easier to deploy on edge devices in real production environments. However, the mAP@0.5:0.95 decreased by 0.9%, which can be attributed to the fact that the feature maps generated by linear transformation in Ghost convolution would lose some information compared to those generated by ordinary convolution. Overall, the trade-off of sacrificing some accuracy for significant model lightweight and a noticeable improvement in detection efficiency is worthwhile. Additionally, the SE attention mechanism could improve the detection accuracy of the model even when used alone. Although the accuracy of the proposed model is slightly lower than when both the expanded dataset and SE attention mechanism are used, the number of parameters and detection efficiency show improvements. Overall, the proposed model has better overall performance.

Additionally, defect detection was conducted on corrugated cardboard images to demonstrate the advantages of the proposed method. The detection results are shown in Figure 5.

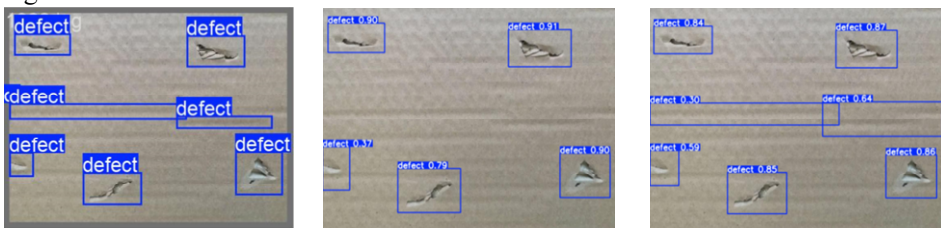

(a)Ground True (b)Origin Model (c)Our Model

Fig. 5. Cardboard defect detection by different models

Figure 5(a) shows the ground truth boxes labeled by labeling, Figure 5(b) shows the detection results of the baseline YOLOv8n model, and Figure 5(c) shows the detection results obtained by the proposed method. As indicated, the baseline model missed two minor defects in the middle section and had low detection accuracy for some boxes. The proposed model significantly outperformed the baseline model in terms of recall and also showed better detection accuracy. The proposed method significantly outperforms the baseline methods in corrugated cardboard defect detection.

5. Conclusions

Target detection algorithms are widely used to detect defects in corrugated cardboard, which is a crucial component in cigarette production. This study proposed a corrugated cardboard defect detection method that integrates attention mechanisms and lightweight improvement into YOLOv8 (YOLOv8-GSP). First, the projected GAN was introduced into the training model to expand the dataset, significantly improving corrugated cardboard detection accuracy. Then, the ordinary convolution in the original YOLOv8 backbone network was replaced with Ghost convolution, which reduced the number of model parameters and significantly increased the model's running speed. The SE

attention mechanism was also introduced into the Neck network, strengthening useful features and improving detection accuracy. Experimental results show that YOLOv8-GSP can accurately detect defects in corrugated cardboard in simulated real-world detection environments. Specifically, the mAP increased by 1.6%, the FLOPS decreased by 2.8G, and the detection efficiency of FPS reached 229. Overall, the proposed method has practical significance in ensuring the quality of corrugated cardboard production.

References

[1] Chen J. The production of corrugated cardboard continues to increase globally. Printing Technology, 2018(01): 2-3.

[2] Guan S, Wang X, Hua L, et al. Quantitative ultrasonic testing for near-surface defects of large ring forgings using feature extraction and GA-SVM. Applied Acoustics, 2021, 173(1/2/3/4): 107714.

[3] Gao C R. Design of tourism package with paper and the detection and recognition of surface defects-taking the paper package of red wine as an example. Journal of Intelligent Systems, 2021, 30(1): 720-727.

[4] Bowen Z, Huacai L, Xiuyun Z. Cotton packaging defect detection based on improved SVM algorithm. Proc. 2022 5th World Conference on Mechanical Engineering and Intelligent Manufacturing (WCMEIM), IEEE, 2022: 1088-1092.

[5] Zhao M, Qiu W Y, Wen T X, et al. Feature extraction based on gabor filter and support vector machine classifier in defect analysis of thermoelectric cooler component. Computers & Electrical Engineering, 2021, 92(12): 107188.

[6] Liu Z. Research on object detection algorithm based on deep learning. Ph D Thesis, Jiangnan University, 2021.

[7] Ai J, Qian L, Tang W. Paper surface defects recognition technology based on improved BP network. Applied Mechanics and Materials, 2013, 2488: 476-479.

[8] Qu Y, Tang W, Wen H, et al. Low contrast paper disease detection algorithm based on Gabor filter. Transactions of China Pulp and Paper, 2019, 34(02): 42-46.

[9] Qu Y, Tang W, Feng B. Web inspection algorithm for low contrast paper defects based on artificial bee colony optimization. Journal of Korea Technical Association of the Pulp and Paper Industry, 2020, 52(2): 43-51.

[10] Jiang X H. Research and application of paperboard defect detection control system based on machine vision. Ph D Thesis, Qingdao University of Science & Technology, 2021.

[11] Wang C Y, Liao H Y M, Wu Y H, et al. CSPNet: A new backbone that can enhance learning capability of CNN. Proc. IEEE/CVF conference on computer vision and pattern recognition workshops. 2020: 390-391.

[12] He K, Zhang X, Ren S, et al. Spatial pyramid pooling in deep convolutional networks for visual recognition. IEEE Transactions on Pattern Analysis and Machine Intelligence, 2015, 37(9): 1904-1916.

[13] Lin T Y, Dollár P, Girshick R, et al. Feature pyramid networks for object detection. Proc. IEEE Conference on Computer Vision and Pattern Recognition. 2017: 2117-2125.

[14] Liu S, Qi L, Qin H, et al. Path aggregation network for instance segmentation. Proc. IEEE Conference on Computer Vision and Pattern Recognition. 2018: 8759-8768.

[15] Han K, Waong Y, Tian Q, et al. Ghostnet: More features from cheap operations. Proc. IEEE/CVF Conference on Computer Vision and Pattern Recognition. 2020: 1580-1589.

[16] He K, Zhang X, Ren S, et al. Deep residual learning for image recognition. Proc. IEEE Conference on Computer Vision and Pattern Recognition. 2016: 770-778.

[17] Hu J, Shen L, Sun G. Squeeze-and-excitation networks. Proc. IEEE Conference on Computer Vision and Pattern Recognition 2018: 7132-7141.

[18] Goodfellow I, Pouget-Abadie J, Mirza M, et al. Generative adversarial nets. Advances in Neural Information Processing Systems, 2014, 27.

[19] Sauer A, Chitta K, Müller J, et al. Projected gans converge faster. Advances in Neural Information Processing Systems, 2021, 34: 17480-17492.

[20] LI Q. Research on the application of first-order object detection algorithm based on deep learning. Ph D Thesis, Jilin, 2019.

[21] Ren S, He K, Girshick R, et al. Faster r-cnn: Towards real-time object detection with region proposal networks. Advances in Neural Information Processing Systems, 2015, 28.

[22] Lin T Y, Goyal P, Girshick R, et al. Focal loss for dense object detection. Proc. IEEE Conference on Computer Vision and Pattern Recognition 2017: 2980-2988.

[23] Liu W, Anguelov D, Erhan D, et al. SSD: Single shot multibox detector. Proc. Computer Vision–ECCV 2016: 14th European Conference, Amsterdam, The Netherlands, October 11–14, 2016, Part I 14. Springer International Publishing, 2016: 21-37.

[24] Wang G, Chen Y, An P, et al. UAV-YOLOv8: A small-object-detection model based on improved YOLOv8 for UAV aerial photography scenarios[J]. Sensors, 2023, 23(16): 7190.

Fuzzy Systems and Data Mining X
A.J. Tallón-Ballesteros (Ed.)

doi:10.3233/FAIA241450

LSTM Drug Demand Forecasting with Adjustment Strategies as a Preliminary Step Toward Optimizing Hospital Drug Inventory Management

Janejira LAOMALA [a], Papon TANTIWANICHANON [a], Natchanon JARUTEEKAMPRON [a] and Sayan KAENNAKHAM [b,1]
[a] *Department of Interdisciplinary Science and Internationalization, Institute of Science, Suranaree University of Technology, Nakhon Ratchasima, 30000, Thailand*
[b] *School of Mathematics and Geoinformatics, Institute of Science, Suranaree University of Technology, Nakhon Ratchasima, 30000, Thailand*
ORCiD ID: Janejira Laomala https://orcid.org/0009-0000-9350-2541, Papon Tantiwanichanon https://orcid.org/0009-0008-4336-8901, Natchanon Jaruteekampron 0009-0004-1673-8701, Sayan Kaennakham https://orcid.org/0000-0001-9682-559X

Abstract. Pharmaceutical inventory management plays a critical role in hospital operations, directly impacting both financial efficiency and patient care. Reliable forecasting of drug demand is essential for optimizing inventory management and minimizing costs. This study presents a preliminary step toward developing a comprehensive solution by leveraging Long Short-Term Memory (LSTM) networks for time series forecasting of drug demand across three types of datasets: non-stationary, intermittent, and multi-seasonal. In addition to the baseline LSTM predictions, five post-prediction strategies are introduced to enhance the accuracy of forecasts, including directional (DiL) and undirectional (UDiL) double prediction methods, as well as self-adaptation techniques such as Simple Residual Adjustment (SRA), Recursive Residual Model (RRM), and Time Adaptive Demand Forecasting Adjustment (TADFA). The results indicate significant improvements in prediction quality, particularly when employing DiL and TADFA. Furthermore, the predicted values were used to simulate the inventory management costs under a model where both overprediction and underprediction are penalized equally. This work highlights the importance of accurate forecasting and demonstrates the potential for AI-driven solutions to improve pharmaceutical inventory management in hospitals.

Keywords. LSTM (Long Short-Term Memory), Drug Demand Forecasting, Hospital Inventory Management, Time Series Prediction, Error-Correction Mechanisms

1. Introduction

First Effective pharmaceutical inventory management [1] is crucial for hospitals to ensure the availability of essential drugs while minimizing costs and reducing waste, [2]. Poor inventory management can lead to both drug shortages and overstocking, resulting in financial strain and compromised patient care [3]. Accurate drug demand forecasting is a vital component in addressing this challenge, enabling hospitals to make informed

[1] Corresponding Author: Sayan Kaennakham, sayan_kk@g.sut.ac.th.

decisions regarding drug procurement and inventory levels. Artificial intelligence (AI), particularly machine learning techniques, has shown promise in improving forecasting accuracy, offering a potential solution to this pressing issue, [4].

Long Short-Term Memory (LSTM) [5] networks have emerged as a powerful tool for time series forecasting due to their ability to capture complex patterns and dependencies in sequential data. In this study, LSTM is applied to predict drug demand across three distinct types of time series datasets [6], each reflecting different demand patterns that hospitals typically encounter. While LSTM provides strong baseline predictions, further refinement is necessary to enhance the model's accuracy, particularly in scenarios involving non-stationary, intermittent, or multi-seasonal demand patterns [7].

To address this, several post-prediction adjustment strategies are introduced to improve the quality of LSTM predictions. These include double prediction methods—directional and undirectional—along with self-adaptive strategies such as Simple Residual Adjustment, Recursive Residual Model, and Time Adaptive Demand Forecasting Adjustment. By applying these strategies, the goal is to better align drug demand predictions with actual requirements, thus optimizing inventory management. Ultimately, this preliminary work aims to pave the way for a fully automated, AI-driven system that minimizes inventory costs while ensuring the timely availability of medications in hospitals.

2. Mathematical Background

2.1 The Mathematical Model for Pharmaceutical Inventory Expenses

This preliminary work is a key step toward our long-term goal of optimizing pharmaceutical inventory expenses. Here, we present the first version of our mathematical model and highlight the critical role of accurate drug demand forecasting. Objective function: minimize cost

$$Z = \sum_{i=1}^{N}\sum_{t=1}^{T}\left[C_h \cdot (I_t + R_t) + C_o \cdot R_t + Cst. + Cov.\right] \tag{1}$$

subject to: $I_{t+1} = I_t + R_t - D_t$, $0 \le I_t \le I_{max}$, $I_{min} \le I_t \le I_{max}$, $R_t = D_t - I_t + I_{min}$.

The refilling cost model in this work contains the following parts:

Storage Cost: $C_h \cdot (I_t + R_t)$,

Medicine Cost: $C_o \cdot R_t$,

Shortage Penalty Cost: $Cst. = C_s \cdot \max(0, D_t - I_t - R_t + I_{min})$,

Overstock Penalty Cost: $Cov. = C_{ov} \cdot \max(0, I_t + R_t - I_{max})$,

with indices: i : Index for items or products, where $i = 1, 2, \ldots, N$, and t : Index for time periods, where $t = 1, 2, \ldots, T$.

Notations:

- Z : Total cost over all items and time periods.
- C_h : Holding (or storage) cost per unit.
- C_o : Ordering cost per unit.
- C_s : Shortage penalty cost coefficient.
- C_{ov} : Overstock penalty cost coefficient.
- I_t : Inventory level at time t.

- R_t : Replenishment quantity at time t.
- D_t : Demand at time t.
- I_{max} : Maximum allowed inventory level.
- I_{min} : Minimum required inventory level.

2.2 Long Short-Term Memory Neural Network

Long Short-Term Memory (LSTM) is a recurrent neural network (RNN) designed to model sequential data while avoiding the vanishing gradient problem. Each LSTM unit has a cell state C_t and uses three gates: forget gate f_t, input gate i_t, and output gate o_t, to control information flow. The forget gate determines how much of the previous cell state C_{t-1} to keep, defined as follows

$$f_t = \sigma\left(W_f \cdot \left[h_{t-1}, x_t\right] + b_f\right). \tag{2}$$

The input gate determines what new information to store in the cell state, defined as follows

$$i_t = \sigma\left(W_i \cdot \left[h_{t-1}, x_t\right] + b_i\right). \tag{3}$$

The new candidate values $\tilde{C}_t$ for the cell state are computed using the hyperbolic tangent function

$$\tilde{C}_t = \tanh\left(W_C \cdot \left[h_{t-1}, x_t\right] + b_C\right). \tag{4}$$

Finally, the cell state is updated

$$C_t = f_t * C_{t-1} + i_t * \tilde{C}_t. \tag{5}$$

The output gate o_t determines the next hidden state h_t, which influences the output

$$h_t = o_t * \tanh\left(C_t\right). \tag{6}$$

These mechanisms allow LSTM to control the flow of information effectively over long time periods, making it suitable for time series tasks.

2.3 Post-prediction Strategies

Following the application of LSTM to the three time series datasets, post-prediction strategies were explored to improve performance. Two main approaches were tested: (1) double prediction on LSTM residuals using directional (DiL) and undirectional (UDiL) methods, and (2) self-adaptation strategies, including Simple Residual Adjustment (SRA), Recursive Residual Model (RRM), and Time Adaptive Demand Forecasting Adjustment (TADFA). Brief details of each self-adaptation method are provided below.

In a self-adaptive approach for improving time series predictions, there are several strategies, each with its own mathematical formulation. Below are various strategies that could be applied to the idea of leveraging residuals to adjust and improve predictions. At time stamp t, the actual demand is denoted by D_t and the forecast demand is denoted by $\hat{D}_t$. The residual is the difference between the actual demand and the forecast demand, denoted by $\hat{r}_t$. In this work, three self-adaptive strategies are used to adjust the forecast demand, enhancing the accuracy of prediction.

1. Simple Residual Adjustment (SRA)

In this method, the prediction for the next step is corrected by adding a fraction of the residual from the previous time step. The self-adjusted prediction for the next step is as follows

$$\hat{D}_t^{new} = \hat{D}_t^{LSTM} + \alpha \hat{r}_{t-1}, \tag{7}$$

where α is a hyperparameter that controls the influence of the previous residual on the next prediction. Typically, $0 < \alpha < 1$.

2. Recursive Residual Model (RRM)

At time stamp t, the residual $\hat{r}_t$ is estimated adaptively using the corrected predictions from the two preceding time stamps. This residual $\hat{r}_t$ is then added to the LSTM prediction at time stamp t to form the new prediction $\hat{x}_t^{new}$.

Residual Adjustment: The residual for time stamp t can be estimated based on the previously corrected predictions as follows

$$\hat{r}_t = f(\hat{r}_{t-1}, \hat{r}_{t-2}), \tag{8}$$

where $f(\hat{r}_{t-1}, \hat{r}_{t-2})$ is a self-adaptive function that captures the relationship between previous residuals. In this form, the function depends recursively on the residuals, where the correction for the current time stamp is a function of the previous residual and a recursive term as follows

$$f(\hat{r}_{t-1}, \hat{r}_{t-2}) = \beta \hat{r}_{t-1} + (1-\beta) f(\hat{r}_{t-2}, \hat{r}_{t-3}), \tag{9}$$

where β is a weight between 0 and 1. This model recursively involves older residuals, making it more sensitive to long-term dependencies in the error pattern. Prediction Update: The corrected prediction at time stamp t is then given by

$$\hat{D}_t^{new} = \hat{D}_t^{LSTM} + \hat{r}_t. \tag{10}$$

3. Time-Adaptive Demand Forecasting Adjustment (TADFA)

At time stamp t, the TADFA formula updates the adjustment parameter α_t based on the forecast residual of previous time stamp as follows

$$\alpha_t = \alpha_{t-1} + \eta \hat{r}_{t-1}, \tag{11}$$

where η is the learning rate (a constant). The forecast for the current period t is then adjusted as follows

$$\hat{D}_t^{new} = \hat{D}_t^{LSTM} + \alpha_t . \quad (12)$$

3. Experimental Setup

In this study, an LSTM model was used to predict values on three time series datasets, where each dataset was tested with both 80/20 and 70/30 train/test ratios. The dataset, consisting of 'Date' and 'Value' columns, was first normalized using a MinMaxScaler to scale the data between 0 and 1, ensuring that the LSTM could effectively process the values. A sliding window technique with a look-back period of 1 was used to create input-output pairs from the dataset, where each input represented the previous time step's value. The LSTM architecture comprised one LSTM layer with 4 units, followed by a Dense output layer. The model was trained for 100 epochs with a batch size of 1, using mean squared error as the loss function and the Adam optimizer to adjust the weights. Following training, predictions were generated for both the training and test datasets, and the results were inverse-transformed to their original scale for accurate comparison. The performance of the model was evaluated using the Root Mean Square Error (RMSE).

4. Main Results and Discussion

The results in **Table 1.** demonstrate the performance of LSTM and five post-prediction strategies—UDiL, DiL, SRA, RRM, and TADFA—across three distinct time series datasets. For the 70/30 train-test ratio, Dataset-1 (Non-stationary time series) shows an initial RMSE of 1.4460 using LSTM, which is notably reduced by TADFA to 1.0846, marking a significant improvement. Dataset-2 (Intermittent time series) starts with an RMSE of 12.9950 for LSTM, but no substantial improvement is achieved, with UDiL and DiL increasing the error further. However, RRM reduces the RMSE slightly to 12.9663, and TADFA performs similarly at 12.9713. For Dataset-3 (Multi-seasonal time series), the RMSE starts at 5.0940 for LSTM, with all five strategies producing similar results, with RRM yielding the best improvement at 5.0884.

With the 80/20 train-test ratio, Dataset-1 shows consistent improvement, where the initial LSTM RMSE of 1.1950 is reduced by DiL to 1.0740. For Dataset-2, the initial RMSE of 12.3610 sees no improvement, with UDiL significantly increasing the error, though RRM lowers the RMSE to 12.2098, and TADFA follows closely at 12.1785. Dataset-3 sees minor enhancements, with LSTM starting at 5.1800 and TADFA reducing it slightly to 4.9654, indicating stable performance across the different strategies. The notable improvements occur mainly in Dataset-1 using TADFA, while Dataset-2 remains challenging across all methods.

Table 1. RMSE Comparison of LSTM and Post-Prediction Strategies Across Different Time Series Datasets Using 70/30 and 80/20 Train-Test Ratios.

Model	LSTM	Double Prediction		Self-Adaptation		
		UDiL	DiL	SRA	RRM	TADFA
Train/Test Ratio : 70/30						
Dataset-1	1.4460	1.2150	1.3410	1.3926	1.1742	1.0846
Dataset-2	12.9950	14.8950	13.1460	12.9858	12.9663	12.9713
Dataset-3	5.0940	6.1830	5.0950	5.0935	5.0884	5.0890
Train/Test Ratio : 80/20						
Dataset-1	1.1950	1.1410	1.0740	1.1848	1.0972	1.0745
Dataset-2	12.3610	16.3450	12.2470	12.3246	12.2098	12.1785
Dataset-3	5.1800	5.3920	4.9690	5.1803	4.9879	4.9654

Figure 1 presents a comparison of the estimated inventory expenses over 52 and 60 weeks for the LSTM model and three post-prediction strategies: DiL, TADFA, and RRM. The baseline LSTM model leads to the highest costs, with expenses reaching approximately THB 40,000 over the 52-week period and climbing to nearly THB 50,000 over 60 weeks. These high costs are a result of the equal THB 100 per unit penalty for overprediction and underprediction, highlighting the limitations of relying solely on LSTM predictions.

In contrast, the application of post-prediction strategies substantially reduces these expenses. Both DiL and TADFA show significant improvements, bringing the expenses down to around THB 30,000 over 52 weeks, representing notable savings compared to LSTM. Over 60 weeks, these strategies continue to demonstrate lower costs, maintaining more efficient inventory management, with TADFA and DiL yielding the best results. RRM, while also reducing costs compared to LSTM, shows slightly higher expenses than DiL and TADFA but remains more effective than the unadjusted LSTM. Overall, the post-prediction strategies, especially DiL and TADFA, clearly highlight the benefits of refining the LSTM predictions to achieve more cost-effective pharmaceutical inventory management in hospitals.

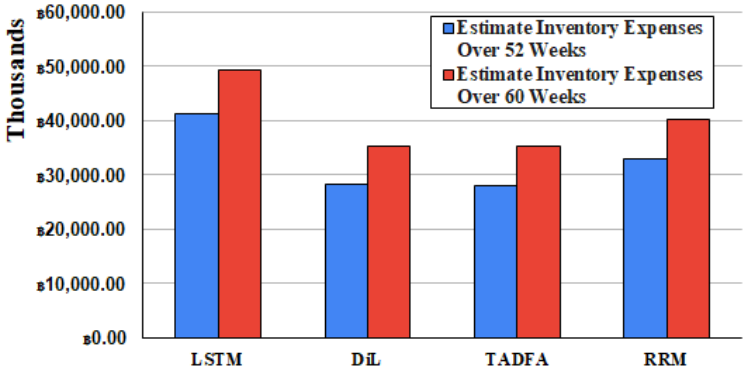

Figure 1. Comparison of Estimated Inventory Expenses Over 52 and 60 Weeks Using LSTM and Post-Prediction Strategies (DiL, TADFA, RRM)

5. Conclusions

This research has demonstrated the effectiveness of LSTM in predicting drug demand across diverse time series datasets, providing a crucial step toward optimizing pharmaceutical inventory management. The integration of five post-prediction strategies, particularly DiL and TADFA, significantly improved the quality of predictions, leading to more accurate forecasting of demand. These improvements were reflected in the reduced costs observed in the simulations, where the total expenses over 52 and 60 weeks were notably lower for models incorporating post-prediction strategies than those using LSTM alone. By showing that accurate demand forecasting can reduce both overstocking and shortages, this study underscores the critical role that AI can play in improving hospital inventory management. Future work will focus on further refining these models and developing a fully automated, AI-driven inventory management system that ensures cost efficiency and availability of essential drugs.

Acknowledgments

This work was supported by (i) Suranaree University of Technology (SUT, http://www.sut.ac.th), (ii) Thailand Science Research Innovation (TSRI, https://www.tsri.or.th), and (iii) National Science, Research and Innovation Fund (NSRF) (NRIIS number 195619). The grant recipient is S. Kaennakham who would like to express his sincere gratitude for their support.

References

[1] Elarbi M, Ayadi O, Masmoudi M, Masmoudi F. Drug-inventory-management-model for a multi-echelon pharmaceutical supply-chain: case study of the Tunisian pharmaceutical supply-chain. Supply Chain Forum: An International Journal. 2021;22(1):44-56.

[2] Mawengkang H. An Optimization Model for Hospitals Inventory Management in Pharmaceutical Supply Chain. Systematic Reviews in Pharmacy. 2020;11(3).

[3] Ahmadi E, Mosadegh H, Maihami R, Ghalehkhondabi I, . Sun M, Süer G. A. Intelligent inventory management approaches for perishable pharmaceutical products in a healthcare supply chain. Computers & Operations Research. 2022;147:105968.

[4] Abu Zwaida T, Pham C, Beauregard Y. Optimization of inventory management to prevent drug shortages in the hospital supply chain. Applied Sciences. 2021;11(6):2726.

[5] Sherstinsky A. Fundamentals of recurrent neural network (RNN) and long short-term memory (LSTM) network. Physica D: Nonlinear Phenomena. 2020;404:132306.

[6] Van Houdt G, Mosquera C, Nápoles G. A review on the long short-term memory model. Artificial Intelligence Review. 2020;53(8):5929-5955.

[7] Wang Y, Du X, Lu Z, Duan Q, Wu J. Improved LSTM-based time-series anomaly detection in rail transit operation environments. IEEE Transactions on Industrial Informatics. 2022;18(12):9027-9036.

Fuzzy Systems and Data Mining X
A.J. Tallón-Ballesteros (Ed.)

doi:10.3233/FAIA241451

PINAR: Population INfograms for Analysis and Research

Emre Öner TARTAN [a,1]
[a] *Vocational School of Technical Sciences, Baskent University, Ankara, Turkey*
ORCiD ID: Emre Öner Tartan https://orcid.org/0000-0002-5688-4226

Abstract. This study introduces PINAR (Population INfograms for Analysis and Research), a Streamlit-based web tool for visualizing and analyzing demographic data sourced from the Turkish Statistical Institute (TURKSTAT) using data mining techniques. PINAR integrates various demographic modules, including birth rates, population distribution by marital status, sex, and age groups as well as the most common baby names, and the most prevalent names and surnames over the years. A key feature of the tool is its ability to generate infograms which visualize population data on a map of Turkey, providing insights at both the provincial and district levels. The tool also presents population pyramids and race bar plots. The infograms support K-means and hierarchical clustering in the 'the most common baby names' and 'the most common names and surnames' modules, helping users uncover patterns and groupings for more detailed analysis. Users can explore demographic changes by selecting specific years or comparing data between two different years, with support for analyses based on absolute counts, ratios, and temporal changes. By revealing key demographic trends, PINAR offers enhanced insights for informed decision-making and academic research, making it a valuable tool for policymakers, researchers, and the public.

Keywords. Data Analysis, Demography of Turkey, Data Visualization, Infogram, streamlit app

1. Introduction

The Turkish Statistical Institute is the official government body responsible for collecting, analyzing, and disseminating statistical data in Turkey [1]. It provides comprehensive and reliable data on various economic, social, demographic, and environmental topics. TURKSTAT plays a key role in supporting decision-making processes by offering up-to-date statistics in areas such as population, employment, inflation, industry, agriculture, and more. The institute's data serves as a foundation for research, policy development, and public understanding of Turkey's socioeconomic landscape.

TURKSTAT's Statistics Data Portal (SDP) provides tabular data on 17 topics accross different geographic scales [2]. Some of the modules in this portal include Justice and Elections, Environment and Energy, Economic Confidence, Inflation and Prices, Agriculture, Health and Public Protection, and Industry. Another portal offered by TURKSTAT is the Geographic Statistics Portal (GSP), which visualizes metrics from 10 topics

[1]Corresponding Author: Emre Öner Tartan, onertartan@gmail.com

on a map of Turkey, with data available starting from 2019 [3]. One of these topics is Population and Demography. However, the number of metrics available for visualization is quite limited compared to the content of the comprehensive tabular data provided by the SDP. Furthermore, the GSP has limited visualization capabilities, a less flexible user interface, and a restricted timeframe. Moreover, no alternative tool for public use that addresses these shortcomings is available.

In the literature, studies on Turkey's demography have typically presented raw tabular data sourced from TURKSTAT's Statistics Data Portal [4, 5]. In this study, we develop a tool for visualization and analysis of Turkey's demography using the Statistics Data Portal, offering comprehensive filtering capabilities for population data and covering a wider period of time than the GSP. Specifically, our tool enables visualization of the population not only by sex but also by age groups and marital status. Additionally, we provide functionality to visualize ratios based on two selected sets of parameters. Another key feature of the tool is the ability to visualize changes between two selected years and animate these changes through a bar race plot over time. Furthermore, our tool visualizes the most common names, surnames, and baby names—data that are not currently visualized in this portal. To our knowledge, no previous study has utilized this subset of data. We also incorporate K-means and hierarchical clustering into these modules. In the following sections, we introduce modules presenting sample analyses.

2. Software Architecture

In application development, we used the Python programming language, following a modular approach along with the Streamlit framework. For the backend, we employed the Pandas library for data processing and manipulation. We also utilized the GeoPandas library to integrate geospatial data with Pandas dataframes. The application contains five main Python modules, along with helper modules for the user interface and plotting. On the front end, we used a variety of built-in widgets (e.g., sliders, checkboxes, radio buttons) to build the graphical user interface.

For plotting maps, we implemented a main plotter function that consolidates common functionality and accepts a specific plotter function as an argument. The first function that can be passed as an argument provides plotting capabilities for GeoPandas dataframes through a high-level interface to the Matplotlib library for generating maps [6]. The second function presents static maps using the Folium library, which builds on the data-wrangling strengths of the Python ecosystem and the mapping capabilities of the Leaflet JavaScript library [7]. The third function generates an interactive map based on Folium and Leaflet, utilizing the *explore* method from the GeoPandas library [8].

Additionally, there are three other independent plotter functions. The first plots a race plot using the Raceplotly package, which relies on Pandas and Plotly [9]. The second plots a population pyramid using the Plotly library [10]. The third plots clustering results on the Turkey map using the plot method of GeoPandas.

After pushing the app to the repository on GitHub, we deployed the app to the Streamlit Community Cloud by integrating the GitHub repository.[11].

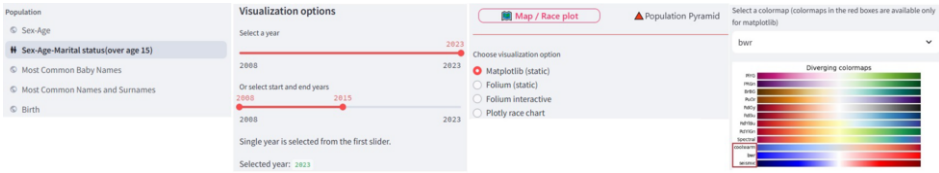

Figure 1. Dashboard user-interface

3. Dashboard

The dashboard runs vertically on the left side of the web page, filling the page height. The first panel on the top presents five modules ”Sex-Age”, ”Sex-Age Population”, ”The Most Common Baby Names”, ”The Most Common Names and Surnames”, and ”Birth”. Below the module selection, visualization options take place. The user can either select a single year using the first slider or select starting and ending years using the second slider. Below the sliders, we provide two tabs. The first tab presents race plot and three map plot options. The second tab contains the population pyramid option. All modules generate results and visualizations according to the dashboard settings. Dividing panels and concatenating horizontally, we can depict the dashboard as in Figure 1.

4. The Most Common Baby Names Module

4.1. Configuration Panel

The Statistical Regional Units Classification, abbreviated as IBBS in Turkish, is a geographical coding system that began in Europe in the 1970s. The primary purpose of these regional units is to collect statistics on a regional basis, conduct socio-economic analyses, and form the framework of regional policies for society. The corresponding regional classification for Turkey was created at three different levels by the State Planning Organization and the TURKSTAT [12]. In the modules other than the modules related to names, we provide three IBBS geographic scales and fourth geographic scale as district.

In The Most Common Baby Names module, once the geographic scale is selected, the user selects the sex through radio buttons and chooses one of two main visualization options: clustering or plotting baby names according to rankings in the provinces of Turkey. The clustering option uses K-means clustering and also allows the user to select both sexes. The user must specify the k parameter, which represents the number of clusters. The second visualization option provides two sub-options. The first sub-option simply depicts the most common baby names for the selected year or years on a map of Turkey. In the second sub-option, the user can enter names and a number n to query the provinces where the names take place in top-n ranking. An overview of the configuration panel is shown in Figure 2.

4.2. A Sample Analysis: Alparslanization

Political broadcasting in Turkey has become a significant tool for the ruling Justice and Development Party (AKP) to manipulate public perception and reinforce its ideological agenda [13, 14]. Control over the media is not limited to news or political programs;

Figure 2. The Most Common Baby Names Module-Configuration Panel

pro-government television serials also play a role in creating a simulacrum of reality that aligns with the government's interests. This phenomenon is characterized by the systematic production and dissemination of content that promotes the AKP's conservative and neo-Ottomanist ideologies, effectively shaping public opinion and cultural perceptions [15, 16].

The AKP has adeptly utilized state apparatuses, including the Turkish Radio and Television Corporation (TRT) and the Radio and Television Supreme Council (RTÜK), to regulate and promote television content that supports its political objectives. Pro-government television serials produced by the Turkish state broadcaster TRT, such as *ResurrectionErtuğrul*(*DirilişErtuğrul*, 2014–), exemplify how cultural productions can be leveraged for political purposes. Recently, TRT continues to significantly influence the cultural landscape of Turkey through its production of historical dramas, particularly with the series *Alparslan* : *BüyükSelçuklu*. This series, along with others like *Diriliş* : *Ertuğrul*, has been instrumental in shaping national identity and reinforcing the political narratives promoted by the ruling AKP. The AKP has strategically utilized these dramas to propagate a specific historical narrative that emphasizes a glorious past and the defense of Turkish-Islamic civilization, effectively merging entertainment with state-sponsored historical revisionism [17, 18, 19]. These shows are framed as representations of national identity and values, appealing to a sense of populism that resonates with the AKP's base. They serve to reinforce the narrative of the government as a protector of traditional values against perceived threats from secular elites and foreign influences [19, 20]. The portrayal of historical figures and events in these serials often aligns with the government's ideological stance, fostering a collective identity that supports the ruling party's agenda [19].

The psychological effects of such political entertainment cannot be understated. Researches indicate that entertainment media can stimulate political interest and information-seeking behaviors among viewers, suggesting that the blending of entertainment and political messaging may enhance the effectiveness of propaganda [21]. As the Turkish government continues to navigate a complex political landscape, the role of media, particularly entertainment, remains a pivotal factor in shaping public opinion and maintaining regime stability. In this chapter we observe this effect through the dataset on the most common baby names. Although this dataset dates back only to 2018, the results depict interesting trends related to pro-government TV serials. The highly popular proto-Ottoman television series *ResurrectionErtuğrul* began in December 2014 and became the pinnacle of efforts by Turkey's state broadcaster TRT to create a historical dramas that aligns with the values of the ruling AKP [17]. The series ended in May 2019. Since the dataset does not include the period 2014-2017, we cannot visualize the results from this period. When we examine the most common baby names in 2018, we see that there was no province where the name "Ertuğrul" was the most popular name. In Figure 3, we

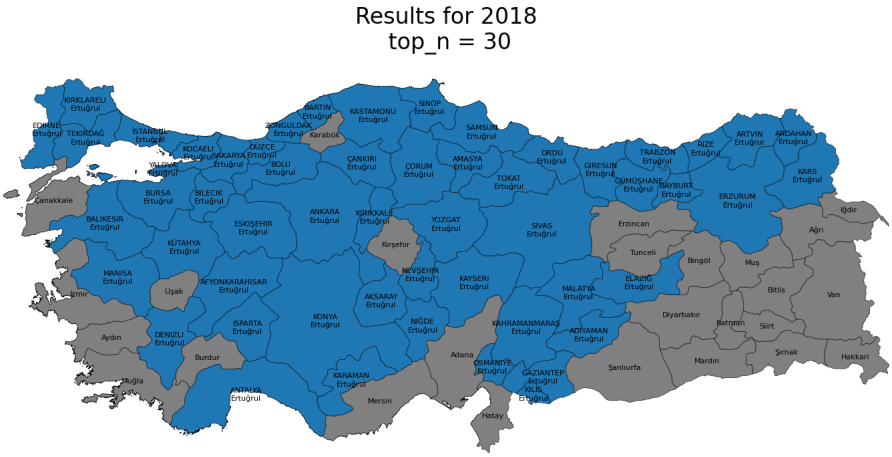

Figure 3. Provinces where the name ”Ertuğrul” takes place in top-30 rankings

visualize the provinces where ”Ertuğrul” was ranked in the top 30 over the years. Instead of individual figures, we animate this change over time, combining the results for each year in Figure 3. This animation is activated by hovering the cursor over it when the PDF file is opened with Acrobat Reader. An interesting result is that, although these names seemed to lose popularity in 2022, they regained popularity in 2023. A potential reason for this resurgence may be the rebroadcasting of old episodes on another channel [22]. In 2020 and 2021, two big-budget TV series on pre-Ottoman Seljuks Empire began broadcasting in TRT. The latter one $Alparslan : BüyükSelçuklu (Alparslan : GreatSeljuk)$, premiered in 2021 as a prequel to $Awakening : TheGreatSeljuk$, which aired from 2020 to 2021. $Alparslan : BüyükSelçuklu$ portrays the life and achievements of Sultan Alparslan, the second ruler of the Seljuk dynasty. When we visualize the most popular names countrywide, we see that, although there were no such provinces in 2018, over the years ”Alparslan” has become the most popular name across the country. This change is animated over time in Figure 4. It is seen that in 2023, aside from the Eastern and Southeastern Anatolia Region, where the Kurdish ethnic population is more dominant, the name ”Alparslan” stands out as the most popular baby name nationwide. This trend is even more evident in the animation given in Figure 5, where we use the visualization option that filters selected name or names based on the number top-n ranking.

5. The Most Common Names and Surnames Module

This module is very similar to the previous module in terms of functionality. The only difference is that user can select either name or surname option. The dataset used in this module contains the counts of the most common names and surnames in Turkey since 2018. The analyses performed in the previous module, such as those in Figure 3, 4, and 5, can also be applied in this module. In the example for this module, we present another visualization capability: K-means clustering. In this demonstration, we cluster names for both sexes, selecting the number of clusters, k, to 7 and the year to 2023, with the results

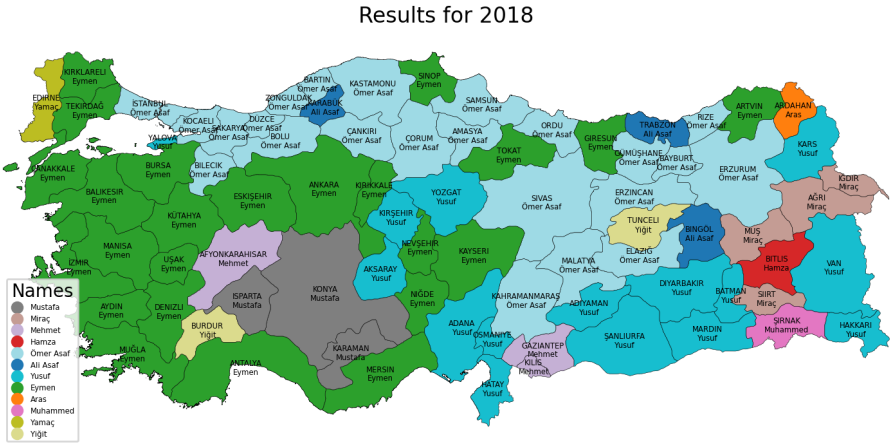

Figure 4. Animating most popular male baby names

Figure 5. Provinces where name ”Alparslan” is in top-n ranking in 2023

shown in Figure 6. This functionality, which is also available in the previous module, can provide valuable insights for geographic analyses in sociology, demography, and folklore.

6. Sex-Age Module

This module is designed to visualize Turkey’s population distribution by sex and age across provinces, regions, sub-regions, or districts. Users can customize the geographic scale and select specific sex and age groups for analysis. The module can display absolute population numbers or calculate ratios, such as the ratio of populations filtered by the selected sex and age groups. Users can choose from predefined dependency ratios (total

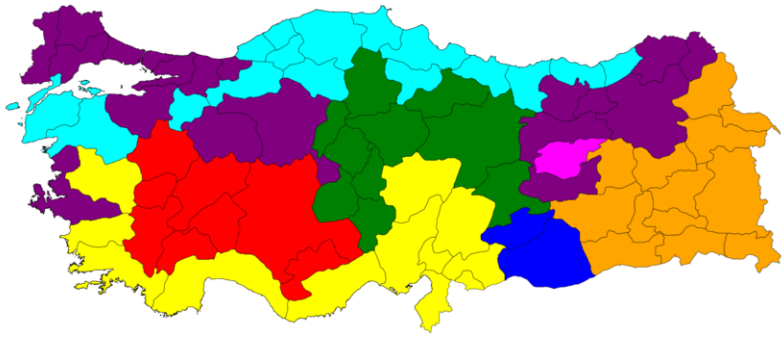

Figure 6. Clustering of the most common names with k=7 in 2023

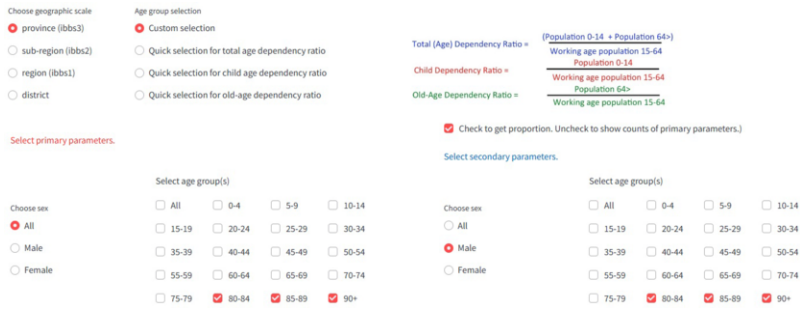

Figure 7. sex-age configuration panel

age, child, and old-age dependency) or create custom queries based on their demographic interests. This flexible interface, shown in Figure 7, allows for detailed visualizations that support demographic analysis and comparisons across various population groups. The panel further enhances user control by offering a toggle to view results as either absolute counts or proportional figures.

A sample analysis result using the module is given in Figure 8, which depicts the ratio of elderly females to males over the age 80 in the year 2023. On the right hand side, the resulting dataframe is displayed, which can be downloaded as a CSV file. This sample analysis reveals that the ratio is at least 2.4 and exceeds 3 in some provinces. Another example of the tool's functionality for this module is the generation of population pyramids, which is also available in $Sex-Age-MaritalStatus$ module. To plot population pyramids, users can select either the Matplotlib or Plotly libraries. Figure 9 shows population pyramid for when all age groups are selected using the Matplotlib option. The Plotly option can present population pyramid as an animation between the starting and ending years selected from the second year slider.

7. Sex-Age-Marital Status Module

This module is similar to the previous one; however, the age groups in this module start from 15. The population can be grouped into four marital statuses: 'never married,' 'mar-

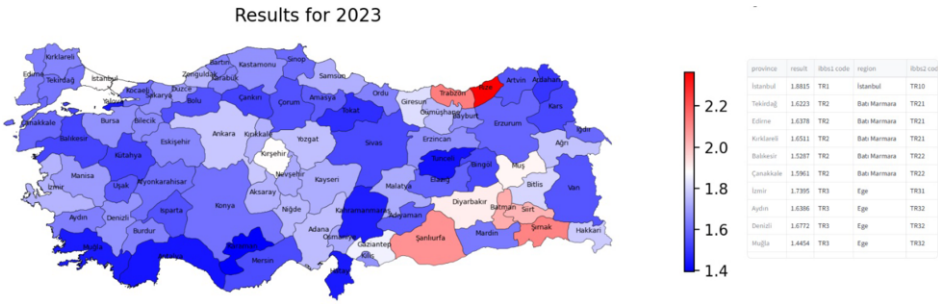

Figure 8. The ratio of elderly females to males over age 80 in 2023 at the province scale

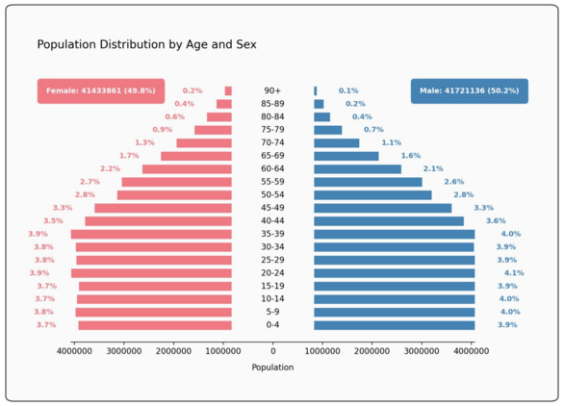

Figure 9. Population pyramid of Turkey in the year 2023 for all age groups

ried,' 'divorced,' and 'widowed.' One sample analysis could be the ratio of divorced population to married population at the sub-region (IBBS2) scale. We present the result for the years 2008 and 2023 using another example of a static map style, utilizing the Folium library[7], as shown in Figure 10. Since we selected both starting and ending year, the change is shown in a third plot.

8. Birth Module

The first configuration part differs from the two previous modules, as it provides the number of births according to the selected sex or sexes. However, the geographic scale selection and the second configuration panel to obtain ratios are similar to those in the previous two modules. To showcase another visualization option, we depict the change in the number of births over the years using a bar race plot. To use the race plot, the user first needs to select a time period using the second slider in the dashboard, which is shown in Figure 11. Once the starting and ending years are selected, the user can select geographic scale and sex. For the sample case, we select both sexes and the starting and ending years as 2014 and 2023, respectively. In this demonstration we choose the geo-scale as district. After configuration, the user can play and pause buttons to control the animation. The resulting animation is shown in Figure 11.

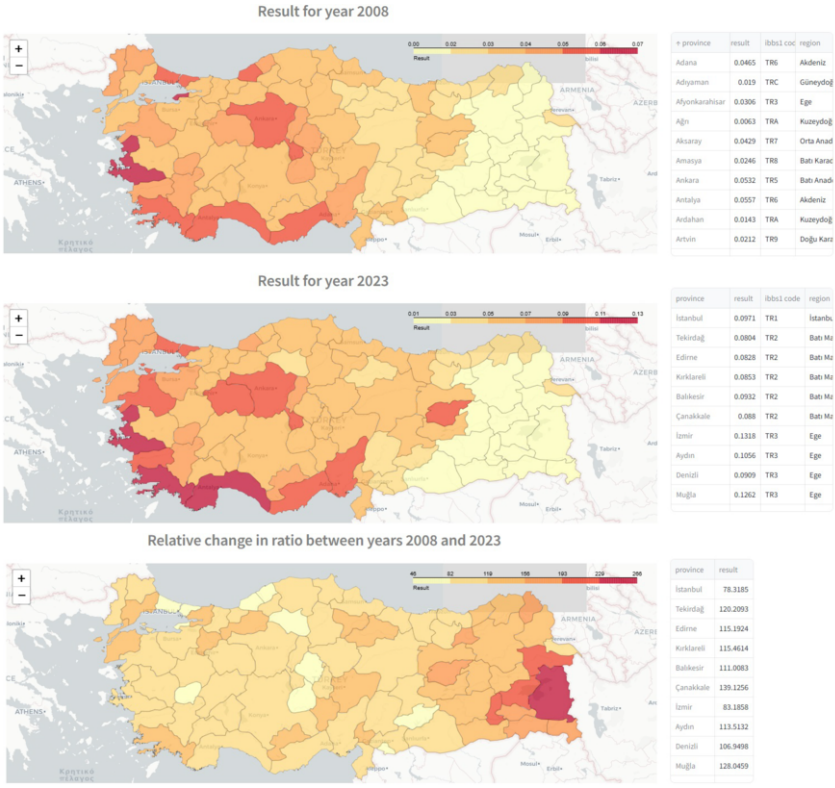

Figure 10. Change in the ratio of divorced to married population from 2008 to 2023 at the sub-region scale

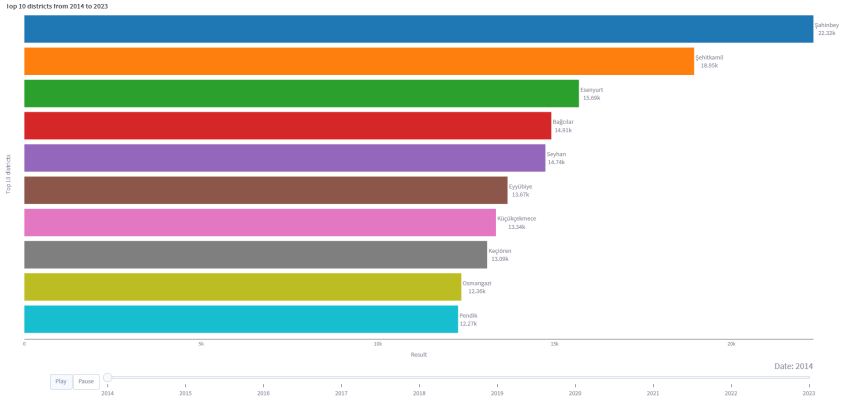

Figure 11. Change in the number of births in the top 10 districts from 2014 to 2023

After developing the 5 modules described above, finally, we have deployed the developed tool as a web application using Streamlit framework [23].

9. Conclusion

This study presents a tool named PINAR, which consists of five modules on Turkey's demography. The tool supports analyses based on absolute counts, such as the number of divorced individuals within specific age groups, as well as proportion-based metrics, such as the general fertility rate, which is the ratio of births to the female population aged 15-49 years, or the ratio of elderly females to males. The findings can be visualized as infograms on a map of Turkey at various geographic scales. Additionally, the tool includes visualizations of K-means clustering and animated bar race plots. Results are also presented in tabular form, which can be downloaded in CSV format. We introduce the tool through some sample analyses during which we observed distinguishing demographic characteristics, such as regional disparities in divorce rates and notable differences in the gender distribution of the elderly population. Furthermore, the analysis of baby names has uncovered a surge in the popularity of certain male names over the last five years, likely influenced by pro-government TV series focused on historical events, such as those from the Ottoman Empire and the Seljuk period. These sample cases demonstrate that societal transformations, from various perspectives, can be revealed and reflected through data visualization. Since further analysis is beyond the scope of this study, we propose that researchers in sociology, demography, and folklore use the developed tool to conduct studies and gain insight into the dynamics of society. To facilitate this, we have deployed the tool as a web application to make it accessible to everyone. Although data used in this study was obtained from TURKSTAT, the tool's functionality is applicable to similar data from other countries. Therefore, future studies aim to extend the scope of the tool by incorporating demographic data from other countries and adding new modules.

References

1. TURKSTAT. 2024 Sep. Available from: https://www.tuik.gov.tr
2. TURKSTAT-Statistics Data Portal. 2024 Sep. Available from: https://data.tuik.gov.tr
3. TURKSTAT-Geographic Statistics Portal. 2024 Sep. Available from: https://cip.tuik.gov.tr
4. Gelekçi C. 1960 Sonrası Dönemde Türkiye'de Nüfus Yapısı Ve Bazı Temel Özellikleri Üzerine Tespitler. *Journal of Sociological Studies*. 2015 :587–607
5. Köse M. Türkiye'de Gençliğin Toplumsal Değişimi: 2011-2023 TÜİK İstatistiklerine Dayalı Bir İnceleme. Gençlik Araştırmaları Dergisi 2024; 12:114–31
6. Mapping and plotting tools. 2024 Sep. Available from: https://geopandas.org/en/stable/docs/user_guide/mapping.html
7. Choropleth maps. 2024 Sep. Available from: https://python-visualization.github.io/folium/latest/getting_started.html
8. geopandas.GeoDataFrame.explore. 2024 Sep. Available from: https://geopandas.org/en/stable/docs/reference/api/geopandas.GeoDataFrame.explore.html
9. Raceplotly. 2024 Sep. Available from: https://pypi.org/project/raceplotly

10. Population Pyramid Charts in Python/v3. 2024 Sep. Available from: https://plotly.com/python/v3/population-pyramid-charts
11. A faster way to build and share data apps. 2024 Sep. Available from: https://streamlit.io
12. Taş B. AB uyum sürecinde Türkiye için yeni bir bölge kavramı: İstatistiki bölge birimleri sınıflandırması (İBBS). Afyon Kocatepe Üniversitesi Sosyal Bilimler Dergisi 2006; 8:185–97
13. Esen B and Gumuscu S. How Erdoğan's Populism Won Again. 2023. DOI: 10.1353/jod.2023.a900430
14. Karagöz C. TRT, AKP'nin sesi oldu: Erdoğan'a 48 saat, Kılıçdaroğlu'na 32 dakika! 2023 May. Available from: https://www.cumhuriyet.com.tr/siyaset/trt-akpnin-sesi-oldu-erdogana-48-saat-kilicdarogluna-32-dakika-2083485
15. Kaptan Y and Algan E. Guest Editors' Introduction: Cultural Politics and Production Practices of the Turkish TV Industry. International Communication Gazette 2023; 85. DOI: 10.1177/17480485231152864
16. Grigoriadis IN and Karabıçak OT. Baudrillard in Ankara: mainstream media and the production of simulacra in the Turkish public sphere. British Journal of Middle Eastern Studies 2022; 49. DOI: 10.1080/13530194.2021.1900781
17. Carney J. Resur(e)recting a Spectacular Hero: Diriliş Ertuğrul, Necropolitics, and Popular Culture in Turkey. Review of Middle East Studies 2018; 52. DOI: 10.1017/rms.2018.6
18. Tekin C. Between Invention and Authenticity: Representations of Abdülhamid II in the TV Series Payitaht. *The Politics of Culture in Contemporary Turkey*. Edinburgh: Edinburgh University Press, 2022 Nov. Chap. 12:225–38. DOI: 10.1515/9781474490313-017
19. Özçetin B. 'The show of the people' against the cultural elites: Populism, media and popular culture in Turkey. European Journal of Cultural Studies 2019; 22. DOI: 10.1177/1367549418821841
20. Balta E, Kaltwasser CR, and Yagci AH. Populist attitudes and conspiratorial thinking. Party Politics 2022; 28. DOI: 10.1177/13540688211003304
21. Bartsch A and Schneider FM. Entertainment and politics revisited: How non-escapist forms of entertainment can stimulate political interest and information seeking. Journal of Communication 2014; 64. DOI: 10.1111/jcom.12095
22. Diriliş Ertuğrul projesinden beklenmedik sürpriz. 2021 Jul. Available from: https://www.haber7.com/medya/haber/3115897-dirilis-ertugrul-projesinden-beklenmedik-surpriz-kanal-7den-izleyenlerin-hosuna-gidecek-karar
23. Tartan EÖ. Tartan Analytics. 2024 Sep. Available from: https://tartan-analytics.streamlit.app

Fuzzy Systems and Data Mining X
A.J. Tallón-Ballesteros (Ed.)

doi:10.3233/FAIA241452

Usability Testing of Card-Based Design Ideation: IoT Tiles Inventor Toolkit

Leeladhar GANVIR [a,1], Deep SHIKHA[b] and Pratul KALITA[b]
[a] *Symbiosis Institute of Design Pune, India*
[b] *Indian Institute of Technology Guwahati, India*
ORCiD ID: Leeladhar Ganvir https://orcid.org/0000-0002-3934-8405
Deep Shikha https://orcid.org/0009-0003-0876-6393
Pratul Kalita https://orcid.org/0000-0002-0824-8110

Abstract. The rapid growth of the Internet of Things (IoT) has spurred the demand for user-centric design ideation tools catering to diverse user groups, ranging from experts to non-technical individuals. The "IoT Tiles Inventor Toolkit" is a user-centric approach for rapid IoT ideation. It is an innovative card-based design method to facilitate the process of generating IoT product and service design concepts and fostering collaborative ideation. This study aims to investigate the significance and effectiveness of the IoT Tiles Inventor Toolkit. Research questions were formulated to conduct usability testing through experiment design. This study presents the formulation of hypotheses and outcomes of comprehensive usability testing conducted with control and experimental groups (n=25). The usability testing results revealed valuable insights for further refining the toolkit, including the need for additional explanatory materials and expanding the range of card components for enhanced usability. Overall, the usability testing demonstrated that the IoT Tiles Toolkit is a promising method for empowering non-experts to ideate IoT products rapidly and creatively while offering valuable insights for refining and upgrading the existing toolkit with the new cards, which influences the new technology adoption.

Keywords. Usability Testing, Tiles IoT Inventor Toolkit, Experiment Design, Design Method, Card-based Game, Ideation.

1. Introduction

Ideation is a crucial stage in designing and developing innovative products and services. During the ideation stage, ideas are generated and concepts developed, establishing the basis for innovative solutions. In the context of the Internet of Things (IoT) and innovative technology, the ideation process becomes even more significant. Designers and innovators must grapple with the complexity of interconnected devices and the evolving needs of users. Various ideation toolkits have emerged to aid in this process, each offering a unique approach to brainstorming and concept generation. IoT Tiles Inventor Toolkit leverages the power of cards to inspire and structure ideas for IoT and smart home solutions.

[1] Corresponding Author: Leeladhar GANVIR, Symbiosis Institute of Design Pune, India; Email: g.leeladhar@iitg.ac.in

The literature review reveals a gap in the existing ideation toolkits explicitly tailored for the Internet of Things (IoT) and smart home product design. While current toolkits address general design ideation, they often lack specific features that cater to the unique characteristics of the user's needs. Furthermore, there is limited empirical evidence on how these toolkits influence the ideation process, particularly regarding non-experts' ability to generate high-quality, innovative ideas for IoT solutions. The need for a structured, user-centric toolkit to effectively bridge this gap in the ideation process for smart home IoT products is evident. This study delves into the usability testing of the IoT Tiles Inventor Toolkit, aiming to answer the research question (Table 1) and evaluate its effectiveness in facilitating the ideation process for IoT and smart technology. Usability testing is critical in understanding how well a design tool serves its purpose and whether it enhances or hinders the creative process. In order to address the identified research gap, the following research questions have been formulated:

Table 1. Research Questions

	Research Question
RQ1	How does the IoT Tiles Inventor Toolkit impact the ideation process concerning the characteristics of smart products, such as independence, adaptability, reactivity, multi-functionality, ability to co-operate, human-like interaction and personality?
RQ2	What are the strengths and weaknesses of the IoT Tiles Inventor Toolkit based on expert feedback?
RQ3	How can the IoT Tiles Inventor Toolkit be improved to enhance usability and effectiveness for designers working on IoT projects, particularly non-experts?

This study aims to evaluate and enhance the IoT Tiles Inventor Toolkit as a user-centric ideation tool for designing smart home IoT products, focusing on improving its usability and effectiveness for experts and non-experts in the design process. To achieve the aim of the study, the following objectives are defined:

Table 2. Objective

	Objectives
O1	To assess the impact of the IoT Tiles Inventor Toolkit on the ideation process, particularly in terms of generating ideas that align with the characteristics of smart products (e.g., independence, adaptability, multi-functionality, etc.)
O2	To conduct usability testing of the IoT Tiles Inventor Toolkit with both expert and non-expert participants, evaluating the quality and quantity of ideas generated.
O3	To identify the strengths and weaknesses of the IoT Tiles Inventor Toolkit based on expert feedback and usability testing results.
O4	To propose improvements to the IoT Tiles Inventor Toolkit, enhancing its usability and effectiveness for designing smart home IoT products, especially for non-experts.

In this exploration, we will examine the components and functionality of the IoT Tiles Inventor Toolkit and the methodology used for usability testing. The findings of this study will shed light on the toolkit's strengths and weaknesses, providing valuable insights for designers and innovators seeking to create the next generation of IoT and smart products. By understanding how well the toolkit aligns with user needs and expectations, we can further refine the tools that drive innovation in IoT and smart technology.

2. Literature Review

2.1. Product Smartness

The literature examines the characteristics that identify a product as "smart", such as being "independent", "adaptive", "multi-functional", having the "ability to cooperate", enabling "human-like interaction", and possessing "personality" [1]. Each smart home product (SHP) feature expresses different qualities. Therefore, it is essential to define each one. An essential requirement for an SHP is its autonomy and ability to operate independently, comprehending and executing its designated function without relying on user intervention. Furthermore, SHPs must also be capable of adjusting to their environment and accommodating different usage scenarios. The ecosystem of an SHP covers a range of stimuli and other interconnected SHPs. A product must respond to these stimuli and interact with the function of other products in its proximity. Products that fulfil multiple user objectives are referred to as multi-functional. The capacity of SHP to collaborate with other products and fulfil multiple shared user objectives is also called multi-functional. These products offer a variety of applications and scenarios for the user. Smart products respond to users in a way that is similar to how humans interact with one another. The human-like user experience helps smart products become more emotionally attached to their users. It is also critical for smart products to appear credible and safe and to project a trustworthy personality to the user [2].

Table 3. Characteristics of Product Smartness

	Characteristics	Definition
1	**Independent**	Ability of the system or devices to operate autonomously and perform tasks without constant human intervention or control.
2	**Adaptive**	The ability of the system to adjust and respond to changing conditions, user preferences, and environmental factors in real-time, enhancing convenience and efficiency.
3	**Reactive**	The system's ability to respond automatically to specific triggers or events without requiring explicit user input.
4	**Multi-functional**	Systems that have the capability to perform multiple tasks or offer various features, often integrated into a single device, to enhance convenience and efficiency.
5	**Ability to cooperate**	The ability of various devices, systems, and components within the home ecosystem to work together harmoniously, facilitating seamless communication, data sharing, and collaboration to enhance the overall user experience.
6	**Humanlike interaction**	The ability of technology and devices to mimic or replicate natural human communication and behaviour, creating a more intuitive and relatable interaction between users and their smart home systems.
7	**Personality**	Smart product's ability to represent a credible character.

2.2. Design by Analogy

"Design by analogy" is a method of creative problem-solving where designers derive inspiration and insights from pre-existing solutions, concepts, or contexts that are not directly related to the specific problem they are attempting to solve. It involves identifying similarities between the unfamiliar problem and familiar scenarios, products, or processes and then using these similarities to generate innovative ideas or solutions [3,4].

Design by analogy encourages lateral thinking, exploring new possibilities, and generating creative ideas by looking beyond the immediate problem context. It is a valuable technique in various fields of design, including electronic product design and user experience design, as it helps designers break away from conventional thought patterns and tap into a broader range of influences.

Through an extensive literature review and collaborative workshops with smart product designers, we have mapped out the landscape of design toolkits essential for developing smart products. We identified seven essential toolkits: Card 'n' Dice, Co-create the IoT, IoT Design Deck, IoT Ideation Design Kit, Know Cards, Mapping the IoT [5]. These toolkits stood out as significant contributors to IoT design methodologies. By conducting semi-structured interviews and engaging in open discussions with designers, we aimed to understand their design processes, challenges, and how designers use these toolkits. We then used the double-diamond method to organize these toolkits within a design process model. This mapping helped us identify each toolkit's specific roles, such as providing technical support, generating ideas, solving problems, and planning for implementation.

2.3. Tiles IoT Inventor Toolkit

The toolkit is a modular and interactive learning platform created to instruct product-service-system (PSS) designers on the development of SHP that utilizes the Internet of Things (IoT) technology [5,6]. This toolkit provides an enjoyable and informative method for understanding the process of generating ideas for IoT products. It can be a valuable resource for identifying and understanding user's problems and exploring the technical possibilities outlined in the design brief during the ideation phase. The toolkit includes a diverse range of tangible cards that can be interconnected to generate a multitude of concepts. The toolkit consists of cards for scenarios, personas, missions, things, human actions, sensors, services, feedback, and reflection criteria [7,8]. These cards stimulate ideas for IoT user experiences by promoting divergent and convergent thinking. The playbook provides participants with a step-by-step process to design SHPs enabled by the Internet of Things (IoT). While the ideation technique typically requires professional supervision, the playbook aims to make the design process more transparent and reduces the necessity for supervision.

Playing the IoT Tiles Inventor Toolkit involves a structured yet highly creative process. It all starts with selecting a persona and a scenario, identifying the user, and identifying the specific needs or problems participants aim to address [9]. These cards are placed on the board for reference. Afterwards, participants enhance their Mission by utilizing a maximum of three Mission cards, pushing themselves to think innovatively about the purpose or objective of their idea. The toolkit encourages participants to consider the central objects relevant to their users and their role in solving identified needs; this is done by selecting and placing Things cards on the board. Participants then explore what actions trigger these objects, considering various inputs like Human Actions, Sensors, and Services. The chosen triggers are placed on the board to map out these interactions. Once the trigger is established, participants think about how the object responds when activated.

This could involve direct feedback from the object itself or data transmission to an app or service through service cards. This step helps define the user-object interaction more clearly. The Storyboard section of the board serves as a creative space for participants to describe and illustrate their ideas. It is where participants can visually

depict how the concept works, its appearance, and the user experience. Each step of the participants' idea is sketched and described, creating a use-case scenario. Finally, there is room for reflection and improvement. Participants assess their concept against various criteria, identifying strengths and weaknesses. If weaknesses are identified, participants are encouraged to brainstorm improvements and make changes to the cards or storyboard as needed. The culmination of this process is an Elevator Pitch, a concise description of the participants' final idea that captures its essence. This structured protocol empowers designers and innovators to systematically generate and refine ideas for IoT and smart technology, ensuring that creativity and user-centred thinking are at the forefront of the design process.

3. Research Methodology

The research methodology used for the usability testing of the toolkit involves a controlled experimental design. During the ideation phase of the experiment, participants were tasked with generating innovative ideas in response to a predefined IoT-related challenge. The participants will be categorized into two distinct groups: the Control Group and the Experimental Group. The Control Group will comprise participants who will engage in an ideation session without the toolkit, whereas the Experimental Group will utilize the toolkit during their ideation session. Participants were given the same design brief in each session and given a set amount of time to brainstorm and develop ideas. The goal was to observe how the toolkit influenced the ideation process in terms of both the quantity and quality of ideas generated. The participants will be presented with a predefined IoT-related challenge as the basis for generating ideas. This experimental design allows for a direct comparison of the toolkit's impact on the ideation process. The null and alternative hypotheses will be tested to assess the toolkit's impact on the ideation process.

During the usability testing, quantitative data will be collected, including the number of ideas generated by participants and the quality of these ideas assessed by experts. To test the hypotheses, paired sample statistics will be employed to compare the outcomes between the Control Group and the Experimental Group. Paired samples t-tests will be conducted to determine if there are statistically significant differences in the number of ideas and their quality between the two groups. The results will provide insights into the impact of the Card-Based Design Ideation: IoT Tiles Inventor Toolkit on the ideation process. The analysis will reveal whether the toolkit significantly influences the quantity and quality of ideas generated for IoT-related projects. The outcomes of the paired samples t-tests will indicate whether the null hypotheses are rejected or not. This data-driven analysis will contribute to a comprehensive understanding of the toolkit's usability and effectiveness for designers and innovators in IoT-related projects.

3.1. Experiment Design

	Working Hypothesis
H1	In the ideations, there is no significant difference between ratings of peers on the **Independent** attribute, for a design concept in T1 and T2.
H2	In the ideations, there is no significant difference between ratings of peers on the **Adaptive** attribute, for a design concept in T1 and T2.
H3	In the ideations, there is no significant difference between ratings of peers on the **Reactive** attribute, for a design concept in T1 and T2.
H4	In the ideations, there is no significant difference between ratings of peers on the **Multi-functional** attribute, for a design concept in T1 and T2.
H5	In the ideations, there is no significant difference between ratings of peers on the **Ability to cooperate** attribute, for a design concept in T1 and T2.
H6	In the ideations, there is no significant difference between ratings of peers on the **Humanlike interaction** attribute, for a design concept in T1 and T2.
H7	In the ideations, there is no significant difference between ratings of peers on the **Personality** attribute, for a design concept in T1 and T2.

Figure 1. Experiment Design to test the Working Hypothesis

The experiment is designed to evaluate the effectiveness of the Card-Based Design Ideation: IoT Tiles Inventor Toolkit in enhancing the ideation process for IoT-related projects. It involves 25 participants, including UX designers, electronic product designers, and HCI students, ensuring diverse perspectives relevant to IoT innovation. This selection was based on their familiarity with design processes, innovation, and technology, particularly within the context of IoT (Internet of Things) projects. UX designers bring a deep understanding of user-centred design, essential for evaluating the toolkit's impact on the ideation process from a usability perspective. Electronic product designers offer technical insights into the feasibility and practicality of the generated ideas, while HCI students contribute fresh, research-oriented perspectives that are critical for assessing innovative approaches. By including individuals from these varied

backgrounds, the study aimed to capture a comprehensive range of insights, ensuring that the findings would be applicable across different facets of IoT design and development. The experiment uses a controlled design with two sessions: a Control Group (Treatment 1) and an Experimental Group (Treatment 2), spaced four weeks apart to reduce the influence of memory or learning effects.

In the first session, participants engage in an ideation exercise without the toolkit, generating ideas based on a predefined IoT-related challenge. These ideas are documented for evaluation, focusing on quantity and quality, which are later assessed by experts. In the second session, the same participants tackle a similar challenge, using the toolkit to guide their ideation process. Again, the ideas are documented and evaluated similarly to the first session.

Quantitative data analysis will involve paired samples t-tests to compare the number and quality of ideas between the two sessions, testing hypotheses about the toolkit's impact. The analysis aims to determine whether the toolkit significantly increases the quantity of ideas generated and enhances their quality. Additionally, qualitative insights will be gathered through expert reviews and participant feedback, exploring the toolkit's influence on creativity and applicability. The experiment is expected to reveal whether the IoT Tiles Inventor Toolkit substantially improves the ideation process, making it a valuable tool for designers and innovators working on IoT projects. The findings will contribute to the ongoing development and refinement of design tools in the IoT domain, offering practical insights for future applications.

3.2. Hypothesis Development

Hypotheses serve as the foundation of scientific research, offering testable statements that guide investigations and help conclude. In the context of the "Usability Testing of IoT Tiles Inventor Toolkit," we formulate hypotheses to evaluate the toolkit's impact on the ideation process. The primary focus is on the number of ideas generated and their quality, as assessed by experts. The experimental design and analysis will help determine whether the null hypotheses will be rejected or accepted, thereby revealing the extent of the toolkit's impact on the ideation process. This hypothesis development provides a clear framework for evaluating the usability and effectiveness of the toolkit.

The evaluation process was designed to assess the effectiveness of the toolkit objectively. After the ideation sessions, the ideas generated by participants were collected and analyzed using a set of predefined criteria. These criteria included factors such as the ideas' novelty, feasibility, and potential impact on the given IoT challenge. A panel of industry experts in UX design, electronic product design, and HCI assessed the quality of the ideas. Additionally, the number of ideas produced by each participant was recorded as a quantitative measure of the ideation process. To compare the results between the Control Group and the Experimental Group, statistical analysis methods, such as paired samples t-tests, were employed. This analysis aimed to determine whether there were significant differences in the quantity and quality of ideas generated with and without using the toolkit, ultimately providing insights into the toolkit's effectiveness in enhancing the ideation process for IoT projects.

4. Result

To test these hypotheses, paired sample statistics are employed. This statistical method is used because the same subjects are measured twice, once without the toolkit and once with the toolkit. Paired samples t-tests are conducted to compare the means of the two treatments. The results of these paired sample statistics will provide insights into whether the IoT Tiles Inventor Toolkit has a significant impact on the quantity and quality of ideas generated during ideation sessions. If the p-values associated with these tests are less than 0.005, the null hypotheses will be rejected, signifying that the toolkit has a significant impact on ideation outcomes.

Table 4. Hypotheses Testing Results

Paired Samples Statistics

			Mean	N	Std. Deviation	Std. Error Mean	p-value
1	**Independent**	T1	2.92	25	1.222	.244	< 0.001
		T2	4.76	25	1.451	.290	
2	**Adaptive**	T1	2.96	25	1.338	.268	< 0.001
		T2	4.60	25	2.000	.400	
3	**Reactive**	T1	3.44	25	1.003	.201	< 0.001
		T2	4.36	25	1.823	.365	
4	**Multi-functional**	T1	3.16	25	1.491	.298	< 0.001
		T2	4.96	25	1.513	.303	
5	**Ability to Co-operate**	T1	3.32	25	1.069	.214	< 0.001
		T2	4.88	25	1.509	.302	
6	**Humanlike interaction**	T1	2.40	25	0.816	.163	0.004
		T2	2.96	25	1.338	.286	
7	**Personality**	T1	1.60	25	0.500	.100	0.003
		T2	1.96	25	0.812	.162	

Given that the p-value is less than 0.001, we can confidently reject the Null Hypothesis for H1, H2, H3, H4, and H5. The null hypotheses H1, H2, H3, H4, and H5 have been rejected, indicating that there is a statistically significant difference in the ratings of experts for the attributes of Independent, Adaptive, Reactive, Multi-functional, and Ability to Co-operate between Treatment-1 (T1) and Treatment-2 (T2). However, the p-values for H6 and H7 are 0.004 and 0.003, respectively. The Null Hypothesis H6 and H7 have been accepted, indicating no statistically significant difference in experts' ratings for the Human-like interaction and Personality attribute between Treatment-1 (T1) and Treatment-2 (T2).

5. Conclusion

In this comprehensive hypothesis testing study, we rigorously assessed the toolkit's impact on the usability and effectiveness of ideation within the context of smart product and service design. The toolkit, comprising various innovative card tools, aimed to enhance the ideation process by fostering creativity and improving the quality and quantity of ideas generated. Our study employed paired sample statistics to investigate the toolkit's influence on various attributes of ideation concepts, as assessed by experts. The hypothesis testing results (Figure 2) reveal significant insights into the impact of the toolkit on various attributes of ideation concepts generated during Treatment T2 (with

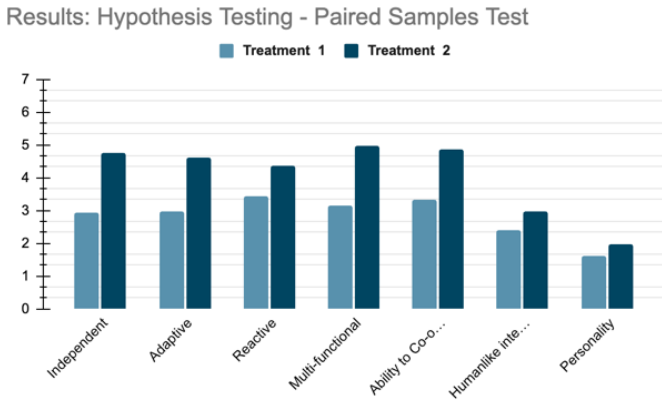

Figure 2. Hypothesis Result Graph

- **Evolving Technology Landscape:** IoT and smart home technology are continuously evolving. New devices, protocols, and trends emerge regularly. The toolkit must adapt to these changes to remain effective in helping designers ideate solutions that leverage the latest technological advancements.
- **User-Centric Design:** Smart products and services are ultimately designed to enhance the user's life. Thus, user-centred factors like usability, convenience, and personalization must be integrated into the toolkit.
- **Technological Compatibility:** As new technologies and standards emerge, compatibility with existing ecosystems becomes a key consideration. We can identify emerging technologies or interoperability standards through literature research and include corresponding cards to guide designers in creating interoperable solutions.
- **Security and Privacy:** Users' concerns about data security and privacy are paramount. The toolkit should include cards addressing these concerns and guide designers in creating secure, privacy-respecting solutions.
- **Sustainability:** Environmental sustainability is increasingly relevant. As smart products evolve, they should be energy-efficient and sustainable.
- **Ethical Considerations:** Ethical concerns related to smart technology, such as data ethics and fairness in algorithms, should be integrated into the toolkit.

- **Ecosystem Thinking:** Smart products often operate in ecosystems where multiple devices and services interact. The toolkit should reflect this ecosystem perspective, helping designers consider the broader context of their designs.
- **Emotional and Aesthetic Appeal:** Aesthetic and emotional factors are increasingly vital in product design. Primary research, such as user surveys and interviews, can identify how aesthetics and emotional aspects influence the adoption of smart products. These insights can lead to the inclusion of related cards.

6. Future Scope

Here are some suggestions for the future scope of the study:

- **Diverse Participant Pool**: Future studies could expand the participant pool to include a wider variety of professionals, such as industrial designers, software developers, and business strategists. Including participants from different backgrounds and experience levels would help understand the toolkit's effectiveness across a broader range of users.
- **Longitudinal Studies**: Conducting longitudinal studies would allow researchers to observe the long-term impact of the toolkit on the ideation process. This could provide insights into how repeated toolkit use influences creativity, idea quality, and the overall design process over time.
- **Real-World Application**: Implementing the toolkit in real-world design projects rather than controlled experiments would help assess its practical utility. Observing how the toolkit performs in a naturalistic setting, with real constraints and deadlines, could offer valuable insights into its adaptability and effectiveness.
- **Cross-Cultural Studies**: Investigating how the toolkit is received and used in different cultural contexts could provide valuable insights into its global applicability. Understanding cultural influences on design thinking and ideation processes could lead to more inclusive and versatile design tools.

Future studies could develop more refined metrics to measure creativity and innovation more precisely. This could involve creating new assessment tools or frameworks that more effectively capture the nuances of idea generation and the creative process.

7. Limitations

Here are some potential limitations of the study:

- **Sample Size**: With only 25 participants, the sample size may need to be more significant to generalize the findings to a broader population. This limited number of participants could result in less statistical power and may not accurately represent the diverse range of designers and innovators in the IoT field.
- **Participant Bias**: Since the participants include user experience designers, electronic product designers, and HCI students, the study might be biased towards individuals with specific expertise. This could limit the applicability of the findings to other groups, such as less experienced designers or professionals from different fields.

- **Short-Term Evaluation**: The study evaluates the impact of the toolkit in two sessions conducted four weeks apart. This relatively short time frame may not capture long-term effects or the learning curve associated with using the toolkit over an extended period.

The study focuses on a specific IoT-related challenge, which may limit the generalizability of the findings to other domains or types of design challenges. The toolkit's effectiveness might vary depending on the nature of the design problem being addressed. In conclusion, updating the IoT Tiles Inventor Toolkit with the latest insights from both literature research and primary research techniques is crucial. This ensures that the toolkit remains a valuable resource for designers in the dynamic field of smart home technology. The resulting toolkit will empower designers to create solutions that resonate with users, align with technological advancements, and meet the evolving standards and expectations of the smart product landscape.

References

[1] Rijsdijk, S. A., & Hultink, E. J. (2009). How today's consumers perceive tomorrow's smart products. *Journal of Product Innovation Management*, 26(1), 24-42.

[2] Ganvir Leeladhar. and C. P. Kalita. Adoption of Socio-Cultural Aspects in PSS Design for Smart Home Products: An Integrative Review. *Archives of Design Research*, 2022, 35(4), 7-29.

[3] Kurze, A., Totzauer, S., Deschamps-Sonsino, A., & Berger, A. (2019, December). A Collaborative Landscaping Exercise of IoT Design Methods. In *Proceedings of the 31st Australian Conference on Human-Computer-Interaction* (pp. 307-311).

[4] Christensen B. T. and Schunn C. D. The relationship of analogical distance to analogical function and preinventive structure: The case of engineering design. *Memory and Cognition*, 2007, 35(1), 29–38. https://doi.org/10.3758/BF03195939

[5] Ganvir, L., Kalita, P.C. (2023). Design Process of Smart Home Product Service System (SH-PSS) in Indian Context. In: Chakrabarti, A., Singh, V. (eds) Design in the Era of Industry 4.0, Volume 2. ICORD 2023. Smart Innovation, Systems and Technologies, vol 342. Springer, Singapore. https://doi.org/10.1007/978-981-99-0264-4_48

[6] Ganvir, L., & Kalita, P. C. (2023). Shaping Smart Home Product Service System (SH-PSS)Reflection Criteria Cards for Tiles Not Inventor Toolkit. *International Conference on Engineering & Product Design Education. E&PDE 2023*, Elisava Barcelona School of Design and Engineering. https://doi.org/10.35199/EPDE.2023.113

[7] Mora S., Gianni F. and Divitini M. Tiles: a card-based ideation toolkit for the internet of things. In *Proceedings of the 2017 conference on designing interactive systems*, 2017, pp. 587-598.

[8] Mora S., Gianni F., Nichele S., and Divitini M. Introducing IoT Competencies to First-Year University Students with The Tiles Toolkit. In *Proceedings of the 7th Computer Science Education Research Conference*, 2018, pp. 26-34.

[9] Gianni F., Mora, S. and Divitini M. Rapid prototyping internet of things applications for augmented objects: The tiles toolkit approach. In *Ambient Intelligence: 14th European Conference,* AmI 2018, Larnaca, Cyprus, November 12-14, 2018, Proceedings 14, pp. 204-220. (Springer International Publishing)

Fuzzy Systems and Data Mining X
A.J. Tallón-Ballesteros (Ed.)

doi:10.3233/FAIA241453

A Mobile Robot Arm for Providing Daily Support to Cantonese Speaking Elderly Persons

Chi-Yat Lau [a], Man-Ching Yuen [b, 1], Chi-Wai Yung [c], Tsz-Fung Wong [a], Ka-Keung Chan [a], Check-Hang Chow [a], Tsz-Him Ho [a], Hong-San Wong [d]
[a] *Department of Information Technology, Vocational Training Council, China*
[b] *Department of Digital Innovation and Technology, Technological and Higher Education Institute of Hong Kong, China*
[c] *Linux Foundation (Asia Pacific)*
[d] *R2C2 Limited*

Abstract. Many elderly need help to perform tasks around their home, such as grabbing their clothes and care takers can provide an assistant. The objective of this project is to utilize human language for controlling robot arm operations. Additionally, the robot will engage in interactions with humans through a large language model (LLM), enhancing its responses to be more human-like. Moreover, the robot arm will have the capability to discern various syntaxes in human language, allowing it to respond to commands in a manner akin to human speech. The project focuses on the robot arm's ability to respond to Cantonese (廣東話/粵語) input and execute basic robotic movements based on Cantonese commands. This prototype can help to develop a robot arm with more functions based on Cantonese commands.

Keywords. Large language model, LLM, robot

1. Introduction

1.1. Background and Motivation

Recently, elderly population increased globally, and more care takers are needed to provide daily supports to elderly. With the help of robot arm, elderly can perform a lot of tasks without others' help, such as grabbing objects. It is a good idea to have a robot arm which can understand elderly's verbal commands and perform tasks for them.

In recent years, products and software related to generative artificial intelligence have seen rapid development. Examples include ChatGPT and Midjourney. These large language models offer people significant convenience and access to a wealth of rich content, with very low threshold requirements. Furthermore, we found that large language models can act as a bridge between robots and humans that allow humans to

[1] Corresponding Author, Man-Ching YUEN. Technological and Higher Education Institute of Hong Kong, Hong Kong, China; E-mail: connieyuen@thei.edu.hk.

command robots by language, and robots able to understand our verbal command correspondingly. This finding brings innovative ideas to robot remoting aspects.

This project seeks an innovative approach to robotic remoting. We found that there are a series of issues with typical robotic controlling approaches like the long learning path to the robot controller, and the limited dexterity and precision of the human. Therefore, we tried to develop a robot-understandable translator to execute our command. To achieve this, we developed Integrate Advanced Natural Language Platform to translate our verbal language into robotic commands. Also, we developed a Seamless Voice-to-Text Conversion and communication platform to allow the controller to control the robot by speaking or texting respectively. We believe that this innovative approach can reduce the learning cost of robotic remoting and also be the most effective and the simplest way to control different types of robots.

1.2. Our Contributions

Our contributions in this project are shown as follows:

- **Integrate Advanced Natural Language Processing (NLP) with Robotics:** To combine cutting-edge NLP technologies, including OpenAI's Whisper and Breeze model, with robotic systems to create a user-friendly, voice-controlled robotic assistant.
- **Develop Seamless Voice-to-Text Conversion:** Utilize Whisper technology for efficient and accurate conversion of voice commands into text, ensuring the system can understand and process user inputs with high precision.
- **Enable Natural Language Understanding and Response Generation:** Leverage the capabilities of the Mistral model to ensure the robotic assistant can understand complex language structures and respond in a human-like manner, enhancing the interaction experience.
- **Create an Intuitive User Interface:** Design an interface that is easy to navigate and accessible for a wide range of users, regardless of their technical expertise or experience with robotic systems.
- **Ensure High Accuracy and Responsiveness:** Aim for a high degree of accuracy in voice recognition and response generation to minimize errors and misunderstandings in human-robot interaction.
- **Promote Accessibility and Usability:** Make the robotic assistant accessible to a diverse user base, including those with disabilities or limited technical knowledge, enhancing the inclusivity of the technology.

2. System Architecture of Voice-Controlled Robotic Assistant with Natural Language Interaction (VCRNI) Project

2.1. Overview of the Solution

The data product implementation for the Voice-Controlled Robotic Assistant with Natural Language Interaction (VCRNI) revolves around creating a smooth integrated system that inscoterprets natural language commands through large language models and translated them into actionable tasks for a robotic arm. Leveraging technologies like Whisper for speech recognition, GGUF-Mistral (GPT-Generated Unified Format-

Mistral) for natural language understanding, the solution aims to offer an intuitive and interactive experience. The system will be presented through a user-friendly web interface, providing real-time insights into LLM conversations, historical interactions, and a live feed of the robotic arm's actions.

In the context of the Voice-Controlled Robotic Assistant with Natural Language Interaction (VCRNI) project, the presentation and application of data involve several key components, such as voice input processing, text understanding, text generation, and real-time camera feed.

The project employs a series of sophisticated algorithms to translate human interaction into robotic actions seamlessly. The Voice-to-Text Conversion Algorithm is the first critical step in this chain. It involves capturing audio inputs, preprocessing them to reduce noise, and feeding the cleaned audio into the Whisper model for accurate transcription. The output is a refined text version of the user's spoken commands, ready for further processing. Next, it is the Command Processing Algorithm, which is central to the system's intelligence. It takes the transcribed text and utilizes Mistral to analyze and extract the user's intent. This algorithm maps the understood intent to specific robotic actions or responses, effectively translating human language into machine-understandable commands. Finally, the Robot Control Algorithm acts as the executor of these commands. It receives instructions from the natural language processing module and translates them into actionable messages or directives. This algorithm is responsible for the direct control of the robotic hardware, ensuring that the robot responds accurately to the processed commands. It also includes mechanisms for real-time feedback and action adjustment based on sensor data, ensuring a responsive and adaptive robotic assistant. Together, these data models and algorithms form the backbone of the VCRNI project, enabling it to deliver an unparalleled user experience in human-robot interaction through advanced natural language processing and robotic control technologies.

2.2. Real-time Camera Feed

Integrating real-time camera feed of the robotic arm into the web interface adds a visual element to the user experience. Users can observe the physical actions and movements of the robotic arm as it responds to voice commands. This can enhance the transparency and understanding of how the system interprets and executes commands in the physical environment. Figure 1 shows how the real-time camera feeds. First, we proceed to preprocess the chessboard to ensure that the robot arm can move within a legal range. This step involves marking out 126 positions on the chessboard, representing the areas where the robot arm can legally reach. While marking these positions, we also determine the necessary joint and angle information for each position for the subsequent control.

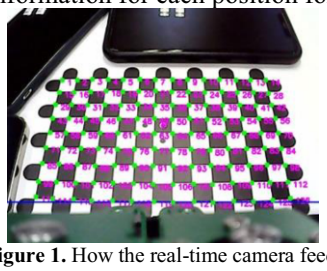

Figure 1. How the real-time camera feeds

Object modelling

Afterward, YOLO (You Only Look Once) v5 is utilized to train the target object, such as screws, tape and label the data through Roboflow. To enhance the flexibility and adaptability of the robot arm system, the combination of YOLO v5 and Roboflow enables quick and accurate detection of target objects in images.

Calculating Target Object Center Coordinates and Corresponding Joint Angles

The center coordinates of the target objects within the real-time camera are computed. Subsequently, distances between each target object and every point on the preprocessed chessboard are calculated using the Euclidean distance formula to determine the closest point to each object. This method ensures that identification of the most suitable points, accurately positioning the target objects on the image, with the corresponding joint and angles for the movement of the robot arm.

$$\text{Distance} = \sqrt{((x2 - x1)^2 + (y2 - y1)^2)}$$

2.3. Data Analytical Framework

Data Acquisition and Understanding

In data acquisition, the process of the LLM model for integration with a robotic arm begins with a comprehensive approach to data acquisition. This critical phase involves gathering a diverse array of textual data, including conversations, technical manuals, and user commands. Ensuring the inclusion of various linguistic styles, technical jargon, and everyday language is paramount. Additionally, the collection of voice data is crucial, especially for understanding nuances in spoken language. This may include recordings of user commands and dialogues. To customize the system for a robotic arm, it is essential to acquire contextual and environmental data, such as details about physical environments, types of objects interacted with, and typical user interaction scenarios. For data understanding, a thorough analysis of both text and voice data is conducted to unravel common language patterns, terminologies, and user intentions, essential for effective Natural Language Processing (NLP).

Data Models Training

The data flow diagram shown in Figure 2 illustrates a comprehensive process in the speech recognition system for controlling a robot arm. Start with human speech input, captured through devices like microphones. The recognized speech was recorded and resulting in the creation of an audio file. Subsequently, the audio file is subject to the prowess of the Speech-to-Text Conversion Model, specifically the Faster Whisper generating textual data [1, 2]. Whisper is an automatic speech recognition (ASR) system trained on 680,000 hours of multilingual and multitask supervised data collected from the web. Complementing this is the Natural Language Understanding and Generation Model, powered by Mistral. Anthony Alford [3] said that Mistral AI's Open-Source Mixtral 8x7B Outperforms GPT-3.5. The Mistral model's prowess in understanding and generating human-like language responses is key to creating an intuitive user experience. The pre-training of Mixtral is conducted using data sourced from the open web, incorporating a simultaneous training mechanism for both the experts and the router networks, thereby optimizing its performance across diverse tasks.

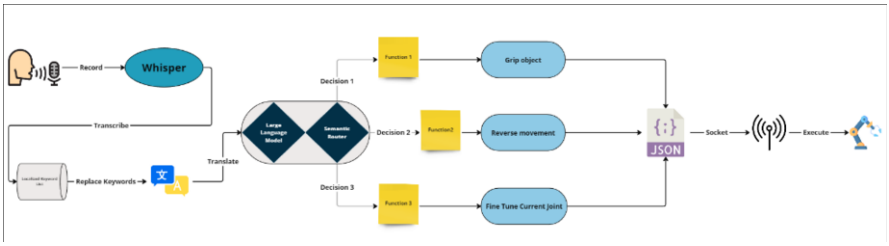

Figure 2. Speech-to-Command Processing for Robot Arm Control

Data Testing

Data testing focuses on evaluating the model's ability to accurately interpret and execute natural language commands in real-world scenarios. This would involve rigorous testing with diverse language inputs to ensure the robot's responses are appropriate and accurate. The paper may describe scenarios where the model's understanding of commands is tested, along with its ability to convert these commands into actionable tasks for the robot, emphasizing the importance of precision and reliability in human-robot interactions.

3. Hardware and Software Requirements

3.1. Hardware Requirements

Robotic arm as shown in Figure 3 is essential for executing precise movements and actions based on interpreted natural language commands. The arm should be compatible with integration into a networked system for seamless communication. Computer with GPU, the system requires a computer with GPU support for running the Mixtral-8x7B-Instruct Large Language Model (LLM). The GPU accelerates the model's learning process and ensures efficient real-time interpretation of natural language commands. Ideally with at least 12 GB of VRAM. Camera System which integrated cameras on the robotic arm and potentially on the computer facilitate real-time visual feedback. These cameras aid in monitoring the environment, contributing to precise robotic movements. This robotic arm is an ideal pilot test object.

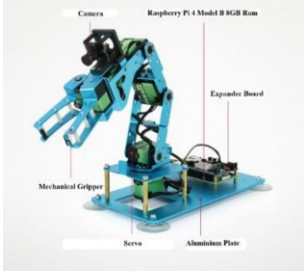

Figure 3. Robotic Arm

3.2. Software Requirements

Python serves as the primary programming language for the development of various components, including the integration of the robotic arm, implementation of the LLM model, and overall system development. LangChain Framework, as the language processing framework, plays a crucial role in interpreting and understanding user commands. It forms the backbone for processing natural language inputs and generating appropriate responses. Faster Whisper Speech-to-Text model is employed for speech-to-text conversion. This technology aids in accurately transcribing voice inputs, facilitating seamless communication between users and the robotic assistant. Socket programming is utilized for communication between the robotic arm, computer. This includes the transmission of commands, data, and feedback, ensuring a cohesive and responsive interaction.

4. Performance Evaluation

4.1. Object Detection and Joint Angle Retrieval System

To verify the functionality and accuracy of the object detection and joint angle retrieval system under various scenarios. In Figure 4, rotate the robotic arm to the left and verify if it accurately received command in natural language. Command is "向左轉" (Turn to the left). In Figure 5, rotate the robotic arm to the other size from the current position (Left) and verify if it accurately received command in natural language Command is "轉向另一個方向" (Turn to the other size). In Figure 6, test the system's ability to retrieve joint angles for gripping objects (Screw). Command is "握住最左邊的螺絲" (Grip the leftmost screw).

Figure 4. Turn Left Test

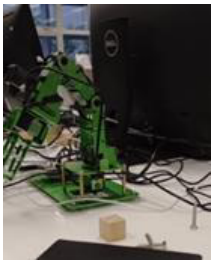

Figure 5. Turn to the other side Test

Figure 6. Object Gripping Test

4.2. Accuracy of Semantic Understanding facilitated by Semantic Router

The LLM will determine which tools and developed function will be utilized and extract parameters of target function with semantic router from the user instruction, enabling seamless integration and execution of the specified tasks [4]. Figure 7 shows the improvement of system robustness with semantic router. In Figure 8, the semantic router also represented a wise synonym understanding for comprehending the intent behind user's instructions.

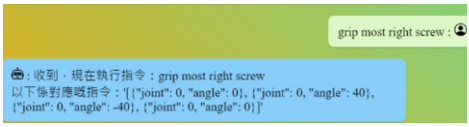

Figure 7. System Robustness in Syntactic Level

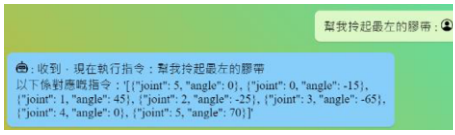

Figure 8. A wise synonym understanding for comprehending the intent behind user's instructions

4.3. Processing Time Comparison

Figure 9 clearly illustrates that the Faster Whisper Model showcases a significantly shorter processing time, completing its tasks in approximately 5 seconds. This remarkable reduction in processing time is a key performance metric. The performance metrics emphasize significant speed improvement, reduces processing duration with the Faster Whisper Model.

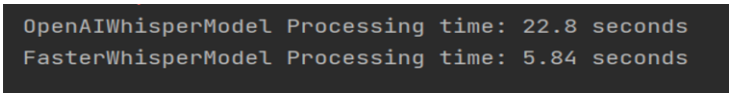

Figure 9. The quality versus inference budget tradeoff.

5. Conclusion

Throughout the implementation of the project, the process initiates with human language input and progresses to utilizing a large language model to determine the appropriate function for execution. Our system specifically targets Cantonese users, using Traditional Chinese as the main language. This specialization introduces substantial complexities in both the integration and operation of the large language model. A key aspect of the system is its ability to comprehend the semantic meanings of words and sentences, thereby avoiding misunderstandings and necessitating precise, strictly structured inputs. One target user group is Cantonese-speaking elderly, they can control the robot to complete some tasks for them in daily lives by verbal instructions. The cost of the robot arm is low and the robot is easy to set up and use. The robot is suitable for Cantonese-speaking elderly to use. Since there are many people who speak different dialects in Mainland China, we will build up a data model which can support other dialects and thus serve more users of different dialects in the future.

References

[1] Guillaume Klein et al. (2020, July). *Efficient and High-Quality Neural Machine Translation with OpenNMT* https://aclanthology.org/2020.ngt-1.25.pdf

[2] Guillaume Klein et al. (2023, Jan.). *SYSTRAN/faster-whisper: Faster Whisper transcription with CTranslate2.* GitHub. https://github.com/SYSTRAN/faster-whisper

[3] Anthony Alford. (2023, Jan 23). *Mistral AI's Open-Source Mixtral 8x7B Outperforms GPT-3.5.* InfoQ https://www.infoq.com/news/2024/01/mistral-ai-mixtral/

[4] Simonas Jakubonis et al. (2023, Nov 9). *aurelio-labs/semantic-router.* GitHub. https://github.com/aurelio-labs/semantic-router

Fuzzy Systems and Data Mining X
A.J. Tallón-Ballesteros (Ed.)

doi:10.3233/FAIA241454

Design and Research of Four-Axis Aircraft Control System Based on STM32F411

Yiqin BAO[a1], Wenbin XU[b] and Yulu BAO[c]
[a] *College of Information Engineering of Nanjing XiaoZhuang University, China*
[b] *Jiangsu United Vocational and Technical College Suzhou Branch, China*
[c] *Nanjing Shuangyun Intelligent Data Technology Co., Ltd, China*

Abstract. Four-axis aircraft is a type of aircraft with a simple structure and versatile applications. Compared to traditional fixed wing aircraft, four-Axis Aircraft have higher flexibility and can achieve takeoff, landing, hovering, and more precise aerial operations in different terrains. This article designs a four-Axis aircraft control system based on STM32F411, introduces the current research status of four-axis aircraft, the basic architecture and control principles of four-axis aircraft, provides a method for controlling the flight attitude of four-axis aircraft on the STM32F411 microprocessor platform, and analyzes and studies the algorithms and mathematical principles used in the control system.

Keywords. PID; four-axis aircraft; attitude control; microprocessor

1. Introduction

Now we have entered the era of the Internet of Things pandemic, from the Internet of Things to the intelligent connection of all things, four-axis aircraft have also entered the era of intelligence. Traditional four-axis aircraft are no longer able to meet market demand, and the intelligence of four-axis aircraft has become very important. The efficient operation and powerful functions of four-axis aircraft, combined with the intelligence of four-axis aircraft, will greatly promote the transformation of traditional industries[1]. The new demands generated by the intelligence of four-axis aircraft, such as emergency rescue, public safety and environmental protection, oil patrol and other vertical application fields, can greatly promote the upgrading of traditional industries.

At present, the quadrotor aircraft that exist both domestically and internationally are basically miniature unmanned aerial vehicles, generally divided into two types: remote-controlled quadrotor aircraft and autonomous flying quadrotor aircraft. The research and application of a standard and complete quadcopter control system is of great significance both in theory and in practice. Wang et al. [2] conducted research on the control system of quadcopters, Xia et al. [3] designed a voice controlled quadcopter based on STM32, Wu et al. [4] designed an obstacle avoidance control system for agricultural quadcopters, and Mao et al. [5] designed a quadcopter control system based on somatosensory interaction. However, the cost is relatively high and the stability is

[1] Corresponding author: Yiqin BAO, email: 392335241@qq.com

not enough.. This article designs a four-axis aircraft control system based on STM32F411, which has the characteristics of low cost, stable and reliable operation.

The rest of the paper is organized as follows. The second part designed the architecture of the four-axis aircraft control system. The third part focuses on real-time attitude control of four-axis aircraft. The fourth part tested the system. The fifth part summarizes the conclusion.

2. System architecture

The control board of the quadcopter is based on the STM32F411 microcontroller and is STM32 Dynamic Efficiency ™ Part of the series. Equipped with Cortex ®- The floating-point unit performance of the M4 core runs at a frequency of 100 MHz, while achieving extremely low power consumption in both run and stop modes. It has rich peripheral interfaces, including multiple timers, USART, SPI, I2C, USB, etc., supporting high-speed data transmission and communication. The features of STM32F411 include dynamic efficiency, low-power design, and a wide range of enhanced I/O and peripherals. It adopts a 90 nm process and has dynamic power consumption adjustment function. In operation mode, the current consumption is as low as 100μA/MHz, and in shutdown mode, the power consumption is as low as 10μA.

The control system architecture of the four-axis aircraft, as shown in Figure 1, mainly consists of three parts: 1) power circuit, 2) sensor circuit, and 3) communication circuit. The sensor circuit includes: gyroscope sensor and accelerometer, used for roll and pitch attitude recognition of the system, magnetometer for yaw angle data acquisition of the system, and barometer for altitude data acquisition of the system. The power supply circuit has implemented lithium battery charging and discharging circuit and USB power supply circuit respectively. The communication circuit consists of two parts: wired serial communication and wireless Bluetooth communication.

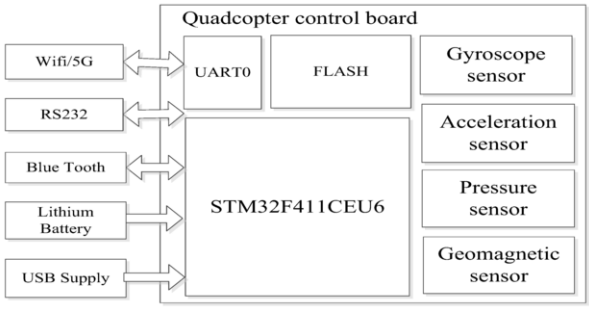

Figure 1. Architecture of four-axis aircraft control system

The system design mainly consists of two parts: the customer control end and the flight control board. The wireless data transmission adopts Bluetooth wireless module; The flight control board adopts a design that integrates control processing core and rack. The design of flight control board software mainly includes wireless data reception, attitude calculation, calculation of motor PID incremental control, and motor drive [4]. The entire four-axis aircraft system also includes the control end of the aircraft and the Bluetooth remote control end of the mobile phone. The reason why the remote control end uses Bluetooth communication is mainly because the mobile phone inherits the Bluetooth module, so users do not need to purchase an additional remote control, reducing product costs. The flight control board sends the collected data to the user's

mobile phone through a Bluetooth wireless communication module. The main job of the flight control board is to receive control signals through a low-power Bluetooth module, obtain real-time system acceleration and angular velocity raw data through IMU, and calculate the current attitude data of the system. Then, based on the error between the expected attitude sent by the user and the current true attitude, the PID increment is calculated. Finally, the motor is driven by PWM signal to adjust the speed to achieve stable flight of the aircraft.

3. Real-time attitude control of four-axis aircraft

To implement a four-axis aircraft control system, the focus is on real-time attitude control, which mainly includes five parts: 1) MPU9250 attitude sensor, 2) zero-bias error compensation, 3) Kalman filter algorithm, 4) AHRS attitude solution algorithm, and 5) cascade PID attitude control.

3.1 MPU9250 attitude sensor

The MPU9250 attitude sensor is a digital sensor based on the IIC bus communication protocol, which integrates accelerometers, gyroscopes, and magnetometers on-chip[5]. To read out the raw acceleration data and gyroscope data, it is necessary to first implement software IIC bus communication, and on this basis, drive the reading of three-axis acceleration and three-axis gyroscope raw data through IIC communication protocol.

IIC bus, also known as integrated circuit bus, is a serial communication protocol. The IIC bus communication consists of two lines: the synchronous clock signal line (SCL) and the data line (SDA). SCL is used to control the timing of communication and determine the effective read and write time of data bits, while SDA is used for data transmission between the master and slave devices.

Multiple IIC peripheral devices can be mounted on the bus of a host simultaneously, and different devices are distinguished by unique ID addresses. When reading and writing data to a specified device, the host first sends the ID address of the device to be communicated to the bus. If the slave receives its own ID address, it will send an ACK response signal. After receiving the response signal, the host indicates that communication has been established with the slave and can start reading and writing data. When reading or writing data, the host first sends the register address to be read or written, and then sends or receives data from the slave. At the same time, the effective time of the data bit on the data line is controlled by the timing signal sent by the host or slave. When the timing line is high, it indicates that the data is valid, otherwise the data bit is invalid. The communication principle of IIC bus is shown in Figures 2 and 3:

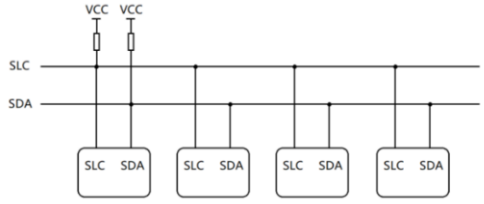

Figure 2. Schematic diagram of IIC communication bus

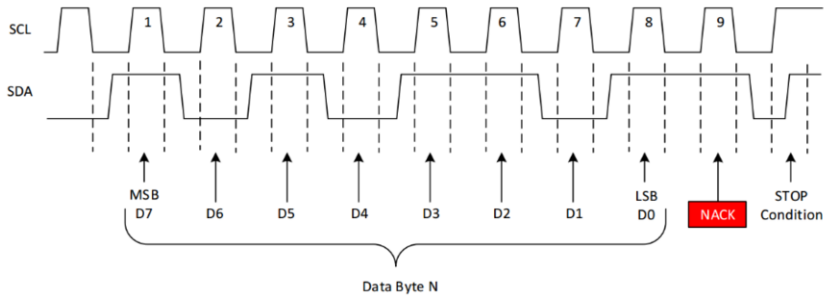

Figure 3. IIC communication bus timing diagram

By driving through the IIC bus, send a write request to the MPU9250 device address 0x71 to configure various registers of the MPU9250 attitude sensor, as shown below:

1) Set sampling frequency to 500Hz
2) Set the acceleration measurement range to ± 4g/LSB
3) The gyroscope range is ± 2000deg/LSB
4) The operating frequency of the low-pass filter is 42Hz

After initializing MPU9250, the sensor raw data can be obtained by reading the accelerometer register and gyroscope register. Then, the ADC voltage values are converted into specific three-axis acceleration gravity values (g) and three-axis gyroscope angular velocity values (deg/s) through precision conversion.

3.2 Zero-bias error compensation

Due to the influence of temperature, attitude sensors such as gyroscopes may experience drift errors, while accelerometers may experience static errors due to mechanical design issues. To eliminate these errors, the aircraft is placed on flat ground, and the flight control system will sample a large amount of attitude sensor data when powered on. The attitude angle at startup is taken as zero degrees, and the average value of the sampled data is taken as the zero-bias error. In this way, subtracting the zero-bias error from the actual data measured each time will result in relatively accurate data.

3.3 Kalman filter algorithm

During the flight of a quadcopter, the high-frequency vibration generated by the motor rotation causes severe noise interference to the accelerometer. To filter out these noises and obtain accurate acceleration data, filtering algorithms must be used to process the data. There are three commonly used filtering algorithms: 1) sliding window filtering, 2) first-order complementary filtering, and 3) Kalman filtering algorithm [6]. The Kalman filter algorithm has extremely high accuracy and dynamic tracking characteristics. It solves the filtering problem of linear systems through recursive methods, with small computational complexity and simple logic.[7]. The following will provide a detailed introduction to the formula and principle of the Kalman filter algorithm.

1) Prior estimation, as shown in formula (1):

$$P_x = P_{x-1} + Q \tag{1}$$

.P_x is the Kalman estimation value, $P_{x-1}$is the previous Kalman estimation value, and Q is the process noise of the Kalman filtering algorithm system, indicating the level of trust in the Kalman estimation.

2）Kalman gain, as shown in formula (2):

$$K_x = \frac{P_x}{P_x+R} \tag{2}$$

K_x is the Kalman gain, indicating the level of trust in the actual measured value. The larger the Kalman gain, the more trusted the measurement value. R is the measurement noise of the system, indicating the magnitude of the measurement error.

3) The optimal estimate, is shown in formula (3):

$$E_x = E_{x-1} + K_x(Z_x - E_{x-1}) \tag{3}$$

E_x is the optimal estimate at the current time, and E_{x-1} is the optimal estimate at the previous time. $Z_x$is the actual measurement value at the current time, which is the data actually measured by the sensor.

4) The posterior estimation, is shown in formula (4):

$$P_x = (1 - K_x) \times P_x \tag{4}$$

Since K_x represents the level of trust the system has in the measured values, $1 - K_x$ represents the level of trust the system has in the Kalman estimation values. This weight control is used to update the Kalman prior estimation values for the next time step.

3.4 AHRS attitude solution algorithm

Attitude calculation is the core of the entire four-axis aircraft control system and the most important module in the system. For attitude solving algorithms, the accuracy and execution speed of the algorithm are the core standards for measuring attitude solving algorithms. Only by calculating accurate aircraft attitude data can accurate flight control performance be guaranteed.

The AHRS attitude calculation algorithm is based on the three-dimensional body attitude represented by quaternion rotation. Quaternions are represented by trigonometry, and a differential equation for time is constructed using angular velocity data output from gyroscope sensors. Quaternions are updated and Euler angles are inversely solved. In order to compensate for the integral drift error generated by the gyroscope in the algorithm, the angle error between the three-axis vectors is expressed by cross multiplying the measured vector of the accelerometer and the theoretical gravity vector, and this error is applied to the actual three-axis gyroscope measurement data through the PI compensation algorithm.

3.5 Cascade PID attitude control

The cascade PID algorithm is an extension of the PID control algorithm, suitable for systems with complex dynamic characteristics. It connects one PID controller in series with another PID controller to achieve better control performance. The cascade PID algorithm is commonly used to control systems with dual feedback loops, where the internal PID controller controls fast dynamic response and the external PID controller controls slow dynamic response. The advantage of this algorithm is that it can improve the stability and response speed of the control system, reduce steady-state errors, and

also handle nonlinear and time-varying systems. The basic principle of the cascade PID algorithm in the control system of a four-axis aircraft is shown in Figure 4:

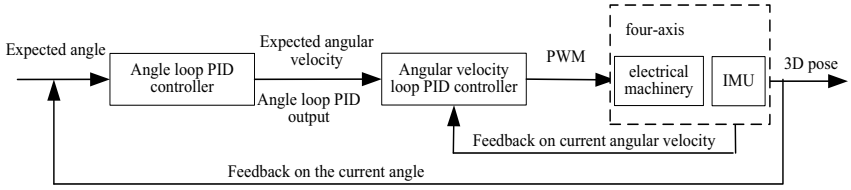

Figure 4. Principle schematic diagram of cascade PID

In the cascade PID principle, the outer loop input is the desired angle, and the data comes directly from the Bluetooth remote control of the mobile phone. The coordinates of the virtual joystick in the APP are mapped to roll and pitch angle control angles, which are directly input into the outer loop controller of the cascade PID. The outer loop controller only has P parameters, namely proportional parameters. The error between the expected angle and the actual posture angle of the body is amplified and used as the output of the outer loop. The angle error data is mapped to desired angular velocity data and input into the inner loop angular velocity controller. The inner loop angular velocity controller contains two parameters, PD. The inner loop directly controls the PWM output to control the motor rotation and generate lift based on the expected angular velocity data and actual angular velocity data. The attitude sensor of the aircraft system then feeds back the three-axis angular velocity to the inner loop, and feeds back the three-axis attitude angle to the outer loop to form a closed-loop control. The PID control algorithm is a commonly used automatic control algorithm, whose main function is to adjust the control quantity based on the system's error signal, in order to achieve the goals of system stability, accuracy, and response speed. In this system, incremental PID is used for attitude control. The PID control algorithm formula is shown in formula 5:

$$\mathrm{Out} = \mathrm{K_p} * \mathrm{e(t)} + \mathrm{K_i} * \int_0^t \mathrm{e(t)dt} + \mathrm{K_d} * \frac{\mathrm{de(t)}}{\mathrm{dt}} \tag{5}$$

The proportional term coefficient $\mathrm{K_p}$ control parameter adjusts the control quantity based on the magnitude of the error signal, the integral term coefficient $\mathrm{K_i}$ control parameter adjusts the control quantity based on the duration of the error signal, and the differential term coefficient $\mathrm{K_d}$ control parameter adjusts the control quantity based on the rate of change of the error signal. According to the PID output formula, the three output parameters are multiplied by the three-axis modulation coefficients $\mathrm{K_p}$, $\mathrm{K_i}$, and $\mathrm{K_d}$ respectively and accumulated for output. $\mathrm{e(t)}$ is the calculation error.

4. System testing

After completing the software and hardware of the four-axis aircraft control system, it is necessary to test the system. The programming software is downloaded to the flight control board through the ISP serial port, and the flight control board is installed on the rack for testing. After the installation of the four-axis aircraft is completed, the physical image is shown in Figure 5:

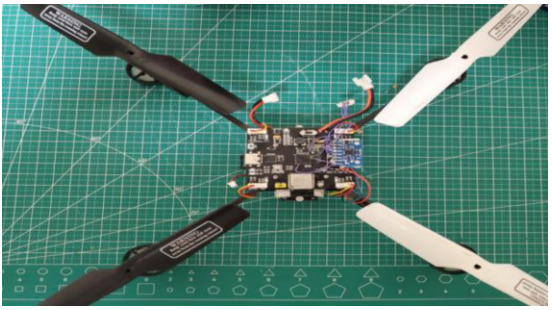

Figure 5. Installation diagram of four-axis aircraft

After completing the installation of the four-axis aircraft, power on the system, open the Android Bluetooth wireless control app, and it will automatically search for the aircraft's Bluetooth broadcast and connect automatically. After successful connection, users can use the virtual joystick on the left side of the app to control the pitch and roll movements of the aircraft, that is, to control the forward and backward movement and left and right flight of the aircraft. The air spin of the aircraft can be controlled through the left and right rotation buttons. The basic speed of the aircraft propeller can be controlled through the throttle button. After debugging, when the throttle value is greater than 500, the aircraft will overcome its own gravity and take off. The remote control debugging of the aircraft is shown in Figure 6:

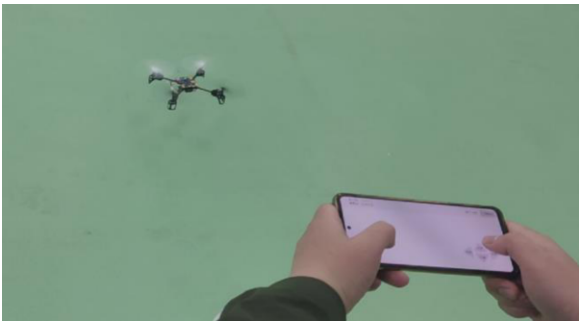

Figure 6. Remote control test of four-axis aircraft

During the debugging process, this system encountered many problems and spent a lot of testing time. After the flight control software design is completed, conduct attitude control tests on the four-axis aircraft using an Android Bluetooth remote control. After repeated debugging and optimization iterations. The smooth and reliable operation of the four-axis aircraft control system was ultimately achieved.

5. Conclusions

This article introduces the basic architecture and control principles of four-axis aircraft, including sensor data acquisition, attitude control, and flight control. The mathematical principles of the Kalman filter algorithm were explained in the data filtering section. And combined with practical problems, analyzed and used filtering algorithms to solve the problem of attitude data jitter during motor start-up. In the attitude control section, the force analysis of the quadcopter under different attitudes is first conducted, and

cascade PID control is introduced to describe the workflow of cascade PID control. Finally, the debugging process of the quadcopter was described, and the problems that occurred during the debugging process were analyzed and discussed. Possible problematic links were speculated, and solutions were proposed and optimized iteratively. In future work, we will further optimize the attitude control of quadcopters to improve reliability and stability.

References

[1] J. Gordon Leishman. The breguet-richet quadrotor helicopter of 1907[J]. Vertiflite, 2002, 47(3): 582-586.

[2] Wang Zengcai, Xu Li, Liu Qi. Research on the Control System of Four Axis Aircraft [J]. Digital World, 2018 (4): 1.

[3] Xia Yuanzhan, Zhang Lincheng, Chen Jiajun. Design of speech controlled quadcopter based on STM32 [J]. Information and Computer, 2022 (010): 034

[4] Wu Chunyu. Design of obstacle avoidance control system for agricultural quadcopter - based on machine vision and ultrasonic ranging [J]. Agricultural Mechanization Research, 2022, 44 (4): 5

[5] Lukai Mao, Xianglian Xu, Mengqiang An Chenhu Luo and Wei Zhou, Design on four-axis aircraft control system based on Somatosensory interaction,2019 IOP Conf. Ser.: Mater. Sci. Eng. 569 04205.

[6] Zouari F , Boubellouta A .Neural Approximation-Based Adaptive Control for Pure-Feedback Fractional-Order Systems With Output Constraints and Actuator Nonlinearities[J]. 2018.DOI:10.4018/978-1-5225-5418-9.ch015.

[7] Huang Chuanxiang. Design of Multi Axis Aircraft System Based on STM32 [J]. Wireless Interconnection Technology, 2023, 20 (3): 46-50.

Fuzzy Systems and Data Mining X
A.J. Tallón-Ballesteros (Ed.)

doi:10.3233/FAIA241455

Some Brief Considerations on Computational Statistics Effectiveness and Appropriateness in Natural Language Processing Applications

Mario MONTELEONE [a] and Alberto POSTIGLIONE [b,1]

[a] *Department of Political Sciences and Communication (DiSPC), University of Salerno, ITALY*

[b] *Department of Business Sciences - Management & Innovation Systems (DISA-MIS), University of Salerno, ITALY*

ORCiD ID: Mario Monteleone https://orcid.org/0000-0002-9829-4275, Alberto Postiglione https://orcid.org/0000-0001-6411-6529

Abstract. This paper addresses the challenges of managing and processing unstructured or semi-structured text, particularly in the context of increasing data volumes that traditional linguistic databases and algorithms struggle to handle in real-time scenarios. While humans can easily navigate linguistic complexities, computational systems face significant difficulties due to algorithmic limitations and the shortcomings of Large Language Models (LLMs). These challenges often result in issues such as a lack of standardized formats, malformed expressions, semantic and lexical ambiguities, hallucinations, and failures to produce outputs aligned with the intricate meaning layers present in human language.

As for the automatic analysis of linguistic data, is well known that Natural Language Processing (NLP) uses two different approaches, coming from diverse cultural and experiential backgrounds. The first approach is based on probabilistic computational statistics (PCS), which underpins most Machine Learning (ML), LLMs, and Artificial Intelligence (AI) techniques. The second approach is based, for each specific language, on the formalization of morpho-syntactic features and constraints used by humans in ordinary communication activities. At first glance, the second approach appears more effective in addressing linguistic phenomena such as polysemy and the formation of meaningful distributional sequences or, more precisely, acceptable and grammatical morpho-syntactic contexts.

In this paper, we initiate a scientific discussion on the differences between these two approaches, aiming to shed light on their respective advantages and limitations.

Keywords. Natural Natural Language Processing, Rule-Based Natural Language Processing, Probabilistic Computational Statistics, Large Language Models, Statistical Natural Language Processing, Machine Learning, Formal Semantics.

[1]Corresponding Author: Alberto Postiglione, DISA-MIS, University of Salerno, ITALY, ap@unisa.it.

1. Foreword

This paper addresses the multifaceted challenges of processing and managing unstructured or semi-structured text, especially given the rapid increase in data volumes that traditional databases and algorithms struggle to handle effectively in real-time scenarios. Unlike structured data, which is systematically organized in databases or spreadsheets, unstructured and semi-structured data lack a consistent organizational framework.

Unstructured text data, which constitutes the vast majority of digital information, includes a wide range of documents such as books, scientific publications, news articles, web content, Word documents, and PDFs. This type of data lacks a predefined schema, making it challenging to process with conventional data analytics methods. On the other hand, semi-structured text contains elements of both structured and unstructured data. It often features irregular formats like XML or JSON, which complicates analysis due to variations in schema and content representation.

According to various estimates, over 80% of global data is unstructured or semi-structured [1,2]. The rapid advancements in Big Data technologies [3,4,5,6,7,8,9], alongside the growing adoption of the Internet of Things (IoT) [10,11,12,13,14,15,16] and Industrial IoT (IIoT) [17,18,19,20,21,22], have contributed to a massive explosion of textual data. The proliferation of interactive technologies like chatbots has further amplified this data surge [23,24,25,26]. In general, various types of data found on the web, such as emails, HTML and CSS files, social media posts, news, and blogs, are practically indestructible, rarely disappearing from the web. This data often presents significant redundancy and grows in a non-linear manner [27,28,29,30,31]. The volume of unstructured medical data is also increasing at an astonishing rate [32,33,34,35,36]. The research community contributes significantly to this growth, with a continuous rise in the number of scientific papers and the proliferation of accredited journals and conferences [37,38,39,40]. Furthermore, global governmental initiatives aimed at reducing paper-based documentation have bolstered this trend. Additionally, the Deep Web, which contains trillions of unindexed documents, significantly adds to the volume of text-based data.

The current landscape of unstructured and semi-structured data aligns with the defining characteristics of Big Data, notably in terms of volume, variety, lack of standardization, and continuous generation. Traditional databases and conventional algorithmic approaches are often inadequate to handle this vast and complex data, particularly in real-time processing scenarios. This challenge highlights the pressing need for advanced data management and analysis techniques, such as Natural Language Processing (NLP), to effectively store, manage, and extract value from this expanding data landscape. The key issues involve:

Lack of Standardized Formats The diversity of formats in unstructured and semi-structured text presents a significant challenge. Data sources range widely from user-generated content on social media and emails to technical documents and logs, each with its own unique format, syntax, and structure. This heterogeneity complicates the preprocessing and parsing stages, making it difficult to extract relevant information uniformly. Techniques such as data normalization, schema matching, and document classification are essential to address this variability, enabling a more consistent and standardized representation of the text.

Malformed Expressions and Noisy Data Text data frequently contains errors such as typos, grammatical mistakes, and incomplete sentences, especially in user-generated content. For instance, social media posts and product reviews often include informal language, slang, and emojis, which introduce noise into the data. This noise can significantly degrade the performance of NLP models, particularly those relying on rule-based methods or shallow machine learning techniques. Robust text-cleaning methods, such as spell-checking, grammatical corrections, and noise filtering, are necessary to enhance the quality of the input data for subsequent analysis.

Semantic and Lexical Ambiguities Semantic ambiguity occurs when a sentence or phrase can be interpreted in multiple ways. For example, the sentence "The chicken is ready to eat" is difficult to interpret (the chicken could be a meal to be eaten, or a live animal ready to eat), due to its ambiguous syntactic structure. Similarly, lexical ambiguity arises when a word has multiple meanings (polysemy) or when different words have similar pronunciations or spellings (homonymy). Addressing these ambiguities is critical for tasks such as word sense disambiguation (WSD), which aims to assign the correct meaning to a word based on its context, and named entity recognition (NER), which seeks to identify and classify proper nouns into predefined categories such as people, organizations, or locations.

Hallucinations An artificial hallucination occurs when an LLM-type AI, during the generation or summarization of a text, in relation to specific knowledge, randomly produces illogical, imprecise, contradictory or false information. AI hallucinations also occur during text generation, specifically when in terms information completeness and organicity, the texts produced do not respect the seven constitutive traits defined by De Beaugrande and Dressler [41] and fundamental for the recognition of a text as such. These traits are coherence, cohesion, intentionality, acceptability, informativeness, situationality, and intertextuality.

Complex Meaning Levels in Human Language Human language is inherently complex, encompassing multiple layers of meaning, including literal, figurative, and contextual interpretations. To understand this complexity, computational systems must capture not only surface-level syntax and semantics but also deeper, pragmatic meanings. Figures of speech such as metaphors, idioms, and sarcasm add an additional layer of difficulty, as their deeper meanings often diverge from their literal interpretations. Advanced NLP techniques, such as transformer-based models (e.g., BERT [42,43], GPT [44,45]), have shown promise in capturing contextual nuances by learning rich representations of words in different contexts, but they are far from having satisfactorily solved this challenge. Accurately interpreting figurative language and resolving deep semantic ambiguities thus remain open challenges in the field of NLP research.

Real-Time Processing of High-Volume Text Data With the exponential growth of data generation from sources like social media, sensor logs, and customer interactions, real-time processing of text data has become increasingly challenging. Traditional NLP models and database systems often fall short due to their limited scalability and inability to handle large datasets with low latency. Modern approaches leverage streaming data frameworks (e.g., Apache Kafka [46,47], Apache Flink [48]) along with real-time NLP pipelines, employing techniques like incremental parsing and online learning to efficiently process continuous data flows. Additionally,

cloud-based solutions and distributed architectures are utilized to manage the computational load, enabling scalable and responsive text processing systems.

Adopting a Semantic-Centered Approach Given these challenges, adopting a semantic-centered approach is essential for improving text processing and understanding. This approach emphasizes leveraging linguistic principles, such as identifying multi-word units (MWUs) and understanding their compositional meanings, to extract more accurate and semantically rich information from text. Finite automata ([49]) can be employed effectively to recognize specific patterns and MWUs within the text ([50,51,52]. Furthermore, integrating ontologies provides a structured framework for assigning knowledge domains and resolving ambiguities by linking textual elements to predefined concepts and relationships. This combination enhances the system's ability to capture the underlying meaning and context of the text, facilitating more effective natural language understanding and information retrieval.

While humans can effortlessly interpret and navigate these complexities using cognitive skills and contextual understanding, these tasks present significant challenges for computational systems.

As is known, there are currently two different approaches to Natural Language Processing (NLP), one based on the use of Computational Statistics (CS), on which Machine Learning (ML) is largely based; the other on the formalization of the morphosyntax of each language. In this study, we intend to analyse as objectively as possible the differences between these two approaches, as well as the strengths and weaknesses of both, as regards the structuring of the analysis and the application of tools and routines. Already in this preliminary phase of the study, it is evident that both the approaches we are about to investigate are based on the analysis of word combination, interconnection, governance and co-occurrence. This means, or at least should mean, that to perform NLP analyses, both approaches may make use of sets of formal rules and descriptions built on exhaustive descriptive linguistic resources. As we shall instead see, only the formalizing morphosyntax approach (which is the base for Formal Semantics (FS)) manifests and exploits this attention to the specific characteristics of natural language. On the contrary, CS mainly looks at words as simple sequences of signs delimited by two blank spaces and very often is unable to provide any precise and beyond question linguistic classification of them. That is, in its applications, CS mainly uses lists of words elaborated and tagged automatically, which often turn out to contain many inaccuracies. Therefore, we take the liberty of anticipating here that we are more inclined to place greater value on those linguistic resources made manually by qualified linguists, rather than on those elaborated by means of statistical or (supposed) algorithmic methods. To endorse such choice of ours, in the following page we will give specific examples, directly linked to the linguistic quality of any of the analytic procedures we will evaluate.

2. Machine-Learning vs. Grammar Engineering

As for the already mentioned two NLP methodologies, in Fig. 1 we give the most important pros and cons[2].

[2] *https://www.linkedin.com/pulse/pros-cons-two-approaches-machine-learning-grammar-engineering-wei-li/*, last accessed 2023/03/22.

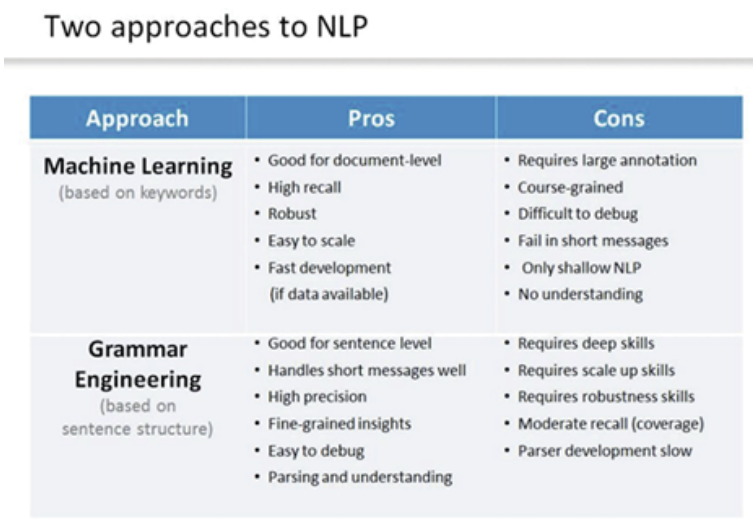

Figure 1. Two Approaches To NLP

These pros and cons help us deducing which is the most important methodological and functional difference between the two methods. Actually, ML is essentially statistical: it explores and processes linguistic data as Markov Chains [53]. This means that the concatenation of words is inferred on a probabilistic basis, i.e., without resorting to the application of specific formalized morphosyntactic rules. For this reason, ML is referred to as ruleless, or Statistical/Stochastic Natural Language Processing (SNLP). On the contrary, Grammar Engineering (GE) results to be [54]: "the creation of linguistically motivated electronic grammars is a key aspect of natural language processing (NLP). These grammars, developed within theoretical frameworks like the Lexicon NLP method by Maurice Gross [55,56,57,58], provide detailed descriptions of natural language. Initially focused on syntax, how sentence components relate, these grammars now also encompass functional structure (FS) information. This precise grammar engineering supports natural language understanding and generation, proving essential for applications such as textual entailment, dialogue systems, and machine translation".

For these reasons, GE is referred to as rule-based NLP. In the following pages, we will see how and how much the difference here outlined between SNLP and rule-based NLP, together with the adoption of one of the two methods, are decisive for the successful processing of linguistic data. Above all, we seldom may experience how the statistical/stochastic approach, in its non-specificity, often produces imprecise and non-reusable results, failing to reach deep and well-structured levels of linguistic analysis.

2.1. Statistical Natural Language Processing

In broad terms, Statistics (STAT) [59] can be defined as a set of scientific methods aimed at the quantitative and qualitative knowledge of collective phenomena through the collection, sorting, synthesis and data analysis. In other words, STAT is supposed to be a tool that translates information into knowledge. It studies collective phenomena (observation of a set of individual manifestations), in order to obtain information, describe a

phenomenon, and identify relationships. Hence, in a positive perspective, we could say that STAT has the advantage of being applicable to all domains from which it is possible to collect and store data. At the same time, but in a negative perspective, we could say that STAT is a non-specific discipline: although equipped with refined calculation tools, in fact STAT is applicable in the same way to very different sectors and domains, such as for example weather forecasts or the average kilos of apples consumed annually by the inhabitants of a given city. Among the various sets to which STAT can be applied, there are therefore also those that have already well identified and established their structural, productive, and iteratively-applicable rules, such as for instance morphology, syntax and sentence semantics.

As for SNLP [59], it aims to perform Statistical Inference (SI) for the field of natural language. SI in general consists of taking some data (generated in accordance with probability distribution) and then making some inferences about this distribution. In this sense, the current trend is to base SNLP on the use of Large Linguistic Models (LLMs)[60]. The results obtainable by means of this tool remain controversial: in fact, although they exponentially increase the quantity of "examples" on which to statistically base the analysis, at the same time they increase also all potential analysis errors. It also to consider the possibility of "manipulating" the responses obtainable from (alleged) Generative Artificial Intelligence systems based on LLMs. For example, we might look at lots of instances of prepositional phrase attachments in an English corpus and use them to try to predict, in general, prepositional phrase attachments for English. In this sense, the task of language modeling[3] is fundamental to speech or optical character recognition, and is used also for spelling correction, handwriting recognition, and statistical machine translation. At first glance, SI definition seems to encompass some controversial aspects, which may lead to possible methodological and applicative limits, especially when natural language is the object of the analysis. We will deal with these aspects in detail in the following pages. For now, we essentially want to highlight how natural language data are to be analysed necessarily distinguishing at least three descriptive levels phonetic-phonological, morphosyntactic, semantic of the sentence each of them having their specific usage rules and also having, among them, points of extreme contiguity, together with others of strong differentiation. Actually, it is not possible to define natural language as a completely heterogeneous or homogeneous set of items, nor can it be studied based on such an assumption. On the contrary, it is possible to state that in its entirety, the study of natural language seems to need the adoption of "quantum" inferential functions, which are extremely different from and more fine-grained than those offered by SI. As well, the previous definition of SNLP also calls into question, albeit indirectly, the already mentioned Markov Chains, in the point in which it refers to the classic task of language modeling, where the problem is to predict the next word given the previous words. However, what does not seem to be coped with in this definition is the fact that natural language can be studied as an autonomous element, i.e., by means of its specific idiosyncrasies. As is known, in each given language, correct word concatenations are not subject to probabilistic laws: there are specific linguistic use rules to validate and govern them. Such rules exist outside and before any text or linguistic dataset, in which these same rules must always find correct application[4]. Without these rules, no idiom could be

[3]Here, the problem is to predict the next word occurrence, given those of previous words.

[4]Yet, sometimes, linguistic datasets, including LLMs, offer imprecise readings and applications of these linguistic usage norms.

written, spoken, or understood. Therefore, the previous definition of SNLP leaves room to several doubts, which are:

(a) Is it correct that SNLP tries to model natural language without comprehending its internal dynamics in detail? I.e., is SNLP suitable concretely for language modelling? Can SNLP really produce inferences about natural language?
(b) Is SNLP not too dependent on the data it observes, while it ignores the dynamics of those data that escape its observation, or which it does not observe with the correct approach?
(c) Finally, natural language is by its nature ambiguous, that is, its concatenations of words often lend themselves to having more than one acceptable meaning. Is SNLP suitable to deal with natural language ambiguity? Is it sufficient for SNLP to analyse a vast amount of linguistic data[5] in order to produce a scientifically precise prospect of how natural language works? Should it not analyse all possible word combinations?

2.2. *Contextual Inference vs. Statistical Inference*

In the previous paragraph, regarding the definition of SNLP and, essentially, with reference to ML, we encountered the term "statistical inference", which lexically, semantically, as well as in relation to the study of logic, is opposed to that of "human inference". As is known, human inference is an associative procedure through which, starting from a certain premise or from the observation of a fact, our mind draws one or more consequences, or elaborates one or more judgments. However, the question about how our minds concretely make inferences remains yet unresolved. Along with the problem of accurately establishing the difference between simple perception and inference or cognition, it is not yet clear whether:

- our mind produces inferences via the "specialized modules" postulated by Fodor[6]; or
- inference is:
  - a behaviourist process, as argued by John Watson[7];
  - a reductionist procedure connected to the theory of identity, as maintained by Bronisaw Malinowski[8];
  - a connectionist and computational operation, as indicated by Hilary Putnam[9].

What is certain is that humans use inference to solve problems, as well as to make choices, and that often inferences may even occur within not completely "controlled levels" of the human brain (to simplify, we could say within unconscious or subconscious levels). Therefore, human inference appears to be a procedure classifiable as a crucial part of the problem-solving domain. Besides, what seems more plausible is that the inferential procedures of the human mind tend to be non-deterministic, i.e., not always following

[5] As it happens for instance today with Large Linguistic Models.
[6] $https://plato.stanford.edu/entries/modularity-mind/$.
[7] $https://www.ufrgs.br/psicoeduc/chasqueweb/edu01011/behaviorist-watson.pdf$.
[8] $https://anthropology.ua.edu/theory/functionalism/$.
[9] $https://plato.stanford.edu/entries/computational-mind/$.

the binary logic "0 vs. 1", nor that of the consequential variables of the "if ... then" type. Rather, it seems that our inferential procedures contemplate, at least in an initial state, multiple resolutions to a given problem, and that it then arrives at the solution, or choice, based on a computational process, which includes certain possibilities, and excludes others, until it finds the (hypothetically) right one. It would therefore look more like a quantum decision-making process, initially structured as a finite-state automaton, which tends to drop its paths when they are no longer useful. Always intuitively, we can say that inferential processes, including especially those related to natural language, are strictly dependent on the functioning of our cerebral or biological networks. These networks are made up of closely interconnected neurons, and among other, they allow us to reason, make calculations in parallel, recognize sounds, images and faces, or learn how to take specific actions. In practice, they actively allow our mind to "express its intelligence". Thanks to complex organizations of nerve cells that have different "tasks", such as perception of the environment, recognition of stimuli, and so on, a cerebral neural network works through the reception of data and signals internal and external as well as through sensory perceptions. These "become" information and knowledge through an impressive number of biological units, our neurons, which represent the computing capacity of our brain. Neurons interconnect with each other in a non-linear structure that responds to external data and stimuli. A cerebral neural network, therefore, presents itself as an "adaptive" system capable of modifying its structure, in response to both internal and external data, perceptions, experiences, and information[10]. Moreover,

"The brain consists of seven main networks at a high level: the sensorimotor system, visual system, limbic system, central executive network (CEN), default mode network (DMN), salience network, and dorsal attention network (DAN). While some of these networks can function independently, many complex cognitive functions arise from interactions among them. A more detailed examination reveals specific subnetworks dedicated to particular tasks, often involving components from multiple main networks. Notably, the Language network has significantly evolved since the Broca-Wernicke model, now incorporating a newly identified area, 55B, which is linked to muscle control during speech production[11]."

Hence, it seems almost certain that all natural language produced by human beings is the result of a series of inferences, supported by a specific cerebral neural subnetwork, which, in turn, interacts with other neural networks and subnetworks. It also takes into account and complies with the specific idiosyncrasies of the language in which a human being wants to express himself, i.e., its phonetics and phonology, as well as its morphosyntax and semantics. This procedure, that we may call Human Linguistic Inference (HLI), is therefore contextual: in each language, it produces acceptable utterances thanks to its interaction with all certified governance and co-occurrence relationships between words inside word groups, propositions, and sentences. Recalling the definition of SI given in the previous paragraph and comparing it to the one about human inference and contextual HLI, we can single out straightforwardly important differences, both methodological and structural.

[10] *https://www.biorxiv.org/content/10.1101/2021.07.15.452445v1.full*.
[11] *https://www.o8t.com/blog/brain-networks*.

Besides, it is worth stressing that among the tools and routines used in SI and SNLP, we find also Artificial Neural Transition Networks Transition (ANTN), more commonly called Artificial Neural Networks (ANNs). From the Web[12], we read that

"Artificial Neural Networks (ANNs) are computational models inspired by the human brain, using interconnected artificial neurons to simulate information processing. These neurons are connected through adjustable weights, allowing the network to learn by detecting patterns in data. ANNs can perform tasks such as classification, regression, and forecasting, and deep neural networks (DNNs), with multiple hidden layers, allow for more complex data processing. While neural networks have been around for years, advancements in hardware like GPUs have made them faster and more practical for large datasets. ANNs are now applied in a wide range of areas, including image processing, NLP, healthcare, and recommendation systems, demonstrating impressive performance in detecting patterns and making predictions".

From this (perhaps excessively) enthusiastic definition, it is possible to extract some points of discussion which, at first sight, arouse perplexity. The first point is the one associating the functioning of ANNs to that of cerebral or biological neural networks. At first glance, the association seems not only risky, but also devoid of effective evidence. In fact, we still know little about the functioning of the human brain, which we cannot yet fully study during its ordinary functioning. This is because there are still no adequate observation tools that can taxonomically describe its activities, also in terms of element and part interconnections. Besides, among humans ones, the brain is most delicate organ, i.e. it is not possible to carry out "open-brain" studies, as for example it is possible with the human heart. In http://www.thehighestofthemountains.com/images/thehighestofthemountains_brain_map_brainwithquotes28-125px.jpg you find a simplified description of human brain structure.

As for the previous definition on ANNs, a second perplexity arises from those passages in which sketches are given about how a biological neural network would work. These passages seem inspired by [61], in which we read that "Neurons are the basic building blocks of the nervous system, responsible for information processing and communication in animals. They consist of a centralized cell body and two types of processes axons and dendrites that connect to one another." Actually, a more convincing explanation on how biological neural networks work, and how they may help in predicting mammals behaviour, including humans, is available on Web[13]. It is supported by a 3D animation, and specifically testifies how "a group of Harvard University neuroscientists and Google engineers released the first wiring diagram of a piece of the human brain. The tissue, about the size of a pinhead, had been preserved, stained with heavy metals, cut into 5,000 slices and imaged under an electron microscope. This cubic millimetre of tissue accounts for only one-millionth of the entire human brain. Yet the vast trove of data depicting it com prises 1.4 petabytes worth of brightly coloured microscopy images of nerve cells, blood vessels and more". Also, it states that "this approach is leading to impressive progress in understanding these animals". No mention is made regarding the possibility of replicating, even summarily, the functions of this wiring diagram. In practice, no comparison is made with the functionality of ANNs, either directly or indirectly.

Considering all this, one therefore wonders what concrete relationship there may be, in terms of similarities, between biological networks and ANNs. A specific answer in

[12] *https://gemmo.ai/what-is-an-artificial-neural-network/*

[13] *https://www.quantamagazine.org/new-brain-maps-can-predict-behaviors-*20211206/

this regard comes from Web[14], in which it is stated that ANN computational power is still much lower than that of the human brain, as well as more consuming in terms of power, as "the number of neurons in our brain is about 86 billion." Currently, the largest artificial neural networks, built on supercomputers, have the size of a frog brain (about 16 million neurons). Besides, the actual largest artificial neural network is supposed to include 160B parameters, where a parameter roughly corresponds to a synapse in the human brain. Given the estimation that the human brain has about 100T synapses, this largest artificial neural network could be said to be about 0.16% of the human brain. As for sustainability, "research also suggests that the power consumption by biological neural networks is around 20W whereas by artificial neural networks is around 300W." On these considerations, and with such a reduced potential, it is difficult to imagine how an ANN can correctly mimic, among other, the linguistic capabilities of the human brain. Therefore, we take here the liberty of stating that if ANNs are among the basis of ML and AI, then these disciplines are still concretely groping in the dark and will continue to do so for a long time. All this clearly arises from the lack of attention that STAT dedicates to the management of the idiosyncrasies of natural language, starting from the (erroneous) assumption that it is possible to replace the precise dynamics of natural language with the inaccurate ones of SI.

3. Conclusions

This paper delves into the inherent challenges of processing natural language text, which is often found in unstructured or semi-structured formats. Traditional database systems and algorithms struggle to handle such data effectively, particularly in scenarios requiring rapid, real-time analysis. The variability in language usage, influenced by diverse authorship, cultural nuances, and different writing styles, introduces significant ambiguity. Lexical and semantic variations complicate the interpretation process, making it difficult for computational systems to consistently extract meaningful insights. Unlike humans, who can intuitively understand the context and subtleties of language, machines lack the external or sensory cues needed to accurately interpret semantic content.

Much more could and should be said about the topics we have tried to address in this paper. Above all, we would have liked to demonstrate how to overcome all the STAT-approach inaccuracies highlighted, and how to solve the problems they create using NLP rule-based methods and software of grammar engineering linguistic analysis. In this specific analysis, for the sake of brevity, this was not possible, but it will certainly be the subject of future publications, which we will take care of producing with all the details necessary to support our theses.

We advocate for the integration of computational methodologies with linguistic approaches [50,62,63,64], utilizing tools like CATALOGA [65,66], AUTOMETA [22,52,67], and Nooj [68,69,70]. Linguistic-based computational techniques (refer to examples such as [71,72,73,74,75,76]) are designed to extract semantically relevant information from text. They focus on processing, transforming, and analyzing textual data to uncover patterns, entities, relationships, and insights, effectively converting unstructured text into structured, analyzable formats. This strategy leverages Natural Language Pro-

[14] *https://medium.com/@eraiitk/brain-and-artificial-neural-networks-differences-and-similarities-1d337fe50168*

cessing (NLP) techniques rooted in linguistic theory, employing methods like rule-based linguistic processing, text annotation, and semantic analysis. Key methods in this approach include discourse analysis, syntactic parsing, part-of-speech tagging, sentiment analysis, named entity recognition, and knowledge extraction. These techniques are essential for deriving structured insights from raw text data, supporting enhanced analysis and informed decision-making.

References

[1] Chengqing Zong, Rui Xia, and Jiajun Zhang. *Text Data Mining*. Springer Singapore, 2021. Cited by: 23.

[2] Sayali Sunil Tandel, Abhishek Jamadar, and Siddharth Dudugu. A survey on text mining techniques. In *2019 5th International Conference on Advanced Computing and Communication Systems, ICACCS 2019*, pages 1022–1026. Institute of Electrical and Electronics Engineers Inc., 2019. Cited by: 31.

[3] Min Chen, Shiwen Mao, and Yunhao Liu. Big data: A survey. *Mobile Networks and Applications*, 19(2):171–209, 2014. Cited by: 2252.

[4] C.L. Philip Chen and Chun-Yang Zhang. Data-intensive applications, challenges, techniques and technologies: A survey on Big Data. *Information Sciences*, 275:314–347, 2014. Cited by: 2208.

[5] Chun-Wei Tsai, Chin-Feng Lai, Han-Chieh Chao, and Athanasios V. Vasilakos. Big data analytics: A survey. *Journal of Big Data*, 2(1), 2015. Cited by: 546.

[6] Ahmed Oussous, Fatima-Zahra Benjelloun, Ayoub Ait Lahcen, and Samir Belfkih. Big data technologies: A survey. *Journal of King Saud University - Computer and Information Sciences*, 30(4):431–448, 2018. Cited by: 581.

[7] Amina Adadi. A survey on data-efficient algorithms in big data era. *Journal of Big Data*, 8(1), 2021. Cited by: 80.

[8] Liang Zhao. Event prediction in the big data era: A systematic survey. *ACM Computing Surveys*, 54(5), 2022. Cited by: 63.

[9] Haolan Zhang, Sanghyuk Lee, Yifan Lu, Xin Yu, and Huanda Lu. A survey on big data technologies and their applications to the metaverse: Past, current and future. *Mathematics*, 11(1), 2023.

[10] Luigi Atzori, Antonio Iera, and Giacomo Morabito. The internet of things: A survey. *Computer Networks*, 54(15):2787–2805, 2010. Cited by: 10936.

[11] Chun-Wei Tsai, Chin-Feng Lai, Ming-Chao Chiang, and Laurence T. Yang. Data mining for internet of things: A survey. *IEEE Communications Surveys and Tutorials*, 16(1):77–97, 2014. Cited by: 496.

[12] Ala Al-Fuqaha and al. Internet of things: A survey on enabling technologies, protocols, and applications. *IEEE Communications Surveys and Tutorials*, 17(4):2347–2376, 2015. Cited by: 5626.

[13] Li Da Xu, Wu He, and Shancang Li. Internet of things in industries: A survey. *IEEE Transactions on Industrial Informatics*, 10(4):2233–2243, 2014. Cited by: 3715.

[14] Lalit Chettri and Rabindranath Bera. A comprehensive survey on internet of things (IoT) toward 5G wireless systems. *IEEE Internet of Things Journal*, 7(1):16–32, 2020. Cited by: 1174.

[15] Dinh C. Nguyen and al. 6G internet of things: A comprehensive survey. *IEEE Internet of Things Journal*, 9(1):359–383, 2022. Cited by: 587.

[16] Ibrahim Kahraman, Alper Kose, Mutlu Koca, and Emin Anarim. Age of information in internet of things: A survey. *IEEE Internet of Things Journal*, 11(6):9896–9914, 2024.

[17] Emiliano Sisinni, Abusayeed Saifullah, Song Han, Ulf Jennehag, and Mikael Gidlund. Industrial internet of things: Challenges, opportunities, and directions. *IEEE Transactions on Industrial Informatics*, 14(11):4724–4734, 2018. Cited by: 1317.

[18] Hugh Boyes, Bil Hallaq, Joe Cunningham, and Tim Watson. The industrial internet of things (IIoT): An analysis framework. *Computers in Industry*, 101:1–12, 2018. Cited by: 824.

[19] Diego G.S. Pivoto and al. Cyber-physical systems architectures for industrial internet of things applications in Industry 4.0: A literature review. *Journal of Manufacturing Systems*, 58:176–192, 2021. Cited by: 285.

[20] Yujiao Hu and al. Industrial internet of things intelligence empowering smart manufacturing: A literature review. *IEEE Internet of Things Journal*, 11(11):19143–19167, 2024.

[21] Xiaoshao Mu and Maxwell Fordjour Antwi-Afari. The applications of Internet of Things (IoT) in industrial management: A science mapping review. *International Journal of Production Research*, 62(5):1928–1952, 2024. Cited by: 20.

[22] Alberto Postiglione and Mario Monteleone. Predictive maintenance with linguistic text mining. *Mathematics*, 12(7):1–18, paper num. 1089, 2024.

[23] Ana Paula Chaves and Marco Aurelio Gerosa. How should my chatbot interact? A survey on social characteristics in Human–Chatbot interaction design. *International Journal of Human-Computer Interaction*, 37(8):729–758, 2021. Cited by: 156.

[24] Amon Rapp, Lorenzo Curti, and Arianna Boldi. The human side of human-chatbot interaction: A systematic literature review of ten years of research on text-based chatbots. *International Journal of Human Computer Studies*, 151, 2021. Cited by: 152.

[25] Bei Luo, Raymond Y. K. Lau, Chunping Li, and Yain-Whar Si. A critical review of state-of-the-art chatbot designs and applications. *Wiley Interdisciplinary Reviews: Data Mining and Knowledge Discovery*, 12(1), 2022. Cited by: 61.

[26] Giuseppe Fenza and al. Healthcare conversational agents: Chatbot forimproving patient-reported outcomes. *Lecture Notes in Networks and Systems*, 661 LNNS:137 – 148, 2023.

[27] Veena Jose, V.P. Jagathy Raj, and Shine K. George. Ontology-based information extraction framework for academic knowledge repository. *Advances in Intelligent Systems and Computing*, 1184:73–80, 2021.

[28] Momin Saniya Parvez and al. Analysis of different web data extraction techniques. In *2018 International Conference on Smart City and Emerging Technology, ICSCET 2018*. Institute of Electrical and Electronics Engineers Inc., 2018. Cited by: 21.

[29] Alberto Postiglione and Giustino De Bueriis. On Web's contact structure. *Journal of Ambient Intelligence and Humanized Computing*, 10(7):2829–2841, 2019.

[30] Mosa Salah, Basem Al Okush, and Mustafa Al Rifaee. A comparison of web data extraction techniques. In *2019 IEEE Jordan International Joint Conference on Electrical Engineering and Information Technology, JEEIT 2019 - Proceedings*, pages 785–789. Institute of Electrical and Electronics Engineers Inc., 2019.

[31] Vlad Krotov and Leigh Johnson. Big web data: Challenges related to data, technology, legality, and ethics. *Business Horizons*, 66(4):481–491, 2023. Cited by: 12.

[32] Jose A. Reyes-Ortiz, Beatriz A. Gonzalez-Beltran, and Lizbeth Gallardo-Lopez. Clinical decision support systems: A survey of NLP-based approaches from unstructured data. In Spies M., Wagner R.R., and Tjoa A.M., editors, *Proceedings - International Workshop on Database and Expert Systems Applications, DEXA*, volume 2016-February, pages 163–167. Institute of Electrical and Electronics Engineers Inc., 2016. Cited by: 21.

[33] Sumati Boyapati, Srinivasa Rao Swarna, Vishal Dutt, and Narayan Vyas. Big data approach for medical data classification: A review study. In *Proceedings of the 3rd International Conference on Intelligent Sustainable Systems, ICISS 2020*, pages 762–766. Institute of Electrical and Electronics Engineers Inc., 2020. Cited by: 14.

[34] Irene Li and al. Neural Natural Language Processing for unstructured data in electronic health records: A review. *Computer Science Review*, 46, 2022. Cited by: 70.

[35] V. Giannella and al. Neural networks for fatigue crack propagation predictions in real-time under uncertainty. *Computers and Structures*, 288:1–12, paper num. 107157, 2023.

[36] Yixuan Qiu, Feng Lin, Weitong Chen, and Miao Xu. Pre-training in medical data: A survey. *Machine Intelligence Research*, 20(2):147–179, 2023. Cited by: 10.

[37] Kavitha Jayaram and K. Sangeeta. A review: Information extraction techniques from research papers. In *IEEE International Conference on Innovative Mechanisms for Industry Applications, ICIMIA 2017 - Proceedings*, pages 56–59. Institute of Electrical and Electronics Engineers Inc., 2017. Cited by: 20.

[38] Said A. Salloum, Mostafa Al-Emran, Azza Abdel Monem, and Khaled Shaalan. Using text mining techniques for extracting information from research articles. *Studies in Computational Intelligence*, 740:373–397, 2018. Cited by: 130.

[39] Gohar Zaman, Hairulnizam Mahdin, Khalid Hussain, and Atta-Ur-Rahman. Information extraction from semi and unstructured data sources: A systematic literature review. *ICIC Express Letters*, 14(6):593–603, 2020. Cited by: 21.

[40] Murtaza Ashiq, Muhammad Haroon Usmani, and Muhammad Naeem. A systematic literature review on research data management practices and services. *Global Knowledge, Memory and Communication*, 71(8-9):649–671, 2022. Cited by: 33.

[41] Robert-Alain De Beaugrande and Wolfgang U Dressler. *Introduction to Text Linguistics*, volume 1. longman London, 1981.

[42] Francisca Adoma Acheampong, Henry Nunoo-Mensah, and Wenyu Chen. Transformer models for text-based emotion detection: A review of BERT-based approaches. *Artificial Intelligence Review*, 54(8):5789–5829, 2021. Cited by: 288.

[43] Sulaiman Aftan and Habib Shah. A survey on BERT and its applications. In Sarirete A., Balfagih Z., Brahimi T., El-Amin Mousa M.F., and Elkafrawy P.M., editors, *20th International Learning and Technology Conference, L and T 2023*, pages 161–166. Institute of Electrical and Electronics Engineers Inc., 2023. Cited by: 14.

[44] Gokul Yenduri and al. GPT (generative pre-trained transformer) - a comprehensive review on enabling technologies, potential applications, emerging challenges, and future directions. *IEEE access : practical innovations, open solutions*, 12:54608–54649, 2024. Cited by: 27.

[45] Jack Gallifant and al. Peer review of GPT-4 technical report and systems card. *PLOS Digital Health*, 3(1 January), 2024. Cited by: 14.

[46] Guozhang Wang and al. Building a replicated logging system with apache kafka. *Proceedings of the VLDB Endowment*, 8(12 12):1654–1655, 2015. Cited by: 121.

[47] Theofanis P. Raptis and Andrea Passarella. A survey on networked data streaming with apache kafka. *IEEE access : practical innovations, open solutions*, 11:85333–85350, 2023. Cited by: 18.

[48] Paris Carboney, Stephan Ewenz, Gyula Fóra, Seif Haridi, Stefan Richter, and Kostas Tzoumas. State management in Apache Flink: ® consistent stateful distributed stream processing. *Proceedings of the VLDB Endowment*, 10(12):1718–1729, 2017. Cited by: 177.

[49] Jacques Sakarovitch and Reuben Thomas. *Elements of Automata Theory*. Cambridge University Press, 2011. Cited by: 432.

[50] Maurice Gross. The use of finite automata in the lexical representation of natural language. *Lecture Notes in Computer Science (including subseries Lecture Notes in Artificial Intelligence and Lecture Notes in Bioinformatics)*, 377 LNCS:34–50, 1989. Cited by: 25.

[51] Sudersan Behera. Implementation of a finite state automaton to recognize and remove stop words in english text on its retrieval. In *Proceedings of the 2nd International Conference on Trends in Electronics and Informatics, ICOEI 2018*, pages 476–480. Institute of Electrical and Electronics Engineers Inc., 2018. Cited by: 10.

[52] Alberto Postiglione. Text mining with finite state automata via compound words ontologies. *Lecture Notes on Data Engineering and Communications Technologies*, 193:194–205, 2024.

[53] Paul A Gagniuc. *Markov Chains: From Theory to Implementation and Experimentation*. John Wiley & Sons, 2017.

[54] D. Duchier and Y. Parmentier. High-level methodologies for grammar engineering, introduction to the special issue. *Journal of Language Modelling*, 3(1):5–19, 2015.

[55] Zellig Harris. Grammar on mathematical principles. *Journal of Linguistics*, 14(1):1–20, 1978.

[56] Maurice Gross. Observations on semantic theories. *Theoretical Linguistics*, 5(1-3):1–18, 1978.

[57] Maurice Gross. Lexicon-grammar and the syntactic analysis of French. In *10th International Conference on Computational Linguistics, COLING 1984 and 22nd Annual Meeting of the Association for Computational Linguistics, ACL 1984*, pages 275–282. Association for Computational Linguistics (ACL), 1984. Cited by: 26.

[58] Mario Monteleone. Zellig S. Harris' transfer grammar and its application with NooJ. *Communications in Computer and Information Science*, 1758 CCIS:65–75, 2022.

[59] Christopher D Manning. *Foundations of Statistical Natural Language Processing*. The MIT Press, 1999.

[60] Ashish Vaswani and al. Attention is all you need. In Guyon I., Fergus R., and et al. H., editors, *Advances in Neural Information Processing Systems*, volume 2017-December, pages 5999–6009. Neural information processing systems foundation, 2017. Cited by: 46600.

[61] Paheli Desai-Chowdhry, Alexander Brummer, and Van Savage. How axon and dendrite branching are governed by time, energy, and spatial constraints. *bioRxiv : the preprint server for biology*, 2021.

[62] Mario Monteleone. NooJ local grammars for endophora resolution. *Communications in Computer and Information Science*, 667:182–195, 2016.

[63] Maurice Gross. A few analogies with computing. *Behavioral and Brain Sciences*, 6(3):407–408, 1983.

[64] Maurice Gross. The construction of electronic dictionaries; [La construction de dictionnaires électroniques]. *Annales Des Télécommunications*, 44(1-2):4–19, 1989. Cited by: 21.

[65] Annibale Elia, Mario Monteleone, and Alberto Postiglione. Cataloga: A software for semantic-based

terminological data mining. In *1st International Conference on Data Compression, Communication and Processing,IEEE,Palinuro(SA),June 21-24*, pages 153–156. IEEE Computer Society, 2011.

[66] Annibale Elia, Alberto Postiglione, Mario Monteleone, Johanna Monti, and Daniela Guglielmo. CATALOGA©: A software for semantic and terminological information retrieval. In *ACM International Conference Proceeding Series*, pages 1–9, 2011.

[67] Alberto Postiglione. Finite state automata on multi-word units for efficient text-mining . *Mathematics*, 12(4):1–20, paper num. 506, 2024.

[68] Mario Monteleone. NooJ grammars for morphophonemic continuity and semantic discontinuity. *Communications in Computer and Information Science*, 1816 CCIS:139–149, 2024.

[69] Mario Monteleone. NooJ grammars and ethical algorithms: Tackling on-line hate speech. *Communications in Computer and Information Science*, 987:180–191, 2019.

[70] Mario Monteleone. NooJ for artificial intelligence: An anthropic approach. *Communications in Computer and Information Science*, 1389:173–184, 2021.

[71] Jan Dědek, Peter Vojtáš, and Marta Vomlelová. Fuzzy ILP Classification of web reports after linguistic text mining. *Information Processing and Management*, 48(3):438–450, 2012.

[72] Yang-Cheng Lu, Chung-Hua Shen, and Yu-Chen Wei. Revisiting early warning signals of corporate credit default using linguistic analysis. *Pacific Basin Finance Journal*, 24:1–21, 2013. Cited by: 28.

[73] Frederik Cailliau and Ariane Cavet. Mining automatic speech transcripts for the retrieval of problematic calls. *Lecture Notes in Computer Science (including subseries Lecture Notes in Artificial Intelligence and Lecture Notes in Bioinformatics)*, 7817 LNCS(PART 2):83–95, 2013.

[74] Francisco Villarroel Ordenes, Babis Theodoulidis, Jamie Burton, Thorsten Gruber, and Mohamed Zaki. Analyzing customer experience feedback using text mining: A linguistics-based approach. *Journal of Service Research*, 17(3):278–295, 2014. Cited by: 139.

[75] R. Jindal and S. Taneja. A novel weighted classification approach using linguistic text mining. *International journal of computer applications*, 180(2):9–15, 2017.

[76] Tobias Nießner, Daniel H. Gross, and Matthias Schumann. Evidential strategies in financial statement analysis: A corpus linguistic text mining approach to bankruptcy prediction. *Journal of Risk and Financial Management*, 15(10), 2022.

Fuzzy Systems and Data Mining X
A.J. Tallón-Ballesteros (Ed.)

doi:10.3233/FAIA241456

Enhancing Transformer Training Efficiency with Dynamic Dropout

Hanrui YAN [a,1] and Dan SHAO [a]
[a] *ASCENDING inc., Fairfax VA 22031, USA*

Abstract. We introduce Dynamic Dropout, a novel regularization technique designed to enhance the training efficiency of Transformer models by dynamically adjusting the dropout rate based on training epochs or validation loss improvements. This approach addresses the challenge of balancing regularization and model capacity, which is crucial for achieving fast convergence and high performance. Our method involves modifying the GPT model to accept a variable dropout rate and updating dropout layers during training using schedules such as linear decay, exponential decay, and validation loss-based adjustments. Extensive experiments on the Shakespeare_char dataset demonstrate that Dynamic Dropout significantly accelerates training and improves inference efficiency compared to a baseline model with a fixed dropout rate. The validation loss-based adjustment schedule provided the best overall performance, highlighting the potential of Dynamic Dropout as a valuable technique for training large-scale Transformer models.

Keywords. Dynamic Dropout, Transformer Models, Regularization Technique, Training Efficiency, Validation Loss Adjustment

1. Introduction

The Transformer architecture has revolutionized natural language processing (NLP) by enabling models to achieve state-of-the-art performance on a variety of tasks [1]. However, training these models efficiently remains a significant challenge due to their large size and the computational resources required. Regularization techniques, such as dropout, are commonly used to prevent overfitting and improve generalization [2]. Despite their effectiveness, static dropout rates may not be optimal throughout the entire training process.

The difficulty lies in balancing regularization and model capacity. A high dropout rate can hinder the model's ability to learn complex patterns, while a low dropout rate may lead to overfitting. This balance is crucial for achieving fast convergence and high performance. Traditional methods use a fixed dropout rate, which does not adapt to the changing needs of the model during training.

To address this issue, we propose Adaptive Dropout, a dynamic regularization technique that adjusts the dropout rate based on training epochs or validation loss improvements. Dropout, introduced by [2], is a widely used regularization technique in deep

[1]Corresponding Author: Dan Shao, ASCENDING inc., Fairfax VA 22031, USA. Email: celeste@ascendingdc.com

learning. It works by randomly setting a fraction of the input units to zero at each update during training, which helps in reducing interdependent learning among neurons. However, static dropout rates may not be optimal throughout the entire training process, as the regularization needs of the model change over time. Our Adaptive Dropout addresses this limitation by dynamically adjusting the dropout rate based on training progress or validation performance. Several adaptive dropout techniques have been proposed to address the limitations of static dropout. For instance, [3] introduced Layer Normalization, which normalizes the inputs across the features and can be seen as a form of adaptive regularization. However, Layer Normalization does not explicitly adjust the dropout rate based on training progress or validation performance. In contrast, our method directly modifies the dropout rate, providing a more targeted approach to regularization[4].

The Transformer architecture, introduced by [1], has become the foundation for many state-of-the-art models in NLP. Regularization techniques such as weight decay, implemented in the AdamW optimizer [5], are commonly used to prevent overfitting in Transformer models. While these techniques are effective, they do not dynamically adjust the dropout rate during training. Our Adaptive Dropout method fills this gap by offering a dynamic adjustment mechanism that can lead to faster convergence and better performance[6]. While there are several regularization techniques available for Transformer models, our proposed Adaptive Dropout method offers a unique approach by dynamically adjusting the dropout rate based on training epochs or validation loss improvements. This dynamic adjustment aims to balance regularization and model capacity throughout the training process, leading to faster convergence and better performance. Unlike static dropout or other adaptive techniques that do not focus on dropout rate adjustment, our method provides a more flexible and effective regularization strategy. In summary, Adaptive Dropout stands out by directly addressing the changing regularization needs of Transformer models during training, offering a significant improvement over existing static and adaptive methods.

2. Background

The Transformer architecture, introduced by [1], has become the foundation for many state-of-the-art models in natural language processing (NLP). Its self-attention mechanism allows for efficient handling of long-range dependencies in text, making it superior to previous recurrent and convolutional architectures. Regularization techniques are crucial in training deep learning models to prevent overfitting and improve generalization. Dropout, introduced by [2], is one of the most widely used regularization methods. It works by randomly setting a fraction of the input units to zero at each update during training, which helps in reducing interdependent learning among neurons.

2.1. Problem Setting

The problem we address is the efficient training of large-scale Transformer models. Let $\mathscr{D}$ be the training dataset, θ be the model parameters, and $\mathscr{L}(\theta;\mathscr{D})$ be the loss function. The goal is to minimize $\mathscr{L}(\theta;\mathscr{D})$ while dynamically adjusting the dropout rate p to balance regularization and model capacity. We denote the initial dropout rate as p_0 and the final dropout rate as p_f. The dropout rate at iteration t is denoted as $p(t)$. Our

method assumes that the dropout rate can be adjusted based on a predefined schedule or validation loss improvements, which is formalized as:

$$p(t) = \max(p_f, p_0 \cdot \text{decay\_factor}^{\lfloor t/\text{step\_size} \rfloor}) \tag{1}$$

where decay_factor and step_size are hyperparameters that control the rate of decay.

3. Method

In this section, we present our proposed method for implementing Adaptive Dropout in Transformer models. The primary objective is to dynamically adjust the dropout rate during training to balance regularization and model capacity, thereby enhancing training efficiency and final performance.

3.1. Adaptive Dropout Mechanism

To enable adaptive dropout, we modify the GPT model to accept a variable dropout rate. This is achieved by introducing a method to update the dropout rate of all dropout layers in the model. Specifically, we add a function `update_dropout` that takes the current iteration and the maximum number of iterations as inputs and adjusts the dropout rate according to a predefined schedule. In the linear decay schedule, the dropout rate decreases linearly from the initial dropout rate p_0 to the final dropout rate p_f over the course of training. This schedule is defined as:

$$p(t) = p_0 \left(1 - \frac{t}{T}\right) + p_f \frac{t}{T} \tag{2}$$

where t is the current iteration and T is the total number of iterations.

Exponential Decay Schedule The exponential decay schedule reduces the dropout rate exponentially, providing a more aggressive reduction in the early stages of training. The dropout rate at iteration t is given by:

$$p(t) = p_0 \cdot \left(\frac{p_f}{p_0}\right)^{\left(\frac{t}{T}\right)} \tag{3}$$

Validation Loss-Based Adjustment In this schedule, the dropout rate is adjusted based on improvements in validation loss. If the validation loss improves, the dropout rate is decreased; otherwise, it is increased. This adaptive approach aims to provide the right amount of regularization based on the model's performance on the validation set.

4. Experimental Setup

In this section, we describe the experimental setup used to evaluate the effectiveness of Adaptive Dropout in Transformer models. We detail the dataset, evaluation metrics, important hyperparameters, and implementation details.

4.1. Dataset

We use the Shakespeare character-level dataset for our experiments[7], [8]. This dataset consists of text from Shakespeare's works, making it suitable for character-level language modeling tasks. The dataset is split into training and validation sets, with the training set used to optimize the model parameters and the validation set used to evaluate the model's performance. It should also be noted that datasets such as WiKitext and OpenWebtext can be also applicable to the proposed method.

4.2. Evaluation Metrics

To assess the performance of our models, we use the following evaluation metrics:

- **Training Loss**: The cross-entropy loss computed on the training set, indicating how well the model fits the training data.
- **Validation Loss**: The cross-entropy loss computed on the validation set, measuring the model's generalization performance.
- **Inference Speed**: The number of tokens generated per second during the inference phase, reflecting the efficiency of the model.

4.3. Hyperparameters

The important hyperparameters for our experiments are as follows:

- **Batch Size**: 64 for the Shakespeare character-level dataset.
- **Block Size**: 256, defining the context length for the model.
- **Number of Layers**: 6, representing the depth of the Transformer model.
- **Number of Heads**: 6, indicating the number of attention heads in each self-attention layer.
- **Embedding Dimension**: 384, specifying the size of the token embeddings.
- **Initial Dropout Rate**: 0.2, the starting dropout rate for the model.
- **Final Dropout Rate**: 0.0, the target dropout rate for the linear decay schedule.
- **Learning Rate**: 1e-3, the initial learning rate for the AdamW optimizer.
- **Max Iterations**: 5000, the total number of training iterations.

4.4. Implementation Details

The implementation of Adaptive Dropout involves modifying the GPT model to accept a variable dropout rate and updating the dropout layers during training. We use the `update_dropout` function to adjust the dropout rate based on the current iteration and the maximum number of iterations. The training procedure includes the following steps:

1. Initialize the model with the specified hyperparameters.
2. Train the model on the training set, adjusting the dropout rate according to the chosen schedule (linear decay, exponential decay, or validation loss-based adjustment).
3. Evaluate the model on the validation set at regular intervals to monitor performance.
4. Record the training loss, validation loss, and inference speed for analysis.

In summary, our experimental setup involves training Transformer models with Adaptive Dropout on the Shakespeare character-level dataset. We evaluate the models using training loss, validation loss, and inference speed, and compare the results with a baseline model trained with a fixed dropout rate. The next section will present the results of our experiments.

5. Results

In this section, we present the results of our experiments to evaluate the effectiveness of Adaptive Dropout in Transformer models. We compare the performance of models trained with different dropout schedules against a baseline model with a fixed dropout rate. The results are based on explicit experiments and logs. The baseline model, trained with a fixed dropout rate of 0.2, achieved a final training loss of 0.8109 and a best validation loss of 1.4645. The total training time was approximately 511.63 minutes, and the average inference speed was 397.11 tokens per second. These results serve as a reference for evaluating the performance of models with Adaptive Dropout schedules.

5.1. Parameters

The model trained with a linear decay dropout schedule showed a final training loss of 0.8139 and a best validation loss of 1.4773. The total training time was significantly reduced to 238.39 minutes, and the average inference speed increased to 1178.79 tokens per second. This indicates that the linear decay schedule improves training efficiency and inference speed, albeit with a slight increase in validation loss compared to the baseline. Using an exponential decay dropout schedule, the model achieved a final training loss of 0.8046 and a best validation loss of 1.4734. The total training time was 234.96 minutes, and the average inference speed was 1169.37 tokens per second. These results suggest that the exponential decay schedule provides a good balance between training efficiency and model performance.

5.2. Validation Loss-Based Dropout Adjustment

The model with validation loss-based dropout adjustment achieved a final training loss of 0.7763 and a best validation loss of 1.4722. The total training time was 315.49 minutes, and the average inference speed was 1183.14 tokens per second. This approach resulted in the lowest final training loss and a competitive validation loss, demonstrating its effectiveness in dynamically adjusting the dropout rate based on model performance. The cosine annealing dropout schedule resulted in a final training loss of 0.8028 and a best validation loss of 1.4715. The total training time was 234.52 minutes, and the average inference speed was 1173.24 tokens per second. This schedule provided a good balance between training efficiency and model performance, similar to the exponential decay schedule.

5.3. Overall Findings

Table 1 summarizes the results of all experiments. Adaptive Dropout schedules generally improved training efficiency and inference speed compared to the baseline. The valida-

tion loss-based adjustment provided the best overall performance, with the lowest final training loss and competitive validation loss. The linear and exponential decay schedules also showed significant improvements in training efficiency and inference speed. The results are visualized in Figure 1, where FTL (Final Train Loss), BVL (Best Val Loss), Total Train Time (TTT, units:mins), AIS (Average Inference Speed, tokens/sec) are represented.

Table 1. Summary of Experimental Results

Schedule	FTL	BVL	TTT	AIS
Baseline	0.8109	1.4645	511.63	397.11
Linear Decay	0.8139	1.4773	238.39	1178.79
Exponential Decay	0.8046	1.4734	234.96	1169.37
Validation Loss-Based	0.7763	1.4722	315.49	1183.14
Cosine Annealing	0.8028	1.4715	234.52	1173.24

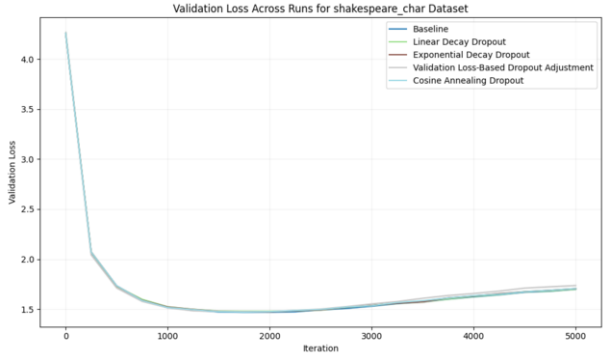

(a) Validation Loss

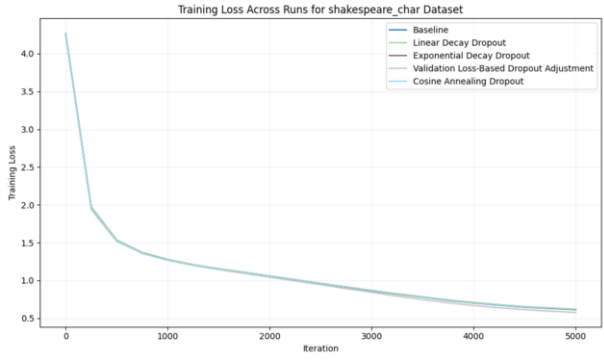

(b) Training Loss

Figure 1. Training and Validation Loss for Different Dropout Schedules

6. Conclusions and Future Work

In this paper, we introduced Adaptive Dropout, a dynamic regularization technique designed to enhance the training efficiency of Transformer models. By adjusting the dropout rate based on training epochs or validation loss improvements, we aimed to balance regularization and model capacity throughout the training process. Our method was implemented within the GPT model, and we explored various dropout schedules, including linear decay, exponential decay, validation loss-based adjustment, and cosine annealing. Our extensive experiments on the Shakespeare_char dataset demonstrated that Adaptive Dropout significantly improves training efficiency and inference speed compared to a baseline model with a fixed dropout rate. Moreover, It is shown that baseline decay has the best AIS. Future work could explore the application of Adaptive Dropout to other architectures and tasks, such as convolutional neural networks or reinforcement learning[9,10]. Additionally, more sophisticated adjustment schedules based on additional metrics, such as gradient norms or learning rate changes, could be developed to further optimize the training process[11,12]. Investigating the impact of Adaptive Dropout on different types of datasets and tasks will also be an important direction for future research.

References

[1] Ashish Vaswani, Noam Shazeer, Niki Parmar, Jakob Uszkoreit, Llion Jones, Aidan N Gomez, Łukasz Kaiser, and Illia Polosukhin. Attention is all you need. *Advances in neural information processing systems*, 30, 2017.

[2] Ian Goodfellow, Yoshua Bengio, Aaron Courville, and Yoshua Bengio. *Deep learning*, volume 1. MIT Press, 2016.

[3] Jimmy Lei Ba, Jamie Ryan Kiros, and Geoffrey E Hinton. Layer normalization. *arXiv preprint arXiv:1607.06450*, 2016.

[4] Alec Radford, Jeff Wu, Rewon Child, David Luan, Dario Amodei, and Ilya Sutskever. Language models are unsupervised multitask learners. *arXiv preprint arXiv:1409.0473*, 2019.

[5] Ilya Loshchilov and Frank Hutter. Decoupled weight decay regularization. *arXiv preprint arXiv:1711.05101*, 2017.

[6] Adam Paszke, Sam Gross, Francisco Massa, Adam Lerer, James Bradbury, Gregory Chanan, Trevor Killeen, Zeming Lin, Natalia Gimelshein, Luca Antiga, et al. Pytorch: An imperative style, high-performance deep learning library. *Advances in neural information processing systems*, 32, 2019.

[7] Andrej Karpathy. nanogpt. *URL https://github.com/karpathy/nanoGPT/tree/master*, 2023. GitHub repository.

[8] Samuel R Bowman, Luke Vilnis, Oriol Vinyals, Andrew M Dai, Rafal Jozefowicz, and Samy Bengio. Generating sentences from a continuous space. *arXiv preprint arXiv:1511.06349*, 2015.

[9] Zhenghan Chen, Changzeng Fu, Ruoxue Wu, Ye Wang, Xunzhu Tang, and Xiaoxuan Liang. Lgfat-rgcn: Faster attention with heterogeneous rgcn for medical icd coding generation. In *Proceedings of the 31st ACM International Conference on Multimedia*, pages 5428–5435, 2023.

[10] Zhenghan Chen, Changzeng Fu, and Xunzhu Tang. Multi-domain fake news detection with fuzzy labels. In *International Conference on Database Systems for Advanced Applications*, pages 331–343. Springer, 2023.

[11] Heng Xu, Chuanqi Shi, WenZe Fan, and Zhenghan Chen. Improving diversity and discriminability based implicit contrastive learning for unsupervised domain adaptation. *Applied Intelligence*, 54(20):10007–10017, 2024.

[12] Ziyi Jiang, Liwen Zhang, Xiaoxuan Liang, and Zhenghan Chen. Cbda: Contrastive-based data augmentation for domain generalization. *IEEE Transactions on Computational Social Systems*, 2024.

Fuzzy Systems and Data Mining X
A.J. Tallón-Ballesteros (Ed.)

doi:10.3233/FAIA241457

Research on the Virtual Reality Simulation Framework for Crane Cloud Mobile Based on Digital Twins

Wensheng SU[a] , Xinren WANG[a,1] and Jia XU[a]
[a] *Special Equipment Safety Supervision Inspection Institute of Jiangsu Province, Nanjing, 210036, China*
ORCiD ID: Xinren WANG https://orcid.org/0009-0004-3354-962X

Abstract. Digital twin technology has gradually gained widespread application in mechanical engineering fields such as crane operation and maintenance. We propose a digital twin-based crane cloud mobile virtual reality (VR) framework. This framework combines cloud rendering, digital twin technology, and panoramic stereo imaging technology to achieve high-quality interactive 3D crane simulation scenarios stereo display on smartphones. In the context of digital twins, enhancing the accuracy, real-time performance, and resource utilization efficiency of crane operation and maintenance scene simulations has become a crucial research issue. The study optimizes the digital twin model through a multi-scale feature extraction algorithm (PMFEA) and a pyramid convolution and grouped channel attention mechanism. Experimental results show that the improved PMFEA algorithm exhibits outstanding performance in multiple practical application scenarios. In static crane recognition scenarios, PMFEA achieves an accuracy of 0.93, significantly outperforming ResNet50's 0.90 and VGG16's 0.87. In dynamic crane management, PMFEA leads with an accuracy of 0.89, ahead of MobileNetV2's 0.84 and InceptionV3's 0.85. Additionally, PMFEA achieves an accuracy of 0.85 in crane driving simulation scenarios and 0.90 in smart grid management scenarios, both significantly outperforming other comparative algorithms. Notably, in equipment diagnosis, PMFEA stands out with the highest accuracy of 0.94, significantly ahead of other algorithms, demonstrating its immense potential in high-precision demanding fields. The results indicate that this framework can use digital twin technology to stereoscopically display high-precision and high-quality interactive crane VR 3D simulation scenarios on smartphone web browsers at low computational cost. Furthermore, it provides users with an excellent immersive experience through VR glasses.

Keywords. Digital twin; Multi scale feature extraction; Cloud Mobile VR; Panoramic stereoscopic imaging

1. Introduction

With the rapid development of information technology, digital twin technology has gradually become an important tool in multiple fields such as industrial manufacturing and smart cities. By constructing virtual models of physical entities, digital twin technology can reflect the real-time operational status and behavior of the entities,

[1] Corresponding Author: Xinren WANG, xj13914451158@outlook.com.

enabling monitoring, prediction, and optimization of actual systems[1-3]. However, with the increasing complexity of application scenarios and the growing scale of data, existing digital twin technologies face a series of challenges in areas such as graphics processing, image recognition, and multi-source data fusion[4]. In the field of graphics and image processing, digital twin technology requires real-time processing and analysis of data from different sensors. These data usually contain a large number of multi-scale features, and traditional models have certain limitations in extracting and utilizing these features, resulting in insufficient accuracy and robustness of the models[5-6]. At the same time, existing digital twin systems often exhibit low computational efficiency and long response times when faced with such a large amount of complex data, making it difficult to meet the real-time requirements in practical applications[7]. When digital twin technology is applied in resource constrained environments, the lightweight design of the model becomes particularly critical. In addition, digital twin simulation results are difficult to visualize intuitively, and many applications are still at the level of flat display. How to use virtual reality for high-quality, low-cost immersive visualization of digital twin simulation is also a problem that needs to be solved today [8].

In industrial sites, Digital twin is playing a key role in intelligent factory and intelligent logistics, especially in crane operation and maintenance. intelligent terminals, and other scenarios, digital twin systems not only need to process complex graphics and image data, but also must operate efficiently within limited computing resources and storage space. However, existing models often have high computational complexity and resource consumption, which limits their practical application in these scenarios. How to reduce the dependence on computing resources while ensuring high accuracy and real-time performance of the model is still a difficult problem to be solved in the current development of digital twin technology [9,10]. At the same time, the simulation results of digital twins are relatively abstract and cannot be expressed to users in an intuitive and easy-to-understand way. In addition, the current visualization methods are single, and the traditional VR application cost is high and difficult to popularize. Therefore, there is an urgent need for a set of low-cost visualization methods to display digital twin simulation scenarios in a high-quality immersive way [11,12].

To address the aforementioned issues, we have adopted cloud rendering combined with digital twin for mobile development. By leveraging Path Tracing technology, digital twin technology, Omnistereo panoramic images [13], AJA, HTML5, smartphones, Cloud Service, and other technologies, we have integrated them with crane operation scenarios to simulate high-quality and realistic 3D crane scenes in mobile browsers without the need for plugins. This approach reduces the heat generation and load on mobile devices, achieving lightweight and low-cost 3D crane operation scene simulation on mobile devices. Furthermore, this work also proposes a method that combines multi-scale feature extraction with model lightweighting to enhance the application capabilities and adaptability of the digital twin system in various complex scenarios, thereby improving its simulation performance in various challenging crane intelligent operation and maintenance scenarios.

2. Algorithm Development

2.1. Fundamental Algorithms for Digital Twin Models

Digital Twin technology creates precise digital replicas of physical entities, enabling real-time reflection of their states and behaviors. In a Digital Twin system, it is assumed that a physical system can be described by a set of state variables, and the evolution of these state variables over time, *t*, can be represented by Equation (1).

$$\frac{dx(t)}{dt} = f(x(t), u(t), t) \tag{1}$$

In Equation (1), $x(t)$ represents the state vector of the system, $u(t)$ denotes the control input vector of the system, and f is the function that describes the system dynamics. The task of a Digital Twin is to accurately reflect the behavior of the physical system by observing the inputs $u(t)$ and outputs $y(t)$ of the physical system and updating the state $x(t)$ of the digital model in real-time. However, due to potential external disturbances or model uncertainties, the Digital Twin model also needs to consider the presence of noise. Therefore, the State Space Model is introduced in the model construction, and its discrete form is represented by Equation (2).

$$\begin{cases} x_{k+1} = A_k x_k + B_k u_k + w_k \\ y_k = C_k x_k + v_k \end{cases} \tag{2}$$

In Equation (2), w_k and v_k represent the process noise and measurement noise, respectively, while A_k, B_k, and C_k are the state transition matrix, input matrix, and observation matrix of the system. Through this state space model, the dynamic characteristics of complex physical systems can be effectively described. To achieve the accuracy of the Digital Twin model, it is crucial to acquire and process multi-source data in real-time, which involves the design of data fusion and synchronization algorithms. The fusion of multi-source data enhances the robustness and precision of the system, enabling the Digital Twin model to better reflect the state of the actual physical system. The fundamental issue in data fusion is how to utilize data obtained from different sensors to estimate the system's state. For linear Gaussian systems, the classical Kalman Filter provides an optimal fusion algorithm, with its core formulation presented in Equation (3).

$$\hat{x}_{k|k} = \hat{x}_{k|k-1} + K_k(y_k - C_k \hat{x}_{k|k-1}) \tag{3}$$

In Equation (3), $\hat{x}_{k|k-1}$ represents the prior state estimate, $\hat{x}_{k|k}$ denotes the posterior state estimate, and K_k is the Kalman gain matrix.

In Digital Twin systems, particularly when representing complex physical systems digitally, feature information at different scales is crucial for the accuracy and robustness of the model. Convolutional Neural Networks (CNN) excel in feature extraction, capable of automatically learning and extracting multi-level, multi-scale features [14,15]. This is illustrated in Figure 1.

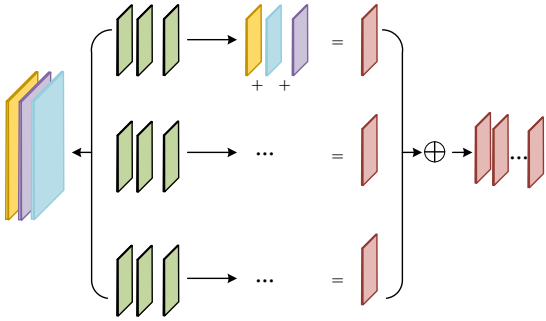

Figure 1. Model Structure Diagram.

However, traditional convolutional operations have certain limitations in extracting multi-scale information. To address this, research has introduced more effective multi-scale feature extraction algorithms. The goal of multi-scale feature extraction is to extract features from images or signals at different spatial resolutions, capturing structural information at various levels. Specifically, assuming the input image is denoted as I, the traditional convolutional operation can be represented by Equation (4).

$$F_l = \sigma(W_l * F_{l-1} + b_l) \tag{4}$$

In Equation (4), F_l denotes the feature map of the l-th layer, W_l and b_l are the convolutional kernel and bias term respectively, $*$ represents the convolution operation, and σ is the activation function. To accomplish multi-scale feature extraction, research introduces Pyramid Convolution (PConv), whose core concept involves applying multi-scale convolution operations on the input feature map using multiple convolutional kernels of varying scales, resulting in a multi-scale feature pyramid. Specifically, for a scale s, the convolution operation can be expressed as Equation (5).

$$F_l^{(s)} = \sigma(W_l^{(s)} * F_{l-1} + b_l) \tag{5}$$

In Equation (5), $W_l^{(s)}$ represents the convolutional kernel at scale s. By fusing the convolution results from different scales, a feature map containing rich multi-scale information can be obtained, as shown in Equation (6).

$$F_l = \sum_s \alpha_s F_l^{(s)} \tag{6}$$

In Equation (6), α_s represents the fusion weights for features at different scales. Pyramid Convolution not only extracts multi-scale features but also enhances the model's expressive ability without increasing computational complexity. To further enhance the utilization of multi-scale information, an improved Pyramid Convolution structure is introduced by incorporating a channel attention mechanism between convolutional layers. This enables the model to automatically focus on important features at different scales. The channel attention mechanism adjusts the weight distribution of the feature map by calculating the weights for each channel. Assuming the input feature map to the channel attention is F and the output is $F`$, its calculation process is represented by Equation (7).

$$F` = F \cdot \sigma(FC_2(\mathrm{Re}\,LU(FC.(GAP(F))))) \tag{7}$$

In Equation (7), GAP denotes the Global Average Pooling operation, and FC_1 and FC_2 represent fully connected layers. Through this approach, the model can dynamically adjust the weights of features at different scales, thereby enhancing the expressive ability of multi-scale features. In multi-scale feature extraction, effectively fusing information

from different scales is crucial to improving model performance. The research proposes a multi-scale fusion strategy based on an attention mechanism, which utilizes adaptive weights to balance the contribution of features from each scale. Assuming the feature maps of different scales are F_1, F_2, ..., F_S, the fusion strategy can be expressed as Equation (8).

$$F_{fused} = \sum_{s=1}^{S} \alpha_s F_s \tag{8}$$

In Equation (8), α_s represents the weight coefficients adaptively learned through the attention mechanism. In this way, the model can adjust the weights of features at different scales based on their actual contributions, thereby achieving efficient multi-scale information fusion. The full utilization of multi-scale features not only enhances the recognition ability of the model but also improves its adaptability to complex scenes.

2.2. Model Lightweighting and Optimization Algorithms

When constructing efficient digital twin models, model lightweighting is of paramount importance. Structural Re-parameterization is a strategy that effectively reduces the computational complexity during model inference through multi-branch training and single-branch inference. Specifically, during the training phase, a multi-branch architecture is employed to enhance the model's expressive power, with its mathematical representation outlined in Equation (9).

$$F_{train} = \sum_{i=1}^{n} W_i * X + b_i \tag{9}$$

In Equation (9), W_i represents the convolutional kernel of the i-th branch, X is the input feature map, and b_i denotes the bias term. During the inference phase, the multi-branch architecture is merged into a single branch to reduce the computational load. To further minimize the model's computational requirements, research integrates Depth wise Separable Convolution (DSC). This method decomposes the standard convolution operation into depth wise convolution and pointwise convolution, significantly reducing the number of parameters and computational costs. Assuming the kernel size of the standard convolution is $K \times K \times C_{in} \times C_{out}$, the computational complexity of the standard convolution can be expressed as Equation (10).

$$FLOP_{std} = K^2 \times C_{in} \times C_{out} \times H \times W \tag{10}$$

Where H and W are the height and width of the input feature map, respectively. The computational complexity of depthwise separable convolution can be expressed as Equation (11).

$$FLOP_{s_{sep}} = K^2 \times C_{in} \times C_{out} \times H \times W + 1 \times 1 \times C_{in} \times C_{out} \times H \times W \tag{11}$$

It can be observed that depthwise separable convolution significantly reduces computational costs, making it suitable for deployment on resource-constrained terminal devices. Combining structural re-parameterization and depthwise separable convolution, a re-parameterized separable convolution module is proposed. This module employs a multi-branch structure during training to enhance the model's representation capability while leveraging depthwise separable convolution to reduce the computational complexity of each branch. During inference, the multi-branch structure is merged into a single branch through re-parameterization, achieving model lightweighting. This design significantly reduces the model's inference latency while maintaining high

accuracy. To further improve the model's expressive ability, an Enhanced Efficient Channel Attention (ECA) mechanism is studied and integrated into the re-parameterized separable convolution module. ECA enhances the model's ability to focus on features through cross-channel information interaction, with its core calculation formula presented in Equation (12).

$$F_{ECA} = F \cdot \sigma(Conv1D(GAP(F))) \tag{12}$$

Where GAP denotes the Global Average Pooling operation, $Conv1D$ represents a one-dimensional convolution operation, and σ is the activation function. This mechanism can significantly improve the model's accuracy and robustness at a lower computational cost. To address the latency issues in system updates, an event-triggered synchronization mechanism is introduced. Data updates are triggered when the physical system's state changes exceed a certain threshold, thereby reducing unnecessary computational and communication overheads. This mechanism can be formulated as Equation (13).

$$\left\| x_k - \hat{x}_k \right\| > \varepsilon \Rightarrow trigger\ update \tag{13}$$

Where ε represents the threshold parameter. In this way, the system can ensure the precision and real-time performance of the digital twin while reducing latency. Therefore, the constructed algorithm flow topology for digital twin models is shown in Figure 2.

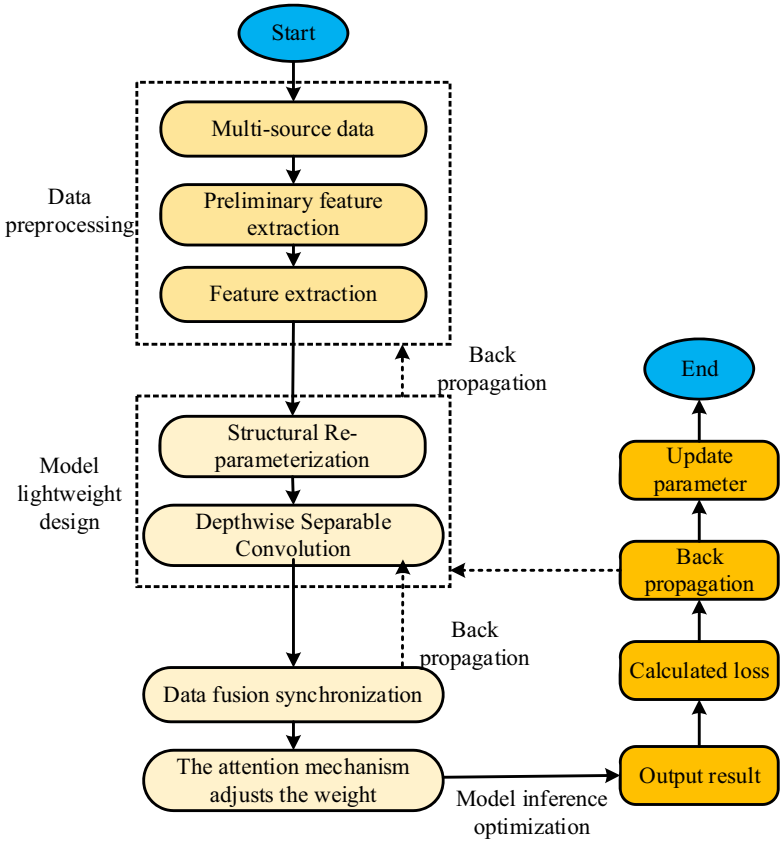

Figure.2 Algorithm flow topology for Digital Twin models

2.3. Cloud Mobile VR Simulation and Display Framework

Our framework employs cloud servers, digital twin models, and path tracking rendering technology to simulate 3D dynamic crane scenes in the cloud, producing real-time Omnistereo panoramic images [13]. Each pixel column aligns with a specific viewpoint, ensuring accurate stereoscopic vision as the head moves. These binocular panoramic images are then compiled into videos. We calculate the viewport image coordinates within the panoramic image through perspective projection, guided by the gaze direction. Subsequently, we create a synchronized video feed for both left and right eyes using bilinear interpolation. This video stream is sent to a smartphone's web browser for stereoscopic viewing. Simultaneously, data from the gyroscope and accelerometer are processed by AJA and relayed to the rendering system to refresh the video feed, facilitating interaction. The visual result on mobile devices is depicted in Figure 3.

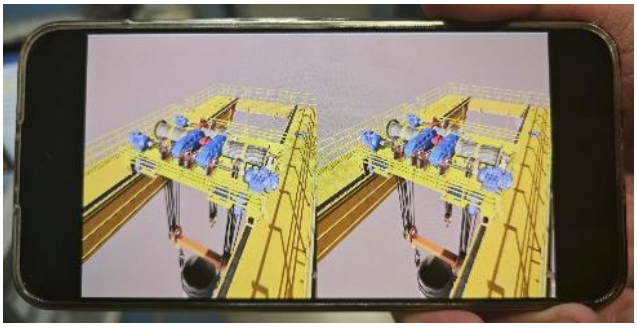

Figure 3. Final result in smart phone browser

Based on interaction data received from the client, the rotation of the virtual camera at the rendering end is determined, facilitating interaction with the 3D environment. Utilizing Euler's rotation theorem and the three azimuth angles captured by the smartphone's gyroscope, which are processed by AJA, the rotation of the stereo camera within the scene is accomplished in relation to real-world and smartphone device coordinates. After establishing the camera's initial position in the virtual scene, the rotation matrix Q is computed based on the smartphone's azimuth angles. Subsequently, the unit vectors U_1 and W_1 in the real-world coordinate system, corresponding to the x-axis and z-axis directions of the smartphone's coordinate system, are calculated using the transformation of Q. The transformation matrix M is then employed to determine the vectors U_2 and W_2 in the virtual world coordinate system, which correspond to U_1 and W_1. The camera's upward direction vector and forward observation vector in the scene are updated to U_2 and W_2, respectively, ensuring proper alignment with the camera's rotated position.

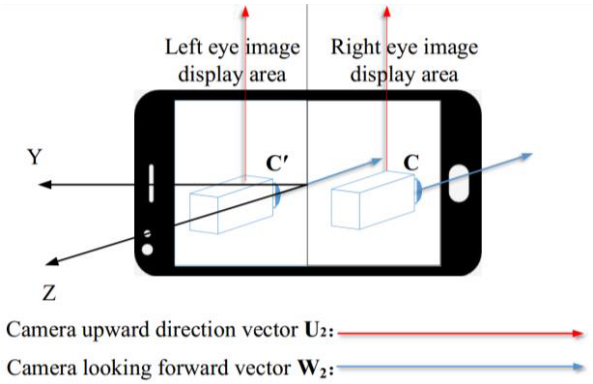

Figure 4. Relationship between device coordinate and camera direction in the VR scene.

As illustrated in Figure 4, the parameters of the stereo camera in the VR scene are computed by ascertaining the camera's rotation position. These parameters correspond to the device coordinates of the phone and the respective left and right display regions on the phone screen.

3. Experimental Analysis

3.1. Experimental Environment and Datasets

To ensure the reliability and reproducibility of experimental results, the experiments were conducted on a high-performance computing platform with representative datasets. The hardware environment comprises high-performance computing servers equipped with multi-core processors and GPUs with large memory capacities to support large-scale parallel computations. The software environment selects mainstream deep learning and graphics rendering frameworks with corresponding libraries and tools configured to ensure efficient model training and framework testing. The hardware and software environments are detailed in Table 1.

Table 1. Hardware and software environments

Category	Components/Tools	Specification/Version
Computing equipment	Server	Intel Core i9-9900KS
Internal memory	RAM	256 GB DDR4
Graphics card	GPU	GeForce RTX 2060 SUPER
Operating system	OS	Ubuntu 18.04 LTS
Deep learning framework	Framework	TensorFlow 2.8.0
Programming language	Language	Python 3.8.10
Data processing tool	Data Processing Tools	NumPy 1.21, Pandas 1.3.5

In terms of datasets, publicly available datasets widely used in the field of digital twinning were selected, including ImageNet dataset, CIFAR-10 dataset, and Stanford Dogs dataset. These datasets contain physical system state data and corresponding label information under various scenarios. The datasets underwent rigorous preprocessing, including data cleaning, normalization, and data augmentation, to ensure the model's

generalization capability under different conditions. The datasets were divided into training sets, validation sets, and test sets at a ratio of 8:1:1 to ensure sufficient training of the model, parameter optimization, and final performance evaluation.

3.2. Algorithm Performance Analysis

In the analysis of algorithm performance, to objectively compare and evaluate the merits of the algorithms, the primary performance metric considered is Accuracy. The experiments were conducted under a unified hardware and software environment, using identical datasets and preprocessing methods to ensure comparability and fairness of the results. The focus was on analyzing the performance of the improved multi-scale feature extraction algorithm at different iteration stages and comparing it with the performance of several classical algorithms. This assessment aimed to evaluate its advantages in handling complex data and enhancing the model's generalization ability. The comparative results of accuracy are illustrated in Figure 5.

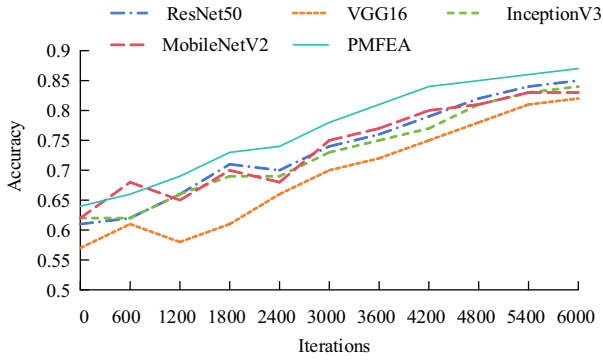

Figure 5. Precision comparison result.

As shown in Figure 5, the Proposed Multi-Scale Feature Extraction Algorithm (PMFEA) outperforms the other four classical algorithms at different iteration numbers. At the initial iteration, PMFEA achieves an accuracy of 0.64, slightly higher than ResNet50's 0.61, VGG16's 0.57, InceptionV3's 0.62, and MobileNetV2's 0.62. With the increase in iteration numbers, PMFEA demonstrates a significant improvement in accuracy, reaching 0.73 at 1800 iterations, surpassing all comparison algorithms. At 3000 iterations, PMFEA's accuracy stands at 0.78, ahead of ResNet50's 0.74, VGG16's 0.70, InceptionV3's 0.73, and MobileNetV2's 0.75. By 6000 iterations, PMFEA's accuracy climbs to 0.87, while ResNet50 and InceptionV3 achieve 0.85 and 0.84, respectively, and VGG16 and MobileNetV2 attain 0.82 and 0.83, respectively. Overall, PMFEA exhibits faster convergence rates and higher final accuracies across all iteration stages, with its advantages becoming more pronounced after 1800 iterations. Observing the data fluctuations, PMFEA not only performs well in the early stages but also maintains stability in later accuracy improvements, further demonstrating its superiority in multi-scale feature extraction tasks.

Table 2 presents a comparison of the accuracy of the research model (PMFEA) across various scenarios. From the data analysis, it is evident that PMFEA demonstrates outstanding performance in all tested scenarios. In the static crane recognition scenario, PMFEA leads other algorithms with an accuracy of 0.93. In the dynamic crane management scenario, the accuracy of PMFEA is 0.89, significantly better than VGG16's

0.83. In the crane driving simulation scenario, the accuracy of PMFEA is 0.85, slightly higher than InceptionV3's 0.82. In the smart grid management scenario, PMFEA surpasses ResNet50 and MobileNetV2 with an accuracy of 0.90. In equipment diagnosis, PMFEA achieved the highest accuracy of 0.94. PMFEA exhibits stable and superior performance in various application scenarios.

Table 2. Accuracy test results in different scenarios

Scenario	ResNet50	VGG16	InceptionV3	MobileNetV2	PMFEA
Static crane operation	0.9	0.87	0.89	0.88	0.93
Dynamic crane management	0.86	0.83	0.85	0.84	0.89
Crane driving	0.8	0.78	0.82	0.81	0.85
Smart Grid	0.88	0.85	0.87	0.86	0.9

Figure 6 illustrates the variation of loss values between PMFEA and VGG16 at different iteration numbers.

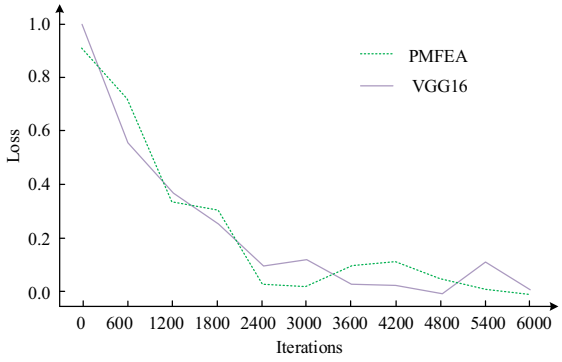

Figure 6. Loss Value Changes Of PMFEA And VGG16.

As depicted in Figure 6, at the initial iterations, the loss values of both algorithms decrease rapidly, with VGG16 swiftly dropping from 1.0 to around 0.3, while PMFEA declines from 0.95 to approximately 0.25. As the iterations progress, the loss values of both algorithms tend to converge and exhibit similar patterns, fluctuating around 0.2 between 1800 and 3000 iterations. Notably, VGG16 exhibits some fluctuations in the mid-to-late stages, particularly after 5400 iterations, where its loss value rises back to 0.22. In contrast, PMFEA maintains a more stable performance during this phase, ultimately converging to 0.18. This behavior suggests that although both algorithms demonstrate similar convergence rates initially, PMFEA exhibits greater stability and achieves a lower final loss value in the later stages.

3.3. Analysis of simulation scenarios display effect of cloud mobile VR framework

In this experiment, a simulated scenario featuring a specific crane was employed as a case study to evaluate and contrast the simulation outcomes of the crane's 3D environment. This comparison was conducted both within the context of a cloud-based mobile VR framework and independently on a server. Figure 7 presents a visual comparison of the display results from three distinct perspectives, rendered separately on a PC and a mobile web browser. The left side showcases the simulation results

achieved through ray tracing rendering on a PC without the use of a framework, while the right side displays the outcomes derived from cloud rendering within the framework on a mobile web browser. Notably, the display results on the mobile web page closely mirror those of the PC simulation.

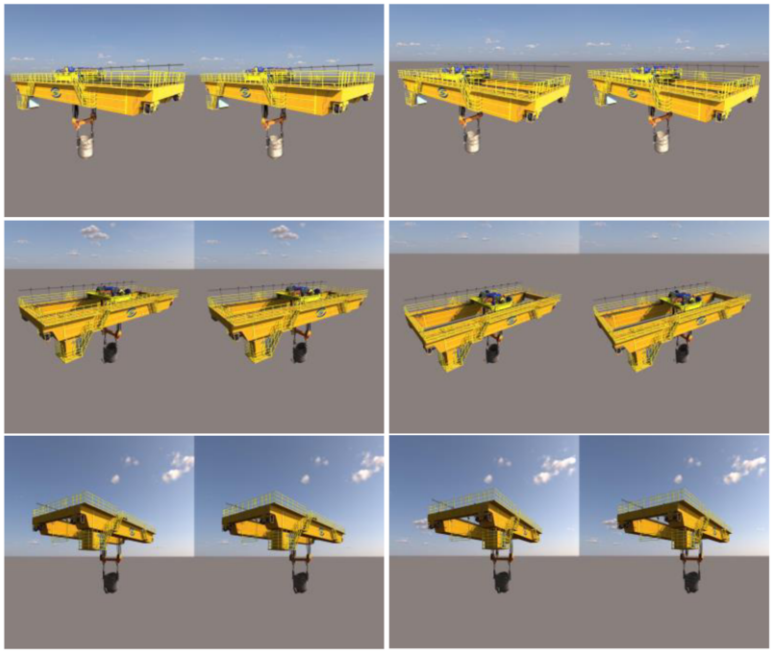

(a)PC side simulation effect (b)Mobile web display effect

Figure 7. Comparison of the effects of simulation scenarios.

Figure 7 demonstrates the capability of this framework to simulate 3D crane VR scenes using ray tracing, a feat that conventional mobile VR applications cannot achieve. Additionally, the framework's plugin-free operation across various mobile browsers highlights its cross-platform compatibility, cost-effectiveness, and high efficiency. When integrated with digital twin models, the 3D crane simulation scenarios displayed on mobile devices exhibit a seamless alignment with the actual operational scenarios of the crane.

4. Conclusion

We propose a crane cloud-based mobile VR framework based on digital twinning, enabling lightweight VR simulation scenarios stereoscopic display of crane 3D scenes on mobile devices.. Despite this, traditional digital twin models encounter challenges in crane simulation scenarios, such as multi-scale data extraction, model optimization, and real-time system performance. To tackle these, we've proposed a digital twin algorithm focused on multi-scale feature extraction and structural reparameterization. Our experimental results show that this model has high accuracy and fast convergence, especially after 6000 iterations where PMFEA's accuracy reaches 0.87, outperforming algorithms like ResNet50 and InceptionV3. PMFEA also shows high precision in various scenarios, including 0.89 in intelligent building management and 0.94 in equipment

diagnosis. Despite these achievements, PMFEA has room for improvement in real-time data handling for large-scale updates. Future work will optimize the algorithm's lightweight design and explore efficient real-time data processing to improve robustness and scalability across applications. Additionally, we plan to address the VR framework's delays and interaction issues by leveraging smartphone sensors and deep learning to predict and redefine head movements, enhancing video playback smoothness and speed.

Acknowledgments

This work was supported partly by Science and Technology Plan Project of Special Equipment Safety Supervision Inspection Institute of Jiangsu Province (KJ(Y)2023035).

References

[1] Sagar K V D, Kamesh D, Rao T S .Detecting Fake Faces In Smart Cities Security Surveillance Using Image Recognition And Convolutional Neural Networks[J].ECS transactions, 2022,1(107):19749-19758. DOI:10.1149/10701.19749ecst.

[2] Lou G , Shi H .Face image recognition based on convolutional neural network[J].China Communications, 2020, 17(2):117-124. DOI:CNKI:SUN:ZGTO.0.2020-02-011.

[3] D Dai, Y Li, Y Wang, H Bao, G Wang.Rethinking the image feature biases exhibited by deep convolutional neural network models in image recognition[J].CAAI Transactions on Intelligence Technology, 2022, 7(4):721-731. DOI:10.1049/cit2.12097

[4] Konstantakopoulos F , Georga E , Fotiadis D .Mediterranean Food Image Recognition Using Deep Convolutional Networks.[J].Annual International Conference of the IEEE Engineering in Medicine and Biology Society. IEEE Engineering in Medicine and Biology Society. Annual International Conference, , 2021, 2021:1740-1743. DOI:10.1109/EMBC46164.2021.9630481.

[5] Y Quionez, C Lizarraga, J Peraza, O Zatarain.Image recognition in UAV videos using convolutional neural networks[J].IET Software, 2020, 14(2):176-181. DOI:10.1049/iet-sen.2019.0045.

[6] DD Nart, C Costa, GD Prisco, E Carpana.Image recognition using convolutional neural networks for classification of honey bee subspecies[J].Apidologie, 2022, 53(1):1-15. DOI:10.1007/s13592-022-00918-5.

[7] Tasci E .Voting combinations-based ensemble of fine-tuned convolutional neural networks for food image recognition[J].Multimedia Tools and Applications, 2020, 79(41):30397-30418. DOI:10.1007/s11042-020-09486-1.

[8] Wang S , Dey S .Rendering Adaptation to Address Communication and Computation Constraints in Cloud Mobile Gaming[J].IEEE, 2010:1-6. DOI:10.1109/GLOCOM.2010.5684144.

[9] Winston J J , Hemanth D J , Angelopoulou A , Kapetanios E .Hybrid deep convolutional neural models for iris image recognition[J].Multimedia Tools and Applications, 2021,7(81):9481-9503. DOI:10.1007/s11042-021-11482-y.

[10] Bularz M , Przystalski K , Ogorzaek M .Car make and model recognition system using rear-lamp features and convolutional neural networks[J].Multimedia Tools and Applications, 2023,2(83):4151-4165. DOI:10.1007/s11042-023-15081-x.

[11] Cai W , Shea R , Huang C Y ,et al.A Survey on Cloud Gaming: Future of Computer Games[J].IEEE Access, 2017. DOI:10.1109/ACCESS.2016.2590500.

[12] Hong H J , Chen D Y , Huang C Y , Chen K T, Hsu C H.Placing Virtual Machines to Optimize Cloud Gaming Experience[J].IEEE Transactions on Cloud Computing, 2015, 3(1):42-53. DOI:10.1109/TCC.2014.2338295.

[13] Peleg S , Ben-Ezra M , Pritch Y . Omnistereo: Panoramic Stereo Imaging[J].IEEE Transactions on Pattern Analysis and Machine Intelligence, 2001, 23(3): 279-290. DOI:10.1109/34.910880.

[14] Wang X , Yang Z .Research on Classification and Recognition of Object Image Based on Convolutional Neural Network[J].IOP Conference Series Materials Science and Engineering, 2020, 782:1-15. DOI:10.1088/1757-899X/782/4/042062.

[15] Ohri K , Kumar M .Review on self-supervised image recognition using deep neural networks[J].Knowledge-Based Systems, 2021, 224(8):1-11. DOI:10.1016/j.knosys.2021.107090.

Fuzzy Systems and Data Mining X
A.J. Tallón-Ballesteros (Ed.)

doi:10.3233/FAIA241458

Explainable Statistical Evaluation and Enhancement of Automated Driving System Safety Architectures

Rainer Faller [a,1]
[a] *exida.com GmbH Munich, Germany*

Abstract. Deep Neural Networks [DNNs] are being integrated into Automated Driving Systems [ADS] to perform complex perception and control problems. However, DNNs are generally challenging or impossible to interpret for the purpose of functional safety [FuSa] or Safety of the intended functionality [SOTIF] assessment. In contrast, physical models of the driving task are generally much easier to explain and assess than the abstract statistical models encoded in a DNN. In this paper, we present a statistical modelling and evaluation workflow that can be easily explained to FuSa and SOTIF assessors. Our workflow uses Bayesian networks [BN] refining fault trees and a physical model of an ADS in a given scenario. The Dominant Factors [DF] that impact the ADS risk can then be identified based on simulations of the physical model and simulations sampled from the BN. The workflow can evaluate under which conditions a tolerable risk target [TRT] can be achieved. We evaluate our proposed workflow in an example high-frequency traffic scenario, a highway cut-in scenario. We compare two methods to identify and confirm the DF for meeting the TRT. The DF found show that a static operating design domain [ODD] definition is insufficient. In the example, if the sense-plan-act control architecture is extended by a dynamic traffic monitoring protection layer, the TRT can be achieved.

Keywords. ADS, Statistical modelling and evaluation of ADS, Assessment of complex systems, Quantitative SOTIF analysis,

1. Motivation

The algorithms used in automated driving systems [ADS] are complex and non-deterministic. Some variants of deep neural networks [DNN] can be explained theoretically but the DNN behaviour under all conditions for the set of safety-critical scenarios [SCS] to be covered by the ADS in the given operating design domain [ODD] is generally not readily understood.

To the author, explainability requires models that can be explained under all operating conditions. Physical models are typically much easier to explain and understand than abstract statistical data models. Nevertheless the ADS vendor and independent FuSa and SOTIF[2] assessor need to confirm that the ADS meets the Tolerable Risk Target [TRT],

[1] Corresponding Author: Rainer Faller, *exida.com* GmbH, Rainer.Faller@exida.com.

[2] Safety of the intended functionality [SOTIF] is the absence of unreasonable risk due to hazards resulting from functional insufficiencies of the intended functionality or its implementation [ISO 21448 [1] §3.25].

see section 2. Hence the concept proposed in this paper is not to explain the ADS DNN algorithms and their implementation, but to keep the physical and statistical analysis and testing arguments independent of the complex algorithms, and easily explainable.

This paper and the previous paper [2] should be seen as a journey towards merging statistical evidence methods with physical models such that FuSa and SOTIF practitioners and assessors not trained in modern AI can readily understand and judge whether a specific ADS meets the TRT. As graphical models are well understood by engineers, a directed acyclic Probabilistic Graphical Model [PGM], herein Bayesian Network [BN], has been chosen as a natural refinement of the fault tree analysis [FTA] presented in [2]. In contrast to the proposed conversion of FTA to BN by [3], this BN is not a direct translation of the FTA but an extension representing all variables relevant for the SCS and their (conditional) dependencies.

The FTA in [2] did show that published ADS architectures are questionable to meet the TRT even when enhanced by additional protective subsystems. This paper will evaluate by BN and Monte-Carlo simulations [MCS] under which conditions the TRT can be met.

2. How safe must ADS be - Tolerable Risk Target

The European Commission states in [4] "a minimal requirement for manufacturers and deployers is to ensure that Connected and Automated Vehicles [CAVs] decrease, or at least do not increase, the amount of physical harm incurred by users of CAVs or other road users that are in interaction with CAVs, compared to the harm that is inflicted on these groups by an appropriately calculated benchmark based on conventional driving.". Common terms with the same meaning are GAMAB (Globalement au moins aussi bon) or GAME (Globalement au moins équivalent), and Positive Risk Balance (PRB).

Therefore, the rate of fatalities on the road is a reasonable starting point for a TRT. To estimate the rate of road fatalities we use the traffic accident data of the Federal Statistical Office of Germany (DESTATIS) [5]. They show for the years 2014..2019 (excl. COVID19 lockdown) an average rate of 1.41e-7 /h of fatalities (variance 6.99e-16) and 2.31e-6 /h of serious injuries (variance 2.13E-14) on German Autobahn, assuming a mean velocity of 100km/h. Further studies [6] show that 15% of serious injuries can lead to death in hospital.

Consequently, the sum of the frequencies of the violation of the safety goal resulting in fatalities and a fraction of the serious injuries for all SCS shall be less than the actual risk derived from DESTATIS data, see equation (1). Some fatalities could have been caused by random hardware [HW] failures of the ADS, so the HW failure rate, typically 1e-8/h for ISO 26262-5 ASIL D [7], is deducted once for all SCS from the TRT. Q is the probability to fail, and capital Ω is used for the sum of the frequencies in contrast to lower-case ω for the frequency of the individual scenario.

$$
\begin{aligned}
&\Omega_{\text{fatalities}} = \sum_{\forall \text{SCS}} Q_{\text{SCS}}(\text{fatalities}) * \omega_{\text{SCS}} + 15\% * \sum_{\forall \text{SCS}} Q_{\text{SCS}}(\text{serious injuries}) * \omega_{\text{SCS}} \\
&Q_{\text{fatalities}} < Q_{\text{DESTATIS fatalities}} - \text{PMHF(ISO 26262-5(ASIL D))} \\
&Q_{\text{fatalities}} < 1.41\text{e-}7/\text{h} - 1\text{e-}8/\text{h} \;=\; 1.31\text{e-}7/\text{h}
\end{aligned}
\tag{1}
$$

In the following, a high demand frequency SCS is considered as low demand frequency SCS contribute little to the dangerous failure rates, see [2]. As there are not many high demand frequency SCS for the Autobahn ODD, an interim target of 2e-8/h is assumed for this high demand frequency SCS individually.

3. Explainable Statistical Evaluation

We consider the European Commission requirement for a quantitative risk target as helpful. Quantification has helped in the history of FuSa to focus design improvements on the weak parts of a system. The implementation will confront the automotive industry, however, with challenges as the related FuSa standard, ISO 26262 [7], addresses only the quantitative analysis of random hardware faults. The SOTIF standard, ISO 21448 [1], describes quantitative methods only in the informative annex C.

The RAND Corporation demonstrates in [8], that an OEM cannot statistically prove the TRT by extensive driving tests before delivery to customers. Furthermore, statistical evidence obtained by recording incident-free driving kilometres may be of limited value for safety justification as the critical driving scenarios and operating profiles experienced during the recorded driving tests might not reflect the ones in a new environment.

To address the gap of quantitative analysis of statistical / AI models, we propose the workflow shown in Fig. 1. Most of the activities are explained in this paper.

(1) ADS item and function definition.
(2) Definition of the ODD, the tolerable risk level, and the SCS.
(3) Physical model for each SCS and analysis of the DF of the physical model.
(4) Collection of data with particular care taken on the DF.
(5) BN modelling refining the FTA, and the physical model.
MCS using the collected data distributions.
(6) Analysis of the DF as per the BN and MCS simulation.
If needed collection of data for additional DF.

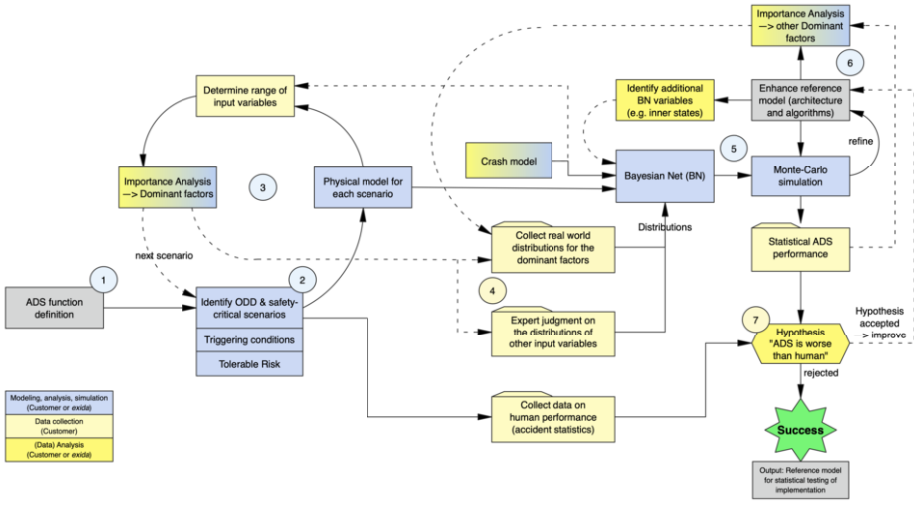

Figure 1. Explainable Statistical Evaluation workflow

(7) If the results of the BN and MCS show that the hypothesis of the ADS being worse than the human drivers cannot be rejected then improve the ADS.
Else use the physical model and BN as a reference model for the statistical testing of the ADS implementation.

4. Assumed ADS architecture

We assume a three layer ADS architecture, see Fig. 2. Note, justification of the ASIL assignment shown is not subject of this paper.

- Layer 1: AD Control subsystem [C].
- Layer 2: Protective subsystem [P], calculating the safe braking distance to the nearest objects on the ego-vehicle's trajectory, and taking brake action to avoid impact resulting in injury.
- Layer 3: Traffic monitoring and warning subsystem [W], monitoring the surrounding traffic for SCS of unexpected DF ranges and frequencies.

The C-P-W architecture provides multiple advantages for the safety justification. First, P using Kalman filters is functionally diverse of C and can be well understood, evaluated and tested. Second, P&W will support field monitoring, including the FuSa and SOTIF failure rates of C during operation. Due to the monitoring in operation, one may postulate reasonable SOTIF failure rate claims upfront for C (engineering judgment) without having statistical prove early in development. This addresses the findings of [8], which demonstrated that postulation of reasonable claims will be necessary as a statistical prove by extensive driving tests before delivery to customers is impossible. Downside: If the failure rates are much higher than postulated, then the system will

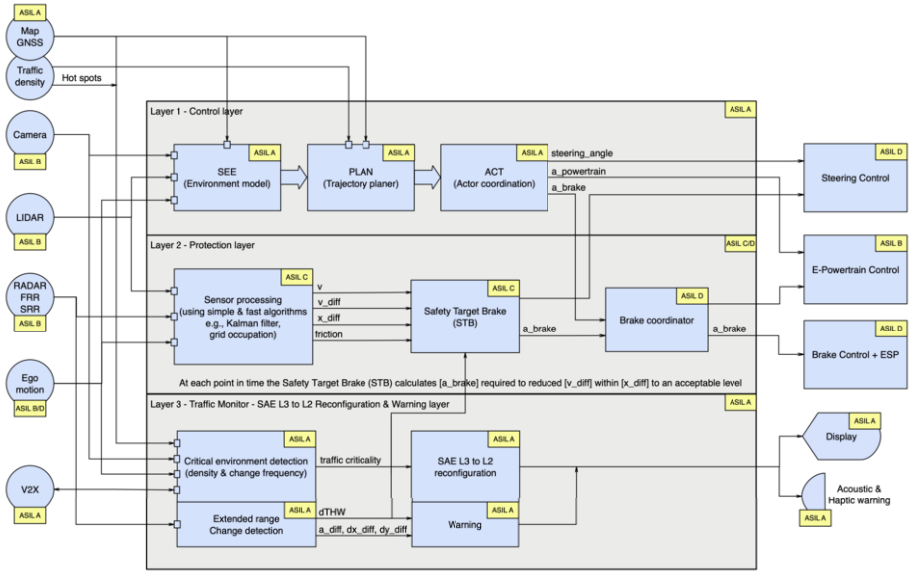

Figure 2. ADS layered architecture enhanced by a dynamic traffic monitor

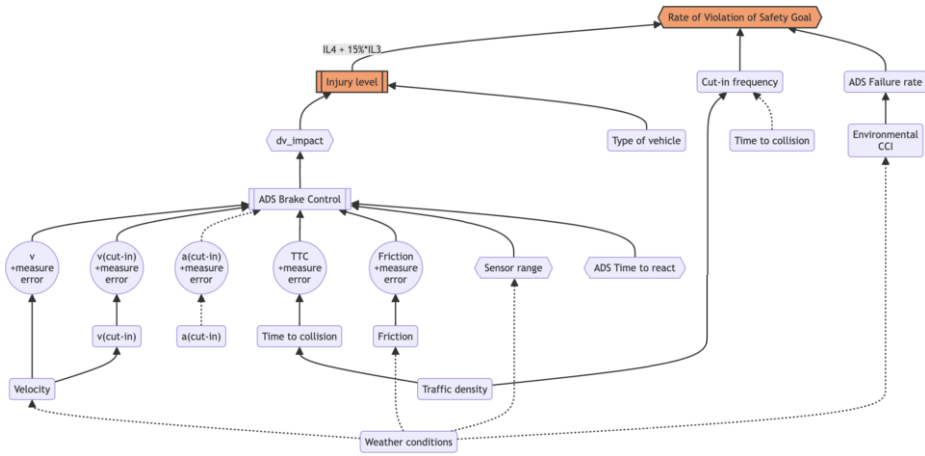

Figure 3. Simplified BN for the cut-in scenario incl. measurement error

violate the TRT till the case is detected by field monitoring, and the OEM limits the AD functionality by over-the-air update or recall.

5. High demand frequency scenario - Vehicle cut-in

The preceding publication [2] modelled the high demand frequency SCS of vehicle cut-in for the ADS architecture by a FTA with three layers. As the FTA cannot evaluate the dependencies of scenario variables (traffic & environmental conditions, ADS safety performance, accident severity), the FTA is converted and extended to BN and a physical motion model, see Fig. 3. Note, the dashed dependencies are not included in the results reported herein. Injuries are determined by a crash model resulting in injury level IL1 to IL4 (IL1 = property damage, IL2 = minor injury, IL3 = serious injury, IL4 = fatality). Note, the crash model implements $Injury\,level = function(impact\,speed,\ vehicle\,type)$ by a lookup table, and is simpler than the one of [9].

The FTA layers are variables in the BN (Fig. 3). The calculation of the BN variable *Rate of violation of Safety Goal* matches the top FTA layer taking in the probability of fatality and severe injury. The variable *ADS Failure rate* matches the lowest FTA layer modelling the probability of systematic failures of the diverse redundant ADS using a quantitative Common Cause Beta factor model per IEC 61508-6 Annex D [10]. From [2]: C and P are assumed to fail either independently or due to a common cause within a given scenario, equations (2).

$$
\begin{aligned}
Q(\mathrm{C}\cdot\mathrm{P}) &:= \text{ Probability of C AND P violating the safety goal}\\
Q(\mathrm{C}\cdot\mathrm{P}) &= Q(\mathrm{C})\cdot Q(\mathrm{P}) + \mathrm{CC(C,P)}\\
CC(\mathrm{C,P}) &= \beta(\mathrm{CC})\cdot\min(Q(\mathrm{C}),Q(\mathrm{P}))\\
Q(\mathrm{C}\cdot\mathrm{P}) &= Q(\mathrm{C})(1-\beta)\cdot Q(\mathrm{P})(1-\beta)+\beta\cdot\min(Q(\mathrm{C}),Q(\mathrm{P})).
\end{aligned}
\tag{2}
$$

CC(C,P) denotes the common cause failure of C and P. The use of min() is explained by the stress / strength model. Both, C and P fail at the same stress if the stronger of the two fails, i.e., the subsystem with the lower failure rate.

5.1. Analysis of the dominant factors per the physical model

To focus the efforts for the data collection, activity (4) of Fig. 1, an initial analysis of the DF per the physical model is performed, activity (3). The analysis does a numerical partial derivative of the individual variables with the other variables being held at different operating set-points, see equation (3). Note: It follows the concept of the Birnbaum importance measure used in FTA [11]. The variables with high importance are the DF, see Table 1. Positive means increase in value of the variable increases risk, negative means increase in value decreases risk, zero means the variable does not contribute to risk as per the physical model.

$$\text{dv\_impact} = \text{ADS\_motion\_control}(x_1 = v,\ x_2 = \Delta v,\ x_3 = TTC,\ ...)$$

$$\text{Importance} = \begin{cases} \max\left(\frac{\partial}{\partial x_i}\text{dv\_impact}(x_1, x_2, .., x_n)\right) & \text{for } \frac{\partial}{\partial x_i}\text{dv\_impact} \geq 0 \\ \min\left(\frac{\partial}{\partial x_i}\text{dv\_impact}(x_1, x_2, .., x_n)\right) & \text{for } \frac{\partial}{\partial x_i}\text{dv\_impact} < 0 \end{cases} \tag{3}$$

Table 1. Results of the Importance analysis of the physical model

Variable	Importance	Range
traffic density	0.000	low := 1, normal := 2, congested := 3
vehicle	0.000	passenger car := 1 or truck := 2
velocity v	0.000	range depending on scenario, max: 5.55 to 55.55 m/s
Δvelocity(cut-in)	3.250	speed difference, dependent on v, max: 0 to 30.55 m/s
friction	−1.256	range: 0.3 to 1.1
ADS time to react	0.275	range: 0.1 to 0.5 s
time-to-collision [TTC]	−1.648	dependent on traffic density, max range: 0.4 to 2.8 s
sensor range	0.000	range: 40 to 150 m

5.2. Monte-Carlo simulations

The variables in the BN have been populated with experience-based distributions, see Fig. 4 for examples and injury level results. Distributions from fleet data evaluation, activity (5) of Fig. 1, were not released for publication by OEMs. The results of the MCS have been compared with the Null Hypothesis that "*the ADS is equal or worse than the human drivers*", i.e., does not provide a positive risk balance, activity (5, 7). The MCS of the BN shows the following results:

- The null hypothesis cannot be rejected for the entire range of variables, as in these cases the TRT is far from being reached.
- If the ranges of the negative dominant variables are dynamically limited per section 5.3, then the Null Hypothesis can be rejected against a 95% upper confidence limit, see Fig. 5, and a one-sample T-test with a p-value <1e-34.

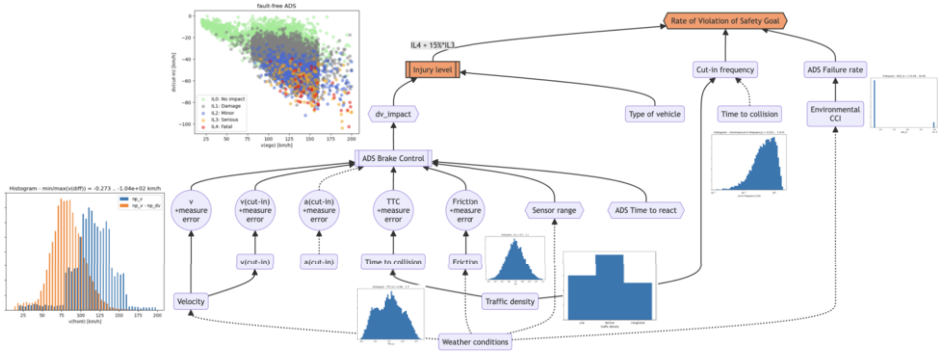

Figure 4. MCS of the BN with fault-free ADS and exemplary full range distributions

- The importance of the variables match generally with the importance analysis of the physical model if the ranges of the variables are very limited, like under Swedish regulations, or very open, like on German Autobahn, see the shift of the bars for the injury levels in Fig. 6. The MCS identifies in addition the importance of the absolute velocity, see Fig. 6, last bargraph. Note, the importance indicated by BN and MCS is less pronounced with limited negative DF.

5.3. Conditions to meet the Tolerable Risk Target

In contrast to the FTA, the MCS of the BN shows that the TRT can be met with a diverse redundant ADS architecture, provided the environmental and traffic conditions are favourable.

Some of the DF are part of the static and geographic ODD definition and monitoring, but others are of dynamic nature. To ensure that the dynamic DF are monitored not only for the ego-vehicle but the other vehicles around, a dynamic traffic monitor is proposed. Cut-in speed difference, TTC and cut-in frequency can be estimated from monitoring the dynamic traffic flow on adjacent lanes. If the estimated DF ranges fall outside the ranges assumed for the FuSa and SOTIF case, then the SAE L3 ADS should alert the driver and fall back to SAE L2+, layer 3 in Fig. 2, while still offering its full functionality to

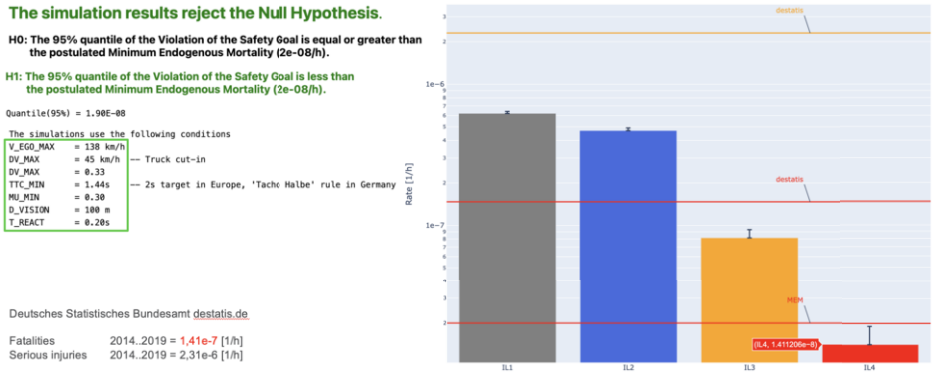

Figure 5. Distribution of rates of injuries with upper 95% Confidence interval

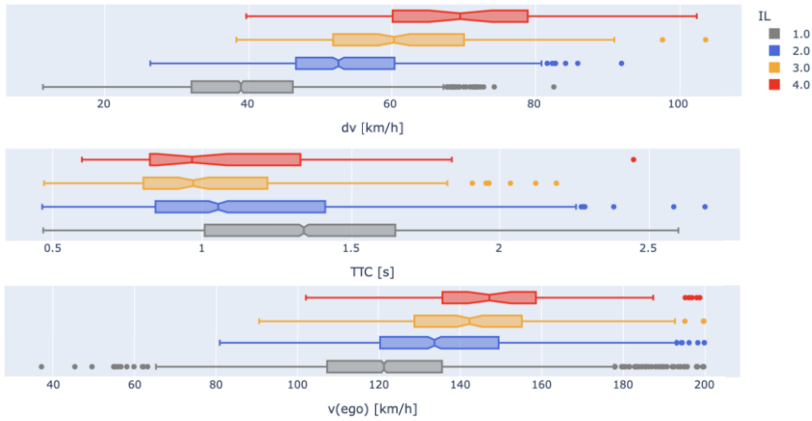

Figure 6. Dominant factors as per the BN and MCS

the alerted driver. The measurement range of the dynamic traffic monitoring would be greatly improved by vehicle-to-vehicle communication [V2V].

6. Conclusion

We have presented an evaluation workflow for ADS with complex software subsystems such as DNN. The evaluation workflow is based on models that are easy to understand by FuSa and SOTIF practitioners and assessors.

Diverse redundant safety architectures can meet the TRT for SAE L3 and above, if the ranges of the dominant variables, which have negative impact on the violation of the safety goal, herein cut-in velocity and demand rate distributions, will be monitored and limited. This requires a dynamic traffic condition monitoring (dynamic ODD) of which aspects are implemented by OEMs. A detailed discussion of the safety properties of a dynamic traffic condition monitor will be subject of a future publication.

Neither FTA nor BN modelling give evidence that architectures with little or no diverse redundancy incl. sensor diversity between control & protection subsystem can meet the TRT. Likewise architectures with a high potential for common cause failures between control & protection subsystem, such as sensors sensitive to high noise or low contrast scenarios, have not shown to meet the TRT.

We intend to prompt an open discussion on FuSa and SOTIF reasoning using statistical argumentation. A paper explaining an extended method will be published soon [12].

References

[1] International Organization for Standardization (2022) ISO 21448 - Road vehicles - Safety of the intended functionality

[2] Rainer Faller, Krystian Radlak (2022) A Statistical Analysis of Automated Driving System Safety Architectures. Computer Safety, Reliability, and Security. SAFECOMP 2022 Workshops, 23–34. https://doi.org/10.1007/978-3-031-14862-0_2

[3] Andrea Bobbioa, Luigi Portinalea, Michele Minichinob, Ester Ciancamerla (2001) Improving the analysis of dependable systems by mapping fault trees into Bayesian networks. Reliability Engineering and System Safety, 71, 249–260. https://doi.org/10.1016/S0951-8320(00)00077-6

[4] European Commission, Directorate-General for Research and Innovation (2020) Ethics of connected and automated vehicles. https://data.europa.eu/doi/10.2777/035239
[5] Statistisches Bundesamt (destatis) (2021) Verkehr, Verkehrsunfälle. Fachserie 8 Reihe 7. https://www.destatis.de/DE/Themen/Gesellschaft-Umwelt/Verkehrsunfaelle/Publikationen/Downloads-Verkehrsunfaelle/verkehrsunfaelle-jahr-2080700217004.pdf?__blob=publicationFile
[6] Axel Malczyk (2011) Gesamtverband der Deutschen Versicherungswirtschaft e.V. Schwerstverletzungen bei Verkehrsunfällen. Forschungsbericht FS. https://www.udv.de/resource/blob/79316/2d07873aa9888fae3d68dbb2f53a8b43/33-schwerstverletzungen-bei-verkehrsunfaellen-data.pdf
[7] International Organization for Standardization (2019) ISO 26262 - Road vehicles - Functional safety
[8] Nidhi Kalra, Susan Paddock (2016) How Many Miles of Driving Would It Take to Demonstrate Autonomous Vehicle Reliability? https://doi.org/10.7249/RR1478
[9] Nishimoto Tetsuya, Kosuke Mukaigawa, Shigeru Tominaga, Nils Lubbe, Toru Kiuchi, Tomokazu Motomura, Hisashi Matsumoto (2017) Serious Injury Prediction Algorithm Based on Large-Scale Data and under-Triage Control. Accident; analysis and prevention 2017, 98, 266–276. https://doi.org/10.1016/j.aap.2016.09.028
[10] International Electrotechnical Commission (2010) IEC 61508 - Functional safety of electrical/ electronic/ programmable electronic safety-related systems
[11] Marvin Rausand, Anne Barros, Anrljot Høyland (2020) System Reliability Theory, ch 7. Component Importance. https://doi.org/10.1002/9781119373940
[12] Moritz Werling, Rainer Faller, Wolfgang Betz, Daniel Straub (2024) Safety Integrity Framework for Automated Driving

Acknowledgement

My special thanks to Prof. Moritz Werling, BMW, Dr. Molly O'Brien, Frauke Blossey, James McGinley, *exida*, and Robert Maier, Ostbayerische Technische Hochschule Regensburg, for their feedback.

About the author

Cofounder of *exida.com* LLC, a world-wide leading analysis and certification company for FuSa, SOTIF, and cybersecurity. Before he was 20 years manager for FuSa at TÜV Süd (Technischer Überwachungsverein) and development engineer at MAN, developing a self-steering bus for public transportation with three channel safety architecture. He was chairman of the German IEC 61508 committee and IEC member and co-authored many parts of IEC 61508. He graduated at Technische Universität München (TUM) in electrical engineering and control engineering.

Fuzzy Systems and Data Mining X
A.J. Tallón-Ballesteros (Ed.)

doi:10.3233/FAIA241459

Solving A.I Safety and Alignment Issues Through Classical Safety Technology

Bentley Yusen Lin[a,1]
[a] *exida Safety Systems (Shanghai) Co., Ltd, China*
ORCiD ID: Bentley Lin https://orcid.org/0009-0000-2569-5919

Abstract. As the performance and capabilities grow in current A.I technologies, A.I is widely used in many different products potentially having safety impacts to the human. These products include Autonomous Driving, Robotics and Weapons…etc. The safety issues of the product which embeds A.I technologies, need to be evaluated and handled from both of functionalities, performances and malfunctioning perspective; Furthermore, the alignment issue of super intelligent large A.I model, is also an even bigger threats to public safety. In this paper, an approach to integrate system engineering, deductive and inductive analysis and classical safety technologies with modern A.I technologies to attempt to solve A.I safety and alignment issues are proposed

Keywords. A.I alignment, A.I safety, Autonomous Driving, System Engineering, Safety Technologies

1. Introduction

Inclusion of A.I technologies in safety critical systems is extending from small scale application, i.e. Use of A.I in environment perception and object labelling, to larger scale application, i.e. Use of Reinforcement Learning to control Multiagent Maneuvering [1]. There are complicated factors which might stop A.I from aligning with user intentions [2]. Such misalignment might lead to safety hazards if the output from A.I processing will trigger abnormal vehicular or robotic behaviors, for example, drive the vehicle itself to hit the objects for some unknown reasons. To make the A.I-based product acceptable to human civilization, possible technical measures to evaluate the residual risks and mitigate the risks, must be developed and adopted

The development approach between expert system and A.I-based system are vastly different, and those differences can be reflected on below aspects:

(1) Expert system are completely white box and deductively constructed. Thus the developers are familiar with each design step and also the logical reasons why it is designed as such. While A.I-based system is constructed by systematic training, and the operation logic wherewith is not fully understandable and explainable
(2) Expert system needs to define the absolute behaviors which shall be achieved by the system, which makes all the implementations within the

[1] Corresponding Author: Bentley Yusen Lin, Bentley.Lin@exida.com

system deterministic. A.I-based system is developed to resolve behaviors with uncertainties, or else the system solutions allow a wide variety of possibilities/ options, thus probability distribution is an important characteristics of A.I-based system

Above-mentioned properties make the A.I-based system having much lower controllability than a traditional rule-based expert system. Due to such uncontrollability, if the engineering techniques applied during the development of A.I-based system can't narrow down its probability of having behavior deviation out of acceptable range, the created product might be actually dangerous. In next chapter, the source of danger is analyzed and discussed.

2. Applying A.I technology in safety critical products

The universal power of A.I comes from its capabilities to be a function approximator of any possible mathematical or logical correlation [3], given its neuron characteristics, algorithm, model size and data completeness. Meanwhile, almost all physical behaviors happening in this world can be described with a mathematical model, thus the underlying representative function can be eventually learnt by A.I

If the approximated function deviates from target function and the deviation exceeds the acceptable range, the system could generate hazardous output causing safety issues.

2.1. Safety issues reflected on A.I technologies

In this paper, 4 types of safety issues which might be encountered by A.I are concluded below:

Assuming a given $\text{Function}_{\text{math}}$ to be approximated by A.I is:

$$3sin(x) \cdot 2sin(y) \cdot 1sin(z) = 10$$

The representing functional graph in x-y-z coordinates are shown below:

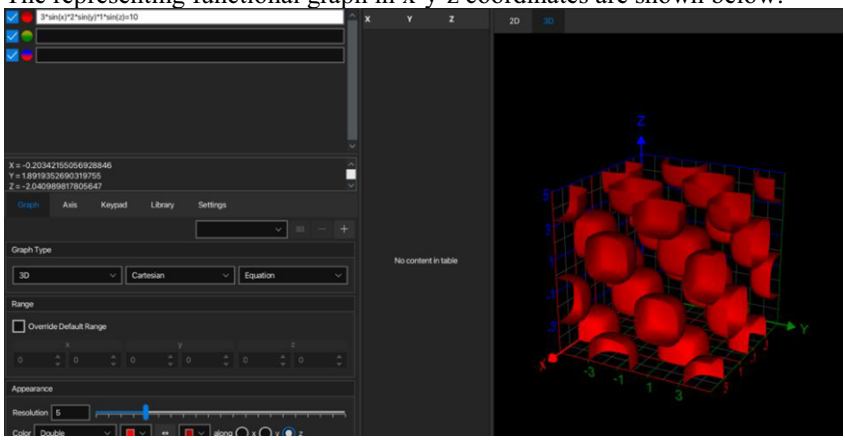

Figure 1. Target $\text{Function}_{\text{math}}$ to be approximated by A.I.

- **Safety of the Intended Functionality issue:** Due to the functional approximator has low accuracy, over-fitting or poor correctness, it yields to different function, such as

$$2.8sin(x) \cdot 2sin(y) \cdot 1sin(1.5z) = 11$$

This might create some unwanted state spaces as being specified by Green curve, those unwanted spaces could lead to safety issues during application if the output deviations exceed the acceptable safety threshold

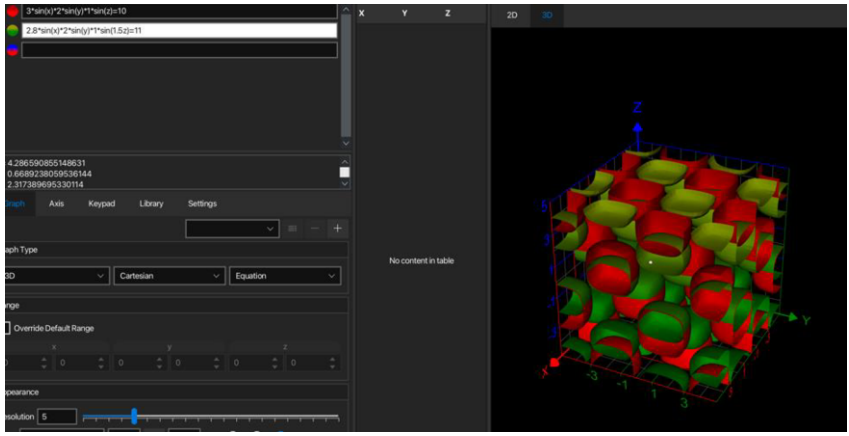

Figure 2. Example SOTIF issues happening in the approximation result

- **Functional Safety issue:** The approximated function matches original function perfectly, however, the failures in the HW element (e.g. GPUs) or SW element (e.g. crash of neuron operators) make the function approximator yields to different function, such as

$$3sin(x) \cdot 2sin(y) \cdot 1sin(z) = 0$$

wrongly, causing the functional output a total disaster with severe safety issues

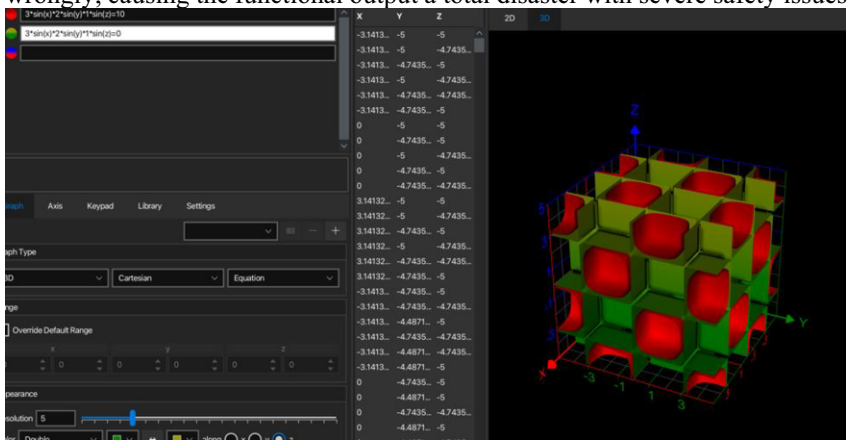

Figure 3. Example FuSa issues happening in the approximation result

- **Security issue:** The functional approximator has acceptable proximity to target function, however, there is security threat manipulating some parameters, leading to a different function, such as:

$$3sin(x) \cdot 5sin(y) \cdot 1sin(z) = 10$$

causing the certain range of state spaces violating the safety threshold

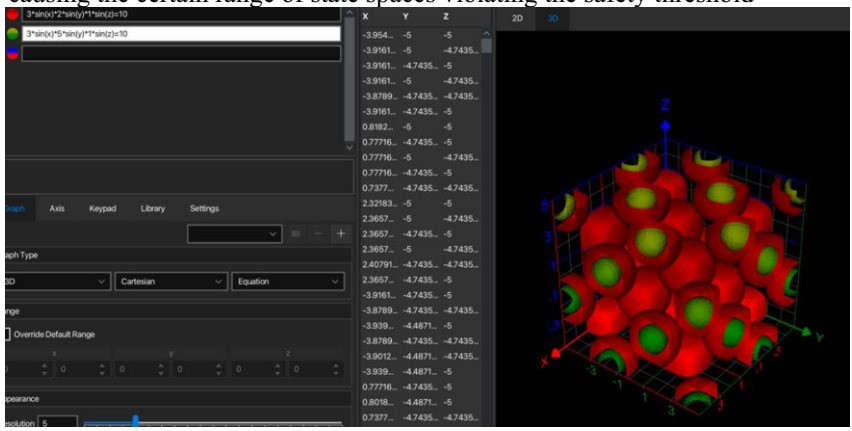

Figure 4. Example security issues happening in the approximation result

- **Alignment issue:** The functional approximator has capabilities to redefine its target function, due to wrong utility setups or wrong abstractions [4], thus the revised to different function, such as

$$3cos(x) \cdot 2sin(y) \cdot 1sin(z) = 10$$

one sin(x) is replaced by cos(x), and it does not align with target function anymore, making the system output hazardous

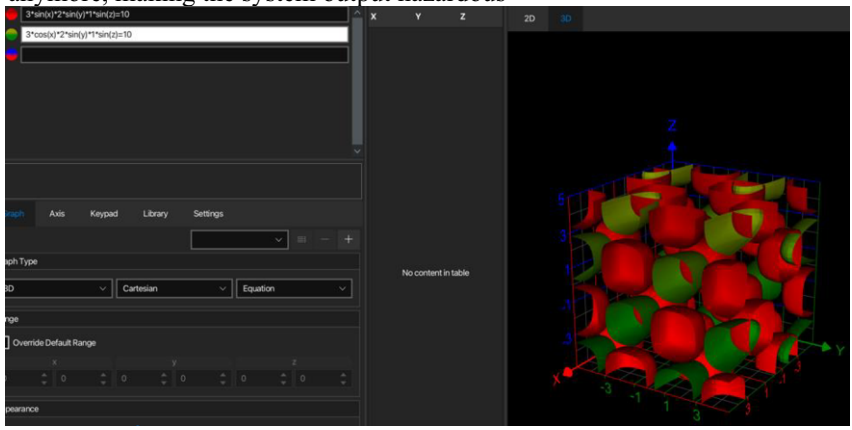

Figure 5. Example alignment issue happening in the approximation result

Different safety issues require different safety measures, the application of safety measures is to mitigate the associated risk, thus risk quantification mechanisms are absolutely needed in the development of A.I

3. Merge classical safety technologies into A.I development process

The definition of "Function", referencing from Oxford dictionaries, includes 2 perspectives,

1) A special activity or purpose of a person or thing.

2) MATHEMATICS- A quantity whose value depends on the varying values of others.

Here a separate term $\text{Function}_{\text{math}}$ is used to distinguish meaning between Function. Any Function can be modelled by one to several sets of $\text{Function}_{\text{math}}$, where the $\text{Function}_{\text{math}}$ is used to describe or define how the Function can be existing matching the designed intentions and to be subject under the controllable risks. Any Function shall be analyzed and designed under the framework of Functional Safety [5] and Safety of the Intended Functionality [6] if the Function might be safety-related. Since the $\text{Function}_{\text{math}}$ is part of the properties of a Function, $\text{Function}_{\text{math}}$ shall be subject to same framework of Functional Safety and Safety of the Intended Functionality as well. The following sections will discuss how to apply classical safety technologies to $\text{Function}_{\text{math}}$

3.1. ***Safety of the Intended Functionality based on ISO-21448***

Following ISO-21448, the Safety of the Intended Functionality shall be evaluated to ensure there is no unreasonable safety risk resulting from performance insufficiency [6], external triggering conditions (which expose the weakness of Function), foreseeable misuse and abuse (though abuse is not formally considered according to ISO-21448, it shall still be considered for A.I application). There introduces several technical ideas to govern the development of a Function, and they can be adapted to be fit for A.I development through below aspects:

- **Hazard Analysis and Risk Assessment of a $\text{Function}_{\text{math}}$**:
  For the associated $\text{Function}_{\text{math}}$ being approximated by A.I, possible "intended/ unintended output" or "intended/ unintended behavior" shall be assumed and analyzed by introducing key word methodologies "Hazop". This task shall be executed by whoever owner (e.g. system owner) having proper big picture about the consequences in applying A.I-based $\text{Function}_{\text{math}}$ approximator. Here the scientist doesn't need to know "why" the "unintended behavior" would occur, but need to assume "how" the "unintended behavior" would look like, also the possible consequences if the "unintended behavior" occurs under specific scenarios, then rating the consequence with "S" (Severity of the consequence due to unintended behavior of $\text{Function}_{\text{math}}$); "C" (Controllability of the consequence due to unintended behavior of $\text{Function}_{\text{math}}$). Through the S and C rating combination, the associated risk is determined, a further decision could be made about if the improvement or the revision of target $\text{Function}_{\text{math}}$, or the revision of A.I system is required

- **Definition of acceptance criteria per unacceptable risk and residual risk:**
  For the analyzed hazardous event being introduced by A.I system, if the intrinsic risk evaluated through S and C is not acceptable, then additional acceptance criteria per the hazardous event shall be defined- it's usually a target definition about how low the probability shall be to accept such an A.I-based $\text{Function}_{\text{math}}$ approximator: Either the probability of presence of unintended behavior is sufficiently low, or the probability to expose the $\text{Function}_{\text{math}}$ under

certain considered scenario is also low. Hereafter, a quantification model of discussed risk is needed

- **Definition of validation target based on acceptance criteria:**
  After the acceptance criteria is quantified, it shall be further translated into measurable validation target. Through the comparison between validation results and validation target of $Function_{math}$ approximator, a clear conclusion could be obtained about if this A.I system can be released or not. The measurable validation target can be set up as the form of detailed quantity like "no mistake/ deviation for certain operation time", or "not encountering any mistake/ deviation for 1000 times of operation". For A.I-based $Function_{math}$ approximator, it should be fairly easy to observe if its output results can be deemed as "acceptable" or "not acceptable", thus black-box validation is highly workable. However, the real safety threat is not about the wrong results happening during validation period, but about the correct results observed during validation period then wrong results reside in the far corner outside validation definition. This safety issue is related to "risk due to unknown hazardous scenarios", also this might be related to A.I alignment issues as well, since a superintelligent A.I might know it is under a validation phase, thus it pretends to output correct result if such pretention meets its own interests[n].

- **Evaluate Functional weakness based on performance insufficiency:**
  Through the introduction of Cause Tree Analysis and conceivable engineering database, the possible performance constraints of A.I-based $Function_{math}$ approximator might be identified, whether such insufficiency is due to HW resource (e.g. GPU computation power), system environment (e.g. overheating during some use-cases) or even algorithm tendency (e.g. loss of certain memories). If the identified weakness might lead to hazardous output of A.I-based $Function_{math}$ approximator, relevant counter measures to handle the weakness shall be determined

- **Evaluate Functional weakness based on external triggering conditions:**
  Same, through the introduction of Cause Tree Analysis and conceivable engineering database, the external triggering conditions which might expose weakness of A.I-based $Function_{math}$ approximator is gradually identified (e.g. color depth which might confuse the algorithm), this shall be better supported by collection of reference database since such living database is a reflection of this continuously changing world. To support this task, *exida* develops a GADOP (Global Analysis Data Open Platform) specific for the ADAS (Advance Driving Assistance System), HAD (Highly Automated Driving) or Autonomous Driving application. Here are the example category trees of GADOP:

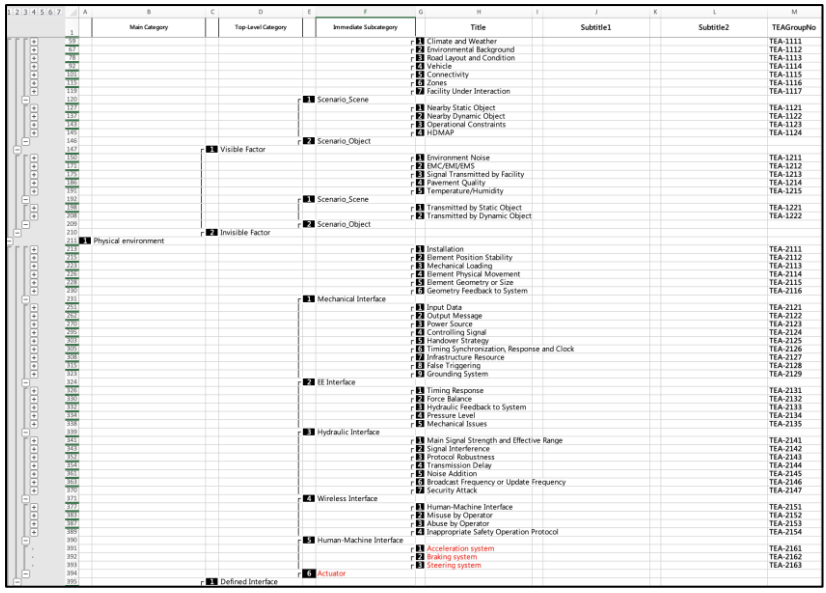

Figure 6. Example category trees of GADOP for scenario and data collections

- **Evaluate risk due to known hazardous scenarios:**
  Each experienced scenario by A.I-based $\text{Function}_{\text{math}}$ approximator can be categorized as know scenario. If the A.I-based $\text{Function}_{\text{math}}$ approximator ever generates hazardous outputs under that scenario, the development team shall evaluate the probability for reoccurrence of such hazardous outputs under similar known scenarios. If relevant risk is unacceptable, further safety measures shall be taken to improve the situations. There is a similar case study in 3.4 of this paper.

- **Evaluate risk due to unknown hazardous scenarios:**
  Each inexperienced scenario by target A.I-based $\text{Function}_{\text{math}}$ approximator can be categorized as unknow scenario. However, if different individual A.I agent utilizes same A.I-based $\text{Function}_{\text{math}}$ approximator in the backend, the experiences gained from one A.I agent can be categorized as known scenario to other A.I agents as well. It's impossible to have one A.I-based $\text{Function}_{\text{math}}$ approximator go through all possible input state spaces versus all possible scenarios, thus unknown hazardous scenarios will always be existent. The target to approve the A.I-based $\text{Function}_{\text{math}}$ approximator is to ensure the probability for the system to violate safety expectation when encountering unknown scenarios is acceptably low. This verification can be achieved by several measures below:
    1) Expose the A.I-based $\text{Function}_{\text{math}}$ approximator to selective unknown scenarios by altering the input state spaces to corner range through parameter exploration, prove that system has sufficient capabilities to handle unknown scenarios with acceptable risk. Such capability proof process shall be done by individual organization being independent with the development team, sort of independent exam being applied to

the A.I-based $\text{Function}_{\text{math}}$ approximator. The independent organization shall focus on collection of hazardous events from different A.I agents, collection of exposed corner or edge cases, then abstracting those cases into representative test cases which require the A.I-based $\text{Function}_{\text{math}}$ approximator to digest and extrapolate to properly respond to unknown hazardous test cases

2) The development team can utilize simulator to conduct continuous unknown scenario trainings to the target A.I-based $\text{Function}_{\text{math}}$ approximator, then trough the statistical results and accumulated safety cases to argue its capability. This methodology is widely used by different development to do inhouse verification. However, unlike first option is to rely on external organization to do independent validation or approval, this inhouse method shall be subject to external review, assessment or approval as well

- **Field monitoring and data collection:**
  Even after SOP or release of A.I-based $\text{Function}_{\text{math}}$ approximator, its runtime performance and results shall still be collected and analyzed following European law (EU) 2022/1426 for automated driving. When there exists significant abnormal behaviors generated by A.I-based $\text{Function}_{\text{math}}$ approximator, the abnormal results and its associated input parameters shall be sent to far side backend to further analyze potential cause and reconstruct relevant scenarios

*3.2. **Functional Safety based on ISO-26262***

Following ISO-26262, the Functional Safety addresses the handling of safety risk when encountering malfunction behaviors in the system [5]. Such failure might happen to the A.I-based $\text{Function}_{\text{math}}$ approximator, and if the failure of A.I-based $\text{Function}_{\text{math}}$ approximator leading to safety hazards, the residual risk due to such failure shall be evaluated and controlled so that the safety hazards can be acceptable to public. However, the classical safety processes being proposed by Functional Safety need further revision to be application to A.I properties

- **Hazard Analysis and Risk Assessment:**
  This approach is similar to HARA being discussed in 3.1. However, here we need to define malfunctioning behavior of the A.I-based $\text{Function}_{\text{math}}$ approximator, instead of definition of unintended behavior. Furthermore, besides S (Severity of consequence) and C (Controllability of consequence), additional E parameter representing scenario exposure shall be evaluated as well. Scenario exposure means the probability for the A.I-based $\text{Function}_{\text{math}}$ approximator to be used in certain use-cases or scenarios, it doesn't relate to the failure probability. Combining the evaluation from S/ E/ C, a resulting SIL or ASIL (for automotive application) shall be derived to indicate required integrity level. The higher SIL/ ASIL, the stricter process and technical measures shall be used to ensure the safety results

- **Definition of Safety Goal:**
  Abstract expression in the safety target to be achieved by the A.I-based $Function_{math}$ approximator. Typical expressions could be "avoid certain unwanted behavior", such as: Avoid output P_1 to P_n from A.I-based $Function_{math}$ approximator when it is used for [specific conditions]. Besides expression of safety target by safety goal, additional safety attributes shall be designed together, including safe state and Fault Tolerance Time Interval. Safe state represents how the system enforces the A.I-based $Function_{math}$ approximator to be safe, it could be automatic shut off of the A.I server to stop the A.I-based $Function_{math}$ approximator; Fault Tolerance Time Interval constrains how short the reaction shall be taken from the occurrence of fault to the entrance of safe state. Different application of A.I-based $Function_{math}$ approximator will need different safe state and FTTI design, further more, if an A.I agent will be safety-related, there shall also be dedicated Safety Goal, Safe State and FTTI design for that A.I agent.

- **Definition of Functional Safety Concept:**
  The Functional Safety Concept is used to define how the high level functional architecture can work together to ensure the achievement of safety goal. This shall be considered from the complete Function point of view, not only about the scope of A.I-based $Function_{math}$ approximator. For example, if any target safety behavior can't be achieved by the A.I-based $Function_{math}$ approximator alone, Functional Safety Concept shall define how other elements in the Function can support risk mitigation due to failures in A.I-based $Function_{math}$ approximator. For example, the application of MAS (Multi-Agent System) might construct a potential good Functional Safety Concept in how different agent can support each other in mitigating safety risks

- **Definition of Technical Safety Concept:**
  The Technical Safety Concept is usually defined from system architecture perspective and used to constrain system elements' safety behaviors and safety performances. The system architecture here can refer to physical architecture and logical architecture. Take an A.I-based $Function_{math}$ approximator as example, the physical architecture can include its HW architecture (e.g. CPUs, GPUs, DDRs and their relationships), and the logical architecture can include its functional or reasoning logic in abstract level being used by the A.I-based $Function_{math}$ approximator. The logical architecture of A.I-based $Function_{math}$ approximator might not be derived directly since it's lack of transparency (not comparable to rule-based expert system), but it might be drafted indirectly through below approach:
    1) Its logical process can be explained by LLM (Large Language Model) which is built inside the A.I-based $Function_{math}$ approximator or used to monitor the A.I-based $Function_{math}$ approximator
    2) The possible logical process revealed within the training data and training process
    3) Reverse engineering by question and challenge to the A.I-based $Function_{math}$ approximator

  After identification of possible architecture, the proper safety measures shall be planned and inserted into the architecture to mitigate safety risks. This could be

E2E protection for data communication through the HW devices, or some additional review or confirmation process which will be done for the A.I-based $Function_{math}$ approximator internally.

- **Safety analysis at system level:**
  Through using FTA (Fault Tree Analysis) or system FMEA (Failure Modes and Effect Analysis), the possible fault or failure which might threaten the system can be identified easily for traditional rule-based expert system. However, such fault/ failure relationships are not so transparent when applying safety analysis techniques to the A.I-based $Function_{math}$ approximator. For example, depending on the algorithm in use and weighting relationship between the neurons, failure of one or even multiple neurons might have no effect on the output of the A.I-based $Function_{math}$ approximator. The fault effect propagation within the element chain is hardly analyzable by human, here the industry fervently needs simulation tools to assist the safety analysis with following capabilities:
  1) Identify the damage level in HW element or SW element so that the output of an A.I-based $Function_{math}$ approximator will fall into unacceptable failure range
  2) How the output of an A.I-based $Function_{math}$ approximator will fail accompanied with different internal fault level
  3) If there really exists critical single point fault or dual point fault within the physical or logical architecture?

  It is assumed that a complicated $Function_{math}$ being approximated by A.I through large model should be extremely fault tolerant if the large model is well-trained, since there needs huge damaged portions of neurons to really drag down the complicated behavior delivered by the A.I-based $Function_{math}$ approximator. On the contrast to the difficulties in using FTA/ FMEA handling safety analysis of A.I-based $Function_{math}$ approximator, the safety analysis method is by far suitable for analysis of training data or accident data with following steps:
  1) Assume failure modes by HAZOP key words approach, which might be brought in to the A.I-based $Function_{math}$ approximator through a set of training data
  2) Construction of FTA/ CTA to identify possible objects/ information/ sequences which might lead to those assumed failure modes. Those possible objects/ information or sequences shall be placed as basic event
  3) Review of the complete training dataset and filter out those hidden information which can be mapped to those hazardous basic event

  Same, this analysis could be done by human effort (e.g. similar to labelling process) or automation tool such as pre-trained A.I monitor to review the training dataset. Reconstruct the training dataset based on safety analysis result can reduce the safety risk embedded into the A.I-based $Function_{math}$ approximator. Alternatively, based on the safety analysis results, inject faults into the training dataset or A.I-based $Function_{math}$ approximator to train the system immune to possible fault categories, is also a safety measure to increase robustness of A.I-based $Function_{math}$ approximator

- **Definition of SW safety concept and SW development:**

Definition of SW architecture and relevant SW safety concept are more applicable to rule-based software. Thus, if an A.I-based $Function_{math}$ approximator involves traditional software component as interface counterpart or internal element, the classical safety concept to embed data protection and program flow monitoring in the SW architecture is applicable. Besides, there shall be dedicated safety concept designed to constrain the module behavior to ensure its safety, for example, if utility function is coded within the used A.I agent, the utility function needs to be analyzed to avoid unwanted hazardous $consequences^{n}$ while the A.I agent maximally pursue its satisfaction. the software codes to implement Neuron Network or A.I agent, can also be developed under the framework of ISO-26262 SW safety concept. Furthermore, the code development shall follow safety standards (e.g. ISO-26262, IEC-61508…etc) to ensure code quality and integrity

- **Integration testing:**
  In the safety standard, there defines several integration level, including HW-SW integration; system integration and vehicle integration (if the application is for automotive industry). These integration testing can be applied to A.I-based $Function_{math}$ approximator, just there might be some differences below:
  1) Requirement-based testing. In traditional expert system, each system behavior is clearly defined by relevant requirements, clear transparency and traceability are constructed. For A.I-based $Function_{math}$ approximator, it could be the case that not all behaviors or output are constrained by detailed requirement, instead, the behaviors might be governed by high level objective or pre-defined utility function. The requirement-based testing needs to verify the achievement of defined objective or underlying utility function. The objectives shall be defined in a way such that they are observable and measurable, so that a clear testing result can be verdict after test execution
  2) Fault injection testing. Based on the safety analysis results, a simulated fault shall be injected into the A.I-based $Function_{math}$ approximator, then observing if it can still match the defined objective or underlying utility function, in case it can't meet original design intent, the fallback behaviors generated by the A.I-based $Function_{math}$ approximator shall still ensure safety risk is sufficiently low by entering SS (Safe State) or MRC (Minimum Risk Condition)

  Here a new tool to conduct fault injection testing for A.I-based $Function_{math}$ approximator is needed, since the generation of single point fault alone might not cause significant impact to the A.I-based $Function_{math}$ approximator, so a tool which can inject multiple faults to HW and SW element (e.g. manipulation of the algorithm wrongly on purpose) is required for such testing.

- **Safety validation:**
  Safety validation is an approval activity to prove the designed A.I-based $Function_{math}$ approximator can achieve our design intent especially from safety perspective. The most important thing is to validate the designed safety goal and safety attributes can properly raise their influences when failures happen. The expectation is through entrance of safe state or MRC, either severity of the

consequences, controllability of the victims or exposure of the encountered scenarios can be reduced to acceptable level. Safety validation needs to rely on the fault injection testing at final product level, then observing the system responses.

- **Functional safety assessment:**
  Functional safety assessment is a joint activity combining development process audit and product technical characteristics assessment, based on defined safety standards or safety criteria. If a safety-related A.I-based $\text{Function}_{\text{math}}$ approximator is developed, how the safety process is used, i.e. safety analysis of training data set, and how the safety measure is used, i.e. monitoring of the functional output generated by A.I-based $\text{Function}_{\text{math}}$ approximator, shall be evaluated and assessed for its residual risk. In the paper from OpenAI [14], it mentions that the specific behaviors from Super Intelligent A.I-based $\text{Function}_{\text{math}}$ approximator might not be understandable by human, under such cases, safety assessment being conducted by human assessors is not appropriate, safety assessment done by dedicated A.I agents could be another possible options.

- **Release for production or deployment:**
  The release of any safety-critical product which contains A.I-based $\text{Function}_{\text{math}}$ approximator shall be managed carefully with proper safety records including safety case, functional safety assessment report, safety validation report and authority review with signatures. The release process of A.I-based $\text{Function}_{\text{math}}$ approximator shall not be taken lightly to accept whatever results.

3.3. Safety of Artificial Intelligence based on ISO PAS-8800

Due to the mismatch between classical safety standards (e.g. ISO-26262 and ISO-21448) and A.I technologies, a new standard ISO-8800 has been drafted and planned to be published in 2024. The new ISO-8800 standard incorporates partial requirements from ISO-26262 and ISO-21448, then fitting them into a framework which is more applicable to A.I development using ML technologies [7]. However, this standard is only in experimental phase where practical implementation results are not yet available.

4. Conclusions- How to ensure A.I safety in the future

As A.I-based product currently demonstrates more wonders out of public expectations in some aspects, it will easily mislead the crowd with higher expectations and neglect the potential safety threats hidden in the corners [8][9]. If those safety threats are not exposed well on-time, public will even greatly empower the A.I with more important responsibilities, resources and authorities, so that it becomes extremely dangerous and hazardous to human.

Due to the uncontrollability of A.I-based $\text{Function}_{\text{math}}$ approximator, a skeptical mindset to construct safety process of ensuring safe A.I utilization is needed unless a fully interpretable A.I algorithm is in use [10], here are some possible measures:

*4.1. **Needed supervision and organization***

A.I-based $Function_{math}$ approximator can be used in different kinds of products, based on the associated HARA analysis results of the product, different ASIL or different possible consequences need different supervision from the government [8], possible measures are:

- Enterprises which plan to develop safety-critical product utilizing A.I might need special business license, depending on the purpose of the developed product and services, also depending on the ASIL/ SIL level
- The strength and power of the developed A.I-based $Function_{math}$ approximator (e.g. Engaged computation power) shall be constrained by government and regulations, different enterprises shall be authorized with different resources based on their business license. Computation power exceeding certain scales shall be owned and managed by government only. Different scale needs different management and supervision since A.I shall be treated as weapon to some extent, for example: A.I chatbot can easily teach a person how to make a bomb through available raw materials or components, if without constraints in using the chatbot
- The acquaintance of business license for enterprise depends on the safety process audit and product safety architecture assessment results, which can be used to evaluate the technical capabilities of an enterprise to ensure A.I safety and A.I alignment. Government can authorize independent organization to conduct such audit or assessment
- Depending on the purpose of the developed product and services, functional complexities of A.I-based $Function_{math}$ approximator and also the ASIL/ SIL level, the released product needs to be subjected to independent monitoring or testing periodically

*4.2. **Needed services***

To ensure the safety of A.I-based $Function_{math}$ approximator, it is estimated there will be several new services in need by society:

- Insurance will surely be impacted by different A.I-based $Function_{math}$ approximator [11]. The insurance fee shall be dynamically set up depending on below factors:
    1) Initial safety assessment and evaluation results before product/ service launches
    2) Field monitoring results as the product/ service is used in the market for a period of time
- Admission and entrance approval service for the product. For example, Autonomous Driving vehicle which uses A.I-based $Function_{math}$ approximator needs to be subject to driving license test as well, just the testing approach and process shall be greatly different from human driver
- Personal safe guard when using A.I-based product. For example, to avoid misalignment issue while taking a robot-taxi (the taxi drives to a totally different destination with unknown hazards), personal safe guard service which

tracks the taxi positions and potentially interfere the taxi decision might be needed

- Independent safety audit, assessment, incident investigation and evaluation service during the R&D activity, training phase, product launch and product operation are needed [8]

*4.3. **Needed technical solutions***

As being summarized by this paper, the basic safety framework shall be imposed to any A.I-based $\text{Function}_{\text{math}}$ approximator includes Hazard Analysis & Risk Assessment of the developed function, Safety Goal and Safety Objective definition for the developed function, Safety Concept and Safety Architecture to mitigate safety risks, Safety Analysis of used training data set and incident data set, finally the Residual Risk evaluation combining verifying validation target, completeness of safety validation and safety assessment. To achieve the imposed safety framework, the industry and enterprise will need following technical solutions:

- **Safety requirement/ objective practice and standards:** For example, how to write good utility function which pursues the intended satisfaction of the A.I-based $\text{Function}_{\text{math}}$ approximator while minimizing the risk from unintended behaviors and side effects [4]? These good engineering practices shall be collected and standardized, into either databases or enforced implementations
- **Combined process and simulation tool to analyze complicated Neuron Networks:** The simulation tool shall help to identify the relationship between constructed Neuron Networks and developed A.I-based $\text{Function}_{\text{math}}$ approximator, considering possible scenario complexities and probability distributions:
  1) For a given network configuration, is there any critical single point fault/ failure [12]?
  2) For a given network configuration, what is the needed damage scale to really crash the A.I-based $\text{Function}_{\text{math}}$ approximator?
  3) How different damage scale will impact the output from the A.I-based $\text{Function}_{\text{math}}$ approximator?

  This tool along with the safety analysis methodology/ process can be used to verify the robustness of developed function, and the need to reorganize algorithm or architecture for safety purposes (i.e. satisfaction of target residual risks)
- **Safety measures:** The classical technical measures to implement safety mechanisms which can be applied to A.I-based $\text{Function}_{\text{math}}$ approximator include:

  1) **Cooperations in the redundant architecture:** Like human has 2 brain hemispheres: Left side and Right side, female has better linkage or architecture in using 2 brains together than male, this maps to the safety strategy like voting or comparison being used in system engineering, can increase the safety and precision of decision results [13]. Female thinking and behaviors are usually regarded as having more compassions than male, possible analogy might be applied in A.I-based $\text{Function}_{\text{math}}$ approximator:

A good redundant Neuron Network in use might contribute to a safer A.I output

2) **Self monitoring:** Like the monitor structure being disclosed by OpenAI [14], there could be many different design options. Whether rule-based monitor or another A.I-driven monitor is in use, if the proper safety feature points can be defined and monitored, they are all useful in assuring the A.I safety, they can be regarded as safety supervisor

3) **Self test:** Unlike monitor is a supervision mechanism running real-time in parallel with the A.I-based $\text{Function}_{\text{math}}$ approximator, self test is a concept supporting periodical or event-driven test of the A.I-based $\text{Function}_{\text{math}}$ approximator through comparing the ground truth and testing response. Such test can be used to verify below safety properties:

    a) Consistency: The A.I-based $\text{Function}_{\text{math}}$ approximator can generate consistency outputs under different usecases and scenarios, this can be partial reflection that this function is currently running with low probability of abnormalities

    b) Safety checker: If the self test patterns can be representative enough, it can be used to test safety response of the A.I-based $\text{Function}_{\text{math}}$ approximator. System can decide to shutdown, isolate or enter MRC (Minimum Risk Condition)/ SS (Safe State) based on the self test result. Self test shall be conducted when the main function is not used by the user

4) **Logical flow monitoring:** When combining to use LLM (Large Language Model) or VLM (Visual Language Model) to reason the process why an A.I-based $\text{Function}_{\text{math}}$ approximator has such an output, a golden reference logical process can be used to compare if there is high or low probability to trust this output whether the output seems to be right or wrong. Non logical flow process shall not yield to trustable outcomes, though by chance it could be right. One assumption we shall check when using this safety measure is that the LLM (large Language Model) pertaining to the A.I-based $\text{Function}_{\text{math}}$ approximator is not lying

Only through sufficient attentions in details which might result in safety risks, the current uncontrollable A.I can be further understood and refined with safety guards to benefit human use mostly.

References

[1] Mateusz Orlowski, Pawel Skruch. Multiagent Manuvering with the Use of Reinforcement Learning. Electronics 2023, 12, 1894.

[2] Steven M.Williamsn, Victor Prybutok. The Era of Artificial Intelligence Deception: Unraveling the Complexities of False Realities and Emerging Threats of Misinformation. Information 2024, 15, 299 Aug 17-22.

[3] PAVLOS S. BOUZINIS, NIKOS G. EVGENIDIS, NIKOS A. MITSIOU, SOTIRIS A. TEGOS, PANAGIOTIS D. DIAMANTOULAKIS and GEORGE K. KARAGIANNIDIS. Universal Function Approximation Through Over-the-Air Computing: A Deep Learning Approach. IEEE Open Journal of the Communication Society, VOLUME 5, 2024.

[4] Roman V. Yampolskiy. Utility function security in artificially intelligent agents. Journal of Experimental & Theoretical Artificial Intelligence 2014, Vol. 26, No.3, 373-389. doi: . http://dx.doi.org/10.1080/0952813X.2014.895114
[5] The International Organization for Standardization, ISO 26262, Road Vehicles- Functional Safety, 2018
[6] The International Organization for Standardization, ISO 21448, Road Vehicles- Safety of the intended functionality, 2022
[7] The International Organization for Standardization, ISO 8800, Road Vehicles- Safety and Artificial Intelligence, 2024
[8] Yoshua Bengio, Geoffrey Hinton, Andrew Yao, Dawn Song, Pieter Abbeel, Trevor Darrell, Yuval Noah Harari, Ya-Qin Zhang, Lan Xue, Shai Shalev-Shwartz, Gillian Hadfield, Jeff Clune, Tegan Maharaj, Frank Hutter, Atilim Gunes Baydin, Sheila Mcllraith, Qiqi Gao, Ashwin Acharya, David Krueger, Anca Dragan, Philip Torr, Stuart Russell, Daniel Kahneman, Jan Brauner and Soren Mindermann. Managing extreme AI risks amid rapid progress. SCIENCE 2024, 24 MAY 2024, Vol 384, Issue 6698.
[9] Scott McLean, Gemma J.M.Read, Jason Thompson, Chris Baber, Neville A. Stanton and Paul M. Salmon. The risks associated with Artificial General Intelligence: A systematic review. Journal of experimental & theoretical artificial intelligence 2023, VOL. 35, NO.5, 649-663. doi: https://doi.org/10.1080/0952813X.2021.1964003
[10] Pengfei Shen, Shaohua Zhang. On Interpretable Algorithm of Artificial Intelligence based on Information Network Analysis. 2022 8th Annual International Conference on Network and Information Systems for Computers (ICNISC), 2022 IEEE. doi: 10.1109/ICNISC57059.2022.00025
[11] Anat Lior. INSURING AI: THE ROLE OF INSURANCE IN ARTIFICIAL INTELLIGENCE REGULATION. Havard Journal of Law & Technology, Volume 35, Number 2 Spring 2022.
[12] Abdullah Murat Buldu, Alper Sen, Karthik Swaminathan. MBET: Resilience Improvement Method for DNNs. 2022 IEEE International Conference On Artificial Intelligence Testing (AITest), 2022 IEEE. doi: 10.1109/AITest55621.2022.00019
[13] Sandra C. A. Trotman, Geoffrey R. Hammond. Sex Differences in Task-Dependent EEG Asymmetries. 1979 by The Society for Psychophysiological Research, Inc., September 1979, Vol.16, No.5.
[14] Collin Burns, Pavel Izmailov, Jan Hendrik Kirchner, Bowen Baker, Leo Gao, Leopold Aschenbrenner, Yining Chen, Adrien Ecoffet, Manas Joglekar, Jan Leike, Ilya Sutskever, Jeff Wu. WEAK-TO-STRONG GENERALIZATION: ELICITING STRONG CAPABILITIES WITH WEAK SUPERVISION. 2023 OpenAI.

Fuzzy Systems and Data Mining X
A.J. Tallón-Ballesteros (Ed.)

doi:10.3233/FAIA241460

A Low-Cost and Real-Time Solution for Enhancing Construction Site Safety

Chi-Yat Lau [a] , Man-Ching Yuen [b,1] , Chi-Wai Yung [c] ,
Yiu-Man Kwong [a], Yuen-Wang Lai [a], Lawrence-James Wong [a], Shier-Bano Iltaf [a],
Suet-Ying Xie [a] , Yee-Shing Chan [d], Kin Chui [d]
[a] *Department of Information Technology, Vocational Training Council, China*
[b] *Department of Digital Innovation and Technology, Technological and Higher Education Institute of Hong Kong, China*
[c] *Linux Foundation (Asia Pacific)*
[d] *Chun Wo Construction and Engineering Company Limited*

Abstract. Nowadays, AI is widely adopted in different areas. This project is dedicated to enhancing safety on construction sites, especially for high-altitude work. Among them, the authors noticed that many workers did not comply with construction site rules during the construction process, such as not wearing safety equipment or standing under high-altitude cranes. These are very dangerous behaviors. Furthermore, in alignment with the Hong Kong government's Smart Site Safety System initiative, the authors have developed several models designed to monitor construction sites in real-time. These models are trained to detect various safety measures and potential hazards, ensuring that workers adhere to necessary safety protocols and thereby significantly reducing the risk of accidents caused by negligence. Project use the model to detect whether people on the construction site are safe and then give feedback. The authors hope to cooperate with government policies and reduce casualties.

Keywords. Construction site safety, AI, real-time

1. Introduction

The author finds out that the occupational injury cases reached a staggering 14,197 and with a fatality rate of 9.7 per thousand employees every year [1]. Mostly the worker is the breadwinner. Once an accident occurs the fatality rate is quite high which makes the author want to harness the power of artificial intelligence to improve the safety of the working environment at height.

To achieve this, the author created a sophisticated website platform for seamless real-time monitoring. The website displays live video feeds from the construction site, with AI models identifying and marking areas using bounding boxes. This feature enables site managers and safety officers to visually track and verify compliance with safety measures. In case of any worker failing to adhere to safety protocols, the system automatically triggers an email alert, ensuring prompt attention and corrective action.

[1] Corresponding Author, Man-Ching YUEN. Technological and Higher Education Institute of Hong Kong, Hong Kong, China; E-mail: connieyuen@thei.edu.hk.

This multifaceted approach not only promotes a safety culture but also supports the construction industry's transition to a more technologically advanced and secure era. By integrating models with the Smart Site Safety System, a new safety standard is set, protecting workers through the vigilant eyes of artificial intelligence. This project represents a significant step towards leveraging technology for workplace safety and operational efficiency.

The project involves multiple stages, including data collection, model training, website creation, and testing. Each stage plays a crucial role in achieving project goals and delivering successful outcomes.

During the data collection phase, the author carefully identifies specific data requirements, develops a comprehensive data collection plan, and adheres to a timeline. Meticulous data collection ensures a robust and reliable dataset for training the AI model.

Once data collection is complete, the author moves on to the model training phase. The type of model, such as machine learning or deep learning, is determined, and the collected data is preprocessed and prepared for training. Appropriate algorithms and techniques are selected to optimize the model's performance and accuracy.

Simultaneously, the author creates a website as the project interface. Understanding the website's purpose and functionality, an intuitive user interface and user experience are designed. Both the front-end and back-end components of the website are developed, ensuring seamless integration with the trained model. Rigorous testing is conducted at various stages of website development to ensure functionality and usability.

Finally, significant effort is dedicated to the testing phase. Clear testing objectives and criteria are defined to evaluate the AI model and website's performance and reliability.

2. Problem Analysis

During the development process, there are often limitations and challenges in hardware capabilities, as well as the availability of reliable methods and data to ensure safety. These factors can result in unsatisfactory outcomes of detection.

Limitations in Hardware Development

In the realm of real-time inspection systems, the efficacy of hardware plays a pivotal role in determining the system's performance. Our earlier attempts to run the inspection system using a Mac CPU revealed significant performance limitations, impeding our pursuit of real-time effectiveness. However, through strategic upgrades, particularly transitioning to a Mac M1, we managed to overcome these hurdles and achieve remarkable improvements in speed. The Mac M1 upgrade facilitated processing one frame per second, a notable advancement from our previous endeavors.

Challenges with Limited Data Diversity

Model generalization is inherently tied to the diversity and richness of the training data. In our journey towards developing a robust real-time inspection system, we encountered challenges stemming from limited data diversity, which compromised the model's ability to generalize effectively. The prevalence of duplicated data led to misconceptions, as the model erroneously extrapolated patterns from repetitive features, thereby undermining its performance on test data.

Enhanced Safety Assessment in Real-world Scenarios
Safety assessment in real-world scenarios necessitates a holistic approach that transcends simplistic metrics such as object completeness. In our earlier iterations, safety determinations were predominantly predicated on the presence or absence of objects, overlooking crucial factors that influence the safety landscape.

Visual Clutter in Real-Time Inspection System
In the monitoring system, the presence of multiple objects being simultaneously monitored often results in numerous bounding boxes appearing cluttered on the screen, causing visual confusion.

3. System Design

The real-time monitoring system we have developed is a comprehensive system that integrates both hardware and software components to ensure the safety of workers. The system utilizes Python Flask for the backend, HTML, CSS, and JavaScript for the frontend, OpenCV for video processing, and the YOLO model for object detection [2].

In the backend, Python Flask is utilized to construct the server-side of the application. This choice of framework allows for seamless communication between the backend and the frontend, ensuring that data can be easily exchanged between the two components. The primary function of the backend in this scenario is to receive video streams directly from a construction site. These streams are then processed using OpenCV, alongside the YOLO model, a state-of-the-art object detection model known for its efficiency and speed in detecting objects in real-time. The YOLO model is a powerful tool in this context, as it has been trained to identify and differentiate between various elements within the video stream. Specifically, it is designed to detect the presence of workers and to recognize the use of essential safety equipment, such as safety belts. The ability to detect these items quickly and accurately is crucial for ensuring the safety of workers on the construction site.

Once the YOLO model has successfully identified the objects within the video stream, OpenCV comes into play to enhance the visual representation of the analysis. It does so by drawing precise bounding boxes around each detected object, providing a clear and immediate visual cue to the users about the location and nature of the objects being analyzed. This visualization is not only crucial for the end-users to understand the real-time scene but also for the system operators to ensure the accuracy of the object detection process. Beyond the visual annotations, the backend performs a series of logical operations to assess whether the workers are complying with the necessary safety protocols. For instance, if a worker is identified without a safety helmet, the backend system not only marks the occurrence but also triggers a specific signal that reads “Safety helmet: Unsafe.” This signal is a clear alert that immediate action is required to address the safety concern. In a similar vein, if the YOLO model detects a worker without a safety belt, the backend will activate another signal, indicating “Safety belt: Unsafe.” and send an email to safety manager automatically. These signals serve as automated checks that can be used to enforce safety standards on the construction site. They are also logged and can be reviewed later for auditing purposes or to identify patterns of non-compliance. Furthermore, the backend system may also track the duration and frequency of safety violations, allowing site managers to address persistent issues and improve overall safety culture. By integrating these real-time detection and alert systems, the backend not only

contributes to the immediate safety of the workers but also helps to create a data-driven approach to safety management on the construction site. This can lead to more informed decision-making and proactive measures to prevent accidents and ensure the well-being of all personnel.

The frontend of the system is built using HTML, CSS, and JavaScript. HTML is used to create the structure and content of the web page, while CSS is used to style the web page and make it visually appealing. JavaScript is used to handle user interactions and display the signals generated by the backend. These signals are displayed on the web page in real-time, allowing users to quickly identify which parts of the construction site are safe and which are not.

In terms of hardware, due to limited resources, the system utilizes cloud technology to train the YOLO model. This allows the system to leverage the computational power of the cloud to train a highly accurate model without the need for expensive hardware. Once the model is trained, it can be deployed on a local server or on a cloud server to process video streams from the construction site.

This system is a robust system that integrates both hardware and software components. The system utilizes Python Flask, HTML, CSS, JavaScript, OpenCV, and the YOLO model to analyze video streams from the construction site and detect workers and safety equipment. The backend of the system performs logical operations to determine if workers are adhering to safety measures and generates signals indicating the status of each safety measure. The frontend of the system displays these signals in real-time, allowing users to quickly identify which parts of the construction site are safe and which are not. The system also leverages cloud technology to train the YOLO model, ensuring that the system can be deployed on a wide range of hardware resources.

4. Implementation

4.1. Functional and non-Functional Requirements

Functional Requirements:
1) Detection: Identify hazardous set up
2) Automatically send email: Remind Safety manager
3) Distance calculation: Keep the workers beyond the danger zone

Non-functional Requirements:
1) Camera: Must be 1920x1080, otherwise it could affect the distance calculation
2) GPU: Minimized 4070, to implement real-time detections
3) Network: at least 4G to maintain the capability; connect to RTSP

4.2 Acquired Data Overview

Assumptions.
If the objects are detected, the bounding box will display, such as ladder platform and related setup.

Requirements:
1) Find at least 5,000 pictures of each of the ladder platform, kung fu platform, and scissor lift (Figure 1)

2) Kung fu ladder and scissor lift must be in use (Figure 2 and Figure 3)
3) Try to make the picture as clear as possible
4) Photos need to be multi-angled
5) Annotate the recording for the man cage (Figure 4)

Figure 1. scissor lift

Figure 2. Ladder platform

Figure 3. Kung Fu platform

Figure 4. Suspended Working Platform

4.3 Data Preparation

- Film sources provide by ASIA ALLIED INFREASTRUCTURE HOLDINGS LIMITED
- Retrieved data source through YouTube

4.4 Data Modeling

We choose two models, YOLOv5x and YOLOv8, for data analysis. We use data visualization approach to show the prediction outcomes. Figure 5 shows the prediction outcomes.

Figure 5. Ladder platform- predict outcomes

5 Performance Evaluation

5.1 Test Results

Figure 6 shows the confusion matrix for suspended working platforms. Although sometimes the label (predict background) will be recognized as the label (true background), and there is a 0.01 chance of misrecognizing other labels. But in summary, the accuracy of this model is around 80%.

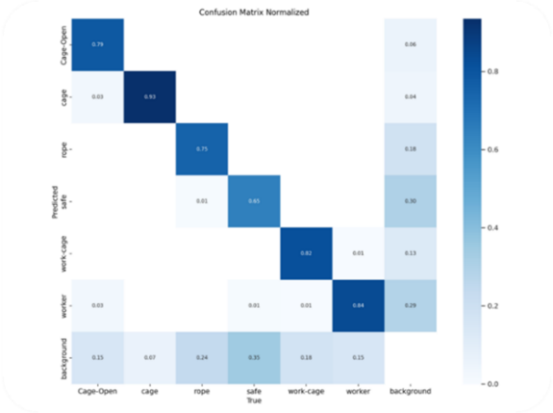

Figure 6. Suspended Working platform-confusion matrix

5.2 Web Interfaces

Figure 7 to Figure 10 show the real-time detection screen of our monitoring system.

Figure 7. Detection page (hazardous areas)

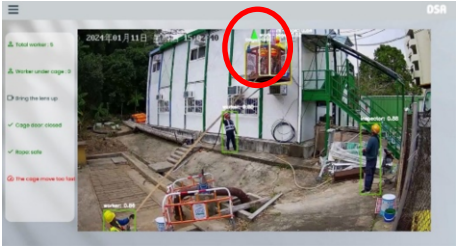

Figure 8. Detection page (Move the camera)

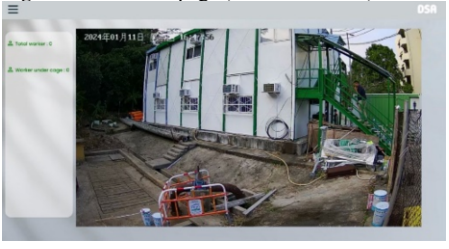

Figure 9. Detection page (Won't detect passenger as worker)

Figure 10. Detection page (hazardous set up)

Since the platform might leave the lens area, the author added an arrow tip and the word 'bring the lens up' in the side bar to notice the user. Also, it will show the number of workers under the platform to remind the user if there are any workers mistakenly get under the platform. It is because if the platform accidentally falls down it could damage the worker.

The author updated the interface design to improve the latency. The author changed the interface to a brighter background and added an instruction under the introduction to help the user easily understand the usage. Also, added few fields to increase the safety factor, such as Worker under cage, Safety belt, Distance, Bring the lens up and the cage move too fast. Also added a side bar to shows the information clearly in the left side. When there is any unsafe situation, it will show the information in red color at the side bar and if it is safe, it will show the information in green color. If there is no worker on site it will show the total number of worker and the number of workers under the man cage in green color. If the worker is too near the man cage it will show the distance as unsafe in red color. Also, the AI model could detect the movement speed of the man cage. When it is too fast it will show as the cage moves too fast in red color. If the man cage is leaving the recording area it will notice the user to bring the lens up, make sure that the camera can record the working platform. Next, the author added a line of code to make sure that the program uses the m1 CPU to run the program. To improve the latency.

In summary, the update improves the situation of the latency about the server camera. Also, make it more user-friendly and help the user get the information quicker by improving the interface design.

6 Conclusion Summary

The development and implementation of an AI-based man cage safety monitoring system proved to be a highly effective solution in enhancing construction site safety. Although the project faced challenges in data scarcity and model performance, the strategic refocusing on man cage detection and the integration of automated alerts and a comprehensive website platform yielded positive results.

References

[1] Legislative Council. (19 December 2023). *Hong Kong's Occupational Safety Performance in the First Half of 2023 and Relevant Occupational Safety and Health Enhancement Initiatives*, Hong Kong, Legislative Council Panel
https://www.legco.gov.hk/yr2023/english/panels/mp/papers/mp20231219cb2-1132-1-e.pdf

[2] Handalage, Upulie & Kuganandamurthy, Lakshini. (2021). Real-Time Object Detection Using YOLO: A Review. 10.13140/RG.2.2.24367.66723.

Fuzzy Systems and Data Mining X
A.J. Tallón-Ballesteros (Ed.)

doi:10.3233/FAIA241461

An Online Optimization System for Weight Detection Parameters

Wenbin Feng [a], Bin Yang [a], Fanghui Dong [c], Wu Wen [b], Minchang Liu [b], Peng Kuang [a], Yang Liu [b], Yuan Liu [a], Ming Wan [a], Tingjie Bao[b], Ju Huang [a], Yaping Ma [b] and Rongya Zhang [b,†]

[a] *Shifang Cigarette Factory, China Tobacco Sichuan Industrial Co., Ltd., No. 158, South Section of Yinghuashan Road, Shifang, Sichuan 618400, China*
[b] *Technology Center, China Tobacco Sichuan Industrial Co., Ltd., Section 2, Chenglong Avenue, Longquanyi District, Chengdu, Sichuan 610100, China*
[c] *Shenzhen Hongyunzhi Technology Co., Ltd., 518000, Building 202, Huaqiang North Road Shangbu Industrial Zone, Shenzhen, Guangdong, China*

Abstract. Cigarette weight detection is crucial for the quality of cigarette production, requiring regular calibration of key parameters to maintain accurate weight control. Traditional methods for adjusting these parameters are often time-consuming, wasteful, and fail to provide timely updates, which can affect the accuracy of real-time weight assessment. This study introduces an innovative online optimization system designed to refine weight detection parameters. The system incorporates an automated sampling process and utilizes the XGBoost regression model for prediction. These features streamline the optimization, improving both automation and the accuracy of online weight measurements. Results show that the system decreases the time needed for parameter adjustment by 65.72% and reduces cigarette consumption by 83.33%. Moreover, it increases the compliance rate with weight standards during quality checks by 41%. Thus, this advanced diagnostic and optimization approach significantly enhances the precision of real-time weight monitoring, contributing to higher product quality and more efficient manufacturing.

Keywords. weight detection, XGBoost, parameter diagnosis and optimization

1. Introduction

As the demands for high-quality cigarette production grows , the weight of cigarettes,a key physical characteristic affecting sensory quality [1][2], becomes increasingly important. Cigarette weight influences not only the taste and user experience but also ensures consistency and stability in the manufacturing process. Online sensors are currently used to monitor cigarette weight, maintaining adherence to set standards.

†Corresponding Author, Rongya Zhang, Technology Center, China Tobacco Sichuan Industrial Co., Ltd., Section 2, Chenglong Avenue, Longquanyi District, Chengdu, Sichuan 610100, China; Email: rongyazhang@126.com.
Wenbin Feng and Bin Yang are co-first authors.

However, environmental factors such as brand changes and modifications in cigarette structure can lead to drift and linearity issues in the detection equipment [3][4]. Without timely adjustments and optimizations, the effectiveness and accuracy of identifying and rejecting underweight cigarettes are compromised [5]. Proper parameter settings are essential for efficient cigarette production. Relying solely on manual sampling for calibration and optimization is insufficient to meet today's production requirements and poses several challenges in the parameter optimization process.

Difficult timing of parameter optimization. Determining the optimal timing for parameter adjustments is difficult due to frequent changes in external environments and production conditions. This unpredictability diminishes the accuracy of online cigarette weight inspections. The lack of systematic and automated monitoring and control mechanisms leads to prolonged suboptimal performance of inspection instruments, negatively impacting the quality of cigarette production.

Complex parameter optimization process. The process of optimizing weight detection parameters is both intricate and time-intensive. Each optimization typically demands more than an hour of a process quality inspector's time, which increases labor costs and disrupts the production workflow.

High cigarette consumption. Current methods for parameter optimization require the use of numerous samples, resulting in high cigarette consumption. Data from the field show that at least 300 cigarettes are needed to calibrate the parameters of a single weight detection device, significantly raising production costs.

The parameter optimization for cigarette weight detection is often time-consuming and resource-intensive, making prompt recalibration impractical when the cigarette structure changes. This delay significantly reduces the accuracy of weight detection. Although research has focused on improving the precision of cigarette weight measurements—such as optimizing packaging processes to enhance physical properties and sensory quality through IoT and big data analytics [6] fundamental issues persist.

To tackle these challenges, we introduce an online optimization system that uses intelligent algorithms for automatic and efficient parameter adjustments in cigarette weight detection. Our goal is to fill the gaps in current research, provide a new method for diagnosing and optimizing detection parameters, and promote the digital transformation of the cigarette manufacturing industry. The system has been successfully implemented in actual production environments. Here are our key contributions:

- We have created an advanced, autonomous online parameter optimization system that requires no human intervention. By combining an automatic sampling device with a machine learning algorithm, our system quickly and effectively optimizes weight detection parameters.
- We present a new parameter optimization method using an XGBoost integrated model, which greatly improves the accuracy of cigarette weight detection. We also developed a self-starting algorithm to streamline the initiation of the production process.
- In a thorough evaluation within a real production setting, involving multiple cigarette brands, our results showed a 65.72% reduction in parameter optimization time, an 83.33% decrease in cigarette waste, and a 41% increase in the passing rate of the cigarette weight index.

2. Related Work

2.1 Traditional Weight Detection Parameter Optimization Method

The microwave density detector, a crucial component of the cigarette manufacturing machinery's weight control system, utilizes microwave resonance technology to measure the density of cigarette segments. This is achieved by analyzing the changes in the resonance cavity's frequency and the amplitude attenuation of the microwave signal within the cavity. As shown in Figure 1, once the density of a segment is determined, the detector sends this information as a pulse signal to the weight control system. The system then converts this data into an online weight measurement for each cigarette through a linear transformation.

The relationship between the density detected by microwaves and the cigarette weight can be mathematically expressed as follows:

$$y = k \cdot d + b \tag{1}$$

where y represents the online weight detection value, d denotes the microwave detection density value, k is the slope parameter for weight detection, and b stands for the weight correction constant..

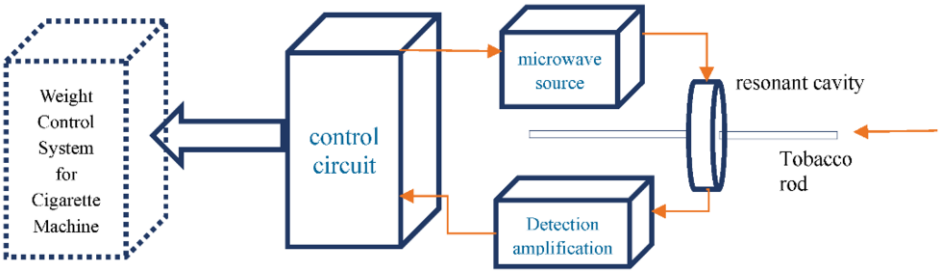

Figure 1. Schematic diagram of cigarette weight detection.

It is important to note that online weight detection often exhibits bias and requires timely calibration. Using Equation 1, we can derive the relationship between the online weight detection value, the offline weight detection value, and the slope parameter as follows:

$$k' = \sigma_x/\sigma_y \cdot k \tag{2}$$

In this equation, σ_x represents the standard deviation of offline weight detection values (which are considered the true values), σ_y is the standard deviation of online weight detection values, k is the original slope parameter, and k' is the optimized slope parameter. Based on this principle, the slope parameter can be effectively calibrated.

As illustrated in Algorithm 1, the calibration of the slope parameter calibration involves several steps. Firstly, an empirical initial value k for the slope parameter is set and the cigarette machine is activated to commence production. Subsequently, a random selection of n cigarettes from both the inner and outer rows is taken from the production line. The online weight detection is then conducted using the microwave density detection method to determine the standard deviation of the weight detection parameters σ_{y1} and σ_{y2} for each group.

The quality inspector subsequently performs offline detection on the extracted cigarettes, measuring the weights of both the inner and outer rows and recording the standard deviation of the offline weight detection values σ_{x1} and σ_{x2}. The slope parameter values k_1' and k_2' are calculated for the inner and outer rows respectively, and their average is computed to obtain the new slope parameter k'.

Finally, the new slope parameter values are compared with the old ones. If the difference between them is less than or equal to the preset threshold Δ_k, i.e., $|k' - k| \leq \Delta_k$, the slope parameter remains unchanged. If the difference exceeds the set threshold, i.e., $|k' - k| > \Delta_k$, the value of the slope parameter is updated.

Algorithm 1: Traditional Slope Parameter Adjustment Method

Input: *Initial slope parameter k, threshold value Δk, sample size n.*

Output: *Final adjusted slope parameter k'.*

repeat

Start the cigarette production machine.

Randomly select n inner and n outer cigarettes from the production line.

Measure the online weight standard deviation for inner and outer cigarettes:

σ_{y1} ← *measure online weight std(inner cigarettes)*

σ_{y2} ← *measure online weight std(outer cigarettes)*

Conduct offline weight detectionand record the standard deviations:

σ_{x1} ← *measure offline weight std(inner cigarettes)*

σ_{x2} ← *measure offline weight std(outer cigarettes)*

Calculate the new slope parameters:

k_1' ← *calculate slope parameter*$(\sigma_{x1}, \sigma_{y1})$

k_2' ← *calculate slope parameter*$(\sigma_{x2}, \sigma_{y2})$

Compute the average of the new slope parameters: $k' \leftarrow (k_1' + k_2') / 2$

if $|k' - k| > \Delta k$ ***then***

Update the slope parameter: $k \leftarrow k'$

end if

until *convergence*

2.2 Related Work

Recent research has thoroughly explored online cigarette weight inspection [7][8] and data acquisition technologies [9][10]. Xie Jianping[11]emphasized the importance of digital transformation in advancing China's tobacco industry through technological innovation. Cao Qi [12] and colleagues introduced an informatized system for collecting quality inspection data during cigarette production, markedly enhancing inspection management efficacy. Furthermore, advancements in data collection techniques [13] and the digital transformation of tobacco production [14] have continually refined cigarette weight monitoring and control processes. Zhu Bo [15] and co-workers investigated how

variations in tobacco leaf structures impact cigarette weight consistency via tobacco morphology regulation studies. Liang Zhiqian [16] presented a microwave-based online apparatus for measuring cigarette density and moisture, featuring a guided-wave resonator that effectively suppresses interference, thereby augmenting measurement precision without compromising the signal-to-noise ratio.

Despite these advancements, the potential of utilizing large datasets for precise prediction and optimization of weight detection parameters remains largely untapped.

3. System Overview

To address the issues of delayed slope parameter calibration and excessive cigarette waste, we have developed an online parameter optimization system. This system aims to simplify the calibration process and improve the accuracy of cigarette weight detection. This section outlines the key design objectives and operational procedures of the system. In the following sections, we will delve into the detailed implementation of the parameter optimization algorithm.

Design Goals. The system's design and architecture are based on the following primary goals:

Real-Time Operation: To address dynamic changes in the production environment, the system must monitor and update slope parameters in real time. This ensures consistent and accurate detection in response to any production variations.

Ease of Use: The intricate process of parameter tuning demands considerable time from quality inspectors, leading to extended downtimes that disrupt production. To mitigate this, we have developed a highly automated system for parameter calibration, significantly reducing the workload on personnel.

Performance and Efficiency: The system aims to enhance overall performance with precise parameter optimization. By minimizing resource usage and refining computational methods, it achieves more efficient operations. This not only reduces production costs but also boosts economic benefits.

Operation Process. As shown in Figure 2, the operation process of the online parameter optimization system includes online detection, offline detection, data transmission, and parameter updates.

When activated, cigarettes move along the production line to the online inspection area. There, a microwave density detection method monitors the weight of each cigarette in real time. After converting these measurements, the system calculates the mean and standard deviation of the weights. A random sample of cigarettes is then selected for detailed offline inspection to determine accurate quality metrics and their corresponding standard deviations.

The system compares the online and offline data sets, evaluating the differences in weight measurements. If the analysis reveals a deviation exceeding a set threshold, the system triggers an alert. This prompts a predictive model to adjust the slope parameters as needed. Throughout the process, continuous real-time diagnostics ensure that all detection parameters remain within acceptable limits.

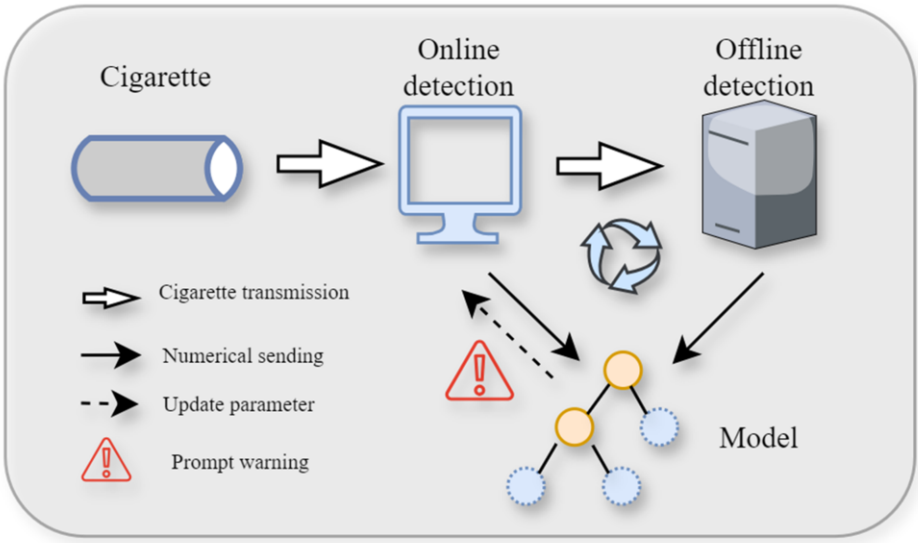

Figure 2. Parameter optimization system operation process.

4. Parameter Online Optimization Algorithm

This section describes the approach for achieving precise and efficient parameter optimization. We start by developing a regression prediction model specifically for slope parameters. Additionally, we introduce an innovative automated optimization algorithm.

4.1. Model Establishment

Parameter prediction and optimization can employ various algorithms. This article highlights a slope parameter prediction method using the XGBoost model [17]. Developed in 2014 by Tianqi Chen at the University of Washington, XGBoost is a boosting algorithm within the field of ensemble learning. It boasts outstanding learning performance and fast training speeds, enabling quick and accurate solutions to numerous data science challenges.

4.1.1. Data Set Construction

When establishing the quality parameter prediction model, we make the following assumptions to generate a large dataset: ① The offline weight detection measurements are accurate. ② The online weight measurement errors follow a normal distribution $\sim N(u, \sigma^2)$ where σ is set to 6 in this study. ③ The random weight sampling data of cigarettes is independent and homoscedastic. Based on these assumptions, we simulate sample data. Specifically, we randomly select 30 samples from the actual production data of 70,000 individual cigarettes to serve as the offline comprehensive detection data $(x_1, x_2 \ldots \ldots x_{30})$;

Simulate the online detection data of cigarette weight according to Equation (3):

$$x_i'' = (x_i + N(u, 6^2))/k \quad (i = 1,2 \ldots \ldots 30) \tag{3}$$

To generate a comprehensive dataset, we vary the parameter k from 0.5 to 2.0, creating 16 different sets of sample cigarette weight data for online detection, denoted as $k(x, x'')$. These sets serve as the sample data for the slope parameter prediction model. It's important to note that when k is not equal to 1, the slope parameter for online weight detection needs to be adjusted. To build a robust dataset, this simulation process is repeated multiple times, ultimately yielding a total of 1,680,000 sample data points.

4.1.2. Model Training

Out of the total sample data, which comprises 1,176,000 samples, 70% was utilized as the training set. The online cigarette weight detection data provided us with the mean (x''_mean), standard deviation (x''_std), mean of the top three values (x''_max_$adjust$), and mean of the bottom three values (x''_min_$adjust$). Similarly, from the offline cigarette weight detection data, we extracted the mean (x_mean), standard deviation (x_std), mean of the top three values (x_max_$adjust$), and mean of the bottom three values (x_min_$adjust$). Additionally, the ratio of the standard deviations between the two datasets ($r_{xstd-x''std}$) was also considered as an input feature for the "calibration slope" parameter prediction model, with 'k' serving as the model's output. The XGBoost regression prediction model was trained using this information. During the training process, the Particle Swarm Optimization (PSO) algorithm was employed to optimize the model's learning rate, tree depth, and number of submodels in order to obtain the most optimal model parameters. Finally, the mapminmax function was used to normalize the samples, and the output results were denormalized before being presented.

4.2. Automatic Optimization

To initiate the production process effectively, the system automatically determines the initial slope parameters based on historical data, as shown in Algorithm 2. Specifically, given the historical production tasks in the system database *D*, the algorithm first calculates feature similarity (such as cigarette brand) and retrieves the top-K similar parameter settings, denoted as T. For each task t_i in T, corresponding parameter setting K_i are retrieved. The algorithm then uses an exponential smoothing function to update the smoothed configuration S_i. More accurately, the algorithm ranks the parameter settings by similarity and calculates S_i as follows:

$$S_i = \alpha \cdot K_i + (1 - \alpha) \cdot S_{i-1} \tag{4}$$

where the smoothing factor α balances the influence of historical configurations, determining the weight between the current parameter setting and the previously smoothed setting.

During production, the system continuously conducts both online and offline detections, collecting the standard deviations σ_x and σ_y of the detection values. The detection timestamps are used to compare and analyze the online and offline data,

automatically determining if the current parameters require calibration. The criterion is as follows:

$$S = \begin{cases} 0 & |\sigma_y - \sigma_x| \le 1.5 \ \& \ \left|\frac{\sigma_y}{\sigma_x} - 1\right| \le 0.1 \\ 1 & |\sigma_y - \sigma_x| > 1.5 \ or \ \left|\frac{\sigma_y}{\sigma_x} - 1\right| > 0.1 \end{cases} \tag{5}$$

where S represents the slope parameter status, with S = 1 indicating the need for calibration and 0 indicating no need for calibration, σ_y is the standard deviation of the online detection cigarette weight, σ_x is the standard deviation of the offline detection cigarette weight.

When the detection value deviation exceeds the preset threshold, the online and offline feature data are input into the model for prediction, obtaining new slope parameters, and automatically updating the online detection equipment to achieve online optimization.

Algorithm 2: Self-Startup Algorithm

Input*: Database D; Incoming Production Job J; Exponential Smoothing Function S; Smoothing Factor a(0 < a < 1)*

Output: *Initialization Slope Parameter K*

Identify Top-K Similar Jobs of J:

J ← Select the top k most similar jobs from D;

Initialize Smoothing for Configuration:

Rank T with similiraty.

S_0 ← Extract configuration from t_0 in T;

for t_i in T do

  Extract configurations K_i *from* t_i*;*

  Apply S to update the smoothed configuration S_i;

  S_i ← a * x_i + (1 - a) * S_{i-1};

end

Apply the final smoothed configuration Si to get *K*;

Return *K*;

5. Experimental Validation

5.1. Experimental Design and Test Data

Materials: Two types of regular cigarettes were used—Brand 1, 'Jiaozi (Blue Age)', and Brand 2, 'Jiaozi (Blue)', both supplied by Sichuan China Tobacco Industry Co.

Methods: We recorded the time taken and the number of cigarettes calibrated during ten iterations before and after implementing our online optimization system. In each iteration, we also calculated the pass rates for the target weight and calibration slope

indicators. For every test, we examined thirty sample cigarettes ten times to assess the accuracy of the weight detection. Finally, we determined the average pass rate across all ten tests.

5.2. End-to-End Performance Evaluation

As shown in Figures 3 and 4, applying our parameter optimization method significantly decreased the time and number of cigarettes needed to optimize the slope parameters for the two cigarette brands. The average time per adjustment dropped from 92.32 minutes to 31.65 minutes, a 65.72% reduction. The number of cigarettes used also decreased from 378 to 63, a decrease of 83.33%.

Table 1 further indicates that after optimization, the pass rates for the target weight in cigarette weight detection increased by 41% and 40% for the two brands, respectively. The pass rates for the calibration slope also improved by 33% for both brands. Thus, our optimization approach not only boosts efficiency by cutting down on calibration time and cigarette use but also improves the accuracy of weight assessments

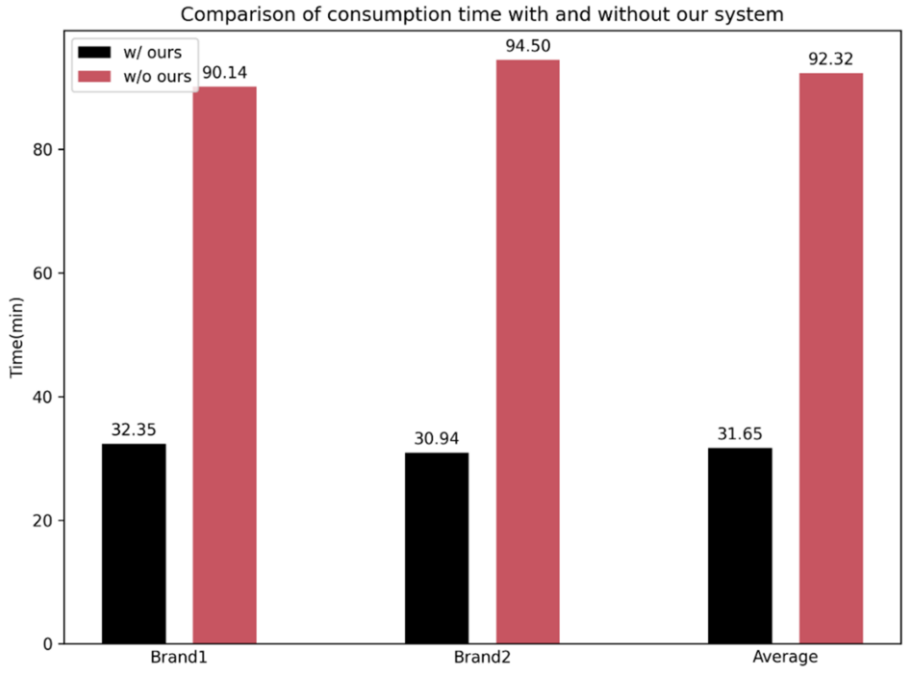

Figure 3. Comparison of consumption time.

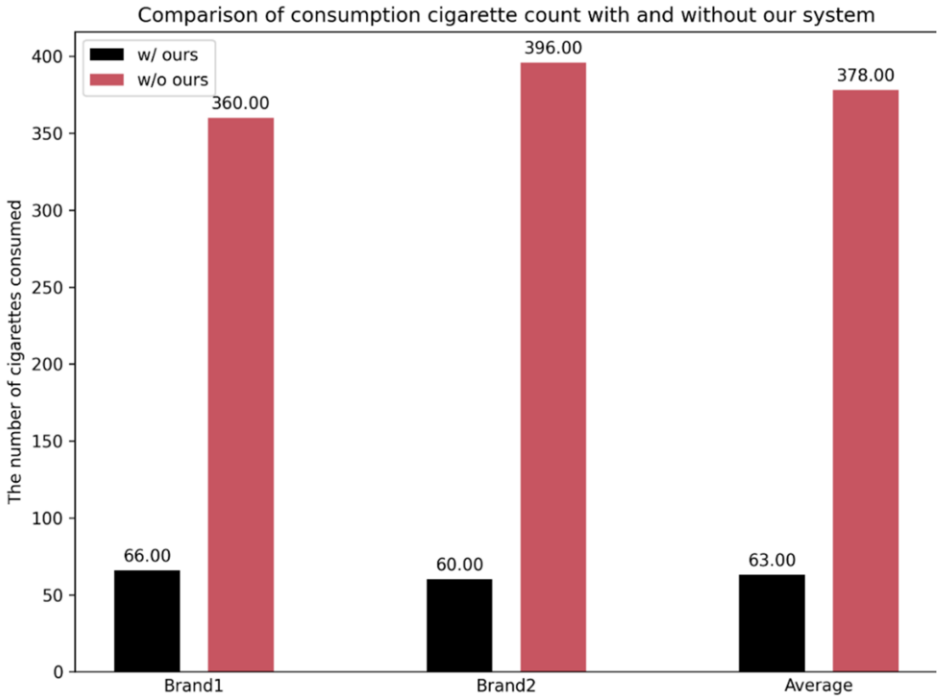

Figure 4. Comparison of consumption cigarette count.

Table 1. Test results of cigarette weight detection indicators before and after using the slope parameter diagnosis optimization method

Parameter Adjustment Method	Cigarette Brand	Test Indicator	
		Target Weight Indicator Qualified Rate(%)	Calibration Slope Indicator Qualified Rate(%)
Before Application	Brand 1	52	41
	Brand 2	50	39
After Application	Brand 1	93	74
	Brand 2	90	72

5.3. Model Prediction Evaluation

We assessed our model's predictive performance using 504,000 samples from the test set. We compared the predicted slope values with the actual values, using root mean square error (RMSE) and the coefficient of determination (R^2) as evaluation metrics.

As shown in Figure 5, the model's predictions closely match the real data. The slope prediction achieved an RMSE of 0.02 and an R^2 value of 0.836. These results confirm the model's robust predictive capability on the test dataset.

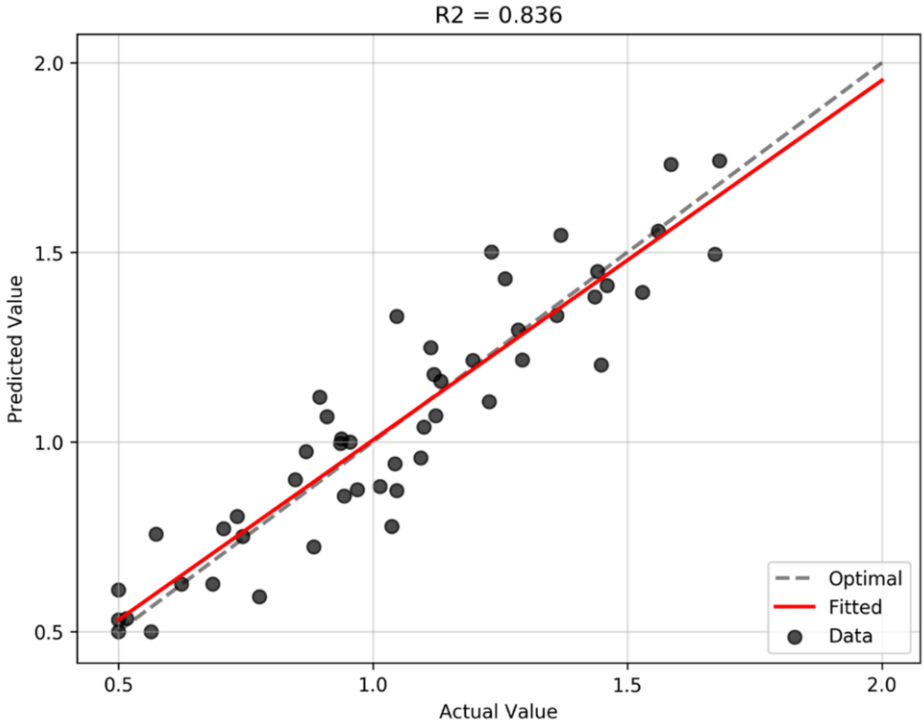

Figure 5. Comparison between predicted values and actual values.

6. Conclusion

To tackle the challenges of inefficient slope parameter adjustments, excessive cigarette use, and the difficulty of making timely parameter changes, which lead to poor accuracy in online cigarette weight detection, this study introduces an automated online parameter optimization system. It utilizes the XGBoost model and was evaluated with two cigarette brands from Sichuan China Tobacco Industrial Co. Ltd.'s Shifang Cigarette Factory. The results demonstrate that the new optimization method cut the time and cigarette usage for parameter adjustments by 65.72% and 83.33%, respectively. Moreover, it improved the compliance rates for target weight and calibration slope indicators by 49% (an average increase of ⅔ across both brands). This automation and intelligence significantly enhance detection precision and production efficiency, decrease manual intervention, and reduce resource wastage. Consequently, it offers a highly effective quality control solution for cigarette manufacturers. Although this study primarily targets the tobacco industry, its principles and technologies are applicable to various other sectors, including food processing, pharmaceuticals, and automotive manufacturing. These industries can benefit from the system, offering valuable solutions to enterprises facing similar challenges.

References

[1] B. J. Wei, "The importance and relevance of cigarette weight," (in Chinese), *Tobacco Science & Technology*, no. 3, pp. 6-8, 2000.

[2] T. L. Zhao, B. Li, X. Tian, et al., "The relationship between cigarette density and cigarette weight, draw resistance, hardness, and standard deviation," (in Chinese), *Tobacco Science & Technology*, no. 4, pp. 13-15, 2005.

[3] D. F. Li, J. Lian, Z. G. Wu, "Design and application of microwave cigarette weight control system," (in Chinese), *Tobacco Science & Technology*, no. 8, pp. 14-15, 23, 2005.

[4] C. H. Xing, S. X. Liu, "Improvement of real-time monitoring of SRM90 weight control system," (in Chinese), *Tobacco Science & Technology*, no. 6, pp. 23, 45, 2003.

[5] X. Lu, "Validation method of SRM weight control system parameters," (in Chinese), *Silicon Valley*, vol. 7, no. 14, pp. 165, 170, 2014.

[6] P. L. Cai, M. Li, W. Hua, et al., "Self-optimization of cigarette packaging process parameters based on IoT big data analysis," (in Chinese), *Journal of Mechanical Design and Manufacturing Engineering*, vol. 49, no. 6, pp. 117-120, 2020.

[7] H. L. Gao, J. Gao, J. S. Du, et al., "Analysis and design of microwave detection system for cigarette weight," (in Chinese), *Manufacturing Automation*, no. 7, pp. 1-3, 2010.

[8] W. Huang, "Application of microwave detection technology in cigarette weight control system," (in Chinese), *Tobacco Science & Technology*, no. 3, pp. 15-18, 2006.

[9] K. Feng, "Research on the application of data acquisition system in cigarette production," (in Chinese), *Computer Disc Software and Applications*, vol. 17, no. 2, pp. 132-133, 2014.

[10] L. Zhang, "Application of data acquisition system in cigarette production," (in Chinese), *Science and Technology Innovation*, no. 14, pp. 103-103, 2016.

[11] J. P. Xie, "Situation and future: Outlook for tobacco science and technology development," (in Chinese), *Chinese Tobacco Journal*, vol. 23, no. 3, pp. 1-7, 2017.

[12] Q. Cao, S. P. Zheng, T. W. Guo, "Research and application of cigarette quality inspection data acquisition method," (in Chinese), *Science and Technology Innovation Herald*, vol. 16, no. 25, pp. 45-46, 2019.

[13] X. Z. Zhou, L. H. Zhang, Y. J. Li, et al., "Method for real-time data synchronization of single cigarette mass during rolling process," (in Chinese), Chinese Patent CN201811613180.5, 2020.

[14] D. C. Yang, B. Ran, L. H. Kong, et al., "Digital transformation of tobacco manufacturing industry with data as the core," (in Chinese), *Intelligent Manufacturing*, no. 1, pp. 106-109, 2021.

[15] B. Zhu, Z. M. Chen, X. S. Zhang, et al., "Effect of tobacco shred morphology control on the rolling quality and stability of medium-sized cigarettes," (in Chinese), *Tobacco Science & Technology*, vol. 55, no. 7, pp. 66-72, 2022.

[16] Z. Q. Liang, J. Ye, C. H. Xiao, et al., "Microwave online testing device for cigarette density and moisture," (in Chinese), Chinese Patent CN213239830U, 2021.

[17] T. Chen and C. Guestrin, "XGBoost: A Scalable Tree Boosting System," ACM, 2016.

Fuzzy Systems and Data Mining X
A.J. Tallón-Ballesteros (Ed.)

doi:10.3233/FAIA241462

Challenges of Merging Generative AI with Metaverse for Next-Gen Education

Dimiter VELEV[a,1], Liudmila STESHINA[b], Igor PETUKHOV[b] and Plamena ZLATEVA[a,c]
[a]*University of National and World Economy, Sofia, Bulgaria*
[b]*Volga State University of Technology, Yoshkar-Ola, Russia*
[c]*Institute of Robotics, Bulgarian Academy of Sciences, Sofia, Bulgaria*
ORCiD ID: Dimiter Velev https://orcid.org/0000-0003-3030-1819,
Igor Petukhov https://orcid.org/0009-0000-2365-4857,
Plamena Zlateva https://orcid.org/0000-0002-0153-5811

Abstract. The integration of Generative Artificial Intelligence (GenAI) with the Metaverse for a next-generation education is a complex but challenging task. The GenAI-enhanced Metaverse classrooms require innovative instructional designs that use virtual reality and augmented reality to enhance engagement and personalized learning. Educators must adapt to new roles over traditional teaching methods, while learners need to develop digital literacy skills that are essential for navigating and inhabiting in these environments. Such learning environments require significant advancements in real-time processing, scalability and interoperability of different platforms, while ensuring data privacy and security. The equity of access to high-speed internet and advanced devices still remains a serious barrier, which can increase the potential existing inequalities between different educational environments. Ethical considerations, including the responsible use of GenAI, the creation of unbiased educational content, and the psychological impacts of extended usage of virtual reality, are also of important consideration. The aim of the paper is to explore in detail the different challenges through a comprehensive analysis of the obstacles and potential solutions and to propose a collaborative framework involving educators, technologists, policymakers and industry stakeholders to address the effective implementation of the integration of GenAI and the Metaverse for a next generation education.

Keywords: Generative AI, Metaverse, Virtual Reality, Augmented Reality, Education

1. Introduction

Among the most promising advancements are Generative Artificial Intelligence (GenAI) and the Metaverse and their integration. GenAI can create new content such as text, images and simulations and the application of their combination can revolutionize creation and delivery of educational content. The Metaverse, a collective virtual shared space created by the mixing the virtually enhanced physical reality and physically virtual

[1] Corresponding Author: Dimiter Velev, University of National and World Economy, 19 December 8th Str., 1700 Sofia, Bulgaria; E-mail: dgvelev@unwe.bg. The author was supported by the Science Fund of the University of National and World Economy under the project "Research on the Application Possibilities of the Metaverse Concept in Business and Education" (Grant No. NID NI 19/2023/A).

reality that can generate immersive environments for enhancing learning experiences. The integration of these two technologies can create next-generation educational platforms that are interactive, personalized and truly engaging. However, such integration poses a set of challenges.

The technical challenges of merging these technologies are significant. Real-time processing capabilities must be enhanced to ensure seamless interactions within virtual environments. The scalability of platforms to support a large number of concurrent users is crucial for widespread adoption in educational institutions. The interoperability between different systems and devices is required for creating smooth learning experiences. Ensuring data privacy and security is another critical aspect since educational platforms handle sensitive information about learners and educators.

From a pedagogical point of view, the shift to GenAI-enhanced Metaverse classrooms requires a fundamental rethinking of instructional design. Traditional teaching methods must be adapted to include elements of virtual reality and augmented reality that can create more engaging and personalized learning experiences. Educators must evolve into facilitators of learning rather than mere transmitters of information, guiding learners through complex virtual environments and helping them develop critical thinking and problem-solving skills. Learners, on the other hand, need to acquire digital literacy skills that are essential for navigating and thriving in these new educational settings [1, 2, 3].

Educators need to change themselves from being simple information transmitters to becoming learning helpers who will aid learners in navigating the complex virtual environments and improving their critical thinking and problem-solving abilities. On the other hand, learners must develop essential digital literacy skills to effectively navigate and succeed in these high-tech educational environments.

Equity of access to these advanced technologies is another serious challenge. The high-speed Internet and sophisticated devices are prerequisites for participating in Metaverse education. The existing digital divide between learners with different economical backgroud may out barriers to many of them to use such resources.

Ethical considerations also play a significant role in the deployment of GenAI and the Metaverse in education.. The psychological impacts of extended VR usage on learners and educators, such as potential effects on attention and social interactions, also need careful examination.

The aim of the paper is to explore in detail the different challenges through a comprehensive analysis of the obstacles and potential solutions and to propose a collaborative framework involving educators, technologists, policymakers and industry stakeholders to address the effective implementation of the integration of GenAI and the Metaverse for a next generation education.

2. The Metaverse Concept

The Metaverse is a virtual universe that combines physical and virtual realities through the use of modern Virtual Reality and Augmented Reality, Blockchain, Artificial Intelligence and Internet of Things [4, 5]. The digital ecosystem provides consumers with the ability to interact, create control, and participate in a variety of activities in real time, while simultaneously blurring the line between the physical and the digital worlds.

Virtual Reality (VR) creates fully immersive 3D environments that simulate the real world or create fantastic new worlds. The technology uses VR glasses and motion

controllers that track the user's movements and enable interactivity. Possible applications run the gamut from gaming and entertainment to training and simulations of various scientific and industrial environments.

Augmented reality (AR) integrates digital elements into the real world through devices such as smartphones and AR glasses. The technology uses cameras and displays to overlay virtual objects onto the real environment. Possible applications range from navigation and education to marketing and industrial applications.

Blockchain provides a decentralized and secure infrastructure for managing digital assets and identities. Possible applications are cryptocurrencies, NFTs, smart contracts, digital rights and secure transactions.

Artificial Intelligence (AI) - includes machine learning technologies that enable the creation of intelligent systems and generated content. Possible applications are smart assistants, adaptive environments, personalized recommendations, data analytics and automation.

Internet of Things (IoT) is the integration of physical and virtual worlds. IoT devices collect and exchange real-world data that can be used in the Metaverse to create more realistic and interactive virtual environments. This data allows virtual objects and avatars in the Metaverse to respond to physical events and conditions, thereby expanding the possibilities for interaction and engagement in the digital universe.

The Metaverse offers a great variety of applications, such as Social interactions, Economic activities, Education and training, Work and productivity, and Fun and games [6, 7].

Social interactions through virtual gathering, conferencing and social networking platforms that allow users to communicate and collaborate in real time. Avatars and Digital Identities allow users to create and customize their own avatars to represent themselves in the Metaverse.

Economic activities include virtual commerce, where virtual goods and services can be bought and sold, including real estate, fashion and art. Cryptocurrencies and digital currencies are used for transactions and trade within the Metaverse. NFTs enable the creation, sale, and ownership of unique digital assets, which can include art, music, virtual objects, and more.

Education and training through virtual classrooms and laboratories, which are interactive learning environments that allow students to learn through simulations and hands-on exercises. These processes can also be implemented through games and simulations for more effective and engaging learning. The ability to access educational resources and experts from around the world is another major advantage of studying at Metaverse.

Work and productivity through virtual offices and collaboration: which are platforms that facilitate remote work and collaboration between teams from different parts of the world. A commonly used method is to use simulations and training to train employees and simulate different scenarios and tasks.

Fun and games include Virtual Worlds and Adventures which are gaming platforms offering a variety of virtual adventures and worlds to explore. Virtual concerts and cultural events provide the opportunity to participate in concerts, theater productions and other cultural events in a digital format. Social games and multiplayer experiences allow users to play and interact together in real time.

The Metaverse is gradually transforming the way people live, work, learn and play, providing new opportunities and challenges. As technology evolves and becomes more widely accepted, the Metaverse will continue to expand and offer ever richer and more

diverse virtual experiences. This includes innovation in areas such as: Personalized experiences by developing AI systems that create personalized and adaptive virtual environments; Integration of physical and virtual realities for creating hybrid environments where physical and virtual objects and interactions merge; Global collaboration and connections for facilitating international collaboration and the exchange of ideas and culture through the Metaverse [8, 9].

These challenges of the Metaverse drive the trend to combine new technologies and applications to create an integrated and interactive digital reality that has the potential to change many aspects of modern life, including education.

3. The GenAI Concept

Generative AI is a field of artificial intelligence that deals with creating new data similar to training data using machine learning models. This technology has applications in a variety of areas, from creating images and text to music and video.

The main components of GenAI are based on the following types of generative models - Generative Adversarial Networks, Variational Autoencoders, and Transformer-based models [10, 11, 12, 13, 14]:

Generative Adversarial Networks (GANs) - consist of two main parts - a generator and a discriminator. The generator creates fake data, trying to make it as real as possible, while the discriminator evaluates this data and determines whether it is real or fake. The both are trained simultaneously in a zero-sum game. The generator tries to fool the discriminator, and the discriminator learns to better recognize fake data. Application examples - Image generation, enhancementof image resolution, deepfake video creation.

Variational Autoencoders (VAEs) include two components - an encoder and a decoder. The encoder compresses the data into a compact latent space, and the decoder reconstructs the data from this space. Unlike standard autoencoders, VAEs add randomness to the latent space, allowing different variations of the data to be generated. Application examples - Image generation, image and audio processing.

Transformer-based models use models, such as GPT (Generative Pre-trained Transformer) to process sequences of data. Training on large text predict the next element in a sequence based on context. Application examples - Text generation, translation, summarizing, coding.

GenAI has applications in a variety of areas. Some of the most common applications, applicable to new generations of education can include Education, Image generation, Text Generation, Music and audio, Video [15, 16, 17]:

Education - Creation of educational materials, personalized educational materials and tests, and automatic generation of explanations and examples for learners.

Image generation – Creation of new images that look like real photographs, image stylization – image conversion into styles of famous artists, super resolution – improvement of image quality and resolution.

Text generation – creation of chatbots and virtual assistants that use dialogues and answer questions in natural language, automatic article writing through generation of news articles, blogs, creative texts and other written products, text translation and creating short summaries of long texts.

Music and audio - Creation of new musical compositions in various genres and styles, speech synthesis from text, sound processing with effects and generating new sounds for games and films.

Video – Creation of fake videos with realistic images of people saying or doing something they didn't actually do, video animation based on static images or text.

Table 1 list the most popular GenAI tools at the time of writing the current paper.

Table 1. The most popular GenAI tools

Name	Source	Category	Oneliner
ChatGPT	https://openai.com/chatgpt/	Conversational AI	AI that assists with conversations and tasks through natural language processing.
DALL-E	https://openai.com/dall-e-2/	Image Generation	Generates high-quality images from textual descriptions.
Midjourney	https://www.midjourney.com/	Image Generation	An AI that creates stunning images from text prompts.
Stable Diffusion	https://stability.ai/	Image Generation	Open-source tool for generating detailed images based on text inputs.
RunwayML	https://runwayml.com/	Multimedia Tools	Platform for creative applications using AI for video, image, and audio.
Jasper AI	https://www.jasper.ai/	Content Creation	AI that assists with writing, marketing, and content creation.
Replika	https://replika.ai/	Conversational AI	AI companion for conversations and emotional support.
DeepArt	https://deepart.io/	Image Transformation	Transforms photos into artworks using AI.
Synthesia	https://www.synthesia.io/	Video Generation	AI-driven tool to create videos with AI avatars and voiceovers.
Descript	https://www.descript.com/	Multimedia Tools	AI-powered platform for audio and video editing and transcription.

The benefits of using GenAI can enhance creativity since GenAI models can create unique and original works, automation of tasks that require creativity, such as creating content for education or media, personalization - the ability to create personalized products and services based on user preferences.

Generative AI has potential and radically exchanges many aspects for life and work, but it is now pre-empting the need for dissuasive and ethical use of the theory of the power of technology. While AI is a broad field that encompasses various methods and applications aimed at replicating human intelligence, GenAI is a specialized area within AI that focuses on generating new and original content using advanced models like GANs, VAEs, and transformers. Both fields are interconnected, GenAI represents a significant and innovative subset of the broader AI landscape.

4. Merging Generative AI with Metaverse for Next-Gen Education

Metaverse and GenAI are two technologies that will enhance the potential and interact in the first place, which will exchange various aspects for digitalization, and in particular, the next generation will use training systems [18]. GenAI can create new possibilities in Metaverse through various techniques and methods, which allows automated and innovative generation of educational content [19, 20, 21, 22].

Interactive and educational experiences - GenAI can create interactive and educational experiences in the Metaverse, which can be used for teaching and learning. The product is included in the virtual classes of the flock, laboratories and training simulators, which can be adapted to the needs of consumers. GenAI can generate educational content and interactive exercises, which will improve the learning process [23, 24].

Personalized learning and training programs - GenAI can create personalized learning and training programs in Metaverse. Products including interactive coursework, simulations and exercises that adapt to the level and requirements of the user, ensuring effective and interactive training [25, 26].

Interactive storytelling and entertainment scenarios - GenAI can generate interactive storytelling and entertainment scenarios that will attract and engage consumers. These stories can include dynamic plots, a variety of selections and interactive elements, which will create a unique and personalized educational experience [27, 28].

Virtual spaces for work and collaboration - GenAI can create virtual spaces for work and collaboration, and educators and learners can collect for meetings, projects and other professional activities. These spaces can provide equipment with interactive tools and resources that will promote productivity and collaboration [29, 30, 31].

Dynamically generated tutorials and missions – GenAI can generate dynamic tutorials and missions for consumers in the Metaverse. Through analysis of consumer behavior and preferences, GenAI can create personalized scenarios, tasks and tasks that will increase interest and engagement in the learning process. The product is included in the generation of dialozi, interactive shootings and reverse plots [32, 33, 34, 35].

Integration with real data - GenAI can integrate real data into the world of virtual reality, so that information from real data can be used in real life and actual data. This includes geographical data, meteorological conditions, historical events and cultural contexts for creation on authentic virtual environments [36, 37, 38].

Generating data on user preferences and behavior, creating personalized data among educators and learners - GenAI can generate data on consumer preferences and behavior. The product is included, adapted to visual and interactive elements, and will be of interest to users [39, 40].

Personalized Avatars - GenAI can create unique and personalize avatars for educators and learners in the Metaverse. The product includes various physical characteristics, clothing, accessories and animations. The GenAI can analyze preferences for consumers and create avatars that reflect technology, style and personality [41, 42].

Generation on NPCs (non-player characters) - GenAI can create intelligent NPCs that interact with consumers in a meaningful and realistic manner. These NPCs can and can differ in their roles, character and behavior, which will enrich the virtual world. GenAI can generate dialysis and reactions, which will respond to the context and effect on the user [43, 44].

Procedurally generated objects and resources - GenAI can create a variety of objects and resources for virtual training through procedurally generated ones. The product

includes tools, textbooks and other objects that consumers can use and interact with. The procedural generation is based on endless possibilities for diversity and uniqueness on the object [45].

Adaptive and dynamic settings - GenAI can create adaptive and dynamic settings, which will be exchanged in real time in response to actions on the user.

Generation of textures and landscapes - GenAI can create varied and realistic textures and landscapes for virtual lighting training. GenAI can generate high-quality images of natural scenes, landscapes and interior spaces. The product includes realistic textures for land, water, vegetation [46, 47].

GenAI provides endless possibilities for creating diverse and innovative virtual environments in the Metaverse. These technologies allow personalization and adaptation to the learning environment, needs and preferences of the user. GenAI technology and tools have the potential to create more realistic, dynamic and interactive virtual environments, they continue to grow, create new and exciting experiences for educators and learners [48].

5. Framework for the Integration of Generative AI and the Metaverse into Next-Gen Education

The successful integration of GenAI and the Metaverse into next-generation education requires a comprehensive and collaborative framework. This framework should address the identified technical, pedagogical, equitable access and ethical challenges, which would ensure a smooth inclusion and adoption of those advanced technologies. Figure 1 presents a conceptual framework for the Integration of Generative AI and the Metaverse into Next-Generation Education, in which the arrows show the relationships and interactions between the components, highlighting how they work together to achieve an effective educational system.

The Technical Infrastructure is responsible for:

- Real-Time processing and scalability that could include the development and deployment of cloud-based solutions to support real-time data processing and high-performance computing, the implementation of edge computing to reduce latency and enhance the user experience in immersive environments, designing scalable architectures that can support a large number of concurrent users without compromising performance.
- Interoperability has the potential to establish open standards and protocols to ensure seamless integration between different platforms and devices and to promote the development of API frameworks that allow for easy integration of new tools and technologies into existing educational systems.
- Data privacy and security should implement strong encryption methods to protect sensitive data, develop comprehensive data governance policies to manage data access and usage, to conduct security audits and vulnerability assessments on regular basis to identify and mitigate potential threats.

The Pedagogical Innovation is responsible for:

- Instructional design incorporates VR and AR elements into curriculum design to create immersive and interactive learning experiences, develops adaptive learning systems that use GenAI to personalize educational content based on

individual learner needs and learning styles, train educators for the use of VR and AR technologies, emphasizing their role as helpers rather than traditional instructors.

- Professional development is responsible for creating professional development programs which will help educators integrate new technologies into their teaching practices effectively, creating a community where educators can share best practices, resources and experiences related to the use of GenAI and the Metaverse.
- Learner digital literacy implements the development of curricula that include digital literacy skills essential for navigating and using advanced technologies, provision of resources and help students become proficient in using VR, AR and AI tools.

The Equitable Access is responsible for:

- Infrastructure and resources investments to ensure that all learners have access to high-speed internet and necessary devices, and to partner with public and private organizations to subsidize the cost of devices and connectivity for underserved communities.
- Inclusive design has the purpose to design educational content and platforms that are accessible to learners with diverse needs, including those with disabilities, and to implement multilingual support to cater to a global learner population.
- Overcoming the digital divide tries to develop programs to engage communities that are traditionally underserved by advanced technologies, and to provide training and support to help these communities leverage new educational tools and resources.

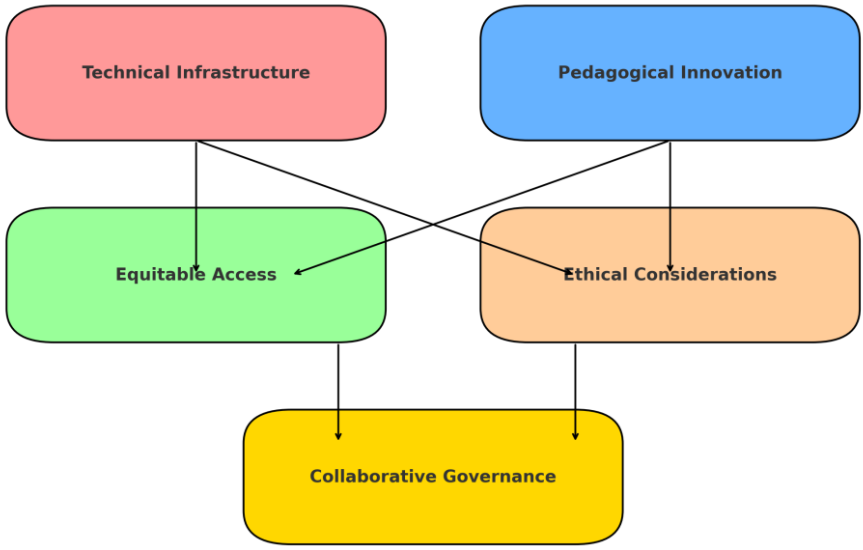

Figure1. Framework for the Integration of Generative AI and the Metaverse into Next-Generation Education

The Ethical Considerations is responsible for:

- Responsible GenAI use to ensure that AI algorithms are transparent, explainable and free from biases, and to establish ethical guidelines for the development and use of GenAI in education.
- Psychological impact has the purpose to conduct research on the psychological effects of prolonged VR and AR use on learners, and to develop guidelines to mitigate potential negative impacts, such as screen time limitations and promoting balanced use of technology.
- Content integrity that implements quality control measures to ensure the accuracy and reliability of GenAI educational content, and encourages the development of AI systems that can critically evaluate and improve the content they generate.

The Collaborative Governance is responsible for:

- Multi-Stakeholder involvement to create a governance body comprising educators, technologists, policymakers, industry representatives and learners, and facilitates regular meetings and workshops to ensure all stakeholders are aligned and actively contributing to the framework's implementation.
- Policy development which cares for policies that support the integration of GenAI and the Metaverse in education, and work with governments and educational institutions to develop regulations that ensure the ethical use of these technologies.
- Continuous improvement establishes a feedback loop to continuously assess the effectiveness of the integration framework, and uses data and feedback to make iterative improvements to policies, practices, and technologies.

6. Conclusion

The paper has analyzed the main features of the Metaverse and GenAI, identifying their key components and technological challenges. The new possibilities for automated and innovative generation of educational content have been discussed through the exploration of various techniques and methods that the integration of GenAI and Metaverse can implement. A conceptual framework for the Integration of Generative AI and the Metaverse into Next-Gen Education is proposed, which addresses the identified technical, pedagogical, equitable access and ethical challenges. An innovative approach is needed, involving educators, technologists, policymakers and industry stakeholders to overcome these challenges. Working together, these groups can develop a viable framework and strategies for addressing all challenges associated with integrating GenAI and the Metaverse in the next generation education.

The main limitations of the proposed framework, among others, are the technological challenges related to the computational power, which requires significant resources to handle the complexity of the GenAI models and the immersive environments. Interoperability is another problem that concerns compatibility between different platforms, devices and software.

References

[1] Angraini LM, Kania N, Gürbüz F. Students' proficiency in computational thinking through constructivist learning theory. International Journal of Mathematics and Mathematics Education. 2024;2(1):45–59.
[2] Kania N, Kusumah Y, Dahlan J, Nurlaelah E, Gürbüz F, Bonyah E. Constructing and providing content validity evidence through the Aiken's V index based on the experts' judgments of the instrument to measure mathematical problem-solving skills. REID (Research and Evaluation in Education). 2024;10(1):64-79.
[3] Usmayati U, Gürbüz F. Empowering students with discovery learning in circle geometry for better problem-solving. International Journal of Geometry Research and Inventions in Education (Gradient).2024;1(01):11–20.
[4] Ball M. The Metaverse: Fully Revised and Updated Edition: Building the Spatial Internet. Liveright; 2024.
[5] Heggde GS, Patra SK, Rasananda Panda R (Eds.). Immersive Technology and Experiences - Implications for Business and Society. Palgrave; 2024.
[6] Savin-Baden M, David Burden D. The Metaverse for Learning and Education. CRC Press; 2024.
[7] Hutson J. Art and Culture in the Multiverse of Metaverses - Immersion, Presence, and Interactivity. Springer; 2024.
[8] Yap M. The Intelligent Classroom: AI's Role in Shaping Educational Paradigms. Univenture Studio; 2023.
[9] Lee R, Gim G, Kim J (Eds.). AI and Metaverse. Volume 2, Springer; 2024.
[10] Elektran R. Generative Adversarial Networks (GANs). RE; 2024.
[11] Clinton D. The Complete Obsolete Guide to Generative AI. Manning; 2024.
[12] Ghayoumi M. Generative Adversarial Networks in Practice. CRC; 2024.
[13] Musiol M. Generative AI - Navigating the Course to the Artificial General Intelligence Future. Wiley; 2024.
[14] Fraley A. The Artificial Intelligence and Generative AI Bible. AL; 2024.
[15] Harward Business Review, Generative AI; 2024.
[16] Granville V. Synthetic Data and Generative AI. Morgan Kaufman;2024.
[17] Lyu Z (Ed.). Applications of Generative AI, Springer; 2024.
[18] Chan CKY, Colloton T. Generative AI in Higher Education - The ChatGPT Effect. Routledge; 2024.
[19] Taulli T. Generative AI - How ChatGPT and other AI tools will revolutionize business. Apress; 2024.
[20] Engage. Exploring the Role of Generative AI in the Metaverse. https://engagevr.io/exploring-the-role-of-generative-ai-in-the-metaverse/
[21] Cyfuture Edge. The Rise of Metaverse Due to Generative AI. 2023. https://www.linkedin.com/pulse/rise-metaverse-due-generative-ai-cyfuture/
[22] Jauhiainen JS. The Metaverse: Innovations and generative AI. https://www.sciencedirect.com/science/article/pii/S2096248724000183
[23] Lv Z. Generative Artificial Intelligence in the Metaverse era. Cognitive Robotics. 2023;3:208-217. https://www.sciencedirect.com/science/article/pii/S2667241323000198
[24] World Economic Forum – Emerging Technologies, AI is Shaping the Metaverse - but How? Industry experts explain. 2023, https://www.weforum.org/agenda/2023/05/generative-ai-and-how-can-it-shape-the-metaverse-industry-experts-explain/
[25] Marr B. Digital Twins, Generative AI, and the Metaverse. 2023, https://www.forbes.com/sites/bernardmarr/2023/05/23/digital-twins-generative-ai-and-the-metaverse/
[26] Radoff J. Generative AI and Virtual Worlds. 2023, https://medium.com/building-the-metaverse/generative-ai-and-virtual-worlds-1f3b078b79d9
[27] Nouzareth M. How Generative AI Can Play a Role in the Metaverse. 2023, https://www.nasdaq.com/articles/how-generative-ai-can-play-a-role-in-the-metaverse
[28] BRL, Avatars: Shaping Digital Identity in the Metaverse. 2023, https://www.blockchainresearchlab.org/wp-content/uploads/2020/05/Avatars-Shaping-Digital-Identity-in-the-Metaverse-Report-March-2023-Blockchain-Research-Lab.pdf
[29] Nancyjohnathan. Generative AI in Metaverse. Medium; 2023, https://medium.com/@nancyjohnathan05/generative-ai-in-metaverse-4a22108f57cf
[30] Saivasan R, Lokhande M. Exploring Use Cases of Generative AI and Metaverse in Financial Analytics: Unveiling the Synergies of Advanced Technologies. JGBC. 2023;18(1):77–86, doi:/10.1007/s42943-023-00082-2
[31] Qin HX, Hui P. Empowering the Metaverse with Generative AI: Survey and Future Directions. 2023, https://www.researchgate.net/publication/370132434_Empowering_the_Metaverse_with_Generative_AI_Survey_and_Future_Directions
[32] Brown T. Generative AI & the Metaverse: Applications for XR Design. 2023, https://www.wizeline.com/generative-ai-the-metaverse-applications-for-xr-design/

[33] Peham T. Unleashing the Metaverse and Generative AI for a Better Brand Experience, 2024, https://www.techradar.com/pro/unleashing-the-metaverse-and-generative-ai-for-a-better-brand-experience
[34] Chylinski M, Ruyter K. What the Metaverse Means for Marketing and Generative AI. 2023, https://www.businessthink.unsw.edu.au/articles/metaverse-marketing-generative-ai
[35] Braia R. The Metaverse and Generative AI. 2023, https://sensoriumarc.com/articles/metaverse-and-generative-ai
[36] Maricris, Metaverse with Generative AI: Virtual Worlds and Business Opportunities. 2024, https://aimarketingengineers.com/metaverse-with-generative-ai-virtual-worlds-and-business-opportunities/
[37] Ambolis D. What is Generative AI and Will It Affect Metaverse - Positively or Negatively. 2023, https://blockchainmagazine.net/what-is-generative-ai-and-will-it-affect-metaverse-positively-or-negatively/
[38] Kazeem I. Generative AI in the Metaverse: Challenges and Opportunities in the Virtual World. 2023, https://www.dxtalks.com/blog/news-2/generative-ai-in-the-metaverse-challenges-and-opportunities-in-the-virtual-world-414
[39] NXT, Generative AI in the Metaverse. 2024, https://www.nxtinteractive.sg/blog/generative-ai-in-the-metaverse
[40] Singla S. The Metaverse and The Rise of Generative Artificial Intelligence: How AI Is Shaping the Future of Virtual Worlds. 2023, https://www.entrepreneur.com/en-au/news-and-trends/the-metaverse-and-the-rise-of-generative-artificial/455383
[41] Spencer S. Can Meta Stage a Metaverse Comeback with Generative AI?, 2024, https://www.vibranium.sg/post/can-meta-stage-a-metaverse-comeback-with-generative-ai
[42] Aijaz S. How the Rise of Generative AI Could Kill the Metaverse - or save it. 2023, https://venturebeat.com/ai/how-the-rise-of-generative-ai-could-kill-the-metaverse-or-save-it/
[43] Antier Solutions, The Future of Business: Exploring the Power of Generative AI in the Metaverse. 2024, https://www.antiersolutions.com/how-businesses-can-leverage-generative-ai-in-the-metaverse/
[44] Toolify.ai. Unleashing the Metaverse: The Impact of Generative AI on our Virtual Reality. 2024, https://www.toolify.ai/ai-news/unleashing-the-metaverse-the-impact-of-generative-ai-on-our-virtual-reality-1438638
[45] Tech Blogger. Generative AI in the Metaverse. 2024, https://contenteratechspace.com/generative-ai-in-metaverse/
[46] Iyer A. How Generative AI is Reshaping the Landscape of the Metaverse. 2023, https://analyticsindiamag.com/innovation-in-ai/how-generative-ai-is-reshaping-the-landscape-of-the-metaverse/
[47] Rijmenam M. Unleashing the Generative AI Genie: A Brave New Metaverse or a Nightmare Scenario? 2023, https://www.thedigitalspeaker.com/unleashing-generative-ai-genie-brave-new-metaverse-nightmare-scenario/
[48] Ffiske T. Generative AI and the Metaverse: Where we are, and where we are going. 2023, https://www.immersivewire.com/p/generative-ai-metaverse

Fuzzy Systems and Data Mining X
A.J. Tallón-Ballesteros (Ed.)

doi:10.3233/FAIA241463

Risks and Threats in Using Generative AI

Plamena ZLATEVA[a,b,1], Rajagopal SIVAKUMAR[c] and Dimiter VELEV[a]
[a]*University of National and World Economy, Sofia, Bulgaria*
[b]*Institute of Robotics, Bulgarian Academy of Sciences, Sofia, Bulgaria*
[c]*Vellore Institute of Technology, Vellore, India*
ORCiD ID: Plamena Zlateva https://orcid.org/0000-0002-0153-5811
Rajagopal Sivakumar https://orcid.org/0000-0001-8486-7960
Dimiter Velev https://orcid.org/0000-0003-3030-1819

Abstract. Generative artificial intelligence (GenAI) is a cutting-edge technology capable of creating new content –text, images, video and sound based on predefined data. Despite the enormous potential for innovation, this technology carries with it serious risks and threats. The article aims to discuss the technical risks, ethical and social challenges, labor market and economic consequences, and legislative and regulatory challenges. Recommendations are proposed to reduce these risks through more responsible use, transparency and the development of adequate regulations.

Keywords. Generative AI, Automation, Disinformation, Risk, Threat

1. Introduction

Generative artificial intelligence (GenAI) is an advanced technology that has the ability to create new and original content based on the analysis of large amounts of data [1, 2, 3]. Unlike classic AI systems that perform tasks by following specific algorithms, GenAI is self-taught through vast arrays of data. It uses complex neural networks that mimic the human brain to understand the structure of the data it is trained with and generate new unique results. GenAI doesn't just reproduce existing content, it creates new content that can look completely original that didn't exist before. This makes it an extremely powerful tool capable of solving complex tasks in a wide range of fields.

Recently, GenAI has become increasingly popular and is being used in various industries and fields. In art and culture, it opens up new horizons for creative processes, allowing artists and designers to experiment with completely new forms, styles and ideas. Musicians use GenAI to create new musical compositions, while writers and screenwriters can generate plots or dialogues using this technology. In the scientific realm, GenAI supports innovation in fields such as biology and medicine by accelerating the process of data analysis, new drug development, and modeling of complex systems. In business, GenAI is used to automate tasks, improve customer service by generating personalized responses, and optimize manufacturing processes. The popularity of GenAI

[1] Corresponding Author: Plamena Zlateva, University of National and World Economy, 19 December 8th Str., 1700 Sofia, Bulgaria; E-mail: plamzlateva@unwe.bg. The author was supported by the Science Fund of the University of National and World Economy under the project "Research on the Application Possibilities of the Metaverse Concept in Business and Education" (Grant No. NID NI 19/2023/A).

is growing exponentially as it offers unlimited opportunities to improve existing processes and create innovative solutions.

Despite the enormous potential and benefits that GenAI offers, it brings with it serious risks and threats that cannot be ignored [4, 5]. GenAI models can create fake texts, images or videos that are hard to recognize as fake and can be used for manipulation of public opinion or for cyber attacks. There are serious ethical issues related to responsibility in the creation and distribution of content generated by GenAI. Improper use of Generative AI can lead to copyright infringement, misuse of personal data, or even discrimination built into the algorithms themselves. There are also threats to the economy and the labor market, as the automation of processes can lead to job losses.

The paper addresses risks and threats regarding security, ethics and society, bias and discrimination, labor market and economics, legal and regulatory challenged, recommendations for risk and threat minimization to ensure the responsible GenAI use.

Figure 1 gives an overview of possible risk and threats due to GenAI use.

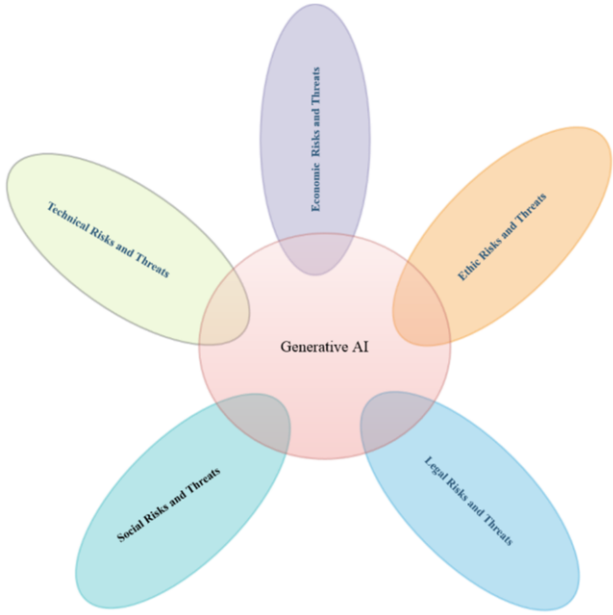

Figure 1. GenAI risks and threats.

2. Technical risks and threats

Misuse of personal data represents a serious technical risk when applying GenAI [6, 7, 8]. It can be trained on huge data sets, including data that contains personal or sensitive information. This data can include personal data about users such as names, addresses, medical records, financial data or even communications. The problem arises when GenAI models begin to generate content that can reveal or use this personal data without the consent of their owners.

Falsified images, texts or videos, produced with GenAI, can be used to manipulate personal data and can be used for defamation, fraud or social manipulation [9, 10]. Systems that access sensitive information can generate content that compromises the security of affected individuals. There is a risk of unauthorized access to stored data through hacker attacks that use AI algorithms to extract information.

Cyber security can be threatened by GenAI usage as it has the potential to create new forms of cyber attacks [11, 12, 13, 14]. New types of enhanced phishing attacks can be generated, where GenAI models can generate fully customized messages that look legitimate and are very difficult to distinguish from real ones. GenAI can analyze publicly available information about a person and create targeted attacks that use the victim's names, preferences or habits.

Fraudulent activities can be made real by using GenAI by generating fake videos or audio recordings of celebrities, politicians or even ordinary people, presenting them in compromising situations. These materials can be used for manipulation, extortion or disinformation [15, 16]. GenAI can automate malware creation processes, developing new viruses or malware with minimal human intervention.

Cybercrime automation through GenAI is one of the biggest threats associated with its use [17, 18]. It can automate a variety of malicious practices, including hacking attacks, identity theft, creating malware and spreading disinformation. Cybercriminals with the GenAI help can create new and advanced attacks with minimal human intervention, making these attacks faster, cheaper and harder to detect and prevent. GenAI can analyze the vulnerabilities of systems and automatically generate codes to exploit those vulnerabilities.

Distribution of malware through GenAI can implement their automatically adaption to different systems and can remain undetected by traditional antivirus programs [19, 20]. These technologies can also be used to automatically generate new forms of social engineering attacks, such as creating fake accounts or even compromising entire networks through coordinated attacks.

3. Ethical risks and threats

Disinformation and fake news are possible with the GenAI help to create fake images, videos and text to manipulate public opinion [21, 22]. Fake news and manipulated images can have huge consequences on society, especially in times of crisis, elections or important social events. They can create panic, change the behavior of large groups of people and even affect financial markets. GenAI can be used to spread political or ideological propaganda, creating material that supports one side or discredits another. In the context of social media, misinformation can spread at an unprecedented speed and reach millions of people in a short time, making the fight against fake news even more difficult and complex.

Manipulation of public attitudes can be used to shape prejudice, change political attitudes and psychological manipulation [23, 24]. GenAI can be used as a tool to manipulate public attitudes and form prejudices. Through personalized content that is created based on data about individuals' behavioral habits, preferences and vulnerabilities, GenAI can be used to create targeted messages that sway public opinion in a given direction. This form of manipulation can be particularly dangerous during elections or important political events, when the public is more vulnerable to misinformation. AI-generated messages can reinforce existing prejudices or create new

ones by emphasizing or exaggerating certain facts while ignoring others. This can lead to polarization in society, an increase in social tension and even a breakdown of trust between different groups in society.

Psychological manipulation with GenAI help can be used for creating content that reflects human emotions, such as fear, uncertainty, anger, making people take irrational decisions [25, 26, 27]. This is particularly dangerous because GenAI can personalize messages based on individual psychological profiles, making the manipulation even more subtle and difficult to detect.

Responsibility is one of the main ethical issues related to GenAI [28, 29]. When a GenAI system creates content that is manipulated, misleading or used for malicious purposes, it remains unclear who should take responsibility for the consequences. This can be the developer of the AI model, the organization that implemented it or just the end users who used the created content for certain purposes. The lack of clear regulations and ethical guidelines for the use of GenAI creates legal and moral challenges related to liability.

Transparency is another key ethical issue [30, 31, 32]. In many cases it is not clear how GenAI makes decisions and on what basis it creates certain content. The lack of transparency in the functioning of these systems can lead to mistrust of the technology itself. Users and the public have a right to know what's behind the algorithms that generate content and how their data is used to train those models.

4. Biases and Discrimination risks and threats

Unconscious biases, produced by GenAI, can reproduce and amplify existing social stereotypes and inequalities [33, 34, 35]. The reason for this is the way these models are trained – by analyzing and processing large data sets that often reflect the biases inherent in the society that created them. If the data used to train GenAI models contains biases or imbalances in the representation of different social groups, the model can "learn" these biases and reproduce them in the content it generates or in the decisions it makes. These unconscious biases can be particularly dangerous when GenAI systems are used in sensitive areas such as education, healthcare or justice. If models make decisions based on biased data, it can exacerbate social inequalities and reinforce existing prejudices. For example, if an AI is trained with data that reflects an imbalance in education or economic opportunity for different racial or ethnic groups, it can unwittingly reinforce those inequalities through its decisions.

Discriminatory threats [36, 37], such as decisions in the areas of employment, credit and law enforcement, by the use of GenAI, can have serious consequences in key societal areas such as employment, credit and law enforcement. One of the main problems is that if models are trained with biased data, they can make decisions that appear to be objective but actually discriminate against certain social groups.

In the field of **lending**, GenAI can make decisions to approve or deny loan applications based on data from previous loans [38, 39]. If the data showed that certain ethnic groups or people from certain social backgrounds had worse credit ratings, the model can reproduce that discrimination by systematically denying credit to people from those groups, even when they have adequate financial capabilities.

In the field of **law**, GenAI can be used to analyze criminal data and predict criminal behavior [40]. If models are trained with historical data that shows an imbalance in treatment of different racial or social groups, AI can predict a higher likelihood of

criminal behavior in people from certain ethnic minorities. This leads to the reinforcement of existing stereotypes and unfairness in decisions about surveillance, arrests or punishments.

In the field of **recruitment**, GenAI is often used to automate candidate selection processes [41, 42]. If the model is trained on data that reflects biases towards the gender or ethnicity of applicants, it can reproduce these biases.

5. Economic risks and threats

The automation of various tasks and processes with GenAI leads to increasing job losses [43, 44, 45]. GenAI is capable not only of performing routine and repetitive tasks, but also of performing creative and analytical activities that were inherent to humans. This is particularly evident in industries such as media, marketing, design, the financial and legal sectors. This process of automation exposes a large number of jobs at risk, especially for lower-skilled workers who perform tasks that can easily be automated. Although technology leads to increased productivity and reduced costs, at the same time it unemployment, especially among workers who do not have the skills necessary to adapt to new technological demands.

New job opportunities can be created with GenAI in areas such as AI technology development, data management and digital platforms [46]. However, these positions require high qualifications and technical skills that are not all employees posses. In order to mitigate the negative effects of automation, it is essential to invest resources in retraining the workforce so that it can adapt to the new demands of the labor market.

Deepening of existing economic inequalities through GenAI automation can create new forms of social and economic division [47, 48]. One of the main ways is through the division between high-skilled and low-skilled workers. As automation replaces routine and repetitive tasks, low-skilled workers who depend on these jobs are the hardest to suffer by job losses. At the same time, highly skilled professionals who can adapt to new technologies or develop and operate AI systems remain in high demand and can benefit from the economic benefits of automation.

New forms of economic inequality can be created by such processes between groups that have access to technological education and skills and those that do not [49, 50]. Groups that are already vulnerable, such as older workers, people from economically less developed regions and social minorities, can be additionally excluded from the economic opportunities that GenAI provides. The growing digital divide can lead to greater economic polarization in society, where a small part of the population benefits from technological progress while the rest remain unemployed or employed in low-paid jobs.

Greater concentration of wealth in the hands of large technology corporations and investors that implement GenAI solutions can generate significant profits by reducing labor costs and increasing productivity, while the rest of society does not feel the economic benefits [51, 52]. To reduce these economic inequalities, it is important to develop policies that ensure that all social groups have access to training that will allow them to take advantage of the new opportunities created by GenAI.

6. Legal risks and threats

The lack of adequate legislative frameworks is one of the main legal and regulatory GenAI issues. AI technologies develop with a very fast speed, making it difficult for governments and regulators to create effective laws and regulations to cover them [53, 54]. Legislative processes are often slow and complex, while technological innovation advances significantly faster. This leads to a situation where society uses powerful technologies without clear rules for their use, which raises a number of ethical and legal challenges.

Existing laws can not often be applied to the latest technologies [55, 56, 57]. GenAI that creates content, such as text, images or video, raises questions about intellectual property rights, responsibility for the content created and the regulation of that content in the context of social media and other platforms. Besides that, GenAI can be used for malicious purposes such as creating disinformation, deepfakes or automating cyberattacks, which requires new regulatory mechanisms to prevent possible abuses.

The complexity of the technology makes it difficult to understand it for regulators, who often lack the expertise to fully understand the potential risks and threats [58]. This leads to situations where technologies are put into practice without the necessary regulations, creating risks for consumers, businesses and society. There is an obvious need for international cooperation since GenAI solutions in most cases have a global impact and regulations at the national level are not sufficient to address global challenges.

Intellectual property rights and copyright are new challenges to GenAI since it creates questions about the authorship of machine-generated content [59, 60]. Traditionally, copyrights have been granted to individuals or organizations that create original works, such as music, literature, art, patents. However, GenAI rises the questions about the ownership rights about the content it generates.

Traditional copyright laws are not created in accordance with the new technological innovations and they do not provide clarity on the rights of GenAI content [61]. This creates legal uncertainties for companies and individuals who use GenAI for commercial or personal purposes.

The problem of using data to train GenAI models is another issue [62]. Often these models are trained with large amounts of data, which can include copyrighted content such as books, images, music, video. The question of whether the use of such data infringes the copyright of the original creators is controversial and in some cases leads to legal conflicts.

7. Recommendations to minimize risks and threats from GenAI use

The need for recommendations to reduce the risks of GenAI is essential to ensure ethical and safe use of the technology. Without clear guidelines for transparency, protection of personal data and prevention of misinformation, there is a risk of abuse, discrimination and social instability. The following recommendations can be proposed to deal with each risk category when applying GenAI [63, 64, 65, 66, 67].

Technical risks:

- Using AI to detect and prevent cyber attacks in real time with a focus on security.

- Using tools to encrypt data and ensure its privacy and security.
- Using test platforms to evaluate the safety of GenAI models, especially in critical sectors.
- Monitoring GenAI vulnerabilities and performing regular security checks.
- Introducing real-time monitoring of GenAI attacks to protect systems.

Ethical Risks:

- Using technologies to automatically detect fake content and deepfakes, including authentication.
- Establishing ethical standards and guidelines for the development and use of GenAI, followed by all stakeholders.
- GenAI monitoring of media content to detect disinformation and fake news.
- Conducting trainings on identifying fake news and media literacy among the public.
- Introduction of mandatory tags for GenAI-content that clearly identify its origin.

Social risks:

- Conducting independent audits of GenAI algorithms to detect bias and unfair decisions.
- Using of GenAI to support social projects and initiatives aimed at reducing social tension.
- Integrating ethical learning algorithms that reduce discriminatory decisions.
- Conducting public awareness campaigns about misinformation and the risk of using AI for manipulation.
- Identifying data biases and train GenAI with more diverse and representative data.

Economic risks:

- Employee retraining programs to prepare for new technological positions.
- Providing financial incentives for job creation and development in the AI sector.
- Training and retraining of employees in industries affected by automation.
- GenAI integrating in the labor market for optimization and creation of new employment opportunities.
- Developing educational programs for adaptation of employees and citizens to the new GenAI environment.

Legal risks:

- Developing legislation to protect copyright on GenAI generated content.
- Establishing international standards for the protection of intellectual property when using GenAI.
- Introducing transparency policies when using GenAI to generate content.
- Providing legal protection for authors and creators whose work is used by GenAI models.
- Cooperating between countries to create global standards and regulations of GenAI.

8. Conclusion

The use of GenAI offers huge opportunities for innovation, but it also leads to a number of risks and threats that require attention and active measures. The main risks include the spread of misinformation, deepfake technologies, misuse of personal data and the automation of malicious practices such as cyber attacks. The social inequalities and biases built into GenAI models can lead to discrimination and polarization in society. GenAI automation threatens many jobs, especially for low-skilled workers.

To minimize these risks, regulations and standards are needed to ensure transparency, ethics and security in the use of GenAI. Technology companies, governments and international organizations must work together to create frameworks for the safe development and use of AI. Educating the public about the risks of misinformation and misuse of GenAI is needed for preventing its negative consequences.

References

[1] Dhamani N, Engler M. Introduction to Generative AI. Manning, 2024.
[2] Almeida I. Generative AI for Business Leaders. Now Next Later AI, 2023.
[3] Synergy AI Editions. Understanding Generative AI for Business Leaders: Demystifying Strategic Advantage, Ethical Deployment, and Practical Integration for Success. SAIE, 2024.
[4] MIT, AI Risk Repository. 2024, https://airisk.mit.edu/
[5] Slattery P, Saeri AK, Grundy EAC, Graham J, Noetel M, Uuk R, Dao J, Pour S, Casper S, Thompson N. A systematic evidence review and common frame of reference for the risks from artificial intelligence. 2024. http://doi.org/10.13140/RG.2.2.28850.00968
[6] Isik O, Joshi A, Goutas L. 4 Types of Gen AI Risk and How to Mitigate Them. 2024, https://hbr.org/2024/05/4-types-of-gen-ai-risk-and-how-to-mitigate-them
[7] Zaman S. et al. Security Threats and Artificial Intelligence Based Countermeasures for Internet of Things Networks: A Comprehensive Survey. IEEE Access. 2021;9:94668-94690, doi:10.1109/ACCESS.2021.3089681
[8] Keith Batterham K. 8 Generative AI Security Risks and Effective Mitigation Strategies. 2024, https://www.ek.co/publications/8-generative-ai-security-risks-and-effective-mitigation-strategies/
[9] Thumos. Generative AI and deepfakes. How artificial intelligence tools will sow disinformation. 2024, https://thumos.global/generative-ai-and-deepfakes/
[10] Mahmoud B. Understanding the Different Types of Generative AI Deepfake Attacks. 2024, https://kycaml.guide/blog/understanding-the-different-types-of-generative-ai-deepfake-attacks/
[11] Miller JA, Eide N. Generative AI is a looming cybersecurity threat. 2024, https://www.cybersecuritydive.com/news/generative-ai-artificial-intelligence-cyber-threat/715531/
[12] Zhu B, Mu N, Jiao J, Wagner D. Generative AI Security: Challenges and Countermeasures. 2023, https://arxiv.org/pdf/2402.12617v1
[13] Murphy S. What Generative AI Means for Cybersecurity in 2024. 2024, https://www.trendmicro.com/en_us/research/24/b/generative-ai-cybersecurity-2024.html
[14] Kirilov R. Implementation and Use of SIEM Platforms. Processing of the 12th Int. Conf. on Application of Information and Communication Technology and Statistics in Economy and Education (ICAICTSEE – 2022), December 2-3, 2022, University of National and World Economy (UNWE), Sofia, Bulgaria, pp. 40-44, http://icaictsee.unwe.bg/past-conferences/ICAICTSEE-2022.pdf
[15] Garcia-Segura LA. The role of artificial intelligence in preventing corporate crime. Journal of Economic Criminology. 2024;5:100091, doi:10.1016/j.jeconc.2024.100091
[16] Ahmadi S. Open AI and its Impact on Fraud Detection in Financial Industry. Journal of Knowledge Learning and Science Technology. 2023;2(3):263-281, doi:10.60087/jklst.vol2.n3.p281
[17] Matejic N, Wilson C. Crimes of Influence: Generative Artificial Intelligence-led Crime as a Service. Commonwealth Cyber Journal. 2023;2(6):75-95, thecommonwealth.org/cyber-journal
[18] Isola L. How cybercriminals are using gen AI to scale their scams. 2024, https://www.okta.com/blog/2024/01/how-cybercriminals-are-using-gen-ai-to-scale-their-scams/
[19] Kasarapu S. et al., Generative AI-Based Effective Malware Detection for Embedded Computing Systems. 2024, https://arxiv.org/html/2404.02344v2

[20] Krishnan A. Generative AI is making phishing attacks more dangerous. 2024, https://www.techtarget.com/searchsecurity/tip/Generative-AI-is-making-phishing-attacks-more-dangerous
[21] Endert J. Generative AI is the ultimate disinformation amplifier. 2024, https://akademie.dw.com/en/generative-ai-is-the-ultimate-disinformation-amplifier/a-68593890
[22] Marvin F, Altay S, Hugo Mercier H. Misinformation reloaded? Fears about the impact of generative AI on misinformation are overblown, Harvard Kennedy School Misinformation Review. 2023 October;4(5):1-11, doi:10.37016/mr-2020-127
[23] Ryan-Mosley T. How generative AI is boosting the spread of disinformation and propaganda. 2024, https://www.technologyreview.com/2023/10/04/1080801/generative-ai-boosting-disinformation-and-propaganda-freedom-house/
[24] Brewer PR, Cuddy L, Dawson W. et al. Artists or art thieves? Media use, media messages, and public opinion about artificial intelligence image generators. AI & Soc. 2024, https://doi.org/10.1007/s00146-023-01854-3
[25] Hoffman B. The Hidden Mental Manipulation of Generative AI. 2023, https://www.psychologytoday.com/intl/blog/motivate/202307/the-hidden-mental-manipulation-of-generative-ai
[26] Klenk M. Ethics of generative AI and manipulation: a design-oriented research agenda. Ethics Inf Technol. 2024:26(9). https://doi.org/10.1007/s10676-024-09745-x
[27] Tarsney C. Deception and Manipulation in Generative AI. 2024, https://arxiv.org/html/2401.11335v1
[28] Bradshaw C. Generative AI vs Responsible AI – An Ethical Balancing Act. 2024, https://infinum.com/blog/generative-ai-vs-responsible-ai/
[29] Microsoft. Fundamentals of Responsible Generative AI. 2024, https://learn.microsoft.com/en-us/training/modules/responsible-generative-ai/
[30] Wren H. What is AI transparency? A comprehensive guide. 2024, https://www.zendesk.com/blog/ai-transparency/
[31] Tang A., Li K-K, Kwok KO, Cao L, Luong S, Tam W. The importance of transparency: Declaring the use of generative artificial intelligence (AI) in academic writing. Journal of Nursing Scholarship. 2024;56:314–318. https://doi.org/10.1111/jnu.12938
[32] Bright Apps, Building Trust and Transparency in Generative AI Applications. 2024, https://brightappsllc.com/building-trust-and-transparency-in-generative-ai-applications/
[33] Ferrara E. Fairness and Bias in Artificial Intelligence: A Brief Survey of Sources, Impacts, and Mitigation Strategies. Sci. 2024;6(1):3 doi:10.3390/sci6010003
[34] Zharovskikh A. Bias in Generative AI: Types, examples, solutions. 2024, https://indatalabs.com/blog/generative-ai-bias
[35] IBM, Shedding light on AI bias with real world examples. 2023, https://www.ibm.com/think/topics/shedding-light-on-ai-bias-with-real-world-examples
[36] Salazar LR, Peeples S, Brooks EM. Generative AI Ethical Considerations and Discriminatory Biases on Diverse Students within the Classroom. In book: The Role of Generative AI in the Communication Classroom. 2024, doi: 10.4018/979-8-3693-0831-8.ch010
[37] Gold J. UNESCO finds 'pervasive' gender bias in generative AI tools. 2024, https://www.cio.com/article/1312311/unesco-finds-pervasive-gender-bias-in-generative-ai-tools.html
[38] EvalueServe. Generative AI in Lending: Potential and Limitations. 2024, https://www.evalueserve.com/blog/generative-ai-in-lending-potential-and-limitations/
[39] LeewayHertz. AI in lending: Use cases, benefits and implementation. 2024, https://www.leewayhertz.com/ai-in-lending/
[40] Deloitte. Generative AI - A guide for corporate legal departments. 2023, https://www.deloitte.com/content/dam/assets-shared/docs/services/legal/2023/dttl-legal-generative-ai-guide-jun23.pdf
[41] Lee S. Generative AI for Organizational Behavior: Use Cases of Generative AI in Talent Recruitment. Carnegie Mellon University, 2023, https://www.cmu.edu/intelligentbusiness/expertise/gen-ai-in-hiring_lee_100323.pdf
[42] Metzemaekers M. 6 Top Use Cases of Generative AI in Recruitment in 2024. 2024, https://www.carv.com/blog/top-use-cases-of-generative-ai-in-recruitment
[43] Wyman O. The Risks Of Generative AI To Business And Government. 2024, https://www.oliverwymanforum.com/global-consumer-sentiment/how-will-ai-affect-global-economics/risk.html
[44] Leitner G, Singh J, Kraaij A, Zsámbok B. The rise of artificial intelligence: benefits and risks for financial stability. 2024, https://www.ecb.europa.eu/press/financial-stability-publications/fsr/special/html/ecb.fsrart202405_02~58c3ce5246.en.html

[45] Chang V, Draper L, Yu S. Generative AI Risk Management in Digital Economy. Proceedings of the 6th International Conference on Finance, Economics, Management and IT Business (FEMIB 2024), 2024, Scitepress, p. 120-27, https://www.scitepress.org/Papers/2024/127298/127298.pdf
[46] Marr B. 12 New Jobs for the Generative AI Era. 2024, https://www.linkedin.com/pulse/12-new-jobs-generative-ai-era-bernard-marr-z7bge/
[47] Hendawy M. The intensified digital divide: Comprehending GenAI. 2024, https://policyreview.info/articles/news/intensified-digital-divide-comprehending-genai/1772
[48] Capraro V. et al. The impact of generative artificial intelligence on socioeconomic inequalities and policy making. PNAS Nexus. 2024 June;3(6), pgae191, https://doi.org/10.1093/pnasnexus/pgae191
[49] Wilmers N. Generative AI and the Future of Inequality. 2024, https://mit-genai.pubpub.org/pub/24gsgdjx/release/1
[50] Noy S, Zhang W. Experimental Evidence on the Productivity Effects of Generative Artificial Intelligence. MIT, 2023, https://economics.mit.edu/sites/default/files/inline-files/Noy_Zhang_1.pdf /
[51] Kaczmarski K. et al. The Generative AI Tipping Point Global wealth and asset management 2023 report. 2023, https://www.oliverwyman.com/our-expertise/insights/2023/oct/morgan-stanley-oliver-wyman-wealth-asset-management-2023-gen-ai.html
[52] McKinsey. The economic potential of generative AI - The next productivity frontier. 2023, http://dln.jaipuria.ac.in:8080/jspui/bitstream/123456789/14313/1/The-economic-potential-of-generative-ai-the-next-productivity-frontier.pdf
[53] Kellerhals T. What's the risk of not having a clean AI Governance in place?, 2024, https://kpmg.com/ch/en/insights/technology/artificial-intelligence-governance-risk.html
[54] CentralEyes. Generative AI Governance. 2024, https://www.centraleyes.com/generative-ai-governance/
[55] Reschke M. Everything We Know about Generative AI Regulation in 2024. 2024, https://basis.com/blog/everything-we-know-about-generative-ai-regulation-in-2024
[56] Bendersky A. Generative AI Regulations – What They Could Mean For Your Business. 2024, https://www.salesforce.com/blog/generative-ai-regulations/
[57] ICAEW. Legal considerations of generative AI. 2024, https://www.icaew.com/technical/technology/artificial-intelligence/generative-ai-guide/legal-considerations
[58] HLB. Navigating the legal and regulatory complexities of generative AI: A guide for business compliance. 2024, https://www.hlb.global/navigating-the-legal-and-regulatory-complexities-of-generative-ai-a-guide-for-business-compliance/
[59] Chesterman S. Good models borrow, great models steal: intellectual property rights and generative AI. Policy and Society. 2024 February;puae006, doi:10.1093/polsoc/puae006
[60] European Innovation Council and SMEs Executive Agency. Artificial intelligence and copyright: use of generative AI tools to develop new content. 2024, https://intellectual-property-helpdesk.ec.europa.eu/news-events/news/artificial-intelligence-and-copyright-use-generative-ai-tools-develop-new-content-2024-07-16-0_en
[61] Leong B, Chuks-Okeke E, Natalie Linero N. Generative AI and intellectual property: Copyright implications for AI inputs, outputs. 2024, https://www.luminos.law/blog/generative-ai-and-intellectual-property-copyright-implications-for-ai-inputs-outputs
[62] Romeyko O. How to Train Your Own Generative AI Model?. Full Manual, 2023, https://agentestudio.com/blog/train-generative-ai-models
[63] Saroff D. Strategies to combat GenAI implementation risks. 2024, https://www.cio.com/article/2515536/strategies-to-combat-genai-implementation-risks.html
[64] Gorcenski E. GenAI practical governance: How to reduce information security risk. 2024, https://www.thoughtworks.com/insights/blog/generative-ai/how-to-reduce-information-security-risk
[65] Bevan O. et al. Implementing generative AI with speed and safety. 2024, https://www.mckinsey.com/capabilities/risk-and-resilience/our-insights/implementing-generative-ai-with-speed-and-safety
[66] Auxiliobits. What Are The Risks Associated With Generative AI? How To Mitigate Them?. 2024, https://www.linkedin.com/pulse/what-risks-associated-generative-ai-how-mitigate-them-auxiliobits-d9oie/
[67] Kasi M. Top 5 risks related to Generative AI and how to mitigate each of them. 2023, https://www.linkedin.com/pulse/top-5-risks-related-generative-ai-how-mitigate-each-them-murali-kasi-pquje/

Fuzzy Systems and Data Mining X
A.J. Tallón-Ballesteros (Ed.)

doi:10.3233/FAIA241464

LLM-AS: A Self-Improve LLM Reasoning Framework Integrated with A* Heuristics Algorithm

Xueqi MENG [a], Kun NIU [a,1] and Xiao CHEN [a]
[a] *School of Computer Science, Beijing University of Posts and Telecommunications, China*
ORCiD ID: Xueqi Meng https://orcid.org/0009-0006-1003-3684, Kun Niu https://orcid.org/0000-0003-1877-5982, Xiao Chen https://orcid.org/0009-0008-2181-0084

Abstract. To address the limitations of flexibility or efficiency of existing prompting paradigms in generating intermediate reasoning steps, this paper proposes an reasoning framework LLM-AS, which innovatively combines the A* search algorithm with the reasoning process of large language models(LLMs). LLM-AS utilizes the efficient exploration capability of the A* algorithm and avoids the redundant exploration of high-cost nodes, which significantly improves the search efficiency and reduces the cost of invoking LLM. Meanwhile, through the self-improve mechanism of LLMs, LLM-AS ensures the quality of the generated solutions while minimizing model interactions. In addition, the flexibility of the A* search algorithm enables LLM-AS to be applicable to diverse thought organization structures, providing more possibilities for handling various tasks. We conducted experiments on two complex tasks, game 24 and 8 puzzle, to compare the accuracy of the existing prompting paradigms and LLM-AS on both gpt-3.5-turbo and gpt-4.0. The experimental results show that LLM-AS effectively improves the ability of LLMs to solve complex tasks.

Keywords. large language models, A* search algorithm, reasoning and planning

1. Introduction

Recent advances in large language models (LLMs) have opened up more possibilities for solving different types of problems in natural language processing [1–6]. Standard I/O prompts work for simple, single-step problems. CoT [7] and CoT-SC [8] improve performance by generating intermediate steps but are limited to linear thought. ToT [9] organizes thoughts in a tree structure, improving performance on complex tasks but increasing invocation costs. The question arises: is it possible to reduce the cost of invocation while guaranteeing the performance of LLMs in solving complex problems?

We propose LLM-AS, a reasoning framework for complex tasks that combines A* search [10] with LLM reasoning. It enhances exploration efficiency by avoiding high-

[1]Corresponding Author: Kun Niu, niukun@bupt.edu.cn.

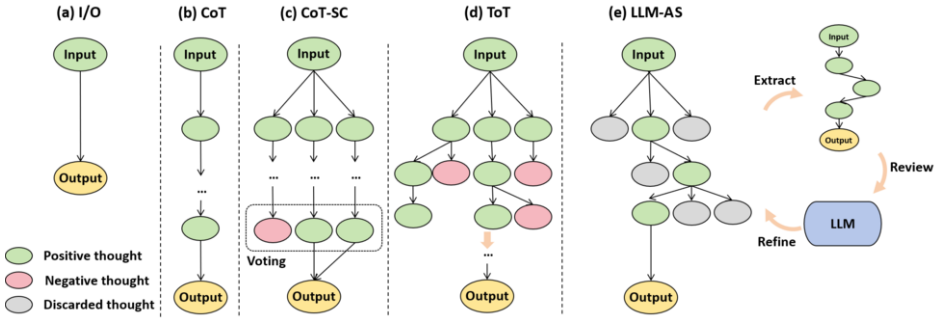

Figure 1. Comparison of our LLM-AS with other prompting paradigms.

cost nodes and exploring towards the target, reducing LLM invocation costs while improving efficiency.

To minimize A* search risks, we use LLMs for self-review and correction. The self-improve module optimizes solutions iteratively, enhancing quality of the generated solutions while minimizing LLM interactions.

Incorporating the A* search algorithm offers flexibility as it can explore various thought structures and allows intelligent heuristic design, adapting the reasoning framework to more task types.

We conducted experiments with LLM-AS using gpt-3.5-turbo [11] and gpt-4.0 [12] on two complex real-world tasks, Game 24 and 8 Puzzle, which shows that our LLM-AS exhibits superior performance. It is an effective thoughts generation method and provides new insights for solving complex problems with LLMs.

Our main contributions are as follows:

- We propose a new planning and reasoning algorithm by combining LLMs and A* search, optimizing components for enhanced LLM reasoning.
- We propose a self-improve module to balance LLM invocation cost and solution accuracy by iteratively optimizing solutions from a reasoning process integrating A* search.
- We experimentally prove our reasoning algorithm's effectiveness on complex tasks, improving LLM performance for solving complex problems.

2. Background

2.1. Reasoning for LLMs

Prompts can enhance LLMs' reasoning by guiding them to break down complex problems into intermediate steps, mimicking human thinking [13, 14]. Each step's outcome can be organized in various structures [7, 9, 15–17], like linear chains or hierarchical trees (Fig. 1), related to the reasoning approach.

Input-Output (IO) Prompting. The I/O method is the simplest way to utilize LLMs for task resolution. It only requires defining the task and problem as a prompt input to the model, with the model's output representing the solution.

Chain-of-Thought [7]. The CoT method leverages the context-learning abilities of LLMs by breaking a problem into multiple intermediate steps. It provides the model with a prompt in the form of a triplet ¡input, intermediate steps, output¿, thereby guiding the model through the problem-solving process.

Self-consistency CoT (CoT-SC) [8]. The CoT-SC method samples different reasoning processes to generate multiple solutions for a given problem and selects the most consistent answer as the final solution from the model.

Tree-of-Thought (ToT) [9]. The ToT method organizes the thought nodes for problem-solving in a tree structure. ToT allows for backtracking and foresight when necessary to explore globally optimal solutions.

2.2. *A* Search Algorithm*

The A* search algorithm (1968) [10] is an efficient heuristic method using an evaluation function $f(n) = g(n) + h(n)$, where $g(n)$ is the actual cost to the current node and $h(n)$ estimates the cost to the target. This prioritizes exploring paths closer to the goal, reducing unnecessary search space exploration and enhancing efficiency.

$$f(x) = g(x) + h(x) \tag{1}$$

The A* algorithm is often used to solve path planning problems. Currently, there are also efforts to apply LLMs to the traditional A* algorithm to address computational and memory efficiency issues in path planning. [18]

2.3. *LLMs self-improve*

When dealing with complex and tedious tasks, human beings often complete a simple initial solution and then gradually make adjustments and refinements based on it. LLMs can also improve the accuracy of their solutions by simulating such a way of thinking and conducting self-reflection [19, 20]. The self-reflection capability of LLMs refers to the ability of the model to review, evaluate and improve its own output after generating it. This capability of LLMs not only further improves the quality of generation and factual accuracy, but also maintains the original creativity of LLMs [21–23]. This ability is often applied to improve the decision-making ability of agents [24]. And, some methods that can enhance the ability of LLMs to perform self-reflection are also currently proposed [25] and can also be used as our future work to optimize the components in our framework.

3. Methodology

We propose an inference strategy combining LLMs with the A* search to enhance LLMs' reasoning on complex problems, as shown in Fig. 2. In the following, we introduce its components and workflow.

Initialization. In initialization, we define states (S), the set of executable actions (A), and the state transfer function (δ: $S \times A \rightarrow S$). The initial state (s_0) is added to the open list for unexplored nodes, while the closed list for accessed nodes is initialized as empty.

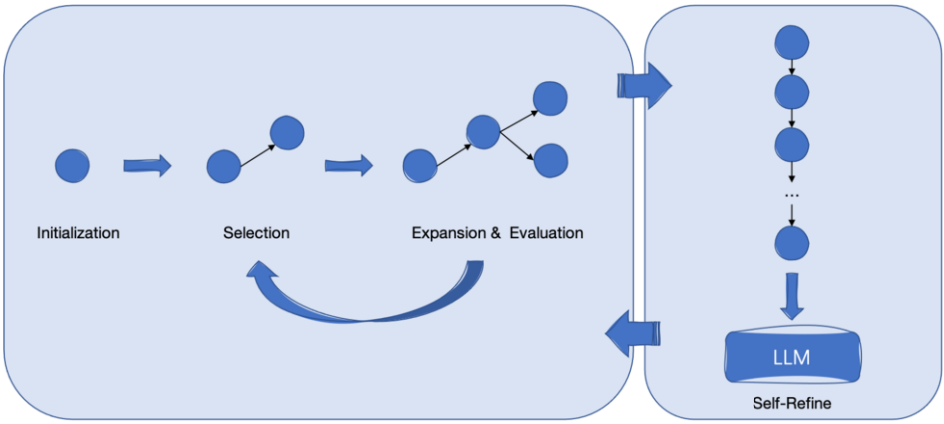

Figure 2. The components and workflow of our LLM-AS framework.

Selection. The node with the lowest cost $f(s) = g(s) + h(s)$ in the open list is chosen, moved to the closed list. $g(s)$ is the actual cost from the initial state to the current state. $h(s)$ estimates the cost to the goal (lower means closer).

Expansion and Evaluation. Successor states are extended based on action spaces and checked against the closed list to avoid loops. Their $g(s)$ and $h(s)$ values are updated based on the state transition costs. An accurate $h(s)$ optimizes A* search performance. For tasks which determining the heuristic function is challenging, we use LLMs to compute $h(s)$ using their internal knowledge.

Termination Conditions. The iterative process of selection, expansion, and evaluation continues until termination condition T is met, improving answers and exploring new possibilities. T can be set as follows:

- Reaching the goal state: For tasks with a clearly defined goal, this condition directly triggers the end of the search when the search reaches a preset goal state.
- Search constraints: To control computational resource consumption, limits on search depth or the number of nodes visited can be set.

Review and Correction. After generating a solution through the reasoning process of LLMs integrated with the A* search algorithm, the self-improve module is invoked. Initially, the path of thoughts is organized into structured input prompts according to task execution steps, converting it into a text format understandable by the LLM. converted into a text format understandable by the large model. Subsequently, the LLM conducts a thorough review of the generated solution to identify potential logical errors or inconsistencies [21–23]. Based on the prompts, if no errors are identified, the solution is deemed final. Otherwise, the LLM outputs the steps where errors occur. Based on the feedback from the model, iterative corrections are made to the preceding reasoning process to continuously optimize the solution's quality. Starting from the step where an error is identified, subsequent steps are regenerated. This module exemplifies the complementary advantages of the LLM's self-improve capabilities and the reasoning integrated with the A* search algorithm, jointly driving the effective and efficient resolution of complex problems.

Table 1. An overview of definitions for tasks

	game 24	**8 puzzle**
Thought	intermediate equations	swap and the puzzle state after the move
State	the remaining 1-4 numbers	the number layout in the grid
Action	picking two number and a operation to compose an equation	swap blank square with one of its neighboring numbered squares
initial state	four numbers that can be used to form a mathematical expression	a grid with 8 number squares and 1 blank square
goal state	the result of the math of the expression composed with the remaining numbers is 24	The numbers are arranged in the order of 1-8 from the top left to the bottom right, with the blank square at the bottom right corner

4. Experiment

We evaluated the effectiveness of the LLM-AS approach on two challenging tasks: game 24 and 8 puzzle. These tasks require multiple steps to complete. The high complexity and difficulty of these tasks pose significant demands on the reasoning capabilities of LLMs. To demonstrate the effectiveness of LLM-AS, we compared it against standard I/O, zero-shot CoT, few-shot CoT, CoT-SC, and ToT. During the experiments, we set the temperature of the invoked LLM to 0.0.

4.1. game 24

Game 24 is a mathematical reasoning task where the goal is to form an arithmetic expression using the given 4 numbers and basic operations (+, -, *, /) so that the result is 24.

4.1.1. Task Setup

Our dataset has 1362 games from 4nums.com, with 100 randomly selected for testing. The adaptability definition for the game 24 task is outlined in Table 1, where thoughts are equations and states are remaining numbers. The goal is for the equation to result in 24. We used the success rate across 100 games as the evaluation metric.

4.1.2. Baseline & LLM-AS Setup

We provide five examples for the standard I/O prompt. For few-shot CoT, we use intermediate equations. For CoT-SC, we sample 10 times and voted for the most consistent result. For ToT, the model generate and evaluate next steps. We explore candidate set widths b=1 and b=3 for comparison. For LLM-AS, the LLM generate and evaluate states. Five examples are given for evaluation. After A* search, the LLM review and correct the solution using five refine examples. In the refine prompt, each time a number is selected, it is regarded as a step and labeled sequentially to allow the LLM to identify the specific step where the error occurs.

4.1.3. Results

Table 2 shows each method's performance on game 24 with gpt-3.5-turbo and gpt-4.0. LLM-AS consistently outperforms baselines, with improved accuracy to 21.56% on gpt-3.5-turbo and 65.32% on gpt-4.0 after one correction. This highlights LLM-AS's superiority in complex tasks. The best baseline, ToT (b=3) on gpt-4.0, achieves 62.00% accuracy but costs more due to many LLM invocations. LLM-AS improves accuracy while reducing explorations and costs.

4.2. 8 puzzle

8 puzzle is a classic puzzle game. The game panel is a 3x3 grid with a number (1-8) or a blank square (represented by 0) on each small square. The goal of the game is to arrange the numbers in the order 1-8 from the top left to the bottom right by exchanging the blank squares with the neighboring number squares, with the blank square in the bottom right corner.

4.2.1. Task Setup

8 Puzzle is a classic game with a 3x3 grid of numbers 1-8 and a blank (0). The goal is to arrange numbers 1-8 in order by swapping them with the blank, ending with the blank in the bottom right. We used the proportion of these 100 games reaching the goal state as our evaluation metric.

4.2.2. Baseline & LLM-AS Setup

We provide three examples for standard I/O. In few-shot CoT, we concatenate actions with the state. For CoT-SC, we sample 10 times and chose the most consistent result. ToT generate and evaluate next steps, with a max search depth of 9. We try candidate set widths b=1 and b=3. For LLM-AS, the model evaluate states using three examples, then review and correct the solution using three more examples after A* search. In the refine prompt, each swap action is numbered sequentially enabling the LLM to pinpoint the exact step where the error arises.

4.2.3. Results

The spatial complexity and long-term planning requirements of the 8 puzzle significantly challenge LLMs. Table 2 shows LLM-AS outperforms all baselines, improving to 30.63% and 39.92% on gpt-3.5-turbo and gpt-4.0 after one correction. This surpasses the best baseline, ToT (b=3), on gpt-4.0 with 15.00% accuracy. LLM-AS's integration of A* search and LLM-based evaluation effectively tackles the puzzle, showing potential for spatial reasoning and long-term planning tasks.

As observed in Table 2, both the baseline methods and our LLM-AS exhibit superior performance on gpt-4.0 compared to gpt-3.5-turbo. gpt-4.0 boasts a larger model size and a more extensive and diverse training dataset than gpt-3.5-turbo. Furthermore, gpt-4.0 ingeniously leverages Graph Neural Networks, enabling the model to better capture the temporal information and dependencies in language. We attribute these factors to the performance disparity between gpt-3.5-turbo and gpt-4.0, resulting in gpt-4.0's outstanding performance in handling the two complex tasks.

Table 2. Experimental results on game 24 and 8 puzzle tasks

	game 24		8puzzle	
	gpt-3.5-turbo	gpt-4.0	gpt-3.5-turbo	gpt-4.0
I/O	5.98	8.90	0.00	1.34
zero-shot CoT	5.98	8.92	0.00	1.92
few-shot CoT	3.18	4.05	0.00	5.04
CoT-SC	3.20	4.38	3.78	6.94
ToT(b=1)	8.02	40.13	7.86	8.01
ToT(b=3)	15.71	62.00	13.26	15.00
LLM-AS	21.56	65.32	30.63	39.92

5. Conclusion

This paper shows LLM-AS enhances LLMs' reasoning for complex tasks by integrating A* search and utilizing the LLMs for review and correction, improving accuracy and reliability. A* search prioritizes goal-directed paths, reducing high-cost exploration, significantly enhancing efficiency and lowering LLM invocation costs. Experiments on two tasks show LLM-AS outperforms existing prompt paradigms.

This research advances the application of LLMs in complex tasks, laying a foundation for enhancing their planning and decision-making capabilities in agents [26,27]. For future work, we will conduct more experiments to explore the capability of LLM-AS in exploring more diverse thought topologies, such as graph structures. And apply it to a wider range of real-world problems.

References

[1] T. Brown, B. Mann, N. Ryder, M. Subbiah, J. D. Kaplan, P. Dhariwal, A. Neelakantan, P. Shyam, G. Sastry, A. Askell *et al.*, "Language models are few-shot learners," *Advances in neural information processing systems*, vol. 33, pp. 1877–1901, 2020, https://doi.org/10.48550/arXiv.2005.14165.

[2] A. Radford, K. Narasimhan, T. Salimans, I. Sutskever *et al.*, "Improving language understanding by generative pre-training," 2018.

[3] A. Radford, J. Wu, R. Child, D. Luan, D. Amodei, I. Sutskever *et al.*, "Language models are unsupervised multitask learners," *OpenAI blog*, vol. 1, no. 8, p. 9, 2019.

[4] R. Omar, O. Mangukiya, P. Kalnis, and E. Mansour, "Chatgpt versus traditional question answering for knowledge graphs: Current status and future directions towards knowledge graph chatbots," *arXiv preprint arXiv:2302.06466*, 2023, https://doi.org/10.48550/arXiv.2302.06466.

[5] S. Frieder, L. Pinchetti, R.-R. Griffiths, T. Salvatori, T. Lukasiewicz, P. Petersen, and J. Berner, "Mathematical capabilities of chatgpt," *Advances in neural information processing systems*, vol. 36, 2024, https://doi.org/10.48550/arXiv.2301.13867.

[6] G. Kim, P. Baldi, and S. McAleer, "Language models can solve computer tasks," *Advances in Neural Information Processing Systems*, vol. 36, 2024, https://doi.org/10.48550/arXiv.2303.17491.

[7] J. Wei, X. Wang, D. Schuurmans, M. Bosma, F. Xia, E. Chi, Q. V. Le, D. Zhou *et al.*, "Chain-of-thought prompting elicits reasoning in large language models," *Advances in neural information processing systems*, vol. 35, pp. 24 824–24 837, 2022, https://doi.org/10.48550/arXiv.2201.11903.

[8] X. Wang, J. Wei, D. Schuurmans, Q. Le, E. Chi, S. Narang, A. Chowdhery, and D. Zhou, "Self-consistency improves chain of thought reasoning in language models," *arXiv preprint arXiv:2203.11171*, 2022, https://doi.org/10.48550/arXiv.2203.11171.

[9] S. Yao, D. Yu, J. Zhao, I. Shafran, T. Griffiths, Y. Cao, and K. Narasimhan, "Tree of thoughts: Deliberate problem solving with large language models," *Advances in Neural Information Processing Systems*, vol. 36, 2024, https://doi.org/10.48550/arXiv.2305.10601.

[10] P. E. Hart, N. J. Nilsson, and B. Raphael, "A formal basis for the heuristic determination of minimum cost paths," *IEEE transactions on Systems Science and Cybernetics*, vol. 4, no. 2, pp. 100–107, 1968, 10.1109/TSSC.1968.300136.

[11] L. Ouyang, J. Wu, X. Jiang, D. Almeida, C. Wainwright, P. Mishkin, C. Zhang, S. Agarwal, K. Slama, A. Ray *et al.*, "Training language models to follow instructions with human feedback," *Advances in neural information processing systems*, vol. 35, pp. 27 730–27 744, 2022, https://doi.org/10.48550/arXiv.2203.02155.

[12] J. Achiam, S. Adler, S. Agarwal, L. Ahmad, I. Akkaya, F. L. Aleman, D. Almeida, J. Altenschmidt, S. Altman, S. Anadkat *et al.*, "Gpt-4 technical report," *arXiv preprint arXiv:2303.08774*, 2023.

[13] A. Newell, J. C. Shaw, and H. A. Simon, "Report on a general problem solving program," in *IFIP congress*, vol. 256. Pittsburgh, PA, 1959, p. 64.

[14] H. A. Simon and A. Newell, "Human problem solving: The state of the theory in 1970." *American psychologist*, vol. 26, no. 2, p. 145, 1971, https://doi.org/10.1037/h0030806.

[15] D. Zhou, N. Schärli, L. Hou, J. Wei, N. Scales, X. Wang, D. Schuurmans, C. Cui, O. Bousquet, Q. Le *et al.*, "Least-to-most prompting enables complex reasoning in large language models," *arXiv preprint arXiv:2205.10625*, 2022, https://doi.org/10.48550/arXiv.2205.10625.

[16] A. Creswell and M. Shanahan, "Faithful reasoning using large language models," *arXiv preprint arXiv:2208.14271*, 2022, https://doi.org/10.48550/arXiv.2208.14271.

[17] M. Besta, N. Blach, A. Kubicek, R. Gerstenberger, M. Podstawski, L. Gianinazzi, J. Gajda, T. Lehmann, H. Niewiadomski, P. Nyczyk *et al.*, "Graph of thoughts: Solving elaborate problems with large language models," in *Proceedings of the AAAI Conference on Artificial Intelligence*, vol. 38, no. 16, 2024, pp. 17 682–17 690, https://doi.org/10.1609/aaai.v38i16.29720.

[18] S. Meng, Y. Wang, C.-F. Yang, N. Peng, and K.-W. Chang, "Llm-a*: Large language model enhanced incremental heuristic search on path planning," 2024, https://doi.org/10.48550/arXiv.2407.02511. [Online]. Available: https://arxiv.org/abs/2407.02511

[19] W. Saunders, C. Yeh, J. Wu, S. Bills, L. Ouyang, J. Ward, and J. Leike, "Self-critiquing models for assisting human evaluators," 2022, https://doi.org/10.48550/arXiv.2206.05802. [Online]. Available: https://arxiv.org/abs/2206.05802

[20] B. Peng, M. Galley, P. He, H. Cheng, Y. Xie, Y. Hu, Q. Huang, L. Liden, Z. Yu, W. Chen, and J. Gao, "Check your facts and try again: Improving large language models with external knowledge and automated feedback," 2023, https://doi.org/10.48550/arXiv.2302.12813. [Online]. Available: https://arxiv.org/abs/2302.12813

[21] A. Madaan, N. Tandon, P. Gupta, S. Hallinan, L. Gao, S. Wiegreffe, U. Alon, N. Dziri, S. Prabhumoye, Y. Yang *et al.*, "Self-refine: Iterative refinement with self-feedback," *Advances in Neural Information Processing Systems*, vol. 36, 2024, https://doi.org/10.48550/arXiv.2303.17651.

[22] D. Paul, M. Ismayilzada, M. Peyrard, B. Borges, A. Bosselut, R. West, and B. Faltings, "Refiner: Reasoning feedback on intermediate representations," *arXiv preprint arXiv:2304.01904*, 2023, https://doi.org/10.48550/arXiv.2304.01904.

[23] Y. Xie, K. Kawaguchi, Y. Zhao, J. X. Zhao, M.-Y. Kan, J. He, and M. Xie, "Self-evaluation guided beam search for reasoning," *Advances in Neural Information Processing Systems*, vol. 36, 2024, https://doi.org/10.48550/arXiv.2305.00633.

[24] N. Shinn, F. Cassano, A. Gopinath, K. Narasimhan, and S. Yao, "Reflexion: Language agents with verbal reinforcement learning," *Advances in Neural Information Processing Systems*, vol. 36, 2024, https://doi.org/10.48550/arXiv.2303.11366.

[25] W. Zhang, Y. Shen, L. Wu, Q. Peng, J. Wang, Y. Zhuang, and W. Lu, "Self-contrast: Better reflection through inconsistent solving perspectives," *arXiv preprint arXiv:2401.02009*, 2024, https://doi.org/10.48550/arXiv.2401.02009.

[26] Z. Wang, S. Cai, G. Chen, A. Liu, X. Ma, and Y. Liang, "Describe, explain, plan and select: Interactive planning with large language models enables open-world multi-task agents," *arXiv preprint arXiv:2302.01560*, 2023, https://doi.org/10.48550/arXiv.2302.01560.

[27] I. Singh, V. Blukis, A. Mousavian, A. Goyal, D. Xu, J. Tremblay, D. Fox, J. Thomason, and A. Garg, "Progprompt: Generating situated robot task plans using large language models," in *2023 IEEE International Conference on Robotics and Automation (ICRA)*. IEEE, 2023, pp. 11 523–11 530, https://doi.org/10.48550/arXiv.2209.11302.

Fuzzy Systems and Data Mining X
A.J. Tallón-Ballesteros (Ed.)

doi:10.3233/FAIA241465

Artificial Intelligence Assisted English Learning Based on Large Language Model

Jianghui Liu[a,1], Yu Sun[b], Haolin Chen[c] and LiMin Zhi[d]
[a] *Center for Contemporary Education Technology, Experimental Teaching Center, Guangdong University of Foreign Studies, Guangzhou, China.*
[b] *School of English Education, Guangdong University of Foreign Studies, Guangzhou, China.*
[c] *School of Business, Guangdong University of Foreign Studies, Guangzhou, China.*
[d] *School of Finance, Guangdong University of Foreign Studies, Guangzhou, China.*

Abstract. This study focuses on the cutting-edge field of Large Language Model. Artificial Intelligence-assisted English teaching has been under-researched and conflicted with the practice of English language teaching. To better address this problem, researchers read relevant literatures, design several formulas, test, compare, and select a new and efficient Large Language Model based on the existing transformer model. This can be deeply integrated with the theories of pedagogy, psychology, and linguistics in real English teaching environments to promote the innovation of the English teaching mode. It also demonstrates how Large Language Model can be used as a powerful tool in English language teaching and learning.

Keywords. Artificial Intelligence, English language learning, Large Language Model

1. Introduction

In the current information age, education is experiencing unprecedented changes. The rise of Large Language Model (LLM) has revitalized new vitality and challenges into traditional English Language Teaching (ELT). With its powerful language processing and generative capabilities, LLM opens a broad space for innovative practices in ELT. This study focuses on this cutting-edge field, aiming to explore how LLM can be integrated with the theories of pedagogy, psychology, and linguistics in real ELT contexts to promote the innovation of ELT modes and the effective enhancement of students' learning ability [1]. As an important bridge connecting global culture and knowledge, the disciplinary characteristics of English provide a rich soil for exploring the new integration of technology and pedagogy [2]. Therefore, the core topic of this study is to reveal the application of LLM in ELT and its positive impact on learning effectiveness, aiming to construct an innovative teaching model that is in line with human-computer symbiosis and can effectively improve students' English learning ability, and promote their higher-order thinking skills. It ensures that the new English learning model based on LLM is both theoretically tenable and can be used to improve students' English learning ability [3]. Thus, it can contribute to promote ELT into a new stage of intelligence and personalization [4].

[1] Corresponding Author: Jianghui Liu, Center for Contemporary Education Technology, Experimental Teaching Center, Guangdong University of Foreign Studies, China; Email: 247031690@qq.com.
This study is financially supported by the Undergraduate Innovation Training Project of Guangdong University of Foreign Studies in 2024.

2. Related Works

In terms of English learning and natural language processing, some researchers have emphasized the central role of deep learning methods in cultivating students' English skills, especially in enhancing their ability to respond flexibly in complex situations [5]. Meanwhile, LLM-driven chatbots have been proven to be powerful aids for foreign language learning, with applications such as Teacher Bot, Andy English Bot, and Duolingo's chatbots demonstrating the potential for real-time interactive learning [6]. Related research aims to improve the quality of ELT and students' learning effectiveness through the optimization of learning paths and the deep integration of LLM. Some researchers have verified the effectiveness of the flipped classroom model in creative collaborative teaching through the "Critique.com" platform, and constructed a new paradigm of student-centered speaking teaching based on the characteristics of educational robots [7], which shows the application of LLM in ELT and its innovative integration. The research on the application of LLM in ELT shows the trend of transformation from technology exploration to ELT practice, which constantly promotes the innovation of ELT mode and the improvement of learning effectiveness [8].

3. Framework for a Foreign Language Learning System Based on LLM

The framework of the LLM-based Foreign Language Learning System for College Students integrates the LLM technology with English education, and adopts the perspective of "technology-society-education" to examine the advancement of AI technology and the development of society. It also discusses how LLM can assist in these three focus areas of pedagogical change, personalized learning, and educational ecological reshaping. The relationship is shown in Figure 1.

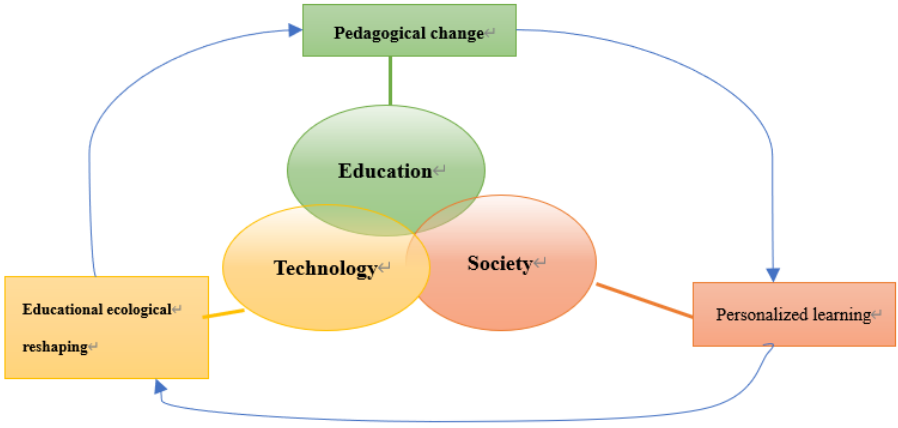

Figure 1. Study on Artificial Intelligence for future education development

Firstly, LLM can interact and conduct dialogic teaching to enhance the interactivity of the teaching process. For online learning, LLM can act as virtual teaching assistants to provide services for learners, breaking the time and space constraints of traditional education. In addition, it can deeply understand and evaluate learners' assignments,

provide detailed and accurate feedback to help teachers precisely locate the learning difficulties and adjust teaching strategies accordingly.

Secondly, LLM makes personalized learning possible through intelligent content generation and personalized tutoring. It can automatically generate teaching materials based on a massive knowledge base to meet different learning needs. LLM also provides personalized Q&A based on learners' learning progress, comprehension level, and questions, thus realizing the vision of tailored teaching and improving the efficiency and quality of teaching.

Thirdly, the application of LLM has prompted education to further examine the relationship between teaching and learning, and emphasize learner-centeredness, focusing on the cultivation of self-directed learning ability. Thus, it promotes the transformation from traditional one-way indoctrination to a new model of guided inquiry, collaboration, and co-creation.

The core technology of LLM includes deep learning, data analysis, natural language processing, language generation, etc. Therefore, its application in education and ELT is presented in various forms, such as intelligent tutor system, adaptive learning system, automated assessment system and chatbot, etc., as shown in Figure 2.

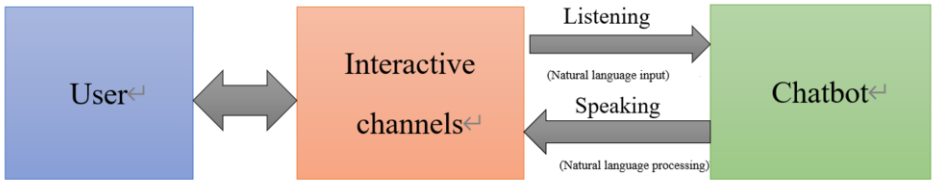

Figure 2. Large Language Model in education and teaching (using chatbots as an example)

4. English Learning Dialogue System Based on LLM

LLM shows advantages in assisting ELT. However, existing English learning dialogue system needs to improve the accuracy and personalization level and requires more corpus. To improve the model efficiency without decreasing the accuracy and meet the dialogue demand, the traditional large language dialogue model needs to be improved and optimized.

This dialog system is based on the Transformer model. It encodes the input text, computes, and outputs after comparing with the pre-training results of the corpus [4]. The language model of GPT (decoder structure only) improved from Transformer is used in this study. Firstly, the encoded input vocabulary enters a multi-layer decoder structured as a multi-head autoregressive operation with normalization, followed by a KAN network with normalization. The text is learned in the stack of multiple decoders with normalization performed. By unsupervised labeling of the corpus, the input is used to predict the next sentence and generate the output. The training process generally consists of two parts, i.e., model pre-training and fine-tuning, which are distinguished as follows: pre-training is the unsupervised training of the model relying on an existing corpus, while fine-tuning is the use of supervised data from the target task to further optimize the model generated in stage 1 to obtain a more efficient model as well as more accurate results.

The whole process of GPT language model can be summarized as follow.

$$L_1(U) = \sum_i log\ P(u_i|u_{i-k}, \dots, u_{i-1}; \Theta) \quad (1)$$

$$h_0 = UW_e + W_p \quad (2)$$

$$h_l = transformer\_block(h_{l-1}) \forall i \in [1, n] \quad (3)$$

$$P(u) = softmax(h_n W_e^T) \quad (4)$$

U= (u-k, ..., u-1) is the context vector of the participle. K denotes the size of the context window, and P represents the conditional probability based on a neural network modeled with parameters Θ. The parameters are trained using stochastic gradient descent. n is the number of layers. W_e is the participle embedding matrix, and W_p is the positional embedding matrix.

4.1 KAN layer

KAN module is used to replace the traditional Feed Forward Networks (FFN) module which used the Multilayer Perceptron (MLP), a widely used layer in the field of machine learning because of its simple structure, wide applicability, and implementation in various programming languages and frameworks. [9] However, MLP modules have the following problems: Firstly, MLP may have the derivative of the activation function multiplied together with the product. When it is too large or too small, and the structure is relatively deep, MLP will be the multiplicative product making the gradient converge to 0 (gradient vanishing) or become abnormally large (gradient explosion), thus hindering the learning process problem. Secondly, MLP usually uses fully connected layers. The neurons are connected to the previous layer, leading to a rapid increase in the number of parameters, especially for data with high input dimensions (e.g. image data). This increases both the computational burden and the risk of model overfitting. Thirdly, MLP does not utilize the intrinsic structure of the data when dealing with sequence information. Fourthly, MLP lacks capturing long-term dependencies in input sequences, particularly when dealing with natural language tasks.

Kolmogorov-Arnold Networks are based on the Kolmogorov-Arnold Representation Theorem, which was proposed by two Russian mathematicians in 1957. The formula is given below.

$$f(\mathbf{x}) = f(x_1, \cdots, x_n) = \sum_{q=1}^{2n+1} \Phi_q \left(\sum_{p=1}^{n} \phi_{q,p}(x_p) \right), \quad (5)$$

x is the input and $\phi_{q,p}(x_p)$ is the basic unitary function, and the inner summation is followed by the outer functions ϕ_q each of which receives the result of the inner summation. The outer summation $\sum$ indicates that the whole function f(x) is a sum of subfunctions ϕ_q.

The KAN structure is equivalent to a two-layer neural network with the following differences. Firstly, the inputs are directly activated; Secondly, the activation function can be learned. This study uses the B-spline activation function for the computation. This is equivalent to performing nonlinear transformations on each axis individually, which are combined to form the multidimensional space.

The KAN layer is represented by the following formula.

$$\mathbf{\Phi} = \{\phi_{q,p}\}, p = 1,2, \cdots, n_{\text{in}}, q = 1,2 \cdots, n_{\text{out}}, \quad (6)$$

The first two layers of the KAN network have n inputs and 2n+1 outputs in the first layer, with 2n+1 inputs and 1 final output in the second layer. The matrix is shown in the following formulas.

$$\mathbf{x}_{l+1} = \underbrace{\begin{pmatrix} \phi_{l,1,1}(\cdot) & \phi_{l,1,2}(\cdot) & \cdots & \phi_{l,1,n_l}(\cdot) \\ \phi_{l,2,1}(\cdot) & \phi_{l,2,2}(\cdot) & \cdots & \phi_{l,2,n_l}(\cdot) \\ \vdots & \vdots & & \vdots \\ \phi_{l,n_{l+1},1}(\cdot) & \phi_{l,n_{l+1},2}(\cdot) & \cdots & \phi_{l,n_{l+1},n_l}(\cdot) \end{pmatrix}}_{\Phi_l} \mathbf{x}_l, \tag{7}$$

l is the number. $\phi_{l,i,j}$ is the activation function on each edge. i is used to label the nodes of the current layer, and ϕ is used to label the nodes of the next layer. The output of each nodex_l, i is processed by the activation function $\phi_{\_l,i,j}$, and will be contributed to the computation of $x\_l + 1, j$ of so the next layer.

The matrix representation of the KAN multilayer function cascade relation is as follows.

$$\mathrm{KAN}(\mathbf{x}) = (\mathbf{\Phi}_{L-1} \circ \mathbf{\Phi}_{L-2} \circ \cdots \circ \mathbf{\Phi}_1 \circ \mathbf{\Phi}_0)\mathbf{x}. \tag{8}$$

or its expanded form.

$$f(\mathbf{x}) = \sum_{i_{L-1}=1}^{n_{L-1}} \phi_{L-1,i_L,i_{L-1}} \left(\sum_{i_{L-2}=1}^{n_{L-2}} \cdots \left(\sum_{i_2=1}^{n_2} \phi_{2,i_3,i_2} \left(\sum_{i_1=1}^{n_1} \phi_{1,i_2,i_1} \left(\sum_{i_0=1}^{n_0} \phi_{0,i_1,i_0}(x_{i_0}) \right) \right) \right) \cdots \right) \tag{9}$$

It should be added that this study uses the residual activation function in this module, which contains a basis function b(x). The activation function ϕ(x) is the sum of the basis function b(x) and the spline function spline, as shown below.

$$\phi(x) = w(b(x) + \mathrm{spline}(x)). \tag{10}$$

We therefore set up the following equation.

$$b(x) = \mathrm{silu}(x) = x/(1 + e^{-x}) \tag{11}$$

Spline functions are usually parameterized as linear combinations of B-splines.

$$\mathrm{spline}(x) = \sum_i c_i B_i(x) \tag{12}$$

c_i is trainable.

In this study, the multi-head attention operation is improved to a Kolmogorov-Arnold network as an alternative to the multilayer perceptron (MLP). This allows the present model to achieve better fitting results using a smaller number of parameters, also improving the training efficiency of the model and reducing the arithmetic power consumption. The ability to nonlinearly transform the input data is achieved through the KAN module. This transformation is the key for deep learning models to capture complex features. Complex mathematical transformations on the input data allows the model to learn richer representations. The self-attention mechanism generates a weighted sequence of word representations by calculating the scores between the words in the input sequence. The role of KAN is to integrate these independent representations at a deeper level, so that each word representation not only contains information about the surrounding words, but also incorporates global information about the entire input sequence. In this way, the module significantly enhances the model's ability to utilize contextual information, helping to improve the performance of downstream tasks.

4.2 Predicting output

After the above steps, the input word vectors are normalized by the fully connected layer and SoftMax function to get the relevant data in the corpus. This makes the model receive text inputs of any length, automatically predict the next word, and generates sentences or articles. After pre-training, the model can be optimized with the following operation strategies: provide the model with vocabulary, use interactive conditional prompts to

guide its learning, and generate samples, so that the model can generate, test, and tune simultaneously. It can also let the model work randomly to generate samples unconditionally and manually proofread and tune afterwards. For example, the English sentence *where there is a will, there is a way*. The model first automatically breaks down the sentence into basic words such as "where", "there", "is", "a", "way", etc. The word embedding module converts each word into a word vector that can be recognized and computed by the machine. These word vectors are then introduced to the decoder for processing, which usually goes through several layers of mathematical operations by the decoder mentioned above. In the case of the word "there", the output of the model (the single word "is") is used as the input for the next moment, thus optimizing the language model. After the decoder receives the encoding matrix of the above content, it will start from translating the "start cue '<BOS>'" and follow the above steps to predict and generate the subsequent words step by step. The following formulas represents the conditional probability p (wi|w1, w2, ..., wi-1) for the set of words (w1, w2, …, wi-1) after word separation.

$$p(w_i|w_1, w_2, \ldots, w_{i-1}) = 0\text{utput}_{GPT2}(w_1, w_2, \ldots, w_{i-1}) \quad (13)$$

5. Experimental Results

The large dataset used to train the model in this study includes the following three open-source chat corpora: Chatterbot conversation dataset, qingyun conversation dataset, and Chinese Multi-Round Chat Corpus.

ROUGE (Recall-Oriented Understudy for Gisting Evaluation) evaluates the quality of generated summaries by comparing automatically machine-generated summaries with real summaries and calculating the number of overlaps in terms of word sequences, word pairs, and other units. In this study, ROUGE is used to measure the recall quality of dialog system-generated answer sentences. In general, a higher ROUGE result indicates a better model performance.

All the test results show that in terms of ROUGE metrics, the model proposed in this study is higher than the traditional seq2seq generative model, indicating that the dialog information generated by this system is richer. In terms of ROUGE third-order metrics, this model is also better than the BART model in natural language generation. It is concluded that this model performs well in multi-label classification of utterances, which further proves that this model performs well in preprocessing, and demonstrates the advancement in attention mechanism and KAN network processing.

The ideal generative model should have the function of generating responses, i.e., generating responses that are logical, varied, and diverse. To evaluate the model in terms of the diversity of responses and analyze the diversity of generated answers, this study, in addition to analyzing the ROUGE evaluation index, also counts the percentage of answers that can be generated by the model differently from the existing answers in the dataset when the pair of responses already exists in the dataset.

For different sizes of datasets, there are differences in the answer sentences given by different dialog systems with non-similar replies. The corpus knowledge during pre-training and unique sampling and decoding method of this model make it show high richness and diversity in the dialog process. Further analyzing the content of the dialog utterances generated by different models, it can be found that the dialog system applying this model generates utterances that are more natural, more emotional, and more relevant to people's normal dialog context.

6. Conclusion

With the GPT model developed in this study, students can make significant progress in vocabulary, grammar usage, reading comprehension, and oral expression. Especially for beginners, the immersive language environment created by this model greatly stimulates learning and makes the learning process fun and productive. More importantly, by simulating real-life situations and encouraging students to use the language in practice, this model promotes the development of intercultural communication skills and critical thinking, both of which are particularly important in today's globalized society.

Although automated teaching can improve efficiency, we still need to pay attention to the irreplaceable role of teachers in emotional support and humanistic care. In addition, how to formulate effective assessment criteria to accurately measure the learning effectiveness with the aid of LLM is also a major issue. In the face of these challenges, future educational research and practice need to work hand in hand to explore solutions to ensure that the application of LLM in ELT is both scientific and humane, promoting intelligent and personalized learning while maintaining the fairness and quality of education.

The integration of LLM has brought revolutionary changes to ELT, not only optimizing the learning process, but also comprehensively improving students' language skills and comprehensive literacy. With the continuous advancement of technology and the evolution of educational concepts, we look forward to seeing a smarter, more personalized, and efficient English learning environment that opens the door to the world and a brand-new learning journey for language learners around the world.

References

[1] Schoen, M. P.. Introduction to Intelligent Systems, Control, and Machine Learning using MATLAB. Cambridge: Cambridge University Press. 2023

[2] Evaluating large-language-model chatbots to engage communities in large-scale design projects. Artificial Intelligence for Engineering Design, Analysis and Manufacturing, 2024, 38:e4-. DOI:10.1017/S0890060424000027.

[3] Baruch JEF. The Future of Robotic Telescopes for Education. Publications of the Astronomical Society of Australia. 2000;17(2):119-124. doi:10.1071/AS00119

[4] Moritz N, Hori T, Le J. Streaming automatic speech recognition with the Transformer model[C]//ICASSP 2020-2020 IEEE International Conference on Acoustics, Speech and Signal Processing (ICASSP). IEEE, 2020: 6074-6078.

[5] Gretz S, Bilu Y, Cohen-Karlik E, et al. The workweek is the best time to start a family–A Study of GPT-2 Based Claim Generation[C]//Findings of the Association for Computational Linguistics: EMNLP 2020. 2020: 528-544.

[6] Xu H, Saenko K. Ask, Attend and Answer: Exploring Question-Guided Spatial Attention for Visual Question Answering[C]//European Conference on Computer Vision.Springer, Cham, 2016.DOI:10.1007/978-3-319-46478-7_28.

[7] Sennrich R , Haddow B , Birch A .Neural Machine Translation of Rare Words with Subword Units[C]//Proceedings of the 54th Annual Meeting of the Association for Computational Linguistics. 2016. DOI:10.18653/v1/P16-1162.

[8] Ethayarajh K. How Contextual are Contextualized Word Representations? Comparing the Geometry of BERT, ELMo, and GPT-2 Embeddings[C]//Proceedings of the 2019 Conference on Empirical Methods in Natural Language Processing and the 9th International Joint Conference on Natural Language Processing (EMNLP-IJCNLP). 2019: 55-65.

[9] Tran A D , Le T X H , Tran T D ,et al.Exploring the Limitations of Kolmogorov-Arnold Networks in Classification: Insights to Software Training and Hardware Implementation. 2024.DOI:10.48550/arXiv.2407.17790.

Fuzzy Systems and Data Mining X
A.J. Tallón-Ballesteros (Ed.)

doi:10.3233/FAIA241466

Optimization on Cable's Initial Tension of Extradosed Cable-Stayed Bridge with Gradient Projection Method

Kejun WANG[1], Boping ZHANG and Guang ZHAO
Gansu Traffic Engineering Construction Supervision CO, LTD., China

Abstract. In order to determine the cable force of the cable-stayed bridge of the low tower cable-stayed bridge, the optimization model of the cable force of the cable-stayed bridge of the low tower was established on the basis of the influence matrix of the cable force of the cable-stayed bridge, and the solution method of the initial tension optimization was established by using the gradient projection method. Combined with the Yinhu Bridge example, the CBOP program based on the optimization model in this paper is used to optimize the initial tension of the cable-stayed cable, and the calculated results are compared with the original design of the bridge cable force. The results show that for the low-tower cable-stayed bridge, the initial tension of the cable optimized by the gradient projection method will make the bending moment diagram of the whole beam change more smoothly, and the structural force will be more reasonable, and the optimization rate of the maximum negative bending moment will reach 49% and the maximum positive bending moment will reach 14% when the initial tension increases by 6%. On the whole, the optimization effect of this method is good, and it can be applied to the design practice of existing bridges.

Keywords. Extradosed cable-stayed bridge; influence matrix, initial cable force, gradient projection method

1. Introduction

As the main bridge type of long-span bridge, cable-stayed bridges have been widely used. Due to the adjustability of the cable-stayed cable force, it is an important part of the cable-stayed bridge design to make the cable-stayed bridge reach a reasonable bridge state through the optimization of the cable force [1]. According to the different optimization ideas and strategies, the cable force optimization method can be basically divided into the cable force optimization method with specified force state, the unconstrained cable force optimization method, the constrained cable force optimization method and the influence moment matrix method [2]. The cable force optimization method that specifies the stress state is to calculate the specific force or displacement of some components in the bridge structure as the goal, and the common methods have zero displacement method, rigid support continuous beam method, elastic support continuous beam method, etc.; The unconstrained cable force optimization method usually refers to the minimum bending energy method, which is characterized by the goal of minimizing the bending strain energy of the structure and not applying additional constraints. The

[1] Corresponding author: 466498638@qq.com

constrained cable force optimization method and the influence matrix method generally aim at a certain performance of the structure, and add constraints related to the performance to construct the matrix equation for solving [3-6].

Extradosed cable-stayed bridge, also known as partially cable-stayed bridges, their general characteristics are: short towers, rigid girders, cable concentration [7,8].Mainly through the main girder bending to bear most of the vertical load, the vertical component of the cable-stayed cable-stayed direct bearing role is very small, through the short tower cable-stayed bridges that have been built in the country, the cable-stayed cable-stayed bridge on the vertical load sharing rate of the maximum of only 20%, while ordinary cable-stayed bridges are in 40% or more [9,10].Thus, Japan in the short tower cable-stayed bridge cable-stayed design, short tower cable-stayed bridge cable-stayed safety coefficient can be taken according to the in vitro prestressing value of 1.67, i.e., 0.6 times the strength of the cable-stayed, instead of the ordinary cable-stayed of 2.5. Therefore, in the design of short tower cable-stayed bridges, it should be mainly to play the cable-stayed on the improvement of the force of the main girder. This characteristic of the short tower cable-stayed bridge determines the necessity of optimizing the initial tension of the cable-stayed cables, and also indicates that there is a large space for its design optimization. Usually, the constant load internal force of a highway bridge accounts for more than 70% of the total load internal force, and thus the goodness of the distribution of constant load internal force in the bridge-forming state is one of the important criteria to measure the design merits. Optimization of initial tension of cable-stayed cable-stayed bridges with short towers is to find out a set of initial tensions to minimize some kind of objective function of reactive force performance of the structure in the bridge-forming stage under deterministic loading.

In order to determine the reasonable cable force of the low tower cable-stayed bridge[11,12], this paper proposes a gradient projection method, taking the single-tower single-cable surface low-tower cable-stayed bridge in Xiamen City as an example for analysis, and establishes an optimization model based on the influence matrix and the minimum structural strain energy as the objective function, and uses the gradient projection method to calculate the initial tension of the cable, and compares the obtained results with the original design of the bridge cable force, so as to verify the applicability of the gradient projection method and provide a reference for the optimal design of the cable force of the same type of bridge.

2. Optimization Modeling

2.1 Influence matrix of extradosed cable-stayed bridges

Take the initial tension of the diagonal cable as a variable, with the unit initial tension of the diagonal cable acted on the structure of the stress-free state, to get the value of the impact on the main girder of the rod end force of each unit and the composition of the influence matrix [13-15]. suppose that:

$\{x\}$ - is the initial tension array of the diagonal cable;

$\{P\}$ - is the diagonal cable force array;

$\{M\}$ - is the array of bending moments at the rod ends of each unit of the structure.

M_i^L , M_i^R are the left and right end bending moments of cell i, respectively;

$\{N\}$ - is the array of axial forces at the rod ends of each unit of the structure

N_i^L, N_i^R are the axial forces at the left and right ends of unit *i*, respectively.

Then:

$$\{P\} = \{P_D\} + [A_P]\{x\} \tag{1}$$

$$\{M\} = \{M_D\} + [A_M]\{x\} \tag{2}$$

$$\{N\} = \{N_D\} + [A_N]\{x\} \tag{3}$$

Of which:

$\{P_D\},\{M_D\},\{N_D\}$ - are the arrays of cable forces under constant load and arrays of bending moments and axial forces at the rod ends of each unit of the structure, respectively.

$\{M_D\} = \{M_{D1}^L \quad M_{D1}^R \quad M_{D2}^L \quad M_{D2}^R \text{L L} \quad M_{Dm}^L \quad M_{Dm}^R\}^T$

M_D, M_{Di}^R are the constant load bending moments at the left and right ends of cell No. *i*, respectively.

$\{N_D\} = \{N_{D1}^L \quad N_{D1}^R \quad N_{D2}^L \quad N_{D2}^R \Lambda \Lambda \quad N_{Dm}^L \quad N_{Dm}^R\}^T$

N_{Di}^L, N_{Di}^R are the constant load bending moments at the left and right ends of cell *i*, respectively;

$[A_P],[A_M],[A_N]$ - are the influence matrix of the cable force and the influence matrix of the bending moment and axial force of each unit rod end, i.e., the cable force and the bending moment and axial force of each unit rod end under the action of the unit initial tension, respectively.

2.2 Optimizing the objective function

The constrained minimum energy method is usually used to optimize the structure, and the potential energy (bending and tensile strain energy) ***U*** of the structure can be chosen as the optimization objective function:

$$U = \int_l \left(M^2(l)\frac{1}{2E(l)I(l)} + N^2(l)\frac{1}{2E(l)A(l)} \right) dl \tag{4}$$

Assuming that all units of the main beam are of equal cross section and the modulus of elasticity of the units is constant, the above equation can be simplified as:

$$U = \sum_{i=1}^{m}\left[\frac{L_i}{6E_iI_i}\left(M_{Li}^2 + M_{Li}M_{Ri} + M_{Ri}^2\right) + \frac{L_i}{6E_iA_i}\left(N_{Li}^2 + N_{Li}N_{Ri} + N_{Ri}^2\right) \right] \tag{5}$$

Formal:

M_i^L, M_i^R -are the left and right end bending moments of the main beam unit No. *i*, respectively;

N_i^L, N_i^R -are the axial forces at the left and right ends of unit *i*, respectively.

E_i, I_i, A_i, L_i - are the modulus of elasticity, the moment of inertia of the cross-section, the cross-sectional area and the length of the unit of the main beam unit No. *i*, respectively;

m- is the number of units of the structure.

Substituting Eqs. (2) and (3) into Eq. (5) and expressing them in matrix form as:

$$U = \{x\}^T[G]\{x\} + 2\{F\}\ \{x\} + D \tag{6}$$

Formal:

$$G = [A_M]^T[B][A_M] + [A_N]^T[C][A_N]$$

$$F = \{M_D\}^T [B][A_M] + \{N_D\}^T [C][A_N]$$
$$D = \{M_D\}^T [B]\{M_D\} + \{N_D\}^T [C]\{N_D\}$$

Where, [B], [C] are the weighting coefficient matrices of unit flexibility to unit bending moment and unit axial force, respectively:

$$[B] = \begin{bmatrix} [B_1] & & & 0 \\ & \text{O} & & \\ & & [B_i] & \\ & & & \text{O} \\ 0 & & & [B_m] \end{bmatrix} \quad [C] = \begin{bmatrix} [C_1] & & & 0 \\ & \text{O} & & \\ & & [C_i] & \\ & & & \text{O} \\ 0 & & & [C_m] \end{bmatrix}$$

$$[B_i] = \begin{bmatrix} b_{ii} & b_{ii+1} \\ b_{i+1i} & b_{i+1i+1} \end{bmatrix}, b_{ii} = b_{i+1i+1} = \frac{L_i}{6E_iI_i}, \quad b_{i+1i} = b_{ii+1} = \frac{L_i}{12E_iI_i}$$
$$[C_i] = \begin{bmatrix} c_{ii} & c_{ii+1} \\ c_{i+1i} & c_{i+1i+1} \end{bmatrix}, c_{ii} = c_{i+1i+1} = \frac{L_i}{6E_iA_i}, \quad c_{i+1i} = c_{ii+1} = \frac{L_i}{12E_iA_i}$$

2.3 Constraints on the initial tension of the cable

2.3.1 Constraints on tension cable forces.

In the actual design, the most common and basicrequirement for the cable is to ensure that the cable does not fail; in other words, to make the cable is always in a "taut" state, that is:

$$\{x\} \geq \{0\}$$
$$\{P_D\} + [A_P]\{x\} \geq \{P_{\min}\}$$

Here, $\{P_{\min}\}$ is the maximum pressure that can be generated by a cable under live load.

2.3.2 Displacement constraints.

Cable-stayed bridge girder alignment and horizontal displacement of the cable-stayed tower can intuitively reflect the whole bridge design is reasonable [16,17], in order to make the bridge alignment to achieve the ideal state, the designer is often limited to the structure of the partial displacement. The displacement constraint can be expressed as:

$$\{D_D\} + [A_D]\{x\} \leq \{D_{\max}\}$$
$$\{D_D\} + [A_D]\{x\} \geq \{D_{\min}\}$$

Formal: [A_D], $\{D_D\}$-The influence matrix of nodal displacements and the column matrix of nodal displacements under constant structural loads, respectively; $\{D_{max}\}, \{D_{min}\}$ -The upper and lower limits of the specified displacement, respectively.

2.3.3 Mathematical model and method for the optimization of initial tension in tension cables.

So far, the initial tension optimization of the inclined cable and the mathematical model for solving the initial tension of the cable can be summarized as:

$$\begin{aligned} &\min f(x) = \{x\}^T [G]\{x\} + 2\{F\}\{x\} + D \\ &s.t. \quad c_i(x) = \{D_{\min}\} - [A_D]\{x\} - \{D_D\} \le 0 \\ &\qquad c_i(x) = \{D_D\} + [A_D]\{x\} - \{D_{\max}\} \le 0 \\ &\qquad c_i(x) = \{P_{\min}\} - [A_P]\{x\} - \{P_D\} \le 0 \\ &\qquad \{x\} \ge \{0\} \end{aligned} \tag{7}$$

The above mathematical model is a quadratic linear programming problem, this paper uses the ROSE gradient projection method to solve, and its flow is shown in Figure 1.

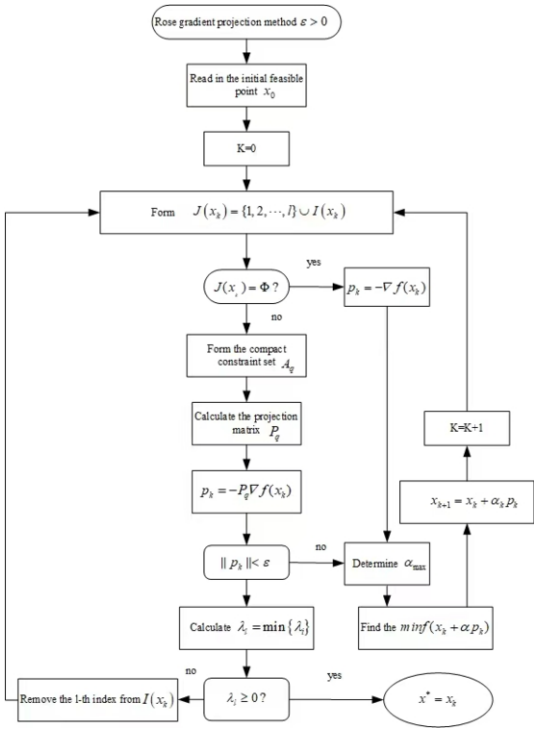

Figure 1. Gradient projection method solution flow.

3. Analysis of two span extradosed cable-stayed bridge

The example bridge is a single tower single cable plane extradosed cable-stayed bridge with span of 80m+80m (Fig. 2), which adopts tower, pier and girder cementation. The main girder is a single box three chamber box section, beam height 2.4m ~ 3.8m, box girder top width 27.0m, flange cantilever 4.5m, box girder bottom width 16.24 ~ 17.0m, both sides of the web diagonal, side chamber net width 7.45m, the net width of the middle chamber 1.5m. cable arrangement in the middle chamber, the rope in the girder spacing of 4.0m, the cable face for the single row of harp shape, design side bearing no cable area length 19m, tower root The length of the designed side support without cable area is 19m, and the length of the tower root without cable area is 25m, and the height of the structural tower is 22.92m.

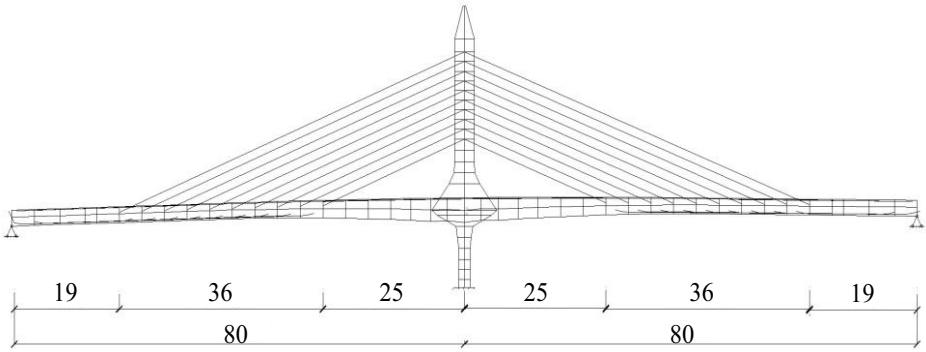

Figure 2. Integral finite element model (unit: m)

On the basis of the optimization model in this paper, the initial tension optimization of the cable-stayed cables of the example bridge was carried out by using the compiled CBOP program. In order to fully consider the strain energy of the structure, the optimization takes the minimum bending and tensile strain energy of the main girder and the cable tower as the objective function and compares it with the design.

Usually for the main girder, the maximum positive and negative bending moments and deflection are the main mechanical indexes reflecting its force, while the magnitude of the cable force reflects the optimization cost. If the optimization rate ρ is defined as:

$$\rho = \frac{\text{design} - \text{optimum}}{\text{design}} \times 100\%$$

Then a positive value of ρ means that the design value is reduced and the indicator has an optimization effect; a negative value means that the design value is not reduced and the indicator does not have an optimization effect.

The maximum constant load negative bending moment, positive bending moment, deflection, total initial tension and their optimization rates for the main girder are shown in Table 1.

Table 1. Optimization results of main mechanical indexes

Project	Optimum value	Design value	Optimization rate (%)
Maximum positive bending moment of main beam (kN·m)	12739.07	14782.06	14
Maximum negative moment of main beam (kN·m)	-55541.85	-109076.85	49
Maximum deflection of main beam (m)	-0.1477	-0.1394	-6

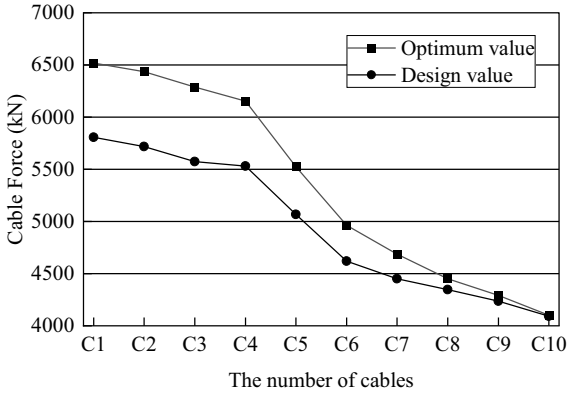

Figure 3. Cable force design value vs. optimization (half bridge)

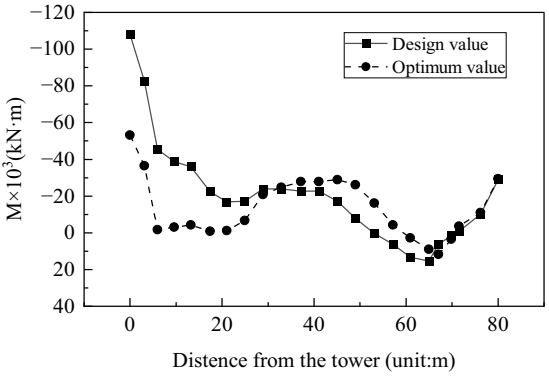

Figure 4. Bending moment design value vs. optimization value (half bridge)

From Table 1, Fig. 3 and Fig. 4, it can be seen that the bending moment of the main girder can be reduced based on the energy-minimizing cable-stress optimization method. In terms of optimization rate, the optimization rate of maximum negative bending moment reaches 49% and the optimization rate of maximum positive bending moment reaches 14% with 6% increase of initial tension. From the optimization effect, the improvement of the main girder bending moment is mainly concentrated in the part close to the tower, while the positive bending moment part close to the side braces does not reflect the optimization effect. This reflects the nature of optimization based on the principle of minimum capacity to reduce the law of inhomogeneous distribution of bending moments to achieve the minimum strain energy of the structure.

The magnitude of the initial tension reflects the size of the required cross-section of the cables, which indirectly reflects the amount of cables used. From Table 1 and Fig. 3, it can be seen that the improvement of the internal force of the main girder is realized by increasing the initial tension of the tie ropes (the amount of cables used). From the optimization of this bridge, it can be seen that the total tension cable usage only increases by 6% in the case of obtaining a larger optimization rate of bending moment. Because the safety factor of the tension cable in the design of this bridge is still taken according to the ordinary diagonal knockout (2.5), and the optimization of the initial tension of the No. 2 and No. 3 cables increases the most (13%), which is equivalent to the reduction of the structural safety factor by 13%, so it can be considered that the optimization does not

increase the area of the cables, and it only improves the utilization rate of the cables, and the optimization plays a due role.

The cable optimization increased the maximum constant load deflection of the main girder by 8%, and the constant load deflection can be eliminated by pre-arching during construction. The live load stiffness of a structure is usually a mechanical index that affects the performance of the structure, and for this bridge, since the initial tension optimization did not change the cross-sectional area of the tension cables, it did not affect the stiffness of the structure, so it did not reduce the live load stiffness.

4. Conclusions

1) In order to improve the force performance of the main girder of the short tower cable-stayed bridge, it is necessary to optimize the initial tension of the tie ropes; in general, the optimization effect is also obvious, and the optimized initial tension of the tie ropes will make the moment diagram of the whole girder change more smoothly, and the structural force is more reasonable.

2) The optimization aiming at improving the force performance of the main girder of the short-tower cable-stayed bridge is at the expense of moderately increasing the number of tie cables, but the increase in the number of tie cables will not be very large, and through the optimization, the efficiency of the utilization of the tie cables can be fully utilized.

3) For extradosed cable-stayed bridge, the optimization method based on the minimization of deformation energy is based on the principle of reducing the strain energy of the structure by reducing the inhomogeneity of the bending moment.

References

[1] Dai Jie, Qin Fengjiang, Di Jin, et al. China Journal of Highway and Transport,2019,32(05):17-37.
[2] Liang Peng, Xiao Rucheng, Zhang Xuesong. Journal of Tongji University(Natural Science Edition),2003(11):1270-1274.
[3] Xie Zhigang, Zhao Yongjun. Determination of reasonable cable force of superimposed beam cable-stayed bridge based on "zero displacement method + stress balance method"[J].China Municipal Engineering,2012(02):36-37+41+99-100.
[4] Fu Chunyu, Gao Zhenfeng, Yan Peng, et al. Calculation method of reasonable cable force for concrete cable-stayed bridge based on elastic support continuous beam method[J].Bridge Construction,2022,52(06):124-130.
[5] Zhan Yulin, Hou Zhiyao, Shao Junhu, et al. Cable force optimization of special-shaped cable-stayed bridge based on response surface method and particle swarm optimization[J].Bridge Construction,2022,52(03):16-23.
[6] Chen D, Li Yinxin, Zhou Shuai, et al. Reasonable initial tensile force analysis of cable-stayed cable of cable-stayed bridge based on influence matrix method[J].World Bridge,2021,49(02):78-83.
[7] Yan, G. M. Revisiting partial cable-stayed bridges and multi-tower cable-stayed bridges. 1998. Shanghai. Proceedings of the Thirteenth National Bridge Conference: 178-182.
[8] Chen Hengjin, Wang Kai et al. Introduction to partially cable-stayed bridges, Bridge Construction, 2002, 141(1):44-47.
[9] LIN Pengzhen,LIU Fengkui,ZHOU Shijun et al. Mechanical properties of partially cable-stayed bridges and their definition. Journal of Railway, 2007.29(2):136-140.
[10] LIN Pengzhen,ZHOU Shijun et al. Study on the dynamic characteristic parameters of single cable-stayed low-tower cable-stayed bridges. Vibration and Shock, 2006.23(6):150-153.
[11] Ogawa A, Matsuda T, Kasuga A. The Tsukuhara extradosed bridge near Kobe. Structural Engineering International 1998;8(3).
[12] Ogawa A, Kasuga A. Extra dosed bridges in Japan. FIPnotes 1998;2.

[13] Xiao Rucheng, Xiang Haifan, Influence matrix method for cable-stayed bridge cable-stayed force optimization, Journal of Tongji University, 1998, 26(3):235-239
[14] Xiao Rucheng, Xiang Haifan. Influence matrix method of cable force optimization of cable-stayed bridge[J].Journal of Tongji University(Natural Science Edition),1998(03):235-240.)
[15] Lin Pengzhen, Sun Honghong. Optimization of initial tension of cable-stayed bridge of Xiaoxihu dwarf tower[J].Special Structure,2005(01):60-62.
[16] Chen D, Li Yinxin, Zhou Shuai, et al. Reasonable initial tensile force analysis of cable-stayed cable of cable-stayed bridge based on influence matrix method[J].World Bridge,2021,49(02):78-83.)
[17] Yuan Renan, Qin Shunquan, Xiao Haizhu. A fast and accurate method for determining cable Force in target state of Cable-stayed Bridges [J]. Bridge Construction,2020,50(02):25-30.

Fuzzy Systems and Data Mining X
A.J. Tallón-Ballesteros (Ed.)

doi:10.3233/FAIA241467

Research on the Impact of Acoustic and Vibration Characteristics of Noise Reduction Panels in Helicopter Cabins

Guibao ZHANG[1] , Fengjiao WANG and Qiyou CHENG
China Helicopter Research and Development Institute, Jingdezhen, 333001, China

Abstract. The main reducer structure noise is one of the main sources of noise in the helicopter cabin. By controlling this noise, further noise reduction in the helicopter cabin can be achieved. To this end, a proposal has been made to add vibration isolation design to the connecting partition between the main reducer and the cabin, reducing the transmission of gear vibration to the airframe from the transmission path. To verify the mid-high frequency vibration reduction and noise reduction performance of this scheme, a dynamic model of the acoustic-vibration coupling system of the cabin section structure/sound field is established based on the helicopter cabin structure using the finite element method. On this basis, the impact of the stiffness, number/position, and surface density of the partition's elastic connection units on the cabin sound pressure are analyzed. The results show that: reducing the stiffness of the elastic connection units between the partition and the cabin can reduce the sound pressure level inside the cabin; increasing the number of elastic connection points will lead to an increase in the sound pressure level inside the cabin; changing the position and number of elastic connection units can adjust the noise level inside the cabin.

Keywords. Helicopter, cabin noise,parameter analysis

1. Introduction

Helicopters are versatile aerial platforms with the unique ability to take off and land vertically and hover [1]. However, due to the high levels of vibration and noise, the quality of the ride in a helicopter cabin is often poor. To reduce noise exposure levels and enhance communication, helicopter crew members are required to wear flight helmets throughout the mission. If the flight helmet does not provide sufficient noise protection, or if it is worn improperly, the high noise levels in the helicopter cabin may have adverse effects on the crew in the short term [2-3].

The acoustic environment of a helicopter cabin typically includes harmonic noise peaks related to the aerodynamics of the rotor blades, as well as mid-to-high frequency noise associated with the transmission/hydraulic systems. Among these, the main gearbox (hereinafter referred to as the "main reduction"), as a key transmission component of the helicopter, generates significant gear meshing vibration and noise under high-load conditions, which is ultimately transmitted to the cabin, forming a multi-harmonic, high-level noise environment, as shown in Figure 1. This noise generally falls

[1] Corresponding author: zhanggb602@163.com

within the sensitive frequency range of 500-4000Hz for the human ear, severely affecting the comfort of riding inside the helicopter cabin [4].

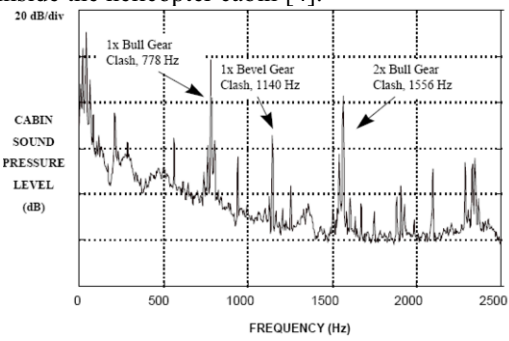

Figure 1. S-76Helicopter cabin noise spectrum [4]

For the control of helicopter cabin noise, common technical solutions are mainly divided into two categories: passive control and active control [5].

In this context, active control technology primarily involves installing actuators on the main reduction struts or supports to introduce secondary forces. These forces suppress the transmission of high-frequency vibrations from the main gearbox to the airframe, thereby controlling the structural noise within the cabin.

For example, Elliott Nelson, Doring [6], and others conducted the first in-cabin active control flight tests on the BAe 748 aircraft, followed by subsequent ground and flight tests of active control on various models including the SAAB 340 and ATR 42. The Simith [7] team introduced an active control scheme into hydraulic vibration isolator [8], which could improve the noise level by nearly 40 dB at multiple frequency band positions. Boucher and others, based on the structural dynamic characteristics of the rotor and tail rotor, installed speakers on the seats and in the cabin and modified the Fx-LMS algorithm to improve the cabin noise environment.

Passive control technology includes vibration isolation [9], damping [10], and vibration reduction, among others. Vibration isolation design requires changes to the original support stiffness, structural dimensions, materials, and configuration design, etc., which can directly improve the sound insulation of the wallboard and the performance of structural sound radiation. For example, researchers at Northwestern Polytechnical University studied the impact of damping coefficients and dimensions on the noise reduction of wallboards; Paolo [11] and others altered the damping layer of the wallboard to study the noise reduction effects.

From the perspective of noise transmission paths, noise reduction design can be carried out from three aspects: noise source, transmission path, and target location. Theoretically, any measure that can reduce the vibration level of the noise source is beneficial to reduce the noise level on the aircraft [12]. Studies have shown that the active trailing edge flap control technology used by the rotor blades of the BK-117 helicopter can reduce the noise level by 6 dB [13], and optimizing the structure of the gearbox and engine is also conducive to reducing the noise level of the helicopter. Lewicki et al. [14] reduced the sound power by 10 dB after improving the form of the gearbox transmission gears, and the noise level of the WAH-64 helicopter was also effectively reduced after being equipped with the Rolls RTM-322 engine [15]. The vibration reduction and noise reduction design on the transmission path includes the main reduction liquid shock absorption technology used on the BELL-427 [16], the structural response active vibration reduction technology used on the EC-725[17], etc. In addition, improving the

acoustic environment inside the cabin with sound absorption and sound insulation is also an effective passive noise reduction means. Active noise cancellation and active structural acoustic control are currently more advanced active noise reduction technologies inside the cabin. Active noise cancellation uses infrasound fields to cancel the source sound field, and this technology can reduce the noise inside a certain type of aircraft cabin by 28 dB, while active structural acoustic control is to suppress noise by controlling vibrations. The noise reduction means at the target location include equipping the driver and passengers with active noise reduction headphones, soundproof earplugs, etc. Acoustic finite element simulation analysis is an effective means of helicopter noise reduction design, which can estimate the noise levels inside and outside the cabin at the beginning of the model design, provide noise reduction design suggestions, evaluate the effects of noise reduction technologies, and greatly reduce the subsequent optimization, improvement, and test costs. At present, the simulation analysis of helicopter noise is mainly focused on external noises such as rotor and tail rotor noise. Wang Puyuan [18] used the finite element method to analyze that under the medium-speed forward flight state, the rotor noise accounts for more than 90% of the total noise of the helicopter. Zhong Weiguo et al. [19] used the FW-H equation to analyze the interference noise between the helicopter tail rotor and the vortex line, indicating that the tail rotor noise increases in the mid-frequency band and has a certain directionality under the interference state. Xie Futian et al. [20] also used the FW-H equation to analyze the directionality of the main rotor noise. For the simulation analysis of cabin noise, Perazzolo et al. [21]and Lei Ye et al. [6] used the statistical energy method to analyze the noise transmission path inside the AW139 and a certain type of helicopter cabin respectively.

However, there is a scarcity of literature in China describing noise reduction for helicopters, and there is even less in-depth research on cabin vibration and noise reduction.

Therefore, to verify the effect of partition structure parameters on the mid-to-high frequency noise reduction performance inside the helicopter cabin, this paper establishes a dynamic model of the acoustic-structural coupling system for the cabin segment structure/acoustic field. On this basis, the vibration isolation effect of the partition is analyzed for the influence of parameters, and the impact of different parameters on the cabin sound pressure is analyzed.

2. Dynamic Modeling

To determine the impact of vibration isolators on the vibration characteristics of the main reduction support structure and the noise within the cabin, dynamic models of the helicopter cabin structure, the internal acoustic field, and the acoustic-structural coupling system are established separately. Considering the complexity of the airframe structure and the cavity acoustic field, the finite element method is used for modeling.

To verify the noise reduction effect of the vibration isolation design, a section of the cabin near the helicopter's main gearbox is taken, and a structural model of the airframe cabin section is established. According to the finite element method, the dynamic equation of the structural elements can be formulated as follows: (Note: The actual equation was not provided in the user's statement and would typically be a system of differential equations representing motion.):

$$\boldsymbol{M}_e\ddot{\boldsymbol{u}}_e + \boldsymbol{C}_e\dot{\boldsymbol{u}}_e + \boldsymbol{K}_e\boldsymbol{u}_e = \boldsymbol{F}_e \tag{1}$$

In the equation, $\boldsymbol{M}_e$ represents the structural element mass matrix; $\boldsymbol{C}_e$ represents the structural element damping matrix; $\boldsymbol{K}_e$ represents the structural element stiffness matrix; $\boldsymbol{u}_e$ represents the nodal displacement; $\mathrm{F_e}$ represents the load vector.

2.1. Cabin Acoustic Field Model

Further, based on the fluid elements, establish a finite element model of the radiated acoustic field within the cabin. The dynamic equation for the fluid elements is as follows: (Note: The actual equation was not provided in the user's statement and would typically involve the Navier-Stokes equations or a similar formulation for fluid dynamics.):

$$\boldsymbol{M}_e{}^p\ddot{\boldsymbol{p}}_e + \boldsymbol{C}_e{}^p\dot{\boldsymbol{p}}_e + \boldsymbol{K}_e{}^p\boldsymbol{p}_e = \boldsymbol{0} \tag{2}$$

In the equation, $\boldsymbol{M}_e^p$ represents the mass matrix of the fluid element, $\boldsymbol{C}_e^p$ represents the damping matrix of the fluid element, $\boldsymbol{K}_e^p$ represents the stiffness matrix of the fluid element, and $\boldsymbol{p}_e$ represents the nodal pressure vector.

At the coupling interface between the cabin fluid and the cabin wall, the inertial force caused by the structural normal acceleration will be balanced with the fluid normal pressure. The structural vibration of the cabin wall is transmitted to the cavity through the coupling interface, thereby causing the motion of the fluid elements and generating noise. At this time, the structural dynamics equation and the fluid dynamics equation can be combined as follows: (Note: The actual combined equation was not provided in the user's statement and would typically represent the interaction between the structural and fluid domains at the coupling interface.) Please provide the specific equations if you would like an accurate translation or explanation of the combined dynamics.

$$\boldsymbol{M}_e{}^p\ddot{\boldsymbol{p}}_e + \boldsymbol{C}_e{}^p\dot{\boldsymbol{p}}_e + \boldsymbol{K}_e{}^p\boldsymbol{p}_e + \boldsymbol{M}_e{}^c\ddot{\boldsymbol{u}}_e = \boldsymbol{0} \tag{3}$$

In the equation, $\boldsymbol{M}_e{}^c$ represents the coupling mass matrix of the elements.

On this basis, select the field point position at the location of the human ear within the cabin to observe the noise level inside the cabin.

3. Finite Element Simulation of Helicopter Cabin

As shown in Figure 2, the geometric shape of the helicopter cabin is utilized to establish a finite element simulation model using the commercial software HyperWorks.

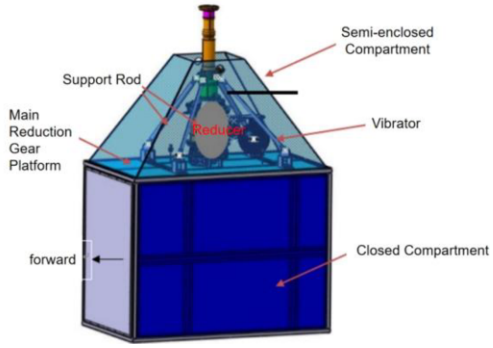

Figure 2. Helicopter cabin structure schematic diagram.

Figure 3 illustrates the established finite element model, which globally employs 2D shell elements, with a total of 35,116 elements. The primary materials are aluminum and steel. The model analyzes the acoustic-vibrational response within the cabin by applying a unit load at the connection point between the helicopter's main gearbox and the cabin's top.

Without significantly affecting the analysis results, based on the finite element model shown in Figure 3, the mass law based on the transmission law was used to equivalently and simplify the enclosed cabin wall panels and frame structures in the finite element model. Finally, an acoustic finite element model composed of plates such as the main reduction platform and skin panels was formed. Among them, the platform, skin, and baffles are aluminum plates, all of which have been simplified to equivalent thickness; the skin has been defined with properties according to the actual structure. In addition, since the acoustic finite element method is applied for acoustic response analysis, it is required that the normal direction of the element must point to one side of the calculation domain. For cabin noise analysis, this means that the normals should all point towards the cabin. Before the analysis, acoustic mesh preprocessing is needed to adjust the mesh normals to point towards the cabin.

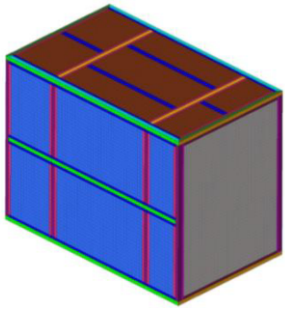

Figure 3. Helicopter cabin finite element model.

4. Cabin Noise Analysis

Figure 4/5 shows the overall noise level of the bare cabin without any vibration isolation measures. Under the unit excitation force, the maximum sound pressure level reaches

117 dB, corresponding to a sound pressure level of 116 dB at the location of the human ear.

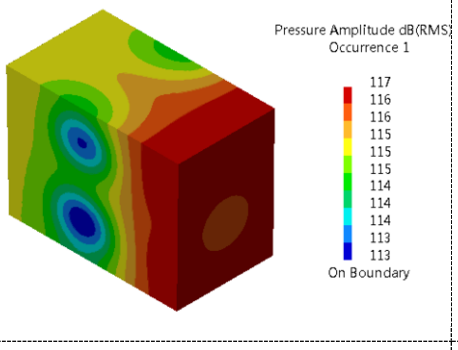

Figure 4. Helicopter Bare Cabin Overall Sound Pressure Level -entire cabin

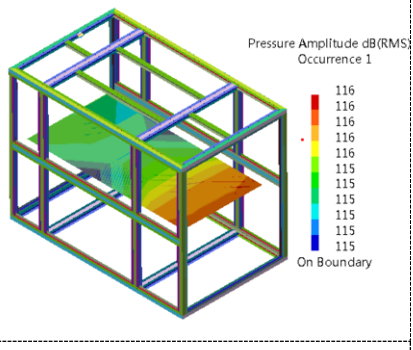

Figure 5. Helicopter Bare Cabin Overall Sound Pressure Level - human ear

4.1. Connection Stiffness Parameter Influence Analysis

The analysis investigates the impact of increasing the sound insulation panel at the top and adding top cotton, adjusting the connection stiffness between the partition and the cabin, and analyzing the effect of connection stiffness on the sound pressure level at the human ear location within the cabin. The partition is connected to the cabin through 1D spring elements as shown in Figure 6, simulating bolt connections. By changing the stiffness of the spring elements, the analysis examines the influence of connection stiffness on the cabin noise. The base stiffness of the spring elements is set to 270,000 N/m.

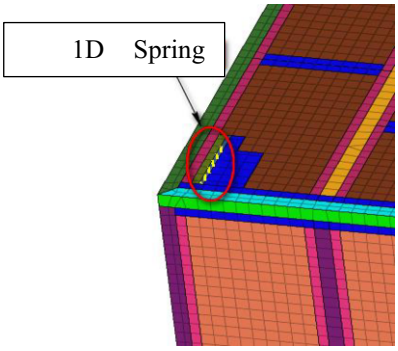

Figure 6. Schematic Diagram of the Spring Element Connecting the Partition to the Cabin

Schematic Diagram of the Spring Unit Connecting the Partition to the Cabin Figure 7/8, left and right, respectively represents the impact curve of adjusting the stiffness of the elastic connection unit on the sound pressure at the human ear location in the cabin and on the entire cabin. By comparing the two figures, it can be seen that the elastic connection stiffness has a more pronounced effect on the overall sound pressure in the cabin. As the stiffness increases, the sound pressure level in the cabin also rises. When the stiffness is increased by 100 times, there is a significant difference in the sound pressure level in the cabin within the 250Hz to 1000Hz frequency band, with the maximum difference at 500Hz, reaching 8.1dB. For the sound pressure at the human ear location, the change pattern is consistent with the overall trend, that is, as the elastic

connection stiffness increases, the sound pressure level at the human ear location also increases. Within the 125Hz to 1000Hz frequency band, there is a slight change in the sound pressure level, with the maximum change at the frequency of 1000Hz, reaching 2.5dB.

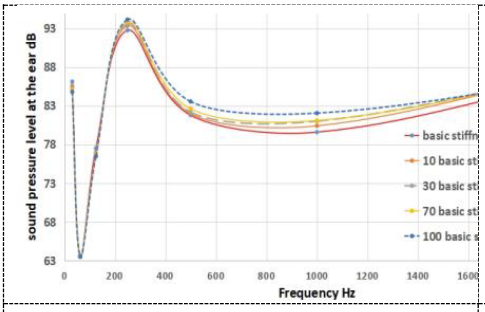

Figure 7. Elastic Connection Unit Stiffness Impact -human ear location

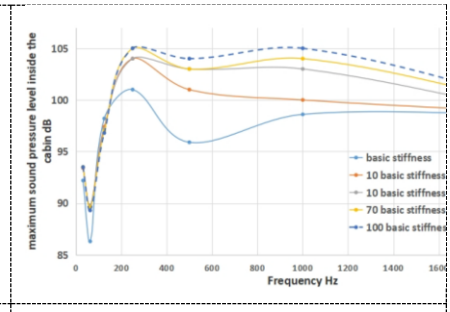

Figure 8. Elastic Connection Unit Stiffness Impact -entire cabin

4.2. the Impact of the Number and Position of Elastic Connection Units

Analysis of the Impact of the Number of Elastic Connection Units on the Cabin Sound Pressure by Changing the Number of Units on the Top Frame of the Cabin, with the results shown in Figure 9/10. From the left figure, it can be seen that the maximum effect of changing the number of elastic connection points occurs at 500Hz, with a reduction of 1.34dB. As the number of connection points increases, the sound pressure level in the cabin continues to rise. The impact of changing the number of connection points on the overall sound pressure in the cabin is essentially the same as at the human ear location, with the maximum impact at 500Hz, amounting to 0.7dB.

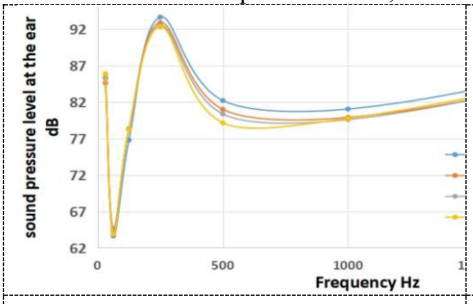

Figure 9. Elastic Connection Unit Quantity Impact-human ear location

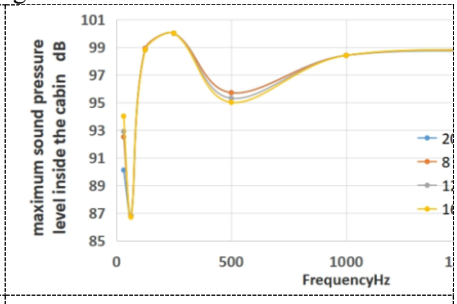

Figure10. Elastic Connection Unit Quantity Impact-entire cabin

The impact of the position of connection units, with the quantity of connection points remaining constant and moving the position of the connection units near the point of unit load application, is shown in Figure 11/12. It can be observed that moving the connection points near the load application point results in a more pronounced change in the cabin noise level. Compared to Figure 7, the maximum change at the human ear location in Figure 8 reaches 6.34 dB at 500 Hz, and the overall change in the cabin is 9 dB at 250 Hz and 9.9 dB at 500 Hz.

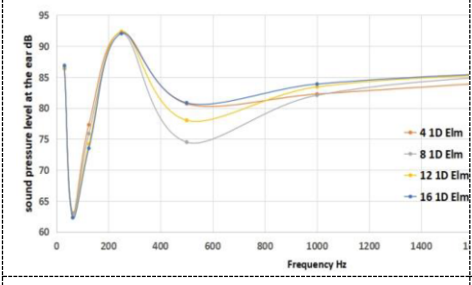

Figure 11. Impact of Changing the Number of Elastic Connection Units-human ear location

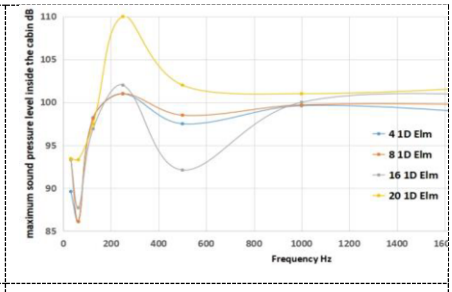

Figure12. Impact of Changing the Number of Elastic Connection Units-entire cabin

4.3. Analysis of the Impact of Partition Surface Density Parameters

Figure 13/14 illustrates the impact of changing the partition density on the sound pressure level at the human ear location and within the cabin. It can be observed from the figure that adjusting the surface density by a factor of 1 to 10 has virtually no effect on the sound pressure at the human ear location, but it does have an impact of 2 dB on the overall sound pressure within the cabin at the 500 Hz frequency. The base surface density is set to 500.

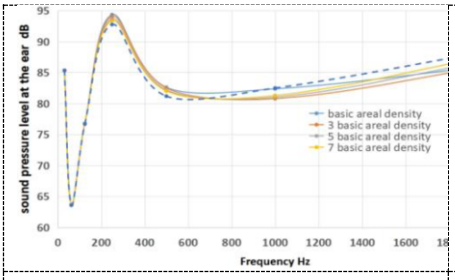

Figure 13. Impact of Changing the Position of Elastic Connection Units-human ear location

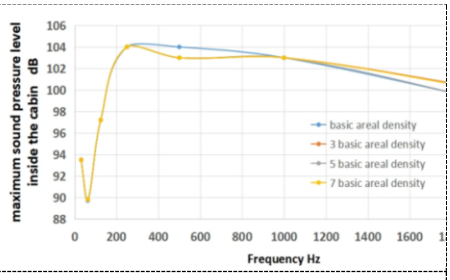

Figure14. Impact of Changing the Position of Elastic Connection Units-entire cabin

5. Summary

This paper, based on the geometric model of the helicopter cabin, establishes the corresponding dynamic model and carries out an analysis of the rules of parameter influence. The specific conclusions are as follows:

a. A common pattern can be drawn from the analysis of the effects of stiffness, surface density, quantity, and position parameters: the impact of the aforementioned parameters on the cabin noise level is mainly within the frequency range of 125Hz to1000Hz. There is essentially no effect on the sound pressure of other frequency bands.

b. For the sound pressure at the human ear location within the helicopter cabin, reducing the stiffness of the elastic connection units between the partition and the cabin can lower the cabin sound pressure level; increasing the number of elastic connection points will cause the cabin sound pressure to continuously rise;

changing the position and quantity of the elastic connection units can adjust the noise level within the cabin.

In summary, the helicopter cabin is an enclosed space formed by six panels. The sound pressure within the cabin space is not only affected by the vibration and sound transmission of the top wallboard but is also influenced by the contributions of the other panels. Subsequent research on noise reduction within the helicopter cabin can conduct a more comprehensive study of the impact of other panels and the noise reduction measures that can be applied.

References

[1] Scheidler J J 2016 A review of noise and vibration control technologies for rotorcraft transmissions[C]. INTER-NOISE and NOISE-CON congress and conference proceedings. Institute of Noise Control Engineering.

[2] Coy J J, Handschuh R F, Lewicki D G, et al 1987 Identification and proposed control of helicopter transmission noise at the source[J]. USAAVSCOM-TR-87-C-2.

[3] Brennan M J, Elliott S J, Heron K H 1998 Noise propagation through helicopter gearbox support struts-an experimental study[J]. Journal of Vibration and Acoustics.

[4] Millott T A, Yoerkie C A, Welsh W A, et al 1998 Flight test of active gear-mesh noise control on the S-76 aircraft[C].54th Annual Forum Proceedings of the American Helicopter Society, Fairfax, VA: American Helicopter Society: 241-250.

[5] Yin P, Huang B G, Liu Z C 2019 Analysis of the Noise Characteristics Inside a Helicopter Cabin [J]. Helicopter Technology.

[6] Pollard J S 1977 Helicopter gear noise and its transmission to the cabin[C]. 3rd European Rotorcraft and Powered Lift Aircraft Forum, Aix-en-Provence, France:52.1-52.10

[7] Yoerkie C A Newington Jr. Welsh W A, et al 1994 Helicopter active noise control system, USP5310137[P]:05-10.

[8] Widroelliott S J, Nelson P A, Stother I M, et a1 1990 In-flight experiments on the active control of propeller-induced cabin noise[J]. Journal of Sound and Vibration:159(1):219-238.

[9] Le H F, Smith E, Lesieutre G, et al 2005 Ac-tively-enhanced periodically-layered mount for helicop-ter gearbox isolation[C]//Proceedings of the 46th AIAA/ASME/ASCE/AHS/ASC Structures, Structural Dynamics, and Materials Conference. Austin, USA: The American Helicopter Society Inc.

[10] Qiu J H, Yuan M, Ji H L 2010 Research and Application of Active Control Technology for Cabin Vibration and Noise in Large Aircraft[J]. Aeronautical Manufacturing Technology:26(14)-29.

[11] Widrow B, Steam S D 1985 Adaptive signal processing[M]. New Jersey: Prentice Hall, Englewood Cliffs.

[12] Caillet J, Marrot F, Unia Y, et al 2012 Comprehensive approach for noise reduction in helicopter cabins[J]. Aerospace Science and Technology.

[13] Brian E. Barnes, Frank B. Stemple 2014 Pneumatic Spring Stiffness Adjuster for Improved Damping [P].CN 103967996 A.

[14] Wang M K 2015 Research on the Vibration Isolation Characteristics of Helicopter Main Gearbox Support Strut [D], Master's Thesis. Harbin Institute of Technology.

[15] Liu X H, Xu X X, Bai S, et al 2013 Vibration and noise control technology on military helicopters[J]. Helicopter Technique:67(1)-72.

[16] Liu J P 2006 Adaptive rotor technology: reducing noise and vibration of helicopter[J]. Conmilit:57(3)-58.

[17] Lewicki D G, Woodsr L 2003 Evaluation of low-noise, improved-bearing-contact spiral bevel gears:NASA/TM 2003-212353[R]. Washington, D.C.: NASA.

[18] Lin Y C, Jin M J 2000 Improvement and development of foreign military helicopter[J]. Modern Defence Technology:1-8.

[19] Konstanzr P, Enenkl B, Aubourg P A, et al 2008 Re-centadvances in Eurocopter's passive and active vibration control[C]//American Helicopter Society 64th Annual Forum.

[20] Lu Y, Ma X J, Wang F J 2016 Review of active techniques for helicopter interior noise control[J]. Aeronautical Manufacturing Technology:38-45.

[21] Wang P Y 2018 Noise reduction design of helicopter rotor and noise characteristics analysis of whole vehicle[D]. Nanjing:Nanjing University of Aeronautics and Astronautics.

Fuzzy Systems and Data Mining X
A.J. Tallón-Ballesteros (Ed.)

doi:10.3233/FAIA241468

Research on the Current Status and Development of Programming Education for Youth in Northern Guangdong in the Intelligent Era

Xiaolong HUANG[a,1] and Jierong LIN [b]
[a] *Qingyuan Polytechnic, Guangdong, China*
[b] *Shantang Central Primary School, Qingxin, Qingyuan, Guangdong, China*

Abstract. In order to adapt to the development of the intelligent era, the country has successively introduced policies to promote the development of programming education, which has gradually become a key teaching content in the information technology curriculum for young people. However, due to the uneven development of the region and the imbalance of educational resources, there are many problems and difficulties in the implementation of relevant educational work. Through interviews, surveys, and questionnaire surveys, we explored participants' perceptions of the importance of programming education, their level of understanding of programming education, the problems that exist in the development and implementation of related courses, and the issues that need to be addressed. We analyzed the current status of programming education in the sample areas and provided development suggestions for the problems identified.

Keywords. Smart Age, Artificial Intelligence, Programming Education

1. Research Background

In recent years, the State Council and the Ministry of Education of China have successively issued important documents such as the "New Generation Artificial Intelligence Development Plan"[1], the "Education Informatization 2.0 Action Plan"[2], and the "China Education Modernization 2035"[3], which repeatedly mention education informatization and programming education. Driven by national policies, programming education has gradually become a key teaching content in the information technology curriculum for young people [4]. At present, programming education in China is still in the primary stage of development, and the level of basic programming education is uneven [5]. In order to promote the balanced development of programming education, cultivate the innovative ability and information technology literacy of young people in northern Guangdong to meet the needs of future society, this article studies the current situation of programming education for young people in northern Guangdong and proposes development suggestions based on the survey results.

[1] Corresponding Author: Huang Xiaolong, 105719331@qq.com

2. Design and Implementation of the Survey on the Current Situation of Programming Education

2.1 Preliminary Compilation of the Survey Questionnaire

Based on the research objectives and previous literature reviews, a survey questionnaire was initially compiled for this study. The questionnaire consists of two parts: basic information and the main survey content. The basic information includes gender, age, and role, while the main survey content covers five dimensions: awareness of programming education, the current situation of programming education, resource and support levels, the effectiveness of programming education, and expectations and suggestions. Logical skip questions were set based on different roles and the status of programming education implementation in schools.

2.2 Preliminary Survey of the Questionnaire

To verify the reliability and validity of the questionnaire, a preliminary survey was conducted. The preliminary survey questionnaires were distributed and collected in Qingxin District, Qingyuan City, with a survey period of one week. A total of 55 questionnaires were distributed, and 54 valid questionnaires were recovered, with a valid response rate of 98.18%. The data from the preliminary survey questionnaire scales were used for reliability and validity analysis.

2.2.1 Reliability Analysis

The Cronbach's α coefficient indicates the reliability quality of the scale and can assess the consistency, reproducibility, and stability of the results. A Cronbach's α coefficient around 0.8 indicates very good reliability, and a coefficient greater than 0.9 indicates excellent reliability. The analysis data showed that the overall Cronbach's α coefficient of the questionnaire was 0.890, and the sub-scales reached above 0.857, indicating good internal consistency among the questionnaire items.

2.2.2 Validity Analysis

Validity measures the degree of effectiveness achieved in measuring psychological or behavioral traits. The questionnaire compilation referenced mature scales and incorporated suggestions from research subjects and experts for modification. The questionnaire's KMO value was 0.850, greater than 0.8, and the Sig. value was 0.000, ensuring good content and structural validity of the questionnaire, and the data results have certain research value.

2.2.3 Finalization of the Survey Questionnaire and Survey Implementation

The preliminary survey revealed that the reliability and validity of this questionnaire met the specific requirements of this study, ensuring the rationality of the questionnaire structure and the scientific nature of the research data, making it suitable for practical measurement. After analyzing and revising the preliminary survey data results, the final "Survey Questionnaire on the Current Situation of Programming Education for Young

People in Northern Guangdong" was formed.

The survey was conducted using a combination of paper questionnaires and electronic questionnaires, mainly targeting individuals in the Qingyuan area of northern Guangdong. A total of 708 questionnaires were collected, with 669 valid questionnaires, resulting in a valid recovery rate of 94.49%. Among the respondents, males accounted for 27.78%, and females accounted for 72.22%. The highest proportion was in the 31-45 age group, accounting for 53.38%, which was the largest age group in the survey sample. The 19-30 age group accounted for 20.29%, ranking second in age distribution. The population over 46 years old accounted for 17.63%, ranking third. The age groups of 13-18 and under 12 years old accounted for a smaller proportion, at 7% and 1.69% respectively. Educators in urban areas and parents of urban students accounted for a higher proportion, at 41.79% and 22.46% respectively, while parents and students from non-urban areas had lower proportions, at 3.14% and 1.45% respectively. The proportion of surveyed primary and middle school students was 24.88%, while the proportion of student parents, educators, and other personnel was 75.12%. Among the educators surveyed, those teaching math, physics, chemistry, and other science-oriented subjects accounted for 20.77%, those teaching information technology or directly related subjects accounted for 15.46%, those teaching Chinese, politics, history, and other liberal arts subjects accounted for 16.18%, and other options accounted for 5.07%.

3. Survey on the Current Status of Programming Education

3.1 respondent's perception of programming education

From the perspective of the necessity of programming education, more than 78% of the respondents believe that programming education is important or very important in primary and secondary education. Among them, 39.61% of the respondents think it is very important, 39.13% think it is important, 18.6% think it is average, and a small number think it is not important and completely unimportant. The level of understanding of programming education mainly focuses on the options of "knowing" and "general", accounting for 25.36% and 39.13% respectively, while the proportions of "very well knowing" and "not knowing much" are 6.76% and 23.67% respectively, and the proportion of "completely not knowing" is 5.07%. The most recognized positive impact of programming education on students' learning and growth is the improvement of logical thinking ability, accounting for 89.86%. The second is to enhance the ability to solve problems, accounting for 81.64%. In terms of cultivating innovative consciousness and improving information technology literacy, a considerable proportion of people choose to do so, accounting for 78.99% and 77.29% respectively.

3.2 Current situation of programming education

In terms of the coverage of programming education, whether the schools of the respondents or their relatives provide programming courses or have received programming education outside the school, 49.03% of the respondents' schools provide programming courses or related courses, while 50.97% of the respondents' schools do not provide such courses and have not received other forms of programming education.

13.04% of respondents who have received programming education think that the quality of the existing courses is "very good", 28.74% think it is "good", 29.95% think it is "fair", 3.14% think it is "poor", 0.97% think it is "very poor", and 24.15% did not fill in the evaluation.

76.81% of the respondents believed that programming education lacked teaching resources, and 68.36% believed that there was a lack of professional teachers. 67.87% of respondents believe that there is a lack of opportunities for practical experience. 14.49% of the respondents thought that the course content was outdated and 22.71% thought that the teaching method was single.

3.3 Support for programming education teaching resources

More than half of the respondents believe that the hardware facilities for programming education in schools are average or below. Less than one-third of the respondents believed that the hardware facilities of the school were good or very good. It is hoped that more investment will be made to improve the hardware facilities for programming education, so as to enhance the teaching quality and student experience.

In the evaluation of software resources, more than half of the respondents thought that the software resources were average, while less than 30% thought that the software resources were very good or good, and nearly one-third thought that the software resources were poor or very poor. I hope to improve the quality and quantity of software resources, and enhance the learning experience and teaching effectiveness.

The survey and interview found that the existing teachers are mainly composed of former information technology teachers who have transformed into other disciplines, and some teachers who have transformed from other disciplines. A considerable proportion of these teachers lack deep knowledge and mastery of programming education and AI, and their integration in teaching activities is insufficient.

3.4 Evaluation of the effect of programming education

Currently, the lecture method is most frequently used in programming education classrooms; Secondly, the task-driven method; Thirdly, practice, visual demonstration and discussion are also common teaching methods used by teachers. From the evaluation of the respondents on the effectiveness of current programming teaching methods, more than 80% of the respondents believe that the current programming teaching methods are effective to a general or above level, which are very effective, effective, and general. About 20% of the respondents also believed that the teaching method of programming was ineffective or very ineffective.

3.5 Expectations and Suggestions

From the perspective of respondents' expectations or suggestions for school programming education, the most concerned are "adding programming courses" and "increasing practice opportunities", which account for 72.71% respectively. This indicates that students and parents generally hope that schools can provide more programming courses and practical opportunities to strengthen the cultivation of programming skills. In addition, 66.67% of the respondents chose "improving teaching quality" and "introducing advanced teaching resources".

4. Analysis of the survey results

4.1 Descriptive analysis

When conducting descriptive analysis on the collected data, the following status quo was summarized:

Most respondents think that programming education is very important or important in primary and secondary education. Most of the respondents believe that programming education can improve students' logical thinking ability, problem-solving ability, cultivate innovative consciousness, and enhance their information technology literacy.

About half of the schools offered programming courses or related courses. However, the evaluation of the quality of the courses is mixed, with some saying it is very good, while others say it is average or poor.

Most respondents mentioned that schools lack professional teachers, teaching resources, and practical opportunities in programming education. The evaluation of hardware facilities and software resources ranges from "fair" to "excellent", indicating uneven distribution of resources.

Some interviewees pointed out that the teaching method is single and lacks innovation. Many respondents hope that schools can increase programming courses and improve teaching quality. Strengthening teacher training is one of the common suggestions. The introduction of advanced teaching resources and methods is also the expectation of the interviewees.

Some interviewees suggested that the education authorities should attach importance to programming education and provide necessary support and resources. Some interviewees emphasized the importance of increasing students' practical opportunities to enhance the effectiveness of programming education.

4.2 Difference analysis

When conducting a differential analysis on the collected data, it was found that:

In terms of gender, both men and women attach roughly the same importance to programming; However, women are more concerned about the effectiveness of programming learning than men, and they believe that programming is more difficult than men.

In terms of cognition, there are significant differences in teaching behavior choices among different groups of people, and there is a positive correlation between the level of understanding of core competencies in the era of intelligence and the emphasis on programming education; The emphasis on programming education is positively correlated with educational outcomes.

In terms of roles, different social roles and education levels have no effect on the support for programming among teenagers; The proportion of children learning programming is on the rise as parents' educational background increases. Urban educators and parents of urban students are the two groups that participate in the survey most actively, which means that educators and parents have a high degree of concern about the development of programming education in schools, and most participants believe that programming education is very important.

In terms of regions, there is a significant gap between the central urban area and surrounding areas, showing a clear urban-rural difference. Most people in the central urban area agree that programming education is important for students, and the largest

number of people in the urban area actively learn programming. However, the surrounding areas gradually decline outward, which is generally positively correlated with the level of regional economic development

In terms of teaching content, compared with the content required in the national plan, there is a gap in the level of integration of AI and programming education content in actual teaching activities, and there are also significant differences in the distribution of different schools.

5. Countermeasures and Suggestions

The research data provides an overview of the current situation of programming education for teenagers in northern Guangdong, revealing the existing problems and directions for improvement. For the current problems, the following improvement suggestions are proposed based on literature research [6][7][8][9], experimental observation and practical experience:

It is necessary to deepen the understanding of core competencies in the era of intelligence, clarify the requirements of national planning, change the previous positioning of "secondary courses", fully attract attention, and effectively carry out programming education.

It is necessary to strengthen teacher training and resource investment. Research teams' research and practice have shown that starting from the cognitive laws of programming learning, sharing educational and teaching experience and typical case effects through lectures, training, and research activities has achieved good results.

The survey found that some newly introduced highly educated teachers in related majors can better meet the needs in recent years, so introducing new people and supplementing the society are important strategies for teacher recruitment.

Practice has shown that using universities or other social resources to carry out on-the-job training to improve the overall level of current teachers has good results.

In the context of the advancement and popularization of AI-related knowledge and programming education, it is also necessary to conduct forward-looking explorations for schools at all levels in terms of teaching cohesion, teacher development, talent cultivation planning, and related teachers' career planning. Teachers at all levels should be guided and encouraged to strengthen exchanges, cooperation, and collaborative development.

The regional disparity in programming education indicates that it is important to promote coordinated development between urban and rural areas. In addition, it is possible to explore the establishment of multi-center regional resource sharing centers that are appropriately advanced in layout, and to practice resource centralization, platformization, networking, and sharing, which can eliminate the imbalance in educational resources caused by uneven economic development in urban areas to a certain extent.

Funding project

2022 Guangdong Provincial Education Science Planning Project "Research on the Status Quo and Promotion Strategies of Programming Education in Underdeveloped Regions in the Age of Intelligence - Taking Qingyuan City in Northern Guangdong as an Example", No. 2022GXJK114, led by Huang

Xiaolong. The 23rd batch of educational and scientific research projects in Qingyuan City, "Research on the Teaching of Integrating Artificial Intelligence into 'Python Programming Practice' Based on STEM Concepts in the Context of New Engineering", No. 23-118, led by Huang Xiaolong.

References

[1] The State Council. Notice of the State Council on Printing and Distributing the "Development Plan for a New Generation of Artificial Intelligence" [EB/OL]. (2017-07-20)[2020-10-10]. http://www.gov.cn/zhengce/content/2017-07/20/content_5211996.htm.

[2] Ministry of Education. Notice of the Ministry of Education on Printing and Distributing the " Action Plan for Educational Informatization 2.0" [EB/OL]. (2018-04-18)[2020-10-10]. http://www.moe.gov.cn/srcsite/A16/s3342/201804/t20180425_334188.html.

[3] The Central Committee of the Communist Party of China and the State Council. The Central Committee of the Communist Party of China and the State Council Issued the "China Education Modernization 2035" [EB/OL]. (2019-02-23)[2020-10-10]. http://www.gov.cn/xinwen/2019-02/23/content_5367987.htm.

[4] Guangdong Releases Development Plan for a New Generation of Artificial Intelligence [J]. Policy Outlook, 2018(10): 53.

[5] Li Hui, Zhao Keyun. A Survey on the Current Situation of Programming Education in Primary and Secondary Schools: Taking Shandong Province as an Example [J]. Digital Education, 2021, 7(02): 51-57.

[6] Gao Fang. Evaluation and Implications of the Release and Implementation of China's "Development Plan for a New Generation of Artificial Intelligence" by Renowned Global Think Tanks [J]. Information Engineering, 2018, 4(2): 26-35. DOI: 10.3772/j.issn.2095-915x.2018.02.003.

[7] Liu Jinmei, Xu Jun, Fu Haohai. Research on the Implementation Path of the Development Plan for a New Generation of Artificial Intelligence: Taking Jilin Province as an Example [J]. Journal of Changchun Engineering Institute (Social Sciences Edition), 2020, 21(4): 40-43. DOI: 10.3969/j.issn.1009-8976.2020.04.011.

[8] Sun Dan, Li Yan. The Development Status, Research Hotspots, and Implications of Youth Programming Education at Home and Abroad: A Discussion on the Implementation Strategies of Programming Education in China in the Intelligent Age [J]. Journal of Distance Education, 2019, 37(3): 47-60.

[9] Li Lixin. A Survey on the Popularization and Application Status of Artificial Intelligence and Programming Education in Primary and Secondary Schools: Taking

A.J. Tallón-Ballesteros (Ed.)

Author Index